

Handbook on the Physics and Chemistry of Rare Earths, volume 33

Elsevier, 2003

Edited by: K. A. Gschneidner, Jr., J.-C. G. Bunzli, and V. K. Pecharsky
ISBN: 978-0-444-51323-6

PREFACE

Karl A. GSCHNEIDNER, Jr., Jean-Claude G. BÜNZLI, and Vitalij K. PECHARSKY

These elements perplex us in our rearches [sic], baffle us in our speculations, and haunt us in our very dreams. They stretch like an unknown sea before us – mocking, mystifying, and murmuring strange revelations and possibilities.

Sir William Crookes (February 16, 1887)

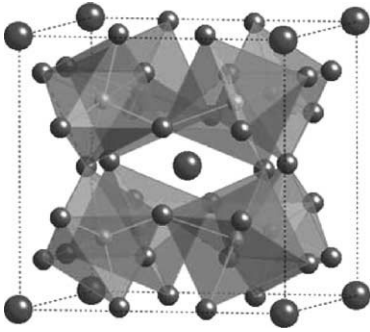
With this volume of the *Handbook on the Physics and Chemistry of Rare Earth* Profs. Jean-Claude Bünzli, Swiss Federal Institute of Technology, Lausanne, and Vitalij K. Pecharsky, Iowa State University, Ames have joined Prof. Karl A. Gschneidner, Jr., one of the founding editors of this series, as editors. Readers of prior volumes of the Handbook will notice that the Preface format has changed with the inclusion of the title and author(s), plus an appropriate figure from each of the chapters, instead of just a brief summary of its contents.

This volume of the Handbook illustrates the rich variety of topics covered by rare earth science. Three chapters are devoted to the description of solid state compounds: skutterudites (Chapter 211), rare earth-antimony systems (Chapter 212), and rare earth-manganese perovskites (Chapter 214). Two other reviews deal with solid state properties: one contribution includes information on existing thermodynamic data of lanthanide trihalides (Chapter 213) while the other one describes optical properties of rare earth compounds under pressure (Chapter 217). Finally, two chapters focus on solution chemistry. The state of the art in unraveling solution structure of lanthanide-containing coordination compounds by paramagnetic nuclear magnetic resonance is outlined in Chapter 215. The potential of time-resolved, laser-induced emission spectroscopy for the analysis of lanthanide and actinide solutions is presented and critically discussed in Chapter 216.

211 Filled Skutterudites

by Brian C. Sales, Oak Ridge, National Laboratory, Tennessee, USA

The lead chapter reviews the remarkable physical behaviors of a distinctive family of intermetallic compounds – the filled lanthanide skutterudites. These unique compounds, which have the RM_4X_{12} stoichiometry (where R = lanthanides, M = Fe, Ru, and Os, and X = P, As and Sb), are best known for their excellent high temperature (> 700 K) thermoelectric properties. But as Brian Sales points out, they also exhibit a rich variety of electronic and

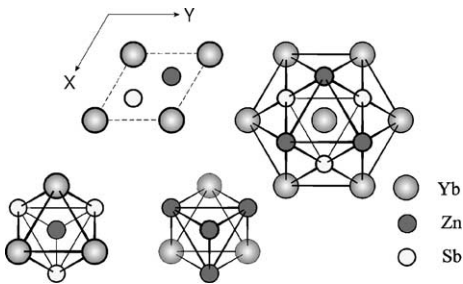


magnetic ground states – heavy fermion mediated superconductivity, ferromagnetism, antiferromagnetism, hybridization gaps (Kondo insulator behavior), non-Fermi-liquid behavior and quantum critical points, quadrupolar ordering, and field-induced heavy fermion states. The Ce-based phases exhibit: heavy fermion behavior – $\text{CeFe}_4\text{Sb}_{12}$; non-Fermi liquid behavior and possibly a quantum critical point – $\text{CeRu}_4\text{Sb}_{12}$; and narrow (hybridized) gap semiconducting behavior – $\text{CeM}_4\text{P}_{12}$ ($M = \text{Fe, Ru, Os}$). However, the most exotic lanthanide skutterudite is $\text{PrFe}_4\text{P}_{12}$ because it has both quadrupole order and heavy fermion ground states, which are extremely close in energy. At low temperatures, < 6 K, a magnetic field of 4 T can drive $\text{PrFe}_4\text{P}_{12}$ between the two ground states leading to some unusual physical properties. Superconductivity is observed in most $\text{LaM}_4\text{X}_{12}$ phases, as well as two of the Pr skutterudites, while those containing Nd, Eu, Gd and Tb exhibit magnetic ordering. Interestingly enough, $\text{EuFe}_4\text{P}_{12}$ has the highest ferromagnetic ordering temperature, 100 K, of the RM_4X_{12} compounds.

212 Rare Earth-Antimony Systems

by Oksana Sologub, University of Wien, Austria,

Petro Salamakha, Institute of Nuclear Technology, Sacavem, Portugal

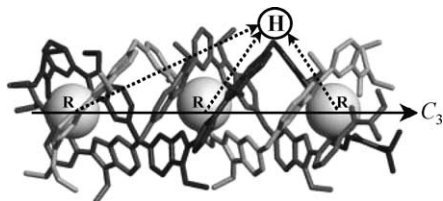


An extensive compilation of the structural and physical properties of rare earth-antimony and of some rare earth-uranium-antimony systems is presented. The first part of the review collects the phase diagrams of binary $R-M$ and ternary $R-M-Sb$, $R-R'-Sb$ or $R-U-Sb$ metal antimonides, along with their crystallographic data and the experimental synthetic methods used to isolate the compounds. A few quaternary systems are also presented. The chapter then focuses on the properties of ternary systems. Atomic coordinates are given for more

than forty types of crystal structures, and magnetic susceptibility and resistivity data are tabulated. The chapter ends with a general discussion on the peculiarities of the rare earth-antimony interaction. The binary systems have been systematically studied and usually yield stoichiometric compounds, $R_5\text{Sb}_3$, $R_4\text{Sb}_3$, RSb , and RSb_2 . Ternary systems are less well known, so that general trends are more difficult to determine, but several families of ternary antimonides crystallize with structures derived from those of binary types.

215 Paramagnetic NMR Lanthanide Induced Shift for Extracting Solution Structure
 by Claude Piguet, University of Geneva, Switzerland,
 Carlos F.G.C. Geraldes, University of Coimbra, Portugal

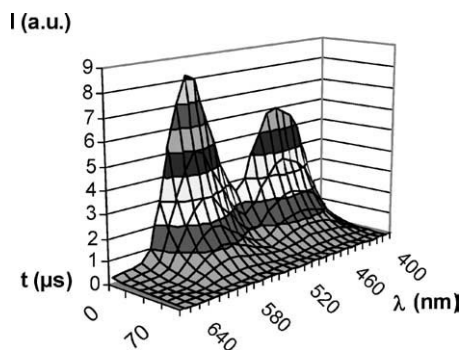
$$\delta_{ij}^{\text{para}} \left(\sum_{m=l}^n F_i^m \right) \langle S_z \rangle_j + \left(\sum_{m=l}^n B_0^{2m} G_i^m \right) C_j$$



The authors summarize the latest advances in one fascinating technique enabling chemists to unravel the solution structures of coordination and supramolecular compounds, nuclear magnetic resonance of paramagnetic species. While paramagnetism is often considered as being a handicap to interpret NMR spectra, detailed structural and electronic information can be extracted from the separation of the contact and pseudo-contact contributions to the paramagnetic NMR shifts induced by the presence of a lanthanide ion. In a

precedent chapter of the Handbook (ch. 153, vol. 23), John Forsberg has reported on the use of a one-nucleus method for determining the structure of axial compounds. Here, the authors outline the general theory and then focus on the limitations of Bleaney's approach for modeling paramagnetic anisotropies and on the description of the new two- and three-nuclei methods, which are independent of changes in crystal field parameters and hyperfine coupling constants. A comprehensive survey of the application of these methods to coordination and supramolecular compounds with three- and fourfold symmetry is presented.

216 Lanthanide and Actinide Solution Chemistry Studied by Time-Resolved Emission Spectroscopy
 by Isabelle Billard, Institut de Recherches Subatomiques, Strasbourg, France

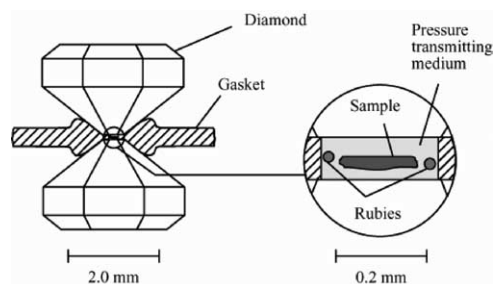


Time-resolved emission spectroscopy is gaining importance in the study of various chemical aspects of luminescent lanthanide and actinide ions in solution. Here, the author describes the theoretical background of this analytical technique and discusses potential applications. Changes in the solution composition and/or in the metal-ion inner coordination sphere induce modifications of the spectroscopic properties of the luminescent species. Both time-resolved spectra and luminescence decays convey useful information. Several models, which are commonly used to extract physico-chemical information from the spectroscopic data, are presented and critically compared. Applications of time-resolved emission spectroscopy are numerous and range from the characterization of the

information from the spectroscopic data, are presented and critically compared. Applications of time-resolved emission spectroscopy are numerous and range from the characterization of the

metal ion solvation sphere, to the evaluation of reaction rate constants and equilibrium constants, and to the quantitative determination of ultra trace amounts of lanthanide and actinide ions in solution, an aspect of importance in environmental chemistry. Potential uses of the technique to study micellar systems and ionic liquids are outlined.

217 Optical Studies on Non-Metallic Rare Earth Compounds under Pressure by Thomas Tröster, University of Paderborn, Germany



In a captivating review, the author surveys the optical properties of non-metallic compounds under pressure. The relationship between the optical properties of compounds and their microscopic structure has always triggered a lot of interest and has been regarded as a fundamental problem. Rare earth ions with partially filled 4f shells provide a detailed fingerprint of the surrounding arrangement of atoms and their interaction with f-electrons. Minute effects can be evidenced by measuring the spectra in various

hosts lattices. However, the presence of impurities somewhat limits the usefulness of the empirical data. In contrast, applying high-pressure to a system usually induces continuous variations in parameters, such as interatomic distances, influencing the optical properties. That is, the experimentalists can alter the energy difference between two states, almost at will, henceforth gathering information on their mutual influence. High pressure techniques are described and experimental data on energy levels, crystal field splittings, intensities and lifetimes of f-f transitions, as well as on electron-phonon interactions, are surveyed.

CONTENTS

Preface v

Contents xi

Contents of Volumes 1–32 xiii

211. Brian C. Sales

Filled skutterudites 1

212. Oksana L. Sologub and Petro S. Salamakha

Rare earth – antimony systems 35

213. R.J.M. Konings and A. Kovács

Thermodynamic properties of the lanthanide(III) halides 147

214. John B. Goodenough

Rare earth – manganese perovskites 249

215. Claude Piguet and Carlos F.G.C. Geraldès

Paramagnetic NMR lanthanide induced shifts for extracting solution structures 353

216. Isabelle Billard

Lanthanide and actinide solution chemistry as studied by time-resolved emission spectroscopy 465

217. Thomas Tröster

Optical studies of non-metallic compounds under pressure 515

Author index 591

Subject index 637

CONTENTS OF VOLUMES 1–32

VOLUME 1: Metals

1978, 1st repr. 1982, 2nd repr. 1991; ISBN 0-444-85020-1

1. Z.B. Goldschmidt, *Atomic properties (free atom)* 1
 2. B.J. Beaudry and K.A. Gschneidner Jr, *Preparation and basic properties of the rare earth metals* 173
 3. S.H. Liu, *Electronic structure of rare earth metals* 233
 4. D.C. Koskenmaki and K.A. Gschneidner Jr, *Cerium* 337
 5. L.J. Sundström, *Low temperature heat capacity of the rare earth metals* 379
 6. K.A. McEwen, *Magnetic and transport properties of the rare earths* 411
 7. S.K. Sinha, *Magnetic structures and inelastic neutron scattering: metals, alloys and compounds* 489
 8. T.E. Scott, *Elastic and mechanical properties* 591
 9. A. Jayaraman, *High pressure studies: metals, alloys and compounds* 707
 10. C. Probst and J. Wittig, *Superconductivity: metals, alloys and compounds* 749
 11. M.B. Maple, L.E. DeLong and B.C. Sales, *Kondo effect: alloys and compounds* 797
 12. M.P. Dariel, *Diffusion in rare earth metals* 847
- Subject index 877

VOLUME 2: Alloys and intermetallics

1979, 1st repr. 1982, 2nd repr. 1991; ISBN 0-444-85021-X

13. A. Iandelli and A. Palenzona, *Crystal chemistry of intermetallic compounds* 1
 14. H.R. Kirchmayr and C.A. Poldy, *Magnetic properties of intermetallic compounds of rare earth metals* 55
 15. A.E. Clark, *Magnetostrictive RFe_2 intermetallic compounds* 231
 16. J.J. Rhyne, *Amorphous magnetic rare earth alloys* 259
 17. P. Fulde, *Crystal fields* 295
 18. R.G. Barnes, *NMR, EPR and Mössbauer effect: metals, alloys and compounds* 387
 19. P. Wachter, *Europium chalcogenides: EuO , EuS , $EuSe$ and $EuTe$* 507
 20. A. Jayaraman, *Valence changes in compounds* 575
- Subject index 613

VOLUME 3: Non-metallic compounds – I

1979, 1st repr. 1984; ISBN 0-444-85215-8

21. L.A. Haskin and T.P. Paster, *Geochemistry and mineralogy of the rare earths* 1
 22. J.E. Powell, *Separation chemistry* 81
 23. C.K. Jørgensen, *Theoretical chemistry of rare earths* 111
 24. W.T. Carnall, *The absorption and fluorescence spectra of rare earth ions in solution* 171
 25. L.C. Thompson, *Complexes* 209
 26. G.G. Libowitz and A.J. Maeland, *Hydrides* 299
 27. L. Eyring, *The binary rare earth oxides* 337
 28. D.J.M. Sevan and E. Summerville, *Mixed rare earth oxides* 401
 29. C.P. Khattak and F.F.Y. Wang, *Perovskites and garnets* 525
 30. L.H. Brixner, J.R. Barkley and W. Jeitschko, *Rare earth molybdates (VI)* 609
- Subject index 655

VOLUME 4: Non-metallic compounds – II

1979, 1st repr. 1984; ISBN 0-444-85216-6

31. J. Flahaut, *Sulfides, selenides and tellurides* 1
32. J.M. Haschke, *Halides* 89
33. F. Hulliger, *Rare earth pnictides* 153
34. G. Blasse, *Chemistry and physics of R-activated phosphors* 237
35. M.J. Weber, *Rare earth lasers* 275
36. F.K. Fong, *Nonradiative processes of rare-earth ions in crystals* 317
- 37A. J.W. O’Laughlin, *Chemical spectrophotometric and polarographic methods* 341
- 37B. S.R. Taylor, *Trace element analysis of rare earth elements by spark source mass spectroscopy* 359
- 37C. R.J. Conzemius, *Analysis of rare earth matrices by spark source mass spectrometry* 377
- 37D. E.L. DeKalb and V.A. Fassel, *Optical atomic emission and absorption methods* 405
- 37E. A.P. D’Silva and V.A. Fassel, *X-ray excited optical luminescence of the rare earths* 441
- 37F. F.W.V. Boynton, *Neutron activation analysis* 457
- 37G. S. Schuhmann and J.A. Philpotts, *Mass-spectrometric stable-isotope dilution analysis for lanthanides in geochemical materials* 471
38. J. Reuben and G.A. Elgavish, *Shift reagents and NMR of paramagnetic lanthanide complexes* 483
39. J. Reuben, *Bioinorganic chemistry: lanthanides as probes in systems of biological interest* 515
40. T.J. Haley, *Toxicity* 553
- Subject index 587

VOLUME 5

1982, 1st repr. 1984; ISBN 0-444-86375-3

41. M. Gasgnier, *Rare earth alloys and compounds as thin films* 1
42. E. Gratz and M.J. Zuckermann, *Transport properties (electrical resistivity, thermoelectric power thermal conductivity) of rare earth intermetallic compounds* 117
43. F.P. Netzer and E. Bertel, *Adsorption and catalysis on rare earth surfaces* 217
44. C. Boulesteix, *Defects and phase transformation near room temperature in rare earth sesquioxides* 321
45. O. Greis and J.M. Haschke, *Rare earth fluorides* 387
46. C.A. Morrison and R.P. Leavitt, *Spectroscopic properties of triply ionized lanthanides in transparent host crystals* 461
- Subject index 693

VOLUME 6

1984; ISBN 0-444-86592-6

47. K.H.J. Buschow, *Hydrogen absorption in intermetallic compounds* 1
48. E. Parthé and B. Chabot, *Crystal structures and crystal chemistry of ternary rare earth–transition metal borides, silicides and homologues* 113
49. P. Rogl, *Phase equilibria in ternary and higher order systems with rare earth elements and boron* 335
50. H.B. Kagan and J.L. Namy, *Preparation of divalent ytterbium and samarium derivatives and their use in organic chemistry* 525
- Subject index 567

VOLUME 7

1984; ISBN 0-444-86851-8

51. P. Rogl, *Phase equilibria in ternary and higher order systems with rare earth elements and silicon* 1
52. K.H.J. Buschow, *Amorphous alloys* 265
53. H. Schumann and W. Genthe, *Organometallic compounds of the rare earths* 446
- Subject index 573

VOLUME 8

1986; ISBN 0-444-86971-9

54. K.A. Gschneidner Jr and F.W. Calderwood, *Intra rare earth binary alloys: phase relationships, lattice parameters and systematics* 1
55. X. Gao, *Polarographic analysis of the rare earths* 163
56. M. Leskelä and L. Niinistö, *Inorganic complex compounds I* 203
57. J.R. Long, *Implications in organic synthesis* 335
- Errata 375
- Subject index 379

VOLUME 9

1987; ISBN 0-444-87045-8

58. R. Reisfeld and C.K. Jørgensen, *Excited state phenomena in vitreous materials* 1
59. L. Niinistö and M. Leskelä, *Inorganic complex compounds II* 91
60. J.-C.G. Bünzli, *Complexes with synthetic ionophores* 321
61. Zhiquan Shen and Jun Ouyang, *Rare earth coordination catalysis in stereospecific polymerization* 395
- Errata 429
- Subject index 431

VOLUME 10: High energy spectroscopy

1988; ISBN 0-444-87063-6

62. Y. Baer and W.-D. Schneider, *High-energy spectroscopy of lanthanide materials – An overview* 1
63. M. Campagna and F.U. Hillebrecht, *f-electron hybridization and dynamical screening of core holes in intermetallic compounds* 75
64. O. Gunnarsson and K. Schönhammer, *Many-body formulation of spectra of mixed valence systems* 103
65. A.J. Freeman, B.I. Min and M.R. Norman, *Local density supercell theory of photoemission and inverse photoemission spectra* 165
66. D.W. Lynch and J.H. Weaver, *Photoemission of Ce and its compounds* 231
67. S. Hüfner, *Photoemission in chalcogenides* 301
68. J.F. Herbst and J.W. Wilkins, *Calculation of 4f excitation energies in the metals and relevance to mixed valence systems* 321
69. B. Johansson and N. Mårtensson, *Thermodynamic aspects of 4f levels in metals and compounds* 361
70. F.U. Hillebrecht and M. Campagna, *Bremsstrahlung isochromat spectroscopy of alloys and mixed valent compounds* 425
71. J. Röhrler, *X-ray absorption and emission spectra* 453
72. F.P. Netzer and J.A.D. Matthew, *Inelastic electron scattering measurements* 547
- Subject index 601

VOLUME 11: Two-hundred-year impact of rare earths on science

1988; ISBN 0-444-87080-6

- H.J. Svec, *Prologue* 1
73. F. Szabadváry, *The history of the discovery and separation of the rare earths* 33
74. B.R. Judd, *Atomic theory and optical spectroscopy* 81
75. C.K. Jørgensen, *Influence of rare earths on chemical understanding and classification* 197
76. J.J. Rhyne, *Highlights from the exotic phenomena of lanthanide magnetism* 293
77. B. Bleaney, *Magnetic resonance spectroscopy and hyperfine interactions* 323
78. K.A. Gschneidner Jr and A.H. Daane, *Physical metallurgy* 409
79. S.R. Taylor and S.M. McLennan, *The significance of the rare earths in geochemistry and cosmochemistry* 485
- Errata 579
- Subject index 581

VOLUME 12

1989; ISBN 0-444-87105-5

80. J.S. Abell, *Preparation and crystal growth of rare earth elements and intermetallic compounds* 1
81. Z. Fisk and J.P. Remeika, *Growth of single crystals from molten metal fluxes* 53
82. E. Burzo and H.R. Kirchmayr, *Physical properties of $R_2Fe_{14}B$ -based alloys* 71
83. A. Szytuła and J. Leciejewicz, *Magnetic properties of ternary intermetallic compounds of the RT_2X_2 type* 133
84. H. Maletta and W. Zinn, *Spin glasses* 213
85. J. van Zytveld, *Liquid metals and alloys* 357
86. M.S. Chandrasekharaiah and K.A. Gingerich, *Thermodynamic properties of gaseous species* 409
87. W.M. Yen, *Laser spectroscopy* 433
Subject index 479

VOLUME 13

1990; ISBN 0-444-88547-1

88. E.I. Gladyshevsky, O.I. Bodak and V.K. Pecharsky, *Phase equilibria and crystal chemistry in ternary rare earth systems with metallic elements* 1
89. A.A. Eliseev and G.M. Kuzmichyeva, *Phase equilibrium and crystal chemistry in ternary rare earth systems with chalcogenide elements* 191
90. N. Kimizuka, E. Takayama-Muromachi and K. Siratori, *The systems R_2O_3 – M_2O_3 – $M'O$* 283
91. R.S. Houk, *Elemental analysis by atomic emission and mass spectrometry with inductively coupled plasmas* 385
92. P.H. Brown, A.H. Rathjen, R.D. Graham and D.E. Tribe, *Rare earth elements in biological systems* 423
Errata 453
Subject index 455

VOLUME 14

1991; ISBN 0-444-88743-1

93. R. Osborn, S.W. Lovesey, A.D. Taylor and E. Balcar, *Intermultiplet transitions using neutron spectroscopy* 1
94. E. Dormann, *NMR in intermetallic compounds* 63
95. E. Zirngiebl and G. Güntherodt, *Light scattering in intermetallic compounds* 163
96. P. Thalmeier and B. Lüthi, *The electron–phonon interaction in intermetallic compounds* 225
97. N. Grewe and F. Steglich, *Heavy fermions* 343
Subject index 475

VOLUME 15

1991; ISBN 0-444-88966-3

98. J.G. Sereni, *Low-temperature behaviour of cerium compounds* 1
99. G.-y. Adachi, N. Imanaka and Zhang Fuzhong, *Rare earth carbides* 61
100. A. Simon, H.J. Mattausch, G.J. Miller, W. Bauhofer and R.K. Kremer, *Metal-rich halides* 191
101. R.M. Almeida, *Fluoride glasses* 287
102. K.L. Nash and J.C. Sullivan, *Kinetics of complexation and redox reactions of the lanthanides in aqueous solutions* 347
103. E.N. Rizkalla and G.R. Choppin, *Hydration and hydrolysis of lanthanides* 393
104. L.M. Vallarino, *Macrocycle complexes of the lanthanide(III) yttrium(III) and dioxouranium(VI) ions from metal-templated syntheses* 443
Errata 513
Subject index 515

MASTER INDEX, Vols. 1–15

1993; ISBN 0-444-89965-0

VOLUME 16

1993; ISBN 0-444-89782-8

105. M. Loewenhaupt and K.H. Fischer, *Valence-fluctuation and heavy-fermion 4f systems* 1
 106. I.A. Smirnov and V.S. Oskotski, *Thermal conductivity of rare earth compounds* 107
 107. M.A. Subramanian and A.W. Sleight, *Rare earths pyrochlores* 225
 108. R. Miyawaki and I. Nakai, *Crystal structures of rare earth minerals* 249
 109. D.R. Chopra, *Appearance potential spectroscopy of lanthanides and their intermetallics* 519
 Author index 547
 Subject index 579

VOLUME 17: Lanthanides/Actinides: Physics – I

1993; ISBN 0-444-81502-3

110. M.R. Norman and D.D. Koelling, *Electronic structure, Fermi surfaces, and superconductivity in f electron metals* 1
 111. S.H. Liu, *Phenomenological approach to heavy-fermion systems* 87
 112. B. Johansson and M.S.S. Brooks, *Theory of cohesion in rare earths and actinides* 149
 113. U. Benedict and W.B. Holzapfel, *High-pressure studies – Structural aspects* 245
 114. O. Vogt and K. Mattenberger, *Magnetic measurements on rare earth and actinide mononictides and monochalcogenides* 301
 115. J.M. Fournier and E. Gratz, *Transport properties of rare earth and actinide intermetallics* 409
 116. W. Potzel, G.M. Kalvius and J. Gal, *Mössbauer studies on electronic structure of intermetallic compounds* 539
 117. G.H. Lander, *Neutron elastic scattering from actinides and anomalous lanthanides* 635
 Author index 711
 Subject index 753

VOLUME 18: Lanthanides/Actinides: Chemistry

1994; ISBN 0-444-81724-7

118. G.T. Seaborg, *Origin of the actinide concept* 1
 119. K. Balasubramanian, *Relativistic effects and electronic structure of lanthanide and actinide molecules* 29
 120. J.V. Beitz, *Similarities and differences in trivalent lanthanide- and actinide-ion solution absorption spectra and luminescence studies* 159
 121. K.L. Nash, *Separation chemistry for lanthanides and trivalent actinides* 197
 122. L.R. Morss, *Comparative thermochemical and oxidation – reduction properties of lanthanides and actinides* 239
 123. J.W. Ward and J.M. Haschke, *Comparison of 4f and 5f element hydride properties* 293
 124. H.A. Eick, *Lanthanide and actinide halides* 365
 125. R.G. Haire and L. Eyring, *Comparisons of the binary oxides* 413
 126. S.A. Kinkad, K.D. Abney and T.A. O'Donnell, *f-element speciation in strongly acidic media: lanthanide and mid-actinide metals, oxides, fluorides and oxide fluorides in superacids* 507
 127. E.N. Rizkalla and G.R. Choppin, *Lanthanides and actinides hydration and hydrolysis* 529
 128. G.R. Choppin and E.N. Rizkalla, *Solution chemistry of actinides and lanthanides* 559
 129. J.R. Duffield, D.M. Taylor and D.R. Williams, *The biochemistry of the f-elements* 591
 Author index 623
 Subject index 659

VOLUME 19: Lanthanides/Actinides: Physics – II

1994; ISBN 0-444-82015-9

130. E. Holland-Moritz and G.H. Lander, *Neutron inelastic scattering from actinides and anomalous lanthanides* 1
131. G. Aeppli and C. Broholm, *Magnetic correlations in heavy-fermion systems: neutron scattering from single crystals* 123
132. P. Wachter, *Intermediate valence and heavy fermions* 177
133. J.D. Thompson and J.M. Lawrence, *High pressure studies – Physical properties of anomalous Ce, Yb and U compounds* 383
134. C. Colinet and A. Pasturel, *Thermodynamic properties of metallic systems* 479
Author index 649
Subject index 693

VOLUME 20

1995; ISBN 0-444-82014-0

135. Y. Ōnuki and A. Hasegawa, *Fermi surfaces of intermetallic compounds* 1
136. M. Gasgnier, *The intricate world of rare earth thin films: metals, alloys, intermetallics, chemical compounds, ...* 105
137. P. Vajda, *Hydrogen in rare-earth metals, including RH_{2+x} phases* 207
138. D. Gignoux and D. Schmitt, *Magnetic properties of intermetallic compounds* 293
Author index 425
Subject index 457

VOLUME 21

1995; ISBN 0-444-82178-3

139. R.G. Bautista, *Separation chemistry* 1
140. B.W. Hinton, *Corrosion prevention and control* 29
141. N.E. Ryan, *High-temperature corrosion protection* 93
142. T. Sakai, M. Matsuoka and C. Iwakura, *Rare earth intermetallics for metal–hydrogen batteries* 133
143. G.-y. Adachi and N. Imanaka, *Chemical sensors* 179
144. D. Garcia and M. Faucher, *Crystal field in non-metallic (rare earth) compounds* 263
145. J.-C.G. Bünzli and A. Milicic-Tang, *Solvation and anion interaction in organic solvents* 305
146. V. Bhagavathy, T. Prasada Rao and A.D. Damodaran, *Trace determination of lanthanides in high-purity rare-earth oxides* 367
Author index 385
Subject index 411

VOLUME 22

1996; ISBN 0-444-82288-7

147. C.P. Flynn and M.B. Salamon, *Synthesis and properties of single-crystal nanostructures* 1
148. Z.S. Shan and D.J. Sellmyer, *Nanoscale rare earth–transition metal multilayers: magnetic structure and properties* 81
149. W. Suski, *The $ThMn_{12}$ -type compounds of rare earths and actinides: structure, magnetic and related properties* 143
150. L.K. Aminov, B.Z. Malkin and M.A. Teplov, *Magnetic properties of nonmetallic lanthanide compounds* 295
151. F. Auzel, *Coherent emission in rare-earth materials* 507
152. M. Dolg and H. Stoll, *Electronic structure calculations for molecules containing lanthanide atoms* 607
Author index 731
Subject index 777

VOLUME 23

1996; ISBN 0-444-82507-X

153. J.H. Forsberg, *NMR studies of paramagnetic lanthanide complexes and shift reagents* 1
 154. N. Sabbatini, M. Guardigli and I. Manet, *Antenna effect in encapsulation complexes of lanthanide ions* 69
 155. C. Görlner-Walrand and K. Binnemans, *Rationalization of crystal-field parametrization* 121
 156. Yu. Kuz'ma and S. Chykhrij, *Phosphides* 285
 157. S. Boghosian and G.N. Papatheodorou, *Halide vapors and vapor complexes* 435
 158. R.H. Byrne and E.R. Sholkovitz, *Marine chemistry and geochemistry of the lanthanides* 497
 Author index 595
 Subject index 631

VOLUME 24

1997; ISBN 0-444-82607-6

159. P.A. Dowben, D.N. McIlroy and Dongqi Li, *Surface magnetism of the lanthanides* 1
 160. P.G. McCormick, *Mechanical alloying and mechanically induced chemical reactions* 47
 161. A. Inoue, *Amorphous, quasicrystalline and nanocrystalline alloys in Al- and Mg-based systems* 83
 162. B. Elschner and A. Loidl, *Electron-spin resonance on localized magnetic moments in metals* 221
 163. N.H. Duc, *Intersublattice exchange coupling in the lanthanide–transition metal intermetallics* 339
 164. R.V. Skolozdra, *Stannides of rare-earth and transition metals* 399
 Author index 519
 Subject index 559

VOLUME 25

1998; ISBN 0-444-82871-0

165. H. Nagai, *Rare earths in steels* 1
 166. R. Marchand, *Ternary and higher order nitride materials* 51
 167. C. Görlner-Walrand and K. Binnemans, *Spectral intensities of $f-f$ transitions* 101
 168. G. Bombieri and G. Paolucci, *Organometallic π complexes of the f -elements* 265
 Author index 415
 Subject index 459

VOLUME 26

1999; ISBN 0-444-50815-1

169. D.F. McMorro, D. Gibbs and J. Bohr, *X-ray scattering studies of lanthanide magnetism* 1
 170. A.M. Tishin, Yu.I. Spichkin and J. Bohr, *Static and dynamic stresses* 87
 171. N.H. Duc and T. Goto, *Itinerant electron metamagnetism of Co sublattice in the lanthanide–cobalt intermetallics* 177
 172. A.J. Arko, P.S. Riseborough, A.B. Andrews, J.J. Joyce, A.N. Tahvildar-Zadeh and M. Jarrell, *Photoelectron spectroscopy in heavy fermion systems: Emphasis on single crystals* 265
 Author index 383
 Subject index 405

VOLUME 27

1999; ISBN 0-444-50342-0

173. P.S. Salamakha, O.L. Sologub and O.I. Bodak, *Ternary rare-earth–germanium systems* 1
 174. P.S. Salamakha, *Crystal structures and crystal chemistry of ternary rare-earth germanides* 225
 175. B. Ya. Kotur and E. Gratz, *Scandium alloy systems and intermetallics* 339
 Author index 535
 Subject index 553

VOLUME 28

2000; ISBN 0-444-50346-3

176. J.-P. Connerade and R.C. Karnatak, *Electronic excitation in atomic species* 1
 177. G. Meyer and M.S. Wickleder, *Simple and complex halides* 53
 178. R.V. Kumar and H. Iwahara, *Solid electrolytes* 131
 179. A. Halperin, *Activated thermoluminescence (TL) dosimeters and related radiation detectors* 187
 180. K.L. Nash and M.P. Jensen, *Analytical separations of the lanthanides: basic chemistry and methods* 311
 Author index 373
 Subject index 401

VOLUME 29: The role of rare earths in catalysis

2000; ISBN 0-444-50472-9

- P. Maestro, *Foreword* 1
 181. V. Paul-Boncour, L. Hilaire and A. Percheron-Guégan, *The metals and alloys in catalysis* 5
 182. H. Imamura, *The metals and alloys (prepared utilizing liquid ammonia solutions) in catalysis II* 45
 183. M.A. Ulla and E.A. Lombardo, *The mixed oxides* 75
 184. J. Kašpar, M. Graziani and P. Fornasiero, *Ceria-containing three-way catalysts* 159
 185. A. Corma and J.M. López Nieto, *The use of rare-earth-containing zeolite catalysts* 269
 186. S. Kobayashi, *Triflates* 315
 Author index 377
 Subject index 409

VOLUME 30: High-Temperature Superconductors – I

2000; ISBN 0-444-50528-8

187. M.B. Maple, *High-temperature superconductivity in layered cuprates: overview* 1
 188. B. Raveau, C. Michel and M. Hervieu, *Crystal chemistry of superconducting rare-earth cuprates* 31
 189. Y. Shiohara and E.A. Goodilin, *Single-crystal growth for science and technology* 67
 190. P. Karen and A. Kjekshus, *Phase diagrams and thermodynamic properties* 229
 191. B. Elschner and A. Loidl, *Electron paramagnetic resonance in cuprate superconductors and in parent compounds* 375
 192. A.A. Manuel, *Positron annihilation in high-temperature superconductors* 417
 193. W.E. Pickett and I.I. Mazin, *RBa₂Cu₃O₇ compounds: electronic theory and physical properties* 453
 194. U. Staub and L. Soderholm, *Electronic 4f state splittings in cuprates* 491
 Author index 547
 Subject index 621

VOLUME 31: High-Temperature Superconductors – II

2001; ISBN 0-444-50719-1

195. E. Kaldis, *Oxygen nonstoichiometry and lattice effects in YBa₂Cu₃O_x. Phase transitions, structural distortions and phase separation* 1
 196. H.W. Weber, *Flux pinning* 187
 197. C.C. Almasan and M.B. Maple, *Magnetoresistance and Hall effect* 251
 198. T.E. Mason, *Neutron scattering studies of spin fluctuations in high-temperature superconductors* 281
 199. J.W. Lynn and S. Skanthakumar, *Neutron scattering studies of lanthanide magnetic ordering* 315
 200. P.M. Allenspach and M.B. Maple, *Heat capacity* 351
 201. M. Schabel and Z.-X. Shen, *Angle-resolved photoemission studies of untwinned yttrium barium copper oxide* 391
 202. D.N. Basov and T. Timusk, *Infrared properties of high-T_c superconductors: an experimental overview* 437
 203. S.L. Cooper, *Electronic and magnetic Raman scattering studies of the high-T_c cuprates* 509

204. H. Sugawara, T. Hasegawa and K. Kitazawa, *Characterization of cuprate superconductors using tunneling spectra and scanning tunneling microscopy* 563
Author index 609
Subject index 677

VOLUME 32

2001; ISBN 0-444-50762-0

205. N.H. Duc, *Giant magnetostriction in lanthanide–transition metal thin films* 1
206. G.M. Kalvius, D.R. Noakes and O. Hartmann, *μ SR studies of rare-earth and actinide magnetic materials* 55
207. Rainer Pöttgen, Dirk Johrendt and Dirk Kußmann, *Structure–property relations of ternary equiatomic YbTX intermetallics* 453
208. Kurima Kobayashi and Satoshi Hirosawa, *Permanent magnets* 515
209. I.G. Vasilyeva, *Polysulfides* 567
210. Dennis K.P. Ng, Jianzhuang Jiang, Kuninobu Kasuga and Kenichi Machida, *Half-sandwich tetrapyrrole complexes of rare earths and actinides* 611
Author index 655
Subject index 733

Chapter 211

FILLED SKUTTERUDITES

Brian C. SALES

Solid State Division, Oak Ridge National Laboratory,

Oak Ridge, TN 37831-6056, USA

Contents

List of symbols	1	11. Gd filled skutterudites	24
List of acronyms	2	12. Tb filled skutterudites	25
1. Introduction	2	13. Yb filled skutterudites	26
2. Structure	3	14. Filled skutterudite thermoelectrics	26
3. Lanthanide skutterudites as Zintl compounds	5	14.1. Introduction to thermoelectric materials and devices	26
4. Synthesis and crystal growth	6	14.2. Electron crystals and phonon glasses	28
5. La filled skutterudites	8	14.3. Future of filled skutterudites as thermoelectrics	30
6. Ce filled skutterudites	12	15. Concluding remarks	31
7. Pr filled skutterudites	17	Acknowledgements	32
8. Nd filled skutterudites	22	References	32
9. Sm filled skutterudites	23		
10. Eu filled skutterudites	23		

List of symbols

B_{eq}	isotropic ADP	T	temperature
C	heat capacity	T	magnetic field in Tesla
C_{RLM}	heat capacity from resonant level model	T_{AF}	antiferromagnetic ordering temperature
C_{ph}	heat capacity from phonons	T_{c}	superconducting transition temperature
e_g	doubly degenerate 3d orbitals	T_{co}	cold temperature of thermoelectric device
H	magnetic field	T_{d}	displacive ordering transition
k_{B}	Boltzmann constant	T_{FM}	ferromagnetic ordering temperature
k	wavevector	t_{2g}	triply degenerate 3d orbitals
m_{e}	free electron mass	T_{h}	hot temperature of thermoelectric device
m^*	effective electron mass	T_{K}	Kondo temperature
n-type	electron doped semiconductor	T^*	characteristic temperature
P	pressure	T_0	characteristic temperature
p-type	hole doped semiconductor	μ_{B}	Bohr magneton
R_{W}	Wilson–Sommerfeld ratio	μ_{eff}	effective magnetic moment
S	Seebeck coefficient	Z	thermoelectric figure of merit

ZT	dimensionless thermoelectric figure of merit	κ	total thermal conductivity of solid
γ	electronic coefficient of heat capacity	κ_e	thermal conductivity of electrons or holes
Γ	$(1 + ZT)^{1/2}$	κ_L	thermal conductivity of lattice
Γ_1	crystal field singlet	κ_{\min}	minimum lattice thermal conductivity
Γ_3	non-Kramers doublet (crystal field state)	ρ	electrical resistivity
Γ_4	crystal field triplet	Θ_D	Debye temperature
Γ_5	crystal field triplet	χ	magnetic susceptibility
Δ	hybridization gap	χ_0	magnetic susceptibility at $T = 0$
ΔC	jump in heat capacity at T_c		

List of acronyms

ADP	atomic displacement parameters	HFSC	heavy-fermion superconductor
AFM	antiferromagnetic metal	LDA	local density approximation
BCS	theory of superconductivity	M	metal
CEF	crystalline electric field	M-I	metal to insulator transition
dHvA	de Hass–van Alphen	NFL	non-Fermi liquid
DOS	density of states	ODS	ordered state
FIHFM	field-induced heavy-fermion metal	QCP	quantum critical point
FMM	ferromagnetic metal	QO	quadrupolar order
HFS	heavy-fermion state	RRR	residual resistance ratio
HFM	heavy-fermion metal	SC	superconductor
HGS	hybridization gap semiconductor	XANES	X-ray absorption near edge spectroscopy

1. Introduction

Skutterudite is the name of a CoAs_3 -based mineral that was first extensively mined as a source of cobalt and nickel in the region of Skutterud Norway. Compounds with the same cubic crystal structure have since been known as “skutterudites”. Oftedal first extensively studied the skutterudite crystal structure in 1928 (Oftedal, 1928). An example of a well-formed natural skutterudite mineral is shown in fig. 1.

The skutterudite structure has two voids in each unit cell that are large enough to accommodate a variety of atoms including most of the light lanthanides (La, Ce, Pr, Nd, Sm, Eu, Gd, Tb) and Yb. The first “filled skutterudites” were synthesized by Prof. Jeitschko and collaborators in the late 1970s (Jeitschko and Braun, 1977; Braun and Jeitschko, 1980a, 1980b, 1980c). The chemical composition of the lanthanide filled skutterudites is given by RM_4X_{12} , where R are the lanthanides noted above, $\text{M} = \text{Fe, Ru, Os}$ and $\text{X} = \text{P, As, Sb}$. For each lanthanide element there is a maximum of nine distinct compounds with the skutterudite structure. In 1996 it was found that some of the lanthanide skutterudites had excellent thermoelectric properties above room temperature (Sales et al., 1996;

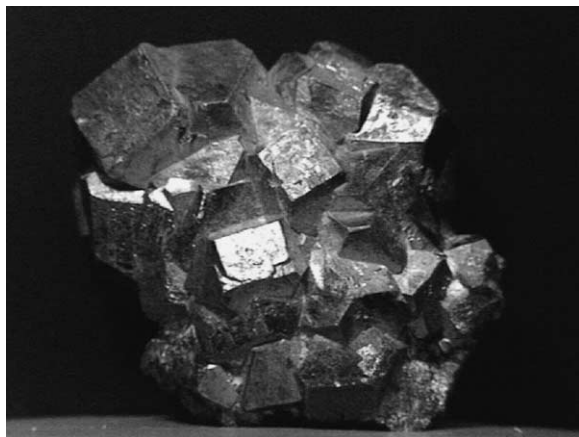


Fig. 1. Photograph of a natural skutterudite mineral. This extremely well crystallized specimen is from the Sandroste Mine near Bou Azzer, Morocco. (Image downloaded from Carnegie–Mellon Mineral Collection Images, Alan Guisewite’s collection.)

Fleurial et al., 1996) and this greatly increased the interest in these materials for thermoelectric applications. In addition to the stoichiometric filled skutterudite compounds of the form RM_4X_{12} , a large number of related alloys were also investigated as possible thermoelectric materials. Most of the research on lanthanide skutterudites in the context of thermoelectric applications has been reviewed recently by Uher (2001), Nolas et al. (1999), and Sales (1998) and hence only a brief summary of the thermoelectric research will be presented at the end of this article. This chapter will focus on what is known about the structural, electronic and magnetic properties of the stoichiometric lanthanide skutterudite compounds of the form RM_4X_{12} . The low temperature properties will be of particular interest since these compounds exhibit a rich variety of electronic and magnetic ground states that include heavy-fermion-mediated superconductivity, ferromagnetism, antiferromagnetism, hybridization gaps (Kondo insulator behavior), non-Fermi-liquid behavior and quantum critical points, quadrupolar ordering, and field-induced heavy-fermion states.

2. Structure

The filled skutterudites crystallize in the cubic space group $Im\bar{3}$ with two formula units (RM_4X_{12}) per unit cell. There are three unique atomic positions in the normalized unit cell. The rare earth position is $(0, 0, 0)$, the transition metal position is $(0.25, 0.25, 0.25)$, and the pnictogen (P, As, Sb) position $(0, y, z)$ is variable with $y \approx 0.35$, $z \approx 0.16$ (fig. 2). The positions of the remaining 31 atoms in the unit cell are determined by the symmetry operations associated with the $Im\bar{3}$ space group (fig. 3). As has been reviewed in detail by Uher (2001), the exact values of y and z for the unique pnictogen position depend on the particular compound, and reflect the fact the pnictogen rings (fig. 4) in the structure are not exactly square and the MX_6 octahedra are slightly distorted. If the pnictogen rings were exactly square and the octahedra symmetric, the pnictogen position would reduce to $(x = 0, y = 0.25, z = 0.25)$. The similarities between the filled skutterudite structure and the more familiar perovskite

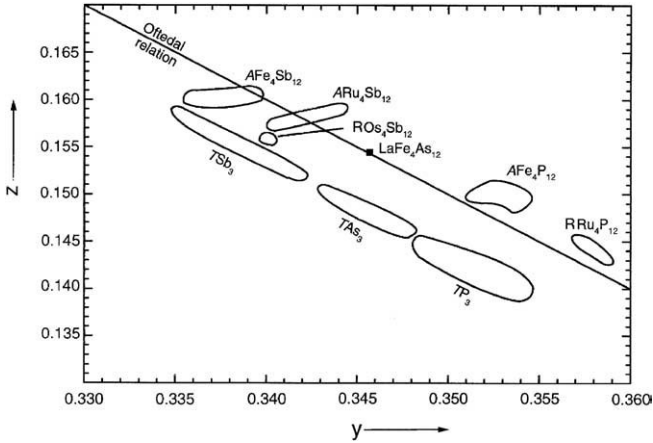


Fig. 2. Positional parameters for the pnictogen atoms of filled and unfilled skutterudites (figure from Kaiser and Jeitschko (1999)). The straight line indicates the condition for square pnictogen rings. In the figure $T = \text{Co, Rh or Ir}$; $A = \text{light lanthanides or Yb, Ca, Sr or Ba}$; $R = \text{light lanthanides}$.

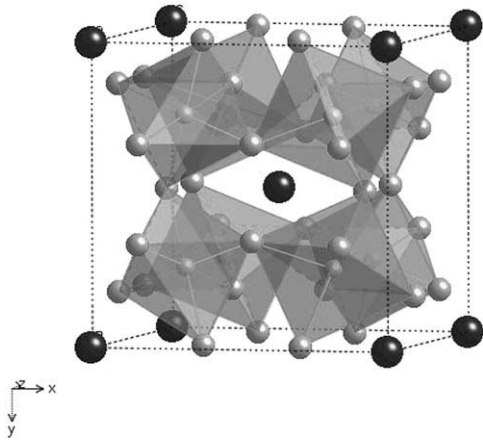


Fig. 3. Model of the filled skutterudite structure. The transition metal atoms (Fe, Ru, or Os – small light blue spheres) are at the center of distorted octahedra formed by the pnictogen atoms (P, As, Sb – green spheres). The lanthanide atoms (red spheres) are located at the center of a cage formed by 12 pnictogen atoms. The skutterudite structure results if the lanthanide atoms are removed from the structure and the transition metals (Fe, Ru or Os) are replaced by transition metals with one more outer shell electron (Co, Rh or Ir).

(e.g., CaTiO_3) and ReO_3 structures have been discussed by Jeitschko and Braun (1977). In the ideal perovskite structure the eight octahedra are not tilted which results in eight voids that are filled by Ca atoms. The tilting of the octahedra in the skutterudite structure reduces the volume of six of these voids which become the centers of rectangular pnictogen (P_4 , As_4 or Sb_4) groups. The remaining two voids are greatly enlarged and can accommodate lanthanide atoms (fig. 4). Each lanthanide atom is located at the center of a distorted icosahedron formed by 12 pnictogen atoms. The size of this icosahedral cage formed by the pnictogen atoms increases as the pnictogen is changed from P to As to Sb. In many of the antimonide compounds the atomic displacement parameters for the lanthanide atoms are unusually large, indicating substantial “rattling” of the R atoms about their equilibrium positions and poor bonding to the antimony atoms forming the cage (Braun and Jeitschko, 1980a; Kaiser and Jeitschko, 1999). The filled skutterudite structure does not form with the smaller

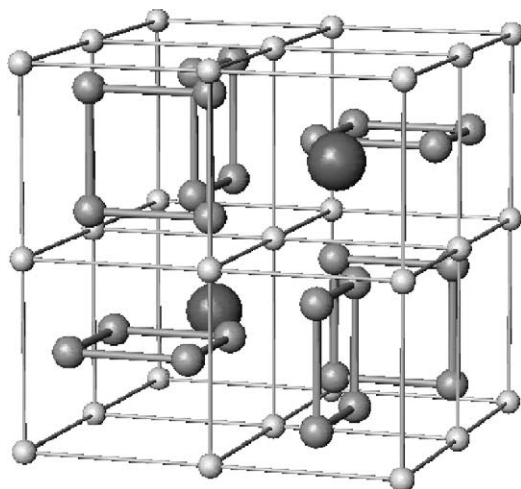


Fig. 4. Model of filled skutterudite structure that emphasizes the pnictogen-pnictogen bonding that results in nearly square pnictogen rings. The transition metal atoms (small white spheres) form a simple cubic lattice as shown. The lines connecting the transition metal atoms have been added for clarity and do not correspond to a chemical bond. The only chemical bonds shown in this model are those that form the pnictogen rings. The lanthanide atoms (large dark spheres) occupy the two voids without a pnictogen ring.

lanthanide elements (Dy–Tm) or Y or Sc because the pnictogen cage is too large for the necessary lanthanide-pnictogen bonding.

3. Lanthanide skutterudites as Zintl compounds

The qualitative electronic structure of the filled skutterudites can be understood within the framework of the Zintl concept (for a good discussion of Zintl's ideas see Corbett (1985), Muller (1993)). Zintl phases are characterized by the presence of covalently bonded anion structures similar to those found in the pure element. In the skutterudites, the pnictogen rings can be considered Zintl anions. The strongly electropositive cations (lanthanide elements and to a lesser extent the transition metal atoms), simply provide the necessary charge to complete the outer electron shell of the pnictogen anions. The Zintl concept can be applied to a huge number of compounds containing elements from the IVB, VB and VIB columns of the periodic table. Zintl compounds tend to be small gap semiconductors or bad metals. For the unfilled skutterudites, such as CoSb_3 , each Sb atom is bonded to two Sb and two Co atoms, and each Co atom is bonded to six Sb atoms (figs. 3 and 4). The outer shell of each Sb atom is $5s^2p^3$ and so to attain a closed shell ($5s^2p^6$) requires 3 electrons. The two covalent Sb–Sb bonds provide two of the electrons. The third electron is donated by the two Co atoms (a half an electron from each). This argument suggests that Co should have a formal valence of +3. In an octahedral site, the crystal field will result in a splitting of the five Co 3d orbitals into a ground state triplet (t_{2g}) and an excited state doublet (e_g). (For an exceptionally clear discussion of why this occurs see Muller (1993).) The six d electrons of Co^{+3} can completely occupy the t_{2g} orbital with no net magnetic moment, which is consistent with the measured diamagnetism for CoSb_3 . This argument would also suggest that CoSb_3 is a semiconductor. Although the simple Zintl concept appears to work for CoSb_3 , it is important

to realize that the Zintl picture is only a guideline and like many of the most useful guidelines they often work but sometimes they do not. In the case of CoSb_3 it is not clear that the Zintl picture should work well since there is not much difference in electronegativity between Co (1.88) and Sb (2.05). Detailed electronic structure calculations (Singh and Pickett, 1994; Sofo and Mahan, 1998) indicate that the electronic structure of CoSb_3 is rather complicated with a small gap of 0.05 eV at the Fermi energy due to a single band that crosses a much larger pseudogap (0.8 eV) between the valence and conduction bands.

The electronic structure of the lanthanide filled skutterudites can also be analyzed using the Zintl picture. The lanthanide filled skutterudites (e.g., $\text{LaFe}_4\text{Sb}_{12}$) form with the transition metals Fe, Ru or Os. These elements have one less outer electron relative to the elements in the next column of the periodic table (Co, Rh, or Ir). If the lanthanide elements contribute three electrons toward satisfying the bonding requirements of the pnictogen atoms, the total electron count is satisfied if each transition metal contributes on average 2.25 electrons. Although in terms of electron count an average valence of 2.25 should result in a semiconductor (within the Zintl picture), an average valence of 2.25 at each transition metal site would also imply a partially filled d band near the Fermi level. Since each transition metal is at a crystallographically equivalent site there is no reason to assume a spatial distribution of different transition metal valence states. This simple argument would suggest that the all of the lanthanide filled skutterudites should be poor metals. If the transition metal has an integer valence of +2, then a better metal should result with holes as the dominant carriers. For most of the lanthanide skutterudites the Zintl picture seems to be qualitatively correct at least as a starting point for understanding the electronic properties of these compounds. These simple ideas are useful but should only be regarded as guidelines and not a substitute for a modern electronic structure calculation. For example, density functional calculations of the electronic structure of $\text{CeFe}_4\text{Sb}_{12}$, and $\text{CeFe}_4\text{P}_{12}$ indicate that both compounds are small band gap semiconductors (Nordstrom and Singh, 1996). The gap is due to strong hybridization between the Ce 4f level and Fe 3d and pnictogen states near the Fermi energy.

4. Synthesis and crystal growth

The skutterudites do not melt congruently and involve pnictogens (P, As, Sb) that generally have high vapor pressures at the formation temperatures of the compounds. The high melting temperatures of Fe, Ru and Os coupled with the reactivity of the lanthanide metals with convenient crucible materials (e.g., SiO_2) makes the synthesis of many of these compounds difficult. As a result, variations in the reported properties of a particular lanthanide skutterudite compound can often be traced to differences in sample composition and quality.

Small single crystals of most of the lanthanide phosphides can be grown in a molten tin flux (Jeitschko and Braun, 1977; Meisner, 1981; Meisner et al., 1985; Delong and Meisner, 1985; Torikachvili et al., 1987; Watcharapasorn et al., 1999; Sato et al., 2000a, 2000b). For example, $\text{LaFe}_4\text{P}_{12}$ crystals were grown using La filings, Fe powder, red phosphorus and Sn in the atomic ratio 1 : 4 : 20 : 50. The mixture was sealed in an evacuated silica tube, annealed for one week at 1050 K, and slow cooled (2 K/h) to about 773 K, followed by rapid cooling to room

temperature. A 1 : 1 mixture of HCl and water was then used to dissolve the Sn flux (Jeitschko and Braun, 1977). Single crystals with typical dimensions from 0.1 to 2 mm can be grown by this method. Although this recipe clearly works and has been used by several authors, it may not be the optimum procedure for growing the largest phosphide crystals based on the known binary phase diagrams. A larger concentration of Sn and a carbonized silica tube along with larger pieces of lanthanide metals and cooling to lower temperatures might result in larger phosphide crystals. Polycrystalline skutterudite phosphides have also been synthesized directly from the elements using a high pressure (4 GPa) and high temperature (800–1200 °C) wedge-type cubic-anvil apparatus (Shirotani et al., 1996, 1997; Sekine et al., 1997; Uchiumi et al., 1999). This technique avoids contamination from residual Sn flux.

Lanthanide arsenides with the filled skutterudite structure were prepared by Braun and Jeitschko (1980b). Lanthanide arsenides, RAs, were first prepared by reacting lanthanide filings with As in a silica tube at 900 K for two days. The RAs material was then ground together with the transition metal and excess As (R : T : As = 1 : 4 : 20) and sealed again in evacuated silica tubes, rapidly heated to 1150 K and kept at temperature for 3 h. The samples were then annealed at 1000 K for 4–7 days. The excess As was removed through sublimation. In spite of this elaborate synthesis procedure, the overall products were only 70–90% single phase. However, small single crystals of the skutterudite phase suitable for X-ray structure refinement could often be isolated from the reaction product. A dense single phase sample of $\text{CeFe}_4\text{As}_{12}$ was prepared by a similar procedure followed by the densification of the powder with a hot-press (Watcharapasorn et al., 2002). Single phase arsenides with a variety of compositions have also been prepared via direct high-pressure high-temperature synthesis from the elements (Shirotani et al., 1997).

Synthesis of the lanthanide antimonides with the filled skutterudite structure have been investigated in much more detail than either the arsenides or phosphides because of the excellent thermoelectric properties of these materials at elevated temperatures. These materials were first synthesized by Braun and Jeitschko (1980a) using a procedure similar to that described above for the synthesis of the arsenides. The phase purity of the antimonides prepared in this manner was only about 80%. A better synthesis procedure was reported by Sales et al. (1996, 1997). A thin layer of carbon was deposited on the inside of a round-bottomed silica tube by the pyrolysis of acetone. Stoichiometric amounts of high purity lanthanide metal pieces (99.99% electropolished bar from Ames laboratory), Fe rod (99.9985% from Alfa Chemical Company), and Sb shot (99.999% from Alfa) were loaded into the precarbonized tube. The tube was sealed under vacuum at a pressure of 10^{-3} Pa and transferred into a programmable furnace. The silica ampoule was heated to 600 °C at 2 °C/min, left at 600 °C for 3 h, and then slowly (0.5 °C/min) heated to 1050 °C and left for about 20–40 h. It is important to slowly heat the tube because of the highly exothermic reaction between the lanthanide elements (particularly Ce) and antimony. The silica ampoule containing the homogeneous molten liquid was removed from the furnace at temperature and quenched into a water bath. The same ampoule (containing the prereacted elements) was then placed in a furnace and annealed at 700 °C for 30 h to form the correct crystallographic phase. The completely reacted solid was removed from the silica tube and cleaned with a wire brush to remove small amounts of carbon from the surface. To form a completely dense polycrys-

talline solid, the reacted material was ball milled into a fine powder in an argon atmosphere, loaded into a graphite die, and hot-pressed (5000 psi) in a helium atmosphere at 700 °C for 40 min. This procedure results in single phase and dense polycrystalline samples suitable for further investigation (transport, magnetic, optical, etc.). Single crystals of the antimonides can also be grown using excess antimony as a flux (Chakoumakos et al., 1999; Takeda and Ishikawa, 2000b; E.D. Bauer et al., 2001a, 2001b). High purity elements in the ratio R:T:Sb = 1:4:20 are loaded into an evacuated carbon coated quartz tube. The tubes are heated to 900 °C for 24 h and then cooled slowly (1–3 °C/h) to 600 °C, followed by a quench to room temperature. The excess Sb flux can be removed by etching in acid (HCl:HNO₃ = 1:1). Small quantities of new compounds with the skutterudite structure can also be synthesized using a clever non-equilibrium thin film method pioneered by D.C. Johnson and collaborators at the University of Oregon (Hornbostel et al., 1997a, 1997b). The new compounds are formed by the low-temperature interdiffusion of multilayer elemental reactants.

5. La filled skutterudites

LaFe₄P₁₂ is a metal that becomes superconducting for temperatures below 4.1 K (Meisner, 1981). The residual resistance ratio (RRR) for these crystals is large $RRR = 90\text{--}1500$ indicating good crystallographic perfection (Torikachvili et al., 1987; Sato et al., 2000a, 2000b; Sugawara et al., 2000). The resistivity at room temperature is about 250 $\mu\Omega\text{ cm}$ (Sugawara et al., 2000) in fair agreement with optical conductivity data which yields a value of 85 $\mu\Omega\text{ cm}$ (Dordevic et al., 1999). Superconductivity is rare in compounds that contain such high concentrations of iron. Mössbauer measurements found that each iron atom in *LaFe₄P₁₂* carried a magnetic moment less than $0.01\mu_B$ (Shenoy et al., 1982; Grandjean et al., 1984). The magnetic susceptibility data is weakly temperature dependent and saturates below 50 K at a value of $8 \times 10^{-4}\text{ cm}^3/\text{mol}$ (emu/mol) (Meisner, 1981; Grandjean et al., 1984). If the iron moments are in a low spin configuration similar to Fe^{+2} , from the Zintl picture discussed in sect. 3, the compound should be a hole doped metal. Hall measurements (Sato et al., 2000b) and band structure calculations (Harima, 1998, 2000) both indicate hole like conduction. Band structure predicts two hole-like Fermi sheets, a nearly spherical sheet composed mainly of Fe 3d states and a multiply connected sheet of mainly P-p character (fig. 5). The band structure calculations are in good agreement with the two masses extracted from dHvA measurements on *LaFe₄P₁₂* crystals (Sugawara et al., 2000). The predicted electronic specific heat coefficient, γ , from the band structure calculations, was 32 $\text{mJ}/\text{mol K}^2$ in fair agreement with the experimental value of 57 $\text{mJ}/\text{mol K}^2$ (Torikachvili et al., 1987). The relatively high density of electronic states and the absence of magnetism suggests that *LaFe₄P₁₂* is a relatively normal BCS superconductor. The jump in the heat capacity at $T_c = 4.1\text{ K}$ is about 87% of the value expected from BCS theory.

LaRu₄P₁₂ is a metal that superconducts below 7.2 K (Meisner, 1981; Delong and Meisner, 1985; Uchiumi et al., 1999). The room temperature resistivity of a polycrystalline sample was 600 $\mu\Omega\text{ cm}$ decreasing to about 20 $\mu\Omega\text{ cm}$ at 8 K (Shirotani et al., 1996). Analysis of the low

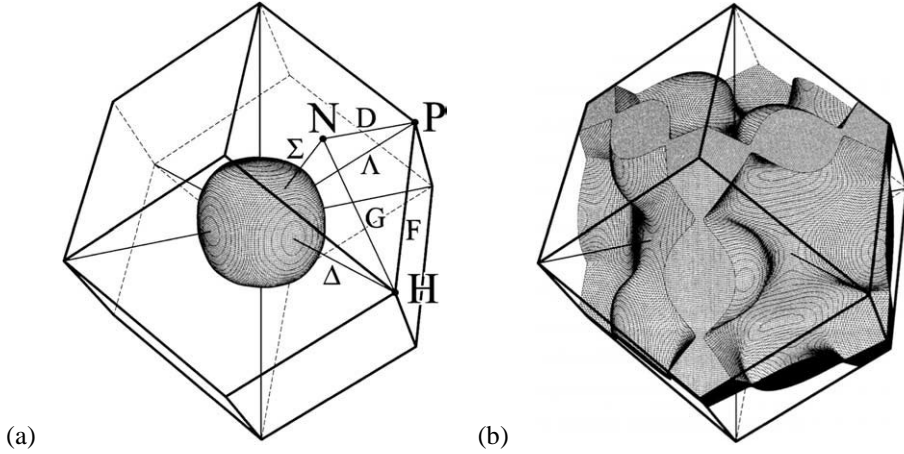


Fig. 5. The Fermi surface of $\text{LaFe}_4\text{P}_{12}$ consists of two hole-like Fermi sheets. The first sheet (a) is nearly spherical with mainly Fe 3d character while the second sheet (b) is multiply connected with mainly P-p character. Both surfaces are centered at the Γ point. Various high-symmetry directions are noted in (a) (Harima, 1998; Sugawara et al., 2000).

temperature heat capacity data yields $\gamma = 26 \text{ mJ/mol K}^2$ and a Debye temperature, $\Theta_D = 446 \text{ K}$. The magnetic susceptibility is essentially temperature independent from 7–300 K, consistent with Pauli paramagnetism (Uchiumi et al., 1999).

$\text{LaOs}_4\text{P}_{12}$ is a metal with a room temperature resistivity of about $400 \mu\Omega \text{ cm}$, which decreases to $50 \mu\Omega \text{ cm}$ at 2 K followed by superconductivity at 1.8 K (Shirotani et al., 1996; Meisner, 1981). There is a weak decrease of T_c with increasing pressure (DeLong and Meisner, 1985).

$\text{LaFe}_4\text{As}_{12}$ is a metal that shows a monotonic decrease in resistivity down to 2 K with no evidence of superconductivity (Shirotani et al., 2000).

$\text{LaRu}_4\text{As}_{12}$ is a poor metal with the highest superconducting transition temperature (10.3 K) of all of the filled skutterudites. Polycrystalline samples can be prepared using high pressure and high temperature (Shirotani et al., 1996, 1997, 2000; Uchiumi et al., 1999). The resistivity at room temperature is $13 \text{ m}\Omega \text{ cm}$ decreasing to $3 \text{ m}\Omega \text{ cm}$ at 12 K. The temperature dependence of the resistivity exhibits a large positive curvature that suggests substantial structure in the electronic density of state near the Fermi energy. Low temperature heat capacity measurements yield $\gamma = 73 \text{ mJ/mol K}^2$, and $\Theta_D = 233 \text{ K}$. The normalized jump in the heat capacity at T_c is 1.75 which is slightly larger than the BCS value of 1.43. With increasing pressure T_c decreases at the rate $dT_c/dP = -0.4 \text{ K/GPa}$ (fig. 6).

$\text{LaOs}_4\text{As}_{12}$ is metallic exhibiting superconductivity below 3.2 K (Shirotani et al., 2000). The resistivity (polycrystalline sample) at room temperature is $0.8 \text{ m}\Omega \text{ cm}$ decreasing to $0.1 \text{ m}\Omega \text{ cm}$ at 4 K.

$\text{LaFe}_4\text{Sb}_{12}$ is a poor metal or heavily doped semiconductor with good thermoelectric properties above room temperature (700–1000 K) (Sales et al., 1996, 1997). Only polycrystalline samples have been investigated. The room temperature resistivity is about $0.5 \text{ m}\Omega \text{ cm}$ de-

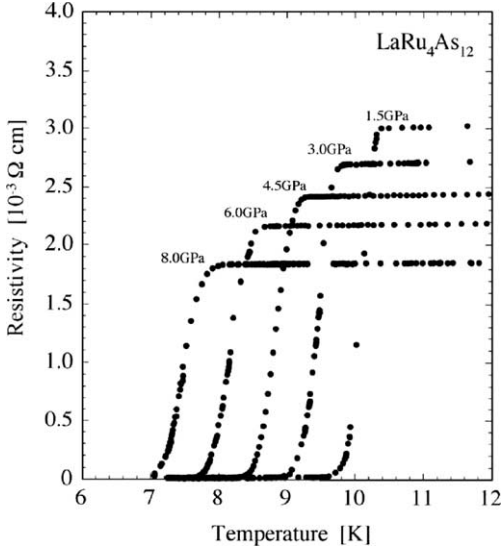


Fig. 6. Electrical resistivity of $\text{LaRu}_4\text{As}_{12}$ vs. temperature and pressure (Shirotani et al., 2000).

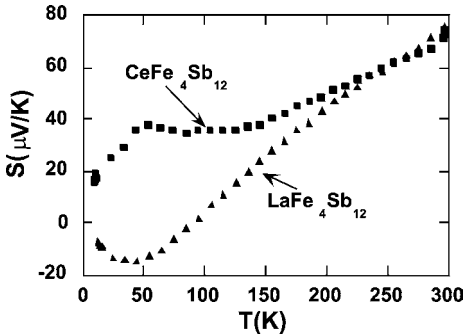


Fig. 7. Seebeck coefficient vs. temperature for $\text{LaFe}_4\text{Sb}_{12}$ and $\text{CeFe}_4\text{Sb}_{12}$ (Sales et al., 1997, unpublished).

creasing to $0.1 \text{ m}\Omega \text{ cm}$ at 10 K. The typical carrier concentration estimated from room temperature Hall data is $2 \times 10^{21} \text{ holes/cm}^3$. The Seebeck coefficient, S , at room temperature is $+75 \text{ }\mu\text{V/K}$ which is typical for a heavily doped semiconductor (the value of S for a good metal is usually less than $10 \text{ }\mu\text{V/K}$ in magnitude). The electronic structure near the Fermi energy has more than one type of band since the Seebeck coefficient changes sign near 100 K (fig. 7). There has been no report of superconductivity in this material above 2 K. There is no evidence of long range magnetic order. The magnetic susceptibility indicates some type of enhanced paramagnetism that is probably associated with nearly itinerant 3d electrons (Ravot et al., 2001; Dannebrock et al., 1996; Sales, unpublished). Although the temperature dependence of the susceptibility is similar for all three samples, the magnitude of the room temperature susceptibility varies substantially from 0.0019 emu/mol (Ravot et al., 2001) to 0.004 (Dannebrock et al., 1996) – note that all of the susceptibility data in Dannebrock’s fig. 2 appears

to be mislabeled since the susceptibility values are too high by a factor of 10). At helium temperatures the susceptibility saturates for all three samples near 0.02 emu/mol. Probably the best interpretation of the susceptibility data was given by Ravot et al. (2001) who were able to account for the nearly Curie–Weiss dependence of the susceptibility in terms of a Stoner band picture. This interpretation is also consistent with the discussion in sect. 3, which implies some type of band magnetism if the average iron valence is 2.25. However, the significant variation of the susceptibility from sample to sample and the difficulty in ruling out small amounts ($< 3\%$) of a magnetic impurity phase suggests that the magnetism may not be intrinsic to the skutterudite phase. Susceptibility measurements should be repeated using a single crystal free of impurity phases.

Braun and Jeitschko (1980a) noted that the lanthanide site in the antimonides is too large for La, the largest trivalent lanthanide element. The poor bonding of La to the surrounding antimony atoms results in a large atomic displacement parameter (ADP) for La and corresponds to the La “rattling” about its equilibrium position. As a first approximation the rattling La atom can be treated as a localized Einstein oscillator. Slack (1995) was first to suggest that if the frequency of the Einstein oscillator is low enough, it could result in a substantial reduction in the lattice thermal conductivity of the filled skutterudites by hybridizing with the acoustic phonons that carry the majority of the heat in most solids. This idea has been experimentally verified by many authors (Morelli and Meisner, 1995; Sales et al., 1996, 1997, 2000, 2001a, 2001b; Fleurial et al., 1996; Nolas et al., 1996a, 1996b, 1998; Morelli et al., 1997; Meisner et al., 1998). A low lattice thermal conductivity, κ_L , is necessary for a good thermoelectric material. The room temperature value of κ_L for dense polycrystalline $\text{LaFe}_4\text{Sb}_{12}$ is approximately 1.5 W/mK. An estimate of the Einstein frequency for La in $\text{LaFe}_4\text{Sb}_{12}$ has been obtained from heat capacity, elastic constant, inelastic neutron scattering (fig. 8), ADP data and theory (Sales et al., 1997, 1999; Keppens et al., 1998; Feldman et al., 2000). All of the measurements indicate a characteristic Einstein temperature of about 75 K for the La atoms.

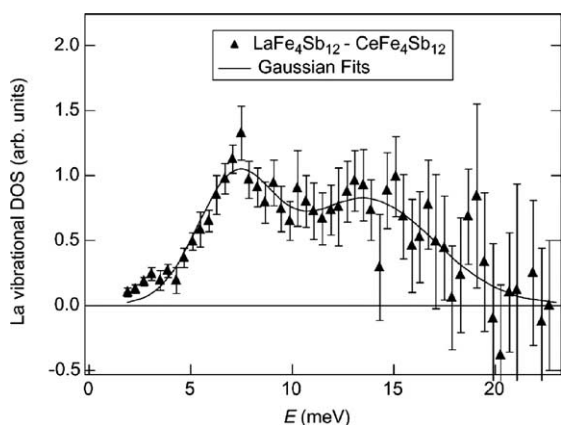


Fig. 8. Difference in the inelastic neutron scattering data between $\text{LaFe}_4\text{Sb}_{12}$ and $\text{CeFe}_4\text{Sb}_{12}$ vs. energy loss (Keppens et al., 1998). $\text{CeFe}_4\text{Sb}_{12}$ was used as a reference compound since the neutron scattering cross section of Ce is much smaller than that of La. The difference spectra therefore reflect the vibrational density of states (DOS) associated with the La atoms. The peak at 7 meV (78 K) corresponds to the quasi-localized La mode. The second broader peak at about 15 meV corresponds to the hybridization of La and Sb vibrational modes. Both peaks can be accounted for using lattice dynamic models based on first-principles calculations (Feldman et al., 2000).

LaRu₄Sb₁₂ is metallic and is superconducting below about 3.6 K (Uchiumi et al., 1999; Takeda and Ishikawa, 2000b; E.D. Bauer et al., 2001a). Low temperature heat capacity data yield $\gamma = 37$ mJ/mol K² and $\Theta_D = 253$ K. The residual resistivity ratio (RRR) is about 69 for the small crystals but no absolute values for the resistivity are reported (Takeda and Ishikawa, 2000b). Polycrystalline samples synthesized at high pressures have a resistivity of 0.7 m Ω cm and a much smaller RRR of 7. The T_c of the polycrystalline material is also significantly lower (2.8 K) (Uchiumi et al., 1999). The normalized jump in the heat capacity at T_c is 2.22, which suggests that *LaRu₄Sb₁₂* is a superconductor with moderate coupling (Takeda and Ishikawa, 2000b). The room temperature magnetic susceptibility of *LaRu₄Sb₁₂* is diamagnetic with a value of -1.93×10^{-4} emu/mol.

LaOs₄Sb₁₂ is presumably a metal although only heat capacity data from small single crystals have been published resulting in $\gamma = 36$ mJ/mol K² and $\Theta_D = 304$ K. There is no evidence for superconductivity above 0.5 K (E.D. Bauer et al., 2001b).

6. Ce filled skutterudites

CeFe₄P₁₂ is a small gap semiconductor with the gap likely arising from the hybridization of the Ce 4f states with the Fe 3d and 5b-p states in the vicinity of the Fermi energy (Meisner et al., 1985; Nordstrom and Singh, 1996). The susceptibility of *CeFe₄P₁₂* is small (2.6×10^{-4} emu/mol), and is roughly a factor of 2 less than its non-magnetic analog *LaFe₄P₁₂*. The lattice constant of *CeFe₄P₁₂* (7.792 Å) is significantly smaller than would be expected for trivalent Ce based on the values for *LaFe₄P₁₂* (7.8316 Å) and *PrFe₄P₁₂* (7.8149 Å). The susceptibility data and the lattice constant suggest the possibility of Ce⁺⁴. However, XANES (X-ray absorption near edge spectroscopy) measurements (Xue et al., 1994) clearly indicate that the Ce is primarily trivalent, though with some evidence of complex electronic behavior. The resistivity increases with decreasing temperature but the behavior is complicated and somewhat sample dependent (Meisner et al., 1985; Sato et al., 2000b). Analysis of single crystal resistivity data above 250 K gives a transport gap of about 0.12 eV (Sato et al., 2000b) which is close to the value of 0.15 eV measured from infrared reflectance spectroscopy (Dordevic et al., 1999). Both values are somewhat smaller than the value of 0.34 eV calculated within the local-density approximation (LDA) (Nordstrom and Singh, 1996). The temperature dependence of the Hall coefficient from 2–300 K appears to be reproducible from crystal to crystal but is difficult to interpret (Sato et al., 2000b). The Seebeck coefficient at room temperature is large for single crystals (≈ 0.5 mV/K) (Sato et al., 2000b) but is about 10 times smaller in hot-pressed polycrystalline samples with small amounts of impurity phases (Watcharapasorn et al., 1999). The room temperature thermal conductivity of a polycrystalline sample is 14 W/mK, which is about ten times larger than the typical values of good thermoelectric materials (Watcharapasorn et al., 1999).

CeRu₄P₁₂ is a narrow gap semiconductor with a gap of 0.075 eV estimated from electrical transport measurements on polycrystalline samples (Shirovani et al., 1996). XANES measurements indicate trivalent Ce with strong hybridization with ligand orbitals. The gap is presumably formed from the hybridization of the Ce 4f states with the Ru d and P-p orbitals

(Kanai et al., 2002). The room temperature thermal conductivity of a dense polycrystalline sample is 8.6 W/m K (Watcharapasorn et al., 1999). The magnetic susceptibility is paramagnetic but relatively small at room temperature ($\approx 0.001 \text{ cm}^3/\text{mol Ce}$) and increases to about $0.018 \text{ cm}^3/\text{mol}$ at 2 K (Shirotani et al., 1999). These values indicate a substantial reduction in the magnetism of the Ce 4f shell due to hybridization.

$\text{CeOs}_4\text{P}_{12}$ is a narrow gap semiconductor with a gap of $\approx 0.036 \text{ eV}$ ($\approx 400 \text{ K}$) estimated from resistivity data (Shirotani et al., 1999). The room temperature resistivity is $\approx 10^{-2} \Omega \text{ cm}$ increasing to $\approx 10^4 \Omega \text{ cm}$ at 2 K. The magnetic susceptibility is similar to that of $\text{CeRu}_4\text{P}_{12}$ (Shirotani et al., 1999). The as-grown samples are p-type with a room temperature Hall mobility of $73 \text{ cm}^2/\text{Vs}$ for a carrier concentration of $5 \times 10^{19} \text{ cm}^{-3}$. The room temperature values of the Seebeck coefficient and thermal conductivity are $+147 \mu\text{V/K}$ and 10.5 W/m K , respectively (Sekine et al., 2001).

$\text{CeFe}_4\text{As}_{12}$ is probably a narrow gap semiconductor, but little low temperature data are available for this compound. The resistivity of a polycrystalline sample indicates a small gap on the order of 0.01 eV (Grandjean et al., 1984). The high temperature thermoelectric properties of this compound were investigated by Watcharapasorn et al. (2002). They found semimetallic behavior with a room temperature resistivity of 0.49 m $\Omega \text{ cm}$, a Seebeck coefficient of $40 \mu\text{V/K}$, and a thermal conductivity of 3.8 W/m K. The maximum value for ZT , the thermoelectric figure of merit, was estimated to be 0.4 at 850 K.

$\text{CeRu}_4\text{As}_{12}$ – only crystallography data has been reported for this compound (see table 1).

$\text{CeFe}_4\text{Sb}_{12}$ is a moderately heavy fermion metal at low temperatures (Morelli and Meisner, 1995; Gajewski et al., 1998; E.D. Bauer et al., 2000) and has excellent thermoelectric properties at elevated temperatures (Sales et al., 1996, 1997; Fleurial et al., 1996). LDA calculations predict a small gap (0.1 eV) that is not observed experimentally (Nordstrom and Singh, 1996). The hybridization between the Ce 4f and the Fe 3d and Sb-p states at the Fermi energy is apparently not large enough to create a gap. XANES measurements (Grandjean et al., 2000) indicate a Ce valence of 3 ± 0.02 , and iron Mössbauer data show no indication of magnetic order (Long et al., 1999). All of the reported data are from polycrystalline samples. Analysis of the low temperature heat capacity and magnetization data are complicated by small amounts of impurity phases (Morelli and Meisner, 1995; Chen et al., 1997; Gajewski et al., 1998). Analysis of the low temperature heat capacity data yields $\gamma = 180 \text{ mJ/mol K}^2$ and $\Theta_D \approx 250 \text{ K}$ (Gajewski et al., 1998). The resistivity of $\text{CeFe}_4\text{Sb}_{12}$ has an unusual ‘‘S’’ shape that is characteristic of many concentrated Kondo compounds (fig. 9b). The rapid decrease in resistivity at about 100 K is caused by the coherent scattering of electrons from the lanthanide sublattice. The interpretation of the magnetic data is complicated by an enhanced Pauli contribution from the Fe (Ravot et al., 2001), a relatively high Kondo temperature, T_K , of about 100 K (Gajewski et al., 1998) and the crystal field splitting of the Ce 4f level in a cubic crystal field. In spite of these complications, it is clear that the value of the Wilson–Sommerfeld ratio $R_w = (\chi_0/\gamma)(\pi^2 k_B^2/\mu_{\text{eff}}^2)$ is of the order unity as expected for heavy fermion systems (Wilson, 1975). In the expression for R_w , χ_0 is the extrapolated Pauli susceptibility at $T = 0$ (0.008 emu/mol Ce), and μ_{eff} is the magnetic moment per Ce ion ($2.54\mu_B$).

Table 1
Crystallography data and ground state properties of filled skutterudites^a

Compound	Lattice constant (Å)	Density (g/cm ³) (X-ray density)	Ground state/transition temperature (K)	Ref.
LaFe ₄ P ₁₂	7.8316	5.08	S, $T_c = 4.1$	1
LaRu ₄ P ₁₂	8.0561	5.81	S, $T_c = 7.2$	1
LaOs ₄ P ₁₂	8.0844	7.99	S, $T_c = 1.8$	1
LaFe ₄ As ₁₂	8.3252	7.26	M	3
LaRu ₄ As ₁₂	8.5081	7.77	S, $T_c = 10.3$	3
LaOs ₄ As ₁₂	8.5437	9.57	S, $T_c = 3.2$	3
LaFe ₄ Sb ₁₂	9.1395	7.93	M	2
LaRu ₄ Sb ₁₂	9.2700	8.35	S, $T_c = 2.8$	2
LaOs ₄ Sb ₁₂	9.3029	9.74	M	2
CeFe ₄ P ₁₂	7.7920	5.16	HGS	1
CeRu ₄ P ₁₂	8.0376	5.86	HGS	1
CeOs ₄ P ₁₂	8.0626	8.06	HGS	1
CeFe ₄ As ₁₂	8.2959	7.34	–	3
CeRu ₄ As ₁₂	8.4908	7.83	–	3
CeOs ₄ As ₁₂	8.5249	9.64	–	3
CeFe ₄ Sb ₁₂	9.1350	7.95	HFM	2
CeRu ₄ Sb ₁₂	9.2657	8.37	NFL, QCP	2
CeOs ₄ Sb ₁₂	9.3011	9.75	HGS	2
PrFe ₄ P ₁₂	7.8149	5.12	QO, $T_{QO} = 6.5$, FIHFM	1
PrRu ₄ P ₁₂	8.0420	5.86	M-I, $T_{M-I} = 60$, $T_{AF} \approx 0.3$	1
PrOs ₄ P ₁₂	8.0710	8.04	M	1
PrFe ₄ As ₁₂	8.3125	7.30	–	3
PrRu ₄ As ₁₂	8.4963	7.82	S, $T_c = 2.4$	3
PrOs ₄ As ₁₂	8.5311	9.62	–	3
PrFe ₄ Sb ₁₂	9.1351	7.95	FMM, $T_{FM} = 5$	2
PrRu ₄ Sb ₁₂	9.2648	8.38	–	2
PrOs ₄ Sb ₁₂	9.2994	9.76	HFSC, $T_{sc} = 1.8$	2
NdFe ₄ P ₁₂	7.8079	5.16	FMM, $T_{FM} = 5$	1
NdRu ₄ P ₁₂	8.0364	5.89	FMM, $T_{FM} = 1.5$	1
NdOs ₄ P ₁₂	8.0638	8.09	–	1
NdFe ₄ As ₁₂	8.309	7.39	–	9
NdRu ₄ As ₁₂	–	–	–	–
NdOs ₄ As ₁₂	8.5291	9.65	–	3
NdFe ₄ Sb ₁₂	9.130	8.04	–	5
NdRu ₄ Sb ₁₂	9.2642	8.39	AFM?, $T_{AF} = 1.3$	2
NdOs ₄ Sb ₁₂	9.2989	9.77	$T_d = 187$	2
SmFe ₄ P ₁₂	7.8029	5.21	M	1
SmRu ₄ P ₁₂	8.0397	5.96	M-I & $T_{AF} = 16$	11
SmFe ₄ Sb ₁₂	9.130	8.06	FMM, $T_{FM} = 45$	5
SmRu ₄ Sb ₁₂	9.259	8.49	–	5
SmOs ₄ Sb ₁₂	9.3009	9.79	–	2
EuFe ₄ P ₁₂	7.8055	5.22	FMM, $T_{FM} = 100$	1
EuRu ₄ P ₁₂	8.0406	5.93	FMM, $T_{FM} = 18$	1

continued on next page

Table 1, *continued*

Compound	Lattice constant (Å)	Density (g/cm ³) (X-ray density)	Ground state/transition temperature (K)	Ref.
EuFe ₄ Sb ₁₂	9.165	7.98	FMM, $T_{\text{FM}} = 84$	5
EuRu ₄ Sb ₁₂	9.2824	8.42	FMM, $T_{\text{FM}} = 3.3$	2
EuOs ₄ Sb ₁₂	9.3187	9.74	–	2
GdFe ₄ P ₁₂	7.795	5.31	FMM, $T_{\text{FM}} = 22$	9
GdRu ₄ P ₁₂	8.0375	6.01	AFM?, $T_{\text{AF}} = 21$	11
TbRu ₄ P ₁₂	8.0338	6.03	AFM?, $T_{\text{AF}} = 20, 10$	11
YbFe ₄ Sb ₁₂	9.1580	8.09	HFM, Mixed Valence	7
YbOs ₄ Sb ₁₂	9.316	9.91		6
ThFe ₄ P ₁₂	7.7999	5.83		4
ThRu ₄ P ₁₂	8.0461	6.47		4
ThOs ₄ As ₁₂	8.5183	10.24		4
UFe ₄ P ₁₂	7.7709	5.94		5
CaFe ₄ Sb ₁₂	9.162	7.5		5
SrFe ₄ Sb ₁₂	9.1782	7.67		10
SrRu ₄ Sb ₁₂	9.2891	8.15		5
SrOs ₄ Sb ₁₂	9.322	9.52		10
BaFe ₄ Sb ₁₂	9.200	7.82		8
BaRu ₄ Sb ₁₂	9.315	8.29		5
BaOs ₄ Sb ₁₂	9.3401	9.68		10

^aSymbols:

S, superconductor;

HGS, hybridization gap semiconductor;

HFM, heavy fermion metal;

M, metallic;

NFL, non-Fermi liquid;

QCP, quantum critical point;

QO, quadrupolar order;

FIHFM, field-induced heavy-fermion metal;

FMM, ferromagnetic metal;

AFM, antiferromagnetic metal;

M-I, metal to insulator transition;

AFM?, unusual magnetic phase transition;

T_{d} , displacive transition.

References

- | | | |
|--------------------------------|--------------------------------|----------------------------|
| 1. Jeitschko and Braun (1977) | 5. Evers et al. (1995) | 9. Jeitschko et al. (2000) |
| 2. Braun and Jeitschko (1980a) | 6. Kaiser and Jeitschko (1999) | 10. Evers et al. (1994) |
| 3. Braun and Jeitschko (1980b) | 7. Dilley et al. (1998) | |
| 4. Braun and Jeitschko (1980c) | 8. Stetson et al. (1991) | 11. Sekine et al. (2000a) |

CeRu₄Sb₁₂ is an unusual metal that exhibits non-Fermi liquid (NFL) behavior in the low temperature specific heat, resistivity, and magnetic susceptibility measurements on single crystals (Takeda and Ishikawa, 2000a, 2000b, 2001; E.D. Bauer et al., 2001a). *CeRu₄Sb₁₂* may be near a ferromagnetic quantum critical point. The low temperature ($T < 4$ K) specific heat (fig. 10) and magnetic susceptibility of *CeRu₄Sb₁₂* are well described by a logarithmic divergence or a power law in temperature. The characteristic temperature, T^* , that is associated with the maximum in the magnetic susceptibility and with the rapid drop in the

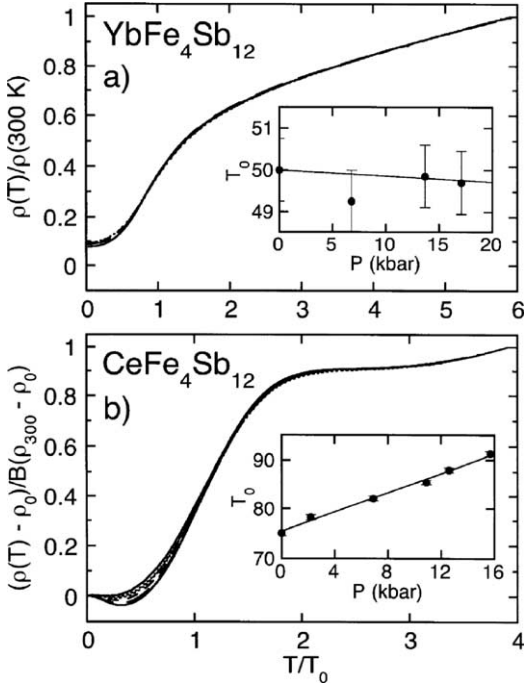


Fig. 9. (a) Scaled resistivity $\rho(T)/\rho(300\text{ K})$ vs. T/T_0 for $\text{YbFe}_4\text{Sb}_{12}$, where T_0 is the scaling temperature. Inset shows the pressure dependence of T_0 . (b) Scaled resistivity of $\text{CeFe}_4\text{Sb}_{12}$ vs. T/T_0 . Inset shows pressure dependence of T_0 . The room temperature resistivity of both compounds was about $0.8\text{ m}\Omega\text{ cm}$ at ambient pressure (E.D. Bauer et al., 2000).

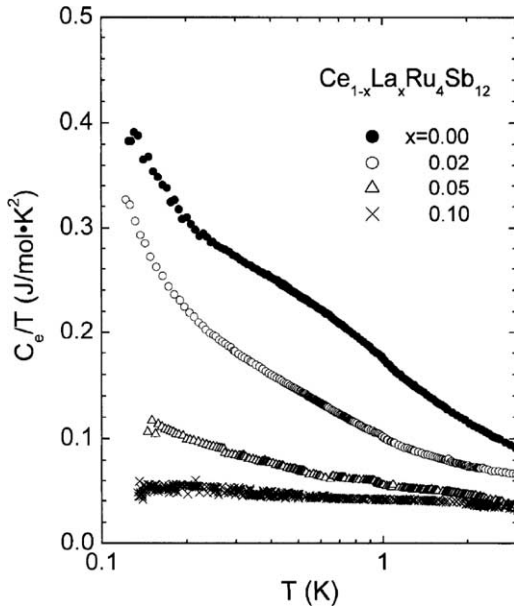


Fig. 10. Electronic contribution to the heat capacity divided by temperature vs. $\log_{10} T$ for a series of La doped alloys of $\text{CeRu}_4\text{Sb}_{12}$. The data has been corrected for a phonon contribution, using heat capacity data from $\text{LaRu}_4\text{Sb}_{12}$, and a nuclear quadrupolar contribution from ^{121}Sb and ^{123}Sb (Takeda and Ishikawa, 2001).

resistivity is about 75 K. The low temperature carrier mass, m^* , estimated from heat capacity and optical studies, is about 85 times the free electron mass (Dordevic et al., 2001). Optical measurements are able to directly measure the pseudo-gap, Δ , created by the hybridization between the Ce 4f states and the extended conduction band states. The mass enhancement scales as $m^*/m_e = (\Delta/T^*)^2$ as predicted by theory (Millis et al., 1987). The low temperature resistivity data for CeRu₄Sb₁₂ reported by Takeda and Ishikawa (2000a, 2000b, 2001) follows a power law in temperature ($\rho \propto T^n$) with $n = 1.65$. A magnetic field greater than 2 T appears to restore Fermi liquid behavior ($n = 2$) for temperatures less than 1 K, as did the substitution of a small amount of La for Ce. The La-doping studies suggest that the parent compound, CeRu₄Sb₁₂, is near a ferromagnetic quantum critical point.

In contrast, E.D. Bauer et al. (2001a) found that the electrical resistivity is sample dependent with some specimens exhibiting NFL behavior below 5 K. For these samples the application of magnetic fields up to $H = 8$ T does not significantly change the non-Fermi liquid ground state. The low temperature transport properties of CeRu₄Sb₁₂ crystals are clearly sensitive to small changes in composition or small concentrations of impurities in the starting materials.

CeOs₄Sb₁₂ is a narrow gap semiconductor with the gap caused by the hybridization of the Ce 4f level with states near the Fermi energy. Transport data on small single crystals shows a weakly activated behavior corresponding to a gap of about 10 K (E.D. Bauer et al., 2001b). Heat capacity data give $\gamma \approx 92$ mJ/mol K² and $\Theta_D = 304$ K. No magnetic order was found above 0.5 K. The temperature dependence of the magnetic susceptibility data suggests a relatively large crystalline electric field splitting (327 K) of the Ce 4f level.

7. Pr filled skutterudites

PrFe₄P₁₂ is quite an unusual compound that exhibits weak semiconducting behavior from 20–300 K followed by an even stranger phase transition near 5 K (fig. 11) (Sato et al., 2000a, 2000b; Aoki et al., 2002). Originally it was thought that the low temperature phase transition corresponded to the onset of antiferromagnetic ordering of the Pr magnetic moments (Torikachvili et al., 1987). More recent work indicates that the phase transition probably corresponds to the ordering of the Pr quadrupole moments since for temperatures below the transition each Pr ion has a low magnetic moment implying a non-magnetic ground state ($< 0.03\mu_B/\text{Pr}$) (Aoki et al., 2002). No magnetic ordering is evident in neutron scattering measurements (Keller et al., 2001). The Hall coefficient changes by more than two orders of magnitude below 5 K but becomes temperature independent below 2 K. The Hall data suggests a gap structure similar to that seen in the resistivity (fig. 11) and heat capacity data. The Seebeck coefficient is extremely large below 5 K reaching a maximum value of -130 $\mu\text{V}/\text{K}$ at 4 K, which reflects an unusually sharp feature in the electronic density of states. The application of a magnetic field induces a transition to a heavy-fermion state (HFS) with a well-defined phase boundary as a function of magnetic field and temperature (figs. 12, 13). A metamagnetic phase transition (fig. 14) is also associated with the phase boundary (Torikachvili et al., 1987; Matsuda et al., 2000; Aoki et al., 2002). It is suggested that the quadrupolar degrees of freedom are essential for the formation of the heavy-fermion state in this material. The crystalline

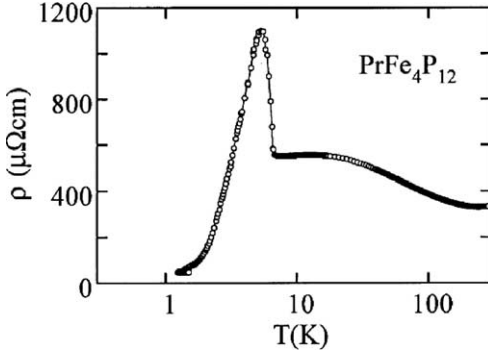


Fig. 11. Electrical resistivity vs. $\log_{10} T$ for $\text{PrFe}_4\text{P}_{12}$. Below 3 K the resistivity is accurately described by $\rho(T) = 20 + 273T^2 \exp(-6.8/T)$, corresponding to the temperature dependence of scattering with a gap structure (Sato et al., 2000a).

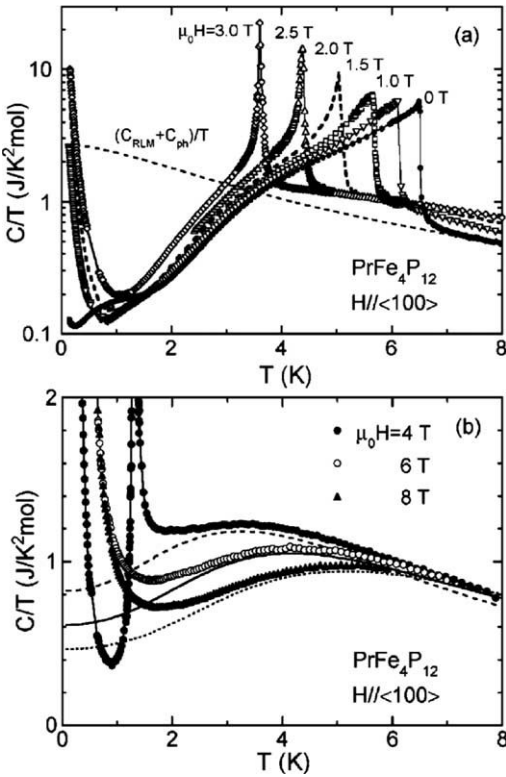


Fig. 12. Total heat capacity of a single crystal of $\text{PrFe}_4\text{P}_{12}$ vs. temperature in various applied magnetic fields: (a) low fields and (b) high fields. The dashed lines in (b) correspond to the best fit of the heavy fermion state to the resonant level model (C_{RLM}). C_{ph} is the estimate of the phonon contribution to the heat capacity (Aoki et al., 2002).

electric field level schemes estimated from the anisotropy in the magnetization are consistent with this conjecture. The de Haas–van Alphen (dHvA) effect has been used to study the electronic structure of $\text{PrFe}_4\text{P}_{12}$. An enormously enhanced cyclotron effective mass of $81 m_e$ was found in the HFS phase. In the low field ordered phase a dHvA branch with a mass of $10 m_e$ was also observed (Sugawara et al., 2001).

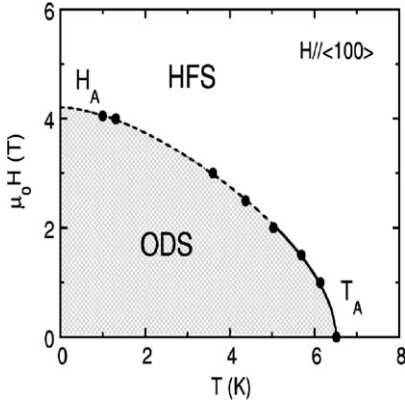


Fig. 13. Magnetic field vs. temperature phase diagram of single crystal $\text{PrFe}_4\text{P}_{12}$ with the magnetic fields applied along the (100) direction. The labels ODS and HFS refer to ordered state and heavy fermion state, respectively. The ordered state is probably due to quadrupolar ordering of the Pr 4f ground state. The solid and broken lines represent second-order and first-order phase boundaries, respectively (Aoki et al., 2002).

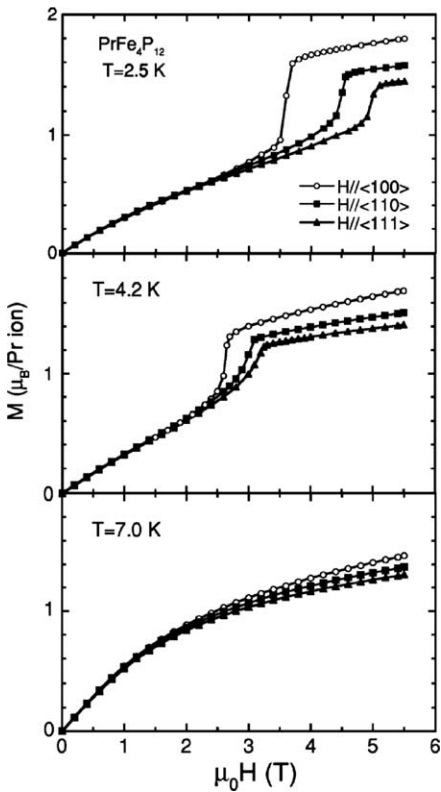


Fig. 14. Magnetization vs. field at 2.5, 4.2 and 7 K with the magnetic field applied along the main symmetry directions of $\text{PrFe}_4\text{P}_{12}$. The observed magnetic anisotropy is a feature of the non-ordered state (Aoki et al., 2002).

$\text{PrRu}_4\text{P}_{12}$ exhibits an unusual metal–insulator transition (M-I) at about 60 K (fig. 15) (Sekine et al., 1997). There is no magnetic anomaly associated with this transition and originally it was thought there is no structural change associated with the M-I. A small struc-

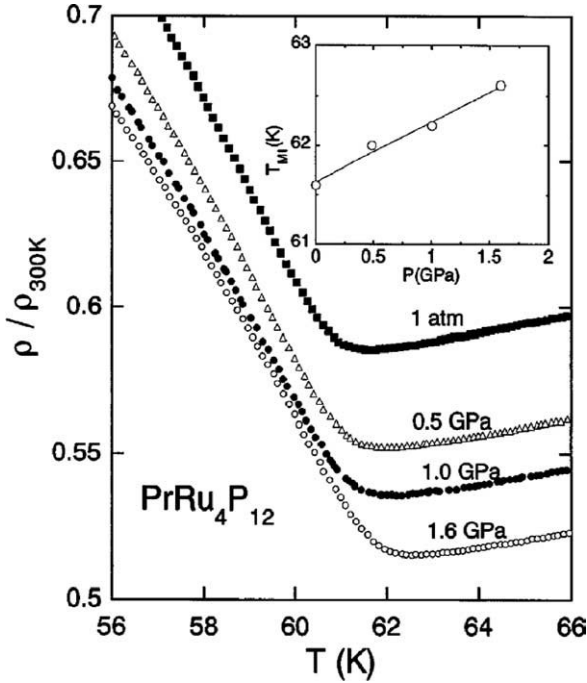


Fig. 15. Normalized resistivity of $\text{PrRu}_4\text{P}_{12}$ vs. temperature at pressures from 1 atm to 1.6 GPa (Sekine et al., 1997).

tural transition was subsequently detected using electron diffraction in which the space group changes from $Im\bar{3}$ (the skutterudite space group) to probably $Pm\bar{3}$ (Lee et al., 2001). XANES measurements give a Pr valence of +3 for temperatures between 20 and 300 K, suggesting that there is no valence transition associated with the M-I (Lee et al., 1999). The opening of a gap at the Fermi energy (Nanba et al., 1999) is either due to a small displacement of the P atoms in the structure or perhaps charge ordering on the phosphorus (Lee et al., 2001). For temperatures near 60 K, Raman measurements on $\text{PrRu}_4\text{P}_{12}$ indicate the softening of a mode at 380 cm^{-1} that is associated with P vibrations (Sekine et al., 1999). There is a small jump in the thermal expansion coefficient at 63 K ($\approx 5 \times 10^{-7}\text{ K}^{-1}$) that shows no evidence of thermal hysteresis, indicating a second order phase transition. The thermal expansion anomaly is unaffected in magnetic fields up to at least 7 T (Matsuhira et al., 2000). The magnetic susceptibility data follow a Curie–Weiss law at high temperatures with an effective moment of $3.8\mu_B$ and a Weiss temperature of -7 K . The low temperature susceptibility ($< 100\text{ K}$) is complicated by the crystalline electric field at the Pr site that splits the $J = 4\text{ f}$ level (Sekine et al., 1997, 2000c). Heat capacity data suggest that the ground state of the Pr 4f shell is a T_3 non-Kramers doublet. Antiferromagnetic order likely occurs for $T < 0.35\text{ K}$ (Meisner, 1981).

$\text{PrOs}_4\text{P}_{12}$ is a metallic with a relatively temperature independent resistivity for temperatures between 50 and 300 K. Below 50 K there is a rapid drop in the resistivity similar to that observed in Pr metal or Kondo lattice Ce compounds such as $\text{CeFe}_4\text{Sb}_{12}$ (fig. 9). There is also a small kink in the resistivity at 7 K of unknown origin. The magnetic susceptibility

data follows a Curie–Weiss law at high temperatures with an effective moment of $3.63\mu_B$ and a Weiss temperature of -17 K. There is no evidence for magnetic order above 1 K. Magnetization measurements at 2 K indicate a non-magnetic ground state caused by the crystalline electric field (Sekine et al., 1997).

PrFe₄As₁₂ – only crystallography data have been reported for this compound (see table 1).

PrRu₄As₁₂ is a superconductor below 2.4 K. The resistivity of a polycrystalline sample changes from 1 mΩ cm at room temperature to 0.25 mΩ cm at 3 K (Shirotani et al., 1997).

PrOs₄As₁₂ – only crystallography data have been reported for this compound (see table 1).

PrFe₄Sb₁₂ is likely a metal. Magnetic measurements on polycrystalline samples that were about 90% phase pure indicated ferromagnetic ordering below 5 K with a moment of $1\mu_B$ per formula unit. The only other phase detected using X-ray diffraction was FeSb₂, which has a weak Pauli paramagnetic susceptibility (Dannebrock et al., 1996).

PrRu₄Sb₁₂ is a metal that becomes superconducting below 1 K. Heat capacity data confirm the bulk nature of the superconductivity with $\Delta C/\gamma T_c = 1.87$, which is larger than the 1.43 value expected from BCS theory. Values for Θ_D and γ are 232 K and 59 mJ/mol K², respectively. The magnetic susceptibility data indicates a non-magnetic ground state for the Pr⁺³ ions and a substantial crystal field splitting greater than 125 K (Takeda and Ishikawa, 2000b).

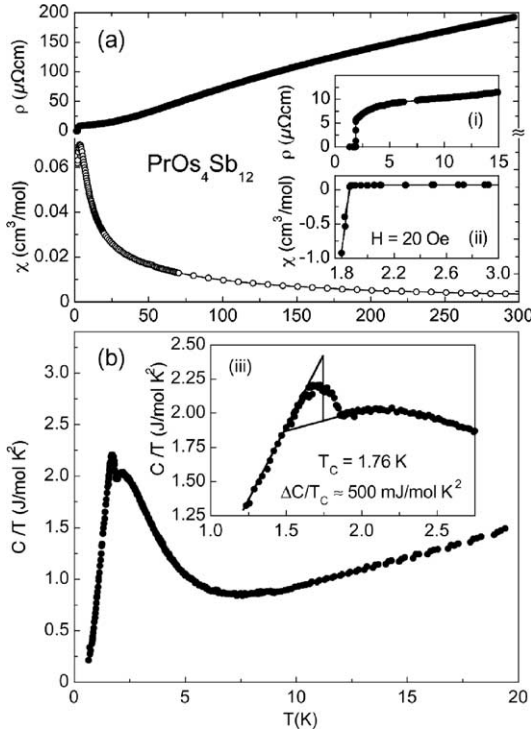


Fig. 16. (a) Resistivity and magnetic susceptibility, and (b) heat capacity data for PrOs₄Sb₁₂ (E.D. Bauer et al., 2002).

$\text{PrOs}_4\text{Sb}_{12}$ is the first known example of a heavy-fermion superconductor containing Pr (E.D. Bauer et al., 2002). Heavy-fermion behavior is inferred by the size of the jump in the heat capacity at $T_c = 1.76$ K and by the slope of the critical field near T_c . Both analyses suggest $\gamma \approx 350$ mJ/mol K² and $m^* \approx 100 m_e$. The resistivity, magnetic susceptibility and heat capacity data are shown in fig. 16. The analysis of the data is complicated by the crystal electric field (CEF) splitting of the Pr levels 4f levels. The resistivity drops by almost a factor of 2 between 7 K and the onset of the superconducting transition at 1.76 K. In many lanthanide compounds this drop is often indicative of low lying CEF levels. The broad Schottky like peak at 2.2 K is also consistent with this hypothesis. Quantitative fits to the magnetic susceptibility data plus an analysis of inelastic neutron scattering (Maple et al., 2002) and heat capacity data imply the $J = 4$ Pr⁺³ level is split into a non-magnetic Γ_3 doublet ground state, a Γ_5 triplet at 8.2 K, a Γ_4 triplet at 133 K and a Γ_1 singlet at 320 K above the ground state. Heavy fermion behavior likely arises in this compound due to the interaction between the charge on the conduction electrons and fluctuations of the Pr⁺³ electric quadrupole moments associated with the Γ_3 doublet ground state. The effect of Pr⁺³ quadrupole fluctuations on the superconductivity of $\text{PrOs}_4\text{Sb}_{12}$ is an open question.

8. Nd filled skutterudites

$\text{NdFe}_4\text{P}_{12}$ is metallic and orders ferromagnetically below 2 K (Torikachvili et al., 1987). The resistivity decreases monotonically from a value of ≈ 150 $\mu\Omega$ cm at room temperature to ≈ 25 $\mu\Omega$ cm at 30 K. Below 30 K the resistivity increases with decreasing temperature (fig. 17) until the ferromagnetic phase transition is reached at 2 K. Below this transition the resistivity decreases as T^4 , rather than the T^2 expected from magnon scattering (Sato et al., 2000a, 2000b). The heat capacity data below 2 K decreases as T^3 rather than the $T^{3/2}$ expected for a simple ferromagnet (Torikachvili et al., 1987). Both the heat capacity data and the resistivity

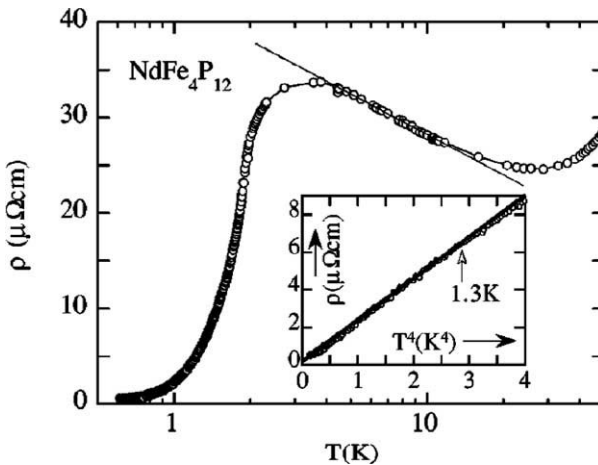


Fig. 17. Low temperature resistivity data for $\text{NdFe}_4\text{P}_{12}$ (Sato et al., 2000b).

can be understood if the magnon energy is linear in wavevector k rather than proportional to k^2 (Sato et al., 2000a, 2000b). The magnetic susceptibility follows a Curie–Weiss law for temperatures between 180 and 300 K with an effective moment of $3.53\mu_B$, close to the Nd^{+3} free ion value of $3.62\mu_B$. Below 150 K the positive curvature in the susceptibility indicates the effects of the CEF. Neutron scattering measurements have confirmed the ferromagnetic ordering of the Nd moments below 2 K (Keller et al., 2001). The ordered moment was found to be $1.6\mu_B$ at 1.5 K. De Hass–van Alfen measurements on $\text{NdFe}_4\text{P}_{12}$ crystals showed a Fermi surface similar to $\text{LaFe}_4\text{P}_{12}$ except for the splitting of the dHvA branches due to the ferromagnetic exchange interaction (Sugawara et al., 2000).

$\text{NdRu}_4\text{P}_{12}$ is a metal that becomes ferromagnetic below 1.5 K (Sekine et al., 1998). Room temperature Raman data have been reported for this compound (Sekine et al., 1998). Three distinct Raman modes at 370, 385, and 415 cm^{-1} were observed, but there was no detailed analysis of exactly which vibrations should be associated with these modes.

$\text{NdOs}_4\text{P}_{12}$ – only crystallography data have been reported for this compound (see table 1).

$\text{NdFe}_4\text{As}_{12}$ – only crystallography data have been reported for this compound (see table 1).

$\text{NdRu}_4\text{As}_{12}$ – has not been synthesized.

$\text{NdOs}_4\text{As}_{12}$ – only crystallography data have been reported for this compound (see table 1).

$\text{NdFe}_4\text{Sb}_{12}$ – only crystallography data have been reported for this compound (see table 1).

$\text{NdRu}_4\text{Sb}_{12}$ is metallic and undergoes some type of magnetic transition near 1.3 K. The magnetic susceptibility follows a Curie–Weiss law above 50 K with an effective moment of $3.45\mu_B$ and a Weiss temperature of -28 K . Crystal fields likely effect the susceptibility and magnetic interactions for temperatures below 50 K. Low temperature heat capacity data confirm the bulk nature of the magnetic transition (Takeda and Ishikawa, 2000b).

$\text{NdOs}_4\text{Sb}_{12}$ may undergo a displacive-type phase transition at -86°C in which the Nd atoms freeze at off center positions (Evers et al., 1995). This transition was proposed on the basis of scanning calorimetry measurements and the huge room temperature value for the Nd atomic displacement parameter ($B_{\text{eq}} = 4\text{ \AA}^2$).

9. Sm filled skutterudites

$\text{SmFe}_4\text{P}_{12}$ is a metal that shows Van Vleck paramagnetism (Jeitschko et al., 2000).

$\text{SmRu}_4\text{P}_{12}$ undergoes a metal to insulator transition in conjunction with antiferromagnetic ordering at 16 K (Sekine et al., 1998).

$\text{SmFe}_4\text{Sb}_{12}$ is metallic and orders ferromagnetically for temperatures below 45 K with a relatively small saturation moment of $0.7\mu_B$ (Dannebrock et al., 1996).

$\text{SmRu}_4\text{Sb}_{12}$ and $\text{SmOs}_4\text{Sb}_{12}$ – only crystallography data have been reported for these compounds (see table 1).

10. Eu filled skutterudites

$\text{EuFe}_4\text{P}_{12}$ is metallic and orders ferromagnetically for temperatures below 100 K (Grandjean et al., 1984). The effective moment, as determined from the high temperature magnetic sus-

ceptibility data, is $6.2\mu_B$ per formula unit which is lower than the value expected for Eu^{+2} of $7.94\mu_B$. The hyperfine parameters as determined from Mössbauer spectroscopy are unusual (Grandjean et al., 1983). The value of the Eu isomer shift in $\text{EuFe}_4\text{P}_{12}$ is -6 mm/s and the isomer shift is independent of temperature from 4 K to 300 K. An isomer shift of -6 mm/s is near the limit for Eu^{+2} compounds which suggests the possibility of a Eu valence that fluctuates between Eu^{+2} and Eu^{+3} configurations. If the Eu^{+3} and Eu^{+2} configurations are energetically degenerate, the average valence is determined by the degeneracy of each level, which implies a temperature independent valence of about $3 - 8/9 = 2.11$. Magnetic order in a mixed valence Eu compound would be extremely interesting. XANES measurements would be helpful in deciding if the Eu valence is intermediate in this material. The reduced moment for Eu^{+2} , however, may simply indicate an incomplete filling of the lanthanide site.

$\text{EuRu}_4\text{P}_{12}$ is metallic and orders ferromagnetically for temperatures below 18 K (Grandjean et al., 1983; Sekine et al., 2000b). The saturation moment is about 10% smaller than the Eu^{+2} value of $7\mu_B$ which could imply an intermediate Eu valence or an incomplete filling of the lanthanide site. The value of the Eu isomer shift in $\text{EuRu}_4\text{P}_{12}$ is -9.3 mm/s, which is compatible with Eu^{+2} in a metallic compound.

$\text{EuFe}_4\text{Sb}_{12}$ is metallic and ferromagnetic below 84 K (Dannebrock et al., 1996; E. Bauer et al., 2001a, 2001b). The low temperature saturation moment, however, is only 64% ($4.5\mu_B$) of the Eu^{+2} value of $7\mu_B$ (Dannebrock et al., 1996; E. Bauer et al., 2001a, 2001b). Part of the decrease is due to the incomplete filling of the Eu site (E. Bauer et al., 2001a, 2001b) which was estimated to be 84%. The Eu Mössbauer isomer shift is -11.7 mm/s and is temperature independent, which clearly indicates divalent Eu. The remainder of the decrease in the saturation moment was attributed to some type of ferrimagnetism, possibly involving the Fe (E. Bauer et al., 2001a, 2001b). The electrical resistivity is sensitive to the exact filling of the lanthanide site and the presence of impurity phases. The room temperature resistivity has been reported as low as $38 \mu\Omega \text{ cm}$ (E. Bauer et al., 2001a, 2001b) to $420 \mu\Omega \text{ cm}$ (Kuznetsov and Rowe, 2000). The samples of Kuznetsov and Rowe appear to be of higher quality and phase purity. The room temperature Seebeck coefficient is $\approx 60 \mu\text{V/K}$ increasing to $\approx 120 \mu\text{V/K}$ at 800 K (Kuznetsov and Rowe, 2000). The thermoelectric properties of $\text{EuFe}_4\text{Sb}_{12}$ are not promising.

$\text{EuRu}_4\text{Sb}_{12}$ is metallic and becomes ferromagnetic for temperatures below 3.3 K (Takeda and Ishikawa, 2000b). The low temperature saturation moment is about $6.2\mu_B$, 89% of the Eu^{+2} value. Low temperature heat capacity measurements indicate that the magnetic entropy removed due to magnetic order is also only about 90% of its expected value (Rln8). It is likely that the lanthanide site is not completely filled in this compound although mixed valence behavior can not be ruled out with the available data.

11. Gd filled skutterudites

$\text{GdFe}_4\text{P}_{12}$ is metallic and a soft ferromagnet with a Curie temperature of 22 K (Jeitschko et al., 2000).

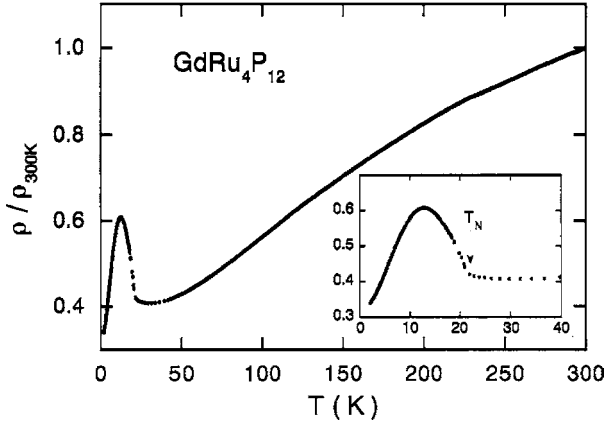


Fig. 18. Resistivity vs. temperature for a polycrystalline sample of $\text{GdRu}_4\text{P}_{12}$ synthesized using high pressures and temperatures (Sekine et al., 2000a).

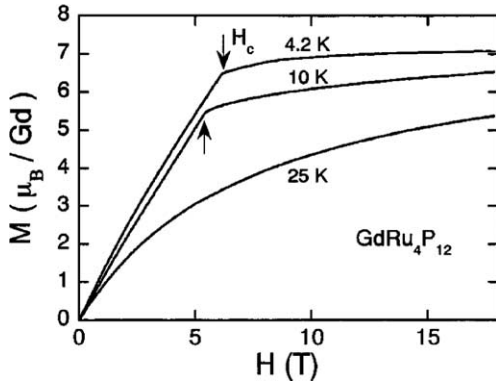


Fig. 19. Low temperature magnetization curves for $\text{GdRu}_4\text{P}_{12}$ that indicate a field induced phase transition (Sekine et al., 2000a).

$\text{GdRu}_4\text{P}_{12}$ is metallic for temperatures between 30 and 300 K, but undergoes an unusual phase transition near 20 K (fig. 18) (Sekine et al., 2000a). The magnetic susceptibility follows a Curie–Weiss law at high temperatures with effective moment of $8.04\mu_B$ and a Weiss temperature of +22 K, which suggests ferromagnetic interactions. Below 22 K, however, the magnetization data are more consistent with a strange type of antiferromagnetic ordering. The magnetization data also indicate a field-induced phase transition at low temperatures for magnetic fields $\approx 5\text{--}6$ T (fig. 19).

12. Tb filled skutterudites

$\text{TbRu}_4\text{P}_{12}$ is metallic with unusual phase transitions at 20 K and 10 K (Sekine et al., 2000a). The resistivity data from $\text{TbRu}_4\text{P}_{12}$ is similar to that of $\text{GdRu}_4\text{P}_{12}$ shown in fig. 18. The high temperature magnetic susceptibility data indicate ferromagnetic interactions (Weiss temperature ≈ 8 K) but low temperature data are more consistent with some type of antiferromagnetic order (fig. 20). Low temperature magnetization data indicate two metamagnetic phase tran-

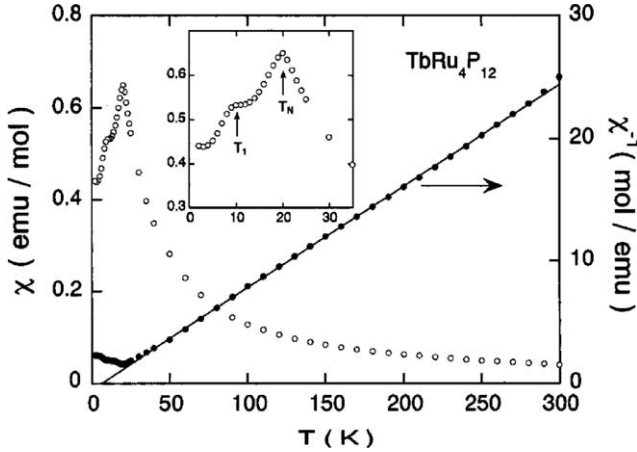


Fig. 20. Inverse magnetic susceptibility of $\text{TbRu}_4\text{P}_{12}$ vs. temperature measured at $H = 1$ T. Inset shows an enlarged view of susceptibility data below 20 K (Sekine et al., 2000a).

sitions. It is possible that the unusual phase transitions at about 20 K in both $\text{GdRu}_4\text{P}_{12}$ and $\text{TbRu}_4\text{P}_{12}$ are related to the freezing of the lanthanide atoms in off-center positions.

13. Yb filled skutterudites

$\text{YbFe}_4\text{Sb}_{12}$ was first synthesized by Dilley et al. (1998). Measurements of the lattice constant, magnetization, resistivity and heat capacity suggest an intermediate valence for the Yb ions. XANES measurements yield a Yb valence of 2.68 (Leithe-Jasper et al., 1999). The electronic specific heat coefficient is estimated to be $\gamma = 140$ mJ/molK² which indicates that the effective mass of the conduction electrons is moderately enhanced at low temperatures. The characteristic temperature, T^* , for the Yb valence fluctuations is estimated to be 50 K (see fig. 9a). The Wilson–Sommerfeld ratio, R_w , is about 2.6 in good agreement with the value of $R_w = 2$ expected for a spin 1/2 Kondo effect. The room temperature value of the resistivity is ≈ 450 $\mu\Omega$ cm as determined from resistivity and optical measurements (Dordevic et al., 2001) and decreases to ≈ 40 $\mu\Omega$ cm at 2 K. Optical measurements also are able to directly measure the pseudogap, $\Delta = 90$ cm⁻¹, created by the hybridization between the Yb 4f states and the extended conduction band states (fig. 21). The mass enhancement scales as $m^*/m_e = (\Delta/T^*)^2$ as predicted by theory (Millis et al., 1987). The thermoelectric properties of $\text{YbFe}_4\text{Sb}_{12}$ were investigated by Dilley et al. (1998, 2000a, 2000b), and Kuznetsov and Rowe (2000). The maximum estimated value of ZT is 0.4 at 670 K.

14. Filled skutterudite thermoelectrics

14.1. Introduction to thermoelectric materials and devices

As mentioned in sect. 1, in 1996 it was found that some of the lanthanide antimony-based skutterudites had excellent thermoelectric properties above room temperature (Sales et al., 1996;

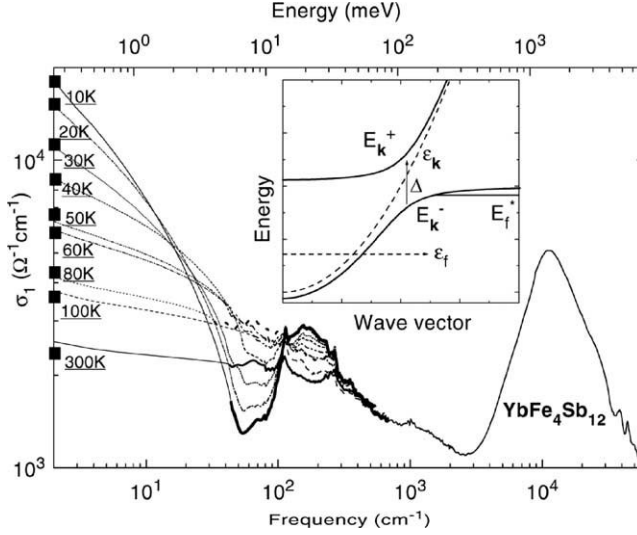


Fig. 21. Real part of the conductivity of $\text{YbFe}_4\text{Sb}_{12}$. The symbols on the left axis represent dc values at different temperatures. Below T^* (≈ 50 K), a narrow peak at zero frequency and a gap-like feature at ≈ 18 meV gradually develop. Inset: Renormalized band structure calculated from the Anderson lattice Hamiltonian. $\varepsilon_{\mathbf{k}}$ and $\varepsilon_{\mathbf{f}}$ denote bands of free carriers and localized electrons, respectively. At low temperatures a direct gap Δ opens. The Fermi level, $E_{\mathbf{F}}^*$ is near the top of the lower band, $E_{\mathbf{k}}^-$, resulting in hole-like character and enhanced effective mass of the quasiparticles (Dordevic et al., 2001).

Fleurial et al., 1996). This discovery greatly increased the interest in these materials for thermoelectric applications. In addition to the stoichiometric filled skutterudite compounds of the form RM_4X_{12} , a large number of related alloys were also investigated as possible thermoelectric materials. Most of the research on lanthanide skutterudites in the context of thermoelectric applications has been reviewed recently by Uher (2001), Nolas et al. (1999), and Sales (1998) and hence only a brief summary of the thermoelectric research will be highlighted in this section.

In a solid that conducts both heat and electricity, the thermal and electrical currents are coupled together. This thermoelectric coupling can be used to construct devices that act as refrigerators, power generators or temperature sensors. The devices work because the electrons or holes in a conducting solid also carry heat as well as electrical charge. The electrical carriers are the “working fluid” in a thermoelectric refrigerator. Thermoelectric devices are attractive for many applications as they have no moving parts (except electrons and holes), use no liquid refrigerant and last indefinitely. The major disadvantage of thermoelectric devices is poor efficiency.

The efficiency of a thermoelectric solid is found to depend on material properties through the dimensionless parameter ZT :

$$ZT = \frac{TS^2}{\rho\kappa} \quad (1)$$

where T is the absolute temperature, ρ is the electrical resistivity, S is the Seebeck coefficient, and κ is the total thermal conductivity. The total thermal conductivity is often broken up into two parts, $\kappa = \kappa_e + \kappa_L$ where κ_e is the heat carried by the electrons and holes and κ_L is the heat carried by the lattice. Z is defined as the figure of merit and ZT is often referred to as the dimensionless figure of merit. For power generation the efficiency is defined as heat in

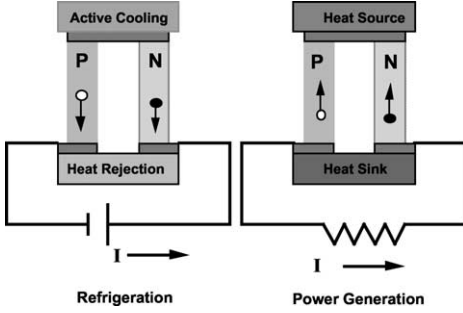


Fig. 22. A single thermoelectric couple is illustrated that has been configured for refrigeration or power generation. The labels “p” (positive) and “n” (negative) refer to the sign of the charge carriers in each leg (open circles correspond to holes and filled circles to electrons). Refrigeration is possible in these devices because electrons (or holes) carry heat, and hot electrons (holes) can be forced away from the cold end of the device by the battery. If a temperature difference is externally imposed on the device, useful power can be extracted.

divided by work out and is given by:

$$\text{Efficiency} = \frac{(T_h - T_{co})(\Gamma - 1)}{(T_{co} + \Gamma T_h)} \quad (2)$$

where T_{co} (T_h) is the temperature of the cold (hot) end and $\Gamma = (1 + ZT)^{1/2}$ varies with the average temperature T . For refrigeration, efficiency is defined as the heat pumped out divided by the work in and is called the Coefficient of Performance (COP). The COP can be greater than 1 and is given by:

$$\text{COP} = \frac{(\Gamma T_{co} - T_h)}{[(T_h - T_{co})(1 + \Gamma)]} \quad (3)$$

For $ZT \gg 1$, Carnot efficiency is obtained for power generation and the Carnot limit to the COP is obtained for refrigeration. Materials currently used in thermoelectric devices have ZT values between 0.4 and 1.0.

All thermoelectric devices are composed of thermoelectric couples such as illustrated in fig. 22. Each leg of the couple is a doped semiconductor (or semimetal) with one p-type and one n-type leg. P-type (n-type) means that the dominant charge carriers are positive (negative). One side of the couple is thermally and electrically shorted together using a metal like copper (brown region). Electrical and thermal contact to a heat sink and the battery or load are made through copper pads at the open end of the couple (brown regions). Since the electrons and holes in a material carry heat, a battery can be used to force the hot electrons and holes away from the cold end of the device resulting in cooling of the cold end. If the direction of the current is reversed, the hot and cold ends are also reversed. If a temperature gradient is imposed across the thermoelectric couple, useful power can be extracted. In an actual thermoelectric device, typically several tens of these couples are connected together in series. For good general reviews of thermoelectric devices, materials and theory refer to Rowe (1995), Goldsmid (1986), Mahan et al. (1997), Mahan (1998), Sales (2002), and Nolas et al. (2001).

14.2. Electron crystals and phonon glasses

In an ideal thermoelectric material the holes and electrons should have high mobilities and high effective masses. A high mobility and a high effective mass result in a large value of

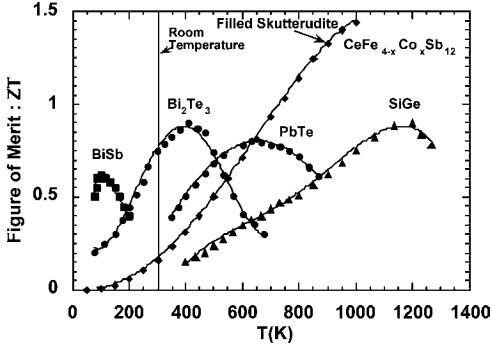


Fig. 23. ZT vs. T for several state-of-the-art thermoelectric materials and for a filled skutterudite with $x \approx 1$. (Figure from T.M. Tritt, unpublished.)

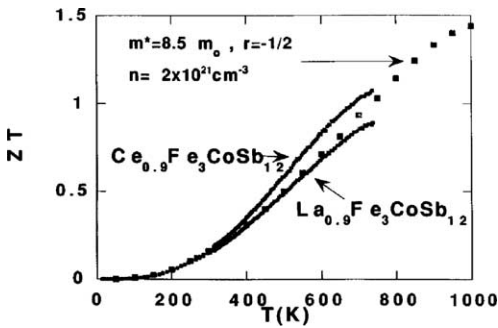


Fig. 24. ZT vs. T for two rare-earth-filled skutterudites. Also shown are the results of a model calculation (squares) (Sales et al., 1997).

S^2/ρ (see eq. (1) and Goldsmid, 1986). High mobilities are typically found in crystals with a high degree of structural perfection. The ideal thermoelectric material should also have the lowest possible lattice thermal conductivity κ_L . The lowest possible value of κ_L for a particular solid is that of a glass with the same chemical composition, κ_{\min} (Slack, 1979). The ideal thermoelectric material should therefore conduct electricity like a crystal but conduct heat like a glass. The skutterudite CoSb_3 has good electronic properties and can be doped n- or p-type (Dudkin and Abrikosov, 1959; Caillat et al., 1996). However, the room temperature lattice thermal conductivity of CoSb_3 is ≈ 10 W/mK, which is an order of magnitude too large for a good thermoelectric material. Slack (1995) suggested filling the voids in the skutterudite structure with weakly bound atoms that “rattle” about their equilibrium positions. He reasoned that heavy “rattlers” with low Einstein temperatures would be effective in scattering the low frequency acoustic phonons that carry most of the heat in a solid. The “rattlers” should therefore dramatically lower κ_L . What was not clear, however, was how the “rattlers” would alter the electronic conduction. Although the electronic properties of the skutterudite antimonides were somewhat degraded by the presence of various rattlers, there was an overall increase in ZT (Morelli and Meisner, 1995; Sales et al., 1996; Fleurial et al., 1996; Nolas et al., 2000; Tang et al., 2001). Representative thermoelectric data from various filled skutterudite antimonides are shown in figs. 23–26. Some of the arsenides and phosphides have been investigated for thermoelectric applications (Watcharapasorn et al., 1999, 2002),

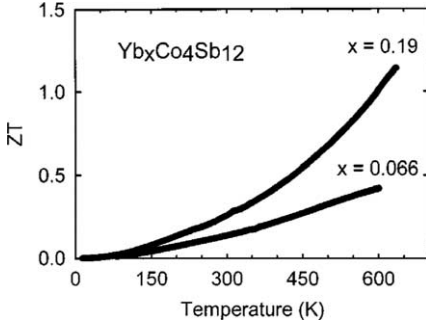


Fig. 25. ZT vs. T for two Yb filled skutterudite samples (Nolas et al., 2000).

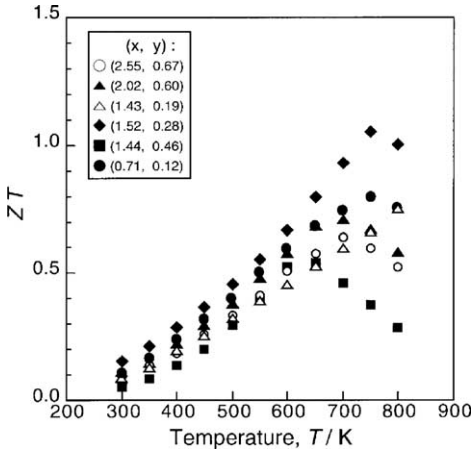


Fig. 26. ZT vs. T for several filled skutterudite samples with the composition $Ce_yFe_xCo_{4-x}Sb_{12}$ (Tang et al., 2001).

but in general these materials are limited by their κ_L values, which are significantly higher than the values for the antimonides. This is not surprising since a lower average mass usually implies a higher sound velocity and a higher κ_L .

14.3. Future of filled skutterudites as thermoelectrics

The filled skutterudite antimonides appear to represent excellent examples of electron–crystal, phonon–glass materials. The incoherent rattling of the loosely bound lanthanide atoms in these materials is inferred from the large values of the ADP parameters obtained in single-crystal structure refinements. This rattling lowers the thermal conductivity at room temperature to values within two to three times κ_{\min} .

The electrical transport in the filled skutterudites is altered by the presence of the rattlers. Relative to the analogous unfilled compounds, the filled skutterudites exhibit larger effective masses and smaller mobilities. Good overall electrical transport is maintained as indicated by the large values of ZT at elevated temperatures (figs. 23–26). The high carrier concentrations in the filled skutterudites are due mostly to the fraction of the lanthanide sites that remain

empty in samples prepared using equilibrium synthesis methods. A simple semiconductor transport model successfully reproduces most of the qualitative features of the resistivity and Seebeck data from these materials (Sales et al., 1997). By varying the extrinsic carrier concentration in the filled skutterudites, this model yields a maximum value for ZT of 1.4 at 1000 K, and a maximum ZT value of 0.3 at 300 K.

The ZT values of the filled skutterudites are too small for room temperature applications. The relatively large band gap of these compounds (≈ 0.6 eV) makes it unlikely that further research will result in a skutterudite-based thermoelectric material with properties better than the Bi_2Te_3 -based materials currently in use near room temperature (see fig. 23). Only at temperatures in the 600–900 K temperature range are the thermoelectric properties of the filled skutterudite antimonides of interest for use in power generation applications. Thermoelectric generators using filled skutterudite antimonides are being investigated by T. Caillat and collaborators at the Jet Propulsion Laboratory. These devices are of interest to NASA as a source of electrical power for deep space missions such as the Cassini and Voyager probes. Filled skutterudites may also be of practical use in the thermoelectric conversion of waste heat into useful electricity.

The filled skutterudite antimonides have demonstrated the validity of the “electron–crystal, phonon–glass” idea in the design of new thermoelectric materials for operation at elevated temperatures. There are many other crystal structures and compounds that contain atomic cages large enough to incorporate additional atoms. It is believed that the filled skutterudite antimonides only represent a small fraction of a more general class of “rattling semiconductors” and that some of these materials will undoubtedly have high values of ZT at room temperature.

15. Concluding remarks

A major theme of contemporary solid state physics is focused on understanding the correlated behavior of electrons in solids. The challenge of this area was succinctly summarized by Anderson’s title “more is different” (1972). The low temperature properties of the lanthanide-filled skutterudites touch on many of the exciting topics at the frontier of correlated electron physics. $\text{CeFe}_4\text{Sb}_{12}$ and $\text{YbFe}_4\text{Sb}_{12}$ are moderately heavy fermion metals. $\text{CeRu}_4\text{Sb}_{12}$ exhibits non-Fermi liquid behavior and may be near a ferromagnetic quantum critical point. $\text{PrOs}_4\text{Sb}_{12}$ is the first example of a Pr compound that exhibits both superconductivity and heavy fermion behavior. $\text{PrRu}_4\text{P}_{12}$ and $\text{SmRu}_4\text{P}_{12}$ each undergo a metal-to-insulator transition and antiferromagnetic order. $\text{PrFe}_4\text{P}_{12}$ is an extremely unusual material in which quadrupolar order (QO) and heavy fermion ground states are extremely close in energy. At low temperatures a magnetic field (≈ 4 T) can drive $\text{PrFe}_4\text{P}_{12}$ between the two ground states. The density of states in $\text{PrFe}_4\text{P}_{12}$ is remarkably sharp in energy as evidenced by a two order of magnitude change in the Hall coefficient below 5 K and a huge value for S at 5 K of -130 $\mu\text{V}/\text{K}$. Most of the La-filled skutterudites and two of the Pr-filled skutterudites are superconductors with a maximum T_c of 10.3 K for $\text{LaRu}_4\text{As}_{12}$. Several of the Ce-filled skutterudites are narrow

gap semiconductors (also called Kondo insulators) where the gap is created by a strong hybridization between the Ce 4f level and the transition metal and pnictogen states near the Fermi energy. The Nd, Eu, Gd and Tb filled skutterudites order magnetically at temperatures ranging from 2 K for NdFe₄P₁₂ to 100 K for EuFe₄P₁₂. The coupling between the lanthanide magnetic moments and the conduction electrons is large in these compounds. This large coupling results in unusual peaks in electrical transport data near the onset of magnetic ordering, and in some cases multiple magnetic transitions. Finally, the thermoelectric figures of merit for the La, Ce and Yb filled skutterudites are among the highest values reported for any material at elevated temperatures (600–1000 K). It is hoped that this article has captured some of the excitement generated by the recent research on the lanthanide filled skutterudites.

Acknowledgements

It is a pleasure to thank Peter Khalifah for many constructive comments and suggestions concerning both the science and the presentation of the work summarized in this chapter. Oak Ridge National Laboratory is managed by UT-Battelle, LLC, for the U.S. Department of Energy under Contract No. DE-AC05-00OR22725.

References

- Anderson, P.W., 1972. *Science* **177**, 393.
- Aoki, Y., Namiki, T., Masuda, T.D., Abe, K., Sugawara, H., Sato, H., 2002. *Phys. Rev. B* **65**, 06446.
- Bauer, E., Berger, S., Galatanu, A., Michor, H., Paul, C., Hilscher, G., Tran, V.H., Grytsiv, A., Rogl, P., 2001a. *J. Magn. Magn. Mater.* **226–230**, 674.
- Bauer, E., Berger, S., Galatanu, A., Galli, M., Michor, H., Hilscher, G., Paul, Ch., Ni, B., Abd-Elmeguid, M.M., Tran, V.H., et al., 2001b. *Phys. Rev. B* **63**, 224414.
- Bauer, E.D., Chau, R., Dilley, N.R., Maple, M.B., Mandrus, D., Sales, B.C., 2000. *J. Phys. Cond. Mater.* **12**, 1261.
- Bauer, E.D., Slebarski, A., Dickey, R.P., Freeman, E.J., Sirvent, C., Zapf, V.S., Dilley, N.R., Maple, M.B., 2001a. *J. Phys. Cond. Mater.* **13**, 5183.
- Bauer, E.D., Slebarski, A., Freeman, E.J., Sirvent, C., Maple, M.B., 2001b. *J. Phys. Cond. Mater.* **13**, 4495.
- Bauer, E.D., Frederick, N.A., Ho, P.-C., Zapf, V.S., Maple, M.B., 2002. *Phys. Rev. B* **65**, 100506.
- Braun, D.J., Jeitschko, W., 1980a. *J. Less Common Metals* **72**, 147.
- Braun, D.J., Jeitschko, W., 1980b. *J. Solid State Chem.* **32**, 357.
- Braun, D.J., Jeitschko, W., 1980c. *J. Less Common Metals* **76**, 33.
- Caillat, T., Borshchevsky, A., Fleurial, J.-P., 1996. *J. Appl. Phys.* **80**, 4442.
- Chakoumakos, B.C., Sales, B.C., Mandrus, D., Keppens, V., 1999. *Acta Crystall. B* **55**, 341.
- Chen, B., Jun-Hao, X., Uher, C., Morelli, D.T., Meisner, G.P., Fleurial, J.-P., Caillat, T., Borshchevsky, A., 1997. *Phys. Rev. B* **55**, 1476.
- Corbett, J.D., 1985. *Chem. Rev.* **85**, 383.
- Dannebrock, M.E., Evers, C.B.H., Jeitschko, W., 1996. *J. Phys. Chem. Solids* **57**, 381.
- Delong, L.E., Meisner, G.P., 1985. *Solid State Commun.* **53**, 119.
- Dilley, N.R., Freeman, E.J., Bauer, E.D., Maple, M.B., 1998. *Phys. Rev. B* **58**, 6287.
- Dilley, N.R., Bauer, E.D., Maple, M.B., Sales, B.C., 2000a. *J. Appl. Phys.* **88**, 1948.
- Dilley, N.R., Bauer, E.D., Maple, M.B., Dordevic, S., Basov, D.N., Freibert, F., Darling, T.W., Migliori, A., Chakoumakos, B.C., Sales, B.C., 2000b. *Phys. Rev. B* **61**, 4608.
- Dordevic, S.V., Dilley, N.R., Bauer, E.D., Basov, D.N., Maple, M.B., 1999. *Phys. Rev. B* **60**, 11321.
- Dordevic, S.V., Basov, D.N., Dilley, N.R., Bauer, E.D., Maple, M.B., 2001. *Phys. Rev. Lett.* **86**, 684.

- Dudkin, L.D., Abrikosov, N.Kh., 1959. *Sov. Phys.-Solid State* **1**, 126.
- Evers, C.B.H., Boonk, L., Jeitschko, W., 1994. *Z. Anorg. Allg. Chem.* **620**, 1028.
- Evers, C.B.H., Jeitschko, W., Boonk, L., Braun, D.J., Ebel, T., Scholz, U.D., 1995. *J. Alloys and Compounds* **224**, 184.
- Feldman, J.L., Singh, D.J., Mazin, I.I., Sales, B.C., Mandrus, D., 2000. *Phys. Rev. B* **61**, R9209.
- Fleurial, J.-P., Borshchevsky, A., Caillat, T., Morelli, D.T., Meisner, G.P., 1996. In: *Proc. 15th International Conference on Thermoelectrics*. In: *IEEE Catalog*, Vol. **96TH8169**. Piscataway, NJ, p. 91.
- Gajewski, D.A., Dilley, N.R., Bauer, E.D., Freeman, E.J., Chau, R., Maple, M.B., Mandrus, D., Sales, B.C., Lacerda, A.H., 1998. *J. Phys. Cond. Mater.* **10**, 6973.
- Goldsmid, H.J., 1986. *Electronic Refrigeration*. Pion Ltd., London.
- Grandjean, F., Gerard, A., Hodges, J., Braun, D.J., Jeitschko, W., 1983. *Hyperfine Interactions* **16**, 765.
- Grandjean, F., Gerard, A., Braun, D.J., Jeitschko, W., 1984. *J. Phys. Chem. Solids* **45**, 877.
- Grandjean, F., Long, G.J., Cortes, R., Morelli, D.T., Meisner, G.P., 2000. *Phys. Rev. B* **62**, 12569.
- Harima, H., 1998. *J. Magn. Magn. Mater.* **177–181**, 321.
- Harima, H., 2000. *Progress of Theoretical Physics, Supplement No. 138*, 117–118.
- Hornbostel, M.D., Hyer, E.J., Edvalson, J.H., Johnson, D.C., 1997a. *Inorg. Chem.* **36**, 4270.
- Hornbostel, M.D., Hyer, E.J., Thiel, J., Johnson, D.C., 1997b. *J. Am. Chem. Soc.* **119**, 2665.
- Jeitschko, W., Braun, D., 1977. *Acta Crystall. B* **33**, 3401.
- Jeitschko, W., Foecker, A.J., Paschke, D., Dewalsky, M.V., Evers, C.B.H., Kunnen, B., Lang, A., Kotzyba, G., Rodewald, U.C., Moller, M.H., 2000. *Z. Anorg. Allg. Chemie* **626**, 1112.
- Kaiser, J.W., Jeitschko, W., 1999. *J. Alloys and Compounds* **291**, 66.
- Kanai, K., Takeda, N., Nozawa, S., Yokoya, T., Ishikawa, M., Shin, S., 2002. *Phys. Rev. B* **65**, 041105(R).
- Keller, L., Fischer, P., Herrmannsdorfer, T., Donni, A., Sugawara, H., Matsuda, T.D., Abe, K., Aoki, Y., Sato, H., 2001. *J. Alloys and Compounds* **323–324**, 516.
- Keppens, V., Mandrus, D., Sales, B.C., Chakoumakos, B.C., Dai, F., Coldea, R., Maple, M.B., Gajewski, D.A., Freeman, E.J., Bennington, S., 1998. *Nature* **395**, 876.
- Kuznetsov, V.L., Rowe, D.M., 2000. *J. Phys. Cond. Mater.* **12**, 7915.
- Lee, C.H., Oyanagi, H., Sekine, C., Shirotani, I., Ishii, M., 1999. *Phys. Rev. B* **60**, 13253.
- Lee, C.H., Matsuhata, H., Yamamoto, A., Ohta, T., Takazawa, H., Ueno, K., Sekine, C., Shirotani, I., Hirayama, T., 2001. *J. Phys. Cond. Mater.* **13**, L45.
- Leithe-Jasper, A., Kaczorowski, D., Rogl, P., Bogner, J., Reissner, M., Steiner, W., Wiesinger, W., Godart, C., 1999. *Solid State Commun.* **109**, 395.
- Long, G.J., Hautot, D., Grandjean, F., Morelli, D.T., Meisner, G.P., 1999. *Phys. Rev. B* **60**, 7410.
- Mahan, G., Sales, B.C., Sharp, J.W., 1997. In: *Physics Today*, March Issue, pp. 42–47.
- Mahan, G.D., 1998. In: *Solid State Physics*, Vol. **51**. Academic Press, San Diego, pp. 81–157 (Chapter 2).
- Maple, M.B., Ho, P.-C., Zapf, V.S., Frederick, N.A., Bauer, E.D., Yuhasz, W.M., Woodward, F.M., Lynn, J.W., 2002. *J. Phys. Soc. Japan (supplement)* **71**, 23.
- Matsuda, T.D., Okada, H., Sugawara, H., Aoki, Y., Sato, H., Andreev, A.V., Shiokawa, Y., Sechovsky, V., Honma, T., Yamamoto, E., et al., 2000. *Physica B* **281–282**, 220.
- Matsuhira, K., Takikawa, T., Sakakibara, T., Sekine, C., Shirotani, I., 2000. *Physica B* **281–282**, 298.
- Meisner, G.P., 1981. *Physica B* **108**, 763.
- Meisner, G.P., Torikachvili, M.S., Yang, K.N., Maple, M.B., Guertin, R.P., 1985. *J. Appl. Phys.* **57**, 3073.
- Meisner, G.P., Morelli, D.T., Hu, S., Yang, J., Uher, C., 1998. *Phys. Rev. Lett.* **80**, 3551.
- Millis, A.J., et al., 1987. *Phys. Rev. B* **35**, 3394.
- Morelli, D.T., Meisner, G.P., 1995. *J. Appl. Phys.* **77**, 3777.
- Morelli, D.T., Meisner, G.P., Chen, B., Hu, S., Uher, C., 1997. *Phys. Rev. B* **56**, 7376.
- Muller, U., 1993. *Inorganic Structural Chemistry*. John Wiley, New York.
- Nanba, T., Hayashi, M., Shirotani, I., Sekine, C., 1999. *Physica B* **259–261**, 853.
- Nolas, G.S., Slack, G.A., Caillat, T., Meisner, G.P., 1996a. *J. Appl. Phys.* **79**, 2622.
- Nolas, G.S., Slack, G.A., Morelli, D.T., Tritt, T.M., Ehrlich, A.C., 1996b. *J. Appl. Phys.* **79**, 4002.
- Nolas, G.S., Cohn, J.L., Slack, G.A., 1998. *Phys. Rev. B* **58**, 164.
- Nolas, G.S., Morelli, D.T., Tritt, T.M., 1999. *Ann. Rev. Mater. Sci.* **29**, 89–116.
- Nolas, G.S., Kaeser, M., Littleton, R.T. IV, Tritt, T.M., 2000. *Appl. Phys. Lett.* **77**, 1855.
- Nolas, G.S., Sharp, J., Goldsmid, H.J., 2001. *Thermoelectrics: Basic Principles and New Materials Developments*. Springer Verlag, New York.
- Nordstrom, L., Singh, D.J., 1996. *Phys. Rev. B* **53**, 1103.
- Oftedal, I., 1928. *Z. Kristallogr. A* **66**, 517.

- Ravot, D., Lafont, U., Chapon, L., Tedenac, J.C., Mauger, A., 2001. *J. Alloys and Compounds* **323**, 389.
- Rowe, D.M. (Ed.), 1995. *CRC Handbook of Thermoelectrics*. Chemical Rubber Press, Boca Raton, FL.
- Sales, B.C., Mandrus, D., Williams, R.K., 1996. *Science* **272**, 1325.
- Sales, B.C., Mandrus, D., Chakoumakos, B.C., Keppens, V., Thompson, J.R., 1997. *Phys. Rev. B* **56**, 15081.
- Sales, B.C., 1998. *MRS Bulletin* **23**, 15.
- Sales, B.C., Chakoumakos, B.C., Mandrus, D., Sharp, J.W., 1999. *J. Solid State Chem.* **146**, 528.
- Sales, B.C., Chakoumakos, B.C., Mandrus, D., 2000. *Phys. Rev. B* **61**, 2475.
- Sales, B.C., Mandrus, D., Chakoumakos, B.C., 2001a. In: *Semiconductors and Semimetals*, Vol. **70**. Academic Press, San Diego, pp. 1–36 (Chapter 1).
- Sales, B.C., Chakoumakos, B.C., Jin, R., Thompson, J.R., Mandrus, D., 2001b. *Phys. Rev. B* **63**, 245113.
- Sales, B.C., 2002. *Science* **295**, 1248.
- Sato, H., Abe, Y., Okada, H., Matsuda, T., Sugawara, H., Aoki, Y., 2000a. *Physica B* **281–282**, 306.
- Sato, H., Abe, Y., Okada, H., Matsuda, T., Sugawara, H., Aoki, Y., 2000b. *Phys. Rev. B* **62**, 15125.
- Sekine, C., Uchiumi, T., Shirotani, I., Yagi, T., 1997. *Phys. Rev. Lett.* **79**, 3218.
- Sekine, C., Saito, H., Uchiumi, T., Sakai, A., Shirotani, I., 1998. *Solid State Commun.* **106**, 441.
- Sekine, C., Saito, H., Sakai, A., Shirotani, I., 1999. *Solid State Commun.* **109**, 449.
- Sekine, C., Uchiumi, T., Shirotani, I., Matsuhira, K., Sakakibara, T., Goto, T., Yagi, T., 2000a. *Phys. Rev. B* **62**, 11581.
- Sekine, C., Inoue, M., Inaba, T., Shirotani, I., 2000b. *Physica B* **281–282**, 308.
- Sekine, C., Inaba, T., Shirotani, I., Yokoyama, M., Amit-suka, H., Sakakibara, T., 2000c. *Physica B* **281–282**, 303.
- Sekine, C., Akita, K., Yanase, N., Shirotani, I., Inagawa, I., Lee, Ch.-H., 2001. *Jap. J. Appl. Phys.* **40**, 3326.
- Shenoy, G.K., Noakes, D.R., Meisner, G.P., 1982. *J. Appl. Phys.* **53**, 2628.
- Shirotani, I., Adachi, T., Tachi, K., Todo, S., Nozawa, K., Yagi, T., Kinoshita, M., 1996. *J. Phys. Chem. Solids* **57**, 211.
- Shirotani, I., Uchiumi, T., Ohno, K., Sekine, C., Nakazawa, Y., Kanoda, K., Todo, S., Yagi, T., 1997. *Phys. Rev. B* **56**, 7866.
- Shirotani, I., Uchiumi, T., Sekine, C., Hori, M., Kimura, S., Hamaya, N., 1999. *J. Solid State Chem.* **142**, 146.
- Shirotani, I., Ohno, K., Sekine, C., Yagi, T., Kawakami, T., Nakanishi, T., Takahashi, H., Tang, J., Matsushita, A., Matsumoto, T., 2000. *Physica B* **281–282**, 1021.
- Singh, D.J., Pickett, W.E., 1994. *Phys. Rev. B* **50**, 11235.
- Slack, G.A., 1979. In: *Solid State Physics*, Vol. **34**. Academic Press, New York, p. 1.
- Slack, G.A., 1995. In: *CRC Handbook of Thermoelectrics*. Chemical Rubber Company, Boca Raton, FL, pp. 407–440.
- Sofo, J.O., Mahan, G.D., 1998. *Phys. Rev. B* **58**, 15620.
- Stetson, N.T., Kauzlarich, S.M., Hope, H., 1991. *J. Solid State Chem.* **91**, 140.
- Sugawara, H., Abe, Y., Aoki, Y., Sato, H., Hedo, M., Settai, R., Onuki, Y., Harima, H., 2000. *J. Phys. Soc. Japan* **69**, 2938.
- Sugawara, H., Matsuda, T.D., Abe, K., Aoki, K., Sato, H., Nojiri, S., Inada, Y., Settai, R., Onuki, Y., 2001. *J. Magn. Magn. Mater.* **226**, 48.
- Takeda, N., Ishikawa, M., 2000a. *Physica B* **281–282**, 388.
- Takeda, N., Ishikawa, M., 2000b. *J. Phys. Soc. Japan* **69**, 868.
- Takeda, N., Ishikawa, M., 2001. *J. Phys. Cond. Mater.* **13**, 5971.
- Tang, X., Chen, L., Goto, T., Hirai, T., 2001. *J. Mater. Res.* **16**, 837.
- Torikachvili, M.S., Chen, J.W., Dalichaouch, Y., Guertin, R.P., McElfresh, M.W., Rossel, C., Maple, M.B., Meisner, G.P., 1987. *Phys. Rev. B* **36**, 8660.
- Uchiumi, T., Shirotani, I., Sekine, C., Todo, S., Yagi, T., Nakazawa, Y., Kanoda, K., 1999. *J. Phys. Chem. Solids* **60**, 689.
- Uher, C., 2001. In: *Semiconductors and Semimetals*, Vol. **69**. Academic Press, San Diego, pp. 139–153 (Chapter 5).
- Watcharapasorn, A., DeMattei, R.C., Feigelson, R.S., Caillat, T., Borschhevsky, A., Snyder, G.J., Fleurial, J.-P., 1999. *J. Appl. Phys.* **86**, 6213.
- Watcharapasorn, A., Feigelson, R.S., Caillat, T., Borschhevsky, A., Snyder, G.J., Fleurial, J.-P., 2002. *J. Appl. Phys.* **91**, 1344.
- Wilson, K.G., 1975. *Rev. Mod. Phys.* **47**, 773.
- Xue, J.S., Antonio, M.A., White, W.T., Soderholm, L., Kauzlarich, S.M., 1994. *J. Alloys and Compounds* **207–208**, 161.

Chapter 212

RARE EARTH – ANTIMONY SYSTEMS

Oksana L. SOLOGUB*, Petro S. SALAMAKHA

Departamento de Química, Instituto Tecnológico e Nuclear;

P-2686-953 Sacavém, Portugal

Contents

List of symbols and abbreviations	36	5. Structure types of the ternary antimonides	95
1. Introduction	36	6. Physical properties of the ternary antimonides	112
2. Binary systems	36	6.1. RM_2Sb_2 compounds	112
3. Ternary systems	37	6.2. $RNiSb$ compounds	115
3.1. $R-M-Sb$ systems	37	6.3. $RMSb_2$ compounds	119
3.1.1. Sc- $M-Sb$ systems	37	6.4. $R_3M_3Sb_4$ compounds	127
3.1.2. Y- $M-Sb$ systems	40	6.5. R_6MSb_{15} compounds	133
3.1.3. La- $M-Sb$ systems	42	6.6. $R_{14}MSb_{11}$ compounds	134
3.1.4. Ce- $M-Sb$ systems	49	7. Peculiarities of the interaction of the rare earths and antimony	135
3.1.5. Pr- $M-Sb$ systems	58	7.1. Binary systems	135
3.1.6. Nd- $M-Sb$ systems	62	7.2. Ternary systems	136
3.1.7. Sm- $M-Sb$ systems	72	7.2.1. $R-s$ -element-Sb	136
3.1.8. Eu- $M-Sb$ systems	76	7.2.2. $R-p$ -element-Sb	136
3.1.9. Gd- $M-Sb$ systems	78	7.2.3. $R-d$ -element-Sb	137
3.1.10. Tb- $M-Sb$	82	7.2.4. $R-f$ -element-Sb	140
3.1.11. Dy- $M-Sb$ systems	84	7.3. Interconnection of the ternary antimonides with the binary structure types	140
3.1.12. Ho- $M-Sb$ systems	86	7.4. Ternary antimonides with the equiatomic composition	140
3.1.13. Er- $M-Sb$ systems	88	7.5. Ternary antimonides with the $R:Sb$ ratio equal to 1:2	141
3.1.14. Tm- $M-Sb$ systems	89	Acknowledgement	142
3.1.15. Yb- $M-Sb$ systems	90	References	142
3.1.16. Lu- $M-Sb$ systems	92		
3.2. $R-R'-Sb$ systems	93		
3.3. $R-U-Sb$ systems	94		
4. Quaternary systems	95		

* Present address: Institut für Anorganische Chemie, Universität Wien, Währingerstraße 42, A-1090 Wien, Austria.

List of symbols and abbreviations

a, b, c	unit cell dimensions (in nm)	x, y	indicate variable component contents, when it is used as index in compound compositional formula. Expressions like: $N - x$ (where N is a number) means N minus x , the x value is given in the text
at.%	composition in atomic percent		
c	concentration		
C	Curie constant		
C	specific heat		
g	gram	Z	formula per unit cell
h	hour	\sim	is used before the composition formula of a compound to indicate that the composition is given approximately
H_{cr}	critical magnetic field	β	unit cell angle (in degrees)
LT	low temperature modification	χ	magnetic susceptibility
HT	high temperature modification	χ_0	temperature independent susceptibility
M	s-, p-, d- element	χ_C	diamagnetic susceptibility
$M_x N_y$	where $x = 2, 3, \dots$ and $y = 0$ or 5 , $M =$ minimum purity and $N =$ nines	γ	electronic specific heat coefficient
R, R'	rare earth metal	μ	magnetic moment
S	Seebeck coefficient	θ_p	paramagnetic Curie temperature
SG	space group	θ_R	characteristic temperature
T	temperature	ρ	electrical resistivity
T_C	Curie temperature	ρ_0	residual resistivity
T_M, T_m	temperature of magnetic transition		
T_N	Néel temperature		

1. Introduction

This chapter presents a review of the current data on phase diagrams and crystal structures of binary, ternary and quaternary metal antimonides with the R elements ($R \equiv \text{Sc, Y}$ and the lanthanides).

Sections 2–4 give the overview of the literature published on these systems, i.e., the isothermal sections and crystallographic characteristics of the binary, ternary and quaternary compounds, as well as, outlines of the experimental methods that have been utilized. A description of the structure types of ternary antimonides is the subject of sect. 5. The physical properties are only briefly presented for the most common isotypic series of compounds (sect. 6). The general features and trends in the R –Sb and R –(s-, p-, d-, f- element)–Sb systems are discussed in sect. 7.

2. Binary systems

Binary systems containing antimony have been investigated by different groups of scientists, and their phase diagrams are mostly compiled by Massalski et al. (1991): Y–Sb (Schmidt and McMasters, 1976), La–Sb (Vogel and Klose, 1954; Lebedev et al., 1983), Ce–Sb (Borsese et al., 1981), Pr–Sb (Abdusalamova et al., 1988), Nd–Sb (Kobzenko et al., 1972), Sm–Sb (Sadygov et al., 1988b; Borzone et al., 1985), Gd–Sb (Abdusalamova et al., 1986), Tb–Sb

(Abdusalamova et al., 1981), Dy–Sb (Ferro et al., 1988), Ho–Sb (Abdusalamova et al., 1984), Er–Sb (Abdusalamova and Rachmatov, 2000), Tm–Sb (Abdusalamova et al., 1991), Yb–Sb (Bodnar and Steinfink, 1967), Lu–Sb (Abdusalamova et al., 1990). Recently, Borzone et al. (2000) presented modified phase diagram for the Gd–Sb system. For the other systems only individual alloys were synthesized and investigated with the aim of finding the isotopic or new compounds.

Information on binary compounds is gathered by Villars and Calvert (1985, 1991), and Villars et al. (1995).

More recently, the compound $\text{Eu}_{16}\text{Sb}_{11}$ has been prepared from the elements in Ta container by heating at 1370 K and then slowly cooled to 1270 K over 4 days (Chan et al., 2000). This compound is isotopic with the Zintl-phase $\text{Ca}_{16}\text{Sb}_{11}$ (X-ray single crystal diffraction).

The crystal structure of the compound previously called “GdSb₂” was determined by X-ray diffraction methods and the true composition was found to be $\text{Gd}_{16}\text{Sb}_{39}$ (Borzone et al., 2000).

The high temperature modification for the Y_5Sb_3 has been reported recently (Mozharivskij and Franzen, 2000b).

Additionally, several compounds not presented on the phase diagrams of the corresponding systems, are listed below.

From metallographic analysis of the sample with composition $\text{Ce}_{33.3}\text{Sb}_{66.6}$, Abulkhaev and Abdusalamova (1989) observed, in addition to the expected CeSb_2 phase and CeSb , needle shaped single crystals of unknown composition and structure. Authors believe that this phase is a high temperature modification of CeSb_2 .

Altmeyer and Jeitschko (1988) reported the existence of new compound with a monoclinic structure, Dy_2Sb_5 , $a = 1.3066$, $b = 0.41627$, $c = 1.4584$, $\beta = 102.21^\circ$. The structure was established by X-ray single crystal diffraction. The Sm_2Sb_5 , Gd_2Sb_5 and Tb_2Sb_5 compounds have been found to be isotopic with Dy_2Sb_5 (Altmeyer and Jeitschko, 1988).

Altmeyer and Jeitschko (1989) observed in the Nd–Sb system at 870 K a new compound with monoclinic symmetry, $\text{Nd}_{8+x}\text{Sb}_{19+y}$, $a = 2.8495$, $b = 0.42489$, $c = 1.34982$, $\beta = 95.476^\circ$ (X-ray single crystal investigation).

Crystallographic data of the binary antimonides of rare earth are listed in table 1.

3. Ternary systems

3.1. *R–M–Sb* systems

3.1.1. *Sc–M–Sb* systems

3.1.1.1. *Sc–Co–Sb*. The crystal structure of the ScCoSb compound was investigated by Kleinke (1998) by X-ray single crystal diffraction. It was found to crystallize with the TiNiSi structure type ($a = 0.6829$, $b = 0.42401$, $c = 0.7358$).

3.1.1.2. *Sc–Ni–Sb*. Early investigations of the ScNiSb compound showed that it had the MgAgAs -type with $a = 0.6062$ (Dwight, 1974) from an X-ray powder analysis of an alloy

Table 1
Crystallographic characteristics of the binary antimonides

Compound	Structure type	Space group	Lattice parameters, nm		
			<i>a</i>	<i>b</i>	<i>c</i>
ScSb	NaCl	$Fm\bar{3}m$	0.58517		
Sc ₅ Sb ₃	Yb ₅ Sb ₃	$Pnma$	1.10792	0.87126	0.76272
Sc ₂ Sb	Cu ₂ Sb	$P4/nmm$	0.42049		0.77902
YSb ₂	HoSb ₂	$C222$	0.3283	0.5907	0.7981
YSb	NaCl	$Fm\bar{3}m$	0.6165		
Y ₄ Sb ₃	anti-Th ₃ P ₄	$I\bar{4}3d$	0.905		
Y ₅ Sb ₃ (LT)	Mn ₅ Si ₃	$P6_3/mcm$	0.89114		0.62960
Y ₅ Sb ₃ (HT)	Yb ₅ Sb ₃	$Pnma$	1.1867	0.92247	0.80977
Y ₃ Sb	Ti ₃ P	$P4_2/n$	1.2361		0.6180
LaSb ₂	SmSb ₂	$Cmca$	0.6314	0.6175	1.856
LaSb	NaCl	$Fm\bar{3}m$	0.6490		
LaSb (HP)	HgMn	$P4/mmm$	0.4019		0.3279
La ₄ Sb ₃	anti-Th ₃ P ₄	$I\bar{4}3d$	0.9649		
La ₅ Sb ₃	Mn ₅ Si ₃	$P6_3/mcm$	0.942		0.662
La ₃ Sb ₂	unknown				
La ₂ Sb	own	$I4/mmm$	0.4626		1.806
CeSb ₂ (HT)	unknown				
CeSb ₂	SmSb ₂	$Cmca$	0.628	0.613	1.826
CeSb	NaCl	$Fm\bar{3}m$	0.6429		
CeSb(HP)	HgMn	$P4/mmm$	0.3975		0.3244
Ce ₄ Sb ₃	anti-Th ₃ P ₄	$I\bar{4}3d$	0.9511		
Ce ₅ Sb ₃	Mn ₅ Si ₃	$P6_3/mcm$	0.931		0.652
Ce ₂ Sb	La ₂ Sb	$I4/mmm$	0.4532		1.784
PrSb ₂	SmSb ₂	$Cmca$	0.626	0.616	1.816
PrSb	NaCl	$Fm\bar{3}m$	0.6361		
Pr ₄ Sb ₃	anti-Th ₃ P ₄	$I\bar{4}3d$	0.948		
Pr ₅ Sb ₃	Mn ₅ Si ₃	$P6_3/mcm$	0.928		0.651
Pr ₂ Sb	La ₂ Sb	$I4/mmm$	0.455		1.782
Nd _{8+x} Sb _{19+y}	own	$C2/m$	2.8495	0.42489 $\beta = 95.476^\circ$	1.34982
NdSb ₂	SmSb ₂	$Cmca$	0.6230	0.6063	1.7892
NdSb	NaCl	$Fm\bar{3}m$	0.6321		
Nd ₄ Sb ₃	anti-Th ₃ P ₄	$I\bar{4}3d$	0.9370		
Nd ₅ Sb ₃	Mn ₅ Si ₃	$P6_3/mcm$	0.9170		0.6460
Nd ₂ Sb	La ₂ Sb	$I4/mmm$	0.4510		1.7610
Sm ₂ Sb ₅	Dy ₂ Sb ₅	$C2/m$			
SmSb ₂	own	$Cmca$	0.6171	0.6051	1.789
SmSb	NaCl	$Fm\bar{3}m$	0.6268		
Sm ₄ Sb ₃	anti-Th ₃ P ₄	$I\bar{4}3d$	0.9308		
Sm ₅ Sb ₃	Mn ₅ Si ₃	$P6_3/mcm$	0.8990		0.6138
Sm ₂ Sb	La ₂ Sb	$I4/mmm$	0.4468		1.746
EuSb ₂	CaSb ₂	$P2_1/m$	0.4768	0.4299 $\beta = 103.01$	0.8970
Eu ₂ Sb ₃	Sr ₂ Sb ₃	$P2_1/c$	0.6570	1.2760 $\beta = 90.04$	1.5028

continued on next page

Table 1, *continued*

Compound	Structure type	Space group	Lattice parameters, nm		
			<i>a</i>	<i>b</i>	<i>c</i>
Eu ₁₁ Sb ₁₀	Ho ₁₁ Ge ₁₀	<i>I4/mmm</i>	1.2325		1.8024
Eu ₁₆ Sb ₁₁	Ca ₁₆ Sb ₁₁	<i>P-421m</i>	1.2674		1.1720
Eu ₅ Sb ₃	Yb ₅ Sb ₃	<i>Pnma</i>	1.29826	1.00033	0.86325
Gd ₂ Sb ₅	Dy ₂ Sb ₅	<i>C2/m</i>			
Gd ₁₆ Sb ₃₉	own	<i>C2/m</i>	0.57395	0.4151	1.3209
				$\beta = 99.21$	
GdSb ₂ (HT)	HoSb ₂	<i>C222</i>	0.3296	0.5930	0.8030
GdSb ₂ (LT)	SmSb ₂	<i>Cmca</i>	0.6157	0.5986	1.783
GdSb (α)	NaCl	<i>Fm$\bar{3}m$</i>	0.6218		
GdSb (β)	unknown				
Gd ₄ Sb ₃	anti-Th ₃ P ₄	<i>I$\bar{4}3d$</i>	0.9220		
Gd ₅ Sb ₃	Mn ₅ Si ₃	<i>P6₃/mcm</i>	0.897		0.632
Tb ₂ Sb ₅	Dy ₂ Sb ₅	<i>C2/m</i>			
TbSb ₂ (HT)	HoSb ₂	<i>C222</i>	0.3282	0.5903	0.7990
TbSb ₂ (LT)	SmSb ₂	<i>Cmca</i>	0.6123	0.5969	1.772
TbSb(α)	NaCl	<i>Fm$\bar{3}m$</i>	0.6178		
Tb ₄ Sb ₃ (α)	anti-Th ₃ P ₄	<i>I$\bar{4}3d$</i>	0.917		
Tb ₅ Sb ₃	Mn ₅ Si ₃	<i>P6₃/mcm</i>	0.89324		0.62887
Dy ₂ Sb ₅	own	<i>C2/m</i>	1.3066	0.41627	1.4584
				$\beta = 102.21^\circ$	
DySb ₂ (HT)	HoSb ₂	<i>C222</i>	0.3273		0.7965
DySb(α)	NaCl	<i>Fm$\bar{3}m$</i>	0.6154		
Dy ₄ Sb ₃ (α)	anti-Th ₃ P ₄	<i>I$\bar{4}3d$</i>	0.9129		
Dy ₅ Sb ₃	Mn ₅ Si ₃	<i>P6₃/mcm</i>	0.8892		0.6270
HoSb ₂	own	<i>C222</i>	0.3343	0.5790	0.7840
HoSb	NaCl	<i>Fm$\bar{3}m$</i>	0.6130		
Ho ₄ Sb ₃	anti-Th ₃ P ₄	<i>I$\bar{4}3d$</i>	0.9071		
Ho ₅ Sb ₃	Mn ₅ Si ₃	<i>P6₃/mcm</i>	0.8851		0.6234
ErSb ₂ (HT)	HoSb ₂	<i>C222</i>	0.3259	0.5866	0.7926
ErSb	NaCl	<i>Fm$\bar{3}m$</i>	0.6106		
Er ₄ Sb ₃	anti-Th ₃ P ₄	<i>I$\bar{4}3d$</i>	0.902		
Er ₅ Sb ₃	Yb ₅ Sb ₃	<i>Pnma</i>	1.1662	0.9136	0.8007
TmSb ₂	HoSb ₂	<i>C222</i>	0.3252	0.5851	0.7912
TmSb	NaCl	<i>Fm$\bar{3}m$</i>	0.6087		
Tm ₅ Sb ₃	Mn ₅ Si ₃	<i>P6₃/mcm</i>			
YbSb ₂	ZrSi ₂	<i>Cmcm</i>	0.4536	1.663	0.4271
YbSb	NaCl	<i>Fm$\bar{3}m$</i>	0.6082		
Yb ₁₁ Sb ₁₀	Ho ₁₁ Ge ₁₀	<i>I4/mmm</i>	1.186		1.710
Yb ₄ Sb ₃	anti-Th ₃ P ₄	<i>I$\bar{4}3d$</i>	0.9320		
Yb ₅ Sb ₃	Mn ₅ Si ₃	<i>P6₃/mcm</i>	0.8995		0.6870
Yb ₅ Sb ₃	own	<i>Pnma</i>	1.2398	0.9562	0.8246
LuSb ₂	HoSb ₂	<i>C222</i>	0.3244	0.5935	0.7885
LuSb	NaCl	<i>Fm$\bar{3}m$</i>	0.6056		
Lu ₅ Sb ₃	Mn ₅ Si ₃	<i>P6₃/mcm</i>	0.890		0.633
Lu ₃ Sb	unknown				

arc melted under argon, annealed at 973 K and furnace cooled. Pecharsky et al. (1983a) confirmed the crystal structure from X-ray powder diffraction and obtained the lattice parameter as $a = 0.6055$. The stoichiometric amounts of the starting components (Sc 99.5%, Ni (4N), Sb (4N)) were arc melted under argon and annealed at 870 K for 200 h.

3.1.1.3. *Sc–Pt–Sb*. ScPtSb belongs to the MgAgAs-type, $a = 0.6312$ (Dwight, 1974) (X-ray powder analysis). Sample preparation, see ScNiSb.

3.1.2. *Y–M–Sb systems*

3.1.2.1. *Y–Li–Sb*. LaLi₃Sb₂ structure type was reported for the YLi₃Sb₂ compound, $a = 0.45251$, $c = 0.7158$ from X-ray single crystal diffraction (Grund et al., 1984).

3.1.2.2. *Y–Zr–Sb*. Morozkin and Sviridov (2001) investigated the crystal structure of the YZrSb compound using X-ray powder diffraction (CeScSi structure type, $a = 0.4245$, $c = 1.6306$).

3.1.2.3. *Y–Ni–Sb*. Figure 1 represents the isothermal section of Y–Ni–Sb phase diagram at 870 K (0–50 at.% Sb) which was studied by Zavali (1982). The isothermal section was constructed by means of X-ray powder analysis of alloys, which were arc melted and subsequently annealed in evacuated silica tubes for 400 h and finally quenched in water. Starting materials were Y 99.8 wt.%, Ni 99.99 wt.% and Sb 99.99 wt.%. The ternary phase equilibria diagram is characterized by the existence of two ternary compounds: $\sim\text{YNi}_2\text{Sb}_2$ (1) and $\sim\text{YNiSb}$ (2).

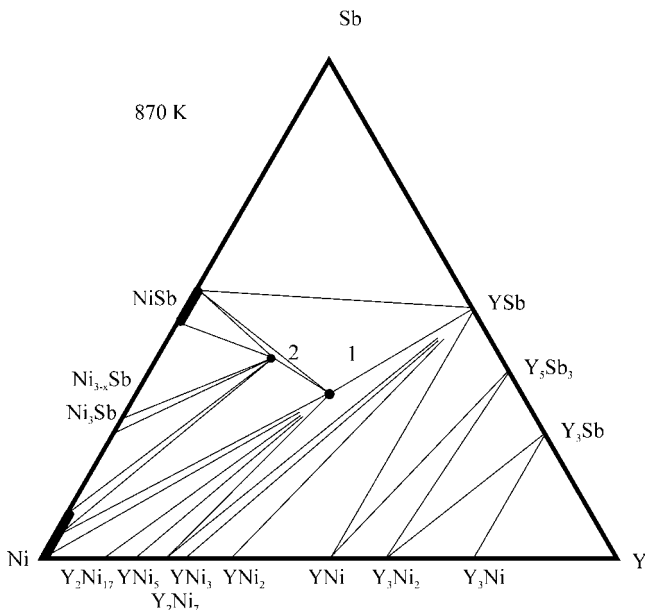


Fig. 1. Y–Ni–Sb, partial isothermal section at 870 K (0–50 at.% Sb).

YNiSb belongs to the MgAgAs-type, $a = 0.6312$ (Dwight, 1974) from X-ray powder analysis. For sample preparation, see ScNiSb.

Sologub et al. (1994) investigated by X-ray powder diffraction the alloy with the nominal composition $Y_{25}Ni_{25}Sb_{50}$ prepared by arc melting ingots of the elements in argon and annealed at 870 K in evacuated quartz tubes for 2 weeks and quenched in water. The sample was found to consist of two phases, namely NiSb (NiAs type, $a = 0.3926$, $c = 0.5134$) and YSb (NaCl type, $a = 0.61707$). The materials used were Y 99.9 wt.%, Ni 99.9 wt.% and Sb 99.9 wt.%.

One more ternary compound has been observed and studied by Mozharivskiy and Kuz'ma (1996) from the arc melted, annealed at 1070 K for 400 h, and finally quenched in cold water alloys. It crystallizes with the Mo_5B_2Si type structure, $a = 0.7662$, $c = 1.3502$ (X-ray powder diffraction). The starting metals were Y, not less than 99.8 wt.%, Ni and Sb 99.9 wt.%.

Mozharivskiy and Franzen (2000a) studied the crystal structure of $Y_5Ni_xSb_{3-x}$ ($0 \leq x \leq 0.38$) by the X-ray single crystal and powder diffraction. The Yb_5Sb_3 structure type ($a = 1.1963$, $b = 0.91330$, $c = 0.80500$) has been observed in the temperature range 1535–1670 K. After annealing the sample for 10 days at 1070 K the structure changes to a Mn_5Si_3 structure type.

3.1.2.4. *Y-Cu-Sb*. No phase diagrams exist for the Y-Cu-Sb system, however two ternary compounds have been observed and characterized.

$YCuSb_2$ was found to crystallize with the $HfCuSi_2$ type with the lattice parameters $a = 0.42617$, $c = 0.9903$ (Sologub et al., 1994). An alloy with the nominal composition $Y_{25}Cu_{25}Sb_{50}$ was prepared by arc melting ingots of the elements in argon and annealed at 1070 K in evacuated quartz tubes for 2 weeks and quenched in water. The materials used were Y 99.9%, Cu 99.9% and Sb 99.9%.

A ternary compound of yttrium with copper and antimony of the stoichiometric ratio 3:3:4 was identified and studied by means of X-ray analysis by Skolozdra et al. (1993). $Y_3Cu_3Sb_4$ compound was found to have the $Y_3Au_3Sb_4$ type with the lattice parameter of $a = 0.9500$ (X-ray powder diffraction). The sample was prepared by melting the metals (around 99.8 wt.% pure for yttrium and 99.99 wt.% for copper and antimony) in an arc furnace and annealing at 870 K for 500 h.

3.1.2.5. *Y-Pd-Sb*. Marazza et al. (1980) established that the YPdSb compound has the MgAgAs type structure with $a = 0.6257$ using X-ray powder diffraction and metallographic analyses. The sample which was enclosed in tantalum vessel under an argon atmosphere, was prepared by melting in an induction furnace and was then annealed at 780 K for 1 week. The metals used had purities greater than 99.9% for Y and greater than 99.99% for Pd and Sb.

YPd_2Sb was reported to be isotypic with the crystal structure of $MnCu_2Al$ with a lattice parameter $a = 0.6691$ (Ishikawa et al., 1982; powder diffraction). The sample was prepared by levitation melting followed by annealing at 1173 K for several days. Riani et al. (1995) confirmed the crystallographic characteristics for this compound, $MnCu_2Al$ type, $a = 0.6691$.

The Y_5Pd_2Sb crystallizes with the Mo_5B_2Si structure type, $a = 0.7733$, $c = 1.3582$ (X-ray powder diffraction; Mozharivskyj and Franzen (2000b)). The sample was annealed at 1070 K for 10 days.

3.1.2.6. *Y–Ag–Sb*. $YAgSb_2$ compound was observed and studied by Sologub et al. (1995a). It was found to crystallize with $HfCuSi_2$ -type structure with lattice parameters $a = 0.42745$, $c = 1.0492$ (X-ray powder diffraction of arc melted and annealed at 1070 K for 14 days alloy). The purity of starting materials was 99.9 wt.%. The existence and crystal structure of $YAgSb_2$ compound were independently confirmed by Brylak et al. (1995) ($a = 0.42765$, $c = 1.0488$; X-ray powder diffraction). The sample was prepared by heating of the mixture of powders of metals with starting composition 1:1:2 in sealed evacuated silica tube for 3 days at 770 K. The reaction product was ground to powder, cold-pressed, sealed again in silica tube, melted in a high frequency furnace, and annealed for 1–2 week at 1070–1170 K. Starting materials were Y 99.9%, Ag M3N, and Sb 325 mesh, M2N5.

3.1.2.7. *Y–Te–Sb*. Complete c – T diagram was presented for the Sb_2Te_3 – Y_2Te_3 section by Geidarova and Rustamov (1985). The YTe_3Sb compound formed by incongruent melting was observed and it had the Bi_2Te_3 structure type, $a = 0.447$, $c = 3.032$ (Geidarova and Rustamov, 1985).

3.1.2.8. *Y–Pt–Sb*. $YPtSb$ crystallizes with the $MgAgAs$ -type, $a = 0.6538$ (Dwight, 1974) (X-ray powder analysis). For sample preparation, see $ScNiSb$.

Mozharivskyj and Franzen (2001) reported the crystal structure for the Y_5Pt_2Sb compound from X-ray powder diffraction and it had the Mo_5B_2Si structure, an ordered version of Cr_5B_3 structure type, $a = 0.7675$, $c = 1.3575$. The starting materials were ingots of Y elements (with purity not less than 99.8%), antimony (99.99%, Johnson Matthey GmbH), and platinum (99.9%, Materials Preparation Center, Ames Laboratory). The mixtures of the components with the initial compositions Y_5Pt_2Sb and with a total weight of 0.5 g were arc-melted in an argon atmosphere, then turned over and remelted to reach homogeneity. The samples were sealed in evacuated silica tubes and annealed at 800 °C for 10 days and then furnace cooled.

3.1.2.9. *Y–Au–Sb*. A new structure type was reported by Dwight (1977) for the $Y_3Au_3Sb_4$ alloy with $a = 0.9818$ from X-ray powder diffraction. The conditions of synthesis were not specified.

3.1.3. *La–M–Sb systems*

3.1.3.1. *La–Li–Sb*. A unique structure type was observed for the $LaLi_3Sb_2$ compound, $a = 0.4619$, $c = 0.7445$ from X-ray single crystal diffraction (Grund et al., 1984).

3.1.3.2. *La–Mg–Sb*. No phase diagram exists for the La – Mg – Sb system. The formation of three compounds was reported by Ganguli et al. (1993) from X-ray single crystal investigations: $La_4Mg_{4.48}Sb_7$, own structure type, $a = 0.46201$, $c = 2.6069$; $La_{4.89}Mg_{1.539}Sb_6$,

own structure type, $a = 0.4616$, $c = 6.767$; $\text{La}_3\text{Mg}_{4.6}\text{Sb}_6$, own structure type, $a = 0.4625$, $c = 6.691$.

3.1.3.3. *La–Al–Sb*. Muravjova (1971) has investigated the La–Al–Sb ternary system (0–33 at.% of La) at 773 K. No ternary phases have been found.

3.1.3.4. *La–Ti–Sb*. The crystal structure of the La_3TiSb_5 compound was investigated by Bollore et al. (1995). The Hf_5CuSn_5 anti-type was established ($a = 0.9528$, $c = 0.6278$, X-ray single crystal diffraction).

3.1.3.5. *La–V–Sb*. The only information available on the interaction of the components in the La–V–Sb system is the formation of the LaVSb_3 compound observed by Brylak and Jeitschko (1995). It was reported to adopt the CeCrSb_3 type structure, $a = 1.3358$, $b = 0.62583$, $c = 0.60551$ from X-ray powder diffraction.

3.1.3.6. *La–Cr–Sb*. LaCrSb_3 crystallizes with a CeCrSb_3 type, $a = 1.3276$, $b = 0.6209$, $c = 0.6114$ (X-ray powder diffraction; Brylak and Jeitschko, 1995). Ferguson et al. (1997) and Raju et al. (1998) confirmed the crystal structure using single crystal ($a = 1.32835$, $b = 0.62127$, $c = 0.6116$) and powder diffraction ($a = 1.3264$, $b = 0.6182$, $c = 0.6094$) respectively.

3.1.3.7. *La–Mn–Sb*. Cordier et al. (1985) reported on the crystal structure for the $\text{LaMn}_{0.65-0.76}\text{Sb}_2$ compound (HfCuSi_2 -type, $a = 0.4387-0.4372$, $c = 1.0780-1.0933$; X-ray single crystal method). Sologub et al. (1995b) observed the ternary phase isotypic with HfCuSi_2 from the alloy with slight different metal deficiency, $\text{LaMn}_{0.87}\text{Sb}_2$ ($a = 0.43657$, $c = 1.0924$; X-ray powder diffraction). Sample was prepared by arc melting ingots of the elements in argon under a low electric current. The weight losses were compensated by adding beforehand an extra amount of Mn. The resulting button was annealed at 1070 K for 350 h. The purity of starting materials was 99.9 wt.%. Wollesen et al. (1996) confirmed the crystal structure using a single crystal method: $a = 0.4381$, $c = 1.0772$ for $\text{LaMn}_{0.721(1)}\text{Sb}_2$. The sample was prepared by annealing cold-pressed pellets of the elemental components taken with the atomic ratio of 1:1:2 in evacuated sealed silica tubes for 10 days at 1070 K followed by cooling at a rate of 100 °C/h. Purities of starting elements were La, greater than 99.9%, Mn, greater than 99.8%, Sb 99.9%.

The crystal structure of the $\text{La}_6\text{MnSb}_{15}$ compound was investigated by Sologub et al. (1996b) by X-ray single crystal and powder diffraction. It was found to crystallize with its own structure type, $a = 1.5376$, $b = 1.9611$, $c = 0.4314$. The single crystal was grown from a melt of the nominal composition $\text{LaMn}_{0.25}\text{Sb}_2$. The sample with a total mass 5 g was heated in a corundum crucible in an argon atmosphere to 1500 K and cooled to room temperature with at a rate of 100 K/h.

3.1.3.8. *La–Fe–Sb*. Leithe-Jasper and Rogl (1994) investigated the formation and crystal structure of the $\text{LaFe}_{1-x}\text{Sb}_2$ compound by X-ray powder analysis of the alloys

$\text{La}_{30-31}\text{Fe}_{13-14}\text{Sb}_{57-55}$ (HfCuSi₂-type, $a = 0.44028-0.44035$, $c = 1.00119-1.00113$). The alloys were obtained by arc melting under low electric current to minimize weight losses by vaporization of Sb, which were compensated beforehand by extra amounts of Sb. The samples were placed in alumina crucibles, sealed in evacuated quartz tubes and annealed for 7 days at 1070 K. After the heat treatment the alloys were quenched by submerging the silica tubes in water. The materials used were 99.9% pure.

The crystal structure of the $\text{LaFe}_4\text{Sb}_{12}$ compound was investigated by Braun and Jeitschko (1980). It was found to adopt the $\text{LaFe}_4\text{P}_{12}$ type structure, $a = 0.91395$ (X-ray single crystal method). The purities of the materials were 99.9% or better. Filings of the lanthanum were prepared under argon and annealed with the corresponding amounts of antimony in evacuated sealed silica tubes for two days at 723 K, followed by five days at 1023 K. The resulting antimonide LaSb was ground together with appropriate amounts of Fe and Sb, pressed into pellets and sealed in evacuated silica tubes. The ampules were quickly heated to 1150 K, were kept at this temperature for 3 h and were then quenched. The starting composition was La:Fe:Sb = 1:4:20. The excess antimony was removed by treating the product for several minutes with concentrated nitric acid. The oxidation products of antimony were then dissolved in concentrated hydrochloric acid.

3.1.3.9. *La-Co-Sb*. Cordier et al. (1985) reported on the crystal structure for the $\text{LaCo}_{0.68}\text{Sb}_2$ compound (HfCuSi₂-type, $a = 0.4394$, $c = 0.9954$; X-ray single crystal method). Leithe-Jasper and Rogl (1994) investigated the formation and crystal structure of the $\text{LaCo}_{1-x}\text{Sb}_2$ compound by X-ray powder analysis of the alloy $\text{La}_{30}\text{Co}_{15}\text{Sb}_{55}$ (HfCuSi₂-type, $a = 0.43854$, $c = 0.99232$). For sample preparation and purity of starting materials, see $\text{LaFe}_{1-x}\text{Sb}_2$. Wollesen et al. (1996) confirmed the crystal structure by using X-ray powder diffraction: $a = 0.43843$, $c = 0.99286$ for $\text{LaCo}_{1-x}\text{Sb}_2$. For synthesis, see $\text{LaMn}_{0.721(1)}\text{Sb}_2$. Purities of starting elements were La, greater than 99.9%, Co, greater than 99.8%, Sb 99.9%.

From a room temperature X-ray powder diffraction analysis $\text{La}_6\text{Co}_{13}\text{Sb}$ was found to crystallize with the ordered $\text{La}_6\text{Co}_{11}\text{Ga}_3$, i.e., the $\text{Nd}_6\text{Fe}_{13}\text{Si}$ type structure, $a = 0.8097$, $c = 2.3289$ (Weitzer et al., 1993). An alloy was synthesized from ingots and compacted powders of the constituting elements (99.9% pure) by arc-melting, followed by annealing at 1073 for 5 days and quenched in cold water.

3.1.3.10. *La-Ni-Sb*. The isothermal section of the La-Ni-Sb phase diagram at 870 K studied by Zavali (1982) is shown in fig. 2. The isothermal section was constructed by means of X-ray powder analysis of alloys, which were arc melted and subsequently annealed in evacuated silica tubes for 400 h and finally quenched in water. Starting materials were La 99.8 wt.%, Ni 99.99 wt.% and Sb 99.99 wt.%. The ternary phase equilibria diagram is characterized by the existence of three ternary compounds: $\text{LaNi}_{2\pm x}\text{Sb}_{2\pm x}$ (1), $\text{LaNiSb}_{2\pm x}$ (2) and LaNiSb (3).

LaNiSb was found to crystallize with the ZrBeSi type with lattice parameters of $a = 0.4404$, $c = 0.8403$ (Hartjes and Jeitschko, 1995; X-ray powder diffraction). Cold-pressed pellets of the ideal composition were arc melted in an atmosphere of argon and annealed at 1120 K for one week. Purities of starting materials were better than 99.9%.

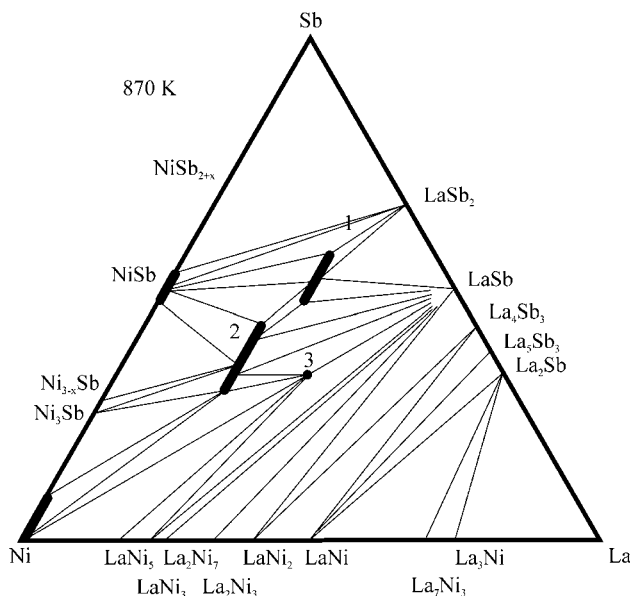


Fig. 2. La–Ni–Sb, isothermal section at 870 K.

Structure refinement from single crystal data established the CaBe_2Ge_2 type structure for the compound $\text{LaNi}_{1.51}\text{Sb}_2$: $a = 0.4466$, $c = 0.991$ (Hoffman and Jeitschko, 1988). The single crystal was selected from a sample prepared by annealing the elemental components for 5 days at 1073 K. The resulting button was melted in a high-frequency furnace and quenched. The CaBe_2Ge_2 type was confirmed from an arc melted alloy of the LaNi_2Sb_2 composition; a monoclinic distortion was observed after annealing it at 1070 K for one week (X-ray powder diffraction; Slebarski et al., 1996).

Pecharsky et al. (1981) reported the BaAl_4 type structure with $a = 0.4433$, $c = 1.0024$ for the LaNi_2Sb_2 compound obtained by arc-melting and annealing at 670 K.

LaNiSb_2 was found to adopt the HfCuSi_2 type structure with the lattice parameters of $a = 0.44269$, $c = 0.9876$ (Sologub et al., 1994). The alloy was prepared by arc melting ingots of the elements with the nominal composition $\text{La}_{25}\text{Ni}_{25}\text{Sb}_{50}$ in argon and annealed at 870 K in evacuated quartz tubes for 2 weeks and quenched in water. The materials used were La 99.9%, Ni 99.9% and Sb 99.9%.

Hoffman and Jeitschko (1988) investigated the antimony rich section of the ternary system La–Ni–Sb from the samples quenched from 1070 K. Except for $\text{LaNi}_{2-x}\text{Sb}_2$, no other ternary compound with a high antimony content was observed. In the various samples, $\text{LaNi}_{2-x}\text{Sb}_2$ was found to be in equilibrium with LaSb, LaSb_2 , NiSb and the high temperature modification of Ni_3Sb .

3.1.3.11. *La–Cu–Sb system.* The isothermal section of the La–Cu–Sb system at 870 K was constructed by Protsyk et al. (2000) (fig. 3). The alloys were synthesized by arc-melting the starting components in an argon atmosphere. The resulting buttons were annealed at 870 K

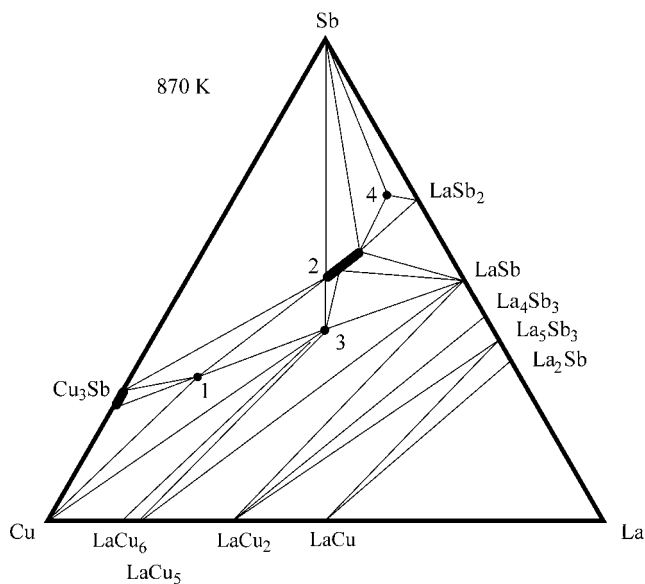


Fig. 3. La-Cu-Sb, isothermal section at 870 K.

for two weeks. Four ternary compounds were observed: $\sim\text{LaCu}_6\text{Sb}_3$ (1), $\text{LaCu}_{1-x}\text{Sb}_2$ (2), $\text{La}_3\text{Cu}_3\text{Sb}_4$ (3) and $\text{La}_6\text{CuSb}_{15}$ (4).

A ternary compound of lanthanum with copper and antimony of the stoichiometric ratio 3:3:4 was identified and studied by means of X-ray analysis by Skolozdra et al. (1993). $\text{La}_3\text{Cu}_3\text{Sb}_4$ (3) compound was found to have the $\text{Y}_3\text{Au}_3\text{Sb}_4$ type with the lattice parameter of $a = 0.9837$ (X-ray powder diffraction). For experimental details, see the Y-Cu-Sb system.

A HfCuSi_2 -type structure was reported for the $\text{LaCu}_{0.82-0.87}\text{Sb}_2$ compound (2), $a = 0.4402-0.4373$, $c = 1.0154-1.0400$ (X-ray single crystal method; Cordier et al. (1985). The crystallographic characteristics for LaCuSb_2 were confirmed by Sologub et al. (1994) from X-ray powder diffraction: HfCuSi_2 type, $a = 0.43690$, $c = 1.0376$. For experimental details, see LaNiSb_2 .

The crystal structure of the $\text{La}_6\text{CuSb}_{15}$ (4) compound was investigated by Sologub et al. (1996b) by X-ray single crystal and powder diffraction. It was found to crystallize with a $\text{La}_6\text{MnSb}_{15}$ structure type, $a = 1.5395$, $b = 1.9465$, $c = 0.4333$. For the sample preparation, see $\text{La}_6\text{MnSb}_{15}$.

The crystal structure of $\sim\text{LaCu}_6\text{Sb}_3$ (1) compound is unknown.

3.1.3.12. *La-Zn-Sb system.* Cordier et al. (1985) reported on the crystal structure for the $\text{LaZn}_{0.52}\text{Sb}_2$ compound (HfCuSi_2 -type, $a = 0.4380$, $c = 1.0488$; X-ray single crystal method). Wollesen et al. (1996) confirmed the crystal structure using X-ray powder diffraction: $a = 0.43883$, $c = 1.0508$ for $\text{LaZn}_{1-x}\text{Sb}_2$. For experimental details, see

$\text{LaMn}_{0.721(1)}\text{Sb}_2$. Purities of starting elements were La, greater than 99.9%, Zn, greater than 99.8%, Sb 99.9%.

Salamakha and Mudryi (2001a) studied the crystal structure of the $\text{LaZn}_{0.6}\text{Sb}_2$ compound. The sample was synthesized in two stages. The proper amounts of the powders were compacted and sealed in evacuated silica capsule. After slowly heating to 1070 K (1st stage), the sample was studied by X-ray powder diffraction. Afterwards, the pellet was reground under C_6H_{12} , recompact and annealed at 870 K for 150 h (2nd stage). The purity of starting materials was 99.9 wt.%. Two modifications of $\text{LaZn}_{0.6}\text{Sb}_2$ compound were observed: $a = 0.43794$, $b = 0.44022$, $c = 1.05044$, NdAgAs₂ type structure (for the sample after 1st stage of annealing) and $a = 0.43900$, $c = 1.0508$, HfCuSi₂ type structure (for the sample after 2nd stage of annealing).

The crystal structure of the $\text{La}_6\text{ZnSb}_{15}$ compound was investigated by Sologub et al. (1996b) by an X-ray single crystal and powder diffraction. It was found to crystallize with the $\text{La}_6\text{MnSb}_{15}$ structure type, $a = 1.5430$, $b = 1.9461$, $c = 0.4351$. For the sample preparation, see $\text{La}_6\text{MnSb}_{15}$.

3.1.3.13. *La–Ga–Sb*. Mills and Mar (2000) reported on the existence of three ternary compounds: $\text{La}_{13}\text{Ga}_8\text{Sb}_{11}$, $\text{La}_{12}\text{Ga}_4\text{Sb}_{23}$ and LaGaSb_2 . The samples have been synthesized by direct reaction of the elements in evacuated silica tubes.

The crystal structure of the $\text{La}_{13}\text{Ga}_8\text{Sb}_{11}$ compound was determined by X-ray single crystal diffraction: own structure type, space group $P6/mmm$, $a = 1.7657$, $c = 0.43378$.

The compound $\text{La}_{12}\text{Ga}_4\text{Sb}_{23}$ was found to adopt the $\text{Pr}_{12}\text{Ga}_4\text{Sb}_{23}$ type structure with the lattice parameters of $a = 0.4344$, $b = 1.9750$, $c = 2.6860$ (X-ray powder diffraction).

The crystal structure of the LaGaSb_2 compound is unknown.

3.1.3.14. *La–Ge–Sb*. Lam et al. (2001) determined the crystal structure of the $\text{La}_6\text{Ge}_{2.8}\text{Sb}_{13.2}$ compound (own structure type, $a = 0.43034$, $b = 1.0851$, $c = 2.7073$) by X-ray single crystal diffraction. The sample had been synthesized by direct reaction of the elements at 1223 K.

3.1.3.15. *La–Zr–Sb*. The crystal structure of the La_3ZrSb_5 compound was investigated by Bollore et al. (1995). It was found to adopt the Hf_5CuSn_3 anti-type structure, $a = 0.9587$, $c = 0.6258$ (X-ray powder diffraction). Ferguson et al. (1997) confirmed the crystal structure of the La_3ZrSb_5 compound using single crystal X-ray diffraction ($a = 0.95743$, $c = 0.63495$).

3.1.3.16. *La–Nb–Sb*. Bollore et al. (1995) determined the crystal structure of La_3NbSb_5 to have the Hf_5CuSn_3 anti-type structure, $a = 0.9534$, $c = 0.6264$ (X-ray powder diffraction).

3.1.3.17. *La–Ru–Sb*. The crystal structure of the $\text{LaRu}_4\text{Sb}_{12}$ compound was studied by Braun and Jeitschko (1980). It was found to crystallize with the $\text{LaFe}_4\text{P}_{12}$ type, $a = 0.92700$ (X-ray powder diffraction). The purities of starting materials and experimental procedure were the same as for $\text{LaFe}_4\text{Sb}_{12}$.

3.1.3.18. *La-Rh-Ge*. Malik and Adroja (1991b) established the KHg_2 type structure with $a = 0.4646$, $b = 0.7547$, $c = 0.7898$ for the LaRhSb compound using X-ray powder diffraction of an arc melted alloy. Purities of the metals were better than 99.99%.

Accordingly to Zeng and Franzen (2000), the $\text{La}_{0.1}\text{Rh}_8\text{Sb}_{24}$ compound belongs to a $\text{LaFe}_4\text{P}_{12}$ type, $a = 0.92213$ (X-ray single crystal diffraction).

Menon Latica and Malik (1996) reported the existence of LaRh_2Sb_2 with a tetragonal structure, but no lattice constants were reported.

3.1.3.19. *La-Pd-Sb*. Marazza et al. (1980) established the CaIn_2 type structure with $a = 0.4610$, $c = 0.8115$ for the LaPdSb compound using X-ray powder diffraction and metallographic analyses. For the sample preparation and purity of starting components, see Y-Pd-Sb system. Malik and Adroja (1991a) confirmed the crystal structure and lattice parameters, $a = 0.4596$, $c = 0.8094$ (X-ray diffraction, arc melted alloy).

LaPdSb_2 was found to form the HfCuSi_2 type structure with the lattice parameters of $a = 0.45309$, $c = 0.9989$ (Sologub et al., 1994). For experimental details, see LaNiSb_2 .

Hoffman and Jeitschko (1985) established the CaBe_2Ge_2 type structure for LaPd_2Sb_2 , $a = 0.4627$, $c = 1.0422$, X-ray powder diffraction. Mixtures of the elemental components were cold pressed, melted in a high frequency furnace, annealed for 3 days at 1170 K and oven cooled.

3.1.3.20. *La-Ag-Sb*. LaAgSb_2 compound was observed and studied by Sologub et al. (1995a). It was found to crystallize with HfCuSi_2 type structure with lattice parameters of $a = 0.43898$, $c = 1.0842$ by X-ray powder diffraction of arc-melted and annealed at 870 K for 14 days alloy. The purity of the starting materials was 99.9 wt.%. The existence and crystal structure of LaAgSb_2 compound were independently confirmed by Brylak et al. (1995) ($a = 0.43903$, $c = 1.0840$; X-ray powder diffraction). For sample preparation, see YAgSb_2 . The starting materials purities were: La 99.9%, Ag M3N, and Sb 325 mesh, M2N5.

3.1.3.21. *La-Cd-Sb*. Sologub et al. (1995b) reported on the crystallographic data for the LaCdSb_2 compound (HfCuSi_2 type structure, $a = 0.44048$, $c = 1.0991$; X-ray powder diffraction) obtained from a multiphase alloy. For the sample preparation and purity of the starting materials, see $\text{CeZn}_{1-x}\text{Sb}_2$. Wollesen et al. (1996) confirmed the crystal structure by using a single crystal method: $a = 0.4399$, $c = 1.0997$ for $\text{CeCd}_{0.700(1)}\text{Sb}_2$. For experimental details, see $\text{LaMn}_{0.721(1)}\text{Sb}_2$. Purities of starting elements were La, greater than 99.9%, Cd, greater than 99.8%, Sb 99.9%.

3.1.3.22. *La-In-Sb*. The crystal structure of the $\text{LaIn}_{0.8}\text{Sb}_2$ compound was investigated by Ferguson et al. (1999) using X-ray single crystal and powder diffraction: own structure type, space group $P2_1/m$, $a = 0.4521$, $b = 0.4331$, $c = 1.1914$, $\beta = 99.66^\circ$.

3.1.3.23. *La-Sn-Sb*. La_4SnSb_2 was investigated by X-ray powder diffraction; the Th_3P_4 type structure was established, $a = 0.9686$ (Hulliger and Ott, 1977). For synthesis, see La_4PbSb_2 .

Wang et al. (1967) studied the $\text{LaSn}_2\text{--LaSb}_2$ section and reported the existence of a ternary compound that they tentatively identified as LaSn_xSb_2 . Ferguson et al. (1996) has determined the crystal structure of LaSn_xSb_2 from single crystal X-ray diffraction method: own structure type, space group $Cmcm$, $a = 0.42425$, $b = 2.3121$, $c = 0.45053$ (for $x = 0.75$). The homogeneity range has been established for the LaSn_xSb_2 ($0.1 \leq x \leq 0.8$) compound. The samples were synthesized by the direct reaction of the elements at 1223 K.

3.1.3.24. *La–Hf–Sb*. The crystal structure of the La_3HfSb_5 compound was investigated by Bollore et al. (1995). It was found to adopt the Hf_5CuSn_3 anti-type structure, $a = 0.9582$, $c = 0.6356$ (X-ray powder diffraction). Ferguson et al. (1997) determined the crystal structure of the compound La_5HfSb_5 by using a single crystal method: $a = 0.9557$, $c = 0.63388$.

3.1.3.25. *La–Os–Sb*. Braun and Jeitschko (1980) investigated the crystal structure of the $\text{LaOs}_4\text{Sb}_{12}$ compound. It was found to form the $\text{LaFe}_4\text{P}_{12}$ type structure, $a = 0.93029$ (X-ray powder diffraction). The purities of starting materials and experimental procedure were the same as for $\text{LaFe}_4\text{Sb}_{12}$.

3.1.3.26. *La–Pt–Sb*. LaPtSb crystallizes with the CaIn_2 -type structure, $a = 0.4560$, $c = 0.8263$ (Rossi et al., 1981; powder X-ray diffraction data). The starting elements (La 3N, Pt 4N, Sb 4N) were melted under argon in tantalum crucible, and annealed at 773 K for one week.

3.1.3.27. *La–Au–Sb*. LaAuSb_2 was found to adopt the HfCuSi_2 type structure with the lattice parameters as $a = 0.44363$, $c = 1.0434$ (Sologub et al., 1994). The alloy was prepared in the same manner as YCuSb_2 . Wollesen et al. (1996) confirmed the crystal structure by using a single crystal method: $a = 0.4436$, $c = 1.0432$. The single crystal was isolated from the sample where the elemental components were annealed together in a NaCl/KCl (1:1) flux for 1 week at 1070 K. The purities of the starting elements were La, greater than 99.9%, Au, greater than 99.9%, Sb 99.9%.

Kasaya et al. (1991) reported an $\text{Y}_3\text{Au}_3\text{Sb}_4$ type structure for the compound $\text{La}_3\text{Au}_3\text{Sb}_4$, $a = 1.0123$ (powder diffraction; powder metallurgical technique).

3.1.3.28. *La–Pb–Sb*. La_4PbSb_2 was investigated by X-ray powder diffraction; the Th_3P_4 type structure was established, $a = 0.9707$ (Hulliger and Ott, 1977). The sample was obtained by heating a mixture of the starting components (with purity (3N) in sealed tantalum tube at 50–100° below the melting point for 8 h.

The formation and crystal structure of the $\text{La}_5\text{Pb}_3\text{Sb}$ compound with the Ti_5Ga_4 type structure was observed by Guloy and Corbett (1994) from X-ray powder diffraction of the sample prepared by a powder metallurgical technique.

3.1.4. *Ce–M–Sb systems*

3.1.4.1. *Ce–Li–Sb*. No ternary phase diagram exists for the Ce–Li–Sb system; however the formation of one ternary compound has been reported by Fischer and Schuster (1982):

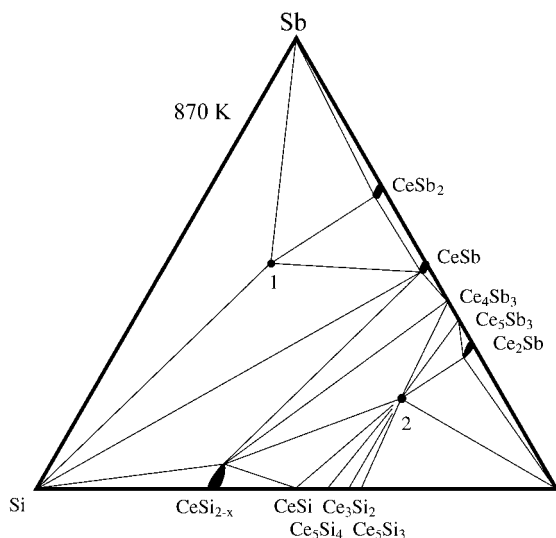


Fig. 4. Ce-Si-Sb, isothermal section at 670 K.

CeLi_2Sb_2 , CaAl_2Si_2 type structure, $a = 0.4311$, $c = 0.6984$. The alloy was prepared by heating the elements in a Ta crucible at 870–1170 K for 24–48 h.

3.1.4.2. *Ce-Si-Sb*. The isothermal section of the phase diagram of the Ce-Si-Sb system (fig. 4) was constructed from an X-ray analysis of 55 alloys prepared by arc melting in an argon atmosphere and annealed in quartz ampoules under vacuum at 670 K for 500 h (Stetskiv, 1999). The purity of the starting metals was better than 99.9 at.%. Two ternary compounds $\sim\text{Ce}_2\text{Si}_3\text{Sb}_5$ (1) (unknown structure), and Ce_3SiSb (2) (La_3GeIn type structure, $a = 1.1948$, $c = 1.5484$) were found. The binary compounds CeSb_2 , CeSb , Ce_2Sb and CeSi_{2-x} dissolve less than 5 at.% of Sb or Si.

3.1.4.3. *Ce-Ti-Sb*. The crystal structure of the Ce_3TiSb_5 compound was investigated by Bollore et al. (1995). It was found to form the Hf_5CuSn_3 anti-type structure, $a = 0.9439$, $c = 0.6235$ (X-ray powder diffraction).

3.1.4.4. *Ce-V-Sb*. CeVSb_3 crystallizes with the CeCrSb_3 type structure, $a = 1.3119$, $b = 0.62392$, $c = 0.60303$ (X-ray powder diffraction; Brylak and Jeitschko, 1995).

3.1.4.5. *Ce-Cr-Sb*. A unique type of structure was reported for CeCrSb_3 , $a = 1.3108$, $b = 0.6184$, $c = 0.6079$ (X-ray single crystal data; Brylak and Jeitschko, 1995). Ferguson et al. (1997) confirmed the structure from X-ray powder diffraction: $a = 1.3127$, $b = 0.6199$, $c = 0.6092$.

3.1.4.6. *Ce-Mn-Sb*. The phase equilibria were established in the ternary system Ce-Mn-Sb for an isothermal section at 870 K (fig. 5). Three ternary compounds were observed:

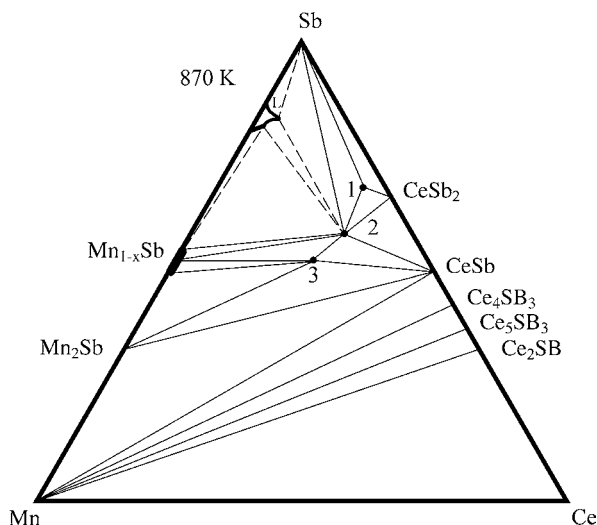


Fig. 5. Ce–Mn–Sb, isothermal section at 870 K.

$\text{CeMn}_{0.85}\text{Sb}_2$ (1), $\text{Ce}_{29}\text{Mn}_{13}\text{Sb}_{58}$ (2) and $\text{Ce}_6\text{MnSb}_{15}$ (3) (Sologub et al., 1995c). The samples were generally prepared by arc melting proper amounts of constituent elements and annealing for 250 h at 870 K. Ternary alloys in the region of 30 to 50 at.% Sb were prepared by heating of compacted mixtures of powders in evacuated quartz tubes from 470 to 870 during a 75 h period, then recompact and heated at 870 K for 150 h, and finally quenched in cold water.

Sologub et al. (1995b) reported on the crystal structure for the $\text{CeMn}_{0.85}\text{Sb}_2$ compound (HfCuSi₂ type structure, $a = 0.43439$, $c = 1.0756$; X-ray powder diffraction). For experimental details, see $\text{LaMn}_{0.87}\text{Sb}_2$. Wollesen et al. (1996) confirmed the crystal structure by using a single crystal method: $a = 0.43514$, $c = 1.0690$ for $\text{CeMn}_{0.741(8)}\text{Sb}_2$. For experimental details, see LaAuSb_2 . The purities of the starting elements were Ce, greater than 99.9%, Mn, greater than 99.8%, Sb 99.9%.

The crystal structure of the $\text{Ce}_6\text{MnSb}_{15}$ compound was investigated by Sologub et al. (1996b) by X-ray powder diffraction. It was found to crystallize with the $\text{La}_6\text{MnSb}_{15}$ structure type, $a = 1.51538$, $b = 1.93646$, $c = 0.42742$. The sample was prepared by arc melting of ingots of the starting elements (purity 99.9 wt.%). Arc melted buttons were annealed at 870 K for 170 h and finally quenched by submerging the capsules into cold water.

The crystal structure of $\text{Ce}_{29}\text{Mn}_{13}\text{Sb}_{58}$ compound was not studied (Sologub et al., 1995c).

3.1.4.7. *Ce–Fe–Sb*. The formation and crystal structure of the $\text{CeFe}_{1-x}\text{Sb}_2$ compound were studied by Leithe-Jasper and Rogl (1994) from X-ray powder analysis of the alloy $\text{Ce}_{30-28}\text{Fe}_{13-17}\text{Sb}_{57-55}$ (HfCuSi₂ type structure, $a = 0.43751-0.43768$, $c = 0.98218-0.98271$). For sample preparation and purity of starting materials, see $\text{LaFe}_{1-x}\text{Sb}_2$.

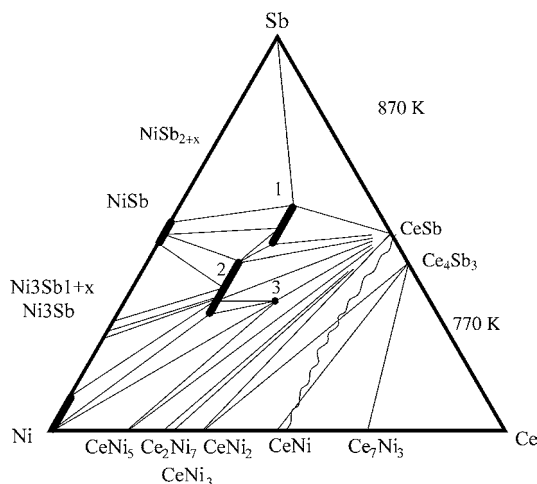


Fig. 6. Ce–Ni–Sb, isothermal section at 870 K.

The crystal structure of the $\text{CeFe}_4\text{Sb}_{12}$ compound was investigated by Braun and Jeitschko (1980). It was found to adopt the $\text{LaFe}_4\text{P}_{12}$ type, $a = 0.91350$ (X-ray powder diffraction). The purities of starting materials and experimental procedure were the same as for $\text{LaFe}_4\text{Sb}_{12}$.

Kaiser and Jeitschko (1999) investigated the phase relations in the Ce–Fe–Sb ternary system at 1173 K for the antimony-rich corner. They found three ternary compounds: CeFeSb_2 , $\text{CeFe}_4\text{Sb}_{12}$ and $\text{Ce}_2\text{Fe}_4\text{Sb}_5$.

3.1.4.8. *Ce–Co–Sb*. Leithe-Jasper and Rogl (1994) investigated the formation and crystal structure of the $\text{CeCo}_{1-x}\text{Sb}_2$ compound from X-ray powder analysis of the alloy $\text{Ce}_{30-25}\text{Co}_{15-25}\text{Sb}_{55-50}$ (HfCuSi_2 type structure, $a = 0.43588-0.43747$, $c = 0.97479-0.98214$). For sample preparation and purity of starting materials, see $\text{LaFe}_{1-x}\text{Sb}_2$. Wollesen et al. (1996) confirmed the crystal structure by using X-ray powder diffraction: $a = 0.43579$, $c = 0.9771$ for $\text{CeCo}_{1-x}\text{Sb}_2$. For synthesis, see $\text{LaMn}_{0.721(1)}\text{Sb}_2$. The purities of starting elements were Ce, greater than 99.9%, Co, greater than 99.8%, Sb 99.9%.

3.1.4.9. *Ce–Ni–Sb*. The isothermal section of Ce–Ni–Sb phase diagram at 870 K studied by Pecharsky et al. (1983b) is given in fig. 6. For the sample preparation, see the La–Ni–Sb system. The ternary phase equilibria diagram is characterized by the existence of three ternary compounds: $\text{CeNiSb}_{2\pm x}$ (1), $\text{CeNi}_{2\pm x}\text{Sb}_{2\pm x}$ (2) and CeNiSb (3).

Pankevich et al. (1983) reported the crystal structure for the CeNiSb_2 compound, HfCuSi_2 type structure, $a = 0.4409$, $c = 0.9750$ (X-ray powder diffraction; arc melted and annealed at 870 K for two weeks). The crystallographic characteristics were confirmed by Sologub et al. (1994), $a = 0.43934$, $c = 0.9750$ and Skolozdra et al. (1994). For experimental details, see LaNiSb_2 .

Early investigations of the CeNiSb compound showed that it had the AlB_2 -type with $a = 0.4384$, $c = 0.4110$ (Pecharsky et al., 1983a; X-ray powder analysis). For experimental

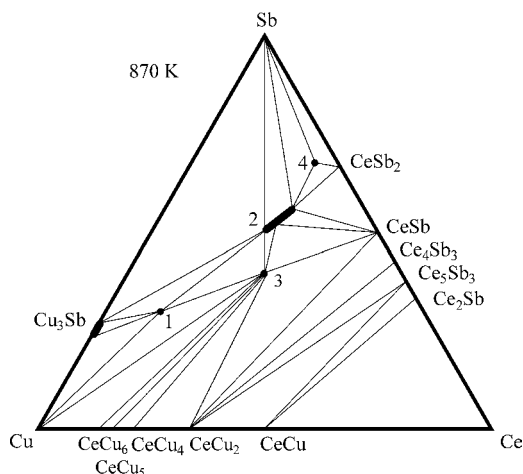


Fig. 7. Ce–Cu–Sb, isothermal section at 870 K.

procedure, see ScNiSb. At variance with these data, Hartjes and Jeitschko (1995) suggested the ZrBeSi type structure, $a = 0.4393$, $c = 0.8257$ from X-ray powder diffraction. For experimental details, see LaNiSb.

The CeGa_2Al_2 type structure was proposed for the CeNi_2Sb_2 compound by Pecharsky et al. (1983b), $a = 0.4395$, $c = 0.9981$ from X-ray powder diffraction of an alloy which was arc melted under argon, annealed at 870 K and quenched. The starting components were Ce 99.5%, Ni and Sb (4N). Hoffman and Jeitschko (1988) established a defect CaBe_2Ge_2 structure for $\text{CeNi}_{2-x}\text{Sb}_2$ alloy, $a = 0.4413$, $c = 0.9846$, X-ray powder diffraction. Mixtures of the elemental components were annealed for about one week between 1023 K and 1073 K, ground to powder, cold pressed, melted in a high frequency furnace and quenched.

A unique structure type was reported for the compound $\text{CeNi}_{2+x}\text{Sb}_{2-x}$ $a = 0.4312$, $b = 0.4285$, $c = 1.0205$ (Pecharsky et al., 1982; X-ray powder diffraction).

3.1.4.10. *Ce–Cu–Sb*. Isothermal section at 870 K for the Ce–Cu–Sb system was constructed by Protsyk et al. (2000) (fig. 7). For experimental procedures, see La–Cu–Sb. Four ternary compounds were observed: $\sim\text{CeCu}_6\text{Sb}_3$ (1), $\text{CeCu}_{1-x}\text{Sb}_2$ (2), $\text{Ce}_3\text{Cu}_3\text{Sb}_4$ (3) and $\text{Ce}_6\text{CuSb}_{15}$ (4).

CeCuSb_2 was found to form a HfCuSi_2 type with the lattice parameters of $a = 0.43378$, $c = 1.02333$ (Sologub et al., 1994). For experimental details, see LaNiSb₂.

A ternary compound of cerium with copper and antimony of the stoichiometric ratio 3:3:4 was identified and studied by means of X-ray analysis by Skolozdra et al. (1993). $\text{Ce}_3\text{Cu}_3\text{Sb}_4$ compound was found to have the $\text{Y}_3\text{Au}_3\text{Sb}_4$ type with the lattice parameters of $a = 0.9721$ (X-ray powder diffraction). For experimental details, see the Y–Cu–Sb system. At variance with this data, Patil et al. (1996) reported a tetragonal distortion of the cubic crystal structure $\text{Y}_3\text{Cu}_3\text{Sb}_4$ for the $\text{Ce}_3\text{Cu}_3\text{Sb}_4$ alloy which was prepared by arc melting the constituent ele-

ments of purity better than 99.9% in an argon atmosphere and annealed at 1070 K for one week ($a = 0.971$, $c = 0.998$; X-ray powder diffraction).

The crystal structure of the $\text{Ce}_6\text{CuSb}_{15}$ compound was investigated by Sologub et al. (1996b) by the X-ray powder diffraction. It was found to crystallize with a $\text{La}_6\text{MnSb}_{15}$ structure type, $a = 1.5452$, $b = 1.9178$, $c = 0.4378$. The sample was synthesized in the same manner as $\text{Ce}_6\text{MnSb}_{15}$.

$\text{CeCu}_{1.33}\text{Sb}_2$ was found to crystallize with the CaBe_2Ge_2 type structure $a = 0.4341$, $c = 1.0256$ from X-ray powder diffraction (Mentink et al., 1994). The starting materials Ce, Cu, Sb were 3 nines pure. The sample was arc melted, wrapped in Ta foil and annealed at 1073 K for 4 weeks. Guzik et al. (1996) reported the crystal structure investigation for the compound with a nominal composition $\text{CeCu}_{1.8}\text{Sb}_2$: CaBe_2Ge_2 type structure, $a = 0.437$, $c = 1.023$ (X-ray powder diffraction, arc melted and annealed at 970 K for one week sample).

3.1.4.11. *Ce–Zn–Sb*. Sologub et al. (1995b) reported on the crystal structure for the $\text{CeZn}_{1-x}\text{Sb}_2$ compound (HfCuSi_2 type structure, $a = 0.43605$, $c = 1.0409$; X-ray powder diffraction). The sample was obtained via a powder metallurgical reaction. The thoroughly mixed blends of powders were compacted and sealed in evacuated silica capsules. After slowly heating to about 870 K for a first reaction, the pellets were reground under C_6H_{12} and recompact for final heat treatment at 870 K for 350 h. The purity of starting materials was 99.9 wt.%. Wollesen et al. (1996) confirmed the crystal structure using X-ray powder diffraction: $a = 0.43449$, $c = 1.05834$ for $\text{CeZn}_{1-x}\text{Sb}_2$. For experimental details, see $\text{LaMn}_{0.721(1)}\text{Sb}_2$. Purities of starting elements were Ce, greater than 99.9%, Zn, greater than 99.8%, Sb 99.9%.

Salamakha and Mudryi (2001a) studied the crystal structure of the $\text{CeZn}_{0.8}\text{Sb}_2$ compound. The sample was synthesized in two stages. Proper amounts of powder were compacted and sealed in evacuated silica capsule. After slowly heating to 1070 K (1st stage), the sample was studied by X-ray powder diffraction. Afterwards, the pellet was reground under C_6H_{12} , recompact and annealed at 870 K for 150 h (2nd stage). The purity of starting materials was 99.9 wt.%. Two modifications of $\text{CeZn}_{0.8}\text{Sb}_2$ compound were observed to form: $a = 0.43493$, $b = 0.43742$, $c = 1.04763$, NdAgAs_2 type structure (for the sample after 1st stage of annealing) and $a = 0.43635$, $c = 1.04160$, HfCuSi_2 (for the sample after 2nd stage of annealing).

The crystal structure of the $\text{Ce}_6\text{ZnSb}_{15}$ compound was investigated by Sologub et al. (1996b) by the X-ray powder diffraction. It was found to crystallize with the $\text{La}_6\text{MnSb}_{15}$ structure type, $a = 1.5215$, $b = 1.9264$, $c = 0.43215$. Sample was synthesized by repeated reaction of sintering of stoichiometric amounts of the starting elements. A proper powder blend was compacted into small pellet, sealed in evacuated quartz tube and slowly heated (within 100 h) to the annealing temperature of 870 K.

3.1.4.12. *Ce–Ga–Sb*. Mills and Mar (2000) investigated the crystal structure of the $\text{Ce}_{12}\text{Ga}_4\text{Sb}_{23}$ compound, with the $\text{Pr}_{12}\text{Ga}_4\text{Sb}_{23}$ type structure, $a = 0.4308$, $b = 1.9509$, $c = 2.6667$ (X-ray powder diffraction). The sample was synthesized by a direct reaction of the elements in evacuated silica tubes.

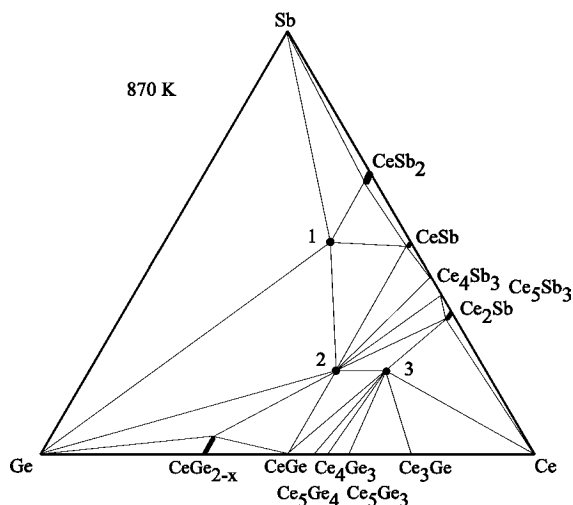


Fig. 8. Ce-Ge-Sb, isothermal section at 870 K.

3.1.4.13. *Ce-Ge-Sb*. The isothermal section of the Ce-Ge-Sb phase diagram (fig. 8) was constructed by X-ray analysis of 50 alloys prepared by arc melting in an argon atmosphere and annealed in quartz ampoules under vacuum at 670 K for 500 h (Stetskiv et al., 1998). The purity of the starting metals was better than 99.9 at.%. Three ternary compounds Ce_2GeSb_3 (1), $\sim\text{Ce}_5\text{Ge}_3\text{Sb}_2$ (2) and Ce_3GeSb (3) were found.

Ce_2GeSb_3 is a superstructure of the ThGe_2 type structure, $a = 1.8894$, $b = 0.4650$, $c = 0.4299$; Ce_3GeSb crystallizes in the La_3GeIn type structure, $a = 1.2012$, $c = 1.5485$; the crystal structure of the $\sim\text{Ce}_5\text{Ge}_3\text{Sb}_2$ is unknown (Stetskiv et al., 1998).

One more compound was found and investigated by Lam et al. (2000) from X-ray powder diffraction: $\text{Ce}_6\text{Ge}_{5-x}\text{Sb}_{11+x}$, $a = 0.42972$, $b = 1.0740$, $c = 2.6791$.

3.1.4.14. *Ce-As-Sb*. The compounds $\text{CeAs}_x\text{Sb}_{1-x}$, NaCl type, were synthesized and investigated by different groups of authors: $\text{Ce}_{50}\text{As}_{10}\text{Sb}_{40}$, $a = 0.6354$ (Burllet et al., 1980); Ce_3AsSb_2 , $a = 0.61865$ (Ott et al., 1978); $\text{Ce}_4\text{As}_{0.8}\text{Sb}_{3.2}$, $a = 0.6363$ (Rossat-Mignod et al., 1983).

3.1.4.15. *Ce-Se-Sb*. A complete c - T diagram was presented for the Ce_2Se_3 - Sb_2Se_3 section by Aliev et al. (1977). $\text{CeSe}_3\text{Sb}_{19}$ was found to form a S_3Sb_2 structure type, $a = 1.159$, $b = 0.412$, $c = 1.183$. A homogeneity field was observed for the $(\text{Ce}_x\text{Sb}_{1-x})_2\text{Se}_3$, $x = 0$ – 0.05 , $a = 1.162$ – 1.159 , $b = 0.396$ – 0.412 , $c = 1.177$ – 1.183 . The sample was annealed at 723–773 K for 300 h.

3.1.4.16. *Ce-Zr, Nb-Sb*. The compounds Ce_3ZrSb_5 and Ce_3NbSb_5 belong to the Hf_5CuSn_3 anti-type. The lattice parameters are $a = 0.9506$, $c = 0.6318$, and $a = 0.9438$, $c = 0.6219$ respectively (Bollore et al., 1995; X-ray powder diffraction).

3.1.4.17. *Ce–Ru–Sb*. The crystal structure of the $\text{CeRu}_4\text{Sb}_{12}$ compound was investigated by Braun and Jeitschko (1980). It was found to crystallize with the $\text{LaFe}_4\text{P}_{12}$ type structure, $a = 0.92657$ (X-ray powder diffraction). The purities of starting materials and experimental procedure were the same as for $\text{LaFe}_4\text{Sb}_{12}$.

3.1.4.18. *Ce–Rh–Sb*. Malik and Adroja (1991b) observed a KHg_2 type with $a = 0.4609$, $b = 0.7416$, $c = 0.7846$ for the CeRhSb compound using X-ray powder diffraction of an arc melted alloy. The purities of the metals were better than 99.99%. Salamakha et al. (2000) reinvestigated the crystal structure of the CeRhSb compound, and found it had the TiNiSi structure type, $a = 0.74150$, $b = 0.46185$, $c = 0.78570$.

The existence of CeRh_2Sb_2 with a tetragonal structure was reported by Menon Latica and Malik (1996).

The $\text{Y}_3\text{Au}_3\text{Sb}_4$ structure type has been reported for the $\text{Ce}_3\text{Rh}_3\text{Sb}_4$ compound by Patil et al. (1998).

3.1.4.19. *Ce–Pd–Sb*. Marazza et al. (1980) established the CaIn_2 type structure with $a = 0.4595$, $c = 0.7894$ for the CePdSb compound using X-ray powder diffraction and metallographic analyses. For sample preparation and purity of starting components, see *Y–Pd–Sb* system. Malik and Adroja (1991a) confirmed the crystal structure and lattice parameters, $a = 0.4594$, $c = 0.7913$ (X-ray diffraction; arc melted alloy). CePdSb_2 was found to adopt a HfCuSi_2 type with the lattice parameters as $a = 0.44899$, $c = 0.9893$ (Sologub et al., 1994). For experimental details, see LaNiSb_2 .

Hoffman and Jeitschko (1985) reported the CaBe_2Ge_2 type structure for CePd_2Sb_2 , $a = 0.4505$, $c = 1.0230$, X-ray powder diffraction. The sample was synthesized in the same manner as LaPd_2Sb_2 . The same structure type however with different lattice parameters values, i.e., $a = 0.4482$, $c = 0.9860$ was reported for the CePdSb_3 sample by Cava et al. (1993).

A new ternary antimonide, $\text{Ce}_3\text{Pd}_6\text{Sb}_5$ was prepared by arc melting of the elemental components and subsequent annealing at 1023 K by Gordon et al. (1995). Its orthorhombic crystal structure was determined from single crystal X-ray data: $a = 1.3481$, $b = 0.4459$, $c = 1.0050$. Purity of the elements was at least 99.9%.

Crystal structure of two ternary compounds $\text{Ce}_8\text{Pd}_{24}\text{Sb}$ and $\text{Ce}_2\text{Pd}_9\text{Sb}_3$ was studied by Gordon and DiSalvo (1996) and Gordon et al. (1996) respectively: $\text{Ce}_8\text{Pd}_{24}\text{Sb}$, own structure type, space group $Pm\bar{3}m$, $a = 0.8461$ and $\text{Ce}_2\text{Pd}_9\text{Sb}_3$, own structure type, space group $Cmcm$, $a = 1.3769$, $b = 0.80412$, $c = 0.93482$ (X-ray single crystal diffraction).

3.1.4.20. *Ce–Ag–Sb*. The CeAgSb_2 compound was observed and studied by Sologub et al. (1995a). It was found to crystallize with HfCuSi_2 type structure with the lattice parameters as follows $a = 0.43641$, $c = 1.0722$ by X-ray single crystal diffraction of an arc melted and annealed at 870 K for 14 days sample. The purity of starting materials was 99.9 wt.%. The existence and crystal structure of CeAgSb_2 compound were independently confirmed by Brylak et al. (1995) ($a = 0.4363$, $c = 1.0699$; X-ray single crystal method). A single crystal was obtained by reaction of the elemental components in a NaCl/KCl flux. The starting ratio was $\text{Ce:Ag:Sb:NaCl/KCl} = 1:1:2:20$. The sample was annealed for 2 weeks at 1070 K, cooled to

960 K at a rate of 3 °C/hr, and quenched in ice water. The NaCl/KCl flux was dissolved in H₂O using an ultrasonic bath. The starting metals were Ce 99.9%, Ag M3N, and Sb 325 mesh, M2N5.

3.1.4.21. *Ce–Cd–Sb*. Sologub et al. (1995b) reported the crystallographic data for the CeCdSb₂ compound (HfCuSi₂ type structure, $a = 0.43751$, $c = 1.0900$; X-ray powder diffraction) which had been obtained from a multiphase alloy. For sample preparation and purity of starting materials, see CeZn_{1-x}Sb₂. Wollesen et al. (1996) confirmed the crystal structure using X-ray powder diffraction: $a = 0.43761$, $c = 1.0912$ for CeCd_{1-x}Sb₂. For experimental details, see LaMn_{0.721(1)}Sb₂. The purities of the starting elements were Ce, greater than 99.9%, Cd, greater than 99.8%, Sb 99.9%.

3.1.4.22. *Ce–In–Sb*. The crystal structure of the CeIn_{0.8}Sb₂ compound (LaIn_{0.8}Sb₂ structure type, $a = 0.4478$, $b = 0.4323$, $c = 1.1796$, $\beta = 99.36^\circ$) was investigated by Ferguson et al. (1999) from X-ray powder diffraction.

3.1.4.23. *Ce–Sn–Sb*. Ferguson et al. (1996) studied the crystal structure of the CeSn_xSb₂ by powder diffraction, LaSnSb₂ structure type, $a = 0.4228$, $b = 2.2868$, $c = 0.4478$. The sample has been synthesized through direct reaction of the elements at 1223 K.

3.1.4.24. *Ce–Te–Sb*. The formation and crystal structure of CeTe_xSb_{1-x} was studied by Ravot et al. (1982) and Rossat-Mignod et al. (1983) from the samples obtained by heating in molybdenum crucibles at 2273 K and slow cooling: NaCl structure type, $x = 0-0.5$, $a = 0.6422-0.6403$.

Charvillat et al. (1977) established the Cu₂Sb structure type for the CeSbTe compound, $a = 0.4365$, $c = 0.945$.

3.1.4.25. *Ce–Hf–Sb*. The crystal structure of the Ce₃HfSb₅ compound was determined by Bollore et al. (1995). It was found to adopt the Hf₅CuSn₃ anti-type structure, $a = 0.9483$, $c = 0.6298$ (X-ray powder diffraction).

3.1.4.26. *Ce–Os–Sb*. The crystal structure of the CeOs₄Sb₁₂ compound was investigated by Braun and Jeitschko (1980). It forms the LaFe₄P₁₂ type structure, $a = 0.93011$ (X-ray powder diffraction). The purities of starting materials and experimental procedure were the same as for LaFe₄Sb₁₂.

3.1.4.27. *Ce–Pt–Sb*. CePtSb belongs to the CaIn₂ type structure, $a = 0.4550$, $c = 0.8077$ (powder diffraction; Rossi et al., 1981). The alloy was melted in an induction furnace under argon in tantalum crucible, annealed at 773 for 1 week. The purity of starting materials was Ce (3N), Pt and Sb (4N) each.

Kasaya et al. (1991) reported the Y₃Au₃Sb₄ type structure for the compound Ce₃Pt₃Sb₄, $a = 0.9820$ (powder diffraction; arc melted alloy).

3.1.4.28. *Ce–Au–Sb*. The HfCuSi_2 type structure with the lattice parameters as $a = 0.44081$, $c = 1.0339$ was reported for the CeAuSb_2 compound (Sologub et al., 1994). The alloy was prepared by argon arc melting ingots of the elements with the nominal composition $\text{Ce}_{25}\text{Au}_{25}\text{Sb}_{50}$ and annealed at 670 K in evacuated quartz tubes for 2 weeks and quenched in water. The materials used were Ce 99.9%, Au 99.9%, and Sb 99.9%. Wollesen et al. (1996) confirmed the crystal structure using X-ray powder diffraction: $a = 0.4381$, $c = 1.0772$ for CeAuSb_2 . The sample was prepared by annealing cold-pressed and arc melted mixtures of starting materials taken with the atomic ratio 1:1:2 in evacuated sealed silica tubes for 10 days at 1070 K followed by cooling at a rate of 100 °C/h. The purities of starting elements were Ce, greater than 99.9%, Au, greater than 99.9%, Sb 99.9%.

CeAuSb crystallizes with CaIn_2 type structure, $a = 0.4616$, $c = 0.8322$ after Suzuki et al. (1993) from powder diffraction of arc melted and annealed at 1273 K for 48 h alloy.

Kasaya et al. (1991) reported a $\text{Y}_3\text{Au}_3\text{Sb}_4$ type structure for the compound $\text{Ce}_3\text{Au}_3\text{Sb}_4$, $a = 1.0058$ (powder diffraction; powder metallurgical technique). The formation and crystal structure of this compound ($\text{Y}_3\text{Au}_3\text{Sb}_4$ type, $a = 1.00443$) was confirmed by Sologub et al. (1998) from X-ray powder diffraction of arc melted and annealed at 1070 K for two weeks alloys.

3.1.5. *Pr–M–Sb systems*

3.1.5.1. *Pr–Li–Sb*. The formation of one ternary compound was reported by Fischer and Schuster (1982): PrLi_2Sb_2 , CaBe_2Ge_2 type structure, $a = 0.4329$, $c = 1.0990$ (X-ray single crystal data). The alloy was prepared by heating the elements in a Ta crucible at 870–1170 K for 24–48 h.

3.1.5.2. *Pr–Ti–Sb*. Bollore et al. (1995) investigated the crystal structure of the Pr_3TiSb_5 compound by X-ray powder diffraction. It crystallizes with the Hf_5CuSn_3 anti-type structure, $a = 0.9401$, $c = 0.6224$.

3.1.5.3. *Pr–V–Sb*. PrVSb_3 has the CeCrSb_3 structure type structure, $a = 1.3121$, $b = 0.62380$, $c = 0.60182$ (X-ray powder diffraction; Brylak and Jeitschko, 1995).

3.1.5.4. *Pr–Cr–Sb*. PrCrSb_3 crystallizes with the CeCrSb_3 type structure: $a = 1.3043$, $b = 0.618831$, $c = 0.60738$ (X-ray powder diffraction; Brylak and Jeitschko, 1995). The crystal structure was confirmed by Ferguson et al. (1997) $a = 1.3127$, $b = 0.6199$, $c = 0.6092$ (X-ray powder diffraction).

3.1.5.5. *Pr–Mn–Sb*. Sologub et al. (1995b) reported the lattice parameters for $\text{PrMn}_{0.82}\text{Sb}_2$ (HfCuSi_2 -type, $a = 0.43362$, $c = 1.0628$; X-ray powder diffraction) obtained from a multi-phase alloy. For experimental details, see $\text{LaMn}_{0.87}\text{Sb}_2$. Wollesen et al. (1996) confirmed the crystal structure using X-ray powder diffraction: $a = 0.4333$, $c = 1.0627$ for $\text{PrMn}_{1-x}\text{Sb}_2$. For experimental details, see $\text{LaMn}_{0.721(1)}\text{Sb}_2$. The purities of the starting elements were Pr, greater than 99.9%, Mn, greater than 99.8%, Sb 99.9%.

3.1.5.6. *Pr-Fe-Sb*. Leithe-Jasper and Rogl (1994) investigated the formation and crystal structure of the $\text{PrFe}_{1-x}\text{Sb}_2$ compound by X-ray powder analysis of the alloy $\text{Pr}_{30-30.5}\text{Fe}_{13-14.5}\text{Sb}_{57-55}$ (HfCuSi₂ type structure, $a = 0.43638-0.43616$, $c = 0.97390-0.97552$). For sample preparation and purity of starting materials, see $\text{LaFe}_{1-x}\text{Sb}_2$.

The crystal structure of the $\text{PrFe}_4\text{Sb}_{12}$ compound was studied by Braun and Jeitschko (1980). It was found to form the $\text{LaFe}_4\text{P}_{12}$ type structure, $a = 0.91351$ (X-ray powder diffraction). The purities of starting materials and experimental procedure were the same as for $\text{LaFe}_4\text{Sb}_{12}$.

From room temperature X-ray powder diffraction analysis the $\text{Pr}_6\text{Fe}_{13}\text{Sb}$ was found to crystallize with the ordered $\text{La}_6\text{Co}_{11}\text{Ga}_3$, i.e., the $\text{Nd}_6\text{Fe}_{13}\text{Si}$ type, $a = 0.8108$, $c = 2.3303$ (Weitzer et al., 1993). An alloy was synthesized from ingots and compacted powders of the constituent elements, 99.9% pure, by arc melting, followed by annealing at 1273 for 2 days and quenched in cold water.

3.1.5.7. *Pr-Co-Sb*. Leithe-Jasper and Rogl (1994) investigated the formation and crystal structure of the $\text{PrCo}_{1-x}\text{Sb}_2$ compound by X-ray powder analysis of the alloy $\text{Pr}_{28}\text{Co}_{17}\text{Sb}_{55}$ (HfCuSi₂-type structure, $a = 0.43415$, $c = 0.96700$). For sample preparation and purity of starting materials, see $\text{LaFe}_{1-x}\text{Sb}_2$. Wollesen et al. (1996) confirmed the crystal structure using X-ray powder diffraction: $a = 0.43463$, $c = 0.9694$ for $\text{PrCo}_{1-x}\text{Sb}_2$. For synthesis, see $\text{LaMn}_{0.721(1)}\text{Sb}_2$. The purities of the starting elements were Pr, greater than 99.9%, Co, greater than 99.8%, Sb 99.9%.

3.1.5.8. *Pr-Ni-Sb*. Pankevich et al. (1983) reported the crystal structure for the PrNiSb_2 compound to have the HfCuSi₂ type structure, $a = 0.4379$, $c = 0.9672$ (X-ray powder diffraction; arc melted and annealed at 870 K for two weeks alloy). The crystallographic characteristics were confirmed by Sologub et al. (1994), $a = 0.43853$, $c = 0.9699$. For experimental details, see LaNiSb_2 .

Early investigations of the PrNiSb compound showed that it had the AlB_2 -type structure with $a = 0.4376$, $c = 0.4053$ (Pecharsky et al., 1983a; X-ray powder analysis). For experimental procedure, see ScNiSb . At variance with these data, Hartjes and Jeitschko (1995) suggested a ZrBeSi type structure, $a = 0.4375$, $c = 0.8123$ from X-ray powder diffraction. For experimental details, see LaNiSb .

The CeGa_2Al_2 type structure was announced for PrNi_2Sb_2 compound by Pecharsky et al. (1982), $a = 0.4367$, $c = 0.9904$ from X-ray powder diffraction. For sample preparation, see CeNi_2Sb_2 . Hoffman and Jeitschko (1988) established the defect CaBe_2Ge_2 type structure for $\text{PrNi}_{2-x}\text{Sb}_2$, $a = 0.4399$, $c = 0.9778$, X-ray powder diffraction. For the experimental details, see $\text{CeNi}_{2-x}\text{Sb}_2$. CaBe_2Ge_2 type structure was confirmed from an arc melted alloy PrNi_2Sb_2 : $a = 0.4360$, $c = 0.9970$; a monoclinic distortion was observed after annealing at 1070 K for one week: $a = 0.4365$, $b = 0.4355$, $c = 0.9969$, $\beta = 90.20^\circ$ (X-ray powder diffraction; Slebarski et al., 1996).

3.1.5.9. *Pr-Cu-Sb*. A ternary compound of praseodymium with copper and antimony of the stoichiometric ratio 3:3:4 was identified and studied by means of X-ray analysis by Skolozdra

et al. (1993). $\text{Pr}_3\text{Cu}_3\text{Sb}_4$ compound was found to have the $\text{Y}_3\text{Au}_3\text{Sb}_4$ type structure with the lattice parameter of $a = 0.9695$ (X-ray powder diffraction). For experimental details, see the Y–Cu–Sb system.

PrCuSb_2 was found to form the HfCuSi_2 type structure with the lattice parameters of $a = 0.43250$, $c = 1.0159$ (Sologub et al., 1994). For experimental details, see LaNiSb_2 .

The CaBe_2Ge_2 type structure was established for PrCu_2Sb_2 from an arc melted alloy: $a = 0.4329$, $c = 1.0183$ (X-ray powder diffraction; Slebarski et al., 1996).

3.1.5.10. *Pr–Zn–Sb*. Sologub et al. (1995b) reported on the crystallographic data for the $\text{PrZn}_{1-x}\text{Sb}_2$ compound (HfCuSi_2 type structure, $a = 0.43398$, $c = 1.0373$; X-ray powder diffraction) obtained from a multiphase alloy. For the sample preparation and the purity of the starting materials, see $\text{CeZn}_{1-x}\text{Sb}_2$. Wollesen et al. (1996) confirmed the crystal structure by using X-ray powder diffraction: $a = 0.43400$, $c = 1.0358$ for $\text{PrZn}_{1-x}\text{Sb}_2$. For experimental details, see $\text{LaMn}_{0.721(1)}\text{Sb}_2$. The purities of the starting elements were Pr, greater than 99.9%, Zn, greater than 99.8%, Sb 99.9%.

The crystal structure of the $\text{Pr}_6\text{ZnSb}_{15}$ compound was investigated by Sologub et al. (1996b) by X-ray powder diffraction. It was found to crystallize with the $\text{La}_6\text{MnSb}_{15}$ structure type, $a = 1.5136$, $b = 1.9180$, $c = 0.42898$. For sample preparation, see $\text{Ce}_6\text{ZnSb}_{15}$.

3.1.5.11. *Pr–Ga–Sb*. Mills and Mar (2000) studied the crystal structure of $\text{Pr}_{12}\text{Ga}_4\text{Sb}_{23}$ by X-ray single crystal diffraction. This compound has its own structure type, space group *Immm*, $a = 0.4283$, $b = 1.9394$, $c = 2.6553$. The crystal was obtained from the sample synthesized through the direct reaction of the elements in evacuated silica tubes.

3.1.5.12. *Pr–Ge–Sb*. The $\text{Pr}_6\text{Ge}_{5-x}\text{Sb}_{11+x}$ compound was observed and investigated by Lam et al. (2001) using X-ray powder diffraction and found that it had the $\text{La}_6\text{Ge}_{2.8}\text{Sb}_{13.2}$ structure type, $a = 0.42674$, $b = 1.0677$, $c = 2.6626$.

3.1.5.13. *Pr–Zr; Nb–Sb*. The Pr_3ZrSb_5 and Pr_3NbSb_5 compounds belong to the Hf_5CuSn_3 anti-type structure with lattice parameters of $a = 0.9450$, $c = 0.6293$ and $a = 0.9396$, $c = 0.6201$ respectively (Bollere et al., 1995; X-ray powder diffraction).

3.1.5.14. *Pr–Ru–Sb*. Braun and Jeitschko (1980) reported the crystal structure of the $\text{PrRu}_4\text{Sb}_{12}$ compound to be of the $\text{LaFe}_4\text{P}_{12}$ type structure, $a = 0.92648$ (X-ray powder diffraction). The purities of starting materials and experimental procedure were the same as for $\text{LaFe}_4\text{Sb}_{12}$.

3.1.5.15. *Pr–Rh–Sb*. Malik and Adroja (1991b) established a KHg_2 type with $a = 0.4596$, $b = 0.7391$, $c = 0.7848$ for the PrRhSb compound by using X-ray powder diffraction of an arc melted alloy. The purities of the metals were better than 99.99%. Adroja et al. (1999) observed the TiNiSi structure type for the $\text{PrRhSb}_{0.976}$ compound from metallographic analyses and powder diffraction.

The existence of PrRh_2Sb_2 with a tetragonal structure was reported by Menon Latica and Malik (1996).

3.1.5.16. *Pr–Pd–Sb*. Marazza et al. (1980) reported the CaIn_2 type structure with $a = 0.4593$, $c = 0.7805$ for the PrPdSb compound from X-ray powder diffraction and metallographic analyses. For the sample preparation and the purity of starting components, see Y–Pd–Sb system. The crystallographic characteristics were also confirmed from powder diffraction data of arc melted and annealed at 1073 K alloys (Zygmunt and Szytula, 1995): CaIn_2 type structure, $a = 0.4588$, $c = 0.7836$. Adroja et al. (1999) observed a LiGaGe structure type for the $\text{PrPdSb}_{0.952}$ compound from metallographic analyses and powder diffraction.

PrPdSb_2 was found to adopt the HfCuSi_2 type structure with the lattice parameters as $a = 0.44707$, $c = 0.9790$ (Sologub et al., 1994). For experimental details, see LaNiSb_2 .

Hoffman and Jeitschko (1988) established a CaBe_2Ge_2 structure for PrPd_2Sb_2 alloy, X-ray powder diffraction. Sample was synthesized in the same manner as LaPd_2Sb_2 .

3.1.5.17. *Pr–Ag–Sb*. The PrAgSb_2 compound was observed and studied by Sologub et al. (1995a). It was found to crystallize with HfCuSi_2 type structure with lattice parameters as follows $a = 0.43506$, $c = 1.0679$ by X-ray powder diffraction of arc melted and annealed at 870 K for 14 days alloy. The purity of starting materials was 99.9 wt.%. The existence and crystal structure of PrAgSb_2 were independently confirmed by Brylak et al. (1995) ($a = 0.43499$, $c = 1.0670$; X-ray powder diffraction). For sample preparation, see YAgSb_2 . The starting materials purities were Pr 99.9%, Ag M3N, and Sb 325 mesh, M2N5.

3.1.5.18. *Pr–Cd–Sb*. Sologub et al. (1995b) reported on the crystallographic data for the PrCdSb_2 compound (HfCuSi_2 type structure, $a = 0.43574$, $c = 1.0864$; X-ray powder diffraction) obtained from a multiphase alloy. For the sample preparation and the purity of the starting materials, see $\text{CeZn}_{1-x}\text{Sb}_2$. Wollesen et al. (1996) confirmed the crystal structure using X-ray powder diffraction: $a = 0.43588$, $c = 1.08555$ for $\text{PrCd}_{1-x}\text{Sb}_2$. For experimental details, see $\text{LaMn}_{0.721(1)}\text{Sb}_2$. The purities of the starting elements were Pr, greater than 99.9%, Cd, greater than 99.8%, Sb 99.9%.

3.1.5.19. *Pr–In–Sb*. The crystal structure of the $\text{PrIn}_{0.8}\text{Sb}_2$ ($\text{LaIn}_{0.8}\text{Sb}_2$ structure type, $a = 0.4465$, $b = 0.4303$, $c = 1.1733$, $\beta = 99.45^\circ$) was investigated by Ferguson et al. (1999) by using X-ray powder diffraction.

3.1.5.20. *Pr–Sn–Sb*. Ferguson et al. (1996) investigated the crystal structure of the PrSn_xSb_2 compound by X-ray powder diffraction: LaSnSb_2 structure type, $a = 0.4204$, $b = 2.2700$, $c = 0.4469$. The sample was synthesized by direct reaction of the elements at 1223 K.

3.1.5.21. *Pr–Te–Sb*. Charvillat et al. (1977) reported a Cu_2Sb structure type for the PrTeSb compound, $a = 0.4344$, $c = 0.9396$.

3.1.5.22. *Pr-Hf-Sb*. The crystal structure of the Pr_3HfSb_5 compound was studied by Bollore et al. (1995). It was found to form the Hf_5CuSn_3 anti-type, $a = 0.9419$, $c = 0.6271$ (X-ray powder diffraction).

3.1.5.23. *Pr-Os-Sb*. The crystal structure of the $\text{PrOs}_4\text{Sb}_{12}$ compound was investigated by Braun and Jeitschko (1980). It belongs to the $\text{LaFe}_4\text{P}_{12}$ type structure, $a = 0.92994$ (X-ray powder diffraction). The purities of the starting materials and the experimental procedure were the same as for $\text{LaFe}_4\text{Sb}_{12}$.

3.1.5.24. *Pr-Pt-Sb*. Wenski and Mewis (1986a) reported the LiGaGe type structure for the PrPtSb compound, $a = 4537$, $c = 0.7963$ from X-ray powder diffraction. The sample was arc melted and annealed at 1273–1373 K for 3–4 weeks. The starting components were Pr (3N), Pt (3N), Sb (3N).

Kasaya et al. (1991) observed the $\text{Y}_3\text{Au}_3\text{Sb}_4$ type structure for the compound $\text{Pr}_3\text{Pt}_3\text{Sb}_4$, $a = 0.9981$ (powder diffraction; arc melted alloy).

3.1.5.25. *Pr-Au-Sb*. PrAuSb_2 was found to adopt a HfCuSi_2 type structure with the lattice parameters as $a = 0.43933$, $c = 1.0290$ (Sologub et al., 1994). The alloy was prepared in the same manner as YCuSb_2 .

Kasaya et al. (1991) reported the $\text{Y}_3\text{Au}_3\text{Sb}_4$ type structure for the compound $\text{Pr}_3\text{Au}_3\text{Sb}_4$, $a = 1.0013$ (powder diffraction; powder metallurgical technique).

3.1.6. *Nd-M-Sb systems*

3.1.6.1. *Nd-Li-Sb*. No ternary phase diagram exists for the Nd-Li-Sb system, however the formation of one ternary compound has been reported by Fischer and Schuster (1982): NdLi_2Sb_2 with the CaBe_2Ge_2 type structure, $a = 0.4280$, $c = 1.0910$ (X-ray single crystal data). The alloy was prepared by heating the elements in a Ta crucible at 870–1170 K for 24–48 h.

3.1.6.2. *Nd-Ti-Sb*. The crystal structure of the Nd_3TiSb_5 compound was investigated by Bollore et al. (1995). It was found to form the Hf_5CuSn_3 anti-type structure, $a = 0.9353$, $c = 0.6196$ (X-ray powder diffraction).

3.1.6.3. *Nd-V-Sb*. The only information available on the interaction of the components in the Nd-V-Sb system is the formation of the NdVSb_3 compound observed by Brylak and Jeitschko (1995). It was reported to adopt the CeCrSb_3 type structure, $a = 1.3040$, $b = 0.6226$, $c = 0.6008$ from X-ray powder diffraction.

3.1.6.4. *Nd-Cr-Sb*. The partial isothermal section of the Nd-Cr-Sb system (33.0–100.0 at.% Sb) at 870 K was constructed by Sologub and Salamakha (1999) (fig. 9). The formation and crystal structure of one ternary compound NdCrSb_3 (1) has been confirmed: CeCrSb_3 type structure, $a = 1.2970$, $b = 0.61679$, $c = 0.60592$ (Brylak and Jeitschko, 1995 and Ferguson

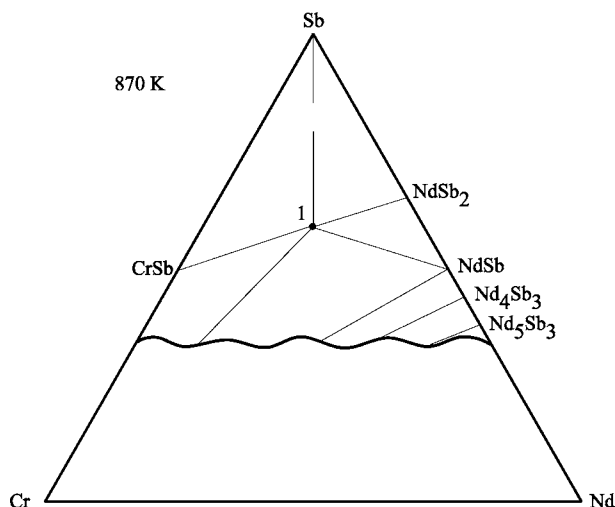


Fig. 9. Nd–Cr–Sb, partial isothermal section at 870 K (33.0–100.0 at.% Sb).

et al., 1997). The solubility of third component in the binary compounds was found to be negligible. The ternary samples used to derive the phase relations in the ternary sections at 870 K, each weighting 1 g, were synthesized by arc melting the proper amounts of the constituent elements under high purity argon on a water cooled copper hearth. The starting materials were used in the form of ingots of high purity elements – Nd (99.9%), Cr (99.99%), Sb (99.999%). The alloys were annealed at 870 K in evacuated quartz tubes for 2 weeks and quenched in water.

3.1.6.5. *Nd–Mn–Sb*. Phase equilibria were established in the Nd–Mn–Sb ternary system for an isothermal section at 870 K by Sologub et al. (1996a) (fig. 10). Three ternary compounds were observed: $\sim\text{Nd}_{26}\text{Mn}_8\text{Sb}_{66}$ (1) (type unknown), $\text{Nd}_{29}\text{Mn}_{13}\text{Sb}_{58}$ (2) (type unknown) and $\text{NdMn}_{1-x}\text{Sb}_2$, $x \sim 0.15$ (3). For the sample preparation, see Ce–Mn–Sb system.

Sologub et al. (1995b) reported on the crystal structure for the $\text{NdMn}_{0.83}\text{Sb}_2$ compound (HfCuSi₂ type structure, $a = 0.43097$, $c = 1.0672$; X-ray powder diffraction). For experimental details, see $\text{LaMn}_{0.87}\text{Sb}_2$. Wollesen et al. (1996) confirmed the crystal structure using X-ray powder diffraction: $a = 0.43174$, $c = 1.0599$ for $\text{NdMn}_{1-x}\text{Sb}_2$. For experimental details, see $\text{LaMn}_{0.721(1)}\text{Sb}_2$. The purities of the starting elements were: Nd, greater than 99.9%, Mn, greater than 99.8%, Sb 99.9%.

3.1.6.6. *Nd–Fe–Sb*. Two ternary compounds ($\text{NdFe}_4\text{Sb}_{12}$ (1) and $\text{NdFe}_{1-x}\text{Sb}_2$ (2)) have been observed as a result of X-ray phase analyses of 30 ternary neodymium–iron–antimony alloys within the concentration region 33.0–100.0 at.% Sb at 870 K (fig. 11) (Sologub and Salamakha, 1999). The solubilities of third component in the binary compounds were found to be negligible. A small homogeneity range was observed for the $\text{NdFe}_{1-x}\text{Sb}_2$ compound. For the sample preparation, see Nd–Cr–Sb system. The starting materials were used in the form of ingots of high purity elements – Nd (99.9%), Fe (99.99%), Sb (99.999%).

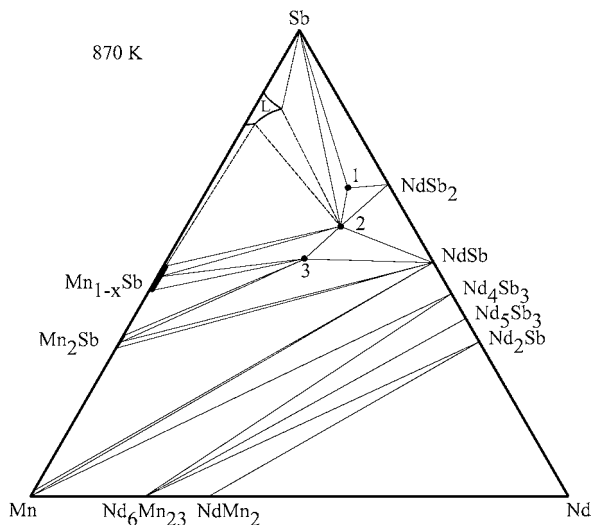


Fig. 10. Nd-Mn-Sb, isothermal section at 870 K.

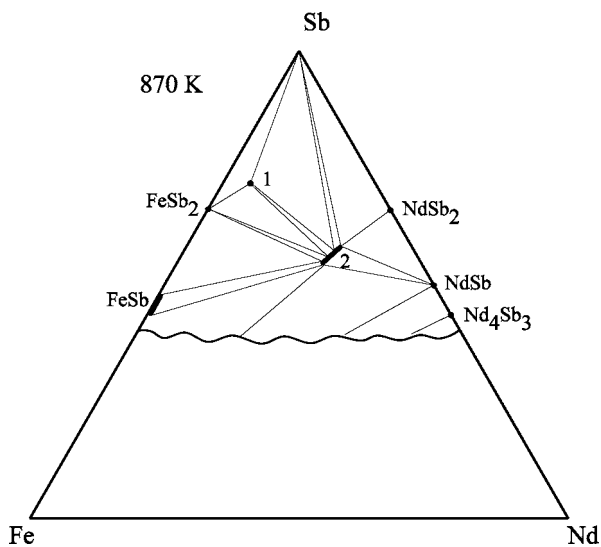


Fig. 11. Nd-Fe-Sb, partial isothermal section at 870 K (33.0–100.0 at.% Sb).

Leithe-Jasper and Rogl (1994) investigated the formation and crystal structure of the $\text{NdFe}_{1-x}\text{Sb}_2$ compound by X-ray powder analysis of the alloy $\text{Nd}_{31-32}\text{Fe}_{14-13}\text{Sb}_{57-55}$ (HfCuSi_2 type structure, $a = 0.43457\text{--}0.43479$, $c = 0.96405\text{--}0.96554$). These results were confirmed by the same authors using X-ray single crystal analysis: $\text{NdFe}_{0.6}\text{Sb}_2$, HfCuSi_2 type structure, $a = 0.43514$, $c = 0.96518$. For the sample preparation and the purity of starting materials, see $\text{LaFe}_{1-x}\text{Sb}_2$.

The crystal structure of the $\text{NdFe}_4\text{Sb}_{12}$ compound was studied Evers et al. (1995). It was found to adopt the $\text{LaFe}_4\text{P}_{12}$ type structure, $a = 0.9130$ (X-ray powder and single crystal diffraction). The purities of the materials were 99.9% or better. Filings of the neodymium were prepared under argon and annealed with the corresponding amounts of antimony in evacuated sealed silica tubes for two days at 723 K, followed by five days at 1023 K. The resulting antimonide NdSb was ground together with appropriate amounts of Fe and Sb, pressed into pellets and sealed in evacuated silica tubes. The ampules were quickly heated to 933 K, kept at this temperature for 3 h, cooled at 1°C/h to 873 K and then quenched. The starting composition was $\text{Nd:Fe:Sb} = 2:4:13$. The excess antimony was removed by treating the product for several days with concentrated hydrochloric acid.

From room temperature X-ray powder diffraction analysis $\text{Nd}_6\text{Fe}_{13}\text{Sb}$ was found to crystallize with the ordered $\text{La}_6\text{Co}_{11}\text{Ga}_3$, i.e., the $\text{Nd}_6\text{Fe}_{13}\text{Si}$ type structure, $a = 0.8098$, $c = 2.3232$ (Weitzer et al., 1993). An alloy was synthesized from ingots and compacted powders of the constituent elements, 99.9% pure, by arc melting, followed by annealing at 1073 for 7 days and quenched in cold water.

Leithe-Jasper (1994) reported the single crystal investigations for two compounds with unique structure types: NdFe_3Sb_2 , $a = 0.42879$, $c = 2.57048$ and $\text{NdFe}_{2-x}\text{Sb}_2$, $a = 0.42965$, $b = 0.42759$, $c = 2.57887$.

Zhang et al. (2000) reported that the $\text{Nd}_2\text{Fe}_{17}$ binary compound dissolves about 3 at.% of Sb at 1223 K.

3.1.6.7. *Nd–Co–Sb*. The 870 K isothermal section of the Nd–Co–Sb system was reported by Sologub and Salamakha (1999) from an X-ray powder analysis of 68 alloys (fig. 12). For the sample preparation, see Nd–Cr–Sb system. The purity of the starting components

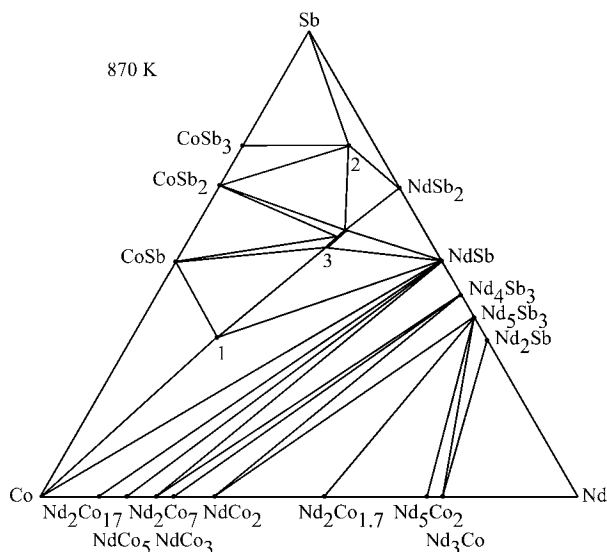


Fig. 12. Nd–Co–Sb, isothermal section at 870 K.

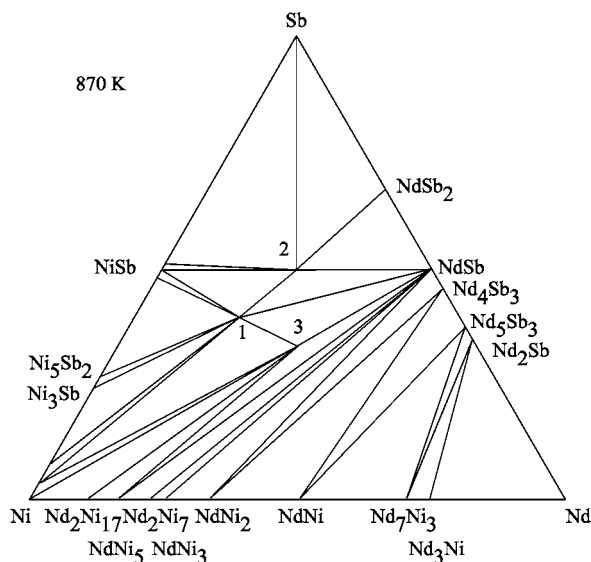


Fig. 13. Nd–Ni–Sb, isothermal section at 870 K.

was Nd 99.9%, Co 99.99%, and Sb 99.999%. The existence of the ternary $\text{NdCo}_{1-x}\text{Sb}_2$ (3) phase has been confirmed. The crystal structures of two other compounds, NdCo_3Sb_2 (1) and $\text{Nd}_6\text{CoSb}_{15}$ (2) have not been investigated.

Leithe-Jasper and Rogl (1994) investigated the formation and crystal structure of the $\text{NdCo}_{1-x}\text{Sb}_2$ compound by X-ray powder analysis of $\text{Nd}_{30-25}\text{Co}_{15-25}\text{Sb}_{55-50}$ (HfCuSi_2 -type structure, $a = 0.43306\text{--}0.43453$, $c = 0.96138\text{--}0.96918$). For the sample preparation and the purity of the starting materials, see $\text{LaFe}_{1-x}\text{Sb}_2$. Wollesen et al. (1996) confirmed the crystal structure using X-ray powder diffraction: $a = 0.43357$, $c = 0.96587$ for $\text{NdCo}_{1-x}\text{Sb}_2$. For synthesis, see $\text{LaMn}_{0.721(1)}\text{Sb}_2$. The purities of the starting elements were: Nd, greater than 99.9%, Co, greater than 99.8%, Sb 99.9%.

3.1.6.8. *Nd–Ni–Sb*. The isothermal section of the Nd–Ni–Sb system at 870 K is shown in fig. 13, after Salamakha (1998). Three ternary compounds have been found: NdNi_2Sb_2 (1), NdNiSb_2 (2) and NdNiSb (3). The solubility of third component in the binary compounds was found to be negligible. For the sample preparation, see Nd–Cr–Sb system. The purity of the starting components was: Nd 99.9%, Ni 99.99%, and Sb 99.999%.

Pankevich et al. (1983) reported the crystal structure of NdNiSb_2 to be the HfCuSi_2 type, $a = 0.4364$, $c = 0.9614$ (X-ray powder diffraction; arc melted and annealed at 870 K for two weeks). The crystallographic characteristics were confirmed by Sologub et al. (1994), $a = 0.43674$, $c = 0.9629$. For experimental details, see LaNiSb_2 .

Early investigations of the NdNiSb compound showed that it had the AlB_2 -type with $a = 0.4372$, $c = 0.3991$ (Pecharsky et al., 1983a; X-ray powder analysis). For the experimental procedure, see ScNiSb . At variance with these data, Hartjes and Jeitschko (1995) suggested

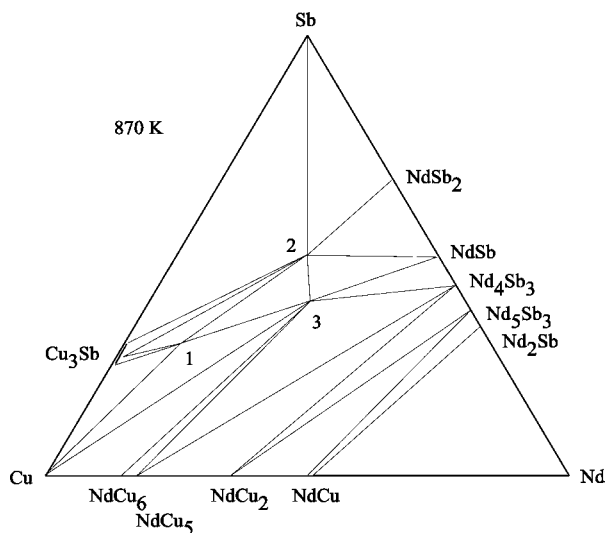


Fig. 14. Nd–Cu–Sb, isothermal section at 870 K.

that the compound had the ZrBeSi type structure, $a = 0.4377$, $c = 0.7997$ from X-ray powder diffraction. For experimental details, see LaNiSb.

The CeGa_2Al_2 type structure was reported for NdNi_2Sb_2 by Pecharsky et al. (1982), $a = 0.43022$, $c = 0.99125$ from X-ray powder diffraction. For sample preparation, see CeNi_2Sb_2 . Hoffman and Jeitschko (1988) established a defect CaBe_2Ge_2 type structure for $\text{NdNi}_{2-x}\text{Sb}_2$ alloy, $a = 0.4300$, $c = 1.001$, X-ray powder diffraction. For the experimental details, see $\text{CeNi}_{2-x}\text{Sb}_2$.

3.1.6.9. *Nd–Cu–Sb*. The isothermal section for the Nd–Cu–Sb system at 870 K was established by Zaplatynsky and Salamakha (1994) (fig. 14). For sample preparation, see Nd–Cr–Sb. The purity of the starting components was: Nd 99.9%, Ni 99.99%, and Sb 99.999%. Three ternary compounds were found to exist. No homogeneous ranges were encountered for the ternary compounds.

A ternary compound of neodymium with copper and antimony of the stoichiometric ratio 3:3:4 was identified and studied by means of X-ray analysis by Skolozdra et al. (1993). The $\text{Nd}_3\text{Cu}_3\text{Sb}_4$ compound (3) was found to have the $\text{Y}_3\text{Au}_3\text{Sb}_4$ type structure with a lattice parameter of $a = 0.9661$ (X-ray powder diffraction). For experimental details, see the Y–Cu–Sb system.

NdCuSb_2 (2) was found to adopt a HfCuSi_2 type structure with lattice parameters of $a = 0.43118$, $c = 1.0111$ (Sologub et al., 1994). For experimental details, see LaNiSb₂.

Crystal structure of the compound NdCu_6Sb_3 (1) has not been investigated.

3.1.6.10. *Nd–Zn–Sb*. The results of an X-ray phase analysis of 25 ternary neodymium-zinc-antimony alloys for the Sb-rich region (33.0–100.0 at.% of Sb) are presented in fig. 15 (Sologub and Salamakha, 1999). The alloys were obtained via a powder metallurgical reaction,

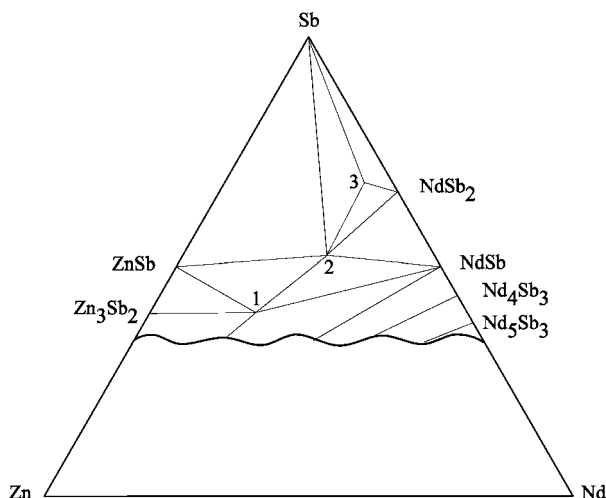


Fig. 15. Nd–Zn–Sb, partial isothermal section at 870 K (33.0–100.0 at.% Sb).

the sintering of Zn and Sb powders with fine filings of neodymium. The thoroughly mixed blends were compacted in the steel dies and then sealed in evacuated silica ampoules. After slowly heating to about 870 K for the first reaction, the hard sintered pellets were reground under C_6H_{12} and recompact for the final heat treatment at 870 K for 300 h and finally quenched by submerging the silica capsules in cold water.

Phase field distribution is characterized by the existence of three ternary compounds. The obtained data on formation and crystal structure of two compounds $NdZn_{1-x}Sb_2$ (2) (HfCuSi₂ type structure, $a = 0.43305$, $c = 1.03482$, X-ray powder diffraction) and Nd_6ZnSb_{15} (3) (La_6MnSb_{15} type, $a = 1.5109$, $b = 1.9026$, $c = 0.42447$, X-ray powder diffraction) are in good agreement with the results of former investigations (Sologub et al., 1995b; Sologub et al., 1996b). Wollesen et al. (1996) confirmed the crystal structure for the $NdZn_{1-x}Sb_2$ ($a = 0.43229$, $c = 1.03334$) from the X-ray powder diffraction. The purity of the starting components and the sample preparation procedure were the same as for $LaMn_{0.721(1)}Sb_2$.

The crystal structure of the $\sim NdZn_2Sb_2$ (1) ternary phase has not been determined yet (Sologub and Salamakha, 1999).

3.1.6.11. *Nd–Ga–Sb*. Mills and Mar (2000) investigated by X-ray powder diffraction the crystal structure of the $Nd_{12}Ga_4Sb_{23}$ compound, $Pr_{12}Ga_4Sb_{23}$ type structure, $a = 0.4268$, $b = 1.308$, $c = 2.6425$. The sample was synthesized by direct reaction of the elements in evacuated silica tubes.

3.1.6.12. *Nd–Ge–Sb*. Lam et al. (2001) determined the crystal structure of the $Nd_6Ge_{3.6}Sb_{12.4}$ compound from X-ray single crystal diffraction, $La_6Ge_{2.8}Sb_{13.2}$ structure type, $a = 0.4210$, $b = 1.06362$, $c = 2.6536$. The crystal was obtained from a sample synthesized by direct reaction of the elements at 1223 K.

3.1.6.13. *Nd–Zr, Nb–Sb*. The compounds Nd_3ZrSb_5 and Nd_3NbSb_5 belong to the Hf_5CuSn_3 anti-type structure with the lattice parameters $a = 0.9413$, $c = 0.6275$, and $a = 0.9360$, $c = 0.6186$, respectively (Bollere et al., 1995; X-ray powder diffraction).

3.1.6.14. *Nd–Ru–Sb*. The crystal structure of the $\text{NdRu}_4\text{Sb}_{12}$ compound was investigated by Braun and Jeitschko (1980). It was found to form the $\text{LaFe}_4\text{P}_{12}$ type, $a = 0.92642$ (X-ray powder diffraction). The purities of the starting materials and the experimental procedure were the same as for $\text{LaFe}_4\text{Sb}_{12}$.

3.1.6.15. *Nd–Rh–Ge*. Malik and Adroja (1991b) established the KHg_2 type structure with $a = 0.4584$, $b = 0.7329$, $c = 0.7838$ for the NdRhSb compound by using X-ray powder diffraction of an arc melted alloy. The purities of the metals were better than 99.99%.

The existence of NdRh_2Sb_2 with a tetragonal structure was reported by Menon Latica and Malik (1996).

3.1.6.16. *Nd–Pd–Sb*. Marazza et al. (1980) established the CaIn_2 type structure with $a = 0.4580$, $c = 0.7716$ for NdPdSb compound by using X-ray powder diffraction and metallographic analyses. For the sample preparation and the purity of starting components, see Y–Pd–Sb system. The crystallographic characteristics were confirmed from powder diffraction of arc melted and annealed at 1073 K alloys with $a = 0.4577$, $c = 0.7676$ (Zygmunt and Szytula, 1995). Mehta et al. (1995) reported an orthorhombic structure for NdPdSb at room temperature: SG $Pmma$, $a = 0.45833$, $b = 0.77189$, $c = 0.7937$.

NdPdSb_2 was found to crystallize with the HfCuSi_2 type structure with lattice parameters of $a = 0.44647$, $c = 0.9738$ (Sologub et al., 1994). For experimental details, see LaNiSb_2 .

Hoffman and Jeitschko (1988) established the CaBe_2Ge_2 type structure for NdPd_2Sb_2 , X-ray powder diffraction. The sample was synthesized in the same manner as LaPd_2Sb_2 .

3.1.6.17. *Nd–Ag–Sb*. The isothermal section for the Nd–Ag–Sb system at 870 K was established by Zaplatynsky and Salamakha (1994) (fig. 16). For the sample preparation, see Nd–Cr–Sb. The purity of the starting components was: Nd 99.9%, Ag 99.99%, and Sb 99.999%. One ternary compound NdAgSb_2 (1) was found to exist. Its crystal structure was independently investigated by two groups of authors (Sologub et al., 1995a; Brylak et al., 1995). This compound was found to belong to the HfCuSi_2 type structure, $a = 0.43357$, $c = 1.0624$. The alloys were prepared in the same manner as YAgSb_2 .

3.1.6.18. *Nd–Cd–Sb*. Figure 17 represents the partial isothermal section of the Nd–Cd–Sb system (33.0–100.0 at.% of Sb) at 870 K, after Sologub and Salamakha (1999). For the sample preparation, see Nd–Zn–Sb system. The phase relations are characterized by the existence of three ternary compounds: NdCdSb_2 (1), $\sim\text{Nd}_6\text{CdSb}_{15}$ (2) and $\sim\text{NdCdSb}$ (3).

Sologub et al. (1995b) reported on the crystallographic data for the NdCdSb_2 (1) compound (HfCuSi_2 -type structure, $a = 0.43454$, $c = 1.0827$; X-ray powder diffraction) obtained from a multiphase alloy. For the sample preparation and the purity of the starting materials,

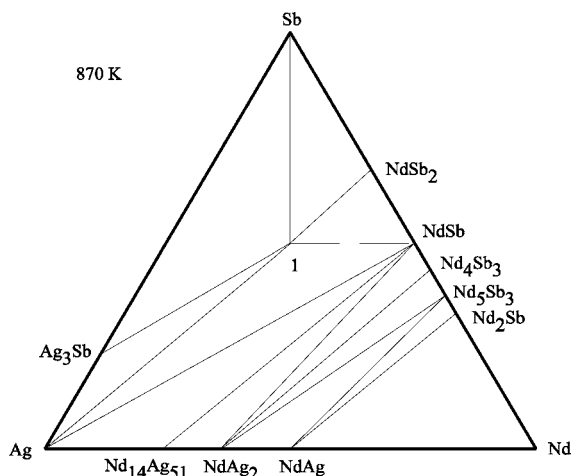


Fig. 16. Nd–Ag–Sb, isothermal section at 870 K.

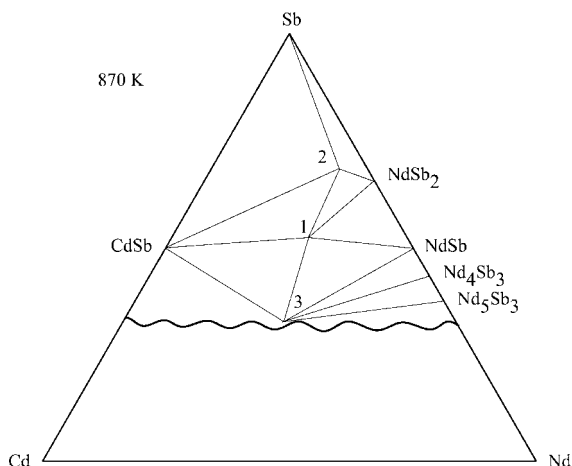


Fig. 17. Nd–Cd–Sb, partial isothermal section at 870 K (33.0–100.0 at.% Sb).

see $\text{CeZn}_{1-x}\text{Sb}_2$. Wollesen et al. (1996) confirmed the crystal structure using X-ray powder diffraction: $a = 0.43405$, $c = 1.0820$ for $\text{NdCd}_{1-x}\text{Sb}_2$. For experimental details, see $\text{LaMn}_{0.721(1)}\text{Sb}_2$. The purities of the starting elements were: Nd, greater than 99.9%, Cd, greater than 99.8%, Sb 99.9%.

3.1.6.19. *Nd–In–Sb*. The crystal structure of the $\text{NdIn}_{0.8}\text{Sb}_2$ compound was investigated by Ferguson et al. (1999) using X-ray powder diffraction: $\text{LaIn}_{0.8}\text{Sb}_2$ structure type, $a = 0.4445$, $b = 0.4297$, $c = 1.1677$, $\beta = 99.22^\circ$.

3.1.6.20. *Nd–Sn–Sb*. Ferguson et al. (1996) studied the crystal structure of the NdSn_xSb_2 by using a powder diffraction method, $a = 0.4195$, $b = 2.2606$, $c = 0.4449$. The sample was synthesized by direct reaction of the elements at 1223 K.

3.1.6.21. *Nd–Te–Sb*. The complete c – T diagram was presented for the Nd_2Te_3 – Sb_2Te_3 section by Geidarova and Rustamov (1985). The NdTe_3Sb compound, which formed incongruently, was observed to have the: Bi_2Te_3 structure type, $a = 0.432$, $c = 2.940$ (Geidarova and Rustamov, 1985).

NdSbTe has the Cu_2Sb type structure, $a = 0.4312$, $c = 0.9371$ (Charvillat et al., 1977).

3.1.6.22. *Nd–Hf–Sb*. Bollore et al. (1995) reported that Nd_3HfSb_5 (studied by X-ray powder diffraction) has the Hf_5CuSn_3 anti-type structure, $a = 0.9390$, $c = 0.6261$.

3.1.6.23. *Nd–Os–Sb*. The crystal structure of the $\text{NdOs}_4\text{Sb}_{12}$ compound was investigated by Braun and Jeitschko (1980). It was found to adopt the $\text{LaFe}_4\text{P}_{12}$ type structure, $a = 0.92989$ (X-ray powder diffraction). The purities of the starting materials and the experimental procedures were the same as for $\text{LaFe}_4\text{Sb}_{12}$. These results were confirmed by Evers et al. (1995), $a = 0.9300$ from X-ray single crystal analysis.

3.1.6.24. *Nd–Pt–Sb*. NdPtSb crystallizes with the CaIn_2 type structure, $a = 0.4544$, $c = 0.7878$ (Rossi et al., 1981; powder X-ray diffraction data). For the experimental details, see the LaPtSb . At variance with these data, Wenski and Mewis (1986a) reported the LiGaGe type structure for the NdPtSb compound, $a = 0.4535$, $c = 0.7866$ from X-ray single crystal investigation. For the sample preparation, see PrPtSb .

3.1.6.25. *Nd–Au–Sb*. The partial isothermal section of the Nd–Au–Sb system (33.0–100.0 at.% of Sb) at 870 K is shown in fig. 18 after Zaplatynsky (2000). Two ternary compounds were found to exist within investigated concentration region. For sample preparation, see Nd–Zn–Sb system.

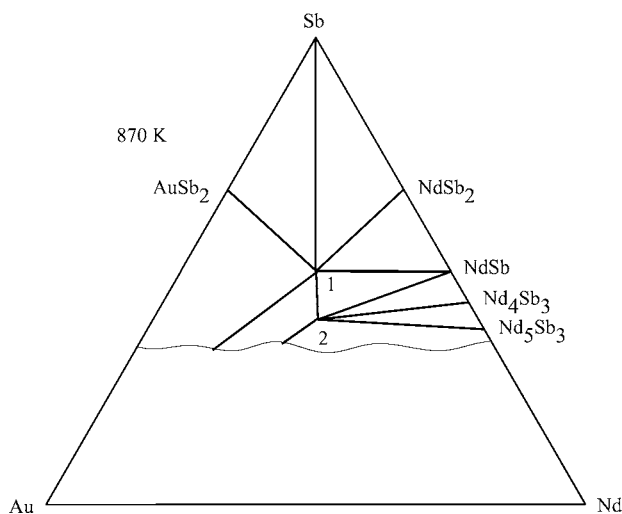


Fig. 18. Nd–Au–Sb , partial isothermal section at 870 K (33.0–100.0 at.% Sb).

The $Y_3Au_3Sb_4$ type structure was reported by Dwight (1977) for the $Nd_3Au_3Sb_4$ alloy (2) ($a = 0.9961$; X-ray powder diffraction). The conditions of synthesis were not specified. The formation and crystal structure of the $Nd_3Au_3Sb_4$ compound ($Y_3Au_3Sb_4$ type, $a = 1.99716$) was confirmed by Sologub et al. (1998). For the sample preparation, see $Nd_3Au_3Sb_4$.

$NdAuSb_2$ (1) was found to adopt the $HfCuSi_2$ type structure with the lattice parameters as $a = 0.43870$, $c = 1.0192$ (Sologub et al., 1994). The alloy was prepared in the same manner as $YCuSb_2$.

3.1.7. *Sm–M–Sb systems*

3.1.7.1. *Sm–Ti–Sb*. The crystal structure of the Sm_3TiSb_5 compound was investigated by Bollore et al. (1995). It was found to form the Hf_5CuSn_3 anti-type structure, $a = 0.9275$, $c = 0.6162$ (X-ray powder diffraction).

3.1.7.2. *Sm–V–Sb*. The $SmVSb_3$ compound has the $CeCrSb_3$ type structure: $a = 1.2904$, $b = 0.6213$, $c = 0.5980$ (X-ray powder diffraction; Brylak and Jeitschko, 1995).

3.1.7.3. *Sm–Cr–Sb*. $SmCrSb_3$ crystallizes with the $CeCrSb_3$ type structure: $a = 1.2838$, $b = 0.61594$, $c = 0.6032$ (X-ray powder diffraction; Brylak and Jeitschko, 1995). The structure was confirmed by Ferguson et al. (1997), $a = 1.2847$, $b = 0.6164$, $c = 0.6038$ (X-ray powder diffraction).

3.1.7.4. *Sm–Mn–Sb*. Sologub et al. (1995b) reported on the lattice parameters for the $SmMn_{0.90}Sb_2$ compound ($HfCuSi_2$ -type, $a = 0.42899$, $c = 1.0569$; X-ray powder diffraction) which was obtained from a multiphase alloy. For experimental details, see $LaMn_{0.87}Sb_2$. Wollesen et al. (1996) confirmed the crystal structure using X-ray powder diffraction: $a = 0.4298$, $c = 1.0520$ for $SmMn_{1-x}Sb_2$. For experimental details, see $LaMn_{0.721}Sb_2$. The purities of the starting elements were: Sm, greater than 99.9%, Mn, greater than 99.8%, Sb 99.9%.

3.1.7.5. *Sm–Fe–Sb*. Leithe-Jasper and Rogl (1994) investigated the formation and crystal structure of the $SmFe_{1-x}Sb_2$ compound by X-ray powder analysis of the alloy $Sm_{30-32}Fe_{13}Sb_{57-55}$ ($HfCuSi_2$ type structure, $a = 0.43252-0.43261$, $c = 0.95025-0.95156$). For the sample preparation and the purity of starting materials, see $LaFe_{1-x}Sb_2$.

The crystal structure of the $SmFe_4Sb_{12}$ compound was studied by Evers et al. (1995). It was found to adopt the $LaFe_4P_{12}$ type, $a = 0.9130$ (X-ray powder diffraction). The purities of the materials were 99.9% or better. Filings of the samarium were prepared under argon and annealed with the corresponding amounts of antimony in evacuated sealed silica tubes for two days at 723 K, followed by five days at 1023 K. The resulting antimonide $SmSb$ was ground together with appropriate amounts of Fe and Sb, pressed into pellets and sealed in evacuated silica tubes. The ampoules were quickly heated to 913 K, kept at this temperature for 24 h, and then quenched. The starting composition was $Sm:Fe:Sb = 2:4:13$. The excess antimony was removed by treating the product for several days with concentrated hydrochloric acid.

From a room temperature X-ray powder diffraction analysis $Sm_6Fe_{13}Sb$ was found to crystallize with the ordered $La_6Co_{11}Ga_3$, i.e., the $Nd_6Fe_{13}Si$ type, $a = 0.8041$, $c = 2.3048$

(Weitzer et al., 1993). An alloy was synthesized from ingots and compacted powders of the constituent elements 99.9% pure by arc melting followed by annealing at 1073 for 3 days and quenched in cold water.

The binary $\text{Sm}_2\text{Fe}_{17}$ compound dissolves about 6 at.% of Sb at 1223 K (Zhang et al., 2000).

3.1.7.6. *Sm–Co–Sb*. Leithe-Jasper and Rogl (1994) investigated the formation and crystal structure of the $\text{SmCo}_{1-x}\text{Sb}_2$ compound by X-ray powder analysis of the alloy $\text{Sm}_{28}\text{Co}_{17}\text{Sb}_{55}$ (HfCuSi₂ type structure, $a = 0.43415$, $c = 0.96700$). For the sample preparation and the purity of starting materials, see $\text{LaFe}_{1-x}\text{Sb}_2$. Wollesen et al. (1996) confirmed the crystal structure by using X-ray powder diffraction: $a = 0.43346$, $c = 0.9650$ for $\text{SmCo}_{1-x}\text{Sb}_2$. For synthesis, see $\text{LaMn}_{0.721}\text{Sb}_2$. The purities of the starting elements were: Sm, greater than 99.9%, Co, greater than 99.8%, Sb 99.9%.

3.1.7.7. *Sm–Ni–Sb*. Pankevich et al. (1983) reported the crystal structure for the SmNiSb_2 compound, HfCuSi₂ type structure, $a = 0.4335$, $c = 0.9513$ (X-ray powder diffraction; arc melted and annealed at 870 K for two weeks). The crystallographic characteristics were confirmed by Sologub et al. (1994), $a = 0.43406$, $c = 0.9523$. For experimental details, see LaNiSb_2 .

Early investigations of SmNiSb showed that it had the AlB_2 type structure with $a = 0.4372$, $c = 0.3843$ (Pecharsky et al., 1983a; X-ray powder analysis). For experimental procedure, see ScNiSb . At variance with these data, Hartjes and Jeitschko (1995) suggested ZrBeSi type structure, $a = 0.4387$, $c = 0.7699$ from X-ray powder diffraction. For experimental details, see LaNiSb .

CeGa_2Al_2 type structure was reported for SmNi_2Sb_2 by Pecharsky et al. (1982), $a = 0.4261$, $c = 0.9838$ from X-ray powder diffraction. For sample preparation, see CeNi_2Sb_2 . Hoffman and Jeitschko (1988) established a defect CaBe_2Ge_2 type structure for $\text{SmNi}_{2-x}\text{Sb}_2$ alloy, $a = 0.4281$, $c = 0.9838$, X-ray powder diffraction. Sample preparation, see $\text{CeNi}_{2-x}\text{Sb}_2$.

3.1.7.8. *Sm–Cu–Sb*. A ternary compound of samarium with copper and antimony of the stoichiometric ratio 3:3:4 was identified and studied by means of X-ray analysis by Skolozdra et al. (1993). The compound $\text{Sm}_3\text{Cu}_3\text{Sb}_4$ was found to have the $\text{Y}_3\text{Au}_3\text{Sb}_4$ type structure with a lattice parameter of $a = 0.9620$ (X-ray powder diffraction). For experimental details, see the Y–Cu–Sb system.

SmCuSb_2 crystallizes with a HfCuSi₂ type structure with the lattice parameters of $a = 0.42939$, $c = 0.9999$ (Sologub et al., 1994). For experimental details, see LaNiSb_2 .

3.1.7.9. *Sm–Zn–Sb*. Sologub et al. (1995b) reported on the crystallographic data for the $\text{SmZn}_{1-x}\text{Sb}_2$ compound (HfCuSi₂ type structure, $a = 0.42997$, $c = 1.0272$; X-ray powder diffraction) which was obtained from a multiphase alloy. For the sample preparation and the purity of starting materials, see $\text{CeZn}_{1-x}\text{Sb}_2$. Wollesen et al. (1996) confirmed the crystal structure of $\text{SmZn}_{1-x}\text{Sb}_2$ by using X-ray powder diffraction: $a = 0.43010$, $c = 1.0271$.

For experimental details, see $\text{LaMn}_{0.721}\text{Sb}_2$. The purities of the starting elements were: Sm, greater than 99.9%, Zn, greater than 99.8%, Sb 99.9%.

The crystal structure of the $\text{Sm}_6\text{ZnSb}_{15}$ compound was investigated by Sologub et al. (1996b) by the X-ray powder diffraction. It was found to crystallize with the $\text{La}_6\text{MnSb}_{15}$ structure type, $a = 1.5004$, $b = 1.8794$, $c = 0.41769$. For sample preparation, see $\text{Ce}_6\text{ZnSb}_{15}$.

3.1.7.10. *Sm–Ga–Sb*. SmGaSb_2 crystallizes with the NaCl type structure, $a = 0.60896$ (Kuliev et al., 1990).

Mills and Mar (2000) established the crystal structure for the $\text{Sm}_{12}\text{Ga}_4\text{Sb}_{23}$ compound from X-ray powder diffraction ($\text{Pr}_{12}\text{Ga}_4\text{Sb}_{23}$ type, $a = 0.4213$, $b = 1.9120$, $c = 2.6009$). The sample was synthesized by direct reaction of the elements in evacuated silica tubes.

3.1.7.11. *Sm–Ge–Sb*. Lam et al. (2001) investigated the crystal structure of the $\text{Sm}_6\text{Ge}_{5-x}\text{Sb}_{11+x}$ compound using X-ray powder diffraction ($\text{La}_6\text{Ge}_{2.8}\text{Sb}_{13.2}$ type structure, $a = 0.41942$, $b = 1.0537$, $c = 2.6350$).

3.1.7.12. *Sm–Se–Sb*. Rustamov et al. (1981b) reported from X-ray powder diffraction the crystal structure of the compound $\text{Sm}_3\text{Se}_9\text{Sb}_4$ obtained by using a chemical vapour transport technique, $\text{Eu}_3\text{S}_9\text{Sb}_4$ structure type, $a = 1.744$, $b = 0.410$, $c = 2.492$.

3.1.7.13. *Sm–Nb–Sb*. Sm_3NbSb_5 crystallizes with the Hf_5CuSn_3 anti-type structure, $a = 0.9344$, $c = 0.6234$ (X-ray powder diffraction; Bollere et al., 1995).

3.1.7.14. *Sm–Ru–Sb*. The crystal structure of the $\text{SmRu}_4\text{Sb}_{12}$ compound was investigated by Evers et al. (1995). It crystallizes with the $\text{LaFe}_4\text{P}_{12}$ type structure, $a = 0.9259$ (X-ray powder diffraction). The purities of the materials were 99.9% or better. Filings of samarium were prepared under argon and annealed with the corresponding amounts of antimony in evacuated sealed silica tubes for two days at 723 K, followed by five days at 1023 K. The resulting antimonide SmSb was ground together with appropriate amounts of Ru and Sb, pressed into pellets and sealed in evacuated silica tubes. The ampules were quickly heated to 873 K, were kept at this temperature for 24 h, and were then quenched. The starting composition was Sm:Ru:Sb = 2:4:13. The excess antimony was removed by treating the product for several days with concentrated hydrochloric acid.

3.1.7.15. *Sm–Pd–Sb*. Marazza et al. (1980) established the CaIn_2 type structure with $a = 0.4572$, $c = 0.7546$ for the SmPdSb compound by using X-ray powder diffraction and metallographic analyses. For the sample preparation and the purity of the starting components, see Y–Pd–Sb system. The crystallographic characteristics were confirmed from X-ray powder diffraction of arc-melted and annealed at 1073 K alloys: CaIn_2 type, $a = 0.4578$, $c = 0.7527$ (Zygmunt and Szytula, 1995).

SmPdSb_2 was found to adopt the HfCuSi_2 type structure with lattice parameters of $a = 0.44315$, $c = 0.9627$ (Sologub et al., 1994). For experimental details, see LaNiSb_2 .

Hoffman and Jeitschko (1988) established the CaBe_2Ge_2 type structure for SmPd_2Sb_2 , X-ray powder diffraction. The sample was synthesized in the same manner as LaPd_2Sb_2 .

3.1.7.16. *Sm–Ag–Sb*. SmAgSb_2 was observed and studied by Sologub et al. (1995a). It was found to crystallize with HfCuSi_2 type structure with lattice parameters as follows $a = 0.43126$, $c = 1.0548$ by X-ray powder diffraction of arc melted and annealed at 870 K for 14 days alloy. The purity of the starting materials was 99.9 wt.%. The existence and crystal structure of SmAgSb_2 compound were independently confirmed by Brylak et al. (1995) ($a = 0.4312$, $c = 1.0555$; X-ray powder diffraction). For sample preparation, see YAgSb_2 . The starting materials were: Sm 99.9%, Ag M3N, and Sb 325 mesh, M2N5.

3.1.7.17. *Sm–Cd–Sb*. Sologub et al. (1995b) reported on the crystallographic data for the SmCdSb_2 compound (HfCuSi_2 type structure, $a = 0.43301$, $c = 1.0782$; X-ray powder diffraction) which obtained from a multiphase alloy. For the sample preparation and the purity of the starting materials, see $\text{CeZn}_{1-x}\text{Sb}_2$. Wollesen et al. (1996) confirmed the crystal structure by using X-ray powder diffraction: $a = 0.43165$, $c = 1.078$ for $\text{SmCd}_{1-x}\text{Sb}_2$. For experimental details, see $\text{LaMn}_{0.721(1)}\text{Sb}_2$. The purities of the starting elements were: Sm, greater than 99.9%, Cd, greater than 99.8%, Sb 99.9%.

3.1.7.18. *Sm–Sn–Sb*. The NdTe_3 type structure was reported for Sm_2SnSb_3 , $a = 0.4228$, $b = 2.299$, $c = 0.4478$ from an X-ray single crystal investigation (Wang et al., 1967). The single crystal was isolated from a sample obtained by heating starting components at 773 K for 24 h, 973 K for 1 week and 1023 K for 15 days.

Ferguson et al. (1996) investigated the crystal structure of the SmSn_xSb_2 by using X-ray powder diffraction $a = 0.4174$, $b = 2.2384$, $c = 0.4416$. The sample was synthesized by direct reaction of the elements at 1223 K.

3.1.7.19. *Sm–Te–Sb*. The complete c – T diagrams were presented for the Sb_2Te_3 – Sm_2Te_3 and Sb_2Te_3 – SmTe sections by Geidarova and Rustamov (1985) and Sadygov et al. (1988a), respectively. The SmTe_3Sb compound, which formed by incongruent melting, was observed by Geidarova and Rustamov (1985) to have the Bi_2Te_3 structure type, $a = 0.446$, $c = 3.020$. Sadygov et al. (1988a) reported from X-ray powder diffraction the crystal structure for two compounds: SmTe_4Sb_2 , Th_3P_4 structure type, $a = 1.049$ and SmTe_7Sb_4 , Th_3P_4 , $a = 1.072$. The samples were prepared by heating in evacuated quartz tubes at 1450 K and oven cooling.

SmSbTe crystallizes with the Cu_2Sb structure type, $a = 0.4287$, $c = 0.9307$ after Charvillat et al. (1977).

3.1.7.20. *Sm–Hf–Sb*. Bollore et al. (1995) studied the crystal structure of the Sm_3HfSb_5 compound. It was found to form the Hf_5CuSn_3 anti-type structure, $a = 0.9340$, $c = 0.6230$ (X-ray powder diffraction).

3.1.7.21. *Sm–Os–Sb*. The $\text{SmOs}_4\text{Sb}_{12}$ compound forms the $\text{LaFe}_4\text{P}_{12}$ type structure, $a = 0.93009$ after Braun and Jeitschko (1980) (X-ray powder diffraction). The purities of the starting materials and the experimental procedure were the same as for $\text{LaFe}_4\text{Sb}_{12}$.

3.1.7.22. *Sm–Pt–Sb*. SmPtSb crystallizes with the MgAgAs -type structure, $a = 0.6554$ (Rossi et al., 1981; powder X-ray diffraction data). For the experimental details, see the LaPtSb system.

3.1.7.23. *Sm–Au–Sb*. The $\text{Y}_3\text{Au}_3\text{Sb}_4$ type structure was reported by Dwight (1977) for the $\text{Sm}_3\text{Au}_3\text{Sb}_4$ alloy ($a = 0.9909$; X-ray powder diffraction). The conditions of synthesis were not specified.

SmAuSb_2 was found to adopt the HfCuSi_2 type structure with lattice parameters of $a = 0.43653$, $c = 1.0134$ (Sologub et al., 1994). For experimental details, see LaNiSb_2 .

3.1.8. *Eu–M–Sb systems*

3.1.8.1. *Eu–Li–Sb*. The EuLiSb compound has the TiNiSi structure type: $a = 0.7914$, $b = 0.4773$, $c = 0.8358$ (Albering et al., 1997).

3.1.8.2. *Eu–Mn–Sb*. Rühl and Jeitschko (1979) reported the results of an X-ray powder investigation of EuMn_2Sb_2 which has the CaAl_2Si_2 type structure, $a = 0.4570$, $c = 0.7660$. The proper amounts of the starting elements were heated in an evacuated tube at 1200–1250 K for 1 week and rapidly quenched.

$\text{Eu}_{14}\text{MnSb}_{11}$ forms the $\text{Ca}_{14}\text{AlSb}_{11}$ type structure, $a = 1.7300$, $c = 2.2746$ (X-ray single crystal diffraction; Rehr and Kauzlarich, 1994). A single crystal was isolated from a sample obtained by heating the starting components (Eu, Mn, and Sb (6N)) in a quartz tube under argon at 1523 K for 24 hours.

3.1.8.3. *Eu–Fe–Sb*. The crystal structure of the $\text{EuFe}_4\text{Sb}_{12}$ compound was investigated by Evers et al. (1995). It was found to adopt the $\text{LaFe}_4\text{P}_{12}$ type structure, $a = 0.9165$ (X-ray powder diffraction). The purities of the materials were 99.9% or better. Filings of europium were prepared under argon and annealed with the corresponding amounts of antimony in evacuated sealed silica tubes for two days at 723 K, followed by five days at 1023 K. The resulting antimonide EuSb_2 was ground together with the appropriate amounts of Fe and Sb, pressed into pellets and sealed in evacuated silica tubes. The ampules were quickly heated to 933 K, kept at this temperature for 3 h, cooled at $1^\circ\text{C}/\text{h}$ to 873 K and then quenched. The starting composition was $\text{Eu}:\text{Fe}:\text{Sb} = 2:4:14$. The excess antimony was removed by treating the product for several days with concentrated hydrochloric acid.

3.1.8.4. *Eu–Ni–Sb*. Marchand and Jeitschko (1978) investigated the crystal structure of the EuNi_2Sb_2 compound (ThCr_2Si_2 type structure: $a = 0.43834$, $c = 1.0664$; X-ray powder diffraction). Stoichiometric amounts of the elemental components (Eu, Ni better than 99.5%, Sb better than 99%) were sealed under argon in silica tubes, heated at 920 K for 12 h, followed by 4 h at 1250 K and rapid cooling. The samples were then ground to powder, cold pressed to

small pellets, resealed in silica tubes under Ar, and annealed for 15 h at 1250 K. The structure refinement from single crystal data confirmed the structure type and established the composition as $\text{EuNi}_{1.53}\text{Sb}_2$ and the lattice parameters as $a = 0.4340$, $c = 1.0597$ (Hoffman and Jeitschko, 1985). A single crystal was selected from a sample prepared by annealing the elemental components for 5 days at 1073 K. The resulting button was melted in a high-frequency furnace and quenched.

3.1.8.5. *Eu–Cu–Sb*. EuCuSb was found to crystallize with the ZrBeSi type structure with lattice parameters of $a = 0.4512$, $c = 0.8542$ (Tomuschat and Schuster, 1981; X-ray photographic powder method).

Dunner et al. (1995) reported the crystal structure for the EuCu_2Sb_2 compound to have the CaBe_2Ge_2 type structure, $a = 0.4504$, $c = 1.0824$ (powder and single crystal diffraction). The sample was obtained by the reaction: $2\text{Eu} + 2\text{CuCl} + 2\text{Sb} \rightarrow \text{EuCu}_2\text{Sb}_2 + \text{EuCl}_2$, and annealed at 1120 K for 100 h.

3.1.8.6. *Eu–Zn–Sb*. EuZn_2Sb_2 with the CaAl_2Si_2 type structure ($a = 0.4489$, $c = 0.7609$; X-ray powder diffraction data) was obtained by Klüfers et al. (1980) from an alloy melted in a corundum crucible at 1173–1373 K for 4–6 hours and annealed at 1373–1473 K for 4–48 hours.

3.1.8.7. *Eu–Se–Sb*. EuSe_4Sb_2 was found by Rustamov et al. (1977) to form PbS_4Bi_2 structure type, $a = 1.14$, $b = 0.376$, $c = 1.42$ in an alloy obtained by melting the starting components in evacuated quartz tube at 1373–1423 K. The crystal structure was confirmed by Aliev et al. (1978) for a sample prepared by a chemical transport reaction technique: $a = 1.137$, $b = 0.400$, $c = 1.135$ from single crystal X-ray diffraction.

Rustamov et al. (1981b) and Aliev et al. (1986) reported the crystal structure for the $\text{Eu}_3\text{Se}_9\text{Sb}_4$ compound, $\text{Eu}_3\text{S}_9\text{Sb}_4$ structure type, $a = 1.717$, $b = 0.406$, $c = 2.488$ from X-ray powder diffraction. The sample was prepared by a chemical vapour transport technique.

3.1.8.8. *Eu–Ru–Sb*. The crystal structure of the $\text{EuRu}_4\text{Sb}_{12}$ compound was investigated by Braun and Jeitschko (1980). It was found to form the $\text{LaFe}_4\text{P}_{12}$ type structure, $a = 0.92824$ (X-ray powder diffraction). The purities of starting materials and experimental procedure were the same as for $\text{LaRu}_4\text{Sb}_{12}$. These results were confirmed by Evers et al. (1995), $a = 0.9284$ from an X-ray single crystal analysis.

3.1.8.9. *Eu–Pd–Sb*. The structure refinement from single crystal data established the CaBe_2Ge_2 type structure for EuPd_2Sb_2 $a = 0.4629$, $c = 1.0568$ (Hoffman and Jeitschko, 1985). A single crystal was isolated from the sample prepared by annealing the elemental components for 10 days at 1020 K. The resulting button was oven cooled.

EuPdSb crystallizes with the TiNiSi type structure, $a = 0.7627$, $b = 0.4695$, $c = 0.7925$ (Malik and Adroja, 1991c; powder X-ray diffraction data). Starting elements (Eu 4N, Pd 4N, Sb 4N) were arc melted under argon.

3.1.8.10. *Eu–Ag–Sb*. EuAgSb was found to crystallize with the ZrBeSi type structure with lattice parameters of $a = 0.4755$, $c = 0.8283$ (Tomuschat and Schuster, 1981).

3.1.8.11. *Eu–Sn–Sb*. The ternary compound EuSn₃Sb₄ was synthesized at 1173 K in a tin flux, and its crystal structure was determined by X-ray single crystal diffraction methods. It crystallizes in the orthorhombic *Pnma* space group with lattice parameters $a = 0.9954$, $b = 0.43516$, $c = 2.2650$ (Lam et al., 2000).

3.1.8.12. *Eu–Te–Sb*. Aliev and Rustamov (1978) reported the *c–T* diagram for the EuTe–Sb₂Te₃ section.

EuTe₄Sb₂ belongs to a Th₃P₄ structure type, $a = 1.044$ after Aliev et al. (1985). The same group of authors studied the crystal structure for EuTe₇Sb₄, Th₃P₄ structure type, $a = 1.062$ (Aliev et al., 1986).

Hulliger and Ott (1977) reported the anti-Th₃P₄ structure type for Eu₄TeSb₂, $a = 0.9814$ from X-ray powder diffraction. The sample was placed in tantalum or molybdenum crucible and heated in quartz tube below 1273 K.

3.1.8.13. *Eu–Os–Sb*. The crystal structure of the EuOs₄Sb₁₂ compound was investigated by Braun and Jeitschko (1980). It belongs to the LaFe₄P₁₂ type structure, $a = 0.93187$ (X-ray powder diffraction). The purities of the starting materials and the experimental procedure were the same as for LaFe₄Sb₁₂.

3.1.8.14. *Eu–Pt–Sb*. EuPtSb was found to form the TiNiSi type structure ($a = 0.7581$, $b = 0.4642$, $c = 0.7893$) from X-ray single crystal diffraction by Wenski and Mewis (1986b).

3.1.8.15. *Eu–Au–Sb*. Tomuschat and Schuster (1981) reported the ZrBeSi type structure for EuAuSb, $a = 0.4669$, $c = 0.8486$ (X-ray photographic powder method). The sample was synthesized by melting the starting components in corundum crucible under argon at 1273 K 12–16 h and annealing at 1373 K 14 h. Suzuki et al. (1993) established a CaIn₂ type structure for EuAuSb, $a = 0.4681$, $c = 0.8422$. For the sample preparation, see CeAuSb.

3.1.9. *Gd–M–Sb systems*

3.1.9.1. *Gd–Li–Sb*. A systematic study of the Gd–Li–Sb system at 470 K was performed by Pavlyuk (1993) over the whole concentration region by means of X-ray powder analysis (fig. 19). The samples were prepared by arc melting under argon and annealed in evacuated quartz ampoules at 470 K for 10 days. Five ternary phases were observed, the crystal structure was established only for two of them: GdLi₃Sb₂ (2), YLi₃Sb₂ type structure, $a = 0.4547$, $c = 0.7196$ (powder diffraction) and Gd₃Li₄Sb₄ (3), Gd₆Cu₈Ge₈ type structure, $a = 1.4594$, $b = 0.4513$, $c = 0.7100$ (powder diffraction). Crystal structure for last three compounds ~GdLi₇Sb₂ (1), ~Gd₄Li₃Sb₄ (4) and ~Gd₂LiSb (5) have not been investigated. No homogeneous ranges were encountered for the ternary compounds. The liquid immiscibility region, existing in the Gd–Li binary system, extends to 20 at.% Ge in the ternary system.

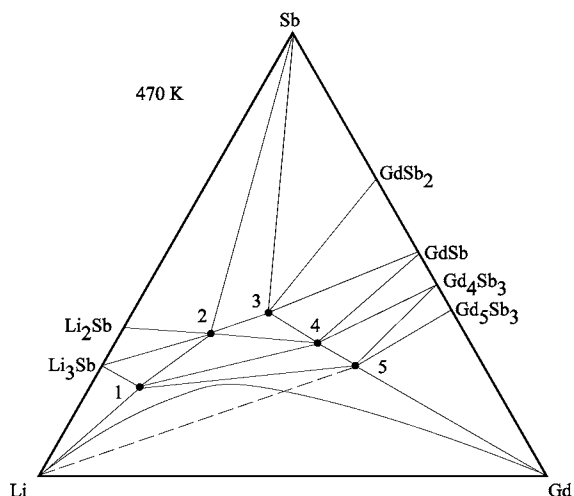


Fig. 19. Gd–Li–Sb, isothermal section at 470 K.

3.1.9.2. *Gd–Cr–Sb*. Ferguson et al. (1997) investigated the crystal structure of the GdCrSb_3 compound (CeCrSb₃ type structure: $a = 1.2760$, $b = 0.6153$, $c = 0.6004$, X-ray powder diffraction).

3.1.9.3. *Gd–Fe–Sb*. Leithe-Jasper and Rogl (1994) investigated the formation and crystal structure of the $\text{GdFe}_{1-x}\text{Sb}_2$ compound by X-ray powder analysis of the alloy $\text{Gd}_{35}\text{Fe}_{10}\text{Sb}_{55}$ (HfCuSi₂ type structure, $a = 0.43080$, $c = 0.94125$). For the sample preparation and the purity of the starting materials, see $\text{LaFe}_{1-x}\text{Sb}_2$.

3.1.9.4. *Gd–Ni–Sb*. GdNiSb_2 is isostructural with the HfCuSi₂ type structure with lattice parameters of $a = 0.43345$, $c = 0.9452$ (Sologub et al., 1994). The alloy was prepared in the same manner as YCuSb_2 .

Early investigations of the GdNiSb compound showed that it had the MgAgAs-type with $a = 0.6340$ (Dwight, 1974) from X-ray powder analysis of an alloy arc melted under argon and annealed at 973 K. Hartjes and Jeitschko (1995) confirmed the crystal structure and obtained the lattice parameter of $a = 0.6323$ by X-ray powder diffraction. For experimental details, see LaNiSb . At variance to these data, Pecharsky et al. (1983a) suggested the AlB_2 type structure with $a = 0.4329$, $c = 0.3918$ from X-ray powder analysis of an alloy arc melted under argon and annealed at 870 K.

Marchand and Jeitschko (1978) investigated the crystal structure of GdNi_2Sb_2 compound (ThCr_2Si_2 type structure: $a = 0.4259$, $c = 0.9809$; X-ray powder diffraction). For the sample preparation, see EuNi_2Sb_2 . A later investigation (Hoffman and Jeitschko, 1988) established the defect CaBe_2Ge_2 type structure for the $\text{GdNi}_{2-x}\text{Sb}_2$ alloy, $a = 0.4261$, $c = 0.9741$, X-ray powder diffraction. For the experimental details, see $\text{CeNi}_{2-x}\text{Sb}_2$. The same authors investigated the antimony rich section of the ternary system Gd–Ni–Sb at 1070 K. Except for $\text{GdNi}_{2-x}\text{Sb}_2$, no other ternary compound with a high antimony content was observed. In sam-

ples quenched from 1070 K $\text{GdNi}_{2-x}\text{Sb}_2$ was found to be in equilibrium with GdSb, elemental antimony, NiSb and the high temperature modification of Ni_3Sb . Kaczmarek et al. (1995) confirmed the crystal structure with similar lattice parameters for GdNi_2Sb_2 ; CaBe_2Ge_2 type structure, $a = 0.4288$, $c = 0.9763$ from powder diffraction of arc melted alloys.

Mozharivskij and Franzen (2000b) reported the crystal structure of the $\text{Gd}_5\text{Ni}_2\text{Sb}$ ($\text{Mo}_5\text{B}_2\text{Si}$ structure type, $a = 0.7698$, $c = 1.3403$) from X-ray powder diffraction of arc melted and annealed at 1070 K for 10 days alloy.

3.1.9.5. *Gd-Cu-Sb*. A ternary compound of gadolinium with copper and antimony of the 3:3:4 stoichiometric ratio was identified and studied by means of X-ray analysis by Skolozdra et al. (1993). $\text{Gd}_3\text{Cu}_3\text{Sb}_4$ compound was found to have the $\text{Y}_3\text{Au}_3\text{Sb}_4$ type with the lattice parameter of $a = 0.9571$ (X-ray powder diffraction). For experimental details, see the Y-Cu-Sb system. At variance with these data, Patil et al. (1996) reported a tetragonal distortion of the cubic crystal structure $\text{Y}_3\text{Cu}_3\text{Sb}_4$ for the $\text{Gd}_3\text{Cu}_3\text{Sb}_4$ alloy which was prepared by arc melting the constituent elements of purity better than 99.9% in an argon atmosphere and annealed at 1070 K for one week ($a = 0.958$, $c = 0.972$; X-ray powder diffraction).

GdCuSb_2 was found to form the HfCuSi_2 type structure with lattice parameters of $a = 0.42783$, $c = 0.9946$ (Sologub et al., 1994). For experimental details, see LaNiSb_2 .

Kaczmarek et al. (1995) established the crystal structure for the GdCu_2Sb_2 compound; CaBe_2Ge_2 type structure, $a = 0.4266$, $c = 0.9953$ from powder diffraction of arc melted alloys.

3.1.9.6. *Gd-Zn-Sb*. Sologub et al. (1995b) reported on the crystallographic data for the $\text{GdZn}_{1-x}\text{Sb}_2$ compound (HfCuSi_2 type structure, $a = 0.42838$, $c = 1.0242$; X-ray powder diffraction) which was obtained from a multiphase alloy. For the sample preparation and the purity of the starting materials, see $\text{CeZn}_{1-x}\text{Sb}_2$. Wollesen et al. (1996) confirmed the crystal structure by using X-ray powder diffraction: $a = 0.42748$, $c = 1.02614$ for $\text{GdZn}_{1-x}\text{Sb}_2$. For experimental details, see $\text{LaMn}_{0.721(1)}\text{Sb}_2$. The purities of the starting elements were: Gd, greater than 99.9%, Zn, greater than 99.8%, Sb 99.9%.

The crystal structure of the $\text{Gd}_6\text{ZnSb}_{15}$ compound was investigated by Sologub et al. (1996a) by the X-ray powder diffraction. It was found to crystallize with the $\text{La}_6\text{MnSb}_{15}$ structure type, $a = 1.4942$, $b = 1.8740$, $c = 0.41528$. For the sample preparation, see $\text{Ce}_6\text{ZnSb}_{15}$.

3.1.9.7. *Gd-Ge-Sb*. Lam et al. (2001) determined the crystal structure of the $\text{Gd}_6\text{Ge}_{4.3}\text{Sb}_{11.7}$ compound, $a = 0.41509$, $b = 1.04438$, $c = 2.6240$ from X-ray single crystal diffraction data. The sample was synthesized by direct reaction of the elements at 1223 K.

3.1.9.8. *Gd-Se-Sb*. Aliev et al. (1977) constructed the complete c - T diagram for the Gd_2Se_3 - Sb_2Se_3 section. The $\text{GdSe}_{30}\text{Sb}_{19}$ compound with the S_3Sb_2 type structure, $a = 1.173$, $b = 0.412$, $c = 1.1846$ was observed from a sample annealed at 723–773 K for 300 h. A small homogeneity field was found for $(\text{Gd}_x\text{Sb}_{1-x})_2\text{Se}_3$: $x = 0$ –0.05, $a = 1.162$ –1.173, $b = 0.396$ –0.412, $c = 1.177$ –1.1846.

3.1.9.9. *Gd–Zr–Sb*. Morozkin and Sviridov (2001) investigated the crystal structure of the GdZrSb compound by X-ray powder diffraction. The CeScSi structure type was established, $a = 0.4261$, $c = 1.6455$.

3.1.9.10. *Gd–Pd–Sb*. Marazza et al. (1980) established the CaIn₂ type structure with $a = 0.4566$, $c = 0.7452$ for the GdPdSb compound by using X-ray powder diffraction and metallographic analyses. For the sample preparation and the purity of the starting components, see Y–Pd–Sb system. Malik and Adroja (1991a) confirmed the crystal structure and lattice parameters, $a = 0.4565$, $c = 0.7443$ (X-ray diffraction; arc melted alloy).

GdPdSb₂ was found to adopt a HfCuSi₂ type structure with lattice parameters of $a = 0.44150$, $c = 0.9567$ (Sologub et al., 1994). For experimental details, see LaNiSb₂.

Mozharivskyj and Franzen (2000b) established the crystal structure of Gd₅Pd₂Sb to be isotypic with Mo₅B₂Si type structure, $a = 0.7812$, $c = 1.3645$ from the X-ray powder diffraction of arc melted and annealed at 1070 K for 10 days alloy.

3.1.9.11. *Gd–Ag–Sb*. GdAgSb₂ compound was observed and studied by Sologub et al. (1995a). It was found to crystallize with HfCuSi₂ type structure with lattice parameters of $a = 0.42965$, $c = 1.0518$ by X-ray powder diffraction of arc melted and annealed at 870 K for 14 days alloy. The purity of the starting materials was 99.9 wt.%. The existence and crystal structure of GdAgSb₂ compound were independently confirmed by Brylak et al. (1995) ($a = 0.42952$, $c = 1.0506$; X-ray powder diffraction). For the sample preparation, see YAgSb₂. The purity of the starting materials was: Gd 99.9%, Ag M3N, and Sb 325 mesh, M2N5.

3.1.9.12. *Gd–Te–Sb*. The complete c – T diagram was presented for the GdTe–Sb₂Te₃ section by Rustamov and Geidarova (1984).

Charvillat et al. (1977) determined the Cu₂Sb structure type for the GdSbTe compound, $a = 0.4262$, $c = 0.9258$ from a GdSb_{0.97}Te alloy and observed the existence of a homogeneity field: GdTe _{x} Sb, $x = 0.86$ – 0.97 , $a = 0.4274$ – 0.4262 , $c = 0.9243$ – 0.9258 .

3.1.9.13. *Gd–Pt–Sb*. The X-ray powder analysis of the GdPtSb compound showed that it had the MgAgAs type structure with $a = 0.6585$ (Dwight, 1974). For the sample preparation, see ScNiSb.

Mozharivskyj and Franzen (2001) reported the crystal structure for the Gd₅Pt₂Sb compound from X-ray powder diffraction data: Mo₅B₂Si type structure, which is an ordered version of the Cr₅B₃ structure type, $a = 0.7801$, $c = 1.3556$. For the experimental procedure, see Y₅Pt₂Sb.

3.1.9.14. *Gd–Au–Sb system*. The Y₃Au₃Sb₄ type structure was reported by Dwight (1977) for the Gd₃Au₃Sb₄ alloy ($a = 0.9864$; X-ray powder diffraction). The conditions of synthesis were not specified.

Table 2
Lattice parameters of the $Gd_4(Bi_xSb_{1-x})_3$ alloys

Bi concentration, x	a
0	0.92328
0.25	0.92680
0.50	0.93072
0.75	0.93449
1.00	0.93906

3.1.9.15. *Gd-Bi-Sb*. Niu et al. (2001) reported on the lattice parameters for the $Gd_4(Bi_xSb_{1-x})_3$ series with $x = 0, 0.25, 0.5, 0.75$ and 1 (table 2).

3.1.10. *Tb-M-Sb*

3.1.10.1. *Tb-Li-Sb*. One ternary compound, $TbLi_2Sb_2$, was observed with an unknown crystal structure (Pavlyuk, 1993).

3.1.10.2. *Tb-Cr-Sb*. Ferguson et al. (1997) established the crystal structure of the $TbCrSb_3$ compound: $CeCrSb_3$ type structure, $a = 1.2680$, $b = 0.6143$, $c = 0.6003$ from X-ray powder diffraction.

3.1.10.3. *Tb-Ni-Sb*. Mozharivskiy and Kuz'ma (1996) investigated the crystal structure of Tb_5Ni_2Sb (Mo_5B_2Si type structure, $a = 0.7641$, $c = 1.3266$; X-ray powder diffraction). The alloy was prepared in the same manner as Y_5Ni_2Sb . The starting materials were Tb not less than 99.8 wt.%, Ni and Sb 99.9 mass%.

$TbNiSb_2$ was found to crystallize with the $HfCuSi_2$ type structure with lattice parameters of $a = 0.43201$, $c = 0.9361$ (Sologub et al., 1994). The alloy was prepared in the same manner as $YCuSb_2$.

An early investigation of the $TbNiSb$ compound showed that it had the $MgAgAs$ -type with $a = 0.6327$ (Dwight, 1974), from an X-ray powder analysis of an alloy arc melted under argon and annealed at 973 K. Pecharsky et al. (1983a) and Hartjes and Jeitschko (1995) confirmed the crystal structure and obtained the lattice parameters as $a = 0.6302$ and $a = 0.6304$, respectively, by X-ray powder diffraction. For experimental details, see $ScNiSb$ and $LaNiSb$ respectively.

Hoffman and Jeitschko (1988) established the defect $CaBe_2Ge_2$ type structure for $TbNi_{2-x}Sb_2$, $a = 0.42496$, $c = 0.9649$, X-ray powder diffraction. For the sample preparation, see $CeNi_{2-x}Sb_2$.

3.1.10.4. *Tb-Cu-Sb*. A ternary compound of terbium with copper and antimony of the 3:3:4 stoichiometric ratio was identified and studied by means of X-ray analysis by Skolozdra et al. (1993). $Tb_3Cu_3Sb_4$ was found to have the $Y_3Au_3Sb_4$ type structure with a lattice parameter of $a = 0.9522$ (X-ray powder diffraction). For experimental details, see the $Y-Cu-Sb$ system.

$TbCuSb_2$ was found to adopt the $HfCuSi_2$ type structure with lattice parameters of $a = 0.42683$, $c = 0.9877$ (Sologub et al., 1994). The alloy was prepared in the same manner as $YCuSb_2$.

3.1.10.5. *Tb–Zn–Sb*. Wollesen et al. (1996) reported on the crystallographic data for the $\text{TbZn}_{1-x}\text{Sb}_2$ compound (HfCuSi₂ type structure, $a = 0.42611$, $c = 1.02297$; X-ray powder diffraction). For experimental details, see $\text{LaMn}_{0.721(1)}\text{Sb}_2$. The purities of the starting elements were: Tb, greater than 99.9%, Zn, greater than 99.8%, Sb 99.9%.

3.1.10.6. *Tb–Ge–Sb*. Lam et al. (2001) investigated the crystal structure of the $\text{Tb}_6\text{Ge}_{5-x}\text{Sb}_{11+x}$ compound using X-ray powder diffraction: $a = 0.41305$, $b = 1.0393$, $c = 2.6139$.

3.1.10.7. *Tb–Zr–Sb*. Morozkin and Sviridov (2001) reported the crystal structure for the TbZrSb compound from X-ray powder diffraction data: CeScSi type structure, $a = 0.4251$, $c = 1.6380$.

3.1.10.8. *Tb–Pd–Sb*. Marazza et al. (1980) established the CaIn_2 type structure with $a = 0.4550$, $c = 0.7384$ for the TbPdSb compound by using X-ray powder diffraction and metallographic analyses. For the sample preparation and the purity of the starting components, see Y–Pd–Sb system. The crystallographic characteristics were confirmed from powder diffraction data of arc melted and annealed at 1073 K alloys: CaIn_2 type structure, $a = 0.4551$, $c = 0.7411$ (Zygmunt and Szytula, 1995).

TbPdSb_2 was found to adopt the HfCuSi₂ type structure with lattice parameters of $a = 0.44097$, $c = 0.9480$ (Sologub et al., 1994). For experimental details, see LaNiSb_2 .

Mozharivskiy and Franzen (2000b) investigated the crystal structure of $\text{Tb}_5\text{Pd}_2\text{Sb}$, which has the $\text{Mo}_5\text{B}_2\text{Si}$ structure type, $a = 0.7730$, $c = 1.3508$ by X-ray powder diffraction of arc melted and annealed at 1070 K for 10 days alloy.

3.1.10.9. *Tb–Ag–Sb*. TbAgSb_2 compound was observed and studied by Sologub et al. (1995a). It was found to crystallize with HfCuSi₂ type structure with lattice parameters as follows: $a = 0.42774$, $c = 1.0477$ by X-ray powder diffraction of arc an melted and annealed at 870 K for 14 days alloy. The purity of starting materials was 99.9 wt.%. The existence and crystal structure of the TbAgSb_2 compound were independently confirmed by Brylak et al. (1995) ($a = 0.42833$, $c = 1.0476$; X-ray powder diffraction). For the sample preparation, see YAgSb_2 . The starting materials were: Tb 99.9%, Ag M3N, and Sb 325 mesh, M2N5.

3.1.10.10. *Tb–Te–Sb*. Rustamov and Geidarova (1984) constructed the complete c – T diagram for the $\text{TbTe–Sb}_2\text{Te}_3$ section.

3.1.10.11. *Tb–Pt–Sb*. An investigation of the TbPtSb compound by X-ray powder diffraction showed that it had the MgAgAs type structure with $a = 0.6540$ (Dwight, 1974). For the sample preparation, see ScNiSb .

Mozharivskiy and Franzen (2001) reported the crystal structure for the $\text{Tb}_5\text{Pt}_2\text{Sb}$ compound from X-ray powder diffraction data: $\text{Mo}_5\text{B}_2\text{Si}$ type structure, which is an ordered version of the Cr_5B_3 structure type, $a = 0.7748$, $c = 1.3463$. For the experimental procedure, see $\text{Y}_5\text{Pt}_2\text{Sb}$.

3.1.10.12. *Tb–Au–Sb*. The $\text{Tb}_3\text{Au}_3\text{Sb}_4$ alloy was reported by Dwight (1974) to have the $\text{Y}_3\text{Au}_3\text{Sb}_4$ type structure ($a = 0.9834$; X-ray powder diffraction). The conditions of synthesis were not specified. The same structure type was confirmed by Shaked et al. (1979) for a $\text{Tb}_3\text{Au}_3\text{Sb}_4$ sample obtained by arc melting the correct amounts of the elemental materials in a helium/argon atmosphere. The alloy was annealed at 960 K for one week and water quenched.

3.1.11. *Dy–M–Sb systems*

3.1.11.1. *Dy–Cr–Sb*. Ferguson et al. (1997) investigated the crystal structure of the DyCrSb_3 compound, CeCrSb_3 type structure: $a = 1.229$, $b = 0.6135$, $c = 0.5978$ by X-ray powder diffraction.

3.1.11.2. *Dy–Ni–Sb*. Mozharivskiy and Kuz'ma (1996) investigated the crystal structure of $\text{Dy}_5\text{Ni}_2\text{Sb}$ ($\text{Mo}_5\text{B}_2\text{Si}$ type structure, $a = 0.7593$, $c = 1.3258$; X-ray powder diffraction). The alloy was prepared in the same manner as $\text{Y}_5\text{Ni}_2\text{Sb}$. The starting materials were: Dy not less than 99.8 wt.%, Ni and Sb 99.9 wt.%.

DyNiSb_2 was found to adopt the HfCuSi_2 type structure with the lattice parameters of $a = 0.43029$, $c = 0.9305$ (Sologub et al., 1994). For experimental details, see LaNiSb_2 .

Dwight (1974) investigated the solubility of Ni in DySb : $(\text{DySb})_{1-x}\text{Ni}_x$, $x = 0-0.26$, NaCl type structure, $a = 0.6155-0.6255$. The same author established from X-ray powder analysis the crystal structure of DyNiSb : MgAgAs-type, $a = 0.6308$ (Dwight, 1974). For the sample preparation, see ScNiSb . Pecharsky et al. (1983a) and Hartjes and Jeitschko (1995) confirmed the crystal structure and obtained lattice parameters of $a = 0.6279$ and $a = 0.6298$, respectively, by X-ray powder diffraction. For experimental details, see ScNiSb and LaNiSb , respectively.

Hoffman and Jeitschko (1988) established the defect CaBe_2Ge_2 type structure for $\text{DyNi}_{2-x}\text{Sb}_2$ alloy, $a = 0.4207$, $c = 0.9587$, X-ray powder diffraction. For the sample preparation, see $\text{CeNi}_{2-x}\text{Sb}_2$.

3.1.11.3. *Dy–Cu–Sb*. A ternary compound of dysprosium with copper and antimony of the 3:3:4 stoichiometric ratio was identified and studied by means of X-ray analysis by Skolozdra et al. (1993). $\text{Dy}_3\text{Cu}_3\text{Sb}_4$ compound was found to have the $\text{Y}_3\text{Au}_3\text{Sb}_4$ type structure with a lattice parameter of $a = 0.9503$ (X-ray powder diffraction). For experimental details, see the Y–Cu–Sb system.

DyCuSb_2 was found to form the HfCuSi_2 type structure with lattice parameters of $a = 0.42669$, $c = 0.9817$ (Sologub et al., 1994). For the experimental details, see LaNiSb_2 .

3.1.11.4. *Dy–Ge–Sb*. Lam et al. (2001) investigated the crystal structure of the $\text{Dy}_6\text{Ge}_{5-x}\text{Sb}_{11+x}$ compound by using an X-ray powder diffraction method: $\text{La}_6\text{Ge}_{2.8}\text{Sb}_{13.2}$ type structure, $a = 0.41032$, $b = 1.0345$, $c = 2.6041$.

3.1.11.5. *Dy–Zr–Sb*. Morozkin and Sviridov (2001) determined the crystal structure of the DyZrSb compound from X-ray powder diffraction data, CeScSi type structure, $a = 0.4240$,

$c = 1.6349$. Later Morozkin et al. (2002) from phase diagram investigation at 1070 K established that this compound has a homogeneity field: $\text{Dy}_{33-28}\text{Zr}_{33-38}\text{Sb}_{33}$.

3.1.11.6. *Dy-Pd-Sb*. Marazza et al. (1980) established the MgAgAs type structure with $a = 0.6533$ for the DyPdSb compound using X-ray powder diffraction and metallographic analyses. For the sample preparation and the purity of the starting components, see *Y-Pd-Sb* system. At variance with these data, Zygmunt and Szytula (1995) reported the CaIn_2 type structure for this compound, $a = 0.4543$, $c = 0.7352$ from powder diffraction of arc melted and annealed at 1073 K alloys. Malik and Adroja (1991c) also observed CaIn_2 type structure, $a = 0.4526$, $c = 0.7325$ for DyPdSb (powder X-ray diffraction data). Their sample also contained the MgAgAs phase. For the experimental details, see *EuPdSb*.

DyPd_2Sb was reported to be isotypic with the crystal structure of MnCu_2Al with a lattice parameter of $a = 0.6682$ (Riani et al., 1995) from powder diffraction of the induction melted alloy.

Mozharivskiy and Franzen (2000b) investigated the crystal structure of the $\text{Dy}_5\text{Pd}_2\text{Sb}$ compound from an arc melted and annealed at 1070 K for 10 days alloy by using X-ray powder diffraction. The $\text{Mo}_5\text{B}_2\text{Si}$ type structure was established, $a = 0.7715$, $c = 1.3507$.

3.1.11.7. *Dy-Ag-Sb*. DyAgSb_2 compound was observed and studied by Sologub et al. (1995a) It was found to crystallize with the HfCuSi_2 type structure with lattice parameters as follows $a = 0.42733$, $c = 1.0453$ by X-ray powder diffraction of an arc melted and annealed at 870 K for 14 days alloy. The purity of starting materials was 99.9 wt.%. The existence and crystal structure of DyAgSb_2 were independently confirmed by Brylak et al. (1995) ($a = 0.42743$, $c = 1.0442$; X-ray powder diffraction). For the sample preparation, see *YAgSb}_2*. The starting materials were: Dy 99.9%, Ag M3N, and Sb 325 mesh, M2N5.

3.1.11.8. *Dy-Te-Sb*. The complete c - T diagrams were presented for the Sb_2Te_3 - Dy_2Te_3 section by Geidarova and Rustamov (1985) and by Geydarova et al. (1985), respectively. The DyTe_3Sb compound formed by incongruent melting and has the Bi_2Te_3 structure type, $a = 0.446$, $c = 3.020$ (Geidarova and Rustamov, 1985).

3.1.11.9. *Dy-Pt-Sb*. An investigation of DyPtSb showed that it had the MgAgAs -type with $a = 0.6531$ (Dwight, 1974) from X-ray powder analysis. For the sample preparation, see *ScNiSb*.

Mozharivskiy and Franzen (2001) reported the crystal structure for the $\text{Dy}_5\text{Pt}_2\text{Sb}$ compound from X-ray powder diffraction: $\text{Mo}_5\text{B}_2\text{Si}$ type structure, which is an ordered version of the Cr_5B_3 structure type, $a = 0.7686$, $c = 1.3420$. For the experimental procedure, see $\text{Y}_5\text{Pt}_2\text{Sb}$.

3.1.11.10. *Dy-Au-Sb*. The $\text{Y}_3\text{Au}_3\text{Sb}_4$ type structure was reported by Dwight (1977) for the $\text{Dy}_3\text{Au}_3\text{Sb}_4$ alloy ($a = 0.9811$; X-ray powder diffraction). The conditions of synthesis were not specified.

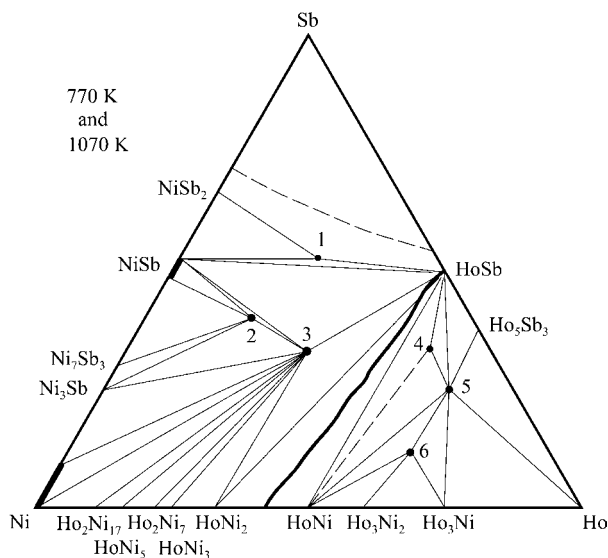


Fig. 20. Ho–Ni–Sb, isothermal sections at 770 K (0–50 at.% Sb) and 1070 K (50–100 at.% Sb).

3.1.12. Ho–M–Sb systems

3.1.12.1. *Ho–Ni–Sb*. Information on the phase equilibria in the ternary Ho–Ni–Sb system is due to the work of Mozharivskiy et al. (1997) (fig. 20) who employed X-ray powder diffraction on samples prepared by arc melting of the pure components. The resulting alloys were annealed at 770 K (0–50 at.% Sb) and 1070 K (50–100 at.% Sb) for 300 hours. The isothermal sections are shown in fig. 20. Six ternary compounds were observed.

Mozharivskiy and Kuz'ma (1996) investigated the crystal structure for $\text{Ho}_5\text{Ni}_2\text{Sb}$ (6) ($\text{Mo}_5\text{B}_2\text{Si}$ type structure, $a = 0.7563$, $c = 1.3250$; X-ray powder diffraction). The alloy was prepared in the same manner as $\text{Y}_5\text{Ni}_2\text{Sb}$. The starting materials were: Ho not less than 99.8 wt.%, Ni and Sb 99.9 wt.%.

HoNiSb_2 (1) was found to adopt the HfCuSi_2 type structure with lattice parameters of $a = 0.42989$, $c = 0.9257$ (Sologub et al., 1994). The alloy was prepared in the same manner as YCuSb_2 .

An early investigation of the HoNiSb (3) compound showed that it had the MgAgAs -type with $a = 0.6290$ (Dwight, 1974) from an X-ray powder analysis. For the sample preparation, see ScNiSb . Pecharsky et al. (1983a) and Hartjes and Jeitschko (1995) confirmed the crystal structure and obtained the same lattice parameter of $a = 0.6262$ by X-ray powder diffraction. For experimental details, see ScNiSb and LaNiSb , respectively.

Hoffman and Jeitschko (1988) established the defect CaBe_2Ge_2 type structure for the $\text{HoNi}_{2-x}\text{Sb}_2$ (2) alloy, $a = 0.4202$, $c = 0.9564$, X-ray powder diffraction. For the sample preparation, see $\text{CeNi}_{2-x}\text{Sb}_2$.

3.1.12.2. *Ho–Cu–Sb*. A ternary compound of holmium with copper and antimony of the 3:3:4 stoichiometric ratio was identified and studied by means of an X-ray analysis by Skoloz-

dra et al. (1993). $\text{Ho}_3\text{Cu}_3\text{Sb}_4$ compound was found to have the $\text{Y}_3\text{Au}_3\text{Sb}_4$ type structure with the lattice parameter of $a = 0.9482$ (X-ray powder diffraction). For experimental details, see the Y–Cu–Sb system.

HoCuSb_2 was found to form the HfCuSi_2 type structure with lattice parameters of $a = 0.42529$, $c = 0.9811$ (Sologub et al., 1994). For experimental details, see LaNiSb_2 .

3.1.12.3. *Ho–Zr–Sb*. Morozkin and Sviridov (2001) established the CeScSi structure type, $a = 0.4201$, $c = 1.6143$, for the HoZrSb compound from X-ray powder diffraction data.

3.1.12.4. *Ho–Pd–Sb*. Mozharivskiy and Kuz'ma (1996) investigated the crystal structure for $\text{Ho}_5\text{Pd}_2\text{Sb}$ ($\text{Mo}_5\text{B}_2\text{Si}$ type, $a = 0.76795$, $c = 1.3476$; X-ray powder diffraction). The alloy was prepared in the same manner as $\text{Y}_5\text{Ni}_2\text{Sb}$. The starting materials were: Ho not less than 99.8 wt.%, Pd and Sb 99.9 wt.%.

Marazza et al. (1980) established the MgAgAs type structure with $a = 0.6509$ for the HoPdSb compound by using X-ray powder diffraction and metallographic analyses. For the sample preparation and the purity of the starting components, see Y–Pd–Sb system. The crystallographic characteristics were confirmed from powder diffraction of arc melted and annealed at 1073 K alloys: MgAgAs type, $a = 0.6495$ (Zygmunt and Szytula, 1995).

HoPd_2Sb was reported to be isotopic with the crystal structure of MnCu_2Al with a lattice parameter of $a = 0.6677$ (Riani et al., 1995) from powder diffraction of an induction melted alloy.

3.1.12.5. *Ho–Ag–Sb*. HoAgSb_2 was observed and studied by Sologub et al. (1995a). It was found to crystallize with HfCuSi_2 type structure with lattice parameters as follows $a = 0.42665$, $c = 1.0427$ by X-ray powder diffraction of an arc melted and annealed at 870 K for 14 days alloy. The purity of the starting materials was 99.9 wt.%. The existence and crystal structure of HoAgSb_2 compound were independently confirmed by Brylak et al. (1995) ($a = 0.42662$, $c = 1.0422$; X-ray powder diffraction). For sample preparation, see YAgSb_2 . The starting materials were: Ho 99.9%, Ag M3N, and Sb 325 mesh, M2N5.

3.1.12.6. *Ho–Pt–Sb*. An X-ray powder diffraction analysis of the HoPtSb compound showed that it had the MgAgAs type structure with $a = 0.6508$ (Dwight, 1974). For the sample preparation, see ScNiSb .

Mozharivskiy and Franzen (2001) reported the crystal structure for the $\text{Ho}_5\text{Pt}_2\text{Sb}$ compound from X-ray powder diffraction data: $\text{Mo}_5\text{B}_2\text{Si}$ type structure, which is an ordered version of the Cr_5B_3 structure type, $a = 0.7681$, $c = 1.3365$. For the experimental procedure, see $\text{Y}_5\text{Pt}_2\text{Sb}$.

3.1.12.7. *Ho–Au–Sb*. The $\text{Ho}_3\text{Au}_3\text{Sb}_4$ alloy was reported by Dwight (1977) to have the $\text{Y}_3\text{Au}_3\text{Sb}_4$ type structure ($a = 0.788$; X-ray powder diffraction). The conditions of synthesis were not specified. These results were confirmed by Shaked et al. (1979) for a $\text{Ho}_3\text{Au}_3\text{Sb}_4$ sample obtained by arc melting the appropriate amounts of the elemental materials in a helium/argon atmosphere. The alloy was annealed at 960 K for one week and water quenched.

3.1.13. *Er–M–Sb systems*

3.1.13.1. *Er–Ni–Sb*. Mozharivskiy and Kuz'ma (1996) investigated the crystal structure of $\text{Er}_5\text{Ni}_2\text{Sb}$ ($\text{Mo}_5\text{B}_2\text{Si}$ type structure, $a = 0.7531$, $c = 1.3178$; X-ray powder diffraction). The alloy was prepared in the same manner as $\text{Y}_5\text{Ni}_2\text{Sb}$. The starting materials were: Er not less than 99.8 wt.%, Ni and Sb 99.9 wt.%.

Dwight (1974) investigated the solubility of Ni in ErSb : $(\text{ErSb})_{1-x}\text{Ni}_x$, $x = 0-0.27$, NaCl type structure, $a = 0.6105-0.6220$. The same author established from an X-ray powder analysis the crystal structure of ErNiSb : MgAgAs-type, $a = 0.6271$ (Dwight, 1974). For the sample preparation, see ScNiSb . Pecharsky et al. (1983a) and Hartjes and Jeitschko (1995) confirmed the crystal structure and obtained lattice parameters of $a = 0.6229$ and $a = 0.6247$, respectively, by X-ray powder diffraction. For experimental details, see ScNiSb and LaNiSb respectively.

Hoffman and Jeitschko (1988) established a defect CaBe_2Ge_2 type structure for $\text{ErNi}_{2-x}\text{Sb}_2$, $a = 0.4194$, $c = 0.9608$, X-ray powder diffraction. For the sample preparation, see $\text{CeNi}_{2-x}\text{Sb}_2$.

3.1.13.2. *Er–Cu–Sb*. ErCuSb_2 was found to crystallize with the HfCuSi_2 type structure and lattice parameters of $a = 0.42433$, $c = 0.9788$ (Sologub et al., 1994). The alloy was prepared in the same manner as YCuSb_2 .

A ternary compound of erbium with copper and antimony of the 3:3:4 stoichiometric ratio was identified and studied by means of an X-ray analysis by Skolozdra et al. (1993). The $\text{Er}_3\text{Cu}_3\text{Sb}_4$ compound was found to have the $\text{Y}_3\text{Au}_3\text{Sb}_4$ type structure with a lattice parameter of $a = 0.9458$ (X-ray powder diffraction). For experimental details, see the Y–Cu–Sb system.

3.1.13.3. *Er–Zr–Sb*. Morozkin and Sviridov (2001) investigated the crystal structure of the ErZrSb compound by using an X-ray powder diffraction method: CeScSi structure type, $a = 0.4204$, $c = 1.6159$.

3.1.13.4. *Er–Pd–Sb*. Marazza et al. (1980) established the MgAgAs type structure with $a = 0.6467$ for the ErPdSb compound by using X-ray powder diffraction and metallographic analyses. For the sample preparation and the purity of the starting components, see Y–Pd–Sb system.

ErPd_2Sb was reported to be isotypic with the crystal structure of MnCu_2Al with a lattice parameter $a = 0.6667$ (Riani et al., 1995) from X-ray powder diffraction of an induction melted alloy.

Mozharivskiy and Franzen (2000b) investigated the crystal structure of the $\text{Er}_3\text{Pd}_2\text{Sb}$ compound from arc melted and annealed at 1070 K for 10 days alloy by using X-ray powder diffraction. The $\text{Mo}_5\text{B}_2\text{Si}$ structure type was established for this compound, $a = 0.7641$, $c = 1.3465$.

3.1.13.5. *Er–Ag–Sb*. ErAgSb_2 was observed and studied by Sologub et al. (1995a). It was found to crystallize with the HfCuSi_2 type structure with lattice parameters as follows $a = 0.42541$, $c = 1.0413$ by X-ray powder diffraction of an arc melted and annealed at 1070 K for

14 days alloy. The purity of the starting materials was 99.9 wt.%. The existence and crystal structure of the ErAgSb_2 compound were independently confirmed by Brylak et al. (1995) ($a = 0.42565$, $c = 1.03900$; X-ray powder diffraction). For sample preparation, see YAgSb_2 . The starting materials were: Er 99.9%, Ag M3N, and Sb 325 mesh, M2N5.

3.1.13.6. *Er–Pt–Sb*. An investigation of ErPtSb showed that it had the MgAgAs type structure with $a = 0.6498$ (Dwight, 1974) from an X-ray powder analysis. For the sample preparation, see ScNiSb .

Mozharivskyj and Franzen (2001) reported the crystal structure of the $\text{Er}_5\text{Pt}_2\text{Sb}$ compound from X-ray powder diffraction data: $\text{Mo}_5\text{B}_2\text{Si}$ type structure, which is an ordered version of Cr_5B_3 structure type, $a = 0.7666$, $c = 1.3391$. For the experimental procedure, see $\text{Y}_5\text{Pt}_2\text{Sb}$.

3.1.13.7. *Er–Au–Sb*. The $\text{Y}_3\text{Au}_3\text{Sb}_4$ type structure was reported by Dwight (1977) for the $\text{Er}_3\text{Au}_3\text{Sb}_4$ alloy ($a = 0.9768$; X-ray powder diffraction). The conditions of synthesis were not specified. The same structure type was confirmed by Shaked et al. (1979) for an $\text{Er}_3\text{Au}_3\text{Sb}_4$ sample obtained by arc melting the appropriate amounts of the elemental materials in a helium/argon atmosphere. The alloy was annealed at 960 K for one week and water quenched.

3.1.14. *Tm–M–Sb systems*

3.1.14.1. *Tm–Ni–Sb*. An early investigation of the TmNiSb compound showed that it had the MgAgAs type structure with $a = 0.6241$ (Dwight, 1974) from X-ray powder analysis. For the sample preparation, see ScNiSb . Pecharsky et al. (1983a) and Hartjes and Jeitschko (1995) confirmed the crystal structure and obtained lattice parameters of $a = 0.6225$ and $a = 0.6237$, respectively, by X-ray powder diffraction. For the experimental details, see ScNiSb and LaNiSb , respectively.

Mozharivskyj and Franzen (2000b) investigated the crystal structure of the $\text{Tm}_5\text{Ni}_2\text{Sb}$ compound of an melted and annealed at 1070 K for 10 days alloy by using X-ray powder diffraction. The $\text{Mo}_5\text{B}_2\text{Si}$ structure type was established, $a = 0.7459$, $c = 1.325$.

3.1.14.2. *Tm–Cu–Sb*. TmCuSb_2 was found to form the HfCuSi_2 type structure with the lattice parameters of $a = 0.42437$, $c = 0.9742$ (Sologub et al., 1994). For experimental details, see LaNiSb_2 .

3.1.14.3. *Tm–Zr–Sb*. Morozkin and Sviridov (2001) established the CeScSi structure type with $a = 0.4174$, $c = 1.5997$ for the TmZrSb compound from X-ray powder diffraction data.

3.1.14.4. *Tm–Pd–Sb*. TmPdSb crystallizes with the MgAgAs -type structure, $a = 0.6454$ (Malik and Adroja, 1991c; powder X-ray diffraction data). For the experimental details, see EuPdSb .

A $\text{Mo}_5\text{B}_2\text{Si}$ structure type was established by Mozharivskyj and Franzen (2000b) for the $\text{Tm}_5\text{Pd}_2\text{Sb}$ compound, $a = 0.7585$, $c = 1.3457$ (X-ray powder diffraction of an arc melted and annealed at 1070 K for 10 days alloy).

3.1.14.5. *Tm–Ag–Sb*. TmAgSb_2 was observed and studied by Sologub et al. (1995a). It was found to crystallize with the HfCuSi_2 type structure with lattice parameters as follows $a = 0.42481$, $c = 1.0395$, by X-ray powder diffraction of an arc melted and annealed at 870 K for 14 days alloy. The purity of the starting materials was 99.9 wt.%. The existence and crystal structure of TmAgSb_2 were independently confirmed by Brylak et al. (1995) ($a = 0.42529$, $c = 1.0390$; X-ray powder diffraction). For the sample preparation, see YAgSb_2 . The starting materials were: Tm 99.9%, Ag M3N, and Sb 325 mesh, M2N5.

3.1.14.6. *Tm–Pt–Sb*. TmPtSb forms the MgAgAs -type with $a = 0.6483$, Dwight (1974) from an X-ray powder analysis. For the sample preparation, see ScNiSb .

Mozharivskyj and Franzen (2001) reported the crystal structure of the $\text{Tm}_5\text{Pt}_2\text{Sb}$ compound from X-ray powder diffraction data: $\text{Mo}_5\text{B}_2\text{Si}$ type structure, which is an ordered version of the Cr_5B_3 structure type, $a = 0.7584$, $c = 1.3394$. For the experimental procedure, see $\text{Y}_5\text{Pt}_2\text{Sb}$.

3.1.14.7. *Tm–Au–Sb*. The $\text{Y}_3\text{Au}_3\text{Sb}_4$ type structure was reported by Dwight (1977) for the $\text{Tm}_3\text{Au}_3\text{Sb}_4$ alloy ($a = 0.9752$; X-ray powder diffraction). The conditions of synthesis were not specified. The same structure type was confirmed by Shaked et al. (1979) for a $\text{Tm}_3\text{Au}_3\text{Sb}_4$ sample obtained by arc melting the stoichiometric amounts of the elemental materials in a helium/argon atmosphere. The alloy was annealed at 960 K for one week and water quenched.

3.1.15. *Yb–M–Sb systems*

3.1.15.1. *Yb–Li–Sb*. YbLiSb belongs to the TiNiSi structure type with the lattice parameters of $a = 0.7553$, $b = 0.4643$, $c = 0.8200$ (Albering et al., 1997).

3.1.15.2. *Yb–Al–Sb*. Fisher et al. (2000) reported the crystal structure of the Zintl compound $\text{Yb}_{14}\text{AlSb}_{11}$, to have the $\text{Ca}_{14}\text{AlSb}_{11}$ structure type, $a = 1.6561$, $c = 2.2102$ (X-ray single crystal diffraction).

3.1.15.3. *Yb–Mn–Sb*. Rühl and Jeitschko (1979) reported the results of an X-ray powder investigation of the YbMn_2Sb_2 compound, CaAl_2Si_2 type, $a = 0.4522$, $c = 0.7439$. For the experimental details, see EuMn_2Sb_2 .

$\text{Yb}_{14}\text{MnSb}_{11}$ crystallizes with the $\text{Ca}_{14}\text{AlSb}_{11}$ structure type: $a = 1.6615$, $c = 2.1948$ after Chan et al. (1998) from X-ray single crystal diffraction. A single crystal was obtained by heating a mixture of elements to 1273–1473 K for 5–10 days and cooling the reaction to room temperature at a rate of 60 °C/h. The starting materials were: dendritic Yb metal 99.9999%; Sb 99.9999%; Mn flakes 99.98%.

3.1.15.4. *Yb–Ni–Sb*. YbNiSb belongs to the MgAgAs type structure with $a = 0.6238$ (Dwight, 1974), from an X-ray powder analysis. For the sample preparation, ScNiSb .

3.1.15.5. *Yb–Cu–Sb*. YbCuSb_2 was found to form the HfCuSi_2 type structure with lattice parameters of $a = 0.43229$, $c = 0.9689$ (Sologub et al., 1994). For experimental details, see LaNiSb_2 .

The LiGaGe type structure was established for the YbCuSb compound ($a = 0.4452$, $c = 0.7995$) by Merlo et al. (1990) by the means of powder and single crystal diffraction data of a sample obtained by melting stoichiometric amounts of the components in iron or in tantalum crucibles and arc welded shut under an argon atmosphere. After slow cooling, no further thermal treatments were applied. The purities of the metals were: Yb 99.9%, Cu and Sb 99.999%. At variance with these data, the ZrBeSi structure type was reported for the YbCuSb compound, $a = 0.4456$, $c = 0.8006$ by Flandorfer et al. (1997) from a sample prepared by high frequency melting of the components in a sealed Ta-crucible and annealed at 723 K for 168 h and finally quenched in cold water.

3.1.15.6. *Yb–Zn–Sb*. YbZn_2Sb_2 with the CaAl_2Si_2 type of structure ($a = 0.4444$, $c = 0.7424$; X-ray powder diffraction data) was observed by Klüfers et al. (1980) from an alloy melted in a corundum crucible at 1173–1373 K for 4–6 hours and annealed at 1373–1473 K for 4–48 hours. The crystal structure was refined by Salamakha and Mudryi (2001b) from an alloy obtained by a powder metallurgical reaction, $a = 0.444194$, $c = 0.741913$. The proper amounts of the respective powders were compacted and sealed in an evacuated silica capsule. After slowly heating to 870 K, the pellet was reground under C_6H_{12} , recompact and annealed at 870 K for 400 h. The purity of starting materials was 99.9 wt.%.

According to Fisher et al. (2000), $\text{Yb}_{14}\text{ZnSb}_{11}$ compound crystallized in the $\text{Ca}_{14}\text{AlSb}_{11}$ structure type: $a = 1.6562$, $c = 2.1859$. The single crystal was grown from a Sn flux. Sologub et al. (2001) confirmed the crystal structure from an alloy produced by powder reaction sintering, and they obtained slightly enlarged lattice parameters, $a = 1.6615$, $c = 2.1948$ (X-ray powder diffraction).

3.1.15.7. *Yb–Se–Sb*. The YbSe_4Sb_2 compound belongs to the PbS_4Bi_2 structure type, $a = 1.150$, $b = 0.400$, $c = 1.402$ (Aliev et al., 1986).

3.1.15.8. *Yb–Pd–Sb*. Marazza et al. (1980) established the MgAgAs type structure with $a = 0.6471$ for the YbPdSb compound by using X-ray powder diffraction and metallographic analyses. For the sample preparation and the purity of starting components, see Y–Pd–Sb system.

YbPd_2Sb was reported to be isotypic with the crystal structure of MnCu_2Al with a lattice parameter $a = 0.6669$ (Riani et al., 1995) from powder diffraction data of an induction melted alloy.

3.1.15.9. *Yb–Cd–Sb*. Salamakha and Mudryi (2001b) observed the YbCd_2Sb_2 compound and refined its crystal structure from X-ray powder diffraction data, CeAl_2Si_2 type structure, $a = 0.46494$, $c = 0.75673$. For the synthesis, see YbZn_2Sb_2 .

3.1.15.10. *Yb–Ag–Sb*. The TiNiSi type structure was established for the YbAgSb compound ($a = 0.7668$, $b = 0.4596$, $c = 0.8353$) by Merlo et al. (1990) by the means of powder and single crystal diffraction data on a sample obtained by melting stoichiometric amounts of the components in iron or in tantalum crucibles and arc welded shut under an argon atmosphere. After slow cooling, no further thermal treatments were applied. Purities of the metals were Yb 99.9%, Ag and Sb 99.999%. The formation and crystal structure of this compound was confirmed by Sologub et al. (1995a) from an arc melted and annealed at 870 K alloy by X-ray powder diffraction data and also by Flandorfer et al. (1997).

3.1.15.11. *Yb–In–Sb*. The ternary Yb₅In₂Sb₆ compound was obtained from a direct element combination reaction in a sealed graphite tube at 973 K, and its crystal structure was determined by X-ray single crystal diffraction methods. It crystallizes in the Ba₅In₂Sb₆ structure type with a unit cell of $a = 0.73992$, $b = 2.3001$, $c = 0.45139$ (Kim et al., 2000).

3.1.15.12. *Yb–Te–Sb*. Aliev et al. (1985) constructed the complete c – T diagrams for the Sb₂Te₃–Sb₃Yb₄, Sb₂Te₃–Yb, Sb₄Te₇Yb–Te and Sb₄Te₇Yb–Yb sections.

The Sb₂Te₃–TeYb section was studied by Aliev and Rustamov (1978) and Rustamov et al. (1981a). Three ternary phases were observed by X-ray powder diffraction method for samples annealed at 673–773 K: Sb₂Te₄Yb, Th₃P₄ structure type, $a = 1.040$; Sb₄Te₇Yb, Th₃P₄ structure type, $a = 1.0625$; (YbTe) _{x} (Te₃Sb₂)_{1– x} , $x = 0$ – 0.06 , Te₃Bi₂ structure type, $a = 0.425$ – 0.425 , $c = 3.020$ – 3.038 .

3.1.15.13. *Yb–Pt–Sb*. An early investigation of the YbPtSb compound showed that it had the MgAgAs-type with $a = 0.647$ (Dwight, 1974) from X-ray powder analysis. For the sample preparation, see ScNiSb.

3.1.15.14. *Yb–Au–Sb*. The LiGaGe type was established for the YbAuSb compound ($a = 0.4635$, $c = 0.7765$) by Merlo et al. (1990) by means of powder and single crystal diffraction method on a sample obtained by melting stoichiometric amounts of the components in iron or in tantalum crucibles and arc welded shut under an argon atmosphere. After slow cooling, no further thermal treatments were applied. The purities of the metals were: Yb 99.9%, Au and Sb 99.999%. The crystal structure was confirmed by Flandorfer et al. (1997) by X-ray powder diffraction.

3.1.16. *Lu–M–Sb systems*

3.1.16.1. *Lu–Ni–Sb*. Mozharivskiy and Kuz'ma (1996) investigated the crystal structure of Lu₅Ni₂Sb (Mo₅B₂Si type, $a = 0.7429$, $c = 1.3190$; X-ray powder diffraction). The alloy was prepared in the same manner as Y₅Ni₂Sb. The starting materials were: Lu not less than 99.8 wt.%, Ni and Sb 99.9 wt.%.

An early investigation of the LuNiSb compound showed that it had the MgAgAs-type with $a = 0.6219$ (Dwight, 1974) from X-ray powder analysis. For the sample preparation, ScNiSb. Pecharsky et al. (1983a) and Hartjes and Jeitschko (1995) confirmed the crystal structure and

obtained the lattice parameters of $a = 0.6187$ and $a = 0.6218$, respectively, by X-ray powder diffraction. For experimental details, see ScNiSb and LaNiSb, respectively.

3.1.16.2. *Lu–Cu–Sb*. LuCuSb₂ was found to form the HfCuSi₂ type structure with lattice parameters of $a = 0.42347$, $c = 0.9705$ (Sologub et al., 1994) from an arc melted alloy. The materials used were: Lu 99.9%, Cu 99.9%, and Sb 99.9%.

3.1.16.3. *Lu–Zr–Sb*. Morozkin and Sviridov (2001) investigated the crystal structure of the LuZrSb compound by using X-ray powder diffraction. The CeScSi structure type was reported, $a = 0.4178$, $c = 1.5952$.

3.1.16.4. *Lu–Pd–Sb*. Mozharivskiy and Franzen (2000b) investigated the crystal structure of the Lu₅Pd₂Sb compound from an arc melted and annealed at 1070 K for 10 days alloy by using X-ray powder diffraction. The Mo₅B₂Si structure type was established, $a = 0.75531$, $c = 1.3345$.

3.1.16.5. *Lu–Ag–Sb*. The formation of LuAgSb compound with TiNiSi type was observed by Sologub et al. (1995a) from an arc melted and annealed at 870 K alloy by using X-ray powder diffraction.

3.1.16.6. *Lu–Pt–Sb*. The X-ray powder diffraction analysis of the LuPtSb compound showed that it had the MgAgAs type structure with $a = 0.6457$ (Dwight, 1974). For the sample preparation, see ScNiSb.

Mozharivskiy and Franzen (2001) reported the crystal structure for the Lu₅Pt₂Sb compound from X-ray powder diffraction data: Mo₅B₂Si type structure, which is an ordered version of the Cr₅B₃ structure type, $a = 0.7519$, $c = 1.3326$. For the experimental procedure, see Y₅Pt₂Sb.

3.1.16.7. *Lu–Au–Sb*. The Y₃Au₃Sb₄ type structure was reported by Dwight (1977) for the Lu₃Au₃Sb₄ alloy ($a = 0.9723$; X-ray powder diffraction). The conditions of synthesis were not specified.

3.2. *R–R'–Sb systems*

The ternary *R–R'–Sb* systems have been studied mostly with respect to the formation of compounds with specific compositions and structures (see table 3).

Ternary Nd–Pr–Sb alloys were studied by Riani et al. (1993) by using X-ray powder diffraction, and optical and electron microscopy of the samples prepared by induction melting of mixtures of the elements in small tantalum crucibles sealed by welding shut under argon. (Nd,Pr)₂Sb (La₂Sb type), (Nd,Pr)₄Sb₃ (anti-Th₃P₄ type), (Nd,Pr)Sb (NaCl type) and (Nd,Pr)Sb₂ (SmSb₂ type) show complete solubility between Nd and Pr. The variation of the lattice parameters as a function of the Nd to Pr ratio was determined. The alloy Nd_{0.475}Pr_{0.475}Sb_{0.05} was investigated by differential thermal analysis; thermal effects were

Table 3
Crystallographic characteristics of the compounds of the $R-R'-Sb$ systems

Compound	Structure type	Space group	Lattice parameters, nm <i>a</i>	References
La ₃ YSb ₃	anti-Th ₃ P ₄	$\bar{I}43d$	0.9553	Hulliger and Ott, 1977
Yb ₃ DySb ₃	anti-Th ₃ P ₄	$\bar{I}43d$	0.9333	Gambino, 1967
Eu ₃ GdSb ₃	anti-Th ₃ P ₄	$\bar{I}43d$	0.8868	Gambino, 1967
Sm ₃ NdSb ₃	anti-Th ₃ P ₄	$\bar{I}43d$	0.935	Gambino, 1967
Sm ₃ GdSb ₃	anti-Th ₃ P ₄	$\bar{I}43d$	0.930	Gambino, 1967
Yb ₃ GdSb ₃	anti-Th ₃ P ₄	$\bar{I}43d$	0.936	Gambino, 1967

observed at 1090 K and 1170 K corresponding to the eutectoid ($\beta R \rightarrow R + R_2Sb$) and eutectic ($L \rightarrow \beta R + R_2Sb$) reactions respectively.

Abulkhaev et al. (1989) reported the formation of continuous solid solutions Gd_xR_{5-x}Sb₃ when $R = Y, Tb, Dy, Ho$ with the structure of Mn₅Si₃ type which originated at the isotypic binary compounds.

3.3. $R-U-Sb$ systems

$R-U-Sb$. A NaCl structure type was observed for continuous solid solution Y_{1-x}U_xSb alloys, $x = 0-1$, $a = 0.6165-0.6208$ by using X-ray powder diffraction method (Frick et al., 1984).

Schmidt and Jeitschko (1998) reported the crystallographic data for the $(R,U)_3Sb_7$, $R = Gd, Tb, Dy, Ho$ (table 4) and $(R,U)Sb_2$, $R = Ce-Sm, Gd-Tm$ (table 5).

Table 4
Lattice parameters for the $(R,U)_3Sb_7$ ($R = Gd, Tb, Dy, Ho$) compounds, space group $Immm$

Compound	<i>a</i>	<i>b</i>	<i>c</i>
Gd _{2.31} U _{0.69} Sb ₇	0.4102	1.4643	1.8370
Gd _{1.5} U _{1.5} Sb ₇	0.4114	1.4532	1.8252
Tb _{1.5} U _{1.5} Sb ₇	0.4110	1.4517	1.8234
Dy _{1.5} U _{1.5} Sb ₇	0.4103	1.4500	1.8268
Ho _{1.47} U _{1.53} Sb ₇	0.4101	1.4477	1.8212

Table 5
Lattice parameters for the $(R,U)Sb_2$ ($R = Ce-Sm, Gd-Tm$) compounds, space group $Pnma$

Compound	<i>a</i>	<i>b</i>	<i>c</i>
Ce _{0.33} U _{0.67} Sb ₂	0.7582	0.4237	1.0348
Pr _{0.33} U _{0.67} Sb ₂	0.7582	0.4231	1.0323
Nd _{0.33} U _{0.67} Sb ₂	0.7579	0.4225	1.0317
Sm _{0.33} U _{0.67} Sb ₂	0.7553	0.4203	1.0274
Gd _{0.32} U _{0.68} Sb ₂	0.7546	0.4196	1.0257
Tb _{0.33} U _{0.67} Sb ₂	0.7546	0.4186	1.0242
Dy _{0.33} U _{0.67} Sb ₂	0.7543	0.4183	1.0236
Ho _{0.33} U _{0.67} Sb ₂	0.7539	0.4179	1.0231
Er _{0.33} U _{0.67} Sb ₂	0.7533	0.4179	1.0219
Tm _{0.33} U _{0.67} Sb ₂	0.7531	0.4172	1.0209

Table 6
Lattice parameters of the $Ce_{1-x}La_xRhSb$ alloys, TiNiSi type structure

Composition	Lattice parameters, nm		
	<i>a</i>	<i>b</i>	<i>c</i>
CeRhSb	0.742	0.469	0.7859
$Ce_{1-x}La_xRhSb$ <i>x</i> = 0.1	0.743	0.4626	0.7869
$Ce_{1-x}La_xRhSb$ <i>x</i> = 0.2	0.7455	0.4626	0.7876
$Ce_{1-x}La_xRhSb$ <i>x</i> = 0.4	0.747	0.4636	0.7888
$Ce_{1-x}La_xRhSb$ <i>x</i> = 0.6	0.7502	0.4639	0.7892
$Ce_{1-x}La_xRhSb$ <i>x</i> = 0.8	0.7521	0.4648	0.7905
LaRhSb	0.7541	0.4658	0.7924

Table 7
Crystallographic data for the $EuCu_{1.75}As_2-EuCu_2Sb_2$ alloys

Composition	Structure type	Lattice parameters, nm	
		<i>a</i>	<i>c</i>
$EuCu_{1.75}As_2$	ThCr ₂ Si ₂	0.4215	1.0185
$EuCu_{1.8}As_{1.5}Sb_{0.5}$	ThCr ₂ Si ₂	0.4277	1.0368
$EuCu_{1.85}AsSb$	ThCr ₂ Si ₂	0.4349	1.0534
$EuCu_{1.9}As_{0.85}Sb_{1.15}$	ThCr ₂ Si ₂	0.4360	1.0579
$EuCu_2As_{0.65}Sb_{1.35}$	CaBe ₂ Ge ₂	0.4407	1.0619
$EuCu_2As_{0.6}Sb_{1.4}$	CaBe ₂ Ge ₂	0.4410	1.0614
$EuCu_2As_{0.5}Sb_{1.5}$	CaBe ₂ Ge ₂	0.4433	1.0644
$EuCu_2Sb_2$	CaBe ₂ Ge ₂	0.4501	1.0824

Slovyanskikh et al. (1990) established the lattice parameters $a = 13.67$, $b = 11.59$, $c = 7.26$, and the space group $P2_12_12$ for GdU_2Sb_6 .

4. Quaternary systems

Substitution of Ce by La in $Ce_{1-x}La_xRhSb$, $x = 0.1-1.0$, TiNiSi type structure (table 6) was investigated by Malik et al. (1995) in the course of studying of some of the physical properties of these phases.

Dunner et al. (1995) investigated the crystallographic characteristics of the alloys with modified $BaAl_4$ type structures within the $EuCu_{1.75}As_2-EuCu_2Sb_2$ region (table 7).

5. Structure types of the ternary antimonides

LaFe₄P₁₂ structure type. See fig. 21, table 8. SG $Im\bar{3}$, $Z = 2$, $a = 0.9300$ nm for $NdOs_4Sb_{12}$ (Evers et al., 1995).

Ce₂Pd₉Sb₃ structure type. See table 9. SG $Cmcm$, $Z = 8$, $a = 1.3769$, $b = 0.80412$, $c = 0.93482$ (Gordon et al., 1996).

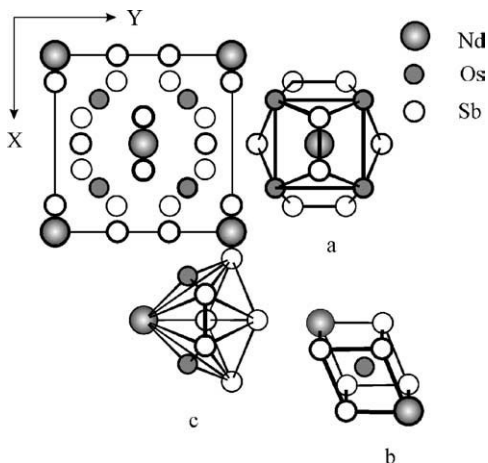


Fig. 21. Projection of the $\text{NdOs}_4\text{Sb}_{12}$ unit cell and coordination polyhedra of atoms.

Table 8

Atom	Wyckoff notation	x/a	y/b	z/c	$G, \%$
Nd	2(a)	0	0	0	100
Os	8(c)	1/4	1/4	1/4	100
Sb	24(g)	0	0.34021	0.15591	100

Table 9

Atom	Wyckoff notation	x/a	y/b	z/c	$G, \%$
Ce1	8(g)	0.34547	0.32828	1/4	100
Pd1	16(h)	0.17109	0.17061	0.08478	100
Pd2	8(f)	0	0.3323	0.5268	100
Pd3	4(c)	0	0.1457	1/4	100
Pd4	8(g)	0.09840	0.4582	1/4	100
Sb1	4(a)	0	0	0	100
Sb2	8(e)	0.32369	0	0	100

Table 10

Atom	Wyckoff notation	x/a	y/b	z/c	$G, \%$
Nd1	2(a)	0	0	0.1527	100
Fe1	8(g)	0	1/2	0.0517	100
Fe2	2(b)	0	0	1/2	100
Fe3	2(a)	0	0	0	100
Sb1	4(e)	0	0	0.3895	100
Sb2	4(d)	0	1/2	1/4	100

NdFe_3Sb_2 structure type. See fig. 22, table 10. SG $I4/mmm$, $Z = 4$, $a = 0.42879$, $c = 2.57048$ (Leithe-Jasper, 1994).

LaLi_3Sb_2 structure type. See table 11. SG $P\bar{3}m1$, $Z = 1$, $a = 0.4619$, $c = 0.7445$ (Grund et al., 1984).

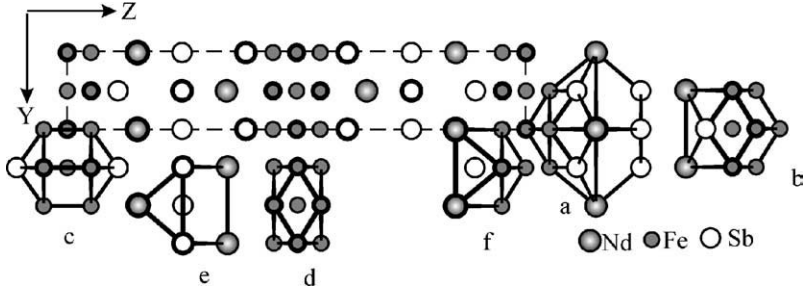


Fig. 22. Projection of the NdFe_3Sb_2 unit cell and coordination polyhedra of atoms.

Table 11

Atom	Wyckoff notation	x/a	y/b	z/c	$G, \%$
La	1(a)	0	0	0	100
Li1	2(d)	1/3	2/3	0.658	100
Li2	1(b)	0	0	1/2	100
Sb	2(d)	1/3	2/3	0.2577	100

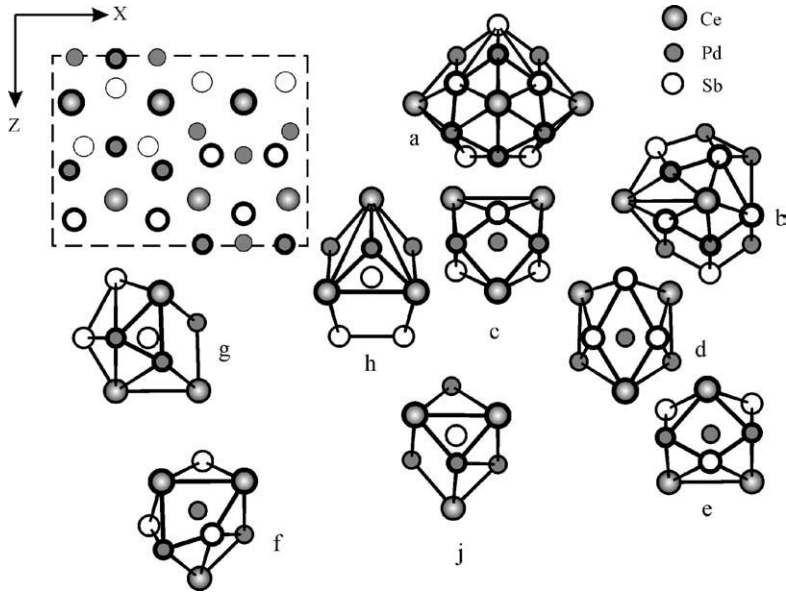


Fig. 23. Projection of the $\text{Ce}_3\text{Pd}_6\text{Sb}_5$ unit cell and coordination polyhedra of atoms.

Ce₃Pd₆Sb₅ structure type. See fig. 23, table 12. SG $Pm\bar{m}n$, $Z = 2$, $a = 1.3481$, $b = 0.4459$, $c = 1.0050$ nm (Gordon et al., 1995).

Table 12

Atom	Wyckoff notation	x/a	y/b	z/c	$G, \%$
Ce1	2(a)	1/4	1/4	0.75756	100
Ce2	4(f)	0.57480	1/4	0.75467	100
Pd1	4(f)	0.41109	1/4	0.00819	100
Pd2	2(b)	1/4	3/4	0.01545	100
Pd3	4(f)	0.56761	1/4	0.39730	100
Pd4	2(b)	1/4	3/4	0.47745	100
Sb1	4(f)	0.37627	1/4	0.47697	100
Sb2	4(f)	0.58653	1/4	0.13700	100
Sb3	2(a)	1/4	1/4	0.16899	100

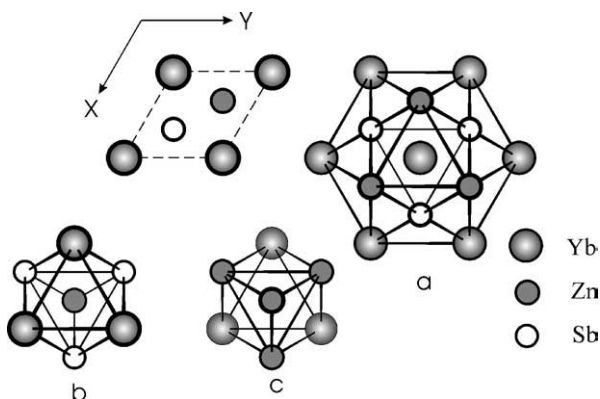
Fig. 24. Projection of the YbZn_2Sb_2 unit cell and coordination polyhedra of atoms.

Table 13

Atom	Wyckoff notation	x/a	y/b	z/c	$G, \%$
Yb	1(a)	0	0	0	100
Zn	2(d)	1/3	2/3	0.3619	100
Sb	2(d)	1/3	2/3	0.7407	100

Table 14

Atom	Wyckoff notation	x/a	y/b	z/c	$G, \%$
La	2(a)	0	0	0	100
X1	4(d)	0	1/2	1/4	100
X2	4(e)	0	0	0.383	100

$$\text{X1} = 0.83\text{Sb} + 0.17\text{Ni}$$

$$\text{X2} = 0.17\text{Sb} + 0.83\text{Ni}$$

CaAl₂Si₂ structure type. See fig. 24, table 13. SG $P\bar{3}m1$, $Z = 1$, $a = 0.444194$, $c = 0.741913$ nm for YbZn_2Sb_2 (Salamakha and Mudryi, 2001b).

BaAl₄ structure type. See table 14. SG $I4/mmm$, $Z = 2$, $a = 0.4433$, $c = 1.0024$ nm for LaNi_2Sb_2 (Pecharsky et al., 1981).

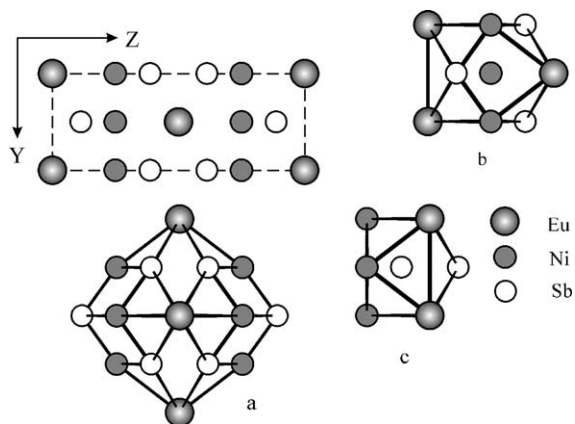


Fig. 25. Projection of the $\text{EuNi}_{1.53}\text{Sb}_2$ unit cell and coordination polyhedra of atoms.

Table 15

Atom	Wyckoff notation	x/a	y/b	z/c	$G, \%$
Eu	2(a)	0	0	0	100
Ni	4(d)	0	1/2	1/4	76.6
Sb	4(e)	0	0	0.35895	99.5

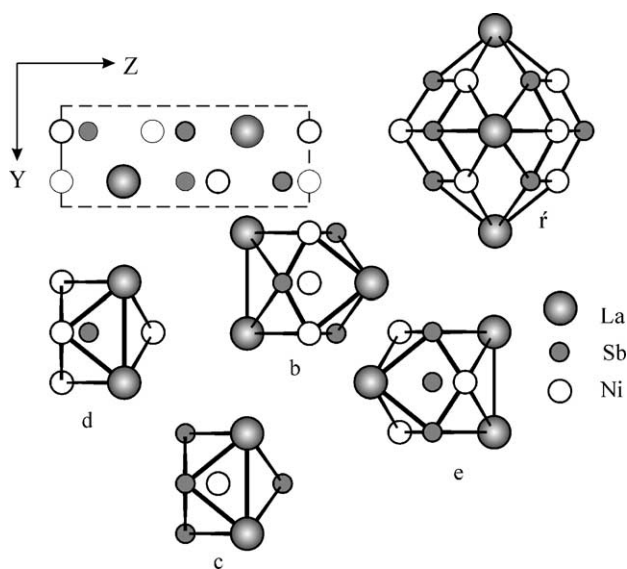


Fig. 26. Projection of the $\text{LaNi}_{1.51}\text{Ge}_2$ unit cell and coordination polyhedra of atoms.

CeGa₂Al₂ structure type. See fig. 25, table 15. SG $I4/mmm$, $Z = 2$, $a = 0.4340$, $c = 1.0597$ nm for $\text{EuNi}_{1.53}\text{Sb}_2$ (Hoffman and Jeitschko, 1988).

CaBe₂Ge₂ structure type. See fig. 26, table 16. SG $P4/nmm$, $Z = 2$, $a = 0.4466$, $c = 0.9918$ nm for $\text{LaNi}_{1.51}\text{Sb}_2$ (Hoffman and Jeitschko, 1988).

Table 16

Atom	Wyckoff notation	x/a	y/b	z/c	$G, \%$
La	2(c)	1/4	1/4	0.74000	100
Ni1	2(a)	3/4	1/4	0	89.8
Ni2	2(c)	1/4	1/4	0.368	61.2
Sb1	2(b)	3/4	1/4	1/2	100
Sb2	2(c)	1/4	1/4	0.12653	100

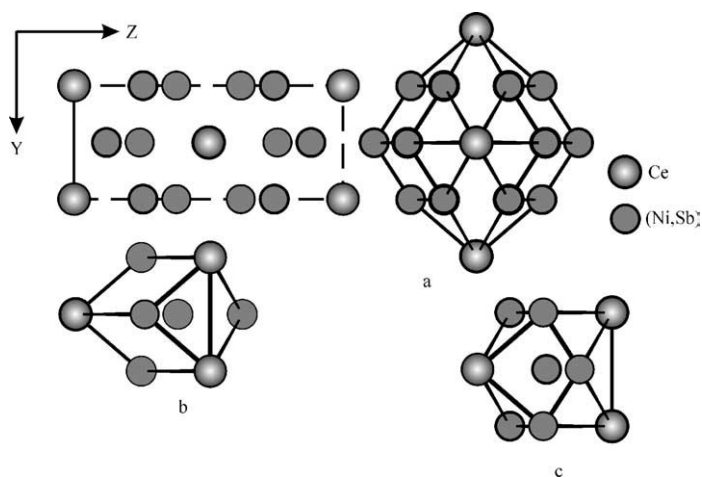


Fig. 27. Projection of the $\text{CeNi}_{2.36}\text{Sb}_{1.64}$ unit cell and coordination polyhedra of atoms.

Table 17

Atom	Wyckoff notation	x/a	y/b	z/c	$G, \%$
Ce	2(a)	0	0	0	100
X1	4(j)	1/2	0	0.256	100
X2	4(i)	0	0	0.3800	100

$$X = 0.59\text{Ni} + 0.41\text{Sb}$$

LaPt₂Ge₂ structure type. SG $P21m$, $Z = 2$, $a = 0.4365$, $b = 0.4355$, $c = 0.9969$ nm, $\beta = 90.20^\circ$ for PrNi_2Sb_2 (Slebarski et al., 1996). Atomic coordinates have not been determined.

CeNi_{2+x}Sb_{2-x} structure type. See fig. 27, table 17. SG $Immm$, $Z = 2$, $a = 0.4285$, $b = 0.4312$, $c = 1.0205$ for $\text{CeNi}_{2.36}\text{Sb}_{1.64}$ (Pecharsky et al., 1982).

NdFe₂Sb₂ structure type. See fig. 28, table 18. SG $Imm2$, $Z = 2$, $a = 0.42965$, $b = 0.42759$, $c = 2.57887$ (Leithe-Jasper, 1994).

Ce₈Pd₂₄Sb structure type. See table 19. SG $Pm\bar{3}m$, $Z = 1$, $a = 0.8461$ nm (Gordon and DiSalvo, 1996).

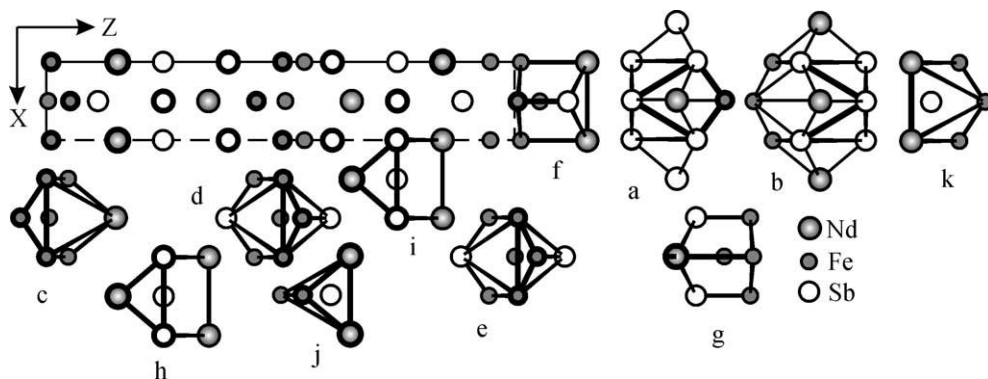
Fig. 28. Projection of the NdFe_2Sb_2 unit cell and coordination polyhedra of atoms.

Table 18

Atom	Wyckoff notation	x/a	y/b	z/c	$G, \%$
Nd1	2(a)	0	0	0.1526	100
Nd2	2(a)	0	0	0.8462	100
Sb1	2(a)	0	0	0.3888	100
Sb2	2(a)	0	0	0.6109	100
Sb3	2(b)	1/2	0	1/4	100
Sb4	2(b)	1/2	0	0.7499	100
Fe1	2(a)	0	0	0.5044	100
Fe2	2(a)	0	0	0.0105	100
Fe3	2(b)	1/2	0	0.0513	100
Fe4	2(b)	1/2	0	0.4490	100

Table 19

Atom	Wyckoff notation	x/a	y/b	z/c	$G, \%$
Ce1	8(g)	0.25140	0.25140	0.25140	100
Pd1	6(f)	0.25552	1/2	1/2	100
Pd2	6(e)	0.31118	0	0	100
Pd3	12(h)	0.26675	1/2	0	100
Sb	1(a)	0	0	1/4	100

Table 20

Atom	Wyckoff notation	x/a	y/b	z/c	$G, \%$
Y	4(a)	0	0	0	100
Sb	4(b)	1/2	1/2	1/2	100
Pd	8(c)	1/4	1/4	1/4	100

MnCu₂Al structure type. See table 20. SG $Fm\bar{3}m$, $Z = 4$, $a = 0.6691$ nm for YPd_2Sb (Ishikawa et al., 1982).

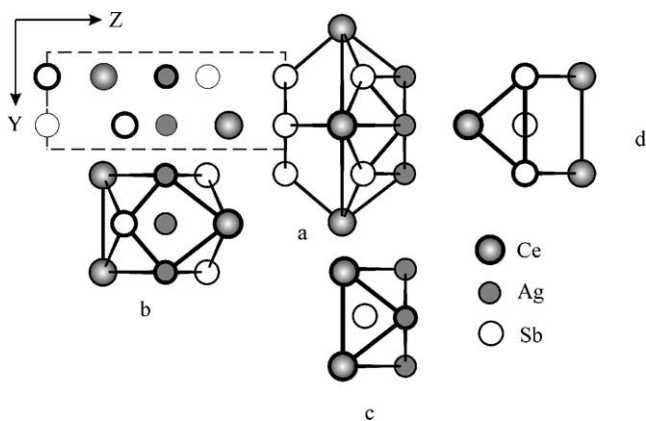


Fig. 29. Projection of the CeAgSb_2 unit cell and coordination polyhedra of atoms.

Table 21

Atom	Wyckoff notation	x/a	y/b	z/c	$G, \%$
Ce	2(c)	1/4	1/4	0.23788	100
Ag	2(b)	3/4	1/4	1/2	99
Sb1	2(a)	3/4	1/4	0	100
Sb2	2(c)	1/4	1/4	0.67363	100

Table 22

Atom	Wyckoff notation	x/a	y/b	z/c	$G, \%$
La	2(a)	1/4	1/4	0.74071	100
Zn	2(b)	1/4	3/4	0.00299	60
Sb1	2(b)	3/4	1/4	0.49962	100
Sb2	2(a)	1/4	1/4	0.15410	100

Table 23

Atom	Wyckoff notation	x/a	y/b	z/c	$G, \%$
La	2(e)	0.8440	1/4	0.2160	100
In	2(e)	0.2139	1/4	0.4846	81
Sb1	2(e)	0.6158	1/4	0.6951	100
Sb2	2(e)	0.2489	1/4	0.0016	100

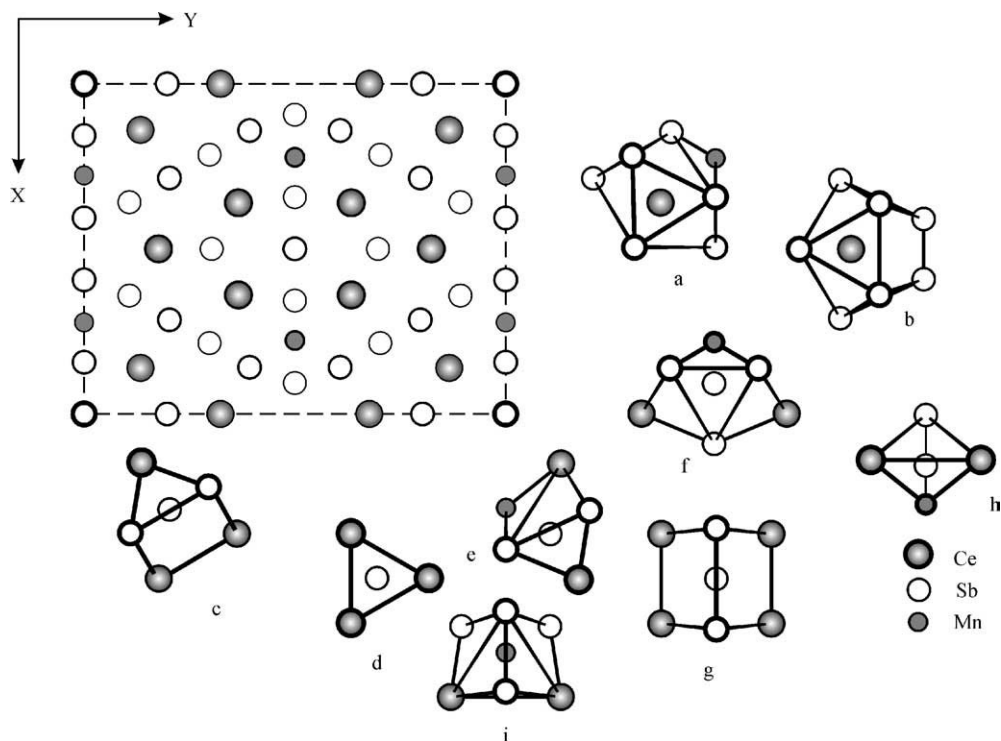
HfCuSi₂ structure type. See fig. 29, table 21. SG $P4/nmm$, $Z = 2$, $a = 0.43641$, $c = 1.0722$ nm for CeAgSb_2 (Sologub et al., 1995a).

NdAgAs₂ structure type. See table 22, SG $Pmmn$, $Z = 2$, $a = 0.437935$, $b = 0.440222$, $c = 1.050438$ nm for LaZnSb_2 (Salamakha and Mudryi, 2001a).

LaInSb₂ structure type. See table 23. SG $P21/m$, $Z = 2$, $a = 0.4521$, $b = 0.4331$, $c = 1.1913$ nm, $\beta = 99.66^\circ$ (Ferguson et al., 1999).

Table 24

Atom	Wyckoff notation	x/a	y/b	z/c	$G, \%$
La	4(c)	0	0.86085	1/4	100
Sb1	4(c)	0	0.24860	1/4	81
Sb2	4(c)	0	0.59076	1/4	100
Sn1	8(f)	0	0.0065	0.1238	18.6
Sn2	4(c)	0	0.0089	1/4	18.6
Sn3	4(a)	0	0	0	19.7

Fig. 30. Projection of the $\text{La}_6\text{MnSb}_{15}$ unit cell and coordination polyhedra of atoms.

LaSn_xSb_2 ($x = 0.75$) structure type. See table 24. SG $Cmcm$, $Z = 4$, $a = 0.42435$, $b = 2.3121$, $c = 0.45053$ nm (Ferguson et al., 1996).

$\text{La}_6\text{MnSb}_{15}$ structure type. See fig. 30, table 25. SG $Imm2$, $Z = 2$, $a = 1.51538$, $b = 1.93646$, $c = 0.427422$ nm for $\text{Ce}_6\text{Mn}_{0.4}\text{Sb}_{15}$ (Sologub et al., 1996b).

$\text{La}_6\text{Ge}_{5-x}\text{Sb}_{11+x}$ structure type. See table 26. SG $Immm$, $Z = 2$, $a = 0.43034$, $b = 1.0851$, $c = 27.073$ nm (Lam et al., 2001).

Table 25

Atom	Wyckoff notation	x/a	y/b	z/c	$G, \%$
Ce1	8(e)	0.1408	0.1322	0.0787	100
Ce2	4(d)	0	0.3232	0.0787	100
Mn	4(c)	0.2751	0	0.0787	40
Sb1	8(e)	0.2139	0.2979	0.0787	100
Sb2	8(e)	0.3595	0.1062	0.0787	100
Sb3	4(d)	0	0.1968	0.5787	100
Sb4	4(c)	0.1603	0	0.5787	100
Sb5	4(c)	0.4066	0	0.5787	100
Sb6	2(a)	0	0	0.0000	100

Table 26

Atom	Wyckoff notation	x/a	y/b	z/c	$G, \%$
La1	4(i)	0	0	0.26676	100
La2	8(l)	0	0.19435	0.40544	100
Sb1	4(j)	1/2	0	0.35768	100
Sb2	8(l)	0	0.30535	0.28862	100
Sb3	4(g)	0	0.29207	0	100
Sb4	4(f)	0.4300	1/2	0	50
Sb5	4(f)	1/2	0	0.07187	100
X1	8(l)	0	0.1205	0.14765	100
X2	4(g)	0	0.03926	0	50

X1 = 61% Ge + 39% Sb

X2 = 19% Ge + 31% Sb

Table 27

Atom	Wyckoff notation	x/a	y/b	z/c	$G, \%$
La1	6(m)	0.58274	0.16547	1/2	100
La2	6(m)	0.16800	0.33600	1/2	100
La3	1a	0	0	0	86
Ga1	12(n)	0.1343	0	0.443	47
Ga2	4(h)	1/3	2/3	0.0663	47
Sb1	6(l)	0.24818	0.49636	0	100
Sb2	6(j)	0.24697	0	0	100
Sb3	6(k)	0.37508	0	1/2	100
Sb4	3(f)	1/2	0	0	100

$La_{13}Ga_8Sb_{21}$ structure type. See table 27. SG $P6/mmm$, $Z = 1$, $a = 1.7657$, $c = 0.43378$ nm (Mills and Mar, 2000).

$Pr_{12}Ga_4Sb_{23}$ structure type. See table 28. SG $Immm$, $Z = 2$, $a = 0.42162$, $b = 1.94070$, $c = 2.63972$ nm (Mills and Mar, 2000).

$Nd_6Fe_{13}Si$ structure type. See fig. 31, table 29. SG $I4/mcm$, $Z = 4$, $a = 0.80978$, $c = 2.32317$ nm for $Nd_6Fe_{13}Sb$ (Leithe-Jasper, 1994).

Table 28

Atom	Wyckoff notation	x/a	y/b	z/c	$G, \%$
Pr1	8(l)	0	0.27695	0.40559	100
Pr2	8(l)	0	0.38900	0.26312	100
Pr3	4(j)	1/2	0	0.09340	100
Pr4	4(j)	1/2	0	0.38118	100
Ga1	4(i)	0	0	0.18986	96
Ga2	4(h)	0	0.181	1/2	2.7
Ga3	4(g)	0	0.43337	0	100
Sb1	8(l)	0	0.11138	0.43300	97.3
Sb2	8(l)	0	0.11584	0.14030	100
Sb3	8(l)	0	0.22151	0.28669	100
Sb4	8(l)	0	0.33456	0.14421	100
Sb5	4(i)	0	0	0.28911	100
Sb6	4(h)	0	0.38335	1/2	100
Sb7	4(g)	0	0.23336	0	100
Sb8	2(a)	0	0	0	100

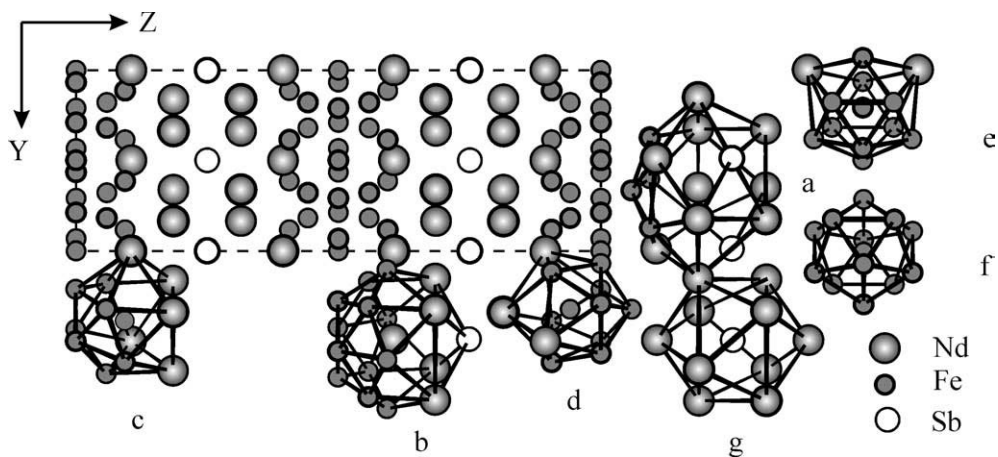
Fig. 31. Projection of the $\text{Nd}_6\text{Fe}_{13}\text{Sb}$ unit cell and coordination polyhedra of atoms.

Table 29

Atom	Wyckoff notation	x/a	y/b	z/c	$G, \%$
Nd1	16(l)	0.1691	0.6691	0.18595	100
Nd2	8(f)	0	0	0.39777	100
Fe1	16(l)	0.3824	0.8824	0.0917	100
Fe2	16(l)	0.1767	0.6767	0.0557	100
Fe3	16(k)	0.0652	0.2103	0	100
Fe4	4(d)	0	1/2	0	100
Sb	4(a)	0	0	1/4	100

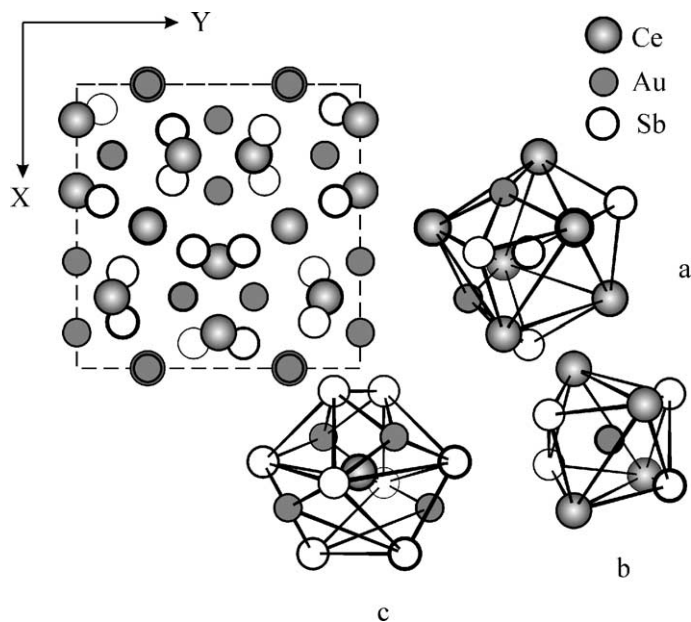


Fig. 32. Projection of the $\text{Ce}_3\text{Au}_3\text{Sb}_4$ unit cell and coordination polyhedra of atoms.

Table 30

Atom	Wyckoff notation	x/a	y/b	z/c	$G, \%$
Ce	12(a)	3/8	0	1/4	100
Au	12(b)	7/8	0	1/4	100
Sb	16(c)	0.0844	0.0844	0.0844	100

Table 31

Atom	Wyckoff notation	x/a	y/b	z/c	$G, \%$
Sm	1(a)	0	0	0	100
X	2(d)	1/3	2/3	1/2	100

$$X = 0.5\text{Ni} + 0.5\text{Sb}$$

$Y_3\text{Au}_3\text{Sb}_4$ structure type. See fig. 32, table 30. SG $\bar{I}43d$, $Z = 4$, $a = 1.00443$ for $\text{Ce}_3\text{Au}_3\text{Sb}_4$ (Sologub et al., 1998).

AlB_2 structure type. See fig. 33, table 31. SG $P6/mmm$, $Z = 1$, $a = 0.4372$, $c = 0.3843$ nm for SmNiSb (Pecharsky et al., 1983a, 1983b).

ZrBeSi structure type. See fig. 34, table 32. SG $P6_3/mmc$, $a = 0.4404$, $c = 0.8403$ nm for LaNiSb (Hartjes and Jeitschko, 1995).

CaIn_2 structure type. See table 33. SG $P6_3/mmc$, $Z = 2$, $a = 0.4580$, $c = 0.7716$ for NdPdSb (Marazza et al., 1980).

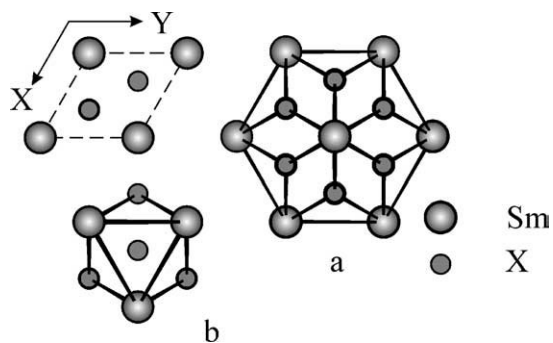


Fig. 33. Projection of the SmNiSb unit cell and coordination polyhedra of atoms.

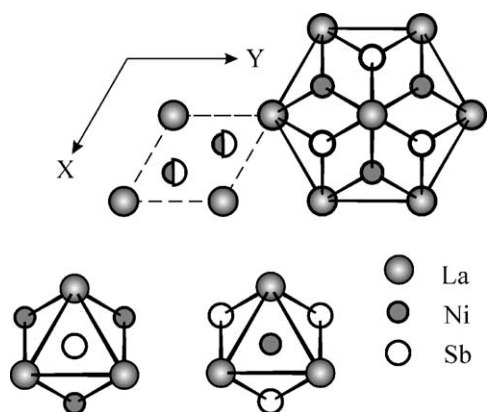


Fig. 34. Projection of the LaNiSb unit cell and coordination polyhedra of atoms.

Table 32

Atom	Wyckoff notation	x/a	y/b	z/c	$G, \%$
La	2(a)	0	0	0	100
Ni	2(c)	1/3	2/3	1/4	100
Sb	2(d)	1/3	2/3	3/4	100

Table 33

Atom	Wyckoff notation	x/a	y/b	z/c	$G, \%$
Nd	2(b)	0	0	0.25	100
X	4(f)	1/3	2/3	0.04	100

$X = 0.5\text{Pd} + 0.5\text{Sb}$

NdPtSb (or *LiGaGe*) structure type. See fig. 35, table 34. SG $P6_3mc$, $Z = 2$, $a = 0.4534$, $c = 0.7866$ nm (Wenski and Mewis, 1986a).

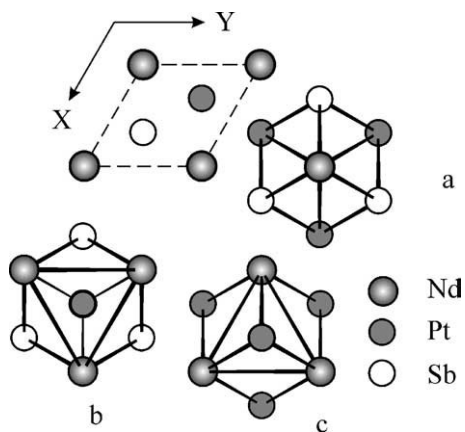


Fig. 35. Projection of the NdPtSb (or LiGaGe) unit cell and coordination polyhedra of atoms.

Table 34

Atom	Wyckoff notation	x/a	y/b	z/c	$G, \%$
Nd	2(a)	0	0	0.000	100
Pt	2(b)	1/3	2/3	0.7137	100
Sb	2(b)	1/3	2/3	0.2635	100

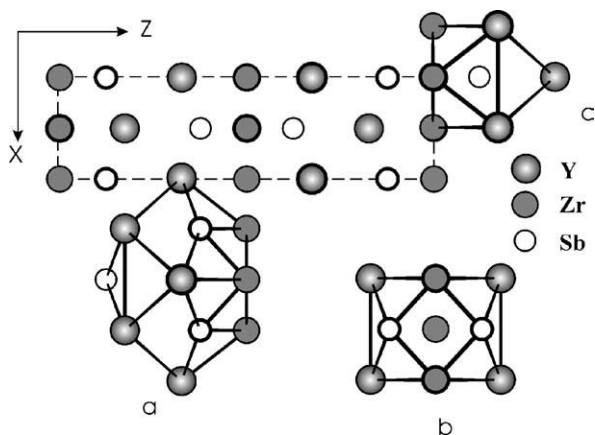


Fig. 36. Projection of the YZrSb unit cell and coordination polyhedra of atoms.

KHg₂ structure type. SG *Imma* $Z = 4$, $a = 0.4584$, $b = 0.7329$, $c = 0.7838$ nm for NdRhSb (Malik and Adroja, 1991b). Atomic coordinates have not been determined.

CeScSi structure type. See fig. 36, table 35. SG *I4/mmm*, $Z = 4$, $a = 0.4245$, $c = 1.6306$ nm for YZrSb (Morozkin and Sviridov, 2001).

Table 35

Atom	Wyckoff notation	x/a	y/b	z/c	$G, \%$
Y	4(e)	0	0	0.335	100
Zr	4(c)	0	1/2	0	100
Sb	4(e)	0	0	0.143	100

Table 36

Atom	Wyckoff notation	x/a	y/b	z/c	$G, \%$
Ce	4(c)	0.0118	1/4	0.7008	100
Rh	4(c)	0.2997	1/4	0.4172	96.6
Sb	4(c)	0.1908	1/4	0.0900	100

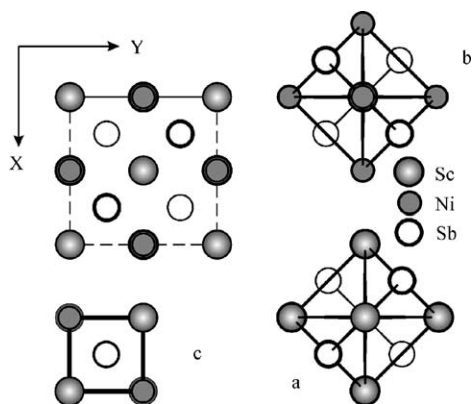


Fig. 37. Projection of the ScNiSb unit cell and coordination polyhedra of atoms.

Table 37

Atom	Wyckoff notation	x/a	y/b	z/c	$G, \%$
Sc	4(b)	1/2	1/2	1/2	100
Ni	4(c)	1/4	1/4	1/4	100
Sb	4(a)	0	0	0	100

Table 38

Atom	Wyckoff notation	x/a	y/b	z/c	$G, \%$
Ce	4(g)	0.1406	0	0	100
Ge	2(d)	0	0	0	100
Sb1	2(b)	1/2	0	0	100
Sb2	4(h)	0.3047	0	1/2	100

TiNiSi structure type. See table 36. SG $Pnma$, $Z = 4$, $a = 0.7581$, $b = 0.4642$, $c = 0.7893$ nm for CeRhSb (Salamakha et al., 2000).

MgAgAs structure type. See fig. 37, table 37. SG $F\bar{4}3m$, $Z = 4$, $a = 0.6055$ nm for ScNiSb (Pecharsky et al., 1983a, 1983b).

Te₂Ag₃Tl structure type. See fig. 38, table 38. SG $Cmmm$, $Z = 4$, $a = 1.8894$, $b = 0.4650$, $c = 0.4299$ for Ce₂GeSb₃ (Stetskiv et al., 1998).

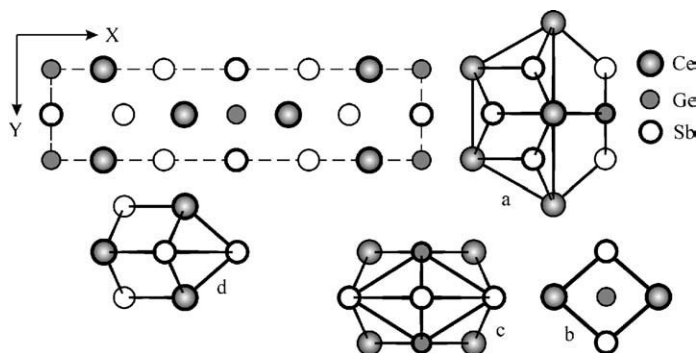
Fig. 38. Projection of the Ce_2GeSb_3 unit cell and coordination polyhedra of atoms.

Table 39

Atom	Wyckoff notation	x/a	y/b	z/c	$G, \%$
La	6(g)	0.6176	0	1/4	100
Ti	2(b)	0	0	0	100
Sb1	6(g)	0.2507	0	1/4	100
Sb2	4(d)	1/3	2/3	0	100

Table 40

Atom	Wyckoff notation	x/a	y/b	z/c	$G, \%$
La1	2(d)	1/3	2/3	0.07041	100
La2	2(c)	0	0	0.21173	100
Mg1	2(d)	1/3	2/3	0.4031	83
Mg2	2(d)	1/3	2/3	0.6733	100
Mg3	1(b)	0	0	1/2	82
Sb1	2(d)	1/3	2/3	0.28754	100
Sb2	2(d)	1/3	2/3	0.56417	100
Sb3	2(d)	1/3	2/3	0.85691	100
Sb4	1(a)	0	0	0	100

U_3CrSb_5 structure type (Hf_5CuSb_3 -anti type). See table 39. SG $P6_3/mcm$, $Z = 2$, $a = 0.95294$, $c = 0.62801$ nm for La_3TiSb_5 (Bollere et al., 1995).

$La_4Mg_{5-x}Sb_7$ structure type. See table 40. SG $P\bar{3}m1$, $Z = 1$, $a = 0.46201$, $c = 2.6069$ for $La_4Mg_{4.48}Sb_7$ structure (Ganguli et al., 1993).

$La_{5-y}Mg_{2-x}Sb_6$ structure type. See table 41. SG $R\bar{3}m$, $Z = 3$, $a = 0.4616$, $c = 6.767$ for $La_{4.89}Mg_{1.539}Sb_6$ (Ganguli et al., 1993).

$La_3Mg_{5-x}Sb_6$ structure type. See table 42. SG $R\bar{3}m$, $Z = 3$, $a = 0.4625$, $c = 6.691$ for $La_3Mg_{4.6}Sb_6$ (Ganguli et al., 1993).

Table 41

Atom	Wyckoff notation	x/a	y/b	z/c	$G, \%$
La1	6(c)	0	0	0.27869	100
La2	6(c)	0	0	0.44266	94.5
La3	3(a)	0	0	0	100
Mg	6(c)	0	0	0.15230	83.0
Sb1	6(c)	0	0	0.08289	100
Sb2	6(c)	0	0	0.19509	100
Sb3	6(c)	0	0	0.36087	100

Table 42

Atom	Wyckoff notation	x/a	y/b	z/c	$G, \%$
La1	6(c)	0	0	0.38795	100
La2	3(a)	0	0	0	100
Mg1	6(c)	0	0	0.12927	90
Mg2	6(c)	0	0	0.23407	100
Mg3	3(b)	0	0	1/2	80
Sb1	6(c)	0	0	0.08404	100
Sb2	6(c)	0	0	0.19154	100
Sb3	6(c)	0	0	0.30550	100

Table 43

Atom	Wyckoff notation	x/a	y/b	z/c	$G, \%$
Eu1	16(e)	1/4	0.6432	1/8	100
Eu2	32(g)	0.9565	0.6768	0.9528	100
Eu3	32(g)	0.9786	0.8741	0.1260	100
Eu4	32(g)	0.1808	0.1589	0.9679	100
Mn	8(a)	0	0	0	100
Sb1	8(b)	0	0	1/4	100
Sb2	16(f)	0.1332	0.1332	1/4	100
Sb3	32(g)	0.0034	0.8614	0.9374	100
Sb4	32(g)	0.8685	0.7244	0.0783	100

$Ca_{14}AlSb_{11}$ structure type. See table 43. SG $I4_1/acd$, $Z = 8$, $a = 1.7300$, $c = 2.2746$ nm for $Eu_{14}MnSb_{11}$ (Rehr and Kauzlarich, 1994).

$Ba_5Al_2Sb_6$ structure type. See table 44. SG $Pbam$, $Z = 2$, $a = 0.73992$, $b = 2.3001$, $c = 0.45139$ nm for $Yb_5In_2Sb_6$ (Mills and Mar, 2000).

La_3InGe structure type. SG $I4/mcm$, $Z = 16$, $a = 1.2012$, $c = 1.5485$ nm for Ce_3GeSb (Stetskiv et al., 1998). Atomic coordinates have not been determined.

Mo_5B_2Si structure type. See table 45. SG $I4/mcm$, $Z = 4$, $a = 0.7593$, $c = 1.3258$ nm for Dy_5Ni_2Sb (Mozharivskiy and Kuz'ma, 1996).

Table 44

Atom	x/a	y/b	z/c	$G, \%$
Yb1	0.9584	0.0895	1/2	100
Yb2	0.0269	0.2446	1/2	100
Yb3	1/2	0	1/2	100
In	0.3244	0.1202	0	100
Sb1	0.5465	0.1369	0	100
Sb2	0.05465	0.1897	0	100
Sb3	0.1989	0.9992	0	100

Table 45

Atom	Wyckoff notation	x/a	y/b	z/c	$G, \%$
Dy1	4(c)	0	0	0	100
Dy2	16(i)	0.1597	0.6597	0.1385	100
Ni	8(h)	0.372	0.872	0	100
Sb	4(a)	0	0	1/4	100

6. Physical properties of the ternary antimonides

6.1. RM_2Sb_2 compounds

The $CeNi_2Sb_2$ compound was classified as Kondo system by Kaczmarek et al. (1993) from magnetic properties and resistivity measurements. The resistivity shows a maximum at 2.5 K and a minimum at 28 K (fig. 39). As reported by Skolozdra et al. (1994), it has a Curie–Weiss

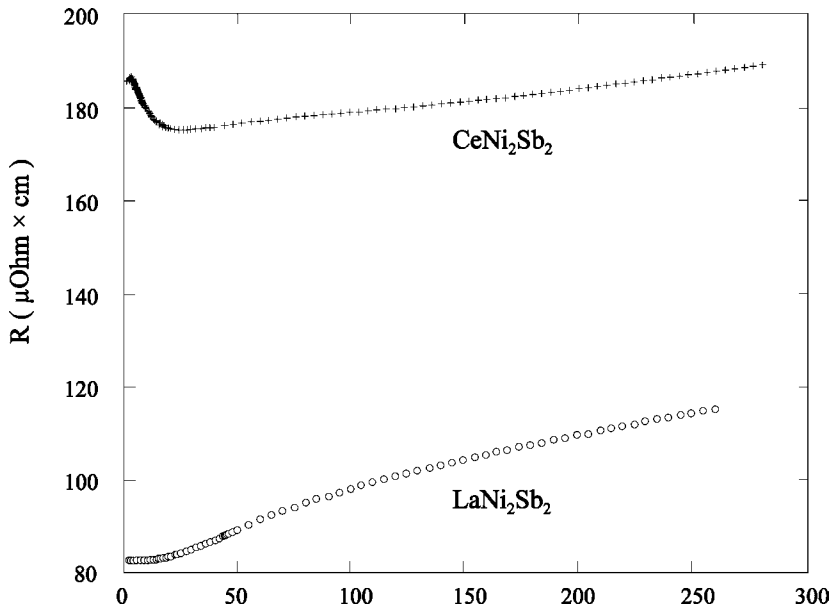


Fig. 39. Resistivity vs T for $LaNi_2Sb_2$ and $CeNi_2Sb_2$.

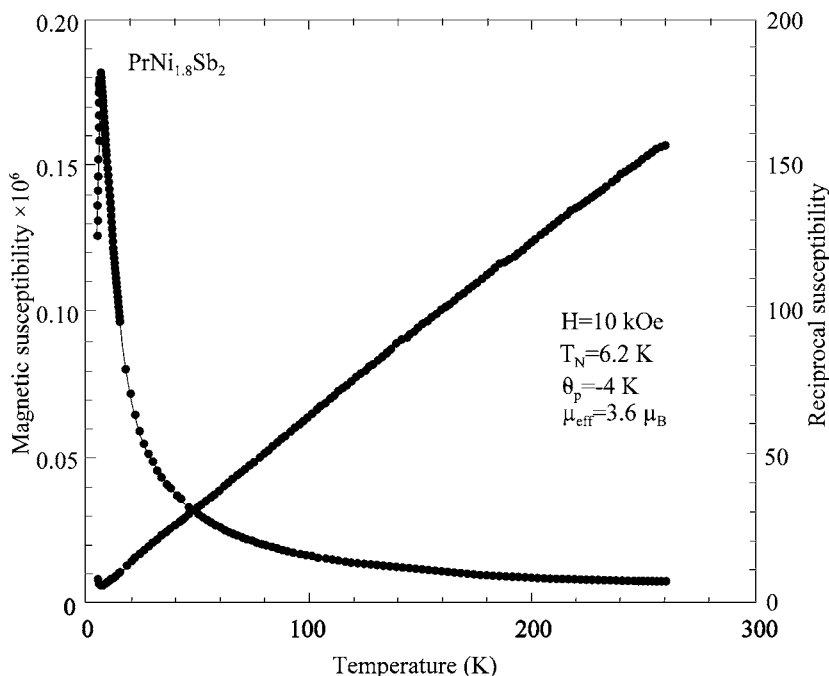


Fig. 40. χ in emu/g and $1/\chi$ in $(\text{emu/mole})^{-1}$ vs T for $\text{PrNi}_{1.8}\text{Sb}_2$.

temperature θ_p of -28 K, $T_N = 2.5$ K and $\mu_{\text{eff}} = 2.60\mu_B$. The residual resistivity of LaNi_2Sb_2 is $80 \mu\Omega \text{ cm}$ after Kaczmarzka et al. (1993).

Slebarski et al. (1996) measured the magnetic properties for the PrM_2Sb_2 compounds (fig. 40–42: $T_N = 6.24$ K, $\theta_p = -4.0$ K, $\mu_{\text{eff}} = 3.60\mu_B$, $H_{\text{cr}} = 10.0$ kOe at $T = 4.2$ for $\text{PrNi}_{1.8}\text{Sb}_2$ (fig. 40); $T_N = 6.5$ K, $\theta_p = -3.5$ K, $\mu_{\text{eff}} = 3.58\mu_B$, $H_{\text{cr}} = 10.3$ kOe at $T = 4.2$ for PrNi_2Sb_2 (fig. 41); $T_N = 6.0$ K, $\theta_p = -1.5$ K, $\mu_{\text{eff}} = 3.51\mu_B$, $H_{\text{cr}} \leq 1.0$ kOe at $T = 4.2$ for PrCu_2Sb_2 (fig. 42). It was found from magnetic susceptibility measurements that Pr is nearly trivalent.

Guzik and Pierre (1998) presented the magnetotransport properties of LaCu_2Sb_2 (fig. 43), LaAg_2Sb_2 (fig. 43) and CeAg_2Sb_2 compounds (fig. 44). The resistivity of CeAg_2Sb_2 exhibits a very broad plateau from room temperature down to 100 K then a slight increase down to 20 K followed by a sharp drop at the Néel temperature 9 K.

Skolozdra et al. (1994) reported Kondo-like behavior for the resistivity of CeCu_2Sb_2 , with a maximum at 17 K and a minimum at about 140 K of (fig. 45) and $\theta_p = -7$ K, $T_N = 3$ K and $\mu_{\text{eff}} = 2.60\mu_B$.

Gordon et al. (1995) reported the physical properties of $\text{Ce}_3\text{Pd}_6\text{Sb}_5$. The magnetic susceptibility exhibits significant anisotropy with an effective high temperature moment per Ce of $2.67\mu_B$ and antiferromagnetic ordering at 6 K. The resistance shows a minimum near 17 K and an anomaly at 6 K.

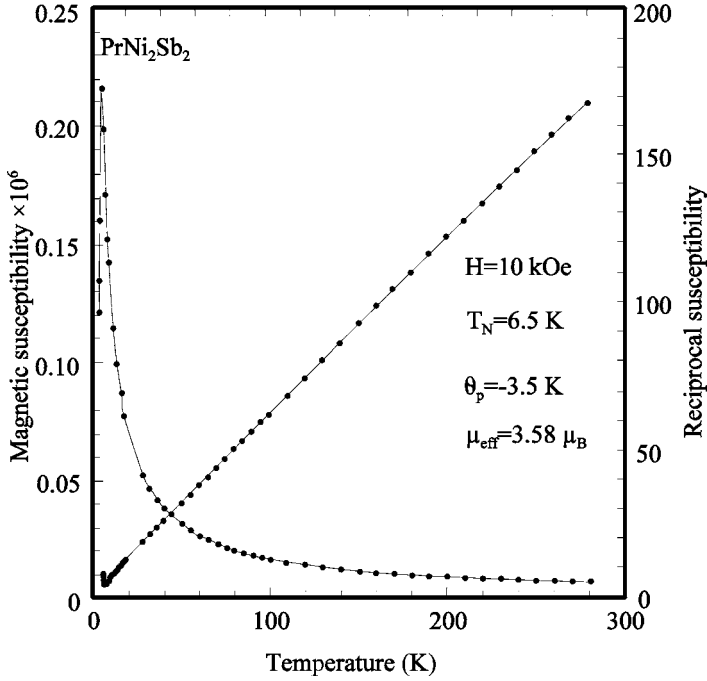


Fig. 41. χ in emu/g and $1/\chi$ in $(\text{emu/mole})^{-1}$ vs T for PrNi₂Sb₂.

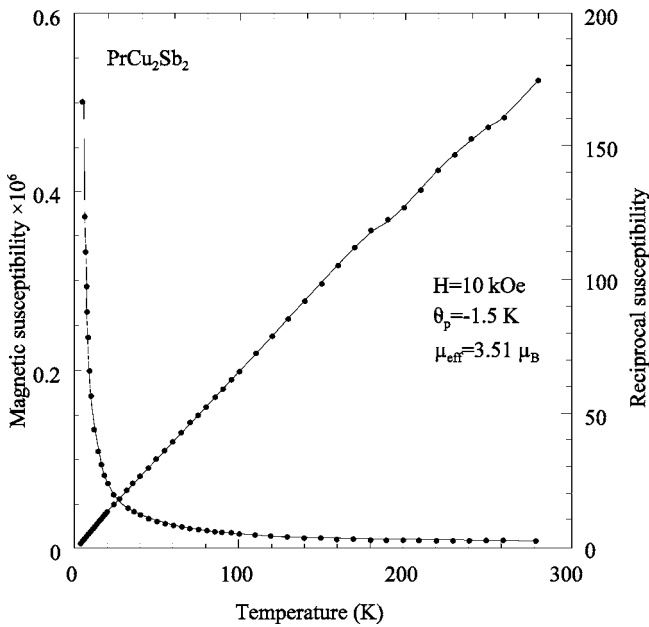


Fig. 42. χ in emu/g and $1/\chi$ in $(\text{emu/mole})^{-1}$ vs T for PrCu₂Sb₂.

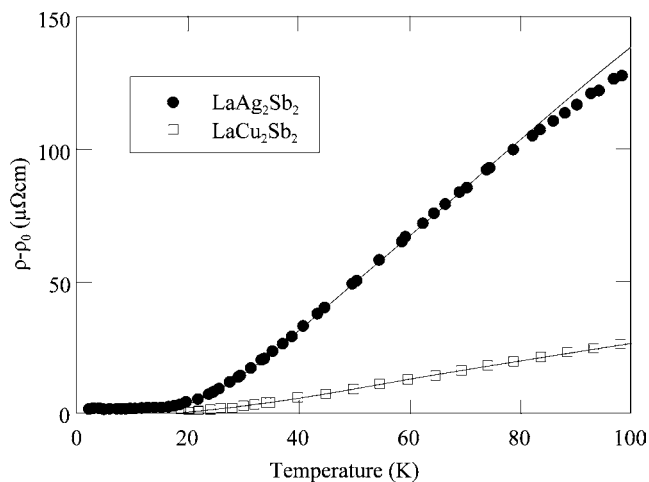


Fig. 43. Resistivity of LaCu₂Sb₂ and LaAg₂Sb₂.

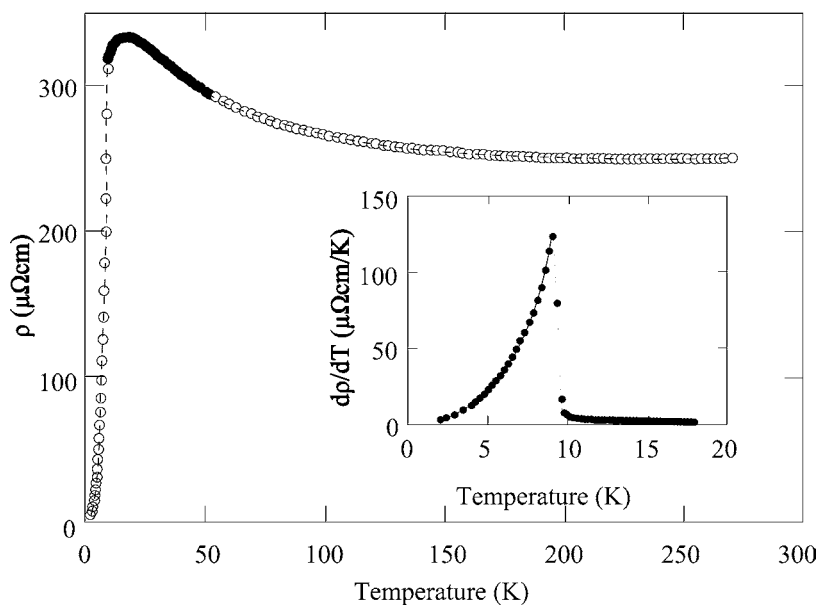


Fig. 44. Resistivity of CeAg₂Sb₂.

6.2. RNiSb compounds

Hartjes and Jeitschko (1995) measured the magnetic characteristics of the RNiSb compounds (table 46). It was observed that the magnetic susceptibility of LaNiSb is nearly temperature independent. The average value of the susceptibility for the temperature range between 100

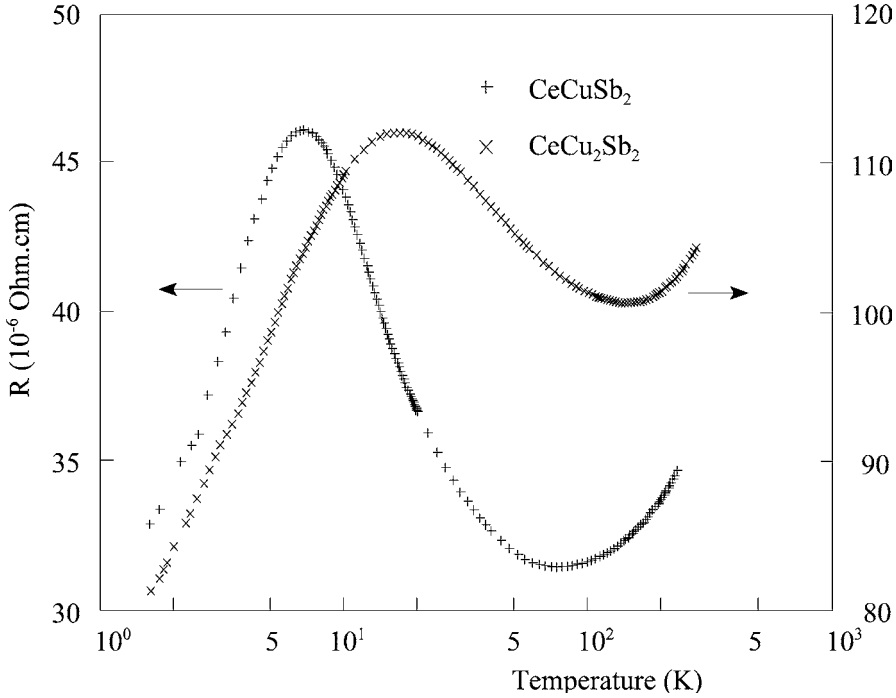


Fig. 45. Resistivity of CeCu_2Sb_2 (right hand scale) and CeCuSb_2 (left hand scale).

Table 46
Magnetic properties of $R\text{NiSb}$ compounds (Hartjes and Jeitschko, 1995)

Compound	Structure type	$\mu_{\text{exp}} (\mu_B)$	$\mu_{\text{eff}} (R^{3+}) (\mu_B)$ (theory)	θ (K)	Type of magnetism
LaNiSb	ZrBeSi	0	0	–	Pauli paramagnetic
CeNiSb	ZrBeSi	2.59(5)	2.54	–9(1)	Curie–Weiss
PrNiSb	ZrBeSi	3.68(4)	3.58	0(1)	Curie–Weiss
NdNiSb	ZrBeSi	3.68(4)	3.62	16(2)	Curie–Weiss
SmNiSb	ZrBeSi	1.58(8)	1.60	–	Van Vleck paramagnetic
GdNiSb	MgAgAs	8.1(5)	7.94	–15(5)	Curie–Weiss
TbNiSb	MgAgAs	10.2(4)	9.72	–13(2)	Curie–Weiss
DyNiSb	MgAgAs	10.6(4)	10.63	–6(2)	Curie–Weiss
HoNiSb	MgAgAs	10.7(4)	10.60	0(3)	Curie–Weiss
ErNiSb	MgAgAs	9.5(3)	9.59	0(2)	Curie–Weiss
TmNiSb	MgAgAs	7.6(3)	7.57	0(1)	Curie–Weiss
LuNiSb	MgAgAs	0	0	–	Pauli paramagnetic

and 300 K is $\chi = 1.8 \times (\pm 0.1) \times 10^{-9} \text{ m}^3/\text{mol}$ which is typical for the Pauli paramagnetism of metallic conductors. The lutetium compound is also assumed to be Pauli paramagnetic. The magnetic susceptibilities between 250 and 300 K are equally small as they are for LaNiSb. It

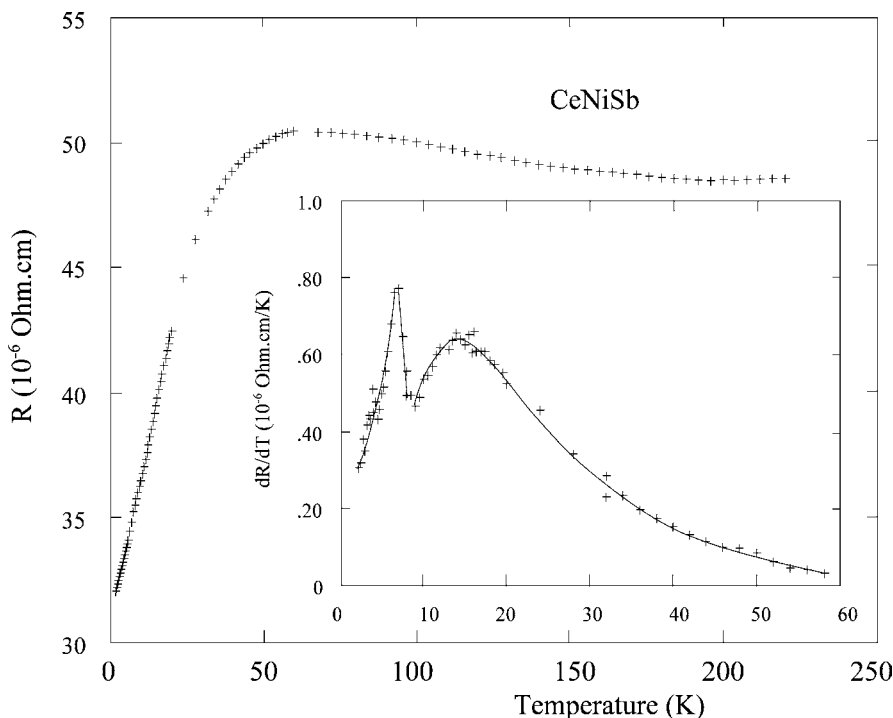


Fig. 46. Resistivity vs temperature for CeNiSb.

was also reported in the same work that for compounds with magnetic lanthanide elements, the magnetism is dominated by the magnetic moments of these elements. The samarium compound shows van Vleck paramagnetism. All other compounds exhibit Curie–Weiss behavior.

The magnetism and resistivity of CeNiSb were investigated by Skolozdra et al. (1994). The susceptibility of CeNiSb follows a Curie–Weiss law above 35 K, with an effective moment of $2.70(5)\mu_B$ and a Curie–Weiss temperature of ~ 15 K. However, susceptibility deviates from this law at lowest temperatures, and diverges near $T_C = 7$ K, where spontaneous magnetization appears. The ferromagnetic moment reaches $0.48\mu_B$ at 1.5 K. The resistivity exhibits a maximum at about 60 K and a minimum around 200 K (fig. 46). A kink in the curve occurs at 7 K, which confirms the Curie temperature. The maximum slope of resistivity vs temperature is reached near 15 K. The magnetoresistance at low temperature is negative. The initial slope is vanishing small in the paramagnetic range, and negative in the ferromagnetic state. Based on these results, the authors announced CeNiSb to be a new ferromagnetic Kondo system. In contrast to this investigation, measurements on a sample in the later work performed by Hartjes and Jeitschko (1995) show a normal Curie–Weiss behavior, and the effective magnetic moment calculated from the linear portion of the $1/\chi$ vs T plot above 50 K of $\mu_{\text{exp}} = 2.59(5)\mu_B$

which is in good agreement with the theoretically expected effective moment for a free Ce^{3+} ion of $2.54\mu_{\text{B}}$.

Magnetic susceptibility and electrical resistivity measurements on CePdSb and GdPdSb were carried out in the temperature range of 4.2–300 K by Malik and Adroja (1991a). The measurements reveal that CePdSb orders ferromagnetically with an ordering temperature of 17 K while GdPdSb orders antiferromagnetically with a Néel temperature of 15.5 K. In the paramagnetic state, the susceptibility of CePdSb follows Curie–Weiss behavior between 50 and 300 K but deviates from it below 50 K. Its saturation magnetic moment per formula unit at 4.2 K is $1.2\mu_{\text{B}}$ which is reduced from the free ion value of $2.14\mu_{\text{B}}$ for the Ce^{3+} ion. The resistivity of CePdSb shows a broad maximum at about 150 K and a $\ln(T)$ behavior at high temperatures, indicating the combined influence of crystalline electric fields and the Kondo effect on the 4f moments. Thus the authors suggest that CePdSb is a Kondo-lattice system with ferromagnetic ordering of cerium moments.

The compound CeRhSb, which crystallizes in the orthorhombic CeCu₂-type structure, has been synthesized by Malik and Adroja (1991b). Its unit-cell volume is anomalous in relation to that of the isostructural RRhSb compounds. Its magnetic susceptibility is weakly temperature dependent and exhibits a broad maximum at about 113 K, characteristic of valence-fluctuating Ce compounds. The resistivity also shows a broad maximum at 113 K followed by a rapid rise below 21 K. The latter indicates gap formation in the electronic density of states. The gap energy is estimated to be about 4 K. Thus CeRhSb appears to represent a valence fluctuating cerium compound in which a pseudogap develops in the electronic density of states at low temperatures. Adroja et al. (1999) performed the neutron scattering studies on CeRhSb and PrMSb ($M = \text{Rh}, \text{Pd}$).

Aliev et al. (1988) reported the results of transport and magnetic measurements of RNiSb, $R = \text{Sc}, \text{Er}, \text{Ho}, \text{Tm}, \text{Yb}$. It was suggested that the gap in the electron energy spectrum in these systems is due to the specific crystal structure with a vacancy in the Ni sublattice. It was found that properties of RNiM compounds are strongly influenced by the annealing process.

Preliminary results on low temperature transport properties in YbPdSb system with MgAgAs type structure are presented by Aliev et al. (1988). Resistivity shows a maximum at $T = 50\text{--}100$ K and the Fermi-liquid decrease of $\rho \approx \rho_0 + AT^2$ at helium temperatures. The high value of the A coefficient $5 \mu\Omega \text{ cm/K}^2$ indicates the possibility of the heavy fermion behavior with γ about 300–400 mJ/mol K². The Seebeck coefficient S is positive and shows a maximum $S_{\text{max}} \approx 22 \mu\text{V/K}$ at $T \approx 200$ K.

The electrical resistivity, magnetic susceptibility and magnetization for YbTSb compounds ($T = \text{Cu}, \text{Ag}, \text{Au}$) were measured by Katoh et al. (1997); the results are presented in table 47 and fig. 47. Also, Flandorfer et al. (1997) classified the YbCuSb and YbAgSb compounds as temperature independent Pauli-type paramagnets whereas a small magnetic moment $\approx 1\mu_{\text{B}}$ was observed for YbAuSb. From X-ray absorption spectroscopy at 10 and 300 K, Yb was determined to be dipositive with temperature independent valences for all compounds: 2.06 for $M = \text{Ag}$, 2.08 for $M = \text{Cu}$ and 2.14 for $M = \text{Au}$.

Table 47

Fitting parameters of magnetic susceptibility and electrical resistivity of YbTbSb : C, Curie constant; θ_p , paramagnetic Curie temperature; χ_0 , temperature independent susceptibility; χ_C , diamagnetic susceptibility; R, high temperature slope; θ_R , characteristic temperature, ϱ_0 , residual resistivity

Compound	C, e.m.u.Kmol ⁻¹	θ_p , K	χ_0 , e.m.u.mol ⁻¹	χ_C , e.m.u.mol ⁻¹	R, $\mu\Omega \text{ cm K}^{-1}$	θ_R , K	ϱ_0 , $\mu\Omega \text{ cm}$
YbCuSb	0.0376	-35.8	1.38×10^{-4}	-4.9×10^{-5}	0.44	170	260
YbAgSb	0.00245	-4.42	-7.69×10^{-5}	-6.1×10^{-5}	0.26	150	46
YbAuSb	0.00339	-4.37	-8.47×10^{-5}	-7.7×10^{-5}	0.21	140	48

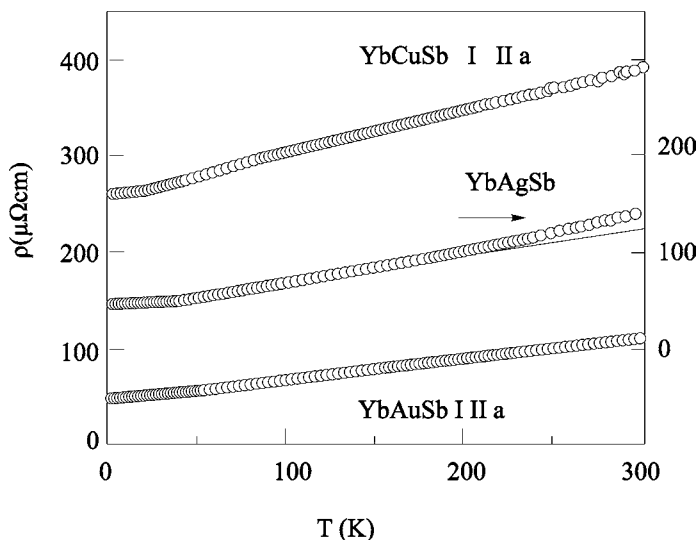


Fig. 47. Electrical resistivity vs for YbTbSb compounds ($T = \text{Cu, Ag, Au}$).

6.3. RMSb_2 compounds

The magnetic data on the $\text{RM}_{1-x}\text{Sb}_2$ ($R = \text{La, Ce, Pr, Nd}$ and Sm and $M = \text{Mn, Zn}$) compounds are summarized in table 48 (Sologub et al., 1995a). The magnetic behavior of the RMnSb_2 compounds is characterized by the onset of ferromagnetism of the Mn sublattice in the temperature range between 100 and 520 K. Ordering of the rare earth sublattice below 50 K was observed for samples containing Ce, Pr and Nd. CeZnSb_2 remains paramagnetic over the temperature range investigated (4.2–550 K). From isothermal magnetization data at 5 K (fig. 48) the magnetic structures of the $\text{RM}_{1-x}\text{Sb}_2$ phases ($R = \text{La, Ce, Pr, Nd}$ and Sm) were thought to be rather complex (metamagnetism).

The magnetic susceptibilities of the RMSb_2 ($M = \text{Ni, Pd, Cu, Au}$) phases were generally measured over the temperature range from 4 K to 100 K (Sologub et al., 1994) (table 49, figs. 49, 50). YCuSb_2 and LaMSb_2 are temperature independent paramagnets. The RMSb_2 compounds are found to order antiferromagnetically below $T = 20$ K. PrPdSb_2 and TbPdSb_2 undergo metamagnetic transitions, whereas PrCuSb_2 and ErCuSb_2 are simple fer-

Table 48
Magnetic characteristics for the $RMn_{1-x}Sb_2$ compounds, $M = Mn, Zn$

Compound	T_c (K)	σ (μ_a)	θ_p (K)	$\mu_{\text{eff/f.u.}}$ (μ_B)	$\mu_{\text{eff/Mn}}$ (μ_B)
$LaMn_{0.87}Sb_2$	~ 310	0.8^b	228	4.6	4.6
$CeMn_{0.85}Sb_2$	~ 310	1.2^c	104	4.8	4.3
$PrMn_{0.82}Sb_2^a$	~ 390	1.0^c			
$NdMn_{0.83}Sb_2$	~ 250	0.6^c	225	5.5	4.5
$SmMn_{0.90}Sb_2^a$	~ 250	0.4^b			
$CeZn_{1-x}Sb_2$			-11	2.6	

^aMultiphase samples.

^b $T = 5$ K, $H = 2$ Tesla.

^c $T = 5$ K, $H = 3$ Tesla.

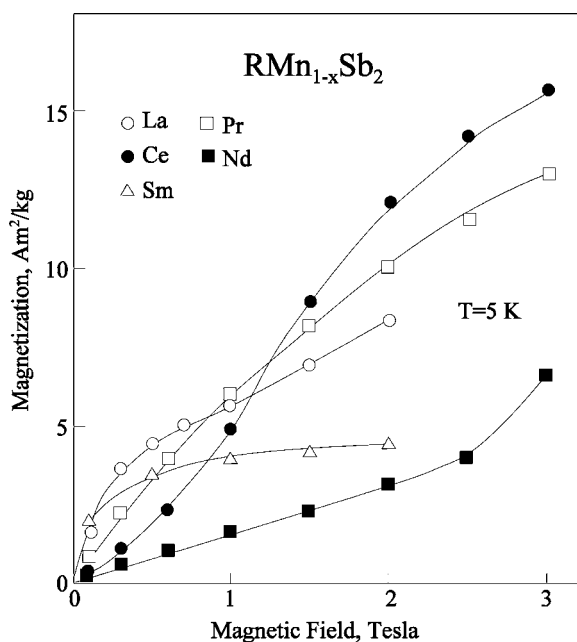


Fig. 48. Magnetization vs magnetic field for $RMn_{1-x}Sb_2$ after Sologub et al. (1995a, 1995b, 1995c).

romagnets. The Sm-containing compounds are typical Van Vleck paramagnets owing to the closely spaced multiplets.

According to Skolozdra et al. (1994), the resistivity for $CeCuSb_2$ shows a maximum at 7 K and a minimum at 70 K, as for concentrated Kondo systems (fig. 45). The resistivity of $LaCuSb_2$ is that of a classical metallic system. The $La_{0.4}Ce_{0.6}CuSb_2$ solid solution alloy exhibits a strong increase of the resistivity at low temperature similar to that of the pure compound with a maximum at 9 K. The magnetoresistance has been measured for the $CeCuSb_2$ up to 5 T; a huge drop of resistivity is observed under a magnetic field. The summary of magnetic properties of $CeCuSb_2$, $CeNiSb_2$ and $(Ce_{1-x}La_x)CuSb_2$ obtained by Skolozdra et al.

Table 49
Magnetic characteristics of the $RMSb_2$ compounds, $M = Ni, Pd, Cu, Au$ (Sologub et al., 1994)

Compound	T_N (K)	θ_p (K)	μ_{eff} (μ_B)
LaNiSb ₂	TIP		
CeNiSb ₂	< 4.0	0.0	1.44
PrNiSb ₂	6.0	-4.0	4.00
NdNiSb ₂	< 4.0	-12.0	4.30
SmNiSb ₂			1.80 ^a
GdNiSb ₂	9.0	-44.0	9.60
TbNiSb ₂	12.0	-44.0	10.80
DyNiSb ₂	10.0	-27.0	12.00
HoNiSb ₂	< 4.0	-12.0	10.20
LaPdSb ₂	TIP		
CePdSb ₂	< 4.0	-65.0	3.04
PrPdSb ₂	8.0 ^b	-13.0	4.00
NdPdSb ₂	< 4.0	-30.	3.50
SmPdSb ₂			1.50 ^a
GdPdSb ₂	15.0	-41.0	7.90
TbPdSb ₂	18.0 ^b	-30.0	9.80
YCuSb ₂	TIP		
LaCuSb ₂	TIP		
CeCuSb ₂	8.0	-7.0	2.50
PrCuSb ₂	5.0 ^c	3.5	3.60
NdCuSb ₂	< 4.0	-9.0	3.70
SmCuSb ₂			1.30 ^a
GdCuSb ₂	12.0	-33.0	8.90
TbCuSb ₂	9.0	-23.0	9.40
DyCuSb ₂	6.0	-9.0	10.30
HoCuSb ₂	< 4.0	-4.0	10.40
ErCuSb ₂	< 4.0 ^d	-3.0	9.80
TmCuSb ₂	< 4.0	-3.0	7.30
LaAuSb ₂	TIP		
CeAuSb ₂	6.0	2.0	2.30
PrAuSb ₂	9.0	-6.0	3.90
NdAuSb ₂	< 4.0	-9.6	3.40
SmAuSb ₂			1.50 ^c

TIP temperature independent paramagnet.

^aEffective moment at 80 K.

^bMetamagnetism, $\mu_0 H_{crit} > 2.5$ T.

^cFerromagnetic, magnetic moment ($\mu_0 H = 3$ T at 5 K) = $1.7\mu_B$.

^dFerromagnetic, magnetic moment ($\mu_0 H = 3$ T at 5 K) = $5.6\mu_B$.

(1994) are presented in table 50, and the reciprocal magnetic susceptibility of the first and last compounds is shown in fig. 51.

Vijaya Lakshmi et al. (1996) performed magnetic and electrical resistivity measurements on $LaMSb_2$ and $CeMSb_2$, $M = Ni, Cu$ (see fig. 52). $CeNiSb_2$ orders ferromagnetically at 6 K while $CeCuSb_2$ orders antiferromagnetically at 5 K. The electrical resistivity of the two La compounds, $LaCuSb_2$ and $LaNiSb_2$ show normal metallic behavior down to 5.4 K with no

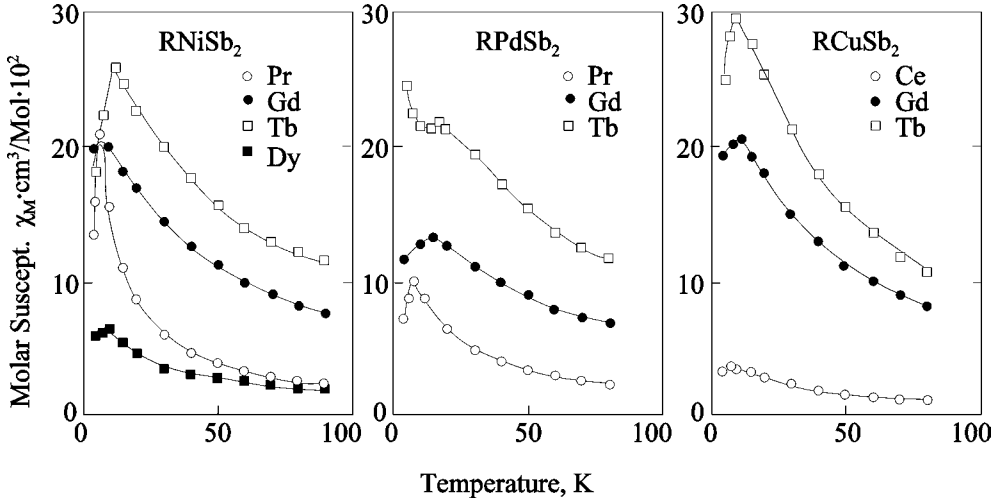


Fig. 49. Molar susceptibility vs T for the RMSb_2 , $M = \text{Ni, Pd, Cu}$ after Sologub et al. (1994).

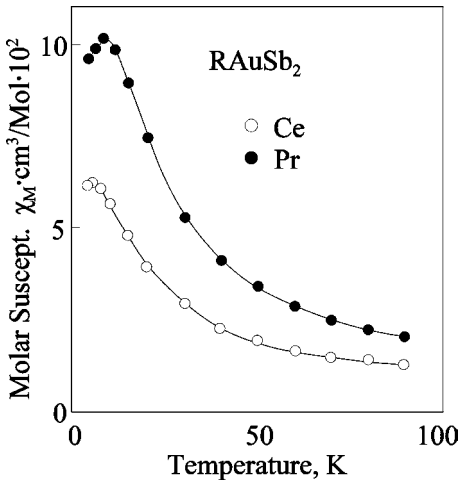


Fig. 50. Molar susceptibility vs T for the RAuSb_2 , $R = \text{Ce, Pr}$ after Sologub et al. (1994).

Table 50

Magnetic characteristics of the RMSb_2 compounds, $M = \text{Ni, Cu}$ (Skolozdra et al., 1994)

Compound	$\mu_{\text{eff}} (\mu_B)$	θ_p (K)	T_C, T_N (K)
CeCuSb ₂	2.57	-11	7
CeNiSb ₂	2.45	+6	7
Ce _{0.8} La _{0.2} CuSb ₂	2.59	-12	4
Ce _{0.6} La _{0.4} CuSb ₂	2.59	-11	< 2

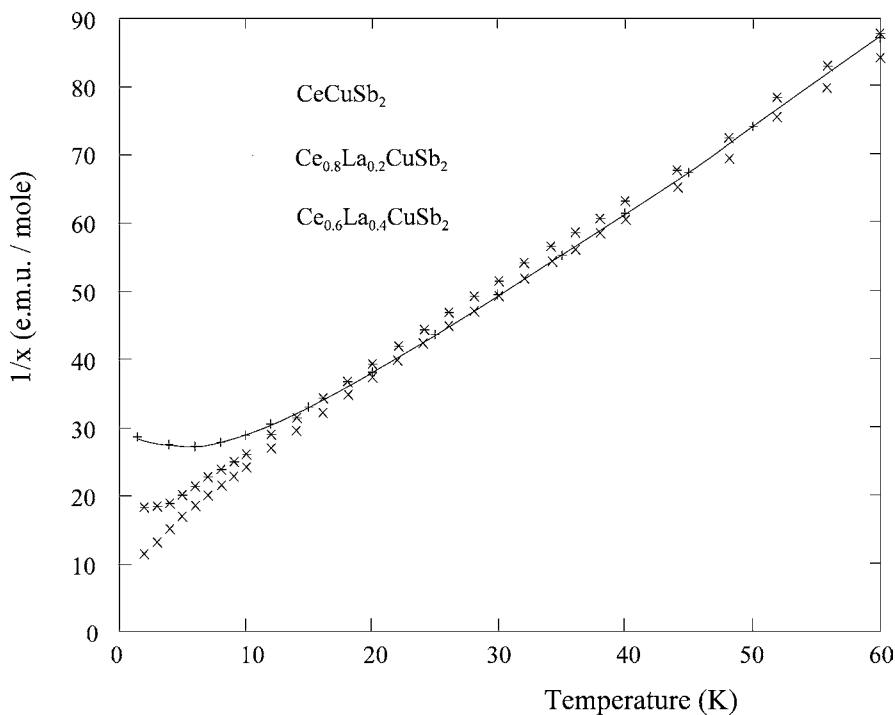


Fig. 51. $1/\chi$ vs T for CeCuSb_2 and $(\text{Ce}_{1-x}\text{La}_x)\text{CuSb}_2$ after Skolozdra et al. (1994).

superconducting transitions. The resistivity of CeCuSb_2 and CeNiSb_2 show broad minimum typical for Kondo lattice systems. There is a low temperature drop in resistivity in both the compounds due to magnetic ordering. In CeNiSb_2 a second minimum (at 10 K) followed by a maximum at 6 K is also observed. All compounds except CeNiSb_2 exhibit positive magnetoresistance in the temperature range 1.5–4.5 K in fields up to 45 kOe. The CeNiSb_2 compound shows negative magnetoresistance.

Accordingly to Sologub et al. (1995a), magnetism of the RAgSb_2 phases over the 2.5 to 300 K temperature range is characterized by tripositive paramagnetic behavior of the lanthanide atoms (table 51, fig. 53). RAgSb_2 with $R = \text{Y, La}$ are weakly temperature dependent paramagnets. In contrast, RAgSb_2 compounds with $R = \text{Pr, Nd, Sm, Gd, Dy, Ho, Er, Tm}$ are weak antiferromagnets with ordering temperatures lower than $T_N \sim 13$ K, and CeAgSb_2 is a noncollinear antiferromagnet ($T_M \sim 12$ K) with a remanent magnetization $\mu = 0.15\mu_B$ per Ce atom.

André et al. (2000) reported results of neutron diffraction measurements performed on RAgSb_2 ($R = \text{Ce, Pr, Nd, Tb, Dy, Ho, Er, Tm}$). All compounds were found to be collinear antiferromagnets with the Néel temperature between 2.0 K (for TmAgSb_2) and 11.1 K (for

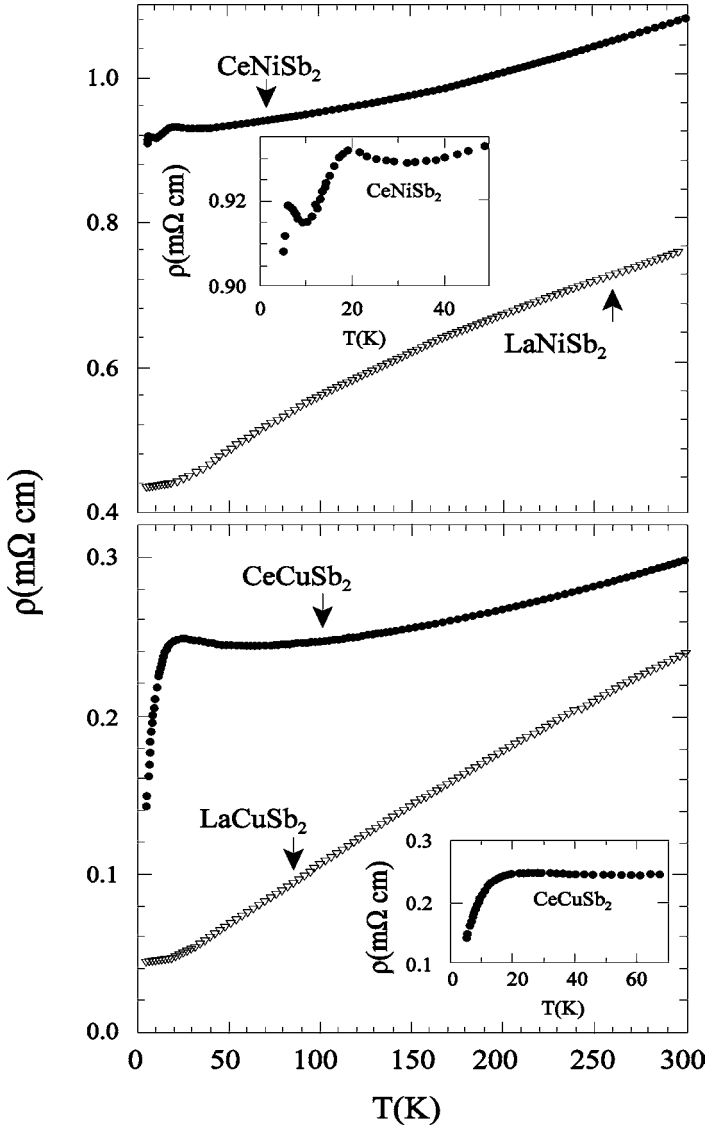


Fig. 52. Resistivity vs T for LaCuSb_2 , CeCuSb_2 , LaNiSb_2 and CeNiSb_2 after Vijaya Lakshmi et al. (1996).

TbAgSb_2), except for CeAgSb_2 which is a ferromagnet with a Ce magnetic moment equal to $0.33\mu_B$ and parallel to the c -axis.

Thermal expansion, magnetostriction and magnetic susceptibility under pressure have been measured on a polycrystalline CeAgSb_2 sample by Thornton et al. (1999). It was observed that in zero magnetic field the magnetic contribution to the linear thermal expansion coefficient

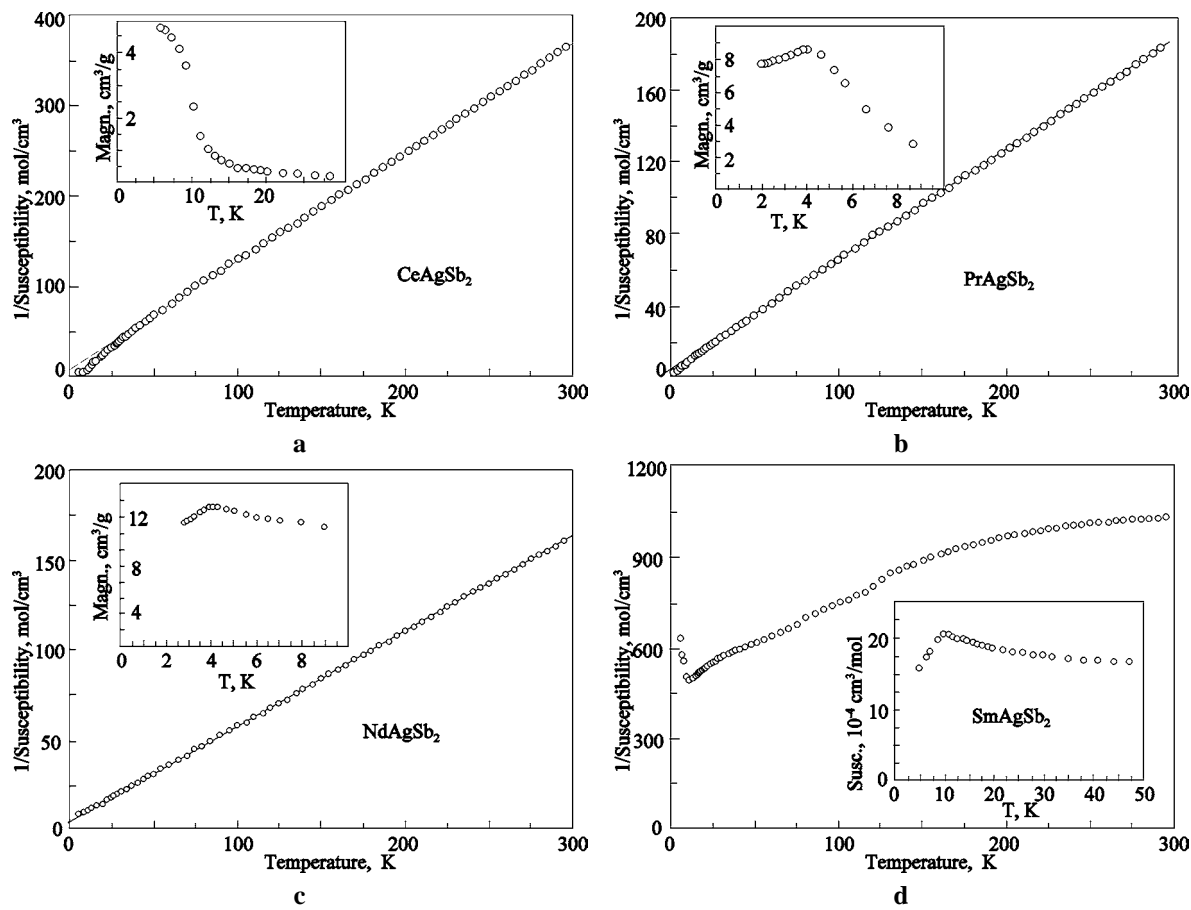


Fig. 53. $1/\chi$ vs T for RAgSb₂, $R = \text{Ce, Pr, Nd, Sm, Gd, Tb, Dy, Ho, Er, Tm}$.

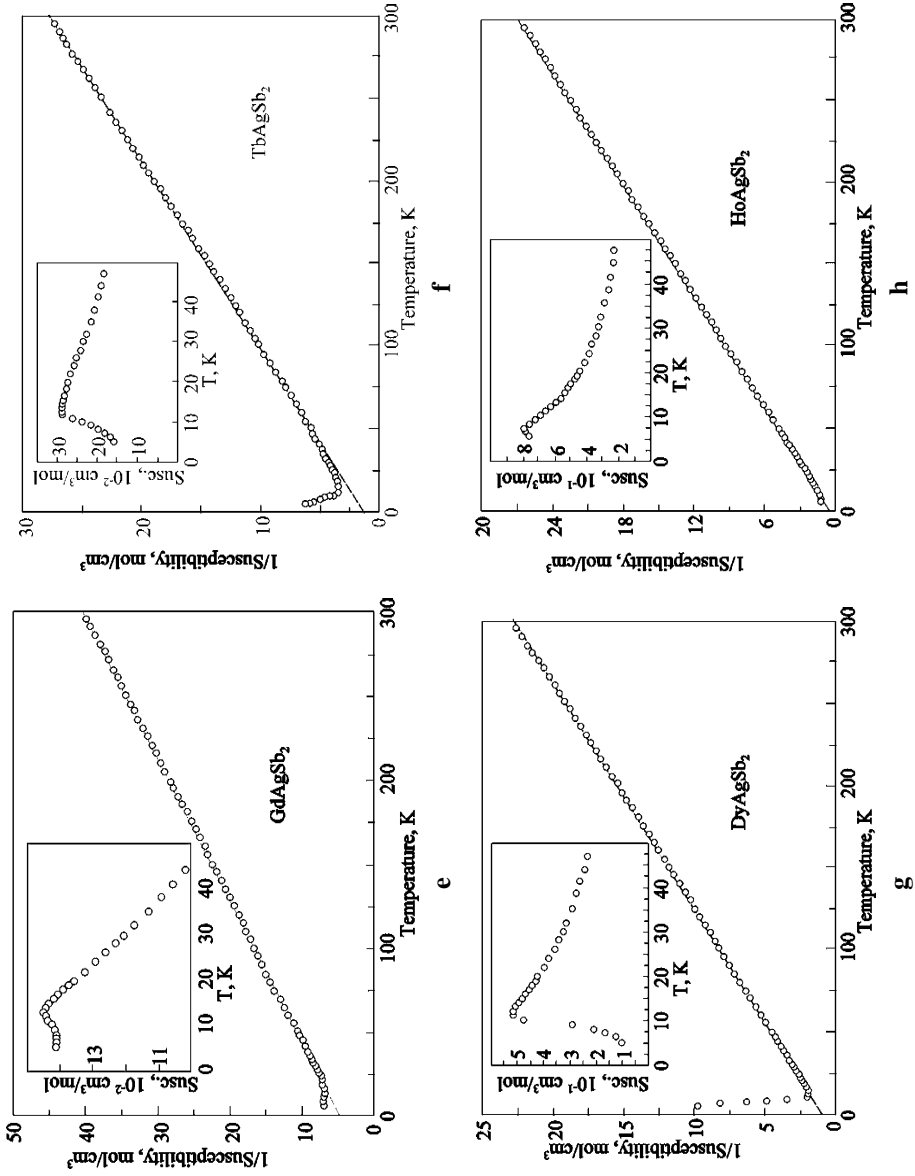


Fig. 53. Continued

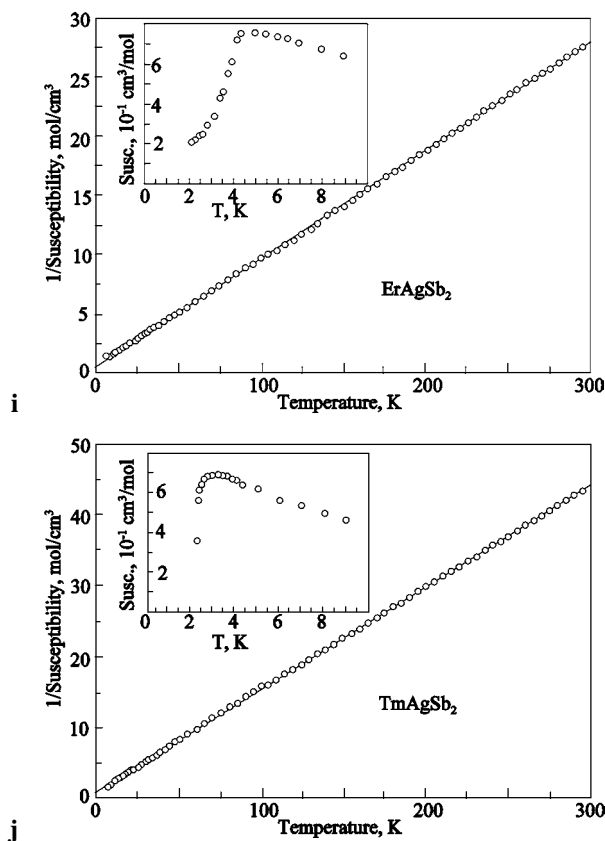


Fig. 53. Continued

has a broad maximum near 17 K with the value of $7.9 \times 10^{-6} \text{ K}^{-1}$ but there is no peak at the $T_N = 9.5 \text{ K}$. T_N was found to decrease under pressure at the rate -10.1 Mbar^{-1} .

Flandorfer et al. (1996) reported on the magnetic properties of $\text{CeFe}_{0.6}\text{Sb}_2$: $T_M = 9.5 \text{ K}$, $\theta_p = -23 \text{ K}$, $\mu_{\text{eff}}/\text{f.u.} = 2.6\mu_B$. Magnetic characteristics for the $\text{Ce}M_{1-x}\text{Sb}_2$ compounds, $M = \text{Mn, Ni, Pd, Cu, Ag, Au, Zn}$ were also measured (fig. 54). The L_{III} absorption edge measurements were performed on the $\text{Ce}M\text{Sb}_2$ compounds, $M = \text{Fe, Co, Ni, Pd, Cu, Ag}$ and Au at 10 K and 300 K. The L_{III} absorption edge spectra are similar at both temperatures and show that Ce in all compounds is in the trivalent, or nearly trivalent state.

6.4. $R_3M_3\text{Sb}_4$ compounds

Shaked et al. (1979) reported on the results of magnetic susceptibilities measurements on the $R_3\text{Au}_3\text{Sb}_4$ compounds ($R = \text{Tb, Ho, Er}$ and Tm) between 4 and 300 K (table 52, fig. 55). The compounds were found to be paramagnetic down to 4 K.

Electrical resistivity, Hall constant, magnetic susceptibility and specific heat measurements were performed on the $R_3\text{Au}_3\text{Sb}_4$ ($R = \text{La, Ce, Pr}$) and the $R_3\text{Pt}_3\text{Sb}_4$ ($R = \text{Ce, Pr}$) com-

Table 51
Magnetic data of ternary RAgSb₂ compounds

Compound	T_N (K)	θ_p (K)	μ_{eff} (μ_B)
YAgSb ₂	$\chi_0 = 0.7 \times 10^{-6} \text{ cm}^3 \text{ g}^{-1}$		
LaAgSb ₂	$\chi_0 = 0.6 \times 10^{-6} \text{ cm}^3 \text{ g}^{-1}$		
CeAgSb ₂	12.0 ^a	-6	2.57
PrAgSb ₂	4.3	-2	3.61
NdAgSb ₂	4.4	-9	3.91
SmAgSb ₂	10.0	-41	0.8 ^b
GdAgSb ₂	14.0	-35	7.8
TbAgSb ₂	13.0	-14	9.6
DyAgSb ₂	12.0	-12	10.5
HoAgSb ₂	6.0	-6	10.3 ^c
ErAgSb ₂	4.8	-6	9.4
TmAgSb ₂	3.1	-8	7.5

Note. Error limits on T_N , θ_p and μ_{eff} are ± 0.5 K, ± 1 K and $\pm 0.05\mu_B$, respectively.

^aNoncolinear antiferromagnet, remanent magnetization $\mu = 0.15\mu_B/\text{Ce}$.

^b $\chi_0 = 1.8 \times 10^{-6} \text{ cm}^3 \text{ g}^{-1}$.

^cCorrected for ~ 15 mole% of excess free (Sb) in the alloy.

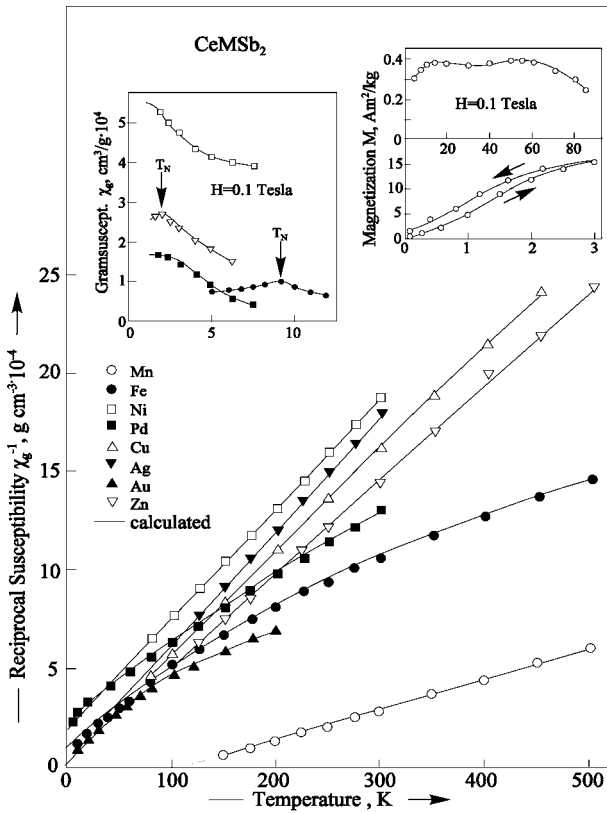


Fig. 54. Reciprocal susceptibility for the $\text{CeM}_{1-x}\text{Sb}_2$, $M = \text{Mn, Fe, Ni, Pd, Cu, Ag, Au, Zn}$.

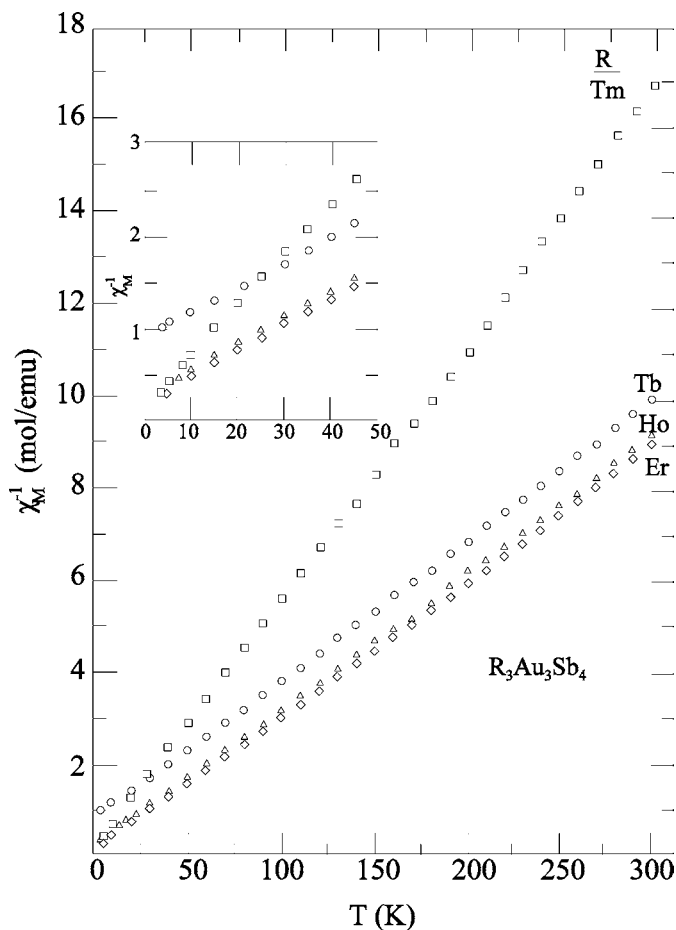


Fig. 55. $1/\chi$ vs T for $R_3Au_3Sb_4$, $R = Tb, Ho, Er, Tm$ after Shaked et al. (1979).

Table 52

The experimental effective magnetic moment of the $R_3Au_3Sb_4$ compounds ($R = Tb, Ho, Er$ and Tm) at 300 K after Shaked et al. (1979)

	Tb^{3+}	Ho^{3+}	Er^{3+}	Tm^{3+}
μ_{eff} (μ_B)	8.94	9.30	9.42	6.91

pounds by Kasaya et al. (1991). $La_3Au_3Sb_4$ and $Ce_3Au_3Sb_4$ show semi-metallic or semi-conducting behaviors whereas $Pr_3Pt_3Sb_4$ shows a metallic one. The valence of the Ce ions in $Ce_3Au_3Sb_4$ is 3+. The results indicate that $R_3Au_3Sb_4$ and $R_3Pt_3Sb_4$ are narrow-gap semiconductors and metals respectively. $Ce_3Pt_3Sb_4$ shows semiconducting behavior and that the Ce ions are in a mixed valence state. Magnetic susceptibility and inverse magnetic susceptibility vs T curves for $Ce_3Au_3Sb_4$ and $Ce_3Pt_3Sb_4$ are presented in fig. 56.

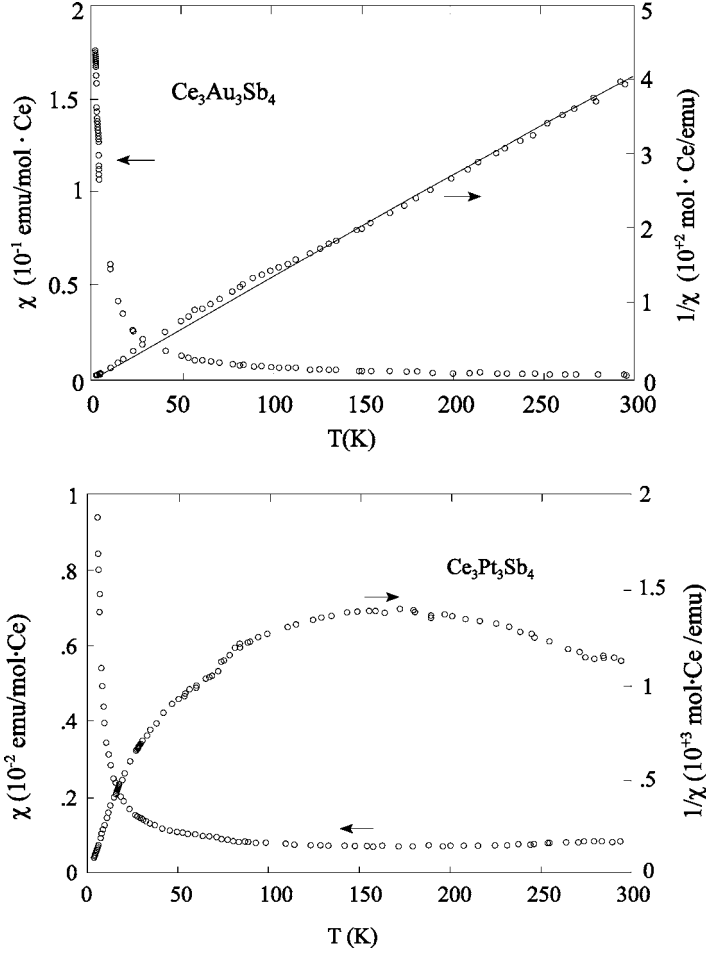
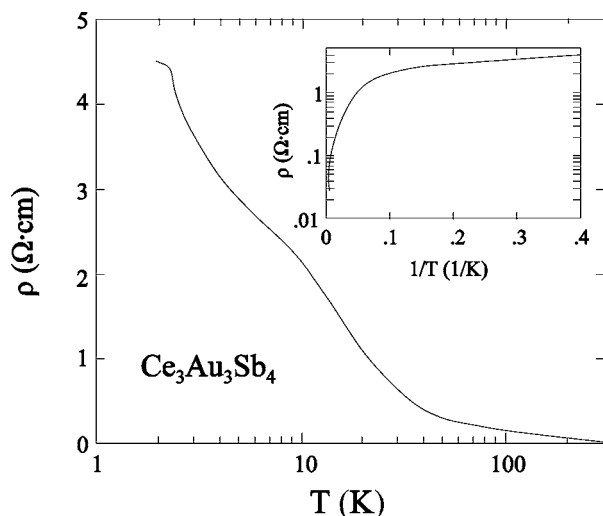
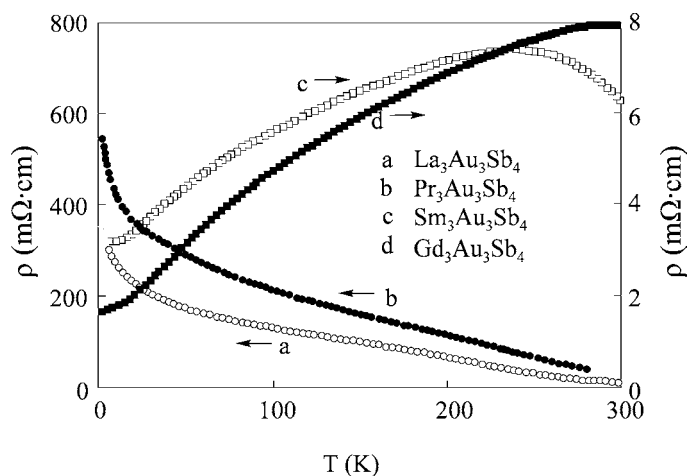


Fig. 56. χ and $1/\chi$ vs T for $Ce_3Au_3Sb_4$ and $Ce_3Pt_3Sb_4$ after Kasaya et al. (1991).

$R_3Au_3Sb_4$ ($R = Sm, Gd$) showed semi-metallic behaviors (Katoh and Kasaya, 1993). They are antiferromagnets with T_N of 2 and 11 K, respectively. The same authors observed no magnetic transitions down to 1.5 K in $Ce_3Au_3Sb_4$ and found $C/T = 2500$ mJ/molK² at 1.5 K which makes this compound a heavy Fermion material. The $\rho(T)$ curves for $R_3Au_3Sb_4$ ($R = La, Ce, Pr, Sm, Gd$) given by Katoh and Kasaya (1993) are presented in figs. 57 and 58.

Kimura et al. (1995) reported on an investigation of the electronic structure of $R_3Au_3Sb_4$ ($R = La, Ce, Pr$) by reflectivity and resonant photoemission spectra. The hybridization between the Ce4f state and the Sb5p state valence band was found to be weak as deduced from the resonant photoemission spectra of $Ce_3Au_3Sb_4$. This result was found to be consistent with the electronic structure derived from an analysis of the optical data about the energy gap.

Fig. 57. ρ vs T for $\text{Ce}_3\text{Au}_3\text{Sb}_4$.Fig. 58. ρ vs T for $R_3\text{Au}_3\text{Sb}_4$ ($R = \text{La, Pr, Sm, Gd}$).

Resistivity, magnetic susceptibility, specific heat and inelastic neutron scattering were measured for $\text{Ce}_3\text{Au}_3\text{Sb}_4$ by Kasaya et al. (1994). The compound was found to be a semiconductor with a resistivity of $22 \text{ } \Omega \text{ cm}$ at 0.13 K . Magnetic susceptibility and inelastic neutron scattering show that $4f$ electrons are in the localized $4f^1$ state. No anomaly in the thermomagnetic curve down to 0.5 K has been observed. However, there exist a broad peak at 1.5 K in the specific heat at $C/T \sim 2500 \text{ mJ/mole K}^2$ and the peak, which is symmetrical in a $\log T$ plot, shifts towards higher temperature values under the influence of a magnetic field.

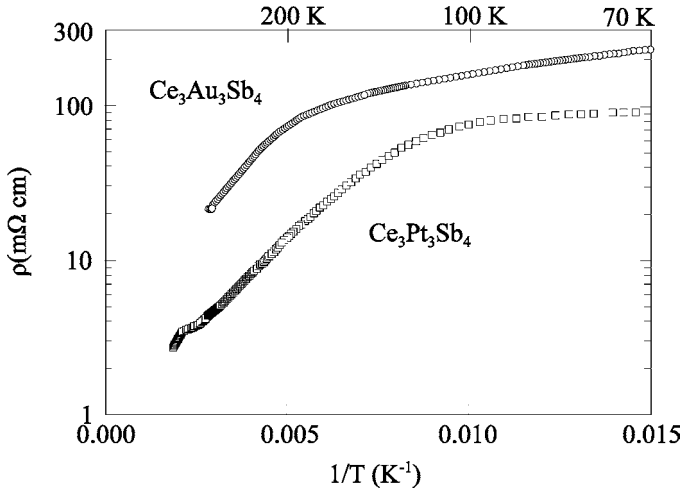


Fig. 59. Temperature dependence of the electrical resistivity for $\text{Ce}_3\text{Au}_3\text{Sb}_4$ and $\text{Ce}_3\text{Pt}_3\text{Sb}_4$ after Katoh and Kasaya (1996).

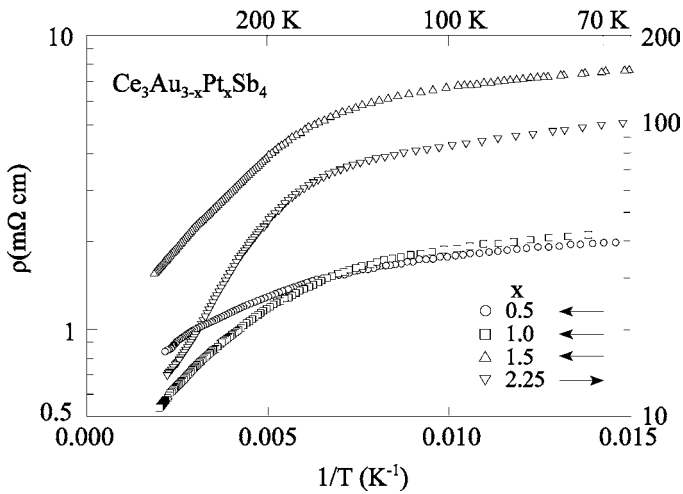


Fig. 60. Temperature dependence of the electrical resistivity for $\text{Ce}_3\text{Au}_{3-x}\text{Pt}_x\text{Sb}_4$ ($x = 0.5, 1.0, 1.5, 2.25$).

Kasaya et al. (1994) and Katoh and Kasaya (1996) measured the electrical resistivity, Hall constant and magnetic susceptibility for the $\text{Ce}_3\text{Au}_{3-x}\text{Pt}_x\text{Sb}_4$ ($x = 0.0, 0.5, 1.0, 1.5, 2.25, 3.0$) (figs. 59, 60, table 53).

Resistivity and magnetic susceptibility were studied for the $R_3\text{Cu}_3\text{Sb}_4$ compounds ($R = \text{Y}, \text{La}, \text{Ce}, \text{Pr}, \text{Nd}, \text{Sm}, \text{Gd}, \text{Tb}, \text{Dy}, \text{Ho}, \text{Er}$) by Skolozdra et al. (1993) (table 54). Resistivity measurements indicates that all compounds are semiconductors. A linear $\varrho(T)$ dependence was observed for $\text{Y}_3\text{Cu}_3\text{Sb}_4$, $\text{Nd}_3\text{Cu}_3\text{Sb}_4$ and $\text{Gd}_3\text{Cu}_3\text{Sb}_4$ while for $\text{Ce}_3\text{Cu}_3\text{Sb}_4$ a minima was observed at ~ 250 K. The temperature dependence of the magnetic susceptibility $\chi(T)$ for $R_3\text{Cu}_3\text{Sb}_4$, $R = \text{Ce}, \text{Pr}, \text{Nd}, \text{Gd}, \text{Tb}, \text{Dy}, \text{Er}$ can be described by the Curie–Weiss law with

Table 53
Magnetic data for $Ce_3Au_{3-x}Pt_xSb_4$ compounds ($x = 0.0, 0.5, 1.0, 1.5, 2.25, 3.0$)

Compound	Temperature range	C, emu/mole K	θ_p (K)	μ_{eff} (μ_B)
$Ce_3Au_3Sb_4$	150 ~ 300	0.79	-2.86	2.51
$Ce_3Au_{2.5}Pt_{0.5}Sb_4$	150 ~ 300	0.807	-11.0	2.54
$Ce_3Au_2PtSb_4$	80 ~ 300	0.822	-45.6	2.56
$Ce_3Au_{1.5}Pt_{1.5}Sb_4$	170 ~ 300	0.837	-100	2.59
$Ce_3Au_{0.75}Pt_{2.25}Sb_4$	480 ~ 720	0.868	-236	2.63
$Ce_3Pt_3Sb_4$	450 ~ 700	1.083	-647	2.94

Table 54
Magnetic data for the $R_3Cu_3Sb_4$ (Skolozdra et al., 1993)

Compound	θ_p (K)	μ_{eff} (μ_B /atom R)
$Ce_3Cu_3Sb_4$	10	2.59
$Pr_3Cu_3Sb_4$	11	3.31
$Nd_3Cu_3Sb_4$	11	3.61
$Gd_3Cu_3Sb_4$	59	7.72
$Tb_3Cu_3Sb_4$	-10	9.96
$Dy_3Cu_3Sb_4$	-7	11.02
$Ho_3Cu_3Sb_4$	3	11.11
$Er_3Cu_3Sb_4$	24	9.50

the values of the effective magnetic moments close to that of the free R^{3+} ions. $La_3Cu_3Sb_4$ and $Y_3Cu_3Sb_4$ are diamagnets. For $Sm_3Cu_3Sb_4$, the $\chi(T)$ curve does not obey the Curie-Weiss law.

$Ce_3Cu_3Sb_4$ was found to be a semiconducting ferromagnet with ferromagnetic transition temperature, $T_m = 10$ T while $Gd_3Cu_3Sb_4$ was reported to be a metallic antiferromagnet with $T_N = 12$ K (Patil et al., 1996).

Patil et al. (1998) reported on measurements of magnetic susceptibility, electrical resistivity and magnetoresistivity for the $Ce_3Rh_3Sb_4$ in the temperature range 2 K to 300 K. The compound was found to order antiferromagnetically at 22 K. The magnetic resistivity shows a broad maximum at about 50 K.

6.5. R_6MSb_{15} compounds

Magnetic measurements were performed down to liquid helium temperature by Sologub et al. (1996a) for $R = Ce, Pr, Sm, Gd$ and $M = Mn, Zn$ (table 55, fig. 61). Ce_6MnSb_{15} and Gd_6ZnSb_{15} undergo an antiferromagnetic transition at 7 and 15 K respectively. Ce_6ZnSb_{15} and Pr_6ZnSb_{15} remain paramagnetic in the temperature range investigated, whereas Sm_6ZnSb_{15} is a van Vleck-type paramagnet.

Magnetic and transport properties have been measured by Deakin et al. (2001) for the series of ternary rare-earth antimonides $R_6Ge_{5-x}Sb_{11+x}$ ($R = La-Nd, Sm, Gd-Dy$) (table 56). All are metallic, with the members containing R, other than La, displaying kinks in their resistivity vs temperature curves. Tb and Dy containing compounds exhibit Kondo-like behavior with resistivity minima occurring at 10 and 150 K, respectively. The $R_6Ge_{5-x}Sb_{11+x}$ ($R = Ce-$

Table 55
Magnetic data of the ternary R_6MSb_{15} compounds

Compound	T_N (K)	θ_p (K)	$\mu_{\text{eff.meas.}}$ (μ_B)	$\mu_{\text{eff.theor.}}$ (μ_B)
Ce_6MnSb_{15}	7	-6	8.9	2.54
Ce_6ZnSb_{15}		-10	2.7	2.54
Pr_6ZnSb_{15}		-13	3.6	3.6
Sm_6ZnSb_{15}		9	0.5	
Gd_6ZnSb_{15}	15	-34	7.7	7.9

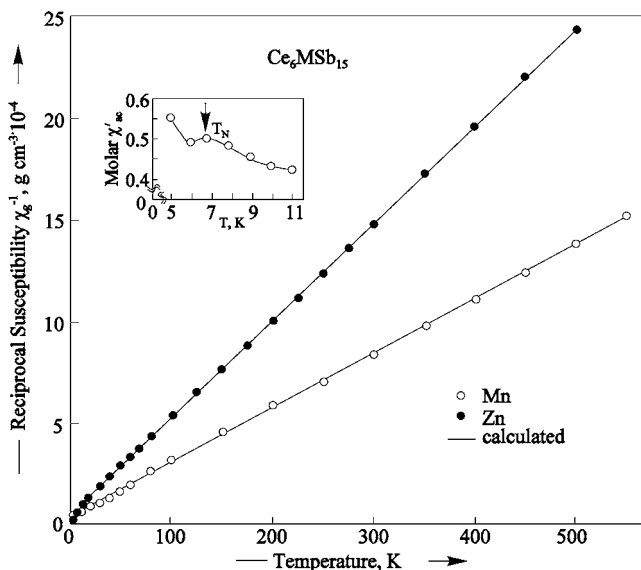


Fig. 61. Reciprocal magnetic susceptibility vs temperature for Ce_6MSb_{15} , $M = Mn, Zn$. Inset: Molar susceptibility vs temperature for Ce_6MnSb_{15} .

Nd, Sm, Gd) members exhibit residual resistivity ratios ($\rho_{300\text{ K}}/\rho_{2\text{ K}}$) close to 2.0, consistent with the partial disorder of Ge and Sb found in the crystal structure of these phases. For the compounds with $R = Ce, Pr, Nd, Sm, Gd, Tb$, the magnetic susceptibility and electrical resistivity measurements reveal long-range antiferromagnetic ordering with $T_N \leq 22$ K. At 2 K, the Ce, Pr, and Nd members undergo metamagnetic transitions at critical fields between 1.0 and 4.0 T, while the Gd containing compound shows spin-flop behavior with $H_{SF} = 1.85$ T and $H_C = 5.75$ T.

6.6. $R_{14}MSb_{11}$ compounds

$Eu_{14}MnSb_{11}$ was reported to be an intermetallic colossal magnetoresistive material having a metal insulator transition associated with a ferromagnetic phase transition at 92 K (Chan et al., 1997).

Temperature dependent dc susceptibility measurements were performed on the $Yb_{14}ZnSb_{11}$ compound in an applied field of 1 kOe in the [100], [110] and [001] directions (Fisher et al., 2000). For temperatures above approximately 150 K, the susceptibility follows a Curie–Weiss

Table 56
Summary of the resistivity and magnetism data for the $R_6\text{Ge}_{5-x}\text{Sb}_{11+x}$ compounds

Compound	$\rho_{300\text{ K}}/\rho_{2\text{ K}}$	$\mu_{\text{eff}}(300\text{ K})$ (μ_{B}/R^{3+})	μ_{RS} (μ_{B}/R^{3+})	θ (K)	T_{N} (K)	$H_{\text{SF}}(2\text{ K})$ (T)	$H_{\text{C}}(2\text{ K})$ (T)
$\text{La}_6\text{Ge}_{5-x}\text{Sb}_{11+x}$	2.18						
$\text{Ce}_6\text{Ge}_{5-x}\text{Sb}_{11+x}$	2.23	2.58	2.54	-27	4.0		1.0
$\text{Pr}_6\text{Ge}_{5-x}\text{Sb}_{11+x}$	2.03	3.54	3.58	-8	2.7		1.5
$\text{Nd}_6\text{Ge}_{5-x}\text{Sb}_{11+x}$	1.70	3.94	3.62	-53	4.2		4.0
$\text{Sm}_6\text{Ge}_{5-x}\text{Sb}_{11+x}$	2.05	1.2	0.85		8.3		
$\text{Gd}_6\text{Ge}_{5-x}\text{Sb}_{11+x}$	1.77	7.08	7.94	-47	12.5	1.85	5.75
$\text{Tb}_6\text{Ge}_{5-x}\text{Sb}_{11+x}$	1.46	8.53	9.72	-10	22		> 7
$\text{Dy}_6\text{Ge}_{5-x}\text{Sb}_{11+x}$	0.92						

temperature dependence with Curie constants (4.63, 4.13 and 5.68) $\pm 0.04 \times 10^{-4}$ emu K/g and Weiss constants (-223, -294 and -474) ± 10 K for the field parallel to [100], [110] and [001] directions, respectively. An intermediate Yb valence behavior with a spin fluctuating temperature of approximately 85 K was determined from thermodynamic, magnetic and transport measurement data. The resistivity of $\text{Yb}_{14}\text{AlSb}_{11}$ is typical of many Zintl compounds and indicates that this material is a small gap semiconductor or a semimetal in contrast to the more metallic behavior of $\text{Yb}_{14}\text{ZnSb}_{11}$ and $\text{Yb}_{14}\text{MnSb}_{11}$ (Fisher et al., 2000).

7. Peculiarities of the interaction of the rare earths and antimony

7.1. Binary systems

Similar to other binary R - p -element systems, the formation of binary rare earth – antimonides with a simple stoichiometry is a characteristic feature of these systems. The largest number of structure types formed was encountered for the group of RSb_2 compounds (4 members). The polymorphic modifications were observed for GdSb_2 and TbSb_2 as well as the RSb ($R = \text{La, Ce}$) and R_5Sb_3 ($R = \text{Yb, Y and Sc}$) compounds were noted to undergo the solid state transformations.

Although the phase diagrams have been constructed for all R - Sb systems except Eu and Sc , there are many reports on the crystal structure of compounds which are not shown in the corresponding phase diagram. The systematic thermochemical investigations of the rare earth antimonides ($R = \text{Y, La, Ce, Pr, Nd, Sm and Dy}$) and optimization of the thermodynamic data have been carried out by Cacciamani et al. (1996) and Ferro et al. (1988) respectively. Later on, the same group of authors (Borzone et al., 2000) suggested that the poor reliability of results for most of the R - Sb phase diagrams are attributable to experimental difficulties arising from the high melting temperatures of the compounds, the high reactivity of samples, and the high volatility of the antimony.

For Gd-Sb phase diagram, as an example, the GdSb_2 (66.6 at% Sb) was reported to be the richest in Sb compound with two structural modifications, SmSb_2 and HoSb_2 (Abdusalamova et al., 1986). In more recent work, Altmeyer and Jeitschko (1998) established the existence the Gd_2Sb_5 compound (71.42 at% Sb) with the monoclinic structure of the Dy_2Sb_5 type.

Table 57
Isotypic compounds of the binary *R*-Sb systems^a

Composition	Structure type	La	Ce	Pr	Nd	Sm	Eu	Gd	Tb	Dy	Ho	Er	Tm	Yb	Lu	Y	Sc
<i>R</i> ₂ Sb	La ₂ Sb	+	+	+	+	+		-	-	-	-	-	-	-	-	-	-
	Cu ₂ Sb	-	-	-	-	-		-	-	-	-	-	-	-	-	-	+
<i>R</i> ₅ Sb ₃	Mn ₅ Sb ₃	+	+	+	+	+		+	+	+	+	-	+	+	+	+	-
	Yb ₅ Sb ₃	-	-	-	-	-		-	-	-	-	+		+		+	+
<i>R</i> ₄ Sb ₃	anti-Th ₃ P ₄	+	+	+	+	+		+	+	+	+	+	-	+	-	+	
<i>R</i> ₁₁ Sb ₁₀	Ho ₁₁ Ge ₁₀	-	-	-	-	-	+	-	-	-	-	-	-	+	-	-	
<i>RSb</i>	NaCl	+	+	+	+	+		+	+	+	+	+	+	+	+	+	+
	HgMn	+	+														
<i>R</i> ₂ Sb ₅	Dy ₂ Sb ₅					+		+	+	+							
<i>RSb</i> ₂	SmSb ₂	+	+	+	+	+	-	+	+	-	-	-	-	-	-	-	-
	HoSb ₂	-	-	-	-	-	-	+	+	+	+	+	+	-	+	+	
	CaSb ₂	-	-	-	-	-	+	-	-	-	-	-	-	-	-	-	
	ZrSi ₂	-	-	-	-	-	-	-	-	-	-	-	-	+	-	-	

^aSign + means that the compound with corresponding structure type exists; - the compound was not observed.

Borzzone et al. (2000) studying the phase diagram of Gd-Sb system, observed and determined the crystal structure of Gd₁₆Sb₃₉ (70.91 at% Sb).

The structures of Eu containing binary antimonides are isotypic with binary antimonides of alkaline earth metals (Ca, Ba, Sr) and do not have the analogues, except for Eu₅Sb₃, in other *R*-Sb systems (table 57).

7.2. Ternary systems

As is evident from the foregoing paragraphs, the interaction of the components in the ternary *R*-*M*-Sb systems have not been adequately studied. The isothermal sections (over all concentration region or partially) have been constructed for the limited number of ternary systems (22), and in other systems only the samples of specific compositions were synthesized and investigated structurally with respect to the formation of isotypic compounds. This paucity of data complicates the pursuance of a proper analysis and the derivation of regularities.

7.2.1. *R*-*s*-element-Sb

Few experimental data are available only for lithium and magnesium containing systems however the isothermal section is constructed for Gd-Li-Sb (5 ternary compounds have been observed). The replacement of R element in the *RLi*₂Sb₂ compounds leads to the formation of different structure type: CaAl₂Si₂ (*R* = Ce) → CaBe₂Ge₂ (*R* = Pr, Nd) → unknown structure (*R* = Tb). No comparative analysis can be made for the magnesium containing systems since only the information regarding the existence of three compounds in the La-Mg-Sb system is presented in the literature.

7.2.2. *R*-*p*-element-Sb

The isothermal sections have been constructed for the La-Al-Sb and Ce-Si(Ge)-Sb systems.

Ternary compounds have been observed for the R -Si, Ge, Sn, Ga, In, Se, Te-Sb systems. The systems with arsenic and bismuth are characterized by formation of substitutional solid solutions between isotypic binary pnictides. No compounds have been found in the partly investigated ternary La-Al-Sb system at 773 K (Muravjova, 1971). For the Yb-Al-Sb, the formation and crystal structure of the $\text{Yb}_{14}\text{AlSb}_{11}$ have been reported (Fisher et al., 2000).

7.2.3. R - d -element-Sb

In spite of the fact that the isothermal sections have been investigated for the 18 ternary systems from 448 possible R - d -element-Sb combinations, a considerable number of publications is devoted to the crystal structure investigations of ternary compounds that enables one to consider more thoroughly the effect of R -element and d -element interaction as well as the formation, composition and crystal structure of ternary antimonides.

7.2.3.1. R -Ti(V, Cr, Zr, Nb, Mo, Hf, Ta, W, Re)-Sb. For this combination of elements, the R -Mo (Ta, W, Re)-Sb systems have not been studied, and as well no information is available on the interaction of Eu and Yb with these d -elements. The $R_3\text{MSb}_5$ series of compounds was observed only for the light lanthanides and the $R\text{ZrSb}$ structure is typical for the yttrium subgroup.

The CeVSb_3 type occurs in the R -V-Sb systems for the ceric subgroup and in the R -Cr-Sb systems for both subgroups ($R = \text{La-Sm, Gd-Dy}$) (table 58).

7.2.3.2. R -Mn(Cd, Zn)-Sb. Analysis of the compositions and crystal structures of the investigated R - $3d$ -element-Sb systems established a vague similarity between R -Mn-Sb and the cadmium and zinc containing systems (table 59):

- (i) the HfCuSi_2 and $\text{La}_6\text{MnSb}_{15}$ structures are typical for the ceric subgroup and Gd;
- (ii) Eu and Yb form the CaAl_2Si_2 and $\text{Ca}_{14}\text{AlSb}_{11}$ types;
- (iii) no compounds have been found in the Tb-Tm, Lu and Y, Sc containing systems.

7.2.3.3. R -Fe(Co, Ru, Rh, Os, Ir)-Sb. Among the ternary R -Fe(Co, Ru, Rh, Os, Ir)-Sb systems, the Nd-Fe-Sb system is the most completely studied (Sologub and Salamakha, 1999;

Table 58
Isotypic compounds of the ternary R -Ti(V, Cr, Zr, Nb, Hf)-Sb systems^a

Structure type	La	Ce	Pr	Nd	Sm	Eu	Gd	Tb	Dy	Ho	Er	Tm	Yb	Lu	Y	Sc
U_3CrSb_5	Ti	+	+	+	+											
	Zr	+	+	+	+											
	Nb	+	+	+	+	-										
	Hf	+	+	+	+	+										
CeVSb_3	V	+	+	+	+											
	Cr	+	+	+	+			+	+	+						
CeScSi	Zr						+	+	+	+	+	+		+	+	

^aSign + means that the compound with corresponding structure type exists; - the compound was not observed.

Table 59
Isotypic compounds of the ternary R -Mn(Zn, Cd)-Sb systems^a

Structure type		La	Ce	Pr	Nd	Sm	Eu	Gd	Tb	Dy	Ho	Er	Tm	Yb	Lu	Y	Sc
HfCuSi ₂	Mn	+	+	+	+	+											
	Zn	+	+	+	+	+		+									
	Cd	+	+	+	+	+											
CaAl ₂ Si ₂	Mn		-		-		+							+			
	Zn				-		+							+			
	Cd				-		+							+			
Ca ₁₄ AlSb ₁₁	Mn		-		-		+							+			
	Zn				-		+							+			
La ₆ MnSb ₁₅	Mn	+	+		-												
	Zn	+	+	+	+	+		+									
NdAgSb ₂	Zn	+	+														

^aSign + means that the compound with corresponding structure type exists; - the compound was not observed.

Table 60
Isotypic compounds of the ternary R -Fe(Co, Ru, Rh, Os, Ir)-Sb systems^a

Structure type		La	Ce	Pr	Nd	Sm	Eu	Gd	Tb	Dy	Ho	Er	Tm	Yb	Lu	Y	Sc
HfCuSi ₂	Fe	+	+	+	+	+		+									
	Co	+	+	+	+	+											
LaFe ₄ Sb ₁₂	Fe	+	+	+	+	+	+							+			
	Ru	+	+	+	+	+	+										
	Rh	+															
	Os	+	+	+	+	+	+							+			
TiNiSi or	Co				-												+
KHg ₂	Rh	+	+	+	+	+											
Nd ₆ Fe ₁₃ Si	Fe	-	+	+	+	+											
	Co	+	-														

^aSign + means that the compound with corresponding structure type exists; - the compound was not observed.

Leithe-Jasper, 1994). Information on the systematic investigations of the interaction of rare earths and antimony with other metals of this subgroup is still lacking. The survey of the isotypic compounds is presented in table 60.

No information is available on the ternary R -Ir-Sb systems.

7.2.3.4. R -Ni(*Pd*, *Pt*)-Sb. Interaction of the components in these systems is the most complicated and highly diversified (table 61).

The greatest efforts have concentrated on the systematic studies of the nickel containing systems. The annealing temperature of the R -Ni-Sb alloys strongly affects the phase equilibria as well as the crystal structure of ternary compounds. The isothermal section of Y-Ni-Sb phase diagram at 870 K (0-50 at.% Sb) was studied by Zavalii (1982). For the La-Ni-Sb, Ce-Ni-Sb and Nd-Ni-Sb systems the isothermal sections at 870 K were constructed by Zavalii (1982), Pecharsky et al. (1983a, 1983b) and Salamakha (1998), respectively. Mozharivskyj

Table 61
Isotypic compounds of the ternary R -Ni(Pd, Pt)-Sb systems^a

Structure type		La	Ce	Pr	Nd	Sm	Eu	Gd	Tb	Dy	Ho	Er	Tm	Yb	Lu	Y	Sc
CeGa ₂ Al ₂	Ni	+	+	+	+	+	+	+	-	-	-	-					
	Pd	-	-	-	-	-	-	-									
CaBe ₂ Ge ₂	Ni	+	+	+	+	+	-	+	+	+	+	+					
	Pd	+	+	+	+	+	+								-		
AlB ₂ or ZrBeSi	Ni	+	+	+	+	+	-	-	-	-	-	-	-	-	-	-	-
	Pd	+	+	+	+	+	-	+	+	+	-	-	-	-	-	-	-
CaIn ₂ or LiGaGe	Pt	+	+	+	+	-	-	-	-	-	-	-	-	-	-	-	-
	Pt	+	+	+	+	-	-	-	-	-	-	-	-	-	-	-	-
MgAgAs	Ni	-	-	-	-	-	-	+	+	+	+	+	+	+	+	+	+
	Pd	-	-	-	-	-	-	-	-	+	+	+		+		+	
	Pt	-	-	-	-	+	-	+	+	+	+	+	+	+	+	+	+
Mo ₅ B ₂ Si	Ni	-	-		-			+	+	+	+	+	+		+	+	
	Pd							+	+	+	+	+	+		+	+	
	Pt							+	+	+	+	+	+		+	+	
HfCuSb ₂	Ni	+	+	+	+	+	-	+	+	+	+						-
	Pd	+	+	+	+	+	-	+	+								
MgCu ₂ Al	Pd									+	+	+		+		+	
TiNiSi	Pd	-	-	-	-	-	+	-	-	-	-	-	-	-	-	-	-
	Pt	-	-	-	-	-	+	-	-	-	-	-	-	-	-	-	-

^aSign + means that the compound with corresponding structure type exists; - the compound was not observed.

et al. (1997) investigated the phase equilibria in the ternary Ho-Ni-Sb system at 770 K (0–50 at.% Sb) and 1070 K (50–100 at.% Sb). Hoffman and Jeitschko (1988) reported some results of phase equilibria studies of the La-Ni-Sb and Gd-Ni-Sb systems at 1070 K. The compounds $RNi_{2-x}Sb_2$ with a defect CaBe₂Ge₂ structure were found and evaluated as the highest antimony content compounds. In variance to these data, Zavali (1982), Pecharsky et al. (1983a, 1983b) and Salamakha (1998) reported on the existence and crystal structure for the $RNiSb_2$ (HfCuSi₂ type structure) and RNi_2Sb_2 (CeGa₂Al₂ type structure) ($R = La, Ce, Nd$) compounds from the alloys annealed at 870 K. Various authors investigated the crystal structure of the $RNiSb$ compounds ($R = La-Sm$) and found them to crystallize either with AlB₂ type (LT form) or ZrBeSi type (HT modification).

Although no phase diagram has been studied for the Ce-Pd-Sb system, seven ternary compounds were observed and their crystal structures were investigated.

In the R -Pt-Sb systems, the compounds with Y₃Au₃Sb₄ structure are found for both the light and heavy rare earth elements. This structure occurs typically for copper and gold containing antimonides, and unexpectedly, it was not observed for the systems with Ni and Pd.

7.2.3.5. R -Cu(Ag, Au)-Sb. The most prevailing structure types among the compounds within R -Cu(Ag, Au)-Sb systems are the HfCuSi₂ and Y₃Au₃Sb₄ types. The compounds of the Y₃Au₃Sb₄ type have not been observed for the systems with silver. Table 62 lists the isotypic series of compounds in the R -Cu(Ag, Au)-Sb systems.

Table 62
Isotypic compounds of the ternary R -Cu(Ag, Au)-Sb systems^a

Structure type		La	Ce	Pr	Nd	Sm	Eu	Gd	Tb	Dy	Ho	Er	Tm	Yb	Lu	Y	Sc
HfCuSi ₂	Cu	+	+	+	+	+	-	+	+	+	+	+	+	+	+	+	+
	Ag	+	+	+	+	+	-	+	+	+	+	+	+	-	-	+	+
	Au	+	+	+	+	+											
Y ₃ Au ₃ Sb ₄	Cu	+	+	+	+	+	-	+	+	+	+	+	-	-	-	+	-
	Au	+	+	+	+	+	-	+	+	+	+	+	+	-	+	+	-
ZrBeSi or	Cu	-	-				+							+			
LiGaGe	Ag						+							-	-		
	Au		+				+							+			
La ₆ MnSb ₁₅	Cu	+	+														
CeGa ₂ Al ₂	Cu	-	+	+	-		+	+									
	Ag	+	+														
TiNiSi	Ag						-							+	+		

^aSign + means that the compound with corresponding structure type exists; - the compound was not observed.

7.2.4. R - f -element-Sb

Only the formation of solid solutions between isotypic compounds has been observed in the R - R' -Sb systems. For the R -U-Sb the formation of both solid solutions (Frick et al., 1984) and ternary compounds (Schmidt and Jeitschko, 1998; Slovyanskikh et al., 1990) have been reported.

7.3. Interconnection of the ternary antimonides with the binary structure types

The structure types of binary antimonides have been described by Hulliger (1984) in chapter 33 of the Handbook.

Several families of ternary antimonides crystallize with structure types derived from those of binary types by an insertion of third component in the structure of binary compounds, i.e., LaFe₄P₁₂ from CoAs₃, Y₃Au₃Sb₄ from Th₄P₃, U₃CrSb₅ from Mn₅Si₃.

Another subgroup of structure types of ternary antimonides contains the superstructures of binary structures: LiGaGe → CaIn₂, ZrBeSi → Ni₂In, Mo₅B₂Si → Cr₅B₃, MgAgAs → CaF₂, TiNiSi → Co₂Si.

The structure of the MnCu₂Al type compound can be considered as both an insertion phase (NaCl) and a superstructure (BiF₃).

The crystal chemistry of the ternary antimonides is discussed in the original papers. Here we present only some regularities and peculiarities of the formation of ternary antimonides and their structures depending on the qualitative and quantitative composition.

7.4. Ternary antimonides with the equiatomic composition

The RMSb compounds crystallize in eight structure types, for some of them the existence of two polymorphic modifications have been reported (table 63). The crystal structure of EuMSb compounds is always different than the structure of other RMSb compounds.

Table 63
Structure types of the *RMSb* ternary antimonides^a

<i>M/R</i>	La	Ce	Pr	Nd	Sm	Eu	Gd	Tb	Dy	Ho	Er	Tm	Yb	Lu	Y	Sc
Ni	1,2	1,2	1,2	1,2	1,2		1,3	3	3	3	3	3	3	3	3	3
Pd	4	4	4	4	4	5	4	4	3,4	3	3	3	3		3	
Pt	4	4	6	4,6	3	5	3	3	3	3	3	3	3	3	3	3
Co																5
Rh	7	5,7	7	7												
Cu						2								6		
Ag						2								5	5	
Au		4				2								6		
Zr							8	8	8	8	8	8		8	8	

^aNumber 1 corresponds to AlB_2 structure type; 2 – $ZrBeSi$; 3 – $MgAgAs$; 4 – $CaIn_2$; 5 – $TiNiSi$; 6 – $LiGaGe$; 7 – KHg_2 ; 8 – $CeScSi$.

7.5. Ternary antimonides with the *R:Sb* ratio equal to 1:2

A $BaAl_4$ fragment is a filled up tetragonal antiprism. The structure types of ternary antimonides related to the $BaAl_4$ type are presented in table 64. In the $La(Ni, Sb)_4$ compound ($BaAl_4$ structure type), the atoms of (Ni, Sb) statistical mixture occupy two different crystallographic positions. For the 1:2:2 composition, two ordered modifications of tetragonal cell – $CeGa_2Al_2$ and $CaBe_2Ge_2$ – are known. An orthorhombic deformation of the $BaAl_4$ with unit cell dimensions similar to the $BaAl_4$ -type unit cell was found for the $CeNi_{2+x}Sb_{2-x}$ compound.

The $LaPt_2Ge_2$ and $Ce_3Pd_6Sb_5$ structure types can be formed in consequence of ordering and distortion of the unit cell of the $CaBe_2Ge_2$ structure.

In the $HfCuSi_2$ structure, a portion of the tetragonal antiprisms is unfilled. The outer deformation of this structure leads to the formation of two new structure types – $NdAgAs_2$ and $LaInSb_2$.

Table 64
Structure types of antimonides with structures related to $BaAl_4$ type structure

Structure types	Space group	Lattice parameters		
		<i>a</i>	<i>b</i>	<i>c</i>
$BaAl_4$	$I4/mmm$	a_1	a_1	c_1
$CeGa_2Al_2$	$I4/mmm$	a_1	a_1	c_1
$CaBe_2Ge_2$	$P4/nmm$	a_1	a_1	c_1
$CeNi_{2+x}Sb_{2-x}$	$Immm$	a_1	a_1	c_1
$LaPt_2Ge_2$	$P2_1$	a_1	a_1	c_1
			$\beta \sim 91^\circ$	
$Ce_3Pd_6Sb_5$	$Pmnn$	$3a_1$	a_1	c_1
$HfCuSi_2$	$P4/nmm$	a_1	a_1	c_1
$NdAgAs_2$	$Pmnn$	a_1	a_1	c_1
$LaInSb_2$	$P2_1/m$	a_1	a_1	c_1
			$\beta \sim 99^\circ$	

The structure of the LaSnSb_2 compound ($Cmcm$ space group) is related to the structure of YbSb_2 (ZrSi_2 structure type, $Cmcm$ space group).

The structure of NdFe_2Sb_2 and NdFe_3Sb_2 compounds can be classified to the structures with two short ($\sim 4 \text{ \AA}$) and one much more longer period ($\sim 25 \text{ \AA}$). These structures contain the fragments of simple structures connected along long period.

The insertion of additional Li atom in the 0 0 0.5 site in the structure of the $R\text{Li}_2\text{Sb}_2$ compounds (CaAl_2Si_2 structure type) leads to the formation of the YLi_3Sb_2 structure type.

Acknowledgement

This work was partially supported by FCT grant in ITN, Portugal (P.S) and NATO Research Fellowship in ITN, Portugal (O.S.).

References

- Abdusalamova, M.N., Rachmatov, O.I., 2000. *J. Alloys Compd.* **299**, L1.
- Abdusalamova, M.N., Burnashev, O.R., Mironov, K.E., 1981. *J. Less-Common Met.* **77**, 81.
- Abdusalamova, M.N., Burnashev, O.R., Mironov, K.E., 1984. *J. Alloys Compd.* **102**, L19.
- Abdusalamova, M.N., Burnashev, O.R., Mironov, K.E., 1986. *J. Less-Common Met.* **125**, 1.
- Abdusalamova, M.N., Rakhmatov, O.I., Fazlyeva, N.D., Tchuiko, A.C., 1988. *J. Less-Common Met.* **141**, L23.
- Abdusalamova, M.N., Faslyeva, N.D., Eliseev, A.A., Shishkin, E.A., Rakhmatov, O.I., Chuiko, A.G., Shumakova, T.P., 1990. *J. Less-Common Met.* **166**, 229.
- Abdusalamova, M.N., Rakhmatov, O.I., Fazlyeva, N.D., Tchuiko, A.C., 1991. *Izv. Akad. Nauk SSSR, Neorg. Mater.* **27** (8), 1386.
- Abulkhaev, V.D., Abdusalamova, M.N., 1989. Phase diagram of the system Ce–Sb. In: *V Vsesoyuzn Soveshchan. "Diagrammy Sost. Metall. Sistem"*, Tezisy dokl., Moskva 1989, p. 137.
- Abulkhaev, V.D., Abdusalamova, M.N., Chuiko, A.G., Timofeev, S.S., 1989. Conditions of formation and crystal chemistry of continuous solutions $\text{Gd}_x\text{Ln}_{5-x}\text{Sb}_3$ ($\text{Ln} = \text{Y, Tb, Dy, Ho}$). In: *V All-Union Conference on the Crystal Chemistry of Intermetallic Compounds, Abstracts*, Lvov, 1989, p. 123.
- Adroja, D.T., Rainford, B.D., Malik, S.K., Takeya, H., Gschneidner, K.A., Pecharsky, V.K., 1999. *J. Alloys Compd.* **288**, 7.
- Albering, J.H., Ebel, T., Jeitschko, W., 1997. *Z. Kristallogr.* **12**, 242.
- Aliev, F.G., Moshchalkov, V.V., Kozyrkov, V.V., Zalyalyutdinov, M.K., Pryadun, V.V., Skolozdra, R.V., 1988. *J. Magn. Magn. Mat.* **76–77**, 295.
- Aliev, O.M., Rustamov, P.G., 1978. *Z. Neorgan. Khimii* **23** (10), 1551.
- Aliev, O.M., Magerramov, E.V., Rustamov, P.G., 1977. *Z. Neorgan. Khimii* **22** (10), 1539.
- Aliev, O.M., Rustamov, P.G., Guseinov, G.G., Guseinov, M.S., 1978. *Izv. Akad. Nauk SSSR, Neorgan. Mater.* **14** (7), 1052.
- Aliev, O.M., Maksudova, T.F., Rustamov, P.G., 1985. *Izv. Akad. Nauk SSSR, Neorgan. Mater.* **21** (9), 1292.
- Aliev, O.M., Maksudova, T.F., Samsonova, N.D., Finkelshtein, L.D., Rustamov, P.G., 1986. *Izv. Akad. Nauk SSSR, Neorgan. Mater.* **22** (1), 23.
- Altmeyer, R.O., Jeitschko, W., 1988. *Z. Kristallogr.* **182**, 3.
- Altmeyer, R.O., Jeitschko, W., 1989. *Z. Kristallogr.* **186**, 5.
- André, G., Bourée, F., Kolenda, M., Leśniewska, B., Oleś, A., Szytuła, A., 2000. *Physica B* **1–2**, 176.
- Bodnar, R.E., Steinfink, H., 1967. *Inorg. Chem.* **6** (2), 527.
- Bollere, G., Ferguson, M.J., Hushagen, R.W., Mar, A., 1995. *Chem. Mater.* **7**, 2229.
- Borsese, A., Borzone, G., Mazzone, D., Ferro, R., 1981. *J. Less-Common Met.* **79** (1), 57.
- Borzone, G., Borsese, A., Delfino, S., Ferro, R., 1985. *Z. Metallkunde* **76** (3), 208.
- Borzone, G., Fornasini, M.L., Parodi, N., Ferro, R., 2000. *Intermetallics* **8**, 189.

- Braun, D.J., Jeitschko, W., 1980. *J. Less-Common Met.* **72**, 147.
- Brylak, M., Jeitschko, W., 1995. *Z. Naturforsch.* **50b**, 899.
- Brylak, M., Moller, M.H., Jeitschko, W., 1995. *J. Solid State Chem.* **115**, 305.
- Burlet, P., Quezel, S., Rossat-Mignod, J., Bartholin, H., Vogt, O., 1980. *Physica B + C* **102B**, 353.
- Cacciamani, G., Borzone, G., Parodi, N., Ferro, R., 1996. *Z. Metallkd.* **87**, 562.
- Cava, R.J., Ramirez, A.P., Takagi, H., Krayevski, J.J., Peck Jr., W.F., 1993. *J. Magn. Magn. Mater.* **128**, 124.
- Chan, J.Y., Wang, M.E., Rehr, A., Kauzlarich, S.M., Webb, D., 1997. *Chem. Mater.* **9**, 3132.
- Chan, J.Y., Olmstead, M.M., Kauzlarich, S.M., Webb, D.J., 1998. *Chem. Mater.* **10**, 3583.
- Chan, J.Y., Olmstead, M.M., Hope, H., Kauzlarich, S.M., 2000. *J. Solid State Chem.* **155** (1), 168.
- Charvillat, J.-P., Damien, D., Wojakowski, A., 1977. *Revue de Chemie Minerale* **14**, 178.
- Cordier, G., Schaffer, H., Woll, P., 1985. *Z. Naturforsch.* **40b**, 1097.
- Deakin, L., Lam, R., Mar, A., 2001. *Inorg. Chem.* **40**, 960.
- Dunner, J., Mewis, A., Reppke, M., Michels, G., 1995. *Z. Anorg. Allg. Chemie* **621**, 1523.
- Dwight, A.E., 1974. Crystal structure of DyNiSb, DyPtSb and related compounds. In: *Proc. Rare Earth Res. Conf.*, 11th, Michigan, Vol. 2, p. 642.
- Dwight, A.E., 1977. *Acta Cryst.* **33B**, 1579.
- Evers, Ch.B.H., Jeitschko, W., Boonk, L., Braun, D.J., Ebel, T., Scholz, U.D., 1995. *J. Alloys Compd.* **224**, 184.
- Ferguson, M.J., Ryan, W., Hushagen, W., Mar, A., 1996. *Inorg. Chem.* **35**, 4505.
- Ferguson, M.J., Hushagen, R.W., Mar, A., 1997. *J. Alloys Compd.* **249**, 191.
- Ferguson, M.J., Ellenwood, R.E., Mar, A., 1999. *Inorg. Chem.* **38**, 4503.
- Ferro, R., Borzone, G., Cacciamani, G., 1988. *Thermochem. Acta* **129**, 99.
- Fischer, H.O., Schuster, H.U., 1982. *Z. Anorg. Allgem. Chem.* **491**, 119.
- Fisher, I.R., Bud'ko, S.L., Song, C., Canfield, P.C., Ozawa, T.C., Kauzlarich, S.M., 2000. *Physical Review Letter* **85** (5), 1120.
- Flandorfer, H., Sologub, O., Godart, C., Hiebl, K., Leithe-Jasper, A., Rogl, P., Noël, H., 1996. *Solid State Commun.* **97** (7), 561.
- Flandorfer, H., Hiebl, K., Godart, C., Rogl, P., Saccone, A., Ferro, R., 1997. *J. Alloys Compd.* **256**, 170.
- Frick, B., Schoenes, J., Hulliger, F., Vogt, O., 1984. *Solid State Communications* **49** (12), 1133.
- Gambino, R.J., 1967. *J. Less-Common Met.* **12**, 344.
- Ganguli, A.K., Kwon, Y.U., Corbett, J.D., 1993. *Inorg. Chem. Acta* **32**, 4354.
- Geidarova, E.A., Rustamov, P.G., 1985. *Z. Neorgan. Khimii* **30** (11), 1705.
- Geydarova, E.N., Bagirova, S.D., Aliyev, I.Ya., Abbasov, A.S., Mustafayev, F.M., 1985. *Doklady Akad. Nauk Azerbajjan. SSR* **41** (11), 35.
- Gordon, R.A., DiSalvo, F.J., 1996. *Z. Naturforsch.* **51b**, 52.
- Gordon, R.A., DiSalvo, F.J., Pöttgen, R., 1995. *J. Alloys Compd.* **228**, 16.
- Gordon, R.A., DiSalvo, F.J., Poettgen, R., Brese, N.E., 1996. *J. Chem. Soc., Faraday Trans* **92**, 2167.
- Grund, I., Schuster, H.-U., Müller, M., 1984. *Z. Anorg. Allgem. Chem.* **515**, 151.
- Guloy, A.M., Corbett, J.D., 1994. *J. Solid State Chem.* **109**, 352.
- Guzik, A., Kaczmarzka, K., Pierre, J., Murani, A.P., 1996. *J. Magn. Magn. Mat.* **161**, 103.
- Guzik, A., Pierre, J., 1998. *J. Alloys Compd.* **264**, 8.
- Hartjes, K., Jeitschko, W., 1995. *J. Alloys Compd.* **226**, 81.
- Hoffman, W.K., Jeitschko, W., 1985. *Monatshefte Chemie* **116**, 569.
- Hoffman, W.K., Jeitschko, W., 1988. *J. Alloys Compd.* **138**, 313.
- Hulliger, F., 1984. Rare earth pnictides. In: Gschneider Jr., K.A., Eyring, L. (Eds.), *Handbook on the Physics and Chemistry of Rare Earth*, Vol. 4. North-Holland Physics Publishing, Amsterdam, pp. 153–237.
- Hulliger, F., Ott, H.R., 1977. *J. Alloys Compd.* **55**, 103.
- Ishikawa, M., Jorda, J.L., Junod, A., 1982. New ternary superconductors of the YPd₂Sn type. In: *Superconductivity in D- and F-band Metals*, Proceedings of the 4th conference, Karlsruhe, p. 141.
- Kaczmarzka, K., Pierre, J., Slebarski, A., Skolozdra, R., 1993. *J. Alloys Compd.* **196**, 165.
- Kaczmarzka, K., Pierre, J., Guzik, A., Slebarski, A., 1995. *J. Magn. Magn. Mat.* **147**, 81.
- Kaiser, J.W., Jeitschko, W., 1999. *J. Alloys Compd.* **291**, 66.
- Kasaya, M., Katoh, K., Takegahara, K., 1991. *Solid State Commun.* **78** (9), 797.
- Kasaya, M., Katoh, K., Kohgi, M., Osakabe, T., Sato, N., 1994. *Physica B* **199–200**, 534.
- Katoh, K., Kasaya, M., 1993. *Physica B* **186–188**, 428.
- Katoh, K., Kasaya, M., 1996. *J. of Physical Society of Japan* **65** (11), 3654.

- Katoh, K., Takabatake, T., Minami, A., Oguro, I., Sawa, H., 1997. *J. Alloys Compd.* **261**, 32.
- Kim, S.-J., Ireland, J.R., Kannewurf, C.R., Kanatsidis, M.G., 2000. *J. Solid State Chem.* **155**, 55.
- Kimura, S., Sato, Y., Arai, F., Ikezawa, M., Kamada, M., Katoh, K., Kasaya, M., 1995. *J. of Physical Society of Japan* **64** (11), 4278.
- Kleinke, H., 1998. *Z. Anorg. Algem. Chem.* **624**, 1771.
- Klüfers, P., Neumann, H., Mewis, A., Schuster, H.-U., 1980. *Z. Naturforsch.* **35b**, 1317.
- Kobzenko, G.F., Chernogorenko, V.B., Martinchuk, E.L., Lynchak, K.A., Skolozdra, R.V., 1972. *Russ. Metall.* **3**, 176.
- Kuliev, A.N., Safaraliev, G.I., Guseinov, G.A., 1990. *Izv. Akad. Nauk SSSR. Neorg. Mater.* **26** (3), 422.
- Lam, R., Zhang, J., Mar, A., 2000. *J. Solid State Chem.* **153**, 371.
- Lam, R., McDonald, R., Mar, A., 2001. *Inorg. Chem.* **40**, 952.
- Lebedev, V.A., Pyatkov, V.I., Ushenin, S.N., 1983. Thermodynamic properties and phase composition of the alloys of the La-Sb system. In: IV All-Union Conference on the Crystal Chemistry of Intermetallic Compounds, Abstracts, Lvov, p. 206.
- Leithe-Jasper, A. 1994. Ph.D. thesis, Vienna University, 84 p.
- Leithe-Jasper, A., Rogl, P., 1994. *J. Alloys Compd.* **203**, 133.
- Malik, S.K., Adroja, D.T., 1991a. *Physical Review B* **43** (7), 6295.
- Malik, S.K., Adroja, D.T., 1991b. *Physical Review B* **43** (7), 6277.
- Malik, S.K., Adroja, D.T., 1991c. *J. Magn. Magn. Mat.* **102**, 42.
- Malik, S.R., Menon Latica, Ghosh, K., Ramakrishnan, S., 1995. *Physical Review B* **51** (1), 399.
- Marazza, R., Rossi, D., Ferro, R., 1980. *J. Less-Common Met.* **75**, P25.
- Marchand, R., Jeitschko, W., 1978. *J. Solid State Chem.* **24**, 351.
- Massalski, T.B., Subramanian, P.R., Okamoto, H., Kacprzak, L. (Eds.), 1991. *Binary Alloy Phase Diagrams*, 2nd ed. and updates. ASM International, Materials Park, OH.
- Mehta, A., Malik, S.K., Yelon, W.B., 1995. *J. Magn. Magn. Mater.* **147**, 309.
- Menon Latica, Malik, S.K., 1996. *Physica B (Amsterdam)* **223-224** (1-4), 286.
- Mentink, S.A.M., van Rossum, B.J., Nieuwenhuys, G.J., Mydosh, J.A., Buschow, K.J., 1994. *J. Alloys Compd.* **216**, 131.
- Merlo, F., Pani, M., Fornasini, M.L., 1990. *J. Less-Common Met.* **166**, 319.
- Mills, A.M., Mar, A., 2000. *Inorg. Chem.* **39**, 4599.
- Morozkin, A.V., Sviridov, L.A., 2001. *Alloys J. Compd.* **320**, L1.
- Morozkin, A.V., Sviridov, L.A., Leonov, A.V., 2002. *Alloys J. Compd.* **335**, 139.
- Mozharivskiy, Yu., Kuz'ma, Yu.B., 1996. *J. Alloys Compd.* **236**, 203.
- Mozharivskiy, Yu., Franzen, H.F., 2000a. *J. Alloys Compd.* **319**, 100.
- Mozharivskiy, Yu., Franzen, H.F., 2000b. *J. Solid State Chem.* **152**, 478.
- Mozharivskiy, Yu., Franzen, H.F., 2001. *Alloys J. Compd.* **327**, 78.
- Mozharivskiy, Yu., Tremel, W., Kuz'ma, Yu.B., 1997. The ternary systems Ho-Ni-(P, As, Sb, Bi). In: 12th International Conference on Solid Compounds of Transition Elements. Saint-Malo, France, UMR6511.
- Muravjova, A.A., 1971. *Visnyk L'viv. University, Ser. Khim.* **12**, 8.
- Niu, X.J., Gschneidner Jr., K.A., Pecharsky, A.O., Pecharsky, V.K., 2001. *J. Magu. Magu. Mat.* **234** (2), 193.
- Ott, H.R., Hulliger, F., Stucki, F., 1978. *Conference Series - Institute of Physics* **37**, 72.
- Pankevich, Yu.V., Pecharsky, V.K., Bodak, O.I., 1983. *Russian Metallurgy* (5), 198. *Transl. from Izvestiya AN SSSR Metall.*
- Patil, S., Hossain, Z., Paulose, P.L., Nagarajan, R., Gupta, L.C., Godart, C., 1996. *J. Solid State Commun.* **99** (6), 419.
- Patil, S., Paulose, P.L., Gupta, L.C., 1998. *Solid State Commun.* **109** (4), 217.
- Pavlyuk, V.V. 1993. Synthesis and crystal chemistry of the intermetallic compounds of lithium, Dr.Sc. Chemistry Thesis, Abstracts, L'viv (L'viv State University, L'viv) pp. 1-46.
- Pecharsky, V.K., Bodak, O.I., Zavalii, I.Yu., 1981. *Vestnik Lvov. Univers. Ser. Khim.* **23**, 38.
- Pecharsky, V.K., Pankevich, Yu.V., Bodak, O.I., 1982. *Dopov. Akad. Nauk URSR, Ser. B*, 46.
- Pecharsky, V.K., Pankevich, Yu.V., Bodak, O.I., 1983a. *Sov. Physics Crystallogr.* **28** (1), 97.
- Pecharsky, V.K., Bodak, O.I., Pankevich, Yu.V., 1983b. *Russian Metallurgy* (1), 173. *Transl. from Izvestiya AN SSSR Metall.*
- Protsyk, O., Salamakha, P., Sologub, O., 2000. Ternary R-Cu-Sb systems, R = La, Ce. In: 4th International Conference on f-elements, Madrid, Spain, 17-21 September 2000, Book of abstracts, AP41.

- Raju, N.P., Greedan, J.E., Ferguson, M.J., Mar, A., 1998. *Chem. Mat.* **10**, 3630.
- Ravot, D., Achard, J.C., Rossat-Mignot, J., 1982. In: *Rare Earth in Modern Science and Technology, Rare Earths Research Conference, Vol. 3*, p. 445.
- Rehr, A., Kauzlarich, S.M., 1994. *J. Alloys Compd.* **207**, 424.
- Riani, P., Marazza, R., Zanicchi, G., Cacciamani, G., Ferro, R., 1993. *J. Alloys Compd.* **202**, L11.
- Riani, P., Mazzone, D., Zanicchi, G., Marazza, R., Ferro, R., 1995. *Z. Metallkunde* **86** (7), 450.
- Rossat-Mignod, J., Buriel, P., Quezel, S., Effantin, J.M., Delacote, D., Bartholin, H., Vogt, O., Ravot, D., 1983. *J. Magn. Magn. Mat.* **31–34**, 398.
- Rossi, D., Marazza, R., Mazzone, D., Ferro, R., 1981. *J. Less-Common Met.* **78**, P1.
- Rustamov, P.G., Geidarova, E.A., 1984. *Z. Neorgan. Khimii* **29** (11), 1706.
- Rustamov, P.G., Godzaev, E.M., Guseinov, M.S., Aliev, O.M., 1977. *Z. Neorgan. Khimii* **22** (2), 298.
- Rustamov, P.G., Aliev, O.M., Maksudova, T.F., 1981a. *Izv. Akad. Nauk SSSR, Neorgan. Mater.* **17** (6), 692.
- Rustamov, P.G., Khasaev, J.P., Aliev, O.M., 1981b. *Izv. Akad. Nauk SSSR, Neorgan. Mater.* **17** (11), 1469.
- Rühl, R., Jeitschko, W., 1979. *Mat. Res. Bull.* **14**, 513.
- Sadygov, F.M., Geidarova, E.A., Aliev, I.I., 1988a. *Z. Neorgan. Khimii* **33** (8), 1238.
- Sadygov, F.M., Shahgulyev, N.S., Aliyev, O.M., 1988b. *J. Less-Common Met.* **144**, L5.
- Salamakha, P., 1998. *J. Alloys Compd.* **267**, L16.
- Salamakha, L.P., Mudryi, S.I. 2001a. Private communication.
- Salamakha, L.P., Mudryi, S.I., 2001b. Synthesis and crystal structure of new antimonides of ytterbium. In: *International Students Conference “Evrika-2001”*, Lviv University.
- Salamakha, P., Sologub, O., Suimetsu, T., Takabatake, T., 2000. *J. Alloys Compd.* **311**, L5.
- Schmidt, F.A., McMasters, D.D., 1976. *J. Less-Common Met.* **21**, 415.
- Schmidt, T., Jeitschko, W., 1998. *Z. Kristallogr.* **15**, 58.
- Shaked, H., Aldred, A.T., Dwight, A.E., 1979. *J. Magn. Magn. Mater.* **10**, 38.
- Skolozdra, R.V., Salamakha, P.S., Ganzzyuk, A.L., Bodak, O.I., 1993. *Neorgan. Mater.* **29**, N1, 25.
- Skolozdra, R.V., Mikhalsky, Ja.F., Kachmarska, K., Pierre, J., 1994. *J. Alloys Compd.* **206**, 141.
- Slebarski, A., Jezierski, A., Zygumt, A., Neumann, M., Mahr, S., Borstel, G., 1996. *J. Magn. Magn. Mat.* **159**, 179.
- Slovyanskikh, V.K., Sanygin, V.P., Kvardakov, A.M., Martynova, L.F., 1990. *Russ. J. Inorg. Chem.* **35**, 603.
- Sologub, O., Salamakha, P., 1999. *J. Alloys Compd.* **285**, L16–18.
- Sologub, O., Hiebl, K., Rogl, P., Noël, H., Bodak, O., 1994. *J. Alloys Compd.* **210**, 153.
- Sologub, O., Noël, H., Leithe-Jasper, A., Rogl, P., Bodak, O., 1995a. *J. Solid State Chem.* **115**, 441.
- Sologub, O., Hiebl, K., Rogl, P., Bodak, O., 1995b. *J. Alloys Compd.* **227**, 40.
- Sologub, O., Rogl, P., Bodak, O., 1995c. *J. Phase Equilib.* **16** (1), 61.
- Sologub, O., Rogl, P., Bodak, O., 1996a. *J. Phase Equilib.* **17** (5), 399.
- Sologub, O., Vybornov, M., Rogl, P., Hiebl, K., Cordier, G., Woll, P., 1996b. *J. Solid State Chem.* **122**, 266.
- Sologub, O.L., Salamakha, P.S., Lueken, H., 1998. New representatives of the $Y_3Au_3Sb_4$ type structure. In: *Proc. International Conf. “28emes Journees des Actinides”*. Uppsala, Sweden, p. P26.
- Sologub, O.L., Salamakha, P.S., Takabatake, T., 2001. Powder diffraction studies of the Yb-Zn-Sb system. In: *Proc. 20th European Crystallographic Meeting, Krakow*, 25–31.
- Stetskiv, A.O. 1999. Interaction of the components in ternary systems Ce-(Si, Ge)-(C, Sn, Sb, Bi), phase equilibria and crystal structure of compounds. Thesis for a Candidate Degree. Lviv State University, Lviv.
- Stetskiv, A.O., Pavlyuk, V.V., Bodak, O.I., 1998. *Polish J. Chem.* **72**, 956.
- Suzuki, H., Yamaguchi, T., Katoh, T., Kasaya, M., 1993. *Physica B: Condensed Matter (Amsterdam)* **186B**, 390.
- Thornton, M.J., Armitage, J.G.M., Tomka, G.J., Riedi, P.C., Houshiar, M., Adroja, D.T., Rainford, B.D., Fort, D., 1999. *Physica B* **259–261**, 101.
- Tomuschat, C., Schuster, H.U., 1981. *Z. Naturforsch.* **36B**, 1193.
- Vijaya Lakshmi, K., Menon Latica, Nigam, A.K., Das, A., Malik, S.K., 1996. *Physica B* **223–224**, 289.
- Villars, P., Calvert, L.D., 1985. *Pearson’s Handbook of Crystallographic Data for Intermetallic Phases*. American Society for Metals, Metals Park, OH, USA.
- Villars, P., Calvert, L.D., 1991. *Pearson’s Handbook of Crystallographic Data for Intermetallic Phases*. ASM International Materials Park, OH, USA.
- Villars, P., Prince, A., Okamoto, H., 1995. *Handbook of Ternary Alloy Phase Diagrams*. ASM International, Materials Park, OH, USA.
- Vogel, R., Klose, H., 1954. *Z. Metallkunde* **45**, 633.
- Wang, R., Steinfink, H., Raman, A., 1967. *Inorg. Chem. (Washington D.C.)* **6** (7), 1298.

- Weitzer, F., Leithe-Jasper, A., Rogl, P., Hiebl, K., Noël, H., Wiesinger, G., Steiner, W., 1993. *J. Solid State Chem.* **104**, 368.
- Wenski, G., Mewis, A., 1986a. *Z. Kristallogr.* **176**, 125.
- Wenski, G., Mewis, A., 1986b. *Z. Anorg. Allgem. Chem.* **543**, 49.
- Wollesen, P., Jeitschko, W., Brylyak, M., Dietrich, L., 1996. *J. Alloys Compd.* **245**, L5.
- Zavaliy, I.Yu. 1982. Thesis for a Master degree, Lviv State university, Lviv, 198.
- Zaplatynsky, O.V. 2000. Thesis for a Candidate Degree. Lviv State University, Lviv, 1999.
- Zaplatynsky, O.V., Salamakha, P.S., 1994. *Visnyk L'viv. University. Ser. Khim.* **33**, 39.
- Zeng, L., Franzen, H.F., 2000. *J. Alloys Compd.* **311**, 224.
- Zhang, J.S., Chen, H.J., Lin, J.H., 2000. *J. Alloys Compd.* **311**, 109.
- Zygmunt, A., Szytula, A., 1995. *J. Alloys Compd.* **219**, 185.

Chapter 213

THERMODYNAMIC PROPERTIES OF THE LANTHANIDE(III) HALIDES

R.J.M. KONINGS* and A. KOVÁCS†

European Commission, Joint Research Centre, Institute for Transuranium Elements,
P.O. Box 2340, 76125 Karlsruhe, Germany; E-mail: konings@itu.fzk.de

Contents

List of symbols	148	6.2. $LnCl_3$	178
List of acronyms	148	6.3. $LnBr_3$ and LnI_3	180
1. Introduction	148	7. Heat capacity of the gaseous trihalides	182
2. Polymorphism	149	7.1. LnX_3 monomers	182
2.1. LnF_3	149	7.2. Ln_2X_6 dimers	190
2.2. $LnCl_3$	150	8. Enthalpy of formation of the gaseous trihalides	191
2.3. $LnBr_3$	152	8.1. LnF_3	191
2.4. LnI_3	152	8.2. $LnCl_3$	193
3. Low-temperature heat capacity and standard entropy of the solid trihalides	154	8.3. $LnBr_3$	194
3.1. LnF_3	154	8.4. LnI_3	196
3.2. $LnCl_3$	158	8.5. Ln_2X_6 dimers	197
3.3. $LnBr_3$ and LnI_3	161	9. Conclusions	198
4. High-temperature heat capacity of the solid trihalides	162	Appendix A. The transition and melting points of the lanthanide trihalides	200
4.1. LnF_3	162	Appendix B. The enthalpies of formation of the solid lanthanide trihalides	209
4.2. $LnCl_3$	166	Appendix C. Experimental data for the liquid trihalides	222
4.3. $LnBr_3$ and LnI_3	168	Appendix D. Molecular parameters of the lanthanide trihalides	224
5. Enthalpy of formation of the solid trihalides	169	Appendix E. The enthalpies of sublimation of the lanthanide trihalides	234
5.1. LnF_3	169	References	241
5.2. $LnCl_3$, $LnBr_3$ and LnI_3	172		
6. Heat capacity of the liquid trihalides	175		
6.1. LnF_3	175		

* Corresponding author.

† On leave from Research Group for Technical Analytical Chemistry of the Hungarian Academy of Sciences at the Institute of General and Analytical Chemistry, Budapest University of Technology and Economics.

List of symbols

A	Madelung constant	T_{trs}	transition temperature
C_p	heat capacity at constant pressure	U	energy
C_{exs}	excess heat capacity	V_m	molar volume
C_{lat}	lattice heat capacity	Z	ionic charge
D	bond energy	$\Delta_f H^\circ$	enthalpy of formation at 298.15 K
d, f, g	polarization functions	$\Delta_r H^\circ$	enthalpy of reaction
Q	molecular partition function	$\Delta_{\text{sub}} H$	enthalpy of sublimation
R	universal gas constant	$\Delta_{\text{trs}} H^\circ$	enthalpy of transition
r_e	equilibrium bond distance	$\Delta_{\text{fus}} S^\circ$	entropy of fusion
r_g	thermal average distance at the temperature of the ED experiment	$\Delta_{\text{trs}} S^\circ$	entropy of transition
r_a	distance between average nuclear positions at a given temperature	ε	electronic energy
S°	standard entropy	ν_1	symmetric stretch
T	temperature	ν_2	symmetric bend (inversion)
T_{fus}	fusion temperature	ν_3	asymmetric stretch
		ν_4	asymmetric bend

List of acronyms

(aq)	aqueous	(g)	gas
BP	Becke–Perdew86 exchange-correlation functional (Perdew, 1986; Becke, 1988)	IR	infrared spectroscopy
B3P	Becke3–Perdew86 exchange-correlation functional (Perdew, 1986; Becke, 1993)	ITS-90	International Temperature Scale of 1999 (www.its-90.com)
(cr)	crystal	(liq)	liquid
DFT	density functional theory	L_n	lanthanide
DS	relativistic Dirac–Slater calculation	MI	matrix isolation
DSC	differential scanning calorimetry	MP2	second order Møller–Plesset perturbation theory (Møller and Plesset, 1934)
ECP _D	relativistic effective core potential of Dolg et al. (1989)	QC	quantum chemical computation
ECP _S	relativistic effective core potential of Stevens et al. (Stevens et al., 1992; Cundari and Stevens, 1993)	(sln)	solution
ED	electron diffraction	TZ	triple-zeta basis set
		VDZ	valence double-zeta basis set
		VTZ	valence triple-zeta basis set

1. Introduction

The lanthanide trihalides have been subject of studies for many decades. The main incentive has been the scientific interest in the physical and chemical properties of compounds of the trivalent lanthanide ions, which are unique in the period system as they regularly vary along

the series. This is due to the fact that the f electrons in the lanthanide ions are localised and do not actively participate in the chemical bonding. A similar effect occurs in the heavy actinide series for the elements beyond plutonium, which exhibit lanthanide-like properties. Because these heavy actinides are highly active materials, understanding of the lanthanide properties is the key to the prediction of the properties of the trivalent actinides, like americium and curium.

The lanthanide halides also have important technological relevance. In the 1950s and 1960s some interest in the fluorides originated from nuclear technology. The molten salt reactor project in the USA initiated many studies on the LnF_3 compounds as these are formed in the (LiF-BeF₂-ThF₄) fuel that was used. Separation of these fission products from the actinides during the pyrochemical reprocessing of the fuel was an important issue. A pyrochemical process was also developed for the reprocessing of the metal fuel for the fast reactor programme in the USA. This process is based on dissolution of the fuel in a high temperature molten chloride salt and selective transport to a metal cathode. In recent years, these technologies have found re-newed interest in the nuclear community, mainly in the frame of the actinide partitioning and transmutation programmes (Baetslé, 1999), for which the separation of the lanthanide fission products from the (trivalent) actinides is a key issue.

Lanthanide bromides and iodides have found important applications in a completely different field. They are added as additives in high-pressure discharge lamps in the lighting industry to improve the arc stability and the colour quality. The latter is due to the contribution of the multiline spectrum of the doped rare earths which are added to the salt mixture. Lanthanide trihalides of dysprosium, holmium, thulium, gadolinium and lutetium are used frequently for this purpose (Hilpert and Niemann, 1997).

These high temperature processes can be modelled adequately by equilibrium thermodynamics. For such calculations reliable thermodynamic data are a priority. Although numerous studies of the thermodynamic properties of the lanthanide trihalides have been published in the past, the available information is still not complete. But because the properties change regularly within the lanthanide series, estimates can help to obtain the data that are lacking.

In the present chapter the existing information is reviewed and emphasis is given to the understanding of the trends in order to establish a basis for the estimations. The cited literature is essentially from the period 1945–2002. The studies made before that period are considered to be less reliable as the separation technology to obtain the lanthanide elements in pure form was not sufficiently well developed before 1945 (Spedding and Daane, 1960).

2. Polymorphism

2.1. LnF_3

Four crystallographic modifications have been reported for the lanthanide trifluorides (Greis and Haschke, 1982; Meyer and Wickleder, 2000). The trifluorides of La, Ce, Pr and Nd have a hexagonal/trigonal structure from room temperature up to the melting point. Greis and Cader (1985) reported that these compounds undergo a λ -type second order transition before melting, which was easier to detect when the samples were heated at low heating rates. As a result

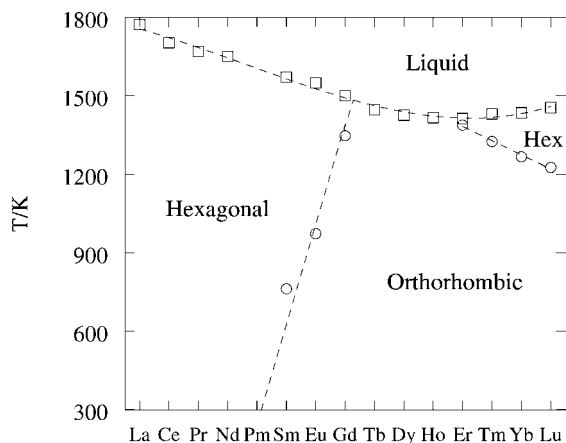


Fig. 1. The polymorphism in the lanthanide trifluorides.

the transition temperatures are not well defined. Greis and Cader (1985) argued that at low temperatures a highly ordered superstructure exists (space group $P\bar{3}c1$) whereas the anion-disordered structure (space group $P6_3cm$) dominates at higher temperatures. The trifluorides of Sm to Lu have an orthorhombic structure (space group $Pnma$) at room temperature. Transitions from the orthorhombic to a hexagonal structure at elevated temperature have been reported for all compounds in the series Sm–Lu: the LaF_3 type hexagonal structure for the trifluorides of Sm to Ho and the YF_3 hexagonal structure for the trifluorides of Er to Lu. Stankus et al. (1999) concluded that the transition involves a deformation mechanism and may occur over a broad temperature range. Pastor and Robinson (1974) and Sobolev et al. (1976a, 1976b) discussed the variation in transition temperatures in view of hydroxide, oxygen and alkaline earth impurities and argued that the transitions in TbF_3 , DyF_3 and HoF_3 do not occur and that the reported claims are due to impurities. The polymorphism as a function of atomic number is shown in fig. 1, which is essentially identical to the figure of Greis and Haschke (1982) in an earlier chapter of this Handbook series.

The reported transition and melting temperatures are summarised in table A.1 of Appendix A. As follows from the discussed above, there is quite some variation in the transition temperatures, but there is generally good agreement for the melting temperatures of the lanthanide trifluorides. The selected values (considering corrections to ITS-90) are summarised in table 1. Figure 1 shows that a minimum in the melting curve of the lanthanide trifluorides occurs at ErF_3 : the melting point steadily decreases with increasing atomic number for the light hexagonal/trigonal and orthorhombic but slightly increases for the heavy hexagonal trifluorides. Since data for PmF_3 are lacking, its melting point has been interpolated.

2.2. $LnCl_3$

The lanthanide trichlorides of La to Eu have a hexagonal crystal structure (space group $P6_3/m$) at room temperature. For $GdCl_3$ the hexagonal as well as the orthorhombic structures have been reported at room temperature. There is some uncertainty which of these is the

Table 1
The selected transition and melting temperatures for the lanthanide trihalides, in K

	F		Cl		Br		I	
	T_{trs}	T_{fus}	T_{trs}	T_{fus}	T_{trs}	T_{fus}	T_{trs}	T_{fus}
La		1766 ± 3		1133 ± 5		1060 ± 3		1045 ± 3
Ce		1703 ± 3		1090 ± 2		1005 ± 2		1033 ± 2
Pr		1670 ± 3		1060 ± 2		965 ± 3		1011 ± 2
Nd		1649 ± 3		1032 ± 2		955 ± 2	859 ± 3	1059 ± 2
Pm		1605 ± 15		994 ± 15		930 ± 15	900 ± 10	1090 ± 10
Sm	743 ± 3	1571 ± 3		950 ± 5		913 ± 5	943 ± 10	1123 ± 5
Eu	973 ± 3	1549 ± 3		894 ± 3		978 ± 10		decomp.
Gd	1347 ± 3	1501 ± 3	872 ± 10	875 ± 2		1043 ± 5	1013 ± 5	1204 ± 3
Tb		1446 ± 3	783 ± 5	855 ± 3		1102 ± 3	1080 ± 5	1229 ± 3
Dy		1426 ± 3	611 ± 5	924 ± 3		1152 ± 3	1101 ± 5	1251 ± 3
Ho		1416 ± 3	820 ± 20	993 ± 3		1192 ± 3	1150 ± 15	1267 ± 5
Er	1388 ± 3	1413 ± 3		1049 ± 5		1196 ± 5	1195 ± 15	1288 ± 3
Tm	1325 ± 3	1431 ± 3		1095 ± 3		1228 ± 3	1240 ± 15	1294 ± 5
Yb	1267 ± 3	1435 ± 3		1138 ± 5		decomp.	1280 ± 15	decomp.
Lu	1230 ± 3	1455 ± 3		1198 ± 5		1298 ± 5	1320 ± 15	1323 ± 5

thermodynamically stable form. Because Sommers and Westrum Jr. (1977) were not able to transform the hexagonal form to the orthorhombic by annealing (367 K, 7 days) or cooling (liquid nitrogen, 7 h), they considered the hexagonal structure to be the thermodynamically stable form. This was confirmed by Raman spectroscopic studies by Daniel et al. (1989). TbCl_3 has an orthorhombic structure (space group $Cmcm$). The trichlorides of Dy to Lu have a monoclinic crystal structure (space group $C2/m$).

The hexagonal structure of the trichlorides of La to Eu persists up to the melting point, whereas GdCl_3 retains its hexagonal structure up to few degrees below to the melting point (Daniel et al., 1989). The high temperature behaviour of the orthorhombic and monoclinic lanthanide trichlorides is not so well known. The enthalpy increment studies for TbCl_3 , DyCl_3 and HoCl_3 (Dworkin and Bredig, 1971) do not reveal any phase transformations up to the melting point (see below), but differential scanning calorimetric measurements of DyCl_3 and ErCl_3 revealed transitions at 611 K and 1025 K (Gaune-Escard et al., 1994), respectively, the nature of which was not explained. Büchel et al. (1995) claimed that in the case of ErCl_3 the DTA peak is due to the reaction with the silica crucible used by Gaune-Escard et al. (1994). Morrison et al. (2000) studied the polymorphism of TbCl_3 by Raman spectroscopy and X-ray diffraction and demonstrated that a phase change occurs around 773 K and tentatively assigned it to a tetragonal structure (space group $P4_2/mnm$), in agreement with the work of Günselius et al. (1988).

The reported transition and melting temperatures are listed in table A.2 of Appendix A. There is general agreement between the studies and the selected values (considering corrections to ITS-90) are summarised in table 1. The polymorphism as a function of atomic number is shown in fig. 2. The minimum in the melting curve of the lanthanide trichlorides occurs at TbCl_3 where a change in structure of the LnCl_3 occurs, as was the case for the trifluorides. Data for PmCl_3 are lacking and its melting point has been interpolated in the LnCl_3 series.

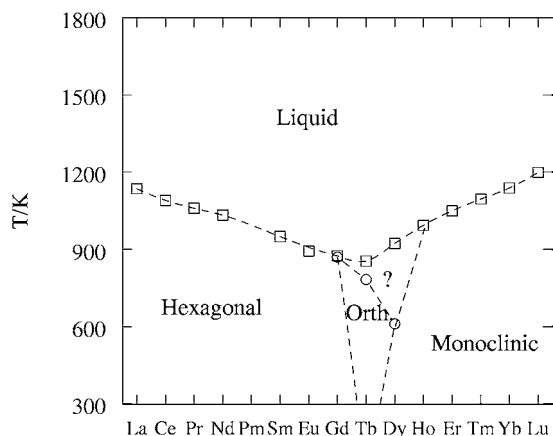


Fig. 2. The polymorphism in the lanthanide trichlorides.

2.3. $LnBr_3$

The tribromides of La, Ce and Pr have a hexagonal structure (space group $P6_3/m$), the tribromides of Nd, Pm, Sm and Eu have an orthorhombic structure (space group $Cmcm$), and the tribromides of Tb to Lu have a hexagonal/rhombohedral structure (space group $R\bar{3}$). For $GdBr_3$ several different crystal structures have been reported: hexagonal/rhombohedral, trigonal and monoclinic, the former being the thermodynamically stable phase.

Phase transformations have not been reported for any of the rare earth tribromides, but only a few detailed studies of the high-temperature phase behaviour have been made. Brown et al. (1968) did not find evidence for polymorphism in $GdBr_3$ by X-ray diffraction; Dworkin and Bredig (1971) none for $LaBr_3$, $CeBr_3$, $PrBr_3$, $NdBr_3$, $GdBr_3$ or $HoBr_3$ by drop-calorimetric measurements; and Cordfunke et al. (Cordfunke and Blacquère, 1997; Cordfunke et al., 1999) none for $NdBr_3$ and $DyBr_3$ by differential scanning calorimetric measurements.

The reported melting points for the tribromides are in good agreement as shown in table A.3 of Appendix A. The recommended melting points (considering corrections to ITS-90) are listed in table 1, and shown as a function of atomic number in fig. 3. The minimum in the melting curve of the lanthanide tribromides occurs at $SmBr_3$ or perhaps $PmBr_3$. Unlike the fluoride, chloride and iodide series, no change in structure has been reported in the bromide series at this point. This observation may, however, be an indication that a high-temperature orthorhombic-hexagonal phase transformation occurs for $EuBr_3$ and eventually for $SmBr_3$, and the stability fields in fig. 3 have been drawn schematically to reflect this. Because of these uncertainties the melting point of $PmBr_3$ is difficult to estimate accurately.

2.4. LnI_3

The triiodides of La to Nd have an orthorhombic structure (space group $Ccmm$), the triiodides of Sm to Lu have a hexagonal/rhombohedral structure (space group $R\bar{3}$). High temperature transformations have been reported for the lanthanide triiodides from NdI_3 to DyI_3 . The orthorhombic NdI_3 probably transforms into the rhombohedral structure (Dworkin and Bredig,

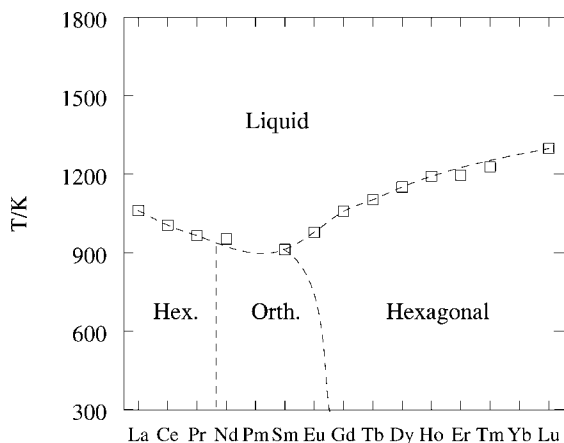


Fig. 3. The polymorphism in the lanthanide tri-bromides.

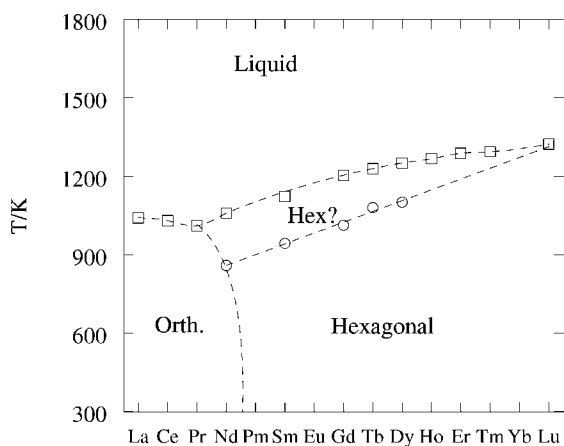


Fig. 4. The polymorphism in the lanthanide tri-iodides.

1971). The nature of the transformations in for the triiodides SmI_3 to DyI_3 is not defined and it is unclear whether this transformation also occurs in HoI_3 , ErI_3 , TmI_3 and LuI_3 as these compounds have hardly been studied. As the enthalpies of these transitions are small, it is most likely that they involve a rearrangement of the rhombohedral lattice. For the diagram in fig. 4 we have linearly extrapolated the transition temperatures beyond DyI_3 based on the straight line established by the LnI_3 transformation temperatures for $\text{Ln} = \text{Nd}, \text{Sm}, \text{Gd}, \text{Tb},$ and Er . This figure is, however, of a speculative nature.

The melting points of LaI_3 to NdI_3 have been studied by several authors and the results agree well and selected values (considering corrections to ITS-90) are given in table 1. For the heavy lanthanide triiodides only a limited number of studies has been made, but the reliability is good (see table A.4 of Appendix A). No experimental studies are known for PmI_3 , EuI_3 and YbI_3 . The latter two compounds start to decompose below the melting point. The melting point of PmI_3 has been interpolated in the LnI_3 series.

3. Low-temperature heat capacity and standard entropy of the solid trihalides

3.1. LnF_3

The heat capacity of hexagonal/trigonal LaF_3 , PrF_3 and NdF_3 and orthorhombic GdF_3 , DyF_3 , ErF_3 and LuF_3 was measured by Lyon et al. (1978, 1979a, 1979b) and Flotow and O'Hare (1981, 1984) using adiabatic low-temperature calorimetry in the 5 to 350 K range. The heat capacity of CeF_3 was measured by King and Christensen (1959) from 51 to 298.15 K, and by Westrum Jr. and Beale Jr. (1961) from 5 to 300 K. The heat capacity curves of all these compounds show a smooth and continuous increase up to 350 K, indicating no transitions.

The heat capacity of the trivalent lanthanide trihalides consists of a lattice component, arising mainly from the vibrations of the ions in the crystal, and an excess component (Westrum Jr. and Grønvold, 1962; Westrum Jr., 1970; Flotow and Tetenbaum, 1981; Westrum Jr., 1983):

$$C_p = C_{lat} + C_{exs}. \quad (1)$$

The excess contribution is due to the distribution of the valence electrons over the energy levels, and includes the splitting of the ground term by the crystalline electric field (Stark effect) and is called the Schottky heat capacity or Schottky anomaly. It can be calculated from

Table 2
The crystal field energy levels for the lanthanide trifluorides (Dieke et al., 1968; Morrison and Leavitt, 1982)

compound	state	$\epsilon_i/\text{cm}^{-1}$
LaF_3	1S_0	0
CeF_3	$^2F_{5/2}$	0, 151, 280
	$^2F_{7/2}$	2160, 2240, 2635, 2845
PrF_3	3H_4	0.0, 59.7, 69.4, 134.7, 202.4, 222.6, 290.4, 330.7, 500.1
NdF_3	$^4I_{9/2}$	0, 45, 136, 296, 500
	$^4I_{11/2}$	1978, 2037, 2068, 2091, 2187, 2223
PmF_3	$^2F_{7/2}$	
SmF_3	$^6H_{5/2}$	0.00, 44.5, 159.4
	$^6H_{7/2}$	1003.4, 1047.0, 1100.6, 1187.0
EuF_3	7F_0	0.00
	7F_1	313, 375, 415
	7F_2	946, 997, 1098
GdF_3	$^8F_{7/2}$	0
TbF_3	7F_6	0, 42, 60, 125, 140, 169, 209, 212, 217, 232, 319, 353, 488
DyF_3	$^6H_{15/2}$	0, 42.3, 61.8, 110.9, 154.9, 210.7, 272.3, 468.5
HoF_3	5I_8	0, 7.3, 18.7, 32.5, 54.1, 76.7, 103.5, 125.3, 149.4, 204.2, 211.1
ErF_3	$^4F_{15/2}$	0, 52.0, 64.3, 96.5, 113.7, 141.6, 181.0, 229.3
TmF_3	3H_6	0, 67, 118, 156, 204, 235, 272, 274, 349, 354, 400, 418, 441
YbF_3	$^3F_{7/2}$	0, 78, 185, 401
LuF_3	1S_0	0

the partitioning function Q , which is described by the Maxwell–Boltzmann distribution law:

$$Q_{\text{exs}} = \sum_{i=0}^n g_i e^{-\varepsilon_i/RT}, \quad (2)$$

where ε_i is the energy and g_i the degeneracy of level i , R is the universal gas constant and T is the absolute temperature. The excess heat capacity is then calculated from the equations:

$$C_{\text{exs}} = R \frac{d}{dT} \left(T^2 \frac{d(\ln Q)}{dT} \right). \quad (3)$$

The electronic states of the lanthanide 3+ ions are characterised by $(2J + 1)$ -fold degeneracy which is removed by the crystalline electric field. For the ground state this results in a set of energy levels generally below 1000 cm^{-1} . These crystal-field states have been identified for most of the lanthanide trifluorides, and are summarised in table 2. Examples of C_{exs} thus calculated are shown in fig. 5 for PrF_3 , NdF_3 , DyF_3 , and ErF_3 .

In LaF_3 , GdF_3 and LuF_3 the excess contribution is zero which is due to the fact that these lanthanide ions have an empty, half-filled and completely filled f-shell, respectively. This is evident from a plot of the C_p values at 298.15 K as a function of the atomic number as shown in fig. 6 which indicates that the values for these three compounds form a straight line, in spite of their different crystal structures. Flotow et al. resolved the lattice and excess contribution by assuming the heat capacity of LaF_3 to represent the lattice component of the other hexagonal earth trifluorides (PrF_3 , NdF_3) and GdF_3 and LuF_3 that of the orthorhombic rare earth trifluorides. Flotow et al. obtained the values in between GdF_3 and LuF_3 by an interpolation using weighing factor f based on the molar volume:

$$C_{\text{lat}} = (1 - f)C_{\text{lat}}(\text{GdF}_3) + fC_{\text{lat}}(\text{LuF}_3). \quad (4)$$

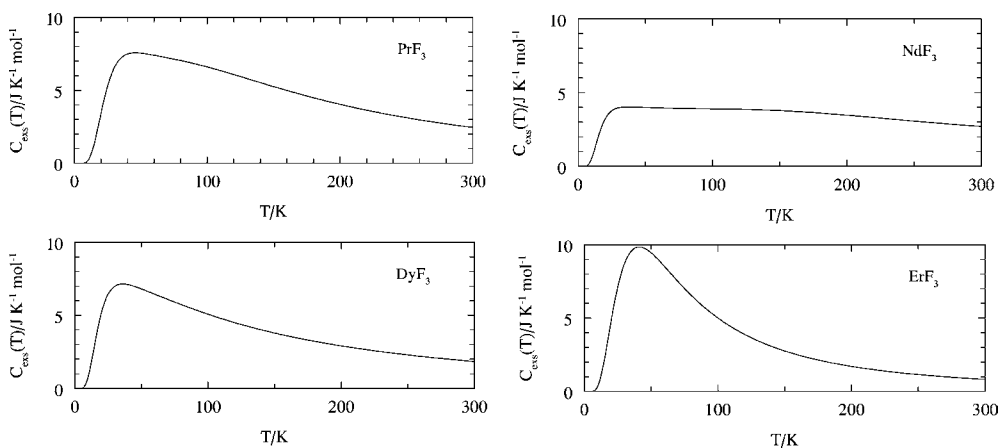


Fig. 5. The excess heat capacity of PrF_3 , NdF_3 , DyF_3 and ErF_3 as calculated from the crystal field energies.

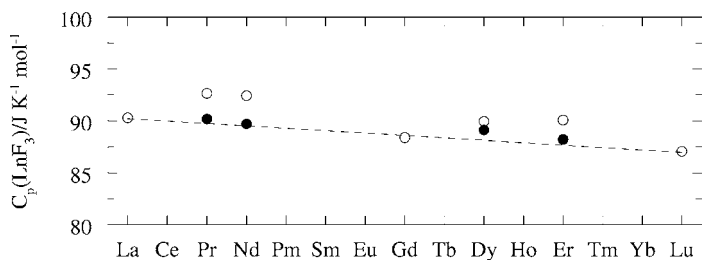


Fig. 6. The variation of C_p (298.15 K) in the lanthanide trifluoride series (\circ). The broken line connects the values for LaF_3 , GdF_3 and LuF_3 for which C_{exs} is zero at 298.15 K. The solid circles show the values of C_{lat} (298.15 K) obtained by subtracting C_{exs} (298.15 K) from the experimental values.

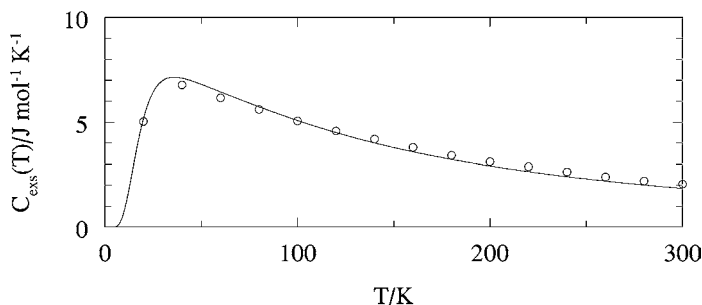


Fig. 7. The excess heat capacity of DyF_3 ; curve shows the values calculated from the crystal field energies, symbols are the values derived from the experimental data by subtracting C_{lat} , as explained in the text.

The experimental excess heat capacity thus obtained as the difference between measured C_p and C_{lat} can then be compared to the values calculated from the crystal field levels. As an example, fig. 7 shows the good agreement of the experimental and calculated excess heat capacity of DyF_3 .

The standard molar entropies at 298.15 K derived from the low-temperature heat capacity measurements are summarized in table 3. Similar to the heat capacity, the entropy can be described as the sum of the lattice and excess components (Konings, 2001, 2002):

$$S = S_{\text{lat}} + S_{\text{exs}}. \quad (5)$$

The excess entropy is then calculated from the following equation:

$$S_{\text{exs}} = R \ln Q_{\text{exs}}. \quad (6)$$

Combining eqs. (2) and (6) gives:

$$S_{\text{exs}} = R \ln(g_0) + R \ln\left(\sum_{i=1}^n g_i e^{-\varepsilon_i/RT}\right). \quad (7)$$

The first term of eq. (7) represents the temperature independent contribution of the ground state, the second term the contribution of the excited energy levels.

The lattice contribution in the lanthanide fluorides is only known with sufficient accuracy when the f shell of the metal ions is empty ($4f^0$) or completely filled ($4f^{14}$). In these cases S_{exs} is zero and the experimental entropy corresponds to S_{lat} . Also in case the f-shell of the metal

Table 3
The entropies of the solid lanthanide(III) fluorides and chlorides at 298.15 K, in $\text{J}\cdot\text{K}^{-1}\cdot\text{mol}^{-1}$

	Calculated			Experimental ^a	
	S_{lat}	S_{exs}	S_{tot}	S_{exp}	References
LaF ₃	105.84	0.00	105.84	106.98 ± 0.11	1
CeF ₃	104.97	13.73	118.70	115.23	2
PrF ₃	104.10	16.75	120.85	121.22 ± 0.12	3
NdF ₃	103.23	17.24	120.47	120.79 ± 0.12	4
PmF ₃	102.37	18.27	120.64	–	
SmF ₃	101.50	15.00	116.50	–	
EuF ₃	100.63	9.44	110.07	–	
GdF ₃	99.76	17.29	117.05	114.77 ± 0.22	5
TbF ₃	98.90	20.07	118.97	–	
DyF ₃	98.03	21.83	119.86	118.07 ± 0.12	6
HoF ₃	97.16	23.18	120.34	–	
ErF ₃	96.29	22.62	118.91	116.86 ± 0.12	6
TmF ₃	95.42	19.56	114.98	–	
YbF ₃	94.55	17.29	111.84	–	
LuF ₃	93.69	0.00	93.69	94.83 ± 0.09	5
LaCl ₃	137.57	0.00	137.57	137.57	7
CeCl ₃	136.71	14.71	151.42	–	
PrCl ₃	136.28	17.87	154.15	153.30	7
NdCl ₃	135.85	18.30	154.15	153.43	7
PmCl ₃	135.42	17.89	153.31	–	
SmCl ₃	134.99	15.27	150.26	150.12	8
EuCl ₃	134.56	9.32	143.88	144.06	8
GdCl ₃	134.13	17.29	151.42	151.42	8
TbCl ₃	133.70	21.15	154.85	–	
DyCl ₃	155.15	22.83	177.98	175.4	9
HoCl ₃	154.72	23.16	177.88	177.1	10
ErCl ₃	154.29	22.60	176.89	175.1	11
TmCl ₃	153.86	20.84	174.70	173.5	12
YbCl ₃	153.43	15.80	169.23	169.3	13
LuCl ₃	153.00	0.00	153.0	153.0	9

^aThe uncertainty for the standard entropies derived from the calorimetric measurements has not been given in some cases.

References

- Lyon et al. (1978)
- Westrum Jr. and Beale Jr. (1961)
- Lyon et al. (1979a)
- Lyon et al. (1979b)
- Flotow and O'Hare (1981)
- Flotow and O'Hare (1984)
- Sommers and Westrum Jr. (1976)
- Sommers and Westrum Jr. (1977)
- Tolmach et al. (1987)
- Tolmach et al. (1990a)
- Tolmach et al. (1990b)
- Tolmach et al. (1990c)
- Gorbunov et al. (1986)

ion is half filled ($4f^7$), S_{lat} can be derived easily from the experimental entropy since only a correction for the temperature independent term in eq. (7) needs to be made in the absence of a significant crystal-field splitting of the ground state.

In fig. 8 the experimental entropies for the lanthanide trifluorides are plotted as a function of the atomic number. The figure shows that S_{lat} for LaF₃, GdF₃ and LuF₃ form approximately

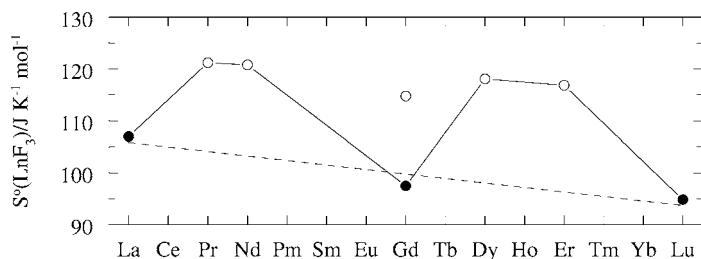


Fig. 8. The variation of the S_{exp} (○) and S_{lat} (●) in the lanthanide trifluorides. The broken line shows S_{lat} derived from the values for LaF_3 , GdF_3 and LuF_3 , the solid line shows S_{exs} derived from the experimental data for the other configurations.

a straight line, as was the case for the heat capacities at 298.15 K. S_{lat} for the other lanthanide compounds is then obtained by inter- or extrapolation of the data (which is a simpler, but essentially identical approximation as the weighing factors based on the molar volume, as indicated by eq. (4)). These numbers are listed in table 3. The excess contribution is calculated from eq. (7) using the crystal field energies listed in table 2, which are mainly based on spectroscopic studies of the lanthanide ions in transparent host crystals. In case of PmF_3 the spectroscopic data are missing, and S_{exs} is calculated from the degeneracy of the ground state of the lanthanide ion. This neglect of the crystal energy splitting leads to a small overestimation of S_{exs} at 298.15 K, which increases when the energy gap of the crystal-field splitting becomes larger. For example, we obtain $S_{\text{exs}} = 17.24 \text{ J} \cdot \text{K}^{-1} \cdot \text{mol}^{-1}$ at 298.15 K for NdF_3 from the known crystal field levels, whereas we obtain $S_{\text{exs}} = R \ln(10) = 19.14 \text{ J} \cdot \text{K}^{-1} \cdot \text{mol}^{-1}$ at 298.15 K from the approximation.

The total entropy values thus obtained for CeF_3 , PrF_3 , NdF_3 , DyF_3 and ErF_3 compare well with the experimental values by Flotow et al. and the difference $S_{\text{exp}} - S_{\text{tot}}$ is in the order of 1–2%. The recommended entropy values are the experimental values of Flotow et al., and the calculated values for those compounds for which no experimental data are available. An uncertainty of $\pm 3.0 \text{ J} \cdot \text{K}^{-1} \cdot \text{mol}^{-1}$ has been assigned to the calculated values.

3.2. LnCl_3

Heat capacity measurements in the 10 to 350 K temperature range have been reported by Sommers and Westrum Jr. (1976, 1977) for the hexagonal lanthanide trichlorides and Tolmach et al. for the monoclinic ones (Gorbunov et al., 1986; Tolmach et al., 1987, 1990a, 1990b, 1990c). No compound was measured in parallel by both groups but remarkable differences are observed between the results of the two groups. This is shown in fig. 9 in which the heat capacity curves of GdCl_3 measured by Sommers and Westrum and LuCl_3 by Tolmach et al. are plotted. It can be seen that the heat capacity curve of LuCl_3 is significantly higher than that of GdCl_3 up to about 150 K above which the heat capacity curve approach each other. This is significantly different from the situation for the trifluorides where the curves of LaF_3 , GdF_3 and LuF_3 have the same shape and the heat capacity slightly decreases with increasing atomic number.

The differences in the entropy values derived for the two groups of compounds are also significant: the lattice values at 298.15 K derived from the work of Tolmach et al. are about $20 \text{ J} \cdot \text{K}^{-1} \cdot \text{mol}^{-1}$ higher than the extrapolation of results for the hexagonal compounds, as

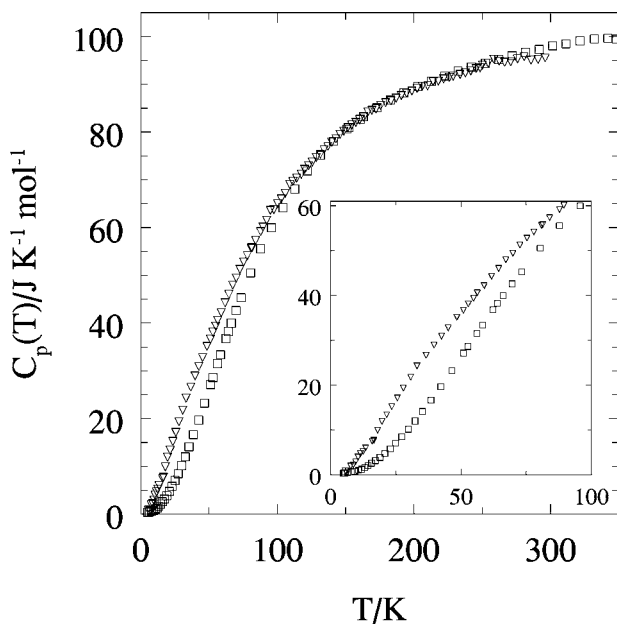


Fig. 9. The heat capacity of GdCl_3 (\square) and LuCl_3 (∇).

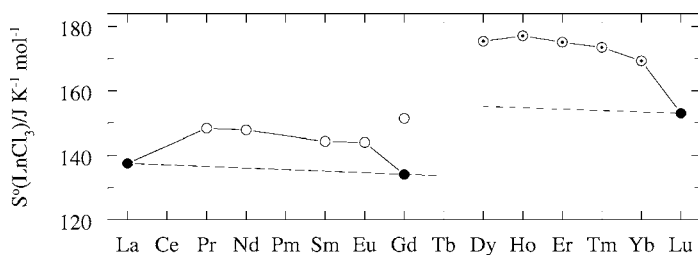


Fig. 10. The variation of S_{exp} (\circ , hexagonal; \odot , monoclinic) and S_{lat} (\bullet) in the lanthanide trichloride series at 298.15 K; the broken line shows the lattice contribution (see text).

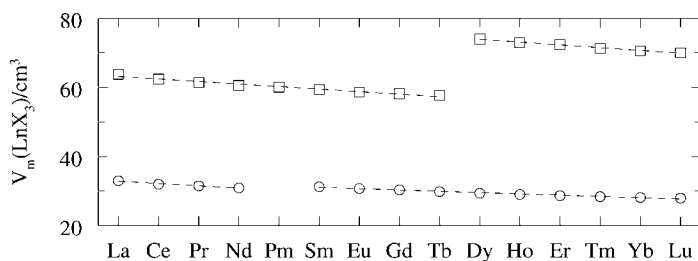


Fig. 11. The molar volumes in the LnF_3 (\circ) and LnCl_3 series (\square) at 298.15 K.

shown in fig. 10. This suggests a distinct difference between entropies of hexagonal and monoclinic crystallographic modifications. This difference is also evident in the molar volumes (fig. 11): V_m of the lanthanide trifluorides, calculated from the lattice constants, decreases lin-

Table 4

The corrected standard entropy values at 298.15 K for the monoclinic lanthanide(III) chlorides (in $\text{J}\cdot\text{K}^{-1}\cdot\text{mol}^{-1}$) as derived from the work of Tolmachev et al. (Tolmachev et al., 1987, 1990a, 1990b, 1990c; Gorbunov et al., 1986); T_{\min} is lower temperature limit of the measurements

	T_{\min}	$S_{\text{exp}}(298.15\text{ K} - T_{\min})$	$S_{\text{lat}}(T_{\min})$	$S_{\text{exs}}(T_{\min})$	$S^{\circ}(298.15\text{ K})$
DyCl ₃	0	169.6	0.00	5.76	175.4
HoCl ₃	6.61	170.1	0.25	6.74	177.1
ErCl ₃	9.86	168.1	1.25	5.76	175.1
TmCl ₃	15.34	166.5	3.35	3.68	173.5
YbCl ₃	0	163.5	0.00	5.76	169.3

Table 5

The crystal field energy levels for the lanthanide trichlorides (Morrison and Leavitt, 1982; Carnall, 1982)

compound	state	$\epsilon_i/\text{cm}^{-1}$
LaCl ₃	¹ S ₀	0
CeCl ₃	² F _{5/2}	0, 37.5, 110
	² F _{5/2}	2166, 2208.6, 2282.6, 2399.5
PrCl ₃	³ H ₄	0, 33.1, 96.4, 130.2, 137.0, 199.1
NdCl ₃	⁴ I _{9/2}	0, 115.4, 123.2, 244.4, 249.4
	⁴ I _{11/2}	1973.85, 2012.58, 2026.90, 2044.19, 2051.60, 2058.90
PmCl ₃	² F _{7/2}	0, 66.6, 84.5, 110.1, 127.0, 240.0
SmCl ₃	⁶ H _{5/2}	0, 40.7, 66.1
	⁶ H _{7/2}	992.8, 1051.2, 1104.7, 1172.6
EuCl ₃	⁷ F ₀	0
	⁷ F ₁	355.05, 405.27
	⁷ F ₂	1022.54, 1027.52, 1084.33
GdCl ₃	⁸ F _{7/2}	0
TbCl ₃	⁷ F ₆	0, 56.8, 90.6, 97.2, 99.3, 104.6, 112.8, 118.0
DyCl ₃	⁶ H _{15/2}	0, 9.82, 9.97, 15.65, 40.8, 80.5, 121.7, 140.5
HoCl ₃	⁵ I ₈	0, 12.5, 43.8, 66.4, 89.9, 104.1, 118.4, 154.2, 155.4, 203.7, 212.8
ErCl ₃	⁴ F _{15/2}	0, 37.9, 64.3, 96.5, 113.7, 141.6, 181.0, 229.43
TmCl ₃	³ H ₆	0, 29, 92, 121, 127, 181, 193, 195, 207
YbCl ₃	³ F _{7/2}	0, 50, 185, 401
LuCl ₃	¹ S ₀	0

early along the series due to the lanthanide contraction with almost no difference between the two crystal structures, whereas V_m of the lanthanide trichlorides shows a distinct difference between the hexagonal and the monoclinic compounds.

The data shown in fig. 10 are not the values reported by Gorbunov et al. (1986) and Tolmachev et al. (1987, 1990a, 1990b, 1990c), because they did not extrapolate their measurements to 0 K in all cases. To derive S° (298.15 K) we have assumed that the heat capacity of LuCl₃ represents the lattice component, and S_{lat} at the lower temperature limit is derived from the results for this compound. The excess contribution at this temperature is calculated from the crystal field energies (see table 5) derived from spectroscopic studies of the ions in transparent host crystals (Dieke et al., 1968; Morrison and Leavitt, 1982;

Carnall, 1982). The 'experimental' standard entropy values thus obtained for the monoclinic lanthanide trichlorides are listed in table 4.

The entropies for those compounds for which no experimental data have been reported (CeCl_3 , PmCl_3 , TbCl_3) are calculated according to the method outlined for the trifluorides. The lattice component has been derived from linear interpolation between LaCl_3 and GdCl_3 for the hexagonal compounds and a parallel relation fitted to the LuCl_3 value for the monoclinic compounds. The excess entropies have been calculated from the energy levels of the Ln^{3+} ions. The calculated values for the standard entropy at 298.15 K (S_{tot}) are in good agreement with the calculated values obtained from the sum of the lattice and excess contribution at 298.15 K, as shown in table 3. Because there is only one 'reference' point for the lattice contribution in the monoclinic series (LuCl_3), the trend along this series is assumed to have the same slope as the hexagonal trichlorides.

3.3. LnBr_3 and LnI_3

Only a few low-temperature heat capacity measurements have been reported for the lanthanide tribromides and triiodides. Deline et al. (1975) measured the low-temperature heat capacity of EuBr_3 , Gavrichev et al. (1992) of LuI_3 . These data are insufficient to derive the lattice component as was done for the trifluorides and the trichlorides. In addition, few data on the crystal field levels for the bromides and iodides are available (Morrison and Leavitt, 1982). A number of assumptions thus had to be made. Figure 12 shows that the trends in the molar volume of the LnBr_3 and LnI_3 series indicate two groups, as is the case for the trichlorides. We therefore conclude that the entropies of the two groups must be derived separately. The lattice entropies of the tribromides in the La–Eu series are obtained by subtracting S_{exs} from the measurements for EuBr_3 and these values are used to approximate S_{lat} , assuming that this quantity will vary regularly through the orthorhombic and hexagonal series. An estimated slope for the relation of S_{lat} versus atomic number dependence was used. The same was done for rhombohedral triiodides using the experimental value for LuI_3 . The lattice entropy of the rhombohedral tribromides and the orthorhombic triiodides have been derived by an extrapolation of the experimental values for the lanthanum (including the value for LaBr_3 obtained indirectly from the experimental value of EuBr_3) and lutetium trihalides, as shown in fig. 13. The entropies of these compounds correlate perfectly with the logarithm of the molecular weight of the halide ion. The crystal field levels in the tribromides and triiodides are assumed to be the same as in the trichlorides, which can be justified by the experimental data for PrBr_3 ,

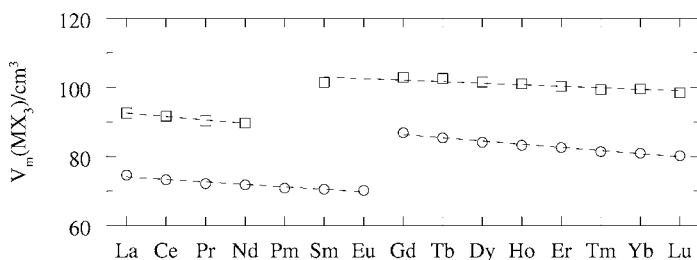


Fig. 12. The molar volumes in the LnBr_3 (○) and LnI_3 series (□) at 298.15 K.

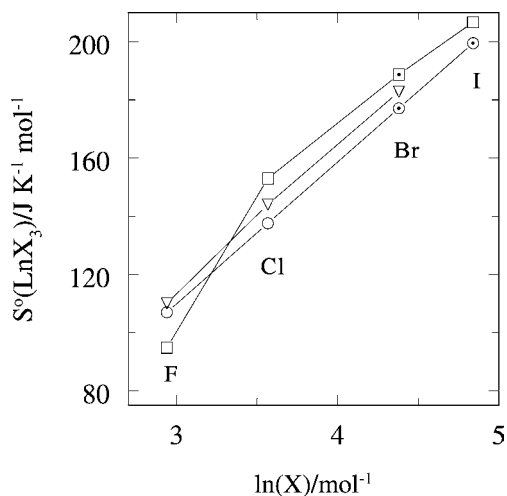


Fig. 13. The standard molar entropy as a function of the logarithm of the molecular weight of the halide atom $\ln(M)$; LaX_3 (\circ), LuX_3 (\square) and EuX_3 (∇); estimated values are indicated by \odot and \square .

NdBr_3 and ErBr_3 doped in LaBr_3 as given by Morrison and Leavitt (1982). The entropy data thus obtained are summarised in table 6.

4. High-temperature heat capacity of the solid trihalides

4.1. LnF_3

Enthalpy increment measurements to derive the high-temperature heat capacity have been reported for all lanthanide trifluorides except PmF_3 , as summarised in table 7. The results of the various authors are compared using the reduced enthalpy increment function:

$$\left\{ H^\circ(T) - H^\circ(298.15 \text{ K}) \right\} / (T - 298.15). \quad (8)$$

Figure 14 shows a plot of this function for LaF_3 . It can be seen that the data for the enthalpy increment by Spedding and Henderson (1971) and Lyon et al. (1978) are in good

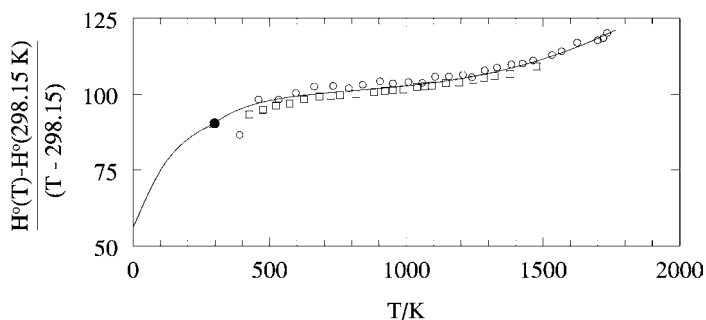


Fig. 14. The reduced enthalpy increment of LaF_3 (in $\text{J}\cdot\text{K}^{-1}\cdot\text{mol}^{-1}$); \circ , Henderson (1970); \square Lyon et al. (1978); \bullet , value at 298.15 K derived from the low-temperature heat capacity measurements of Lyon et al. (1978).

Table 6
The entropies of the solid lanthanide(III) bromides and iodides at 298.15 K, in $\text{J}\cdot\text{K}^{-1}\cdot\text{mol}^{-1}$

	Calculated			Experimental ^a	
	S_{lat}	S_{exs}	S_{tot}	S_{exp}	References
LaBr ₃	177.1	0.00	177.1	–	
CeBr ₃	176.5	14.71	191.2	–	
PrBr ₃	175.9	17.87	193.8	–	
NdBr ₃	175.3	18.30	193.6	–	
PmBr ₃	174.7	17.89	192.6	–	
SmBr ₃	174.1	15.27	189.4	–	
EuBr ₃	173.5	9.32	182.8	182.8	1
GdBr ₃	191.7	17.29	209.0	–	
TbBr ₃	191.1	21.15	212.3	–	
DyBr ₃	190.5	22.83	213.4	–	
HoBr ₃	189.9	23.16	213.1	–	
ErBr ₃	189.6	22.60	212.2	–	
TmBr ₃	189.3	20.84	210.2	–	
YbBr ₃	189.0	15.80	204.8	–	
LuBr ₃	188.7	0.00	188.7	–	
LaI ₃	196.3	0.00	196.3	–	
CeI ₃	195.7	14.71	210.4	–	
PrI ₃	195.1	17.87	213.0	–	
NdI ₃	194.5	18.30	212.8	–	
PmI ₃	212.7	17.89	230.6	–	
SmI ₃	212.1	15.27	227.4	–	
EuI ₃	212.5	9.32	220.8	–	
GdI ₃	210.9	17.29	228.2	–	
TbI ₃	210.3	21.15	231.5	–	
DyI ₃	209.7	22.83	232.5	–	
HoI ₃	209.1	23.16	232.3	–	
ErI ₃	208.5	22.60	231.1	–	
TmI ₃	207.9	20.84	228.7	–	
YbI ₃	207.3	15.80	223.1	–	
LuI ₃	206.7	0.00	206.7	206.7	2

^aThe uncertainty for the standard entropies derived from the calorimetric measurements has not been given in some cases.

References

1. Deline et al. (1975)

2. Gavrichev et al. (1992)

agreement, with the exception of the lowest data point of the former authors. The high-temperature results also reasonably fit the low-temperature results by Lyon et al. (1978). The combined results have been fitted to a polynomial equation, applying as boundary conditions $\{H^\circ(T) - H^\circ(298.15 \text{ K})\} = 0$ at 298.15 K and $C_p(298.15 \text{ K}) = 90.29 \text{ J}\cdot\text{K}^{-1}\cdot\text{mol}^{-1}$, as followed from the low-temperature measurements. The coefficients of the polynomial are given in table 8. The data for the other trifluorides have been evaluated in a similar way, and the results are also listed in table 8. The values for $C_p(298.15 \text{ K})$ of those compounds for which no

Table 7
Summary of the enthalpy increment measurements for the lanthanide trifluorides

compound	T/K	number of data points	References
LaF ₃	390–1831	33	1
	425–1477	23	2
CeF ₃	398–1799	19	3
	575–1373	9	4
	400–1899	20	5
PrF ₃	390–1831	30	1
	727–1243	6	4
NdF ₃	390–1831	31	1
	727–1324	9	4
SmF ₃	400–1887	23	5
EuF ₃	400–1252	?	5
GdF ₃	390–1831	27	1
	576–1249	8	4
	400–1803	?	5
TbF ₃	400–1793	?	5
DyF ₃	577–1173	7	4
	400–1744	?	5
HoF ₃	390–1831	27	1
	432–1588	63	6
ErF ₃	400–1841	21	5
TmF ₃	400–1794	?	5
YbF ₃	577–1175	7	4
	400–1731	?	5
LuF ₃	390–1831	30	1

References

1. Spedding and Henderson (1971)
2. Lyon et al. (1978)
3. King and Christensen (1959)
4. Charlu et al. (1970)
5. Spedding et al. (1974)
6. Lyapunov et al. (2000)

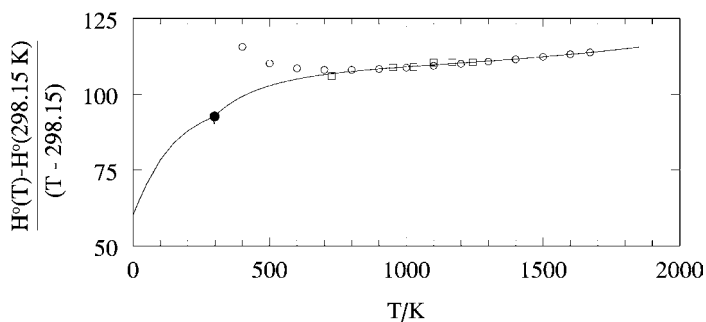


Fig. 15. The reduced enthalpy increment of PrF₃ (in J·K⁻¹·mol⁻¹); o, Henderson (1970); □ Charlu et al. (1970); ●, value at 298.15 K derived from the low-temperature heat capacity measurements of Lyon et al. (1979a).

low-temperature measurements have been reported are calculated from the sum of the lattice and excess contributions (eq. (1)).

For most compounds there is good agreement between the various data sets, although the results of Henderson (1970), Spedding and Henderson (1971), that were reported as poly-

Table 8
Recommended high temperature heat capacity functions for the solid lanthanide trifluorides

compound	$C_p(298.15 \text{ K})$ /kJ·mol ⁻¹	$C_p^\circ(T)/\text{J} \cdot \text{K}^{-1} \cdot \text{mol}^{-1} = a + bT + cT^2 + dT^3 + eT^{-2}$					T_{max} /K	$\Delta_{\text{trs}}H^\circ$ /kJ·mol ⁻¹
		a	$b \times 10^3$	$c \times 10^6$	$d \times 10^9$	$e \times 10^{-6}$		
LaF ₃	90.29 ± 0.09	122.1188	-22.4674	-16.3094	28.1746	-2.17138	1766	
CeF ₃	93.47 ± 0.09	103.2577	-12.9896	24.6881		-0.72087	1703	
PrF ₃	92.65 ± 0.09	130.5994	-32.5026	18.1689		-2.65559	1670	
NdF ₃	92.42 ± 0.09	103.3867	1.66688	10.3935		-1.10117	1649	
PmF ₃	92.0							
SmF ₃	hex	91.7	169.0564	-7.6809		-4.84076	743	1.784
			297.1925	-370.3989	189.2022			1571
EuF ₃	hex	97.9	117.4275			-1.73589	973	8.714
			150.6658					1549
GdF ₃	hex	88.39 ± 0.09	102.3403	6.0945		-1.40162	1347	6.029
			130.834					1501
TbF ₃		90.5	97.5769	19.8845		-1.15610	1446	
DyF ₃		88.94 ± 0.09	91.2338	28.2118	-3.1553	-0.926687	1426	
HoF ₃		88.6	131.7639	-65.0032	44.2500	-2.46383	1416	
ErF ₃	orth	90.07 ± 0.09	121.3374	-30.3149	22.7317	-2.15564	1388	29.47
			135.0177					1413
TmF ₃	orth	90.8	115.6209	-17.1827	12.9143	-1.85306	1325	30.28
			97.8638					1431
YbF ₃	orth	89.4	103.7012	9.2366		-1.51608	1267	24.46
			119.5369					1435
LuF ₃	orth	87.07 ± 0.09	89.0368	19.2857		-0.68598	1230	25.07
			121.7126					1455

nomial equations only, tend to deviate at low temperatures in several of their measurements. This is evident in their tables which show a minimum in C_p around 500–600 K in those cases (e.g., fig. 15). It is very likely caused by small errors which are amplified at low temperatures by the non-constrained fitting procedure they used. In these cases the lowest temperature results have been omitted from our polynomial fitting. Only for GdF₃ and HoF₃ the reported data are discordant. The results of Charlu et al. (1970), Spedding and Henderson (1971) and Spedding et al. (1974) for GdF₃ are significantly different. Since only the latter results agree well with the low-temperature heat capacity, they have been selected here. For HoF₃ the situation is less clear. The results of Spedding and Henderson (1971) and Lyapunov et al. (2000) agree reasonably at low temperature, but the difference systematically increases with increasing temperature. The reason for this is unclear. We have preferred the results of Spedding and Henderson (1971) as their measurements on the other lanthanide trifluorides have proved to be highly reliable.

In analogy with the approach that has been described in the section on the low-temperature heat capacity, the high-temperature heat capacity of the LnX_3 compounds can be described as the sum of the lattice and excess contributions (eq. (1)). However, whereas at low temperature the lattice heat capacity mainly arises from harmonic vibrations, at high temperatures the effects of anharmonicity of the vibrations, of thermal dilation of the lattice and of thermally

induced vacancies in the lattice heat capacity have to be taken into account:

$$C_{\text{lat}} = C_{\text{har}} + C_{\text{anh}} + C_{\text{dil}} + C_{\text{vac}}. \quad (9)$$

According to theory, the molar harmonic contribution approaches the limit of $3R$ per atom, which corresponds to $12R$ for MX_3 compounds. Figure 14 shows that the heat capacity of LaF_3 reaches this value around 900–1000 K but then increases strongly above 1100 K, an effect that is not seen very evident in any other lanthanide trifluoride (e.g., PrF_3 in fig. 15). Lyon et al. (1978) attributed this effect to the contribution of C_{vac} , and suggested that this contribution can amount to about $60 \text{ J}\cdot\text{K}^{-1}\cdot\text{mol}^{-1}$ near the melting point. An alternative/additional and more likely explanation can be found in the observations of Greis and Cader (1985) that the hexagonal/trigonal lanthanide trifluorides undergo a λ -type second order transition before melting, whose effect is strongest for LaF_3 and becomes much weaker going from CeF_3 to EuF_3 .

4.2. LnCl_3

The high-temperature heat capacity data for the lanthanide trichlorides are limited. Walden and Smith (1961) measured the enthalpy increment of CeCl_3 , and Dworkin and Bredig (1971) determined the enthalpy increments of GdCl_3 , TbCl_3 , DyCl_3 , and HoCl_3 by drop calorimetry. Gaune-Escard et al. (Gaune-Escard et al., 1996; Rycerz and Gaune-Escard, 2002a, 2002b) measured the heat capacity of a selected number of compounds by differential scanning calorimetry (DSC). Only in some cases (CeCl_3 , GdCl_3 , DyCl_3) a comparison can be made between these studies and the agreement with the low-temperature heat capacity data checked. In fig. 16 the results for GdCl_3 are compared in a plot of the reduced enthalpy increment, which shows that the low-temperature data of Sommers and Westrum Jr. (1976) and the high-temperature data of Dworkin and Bredig (1971) are in excellent agreement. Also the results of Gaune-Escard et al. (1996) agree well, although they indicate a somewhat different slope of the curve. Figure 17 compares the results for LaCl_3 of Gaune-Escard et al. (1996) again with the low-temperature data of Sommers and Westrum Jr. (1977), but also with the DSC data by Reuter and Seifert (1994). For this compound the results of Gaune-Escard et al. (1996) are significantly lower than those of the other two studies, which agree very well.

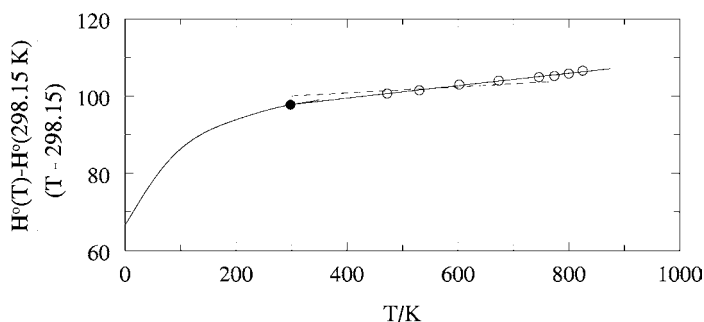


Fig. 16. The reduced enthalpy increment of GdCl_3 (in $\text{J}\cdot\text{K}^{-1}\cdot\text{mol}^{-1}$); ●, Sommers and Westrum Jr. (1977); ○, Dworkin and Bredig (1971); broken line, Gaune-Escard et al. (1996).

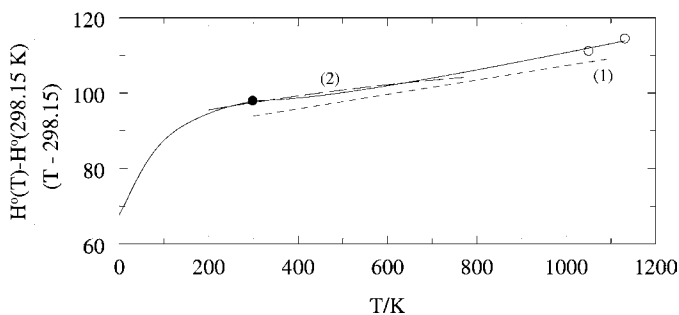


Fig. 17. The reduced enthalpy increment of LaCl_3 (in $\text{J}\cdot\text{K}^{-1}\cdot\text{mol}^{-1}$); ●, Sommers and Westrum Jr. (1976); ○, Dworkin and Bredig (1963a); broken line (1), Gaune-Escard et al. (1996); broken line (2), Reuter and Seifert (1994).

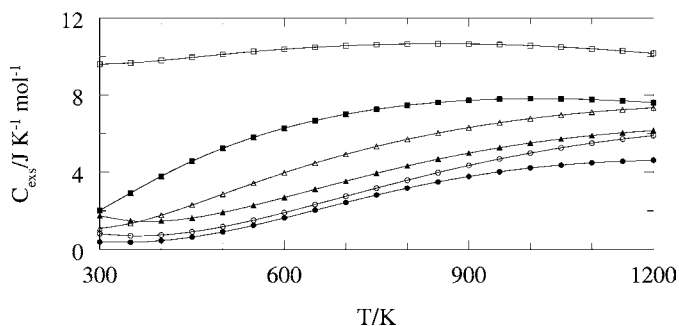


Fig. 18. The excess heat capacity in LnCl_3 compounds; ●, CeCl_3 ; ○, PrCl_3 ; ▲, NdCl_3 ; △, PmCl_3 ; ■, SmCl_3 ; □, EuCl_3 .

It is important to note that the curves for LaCl_3 and GdCl_3 , both of which do not have an electronic excess term due to the stable f^0 and f^7 electron configurations, are almost identical below 1000 K. This indicates that the lattice heat capacities in the hexagonal LnCl_3 compounds between these compounds hardly vary. We thus can obtain the high-temperature heat capacity by adding C_{exs} to the lattice curve of LaCl_3 or GdCl_3 . C_{exs} is calculated from the known energy levels for these compounds, where not only the ground state energy levels but also the excited states are taken into account. The latter values are not shown in table 2, but can be found in the review by Morrison and Leavitt (1982). Figure 18 shows the variation of C_{exs} with temperature for the compounds CeCl_3 to EuCl_3 . Figure 19 shows that the heat capacity of CeCl_3 thus obtained is in good agreement with the results of the enthalpy increment measurements by Walden and Smith (1961), whereas the heat capacity data reported by Gaune-Escard et al. (1996) are significantly lower. Similarly, fig. 20 shows that the calculated heat capacity of PrCl_3 is in much better agreement with the low-temperature data than the experimental results of Gaune-Escard et al. (1996). For the monoclinic lanthanide trichlorides for which no experimental data are available we have estimated the lattice heat capacity by subtracting C_{exs} from the values of DyCl_3 .

The recommended heat capacity equations for the lanthanide trichlorides are listed in table 9.

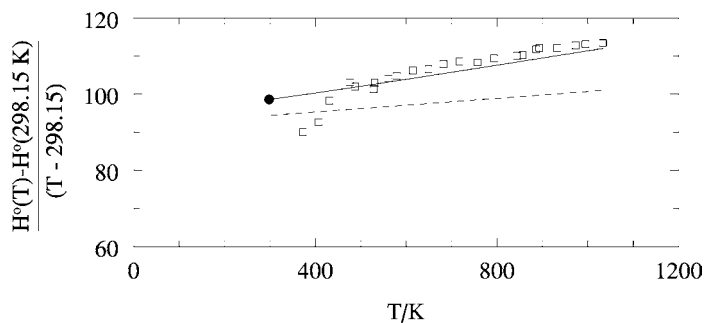


Fig. 19. The reduced enthalpy increment of CeCl_3 (in $\text{J}\cdot\text{K}^{-1}\cdot\text{mol}^{-1}$); \square , Walden and Smith (1961); \bullet , estimated C_p (298.15 K); broken line, Gaune-Escard et al. (1996); solid line, calculated from C_{lat} and C_{exs} .

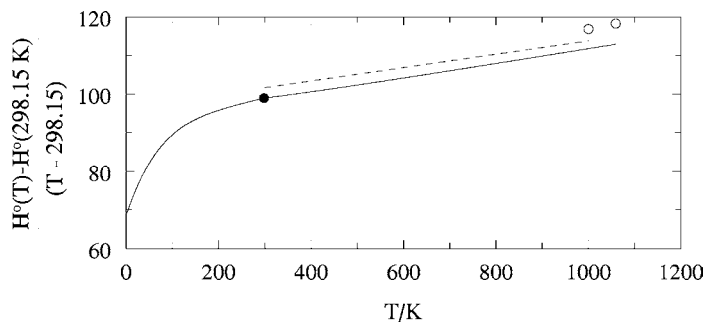


Fig. 20. The reduced enthalpy increment of PrCl_3 (in $\text{J}\cdot\text{K}^{-1}\cdot\text{mol}^{-1}$); \bullet , Sommers and Westrum Jr. (1976); \circ , Dworkin and Bredig (1963a); broken line, Gaune-Escard et al. (1996); solid line, calculated from C_{lat} and C_{exs} .

4.3. LnBr_3 and LnI_3

Dworkin and Bredig (1971) measured the enthalpy increments of the lanthanide tribromides CeBr_3 , NdBr_3 , GdBr_3 and HoBr_3 and triiodides LaI_3 , NdI_3 , GdI_3 and TbI_3 by drop-calorimetry. The heat capacity of LaBr_3 was measured by Rycerz and Gaune-Escard (1999a), that of TmI_3 by Gardner and Preston (1991) using differential scanning calorimetry. Low-temperature data have not been reported for these compounds. As mentioned above, such data are only available for EuBr_3 and LuI_3 . We have fitted the experimental enthalpy data to polynomial equations in the usual way, using estimated C_p (298.15 K) values as constraint. The latter were deduced from the low-temperature measurements by assuming a slight change in the lattice component along the series, as was observed for the trifluorides and trichlorides. This approach was preferred to a non-constrained fitting procedure as this normally results in too high C_p (298.15 K) values. For example, the unconstrained fit of CeBr_3 results in C_p (298.15 K) = $105.1 \text{ J}\cdot\text{K}^{-1}\cdot\text{mol}^{-1}$, whereas the estimated value is $101.9 \text{ J}\cdot\text{K}^{-1}\cdot\text{mol}^{-1}$.

The heat capacities for the other compounds were derived using the estimation procedure described for the trichlorides, i.e., from the lattice and excess contributions. The former was derived from the enthalpy measurements, the latter from the crystal field energies. As the crystal energies of the tribromides and triiodides are poorly known, we have used the values for the trichlorides to approximate C_{exs} . The results thus obtained are listed in tables 10 and 11. The calculated data for TmI_3 agree within 2% with the DSC results of Gardner and Preston (1991).

Table 9
High temperature heat capacity functions for the solid lanthanide trichlorides

compound	$C_p(298.15\text{ K})$ $/\text{J}\cdot\text{K}^{-1}\cdot\text{mol}^{-1}$	$C_p^\circ(T)/\text{J}\cdot\text{K}^{-1}\cdot\text{mol}^{-1} = a + bT + cT^2 + dT^3 + eT^{-2}$					T_{max} $/\text{K}$	$\Delta_{\text{trs}}H^\circ$ $/\text{kJ}\cdot\text{mol}^{-1}$
		a	$b \times 10^3$	$c \times 10^6$	$d \times 10^9$	$e \times 10^{-6}$		
LaCl ₃	98.03	74.9288	51.6544			0.68452	1133	
CeCl ₃	98.6	90.9772	35.8123			-0.27153	1090	
PrCl ₃	98.95	85.6511	39.5240			0.13465	1060	
NdCl ₃	99.24	87.2834	38.5855			0.04021	1032	
PmCl ₃	99.6							
SmCl ₃	99.54	95.3748	33.4442			0.56135	950	
EuCl ₃	106.98	100.9736	30.0922			-0.26362	894	
GdCl ₃	97.78	88.7959	31.4441			-0.03475	875	
TbCl ₃	orth	86.2920	38.5982				783	18.68
	?	123.930					855	
DyCl ₃	100.5	104.5279	-27.0190	45.3111			924	
HoCl ₃	101.9	100.3820	5.0913				993	
ErCl ₃	99.78	101.4247	-16.3266	36.2574			1049	
TmCl ₃	100.0	102.0423	-17.9564	37.2518			1095	
YbCl ₃	101.4	104.8985	-23.8396	40.6023			1138	
LuCl ₃	96.62	98.3259	-17.9501	41.0146			1198	

Table 10
High temperature heat capacity functions for the solid lanthanide tribromides

compound	$C_p(298.15\text{ K})$ $/\text{J}\cdot\text{K}^{-1}\cdot\text{mol}^{-1}$	$C_p^\circ(T)/\text{J}\cdot\text{K}^{-1}\cdot\text{mol}^{-1} = a + bT + cT^2 + dT^3 + eT^{-2}$					T_{max} $/\text{K}$	$\Delta_{\text{trs}}H^\circ$ $/\text{kJ}\cdot\text{mol}^{-1}$
		a	$b \times 10^3$	$c \times 10^6$	$d \times 10^9$	$e \times 10^{-6}$		
LaBr ₃	101.6	97.4736	17.9256			-0.10828	1061	
CeBr ₃	101.9	89.7173	31.6041			0.24534	1005	
PrBr ₃	102.3	93.6869	26.6878			-0.05833	965	
NdBr ₃	103.1	81.7525	42.7393			0.76491	955	
PmBr ₃	103.0							
SmBr ₃	103.1	103.2523	20.7015			-0.56223	913	
EuBr ₃	110.62 ± 0.11	100.8207	18.5433			0.37963	978	
GdBr ₃	100.2	93.8256	14.2533			0.18888	1043	
TbBr ₃	100.5	90.1490	22.3082			0.32889	1102	
DyBr ₃	100.4	92.3542	16.8413			0.26887	1152	
HoBr ₃	100.7	95.5581	15.5998			0.04363	1192	
ErBr ₃	100.7	94.3588	13.7789			0.19850	1196	
TmBr ₃	100.7	94.4929	13.6251			0.19066	1228	
YbBr ₃	101.8	96.5726	11.6884			0.15489	1250 ^a	
LuBr ₃	99.5	95.8694	12.1770				1298	

^aDecomposes before melting.

5. Enthalpy of formation of the solid trihalides

5.1. LnF_3

Three different methods have been used to determine the enthalpies of formation of the lanthanide trifluorides: fluorine combustion calorimetry, precipitation calorimetry and galvanic

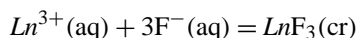
Table 11
High temperature heat capacity functions for the solid lanthanide triiodides

compound	$C_p(298.15 \text{ K})$ /J·K ⁻¹ ·mol ⁻¹	$C_p^\circ(T)/\text{J}\cdot\text{K}^{-1}\cdot\text{mol}^{-1} = a + bT + cT^2 + dT^3 + eT^{-2}$					T_{max} /K	$\Delta_{\text{trs}}H^\circ$ /kJ·mol ⁻¹
		a	$b \times 10^3$	$c \times 10^6$	$d \times 10^9$	$e \times 10^{-6}$		
LaI ₃	102.5	90.1970	27.5096			0.36456	1045	
CeI ₃	102.9	86.8928	35.1439			0.49150	1033	
PrI ₃	103.3	87.7509	34.7680			0.46074	1011	
NdI ₃	orth hex?	104.1	103.6598	-19.9550	52.6734	0.15179	859	13.53
			120.450				1059	
PmI ₃	104.5							
SmI ₃	104.1	100.9741	16.8259			-0.16808	1123	
EuI ₃	111.6	106.0620	14.0032			0.12116	1100 ^a	
GdI ₃	hex hex?	102.0	96.1164	13.1558		0.17434	1013	0.493
			128.189				1204	
TbI ₃	hex hex?	102.3	89.3082	27.8840		0.41585	1080	1.15
			124.334				1229	
DyI ₃	102.3	95.8785	14.3586			0.19028	1251	
HoI ₃	102.6	97.1180	12.2577			0.16244	1267	
ErI ₃	102.7	97.4364	11.7695			0.15597	1288	
TmI ₃	102.8	97.6703	11.4701			0.15200	1294	
YbI ₃	103.9	99.5694	9.6833			0.12832	1300 ^a	
LuI ₃	101.7 ± 0.3	95.6752	13.5944			0.17526	1323	

^aDecomposes before melting.

cell studies. Combustion calorimetry is the most reliable of these three, though it is very sensitive to impurities in the starting metals. It has been applied for most of the lanthanide trifluorides and the results originate essentially from two laboratories, Argonne National Laboratory (ANL) in the USA and Kyoto University in Japan. Unfortunately the agreement between these two laboratories is variable for those cases where a comparison of the results can be made. For GdF₃ and HoF₃ the results agree very well, but for ErF₃ they differ by ~ 25 kJ·mol⁻¹, and for NdF₃ by ~ 19 kJ·mol⁻¹, which is well beyond the possible contribution of impurities.

The precipitation measurements of the equilibrium:



are generally hindered by insufficient knowledge of the precipitated phase, which can be amorphous instead of crystalline. The EMF measurements are in principle very accurate but unwanted electrode reactions may affect the results. Tables B.1 to B.14 of Appendix B summarise the data collected and reviewed for the lanthanide fluorides and show that the agreement between the three techniques is indeed poor.

Several methods have been proposed to check and correlate the data for the LnF₃ compounds. A semi-empirical method was proposed by Kim and Johnson (1981) who used the Born-Landé equation to estimate the lattice energy U_{lat} :

$$U_{\text{lat}} = N_{\text{A}} Z_1 Z_2 e^2 A (1 - 1/n) / r_0, \quad (10)$$

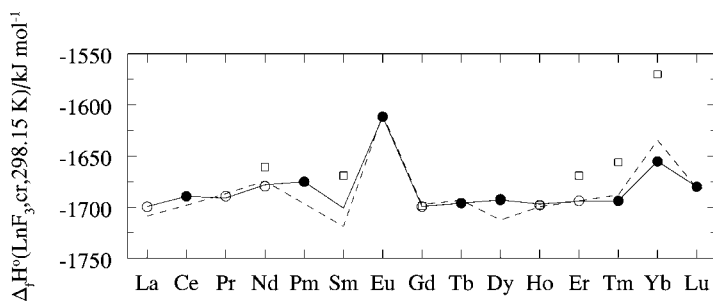


Fig. 21. The enthalpy of formation of the lanthanide trifluorides as a function of the atomic number. \circ and \square indicate the experimental results from fluorine combustion studies at ANL and Kyoto University, respectively; the broken curve shows the estimated values using the Born–Landé equation (Kim and Johnson, 1981); the solid curve shows the values estimated values in this study (\bullet).

where N_A is the Avogadro's constant, Z_1 and Z_2 are the oxidation numbers of the ions, e is the charge of a proton, A is the Madelung constant, n is the Born exponent and r_0 is the characteristic distance of the lattice. The values that were thus obtained agree well with those derived from a Born–Haber cycle using the experimentally determined $\Delta_f H^\circ$ (298.15 K) values. Thus the calculated U_{lat} values could be used to obtain the enthalpies of formation of those trifluorides for which no or no reliable data are available. They are compared to the experimental fluorine combustion results in fig. 21, which shows good agreement for the ANL results, but not for the majority of the results of the Kyoto University.

The trend of the $\Delta_f H^\circ$ along the LnF_3 shows little variation, with the exception of the values for EuF_3 and YbF_3 which are significantly less negative. This can be understood by looking at the Born–Haber cycle for the LnX_3 compounds (fig. 22). Because Eu and Yb are divalent elements whereas the others are trivalent, the ionisation step to form Ln^{3+} in the cycle is different for these two elements as the stable $4f^7$ and $4f^{14}$ configurations have to be broken up to form the $4f^6$ and $4f^{13}$ configurations (Gschneidner Jr., 1969). To eliminate this effect, Morss (1976) and Fuger et al. (1983) proposed to use the quantity

$$\Delta_f H^\circ(LnX_3, \text{cr}, 298.15 \text{ K}) - \Delta_f H^\circ(Ln^{3+}, \text{aq}, 298.15 \text{ K}) \quad (11)$$

to analyse the data for lanthanide compounds. They correlated this quantity with molar volume or ionic radius for the lanthanide and actinide trihalides. The relation with ionic radius is shown in fig. 23, using the enthalpies of formation of the aqueous ions from Cordfunke and Konings (2001a). It can be seen that the ANL results indicate two straight lines for the two crystallographic modifications (as is the case for the lanthanide trichlorides, tribromides and triiodides). The results of the Kyoto University (not shown in this figure) are widely scattered, whereas the values calculated by Kim and Johnson (1981) from the Born–Landé equation approximately agree with the trend, with strongly deviating values for SmF_3 , DyF_3 and YbF_3 . On the basis of these considerations we have based our recommended values (table 12) on the fluorine combustion data from ANL only, and have estimated the values for those compounds for which no data are available by inter- and extrapolation of the linear trends shown in fig. 23.

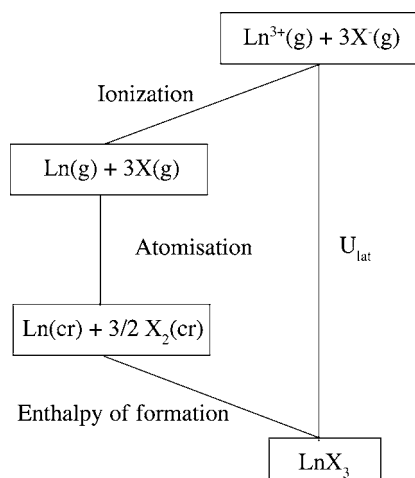
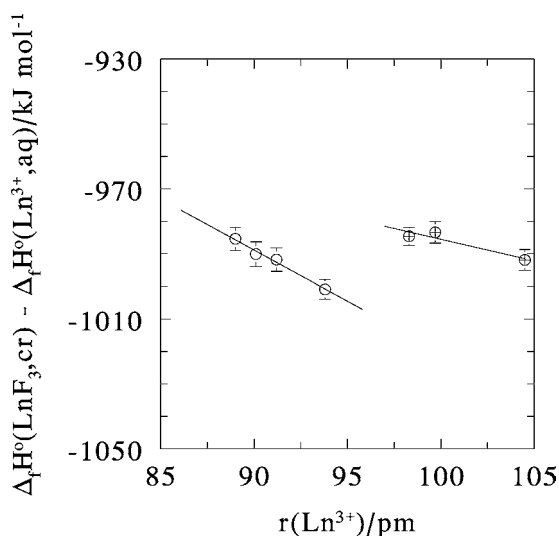


Fig. 22. The Born–Haber cycle for the lanthanide trihalides.

Fig. 23. The quantity $\Delta_f H^\circ(\text{LnF}_3, \text{cr}) - \Delta_f H^\circ(\text{Ln}^{3+}, \text{aq})$ as a function of the ionic radius (coordination number 6); ⊕, hexagonal and ○ orthorhombic structure.

5.2. LnCl_3 , LnBr_3 and LnI_3

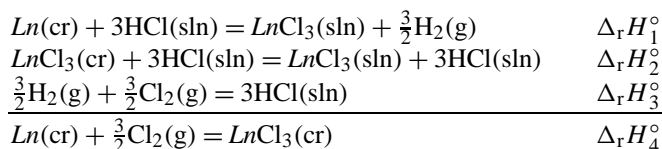
A careful review of all experimental data for the lanthanide chlorides, bromides and iodides, mainly made by solution calorimetry, has been made by Cordfunke and Konings (2001b) recently, who evaluated data from the literature between 1940 and 2000. The tables of this work are reproduced in Appendix B, corrected for some small errors. The present section summarises the justification of the selected values.

Two thermochemical reaction schemes are generally used to derive the enthalpies of formation of these compounds. The first is based on the dissolution of the lanthanide metal as well

Table 12
Selected enthalpies of formation of the solid lanthanide trihalides, in $\text{kJ}\cdot\text{mol}^{-1}$

	F	Cl	Br	I
La	-1699.5 ± 2.0	-1071.6 ± 1.5	-904.4 ± 1.5	-673.9 ± 2.0
Ce	-1689.2 ± 5.0	-1059.7 ± 1.5	-891.2 ± 1.5	-666.8 ± 3.0
Pr	-1689.1 ± 2.6	-1058.6 ± 1.5	-890.5 ± 4.0	-664.7 ± 5.0
Nd	-1679.4 ± 1.9	-1040.9 ± 1.0	-864.0 ± 3.0	-639.2 ± 4.0
Pm	-1675 ± 20	-1030 ± 10	-858 ± 10	-634 ± 10
Sm	-1700.7 ± 5.0	-1025.3 ± 2.0	-853.4 ± 3.0	-621.5 ± 4.0
Eu	-1611.5 ± 5.0	-935.4 ± 3.0	-759 ± 10	-538 ± 10
Gd	-1699.3 ± 2.3	-1018.2 ± 1.5	-838.2 ± 2.0	-624.1 ± 3.0
Tb	-1695.9 ± 5.0	-1010.6 ± 3.0	-843.5 ± 3.0	-623.8 ± 3.0
Dy	-1692.0 ± 1.9	-993.1 ± 3.0	-834.3 ± 2.5	-616.7 ± 3.0
Ho	-1697.8 ± 2.3	-997.7 ± 2.5	-842.1 ± 3.0	-622.9 ± 3.0
Er	-1693.6 ± 1.9	-994.4 ± 2.0	-837.1 ± 3.0	-619.0 ± 3.0
Tm	-1693.7 ± 5.0	-996.3 ± 2.5	-832 ± 10	-619.7 ± 3.5
Yb	-1655.1 ± 5.0	-959.5 ± 3.0	-791.9 ± 2.0	-578 ± 10
Lu	-1679.9 ± 5.0	-987.1 ± 2.5	-814 ± 10	-605.1 ± 2.2

as the lanthanide trihalide in hydrogen-saturated hydrochloric acid $\text{HCl}(\text{sln})$. The reaction scheme for the lanthanide trichlorides looks as follows:

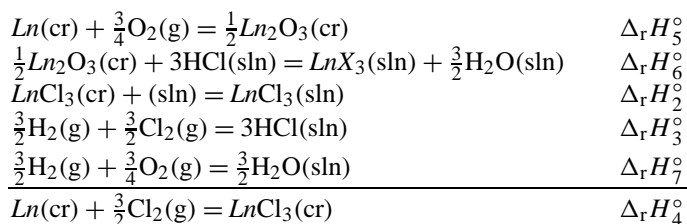


The standard molar enthalpy of formation of $\text{LnCl}_3(\text{cr})$ equals to $\Delta_{\text{r}}H_4^{\circ}$, and can be calculated as:

$$\Delta_{\text{f}}H^{\circ}(\text{LnCl}_3, \text{cr}, 298.15 \text{ K}) = \Delta_{\text{r}}H_1^{\circ} - \Delta_{\text{r}}H_2^{\circ} + \Delta_{\text{r}}H_3^{\circ}. \quad (12)$$

The value $\Delta_{\text{r}}H_3^{\circ}$ is the partial molar enthalpy of formation of $\text{HCl}(\text{sln})$ at the concentration given, and is calculated from the enthalpy of formation of the infinitely dilute acid (Cox et al., 1989), the enthalpy of formation of the HCl solutions (Parker et al., 1976) and the densities of the HCl solution at 298.15 K (Söhnel and Novotný, 1985), neglecting the influence of the lanthanide ion.

The second scheme involves the enthalpy of solution of the lanthanide sesquioxide and the lanthanide trihalide:



For this reaction sequence:

$$\Delta_f H^\circ(\text{LnCl}_3, \text{cr}, 298.15 \text{ K}) = \Delta_r H_5^\circ + \Delta_r H_6^\circ + \Delta_r H_3^\circ - \Delta_r H_7^\circ - \Delta_r H_2^\circ,$$

where $\Delta_r H_7^\circ$ is the partial enthalpy of formation of $\text{H}_2\text{O}(\text{sln})$ in hydrochloric acid. Only in case the enthalpy of formation of the sesquioxide is based on the combustion of the lanthanide metal, the two schemes are really independent.

For the calculation of the enthalpies of formation of the tribromides and triiodides, the same reaction cycles were used as for the trichlorides. However, as the halide ion in the compounds are different from those in the solution (e.g., LnI_3 in $\text{HCl}(\text{aq})$) the calculation of $\Delta_r H_3^\circ$ becomes a bit more complex as we have to deal with the ternary system $\text{H}_2\text{O}-\text{HCl}-\text{HX}$. In that case, it is assumed that the apparent enthalpy of formation of HI and HBr in HCl solutions are the same as in HBr and HI solutions of the same molality.

The results derived in this way by Cordfunke and Konings (2001b) are listed in tables B.1 to B.14 of Appendix B, the recommended values are given in table 12. For the trichlorides several studies have been reported for each compound, except, of course, PmCl_3 . The results quite well agree after recalculation, often with more recent enthalpies of solution of the metals. This is especially true for the results derived from the early measurements by Bommer and Hohmann (1941a, 1941b) which generally deviate significantly when the original value for the enthalpy of solution of the metal is used. This has been explained by the fact that the metals probably contained large fraction impurities, especially of potassium (Spedding and Miller, 1952). For the tribromides and triiodides the situation is less good. Often the number of studies is limited (e.g., for PrI_3 and SmI_3 only the measurements by Bommer and Hohmann (1941b)) or no measurements have been made (EuBr_3 , EuI_3 , TmBr_3 , YbI_3 and LuBr_3 , in addition to PmBr_3 and PmI_3).

In general one can conclude that the enthalpies of solution of the metals form the major source of uncertainty. Cordfunke and Konings (2001b) tried to overcome this by combining results from different sources and by inter- or extrapolation values as a function of the molarity, which was possible in some cases because accurate determinations of the enthalpy of solution as a function of molarity were performed by Merli et al. (1998). But in some cases (e.g., the cerium trihalides) the analysis heavily relies almost completely on a single measurement.

The variation of the enthalpies of formation of the trichlorides, tribromides and triiodides are shown in fig. 24. The general patterns is the same as observed for the trifluorides. Also for the trichlorides, tribromides and triiodides the variation of the quantity $\{\Delta_f H^\circ(\text{LnX}_3, \text{cr}, 298.15 \text{ K}) - \Delta_f H^\circ(\text{Ln}^{3+}, \text{aq}, 298.15 \text{ K})\}$ with the ionic radius has been examined, as shown in figs. 25 to 27. The results for the trichlorides clearly show a difference between the two crystallographic modifications, but for the tribromides and triiodides a difference is not very evident. The trends shown in figs. 25 to 27 have been used to estimate the enthalpies of formation of those compounds for which no or no reliable experimental data are available.

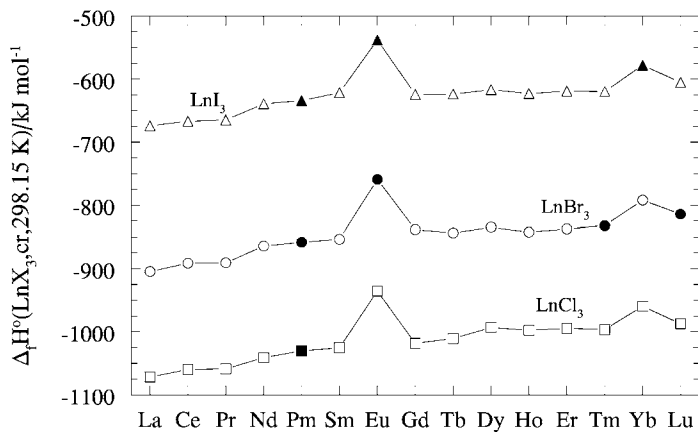


Fig. 24. The enthalpy of formation of the lanthanide trichlorides, tribromides and triiodides as a function of the atomic number. Estimated values are indicated by closed symbols.

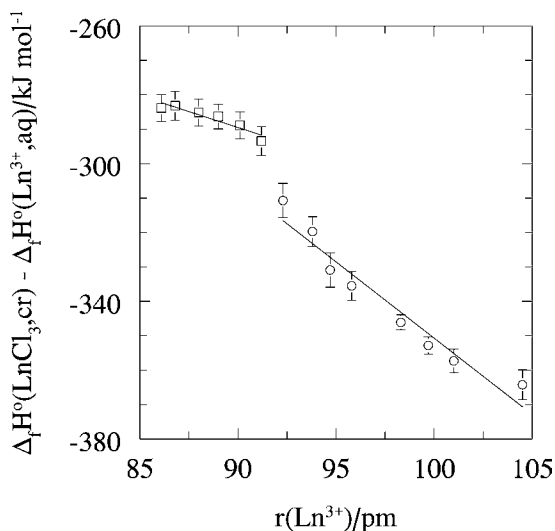


Fig. 25. The quantity $\Delta_f H^\circ(\text{LnCl}_3, \text{cr}) - \Delta_f H^\circ(\text{Ln}^{3+}, \text{aq})$ as a function of the ionic radius (coordination number 6); \square , monoclinic and \circ hexagonal structure.

6. Heat capacity of the liquid trihalides

6.1. LnF_3

The essential thermodynamic quantity for the liquid trihalides is the heat capacity, which in combination with the data for the solid phase gives the enthalpy/entropy of fusion. With these two quantities the Gibbs energy of the liquid phase can be calculated and extrapolated to the super-cooled state, if needed.

The enthalpy increment of the lanthanide trifluorides in the liquid phase has been measured for most compounds (see table 7). The heat capacity has been derived from these results by fitting them to a 2-term equation $\{H^\circ(T) - H^\circ(298.15 \text{ K})\} = a(T/\text{K}) + b$. In

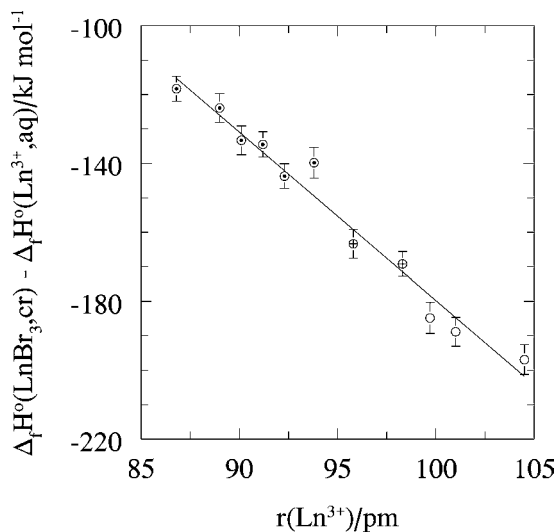


Fig. 26. The quantity $\Delta_f H^\circ(\text{LnBr}_3, \text{cr}) - \Delta_f H^\circ(\text{Ln}^{3+}, \text{aq})$ as a function of the ionic radius (coordination number 6); ○ hexagonal, ⊕, orthorhombic and ⊙ rhombohedral structure.

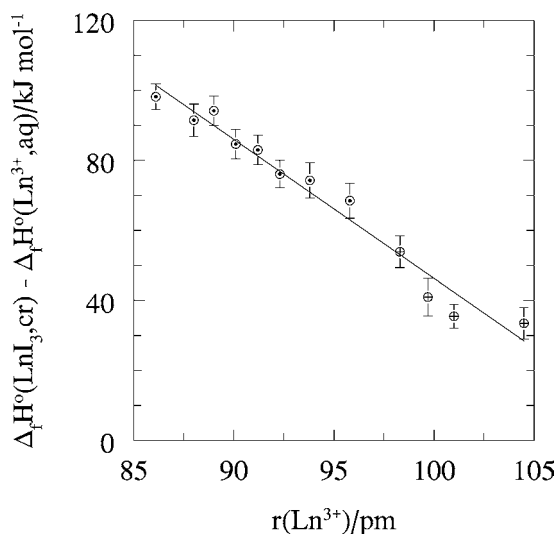


Fig. 27. The quantity $\Delta_f H^\circ(\text{LnI}_3, \text{cr}) - \Delta_f H^\circ(\text{Ln}^{3+}, \text{aq})$ as a function of the ionic radius (coordination number 6); ⊕, orthorhombic and ⊙ rhombohedral structure.

most cases a single set of data by Spedding and coworkers (Spedding and Henderson, 1971; Spedding et al., 1974) is available; only for CeF_3 and HoF_3 other measurements have been reported. For CeF_3 the results of King and Christensen (1959) and Spedding et al. (1974) are in excellent agreement, for HoF_3 the results of Spedding and Henderson (1971) and Lyapunov et al. (2000) disagree up to 6%. We have preferred the results of Spedding and Henderson (1971) for reasons given earlier.

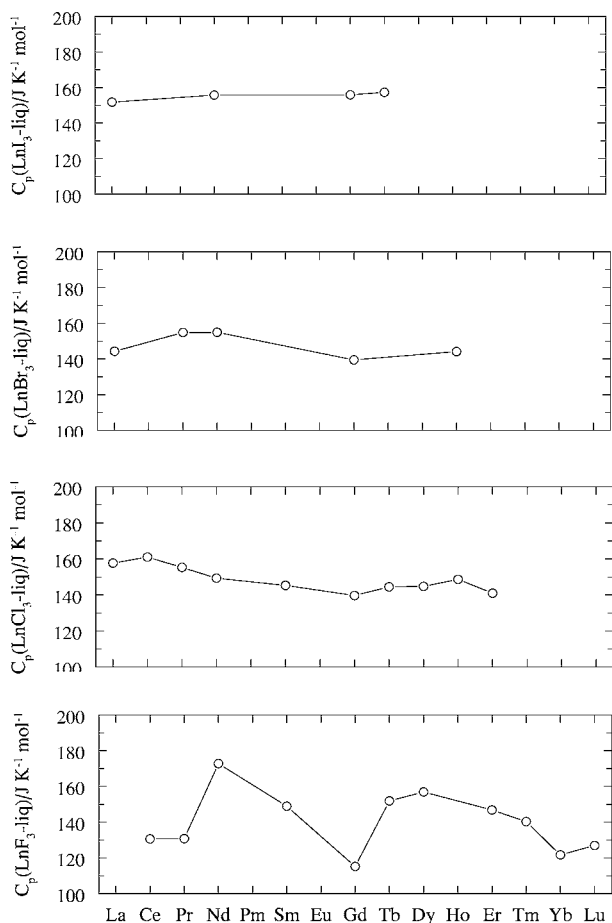


Fig. 28. The heat capacity of the liquid lanthanide trihalides.

Figure 28 shows the trend in the heat capacity of the lanthanide trifluorides. The irregular pattern indicates a large excess term for the compounds with a partially filled lanthanide ion *f*-shell, suggesting that this is of an electronic nature, which is consistent with the strong ionic nature of these liquids. Not shown in fig. 28 is the value for LaF₃ derived from the experimental results. It is unrealistically high: 330.07 J·K⁻¹·mol⁻¹. This is probably due to the fact that the experiments only cover a small temperature range (60 K) in which a post-melting effect cannot be excluded, especially in combination with the anomalous rapid increase already noted for the solid phase. Figure 28 shows that the trend in the lanthanide fluorides (and other trihalides) suggests a value of about 135 J·K⁻¹·mol⁻¹ for LaF₃.

The enthalpies of fusion that have been derived from the enthalpy increment equations for the solid and liquid phase are listed in table 13 and the derived entropies of fusion are plotted in fig. 29. It can be seen that the enthalpies and entropies of fusion for ErF₃ to LuF₃ are significantly lower than those of the other lanthanide trifluorides. Because these four compounds

Table 13
Enthalpy of fusion and heat capacity of the liquid phase for the lanthanide trifluorides

compound	T_{fus} /K	$\Delta_{\text{fus}}H^\circ$ /kJ·mol ⁻¹	$\Delta_{\text{fus}}S^\circ$ /J·K ⁻¹ ·mol ⁻¹	$\Delta V/V_{\text{cr}}^a$ /%	$C_p(\text{liq})$ /J·K ⁻¹ ·mol ⁻¹
LaF ₃	1766	55.87	31.51	29.14	135 ^b
CeF ₃	1703	56.52	33.19	32.92	130.61 ^{b,c}
PrF ₃	1670	57.28	34.30	29.13	130.76 ^b
NdF ₃	1649	54.75	33.20	30.78	172.82 ^b
PmF ₃	1605	53.4	33.3		160
SmF ₃	1571	52.43	33.37	25.58	148.94 ^d
EuF ₃	1549	52.9	34.2		130
GdF ₃	1501	52.44	34.94	25.81	115.20 ^b
TbF ₃	1446	58.44	40.41		151.91 ^d
DyF ₃	1426	58.42	40.97	25.35	156.92 ^d
HoF ₃	1416	56.77	40.09	26.57	135.02 ^b
ErF ₃	1413	27.51	19.47	28.37	146.83 ^d
TmF ₃	1431	28.90	20.20		140.32 ^d
YbF ₃	1435	29.74	20.73	29.99	121.70 ^d
LuF ₃	1455	29.27	20.12	31.95	126.94 ^b

^a $\Delta V = V_{\text{liq}} - V_{\text{cr}}$ where V_{liq} is the volume of the liquid phase at the melting point and V_{cr} the volume of the solid phase at room temperature. Data are taken from Kishenbaum and Cahill (1960), Kishenbaum and Cahill (1962) and Khairulin et al. (2000).

^bSpedding et al. (1974).

^cKing and Christensen (1959).

^dSpedding and Henderson (1971).

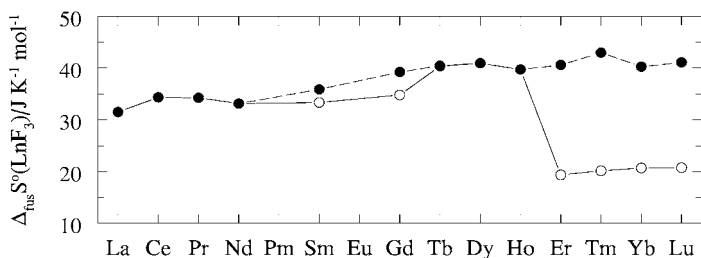


Fig. 29. The entropies of fusion (○) and the sum of the transition and fusion entropies (●) of the LnF_3 compounds.

undergo an orthorhombic to hexagonal transformation before melting, the sum of the transition and fusion entropies are plotted also. This quantity shows a steady but small increase along the lanthanide trihalide series, from which the enthalpies of fusion of PmF₃ and EuF₃ have been estimated.

6.2. $LnCl_3$

For the liquid lanthanide trihalides data from enthalpy-increment measurements and heat capacity (DSC) measurements are available, as summarised in table C.1 of Appendix C, the recommended values are given in table 14. The majority of the results have been reported by two

Table 14
Enthalpy of fusion and heat capacity of the liquid phase for the lanthanide trichlorides

compound	T_{fus} /K	$\Delta_{\text{fus}}H^\circ$ /kJ·mol ⁻¹	$\Delta_{\text{fus}}S^\circ$ /J·K ⁻¹ ·mol ⁻¹	$\Delta V/V_{\text{cr}}$ ^a /%	$C_p(\text{liq})$ /J·K ⁻¹ ·mol ⁻¹
LaCl ₃	1133	55.0 ^b	48.54	19.1	157.7 ^b
CeCl ₃	1090	53.6 ^c	49.17	18.0	161.05 ^c
PrCl ₃	1060	49.9 ^b	47.12	21.0	155.3 ^b
NdCl ₃	1032	49.2 ^b	47.67	21.8	149.5 ^b
PmCl ₃	994	48.7	49		147
SmCl ₃	950	47.6	50.1	24.5	144.4 ^d
EuCl ₃	894	45.0	50.3		142
GdCl ₃	875	40.6 ^b	46.40	26.4	139.7 ^b
TbCl ₃	855	19.5 ^b	22.80	21.0	144.47 ^b
DyCl ₃	924	25.5 ^b	27.75	0.3	144.77 ^b
HoCl ₃	993	32.6 ^b	32.83	1.3	148.67 ^b
ErCl ₃	1049	32.6 ^d	31.08	4.9	141.00 ^b
TmCl ₃	1095	35.6 ^d	32.51		141
YbCl ₃	1138	37.6	33		140
LuCl ₃	1198	39.5	33		141

^aData taken from Iwodate et al. (1995) and Wasse and Salmon (1999b).

^bDworkin and Bredig (1963a, 1963b, 1971).

^cWalden and Smith (1961).

^dGaune-Escard et al. (1994, 1996).

different research groups: Dworkin and Bredig (1963a, 1963b, 1971) using drop calorimetry and Gaune-Escard et al. (Gaune-Escard et al., 1996; Rycerz and Gaune-Escard, 2002a, 2002b) using differential scanning calorimetry. The early results of Dworkin and Bredig (1963a, 1963b) were reported without details and could not be recalculated, in contrast to the later results. In general, the reliability of the results of both studies is limited since the measurements cover small temperature ranges. For NdCl₃ and GdCl₃ the studied temperature range is larger than 50 K, and the agreement is excellent; for PrCl₃ and DyCl₃ it is less than 25 K for the DSC measurement and the agreement is poor.

The trend in the heat capacity of the lanthanide trichlorides is shown in fig. 28. It is clear that the variation in the values is much less pronounced than in case of the trifluorides, the (apparent) electronic excess term being small. This suggests that the structure of the liquid trichlorides is different, i.e., less ionic. The structure of the liquid trichlorides has been studied extensively in recent years (Iwodate et al., 1995; Wasse and Salmon, 1999a, 1999b; Hutchinson et al., 1999; Wasse et al., 2000) by X-ray and neutron diffraction. The results of these studies indeed show that intermediate range order exists in the liquid trichlorides through the formation of molecular species of the type $LnCl_n^{3-n}$ and eventually $Ln_2Cl_n^{6-n}$, yielding a loose ionic network. With decreasing cation size from La to Lu, the ionic character of the liquid reduces further, which is evidenced by the decrease of the electrical conductivity of the liquid trichlorides along the lanthanide series (Wasse and Salmon, 1999a).

As is shown in fig. 30 the variation in $C_p(\text{liq})$ of the hexagonal trichlorides can be correlated to the volume change between the solid (at room temperature) and the liquid: the heat

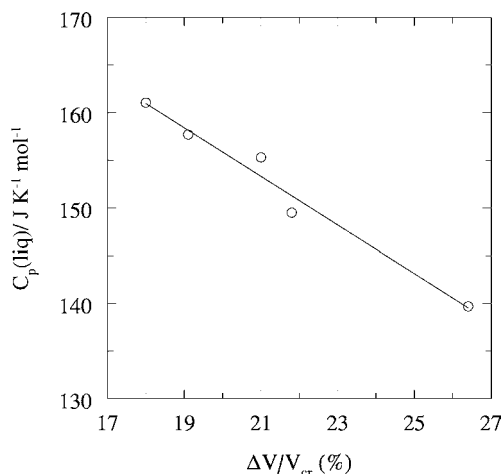


Fig. 30. The heat capacity of liquid lanthanide trichlorides as a function of the volume change $\Delta V/V_{cr}$.

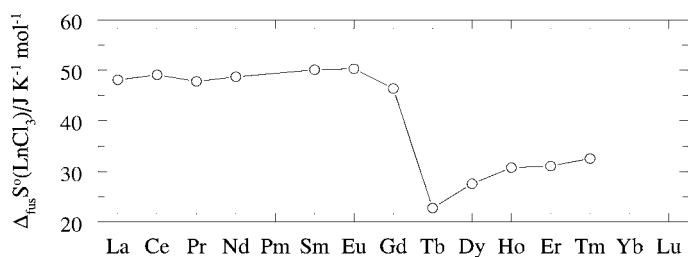


Fig. 31. The entropies of fusion of the $LnCl_3$ compounds.

capacity is low when the volume change is large, indicating that part of the variation in $C_p(\text{liq})$ arises from variation in C_{lat} . Thus the heat capacity of $SmCl_3$ is estimated from the known ΔV , that of $PmCl_3$ and $EuCl_3$ is interpolated. For the monoclinic trichlorides $DyCl_3$, $HoCl_3$ and $ErCl_3$ the volume change is quite small, which is due to the fact that these compounds undergo a solid-solid transformation before melting. The values for these compounds have been estimated from the trend suggested in fig. 28.

The entropies of fusion almost constant in the hexagonal $LnCl_3$ series $LaCl_3$ – $GdCl_3$, as shown in fig. 31. From this trend we estimate $\Delta_{fus} S^0 = 47\ J\cdot K^{-1}\cdot mol^{-1}$ for $PmCl_3$ and $SmCl_3$. In the series $TbCl_3$ to $TmCl_3$ the entropy of fusion increases towards a constant value $\Delta_{fus} S^0 = 33\ J\cdot K^{-1}\cdot mol^{-1}$ which we have taken for $YbCl_3$ and $LuCl_3$. This observation is not in agreement with the experimental DTA data by Goryushkin et al. (1990) who observed a steady increase from $TbCl_3$ to $LuCl_3$. We consider their data, however, not accurate enough.

6.3. $LnBr_3$ and LnI_3

There are only a few measurements of the heat capacity of the liquid tribromides and triiodides and most of them have been made by Dworkin and Bredig (1963a, 1963b, 1971) using drop calorimetry. Rycerz and Gaune-Escard (1999a) measured the heat capacity of $LaBr_3(l)$

Table 15
Enthalpy of fusion and heat capacity of the liquid phase for the lanthanide tribromides and triiodides

compound	T_{fus} /K	$\Delta_{\text{fus}}H^{\circ}$ /kJ·mol ⁻¹	$\Delta_{\text{fus}}S^{\circ}$ /J·K ⁻¹ ·mol ⁻¹	$\Delta V/V_{\text{cr}}^{\text{a}}$ /%	$C_{\text{p}}(\text{liq})$ /J·K ⁻¹ ·mol ⁻¹
LaBr ₃	1061	54.39 ^a	51.26		144.3 ^a
CeBr ₃	1005	51.88 ^a	51.62		149
PrBr ₃	965	47.28 ^a	48.94		154.8 ^a
NdBr ₃	955	45.61 ^a	47.76		154.92 ^a
PmBr ₃	930	48.6	52		155
SmBr ₃	913	47.5	52		149
EuBr ₃	978	50.9	52		144
GdBr ₃	1043	38.07	35.98		139.46 ^a
TbBr ₃	1102	41.9	38		144
DyBr ₃	1152	46.4 ^b	40.31		149
HoBr ₃	1192	50.21 ^a	41.98		149
ErBr ₃	1196	50.2	42		149
TmBr ₃	1228	51.6	42		149
YbBr ₃ ^c					
LuBr ₃	1298	51.8	42		144
LaI ₃	1045	55.45 ^a	53.26		151.77 ^a
CeI ₃	1033	51.88 ^a	50.22		155
PrI ₃	1011	53.14 ^a	52.56		155
NdI ₃	1059	40.94 ^a	38.66		155.74 ^a
PmI ₃	1090	43.6	40		155
SmI ₃	1123	47.2	42		155
EuI ₃ ^c					
GdI ₃	1204	53.97 ^a	44.83		155.85 ^a
TbI ₃	1229	57.48 ^a	46.77		157.50 ^a
DyI ₃	1251	56.5 ^b	45.16		155
HoI ₃	1267	57.0	45		155
ErI ₃	1288	58.0	45		155
TmI ₃	1294	58.2	45		155
YbI ₃ ^c					
LuI ₃	1323	59.5	45		155

^aDworkin and Bredig (1963b, 1971).

^bCordfunke and Booiij (1997).

^cDecomposes before melting.

in a very limited temperature range (1070–1090 K), obtaining a somewhat different value (151.12 J·K⁻¹·mol⁻¹). The results (fig. 28) show that the variation in $C_{\text{p}}(\text{liq})$ along the lanthanide series becomes less prominent going from F to I, indicating that the character becomes increasingly less ionic and more molecular. The heat capacity of the liquid tribromides have therefore been assumed to show a slight trend, those of the triiodides to be approximately constant (table 15).

The enthalpies of fusion of some hexagonal tribromides and orthorhombic triiodides have been measured by drop calorimetry (Dworkin and Bredig, 1963a, 1971). The en-

tries of fusion derived from these values is about $50 \text{ J}\cdot\text{K}^{-1}\cdot\text{mol}^{-1}$ for the first group, and $52 \text{ J}\cdot\text{K}^{-1}\cdot\text{mol}^{-1}$ for the second, except for NdI_3 . This compound, however, undergoes a solid state transition, as discussed before, and the sum of the entropies of transition and fusion is close ($54 \text{ J}\cdot\text{K}^{-1}\cdot\text{mol}^{-1}$). For the orthorhombic tribromides no experimental data are available, and we have assumed the entropy of fusion to be close to that of the isostructural triiodides. The few data for the hexagonal/rhombohedral tribromides suggest an increase with increasing atomic number, whereas the few data for the hexagonal/rhombohedral triiodides suggest a constant value. This may be an indication that the high temperature phase behaviour for GdBr_3 and TbBr_3 is more complex. It should be noted that Goryushkin and coworkers (Goryushkin and Poshevneva, 1992, 1996; Goryushkin et al., 1999; Poshevneva et al., 2002) reported enthalpies and entropies of fusion of LuI_3 , HoI_3 , ErI_3 , and SmI_3 that are very different ($\Delta_{\text{fus}}S^\circ = 22.6 \pm 3.0 \text{ J}\cdot\text{K}^{-1}\cdot\text{mol}^{-1}$ for SmI_3 , $18 \pm 4 \text{ J}\cdot\text{K}^{-1}\cdot\text{mol}^{-1}$ for HoI_3 , $23 \pm 2 \text{ J}\cdot\text{K}^{-1}\cdot\text{mol}^{-1}$ for ErI_3 and $82 \pm 20 \text{ J}\cdot\text{K}^{-1}\cdot\text{mol}^{-1}$ for LuI_3). But since the results for the trichlorides by the same authors are in poor agreement with other experimental determinations, they have not been considered for the recommended values.

7. Heat capacity of the gaseous trihalides

7.1. LnX_3 monomers

The thermodynamic functions of the gaseous lanthanide trihalides have been calculated using standard statistical thermodynamic methods which relate the functions C_p , S , and H to the molecular partition function Q (Lewis et al., 1961):

$$Q = \sum_i g_i e^{-\varepsilon_i/kT}, \quad (13)$$

where ε_i is the energy of state i , which has a statistical weight (degeneracy) g_i , k is the Boltzmann constant and T is the absolute temperature. Using the Bohr–Oppenheimer approximation, the energy can be described as the sum of the translational and the internal energies, the latter being the sum of the electronic, rotational and vibrational contributions. The total partition function thus becomes the product of the individual ones:

$$Q = q_{\text{trs}} \cdot q_{\text{elec}} \cdot q_{\text{vib}} \cdot q_{\text{rot}}. \quad (14)$$

The calculation of thermodynamic functions thus requires accurate knowledge of the molecular geometry, the electronic and vibrational energy levels of the gaseous molecules. The electronic levels of the gaseous LnX_3 molecules have not been determined experimentally, but are estimated from those of the Ln^{3+} ions measured in the crystal phase (Myers and Graves, 1977a). For the molecular geometry and vibrational properties experimental data are available, though incomplete for the whole LnX_3 family. For that reason the experimental data were extended by empirical estimates (Myers and Graves, 1977a) or by results from quantum chemical computations (Joubert et al., 1998) in previous thermodynamic compilations. In this section we will discuss the structural and vibrational properties to derive a consistent set of

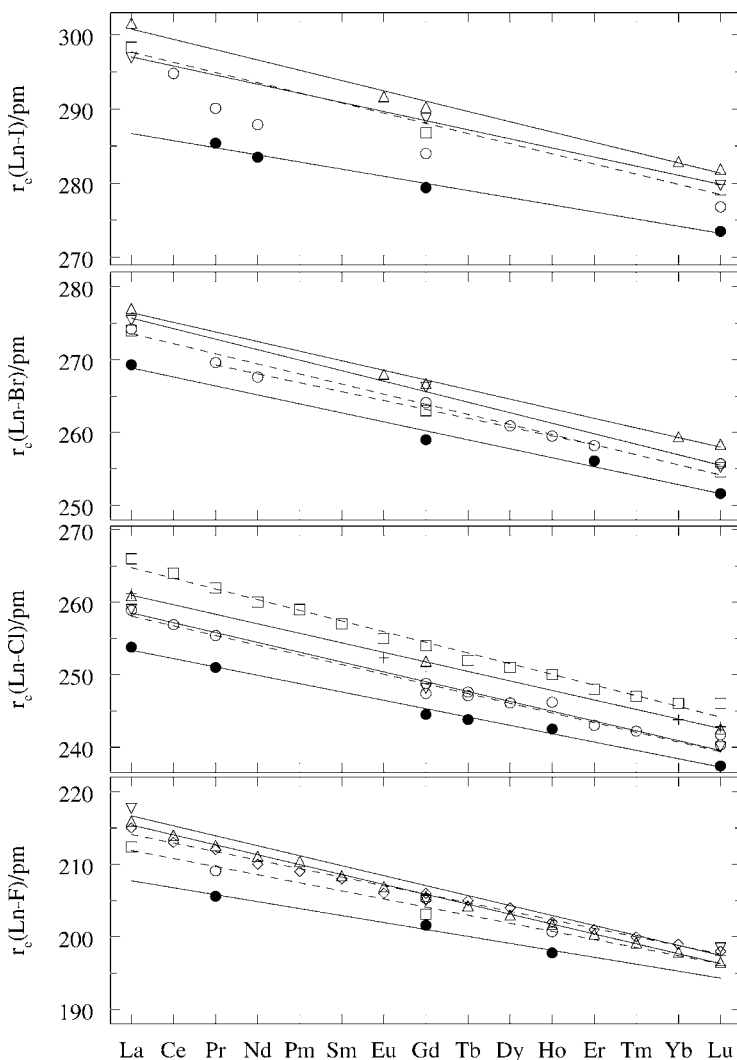


Fig. 32. The bond length of the lanthanide trihalides; ●, experimental values from ED (r_e); ○, experimental values from ED (r_g); □, Adamo and Maldivi (1998) for the BP-DS/TZ, TZd level; ◇ Joubert et al. (1998) at the MP2/ECP_D, VDZd level; △ Dolg et al. (1991) at the CISD + Q/ECP_Df, ECP_Dd level; ▽ Adamo and Maldivi (1998) at the B3P/ECP_S, ECP_Sd level. For details of the computations see original papers.

bond distances, bond angles and vibration frequencies for the thermodynamic calculations. For a more detailed analysis see the review by Kovács and Konings (2002).

The structure and vibrational spectra of the lanthanide trihalides have been studied extensively in the past decade. Due to the recent developments in the experimental and theoretical

Table 16

Ln-*X* equilibrium bond distances (pm)^a

<i>Ln</i>	<i>LnF</i> ₃	<i>LnCl</i> ₃	<i>LnBr</i> ₃	<i>LnI</i> ₃
La	207.7	253.4	268.9	286.7
Ce	206.8	252.2	267.6	285.7
Pr	205.8	251.1	266.4	284.8
Nd	204.9	249.9	265.2	283.8
Pm	203.9	248.8	263.9	282.9
Sm	202.9	247.6	262.7	281.9
Eu	202.0	246.5	261.5	280.9
Gd	201.0	245.3	260.3	280.0
Tb	200.1	244.2	259.0	279.0
Dy	199.1	243.0	257.8	278.1
Ho	198.1	241.9	256.6	277.1
Er	197.2	240.7	255.3	276.1
Tm	196.2	239.6	254.1	275.2
Yb	195.3	238.4	252.9	274.2
Lu	194.3	237.3	251.6	273.3

^aEstimated uncertainty ± 2 pm.

Table 17

X-*Ln*-*X* equilibrium bond angles (in degrees)^a

<i>Ln</i>	<i>LnF</i> ₃	<i>LnCl</i> ₃	<i>LnBr</i> ₃	<i>LnI</i> ₃
La	109.0	118.0	118.0	118.5
Ce	109.5	118.5	118.5	119.0
Pr	110.0	119.0	119.0	119.5
Nd	110.5	119.5	119.5	120.0
Pm	111.0	120.0	120.0	120.0
Sm	111.5	120.0	120.0	120.0
Eu	112.0	120.0	120.0	120.0
Gd	112.5	120.0	120.0	120.0
Tb	113.0	120.0	120.0	120.0
Dy	113.5	120.0	120.0	120.0
Ho	114.0	120.0	120.0	120.0
Er	114.5	120.0	120.0	120.0
Tm	115.0	120.0	120.0	120.0
Yb	115.5	120.0	120.0	120.0
Lu	116.0	120.0	120.0	120.0

^aEstimated uncertainty: for *LnF*₃: $\pm 4^\circ$; for the other halides: $\pm 2^\circ$.

methods the accuracy of the data has been improved considerably. Many early experimental data have been reanalysed, and numerous computations have been performed on some “popular” *LnX*₃ species. The latest experimental and theoretical data, reviewed recently by the present authors (Kovács and Konings, 2002),¹ confirmed previously suggested trends (Myers and Graves, 1977a) and facilitated the estimation of the missing data of the non-investigated molecules or to correct non-reliable earlier ones. Based on the recent experimental and computed results we can make more accurate predictions than obtained previously (Myers and Graves, 1977a; Jia and Zhang, 1988).

The available experimental data on the molecular geometries of the lanthanide trihalides are compiled in tables D.1 to D.4 of Appendix D. Equilibrium geometries (r_e , α_e) from electron diffraction (ED) experiments on 13 lanthanides trihalides have been reported by Zassorin (1988). More recent studies on lanthanide chlorides and bromides by Giricheva et al. (2000a, 2000b, 2000c, 2000d) and Zakharov et al. (2001) gave slightly shorter bond distances. The difference may arise from the neglect of the (small) dimer content of the vapour by Zassorin (Hargittai, 2000). However, the data from the two sources are close and agree within the given experimental errors.

The experimental and selected computed $r(\text{Ln}-X)$ bond lengths are presented in fig. 32. The most important trend that is obvious from the figure is the gradual decrease of $r(\text{Ln}-X)$ along the lanthanide row as a result of the well known “lanthanide contraction”. Although the computations indicate the same trend, they consistently overestimate the bond distances. The best probable values for the equilibrium geometrical parameters are given in tables 16 and 17. They take into account the opposite effects of dimer formation and the harmonic

¹ For earlier reviews on the topic see those of Hargittai (2000) (molecular structure) and Boghosian and Papatheodorou (1996) (vibrational frequencies).

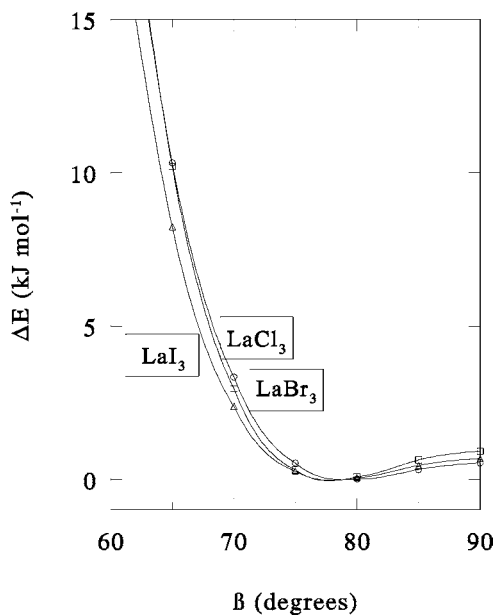


Fig. 33. The computed potential energy curves for the LaX_3 molecules (Kovács and Konings, 1997a); β is the angle between the La–X bond and the symmetry axis; \square , LaCl_3 ; \circ , LaBr_3 ; \triangle , LaI_3 .

approximation in the ED analysis, information on various trends, and the floppy nature of the LnX_3 molecules derived from quantum chemical computations. The latter property is the origin of the controversial results for the molecular symmetry of most LnX_3 species. Until recently (and apart from the early works) ED studies suggested a pyramidal C_{3v} structure for all the lanthanide trihalides (see Zasorin (1988) and references therein). On the other hand, less sophisticated quantum chemical calculations (Cundari et al., 1995; Di Bella et al., 1993) suggested a planar D_{3h} arrangement. The introduction of electron correlation and extended basis sets in the computations resulted generally (although not always) in a more pyramidal character of the LnX_3 species. An application of selectivity rules for the gas-phase IR spectra (Kovács and Konings, 1997a, 1997b) and the different symmetry number (3 for C_{3v} and 6 for D_{3h}) in thermodynamic calculations were not conclusive either.

Most of the recent experimental and computed results indicate a gradual increase of the X–Ln–X bond angle (towards the planar 120°) from F to I and from La to Lu.² This is in agreement with the decreasing polarizability of the ions along the lanthanide series and the weaker polarization abilities of the heavier halides. On the basis of the presently available results (Kovács and Konings, 2002) the LnF_3 halides are most probably pyramidal (C_{3v}), as considerable pyramidal character was obtained by both experiment and computations, and the ν_1 bands were found in the matrix-IR spectra. The absence of the ν_1 bands in the IR spectra (Kovács and Konings, 1997a, 1997b), analysis of the shrinkage effect in CeI_3 (Molnár et al., 1996) and the computed small inversion barriers for LaCl_3 , LaBr_3 and LaI_3 (fig. 33) imply a quasi-planar character for the trihalides of the light lanthanide elements. The most recent

² For a comprehensive overview of the earlier results see the paper by Molnár and Hargittai (1995).

experiments (Giricheva et al., 2000d, 2000c; Zakharov et al., 2001; Molnár et al., 1996) and sophisticated theoretical computations (Adamo and Maldivi, 1998; Adamo and Barone, 2000; Kovács, 2000; Solomonik and Marochko, 2000) indicate a D_{3h} symmetry of the trichlorides, tribromides and triiodides of the heavier lanthanides. The exact border between pyramidal and planar structures cannot be determined presently. It would require highly sophisticated calculations with (nearly) complete electron correlation treatment and saturated basis set.

The available experimental data on the molecular vibrations of lanthanide trihalides are compiled in tables D.1 to D.4 of Appendix D. Early gas-phase IR data on LaCl_3 , PrCl_3 , NdCl_3 , and GdCl_3 (Selivanov et al., 1973) have been extended recently by modern gas-phase Fourier-transform infrared measurements on several trichlorides and on the LaX_3 and DyX_3 ($X = \text{Cl, Br, I}$) series (Kovács and Konings, 1997a, 1997b; Groen, 2002), providing the first experimental information on the symmetric bending ν_2 frequencies of these compounds. They pointed out the error in interpretation of the early gas-phase IR spectra on NdX_3 ($X = \text{Cl, Br, I}$) halides by Wells Jr. et al. (1977). In addition, numerous measurements have been performed on matrix-isolated LnX_3 species using infrared spectroscopy (Hauge et al., 1971; Hastie et al., 1975; Wesley and DeKock, 1971; Bencze et al., 1996; Feltrin and Cesaro, 1996; Perov et al., 1975; Loktyushina and Mal'tsev, 1984; Loktyushina et al., 1987) and in few cases Raman spectroscopy (Lesiecki et al., 1972; Groen, 2002). The data on DyX_3 compounds (Groen, 2002) provided the first experimental information on the symmetric stretching ν_1 vibrations of the trichlorides, tribromides and triiodides. Note, that because of the high evaporation temperatures of LnF_3 compounds only vibrational data of the matrix-isolated species could be obtained hitherto (Hauge et al., 1971; Hastie et al., 1975; Wesley and DeKock, 1971; Bencze et al., 1996).

The experimental and selected computed vibrational frequencies of LnF_3 and LnCl_3 compounds are presented in figs. 34 and 35. The data show a gradually increase along the lanthanide row for all the four fundamentals. They confirm also the earlier linear relationship suggested by Myers and Graves (1977a) for estimation of the frequencies.

Our recommended values for the gas-phase vibrational frequencies are compiled in tables 18 to 21. Most of the estimated data have been derived from the available gas-phase and matrix-isolation vibrational spectra, the latter corrected for matrix-shifts. The LnF_3 compounds deserve a special attention, because for these compounds no reference gas-phase vibrational spectra are available. Hastie et al. (1975) used the relationship $\nu_g = \nu_{\text{Ne}} + (0.8 \pm 0.4)(\nu_{\text{Ne}} - \nu_{\text{Ar}})$ for the stretching frequencies suggested by Hastie et al. (1970), where ν_g is the gas-phase frequency. This formula is, however, not suited for general use as more recent experimental evidence indicates otherwise (see, e.g., the collected vibrational data by Hargittai (2000)). Furthermore, an excellent agreement is found between the gas-phase and Ar-matrix ν_3 frequencies for the LnCl_3 species, as shown in fig. 35. In fact, the clue for the estimation of the gas-phase stretching frequencies of LnF_3 compounds was provided by the computations. The overestimation of the $\text{Ln}-\text{F}$ bond at the most reliable BP-DS/TZ,TZd level (Adamo and Maldivi, 1998) was found to be similar to that of the $\text{Ln}-\text{Cl}$ bonds (cf. fig. 32), thus a similar systematic error for the LnF_3 and LnCl_3 stretching frequencies can also be expected.

For the LnF_3 bending fundamentals ν_4 and ν_2 the mean of the Ne-matrix and Ar-matrix frequencies by Hastie et al. (1975) was accepted. Assumptions had to be made for the ν_4

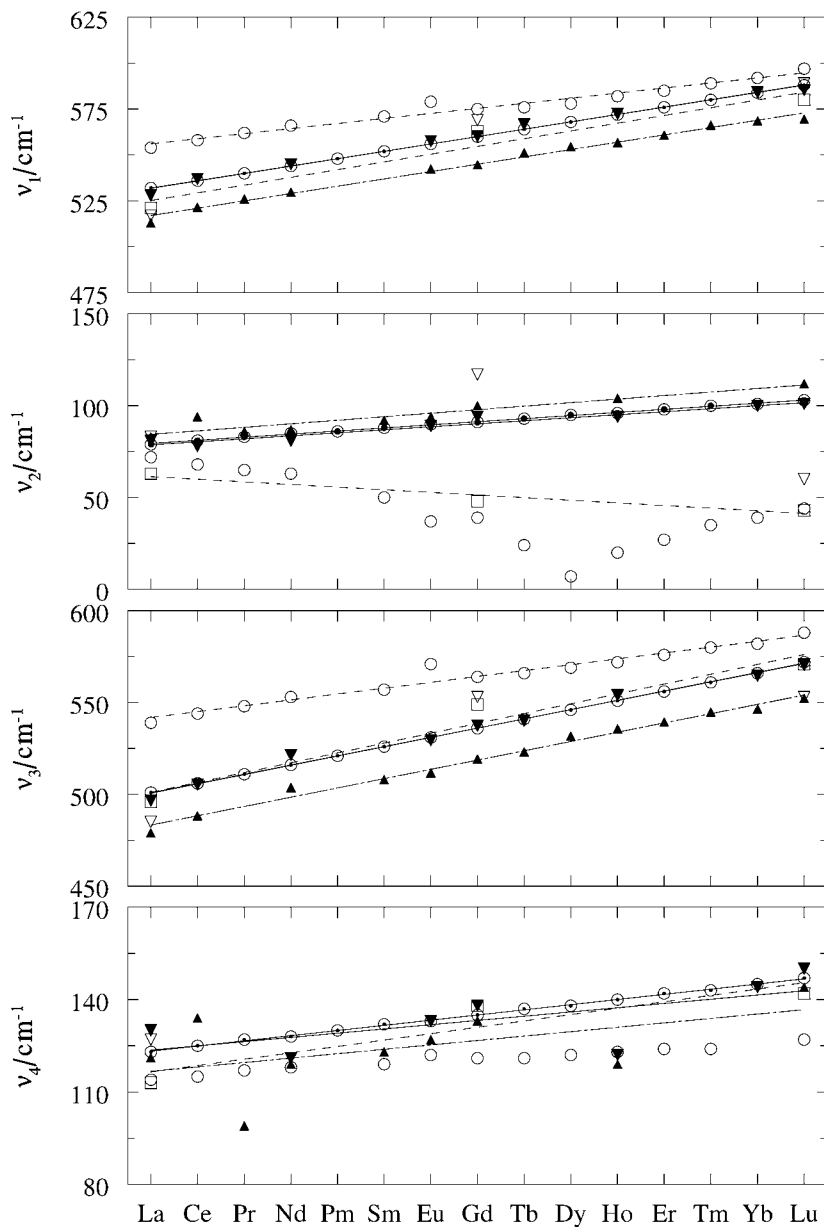


Fig. 34. The vibrational frequencies of the lanthanide trifluorides; \odot , recommended gas-phase frequencies; \blacktriangledown , experimental data for species isolated in neon matrix; \blacktriangle , in argon matrix; \square , Adamo and Maldivi (1998) at the BP-DS/TZ, TZd level; \circ Joubert et al. (1998) at the MP2/ECP_D, VDZd level; \triangle Dolg et al. (1991) for the CISD + Q/ECP_{Df}, ECP_{Dd} level; ∇ Adamo and Maldivi (1998) at the B3P/ECP_S, ECP_{Sd} level.

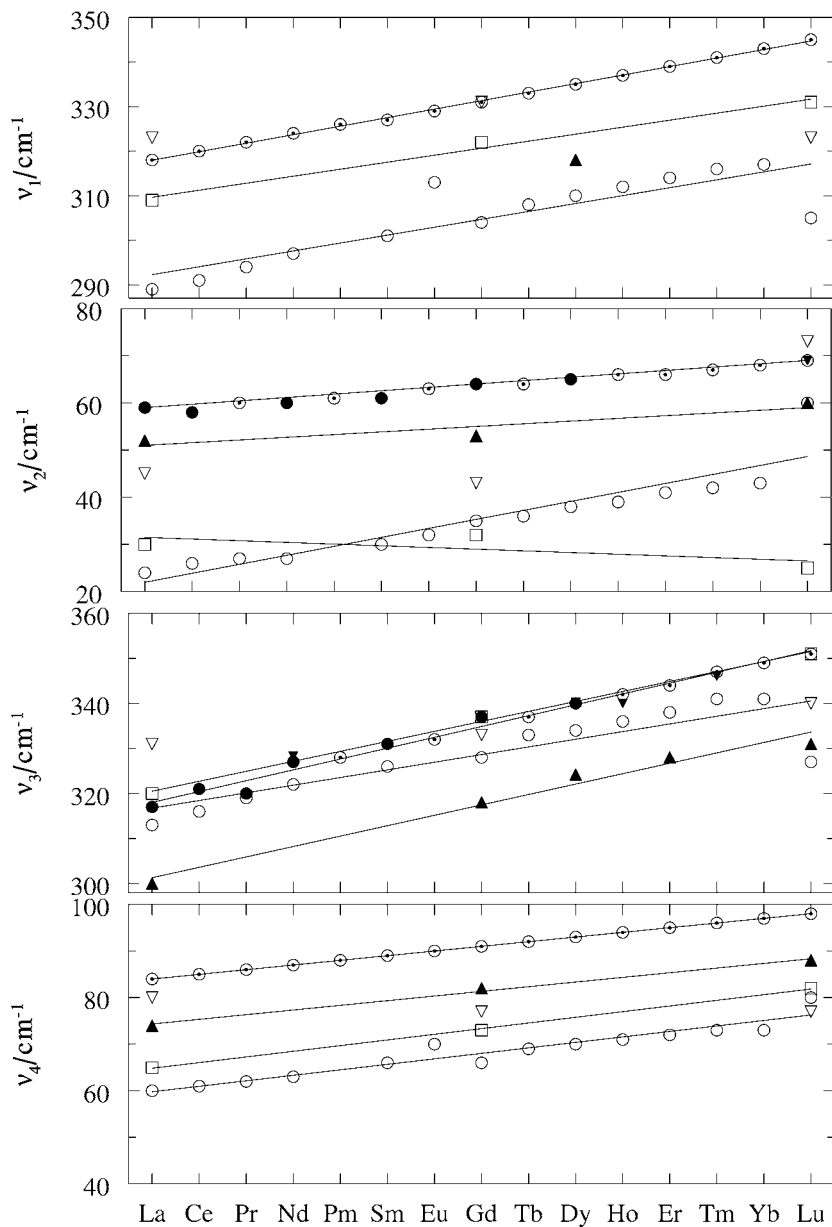


Fig. 35. The vibrational frequencies of the lanthanide trichlorides; ●, experimental gas-phase values; ▼, experimental data for species isolated in argon matrix; ▲, in xenon matrix; ○, estimated gas-phase values; □, Adamo and Maldivi (1998) at the BP-DS/TZ,TZd level; ◊ Joubert et al. (1998) at the MP2/ECP, VDZd level; △ Dolg et al. (1991) for the CISD + Q/ECPf, ECPd level; ▽ Adamo and Maldivi (1998) at the B3P/ECP, ECPd level.

Table 18
Vibrational frequencies (cm^{-1}) for LnF_3 molecules^a

<i>Ln</i>	$\nu_1(A_1)$	$\nu_2(A_1)$	$\nu_3(E)$	$\nu_4(E)$
La	532	79	501	123
Ce	536	81	506	125
Pr	540	83	511	127
Nd	544	85	516	128
Pm	548	86	521	130
Sm	552	88	526	132
Eu	556	90	531	133
Gd	560	91	536	135
Tb	564	93	541	137
Dy	568	95	546	138
Ho	572	96	551	140
Er	576	98	556	142
Tm	580	100	561	143
Yb	584	101	566	145
Lu	588	103	572	147

^aEstimated uncertainty $\pm 10 \text{ cm}^{-1}$.

Table 19
Vibrational frequencies (cm^{-1}) for LnCl_3 molecules^a

<i>Ln</i>	$\nu_1(A_1)$	$\nu_2(A_1)$	$\nu_3(E)$	$\nu_4(E)$
La	318	59 ^b	317 ^b	84
Ce	320	58 ^c	321 ^c	85
Pr	322	60	320 ^d	86
Nd	324	60 ^c	327 ^c	87
Pm	326	61	328	88
Sm	327	61 ^c	331 ^c	89
Eu	329	63	332	90
Gd	331	64 ^c	337 ^c	91
Tb	333	64	337	92
Dy	335	65 ^c	340 ^c	93
Ho	337	66	342	94
Er	339	66	344	95
Tm	341	67	347	96
Yb	343	68	349	97
Lu	345	69	351	98

^aEstimated error for both the experimental and estimated data is $\pm 10 \text{ cm}^{-1}$.

^bMeasured by Kovács and Konings (1997a).

^cMeasured by Kovács and Konings (1997b).

^dMeasured by Selivanov et al. (1973).

frequencies of the bromides and iodides due to the lack of experimental data. Observations made for the LnF_3 and LnCl_3 series (the relative magnitude of the ν_4 and ν_2 frequencies, and the slightly larger slope for the trend in ν_4 than that of ν_2) have been extended to the LnBr_3 and LnI_3 molecules. This explains the larger uncertainty of the ν_4 data for these molecules. The uncertainty of the ν_2 values is due to the fact that the frequencies occur near the lower detection limit of most infrared spectrometers, thus excluding the observation of the complete band envelope in the spectra.

On the basis of the systematic comparison of calculated and experimental results we conclude that present standard theoretical methods are not able to substitute gas-phase experiments on the geometrical and vibrational properties of the LnX_3 molecules. Systematic theoretical studies on the complete lanthanide series or on selected molecules (Cundari et al., 1995; Joubert et al., 1998; Dolg et al., 1991; Lanza and Fragalá, 1996; Adamo and Maldivi, 1997; Adamo and Maldivi, 1998; Adamo and Barone, 2000; Kovács, 2000) showed several deficiencies of the computational methods. These include the overestimation of the equilibrium Ln-X bond distance, uncertainty for the bond angles of planar/quasi-planar structures, a failure in predicting the values and trends of the ν_2 mode. Moreover, the errors are not consistent for different halides, nor for the two (ν_1 and ν_3) stretching frequencies of an LnX_3 molecule. The less sophisticated character of the standard methods used at present shows that the computed results are quite sensitive to the theory and basis set chosen. On the other hand, the trends in the lanthanide row are predicted well by most advanced levels of theory. Furthermore, the error in the computed geometry and vibrational frequencies is strongly related.

Table 20
Vibrational frequencies (cm^{-1}) of LnBr_3 molecules^a

<i>Ln</i>	$\nu_1(A_1)$	$\nu_2(A_1)$	$\nu_3(E)$	$\nu_4(E)$
La	207	30 ^b	232 ^b	57
Ce	208	36	233	57
Pr	209	36	234	58
Nd	210	37	236	58
Pm	211	37	237	59
Sm	212	37	238	59
Eu	213	38	239	60
Gd	214	38	241	60
Tb	215	39	242	61
Dy	216	44 ^c	243 ^c	61
Ho	217	39	244	62
Er	218	40	245	62
Tm	219	40	247	63
Yb	220	41	248	63
Lu	221	41	249	64

^aEstimated error for the experimental ν_3 values is 5 cm^{-1} , while for the experimental ν_2 and estimated frequencies 10 cm^{-1} .

^bMeasured by Kovács and Konings (1997a).

^cMeasured by Groen (2002).

Table 21
Vibrational frequencies (cm^{-1}) of LnI_3 molecules^a

<i>Ln</i>	$\nu_1(A_1)$	$\nu_2(A_1)$	$\nu_3(E)$	$\nu_4(E)$
La	162	25 ^b	191 ^b	40
Ce	163	27	191 ^c	41
Pr	163	28	192	41
Nd	164	28	192	41
Pm	164	28	193	42
Sm	165	28	194	42
Eu	165	28	194	42
Gd	166	29	195	42
Tb	166	29	195	43
Dy	167	32 ^d	195 ^d	43
Ho	167	29	196	43
Er	168	29	197	44
Tm	168	30	198	44
Yb	168	30	198	44
Lu	169	30	199	45

^aEstimated error for the experimental ν_3 values is 5 cm^{-1} , while for the experimental ν_2 and estimated frequencies 10 cm^{-1} .

^bMeasured by Kovács and Konings (1997a).

^cMeasured by Molnár et al. (1996).

^dMeasured by Groen (2002).

Thus, computations can be used to extend partial experimental information. This was shown in joint experimental/computational studies using advanced theoretical methods (Kovács and Konings, 1997a, 1997b; Hargittai, 2000).

7.2. Ln_2X_6 dimers

The structure of the Ln_2X_6 dimers has been derived from electron diffraction (Molnár et al., 1996; Hargittai, 2000; Giricheva et al., 2000c, 2000b; Zakharov et al., 2001) and theoretical studies (Kovács, 1999, 2000, 2002) for a few species (table D.5). They indicated a bridged structure (D_{2h} symmetry), as shown in fig. 36. In most ED investigations a few geometrical

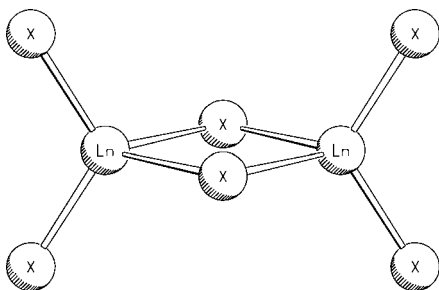


Fig. 36. The molecular geometry of the Ln_2X_6 dimer molecules.

parameters were assumed to be identical to the monomers, the others were treated independently in the refinements (Molnár et al., 1996; Giricheva et al., 2000c, 2000b; Zakharov et al., 2001). However, the small amount of dimeric molecules in the vapour makes such an analysis uncertain and quantum chemical calculations can therefore help to obtain more reliable data (Hargittai, 2000). High-level theoretical calculations indicate shorter terminal $Ln-X$ bonds in the dimers (by ca. 1 pm) and longer ring $Ln-X$ bonds (by ca. 20 pm) with respect to the bond in the monomers (Kovács, 2000). The recent results of Hargittai (2000) for Dy_2Cl_6 and Dy_2Br_6 are in very good agreement with the computations.

Experimental information on the molecular vibrations of the dimers is restricted to a few, mostly, tentative assignments in matrix-IR spectra (Wesley and DeKock, 1971; Hastie et al., 1975; Feltrin and Cesaro, 1996). On the other hand, the complete vibrational spectrum has been computed for La_2X_6 , Dy_2X_6 , Ce_2Br_6 and Ce_2I_6 (Kovács, 1999, 2000; Kapala et al., 2002) and the data are summarised in table D.6. However, due to the failure of the computations to accurately predict the bending frequencies of the monomers at low wavenumbers, the reliability of these frequencies of the dimers may be limited also.

Here we have used a rough approximation by calculating the thermodynamic functions of the Ln_2X_6 molecules from a single set of structural and molecular parameters for the fluorides, chlorides, bromides and iodides each.

8. Enthalpy of formation of the gaseous trihalides

8.1. LnF_3

The vapour pressures of all lanthanide trifluorides have been measured, including PmF_3 . Various techniques have been used, which can be divided in indirect techniques (effusion and boiling point methods) which provide accurate data for the total vapour pressure, and direct mass spectrometric techniques, which are less precise, particularly in case of quadrupole mass spectrometry, but give information on the vapour composition and the presence of dimeric or polymeric molecules or dissociation products.

The enthalpy of formation of the gaseous compounds can be derived from the vapour pressure studies using the thermal functions for the condensed and gaseous states derived in the previous sections. Third-law and second-law thermodynamic analyses of the equilibrium



have been applied, to derive the enthalpy of sublimation at 298.15 K, from which the enthalpy of formation of the gaseous compounds follows as:

$$\Delta_f H^\circ(LnX_3, \text{g}) = \Delta_{\text{sub}} H^\circ + \Delta_f H^\circ(LnX_3, \text{cr}). \quad (16)$$

The third-law value for the enthalpy of sublimation is preferred in view of the accuracy of the thermal functions of the condensed and gaseous states presented in the previous sections, though it should be realised that all uncertainties/errors in the thermal functions (entropy, enthalpy) of solid as well as gaseous phase accumulate in this value. The results are presented in table E.1 of Appendix E.

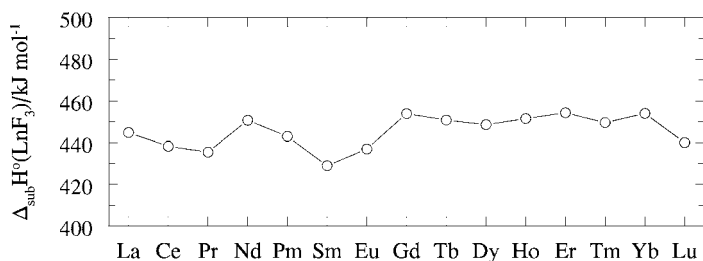


Fig. 37. The sublimation enthalpies at 298.15 K of the lanthanide trifluorides.

Table 22
The selected enthalpies of formation of the gaseous lanthanide trihalides, in $\text{kJ}\cdot\text{mol}^{-1}$

	F	Cl	Br	I
La	-1254.7 ± 3.6	-734.1 ± 5.2	-596.5 ± 5.2	-366.0 ± 8.2
Ce	-1262.4 ± 5.4	-729.3 ± 3.4	-584.5 ± 5.8	-365.0 ± 5.2
Pr	-1253.6 ± 3.3	-729.3 ± 3.4	-587.5 ± 5.7	-367.9 ± 5.8
Nd	-1246.2 ± 5.3	-716.4 ± 2.2	-562.3 ± 5.0	-344.6 ± 5.0
Pm	-1245 ± 25	-710 ± 13	-560 ± 14	-342 ± 14
Sm	-1240 ± 11	-710 ± 9	-562 ± 10	-336 ± 11
Eu	-1175 ± 11	-625 ± 9	-477 ± 14	-255 ± 14
Gd	-1245.4 ± 5.5	-712.2 ± 6.2	-563.5 ± 3.6	-347.7 ± 8.5
Tb	-1245.1 ± 7.1	-712.9 ± 5.0	-570.9 ± 3.6	-350.8 ± 6.5
Dy	-1243.5 ± 3.6	-708.9 ± 3.0	-561.3 ± 5.4	-343.0 ± 5.0
Ho	-1246.3 ± 3.8	-712.9 ± 4.7	-562.1 ± 5.8	-351.0 ± 6.7
Er	-1239.3 ± 2.8	-709.4 ± 8.2	-566.0 ± 5.8	-345.5 ± 6.7
Tm	-1206.4 ± 5.8	-720.3 ± 6.5	-560 ± 11	-347.9 ± 6.9
Yb	-1115.8 ± 5.4	-683 ± 9	-522 ± 10	-308 ± 10
Lu	-1260.8 ± 5.4	-710.0 ± 2.5	-547 ± 14	-335 ± 10

Since most studies were made with indirect techniques assumptions had to be made on the fraction of dimeric molecules in the vapour. Mass spectrometric data are available only for La_2F_6 and Ce_2F_6 (Roberts and Searcy, 1972; Skinner and Searcy, 1971), and show a negligible fraction (10^{-4}) of dimeric molecules in the vapour. On the basis of these observations we have derived the enthalpies of sublimation from the vapour pressure studies assuming only monomeric molecules to be present. The sublimation enthalpy of the trifluorides does not vary much in the lanthanide series (fig. 37), but there is a small distinction between the start and the end of the LnF_3 series. The values for LaF_3 to NdF_3 group around $440\text{--}430 \text{ kJ}\cdot\text{mol}^{-1}$, the values for TbF_3 to YbF_3 around $450 \text{ kJ}\cdot\text{mol}^{-1}$. These two groups correspond to the two different crystallographic modifications in the LnF_3 series. The values of the compounds in between are less well defined: for PmF_3 to GdF_3 only second-law values from mass spectrometric studies are available. These also group around $430 \text{ kJ}\cdot\text{mol}^{-1}$ except PmF_3 which is somewhat higher, probably due to the uncertainties in the result for that compound, that was measured on a mixed $(\text{Pr}_{1/3}\text{Pm}_{1/3}\text{Sm}_{1/3})\text{F}_3$ sample (Gibson and Haire, 1989).

Compared to the critical evaluation by Myers and Graves (1977b) the variation along the LnF_3 series is much more smooth, which we feel is mainly due to the improved thermodynamic functions for the solid and gaseous phases derived in the present study.

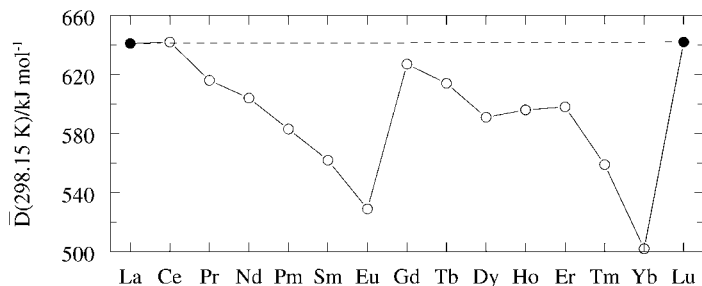


Fig. 38. The mean bond energy at 298.15 K of the lanthanide trifluorides.

The recommended enthalpies of formation of the gaseous trifluorides derived from these values are shown in table 22. From these values the mean bond energy can be derived as one third of the energy of the reaction:



Figure 38 shows the mean bond energy of gaseous trifluorides (for practical reasons expressed as the mean bond enthalpy at 298.15 K). It reveals a regular pattern: the bond energies of LaF_3 , GdF_3 and LuF_3 (f^0 , f^7 and f^{14} configurations) are about equal, in between the bond energy systematically decreases reaching the lowest values at EuF_3 and YbF_3 , indicating that the bond energy becomes weaker with increasing number of electrons in the first and second half of the f shell. This pattern (including the plateau for Dy–Ho–Er) is typical for many atomic properties of the lanthanide elements and ions (e.g., ionisation potential).

8.2. LnCl_3

Also for the trichlorides a large number of vapour pressure studies have been made, and the results of the third-law analysis are shown in table E.2 of Appendix E.

The formation of Ln_2Cl_6 dimers in the vapours of LnCl_3 ($\text{Ln} = \text{La}, \text{Eu}, \text{Lu}$) compounds has been demonstrated by Hastie et al. (1968) by mass spectrometry. They found that the dimer fraction, as derived from the ion-intensity data, is small for LaCl_3 and EuCl_3 (< 0.01), but indicate a dimer fraction of ~ 0.02 in the vapour of LuCl_3 . Kudin et al. (1997, 2000) studied the vapours of DyCl_3 , TbCl_3 , TmCl_3 and YbCl_3 by mass spectrometry. They concluded that for DyCl_3 and TbCl_3 the dimer fraction can be significant (around 0.10 at 1600 K) whereas for TmCl_3 and YbCl_3 it is negligible. These authors also found evidence for the existence of higher polymers (trimers and tetramers) in vapour, but their contribution to the total vapour pressure is negligible. Giricheva et al. (2000c, 2000b) found that the dimer fraction is 0.03 for ErCl_3 and 0.09 for LuCl_3 by mass spectrometry. Kapala et al. (2002) studied the vapour phase of CeCl_3 , PrCl_3 , NdCl_3 and DyCl_3 by mass spectrometry and found dimer fractions smaller than 0.01 for the light lanthanide trichlorides, and ~ 0.02 in the vapour of DyCl_3 . The results of Pogrebnoi et al. (2001) for CeCl_3 and SmCl_3 confirm this.

In the first approximation we have neglected the dimers in the vapour pressure analysis. On the basis of the mass spectrometric results this seems to be justified for the light lanthanide trichlorides, and good agreement is found for the enthalpies of sublimation derived from the

various studies. For the heavy lanthanide trichlorides a comparison to the work of Kudin et al. can be made. The enthalpies of sublimation derived from their results are, however, very discordant. For DyCl_3 and TmCl_3 the difference in the enthalpies of sublimation is far beyond the possible effect of dimers. A sensitivity analysis shows that a correction of the monomer pressure of the effusion studies for a dimer fraction of 0.1 increases the enthalpy of sublimation by $2\text{--}3 \text{ kJ}\cdot\text{mol}^{-1}$. But also for TbCl_3 and YbCl_3 , for which the dimer effect should be small on the basis of Kudin's results, the agreement is poor. We therefore conclude that in these studies the conversion of ion intensity to pressure may not be correct for the heavy dimers. On the basis of these considerations and the absence of a reliable way to systematically quantify the dimer fraction, we have neglected the possible dimer contribution in the analysis, but have raised the uncertainty of the selected enthalpies of sublimation.

Figure 39 shows the variation in the sublimation enthalpy of the trichlorides. On first sight the values for the crystallographic modifications in the LnCl_3 series seem to be different, like was the case for the trifluorides. The enthalpies of sublimation of the hexagonal trichlorides $\text{LaCl}_3\text{--NdCl}_3$ are about $40 \text{ kJ}\cdot\text{mol}^{-1}$ higher than those of the monoclinic compounds. GdCl_3 also has hexagonal crystal structure (fig. 2), but its enthalpy of sublimation is close to that of the monoclinic forms. TbCl_3 is orthorhombic, and its enthalpy of sublimation is also close to the monoclinic series though fig. 11 suggest it is crystallographically more closely related to the hexagonal series. The enthalpy of sublimation of PmCl_3 , SmCl_3 and EuCl_3 have been estimated from these data assuming that the enthalpy of sublimation gradually decreases from LaCl_3 to GdCl_3 . The approximate values for EuCl_3 by Moriarity (1963), although probably subjected to decomposition, and for SmCl_3 by Pogrebnoi et al. (2001) (the mass spectrometric measurements by the group of Kudin are generally discordant as can be seen for TbCl_3 and DyCl_3 in table E.2) might indicate that this leads to a small overestimation. Accurate measurements are needed to resolve this.

A distinct difference can be noted when the variation in the enthalpy of sublimation along the LnCl_3 series is compared to the results of the critical evaluation by Myers and Graves (1977b). The trend for the lanthanide trichlorides is almost linear in our analysis which is not the case in the analysis of Myers and Graves (1977b), who reported a pronounced difference in enthalpy at the mid of the series separating the hexagonal and the monoclinic lanthanide trichlorides. This observation can clearly be related to the distinct different entropies for the solid phase that were selected here, based on new experimental results.

The recommended enthalpies of formation of the gaseous trichlorides derived from the selected enthalpies of sublimation are shown in table 22. The mean bond energies derived from these values is shown in fig. 40, which reveals the same pattern as for the trifluorides, which should be explained by a $f^0\text{--}f^7\text{--}f^{14}$ linear base variation and an excess contribution which is related to the changes in the electronic nature of the lanthanide(III) ions.

8.3. LnBr_3

The number of vapour pressure studies of the tribromides is significantly less. Gietmann et al. (1996) systematically measured the vaporization of the lanthanide bromides using mass spectrometry, showing the importance of the dimeric molecules in the vapour. For the light lanthanide tribromides (La, Ce, Nd) the fraction of dimers is around 0.01, but for TbBr_3 it is 0.03,

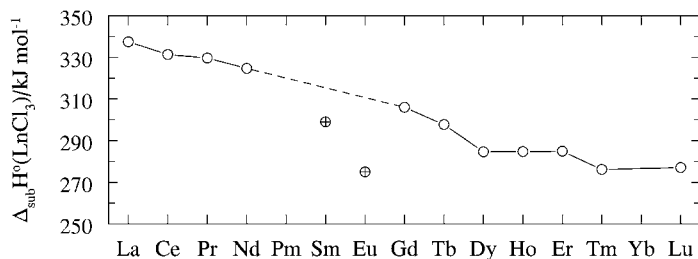


Fig. 39. The sublimation enthalpies at 298.15 K of the lanthanide trichlorides. ⊕ – experimental results for SmCl_3 and EuCl_3 that are not considered (see text).

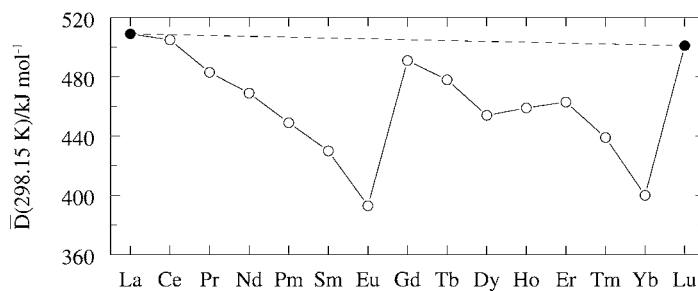


Fig. 40. The mean bond energy at 298.15 K of the lanthanide trichlorides.

for HoBr_3 it is 0.08, and for ErBr_3 and TmBr_3 it is 0.10. The results of Zakharov et al. (2003) for NdBr_3 is in agreement with the above data (0.007) whereas Zakharov et al. (2001) found a lower fraction for ErBr_3 (0.025). As mentioned in the section for the chlorides, such fractions would lead to an error of maximum $2\text{--}3 \text{ kJ}\cdot\text{mol}^{-1}$ in case the dimer contribution is neglected.

The enthalpies of sublimation for the monomer derived from Gietmann's results are generally in reasonable agreement with the values from the indirect measurements although they are almost systematically the lowest (contrary to what one expects), as shown in table E.3 of Appendix E. A comparison with the torsion effusion data of Piacente and coworkers (Brunetti et al., 1999, 2000; Villani et al., 2000a, 2000b; Piacente et al., 2002) for six lanthanide tribromides, shows a difference of $4\text{--}10 \text{ kJ}\cdot\text{mol}^{-1}$, irrespectively of the dimer fraction. It is clear that the effect of the neglect of dimers in the third-law analysis is of the same order as or even smaller than the variation between the various authors, and this has been reflected in the uncertainty. The variation in fig. 41 thus is partly due to systematic errors between the studies which are not eliminated due to the limited number of studies, which is especially true for the tribromides of Gd-Lu. Gietmann's results indicate an almost constant value for this series, as do the results of Makhadmurodov et al. (1975).

The enthalpy of sublimation of PmBr_3 , SmBr_3 and EuBr_3 has been estimated to decrease gradually from NdBr_3 to GdBr_3 . The recommended enthalpies of formation of the gaseous tribromides derived from the selected enthalpies of sublimation are shown in table 22. The mean bond energies derived from these values are shown in fig. 42, which confirms the general patterns found for the other trihalides.

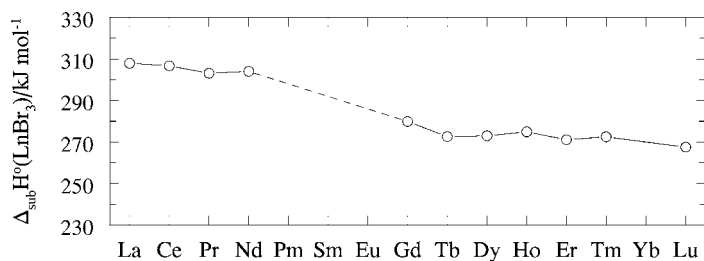


Fig. 41. The sublimation enthalpies at 298.15 K of the lanthanide tribromides.

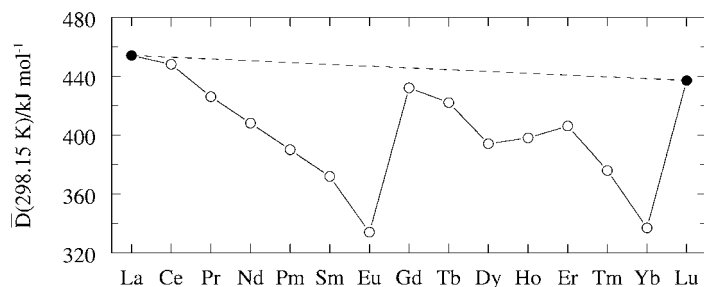


Fig. 42. The mean bond energy at 298.15 K of the lanthanide tribromides.

8.4. LnI_3

The early mass spectrometric studies for the lanthanide triiodides do not mention the dimer formation (Hirayama and Castle, 1973), but in later studies this effect was considered. Hirayama et al. (1976) found that the dimer fraction for LaI_3 is negligible. Kaposi et al. (1983, 1986) found the dimer fraction to be 0.05 and 0.03 for DyI_3 and HoI_3 respectively, whereas Gietmann et al. (1996) found it to be 0.1 for HoI_3 . Struck and Feuersanger (1991), Struck and Baglio (1992) reported mass spectra for CeI_3 and TmI_3 which demonstrate the presence of dimers, with ion-intensity ratios of < 0.01 and ~ 0.03 , respectively. The results for the last compound are in contrast to the large fraction of dimers reported by Dettingmeijer and Dielis (1988) for TmI_3 : 0.21 at 880 K to 0.43 at 1010 K. As discussed by Struck and Feuersanger (1991) quadrupole mass spectrometry, as used by Dettingmeijer and Dielis (1988), is suspect as the conversion from ion current to equilibrium partial pressure is difficult.

In absence of a good way to quantify the dimer fraction of the triiodides and the indication that it is probably below 0.1, the dimers have been neglected in the vapour pressure analysis (table E.4 of Appendix E), similar to the chlorides and bromides. The effect of such small fractions is within the variation between the results of these studies.

The sublimation enthalpy of triiodides vary in a similar way as that of the tribromides (fig. 43), showing the same pattern as the trichlorides and tribromides. The enthalpy of sublimation of PmI_3 , SmI_3 and EuI_3 has been interpolated from the NdI_3 – GdI_3 data; that of YbI_3 and LuI_3 taken close to the values of the TbI_3 – TmI_3 series.

The recommended enthalpies of formation of the gaseous triiodides derived from these values are shown in table 22, the mean bond energies derived from these values in fig. 44.

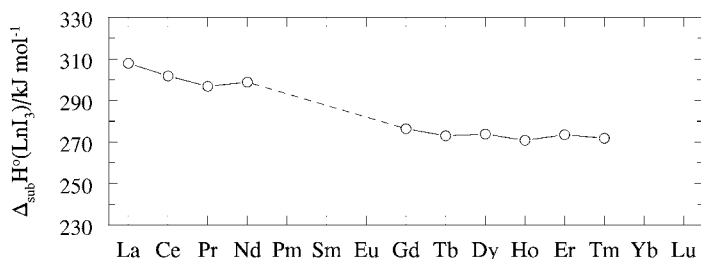


Fig. 43. The sublimation enthalpies at 298.15 K of the lanthanide iodides.

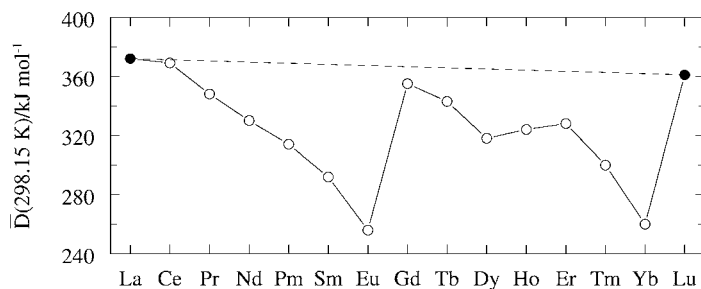


Fig. 44. The mean bond energy at 298.15 K of the lanthanide triiodides.

8.5. Ln_2X_6 dimers

As was already discussed in the previous sections, dimeric molecules contribute significantly (up to 10%) to the total vapour pressure of the lanthanide trihalides. However, experimental information is only available for a few systems, which is often highly uncertain. As a result it is difficult to predict trends in the lanthanide series or estimate unknown values.

The lanthanide tribromide series is an exception as Gietmann et al. (1996) made a systematic study by mass spectrometry. The enthalpies of dimerisation derived from this work are shown in fig. 45. They are almost constant along the series, especially considering that the uncertainty (in the experimental data but also in the thermal functions of the gaseous dimers) is relatively large. Experimental data are also available for all the lanthanum trihalides (Roberts and Searcy, 1972; Hastie et al., 1968; Gietmann et al., 1996; Hirayama et al., 1976), which permits one to investigate the dimerisation enthalpies as a function of the halide atom. In fig. 46 the enthalpies of dimerisation at 298.15 K derived from these studies are plotted as a function of the atomic weight of the halide ion. It can be seen

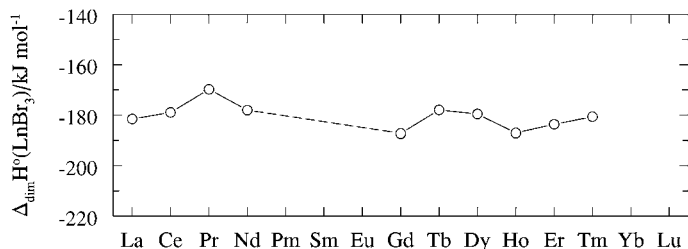


Fig. 45. The enthalpies of dimerisation at 298.15 K of the lanthanide tribromides as derived from the work of Gietmann et al. (1996).

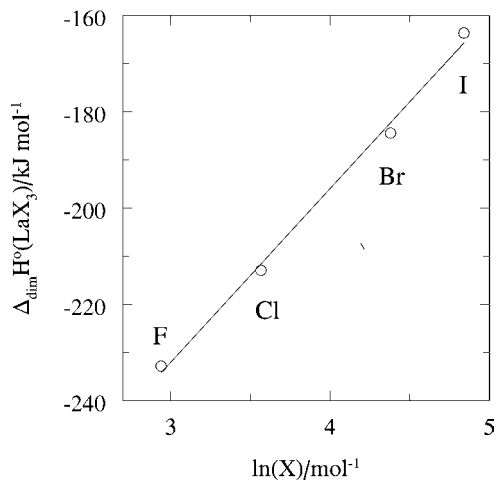


Fig. 46. The enthalpies of dimerisation at 298.15 K of the lanthanum trihalides.

that the dimerisation enthalpy increases linearly from F to I. These results are in excellent agreement with the dimerisation energies (0 K) for LaX_3 and DyX_3 molecules calculated by (Kovács, 2000). Although the dimerisation enthalpies seem to indicate the largest stability of the Ln_2F_6 molecules among the Ln_2X_6 dimers, it should be realised, however, that the derived dimerisation enthalpies refer to 298.15 K and the computations refer to 0 K and thus do not include the entropy contribution that is important at the high temperatures of the experiments.

In absence of more detailed information we suggest therefore that for practical reasons the enthalpies of dimerisation are treated constant in the different lanthanide halides series: $-233 \text{ kJ}\cdot\text{mol}^{-1}$ for the trifluorides, $-213 \text{ kJ}\cdot\text{mol}^{-1}$ for the trichlorides, $-185 \text{ kJ}\cdot\text{mol}^{-1}$ for the tribromides, and $-165 \text{ kJ}\cdot\text{mol}^{-1}$ for the triiodides.

9. Conclusions

In the present chapter we have presented a careful evaluation of the thermodynamic and related properties of the lanthanide trihalides. It is shown that the properties of these compounds vary regularly within the four series (F to I) and in most cases clear trends are observed.

The melting points in all four lanthanide trihalide series exhibit a minimum which shift from the heavy lanthanides to the light lanthanides as the atomic number of the halide increases. In the fluoride series the minimum occurs at ErF_3 , in the chloride series at TbCl_3 , in the bromide series probably at SmBr_3 , and in the iodide series at PrI_3 . This minimum concurs with a change in the stable crystallographic structure, except for the bromide series in which the high temperature polymorphic behaviour is not known.

The variation in the heat capacity and entropy of the solid lanthanide trihalides can be described by a lattice contribution that linearly varies with atomic number within each crystallographic class of compounds, and an excess contribution that depends on the electronic configuration (crystal field) of the lanthanide ions. A distinct difference is observed between

the heat capacity and entropy of the hexagonal and monoclinic lanthanide trichlorides, which clearly correlates with a distinct difference in molar volume between the two modifications. Both effects are absent in the lanthanide trifluoride series. The enthalpies of formation of the solid lanthanide trihalides show a slight increase along the series, with anomalous values for the Eu and Yb compounds, which is due to the fact that Eu and Yb metals have divalent standard states and 88 and 46 kJ·mol⁻¹, respectively, is necessary to form the trivalent state (Gschneidner Jr., 1969; Johansson and Mårtensson, 1987).

The properties of the liquid lanthanide trihalides depend strongly on the atomic number of the halide. The variation in the heat capacity of the lanthanide fluorides indicates a strongly ionic behaviour of the melts with a concomitant irregular trend related to the electronic configuration of the lanthanide ions. In the lanthanide chlorides, bromides and iodides the trend becomes systematically more constant, indicating an increasing molecular nature of the melts.

The molecular parameters of the gaseous lanthanide trihalide molecules exhibit simple linear trends, with decreasing bond length and increasing vibrational frequencies as the atomic number of the lanthanide ion increases. This is in agreement with the well-known lanthanide contraction (Gschneidner Jr., 1989). The *Ln*-*X* bond energies of the lanthanide trihalide molecules are about equal for LaX₃, GdX₃ and LuX₃ (f⁰, f⁷ and f¹⁴ configurations) within each halide series, but in between the bond energy systematically decreases reaching minimum values at EuX₃ and YbX₃. This indicates that the bond energy becomes weaker with increasing number of electrons in the first and second half of the f shell. This pattern is typical for many atomic properties of the lanthanide elements and ions (e.g., ionisation potential). The enthalpies of dimerisation for the *LnX*₃ molecules are about constant within each halide series.

Although the literature on the thermodynamic and related properties of the lanthanide trihalides on which our evaluation and conclusions are based is extensive, it is far from complete. As we have demonstrated in many instances the gaps in the experimental information can be filled with estimates (e.g., the standard entropies and the enthalpies of formation) based on the observed systematics. However, this is not always possible for the following reasons:

- The polymorphism of the trichlorides, tribromides and triiodides is not sufficiently well known to make very reliable estimations and predictions at high temperatures. Further experiments to solve the polymorphism of the middle of the series are required.
- The experimental basis for the recommended heat capacity of the tribromides and triiodides is marginal and more low- as well as high-temperature heat capacity measurements are required.
- The lack of auxiliary data such as crystal field energies for the tribromides and triiodides further limits the value of the semi-empirical approach used here to estimate high temperature heat capacities.
- The experimental basis to derive the enthalpies of formation of the trifluorides is limited. The data selected here are based on the results of a single laboratory. Reliable experiments to verify the selected values and confirm the suggested trend are needed.
- The experimental data on the gaseous compounds are affected by the limited knowledge of the dimer fraction in the vapour. A systemic study is only available for the tribromides.

In spite of these limits, the data presented here form a consistent and reliable basis for thermochemical analysis and modelling.

The information presented in this chapter will be included in the material property database for f-elements and compounds (*f*-MPD) of the Institute of Transuranium Elements, which is accessible through internet.³ Complete thermodynamic tables can be retrieved at that site, which will be updated regularly with new information.

Appendix A. The transition and melting points of the lanthanide trihalides

Table A.1
Transition and melting temperatures for the lanthanide trifluorides

authors	T_{trs}/K	T_{fus}/K
LaF₃		
Spedding and Daane (1960)		1766
Porter and Brown (1962)		1763
Robinson and Cripe (1966)		1768 ± 10
Jones and Shand (1968) ^a		1693
Spedding and Henderson (1971) ^b		1766 ± 3
Dworkin and Bredig (1971)		1768 ± 3
Nafziger et al. (1973)		1760 ± 2
Sobolev et al. (1976a)		1773
Greis and Cader (1985)		1773
Stankus et al. (2000)		1766
selected value:		1766 ± 3
CeF₃		
King and Christensen (1959)		1732
Spedding and Daane (1960)		1703
Porter and Brown (1962)		1710
Robinson and Cripe (1966)		1698 ± 10
Jones and Shand (1968) ^a		1670
Spedding and Henderson (1971) ^b		1703 ± 3
Sobolev et al. (1976a)		1716
Greis and Cader (1985)		1709
selected value:		1703 ± 3
PrF₃		
Spedding and Daane (1960)		1668
Robinson and Cripe (1966)		1673 ± 10
Jones and Shand (1968) ^a		1645
Spedding and Henderson (1971) ^b		1672 ± 3
Sobolev et al. (1976a)		1677
Greis and Cader (1985)		1674
selected value:		1670 ± 3
NdF₃		
Spedding and Daane (1960)		1647
Robinson and Cripe (1966)		1653 ± 10
Jones and Shand (1968) ^a		1620

continued on next page

³ <http://www.f-elements.net>

Table A.1, *continued from previous page*

authors	T_{trs}/K	T_{fus}/K
Spedding and Henderson (1971) ^b		1650 ± 3
Sobolev et al. (1976a)		1645
Greis and Cader (1985)		1651
Stankus et al. (2000)		1649
selected value:		1649 ± 3
SmF₃		
Spedding and Daane (1960)		1579
Thoma and Burton (1966)	828	
Jones and Shand (1968) ^a	852	1568
Spedding and Henderson (1971) ^b	762 ± 3	1571 ± 3
Gogadze et al. (1972a)		1583 ± 5
Sobolev et al. (1976a)	743	1577
Greis and Cader (1985)	753	1582
Stankus et al. (2000)	~760	1572
selected value:	743 ± 3	1571 ± 3
EuF₃		
Spedding and Daane (1960)		1549
Thoma and Burton (1966)	973	
Jones and Shand (1968) ^a	954	1536
Spedding and Henderson (1971) ^b		1549 ± 3
Greis and Cader (1985)	1125	1531
selected value:	973 ± 3	1549 ± 3
GdF₃		
Spedding and Daane (1960)		1504
Porter and Brown (1962)		1501
Thoma and Burton (1966)	1173	
Jones and Shand (1968) ^a	1074	1516
Spedding and Henderson (1971) ^b	1347 ± 3	1503 ± 3
Zhigarnovskii and Ippolitov (1970a)	1338 ± 5	1478 ± 5
Gogadze et al. (1972b)	1293 ± 5	
De Kozak et al. (1973)	1348 ± 5	1523 ± 5
Pastor and Robinson (1974)		1503
Sobolev et al. (1976a)	1343	1501
Greis and Cader (1985)	1338	1508
Stankus et al. (1999)	1310	1509 ± 3
selected value:	1347 ± 3	1501 ± 3
TbF₃		
Spedding and Daane (1960)		1445
Thoma and Burton (1966)	1223 ± 6	
Jones and Shand (1968) ^a	1235	1477
Spedding and Henderson (1971) ^b		1446 ± 3
Sobolev et al. (1976a)		1439
Greis and Cader (1985)		1455
selected value:		1446 ± 3

continued on next page

Table A.1, *continued from previous page*

authors	T_{trs}/K	T_{fus}/K
DyF₃		
Spedding and Daane (1960)		1427
Thoma and Burton (1966)	1303 ± 6	
Jones and Shand (1968) ^a	1418	1432
Spedding and Henderson (1971) ^b		1428 ± 3
Gogadze et al. (1972a)		1381 ± 5
Pastor and Robinson (1974)		1433
Sobolev et al. (1976a)		1420
De Kozak and Almai (1978)		1438
Greis and Cader (1985)		1433
Khairulin et al. (1998)		1427 ± 5
selected value:		1426 ± 3
HoF₃		
Spedding and Daane (1960)		1416
Thoma and Burton (1966)	1343 ± 6	
Jones and Shand (1968) ^a		1407
Spedding and Henderson (1971) ^b		1416 ± 3
Shaimuradov et al. (1974)	1343	1418
Pastor and Robinson (1974)		1423
Sobolev et al. (1976a)		1413
Sobolev et al. (1976c)		1413 ± 5
Greis and Cader (1985)		1420
Stankus et al. (2000)		1416
selected value:		1416 ± 3
ErF₃		
Spedding and Daane (1960)		1413
Thoma and Burton (1966)	1348	
Jones and Shand (1968) ^a	1372	1404
Spedding and Henderson (1971) ^b	1388 ± 3	1416 ± 3
Gogadze et al. (1972c)	1369 ± 5	1418 ± 5
Sobolev et al. (1976a)	1377	1407
Sobolev et al. (1976c)	1390	1413
Greis and Cader (1985)	1392	1420
Stankus et al. (2000)	1372	1414
selected value:	1388 ± 3	1413 ± 3
TmF₃		
Spedding and Daane (1960)		1431
Thoma and Burton (1966)	1303	
Jones and Shand (1968) ^a	1298	1415
Spedding and Henderson (1971) ^b	1325 ± 3	1416 ± 3
Sobolev et al. (1976a)	1320	1432
Greis and Cader (1985)	1322	1431
selected value:	1325 ± 3	1431 ± 3

continued on next page

Table A.1, *continued from previous page*

authors	T_{trs}/K	T_{fus}/K
YbF₃		
Spedding and Daane (1960)		1430
Thoma and Burton (1966)	1258	
Jones and Shand (1968) ^a	1245	1445
Zhigarnovskii and Ippolitov (1970b)	1273 ± 7	
Spedding and Henderson (1971) ^b	1267 ± 3	1416 ± 3
Gogadze et al. (1972c)	1273 ± 5	1418 ± 5
Labeau et al. (1974)	1251	1438
Sobolev et al. (1976a)	1251	1428
Greis and Cader (1985)	1259	1445
Stankus et al. (1999)	1256	1440 ± 5
selected value:	1267 ± 3	1435 ± 5
LuF₃		
Spedding and Daane (1960)		1455
Thoma and Burton (1966)	1218	
Jones and Shand (1968) ^a	1152	1456
Spedding and Henderson (1971) ^b	1230 ± 3	1457 ± 3
Sobolev et al. (1976a)	1226	1455
Greis and Cader (1985)	1216	1453
Stankus et al. (2000)	1220	1461
selected value:	1230 ± 3	1455 ± 3

^aResults published in graphical form only.^bAlso reported by Henderson (1970).Table A.2
Transition and melting temperatures for the lanthanide trichlorides

authors	T_{trs}/K	T_{fus}/K
LaCl₃		
Spedding and Daane (1960)		1135
Dworkin and Bredig (1963a)		1131
Vogel and Schneider (1972)		1123
Nisel'son and Lyzlov (1976)		1125
Lyzlov and Nisel'son (1978)		1125
Seifert et al. (1985)		1117
Laptev et al. (1986)		1118
Igarashi and Mochinaga (1987)		1150
Gaune-Escard et al. (1994)		1127
selected value:		1133 ± 5
CeCl₃		
Spedding and Daane (1960)		1090
Dworkin and Bredig (1971)		1090
Nisel'son and Lyzlov (1976)		1104
Laptev et al. (1986)		1092
Seifert et al. (1988a)		1104
Gaune-Escard et al. (1994)		1086
selected value:		1090 ± 2

continued on next page

Table A.2, *continued from previous page*

authors	T_{trs}/K	T_{fus}/K
PrCl₃		
Spedding and Daane (1960)		1059
Dworkin and Bredig (1963a)		1059
Nisel'son and Lyzlov (1976)		1051
Laptev et al. (1986)		1051
Igarashi and Mochinaga (1987)		1059
Seifert et al. (1987)		1062
Gaune-Escard et al. (1994)		1061
selected value:		1060 ± 2
NdCl₃		
Spedding and Daane (1960)		1031
Druding and Corbett (1961)		1031
Dworkin and Bredig (1963a)		1032
Vogel and Schneider (1972)		1032
Nisel'son and Lyzlov (1976)		1027
Lyzlov and Nisel'son (1978)		1027
Laptev et al. (1986)		1043
Igarashi and Mochinaga (1987)		1029
Seifert et al. (1988b)		1037 ^a
Gaune-Escard et al. (1994)		1032
selected value:		1032 ± 2
SmCl₃		
Spedding and Daane (1960)		955
Korshunov et al. (1964)		938
Vogel and Schneider (1972)		941
Nisel'son and Lyzlov (1976)		941
Laptev et al. (1986)		948
Thiel and Seifert (1988)		941
Rycerz and Gaune-Escard (2002a)		950
selected value:		950 ± 5
EuCl₃		
Spedding and Daane (1960)		decomposes
Korshunov et al. (1966a)		896
Laptev et al. (1986)		893
Kiseleva et al. (1990)		905 ± 7
Seifert and Sandrok (1991)		893
Rycerz and Gaune-Escard (2002b)		894
selected value:		894 ± 3
GdCl₃		
Spedding and Daane (1960)		875
Harris and Veale (1965)	373 ± 10	873 ± 10
Korshunov and Drobot (1965)		882
Dworkin and Bredig (1971)		875
Vogel and Schneider (1972)		873

continued on next page

Table A.2, continued from previous page

authors	T_{trs}/K	T_{fus}/K
Nisel'son and Lyzlov (1976)		901
Lyzlov and Nisel'son (1978)		901
Garton and Walker (1982)		882
Igarashi and Mochinaga (1987)		875
Daniel et al. (1989)	870–875	
Goryushkin et al. (1990)		886.1 ± 3.3
Seifert et al. (1991)		878
Gaune-Escard et al. (1994)		873
selected value:	872 ± 10	875 ± 2
TbCl₃		
Spedding and Daane (1960)	770	855
Korshunov et al. (1966a)		851
Dworkin and Bredig (1971)	783 ± 2	855 ± 2
Lyzlov and Nisel'son (1978)	801	868
Garton and Walker (1982)		860
Goryushkin et al. (1990)	793.1 ± 4.7	856.9 ± 4.7
Rycerz and Gaune-Escard (1999b)	790	854
Morrison et al. (2000)	~ 783	
selected value:	783 ± 5	855 ± 3
DyCl₃		
Spedding and Daane (1960)		920
Korshunov and Drobot (1965)		927
Dworkin and Bredig (1971)		924 ± 2
Lyzlov and Nisel'son (1978)		921
Garton and Walker (1982)		920
Igarashi and Mochinaga (1987)		928
Goryushkin et al. (1990)		929.4 ± 6.8
Gaune-Escard et al. (1996)	611	909
Reuter and Seifert (1994)		919
selected value:	611 ± 5	924 ± 3
HoCl₃		
Spedding and Daane (1960)		993
Korshunov et al. (1966b)		991
Dworkin and Bredig (1971)		993 ± 2
Garton and Walker (1982)		977
Goryushkin et al. (1990)		1014.3 ± 3.4
Roffe and Seifert (1997)		973
selected value:		993 ± 3
ErCl₃		
Spedding and Daane (1960)		1049
Korshunov et al. (1966b)		1037
Dworkin and Bredig (1971)		1049 ± 2
Vogel and Schneider (1972)		1035
Lyzlov and Nisel'son (1978)		1054
Goryushkin et al. (1990)		1064.0 ± 3.0

continued on next page

Table A.2, *continued from previous page*

authors	T_{trs}/K	T_{fus}/K
Büchel et al. (1995)		1024
Gaune-Escard et al. (1996)	1025	1046
Dudek and Seifert (2001)		1024
selected value:		1049 ± 5
TmCl₃		
Spedding and Daane (1960)		1097
Goryushkin et al. (1990)		1110.2 ± 3.5
Gaune-Escard et al. (1996)		1092
selected value:		1095 ± 3
YbCl₃		
Spedding and Daane (1960)		1138
Goryushkin et al. (1990)		1155.5 ± 1.6
selected value:		1138 ± 5
LuCl₃		
Spedding and Daane (1960)		1198
Lyzlov and Nisel'son (1978)		1177
Goryushkin et al. (1990)		1179.4 ± 2.4
selected value:		1198 ± 5

^aValue taken from the graphs, in the text 1104 K is given.

Table A.3
Transition and melting temperatures for the lanthanide tribromides

authors	T_{trs}/K	T_{fus}/K
LaBr₃		
Spedding and Daane (1960)		1062
Shimazaki and Niwa (1962)		1056
Dworkin and Bredig (1971)		1061 ± 2
Rycerz and Gaune-Escard (1999a)		1058
selected value:		1060 ± 3
CeBr₃		
Spedding and Daane (1960)		1005
Shimazaki and Niwa (1962)		1005
Thoma and Burton (1966)		995
Dworkin and Bredig (1971)		1005 ± 2
selected value:		1005 ± 2
PrBr₃		
Spedding and Daane (1960)		964
Dworkin and Bredig (1971)		966 ± 2
selected value:		965 ± 3

continued on next page

Table A.3, *continued from previous page*

authors	T_{trs}/K	T_{fus}/K
NdBr₃		
Spedding and Daane (1960)		955
Shimazaki and Niwa (1962)		957
Dworkin and Bredig (1971)		955 ± 2
Cordfunke et al. (1999)		953.2 ± 0.3
selected value:		955 ± 2
SmBr₃		
Spedding and Daane (1960)		913
selected value:		913 ± 5
EuBr₃		
Spedding and Daane (1960)		decomposes
Thoma and Burton (1966)		978
selected value:		978 ± 10
GdBr₃		
Spedding and Daane (1960)		1043
Thoma and Burton (1966)		1058 ± 2
selected value:		1043 ± 5
TbBr₃		
Spedding and Daane (1960)		1101
Thoma and Burton (1966)		1103 ± 2
selected value:		1102 ± 3
DyBr₃		
Spedding and Daane (1960)		1152
Cordfunke and Blacquière (1997)		1151.0 ± 1.5
selected value:		1152 ± 3
HoBr₃		
Spedding and Daane (1960)		1192
Dworkin and Bredig (1971)		1192 ± 2
Gietmann et al. (1996)		1202
selected value:		1192 ± 3
ErBr₃		
Spedding and Daane (1960)		1196
selected value:		1196 ± 5
TmBr₃		
Spedding and Daane (1960)		1227
Thoma and Burton (1966)		1228 ± 2
selected value:		1228 ± 3
LuBr₃		
Spedding and Daane (1960)		1298
Thoma and Burton (1966)		1233 ± 2
selected value:		1298 ± 5

Table A.4
Transition and melting temperatures for the lanthanide triiodides

authors	T_{trs}/K	T_{fus}/K
LaI₃		
Spedding and Daane (1960)		1045
Corbett et al. (1962)		1051.5
Shimazaki and Niwa (1962)		1034
Dworkin and Bredig (1971)		1051 ± 2
Kutscher and Schneider (1971)		1041
selected value:		1045 ± 3
CeI₃		
Spedding and Daane (1960)		1039
Corbett et al. (1962)		1033–1034
Dworkin and Bredig (1963a)		1033 ± 2
Konings and Kok-Scheele (1999)		1027 ± 1
selected value:		1033 ± 2
PrI₃		
Spedding and Daane (1960)		1010
Shimazaki and Niwa (1962)		1006
Dworkin and Bredig (1963a)		1011 ± 2
Kutscher and Schneider (1971)		1003
Corbett (1972)		1011
selected value:		1011 ± 2
NdI₃		
Spedding and Daane (1960)		1057
Druding and Corbett (1961)	847	1060
Shimazaki and Niwa (1962)		1048
Dworkin and Bredig (1963a)	847 ± 2	1060 ± 2
Kutscher and Schneider (1971)	836	1053
Corbett (1972)		1060
Cordfunke et al. (1999)	859.3 ± 0.6	1058.7 ± 0.6
selected value:	859 ± 3	1059 ± 2
SmI₃		
Spedding and Daane (1960)		1123
Kutscher and Schneider (1971)	943	1089–1097 ^a
Molodkin et al. (1984)		1144–1155
Poshevneva et al. (2002)		1145 ± 9
selected value:	943 ± 10	1123 ± 5
GdI₃		
Spedding and Daane (1960)		1198
Mee and Corbett (1965)		1204
Kutscher and Schneider (1971)	1021	1213
Dworkin and Bredig (1971)	1013 ± 2	1204 ± 2
Corbett (1972)		1204
selected value:	1013 ± 5	1204 ± 3

continued on next page

Table A.4, continued from previous page

authors	T_{trs}/K	T_{fus}/K
TbI₃		
Spedding and Daane (1960)		1230
Dworkin and Bredig (1971)	1080 ± 2	1228 ± 2
selected value:	1080 ± 5	1229 ± 3
DyI₃		
Spedding and Daane (1960)		1251
Kutscher and Schneider (1971)	1246	1250
Corbett (1972)	1101	1256
Cordfunke and Blacquère (1997)		1251.5 ± 1.5
selected value:	1101 ± 5	1251 ± 3
HoI₃		
Spedding and Daane (1960)		1267
Gietmann et al. (1996)		1283
Goryushkin and Poshevneva (1996)		1266 ± 2
selected value:		1267 ± 5
ErI₃		
Spedding and Daane (1960)		1288
Corbett (1972)		1287
Goryushkin et al. (1999)		1282 ± 10
selected value:		1288 ± 3
TmI₃		
Spedding and Daane (1960)		1294
selected value:		1294 ± 5
LuI₃		
Spedding and Daane (1960)		1323
Goryushkin and Poshevneva (1992)		1313 ± 15
selected value:		1323 ± 5

^aUnder decomposition.

Appendix B. The enthalpies of formation of the solid lanthanide trihalides

Table B.1

The enthalpy of formation of $\text{LaX}_3(\text{cr})$ at 298.15 K; ΔH_1° and ΔH_2° are the enthalpies of solution of $\text{La}(\text{cr})$ and $\text{LaX}_3(\text{cr})$ in $\text{HCl}(\text{aq})$, respectively

authors	method ^a	$\Delta H_1^\circ/\text{kJ}\cdot\text{mol}^{-1}$	$\Delta H_2^\circ/\text{kJ}\cdot\text{mol}^{-1}$	$\Delta_f H^\circ/\text{kJ}\cdot\text{mol}^{-1}$
LaF₃				
Polyachenok (1967)	H			-1695
Kondrat'ev ^b	S			-1698.2 ± 6.3
Khanaev et al. (1977)	S			-1630.1 ± 5.0
Rezukhina et al. (1974)	E			-1731.8 ± 5.0
Johnson et al. (1980)	C			-1699.5 ± 2.0
selected value:				-1699.5 ± 2.0

continued on next page

Table B.1, continued from previous page

authors	method ^a	$\Delta H_1^\circ/\text{kJ}\cdot\text{mol}^{-1}$	$\Delta H_2^\circ/\text{kJ}\cdot\text{mol}^{-1}$	$\Delta_f H^\circ/\text{kJ}\cdot\text{mol}^{-1}$
LaCl₃				
Bommer and Hohmann (1941a, 1941b)	S (0.1)	-738.5 ± 2.6	-132.2 ± 0.1	-1105.1 ± 2.6 -1072.2 ± 2.7^c
Lohr and Cunningham (1951)	S (1.5)	-695.0 ± 5.9		
Spedding and Flynn (1954)	S (0.27)	-705.7 ± 0.2	-130.3 ± 0.7	-1073.0 ± 0.9
Montgomery (1959)	S (0.51)		-129.7 ± 0.4	-1070.2 ± 0.7^d -1070.3 ± 1.6^g
Fitzgibbon et al. (1965)	S (1.0)	-705.5 ± 1.3		
Gvelesiani and Yashvili (1967)	S (1.0)	-708.0 ± 2.0		
	S (1.5)	-708.8 ± 1.4		
Morss (1969)	S (1.0)	-703.3 ± 3.8		
Lapteev et al. (1990)	E			-1066.9 ± 1.1
Cordfunke and Booij (1995)	S (1.0)		-126.4 ± 0.5	-1072.3 ± 1.5^e -1071.1 ± 1.4^f
Oppermann et al. (1997)	S (4.0)		-111.8 ± 0.4	-1065.9 ± 0.6^d -1069.4 ± 1.3^g
Merli et al. (1998)	S (1.0)	-704.4 ± 1.2		
	S (6.0)	-707.8 ± 1.2		
selected value:				-1071.6 ± 1.5
LaBr₃				
Hurtgen et al. (1980)	S (1.0)		-158.5 ± 0.2	-905.1 ± 1.4^e -904.0 ± 1.2^f
	S (0.1)		-163.7 ± 0.4	-902.3 ± 0.7^c
Oppermann et al. (1997)	S (4.0)		-146.1 ± 0.4^i	-902.8 ± 1.2^d -904.4 ± 1.5
selected value:				-904.4 ± 1.5
LaI₃				
Hohmann and Bommer (1941)	S (0.1)	-738.5 ± 2.6	-200.6 ± 0.7	-706.5 ± 2.7 -671.9 ± 1.7^c
Furkaliouk et al. (1995)	S (1.0)			-667.9 ± 1.6
Oppermann et al. (1997)	S (4.0)		$[-196.6 \pm 1.1]^h$ -167.5 ± 0.4^j	-673.9 ± 1.6^e -689.4 ± 1.1^d -673.9 ± 2.0
selected value:				-673.9 ± 2.0

^aE: e.m.f. measurements, S: solution calorimetry; values in parentheses give the concentration of the solvent in mol·dm⁻³; H: high temperature equilibria.

^bKondrat'ev Y.V., Thesis, University of Leningrad. Cited and recalculated by Johnson et al. (1980).

^cUsing ΔH_1° from Spedding and Flynn (1954).

^dCycle based on $\Delta_f H^\circ(\text{La}_2\text{O}_3(\text{cr}))$.

^eUsing ΔH_1° from Merli et al. (1998).

^fUsing ΔH_1° from Fitzgibbon et al. (1965).

^gUsing ΔH_1° extra- or interpolated from the results of Merli et al. (1998).

^hDerived from Furkaliouk et al. (1995).

ⁱIn HBr(aq).

^jIn HI(aq).

Table B.2

The enthalpy of formation of $CeX_3(cr)$ at 298.15 K; ΔH_1° and ΔH_2° are the enthalpies of solution of $Ce(cr)$ and $CeX_3(cr)$ in $HCl(aq)$, respectively

authors	method ^a	$\Delta H_1^\circ/kJ\cdot mol^{-1}$	$\Delta H_2^\circ/kJ\cdot mol^{-1}$	$\Delta_f H^\circ/kJ\cdot mol^{-1}$
CeF₃				
Kholokhova and Rezukhina (1976)	E			-1732.6 ± 4.2
selected value:				-1689.2 ± 5.0^b
CeCl₃				
Bommer and Hohmann (1941a, 1941b)	S (0.1)	-726.8 ± 2.9	-136.8 ± 0.7	-1088.8 ± 3.0 -1061.1 ± 0.8^c
Spedding and Miller (1952)	S (0.24)	-699.2 ± 0.2	-137.1 ± 0.4	-1059.6 ± 0.5
	S (0.37)		-134.2 ± 0.9	
Montgomery (1962)	S (1.5)	-690.9 ± 0.6	-129.4 ± 0.3	-1058.9 ± 0.7
Laptev et al. (1990)	E			-1029.2 ± 0.7
Cordfunke and Booiij (1995)	S (0.24)		-136.24 ± 0.48	-1060.5 ± 0.6^c
selected value:				-1059.7 ± 1.5
CeBr₃				
Furkaliouk and Cordfunke (1996)	S (0.25)		-168.87 ± 0.38	-891.5 ± 0.8^c -891.4 ± 1.0^d -890.7 ± 1.7^e
selected value:				-891.2 ± 1.5
CeI₃				
Hohmann and Bommer (1941)	S (0.1)	-726.8	-690.4 ± 2.9 -206.8	-662.8
Furkaliouk and Cordfunke (1996)	S (1.0)		$[-200.0 \pm 0.9]^f$	-669.4 ± 0.9 -667.3 ± 1.0^c -666.4 ± 1.9^e
selected value:				-666.8 ± 3.0

^aE: e.m.f. measurements, S: solution calorimetry; values in parentheses give the concentration of the solvent in $mol\cdot dm^{-3}$.

^bSee main text for explanation of selected value.

^cUsing ΔH_1° from Spedding and Flynn (1954).

^dRecalculation of the reaction cycle in Cordfunke and Booiij (1995) based on KCl/KBr .

^eChloride cycle using $\Delta H_1^\circ(CeCl_3)$ from Cordfunke and Booiij (1995).

^fDerived from the enthalpy of solution of a CeI_3/KCl mixture.

Table B.3

The enthalpy of formation of $\text{PrX}_3(\text{cr})$ at 298.15 K; ΔH_1° and ΔH_2° are the enthalpies of solution of $\text{Pr}(\text{cr})$ and $\text{PrX}_3(\text{cr})$ in $\text{HCl}(\text{aq})$, respectively

authors	method ^a	$\Delta H_1^\circ/\text{kJ}\cdot\text{mol}^{-1}$	$\Delta H_2^\circ/\text{kJ}\cdot\text{mol}^{-1}$	$\Delta_f H^\circ/\text{kJ}\cdot\text{mol}^{-1}$
PrF₃				
Polyachenok (1967)	H			-1678
Kondrat'ev ^b	S			-1689.0 ± 6.3
Rezukhina et al. (1974)	E			-1712.0 ± 5.0
Johnson et al. (1980)	C			-1689.1 ± 2.6
selected value:				-1689.1 ± 2.6
PrCl₃				
Bommer and Hohmann (1941a, 1941b)	S (0.1)	-723.4 ± 1.1	-141.8 ± 2.2	-1081.1 ± 2.5 -1061.8 ^c
Lohr and Cunningham (1951)	S (1.5)	-687.9 ± 9.6		
Spedding and Flynn (1954)	S (0.25)	-704.1	-142.2 ± 0.6	-1059.4
	S (1.47)	-692.8	-125.6 ± 0.9	-1057.7
				-1052.6 ± 9.6 ^d
Stubblefield (1969)	S (1.0)	-687.9 ± 3.4		
Fitzgibbon et al. (1973)	S (2.0)	-692.2 ± 1.3		
Laptev et al. (1990)	E			-1035.9 ± 1.1
selected value:				-1058.6 ± 1.5
PrBr₃				
Hurtgen et al. (1980)	S (1.0)		-171.7 ± 0.7	-874.3 ± 3.4 ^e
	S (0.25)		[-174.8 ± 0.6] ^f	-890.5 ± 4.0 ^e
	S (0.1)		-176.3 ± 0.4	-889.9 ^g
selected value:				-890.5 ± 4.0
PrI₃				
Hohmann and Bommer (1941)	S (0.1)	-723.4 ± 1.1	-208.9 ± 0.1	-683.1 ± 1.1 -664.7 ± 2.0 ^e
selected value:				-664.7 ± 5.0

^aE: e.m.f. measurements, S: solution calorimetry; values in parentheses give the concentration of the solvent in $\text{mol}\cdot\text{dm}^{-3}$; H: high temperature equilibria.

^bKondrat'ev Y.V., Thesis, University of Leningrad. Cited and recalculated by Johnson et al. (1980).

^cUsing ΔH_1° from Spedding and Flynn (1954).

^dUsing ΔH_1° from Lohr and Cunningham (1951).

^eUsing ΔH_1° from Stubblefield (1969).

^fEstimated by interpolation.

^gUsing ΔH_1° from Bommer and Hohmann (1941a).

Table B.4

The enthalpy of formation of $\text{NdX}_3(\text{cr})$ at 298.15 K; ΔH_1° and ΔH_2° are the enthalpies of solution of $\text{Nd}(\text{cr})$ and $\text{NdX}_3(\text{cr})$ in $\text{HCl}(\text{aq})$, respectively

authors	method ^a	$\Delta H_1^\circ/\text{kJ}\cdot\text{mol}^{-1}$	$\Delta H_2^\circ/\text{kJ}\cdot\text{mol}^{-1}$	$\Delta_f H^\circ/\text{kJ}\cdot\text{mol}^{-1}$
NdF₃				
Polyachenok (1967)	H			-1653
Kondrat'ev ^b	S			-1678.1 ± 2.1
Kholokhova and Rezukhina (1976)	E			-1712.9 ± 4.2
Khanaev et al. (1977)	S			-1650.6 ± 4.6
Johnson et al. (1980)	C			-1679.4 ± 1.9
Kim and Oishi (1980)	C			-1660.6 ± 4.9
selected value:				-1679.4 ± 1.9
NdCl₃				
Bommer and Hohmann (1941a, 1941b)	S (0.1)	-717.1 ± 4.3	-150.2 ± 0.2	-1065.7 ± 4.3
		[-688.0 ± 2.5] ^g		-1036.6 ± 2.5
Spedding and Miller (1952)	S (0.25)	-680.3 ± 0.8	-148.7 ± 0.4	-1029.0 ± 0.9
Polyachenok and Novikov (1963a)	S (0.2)	-685.8 ± 5.4	-154.8 ± 0.8	-1028.9 ± 5.5
Stuve (1965a)	S (4.0)	-693.6 ± 0.9	-127.3 ± 0.3	-1041.3 ± 1.0
Popova and Monaenkova (1989)	S (2.19)	-686.8 ± 1.0		
Tiflova (1990)	S (2.3)	-690.8 ± 1.6	-140.0 ± 0.6	-1036.6 ± 1.7
Cordfunke et al. (1996)	S (2.3)		-137.1 ± 0.5	-1039.5 ± 1.7 ^c
		[-692.8 ± 2.0] ^g		-1041.5 ± 2.1 ^d
	S (4.0)		-128.3 ± 0.3	-1040.3 ± 1.0 ^e
		[-695.1 ± 2.0] ^g		-1041.8 ± 2.0 ^d
Merli et al. (1998)	S (1.0)	-689.6 ± 2.0		
	S (3.0)	-693.9 ± 1.3		
	S (6.0)	-695.7 ± 1.8		
Hennig and Oppermann (1998)	S (4.0)		-127.5 ± 0.3	-1037.1 ± 0.6 ^f
				-1042.6 ± 2.0 ^d
selected value:				-1040.9 ± 1.0
NdBr₃				
Hurtgen et al. (1980)	S (0.1)	[-688.0 ± 2.5] ^g	-184.5 ± 0.6	-865.6 ± 2.6
Hennig and Oppermann (1999)	S (4.0) ^g		-169.9 ± 0.2	-862.3 ± 3.1 ^g
selected value:				-864.0 ± 3.0
NdI₃				
Hohmann and Bommer (1941)	S (0.1)	-717.1 ± 4.3	-215.7 ± 0.2	-670.0 ± 4.3
		[-688.0 ± 2.5] ^g		-640.9 ± 2.5
Hennig and Oppermann (2000)	S (4.0) ^h		-201.8 ± 0.6	-637.4 ± 1.6 ^h
selected value:				-639.2 ± 4.0

^aE: e.m.f. measurements, S: solution calorimetry; values in parentheses give the concentration of the solvent in $\text{mol}\cdot\text{dm}^{-3}$; H: high temperature equilibria.

^bKondrat'ev Y.V., Thesis, University of Leningrad. Cited and recalculated by Johnson et al. (1980).

^cUsing ΔH_1° from Tiflova (1990).

^dUsing ΔH_1° (interpolated) from Merli et al. (1998).

^eUsing ΔH_1° from Stuve (1965a).

^fIn $\text{HBr}(\text{aq})$; cycle based on $\Delta_f H^\circ(\text{Nd}_2\text{O}_3(\text{cr}))$.

^gValue estimated by the present authors.

^hIn $\text{HI}(\text{aq})$; cycle based on $\Delta_f H^\circ(\text{Nd}_2\text{O}_3(\text{cr}))$.

Table B.5

The enthalpy of formation of $\text{SmX}_3(\text{cr})$ at 298.15 K; ΔH_1° and ΔH_2° are the enthalpies of solution of $\text{Sm}(\text{cr})$ and $\text{SmX}_3(\text{cr})$ in $\text{HCl}(\text{aq})$, respectively

authors	method ^a	$\Delta H_1^\circ/\text{kJ}\cdot\text{mol}^{-1}$	$\Delta H_2^\circ/\text{kJ}\cdot\text{mol}^{-1}$	$\Delta_f H^\circ/\text{kJ}\cdot\text{mol}^{-1}$
SmF₃				
Kim et al. (1977)	C			-1669.0 ± 4.6
selected value:				-1700.7 ± 5.0^b
SmCl₃				
Bommer and Hohmann (1941b)	S (0.05)		-163.2 ± 0.2	-1025.9 ± 1.7^c
Machlan et al. (1955)	S (6.0)		-123.4 ± 0.8	
Montgomery and Hubert (1959)	S (0.48)		-158.5 ± 1.0	-1025.1 ± 1.8^d
Gvelesiani and Yashvili (1967)	S (0.7)	-683.7 ± 5.4		
	S (1.0)	-682.6 ± 2.4		
Baker et al. (1972)	S (2.0)	-690.1 ± 1.3		
	S (3.99)	-689.5 ± 3.8		
Morss and Fahey (1976)	S (2.0)		-151.9	-1025.8 ± 1.3^e
Khanaev et al. (1987)	S (0.05) ^f	-689.6 ± 1.7		
Hennig and Oppermann (1997)	S (4.0)		-139.2 ± 0.2	-1025.1 ± 1.4^d
				-1025.3 ± 3.8^e
selected value:				-1025.3 ± 2.0
SmBr₃				
Hurtgen et al. (1980)	S (1.0)		-190.2 ± 0.9	-850.5 ± 2.6^g
		$[-689.0 \pm 2.0]^h$		-856.9 ± 2.2
	S (0.1)		-195.4 ± 0.8	-856.3 ± 2.1^c
selected value:				-853.4 ± 3.0
SmI₃				
Hohmann and Bommer (1941)	S (0.05)		-237.0 ± 0.7	-621.5 ± 1.8^c
selected value:				-621.5 ± 4.0

^aE: e.m.f. measurements, S: solution calorimetry; values in parentheses give the concentration of the solvent in $\text{mol}\cdot\text{dm}^{-3}$.

^bSee main text for explanation of selected value.

^cUsing ΔH_1° from Khanaev et al. (1987).

^dCycle based on $\Delta_f H^\circ(\text{Sm}_2\text{O}_3(\text{cr}))$.

^eUsing ΔH_1° from Baker et al. (1972).

^fThe measurements were carried out in $\text{HClO}_4(\text{aq})$.

^gUsing ΔH_1° from Gvelesiani and Yashvili (1967).

^hEstimated.

Table B.6

The enthalpy of formation of $\text{EuX}_3(\text{cr})$ at 298.15 K; ΔH_1° and ΔH_2° are the enthalpies of solution of $\text{Eu}(\text{cr})$ and $\text{EuX}_3(\text{cr})$ in $\text{HCl}(\text{aq})$, respectively

authors	method ^a	$\Delta H_1^\circ/\text{kJ}\cdot\text{mol}^{-1}$	$\Delta H_2^\circ/\text{kJ}\cdot\text{mol}^{-1}$	$\Delta_f H^\circ/\text{kJ}\cdot\text{mol}^{-1}$
EuCl₃				
Bommer and Hohmann (1941b)	S (0.1)		-172.2 ± 0.2	$-872.3 \pm 2.9^{\text{b}}$ $-1015.2 \pm 2.9^{\text{c}}$
Machlan et al. (1955)	S (6.0)		-129.3 ± 0.8	$-920.8 \pm 2.6^{\text{d}}$
Burnett and Cunningham (1964), Burnett (1964)	S (0.1)	-688.6 ± 2.9		
Stuve (1965b)	S (4.0)	$-583.0 \pm 2.5^{\text{e}}$	-143.6 ± 0.4	-914.5 ± 2.5 $-936.6 \pm 2.9^{\text{f}}$ $-936.1 \pm 2.1^{\text{g}}$
Stubblefield et al. (1965)	S (6.0)	-589.9 ± 2.9		
Fitzgibbon et al. (1972)	S (4.0)	-605.2 ± 2.9		
Hennig et al. (1998)	S (4.0)		-146.9 ± 0.2	$-893.6 \pm 2.1^{\text{g}}$ $-911.2 \pm 2.5^{\text{h}}$ $-933.4 \pm 2.9^{\text{f}}$ -935.4 ± 3.0
selected value:				

^aE: e.m.f. measurements, S: solution calorimetry; values in parentheses give the concentration of the solvent in $\text{mol}\cdot\text{dm}^{-3}$.

^bUsing ΔH_1° from Burnett and Cunningham (1964).

^cUsing ΔH_1° from Burnett and Cunningham (1964) neglecting the effect of oxygen in the $\text{HCl}(\text{aq})$ solution.

^dUsing ΔH_1° from Stubblefield et al. (1965).

^eTwo sets of measurements with different samples of $\text{Eu}(\text{cr})$.

^fUsing ΔH_1° from Fitzgibbon et al. (1972).

^gCycle based on $\Delta_f H^\circ(\text{Eu}_2\text{O}_3(\text{cr}))$.

^hUsing ΔH_1° from Stuve (1965b).

Table B.7

The enthalpy of formation of $\text{GdX}_3(\text{cr})$ at 298.15 K; ΔH_1° and ΔH_2° are the enthalpies of solution of $\text{Gd}(\text{cr})$ and $\text{GdX}_3(\text{cr})$ in $\text{HCl}(\text{aq})$, respectively

authors	method ^a	$\Delta H_1^\circ/\text{kJ}\cdot\text{mol}^{-1}$	$\Delta H_2^\circ/\text{kJ}\cdot\text{mol}^{-1}$	$\Delta_f H^\circ/\text{kJ}\cdot\text{mol}^{-1}$
GdF₃				
Rudzitis and Deventer (1965)	C			-1700.8 ± 1.3
Polyachenok (1967)	H			-1628
Kondrat'ev ^b	S			-1672.2 ± 2.1
Kholokhova and Rezukhina (1976)	E			-1713.3 ± 4.6
Storozhenko et al. (1976)	S			-1646.5 ± 3.2
Kim et al. (1978)	C			-1698.7 ± 7.1
Johnson et al. (1980)	C			-1699.3 ± 2.3
selected value:				-1699.3 ± 2.3
GdCl₃				
Bommer and Hohmann (1941a, 1941b)	S (0.1)	-706.3 ± 2.3	-177.4 ± 0.2	-1027.7 ± 2.3 $-1005.0 \pm 1.3^{\text{c}}$
Spedding and Flynn (1954)	S (0.27)	-683.6 ± 1.3	-174.1 ± 0.7	-1006.9 ± 1.5
Daire (1968)	S (1.0)	-682.8 ± 1.3		
Yashvili and Gvelesiani (1971)	S (6.0)	-694.5 ± 1.7		

continued on next page

Table B.7, continued from previous page

authors	method ^a	$\Delta H_1^\circ/\text{kJ}\cdot\text{mol}^{-1}$	$\Delta H_2^\circ/\text{kJ}\cdot\text{mol}^{-1}$	$\Delta_f H^\circ/\text{kJ}\cdot\text{mol}^{-1}$
Tiflova et al. (1989)	S (2.19)	-684.9 ± 0.4 [-695.2 ± 1.5] ^e	-165.3 ± 0.2	-1006.1 ± 0.5 -1016.3 ± 1.5^d
Furkaliouk et al. (1992)	S (1.0)	-683.7 ± 0.7		
Laptey et al. (1993)	E			-1009.8 ± 1.1
Merli et al. (1998)	S (1.0)	-694.9 ± 1.0	-170.5 ± 0.7	-1017.5 ± 1.3
	S (6.0)	-696.1 ± 1.1		
	S (6.1)		-136.4 ± 0.7	-1018.9 ± 1.3
selected value:				-1018.2 ± 1.5
GdBr₃				
Hurtgen et al. (1980)	S (1.0)		-214.8 ± 0.7	-827.0 ± 1.6^c -838.2 ± 1.8^d
	S (0.27)		[-218.4 ± 1.1]	-826.3 ± 2.0^f
	S (0.1)		-219.9 ± 1.1	
selected value:				-838.2 ± 2.0
GdI₃				
Hohmann and Bommer (1941)	S (0.1)	-706.3 ± 2.3	-256.0 ± 2.5^g	-618.9 ± 3.4
Furkaliouk et al. (1992)	S (1.0)	-688.2 ± 0.8	-236.9 ± 0.3	-612.9 ± 0.9
	S (0.1)			-624.1 ± 1.1^d
selected value:				-624.1 ± 3.0

^aE: e.m.f. measurements, S: solution calorimetry; values in parentheses give the concentration of the solvent in mol·dm⁻³; H: high temperature equilibria.

^bKondrat'ev Y.V., Thesis, University of Leningrad. Cited and recalculated by Johnson et al. (1980).

^cUsing ΔH_1° from Spedding and Flynn (1954).

^dUsing ΔH_1° from Merli et al. (1998).

^e ΔH_1° estimated from the results of Merli et al. (1998).

^fThe value obtained by combining ΔH_2° interpolated from the results of Hurtgen et al. (1980) and ΔH_1° from Spedding and Flynn (1954).

^gThe value corrected to 298.15 K.

Table B.8

The enthalpy of formation of TbX₃(cr) at 298.15 K; ΔH_1° and ΔH_2° are the enthalpies of solution of Tb(cr) and TbX₃(cr) in HCl(aq), respectively

authors	method ^a	$\Delta H_1^\circ/\text{kJ}\cdot\text{mol}^{-1}$	$\Delta H_2^\circ/\text{kJ}\cdot\text{mol}^{-1}$	$\Delta_f H^\circ/\text{kJ}\cdot\text{mol}^{-1}$
TbF₃				
Kholokhova and Rezhukhina (1976)	E			-1707.9 ± 5.0
Storozhenko et al. (1976)	S			-1623.3 ± 3.8
selected value:				-1695.9 ± 5.0
TbCl₃				
Stuve (1967a)	S (4.0)	-689.9	-167.9	-997.1
Fitzgibbon and Holley Jr. (1968)	S (1.0)	-701.7 ± 2.5		

continued on next page

Table B.8, *continued from previous page*

authors	method ^a	$\Delta H_1^\circ/\text{kJ}\cdot\text{mol}^{-1}$	$\Delta H_2^\circ/\text{kJ}\cdot\text{mol}^{-1}$	$\Delta_f H^\circ/\text{kJ}\cdot\text{mol}^{-1}$
Morss (1976)	S (0.89)	-696.2	-181.5	-1008.6 ^b -1013.9 ^c -1009.2 ^d -998.2 ^e
Bettonville et al. (1987)	S (1.0)	-697.0 ± 1.2		
Furkaliouk et al. (1993)	S (1.0)	-686.0 ± 0.6		
selected value:				-1010.6 ± 3.0
TbBr₃				
Bettonville et al. (1987)	S (1.0)	-697.0 ± 1.2	-216.0 ± 1.5	-842.1 ± 2.0 -841.5 ^f -846.8 ± 3.0 ^c
selected value:				-843.5 ± 3.0
TbI₃				
Furkaliouk (1993)	S (1.0)	-682.7 ± 0.4	-240.7 ± 0.3	-608.1 ± 0.5
Furkaliouk et al. (1993)	S (1.0)	-686.0 ± 0.6	-240.7 ± 0.3	-611.4 ± 0.7 -621.8 ^f -627.1 ± 1.2 ^c -622.4 ± 2.5 ^d
selected value:				-623.8 ± 3.0

^aE: e.m.f. measurements, S: solution calorimetry; values in parentheses give the concentration of the solvent in mol·dm⁻³.

^bQuoted in Morss (1976).

^cUsing ΔH_1° from Fitzgibbon and Holley Jr. (1968).

^dUsing ΔH_1° from Bettonville et al. (1987).

^eUsing ΔH_1° from Furkaliouk et al. (1993).

^fUsing ΔH_1° from Morss (1976).

Table B.9

The enthalpy of formation of DyX₃(cr) at 298.15 K; ΔH_1° and ΔH_2° are the enthalpies of solution of Dy(cr) and DyX₃(cr) in HCl(aq), respectively

authors	method ^a	$\Delta H_1^\circ/\text{kJ}\cdot\text{mol}^{-1}$	$\Delta H_2^\circ/\text{kJ}\cdot\text{mol}^{-1}$	$\Delta_f H^\circ/\text{kJ}\cdot\text{mol}^{-1}$
DyF₃				
Storozhenko et al. (1976)	S			-1640.2 ± 4.5
Kim et al. (1980)	C			-1678 ± 8
Johnson et al. (1980)	C			-1692.0 ± 1.9
selected value:				-1692.0 ± 1.9
DyCl₃				
Bommer and Hohmann (1941a, 1941b)	S (0.1) ^b	-695.5 ± 0.2	-197.9 ± 0.4	-996.4 ± 0.5
Morss (1976) ^c	S (4.0)	-692.4	-180.4	-987.0 -989.9 ± 3.0 ^d

continued on next page

Table B.9, continued from previous page

authors	method ^a	$\Delta H_1^\circ/\text{kJ}\cdot\text{mol}^{-1}$	$\Delta H_2^\circ/\text{kJ}\cdot\text{mol}^{-1}$	$\Delta_f H^\circ/\text{kJ}\cdot\text{mol}^{-1}$
Huber Jr. et al. (1971)	S (4.0)	-695.3 ± 2.9		
Morss and Fahey (1976)	S (4.0)	-691 ± 9	-180.4 ± 1.1	-985.6 ± 9.1
Monaenkova et al. (1989)	S (2.19)	-704.2 ± 0.6	-190.7 ± 0.2	-999.9 ± 0.7
Tiflova (1990)	S (1.07)	-701.0 ± 0.6	-198.8 ± 0.3	-995.0 ± 0.7
	S (4.01)	-706.5 ± 0.4	-177.2 ± 0.5	-1004.4 ± 0.7
				-993.1 ± 3.0^d
				-992.9 ± 3.1^e
Cordfunke et al. (1996)	S (4.0)	-699.4 ± 1.3	-180.1 ± 0.2	-994.4 ± 1.3
				-990.0 ± 3.0^c
selected value:				-993.1 ± 3.0
DyBr ₃				
Bommer and Hohmann (1941a)	S (0.1) ^b	-694.0 ± 0.2		
Hurtgen et al. (1980)	S (1.0)		-218.9 ± 0.2	-840.2 ± 0.7^f
	S (0.1)		-223.2 ± 1.4	-834.4 ± 1.5^g
	S (0.1)		-223.2 ± 1.4	-838.3 ± 1.7^h
Cordfunke and Booiij (1997)	S (1.0)			-835.0 ± 1.5
			$[-224.9 \pm 0.4]^i$	-834.3 ± 2.2^h
selected value:				-834.3 ± 3.0
DyI ₃				
Hohmann and Bommer (1941)	S (0.1) ^b	-694.8 ± 0.2	-256.7 ± 1.0	-606.7 ± 1.0
Morss and Spence (1992)	S (1.0)	-691 ± 9	-242 ± 8	-615.1 ± 12.0
Cordfunke and Booiij (1997)	S (1.0)			-619.3 ± 1.8
			$[-248.9 \pm 0.4]^i$	-616.7 ± 2.1^h
Leonidov and Furkalyuk (1999)	S (4.0)		-229.0 ± 0.6	-621.7 ± 1.4^j
selected value:				-616.7 ± 3.0

^aE: e.m.f. measurements, S: solution calorimetry; values in parentheses give the concentration of the solvent in mol·dm⁻³.

^bThe measurements were carried out at 294 K.

^cCited in Morss (1976).

^dUsing ΔH_1° from Huber Jr. et al. (1971).

^eCycle based on $\Delta_f H^\circ(\text{Dy}_2\text{O}_3(\text{cr}))$.

^fUsing ΔH_1° from Tiflova (1990).

^gUsing ΔH_1° from Bommer and Hohmann (1941a).

^hCycle based on $\Delta_f H^\circ(\text{CeCl}_3(\text{cr}))$.

ⁱEstimated from Cordfunke and Booiij (1997).

^jUsing ΔH_1° from Cordfunke and Booiij (1997).

Table B.10

The enthalpy of formation of $\text{HoX}_3(\text{cr})$ at 298.15 K; ΔH_1° and ΔH_2° are the enthalpies of solution of $\text{Ho}(\text{cr})$ and $\text{HoX}_3(\text{cr})$ in $\text{HCl}(\text{aq})$, respectively

authors	method ^a	$\Delta H_1^\circ/\text{kJ}\cdot\text{mol}^{-1}$	$\Delta H_2^\circ/\text{kJ}\cdot\text{mol}^{-1}$	$\Delta_f H^\circ/\text{kJ}\cdot\text{mol}^{-1}$
HoF₃				
Rudzitis and Deventer (1965)	C			-1700.8 ± 4.2
Kim and Oishi (1979)	C			-1698 ± 6
Johnson et al. (1980)	C			-1697.8 ± 2.3
selected value:				-1697.8 ± 2.3
HoCl₃				
Bommer and Hohmann (1941a)	S (0.1)	-686.2	-209.2	-975.8
Stuve (1967a)	S (4.0)	-710.5 ± 7.1	-180.5 ± 0.3	-1005.1 ± 7.1
Morss (1976) ^b	S (0.87)	-698.3	-202.3	-980.8
				-997.4^{d}
Bedtonville et al. (1987)	S (1.0) ^c	-705.9 ± 1.9		
Lezhava (1992)	S (1.07)	-704.5 ± 2.2	-199.2 ± 0.8	-998.0 ± 2.4
selected value:				-997.7 ± 2.5
HoBr₃				
Bedtonville et al. (1987)	S (1.0) ^d	-705.9 ± 2.4	-221.9 ± 1.2	-842.1 ± 2.7
selected value:				-842.1 ± 3.0
HoI₃				
Bommer and Hohmann (1941a)	S (0.1)	-686.2	-259.4	-596.4
Lezhava (1992)	S		-255.1 ± 1.2	-622.9 ± 3.2
selected value:				-622.9 ± 3.0

^aE: e.m.f. measurements, S: solution calorimetry; values in parentheses give the concentration of the solvent in $\text{mol}\cdot\text{dm}^{-3}$.

^bQuoted in by Morss (1976).

^cTwo different samples of $\text{Ho}(\text{cr})$ were used.

^dUsing ΔH_1° from Bedtonville et al. (1987).

Table B.11

The enthalpy of formation of $\text{ErX}_3(\text{cr})$ at 298.15 K; ΔH_1° and ΔH_2° are the enthalpies of solution of $\text{Er}(\text{cr})$ and $\text{ErX}_3(\text{cr})$ in $\text{HCl}(\text{aq})$, respectively

authors	method ^a	$\Delta H_1^\circ/\text{kJ}\cdot\text{mol}^{-1}$	$\Delta H_2^\circ/\text{kJ}\cdot\text{mol}^{-1}$	$\Delta_f H^\circ/\text{kJ}\cdot\text{mol}^{-1}$
ErF₃				
Polyachenok (1967)	H			-1582
Kondrat'ev ^b	S			-1635.0 ± 8.4
Kim et al. (1979)	C			-1669 ± 6
Johnson et al. (1980)	C			-1693.6 ± 1.9
selected value:				-1693.6 ± 1.9
ErCl₃				
Bommer and Hohmann (1941a, 1941b)	S (0.1)	-680.1 ± 3.1	-207.3 ± 0.2	-971.6 ± 3.1
Spedding and Flynn (1954)	S (1.42)	-661.4 ± 0.9	-193.3 ± 0.4	-958.9 ± 1.0
Montgomery and Stuve (1961)	S (1.4)		-201.9 ± 0.9	$-994.5 \pm 1.7^{\text{c}}$
				$-994.3 \pm 2.8^{\text{d}}$
Gamanovich and Glybin (1974) ^c	S (2.03)		-201.7 ± 1.2	
Fuger et al. (1980)	S (1.43)	-705.6 ± 1.4	-201.7 ± 0.2	-994.6 ± 1.4

continued on next page

Table B.11, continued from previous page

authors	method ^a	$\Delta H_1^\circ/\text{kJ}\cdot\text{mol}^{-1}$	$\Delta H_2^\circ/\text{kJ}\cdot\text{mol}^{-1}$	$\Delta_f H^\circ/\text{kJ}\cdot\text{mol}^{-1}$
Tiflova (1990) ^e	S (2.19)	-681.9 ± 0.7	-197.3 ± 0.2	-971.1 ± 0.8
	S (2.19)	-682.9 ± 1.8	-197.3 ± 0.2	-972.1 ± 1.8
Furkaliouk et al. (1993)	S (1.0)	-681.8 ± 0.7		
Merli et al. (1998)	S (6.0)	-707.0 ± 1.2		
selected value:				-994.4 ± 2.0
ErBr ₃				
Hurtgen et al. (1980)	S (1.0)	$[-705.0 \pm 3.0]^f$	-226.0 ± 0.5	-837.1 ± 3.0
selected value:				-837.1 ± 3.0
ErI ₃				
Bommer and Hohmann (1941a)	S (0.1)	-680.1 ± 3.1	-261.1 ± 0.6	-587.6 ± 3.2
Furkaliouk and Cordfunke (1996)	S (1.0)	-681.8 ± 0.7	-252.1 ± 0.2	-595.8 ± 0.7
		$[-705.0 \pm 3.0]^f$		-619.0 ± 3.0^f
selected value:				-619.0 ± 3.0

^aE: e.m.f. measurements, S: solution calorimetry; values in parentheses give the concentration of the solvent in mol·dm⁻³; H: high temperature equilibria.

^bKondrat'ev Y.V., Thesis, University of Leningrad. Cited and recalculated by Johnson et al. (1980).

^cUsing ΔH_1° from Fuger et al. (1980).

^dBased on the enthalpy of solution of Er₂O₃.

^eTwo sets of measurements with different samples of Er(cr).

^fThe value estimated from the results of Fuger et al. (1980) and Merli et al. (1998).

Table B.12

The enthalpy of formation of TmX₃(cr) at 298.15 K; ΔH_1° and ΔH_2° are the enthalpies of solution of Tm(cr) and TmX₃(cr) in HCl(aq), respectively

authors	method ^a	$\Delta H_1^\circ/\text{kJ}\cdot\text{mol}^{-1}$	$\Delta H_2^\circ/\text{kJ}\cdot\text{mol}^{-1}$	$\Delta_f H^\circ/\text{kJ}\cdot\text{mol}^{-1}$
TmF ₃				
Kim et al. (1980)	C			-1656 ± 7
selected value:				-1693.7 ± 5.0^b
TmCl ₃				
Bommer and Hohmann (1941a, 1941b)	S (0.1)	-675.7 ± 0.4	-212.9 ± 0.1	-961.6 ± 0.5
Stuve (1967b)	S (4.0)	-698.0 ± 1.3	-186.6 ± 0.9	-986.5 ± 1.6
Morss (1976) ^c		-705.7	-205.8	-993.8
Lezhava (1992) ^d	S (1.07)	-709.3 ± 0.8	-203.3 ± 0.4	-998.7 ± 0.9
selected value:				-996.3 ± 2.5
TmI ₃				
Hohmann and Bommer (1941)	S (0.1)	-675.7 ± 0.4	-261.9	-583.4
Lezhava (1992)	S (H ₂ O)		-261.8 ± 1.8	-619.7 ± 3.5^e
selected value:				-619.7 ± 3.5

^aE: e.m.f. measurements, S: solution calorimetry; values in parentheses give the concentration of the solvent in mol·dm⁻³.

^bSee main text for explanation.

^cQuoted in Morss (1976).

^dTwo sets of measurements with different samples of Tm(cr).

^eBased on $\Delta_f H^\circ(\text{Tm}^{3+}, \text{aq})$ (Cordfunke and Konings, 2001a).

Table B.13

The enthalpy of formation of $\text{YbX}_3(\text{cr})$ at 298.15 K; ΔH_1° and ΔH_2° are the enthalpies of solution of $\text{Yb}(\text{cr})$ and $\text{YbX}_3(\text{cr})$ in $\text{HCl}(\text{aq})$, respectively

authors	method ^a	$\Delta H_1^\circ/\text{kJ}\cdot\text{mol}^{-1}$	$\Delta H_2^\circ/\text{kJ}\cdot\text{mol}^{-1}$	$\Delta_f H^\circ/\text{kJ}\cdot\text{mol}^{-1}$
YbF₃				
Kim et al. (1978)	C			-1569.8 ± 7.1
selected value:				-1655.1 ± 3.0^b
YbCl₃				
Bommer and Hohmann (1941a)	S (0.05)		-213.2 ± 0.2	
Machlan et al. (1955)	S (6.0)		-165.7 ± 1.3	-959.4 ± 1.7^c
Stuve (1967b)	S (4.0)	-671.7 ± 2.8	-187.2 ± 0.8	-959.5 ± 2.9
Bettonville et al. (1987)	S (6.0)	-664.9 ± 1.1		
selected value:				-959.5 ± 3.0
YbBr₃				
Burgess and Kijowski (1981)	S (H ₂ O)		-253.3 ± 3.2	-787.2 ± 4.4^e
Bettonville et al. (1987)	S (6.0)	-664.9 ± 1.1	-199.9 ± 1.4	-792.6 ± 1.8
	S (1.0)	$[-663.0 \pm 3.0]^d$	-229.8 ± 1.5	-791.9 ± 3.4
selected value:				-791.9 ± 5.0

^aE: e.m.f. measurements, S: solution calorimetry; values in parentheses give the concentration of the solvent in $\text{mol}\cdot\text{dm}^{-3}$.

^bSee main text for explanation.

^cUsing ΔH_1° from Bettonville et al. (1987).

^dEstimated by Cordfunke and Konings (2001b).

^eBased on $\Delta_f H^\circ(\text{Yb}^{3+}, \text{aq})$ (Cordfunke and Konings, 2001a).

Table B.14

The enthalpy of formation of $\text{LuX}_3(\text{cr})$ at 298.15 K; ΔH_1° and ΔH_2° are the enthalpies of solution of $\text{Lu}(\text{cr})$ and $\text{LuX}_3(\text{cr})$ in $\text{HCl}(\text{aq})$, respectively

authors	method ^a	$\Delta H_1^\circ/\text{kJ}\cdot\text{mol}^{-1}$	$\Delta H_2^\circ/\text{kJ}\cdot\text{mol}^{-1}$	$\Delta_f H^\circ/\text{kJ}\cdot\text{mol}^{-1}$
LuF₃				
Kholokhova and Rezhukhina (1976)	E			-1700.8 ± 5.0
selected value:				-1679.9 ± 5.0^b
LuCl₃				
Bommer and Hohmann (1941a) ^b	S (0.1)	-670.7	-214.6	-954.9
Morss (1976) ^c	S (0.89)	-700.0	-208.1	-985.6
				-973.3^d
				-987.9^e
Tiflova (1990)	S (2.19)	-694.9 ± 1.0	-199.5 ± 0.3	-981.9 ± 1.1
		$[-702.7 \pm 2.5]^f$		-989.7 ± 2.6
Furkaliouk et al. (1993)	S (1.0)	-687.7 ± 0.5		
Merli et al. (1998)	S (1.0)	-702.3 ± 2.2	-210.5 ± 0.70	-984.9 ± 2.3
	S (3.0)	-703.1 ± 1.3		
	S (6.0)	-703.9 ± 2.2	-175.9 ± 0.90	-988.2 ± 3.0
selected value:				-987.1 ± 2.5

continued on next page

Table B.14, continued from previous page

authors	method ^a	$\Delta H_1^\circ/\text{kJ}\cdot\text{mol}^{-1}$	$\Delta H_2^\circ/\text{kJ}\cdot\text{mol}^{-1}$	$\Delta_f H^\circ/\text{kJ}\cdot\text{mol}^{-1}$
LuI ₃				
Hohmann and Bommer (1941) ^b	S (0.1)	-670.7	-279.8	-559.5
Furkaliouk and Cordfunke (1996)	S (1.0)	-685.0 ± 0.5	-263.3 ± 0.4	-587.8 ± 0.7 -605.1 ± 2.2 ^c
selected value:				-605.1 ± 2.2

^aE: e.m.f. measurements, S: solution calorimetry; values in parentheses give the concentration of the solvent in mol·dm⁻³.

^bSee main text for explanation.

^cQuoted by Morss (1976).

^dUsing ΔH_1° from Furkaliouk and Cordfunke (1996).

^eUsing ΔH_1° from Merli et al. (1998).

^fEstimated value.

Appendix C. Experimental data for the liquid trihalides

Table C.1

Experimental results for the enthalpy of fusion and heat capacity of the liquid lanthanide trichlorides

compound	$\Delta_{\text{fus}} H^\circ$ /kJ·mol ⁻¹	$C_p(\text{liq})$ /J·K ⁻¹ ·mol ⁻¹
LaCl ₃		
Dworkin and Bredig (1963a)	54.4	157.7
Savin et al. (1979)	31.0 ± 2.1	349.4
Gaune-Escard et al. (1994)	55.7	
selected value:	55.0	157.7
CeCl ₃		
Walden and Smith (1961)	53.6	161.05
Savin and Mikhailova (1981)	33.5	
Gaune-Escard et al. (1994)	55.5	
selected value:	53.6	161.05
PrCl ₃		
Dworkin and Bredig (1963a)	50.6	133.9
Savin et al. (1979)	28.9 ± 2.1	179.9
Gaune-Escard et al. (1994)	49.1	155.28
selected value:	49.9	155.3
NdCl ₃		
Dworkin and Bredig (1963a)	50.2	146.4
Savin and Mikhailova (1981)	33.5	
Gaune-Escard et al. (1994)	48.1	149.53
selected value:	49.2	149.5
SmCl ₃		
Rycerz and Gaune-Escard (2002a)	47.6	145.26
selected value:	47.6	145.26

continued on next page

Table C.1, continued from previous page

compound	$\Delta_{\text{fus}} H^\circ$ /kJ·mol ⁻¹	$C_p(\text{liq})$ /J·K ⁻¹ ·mol ⁻¹
EuCl₃		
Rycerz and Gaune-Escard (2002b)	45.0	155.96
selected value:	45.0	149.5
GdCl₃		
Dworkin and Bredig (1963b)	40.2	141.0
Dworkin and Bredig (1971)	40.6	139.52
Goryushkin et al. (1990)	60.3 ± 12	
Gaune-Escard et al. (1994)	40.6	139.89
selected value:	40.6	139.7
DyCl₃		
Dworkin and Bredig (1971)	25.5	144.77
Goryushkin et al. (1990)	36.5 ± 7.3	
Gaune-Escard et al. (1996)	27.6	159.43
selected value:	25.5	144.77
TbCl₃		
Dworkin and Bredig (1963b)	19.5	144.47
Goryushkin et al. (1990)	31.6 ± 6.3	
Rycerz and Gaune-Escard (1999b)	20.8	139.27
selected value:	19.5	144.77
HoCl₃		
Dworkin and Bredig (1963b)	29.3	147.7
Dworkin and Bredig (1971)	32.6	148.66
Goryushkin et al. (1990)	37.9 ± 7.6	
selected value:	32.6	148.66
ErCl₃		
Dworkin and Bredig (1963b)	32.6	141.0
Gaune-Escard et al. (1996)	31.1	
Goryushkin et al. (1990)	38.5 ± 7.7	
selected value:		141.0
TmCl₃		
Goryushkin et al. (1990)	46.9 ± 9.4	
Gaune-Escard et al. (1996)	35.6	
selected value:	35.6	141.0
YbCl₃		
Goryushkin et al. (1990)	58.1 ± 11.6	
selected value:	37.6	
LuCl₃		
Goryushkin et al. (1990)	59.3 ± 11.9	
selected value:	39.5	

Appendix D. Molecular parameters of the lanthanide trihalides

Table D.1

Experimental structural parameters and vibrational frequencies of the lanthanide trifluorides; bond distances in pm, bond angles in degrees, frequencies in cm^{-1}

authors	method	symmetry	$r(Ln-X)$	$\angle(X-Ln-X)$	vibrational frequencies			
					$\nu_1(A_1)$	$\nu_2(A_1)$	$\nu_3(E)$	$\nu_4(E)$
LaF₃								
Akishin et al. (1959)	ED/gas (r_a)	D _{3h}	222(3)					
Hargittai (1999)	ED/gas (r_a)		213(6)					
Wesley and DeKock (1971)	IR/matrix (Ar)	D _{3h}				84	478	120
	IR/matrix (Kr)	D _{3h}					474	
	IR/matrix (N ₂)	D _{3h}					84	457
Hastie et al. (1975)	IR/matrix (Ne)	C _{3v}			527.9	81	496.6	130
	IR/matrix (Ar)	C _{3v}			513.0	83	479.0	121.1
	IR/matrix (N ₂)	C _{3v}			490	94	459	112
	IR/gas (estimated)	C _{3v}			540(10)	82(10)	510(10)	125(10)
CeF₃								
Wesley and DeKock (1971)	IR/matrix (Ar)	D _{3h}				86	483	
	IR/matrix (Kr)	D _{3h}					479	
	IR/matrix (N ₂)	D _{3h}					86	465
Hastie et al. (1975)	IR/matrix (Ne)	C _{3v}			536.9	78	505.3	116
	IR/matrix (Ar)	C _{3v}			521.5	94	488.3	134
	IR/matrix (N ₂)	C _{3v}			506	82	468	121
	IR/gas (estimated)	C _{3v}			549(8)	80(15)	519(8)	115(15)
PrF₃								
Zasorin (1988)	ED/gas (r_g)	C _{3v}	209.1(3)	102.6(28)				
	ED/gas (r_e)	C _{3v}	205.6(5)	105.0(15)				
Wesley and DeKock (1971)	IR/matrix (Ar)	D _{3h}			542	86	458	99
	IR/matrix (Kr)	D _{3h}			538		455	
	IR/matrix (N ₂)	D _{3h}				86	488	118
Lesiecki et al. (1972)	Raman/matrix (Ar)	D _{3h}			526		458	99
	IR/matrix (Ar)	D _{3h}			542	86	458	99

continued on next page

Table D.1, continued from previous page

authors	method	symmetry	$r(Ln-X)$	$\angle(X-Ln-X)$	vibrational frequencies			
					$\nu_1(A_1)$	$\nu_2(A_1)$	$\nu_3(E)$	$\nu_4(E)$
NdF₃								
Wesley and DeKock (1971)	IR/matrix (Ar)	D _{3h}				86	502	118
	IR/matrix (Kr)	D _{3h}					499	
	IR/matrix (N ₂)	D _{3h}				86	482	123
Hastie et al. (1975)	IR/matrix (Ne)	C _{3v}			544.9	81	521.4	121
	IR/matrix (Ar)	C _{3v}			529.7	87	503.7	119
	IR/matrix (N ₂)	C _{3v}			505	103	483	124
	IR/gas (estimated)	C _{3v}			557(10)	80(15)	535(10)	115(15)
SmF₃								
Wesley and DeKock (1971)	IR/matrix (Ar)	D _{3h}				92	508	123
	IR/matrix (Kr)	D _{3h}					504	
	IR/matrix (N ₂)	D _{3h}					491	
EuF₃								
Wesley and DeKock (1971)	IR/matrix (Ar)	D _{3h}				94	511	124
	IR/matrix (Kr)	D _{3h}					507	
	IR/matrix (N ₂)	D _{3h}					502	
Hastie et al. (1975)	IR/matrix (Ne)	C _{3v}			557.5	89	529.5	133
	IR/matrix (Ar)	C _{3v}			542.4	94.0	511.7	127
	IR/matrix (N ₂)	C _{3v}			532	101	504	120
	IR/gas (estimated)	C _{3v}			572(10)	90(15)	544(10)	120(10)
GdF₃								
Zasorin (1988)	ED/gas (r_g)	C _{3v}	205.3(3)	108.4(24)				
	ED/gas (r_e)	C _{3v}	201.6(6)	109.9(23)				
Hastie et al. (1975)	IR/matrix (Ne)	C _{3v}			560.2	94	537.3	138
	IR/matrix (Ar)	C _{3v}			544.7	100	519.2	133
	IR/matrix (N ₂)	C _{3v}			532	116	500	143
	IR/gas (estimated)	C _{3v}			583(10)	95(15)	552(10)	130(10)
TbF₃								
Hauge et al. (1971)	IR/matrix (Ne)	C _{3v}			566.7		540.1	
	IR/matrix (Ar)	C _{3v}			551.1		523.1	
	IR/matrix (N ₂)	C _{3v}					509	

continued on next page

Table D.1, continued from previous page

authors	method	symmetry	$r(Ln-X)$	$\angle(X-Ln-X)$	vibrational frequencies			
					$\nu_1(A_1)$	$\nu_2(A_1)$	$\nu_3(E)$	$\nu_4(E)$
DyF ₃								
Bencze et al. (1996)	IR/matrix (Ar)	C _{3v}			554.4		531.6	
	IR/matrix (N ₂)	C _{3v}			540.2		513	
HoF ₃								
Zasorin (1988)	ED/gas (r_g)	C _{3v}	200.7(3)	105.8(24)				
	ED/gas (r_e)	C _{3v}	197.8(10)	108.2(32)				
Hauge et al. (1971)	IR/matrix (Ne)	C _{3v}			572.4	94	554.0	122
	IR/matrix (Ar)	C _{3v}			556.7	104	535.6	119
	IR/matrix (N ₂)	C _{3v}				124	516	143
ErF ₃								
Bencze et al. (1996)	IR/matrix (Ar)	C _{3v}			560.7		539.4	
	IR/matrix (N ₂)	C _{3v}			546.0		524	
TmF ₃								
Bencze et al. (1996)	IR/matrix (Ar)	C _{3v}			566.2		544.8	
	IR/matrix (N ₂)	C _{3v}			547		529	
YbF ₃								
Hauge et al. (1971)	IR/matrix (Ne)	C _{3v}			584.1	100	564.7	144
	IR/matrix (Ar)	C _{3v}			568.5		546.4	
	IR/matrix (N ₂)	C _{3v}					526	
LuF ₃								
Hauge et al. (1971)	IR/matrix (Ne)	C _{3v}			585.4	101	570.5	150
	IR/matrix (Ar)	C _{3v}			569.6	112	552.2	144
	IR/matrix (N ₂)	C _{3v}				121	530	149

Table D.2

Experimental structural parameters and vibrational frequencies of the lanthanide trichlorides; bond distances in pm, bond angles in degrees, frequencies in cm^{-1}

authors	method	symmetry	$r(Ln-X)$	$\angle(X-Ln-X)$	vibrational frequencies			
					$\nu_1(A_1)$	$\nu_2(A_1)$	$\nu_3(E)$	$\nu_4(E)$
LaCl ₃								
Zasorin (1988)	ED/gas (r_g)	C _{3v}	258.9(5)	112.8(17)				
	ED/gas (r_e)	C _{3v}	253.8(9)	115.4(20)				
Spiridonov et al. (1990)	ED/gas (r_e)	C _{3v}	256.0(6)	116.5(3)				
Girichev (2002)	ED/gas (r_g)	D _{3h}	258.9(6)	116.7(12)				
Selivanov et al. (1973)	IR/gas						316	
Perov et al. (1975)	IR/matrix (Xe)	D _{3h}				52	300	74
Kovács and Konings (1997a)	IR/gas					59	317	
CeCl ₃								
Krasnov (1979)	ED/gas	C _{3v}	256.9(10)	111.6(20)				
Kovács and Konings (1997b)	IR/gas ^a					58	321	
PrCl ₃								
Zasorin (1988)	ED/gas (r_g)	C _{3v}	255.4(5)	112.5(15)				
	ED/gas (r_e)	C _{3v}	251.0(9)	114.3(20)				
Selivanov et al. (1973)	IR/gas						320	
NdCl ₃								
Selivanov et al. (1973)	IR/gas						324	
Wells Jr. et al. (1977)	IR/gas	D _{3h}			349	177	301	120
Feltrin and Cesaro (1996)	IR/matrix (Ar)	D _{3h}					328.3	
Kovács and Konings (1997b)	IR/gas ^a					60	327	
SmCl ₃								
Kovács and Konings (1997b)	IR/gas ^a					61	331	
GdCl ₃								
Zasorin (1988)	ED/gas (r_g)	C _{3v}	248.8(5)	112.3(12)				
	ED/gas (r_e)	C _{3v}	244.5(7)	113.5(21)				
Giricheva et al. (2000d)	ED/gas (r_g)	D _{3h}	247.4(5)	117.0(11)				
Selivanov et al. (1973)	IR/gas						326	
Perov et al. (1975)	IR/matrix (Xe)	D _{3h}				53	318	82
Kovács and Konings (1997b)	IR/gas ^a					64	337	

continued on next page

Table D.2, continued from previous page

authors	method	symmetry	$r(Ln-X)$	$\angle(X-Ln-X)$	vibrational frequencies			
					$\nu_1(A_1)$	$\nu_2(A_1)$	$\nu_3(E)$	$\nu_4(E)$
TbCl ₃								
Zasorin (1988)	ED/gas (r_g)	C _{3v}	247.6(5)	111.2(15)				
	ED/gas (r_e)	C _{3v}	243.8(8)	112.9(19)				
Girichev (2002)	ED/gas (r_g)	D _{3h}	247.1(5)	115.5(11)				
DyCl ₃								
Hargittai (2000)	ED/gas (r_g)		246.1(8)					
Feltrin and Cesaro (1996)	IR/matrix (Ar)	D _{3h}					340.2	
Groen (2002)	Raman/matrix (Xe)				318			
	IR/matrix (Xe)							324.2
Kovács and Konings (1997b)	IR/gas ^a					65		340
HoCl ₃								
Zasorin (1988)	ED/gas (r_g)	C _{3v}	246.2(5)	111.7(15)				
	ED/gas (r_e)	C _{3v}	242.5(9)	112.6(19)				
Loktyushina et al. (1987)	IR/matrix (Ar)							340
ErCl ₃								
Giricheva et al. (2000c)	ED/gas (r_g)	C _{3v}	243.0(5)	112.3(12)				
	ED/gas (r_e)	C _{3v}	239.3(5)					
Perov et al. (1975)	IR/matrix (Xe)	D _{3h}						328
TmCl ₃								
Giricheva et al. (2000a)	ED/gas (r_g)	D _{3h}	242.2(6)	116.2(14)				
Feltrin and Cesaro (1996)	IR/matrix (Ar)	D _{3h}						346.1
LuCl ₃								
Zasorin (1988)	ED/gas (r_g)		241.7(6)	111.5(20)				
	ED/gas (r_e)		237.4(10)	114.5(24)				
Giricheva et al. (2000b)	ED/gas (r_g)		240.3(5)	117.9(13)				
	ED/gas (r_α)	D _{3h}	236.7(6)	120.2(15)				
Perov et al. (1975)	IR/matrix (Xe)	D _{3h}				60	331	88

^aRe-interpretation of the gas-phase spectra presented by Kovács et al. (1995).

Table D.3

Experimental structural parameters and vibrational frequencies of the lanthanide tribromides; bond distances in pm, bond angles in degrees, frequencies in cm^{-1}

authors	method	symmetry	$r(Ln-X)$	$\angle(X-Ln-X)$	vibrational frequencies			
					$\nu_1(A_1)$	$\nu_2(A_1)$	$\nu_3(E)$	$\nu_4(E)$
LaBr₃								
Giricheva et al. (1977)	ED/gas (r_g)	C_{3v}	274.1(5)	115.5(20)				
Zasorin (1988)	ED/gas (r_g)	C_{3v}	274.2(4)	114.3(17)				
	ED/gas (r_e)	C_{3v}	269.3(10)	115.0(23)				
Kovács and Konings (1997a)	IR/gas					ca.30	232	
PrBr₃								
Girichev et al. (2002)	ED/gas (r_g)	D_{3h}	269.6(6)	114.7(10)				
NdBr₃								
Zakharov et al. (2003)	ED/gas (r_g)	D_{3h}	267.5(6)	115.0(12)				
Wells Jr. et al. (1977)	IR/gas	D_{3h}			220	120	188	80
GdBr₃								
Zasorin (1988)	ED/gas (r_g)	C_{3v}	264.1(4)	113.7(20)				
	ED/gas (r_e)	C_{3v}	259.0(9)	115.2(23)				
Loktyushina and Mal'tsev (1984)	IR/matrix (Xe)						255	
	IR/matrix (Ar)						238	
DyBr₃								
Hargittai (2000)	ED/gas (r_g)		260.9(8)					
Feltrin and Cesaro (1996)	IR/matrix (Ar)	D_{3h}					243.1	
Groen (2002)	IR/gas					44	243	
	IR/matrix (Kr)						237.2	
	IR/matrix (Xe)						229.4	
	Raman/matrix (Kr)				210		237	
	Raman/matrix (Xe)				202		227	47
HoBr₃								
Girichev et al. (2002)	ED/gas (r_g)	D_{3h}	259.5(6)	115.3(11)				
Loktyushina et al. (1987)	IR/matrix (Ar)						241.5	
ErBr₃								
Zakharov et al. (2001)	ED/gas (r_g)	D_{3h}	258.2(6)	116.0(14)				
	ED/gas (r_e)	D_{3h}	256.1(9)	120(2)				
TmBr₃								
Feltrin and Cesaro (1996)	IR/matrix (Ar)	D_{3h}					249.9	

continued on next page

Table D.3, continued from previous page

authors	method	symmetry	$r(Ln-X)$	$\angle(X-Ln-X)$	vibrational frequencies			
					$\nu_1(A_1)$	$\nu_2(A_1)$	$\nu_3(E)$	$\nu_4(E)$
LuBr ₃								
Zasorin (1988)	ED/gas (r_g)	C _{3v}	255.7(4)	115.0(11)				
	ED/gas (r_e)	C _{3v}	251.6(8)	117.2(17)				
Loktyushina and Mal'tsev (1984)	IR/matrix (Xe)						231	
	IR/matrix (Ar)						245	

Table D.4

Experimental structural parameters and vibrational frequencies of the lanthanide triiodides; bond distances in pm, bond angles in degrees, frequencies in cm⁻¹

authors	method	symmetry	$r(Ln-X)$	$\angle(X-Ln-X)$	vibrational frequencies			
					$\nu_1(A_1)$	$\nu_2(A_1)$	$\nu_3(E)$	$\nu_4(E)$
LaI ₃								
Hargittai (1999)	ED/gas (r_α)		286(3)					
Kovács and Konings (1997a)	IR/gas					ca.25	191	
CeI ₃								
Molnár et al. (1996)	ED/gas (r_g)	D _{3h}	294.8(9)					
	IR/gas	D _{3h}				ca.25 ^a	191(10)	
PrI ₃								
Zasorin (1988)	ED/gas (r_g)	C _{3v}	290.1(4)	113.4(13)				
	ED/gas (r_e)	C _{3v}	285.4(7)	113.7(19)				
NdI ₃								
Zasorin (1988)	ED/gas (r_g)	C _{3v}	287.9(4)	113.8(11)				
	ED/gas (r_e)	C _{3v}	283.5(8)	113.9(16)				
Ezhov et al. (2000)	ED/gas (r_g)	D _{3h}	287.3(4)	118.6(11)				
	ED/gas (r_e)	D _{3h}	286.6(5)	118(2)				
Wells Jr. et al. (1977)	IR/gas	D _{3h}			195	98	141	72

continued on next page

Table D.4, continued from previous page

authors	method	symmetry	$r(Ln-X)$	$\angle(X-Ln-X)$	vibrational frequencies			
					$\nu_1(A_1)$	$\nu_2(A_1)$	$\nu_3(E)$	$\nu_4(E)$
GdI ₃								
Zasorin (1988)	ED/gas (r_g)	C _{3v}	284.0(4)	115.4(13)				
	ED/gas (r_e)		279.4(7)	115.5(16)				
Loktyushina and Mal'tsev (1984)	IR/matrix (Xe)							183.5
DyI ₃								
Feltrin and Cesaro (1996)	IR/matrix (Ar)	D _{3h}						189.5
Groen (2002)	IR/gas					32		195
	IR/matrix (Xe)							185
	Raman/matrix (Xe)				157			184
HoI ₃								
Loktyushina and Mal'tsev (1984)	IR/matrix (Xe)							185
	IR/matrix (Ar)							196.5
TmI ₃								
Feltrin and Cesaro (1996)	IR/matrix (Ar)	D _{3h}						198.9
LuI ₃								
Zasorin (1988)	ED/gas (r_g)	C _{3v}	276.8(3)	115.6(6)				
	ED/gas (r_e)	C _{3v}	273.5(6)	116.6(10)				
Loktyushina and Mal'tsev (1984)	IR/matrix (Ar)							198

^aBand not assigned in Molnár et al. (1996).

Table D.5

Experimental and computed geometrical parameters of selected Ln_2X_6 dimers; bond distances in pm, bond angles in degrees

Ln_2X_6	Geometry ^a				
	r_r	r_t	α_{r1}	α_{r2}	α_t
La ₂ F ₆ ^b	236.2	212.6	70.6	109.4	116.7
Dy ₂ F ₆ ^b	221.9	200.8	73.0	107.0	117.2
La ₂ Cl ₆ ^b	281.4	258.4	80.6	99.4	117.0
Ce ₂ Cl ₆ ^c	277.5	257.0	82.7	–	116.5
Pr ₂ Cl ₆ ^c	275.4	254.9	83.4	–	116.3
Nd ₂ Cl ₆ ^c	273.5	253.0	81.1	99.4	116.3
Dy ₂ Cl ₆ ^d	268.0(10)	244.9(10)	84.1(34)		
Dy ₂ Cl ₆ ^b	266.4	245.2	83.6	96.4	116.7
Er ₂ Cl ₆ ^e	265(4)	244.4(5)	84(10)		117(5)
Lu ₂ Cl ₆ ^f	258.9(24)	236.6(5)	84(2)		119(7)
La ₂ Br ₆ ^b	297.1	273.9	83.7	96.3	115.0
Ce ₂ Br ₆ ⁱ	301.3	278.1	83.9	96.1	117.0
Dy ₂ Br ₆ ^d	281.1(9)	259.4(8)	91.7(17)		
Dy ₂ Br ₆ ^b	282.0	260.4	87.0	93.0	115.7
Er ₂ Br ₆ ^g	275.8(20)	258.8(6)	81(7)		116(7)
La ₂ I ₆ ^b	318.8	296.1	87.6	92.4	114.5
Ce ₂ I ₆ ^h	320.7(23.8)	294.8(9)			
Ce ₂ I ₆ ⁱ	322.0	299.3	88.5	91.5	116.7
Dy ₂ I ₆ ^b	303.6	282.4	90.8	89.2	115.3

^a r_r , α_{r1} and α_{r2} indicate the geometrical parameters of the ring, while r_t and α_t the terminal ones of the dimer (cf. fig. 36).

^bComputed by Kovács (2000).

^cComputed by Kapala et al. (2002).

^dFrom ED investigations by Hargittai (2000).

^e r_g parameters by Giricheva et al. (2000c).

^f r_g parameters by Giricheva et al. (2000b).

^g r_g parameters by Zakharov et al. (2001).

^h r_g parameters by Molnár et al. (1996).

ⁱComputed by Kovács (1999).

Table D.6
Computed vibrational frequencies of selected Ln_2X_6 compounds, in cm^{-1} ^a

	$\text{La}_2\text{F}_6^{\text{a}}$	$\text{Dy}_2\text{F}_6^{\text{a}}$	$\text{La}_2\text{Cl}_6^{\text{a}}$	$\text{Ce}_2\text{Cl}_6^{\text{b}}$	$\text{Pr}_2\text{Cl}_6^{\text{b}}$	$\text{Nd}_2\text{Cl}_6^{\text{b}}$	$\text{Dy}_2\text{Cl}_6^{\text{a}}$	$\text{La}_2\text{Br}_6^{\text{a}}$	$\text{Ce}_2\text{Br}_6^{\text{a}}$	$\text{Dy}_2\text{Br}_6^{\text{a}}$	$\text{La}_2\text{I}_6^{\text{a}}$	$\text{Ce}_2\text{I}_6^{\text{a}}$	$\text{Dy}_2\text{I}_6^{\text{a}}$
A_u	64	58	29	32	34	34	30	18	19	21	14	14	16
B_{1u}	71	67	33	32	35	38	38	23	28	29	18	21	23
	302	331	226	233	237	240	244	161	164	173	137	140	144
B_{2u}	41	40	14	12	10	12	12	7	9	8	5	5	5
	163	177	88	91	91	92	94	51	53	55	34	36	39
	518	540	333	330	334	336	345	240	239	243	195	195	195
B_{3u}	120	122	64	64	65	66	71	42	43	47	31	31	34
	386	406	230	236	236	236	237	151	151	154	110	110	113
	520	547	317	312	315	317	331	214	212	220	171	169	171
A_g	98	100	54	53	54	55	58	34	34	38	24	24	27
	152	156	97	91	92	94	100	72	72	75	53	54	57
	352	390	234	238	241	243	253	151	152	162	112	113	120
	534	559	328	323	326	328	341	226	223	230	182	180	181
B_{1g}	55	53	32	44	45	47	36	23	25	27	19	20	23
	511	534	329	327	330	332	341	236	236	240	193	193	193
B_{2g}	73	71	42	42	45	46	48	32	37	38	25	28	31
	301	334	190	198	199	200	200	131	136	136	108	112	110
B_{3g}	113	124	65	74	75	76	70	36	38	39	24	26	27

^aComputed by Kovács (1999, 2000).

^bComputed by Kapala et al. (2002).

Appendix E. The enthalpies of sublimation of the lanthanide trihalides

Table E.1
Enthalpy of sublimation of the gaseous lanthanide trifluorides

authors	method ^a	<i>T</i> /K	$\Delta_{\text{sub}}H^\circ(298.15 \text{ K})/\text{kJ}\cdot\text{mol}^{-1}$
LaF₃			
Kent et al. (1966) ^b	K	1200–1405	446.9 ± 0.8
	M	1303–1416	448.5 ± 0.9
Suvorov et al. (1966)	TE	1333–1532	448.5 ± 1.0
Mar and Searcy (1967)	L	1343–1640	440.9 ± 0.2
	T	1378–1573	442.0 ± 0.7
Suvorov and Novikov (1968)	K	1097–1222	359.5 ± 2.4
Skinner and Searcy (1971)	M	1221–1412	447.7 ± 0.6
Roberts and Searcy (1972)	M	1326–1644	441.0
Petzel et al. (1992)	K	1419–1661	443.0 ± 0.7
selected value:			444.8 ± 3.0
CeF₃			
Lim and Searcy (1966)	K	1373–1658	439.4 ± 2.0
Suvorov et al. (1966)	TE	1333–1532	437.8 ± 0.4
Zmbov and Margrave (1968)	M	1301–1485	411.6
Roberts and Searcy (1972)	M	1262–1586	437.6
McCreary and Thorn (1973a)	M	1343–1476	447.5
selected value:			438.3 ± 2.0
PrF₃			
Suvorov et al. (1966)	TE	1335–1465	435.8 ± 0.7
Zmbov and Margrave (1968)	M	1327–1491	419.1
Skinner and Searcy (1968)	K	1430–1586	435.2 ± 0.1
	M	1424–1584	435.4 ± 0.3
selected value:			435.5 ± 2.0
NdF₃			
Suvorov et al. (1966)	TE	1334–1490	450.7 ± 1.1
Zmbov and Margrave (1966) ^b	M	1383–1520	433.2 ± 0.7
McCreary and Thorn (1974a)	M	1325–1470	445.8
selected value:			433.2 ± 5.0
PmF₃			
Gibson and Haire (1989)	M ^c	1373–1553	443
selected value:			430 ± 15
SmF₃			
Zmbov and Margrave (1968)	M	1362–1506	428.7
selected value:			429 ± 10
EuF₃			
Zmbov and Margrave (1968)	M	1382–1522	436.9
selected value:			437 ± 10
GdF₃			
Zmbov and Margrave (1968)	M	1391–1527	414.1
McCreary and Thorn (1973b)	M	1465 ^d	453.9
selected value:			454 ± 5.0

continued on next page

Table E.1, *continued from previous page*

authors	method ^a	T/K	$\Delta_{\text{sub}}H^\circ(298.15\text{ K})/\text{kJ}\cdot\text{mol}^{-1}$
TbF₃			
Zmbov and Margrave (1968)	M	992–1167	445.9
McCreary and Thorn (1973b)	M	1325–1437	450.8
selected value:			450.4 ± 5.0
DyF₃			
Besenbuch et al. (1967)	E	1326–1362	452.1 ± 0.3
	M	1426–1622	445.0 ± 0.5
Zmbov and Margrave (1968)	M	1002–1170	
McCreary and Thorn (1974b)	M	^e	455.7 ± 0.1
Stolyarova et al. (1996)	M	1280–1380	449.5
selected value:			448.6 ± 3.0
HoF₃			
Besenbuch et al. (1967)	E	1328–1406	448.0 ± 0.5
	M	1278–1456	449.6 ± 0.3
McCreary and Thorn (1974b)	M	^e	456.8 ± 0.4
selected value:			451.5 ± 2.0
ErF₃			
Besenbuch et al. (1967)	E	1311–1405	454.8 ± 0.4
	M	1374–1521	452.8 ± 0.2
McCreary and Thorn (1974b)	M	^e	457.3 ± 1.5
Bencze et al. (1996)	M	1288–1635	455.3 ± 0.3
selected value:			454.3 ± 2.0
TmF₃			
Zmbov and Margrave (1967)	M	1273–1415	
Biefeld and Eick (1976)	K	1349–1809	446.6 ± 0.4
Bencze et al. (1996)	K + M	1266–1624	452.6 ± 0.6
selected value:			449.6 ± 3.0
YbF₃			
Zmbov and Margrave (1967)	M	1293–1428	437.9 ± 0.4
Biefeld and Eick (1975)	M	1342–1794	457.3 ± 2.1 ^f
Petzel and Greis (1976)	M	1580–1795	454.0 ± 0.5
selected value:			454.0 ± 2.0
LuF₃			
Zmbov and Margrave (1967)	M	1287–1450	425.2 ± 0.5
Petzel et al. (1992)	K	1471–1945	440.0 ± 1.1
selected value:			440.0 ± 2.0

^aB, boiling point method; E, effusion; K, Knudsen effusion; M, mass spectrometry; TE, torsion effusion.

^bAlso reported by Zmbov and Margrave (1968).

^cMade on a sample (Pr_{1/3}Pm_{1/3}Sm_{1/3})F₃.

^dMean temperature.

^eNo temperature range given.

^fIt was concluded by the authors that the vaporization proceeded according to the reaction YbF_{3,00}(cr) = 0.005YbF_{2,40}(cr) + 0.95YbF₃(g) + 0.003F(g). We have here treated the data as if congruent vaporization took place.

Table E.2
Enthalpy of sublimation of the gaseous lanthanide trichlorides

authors	method ^a	T/K	$\Delta_{\text{sub}}H^\circ(298.15 \text{ K})/\text{kJ}\cdot\text{mol}^{-1}$
LaCl₃			
Harrison (1952)	K	1028–1192	331.9 ± 0.8
Nesmeyanov and Sazonov (1959)	K	842–1101	329.8 ± 1.3
Polyachenok and Novikov (1963b)	B	????–1673	333.2
Novikov and Baev (1962)	B	1397–1493	340.2 ± 1.0
Shimazaki and Niwa (1962)	K	1022–1110	342.7 ± 0.3
Moriarity (1963)	K	1173–1253	319.7 ± 4.3
Hastie et al. (1968)	M	950–1100	331.4
Nisel'son et al. (1978)	B	1373–1573	337.1
Brunetti et al. (2000)	TE	955–1045	337.8 ± 0.2
selected value:			337.5 ± 5.0
CeCl₃			
Harrison (1952)	K	1013–1085	326.0 ± 1.6
Novikov and Baev (1962)	B	1366–1497	332.3 ± 0.8
Shimazaki and Niwa (1962)	K	1012–1071	332.8 ± 0.2
Moriarity (1963)	K	1043–1223	323.7 ± 1.9
Polyachenok and Novikov (1963b)	B	????–1673	312.3
Villani et al. (2000b)	TE	887–1003	329.1 ± 0.1
Pogrebnoi et al. (2001)	M	972–1075	333.5 ± 0.3
Kapala et al. (2002)	M	876–1088	327.1
selected value:			330.3 ± 3.0
PrCl₃			
Harrison (1952)	K	991–1142	320.9 ± 1.8
Novikov and Baev (1962)	B	1314–1465	329.9 ± 0.7
Shimazaki and Niwa (1962)	K	1002–1061	330.6 ± 0.2
Moriarity (1963)	K	1002–1273	330.6 ± 0.2
Polyachenok and Novikov (1963b)	B	????–1673	323.3 ± 3.6
Dudchik et al. (1969a)	B	1374–1636	327.5 ± 0.2
Nisel'son et al. (1978)	B	1373–1573	336.4
Hannay and Myers (1979)	E	914–1056	332.1 ± 0.5
Villani et al. (2000a)	TE	890–1061	327.7 ± 0.3
Kapala et al. (2002)	M	946–1106	326.1
selected value:			329.2 ± 3.0
NdCl₃			
Harrison (1952)	K	964–1107	312.6 ± 2.2
Novikov and Baev (1962)	B	1314–1465	324.0 ± 0.8
Shimazaki and Niwa (1962)	K	973–1032	326.7 ± 0.5
Moriarity (1963)	K	993–1278	323.6 ± 4.2
Polyachenok and Novikov (1963b)	B	????–1673	293.0
Ciach et al. (1973)	M	1055–1093	339.0
Evseeva and Zenkevich (1976)	M		n.a.
Nisel'son et al. (1978)	B	1373–1573	329.1
Villani et al. (2002)	TE	866–1019	324.5 ± 0.3
Kapala et al. (2002)	M	934–1079	323.8
selected value:			324.5 ± 2.0

continued on next page

Table E.2, continued from previous page

authors	method ^a	T/K	$\Delta_{\text{sub}}H^\circ(298.15 \text{ K})/\text{kJ}\cdot\text{mol}^{-1}$
SmCl₃			
Pashinkin et al. (1962)	?	774–854	247.6
Pogrebnoi et al. (2001)	M	972–1075	299.0 ± 0.4
selected value:			315 ± 8
EuCl₃			
Moriarity (1963)	E	953–1188	275.8 ± 10.6
Hastie et al. (1968)	M	1145–1290	decomp.
selected value:			310.0 ± 10
GdCl₃			
Moriarity (1963)	K	871–1119	291.4 ± 3.4
Dudchik et al. (1969a)	B	1369–1603	304.1 ± 0.4
Ciach et al. (1973)	M	963–1075	320.9
Myers and Hannay (1980)	E	938–1044	307.9 ± 0.5
selected value:			306.0 ± 6.0
TbCl₃			
Moriarity (1963)	K	1198–1313	300.5 ± 6.2
Dudchik et al. (1969a)	B	1326–1653	295.1 ± 0.3
Myers and Hannay (1980)	K	926–1044	300.3 ± 0.4
Kudin et al. (2000)	M	900–1100	308.6
selected value:			297.7 ± 3.0
DyCl₃			
Moriarity (1963)	K	1023–1223	269.8 ± 1.1
Dudchik et al. (1969a)	B	1325–1620	282.6 ± 0.5
Myers and Hannay (1980)	K	936–1031	287.9 ± 0.4
Kudin et al. (1997)	M	850–1010	275.1
Brunetti et al. (1999)	TE	924–1214	283.7 ± 0.2
Kapala et al. (2002)	M	930–1027	282.4
selected value:			284.2 ± 4.0
HoCl₃			
Moriarity (1963)	K	1043–1223	275.1 ± 3.2
Dudchik et al. (1969b)	B	1273–1643	279.8
Piacente et al. (2002)	TE	904–1105	284.8 ± 0.3
selected value:			284.8 ± 4.0
ErCl₃			
Moriarity (1963)	K	1043–1283	285.8 ± 9.2
Polyachenok and Novikov (1963b)	B	????–1673	264.0
selected value:			285 ± 8
TmCl₃			
Moriarity (1963)	K	1073–1228	274.6 ± 5.9
Dudchik et al. (1969b)	B	1273–1643	276.2
Kudin et al. (2000)	M	900–1100	283.2
selected value:			276 ± 6

continued on next page

Table E.2, *continued from previous page*

authors	method ^a	T/K	$\Delta_{\text{sub}}H^\circ(298.15 \text{ K})/\text{kJ}\cdot\text{mol}^{-1}$
YbCl₃			
Moriarity (1963)	K	1148–1323	292.1 ± 1.4
Kudin et al. (1997)	M	1000–1130	309.4
selected value:			277 ± 6
LuCl₃			
Moriarity (1963)	K	1168–1228	283.9 ± 2.1
Dudchik et al. (1969b)	B	1273–1643	277.1
Nisel'son et al. (1978)	B	1373–1573	
selected value:			277 ± 6

^aB, boiling point method; E, effusion; K, Knudsen effusion; M, mass spectrometry; TE, torsion effusion.

Table E.3
Enthalpy of sublimation of the gaseous lanthanide tribromides

authors	method ^a	T/K	$\Delta_{\text{sub}}H^\circ(298.15 \text{ K})/\text{kJ}\cdot\text{mol}^{-1}$
LaBr₃			
Harrison (1952)	K	915–1057	295.0 ± 1.4
Shimazaki and Niwa (1962)	K	1002–1052	321.4 ± 0.1
Dudchik et al. (1975)	B	1321–1542	318.0
Gietmann et al. (1996)	M	950–1024	308.8 ± 0.6
Brunetti et al. (2000)	TE	955–1045	316.0 ± 0.1
selected value:			314.3 ± 5.0
CeBr₃			
Harrison (1952)	K	892–1030	286.8 ± 0.8
Shimazaki and Niwa (1962)	E	943–992	311.8 ± 0.4
Dudchik et al. (1975)	B	1306–1518	308.4
Gietmann et al. (1996)	M	962–968	301.1 ± 0.0
Villani et al. (2000b)	TE	887–1003	305.9 ± 0.4
selected value:			306.8 ± 5.0
PrBr₃			
Shimazaki and Niwa (1962)	K	924–973	307.4 ± 0.3
Dudchik et al. (1975)	B	1280–1560	304.4
Gietmann et al. (1996)	M	924–955	298.1 ± 0.2
Villani et al. (2000a)	TE	890–1061	303.0 ± 0.2
selected value:			303.3 ± 4.0
NdBr₃			
Harrison (1952)	K	849–975	274.2 ± 0.4
Shimazaki and Niwa (1962)	K	889–948	305.6 ± 0.1
Dudchik et al. (1975)	B	1258–1559	302.2
Gietmann et al. (1996)	M	923–936	294.6 ± 0.2
Villani et al. (2002)	TE	866–1019	304.2 ± 0.2
selected value:			301.6 ± 4.0
SmBr₃			
Harrison (1952)	K	822–940	260.2 ± 1.4
selected value:			300 ± 10

continued on next page

Table E.3, *continued from previous page*

authors	method ^a	<i>T</i> /K	$\Delta_{\text{sub}}H^\circ(298.15 \text{ K})/\text{kJ}\cdot\text{mol}^{-1}$
GdBr₃			
Makhadmurodov et al. (1975)	B	1120–1532	277.0
Gietmann et al. (1996)	M	1005–1011	272.5 ± 0.1
selected value:			274.8 ± 3.0
TbBr₃			
Makhadmurodov et al. (1975)	B	1219–1536	274.6
Gietmann et al. (1996)	M	964–985	270.6 ± 0.5
selected value:			272.6 ± 3.0
DyBr₃			
Makhadmurodov et al. (1975)	B	1220–1535	273.0
Hilpert et al. (1995)	M	953–1053	269.6 ± 0.4
Brunetti et al. (1999)	TE	878–1151	276.4 ± 0.4
selected value:			273.0 ± 5.0
HoBr₃			
Gietmann et al. (1996)	M	971–1003	275.0 ± 0.5
Piacente et al. (2002)	TE	904–1105	285.0 ± 0.3
selected value:			280.0 ± 5.0
ErBr₃			
Makhadmurodov et al. (1975)	B	1242–1506	270.8
Gietmann et al. (1996)	M	946–995	271.4 ± 0.8
selected value:			271.1 ± 5.0
TmBr₃			
Makhadmurodov et al. (1975)	B	1252–1482	269.5
Gietmann et al. (1996)	M	946–995	275.4 ± 1.7
selected value:			272.5 ± 5.0
LuBr₃			
Makhadmurodov et al. (1975)	B	1305–1468	267.2
selected value:			267.2 ± 10

^aB, boiling point method; E, effusion; K, Knudsen effusion; M, mass spectrometry; TE, torsion effusion.

Table E.4
Enthalpy of sublimation of the gaseous lanthanide triiodides

authors	method ^a	<i>T</i> /K	$\Delta_{\text{sub}}H^\circ(298.15 \text{ K})/\text{kJ}\cdot\text{mol}^{-1}$
LaI₃			
Shimazaki and Niwa (1962)	K	953–1012	315.5 ± 0.4
Hirayama et al. (1976)	M	891–1009	302.7 ± 0.3
Brunetti et al. (2000)	TE	955–1045	307.9 ± 0.3
selected value:			307.9 ± 8.0
CeI₃			
Hirayama and Castle (1973)	M	933 ^b	305.9
Hirayama et al. (1975)	K	870–1015	297.5 ± 0.4
Struck and Feuersanger (1999)	M	841–928	285.6
Villani et al. (2000b)	TE	887–1003	301.8 ± 0.4
selected value:			299.7 ± 5.0

continued on next page

Table E.4, *continued from previous page*

authors	method ^a	T/K	$\Delta_{\text{sub}}H^\circ(298.15 \text{ K})/\text{kJ}\cdot\text{mol}^{-1}$
PrI₃			
Shimazaki and Niwa (1962)	E	933–1002	303.6 ± 0.7
Hirayama and Camp (1972)	E	841–1032	296.5 ± 0.7
Villani et al. (2000a)	TE	890–1061	297.1 ± 0.3
selected value:			296.8 ± 3.0
NdI₃			
Shimazaki and Niwa (1962)	E	953–1002	298.0 ± 0.3
Hirayama and Camp (1972)	E	857–1037	289.7 ± 0.6
Villani et al. (2002)	TE	866–1019	296.0 ± 0.2
selected value:			294.6 ± 3.0
GdI₃			
Hirayama and Castle (1973)	M	943 ^b	270.0
Hirayama et al. (1975)	K	912–1025	276.4 ± 0.8
selected value:			276.4 ± 4.0
TbI₃			
Hirayama and Castle (1973)	M	931 ^b	261.0
Hirayama et al. (1975)	K	883–979	273.0 ± 0.4
selected value:			273.0 ± 6.0
DyI₃			
Hirayama and Castle (1973)	M	916 ^b	266.7
Hirayama et al. (1975)	K	885–1060	272.6 ± 0.4
Kaposi et al. (1983)	M	970–1150	270.8 ± 1.7
Brunetti et al. (1999)	TE	843–1051	274.9 ± 0.4
selected value:			273.8 ± 4.0
HoI₃			
Hirayama and Castle (1973)	M	880 ^b	280.7
Hirayama et al. (1975)	E	924–1029	276.1 ± 0.6
Kaposi et al. (1986)	M	935–1055	275.3 ± 0.5
Gietmann et al. (1996)	M	945–975	269.3 ± 0.8
Piacente et al. (2002)	TE	904–1105	267.1 ± 0.4
selected value:			272.0 ± 6.0
ErI₃			
Hirayama and Castle (1973)	M	895 ^b	259.9
Hirayama et al. (1975)	K	898–1016	273.5 ± 0.6
selected value:			273.5 ± 6.0
TmI₃			
Hirayama et al. (1975)	K	867–990	271.8 ± 0.6
Dettingmeijer and Dielis (1988)	K	874–1012	267.5 ± 0.4 ^c
Struck and Feuersanger (1991)	M	775–900	258.1
selected value:			271.8 ± 6.0

^aB, boiling point method; E, effusion; K, Knudsen effusion; M, mass spectrometry; TE, torsion effusion.

^bOnly mean temperature is given.

^cRecalculated assuming monomeric species only.

References

- Adamo, C., Barone, V., 2000. *J. Comput. Chem.* **21**, 1153–1166.
- Adamo, C., Maldivi, P., 1997. *Chem. Phys. Lett.* **268**, 61–68.
- Adamo, C., Maldivi, P., 1998. *J. Phys. Chem. A* **102**, 6812–6820.
- Akishin, P.A., Naumov, V.A., Tatevskii, V.M., 1959. *Vestn. Mosk. Gos. Univ., Ser. 2, Khim.*, 229–236.
- Baetslé, L.H. (Ed.), 1999. *Actinide and Fission Products Partitioning and Transmutation*. OECD/NEA.
- Baker, F.B., Fitzgibbon, G.C., Pavone, D., Holley, C.E. Jr., Hansen, L.D., Lewis, E.A., 1972. *J. Chem. Thermodyn.* **4**, 621.
- Becke, A.D., 1988. *Phys. Rev. A* **38**, 3098.
- Becke, A.D., 1993. *J. Chem. Phys.* **98**, 5648.
- Bence, L., Feltrin, A., Cesaro, S.N., Popovic, A., 1996. *Rapid Comm. Mass Spectr.* **10**, 1248–1258.
- Besenbuch, G., Charlu, T.V., Zmbov, K.F., Margrave, J.L., 1967. *J. Less-Common Met.* **12**, 375.
- Bettonville, S., Goudiakas, J., Fuger, J., 1987. *J. Chem. Thermodyn.* **19**, 595–604.
- Biefeld, R.M., Eick, H.A., 1975. *J. Chem. Phys.* **63**, 1190.
- Biefeld, R.M., Eick, H.A., 1976. *J. Less-Common Met.* **45**, 117–123.
- Boghosian, S., Papatheodorou, G.N., 1996. In: *Handbook on the Physics and Chemistry of Rare Earths*, Vol. **23**. Elsevier Science B.V., p. 435 (ch. 157).
- Bommer, H., Hohmann, E., 1941a. *Z. anorg. allgem. Chem.* **248**, 373–382.
- Bommer, H., Hohmann, E., 1941b. *Z. anorg. allgem. Chem.* **248**, 357–372.
- Brown, D., Fletcher, S., Holah, D.G., 1968. *J. Chem. Soc. A*, 1889–1894.
- Brunetti, B., Vassallo, P., Piacente, V., Scardala, P., 1999. *J. Chem. Eng. Data* **44**, 509–515.
- Brunetti, B., Villani, A.R., Piacente, V., Scardala, P., 2000. *J. Chem. Eng. Data* **45**, 231–236.
- Büchel, D., Krok-Kowalski, J., Seifert, H.J., 1995. *Thermochim. Acta* **282/283**, 297–304.
- Burgess, J., Kijowski, J., 1981. *J. Inorg. Nucl. Chem.* **43**, 2389.
- Burnett, J.L., 1964. *Tech. Rep. UCRL-11850*.
- Burnett, J.L., Cunningham, B.B., 1964. *Tech. Rep. UCRL-11126*, U.S. At. Energy Comm.
- Carnall, W.T., 1982. *J. Chem. Phys.* **96**, 8713–8726.
- Charlu, T.V., Chaudhuri, A.K., Margrave, J.L., 1970. *High Temp. Sci.* **2**, 1–8.
- Ciach, S., Nicholson, A.J.C., Swingler, D.L., Thistlethwaite, P.J., 1973. *Inorg. Chem.* **12**, 2072–2074.
- Corbett, J.D., 1972. *Inorg. Nucl. Chem. Lett.* **8**, 337–340.
- Corbett, J.D., Druding, L.F., Burkhard, W.J., Lindahl, C.B., 1962. *Discussions Faraday Soc.* **32**, 79.
- Cordfunke, E.H.P., Blacquère, R.J.H., 1997. *Thermochim. Acta* **298**, 195–197.
- Cordfunke, E.H.P., Booij, A.S., 1995. *J. Chem. Thermodyn.* **27**, 897–900.
- Cordfunke, E.H.P., Booij, A.S., 1997. *J. Chem. Thermodyn.* **29**, 715.
- Cordfunke, E.H.P., Konings, R.J.M., 2001a. *Thermochim. Acta* **375**, 61–64.
- Cordfunke, E.H.P., Konings, R.J.M., 2001b. *Thermochim. Acta* **375**, 17–50.
- Cordfunke, E.H.P., Booij, A.S., Furkaliouk, M.Y., 1996. *J. Chem. Thermodyn.* **28**, 1387–1393.
- Cordfunke, E.H.P., Elzinga, G.D., Huntelaar, M.E., van Vlaanderen, P., 1999. *Thermochim. Acta* **338**, 135–138.
- Cox, J.D., Wagman, D.D., Medvedev, V.A., 1989. *CODATA Key Values for Thermodynamics*. Hemisphere, New York.
- Cundari, T.R., Stevens, W.J., 1993. *J. Chem. Phys.* **98**, 5555.
- Cundari, T.R., Sommerer, S.O., Strohecker, L.A., Tipsett, L., 1995. *J. Chem. Phys.* **103**, 7058–7063.
- Daire, M., 1968. *C. R. Acad. Sci. Paris Ser. C* **266**, 1111.
- Daniel, J.F., Wilmarth, W.R., Begun, G.M., Peterson, J.R., 1989. *J. Cryst. Spectrosc. Res.* **19**, 39–49.
- De Kozak, A., Almai, M., 1978. *Rev. Chim. Min.* **15**, 139–144.
- De Kozak, A., Samouël, M., Chrétien, A., 1973. *Rev. Chim. Min.* **10**, 259–271.
- Deline, T.A., Westrum, E.F. Jr., Haschke, J.M., 1975. *J. Chem. Thermodyn.* **7**, 671–675.
- Dettingmeijer, J.H., Dielis, H.R., 1988. *J. Less Common Met.* **139**, 331–343.
- Di Bella, S., Lanza, G., Fragalá, I., 1993. *Chem. Phys. Lett.* **214**, 598.
- Dieke, G.H., Crosswhite, H.M., Crosswhite, H., 1968. *Spectra and Energy Levels of Rare Earth Ions in Crystals*. Interscience Publishers.
- Dolg, M., Stoll, H., Savin, A., Preuss, H., 1989. *Theor. Chim. Acta* **75**, 173.
- Dolg, M., Stoll, H., Preuss, H., 1991. *J. Mol. Struct. (Theochem)* **235**, 67.
- Druding, L.F., Corbett, J.D., 1961. *J. Am. Chem. Soc.* **83**, 2462–2467.
- Dudchik, G.P., Polyachenok, O.G., Novikov, G.I., 1969a. *Russ. J. Phys. Chem.* **43**, 1669.

- Dudchik, G.P., Polyachenok, O.G., Novikov, G.I., 1969b. *Russ. J. Phys. Chem.* **43**, 1203.
- Dudchik, G.P., Makhmadmurodov, A., Polyachenok, O.G., 1975. *Russ. J. Phys. Chem.* **49**, 1094–1095.
- Dudek, H., Seifert, H., 2001. *Z. anorg. allg. Chem.* **627**, 2317–2322.
- Dworkin, A.S., Bredig, M.A., 1963a. *J. Phys. Chem.* **67**, 697–698.
- Dworkin, A.S., Bredig, M.A., 1963b. *J. Phys. Chem.* **67**, 2499–2500.
- Dworkin, A.S., Bredig, M.A., 1971. *High Temp. Sci.* **3**, 81.
- Evseeva, G.V., Zenkevich, L.V., 1976. *Vestn. Mosk. Univ. Khim.* **17**, 110.
- Ezhov, Y.S., Komarov, S.A., Sevast'yanov, V.G., 2000. *J. Struct. Chem.* **41**, 593 (Engl. transl.).
- Feltrin, A., Cesaro, S.N., 1996. *High Temperature and Materials Science* **35**, 203–214.
- Fitzgibbon, G.C., Holley, C.E. Jr., 1968. *J. Chem. Engr. Data* **13**, 63.
- Fitzgibbon, G.C., Holley, C.E. Jr., Wadsö, I., 1965. *J. Phys. Chem.* **69**, 2464–2466.
- Fitzgibbon, G.C., Huber, E.J. Jr., Holley, C.E. Jr., 1972. *J. Chem. Thermodyn.* **4**, 349.
- Fitzgibbon, G.C., Huber, E.J. Jr., Holley, C.E. Jr., 1973. *Rev. Chim. Miner.* **10**, 29.
- Flotow, H.E., O'Hare, P.A.G., 1981. *J. Chem. Phys.* **74**, 3046–3055.
- Flotow, H.E., O'Hare, P.A.G., 1984. *J. Chem. Phys.* **80**, 460–466.
- Flotow, H.E., Tetenbaum, M., 1981. *J. Chem. Phys.* **74**, 5269.
- Fuger, J., Morss, L.R., Brown, D., 1980. *J. Chem. Soc. Dalton Trans.*, 1076–1078.
- Fuger, J., Parker, V.B., Hubbard, W.N., Oetting, F.L., 1983. *The chemical thermodynamics of actinide elements and compounds. Part 8. The Actinide Halides.* IAEA.
- Furkaliouk, M.Y., 1993. Ph.D. thesis, Moscow State University, Chem. Department.
- Furkaliouk, M.Y., Cordfunke, E.H.P., 1996. *J. Chem. Thermodyn.* **28**, 255–259.
- Furkaliouk, M.Y., Efimov, M.E., Goryushkin, V.F., 1992. *Zh. Fiz. Khim.* **66**, 1108.
- Furkaliouk, M.Y., Leonidov, V.Y., Goryushkin, V.F., 1993. *Zh. Fiz. Khim.* **67**, 1947–1949.
- Furkaliouk, M.Y., Booi, A.S., Cordfunke, E.H.P., 1995. *J. Chem. Thermodyn.* **27**, 293–297.
- Gamanovich, N.M., Glybin, V.P., 1974. *Zh. Fiz. Khim.* **48**, 2883.
- Gardner, P.J., Preston, S.R., 1991. *Thermochim. Acta* **175**, 129–134.
- Garton, G., Walker, P.J., 1982. *Mat. Res. Bull.* **17**, 1227–1234.
- Gaune-Escard, M., Rycerz, L., Szczepaniak, W., Bogacz, A., 1994. *J. Alloys Comp.* **204**, 193–196.
- Gaune-Escard, M., Bogacz, A., Rycerz, L., Szczepaniak, W., 1996. *J. Alloys Comp.* **235**, 176–181.
- Gavrichev, K.S., Gorbunov, V.E., Golushina, L.N., Totrova, G.A., Goryushkin, V.F., 1992. *Zh. Fiz. Khim.* **66**, 2829–2831.
- Gibson, J.K., Haire, R.G., 1989. *Thermochim. Acta* **140**, 287–298.
- Gietmann, C., Hilpert, K., Nickel, H., 1996. *Tech. Rep. Internal Report JUEL-3337.*
- Girichev, G.V., 2002. To be published.
- Girichev, G.V., Giricheva, N.I., Shlykov, S.A., Zakharov, A.V., Krasnov, A.V., Krasnova, O.G., 2002. In: *XIX Austin Symposium on Molecular Structure.*
- Giricheva, N.I., Zasorin, E.Z., Girichev, G.V., Krasnov, K.S., Spiridonov, V.P., 1977. *Izv. Vyssh. Uchebn. Zaved., Khim. Khim. Tekhnol.* **20**, 284 (in Russian).
- Giricheva, N.I., Girichev, G.V., Krasnov, A.V., 2000a. *J. Struct. Chem.* **41**, 149 (Engl. transl.).
- Giricheva, N.I., Girichev, G.V., Krasnov, A.V., Krasnova, O.G., 2000b. *J. Struct. Chem.* **41**, 388 (Engl. transl.).
- Giricheva, N.I., Girichev, G.V., Shlykov, S.A., Pelipets, O.V., 2000c. *J. Struct. Chem.* **41**, 231 (Engl. transl.).
- Giricheva, N.I., Zakharov, A.V., Shlykov, S.A., Girichev, G.V., 2000d. *J. Chem. Soc., Dalton Trans.*, 3401–3403.
- Gogadze, N.G., Ippolitov, E.G., Zhigarnovskii, B.M., 1972a. *Russ. J. Inorg. Chem.* **17**, 304–305.
- Gogadze, N.G., Ippolitov, E.G., Zhigarnovskii, B.M., 1972b. *Russ. J. Inorg. Chem.* **17**, 600–601.
- Gogadze, N.G., Ippolitov, E.G., Zhigarnovskii, B.M., 1972c. *Russ. J. Inorg. Chem.* **17**, 1357–1358.
- Gorbunov, V.E., Tolmach, P.I., Gavrichev, K.S., Totrova, G.A., Goryushkin, V.F., 1986. *Russ. J. Phys. Chem.* **60**, 789–790.
- Goryushkin, V.F., Poshevneva, A.I., 1992. *Russ. J. Inorg. Chem.* **37**, 1074–1076.
- Goryushkin, V.F., Poshevneva, A.I., 1996. *Russ. J. Inorg. Chem.* **41**, 1467–1468.
- Goryushkin, V.F., Poshevneva, A.I., Vinokurova, N.G., 1999. *Russ. J. Inorg. Chem.* **44**, 1020–1030.
- Goryushkin, V.F., Zalyмова, S.A., Poshevneva, A.I., 1990. *Russ. J. Inorg. Chem.* **35**, 1749–1752.
- Greis, O., Cader, M.S.R., 1985. *Thermochim. Acta* **87**, 145–150.
- Greis, O., Haschke, J.M., 1982. In: *Handbook on the Physics and Chemistry of Rare Earths, Vol. 5.* North-Holland, pp. 387–460 (ch. 45).

- Groen, P.C., 2002. To be published.
- Gschneidner, K.A. Jr., 1969. *L. Less-Common Met.* **17**, 13–24.
- Gschneidner, K.A. Jr., 1989. *J. Less-Common Met.* **154**, 1–8.
- Gunselius, H., Borrmann, H., Simon, A., Urland, W., 1988. *Z. Naturforsch. B* **43**, 1023.
- Gvelesiani, G.G., Yashvili, T.S., 1967. *Zh. Neorg. Khim.* **12**, 3233.
- Hannay, M.H., Myers, C.E., 1979. *J. Less-Common Met.* **66**, 145–150.
- Hargittai, M., 1999. *J. Phys. Chem. A* **103**, 7552–7553.
- Hargittai, M., 2000. *Chem. Rev.* **100**, 2233–2301.
- Harris, A.L., Veale, C.R., 1965. *J. Inorg. Nucl. Chem.* **27**, 1437–1439.
- Harrison, E.R., 1952. *J. Appl. Chem.* **2**, 601–602.
- Hastie, J.W., Ficalora, P., Margrave, J.L., 1968. *J. Less-Comm. Metals* **14**, 83.
- Hastie, J.W., Hauge, R.H., Margrave, J.L., 1970. *Spectroscopy in Inorganic Chemistry*. Academic Press, p. 57.
- Hastie, J.W., Hauge, R.H., Margrave, J.L., 1975. *J. Less-Common Met.* **39**, 309.
- Hauge, R.H., Hastie, J.W., Margrave, J.L., 1971. *J. Less-Common Met.* **23**, 359–365.
- Henderson, D.C., 1970. Ph.D. thesis, Iowa State University, Ames.
- Hennig, C., Oppermann, H., 1997. *Z. Naturforsch. B* **52**, 1517–1525.
- Hennig, C., Oppermann, H., 1998. *Z. Naturforsch. B* **53**, 175–183.
- Hennig, C., Oppermann, H., 1999. *Z. Naturforsch. B* **54**, 1283–1294.
- Hennig, C., Oppermann, H., 2000. *Z. Naturforsch. B* **55**, 65–73.
- Hennig, C., Oppermann, H., Blonska, A., 1998. *Z. Naturforsch. B* **53**, 1169–1179.
- Hilpert, K., Niemann, U., 1997. *Thermochim. Acta.* **299**, 49–57.
- Hilpert, K., Miller, M., Ramondo, F., 1995. *J. Chem. Phys.* **102**, 6194–6198.
- Hirayama, C., Camp, F.E., 1972. *J. Chem. Eng. Data* **17**, 415.
- Hirayama, C., Castle, P.M., 1973. *J. Phys. Chem.* **77**, 3110.
- Hirayama, C., Rome, J.F., Camp, F.E., 1975. *J. Chem. Eng. Data* **20**, 1.
- Hirayama, C., Carlson, G.L., Castle, P.M., Rome, J.F., Snider, W.E., 1976. *J. Less-Common Met.* **45**, 293–300.
- Hohmann, E., Bommer, H., 1941. *Z. anorg. allgem. Chem.* **248**, 383–396.
- Huber, E.J. Jr., Fitzgibbon, G.C., Holley, C.E. Jr., 1971. *J. Chem. Thermodyn.* **3**, 643.
- Hurtgen, C., Brown, D., Fuger, J., 1980. *J. Chem. Soc., Dalton Trans.*, 70–75.
- Hutchinson, F., Rowley, A.J., Walters, M.K., Wilson, M., Madden, P.A., Wasse, J.C., Salmon, P.S., 1999. *J. Chem. Phys.* **111**, 2028–2037.
- Igarashi, K., Mochinaga, J., 1987. *Z. Naturforsch.* **42a**, 777–778.
- Iwadate, Y., Okako, N., Koyama, Y., Kubo, H., Fukushima, K., 1995. *J. Mol. Liquids* **265/66**, 369–372.
- Jia, Y.Q., Zhang, S.G., 1988. *Inorg. Chim. Acta* **143**, 137–145.
- Johansson, B., Mårtensson, N., 1987. In: *Handbook on the Physics and Chemistry of Rare Earths*, Vol. **10**. North-Holland, Amsterdam, p. 368 (ch. 69).
- Johnson, G.K., Pennell, R.G., Kim, K.Y., Hubbard, W.N., 1980. *J. Chem. Thermodynamics* **12**, 15.
- Jones, D.A., Shand, W.A., 1968. *J. Cryst. Growth* **2**, 361–368.
- Joubert, L., Picard, G., Legendre, J.-J., 1998. *Inorg. Chem.* **37**, 1984.
- Kapala, J., Roszak, S., Nunziante Cesaro, S., Miller, M., 2002. *J. Alloys Comp.* **345**, 90–99.
- Kaposi, O., Lelik, L., Balthazar, K., 1983. *High Temp. Sci.* **16**, 299.
- Kaposi, O., Ajtony, Z., Popovic, A., Marsel, J., 1986. *J. Less-Common Met.* **123**, 199–208.
- Kent, R.A., Zmbov, K.F., Kana'an, A., Besenbruch, G., McDonald, J.D., Margrave, J.L., 1966. *J. Inorg. Nucl. Chem.* **28**, 1419.
- Khairulin, R.A., Stankus, S.V., Tyagel'sky, P.V., 1998. *Inorg. Mat.* **34**, 742–745.
- Khairulin, R.A., Stankus, S.V., Lyapunov, K.M., 2000. *Inorg. Mat.* **36**, 1289–1292.
- Khanaev, E.I., Kotov, M.G., Afanas'ev, Y.A., Il'ina, L.D., 1977. *Sov. Radiochem.* **19**, 221–222.
- Khanaev, E.I., Storozhenko, T.P., Il'ina, L.D., 1987. *Russ. J. Phys. Chem.* **61**, 926–929.
- Kholokhova, L.I., Rezukhina, T.N., 1976. *Russ. J. Phys. Chem.* **50**, 451–452.
- Kim, K.-Y., Johnson, C.E., 1981. *J. Chem. Thermodyn.* **13**, 13–25.
- Kim, Y.C., Oishi, J., 1979. *J. Chem. Thermodynamics* **11**, 657–662.
- Kim, Y.C., Oishi, J., 1980. *J. Chem. Thermodyn.* **12**, 407–413.
- Kim, Y.C., Oishi, J., Kang, S.H., 1977. *J. Chem. Thermodyn.* **9**, 973–977.

- Kim, Y.C., Oishi, J., Kang, S.H., 1978. *J. Chem. Thermodyn.* **10**, 975–981.
- Kim, Y.C., Yano, H., Misumi, M., Oishi, J., 1979. *J. Chem. Thermodyn.* **11**, 429–434.
- Kim, Y.C., Kanazawa, M., Oishi, J., 1980. *J. Chem. Thermodyn.* **12**, 811–816.
- King, E.G., Christensen, A.L., 1959. Tech. Rep. USBM-RI-5510, U.S. Bureau of Mines.
- Kiseleva, T.V., Goryushkin, V.F., Laptev, D.M., 1990. *Russ. J. Inorg. Chem.* **35**, 756–757.
- Kishenbaum, A.D., Cahill, J.A., 1960. *J. Inorg. Nucl. Chem.* **15**, 297–304.
- Kishenbaum, A.D., Cahill, J.A., 1962. *J. Chem. Eng. Data* **7**, 98–99.
- Konings, R.J.M., 2001. *J. Nucl. Mater.* **295**, 57–63.
- Konings, R.J.M., 2002. *J. Nucl. Mater.* **301**, 223–226.
- Konings, R.J.M., Kok-Scheele, A., 1999. *Thermochim. Acta* **331**, 45–48.
- Korshunov, B.G., Drobot, D.V., 1965. *Russ. J. Inorg. Chem.* **10**, 508–510.
- Korshunov, B.G., Drobot, D.V., Bukhtiyarov, V.V., Shevtsova, Z.N., 1964. *Russ. J. Inorg. Chem.* **9**, 773–775.
- Korshunov, B.G., Drobot, D.V., Borodulenko, G.P., Galchenko, I.E., 1966a. *Russ. J. Inorg. Chem.* **11**, 547–550.
- Korshunov, B.G., Drobot, D.V., Borodulenko, G.P., Galchenko, I.E., 1966b. *Russ. J. Inorg. Chem.* **11**, 223–225.
- Kovács, A., 1999. *J. Mol. Struct.* **482–483**, 403–407.
- Kovács, A., 2000. *Chem. Phys. Lett.* **319**, 238–246.
- Kovács, A., Konings, R.J.M., 1997a. *Chem. Phys. Lett.* **268**, 207–212.
- Kovács, A., Konings, R.J.M., 1997b. *Vibr. Spectrosc.* **15**, 131–135.
- Kovács, A., Konings, R.J.M., 2002. *J. Phys. Chem. Ref. Data* submitted.
- Kovács, A., Konings, R.J.M., Booi, A.S., 1995. *Vibr. Spectrosc.* **10**, 65–70.
- Krasnov, K.S., 1979. *Molekulyarn'ie Postoyann'ie Neorganicheskikh Soedinenenii. Khimiya, Leningrad.*
- Kudin, L.S., Pogrebnoi, A.M., Kutnetsov, A.Y., Butman, M.F., Burdukovskaya, G.G., 1997. *High Temp. High Press.* **29**, 389–396.
- Kudin, L.S., Pogrebnoi, A.M., Khasanshin, I.V., Motalov, V.B., 2000. *High Temp. High Press.* **32**, 537–545.
- Kutscher, J., Schneider, A., 1971. *Inorg. Nucl. Chem. Lett.* **7**, 815–819.
- Labeau, M., Aléonard, S., Védrine, A., Boutonnet, R., Cousseins, J.C., 1974. *Mat. Res. Bull.* **9**, 615–624.
- Lanza, G., Fragalá, I.L., 1996. *Chem. Phys. Lett.* **255**, 341–346.
- Laptev, D.M., Kiseleva, T.V., Kulagin, N.M., Goryushkin, V.F., Vorontsov, E.S., 1986. *Russ. J. Inorg. Chem.* **31**, 1131–1133.
- Laptev, D.M., Kiseleva, T.V., Vasil'ev, V.V., 1990. *Zh. Fiz. Khim.* **64**, 1472–1476.
- Laptev, D.M., Kiseleva, T.V., Vasil'ev, V.V., Oshchepkov, D.I., 1993. *Russ. J. Phys. Chem.* **67**, 2172–2174.
- Leonidov, V.Y., Furkalyuk, M.Y., 1999. *Russ. J. Phys. Chem.* **73**, 937–939.
- Lesiecki, M., Nibler, J.W., DeKock, C.W., 1972. *J. Chem. Phys.* **57**, 1352–1353.
- Lewis, G.N., Randall, M., Pizer, K.S., Brewer, L., 1961. *Thermodynamics.* McGraw-Hill.
- Lezhava, S.A., 1992. Ph.D. thesis, Moscow State University, Chem. Department.
- Lim, M., Searcy, A.W., 1966. *J. Phys. Chem.* **70**, 1762.
- Lohr, H.R., Cunningham, B.B., 1951. *J. Am. Chem. Soc.* **73**, 2025–2028.
- Loktyushina, N.S., Mal'tsev, A.A., 1984. *Russ. J. Phys. Chem.* **58**, 1602–1604.
- Loktyushina, N.S., Zaitsev, S.A., Osin, S.B., Shevel'kov, V.F., 1987. *Vest. Mosk. Univ. Ser. 2 Khim.* **42**, 434–436.
- Lyapunov, K.M., Baginskii, A.V., Stankus, S.V., 2000. *J. Alloys Comp.* **306**, 17–20.
- Lyon, W.G., Osborne, D.W., Flotow, H.E., Grandjean, F., Hubbard, W.N., Johnson, G.K., 1978. *J. Chem. Phys.* **69**, 167–173.
- Lyon, W.G., Osborne, D.W., Flotow, H.E., 1979a. *J. Chem. Phys.* **70**, 675–680.
- Lyon, W.G., Osborne, D.W., Flotow, H.E., 1979b. *J. Chem. Phys.* **71**, 4123–4127.
- Lyzlov, Y.N., Nisel'son, L.N., 1978. *Russ. J. Inorg. Chem.* **23**, 857–859.
- Machlan, G.R., Stubblefield, C.T., Eyring, L., 1955. *J. Am. Chem. Soc.* **77**, 2975.
- Makhmadmurodov, A., Dudchik, G.P., Polyachenok, O.G., 1975. *Russ. J. Phys. Chem.* **49**, 1599.
- Mar, R.W., Searcy, A.W., 1967. *J. Phys. Chem.* **71**, 888.
- McCreary, J.R., Thorn, R.J., 1973a. *High Temp. Sci.* **5**, 365.
- McCreary, J.R., Thorn, R.J., 1973b. *High Temp. Sci.* **5**, 97.
- McCreary, J.R., Thorn, R.J., 1974a. *High Temp. Sci.* **6**, 205.
- McCreary, J.R., Thorn, R.J., 1974b. In: *Proceedings of the 11th Rare Earth Conference*, p. 1039.
- Mee, J.E., Corbett, J.D., 1965. *Inorg. Chem.* **4**, 88–93.
- Merli, L., Rorif, F., Fuger, J., 1998. *Radiochim. Acta* **82**, 3–9.

- Meyer, G., Wickleder, M.S., 2000. In: Handbook on the Physics and Chemistry of Rare Earths, Vol. **28**. North-Holland, pp. 53–129 (ch. 177).
- Møller, C., Plessset, M.S., 1934. Phys. Rev. **618**, 46.
- Molnár, J., Hargittai, M., 1995. J. Phys. Chem. **99**, 10780.
- Molnár, J., Konings, R.J.M., Kolonits, M., Hargittai, M., 1996. J. Mol. Struct. **375**, 223–229.
- Molodkin, A.K., Karagodina, A.M., Tupolev, V.S., Dudareva, A.G., Krohina, A.G., 1984. Russ. J. Inorg. Chem. **29**, 614–617.
- Monaenkova, A.S., Tiflova, L.A., Goryushkin, V.F., 1989. Russ. J. Phys. Chem. **63**, 595.
- Montgomery, R.L., 1959. Tech. Rep. USBM-RI-5445, U.S. Bureau of Mines.
- Montgomery, R.L., 1962. Tech. Rep. USBM-RI-6146, U.S. Bureau of Mines.
- Montgomery, R.L., Hubert, T.D., 1959. Tech. Rep. USBM-RI-5525, U.S. Bureau of Mines.
- Montgomery, R.L., Stuve, J.M., 1961. Tech. Rep. USBM-RI-5892, U.S. Bureau of Mines.
- Moriarity, J.L., 1963. J. Chem. Eng. Data **8**, 422.
- Morrison, C.A., Leavitt, R.P., 1982. In: Handbook on the Physics and Chemistry of Rare Earths, Vol. **5**. North-Holland, pp. 461–692 (ch. 46).
- Morrison, H.G., Assefa, Z., Haire, R.G., Peterson, J.R., 2000. J. Alloys Comp. **303–304**, 440–444.
- Morss, L.R., 1969. PhD thesis. Tech. Rep. UCRL-18951, Lawrence Radiation Laboratory University of California Berkeley.
- Morss, L.R., 1976. Chem. Rev. **76**, 827–840.
- Morss, L.R., Fahey, J.A., 1976. In: 12th Rare-Earth Res. Conf., Vol. **1**. Vail, Co., pp. 443–450.
- Morss, L.R., Spence, T.G., 1992. Z. anorg. allgem. Chem. **616**, 162.
- Myers, C.E., Graves, D.T., 1977a. J. Chem. Eng. Data **22**, 436–439.
- Myers, C.E., Graves, D.T., 1977b. J. Chem. Eng. Data **22**, 440–444.
- Myers, C.E., Hannay, M.H., 1980. J. Less-Common Met. **70**, 15–124.
- Nafziger, R.H., Lincoln, R.L., Riazance, N., 1973. J. Inorg. Nucl. Chem. **35**, 421–426.
- Nesmeyanov, A.N., Sazonov, L.A., 1959. Russ. J. Inorg. Chem. **4**, 97–98.
- Nisel'son, L.A., Lyzlov, Y.N., 1976. Russ. J. Inorg. Chem. **21**, 1842–1844.
- Nisel'son, L.N., Lyzlov, Y.N., Slov'ev, S.I., 1978. Russ. J. Inorg. Chem. **23**, 434–435.
- Novikov, G.I., Baev, A.G., 1962. Russ. J. Inorg. Chem. **7**, 1349.
- Oppermann, H., Morgenstern, A., Ehrlich, S., 1997. Z. Naturforsch. B **52**, 1062–1066.
- Parker, V.B., Wagman, D.D., Garvin, D., Oct 1976. Tech. Rep. NBSIR 75, Nat. Bureau Standards, Washington.
- Pashinkin, A.S., Drobot, D.V., Zevtsova, Z.R., Korshunov, B.G., 1962. Russ. J. Inorg. Chem. **7**, 2811.
- Pastor, R.C., Robinson, M., 1974. Mat. Res. Bull. **9**, 569–578.
- Perdew, J.P., 1986. Phys. Rev. B **33**, 8822.
- Perov, P.A., Nedyak, S., Mat'tsev, A., 1975. Vestn. Mosk. Univ. Khim **30**, 281.
- Petzel, T., Greis, O., 1976. J. Less-Common Met. **56**, 197.
- Petzel, T., Marx, V., Potthast, J., Ahnen, T., 1992. Thermochim. Acta **194**, 319–327.
- Piacente, V., Brunetti, B., Scardala, P., Villani, A.R., 2002. J. Chem. Eng. Data **47**, 388–396.
- Pogrebnoi, A.M., Kudin, L.S., Motalov, V.B., Goryushkin, V.F., 2001. Rapid Commun. Mass Spectrom. **15**, 1662–1671.
- Polyachenok, O.G., 1967. Zh. Neorg. Khim. **12**, 449–452.
- Polyachenok, O.G., Novikov, G.I., 1963a. Russ. J. Inorg. Chem. **8**, 816–820.
- Polyachenok, O.G., Novikov, G.I., 1963b. Russ. J. Inorg. Chem. **8**, 793–820.
- Popova, A.A., Monaenkova, A.S., 1989. Zh. Fiz. Khim. **63**, 2340.
- Porter, B., Brown, E., 1962. J. Am. Ceram. Soc. **45**, 49.
- Poshevnova, A.I., Goryushkina, Y.V., Vinokurova, N.G., Goryushkin, V.F., 2002. Russ. J. Inorg. Chem. **47**, 181–182.
- Reuter, G., Seifert, H.J., 1994. Thermochim. Acta **237**, 219–228.
- Rezukhina, T.N., Sisoeva, T.F., Holokhonova, L.I., Ippolitov, E.G., 1974. J. Chem. Thermodyn. **6**, 883–893.
- Roberts, J.A., Searcy, A.W., 1972. High Temp. Sci. **4**, 411.
- Robinson, M., Cripe, D.M., 1966. J. Appl. Phys. **2**, 2072–2074.
- Roffe, M., Seifert, H.J., 1997. J. Alloys Comp. **257**, 128–133.
- Rudzitis, E., Deventer, E.V., 1965. Tech. Rep. ANL-7055, Argonne National Laboratory.
- Rycerz, L., Gaune-Escard, M., 1999a. J. Thermal Anal. Calorim. **56**, 355–363.
- Rycerz, L., Gaune-Escard, M., 1999b. J. Thermal Anal. Calorim. **68**, 973–981.
- Rycerz, L., Gaune-Escard, M., 2002a. Z. Naturforsch. **57a**, 79–84.

- Rycerz, L., Gaune-Escard, M., 2002b. *Z. Naturforsch.* **57a**, 215–220.
- Savin, V.D., Mikhailova, N.P., 1981. *Russ. J. Phys. Chem.* **53**, 2237–2239.
- Savin, V.D., Mikhailova, N.P., Morozova, V.A., 1979. *Russ. J. Phys. Chem.* **53**, 1410–1413.
- Seifert, H.J., Sandrok, J., 1991. *Z. anorg. allg. Chem.* **587**, 110–117.
- Seifert, H.J., Fink, H., Thiel, G., 1985. *J. Less-Common Met.* **110**, 139–147.
- Seifert, H.J., Fink, H., Uebach, W., 1987. *Z. anorg. allg. Chem.* **555**, 143–153.
- Seifert, H.J., Fink, H., Uebach, W., 1988a. *J. Thermal Anal.* **31**, 1309–1315.
- Seifert, H.J., Fink, H., Uebach, W., 1988b. *J. Thermal Anal.* **33**, 625–632.
- Seifert, H.J., Sandrok, J., Thiel, G., 1991. *Z. anorg. allg. Chem.* **598/599**, 307–318.
- Selivanov, G.K., Sekachev, Y.N., Mal'tsev, A.A., 1973. *Russ. J. Phys. Chem.* **47**, 1239.
- Shaimuradov, I.B., Reshetnikova, L.P., Novoselova, A.V., 1974. *Inorg. Mat.* **10**, 1264–1266.
- Shimazaki, E., Niwa, K., 1962. *Z. anorg. allg. Chem.* **314**, 21.
- Skinner, H.B., Searcy, A.W., 1968. *J. Phys. Chem.* **72**, 3375.
- Skinner, H.B., Searcy, A.W., 1971. *J. Phys. Chem.* **75**, 108.
- Sobolev, B.P., Fedorov, P.P., Seirania, K.B., Tkachenko, N.L., 1976a. *J. Solid State Phys.* **17**, 201–212.
- Sobolev, B.P., Fedorov, P.P., Shteynberg, D.B., Sinityn, B.V., Shakhkalamian, G.S., 1976b. *J. Solid State Phys.* **17**, 191–199.
- Sobolev, B.P., Ratnikova, I.D., Fedorov, P.P., Sinityn, B.V., Shakhkalamyan, G.S., 1976c. *Mat. Res. Bull.* **11**, 999–1004.
- Söhnle, O., Novotný, P., 1985. *Densities of Aqueous Solutions of Inorganic Substances*. Elsevier.
- Solomonik, V.G., Marochko, O.Y., 2000. *Russ. J. Phys. Chem.* **74**, 2094–2096.
- Sommers, J.A., Westrum, E.F. Jr., 1976. *J. Chem. Thermodyn.* **8**, 1115–1136.
- Sommers, J.A., Westrum, E.F. Jr., 1977. *J. Chem. Thermodyn.* **9**, 1–26.
- Spedding, F.H., Daane, A.H., 1960. *Metall. Rev.* **5**, 298.
- Spedding, F.H., Flynn, J.P., 1954. *J. Am. Chem. Soc.* **76**, 1474–1477.
- Spedding, F.H., Henderson, D.C., 1971. *J. Chem. Phys.* **54**, 2476–2483.
- Spedding, F.H., Miller, C.F., 1952. *J. Am. Chem. Soc.* **74**, 4195–4198.
- Spedding, F.H., Beaudry, B.J., Henderson, D.C., Moorman, J., 1974. *J. Chem. Phys.* **60**, 1578–1588.
- Spiridonov, V.P., Gershikov, A.G., Lyutsarev, V.S., 1990. *J. Mol. Struct.* **221**, 79.
- Stankus, S.V., Khairulin, R.A., Lyapunov, K.M., 1999. *J. Alloys Comp.* **290**, 30–33.
- Stankus, S.V., Khairulin, R.A., Lyapunov, K.M., 2000. *High Temp.-High Press.* **32**, 467–472.
- Stevens, W.J., Krauss, M., Basch, H., Jasien, P.G., 1992. *Can. J. Chem.* **70**, 612.
- Stolyarova, V.L., Aune, R.E., Seetharaman, S., 1996. *Rapid Comm. Mass Spectrom.* **10**, 501–508.
- Storozhenko, T.P., Khanaev, E.I., Afanas'ev, Y.A., 1976. *Russ. J. Phys. Chem.* **50**, 643–644.
- Struck, C.W., Baglio, J.A., 1992. *High Temp. Sci.* **31**, 209.
- Struck, C.W., Feuersanger, A.E., 1991. *High Temp. Sci.* **31**, 127–145.
- Struck, C.W., Feuersanger, A.E., 1999. *High Temp. Sci.* **31**, 127–145.
- Stubblefield, C.T., 1969. *Rev. Sci. Instr.* **40**, 456.
- Stubblefield, C.T., Rutledge, J.L., Phillips, R., 1965. *J. Phys. Chem.* **69**, 991.
- Stuve, J.M., 1965a. *Tech. Rep. USBM-RI-6697*, U.S. Bureau of Mines.
- Stuve, J.M., 1965b. *Tech. Rep. USBM-RI-6640*, U.S. Bureau of Mines.
- Stuve, J.M., 1967a. *Tech. Rep. USBM-RI-7046*, U.S. Bureau of Mines.
- Stuve, J.M., 1967b. *Tech. Rep. USBM-RI-6902*, U.S. Bureau of Mines.
- Suvorov, A.V., Novikov, G., 1968. *Vestn. Mosk. Univ.* **4**, 83–88.
- Suvorov, A.V., Krzhizhanovskaya, Novikov, G., 1966. *Russ. J. Inorg. Chem.* **11**, 1441.
- Thiel, G., Seifert, H.J., 1988. *Thermochim. Acta.* **133**, 275–282.
- Thoma, R.E., Burton, G.D., 1966. *Inorg. Chem.* **5**, 1937–1939.
- Tiflova, L.A., 1990. Ph.D. thesis, Moscow State University, Chem. Department.
- Tiflova, L.A., Monaenkova, A.S., Goryushkin, V.F., 1989. *Russ. J. Phys. Chem.* **63**, 1082–1084.
- Tolmach, P.I., Gorbunov, V.E., Gavrichev, K.S., Totrova, G.A., Goryushkin, V.F., 1987. *Russ. J. Phys. Chem.* **61**, 1529–1532.
- Tolmach, P.I., Gorbunov, V.E., Gavrichev, K.S., Golushina, L.N., Goryushkin, V.F., 1990a. *Russ. J. Phys. Chem.* **64**, 580–582.
- Tolmach, P.I., Gorbunov, V.E., Gavrichev, K.S., Goryushkin, V.F., 1990b. *Russ. J. Phys. Chem.* **64**, 582–583.

- Tolmach, P.I., Gorbunov, V.E., Gavrichev, K.S., Totrova, G.A., Goryushkin, V.F., 1990c. *Russ. J. Phys. Chem.* **64**, 583–585.
- Villani, A.R., Brunetti, B., Piacente, V., 2000a. *J. Chem. Eng. Data* **45**, 1167–1172.
- Villani, A.R., Brunetti, B., Piacente, V., 2000b. *J. Chem. Eng. Data* **45**, 823–828.
- Villani, A.R., Scardala, P., Brunetti, B., Piacente, V., 2002. *J. Chem. Eng. Data* **47**, 428–434.
- Vogel, G., Schneider, A., 1972. *Inorg. Nucl. Chem. Lett.* **8**, 513–521.
- Walden, G.E., Smith, D.F., 1961. *Tech. Rep. BM-RI 5859*, US Bureau of Mines.
- Wasse, J.C., Salmon, P.S., 1999a. *J. Phys.: Condens. Matter* **11**, 9293–9302.
- Wasse, J.C., Salmon, P.S., 1999b. *J. Phys.: Condens. Matter* **11**, 2171–2177.
- Wasse, J.C., Salmon, P.S., Delaplane, R.G., 2000. *Physica B* **276–278**, 433–434.
- Wells, J.C. Jr., Gruber, J.B., Lewis, M., 1977. *Chem. Phys.* **24**, 391–397.
- Wesley, R.D., DeKock, C.W., 1971. *J. Chem. Phys.* **55**, 3866.
- Westrum, E.F. Jr., 1970. In: *Science and Technology of the Rare Earths*, Vol. 1. Pergamon, pp. 310–350.
- Westrum, E.F. Jr., 1983. *J. Chem. Thermodyn.* **15**, 305–325.
- Westrum, E.F. Jr., Beale, A.F. Jr., 1961. *J. Chem. Phys.* **65**, 353–355.
- Westrum, E.F. Jr., Grøonvold, F., 1962. In: *Thermodynamics of Nuclear Materials. Proceedings of a Symposium*. IAEA, Vienna, p. 3.
- Yashvili, T.S., Gvelesiani, G.G., 1971. *Russ. J. Phys. Chem.* **45**, 551.
- Zakharov, A.V., Giricheva, N.I., Vogt, N., Shlykov, S.A., Vogt, J., Girichev, G.V., 2001. *J. Chem. Soc., Dalton Trans.*, 3160–3162.
- Zakharov, A.V., Giricheva, N.I., Vogt, N., Shlykov, S.A., Vogt, J., Girichev, G.V., 2003. *Struct. Chem.* **14**, 193–197.
- Zasorin, E.Z., 1988. *Russ. J. Phys. Chem.* **62**, 441.
- Zhigarnovskii, B.M., Ippolitov, E.G., 1970a. *Inorg. Mat.* **6**, 1410–1412.
- Zhigarnovskii, B.M., Ippolitov, E.G., 1970b. *Inorg. Mat.* **6**, 1033–1034.
- Zmbov, K.F., Margrave, J.L., 1966. *J. Chem. Phys.* **45**, 3167–3169.
- Zmbov, K.F., Margrave, J.L., 1967. *J. Less-Common Met.* **12**, 494.
- Zmbov, K.F., Margrave, J.L., 1968. *Adv. Chem. Ser.* **72**, 267.

Chapter 214

RARE EARTH – MANGANESE PEROVSKITES

John B. GOODENOUGH

University of Texas at Austin, Austin, TX 78712-1063, USA

Contents

List of acronyms	249	2.6. $\text{Sr}_{1-x}\text{Ca}_x\text{MnO}_3$ ($0 \leq x \leq 1$) and $\text{Sr}_{1-y}\text{Ba}_y\text{MnO}_3$ ($0 \leq y \leq 0.2$)	278
1. Introductory concepts	250	2.7. Bloch's rule	279
1.1. Tolerance factor	250	3. Mixed-valent perovskites	282
1.2. Electronic considerations	252	3.1. Oxygen vacancies	282
1.2.1. Ligand-field considerations	253	3.2. $\text{Ca}_{1-x}\text{La}_x\text{MnO}_3$, $0 \leq x \leq 0.2$	283
1.2.2. Interatomic interactions	256	3.3. $\text{LaMnO}_{3+\delta}$	285
1.2.3. Localized-itinerant electronic transitions	260	3.4. $(\text{La}_{1-y}\text{R}_y)_{0.7}\text{A}_{0.3}\text{MnO}_3$: The CMR phenomenon	290
2. Single-valent perovskites	262	3.5. The system $\text{La}_{1-x}\text{Sr}_x\text{MnO}_3$	311
2.1. LaMnO_3	262	3.6. The system $\text{La}_{1-x}\text{Ca}_x\text{MnO}_3$	323
2.2. $\text{LaMn}_{1-x}\text{Ga}_x\text{O}_3$ and $\text{LaMn}_{1-x}\text{Sc}_x\text{O}_3$	269	3.7. $\text{R}_{0.5}\text{A}_{0.5}\text{MnO}_3$	330
2.3. RMnO_3	275	4. Conclusions	342
2.4. CaMnO_3	276	References	344
2.5. SrMnO_3	277		

List of acronyms

AFI	antiferromagnetic insulator	MCG	magnetic cluster glass
AFM	antiferromagnetic metal	NMR	nuclear magnetic resonance
CO	charge-ordered	NQR	nuclear quadrupole resonance
CAFI	canted-spin antiferromagnetic insulator	OO	orbital-ordered
CDW	charge-density wave	PDF	pair-density function
CMR	colossal negative magnetoresistance	QCP	quantum critical point
ESR	electron spin resonance	SG	spin glass
FC	field-cooled	SDW	spin-density wave
FI	ferromagnetic insulator	SP	superparamagnetic
FM	ferromagnetic metal	ZFC	zero-field-cooled
FV	ferromagnetic vibronic conductor		

1. Introductory concepts

1.1. Tolerance factor

The cubic AMO_3 perovskite structure consists of an MO_3 array of corner-shared $MO_{6/2}$ octahedra with a large A cation at the body-center position. As is illustrated in fig. 1, this structure allows formation of the Ruddlesden–Popper (1957, 1958) rock-salt/perovskite intergrowth structures $MO \cdot (AMO_3)_n$. In all these structures, the mismatch between the equilibrium (A–O) and (M–O) bond lengths is given by the deviation from unity of the geometric tolerance factor

$$t \equiv (A-O)/\sqrt{2}(M-O). \quad (1)$$

This factor may be calculated for room temperature and atmospheric pressure from tabulated sums of ionic radii obtained from X-ray data (Shannon and Prewitt, 1969, 1970). However, it must be recognized that the thermal expansions and the compressibilities of the (A–O) and (M–O) bonds are different, which makes t both pressure and temperature dependent. In the case of a transition-metal atom M , the thermal expansion of the (A–O) bond is the larger, which makes

$$dt/dT > 0. \quad (2)$$

The compressibility of the (A–O) bond is normally the larger (Goodenough et al., 1972), which makes

$$dt/dP < 0, \quad (3a)$$

but at the crossover from localized to itinerant electronic behavior for d electrons of an MO_3 array, a

$$dt/dP > 0 \quad (3b)$$

is found. The origin of this abnormality is discussed in sect. 1.2.3.

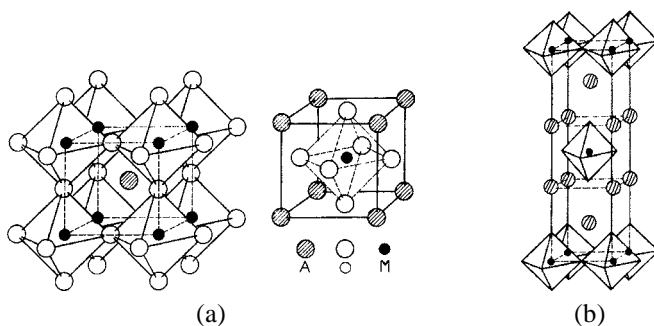


Fig. 1. (a) The ideal cubic perovskite structure and (b) the $n = 1$ Ruddlesden–Popper phase $AO \cdot AMO_3$.

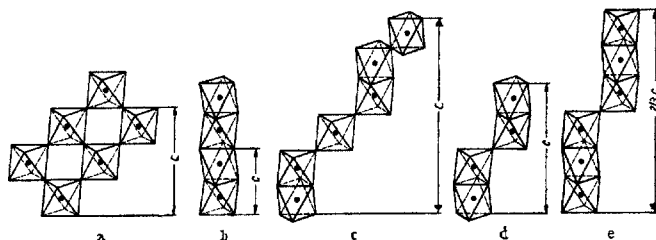


Fig. 2. The hexagonal perovskite polytypes: (a) cubic, (b) hexagonal, (c) 6H, (d) 4H, (e) 9R after Goodenough et al. (1972).

The AMO_3 perovskites adjust to a $t > 1$ by the formation of hexagonal polytypes like those illustrated schematically in fig. 2. In these polytypes, the close-packed (111) AO_3 layers of the cubic phase are changed from all-cubic to cubic + hexagonal or all-hexagonal stacking. Application of hydrostatic pressure normally reduces t , changing hexagonal polytypes successively to structures with more cubic and less hexagonal stacking (Goodenough et al., 1972).

The AMO_3 perovskites adjust to a $t < 1$ by cooperative rotations of the $\text{MO}_{6/2}$ octahedra. These rotations lower the M–O–M bond angle from 180° to $(180^\circ - \phi)$. Three of the common rotations are illustrated in fig. 3. With decreasing t , rotations about a cubic [001] axis to give tetragonal $I4/mcm$ symmetry is followed by those about a [111] axis to give rhombohedral $R\bar{3}c$ symmetry and then about a [110] axis to give orthorhombic $Pbnm$ symmetry with $c/a > \sqrt{2}$ (in the equivalent space group $Pnma$, $b/a > \sqrt{2}$). The bending angle ϕ increases with decreasing t , and ϕ increases discontinuously on going from $R\bar{3}c$ to $Pbnm$ symmetry. The Ruddlesden–Popper phases also adjust to a $t < 1$ by cooperative rotations of the $\text{MO}_{6/2}$ octahedra.

The ability to adjust to a $t < 1$ allows for extensive cation substitutions on both the A and the M sites; the structure is also tolerant of large concentrations of both oxygen and A-cation vacancies. The perovskites do not accept oxygen interstitials, but the Ruddlesden–Popper phases with a $t < 1$ may accept interstitial oxygen between the AO layers of the rock-salt intergrowths in order to increase t . Primary emphasis here is on the oxygen-stoichiometric perovskites containing $\text{M} = \text{Mn}$; the physical properties of these oxides are changed either by a progressive substitution of a lanthanide by an alkaline-earth on the A sites so as to change both t and the $\text{Mn(IV)}/\text{Mn}$ ratio or by a progressive isovalent substitution of one rare-earth by another or one alkaline-earth by another on the A sites so as to change only t while keeping the $\text{Mn(IV)}/\text{Mn}$ ratio fixed. The presence of two or more A-site cations of different radius r_A leads to a variance $\sigma^2 \equiv (\sum_i x_i r_{Ai}^2 - \langle r_A \rangle^2)$, where x_i is the concentration of each A-site cation of radius r_{Ai} ; σ^2 is a measure of the consequent perturbation of the periodic potential of the MO_3 array. Partial substitutions of Mn by other cations on the M sites are also discussed for a few special cases. Several interesting phenomena encountered in Ruddlesden–Popper manganites are not included here.

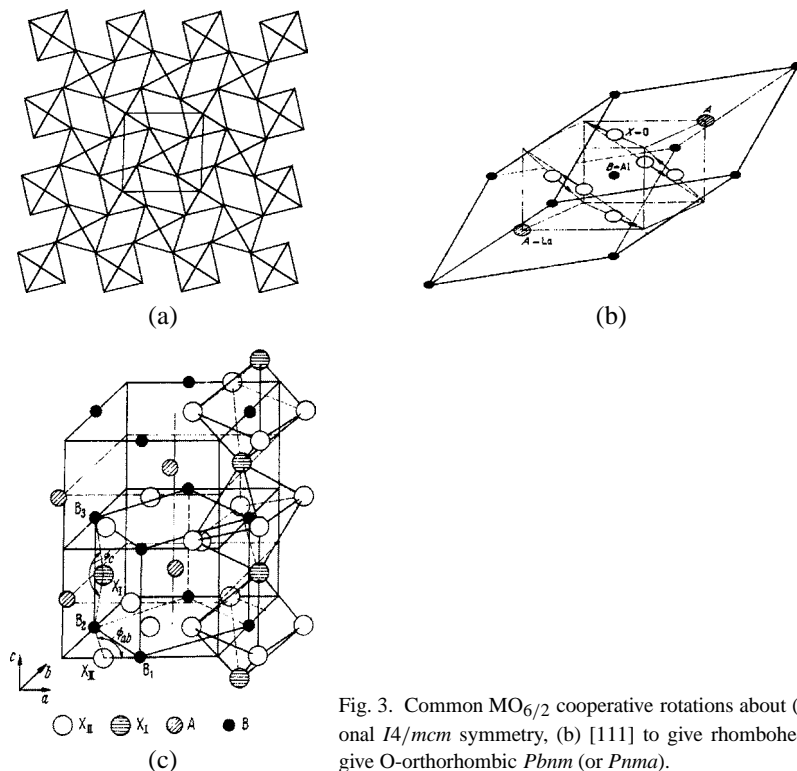


Fig. 3. Common $MO_6/2$ cooperative rotations about (a) $[001]$ to give tetragonal $I4/mcm$ symmetry, (b) $[111]$ to give rhombohedral $R\bar{3}c$, (c) $[110]$ to give O-orthorhombic $Pbnm$ (or $Pnma$).

1.2. Electronic considerations

The AMO_3 perovskites with $M = Mn$ are sufficiently ionic that the Madelung energy stabilizes filled bonding bands that have primarily O-2p character separated from empty antibonding bands of primarily cationic s and p character by a large (~ 6 eV) energy gap. Lanthanide A-site cations introduce empty 5d bands that may overlap the antibonding s bands (Oliver et al., 1972).

The $4f^n$ configurations at the A-site lanthanide ions are localized and the intraatomic electron–electron coulomb energies are large, so the separation between successive $4f^n$ configurations is $U_{fn} > 6$ eV. Moreover, the Ce^{4+} ion is too small to occupy an A site, the Eu^{3+}/Eu^{2+} redox energy lies above the $Mn(III)/Mn(II)$ level, and the Pr^{4+}/Pr^{3+} redox energy lies below the $Mn(IV)/Mn(III)$ level. As illustrated schematically in fig. 4 for $NdMnO_3$, the $Mn(IV)/Mn(III)$ redox energy lies a little above the top of the O-2p bonding bands. Therefore, in the manganese perovskites to be discussed, the rare-earth ions all have $R^{3+}: 4f^0$ or localized $R^{3+}: 4f^n$ configurations with 4f-electron energies well-removed from the Fermi energy. Long-range magnetic ordering of the $R^{3+}: 4f^n$ configurations at low-temperatures is not considered here; the principal interest of the R^{3+} ion is its size, which influences the physical properties of the MnO_3 array through the tolerance factor t and variance σ^2 .

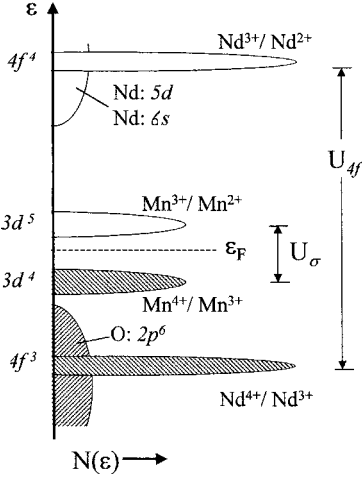


Fig. 4. Schematic one-electron energies for Nd-5d, 6s and O-2p bands of NdMnO_3 and redox energies of Nd(III) and Mn(III) in NdMnO_3 .

The structural, transport, and magnetic properties of a manganese-perovskite system $\text{R}_{1-x}\text{A}_x\text{MnO}_3$ (A = alkaline-earth or alkali atom) are strongly influenced by two features of the MnO_3 array: the orbital degeneracy of the octahedral-site, high-spin Mn(III): d^4 configuration and the possibility of a transition from localized to itinerant electronic behavior of the σ -bonding d electrons with increasing t and Mn(IV)/Mn ratio x . Therefore, we introduce a description of the d-electron manifold before we present and interpret the physical data.

1.2.1. Ligand-field considerations

The five 3d orbitals of a free Mn atom are degenerate; but with more than one electron in the 3d manifold, the spin degeneracy is removed by the ferromagnetic direct-exchange interactions between electron spins in atomic orthogonal orbitals. These exchange interactions produce the Hund intraatomic exchange field H_{ex} . The exchange splitting between spin states will be designated Δ_{ex} .

The atomic orbitals $f_m = R_{nl}(r)P_l^{|m|}(\cos\theta)\exp(\pm im\phi)$ with azimuthal angular momentum quantum number m , where $L_z f_m = -i\hbar(\partial f_m/\partial\phi) = m\hbar f_m$, have the angular dependencies for $l = 2$ (d orbitals)

$$\begin{aligned} f_0 &\sim (\cos^2\theta - 1) \sim [(z^2 - x^2) + (z^2 - y^2)]/r^2, \\ f_{\pm 1} &\sim \sin 2\theta \exp(\pm i\phi) \sim (yz \pm izx)/r^2, \\ f_{\pm 2} &\sim \sin^2\theta \exp(\pm i2\phi) \sim [(x^2 - y^2) \pm ixy]/r^2. \end{aligned} \quad (4)$$

In an isolated octahedral site, the xy and $(yz \pm izx)$ orbitals only overlap the ligand O- $2p_\pi$ orbitals while the $[(z^2 - x^2) + (z^2 - y^2)]$ and $(x^2 - y^2)$ orbitals only overlap the O-2s, $2p_\sigma$ orbitals. The resonance integrals $b^{ca} \equiv (f_m, H' \phi_o) \approx \varepsilon_{mo}(f_m, \phi_o)$ describing the energy of a virtual charge transfer to the empty M-3d orbitals from the same-symmetry sum of near-neighbor oxygen orbitals ϕ_o contain both an overlap integral (f_m, ϕ_o) and a one-electron energy ε_{mo} that are larger for σ -bonding than for π -bonding. Therefore, the antibonding states

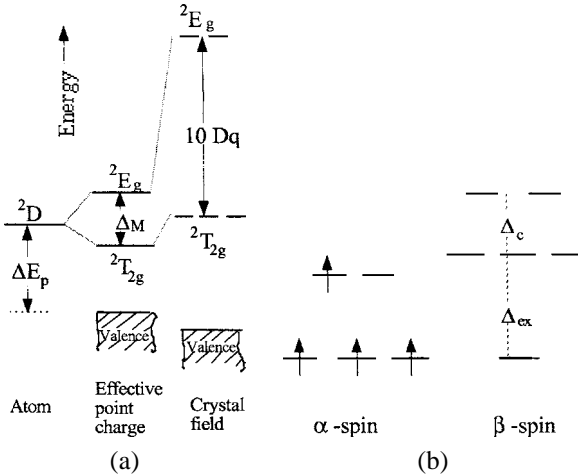


Fig. 5. Octahedral-site splitting of (a) the orbitally fivefold-degenerate d^1 manifold by a cubic crystalline field and (b) the high-spin Mn(III) configuration.

of a σ -bond are raised higher in energy than those of a π -bond and, as a consequence, the cubic symmetry of the octahedral site raises the twofold-degenerate pair of σ -bonding e orbitals, the $[(z^2 - x^2) + (z^2 - y^2)]$ and the $(x^2 - y^2)$ orbitals, above the threefold-degenerate set of π -bonding t orbitals xy , $(yz \pm izx)$ by an energy Δ_c , which quenches the orbital angular momentum associated with $m = \pm 2$ (see fig. 5).

If a point-charge ionic model places the empty 3d orbitals of a degenerate manifold an energy ΔE_p above the O-2p orbitals and ΔE_s above the O-2s orbitals, the antibonding d-like states may be described in second-order perturbation theory to give the ligand-field wavefunctions

$$\begin{aligned}\psi_t &= N_\pi (f_t - \lambda_\pi \phi_\pi), \\ \psi_e &= N_\sigma (f_e - \lambda_\sigma \phi_\sigma - \lambda_s \phi_s),\end{aligned}\quad (5)$$

provided the covalent-mixing parameters are $\lambda_\pi \equiv b_\pi^{ca}/\Delta E_p \ll 1$ and $\lambda_\sigma \equiv b_\sigma^{ca}/\Delta E_p \ll 1$. A larger ΔE_s keeps $\lambda_s \ll 1$ where eq. (5) is applicable. According to second-order perturbation theory, the antibonding states are raised an energy $\Delta E = |b^{ca}|^2/\Delta E_p$ by the Mn-O covalent bonding, and the cubic-field splitting of the e and t orbital energies is

$$\Delta_c = \Delta \varepsilon_\sigma - \Delta \varepsilon_\pi = \Delta_M + (\lambda_\sigma^2 - \lambda_\pi^2)\Delta E_p + \lambda_s^2 \Delta E_s, \quad (6)$$

where Δ_M is a small, purely electrostatic energy of uncertain sign due to the penetration of the O^{2-} -ion electron cloud by the cation wavefunctions. In the perovskite structure, an interaction of the ψ_t electrons with the empty A-cation wavefunctions would lower ε_π and increase Δ_c . This latter interaction does not appear to be of primary importance in the rare-earth manganese perovskites where a $\Delta_{ex} > \Delta_c$ removes the spin degeneracy and maintains, at atmospheric pressure, a high-spin configuration on the Mn(III): t^3e^1 ions; the Mn(IV): t^3e^0 configuration contains no e electron and the high-spin Mn(II): t^3e^2 configuration has two electrons in a σ -bonding e -orbital. The mobile electrons that transport charge are electrons occupying the orbitally twofold-degenerate e orbitals.

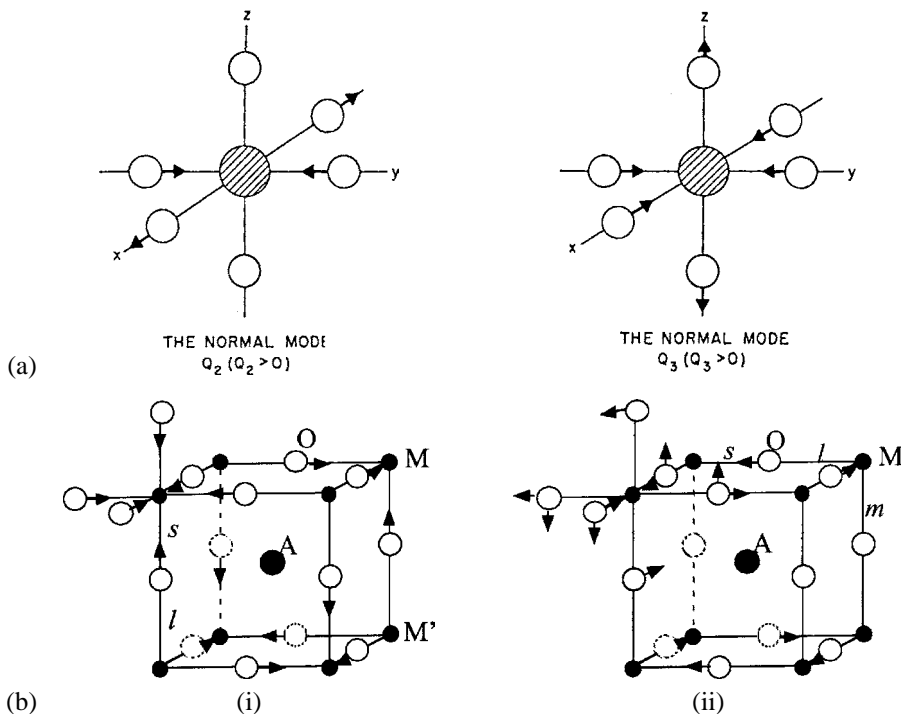


Fig. 6. (a) Jahn-Teller octahedral-site deformations that remove the e-orbital degeneracy of a localized Mn(III): t^3e^1 configuration. (b) Cooperative oxygen displacements that remove the orbital degeneracy of a high-spin, octahedral-site d^4 configuration: (i) disproportionation as in CaFeO_3 below room temperature and (ii) Jahn-Teller orbital ordering in LaMnO_3 .

The twofold e-orbital degeneracy at a localized Mn(III): t^3e^1 configuration may be removed by cooperative oxygen displacements that either lower the site symmetry from cubic to tetragonal or orthorhombic (Jahn-Teller site distortion) as illustrated in fig. 6(a) or transfer an electron from one Mn atom to another as in the disproportionation reaction $2\text{Mn(III)} = \text{Mn(IV)} + \text{Mn(II)}$ that is illustrated in fig. 6(b)(i). These atomic displacements are superimposed on the cooperative rotations of the $\text{MnO}_{6/2}$ octahedra induced by a tolerance factor $t < 1$. In a perovskite with a large concentration of Mn(III) ions, long-range-cooperative Jahn-Teller site distortions reduce the elastic energy associated with the individual site distortions and give a global distortion of the structure. In orthorhombic LaMnO_3 , for example, long-range orbital ordering stabilizes site distortions that create within (001) planes two short and two long Mn-O bonds at each site-centered Mn atom, the direction of the long Mn-O bonds alternating from (100) to (010) in a checkerboard fashion as is illustrated in fig. 6(b)(ii). The long-range orbital ordering changes the orthorhombic axial ratio from $c/a > \sqrt{2}$ to $c/a < \sqrt{2}$. Where the local site distortions are disordered, the axial ratio becomes $c/a \approx \sqrt{2}$. We distinguish the orthorhombic structures as O for a $c/a > \sqrt{2}$ due

to cooperative $\text{MnO}_{6/2}$ rotations alone, O' for a $c/a < \sqrt{2}$ signaling a superimposed long-range-cooperative orbital ordering, and O^* for $c/a \approx \sqrt{2}$ signaling orbital fluctuations with only short-range-cooperative orbital ordering.

1.2.2. Interatomic interactions

In the manganese perovskites, the dominant interactions between d-like orbitals at neighboring Mn atoms are the $(180^\circ - \phi)$ Mn–O–Mn interactions. The spin-independent resonance integrals describing charge transfer between Mn atoms at positions R_i and R_j are

$$\begin{aligned} b_\pi^{cac} &= (\psi_{ti}, H' \psi_{tj}) \approx \varepsilon_\pi \lambda_\pi^2, \\ b_\sigma^{cac} &= (\psi_{ei}, H' \psi_{ej}) \approx \varepsilon_\sigma \lambda_\sigma^2 \cos \phi, \end{aligned} \quad (7)$$

where λ_π varies with the acidity of the A cations as well as with the bending angle ϕ and H' describes the perturbation of the potential at R_j caused by the presence of a Mn atom at R_i . The smaller term $\varepsilon_s \lambda_s^2$ is omitted from b_σ^{cac} for simplicity.

The interactions between localized spins on neighboring cations are treated by a perturbation theory in which the spin-dependent resonance integrals for parallel and antiparallel coupling of spins are

$$t_{ij}^{\uparrow\uparrow} = b_{ij}^{cac} \cos(\theta_{ij}/2) \quad \text{and} \quad t_{ij}^{\uparrow\downarrow} = b_{ij}^{cac} \sin(\theta_{ij}/2) \quad (8)$$

for electron transfer between cations whose spins are rotated by an angle θ_{ij} with respect to one another; $b_{ij}^{cac} \approx \varepsilon_{ij}(\psi_i, \psi_j)$ is the spin-independent resonance integral. The spin angular momentum is conserved in an electron transfer. Rules for the sign of the interatomic spin–spin exchange interactions follow:

- **Direct exchange** between spins in orthogonal orbitals is a *potential exchange* as it does not involve electron transfer; like the intraatomic interactions, it is *ferromagnetic*.

- **Superexchange** interactions between spins S_i and S_j on neighboring atoms is a *kinetic exchange* that involves *virtual* charge transfer between crystal-field orbitals on neighboring cations; spin polarization of the electron cloud on any intervening anion is neglected in this Anderson (1959) formulation of superexchange. However, Goodenough (1963) pointed out that where the superexchange interaction is across an intervening anion, as in the $(180 - \phi)$ Mn–O–Mn interactions in a manganese-oxide perovskite, there is an additional component to the superexchange interaction, which he called “semicovalent exchange” as it involves transfer of two electrons from the intervening oxygen, one each to the two interacting transition-metal atoms. This term does not change the sign of the overall exchange interaction; but it adds a second semicovalent-exchange term to the expression for the superexchange interaction that becomes dominant where the energy ΔE_p becomes smaller than the effective intraatomic energy U_{eff} (Zaanen and Sawatzky, 1987). We shall introduce this second term explicitly in the discussion of the single-valent compounds LaMnO_3 and CaMnO_3 (sects. 2.4 and 2.7). Here we present only the Anderson formulation and its modification to give the rules for the sign of the superexchange spin–spin coupling.

Antiferromagnetic superexchange: Transfer of an electron of α spin from a half-filled orbital to an orbital that is also half-filled is constrained by the Pauli exclusion principle to be most

probable if the spin on the acceptor atom has β spin. From second-order perturbation theory, the bonding energy gained by the virtual electron transfer is, from eq. (8),

$$\Delta\varepsilon^S \approx -|t_{ij}^{\uparrow\downarrow}|^2/U_{\text{eff}} = \text{Const} + J_{ij}S_i \cdot S_j \quad (9)$$

where $J_{ij} \approx |2b_{ij}^2|/4S^2U_{\text{eff}}$ and U_{eff} is the total energy it costs to add an electron to the acceptor. Equation (9) with $J_{ij} \approx 2b_{ij}^2/U_{\text{eff}}$ is the Anderson expression for spin $S = 1/2$.

Ferromagnetic superexchange: Transfer of an electron from a half-filled orbital to an empty orbital on an acceptor atom having a spin S is not constrained by the Pauli exclusion principle, but the intraatomic exchange energy Δ_{ex} makes the transfer most probable if the spin S is parallel to the spin of the transferred electron. From third-order perturbation theory, the bonding energy gained by the virtual electron transfer is, from eq. (8),

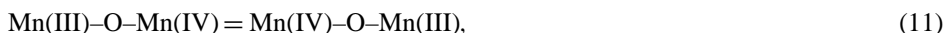
$$\Delta\varepsilon^S \approx -\frac{|t_{ij}^{\uparrow\uparrow}|^2\Delta_{\text{ex}}}{U_{\text{eff}}^2} = \text{Const} - J_{ij}S_i \cdot S_j \quad (10)$$

where $J_{ij} \approx (2b_{ij}^2\Delta_{\text{ex}})/4S^2U_{\text{eff}}^2$.

A similar reasoning applies to virtual transfer of an electron from a filled orbital at an atom of spin S to a half-filled orbital at an acceptor atom.

Vibronic superexchange: In manganese-oxide perovskites, orbital fluctuations at the Jahn–Teller Mn(III) ions of a Mn(III)–O–Mn(III) interaction give rise, over the period of an axial oxygen vibration, to both antiferromagnetic and ferromagnetic superexchange interactions. However, electron transfer to an empty orbital is energetically favored over transfer to a half-filled orbital and the axial oxygen displacements associated with the orbital fluctuations correlate asymmetric e-orbital occupancy on either side of the oxygen atom for minimization of the elastic energy. Consequently, the net vibronic Mn(III)–O–Mn(III) superexchange interaction is *ferromagnetic*.

• **Double exchange** is also a *kinetic exchange*; it involves a *real* charge transfer between like atoms in two different valence states, each carrying a localized spin S . If the charge transfer requires an activation energy as occurs in polaronic conduction, then the individual atomic spins have time to relax between electron jumps and no spin–spin coupling is achieved by the real charge transfer. In this case, a superexchange coupling by virtual charge transfer is still present. Polaronic conduction in a manganese-oxide perovskite occurs where the time τ_h for an electron to hop from one atom to a neighbor is long compared to the period ω_o^{-1} of the cooperative oxygen vibrations that would trap it at the manganese atom of lower valence state. Double exchange was first postulated by Zener (1951) to occur within a Mn(III)–O–Mn(IV) pair by a double electron transfer $\text{O}^{2-}\text{--Mn(IV)} = \text{O}^-\text{--Mn(III)}$ accompanied by $\text{Mn(III)--O}^- = \text{Mn(IV)--O}^{2-}$ on the opposite side in a time $\tau_h < \omega_o^{-1}$ to give a ferromagnetic coupling between localized manganese spins since spin is conserved in the real charge transfer and the intraatomic Δ_{ex} is operative at each Mn atom. This mechanism only provides for ferromagnetically coupled pairs



In order to account for an observed global ferromagnetism, Zener (1951) had to make the further assumption that these pairs do not require an activation energy to diffuse through the lattice. This model leads to a charge-carrier mobility

$$\mu = eD_0/kT \quad (12)$$

where the diffusion coefficient D_0 is temperature-independent. We shall refer to the two-manganese polarons described by eq. (11) as Zener polarons. Following the formulation of eq. (8) by Anderson and Hasegawa (1955). De Gennes (1960) proposed a double-exchange model in which the mobile electrons of e-orbital parentage occupy a narrow σ^* band having no spin degeneracy and a spin-dependent resonance integral $t_{ij}^{\uparrow\uparrow}$ replaces the usual spin-independent integral b_{ij}^{cac} . The tight-binding band model then gives a ferromagnetic stabilization

$$\Delta_{\text{ex}}^D \approx -c(1-c)zt_{ij}^{\uparrow\uparrow} = -c(1-c)zb_{ij}^{cac} \cos(\theta_{ij}/2) \quad (13)$$

where z is the number of manganese near neighbors and $c = \text{Mn(IV)}/\text{Mn}$ is the fractional occupancy of mobile charge carriers in the MnO_3 array.

• **Indirect exchange** is a coupling of localized spins at M atoms by electrons of a partially occupied broad band. Whereas the mobile spins are assumed to couple ferromagnetically to the localized spins in the De Gennes model (minority-spin electrons would couple antiferromagnetically), localized spins only induce a partial intraatomic parallel-spin magnetization of broad-band electrons. The induced magnetization is largest at the position of a localized spin and it oscillates in sign at larger distances from the localized spin. Therefore, indirect exchange may be *ferromagnetic* between close near neighbors and *antiferromagnetic* between more distant neighbors.

• **Antisymmetric exchange** introduces a term of the form $\mathbf{D}_{ij} \cdot \mathbf{S}_i \times \mathbf{S}_j$ that may be added to the symmetric superexchange term of the form $J_{ij} \mathbf{S}_i \cdot \mathbf{S}_j$; it cants antiferromagnetically coupled spins so as to give a ferromagnetic component perpendicular to the vector \mathbf{D}_{ij} . Antisymmetric exchange originates in the orbital angular momentum; it may dominate symmetric exchange in the coupling between localized $4f^n$ configurations on the lanthanide ions, but it is much weaker than the symmetric exchange in the coupling between d^n configurations in the manganese-oxide perovskites. Antisymmetric exchange was introduced by Dzialoshinskii (1958), who pointed out that a $\mathbf{D}_{ij} \neq 0$ can only exist where spin canting leaves the system *invariant* under all symmetry operations of the unit cell. The formalism was developed further by Moriya (1960); \mathbf{D}_{ij} is known as the Dzialoshinskii vector.

In the orthorhombic AMO_3 perovskites, canting of antiferromagnetically coupled M-atom spins to give a weak ferromagnetic component can be accomplished by any of three different mechanisms: magnetocrystalline anisotropy of cooperatively tilted $\text{MO}_{6/2}$ octahedra, Dzialoshinskii–Moriya antisymmetric exchange, or a double-exchange component varying as $\cos(\theta_{ij}/2)$ superimposed on a superexchange component varying as $\cos\theta_{ij}$. Bertaut (1963) has described the possible spin configurations compatible with the $Pbnm$ space group. Figure 7 represents the M atoms of an orthorhombic AMO_3 structure. Linear combinations of the spin components that transform into themselves are chosen as the base vectors of the

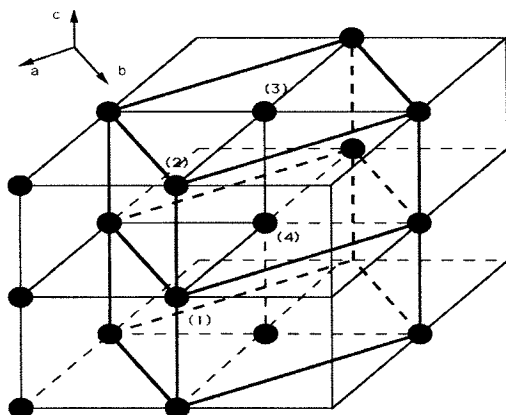


Fig. 7. Labeling of M-atom positions in the orthorhombic ($Pbnm$) structure of an AMO_3 perovskite.

irreducible representations. In the notation of Koehler et al. (1960), these base vectors are

$$\begin{aligned}
 F &= S_1 + S_2 + S_3 + S_4, \\
 G &= S_1 - S_2 + S_3 - S_4, \\
 C &= S_1 + S_2 - S_3 - S_4, \\
 A &= S_1 - S_2 - S_3 + S_4.
 \end{aligned}
 \tag{14}$$

Subjecting these vectors to the crystallographic symmetry operations generates the four possible representations of the base vectors shown in table 1. The x , y , z directions in table 1 are taken parallel to the a , b , c axes of the orthorhombic unit cell in space group $Pbnm$.

Where the MO_3 array is mixed-valent with both orbital and charge ordering, more complex spin configurations are found as is illustrated by $La_{0.5}Ca_{0.5}MnO_3$.

Extrapolation of the rules for the sign of the superexchange interaction, eqs. (9) and (10), to itinerant-electron magnetism leads to the following rules for bands containing n electrons per band orbital ($0 \leq n \leq 2$ because of spin degeneracy):

- Half-filled bands ($n = 1$) are antiferromagnetic.
- Bands with $0 < n \leq 1/2$ or $3/2 \leq n < 2$ would be half-metallic ferromagnets with full magnetization $M = Nn\mu_B$ or $N(2 - n)\mu_B$ per band orbital, where N is the number of transition-metal atoms per unit volume if narrow enough for total removal of the spin de-

Table 1
Representations of base vectors of M-atom spins with space group $Pbnm$

Representations	Base	Vector for	M-atom spin
Γ_1	A_x	G_y	C_z
Γ_2	F_x	C_y	G_z
Γ_3	C_x	F_y	A_z
Γ_4	G_x	A_y	F_z

generacy; if the intraatomic electron–electron interactions are not strong enough to remove completely the spin degeneracy of the band, a spin-density wave (SDW) may be stabilized.

- Bands with $1/2 < n < n_c$ or $n_c < n < 3/2$ would be ferromagnetic with a reduced magnetization $M = N(1 - n)\mu_B$ or $M = N(n - 1)\mu_B$ since only the antibonding states of the band are magnetized. At $n_c \approx 2/3$ or $4/3$ (value depends on bandwidth), there is a transition to antiferromagnetic order as the filling approaches $n = 1$.

The transition from localized to itinerant electronic behavior occurs where the interatomic interactions become greater than the intraatomic interactions. A measure of the strength of the interatomic interactions is the bandwidth W and of the strength of the intraatomic interactions is the energy U_{eff} that separates successive redox energies. The transition from localized to itinerant electronic behavior occurs where

$$W \approx U_{\text{eff}}. \quad (15)$$

Itinerant-electron magnetism is found in a narrow range of bandwidths ΔW near $W \approx U_{\text{eff}}$. For broader bands, localized spins on the M atoms are suppressed, and the tight-binding bandwidths are

$$W_\pi \approx 2zb_\pi^{\text{cac}} \quad \text{and} \quad W_\sigma \approx 2zb_\sigma^{\text{cac}} \quad (16)$$

where the number of like nearest neighbors is $z = 6$ for 3D bands, $z = 4$ for 2D bands, $z = 2$ for 1D bands. From eq. (7), a $\lambda_\sigma > \lambda_\pi$ and a small bending angle ϕ makes

$$W_\sigma > W_\pi. \quad (17)$$

The intraatomic interactions, on the other hand, are stronger the weaker the covalent mixing, which makes the on-site coulomb energies

$$U_{\pi\text{eff}} > U_{\sigma\text{eff}}. \quad (18)$$

Equation (18) is particularly strong at a Mn(III) ion, for example, where $U_{\pi\text{eff}}$ includes the exchange energy Δ_{ex} whereas U_σ includes neither a crystal-field splitting Δ_c nor an exchange splitting Δ_{ex} . A $W_\pi < U_{\pi\text{eff}}$ can leave a t^3 manifold localized in the presence of a $W_\sigma > U_{\sigma\text{eff}}$ that transforms the e electrons of an MO_3 array into itinerant electrons occupying a narrow σ^* band. This situation is found, for example, in the mixed-valent MnO_3 array of $\text{La}_{1-x}\text{Sr}_x\text{MnO}_3$ with $0.17 \leq x < 0.5$.

1.2.3. Localized-itinerant electronic transitions

A fundamental question is whether the transition between localized and itinerant electronic behavior is continuous or discontinuous. Mott (1949) was the first to point out that an on-site electrostatic energy $U_\sigma > W_\sigma$ is needed to account for the fact that NiO is an antiferromagnetic insulator rather than a metal. Hubbard (1963) subsequently introduced U formally as a parameter into the Hamiltonian for band electrons; his model predicted a smooth transition from a Pauli paramagnetic metal to an antiferromagnetic insulator as the ratio W/U decreased to below a critical value of order unity. This metal–insulator transition is known as the Mott–Hubbard transition.

In fact, there is increasing evidence that this transition is not continuous, and independent arguments have been presented that suggest the transition is first-order (Goodenough, 1992; Dagotto et al., 1998; Rozenberg et al., 1994). The simplest argument is based on the virial theorem of mechanics for central-force fields:

$$2\langle T \rangle + \langle V \rangle = 0 \quad (19)$$

where $\langle T \rangle$ is the mean kinetic energy of a system of particles and $\langle V \rangle$ is their mean potential energy. Electrons bound in a crystal have a $\langle V \rangle < 0$. At a transition from localized to itinerant electronic behavior, the volume occupied by an electron increases discontinuously, which means that $\langle T \rangle$ decreases and therefore $|\langle V \rangle|$ decreases discontinuously. For antibonding electrons, a decrease in $|\langle V \rangle|$ is accomplished by a decrease in the equilibrium (M–O) bond length, and a discontinuous decrease in (M–O) gives a first-order transition with

$$(M-O)_{\text{localized}} > (M-O)_{\text{itinerant}} \quad (20)$$

This situation leads to a double-well potential for the (M–O) bond at the crossover between localized and itinerant electronic behavior. A double-well potential for the equilibrium (M–O) bond length gives rise to lattice instabilities and phase segregation. However, the phase segregation may appear at too low a temperature for atomic diffusion. In this case, the perovskite structure accommodates a spinodal phase segregation by cooperative oxygen-atom displacements that create, on a small length scale, fluctuating regions of shorter (M–O) bond length in a matrix of larger (M–O) bond length or vice versa with complex bond-length fluctuations in between that may order at lower temperatures into a charge-density/spin-density wave (CDW/SDW); the CDW/SDW may be mobile or, if commensurate with the lattice, become pinned. A static CDW/SDW is readily observed by a diffraction experiment, a mobile CDW/SDW is not. Similarly, long-range-cooperative orbital ordering at Jahn–Teller ions induce a global lattice distortion and different equilibrium bond lengths are observed directly by neutron diffraction whereas bond-length fluctuations associated with short-range-cooperative orbital fluctuations are not. In the manganese oxides with perovskite structure, bond-length fluctuations due to the localized-itinerant electronic crossover coexist with bond-length fluctuations associated with Jahn–Teller orbital fluctuations. The fluctuations appearing at crossover may be called quantum-critical-point fluctuations.

Egami (2001) has developed pair-density-function analysis of pulsed neutron-diffraction data to determine the structure in a time interval that is short relative to a bond-length fluctuation. This method provides a direct observation of the pattern of bond-length fluctuations. Several other measurements have been shown to provide indirect signatures of the presence of bond-length fluctuations (Goodenough and Zhou, 2001). For example,

- An increase in the tolerance factor with pressure ($dt/dP > 0$) signals an unusually compressible M–O bond length; it has only been found at a crossover where there is a double-well potential for two equilibrium (M–O) bond lengths.
- The bandwidth W depends more sensitively on the M–O–M bond-bending angle ϕ than can be accounted for by eqs. (7) and (16), which suggests

$$W = W_b \exp(-\lambda \varepsilon_{sc} / \hbar \omega_0) \quad \text{with } \lambda \sim \varepsilon_{sc} / W_b, \quad (21)$$

where ε_{sc} is the energy required for an electron to transfer to a strong-correlation fluctuation from an itinerant-electron matrix and W_b is the tight-binding bandwidth of eq. (16). The period ω_0^{-1} of a bond-length fluctuation does not need to be overly sensitive to the angle ϕ to make W sensitive to ϕ .

- $^{18}\text{O}/^{16}\text{O}$ isotope exchange changes ω_0^{-1} and thereby changes W of eq. (21) to give marked changes in transition temperatures.
- The phonon contribution to the thermal conductivity is strongly suppressed by bond-length fluctuations.
- Both the room-temperature thermoelectric power and the phonon-drag component at low temperatures increase with hydrostatic pressure due to a decrease in the volume fraction of strong-correlation fluctuations in an itinerant-electron matrix.
- Where strong-correlation fluctuations are present in an itinerant-electron matrix, the magnetic susceptibility may be interpreted as a coexistence of Curie–Weiss and mass-enhanced Pauli paramagnetism.
- In mixed-valent systems, a spinodal phase segregation into fluctuating hole-rich conductive regions and hole-poor insulating regions gives rise to such unusual phenomena as a colossal magnetoresistance (CMR) in the manganese-oxide perovskites and high- T_c superconductivity in the intergrowth copper oxides.

2. Single-valent perovskites

2.1. LaMnO_3

The most extensively studied RMnO_3 parent compound is LaMnO_3 , which contains high-spin $\text{Mn(III)}:t^3e^1$ ions. It was already recognized in the 1950s that this compound is oxidized in air; oxidation changes the orthorhombic, antiferromagnetic insulator LaMnO_3 into a rhombohedral, ferromagnetic metal $\text{La}_{1-\zeta}\text{Mn}_{1-\varepsilon}\text{O}_3$ ($\zeta + \varepsilon = 0.12$ and $\zeta > \varepsilon$). Stoichiometric LaMnO_3 is stable in an inert atmosphere like N_2 or Ar or in vacuum. Wollan and Koehler (1955) reported the structure and magnetic order of LaMnO_3 at 4 K obtained by neutron diffraction; the data showed an orthorhombic axial ratio $c/a < \sqrt{2}$ and anisotropic ($180^\circ - \phi$) Mn–O–Mn interactions with ferromagnetic (001) MnO_2 planes coupled antiparallel to one another. Goodenough (1955) recognized that both the magnetic order below a Néel temperature $T_N = 135$ K and an axial ratio $c/a < \sqrt{2}$ can be accounted for by a cooperative antiferrodistortive Jahn–Teller ordering of the occupied σ -bonding e orbitals to give the structure of fig. 6(b)(ii). Each oxygen in a puckered (001) plane would be displaced so as to give ($180^\circ - \phi$) Mn–O··Mn bonds containing one short (*s*) and one long (*l*) Mn–O bond. This order would give $e^1 \cdots \text{O} - e^0$ ferromagnetic superexchange interactions by eq. (10) that dominate the $t^3\text{--O--}t^3$ interactions. Along the *c*-axis there would be no oxygen-atom displacement and equal Mn–O bonds would give antiferromagnetic $t^3\text{--O--}t^3$ superexchange interactions by eq. (9). Although the cooperative oxygen displacements were not observed at that time, this fact could be accounted for by the limited resolving power of their early powder diffractometer. Goodenough and Loeb (1955) had previously pointed out that cooperative

ferrodistortive Jahn–Teller orbital ordering occurs in tetragonal spinels containing octahedral-site Mn(III) and Cu(II) ions, and antiferrodistortive cooperative distortions within the (001) planes of LaMnO_3 would provide an experimental demonstration of Goodenough’s postulated rules for the sign of the spin–spin superexchange interactions, rules that were later shown to have general applicability (Goodenough, 1963). Kanamori (1959, 1960) subsequently refined the model; he took account of the crystalline orthorhombic symmetry by admixing the Q_3 and Q_2 deformation modes of fig. 6(a). Recent neutron (Rodríguez-Carvajal et al., 1998) and X-ray (Murakami et al., 1998) diffraction experiments on LaMnO_3 have fully corroborated the predicted oxygen displacements with opposite directions of the cooperative displacements in alternate (001) planes (out-of-phase stacking). Mizokawa et al. (1999) have argued that the degeneracy of the direction of oxygen displacements in the (001) planes is lifted by the A–O interactions to give the long-range orbital order in 3D, a larger tilting of the $\text{MnO}_{6/2}$ octahedra (smaller tolerance factor $t < 1$) favoring in-phase stacking of the oxygen displacements. Kataoka (2001) has extended the theory of Kanamori to include higher-order anharmonic elastic and first-order Jahn–Teller energies to account for the first-order character of the orbital order–disorder transition at $T_{JT} = 750$ K. At temperatures $T > T_{JT}$, the disordered occupied e orbitals fluctuate to give an O^* -orthorhombic symmetry with $c/a \approx \sqrt{2}$. Figure 8 shows the variation of the orthorhombic ($Pbnm$) cell parameters with temperature (Rodríguez-Carvajal et al., 1998). Louca et al. (1997), Egami et al. (1997), and Louca and Egami (1999) have shown with pulsed neutron diffraction and pair-density-function analysis that locally the Jahn–Teller distortions remain on a time scale short compared to 10^{-12} s where disorder reduces the average distortion viewed on a longer time scale. A Raman scattering study by Granado et al. (2000) also indicates that orbital disorder occurs on heating through T_{JT} and that considerable orbital fluctuation occurs on approaching T_{JT} from below. The apparent loss of ordering of the cooperative $\text{MnO}_{6/2}$ rotation in the O^* phase just above T_{JT} is a result of the orbital fluctuations. The cooperative rotations reappear in an O-orthorhombic phase at higher temper-

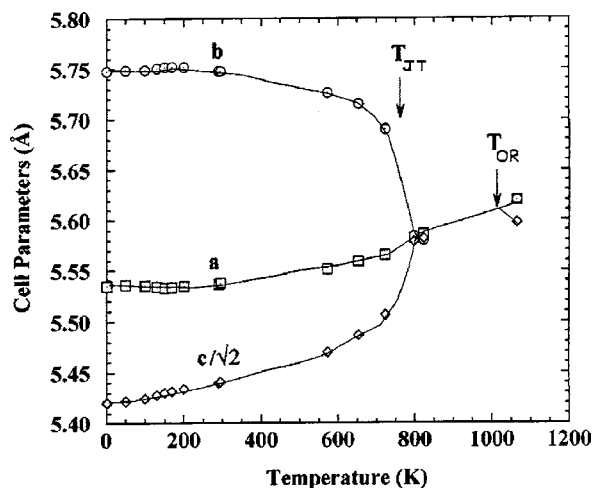


Fig. 8. Orthorhombic ($Pbnm$) lattice parameters of LaMnO_3 as a function of temperature. The $\text{MnO}_{6/2}$ octahedra become nearly regular in the O^* phase ($T > T_{JT}$) on the time scale of the measurement, but the displacement parameter of the oxygen atoms increases significantly; after Rodríguez-Carvajal et al. (1998).

atures ($T > 900$ K) before transforming above ca. 1000 K to the $R\bar{3}c$ rhombohedral structure with cooperative rotations about the [111] axis (Zimmermann et al., 2001). Rhombohedral symmetry does not support removal of the e-orbital degeneracy.

The type-A antiferromagnetic order of eq. (14) is canted by Dzialoshinskii antisymmetric exchange to give a weak canted-spin ferromagnetic moment oriented along the c -axis (type $A_y F_z$ of table 1) (Matsumoto, 1970a); in accordance with table 1, the Dzialoshinskii vector D_{ij} is parallel to the a -axis and the antiferromagnetic component of the Mn-atom spins $S = 2$ is parallel to the b -axis in space group $Pbnm$ (Zhou and Goodenough, 1999). Cestelli Guidé et al. (2001) have measured with muon spin rotation a cant angle of 2° and shown from the critical exponent β of $[1 - (T/T_N)]^\beta$ that LaMnO_3 is a Heisenberg system near T_N with a crossover to Ising behavior at lower temperatures due to magnetocrystalline anisotropy.

The Weiss constant of a Curie-Weiss paramagnetic susceptibility is a measure of the sign of the net spin-spin interactions in the paramagnetic state. Figure 9 shows isotropic paramagnetic data for a single crystal of LaMnO_3 taken under vacuum (Zhou and Goodenough,

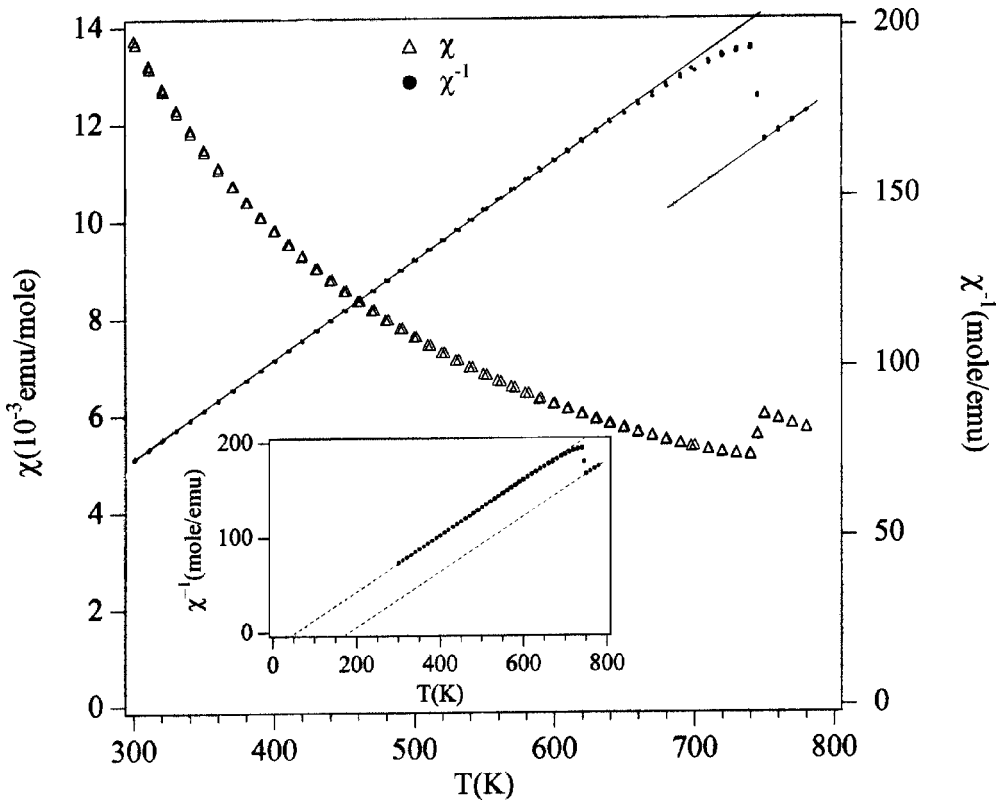


Fig. 9. Magnetic susceptibility $\chi(T)$ and $\chi^{-1}(T)$ for single-crystal LaMnO_3 . χ_{\parallel} and χ_{\perp} could not be resolved in the paramagnetic O' phase ($T_N < T < T_{JT}$), but they are resolved below T_N ; after Zhou and Goodenough (1999).

1999). Early paramagnetic data on a polycrystalline sample showed similar behavior (Jonker and van Santen, 1950). The presence of ferromagnetic interactions within (001) planes and antiferromagnetic interactions between planes in the range $T_N = 135 \text{ K} < T < T_{JT} = 750 \text{ K}$ gives a Curie–Weiss paramagnetic susceptibility with a positive Weiss constant $\theta = 52.5 \text{ K} < T_N$. The magnetic susceptibility increases discontinuously on increasing the temperature through T_{JT} ; the Curie constant C remains unchanged, but a $\theta = 177 \text{ K} > T_N$ for temperatures $T > T_{JT}$ shows that the magnetic interactions become isotropically ferromagnetic where the occupied e orbitals fluctuate. Such a change could be understood as due to the onset of a vibronic superexchange above T_{JT} with no change in the Mn spins provided LaMnO_3 remains an insulator at temperatures $T > T_{JT}$ (Goodenough et al., 1961).

The resistivity $\rho(T)$ and thermoelectric power $\alpha(T)$, obtained under vacuum, of the single crystal of LaMnO_3 used in the magnetic study of fig. 9 are shown in fig. 10(a). These measurements (Zhou and Goodenough, 1999) were made both to determine the oxygen stoichiometry of the crystal and to test the assumption that LaMnO_3 remains an insulator at temperatures $T > T_{JT}$. An initial value of $\alpha(300 \text{ K}) \approx -600 \mu\text{V/K}$ shows a slight oxygen deficiency; on cycling to 1100 K in vacuum, it becomes slightly oxidized to give the $\alpha(300 \text{ K}) \approx 550 \mu\text{V/K}$ of

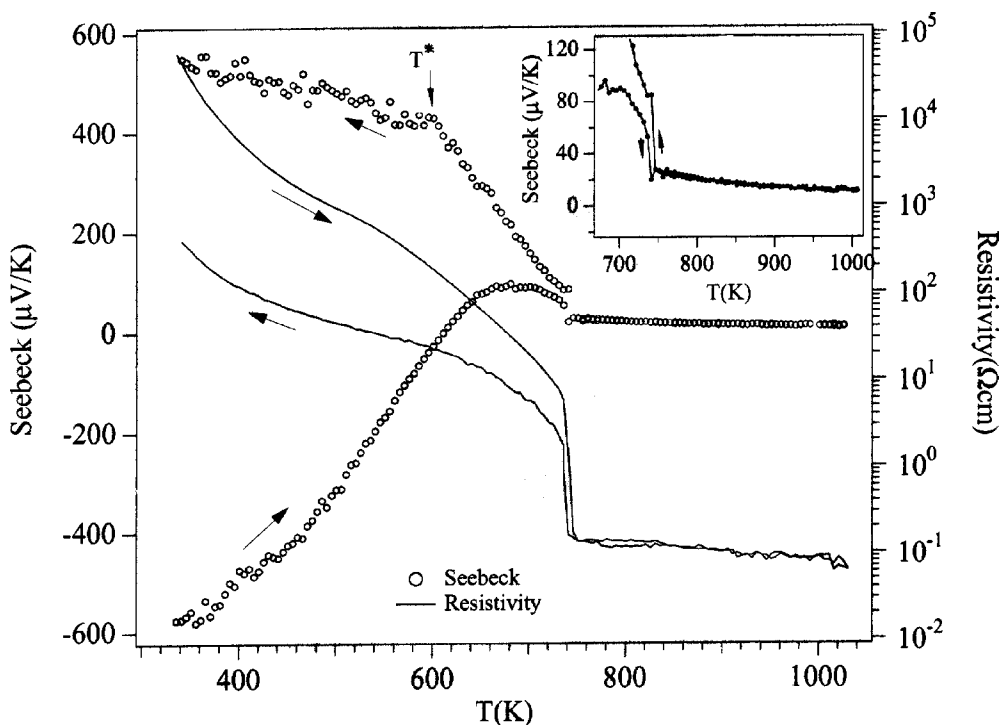


Fig. 10. (a) Resistivity $\rho(T)$ and thermoelectric power $\alpha(T)$ taken on cycling a virgin single crystal of LaMnO_3 from room temperature to 1100 K measured in a vacuum of 10^{-3} torr, after Zhou and Goodenough (1999).

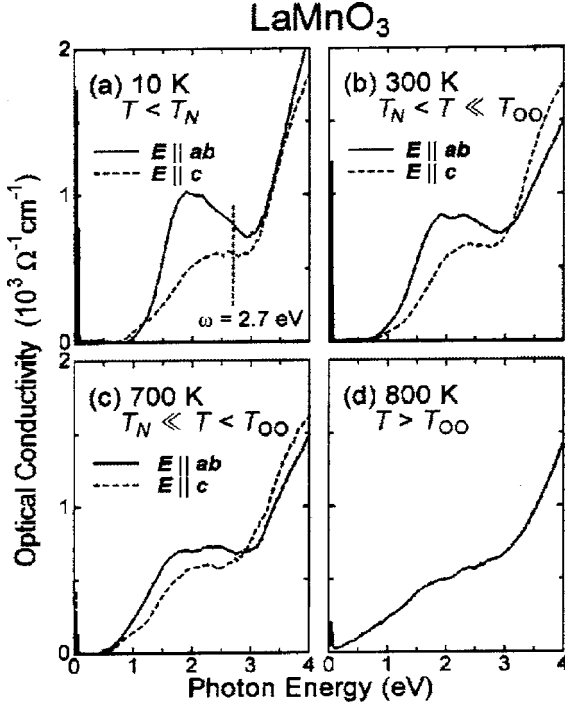


Fig. 10. (b) Optical conductivity spectra for $E \parallel ab$ (solid lines) $E \parallel c$ (dashed lines) of a detwinned LaMnO_3 crystal at representative temperatures: 10 K, 300 K ($T_N < T \ll T_{JT}$), 700 K ($T_N \ll T < T_{JT}$) and 800 K ($T > T_{JT}$) after Tobe et al. (2001).

fig. 10(a). The $\rho(T)$ and $\alpha(T)$ curves were reversible after the first cycle. These data show the sample is oxygen stoichiometric to within 0.1%. Nevertheless, $\rho(T)$ drops abruptly at T_{JT} to a magnitude comparable to that of a “bad metal” and $\alpha(T)$ drops to a low, nearly temperature-independent value. The onset at T^* of a sharper decrease in $\alpha(T)$ and $\rho(T)$ with increasing temperature in the interval $T^* < T < T_{JT}$ correlates with increasing orbital fluctuations on the approach to T_{JT} . The drops in $\alpha(T)$ and $\rho(T)$ represent a change from a small to a large fraction of mobile e electrons even though the crystal remains nominally single-valent Mn(III). Given the strong coupling of the e electrons to local lattice deformations below T_{JT} and the observation that dynamic local Jahn–Teller distortions persist above T_{JT} , we may conclude that LaMnO_3 is a vibronic conductor above T_{JT} and may have double-exchange as well as vibronic superexchange ferromagnetic interactions. The optical conductivity data of fig. 10(b) show the closing of an energy gap at ϵ_F with increasing temperature to T_{JT} , but the absence of a Drude term above T_{JT} that would be present if the conductive electrons were itinerant rather than vibronic.

The transition to a conductive state requires the generation of charge carriers and therefore thermal excitations of the disproportionation reaction



Van Roosmalen and Cordfunke (1994) have analyzed the relation between the partial pressure of oxygen and the value of δ in $\text{LaMnO}_{3+\delta}$ to conclude that a partial disproportionation reaction is responsible for the surprisingly large oxidation of LaMnO_3 in air. This disproportionation reaction accounts for the ready oxidation of LaMnO_3 in air, the Mn(II) being oxidized to Mn(III) to give $\text{La}_{1-\zeta}\text{Mn}_{1-\varepsilon}\text{O}_3$. In 10^{-3} torr vacuum, only a small percentage of the Mn(II) are oxidized to give the large $\alpha(300\text{ K}) > 0$; but at $T > T_{JT}$, the Mn(II) give electronic charge carriers and the Mn(IV) give hole charge carriers of nearly equal concentration, so a temperature-independent $\alpha \approx 0$ is found. The fact that the Curie constant C exhibits little change from its value for $T_N < T < T_{JT}$ to its value for $T > T_{JT}$ is consistent with a partial charge disproportionation; the observed value of C corresponds to a $\mu_{\text{eff}} = 5.2\mu_B$, which is to be compared to a spin-only value $\mu_{\text{eff}} = 4.9\mu_B$ for $S = 2$ and a $\mu_{\text{eff}} = 5.0\mu_B$ for a full disproportionation into Mn(II) with $S = 5/2$ and Mn(IV) with $S = 3/2$. Since the disproportionation reaction would be associated with a cooperative breathing-mode deformation that contracts equally the (Mn–O) bond lengths at Mn(IV) and expands equally the (Mn–O) bond lengths at Mn(II), we are led to the conclusion that the cooperative orbital ordering in the O' -orthorhombic phase suppresses the disproportionation reaction by localizing the Mn(III) e electrons in the long (Mn–O) bonds within the (001) planes, which hinders breathing-mode displacements of the oxygen atoms at the Mn atoms. Although the O' -orthorhombic ($c/a < \sqrt{2}$) structure is retained in the interval $T^* < T < T_{JT}$, which indicates the matrix retains occupied e orbitals preferentially ordered into the (001) planes, orbitally disordered fluctuations above T^* introduce charge carriers that reduce $\alpha(T)$, the volume fraction increasing discontinuously at T_{JT} . On raising the temperature through T_{JT} and in the orbitally disordered clusters in the range $T^* < T < T_{JT}$, the locally cooperative oxygen displacements become short range fluctuations in 3D that permit the formation of breathing-mode displacements of some of the Mn atoms. The formation of six short Mn–O bonds creates empty molecular e orbitals at Mn(IV) ions; the six long (Mn–O) bonds stabilize localized Mn(II): t^3e^2 configurations. The disproportionation reaction may therefore be considered a segregation into localized electrons at Mn(II) and holes delocalized over a Mn(IV) $\text{O}_{6/2}$ cluster as the result of an approach to the condition $U_\sigma \approx W_\sigma$ from the localized electron side. From a theoretical perspective, Ahn and Millis (2001) have used a tight-binding parametrization of band theory and expressions for the elastic energies to argue that the e electrons of LaMnO_3 approach the transition to itinerant-electron behavior from the localized-electron side. Moreover, it is apparent from fig. 10(a) that real charge transfer is occurring, which introduces an isotropic, ferromagnetic double-exchange component to the spin–spin coupling. Therefore, some other experiment is required to establish the existence of a vibronic isotropic superexchange interaction.

Goodenough et al. (1961) explored the $\text{LaMn}_{1-x}\text{Ga}_x\text{O}_3$ for this purpose and Lotgering (1970) studied the system $\text{La}_{1-x}\text{Ba}_x\text{Mn}_{1-x}\text{Ti}_x\text{O}_3$. In each case, all the manganese are Mn(III) and dilution of the Mn(III) by substitution of a non-magnetic ion into the MnO_3 array suppresses a static cooperative Jahn–Teller deformation. In each case a ferromagnetic superexchange in an insulator was observed, indicating the presence of a ferromagnetic vibronic superexchange. However, before turning to more recent studies of $\text{LaMn}_{1-x}\text{Ga}_x\text{O}_3$ and

$\text{LaMn}_{1-x}\text{Sc}_x\text{O}_3$, I draw attention to evidence from high-pressure studies that the σ -bonding e electrons of LaMnO_3 approach the transition from localized to itinerant behavior.

Millis et al. (1995) proposed on theoretical grounds that the cooperative Jahn–Teller orbital ordering makes LaMnO_3 an insulator. This prediction found experimental support in the high-temperature transport measurements of fig. 10(a). Subsequently, Loa et al. (2001) concluded, from their room-temperature structural and reflectance data and from resistivity $\rho(T)$ data all taken to 400 kbar hydrostatic pressure, that (1) the cooperative Jahn–Teller distortion of the Mn(III) octahedra in LaMnO_3 disappears at about 180 kbar although the phase remains an O' -orthorhombic insulator and, therefore, (2) the insulator behavior of LaMnO_3 is not due to the Jahn–Teller orbital ordering. However, the quality of the structural data decreased with increasing pressure, and a closer analysis of their data in comparison with that of Pinsard-Gaudart et al. (2001) shows that these conclusions are not supported by the data. Pinsard-Gaudart et al. (2001) reported room-temperature time-of-flight neutron-diffraction data taken on crushed, oxygen-stoichiometric single-crystal LaMnO_3 , a procedure that gave amazingly high-quality diffraction data. These data show that the cooperative Jahn–Teller distortion is stable to about 70 kbar; the reduction with pressure of the different Mn–O bond lengths is nearly the same and the extent of the cooperative $\text{MnO}_{6/2}$ rotations is continuously reduced. Low-temperature measurements revealed that type-A antiferromagnetic order is retained and T_N increases as a result of the greater overlap of the Mn-3d and O-2p orbitals. However, a transition to an unknown phase occurred between 70 and 80 kbar. The insulator-metal transition found at about 320 kbar by Loa et al. (2001) is consistent with the theoretical deduction by Ahn and Millis (2001) that the σ -bond e electrons of LaMnO_3 approach the transition from localized to itinerant behavior. Pressure experiments (Zhou and Goodenough, 2002a) discussed in sect. 2.7 confirm this deduction. The character of the orbital ordering in the insulator high-pressure phase $P \geq 80$ kbar has yet to be determined.

In order to show that the e -orbital degeneracy is lifted by electron–phonon interactions and not by the superexchange interaction, Allen and Perebeinos (1999) and Perebeinos and Allen (2001) have invoked the Franck–Condon process via self-trapped excitons to predict a Gaussian envelope of vibrational sidebands associated with resonant behavior of a Raman process close to the orbital excitation energy of 2 eV in LaMnO_3 . Features of the Raman spectra of LaMnO_3 obtained (Björnsson et al., 2000; Romero et al., 2001) for a laser frequency around 1100 cm^{-1} are consistent with these predictions. In the first step of the Raman process, the incident photon excites an electron at a Mn(III) ion from the lower to the upper orbital state of the Jahn–Teller doublet. This orbital exciton (also called an “orbiton”) is self-trapped by oxygen rearrangements from the orbitally ordered Jahn–Teller state, which creates a vibrationally excited state of the orbiton. In the second step of the Raman process, this virtual excitation decays back to the orbital ground state, but not to the vibrational ground state. A number of vibrational quanta are also excited (Franck–Condon principle) to give vibrational sidebands of significantly greater magnitude than are found with non-Jahn–Teller ions. Perebeinos and Allen (2000) have also predicted that the vibrational quanta associated with a photoexcited hole in a photoemission experiment are responsible for a ca. 0.5 eV broadening observed in angle-resolved photoemission spectra of the manganese-oxide perovskites (Dessau and Shen, 1998).

If the orbital exciton is not self-trapped by interactions with oxygen optical-mode vibrations, then it may propagate through the crystal as an orbital wave since there is inertia to slow restoration to the ground state (Ishihara et al., 1997). A quantized orbital wave is a new particle, the itinerant orbiton, analogous to the magnon corresponding to a quantized spin wave. The spin waves in a ferromagnetic crystal are detected by changes in the properties of a beam of photons or neutrons that is scattered from a single crystal. Saitoh et al. (2001) have used Raman scattering from a high-quality LaMnO_3 single crystal to detect a frequency shift that weakens as the temperature is increased from 9 K until it completely disappears above T_{JT} . They interpret this shift to be due to the presence of orbital-wave orbitons, but Allen and Perebeinos (2001) cautioned that the theory needs to introduce orbiton–phonon interactions before this demonstration can be considered “air tight”. Subsequently, van den Brink (2001) has developed a theory that introduces the electron–electron correlations and lattice dynamics on the same footing. His analysis accounts for the data of Saitoh et al. (2001) with a relatively weak electron–phonon coupling that, nevertheless, narrows the itinerant orbiton dispersion by a factor of two. The theory of Allen and Perebeinos applies to the strong-coupling limit. Orbitons may influence other physical properties such as heat capacity or thermal conductivity.

Measurements (Tobe et al., 2001; Quijada et al., 2001) of the optical-conductivity spectra of detwined single crystals of LaMnO_3 from $10 \text{ K} < T_N$ to $300 \text{ K} > T_N$ have shown a pronounced difference in the lowest-lying 2 eV excitation for the electric field $E \parallel ab$ and $E \parallel c$ ($Pbnm$ setting) that changed little on crossing T_N , but decreased gradually with increasing temperature to T_{JT} across which it collapsed. The fact that the anisotropy reflects the orbital ordering and not the spin ordering indicates a large O-2p admixture in the Mn(IV)/Mn(III) redox couple to facilitate an allowed 2p–3d transition. Quijada et al. (2001) interpret the 2 eV excitation to be the interatomic $\text{Mn(III)} + \text{Mn(III)} = \text{Mn(IV)} + \text{Mn(II)}$ e–e transition rather than the intraatomic transition examined by Allen and Perebeinos (1999).

2.2. $\text{LaMn}_{1-x}\text{Ga}_x\text{O}_3$ and $\text{LaMn}_{1-x}\text{Sc}_x\text{O}_3$

Reexamination (Töpfer and Goodenough, 1997a) of the insulator system $\text{LaMn}_{1-x}\text{Ga}_x\text{O}_3$ with oxygen-stoichiometric samples confirmed the earlier study (Goodenough et al., 1961) in this system. As shown in fig. 11, the O' -orthorhombic $c/a < \sqrt{2}$ phase is retained to $x = 0.5$, albeit with a c/a approaching $\sqrt{2}$ monotonically with increasing x ; long-range orbital order is retained in a percolating matrix to $x = 0.5$. However, the saturation magnetization at 4 K approaches the spin-only value of $4\mu_B/\text{Mn}$ for $x \geq 0.5$. Moreover, the Néel temperature T_N of the canted-spin, type-A antiferromagnetic order decreases with dilution of the Mn concentration to $x = 0.25$; the magnetic-ordering temperature increases to a higher ferromagnetic Curie temperature T_C at $x \approx 0.30$ that decreases monotonically with increasing x . Moreover, in a field of 100 Oe the paramagnetic Weiss constant θ increases with x , changing from $\theta \leq T_N$ for $x \leq 0.20$ to a $\theta > T_N$ for $x \geq 0.30$.

The magnetization data for these polycrystalline samples prompted a closer look with an oxygen-stoichiometric series of single-crystal samples in the range $0.15 \leq x \leq 0.50$ (Zhou et al., 2001a). The zero-field-cooled (ZFC) and field-cooled (FC) magnetization $M(T)$ under applied fields of 10 Oe, 50 Oe, and 5 kOe as well as the reciprocal magnetization $M^{-1}(T)$

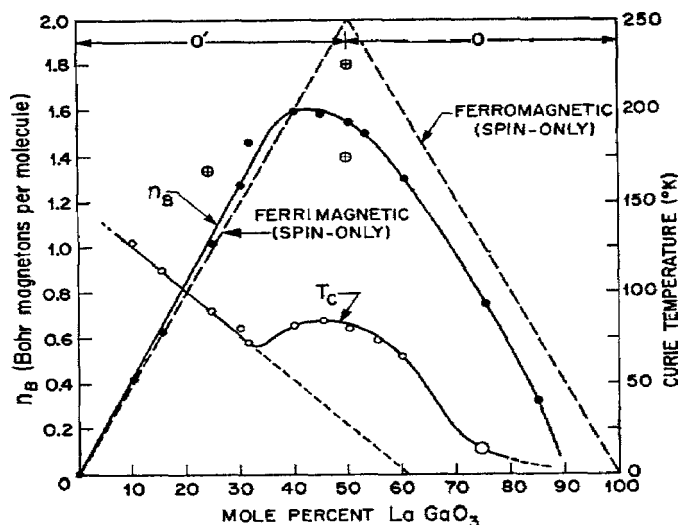


Fig. 11. Variation with x of the magnetic moment per Mn ion in Bohr magnetons at 4 K (straight line represents ferromagnetic spin-only value) and magnetic-ordering temperatures (crossed circles) for $\text{LaMn}_{1-x}\text{Ga}_x\text{O}_3$, after Goodenough et al. (1961).

in 5 kOe are shown in fig. 12 for $x = 0.15, 0.25, 0.35$, and 0.50 samples. Whereas the curves for $x = 0.15$ and 0.25 are typical of a type-A canted-spin antiferromagnet having a $\theta > 0$ because of the ferromagnetic exchange interactions in the basal planes, the low-field $M(T)$ curves for $x = 0.35$ and 0.50 show a maximum in the ZFC curves near the magnetic-ordering temperature, which is typical of a spin glass (Mydosh, 1993). An ac susceptibility $\chi_{ac}(T)$ of the $x = 0.5$ crystal is also plotted; it shows a sharp peak at the spin-freezing temperature T_f . On the other hand, the $M(T)$ curve taken in 5 kOe is typical of a ferromagnet with a $T_C \approx T_f$. Since a saturation spin-only moment of $4\mu_B/\text{Mn}$ is achieved in single-crystal samples under an applied field of only a few kOe (fig. 13) and the hysteresis loop has a small remanence, it is apparent that a modest magnetic field induces a transition from a spin glass to a ferromagnetic phase in the $x = 0.5$ sample. From the inset of fig. 13, this transition is initiated at about $H = 2500$ Oe; the volume fraction of the ferromagnetic phase increases with H , saturating at $H \geq 2$ kOe.

The data of fig. 11 show that for $x > 0.5$ the system has the O^* -orthorhombic structure indicative of orbital disorder in zero field; these polycrystalline samples are ferromagnetic with a saturation magnetization at 4 K approaching $4\mu_B/\text{Mn}$ atom. Since the O' -orthorhombic phase is retained in zero field at $x \leq 0.5$, these results have a straightforward interpretation. In zero field, an orbitally ordered, antiferromagnetic matrix with Néel temperature T_N percolates through the structure if $x \leq 0.5$; but orbitally disordered, ferromagnetic clusters are present in the matrix for $x \geq 0.30$, and these clusters have a $T_C > T_N$. The application of a magnetic field stabilizes the orbitally disordered ferromagnetic phase relative to the orbitally ordered antiferromagnetic phase, and the ferromagnetic clusters grow in a magnetic field at the expense of the antiferromagnetic matrix. In this system, there is no negative magnetoresistance associated with the growth of the ferromagnetic clusters to beyond their percolation threshold; the orbitally disordered phase remains insulating for larger values of x . On the other hand, ap-

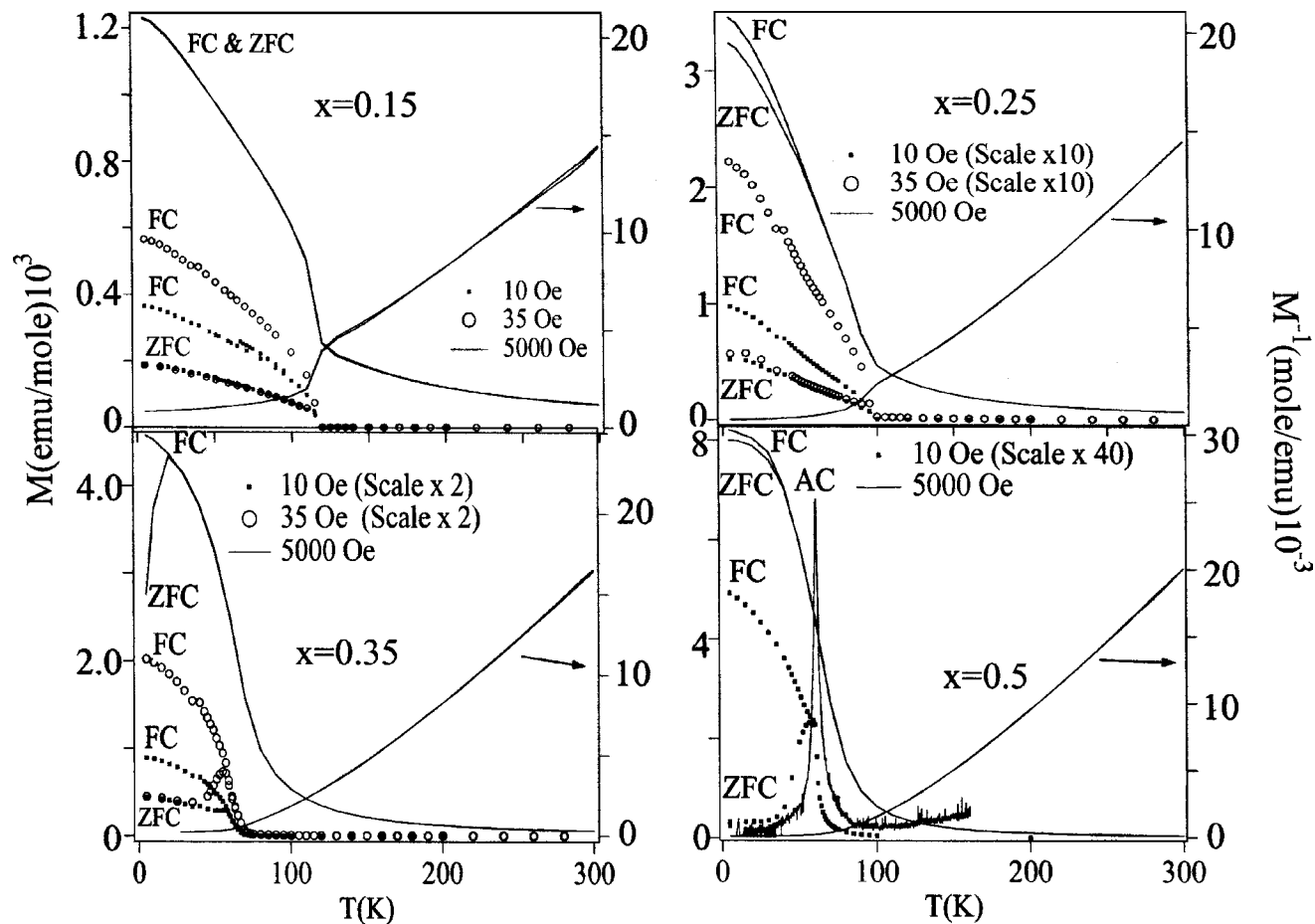


Fig. 12. The temperature dependence of the magnetization $M(T)$ and its reciprocal $M^{-1}(T)$ under different applied fields for single crystals of the system $\text{LaMn}_{1-x}\text{Ga}_x\text{O}_3$. The ac susceptibility $\chi_{ac}(T)$ of the $x = 0.5$ sample is superimposed, after Zhou et al. (2001a).

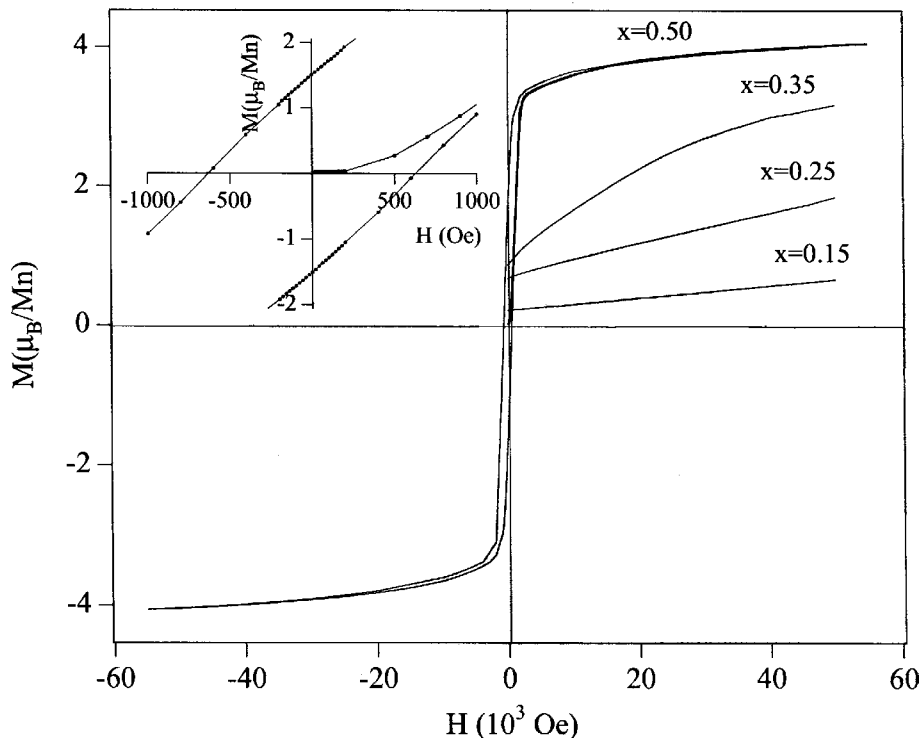


Fig. 13. The magnetization vs. applied magnetic field at $T = 5$ K for single-crystal samples of the $\text{LaMn}_{1-x}\text{Ga}_x\text{O}_3$ system. The full hysteresis loop is shown for the $x = 0.50$ sample; the inset is the detail in low fields, after Zhou et al. (2001a).

plication of hydrostatic pressure appears to stabilize the orbitally ordered matrix, which has a smaller volume (Zhou et al., 2001a).

A zero-field phase diagram for the $\text{LaMn}_{1-x}\text{Ga}_x\text{O}_3$ system is shown in fig. 14. Four important conclusions follow from the studies made of this system: (1) An isotropic ferromagnetic, vibronic Mn(III)–O–Mn(III) superexchange interaction is found where the occupied e orbitals fluctuate. (2) A magnetic field stabilizes the orbitally fluctuating, ferromagnetic phase relative to the orbitally ordered antiferromagnetic phase; and where the two phases coexist, a magnetic field may induce a transition from a spin-glass to a ferromagnetic phase. (3) The σ -bonding e electrons of the Mn(III) ions remain localized in the orbitally fluctuating state where Ga substitutions perturb the periodic potential of the MnO_3 array. (4) Hydrostatic pressure stabilizes an ordering of the occupied e orbitals that decreases the volume fraction of disordered orbitals.

For comparison, Al(III) and Sc(III) were substituted for Mn(III) (Goodenough et al., 2002). These ions also perturb the periodic potential of the MO_3 array to maintain localized e electrons at the Mn(III) ions where the orbitals become disordered. In these solid-solution

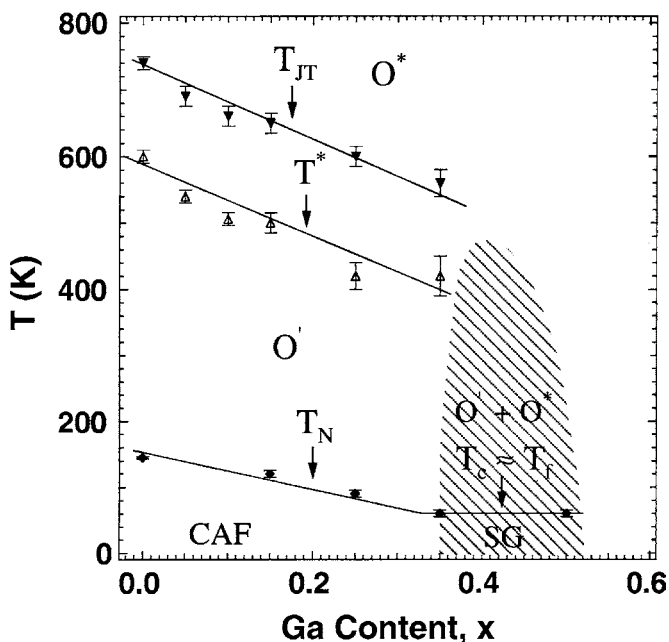


Fig. 14. Phase diagram for the $\text{LaMn}_{1-x}\text{Ga}_x\text{O}_3$ as obtained with single-crystal samples, after Goodenough et al. (2002).

systems also, the disproportionation reaction $2\text{Mn(III)} = \text{Mn(II)} + \text{Mn(IV)}$ is suppressed. Single-phase $\text{LaMn}_{1-x}\text{Al}_x\text{O}_3$ was restricted to the range $0 \leq x \leq 0.20$ where it remained a canted-spin antiferromagnet. On the other hand, single-phase $\text{LaMn}_{1-x}\text{Sc}_x\text{O}_3$ was found over the entire range of solid solutions $0 \leq x \leq 1$. This system showed a smooth crossover from $c/a < \sqrt{2}$ to $c/a > \sqrt{2}$ near $x = 0.35$; $c/a > \sqrt{2}$ became independent of x above $x = 0.75$. The Sc(III) ion is larger and has a stronger octahedral-site preference than Ga(III), which makes Sc(III) more resistant to the cooperative Jahn–Teller distortion induced by the Mn(III) ions. The smaller Al(III) ion, on the other hand, offers little resistance to a cooperative Jahn–Teller distortion, and the c/a ratio changed little in the range $0 \leq x \leq 0.20$ of $\text{LaMn}_{1-x}\text{Al}_x\text{O}_3$.

The phase diagram of fig. 15 for $\text{LaMn}_{1-x}\text{Sc}_x\text{O}_3$ shows an evolution with x from canted-spin antiferromagnetic insulator (CAFI) to spin-glass insulator (SGI) to ferromagnetic insulator (FI) that is similar to that of the $\text{LaMn}_{1-x}\text{Ga}_x\text{O}_3$ system. Moreover, the spin-glass phase transforms to a ferromagnetic phase in a high magnetic field; the evolution with x of the magnetization at 5 K in a field of 50 kOe is shown in fig. 16. In polycrystalline $\text{LaMn}_{1-x}\text{Sc}_x\text{O}_3$, as in polycrystalline $\text{LaMn}_{1-x}\text{Ga}_x\text{O}_3$, the full theoretical spin-only moment of $4\mu_B/\text{Mn}$ is not attained for any value of x whereas the full moment was found in the single crystals of $\text{LaMn}_{1-x}\text{Ga}_x\text{O}_3$. The evolution of the magnetic ordering temperature indicates that spin-glass behavior is found where the ferromagnetic clusters within the antiferromagnetic matrix have a $T_C > T_N$. The more rapid drop-off in T_N with x as x approaches the critical value $x_c \approx 0.30$ where $T_N = T_f \approx T_C$ shows the presence of orbitally disordered clusters appearing for $x < x_c$;

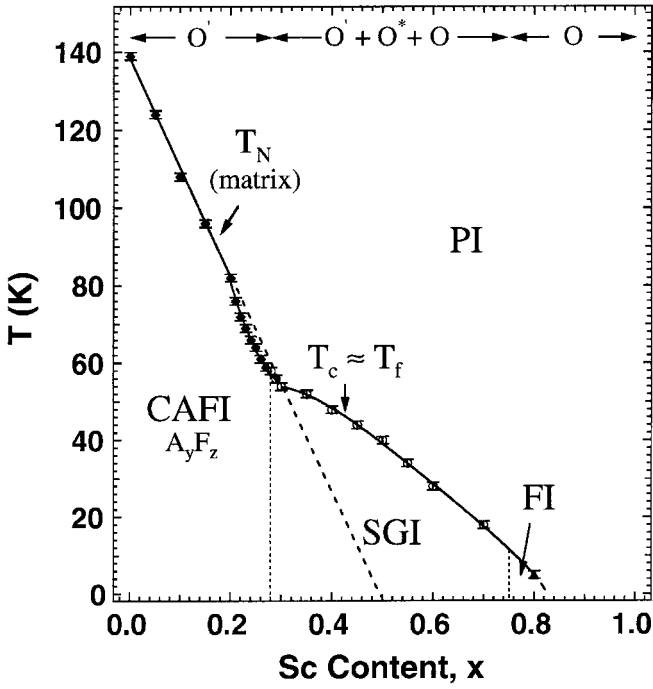


Fig. 15. Phase diagram for the $\text{LaMn}_{1-x}\text{Sc}_x\text{O}_3$ system as obtained with polycrystalline samples, after Goodenough et al. (2002).

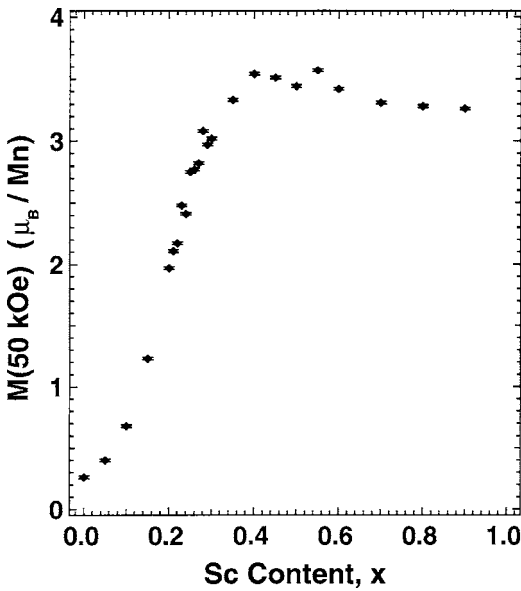


Fig. 16. The magnetization at 50 kOe vs. x at $T = 5 \text{ K}$ for $\text{LaMn}_{1-x}\text{Sc}_x\text{O}_3$, after Goodenough et al. (2002).

the clusters dilute the antiferromagnetic matrix more rapidly than a simple substitution of Sc(III) ions.

2.3. RMnO_3

The stoichiometric manganites RMnO_3 with larger lanthanide ions La to Dy all form the O' -orthorhombic $Pbnm$ structure at room temperature while those with the smaller lanthanide ions Ho to Lu or with Y all take the hexagonal $P6_3cm$ structure of fig. 17. High-resolution electron diffraction taken on single crystals of RMnO_3 ($R = \text{Y, Yb, Lu}$) have demonstrated the formation of Mn trimers within the MnO ab planes as well as a ferroelectric distortion along the c -axis in the hexagonal structure (Katsufuji et al., 2001). Long-range magnetic order is frustrated by competing exchange interactions in the MnO planes, which lowers T_N and sustains spin fluctuations well below T_N . However, an O' -orthorhombic perovskite form of RMnO_3 for the smaller rare-earth ions can be prepared either by high pressure (Wood et al., 1973) or from citrate-based precursors (Szabo, 1969), which has allowed study of the entire RMnO_3 series of perovskite manganites (Szabo, 1969; Quezel-Ambrunat, 1968; Rodríguez-Carvajal et al., 1998; Troyanchuk et al., 1997; Quezel et al., 1974, 1977; Jirák et al., 1997; Matsumoto, 1970b; Brinks et al., 2001).

The cooperative rotations of the $\text{MnO}_{6/2}$ octahedra increase with decreasing radius of the R^{3+} ion, i.e., with decreasing tolerance factor t . As the bending angle ϕ of the $(180^\circ - \phi)$ Mn–O–Mn interactions increases, the strength of the ferromagnetic σ -bond superexchange in the (001) planes is weakened relative to that of the antiferromagnetic t^3 –O– t^3 interactions. As a result, the Néel temperature T_N for ordering of the manganese moments decreases systematically from 141 K for $R = \text{La}$ to 50 K for $R = \text{Eu}$; and for $R = \text{Tb, Ho, and Y}$ the ferromagnetic (001) planes transform to an incommensurate spiral-spin configuration propagating along the b -axis in the bc plane, see fig. 18, with a $T_N \approx 40$ K. The propagation vector $\mathbf{k} = k_y \mathbf{b}^*$ increases with decreasing ionic radius of the R^{3+} ion. In orthorhombic HoMnO_3 , it also in-

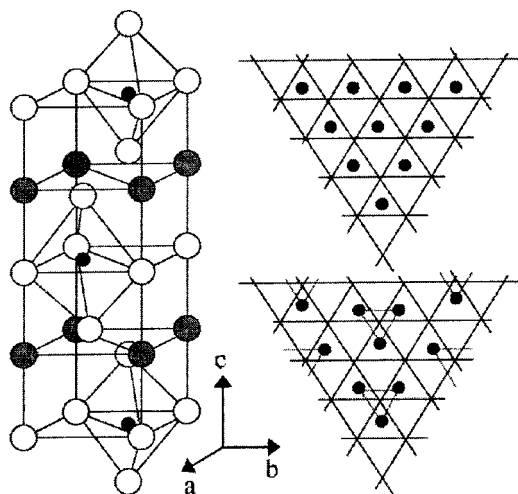


Fig. 17. Hexagonal $P6_3cm$ structure of LuMnO_3 , after Katsufuji et al. (2001).

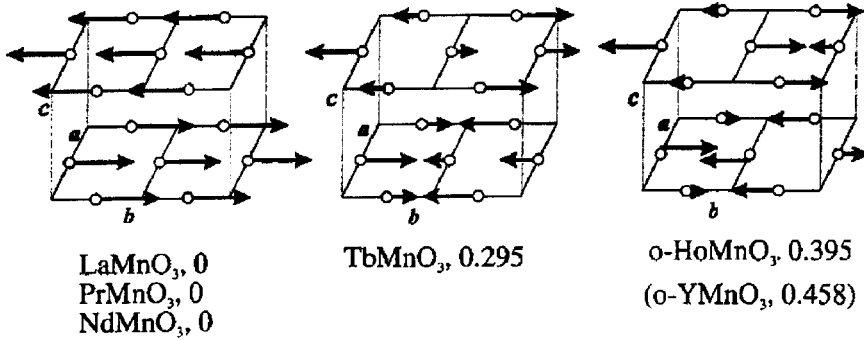


Fig. 18. The magnetic ordering of Mn(III)-ion spins in RMnO_3 , $R = \text{La, Pr, Nd, Tb, Ho}$ (and Y), in two adjacent (001) planes. Not shown is the spin canting to give a small ferromagnetic component along the c -axis for $R = \text{La, Pr, Nd}$. The numerical values refer to the spin periodicity just below T_N , after Brinks et al. (2001).

creases with decreasing temperature from $0.395b^*$ just below T_N to $0.431b^*$ at $T_{\text{Ho}} = 11$ K, the ordering temperature of the Ho^{3+} -ion moments. A $dt/dT > 0$ means that t decreases with temperature as well as with substitution of smaller A cations. The Ho^{3+} moments order in a spiral-spin configuration with the same propagation vector \mathbf{k} as that of the Mn(III) spins. At lowest temperatures, a commensurate spiral-spin configuration coexists with the incommensurate configuration (Brinks et al., 2001).

2.4. CaMnO_3

Oxygen-stoichiometric CaMnO_3 can be prepared in a flowing O_2 atmosphere; at room temperature, it has the O-orthorhombic ($c/a > \sqrt{2}$) perovskite structure. The half-filled t orbitals of the Mn(IV): t^3e^0 ions give rise to antiferromagnetic $t^3\text{-O-t}^3$ superexchange interactions between all nearest neighbors. As there are no other competitive interactions, CaMnO_3 is a type G (see table 1) antiferromagnetic insulator with a Néel temperature $T_N = 125$ K and a spin-only paramagnetic moment $\mu_{\text{eff}} = 3.9\mu_B$; the atomic moment of the antiferromagnetic state, $\mu_{\text{Mn}} \approx 2.64\mu_B$ (Yudin et al., 1966) is reduced from $3.0\mu_B$ by the virtual charge transfer of the antiferromagnetic superexchange interaction.

One remarkable feature of this compound is an anomalously low thermal conductivity $\kappa(T)$ in the paramagnetic phase; $\kappa(T)$ increases abruptly on cooling through T_N (Fujishiro et al., 2000; Zhou and Goodenough, 2002b). Since CaMnO_3 is an insulator, only the magnons and phonons contribute to $\kappa(T)$; therefore, the $\kappa(T)$ data indicate that spin disorder suppresses not only the magnons, but also the phonons. Since the orbital angular momentum is quenched in a t^3e^0 configuration and there are no orbital fluctuations, the spin-lattice interactions would appear to be due to an exchange striction, antiferromagnetic coupling on opposite sides of an oxygen atom giving rise to shorter Mn–O bond lengths. In the paramagnetic phase, random exchange-strictive displacements would perturb the periodicity of the lattice and suppress the optical phonons. However, the superexchange interaction, eq. (9), involves a virtual charge transfer between cations that does not alter the Mn–O equilibrium bond length. Therefore, we

need to introduce the semicovalent-exchange component that was first introduced by Goodenough (1963), who showed it gave the same sign of the exchange coupling. Subsequently, it was given analytic form by Geertsma (1979) and quoted by Zaanen and Sawatzky (1987). This interaction involves a two-electron virtual charge transfer from the intermediate oxygen, one of one spin to one side and one of opposite spin to the other side. Each electron transfer costs an energy Δ if the on-site electrostatic energy for the oxygen 2p electrons is small, i.e., $U_{pp} \ll \Delta$. Addition of the semicovalent exchange component changes the expression for the superexchange interaction from that given in eq. (9) to

$$J_{ij} \sim \frac{2|b^{ca}|^4}{\Delta^2} (1/U_{\text{eff}} + 1/2\Delta), \quad (23)$$

where the first term is just the Anderson superexchange term in which $b_{ij} \sim \Delta^2 \lambda_{\pi}^4$ with $\lambda_{\pi} = b^{ca}/\Delta$ and b^{ca} is the cation–anion resonance (electron-energy transfer) integral. The second term in eq. (23) is the semicovalent-exchange component. Where the highest occupied redox couple in the point-charge model of an ionic crystal lies below the $O^{2-} : 2p^6$ level, a $\Delta < U_{\text{eff}}$ makes the semicovalent exchange larger than the Anderson component of the superexchange interaction. A two-electron transfer from the oxygen, one to each of its neighboring Mn atoms, would increase Mn–O–Mn bonding where the Mn-atom spins on opposite sides of the oxygen are antiparallel. Accordingly, an important exchange-strictive contraction of the Mn–O bond lengths occurs on cooling through T_N (Moritomo et al., 2001). In order to test whether the semicovalent exchange striction is responsible for the surprising suppression of $\kappa(T)$ in the paramagnetic phase of CaMnO_3 , the $\kappa(T)$ of single-crystal CaMnO_3 was compared to that for single-crystal LaMnO_3 , LaGaO_3 , large-grained YCrO_3 , and SmNiO_3 (Zhou and Goodenough, 2002b). The reciprocal thermal conductivity $\kappa^{-1}(T)$ is plotted for these compounds in fig. 19 where the dotted line represents that of an oxide glass. As expected, LaGaO_3 has a normal $\kappa(T)$ behavior whereas $\kappa(T)$ is suppressed in the paramagnetic phase of the four antiferromagnetic compounds; the suppression increases progressively on going from YCrO_3 to LaMnO_3 to CaMnO_3 to SmNiO_3 . This progression correlates with the magnitude of the charge-transfer gap Δ from the O-2p bands to the lowest unoccupied redox energy of the transition-metal atoms, as can be seen from the schematic energy diagrams of fig. 20. This experiment provides a confirmation of the competitive character of the semicovalent exchange component of the superexchange interaction.

2.5. SrMnO_3

SrMnO_3 has a tolerance factor $t > 1$, which places the Mn–O–Mn bonds under tension and the Sr–O bonds under compression. These stresses are relieved by the formation of hexagonal polytypes (Goodenough et al., 1972). SrMnO_3 forms the 6H hexagonal polytype in which the (111) close-packed SrO_3 planes of the cubic structure have hexagonal stacking alternating with two cubic stackings instead of all-cubic stacking. Alternatively, loss of oxygen reduces some of the manganese to Mn(III), thereby increasing the mean ionic radius of the manganese ions to reduce t and stabilize the cubic phase. Oxygen-deficient, cubic $\text{SrMnO}_{3-\delta}$ is a mixed oxide-ion/electron conductor, but in air it picks up oxygen above 600 °C to revert to the hexagonal polytype (Tichy and Goodenough, 2002).

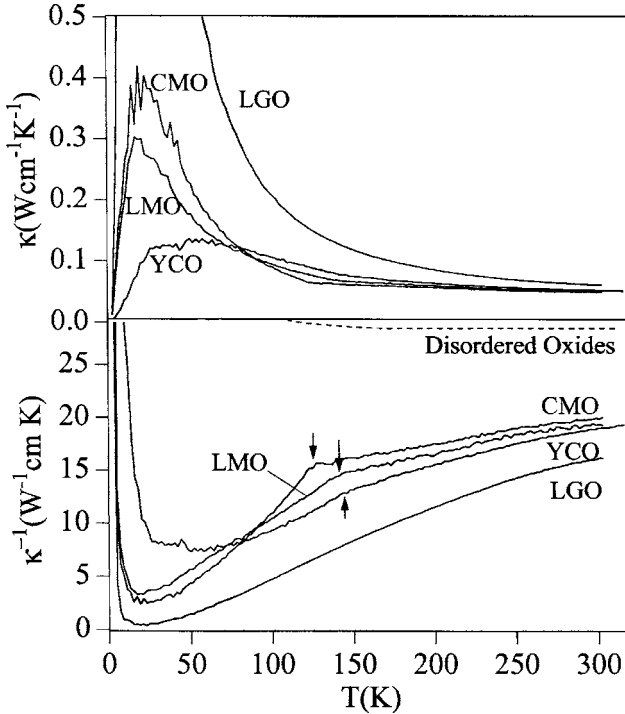


Fig. 19. Thermal conductivity $\kappa(T)$ and its inverse of single-crystal LaGaO_3 (LGO), LaMnO_3 (LMO), CaMnO_3 (CMO), and large grained YCrO_3 (YCO). The dotted line is that of an oxide glass. The arrows indicate the Néel temperatures T_N , after Zhou and Goodenough (2002b).

2.6. $\text{Sr}_{1-x}\text{Ca}_x\text{MnO}_3$ ($0 \leq x \leq 1$) and $\text{Sr}_{1-y}\text{Ba}_y\text{MnO}_3$ ($0 \leq y \leq 0.2$)

According to eqs. (7) and (9), the Néel temperature T_N of the system $\text{Sr}_{1-x}\text{Ca}_x\text{MnO}_3$ and $\text{Sr}_{1-y}\text{Ba}_y\text{MnO}_3$ should increase with increasing x and y as $\langle \cos^2 \theta \rangle$ increases with the tolerance factor t ; $\theta = (180^\circ - \phi)$ is the Mn–O–Mn bond angle. Neumeier et al. (2001) have shown that the transition at T_N in CaMnO_3 is second-order with a jump in the specific heat $\Delta C_p = -9.9 \pm 0.7 \text{ J/mol}$ at $T_N = 124.2 \text{ K}$. Chmaissem et al. (2001) obtained T_N and, with neutron and synchrotron X-ray powder diffraction, the values of $\langle \cos^2 \theta \rangle$ as a function of x and y . The system $\text{Sr}_{1-x}\text{Ca}_x\text{MnO}_3$ is O-orthorhombic ($Pbnm$) for $0.4 < x \leq 1.0$, tetragonal ($I4/mcm$) for $0.3 \leq x \leq 0.4$, and cubic ($Pm\bar{3}m$) for $0 \leq x \leq 0.3$; $\text{Sr}_{1-y}\text{Ba}_y\text{MnO}_3$ is cubic for all values of $y \leq 0.2$ obtained at lower temperatures under a high oxygen pressure. As shown in fig. 21, Chmaissem et al. (2001) found experimentally the relationship

$$T_N(\theta, \sigma^2) = T_{N,\max}(180^\circ, 0) - C_1[1 - \langle \cos^2 \theta \rangle] - C_2\sigma^2, \quad (24)$$

where C_1 and C_2 are constants and $\sigma^2 \equiv (r_A^0 - \langle r_A \rangle)^2$ is the variance of the room-temperature ionic radii associated with different A-site cations; r_A^0 is the radius of Sr^{2+} obtained from cubic SrMnO_3 . To fit the experimental variation of T_N with x and y , it was necessary to add the term $C_2\sigma^2$ to take account of the variation in the periodic potential as a result of changes in θ induced by different A-site cations bonding with the bridging oxygen atoms.

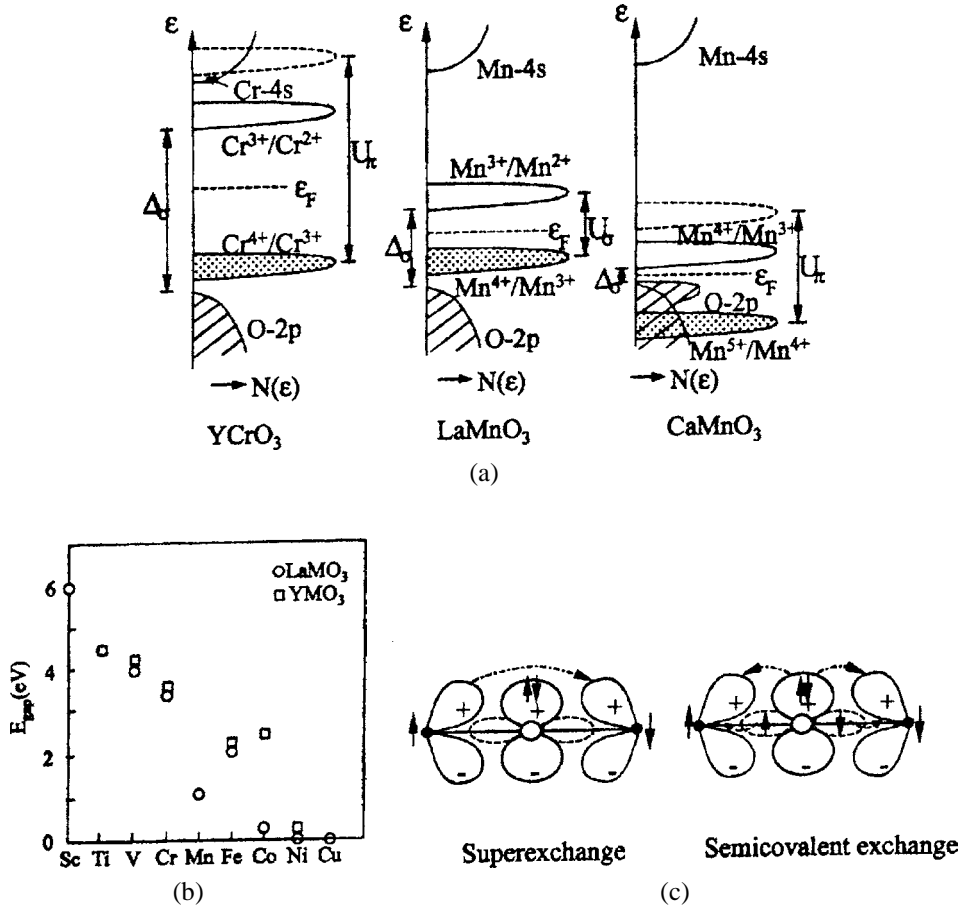


Fig. 20. (a) Schematic energy diagrams for YCrO₃, LaMnO₃, and CaMnO₃. (b) The charge transfer gap Δ measured by optical spectra, after Arima et al. (1993). (c) Virtual electron transfers for 180° t^3e^0 -O- t^3e^0 in Anderson superexchange and semicovalent exchange. In Anderson superexchange, the operative transfer integrals are between the crystal-field orbitals $\psi_i = N_\pi (f_i - \lambda_\pi \phi_\pi)$, after Zhou and Goodenough (2002b).

2.7. Bloch's rule

Bloch (1966) studied the variation of the Néel temperature T_N with volume V for numerous antiferromagnetic insulators and found the general relationship

$$\alpha_B \equiv d \log T_N / d \log V \approx -3.3 \pm 0.4. \tag{25}$$

This relationship, known as Bloch's rule, applies in the localized-electron limit where the interatomic spin-spin interaction is described by the superexchange perturbation theory of eq. (23) with $T_N \sim J$; J is the Heisenberg exchange energy. Calculations by Shrivastava and

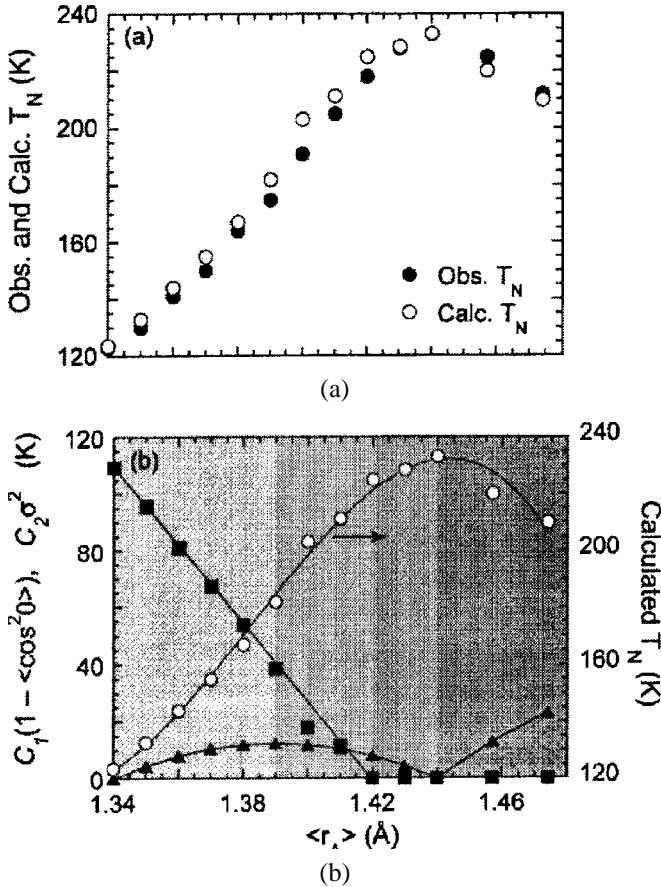


Fig. 21. (a) Observed (filled circles) and calculated (open circles) T_N as a function of $\langle r_A \rangle$. (b) Calculated T_N values (open circles) obtained by subtracting the individual contributions of $C_1[1 - \langle \cos^2 \theta \rangle]$ (filled squares) and $C_2 \sigma^2$ (filled triangles) from $T_{N,\max} = 233$ K (see eq. (24)), after Chmaissem et al. (2001).

Jaccarino (1976) and by Smith (1969) have given a $b^{ca} \sim r^{-n}$ with $n \approx 2.5-3.0$ for an equilibrium M–O bond length r . If U and Δ of eq. (23) are pressure-independent, it follows that $T_N \sim r^{-10} \sim V^{-3.3}$. If the compressibility $K \equiv -V^{-1} \partial V / \partial P$ remains constant, the pressure dependence of T_N should conform to Bloch's rule. Therefore, any deviation from Bloch's rule would be an indication that either the superexchange perturbation approach breaks down or the assumption that U and Δ are pressure-independent is not valid.

A determination of α_B for LaMnO_3 and CaMnO_3 has been compared to α_B for YCrO_3 (Zhou and Goodenough, 2002a). Figure 22 compares T_N vs. hydrostatic pressure P for these three compounds. The data for LaMnO_3 is non-linear below 7 kbar; a first-order phase change at 7 kbar is followed by an unusually large slope $dT_N/dP = 0.55$ K/kbar for $P > 7$ kbar, which is to be compared to a $dT_N/dP = 0.34$ K/kbar for CaMnO_3 and 0.30 K/kbar for YCrO_3 over the entire pressure range. A neutron-diffraction study to 70 kbar by Pinsard-Gaudart et al. (2001) has shown retention over the entire pressure range of the cooperative ordering of the e electrons into the (001) planes and a compressibility $K = 0.70 \times 10^{-6}/\text{bar}$

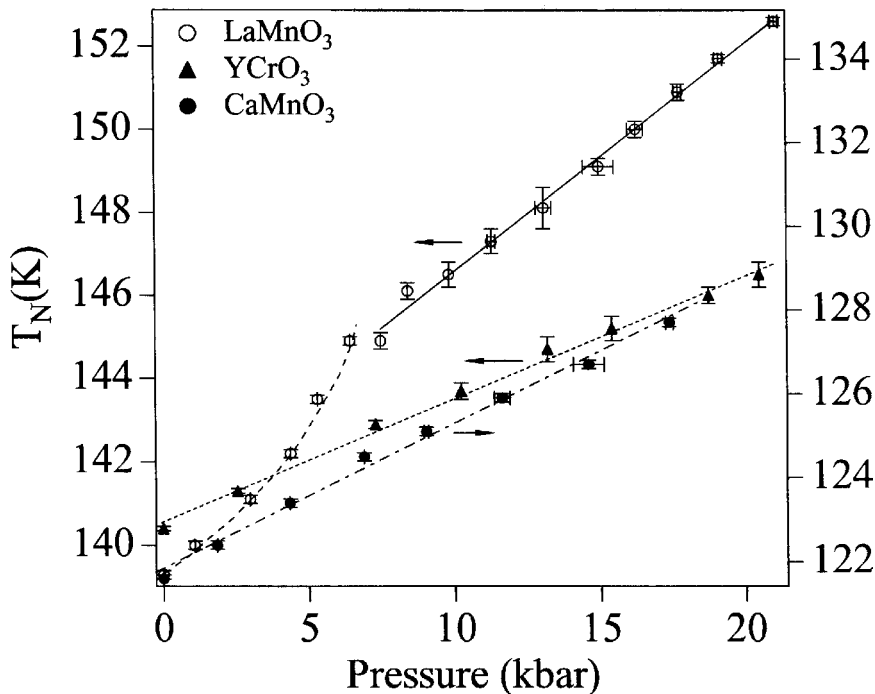


Fig. 22. Pressure dependence of T_N for LaMnO_3 , CaMnO_3 , and YCrO_3 . Straight lines are linear fittings of the data, after Zhou and Goodenough (2002a).

that is comparable to the $K = 0.68 \times 10^{-6}/\text{bar}$ found by Bloch (1966) for other antiferromagnetic insulators. A measured $|\alpha_B| = 5.3$ for LaMnO_3 under $P > 7$ kbar is to be compared with eq. (25) and an estimated (assuming $K = 0.68 \times 10^{-6}/\text{bar}$) $|\alpha_B| = 3.8$ and 3.0 for CaMnO_3 and YCrO_3 , respectively. YCrO_3 clearly obeys the Bloch rule and CaMnO_3 is at its upper limit, but LaMnO_3 has an unusually large $|\alpha_B|$ in the range $P > 7$ kbar as well as an anomalous dT_N/dP in the range $P < 7$ kbar and a two-phase region at $P \approx 7$ kbar.

In YCrO_3 and CaMnO_3 , the $t^3\text{-O-t}^3$ interactions contain an effective on-site energy U_π that is augmented by the intraatomic exchange energy $\Delta_{\text{ex}} > 2.5$ eV whereas the U_σ for the $e^1\text{-O-e}^0$ interactions in the (001) planes of LaMnO_3 is not augmented and is too small to inhibit a disproportionation reaction above T_{JT} . Moreover, the anomalous behavior of dT_N/dP in LaMnO_3 cannot be attributed to either an orbital reorientation or an anomalous compressibility. Therefore, we conclude there is a breakdown of the perturbative description of the spin-spin interactions in the (001) planes and/or the assumption that the factor $[U_\sigma^{-1} + (2\Delta)^{-1}]$ in eq. (23) is pressure-independent. Such a breakdown would occur on the approach to the transition from localized-electron to band magnetism. The on-site energy U collapses due to screening in the band regime where the bandwidth is $W > U$. This collapse at crossover is relatively sharp because the screening is feedback-enhanced on the approach to the localized

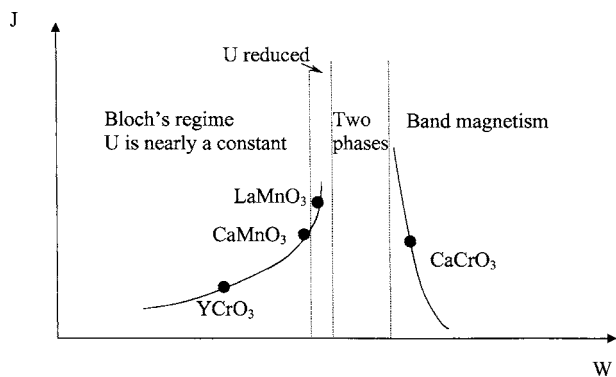


Fig. 23. Schematic energy diagram of the Heisenberg exchange energy J vs. bandwidth W at the crossover from localized-electron to band magnetism, after Zhou and Goodenough (2002a).

to itinerant electronic transition. Moreover, from the virial theorem of eq. (19), we can expect a double-well potential for the equilibrium M–O bondlength at crossover and therefore a first-order phase change with a spinodal phase segregation. In perovskite-related oxides, such spinodal phase segregations set in near room temperature, which is too low for atomic diffusion. Therefore, phase segregations on a small length scale are generated by atomic displacements that give rise to either static charge-density waves or to bond-length fluctuations and dynamic phase segregation. A $dT_N/dP < 0$ is predicted for band antiferromagnetism; it has been confirmed in CaCrO_3 (Goodenough et al., 1968). Therefore, we place the exchange interaction J for the (001) planes of LaMnO_3 at the approach to the crossover from localized-electron to band magnetism where U_σ is decreasing with pressure because of a feedback enhanced screening; the first-order phase change at $P \approx 7$ kbar suggests a spinodal phase segregation into localized-electron and itinerant-electron antiferromagnetism under pressures $P > 7$ kbar as indicated in the schematic J vs. W diagram of fig. 23.

3. Mixed-valent perovskites

3.1. Oxygen vacancies

CaMnO_3 catalyzes the selective oxidation of hydrocarbons by accepting electrons into the MnO_3 array during a dissociative chemisorption of the reactant and then releasing oxygen to the departing species. Each oxygen vacancy captures the two electrons it introduces on the two neighboring, fivefold-coordinated Mn(III) ions. The square-pyramidal configuration of the Mn(III) ions was first detected by Poeppelmeier et al. (1982a) in polycrystalline $\text{CaMnO}_{2.5}$ that was obtained (Poeppelmeier et al., 1982b) by reaction of CaMnO_3 in a 10% H_2/He atmosphere within the narrow temperature interval of 300–325 °C. Reller et al. (1984) subsequently demonstrated the existence of several vacancy-ordered intermediate phases in the interval $0 \leq \delta \leq 0.5$, all of which have the structural configuration of two square-pyramidal Mn(III) ions trapped at opposite sides of an oxygen vacancy. Wiebe et al. (2001) showed that $\text{CaMnO}_{2.94}$ retains the G-type antiferromagnetic order of CaMnO_3 below T_N with

$\mu_{\text{Mn}} = 2.43\mu_{\text{B}}$; the reduction of μ_{Mn} from the spin-only moment of $3.0\mu_{\text{B}}$ reflects the virtual electron transfers of the Mn–O–Mn superexchange interactions. Evidence of a vacancy-ordered phase coexisting with a G-type antiferromagnetic spin configuration was found in a $\text{CaMnO}_{2.89}$ sample; the Mn(III)–□–Mn(III) e^1 –□– e^1 superexchange interaction is antiferromagnetic, and the single Mn(III)–O–Mn(IV) e^1 –O– e^0 interaction on the opposite side does not provide a strong enough ferromagnetic coupling to overcome the six nearest-neighbor antiferromagnetic t^3 –O– t^3 interactions at the Mn(IV) ion.

3.2. $\text{Ca}_{1-x}\text{La}_x\text{MnO}_3$, $0 \leq x \leq 0.2$

Lanthanum substitution for Ca in $\text{Ca}_{1-x}\text{La}_x\text{MnO}_3$, $0 \leq x \leq 0.2$, has been used to introduce electrons into the MnO_3 array while keeping it intact. Each La^{3+} ion creates a shallow donor level below the Mn(IV)/Mn(III) redox level; at lowest temperatures, the electrons are trapped at one (or more) of the eight Mn nearest neighbors of a La^{3+} ion. Neumeier and Cohn (2000) have correlated the electronic resistivity $\rho(T)$ with $M_s(0)$, the saturation magnetization at $T = 0$ K (extrapolated from 5 K). They distinguished four compositional regions in the interval $0 \leq x \leq 0.2$. Region I ($0 < x < 0.02$) contains small-polaron Mn(III) ions that increase the saturation magnetization by $dM_s(0)/dx = 1.20 \pm 0.25\mu_{\text{B}}/\text{Mn}$. Region II ($0.02 < x \leq 0.07$) contains two-manganese (Zener) polarons and a $dM_s(0)/dx = 8.4 \pm 0.35\mu_{\text{B}}/\text{Mn}$. $M_s(0)$ reaches a maximum in the interval $0.07 < x < 0.08$, and Region III ($0.08 < x < 0.17$) shows a $dM_s(0)/dx \approx -4.5\mu_{\text{B}}/\text{Mn}$. Region IV ($0.18 \leq x \leq 0.20$) is a C-type (table 1) antiferromagnet with $M_s(0) = 0\mu_{\text{B}}/\text{Mn}$. At low temperatures ($50 \text{ K} < T < 150 \text{ K}$), the n -type resistivity $\rho(T) \sim \exp(-E_a/kT)$ had an $E_a \approx 85$ meV for $x = 0$, an $E_a \approx 30$ meV independent of x in the interval $0.005 \leq x \leq 0.10$, and an $E_a \approx 85$ to 95 meV for $0.12 \leq x \leq 0.20$. For $T > 200$ K, the $\rho(T)$ curves resembled those of a degenerate semiconductor with variable range hopping below a mobility edge.

Interpretation by Neumeier and Cohn (2000) of the changes in $M_s(0)$ with x was as follows: The small polarons are coupled antiparallel to their nearest neighbors, retaining the G-type antiferromagnetic order, but the e electrons are sufficiently mobile below T_{N} to move to the spin sublattice parallel to the magnetizing field. This model gives a weak ferrimagnetism with a $dM_s(0)/dx = 1\mu_{\text{B}}/\text{Mn}$. The e^1 –O– e^0 ferromagnetic interactions do not dominate the antiferromagnetic t^3 –O– t^3 interactions in this case. On the other hand, Zener polarons have fast ($\tau_{\text{h}} < \omega_{\text{o}}^{-1}$) e -electron transfer between the Mn(III) and Mn(IV) ions of the pair, which introduces two-manganese ferromagnetic clusters via intrapolaron double exchange. If all the electrons formed Zener polarons, $M_s(0)$ would vary with x as $dM_s(0)/dx \approx 7\mu_{\text{B}}/\text{Mn}$ for spin-only moments to give $M_s(0) = 0.5\mu_{\text{B}}/\text{Mn}$ at $x = 0.07$ instead of the observed $0.4\mu_{\text{B}}/\text{Mn}$. It follows that the electrons initially introduced ($0 < x \leq 0.02$) form small polarons; but as x increases, they are progressively transformed into Zener polarons. The activation energy for electron transport by a Zener polaron is smaller than that for a small polaron (0.30 meV vs. 0.85 meV). In the interval $0.08 < x < 0.17$, the electrons segregate into an electron-rich C-type antiferromagnetic phase with no Dzialoshinskii spin canting and an electron-poor phase dominated by small-polaron conduction. Trapping of the Zener polarons in the C-type antiferromagnetic phase causes the resistivity at 5 K, which is a minimum in the range

$0.07 \leq x \leq 0.1$, to increase by over five orders of magnitude as x increases in the range $0.10 < x \leq 0.20$. In the C-type antiferromagnetic order, ferromagnetic c -axis chains are coupled antiparallel to one another, and the e electrons occupy ($3z^2-r^2$) orbitals oriented along the c axis, which inhibits their mobility in 3D. The e electrons probably form a 1D charge-density wave propagating along the c -axis.

Granado et al. (2001) have reported an anomalous softening of the bending modes and hardening of the stretching mode of the oxygen vibrations on cooling through $T_N \approx 120$ K in CaMnO_3 and a complete suppression of the frequency shift on cooling through T_N after doping with only 3% La in $\text{La}_{0.03}\text{Ca}_{0.97}\text{MnO}_3$. The anomalous frequency shift was attributed to a spin-phonon coupling that is dramatically weakened by the introduction of Mn(III), but the origin of the spin-phonon coupling and its suppression were not identified. We attribute the frequency shift to the suppression of phonons in the paramagnetic phase and the appearance of phonons in the antiferromagnetically ordered phase. As discussed above, local exchange-strictive atomic displacements in the paramagnetic phase appear to be induced by the semi-covalent component of the superexchange interactions; random atomic displacements were seen to suppress the phonon contribution to the thermal conductivity, fig. 19. Below T_N , the phonon and/or magnon contributions to $\kappa(T)$ are restored. A similar phenomenon was found in LaMnO_3 . However, the system $\text{LaMn}_{1-x}\text{Ga}_x\text{O}_3$ shows a systematic decrease with x in the phonon contribution to $\kappa(T)$ below T_N , fig. 24, as a result of the bond-length fluctuations associated with orbital fluctuations at some of the Mn(III) ions. A similar phenomenon would occur in lightly doped $\text{Ca}_{1-x}\text{La}_x\text{MnO}_3$; the occupied e orbitals at the Mn(III) ions fluctuate for $x \leq 0.07$ so as to introduce bond-length fluctuations that suppress the formation of phonons below T_N and therefore any frequency shift of the oxygen vibrational modes due to phonon formation on cooling through T_N .

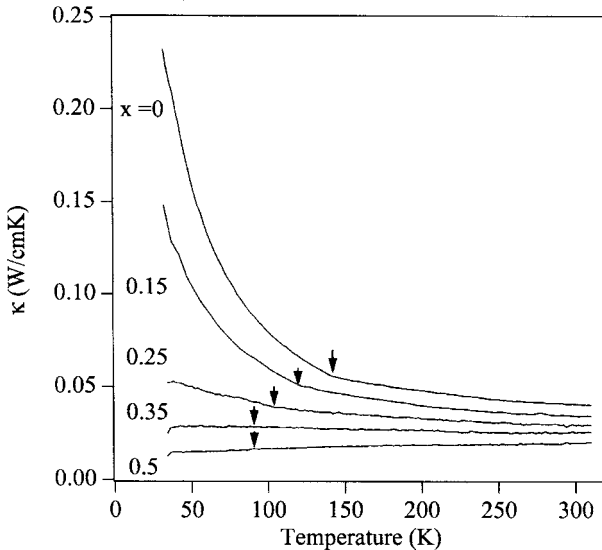


Fig. 24. Temperature dependence of the thermal conductivity κ for single-crystal samples of $\text{LaMn}_{1-x}\text{Ga}_x\text{O}_3$. The arrows mark T_N or T_f obtained from measurement of the magnetic susceptibility, after Zhou et al. (2001a).

Moritomo et al. (2001) have confirmed the drop in polaron activation energy with electron doping in the range $0 < x \leq 0.10$ and the existence of a remarkable increase with x in $M_s(0)$ in the range $0.05 < x < 0.08$; they also found the jump ΔC of the lambda anomaly in the specific heat at T_N was $\Delta C \approx 1.4k$ ($k =$ Boltzmann constant) in the range $0 \leq x \leq 0.03$ and increased linearly with x to $\Delta C \approx 2.3k$ in the range $0.04 \leq x \leq 0.08$. It thus appears that the ferrimagnetic order for small polarons gives an Ising behavior below T_N ($\Delta C = 1.5k$) whereas the spin glass regions associated with Zener polarons give a Heisenberg behavior below T_N ($\Delta C = 2.2k$).

A theoretical model (Chen and Allen, 2001) of the lightly electron-doped MnO_3 array of CaMnO_3 found bipolaron formation unstable, phase separation unlikely, small polarons trapped in seven-manganese clusters for $x < 0.045$, and a transition to metallic behavior at $x \approx 0.045$. The seven-manganese clusters consisted of a central Mn(III) ion and the six nearest-neighbor Mn(IV) with fluctuations of the occupied ($3z^2-r^2$) orbital on the Mn(III) ion between the three ($180^\circ - \phi$) O–Mn–O bond axes. Experimentally, the formation of Zener polarons having a small motional enthalpy develops in the interval $0.02 < x < 0.07$ in place of a global transition to itinerant-electron behavior at temperatures $T < 150$ K. Phase segregation in the interval $0.08 < x < 0.18$ appears to be a result of ordering of the axes of the Zener two-manganese polarons along the c -axis.

3.3. $\text{LaMnO}_{3+\delta}$

Early attempts to prepare the perovskite LaMnO_3 showed that it becomes oxidized on reaction in air. Although the oxidized compound is conveniently characterized as $\text{LaMnO}_{3+\delta}$, its structural formula is $\text{La}_{1-\zeta}\text{Mn}_{1-\varepsilon}\text{O}_3$ ($\zeta > \varepsilon$) since the perovskite structure does not accept interstitial oxygen and tolerates A-cation vacancies more readily than Mn-cation vacancies. Experimentally, the ratio $\text{O}/\text{Mn} = 3 + \delta$ is determined chemically, and the fraction of cation sites that are vacant to give 2δ Mn(IV) is $(\varepsilon + \zeta) \approx 2\delta/3$. Of interest is the evolution of physical properties across the transition from a spin-canted antiferromagnet with small-polaron charge carriers to a ferromagnetic metal via a mixed ferromagnet/antiferromagnet in the interval $0 \leq \delta \leq 0.21$, where $\delta = 0.21$ approaches the oxidation limit.

As shown in fig. 25, there is a first-order transition at room temperature from an O' -orthorhombic ($c/a < \sqrt{2}$) perovskite to a rhombohedral $R\bar{3}c$ perovskite across the interval $0.05 < \delta < 0.10$. The O' structure signals retention of cooperative Jahn–Teller Mn(III)-site distortions that order the occupied e orbitals into the (001) planes to give the canted-spin A-type antiferromagnetic order of the parent compound LaMnO_3 . With the antiferromagnetic component of the spins along the b -axis ($Pbnm$ axes) and a Dzialoshinskii vector along the a -axis, a weak ferromagnetic component is along the c -axis (see table 1). The introduction of Mn(IV) ions leaves unchanged the antiferromagnetic $t^3\text{--O--}t^3$ interactions between the ferromagnetic (001) planes. Within the (001) planes, Mn(IV) ions may create 2D orbital fluctuations and/or formation of two-manganese Zener polarons without disrupting the A-type antiferromagnetic order. On the other hand, rhombohedral symmetry does not remove the e -orbital degeneracy, and this structure is generally associated with itinerant e electrons and therefore with ferromagnetic metallic behavior via de Gennes double exchange. The coexistence of two electronic phases at the crossover from localized to itinerant electronic behavior

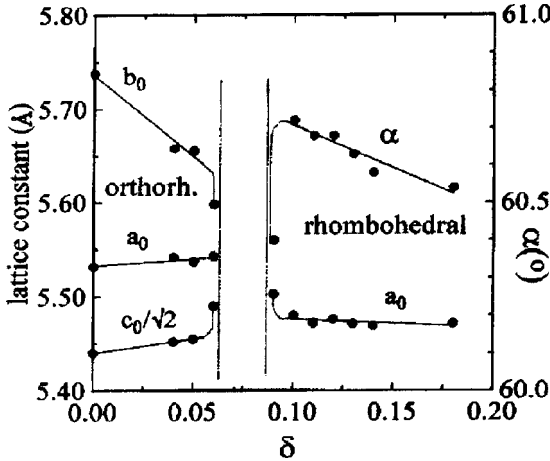


Fig. 25. Variation with δ of room-temperature lattice parameters of $\text{LaMnO}_{3+\delta}$, after Töpfer and Goodenough (1997b).

in the oxides with perovskite-related structures is a recurring theme. In order to investigate how the character of the mobile charge carriers and the magnetic order change on traversing the compositional range of the structural phase change, systematic transport and structural studies were made over the range $0.08 \leq \delta \leq 0.18$ (Töpfer et al., 1996; Töpfer and Goodenough, 1997b). The changes encountered in this system are to be compared with those found in the system $\text{La}_{1-x}\text{Sr}_x\text{MnO}_3$ in sect. 3.5.

At higher temperatures, 700–1000 K, a positive thermoelectric power $\alpha(T)$ is essentially temperature-independent and the evolution of its magnitude with δ is consistent with polaronic conduction described by the statistical component

$$\alpha = (k/e) \ln[\beta(1-c)/c], \quad (26)$$

where c is the fractional occupancy of the Mn atoms by mobile Mn(IV) with a spin-degeneracy factor $\beta = 2$. However, a $\beta = 1$ is to be expected because of the strong intraatomic exchange coupling between the mobile e electrons and the stationary t^3 configuration. On lowering the temperature in the paramagnetic range, the mobile holes condense progressively into clusters and $\alpha(T)$ increases as

$$\alpha(T) = (k/e)(E_g/kT) \quad (27)$$

where $E_g \approx 0.02$ eV is the enthalpy required to free a hole from a hole-rich second-phase cluster. However, $\alpha(T)$ reaches a maximum value at a T_{\max} near the magnetic-ordering temperature in samples with $0.12 \leq x \leq 0.18$; below T_{\max} , $\alpha(T)$ decreases nearly linearly with decreasing temperature, reaching zero at a T_α as is illustrated for $\delta = 0.16$ in fig. 26. The matrix is a ferromagnetic insulator (FI) below T_α where $\alpha \approx 0$ $\mu\text{V}/\text{K}$. The opening of a small energy gap at the Fermi energy in a nearly flat dispersion curve by charge and orbital ordering could give an $\alpha \approx 0$ $\mu\text{V}/\text{K}$ and insulator behavior. This FI phase is to be compared to that found below a $T_{\text{OO}} < T_C$ in the $\text{La}_{1-x}\text{Sr}_x\text{MnO}_3$ system over the range $0.10 < x < 0.17$. In

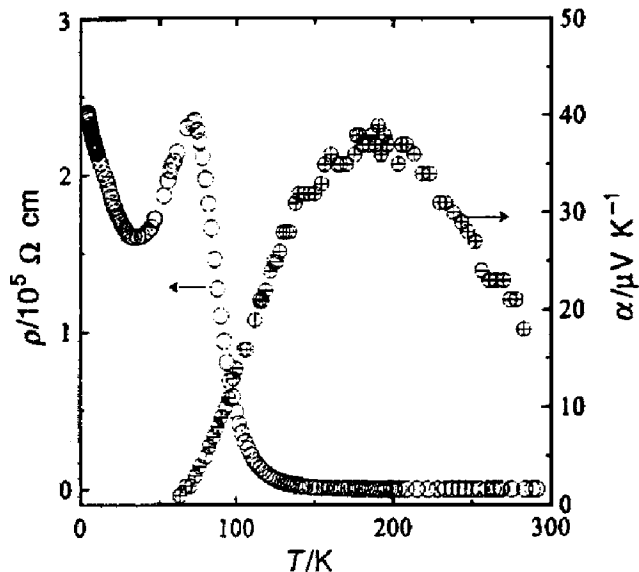


Fig. 26. Temperature variation of the resistivity $\rho(T)$ and thermoelectric power $\alpha(T)$ for $\text{LaMnO}_{3.16}$, after Töpfer et al. (1996).

that system, an orbitally fluctuating O^* -orthorhombic ferromagnetic vibronic (FV) phase appears in the interval $T_{OO} < T < T_C$ between the FI phase and a paramagnetic, polaronic O' phase in the interval $0.10 < x \leq 0.15$; the FV phase transforms abruptly to a ferromagnetic metallic (FM) phase in the interval $0.15 < x \leq 0.16$, see fig. 43. In the $\text{LaMnO}_{3+\delta}$ system, the FM phase is stabilized in the interval $0.18 < \delta < 0.20$. Therefore, we can expect a FV conductive phase to appear in the interval $T_\alpha < T < T_C$ of $\text{LaMnO}_{3+\delta}$, $0.10 < \delta < 0.18$.

The remarkable $\rho(T)$ behavior found in the interval $T_\alpha < T < T_C$ of fig. 26 may be an artifact of the polycrystalline samples reflecting changes in grain-boundary resistance with temperature in the interval $T_\alpha < T < T_C$. Support for this conclusion comes from hydrostatic-pressure measurements of Markovich et al. (2000, 2001). Their initial experiments on $\text{La}_{0.91}\text{Mn}_{0.95}\text{O}_3$ showed that the tolerance factor t increases with pressure; an unusually high compressibility of the mean Mn–O bond is characteristic of a double-well potential for the equilibrium bondlength. A subsequent study of $\rho(T)$ under pressure to 0.94 GPa was made on a $\text{La}_{0.94}\text{Mn}_{0.98}\text{O}_3$ single crystal. At ambient pressure, the single-crystal $\rho(T)$ curve showed a smooth insulator-metal transition on heating at a $T_{FI} = 115$ K and a metal-insulator transition at the Curie temperature $T_C = 210$ K. A minimum resistivity of about $2.53 \Omega \text{ cm}$ at T_{FI} shows the sample is a “bad metal” in the interval $T_{FI} < T < T_C$ typical of a FV percolating phase. Moreover, pressure stabilizes the FV phase relative to both the FI and paramagnetic polaronic phase; $dT_C/dP = 17 \text{ K/GPa}$ and a $dT_{FI}/dP < 0$ suppresses the FI phase by 0.94 GPa. The FI phase in $\text{La}_{1-x}\text{Sr}_x\text{MnO}_3$ is stabilized by pressure, which distinguishes the FI phase below T_{OO} in that system from the FI phase below T_α in $\text{LaMnO}_{3+\delta}$ where cation vacancies can be expected to trap out the holes they introduce. However, a simple trapping out of holes cannot account for the suppression of $\alpha(T)$ and ferromagnetic order.

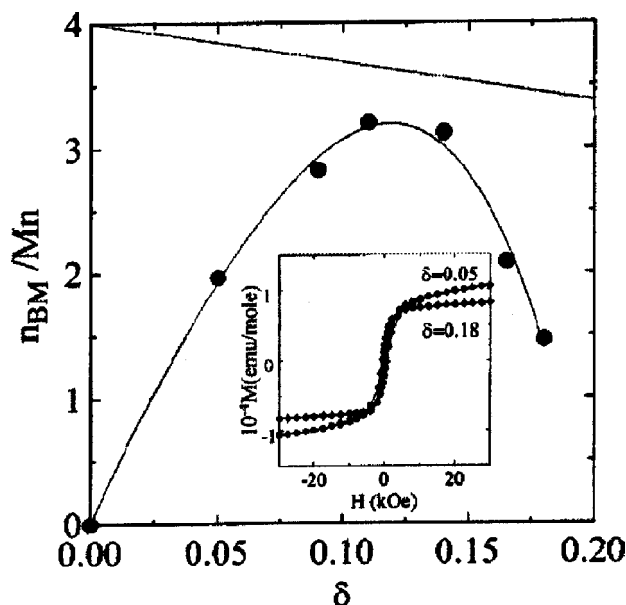


Fig. 27. Variation with δ of magnetization per Mn atom at 5 K in a field $H = 40$ kOe (30 kOe for $\delta = 0.18$). Insert: Magnetization vs. applied field H for $\delta = 0.05$ and $\delta = 0.18$ of $\text{LaMnO}_{3-\delta}$, after Töpfer and Goodenough (1997b).

Figure 27 shows the variation with δ of the magnetization M at 5 K in a field $H = 40$ kOe. M (5 K, 40 kOe) approaches the spin-only ferromagnetic value only for $0.12 \leq \delta \leq 0.14$. As δ increases, another hole-rich antiferromagnetic phase appears within the FV matrix to give a $dM/dT \approx 0$ at lower temperatures. The volume fraction of the antiferromagnetic clusters of the “cluster glass” increases with δ . A candidate for this hole-rich phase is the type-CE antiferromagnetic phase appearing at 50–50 Mn(III)–Mn(IV) in $\text{La}_{0.5}\text{Ca}_{0.5}\text{MnO}_3$ (see sect. 3.6). However, in the rhombohedral phase appearing with $\delta \geq 0.20$, the antiferromagnetic phase cannot compete with the FM phase having itinerant e electrons.

Allodi et al. (2001) found, by following the ^{139}La NMR signal of $\text{LaMnO}_{3+\delta}$ samples as a function of temperature, an inhomogeneous wipeout of the NMR signal in a broad temperature interval for all the lightly doped samples; in $\text{LaMnO}_{3.04}$ ($T_N = 125$ K) it occurred over the range $75 \text{ K} \leq T \leq 140 \text{ K}$. Comparison with muon-spin-rotation data ruled out the possibility that the wipeout is due to spin fluctuations, which means it is due to electric-field-gradient fluctuations associated with orbital and/or bond-length fluctuations. These data reveal fast nuclear relaxations in a volume fraction of vibronic charge transfer and “bad-metal” behavior. This wipeout phenomenon was not observed in either the parent compound LaMnO_3 or in a hole-rich R-rhombohedral matrix; it is associated with phase segregation at the crossover from localized to vibronic behavior of the e electrons. At lower temperatures, the NMR signal was restored, indicating the charge carriers had become static in the time scale $\tau < 10^{-9}$ s as a result of orbital ordering in the FI phase.

The Weiss constant θ of the Curie–Weiss paramagnetic susceptibility plot $\chi^{-1}(T)$ reflects the mean magnitude of the interatomic exchange interactions. LaMnO_3 has a $\theta > 0$, which reveals that the ferromagnetic interactions in the (001) planes are stronger than the c -axis

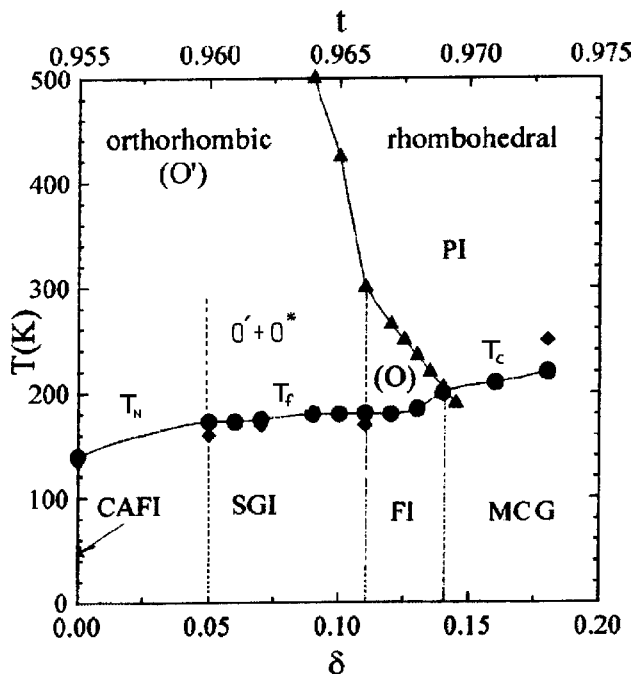


Fig. 28. Tentative phase diagram for $\text{LaMnO}_{3+\delta}$, $0 \leq \delta \leq 0.18$. Data from Töpfer and Goodenough (1997b). PI = paramagnetic insulator, CAFE = canted-spin antiferromagnetic (A-type) insulator, SGI = spin-glass insulator, FI = ferromagnetic insulator, MCS = metamagnetic canted-spin configuration.

antiferromagnetic interaction; but a $\theta < T_N$ signals that the ferromagnetic planes couple antiferromagnetically. As δ increases, the interval $T_N - \theta$ decreases in the range $0 < \delta \leq 0.05$. For the spin-glass ferromagnetic phases $0.08 \leq \delta \leq 0.16$, we find $\theta > T_C$ with $\theta - T_C$ increasing dramatically with δ . In the paramagnetic phase, the strength and fraction of ferromagnetic interactions clearly increases with δ , and a large $\theta - T_C$ signals the presence of considerable short-range ferromagnetic order above T_C . Moreover, a slow rise of $M(T)$ on cooling through T_C indicates the persistence of a paramagnetic volume below T_C (Töpfer et al., 1996). It is clear that the compounds are magnetically inhomogeneous, which is another reflection of the segregation of orbitally disordered and orbitally ordered volumes.

In the O' -orthorhombic $\delta = 0.05$ sample, the magnetization $M(T)$ taken on heating after cooling in zero applied field showed a typical spin-glass behavior (Töpfer and Goodenough, 1997b) indicating the presence of ferromagnetic clusters with a $T_C > T_N$ in the antiferromagnetic matrix. In this insulator, the ferromagnetic coupling would be due to vibronic superexchange in regions of orbital fluctuations.

These considerations lead us to propose the tentative phase diagram of fig. 28. The orthorhombic-rhombohedral transition has been tracked by Wold and Arnett (1959). The two-phase region $0.05 < \delta < 0.10$ observed by room-temperature X-ray diffraction has been shown from the spin-glass behavior below T_f to extend over a wider compositional range below 200 K, which indicates that a spinodal phase segregation separates the O' -orthorhombic ($c/a < \sqrt{2}$) from an O^* -orthorhombic ($c/a \approx \sqrt{2}$) or R-rhombohedral phase. With neutron powder diffraction, Huang et al. (1997) have shown the two-phase region at 300 K in the inter-

val $0.05 < \delta \leq 0.10$ consists of an antiferromagnetic O' phase and a ferromagnetic O^* phase of smaller volume. At a higher value of δ , an R-rhombohedral phase transforms smoothly to a ferromagnetic monoclinic ($P112_1/a$) phase that corresponds to the ferromagnetic cluster glass. At lower temperatures, the transition temperature separating the orbitally fluctuating O^* phase from the R phase extends to a higher value of δ than the transition between the O' and R phases; percolation of the O^* and not the O' phase gives a ferromagnetic matrix that transforms to a ferromagnetic-insulator (FI) phase below T_C in the interval $0.11 < \delta < 0.14$ whereas the spin-glass-insulator (SGI) phase is found for $\delta \leq 0.11$ where the percolating matrix is the O' phase. The O^* -R transition was not tracked below T_C of the metamagnetic "cluster glass" (MCG) appearing in the interval $0.15 \leq x \leq 0.18$.

3.4. $(La_{1-y}R_y)_{0.7}A_{0.3}MnO_3$: The CMR phenomenon

The perovskite systems $R_{1-x}A_xMnO_3$ ($A =$ alkaline-earth) have been studied both extensively and intensively because they exhibit an intrinsic "colossal negative magnetoresistance", known as the CMR phenomenon, at and above a ferromagnetic Curie temperature T_C on application of a high magnetic field (Kusters et al., 1989; von Helmolt et al., 1993; Chahara et al., 1993). They also exhibit below T_C an extrinsic giant magnetoresistance associated with tunneling of electron spins across grain boundaries; the MnO_3 array has only majority-spin conduction electrons in the ferromagnetic state. Here we discuss the intrinsic CMR phenomenon.

In the systems $(La_{1-y}R_y)_{0.7}A_{0.3}MnO_3$, the ratio $Mn(IV)/Mn = 0.3$ is held constant and, by decreasing the tolerance factor t of eq. (1) by decreasing the mean ionic radius of the large A-site cations of the perovskite structure, the MnO_3 array is changed from a ferromagnetic metal with itinerant σ^* electrons of e-orbital parentage in $La_{0.7}Sr_{0.3}MnO_3$ to an antiferromagnetic insulator in $Pr_{0.7}Ca_{0.3}MnO_3$, which has localized e electrons in ordered orbitals and charge ordering of the holes. In all these perovskites, the π -bonding t^3 configuration on the Mn atoms is localized with a spin $S = 3/2$, and dramatic changes in physical properties are found at the crossover from localized to itinerant behavior of the σ -bonding electrons of e orbital parentage. In accordance with the virial theorem of eq. (19), the crossover compositions exhibit a dynamic spinodal phase segregation by cooperative oxygen displacements on a small length scale into either hole-rich itinerant-electron and hole-poor localized-electron regions or into regions of e-orbital and charge disorder and those of e-orbital and charge order. The itinerant-electron and/or orbitally disordered regions are ferromagnetic and conductive; the orbitally ordered, localized-electron regions are poor electronic conductors, especially where they contain ordering of the mobile holes. The ferromagnetic, conductive phase may be stabilized relative to the antiferromagnetic localized-electron phase by various externally applied forces.

The CMR phenomenon is illustrated in fig. 29, which is taken from Hwang et al. (1995) for the system $La_{0.7-x}Pr_xCa_{0.3}MnO_3$ (note: $x = 0.7y$ of $(La_{1-y}R_y)_{0.7}A_{0.3}MnO_3$). The Curie temperatures T_C are marked by arrows. The magnetoresistance between 0 and 5 Tesla, defined here as $(\rho_{0T} - \rho_{5T})/\rho_{5T}$, increases and T_C decreases, both dramatically, as x increases in the range $0 \leq x \leq 0.6$ even though the variation in tolerance factor is small. Moreover,

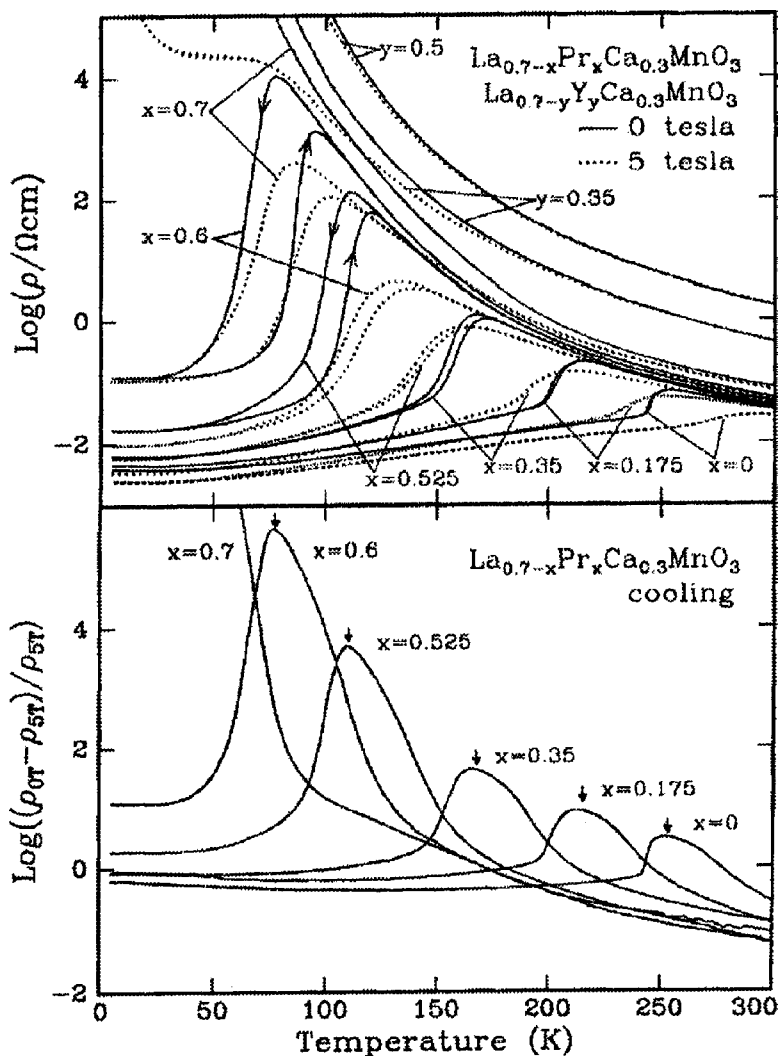


Fig. 29. CMR at 5 T on cooling for different compositions $0 \leq x \leq 0.7$ in the system $\text{La}_{0.7-x}\text{Pr}_x\text{Ca}_{0.3}\text{MnO}_3$. Arrows indicate the Curie temperatures T_C ; after Hwang et al. (1995).

the magnetic transition at T_C is first-order, but the resistance decreases smoothly with temperature on cooling through T_C although exhibiting a thermal hysteresis. The $x = 0.7$ end member $\text{Pr}_{0.7}\text{Ca}_{0.3}\text{MnO}_3$ exhibits an even more complex behavior (Roy et al., 2000; Jirák et al., 1985; Yoshizawa et al., 1995, 1996; Tomioka et al., 1995, 1996; Anane et al., 1999; Lees et al., 1996; Miyano et al., 1997; Fiebig et al., 1998, 1999; Ogawa et al., 1998; Cox et al., 1998; Moritomo et al., 1997a; Kiryukin et al., 1997; Asamitsu et al., 1997; Srivastava et

al., 2000; Stankiewicz et al., 2000); it undergoes, on cooling, a charge-ordering transition at $T_{CO} \approx 230$ K followed by antiferromagnetic order below $T_N \approx 150$ K that develops at lower temperatures a canted-spin ferromagnetic component. The insulating antiferromagnetic state can be driven irreversibly to a ferromagnetic conductive state with a large release of heat not only by an applied magnetic field, but also by the application of pressure, by the irradiation with visible light or X-rays, or by a high current. The complexity is characteristic of antiferromagnetic compositions having a tolerance factor t at the transition from antiferromagnetic to ferromagnetic behavior below their magnetic-ordering temperature. The resistive transition occurs where the localized-electron phase forms a percolating matrix within which the ferromagnetic regions are isolated in the absence of an external input. With the application of the external input, the ferromagnetic regions grow at the expense of the antiferromagnetic volume. The situation is analogous to that found in $\text{LaMn}_{0.5}\text{Ga}_{0.5}\text{O}_3$, fig. 13, except that here the ferromagnetic phase is mixed-valent and conductive.

The tight-binding bandwidth $W_\sigma = 2zt_\sigma^\uparrow$ for the σ^* electrons of a single-phase MnO_3 array with $z = 6$ like nearest neighbors is, from eqs. (7) and (8),

$$W_\sigma \approx 12\varepsilon_\sigma \lambda_\sigma^2 \langle \cos \phi \rangle \cos(\theta_{ij}/2). \quad (28)$$

The small changes in W_σ that result from increasing the bending ϕ of the $(180^\circ - \phi)$ Mn–O–Mn bonds on substitution of Pr^{3+} for La^{3+} cannot account for the dramatic change in T_C , from 250 K for $x = 0$ to 80 K for $x = 0.6$, or for that in the magnitude of the CMR phenomenon shown in fig. 29 even though the increase in $\langle \cos \phi \rangle$ is enhanced by a transition from a larger equilibrium $(\text{Mn–O})_{\text{localized}}$ to a smaller $(\text{Mn–O})_{\text{itinerant}}$ bond length, eq. (20). However, the bandwidth of eq. (21)

$$W = W_\sigma \exp(-\lambda \varepsilon_{sc}/\hbar\omega_0) \quad \text{with } \lambda \sim \varepsilon_s/W_\sigma \quad (29)$$

is applicable where a dynamic spinodal phase segregation occurs; ε_{sc} is the energy required to transfer a hole from the hole-rich ferromagnetic phase to the hole-poor matrix and ω_0 is the frequency of the cooperative oxygen vibrations that separate the two phases. With eq. (29), we can attribute the change in physical properties with tolerance factor t , or bending angle ϕ , to changes in ω_0 with ϕ as well as to changes in the mean equilibrium (Mn–O) bond length. Egami and Louca (1999, 2002) have emphasized that there are two vibrational modes of the oxygen atoms that might impact the Mn–O bond length where the $(180^\circ - \phi)$ Mn–O–Mn bond is bent from 180° : one is the breathing mode in which an oxygen atom moves close to one Mn nearest neighbor and away from the other; the second is a vibration perpendicular to the bond in which the two neighboring Mn atoms are impacted equally. A breathing mode would occur at the interface between localized and itinerant phases; displacements perpendicular to a bond would occur within phases.

Spinodal phase segregation and vibronic conduction occur where the time for a hole to travel from one Mn atom to another is $\tau_h \approx \hbar/W \approx \omega_0^{-1}$, or $W \approx \hbar\omega_0$. Small changes in ω_0 with bending angle ϕ can change a $W < \hbar\omega_0$ where conduction is polaronic into a $W > \hbar\omega_0$ where the electrons become itinerant. A de Gennes double exchange associated with itinerant σ^* electrons would give a much higher T_C than a vibronic superexchange augmented by a Zener double exchange, and T_C increases dramatically where the volume fraction of itinerant

electrons increases just below T_C . Moreover, the first-order character of the transition at T_C signals a discontinuous change in the volume fraction of the itinerant-electron phase, but the heterogeneous character of the material makes the resistivity change smoothly on cooling through T_C . As the tolerance factor t decreases with increasing x , the volume fraction of the itinerant-electron phase above T_C decreases and, therefore, the discontinuity in the volume fraction on cooling through T_C increases. Therefore, the latent heat of the transition at T_C increases with x in $\text{La}_{0.7-x}\text{Pr}_x\text{Ca}_{0.3}\text{MnO}_3$.

With decreasing temperature in the paramagnetic state, polaronic holes progressively condense out below a critical temperature into an itinerant-electron phase. The hole-rich regions have a higher Curie temperature T_C^* than the T_C of the hole-poor matrix; the ferromagnetic spin–spin coupling of the matrix is progressively reduced as it becomes increasingly due to vibronic superexchange and the double-exchange component is reduced by trapping out of the mobile holes into the hole-rich clusters (Goodenough, 1997). The hole-rich clusters, on the other hand, may achieve a de Gennes double-exchange coupling that gives the higher T_C^* . As the bandwidth W decreases with increasing x , the double-exchange component of the coupling in the matrix decreases, so T_C decreases. However, as T_C decreases, more holes are trapped out in the hole-rich clusters in the paramagnetic phase, which feeds back to lower T_C even more. Therefore T_C decreases dramatically with increasing x , but not T_C^* . On application of a magnetic field in the interval $T_C < T < T_C^*$, the ferromagnetic phase is stabilized relative to the paramagnetic phase, and growth of the conductive ferromagnetic clusters to beyond percolation gives the CMR phenomenon. Although, the increase in the volume of the ferromagnetic phase in an applied magnetic field dilutes its hole concentration, orbital disorder introduces ferromagnetic vibronic superexchange interactions. Nevertheless, the hole concentration must remain consistent with itinerant-electron or vibronic conduction in the hole-rich phase. As the temperature decreases, more holes are trapped out into the hole-rich conductive phase and the volume fraction of this phase can grow larger in an applied field of 5 T, which decreases ρ_{5T} at T_C . Moreover, with fewer holes in the matrix, the resistivity ρ_{0T} increases with decreasing temperature. Therefore, the magnetoresistance $(\rho_{0T} - \rho_{5T})/\rho_{5T}$ at T_C increases remarkably as T_C decreases with increasing x .

The growth of a conventional magnetic polaron in a magnetic field also leads to a negative magnetoresistance having a maximum value at T_C , and serious claims have been made (Nagaev, 1999, 2001a; Emin, 1998) that his model is applicable to the CMR phenomenon in the manganese oxides. In this model also, mobile charge carriers achieve a greater stability and mobility by congregating in regions of ferromagnetic order. The analogy is, therefore, quite complete without requiring the strong electron-lattice coupling implicit in a double-well potential at the crossover from localized to itinerant electronic behavior; it relies instead on the electron-spin interactions alone. However, the sensitivity of T_C to the tolerance factor and the data to be presented argue for a model in which the electron-spin interactions are supplemented by strong electron–phonon interactions due to a double-well potential at the crossover from localized to itinerant electronic behavior. On the other hand, phase segregation into hole-rich and hole-poor regions needs to be supplemented in the manganese-oxide perovskites by consideration of the Jahn–Teller site deformations that occur at localized-electron $\text{Mn(III)}: t^3e^1$ configurations. It is the dynamic Jahn–Teller orbital fluctuations that give rise

to the ferromagnetic vibronic-superexchange interactions in the hole-poor matrix. Where the cooperative deformations become long-range statically ordered, anisotropic antiferromagnetic interactions are introduced as in LaMnO_3 . This type of order occurs within a percolating matrix where the tolerance factor is lower than a critical value t_c . Moreover, an applied magnetic field can stabilize an orbitally disordered ferromagnetic phase relative to an orbitally ordered antiferromagnetic phase as was seen to be the case in the single-valent compound $\text{LaMn}_{0.5}\text{Ga}_{0.5}\text{O}_3$, fig. 13. An antiferromagnetic to ferromagnetic transition can also be induced by a pressure that increases a $t < t_c$ to a $t > t_c$ or by a $^{16}\text{O}/^{18}\text{O}$ isotope exchange that changes t_c , as is shown below for the system $(\text{La}_{1-y}\text{Nd}_y)_{0.7}\text{Ca}_{0.3}\text{MnO}_3$. In a mixed-valent system, stabilization of a ferromagnetic phase containing orbital and charge disorder relative to an antiferromagnetic phase having ordered orbitals and charge can also be accomplished by the application of an electric field or by electromagnetic irradiation that disorders the charge and the occupied e orbitals. All these features are illustrated by $\text{Pr}_{0.7}\text{Ca}_{0.3}\text{MnO}_3$.

The Nd^{3+} ion is smaller than Pr^{3+} , so the critical tolerance factor t_c for $(\text{La}_{1-y}\text{Nd}_y)_{0.7}\text{Ca}_{0.3}\text{MnO}_3$ occurs at a $y < 0.6$ rather than at a $y \geq 0.9$ as in $(\text{La}_{1-y}\text{Pr}_y)_{0.7}\text{Ca}_{0.3}\text{MnO}_3$. Figure 30 shows (Archibald et al., 1996) the temperature dependence of the thermoelectric power $\alpha(T)$ for several compositions in the range $0.2 \leq y \leq 0.75$. At atmospheric pressure, the $0.55 < y \leq 1$ samples with $0.946 \leq t \leq 0.952$ are in the O' -orthorhombic ($c/a < \sqrt{2}$) phase and undergo a second-order polaronic-polaronic transition at a Néel temperature T_N to a weakly canted antiferromagnetic spin configuration as occurs in PrMnO_3 . However, a charge-ordering temperature was not noted. The $0 \leq y \leq 0.55$ samples are in the pseudocubic O^* -orthorhombic ($c/a \approx \sqrt{2}$) phase and undergo a first-order phase change at a ferromagnetic Curie temperature T_C , from which we deduce a critical tolerance factor $t_c \approx 0.955$. The temperature dependence of the resistivity $\rho(T)$ exhibits a strong maximum at T_C in the O^* phase as in $\text{La}_{0.7-x}\text{Pr}_x\text{Ca}_{0.3}\text{MnO}_3$ with $x \leq 0.6$, fig. 29; $\rho(T)$ continues to increase with decreasing temperature below T_N in the O' phase, and it was not possible to obtain a stable measure of $\alpha(T)$ below T_N in this phase. The maximum in $\alpha(T)$ occurs at a T_{max} a little above T_C in the O^* phase. Five other features of fig. 30 are noteworthy.

First, $\alpha(T)$ approaches a temperature-independent value of $-20 \mu\text{V}/\text{K}$ in the O^* samples at high temperatures; this value is somewhat larger in the O' sample, fig. 31. A temperature-independent α is indicative of polaronic conduction in which the statistical term, eq. (26), dominates any transport contribution. In eq. (26), the spin-degeneracy factor is $\beta = 1$ because of the strong intraatomic exchange at the Mn atoms; c is the fraction of available sites that are occupied by charge carriers. For small polarons, $c = xN/N = x$ would give a value $\alpha = +38 \mu\text{V}/\text{K}$ whereas a two-Mn Zener polaron would correspond to $c = xN/(N/2) = 2x$ to give the observed $\alpha = -20 \mu\text{V}/\text{K}$. Therefore, we conclude that at high temperatures there is a progressive transition with increasing tolerance factor from small polarons to two-Mn polarons as t increases, complete conversion occurring for $t > 0.995$. At still higher values of t , a transition from two-Mn polarons to itinerant electrons can be anticipated. Indeed, in $\text{La}_{0.7}(\text{Ca}_{1-y}\text{Sr}_y)_{0.3}\text{MnO}_3$ the transition at T_C changes from first-order to second-order with increasing y , fig. 32, and both T_C and dT_C/dy change discontinuously at the crossover of T_C and the orthorhombic-rhombohedral transition temperature T_{OR} , fig. 33; the electrons become itinerant in the paramagnetic state of $\text{La}_{0.7}\text{Sr}_{0.3}\text{MnO}_3$ (Tomioka et al., 2001) and

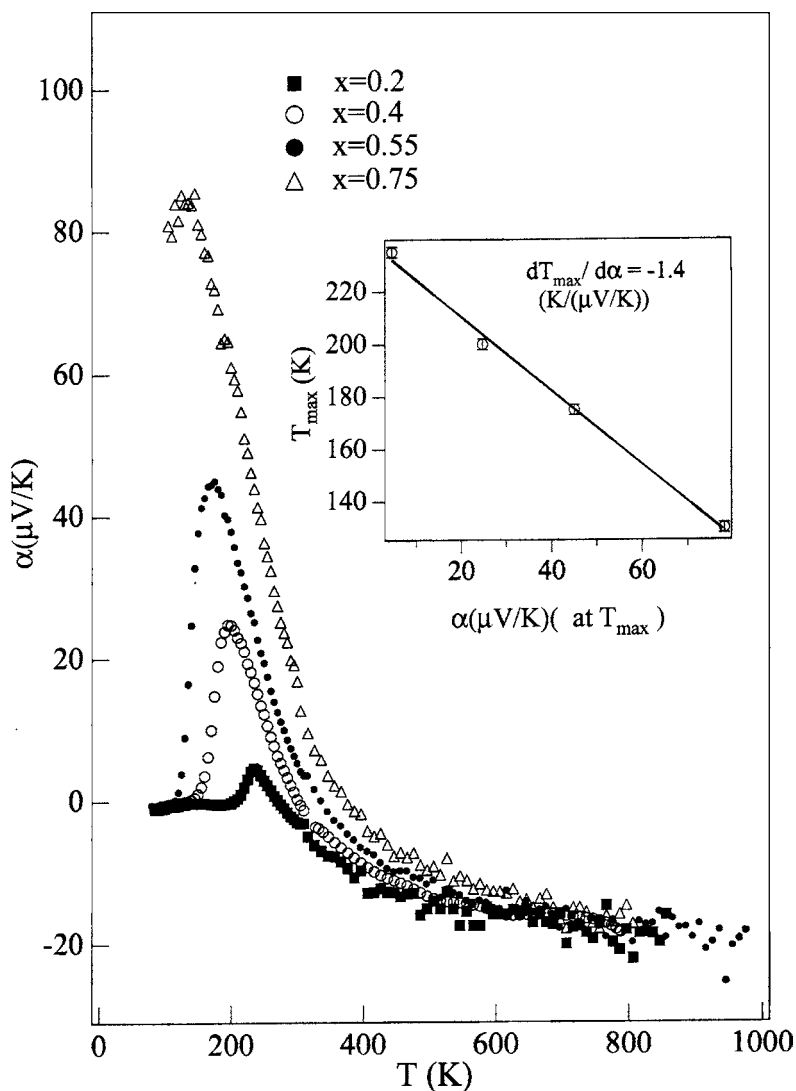


Fig. 30. Thermoelectric power $\alpha(T)$ for several compositions $0.20 \leq y \leq 0.75$ of the system $(\text{La}_{1-y}\text{Nd}_y)_{0.7}\text{Ca}_{0.3}\text{MnO}_3$; after Archibald et al. (1996).

$\text{La}_{2/3}\text{Sr}_{1/3}\text{MnO}_3$ (Mira et al., 1999, 2000) as well as in $\text{La}_{0.65}\text{Ba}_{0.35}\text{MnO}_3$, which has the highest tolerance factor t (McIlroy et al., 1996). Confirmation of two-Mn polarons was found in the $\text{La}_{1-x}\text{Ca}_x\text{MnO}_3$ system by Mössbauer spectroscopy for $x = 0.20$ (Chechersky et al., 1997, 1999a) and by Mn K-edge X-ray extended fine structure (EXAFS) for $x = 0.25$ (Lanzara et al., 1998).

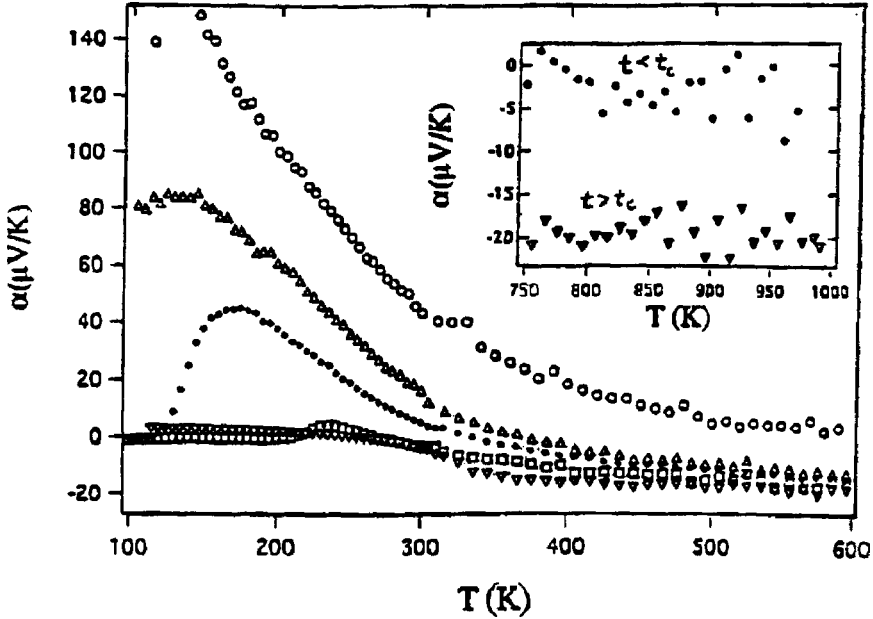


Fig. 31. High-temperature thermoelectric power $\alpha(T)$ for $y = 0.75$ ($t = 0.952 < t_c$) and $y \leq 0.55$ ($t \geq 0.957 > t_c$) of the system $(\text{La}_{1-y}\text{Nd}_y)_{0.7}\text{Ca}_{0.3}\text{MnO}_3$, after Goodenough (1999).

Second, the sharp increase in $\alpha(T)$ as T decreases to T_{\max} reflects a progressive condensation of the mobile holes into a hole-rich phase; shortening of the equilibrium Mn–O bond length in the hole-rich clusters transforms the $\tau_h > \omega_0^{-1}$ of the polaronic matrix to $\tau_h \leq \omega_0^{-1}$ of the hole-rich conductive clusters. The volume of the hole-rich phase increases with the number of holes that are trapped in it. The hole-rich clusters become superparamagnetic below a $T_C^* > T_C$. On cooling through T_C , the Weiss molecular field increases the volume fraction of the conductive phase to well beyond percolation, releasing the trapped holes and lowering $\alpha(T)$. Independent evidence for superparamagnetic clusters in the interval $T_C < T < T_C^*$ appears in the inverse magnetic susceptibility χ^{-1} vs. temperature (Goodenough and Zhou, 1998) shown in fig. 34. The huge difference $\theta - T_C$, where θ is the high-temperature Weiss constant, reveals an anomalously extensive range of short-range ferromagnetic order above T_C . Further evidence for phase segregation above and below T_C has been obtained with a variety of other techniques in addition to Mössbauer (Chechersky et al., 1997, 1999a) and it has been possible to describe the structure of the low-energy optical conductivity with a two-phase model (Quijada et al., 1998). Kim et al. (1998) came to a similar conclusion from their optical-conductivity data, and Y.G. Zhao et al. (1998) used pulsed laser excitation to reveal a fast transient associated with photoionization of the polaronic phase and a slow transient associated with the hole-rich clusters in $\text{La}_{0.7}\text{Ca}_{0.3}\text{MnO}_3$. Sakaie et al. (1999) have confirmed with ^{139}La NMR a slow correlation time for the spin–spin fluctuations

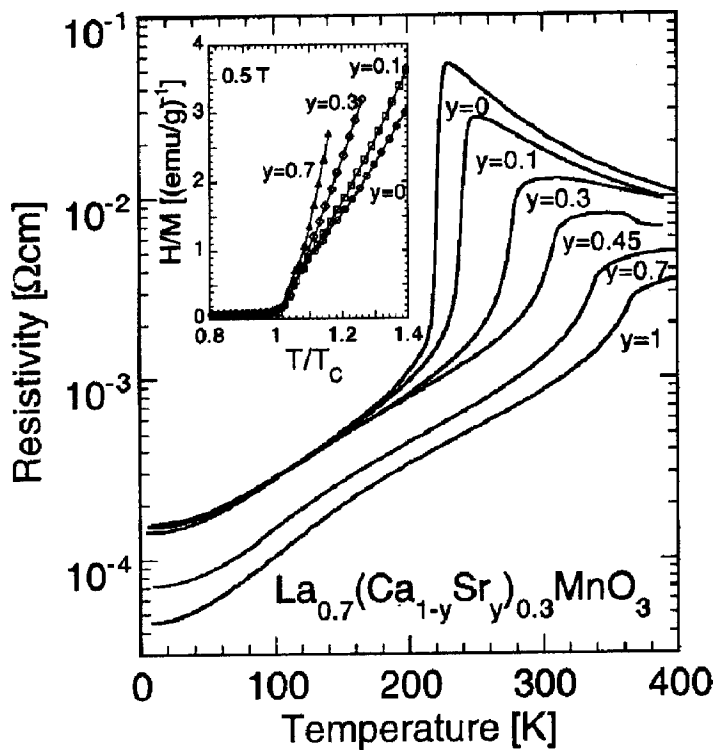


Fig. 32. The resistivity vs. temperature for $\text{La}_{0.7}(\text{Ca}_{1-y}\text{Sr}_y)_{0.3}\text{MnO}_3$ crystals with varying y . The anomaly at ca. 370 K for $y = 0.45$ is due to the orthorhombic-rhombohedral transition. Inset shows inverse susceptibility vs. T/T_C , after Tomioka et al. (2001).

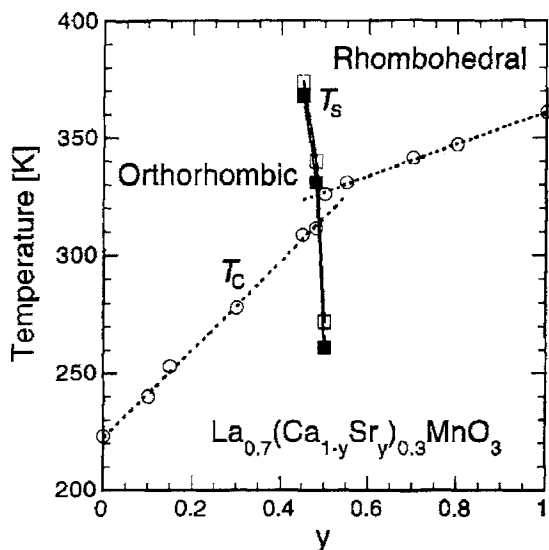


Fig. 33. Phase diagram for $\text{La}_{0.7}(\text{Ca}_{1-y}\text{Sr}_y)_{0.3}\text{MnO}_3$, after Tomioka et al. (2001).

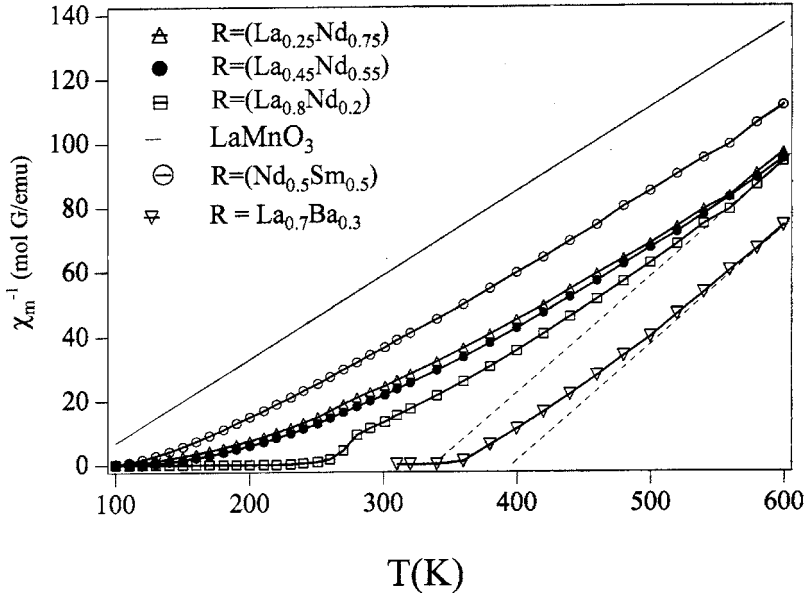


Fig. 34. Inverse magnetic susceptibility vs. absolute temperature for several samples $R_{0.7}Ca_{0.3}MnO_3$ compared with $LaMnO_3$ and $La_{0.7}Ba_{0.3}MnO_3$, after Goodenough and Zhou (1998).

of the ferromagnetic clusters and reported an anomalous temperature and field dependence of the spin-lattice relaxation. Lu et al. (1997) and Fäth et al. (1999) have used tunneling scanning spectroscopy on, respectively, $x = 0.35$ and $x = 0.30$ of $La_{1-x}Ca_xMnO_3$ films deposited epitaxially on a single crystal $SrTiO_3$ substrate to observe directly the coexistence of the ferromagnetic phase and a polaronic phase both above and below T_C and how the spatial extent of the ferromagnetic phase increases to beyond a percolation threshold on decreasing the temperature through T_C or on applying a magnetic field above T_C .

The CMR phenomenon occurs where the conductive ferromagnetic phase reaches a percolation threshold in the paramagnetic phase (Goodenough and Zhou, 1997). De Teresa et al. (1997) with neutron scattering. Chun et al. (2000) have measured the Hall constant and Hall mobility of single-crystal $La_{0.7}Ca_{0.3}MnO_3$ ($T_C = 216.2$ K) to demonstrate a transition from a low-temperature, ferromagnetic phase to a high-temperature polaronic phase in the interval $T_C < T < 1.4T_C$ where ferromagnetic, metallic clusters coexist with the polaronic paramagnetic phase. Chechersky et al. (2000) have used ^{57}Co Mössbauer spectroscopy to identify the coexistence of two distinguishable ferromagnetic phases below T_C in a well-characterized, homogeneous ceramic sample of $La_{0.7}Ca_{0.3}Mn(^{57}Co)O_3$ ($T_C = 245$ K); the volume fraction of the minority phase decreases with decreasing temperature, and they observed a single ferromagnetic phase at lowest temperatures. Neutron-scattering data are consistent with this finding (Adams et al., 2000). Heffner et al. (2000) have used muon spin relaxation and neutron spin-echo measurements in ferromagnetic $La_{1-x}Ca_xMnO_3$ with $x = 0.33$ ($T_C = 262$ K)

and $x = 0.30$ ($T_C = 250$ K), respectively, to identify two phases below T_C that are distinguished by very different spin dynamics. The metallic matrix displayed diffusive relaxation with a diffusion coefficient correlating with that of Mn spin waves obtained (Lynn et al., 1996; Vasiliu-Doloc et al., 1997) from neutron-scattering studies of the metallic ferromagnetic phase. The second phase, which was confined to spatially separated clusters ≤ 30 Å in diameter, possessed more slowly fluctuating spins and a linewidth independent of the muon wave number q , which signals a more insulating phase. We identify the former with the hole-rich phase, the latter with the hole-poor phase. As the temperature decreased below T_C , the matrix grew at the expense of the minority, slow-relaxation phase. X.J. Liu et al. (2001a) have observed photoinduced changes in transmission through $\text{La}_{0.7}\text{Ca}_{0.3}\text{MnO}_3$ ($T_C = 200$ K) films probed with a continuous wave (CW) Ar^+ laser ($E_{\text{probe}} = 2.54$ eV) and a CW $\text{Ti:Al}_2\text{O}_3$ laser ($E_{\text{probe}} = 1.55$ eV). The data showed a photoinduced creation of clusters at temperatures $T < T_C$ and a photoinduced annihilation of clusters at $T > T_C$. X.J. Liu et al. (2001a) interpreted this finding to be the creation of charge-ordered clusters ($T < T_C$) or annihilation of metallic clusters ($T > T_C$) since the matrix changes from polaronic to itinerant/vibronic on cooling through T_C . It is unlikely that electron excitations would create a charge-ordered phase. Therefore, we suggest that the light perturbs the periodic potential of the itinerant-electron phase by exciting electrons from narrow σ^* -band states to localized energy levels such as that of a Mn(II) ion, thereby favoring the polaronic over the itinerant-electron phase. This interpretation is supported by a similar experiment made on a $\text{La}_{0.7}\text{Sr}_{0.3}\text{MnO}_3$ film ($T_C = 350$ K) at temperatures $T < T_C$, which showed the creation of polaronic clusters from the itinerant-electron matrix (X.J. Liu et al., 2001b, 2001c).

The third feature of fig. 30 to be noted is the maximum in $\alpha(T)$ found at a T_{max} a little above T_C ; it increases dramatically as the tolerance factor t is lowered to the $O'-O^*$ phase boundary appearing in the interval $0.952 < t < 0.957$ because the concentration of mobile holes in the matrix decreases with T . Comparison of fig. 30 and fig. 35 shows a pressure dependence $dt/dP > 0$, which is the anomalous case of eq. (3b), indicating the presence of a double-well potential for the equilibrium (Mn–O) bond length in accordance with eq. (20) for the crossover from localized to itinerant behavior of antibonding electrons. The large compressibility of the (Mn–O) bond length in the two-phase domain has been corroborated by several experiments. Radaelli et al. (1997a) have used high-resolution neutron diffraction to show for $\text{La}_{0.75}\text{Ca}_{0.25}\text{MnO}_3$ an anomalous decrease in the volume on cooling through T_C where the fraction of the ferromagnetic itinerant-electron phase increases sharply. The decrease in mean cell volume occurred despite an increase in the $(180^\circ - \phi)$ Mn–O–Mn bond angle because a significant decrease in the (Mn–O) bond length overcompensated for the increase in bond angle. De Teresa et al. (1996a) measured the magnetoresistance (MR) and the magnetothermal expansion (ME) for $\text{La}_{2/3}\text{Ca}_{1/3}\text{MnO}_3$ and found a strong correlation between the two in the paramagnetic phase just above T_C . They concluded that the increase in the volume fraction of the conductive ferromagnetic phase responsible for the MR is also responsible for the large volume contraction. Neumeier et al. (1995) and Laukhin et al. (1997) have found a $dT_C/dP > 0$ that increases as T_C decreases; the effect disappears in the O' phase where there is a T_N . Fontcuberta et al. (1998) have also shown that isovalent substitutions in $(\text{La}_{1-y}\text{R}_y)_{2/3}(\text{Ca}_{1-x}\text{Sr}_x)_{1/3}\text{MnO}_3$ yield a $dT_C/dP > 0$ that increases with the extent of local

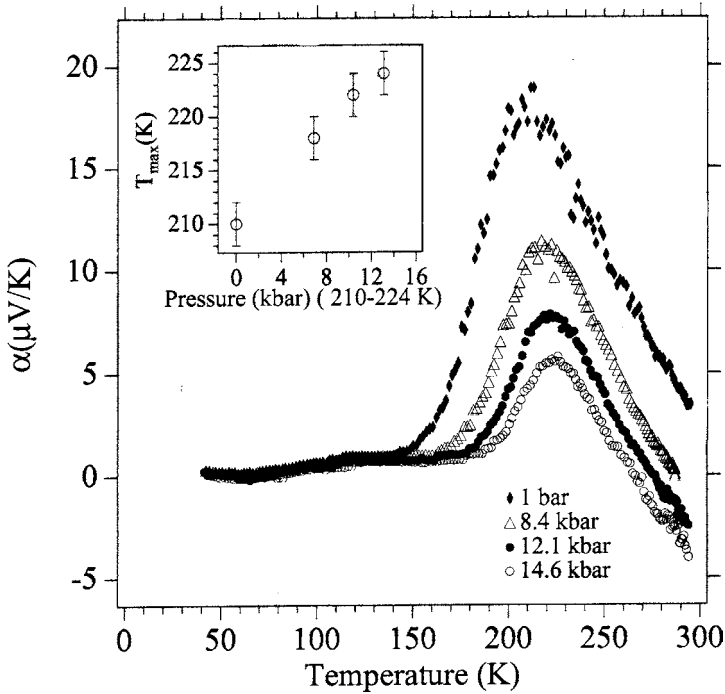


Fig. 35. Pressure dependence of $\alpha(T)$ for $(\text{La}_{0.6}\text{Nd}_{0.4})_{0.7}\text{Ca}_{0.3}\text{MnO}_3$ with $t = 0.960 > t_c$; after Archibald et al. (1996).

disorder at the A-site cations, but the variations with disorder were not enough to account for the large dT_C/dP that was observed. De Teresa et al. (1996b) have provided a comprehensive investigation of $\text{La}_{2/3}\text{Ca}_{1/3}\text{MnO}_3$ that links the large pressure dependence of T_C directly to the coexistence of two distinguishable phases, a conductive ferromagnetic phase of smaller volume and a paramagnetic polaronic phase of larger volume.

Fourth, Jaime and Salamon (1999) have pointed out that $\alpha(T)$ increases more sharply than exponentially on cooling to T_{max} in fig. 30 and that the additional entropy transported increases on crossing the $O'-O^*$ phase boundary at t_c . This observation is consistent with a progressive transformation from Zener to small polarons in the hole-poor phase as the hole concentration $x = 0.30$ in this phase is diluted by the trapping of Zener polarons in the hole-rich phase. Such a transformation would double the number of sites available to a polaron and would therefore increase the α of eq. (26) by reducing $c = (1-r)2x$ toward $c = (1-r)x$, where r is the ratio of trapped to free polarons. In the O' phase, most of the polarons appear to be small polarons at T_N .

Fifth, fig. 36 shows the temperature dependence of the resistivity $\rho(T)$ as a function of pressure for the $y = 0.75$ sample, which is just on the O' side of the $O'-O^*$ phase boundary ($t < t_c$) at atmospheric pressure, and fig. 37 shows the change in $\alpha(T)$ with pressure for the same sample (Zhou et al., 1996). A resistivity maximum occurs at T_C where a long-

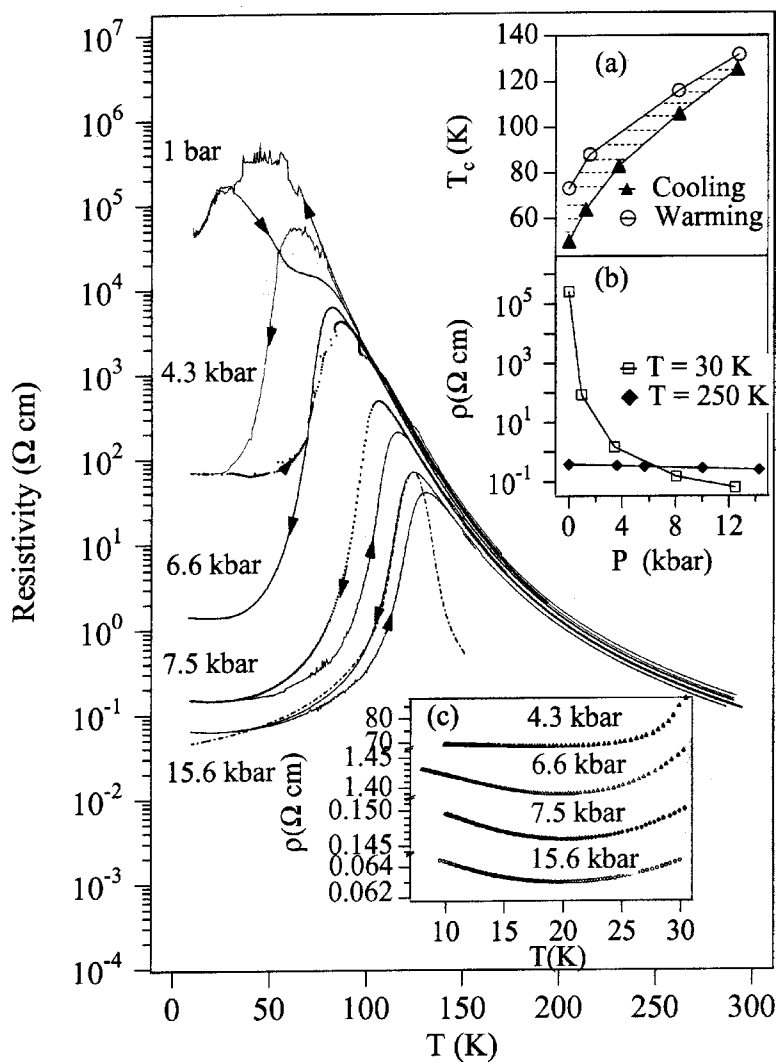


Fig. 36. Pressure dependence of $\rho(T)$ for $(\text{La}_{0.25}\text{Nd}_{0.75})_{0.7}\text{Ca}_{0.3}\text{MnO}_3$ with $t = 0.952 < t_c$; after Zhou et al. (1996). Lower inset shows $\rho(T)$ at low temperatures; upper insets show T_c and $\rho(30\text{ K})$, $\rho(250\text{ K})$ vs. pressure.

range Weiss molecular field increases the volume fraction of the conductive ferromagnetic phase to beyond percolation. The drop in $\rho(T)$ on cooling through T_c is continuous even though the thermal hysteresis in $\rho(T)$ shows that the magnetic transition is first-order. It has been commonly assumed that the metallic temperature dependence of $\rho(T)$ below T_c signals itinerant-electron behavior. However, fig. 36 shows that $\rho(T)$ remains above the itinerant-

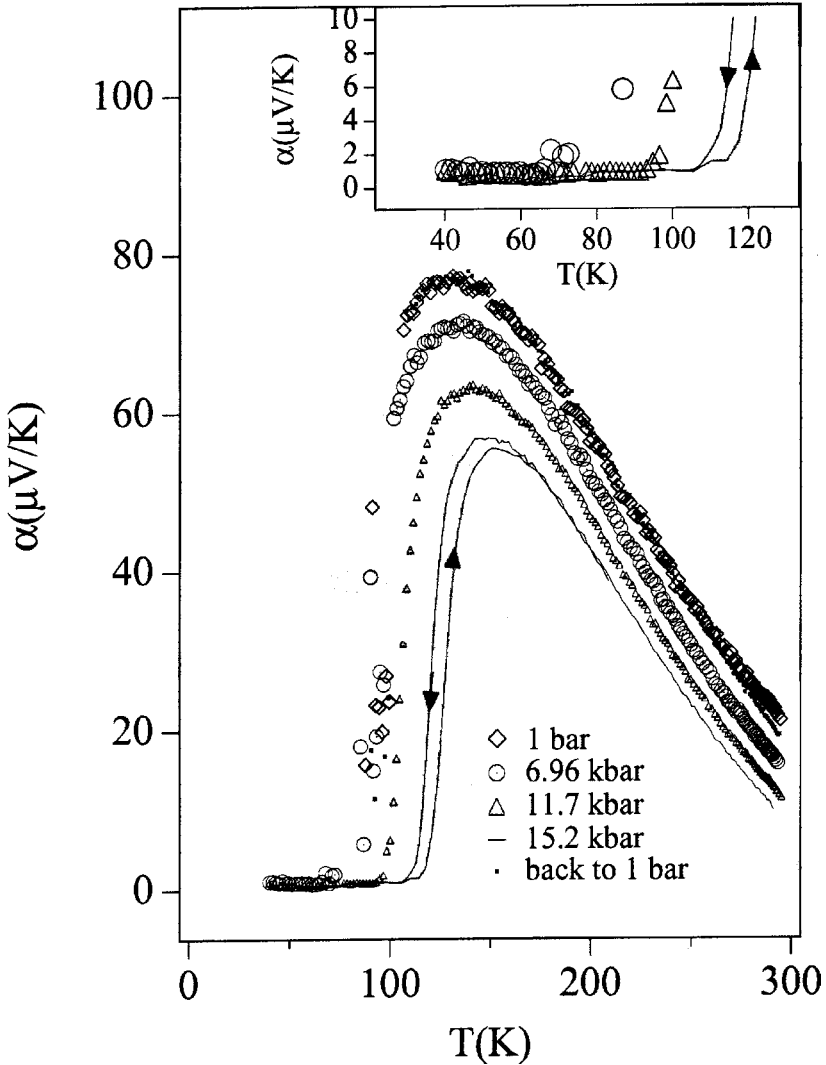


Fig. 37. Pressure dependence of $\alpha(T)$ for $(\text{La}_{0.25}\text{Nd}_{0.75})_{0.7}\text{Ca}_{0.3}\text{MnO}_3$ with $t = 0.952 < t_c$; after Zhou et al. (1996). Inset details low-temperature data.

electron limit, which makes the ferromagnetic phase below T_C a “bad metal”. Moreover, the drop in $\alpha(T)$ to a small, temperature-independent value, as shown in fig. 37, is not characteristic of a conventional metal. Since eq. (26) is not applicable at low temperatures, we turn to the general expression for the thermoelectric power (MacDonald, 1962):

$$\alpha = \alpha_0 + \delta\alpha, \quad (30)$$

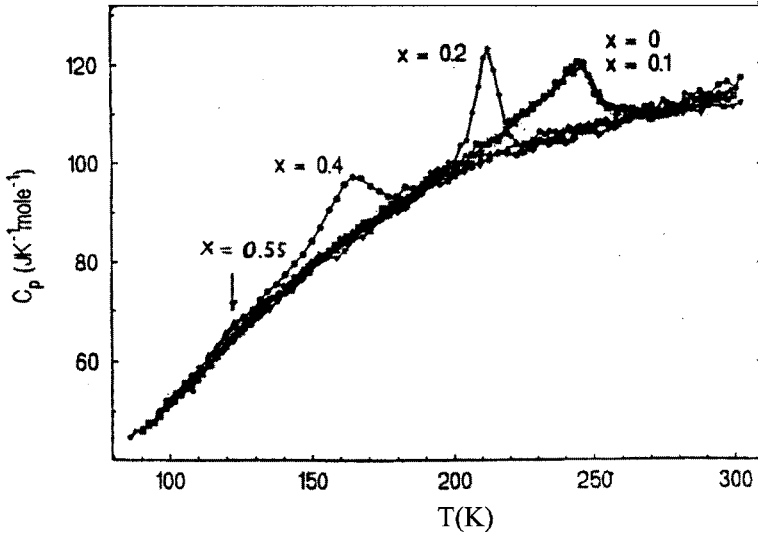


Fig. 38. Specific heat vs. temperature for several samples with $t > t_c$ for $(\text{La}_{1-y}\text{Nd}_y)_{0.7}\text{Ca}_{0.3}\text{MnO}_3$; after Overend et al. (unpublished).

where $\delta\alpha$ is a low-temperature enhancement factor normally associated in a metal with a phonon drag having a maximum contribution at a temperature $T_{\text{max}} \approx 0.2\theta_D$, θ_D is the Debye temperature, and

$$\alpha_0(T) = -\frac{k}{e} \int \frac{(\varepsilon - \varepsilon_F) \sigma(\varepsilon)}{kT} \frac{\sigma(\varepsilon)}{\sigma} d\varepsilon \quad (31)$$

in which $\sigma(\varepsilon) = f(\varepsilon)[1 - f(\varepsilon)]N(\varepsilon)\mu(\varepsilon)$ is the product of the Fermi distribution function $f(\varepsilon)$, the energy density of one-particle states $N(\varepsilon)$, and the particle mobility $\mu(\varepsilon)$ at an energy ε relative to the band edge. In a metallic conductor, α_0 becomes Mott's expression:

$$\alpha_0 \approx -\frac{\pi^2 k^2 T}{3e\varepsilon_F} \left\{ \frac{\partial \ln \sigma(\varepsilon)}{\partial \ln \varepsilon} \right\}_{\varepsilon=\varepsilon_F} \quad (32)$$

Below T_C , the conductive ferromagnetic phase of fig. 37 shows no phonon-drag enhancement ($\delta\alpha = 0$) and does not vary linearly with T as predicted by eq. (32). It follows from eq. (31) that a temperature-independent $\alpha \approx 0 \mu\text{V}/\text{K}$ below T_C implies $\sigma(\varepsilon - \varepsilon_F) \approx \sigma(\varepsilon_F - \varepsilon)$, which means that there is little dispersion in the electron energies $\varepsilon(k)$ of the σ^* band of e-orbital parentage. Moreover, the specific-heat data of fig. 38 (Overend et al., unpublished) show that the Λ -point anomaly at T_C vanishes on the approach to the $O'-O^*$ phase boundary ($y = 0.55$ sample), which is typical of spin-glass behavior below T_C where ferromagnetic clusters are in an antiferromagnetic matrix. At the phase boundary, the Mn(III) e orbitals of the hole-poor matrix order as in the O' phase in zero applied field, but become disordered in a modest applied field as occurs in $\text{LaMn}_{0.5}\text{Ga}_{0.5}\text{O}_3$, fig. 13. We conclude that the charge carriers are

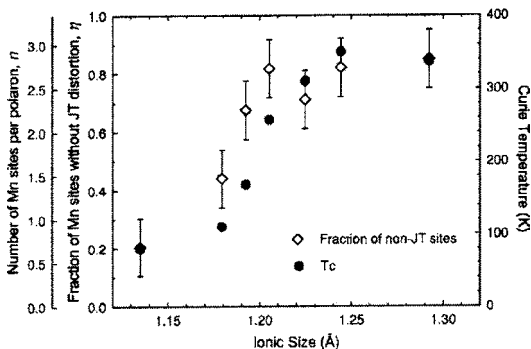


Fig. 39. The fraction η of Mn sites without local Jahn–Teller distortions at 10 K and the Curie temperature T_C of various $R_{0.7}A_{0.3}MnO_3$ compounds vs. the 9-coordinated ionic radii r_A ; after Louca et al. (2001).

vibronic below T_C with a probability of electron transfer from a Mn(III) to a Mn(IV) ion $\tau_h^{-1} \approx \omega_0$; the charge carriers are strongly coupled to local oxygen-vibration modes that, if long-range ordered, could give rise to mobile stripes of alternating itinerant and localized states. Clarification of the character of the charge carriers in the ferromagnetic phase of the materials exhibiting a large CMR phenomenon remains a challenge.

An important tool for investigating the ordering of cooperative bond-length fluctuations at the crossover from localized to itinerant-electron behavior and/or those due to orbital fluctuations is the pulsed-neutron atomic pair-density-function (PDF) method developed by Egami (2001). Louca et al. (2001) have employed this method to determine the nature of the transition from polaronic to itinerant-electron behavior with changes in the mean room-temperature ionic radius $\langle r_A \rangle$ of the A-site ions for a series of $R_{0.7}A_{0.3}MnO_3$ compositions. They found Jahn–Teller distortions and Mn(IV) small polarons at 10 K if $\langle r_A \rangle$ is less than 1.17 \AA and six equivalent (Mn–O) bonds at each Mn atom of itinerant-electron length if $\langle r_A \rangle$ is greater than 1.24 \AA . In the narrow range 1.17 $\text{\AA} < \langle r_A \rangle < 1.24 \text{\AA}$, the volume fraction η of the itinerant-electron phase increased continuously and the Curie temperature T_C tracked η ; fig. 39. Moreover, analysis showed that the short (Mn(IV)–O) bond length corresponded to half the Mn–Mn separation in the (001) planes for an $\langle r_A \rangle$ in the range 1.19 to 1.20 \AA , indicating that an $\langle r_A \rangle$ larger than 1.20 \AA would increase the Mn–O–Mn bond angle to a value that approached and then exceeded the critical angle for crossover from localized to itinerant electronic behavior. A bent ($180^\circ - \phi$) bond angle allows adjustment of the Mn–O–Mn bond length in different domains without changing the Mn–Mn separation by displacements of the oxygen atoms perpendicular to the bond axis and oxygen displacements along a bond axis at a phase interface. Therefore, at the crossover angle, the first-order character of the transition from localized to itinerant electronic behavior allows phase segregation by cooperative oxygen displacement perpendicular to the Mn–O–Mn bond axis that create shorter Mn–O bonds in the itinerant-electron phase and longer Mn–O bonds in the localized-electron phase. These cooperative oxygen displacements may fluctuate to give phase fluctuations. This analysis provides insight into the sensitivity of the bandwidth W of eq. (28) to the vibrational frequency ω_0 at the crossover from polaronic to itinerant-electron behavior; the perpendicular vibrations harden as the Mn–O–Mn bond angle bends from 180° . Billinge et al. (2000) have used the PDF technique to show a similar continuous evolution from polaronic to itinerant-electron behavior on

traversing the insulator-metal transition whether with increasing r_A , i.e., tolerance factor, or decreasing temperature across T_C in the $\text{La}_{1-x}\text{Ca}_x\text{MnO}_3$ system; polaronic behavior sets in at 20 K where $\langle r_A \rangle$ decreases below 1.15 Å. Rivadulla et al. (2001), using literature neutron-diffraction data, have shown that the polaronic, antiferromagnetic phase converts abruptly to the conductive, ferromagnetic phase where the Mn–O–Mn bond angle $\theta = (180^\circ - \phi)$ changes from 157° in $\text{Pr}_{2/3}\text{Ca}_{1/3}\text{MnO}_3$ to $\theta = 159.5^\circ$ in $(\text{La}_{0.78}\text{Pr}_{0.22})_{2/3}\text{Ca}_{1/3}\text{MnO}_3$. At this transition, the ratio Q_3/Q_2 of the tetragonal/orthorhombic Jahn–Teller distortional modes

$$\tan \Phi = \pm(2/\sqrt{6})(2m - l - s)/(2/\sqrt{2})(l - s) \quad (33)$$

changes from $\Phi = 23^\circ$ to $\Phi = 25^\circ$. In eq. (33) s and l are the short and long (Mn–O) bond lengths in the (001) planes and m is the intermediate-length (Mn–O) bond along the [001] axis. A $\Phi = 30^\circ$ is the strong-anisotropy all- Q_3 limit $m = s$ whereas $\Phi = 0$ corresponds to the Q_2 limit where, in the perovskite structure, $m = l = s$ and the six (Mn–O) bond lengths at a Mn atom are equivalent.

For further evidence of strong electron coupling to oxygen vibrations in a system that has two electronic phases, we turn to studies of $^{18}\text{O}/^{16}\text{O}$ isotope exchange. Isotope exchange does not change the Mn–O–Mn bond angle $(180^\circ - \phi)$, which would leave W_σ of eq. (27) unchanged; but it does change $\omega_o \sim M_o^{-1/2}$, where M_o is the oxygen mass, and therefore W of eq. (28) and $\tau_h \approx \hbar/W$. G.-M. Zhao et al. (1996, 1997a, 1997b) were the first to show a dramatic decrease of T_C on the exchange of $^{18}\text{O}/^{16}\text{O}$. If on cooling through T_C the transition was from a global polaronic phase with $\tau_h > \omega_o^{-1}$ to a global itinerant-electron phase with $\tau_h \approx \hbar/W < \omega_o^{-1}$, then the exchange of $^{18}\text{O}/^{16}\text{O}$, which decreases $\omega_o \sim M_o^{-1/2}$, should favor the itinerant-electron phase with $\tau_h < \omega_o^{-1}$ and therefore raise T_C . The fact that $^{18}\text{O}/^{16}\text{O}$ exchange decreases T_C is, therefore, evidence that T_C depends on a bandwidth W described by eq. (28) as a result of the two-phase character of the electronic system; a decrease in W with increasing M_o favors the polaronic phase and lowers T_C if the transition is governed by the bandwidth W rather than by W_σ .

If the dramatic change in T_C with tolerance factor t in fig. 29 is due to a change in $\omega_o(\phi)$, as is suggested by a $T_C \sim W$ and eq. (29), then the critical ambient tolerance factor t_c for the $\text{O}'\text{--O}^*$ transition should increase and T_C decrease accordingly on the exchange of ^{18}O for ^{16}O whereas pressure should have the opposite effect. In order to probe this deduction, Zhou and Goodenough (1998) undertook additional isotope-exchange experiments. Figure 40 compares the $\alpha(T)$ curves at atmospheric pressure for the ^{18}O and ^{16}O $(\text{La}_{0.25}\text{Nd}_{0.75})_{0.7}\text{Ca}_{0.3}\text{MnO}_3$ samples ($t < t_c$) of figs. 36 and 37. Comparison of these two curves with fig. 31 shows that the change in $\alpha(T)$ on exchanging ^{18}O for ^{16}O is equivalent to reducing t . This experiment provides direct evidence that the sensitivity with respect to t of the magnetic and transport properties of fig. 29 depends more on the sensitivity of t to $\omega_o(\phi)$ than to W_σ . Nagaev (2001b) has argued that the isotope effect is due to oxygen off-stoichiometry, but this position does not appear to be tenable. Chechersky et al. (1999b) have provided further confirmation of our conclusion. They followed with Mössbauer spectroscopy the temperature dependence through T_C of the two-phase character of $\text{La}_{0.8}\text{Ca}_{0.2}\text{MnO}_3$ and found the strength of the exchange interactions at 78 K were not changed by $^{18}\text{O}/^{16}\text{O}$ exchange whereas a considerable softening

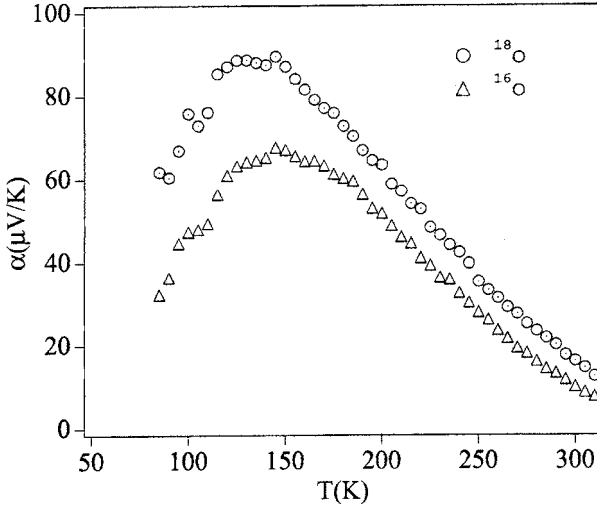


Fig. 40. Comparison of $\alpha(T)$ for ^{18}O and ^{16}O at atmospheric pressure for $(\text{La}_{0.25}\text{Nd}_{0.75})_{0.7}\text{Ca}_{0.3}\text{MnO}_3$ samples of figs. 36 and 37; after Zhou and Goodenough (1998).

of the anharmonic $\text{Mn}-^{18}\text{O}-\text{Mn}$ vibrations reduced the volume fraction of the ferromagnetic phase at a given temperature.

To obtain information on the variation of T_C with pressure for ^{18}O vs. ^{16}O , Zhou and Goodenough (1998) used the fact that $\rho(T)$ for $(\text{La}_{0.25}\text{Nd}_{0.75})_{0.7}\text{Ca}_{0.3}\text{MnO}_3$ in fig. 36 has its maximum value near T_C . Three additional features of fig. 36 are noteworthy:

1. The $\rho(T)$ curves are relatively insensitive to pressure for $T > T_C$, but they change dramatically for $T < T_C$ on crossing a transition at $P_c < 4$ kbar. The transition, not shown in fig. 36, is sharply defined.
2. There is no thermal hysteresis in the $\rho(T)$ curve at atmospheric pressure where $(\text{La}_{0.25}\text{Nd}_{0.75})_{0.7}\text{Ca}_{0.3}\text{MnO}_3$ is in the O' phase at the magnetic-ordering temperature, but a pronounced thermal hysteresis appears at pressures $P > P_c$.
3. The thermal hysteresis, which marks a change from a second-order transition at T_N to a first-order transition at T_C on crossing the $O'-O^*$ phase boundary, decreases as T_C increases with pressure $P > P_c$.

Figure 41 (top) compares the evolution with pressure of T_C and thermal hysteresis at T_C of the $(\text{La}_{0.25}\text{Nd}_{0.75})_{0.7}\text{Ca}_{0.3}\text{MnO}_3$ sample with ^{16}O and ^{18}O . A shift of $\Delta P_c \approx 9$ kbar on isotope exchange reflects the increase in effective t_c , and a giant isotope coefficient $d \ln T_C / d \ln M_o \approx 4.9$ appears abruptly on conversion from the O' to the O^* phase; no measurable isotope shift was found in the antiferromagnetic O' phase containing small-polaron holes. Ordering of the occupied e-electron orbitals into the (001) planes in the O' phase is stabilized by a softer $\omega_o \sim M_o^{-1/2}$, which shows it is not the bending angle $\theta = (180^\circ - \phi)$ of the $\text{Mn}-\text{O}-\text{Mn}$ bond *per se* that controls the $O'-O^*$ transition; it is the dependence of ω_o , and hence of W of eq. (28), on ϕ that makes the polaronic to itinerant-electron transition vary so sensitively with θ . The large isotope shift of T_C is clearly associated with an instability of the static Jahn–Teller orbital ordering on the approach to a transition from localized to itinerant electronic

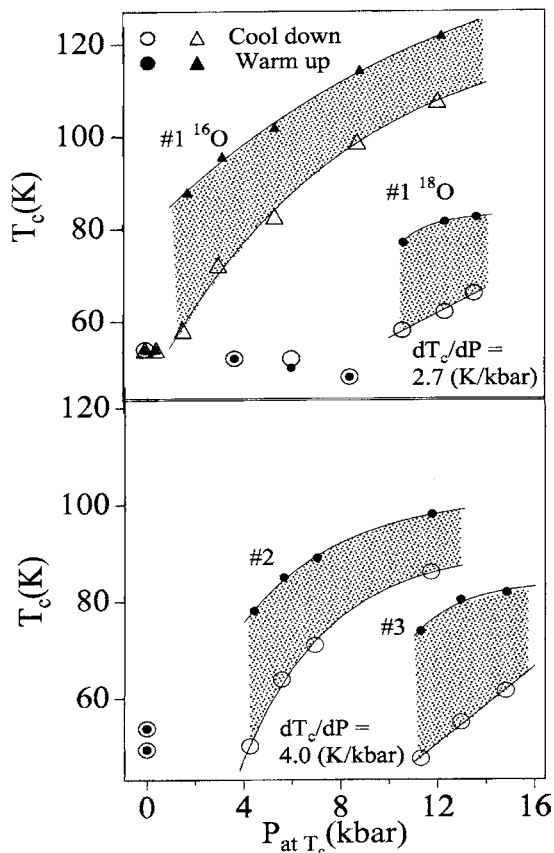


Fig. 41. Variation of T_C with increasing and decreasing pressure for ^{16}O and ^{18}O for three samples of $(\text{La}_{1-y}\text{Nd}_y)_{0.7}\text{Ca}_{0.3}\text{MnO}_3$, of figs. 36 and 37: $y = 0.75$ (#1, top) and $y = 0.8$ and 0.85 (#2 and #3, respectively, bottom); after Zhou and Goodenough (1998).

behavior where the (Mn–O) bond length has a double-well potential. It is at such a transition that we find the coexistence of two phases, one hole-rich with itinerant electrons and the other hole-poor with cooperative Jahn–Teller distortions that may be static or fluctuating.

The magnitude of ΔT_C in the O^* phase on $^{18}\text{O}/^{16}\text{O}$ exchange increases with the magnitude of $dT_C/dt > 0$, which is a maximum just above t_c . The isotope shifts of T_C in samples with $t > t_c$ at ambient pressure were similar to those reported by G.-M. Zhao et al. (1996, 1997a, 1997b). Franck et al. (1999, 2001) have reported an analogous finding in $\text{La}_{1-x}\text{Ca}_x\text{MnO}_3$ for $0.2 < x < 0.3$ and an increase of ΔT_C in the oxygen-excess $x = 0.2$ compound that does not support the Nagaev (2001b) calculation, but is due to the perturbation of the periodic potential of the MnO_3 array as a result of the cation vacancies present.

In the O' phase, T_N is determined only by superexchange interatomic interactions; the small-polaron hopping rate is too slow relative to a spin-relaxation time for a double-exchange coupling to be operative. However, the charge carriers are more mobile in the O^* phase and they contribute a double-exchange component to the vibronic ferromagnetic superexchange interactions of the matrix that increases with the volume fraction of the conductive ferro-

magnetic phase. The $dT_C/dt > 0$ reflects an increase with tolerance factor t in the double-exchange contribution to the magnetic interactions as the $(180^\circ - \phi)$ Mn–O–Mn bond angle increases. The larger mass M_o of an ^{18}O softens $\omega_o \sim M_o^{-1/2}$, which lowers $\omega(\phi)$ for a given value of ϕ ; the volume fraction of the conductive ferromagnetic phase decreases as ω_o softens and the effective t_c increases. Above the temperature of condensation of the itinerant-electron phase, the small polarons break down first by forming two-Mn Zener polarons and then, as W increases further, become itinerant holes. On cooling, the Zener polarons may order or may condense into a 1D or 2D itinerant-electron σ^* band where a 3D σ^* band would be narrow enough for orbital ordering. The reduction of W on ^{18}O substitution for ^{16}O increases the small-polaron/Zener-polaron ratio as is made evident by the increase in the high-temperature magnitude of $\alpha(T)$ in fig. 40.

In order to identify any dependence on M_o of the character of the charge carriers in the majority conductive phase below T_C , we minimized any pressure dependence by examining a ^{16}O sample of lower t having a P_c close to that of the ^{18}O -substituted $(\text{La}_{0.25}\text{Nd}_{0.75})_{0.7}\text{Ca}_{0.3}\text{MnO}_3$ sample. For this purpose, Zhou and Goodenough (1998) measured the pressure dependence of $\rho(T)$ for two additional ^{16}O samples, 2 and 3 with $(\text{La}_{0.2}\text{Nd}_{0.8})$ and $(\text{La}_{0.15}\text{Nd}_{0.85})$ corresponding, respectively, to $t = 0.951$ and 0.949 . Figure 41 (bottom) shows that the ^{16}O sample 3 has nearly the same $P_c \approx 11$ kbar as the ^{18}O sample having a $t = 0.952$. It follows that the exchange of ^{18}O for ^{16}O is equivalent to a shift of tolerance factor $\Delta t \approx -0.03$; hydrostatic pressure is equivalent to an increase of t by $dt/dP \approx 2.7 \times 10^{-3}$ per kbar. From fig. 41, they also observed at $P_c = 11$ kbar for ^{16}O ($\text{La}_{0.15}\text{Nd}_{0.85}$) and ^{18}O ($\text{La}_{0.25}\text{Nd}_{0.75}$), respectively, a thermal hysteresis $\Delta T_C = 27$ K and 19 K; on cooling, a $dT_C/dP = 4.0$ K/kbar and 2.7 K/kbar. The thermal hysteresis ΔT_C should be proportional to the volume change ΔV at the first-order transition, which in turn would be proportional to the change in the mean electronic potential energy $\Delta\langle V \rangle$. From the virial theorem, eq. (19), it follows that

$$\Delta T_C \sim \Delta\langle T \rangle|_{T_C} \quad (34)$$

is a measure of the change $\Delta\langle T \rangle$ in the mean kinetic energy of the charge carriers at the first-order transition at T_C . At temperatures $T > T_C$, the charge carriers are polaronic and the ratio of small to Zener polarons is larger for the ^{18}O sample at P_c . Since itinerant electrons would have a mean kinetic energy essentially independent of M_o , a $\Delta T_C(^{18}\text{O}) > \Delta T_C(^{16}\text{O})$ would follow from eq. (34), which is just the opposite to what is observed. Therefore, these data also lead to the conclusion that in the O^* phase near the $\text{O}'\text{--O}^*$ phase boundary, the charge carriers below T_C are not conventional itinerant electrons, but interact strongly with the lattice to form “vibronic” states with a bandwidth described by eq. (29) rather than eq. (28). We also note that a larger dT_C/dP of the ^{16}O vs. ^{18}O sample is consistent with a smaller trapping energy of the polarons in the paramagnetic state of the ^{16}O sample evident in fig. 40.

G.-M. Zhao et al. (2001) have subsequently shown an isotope shift of the intrinsic resistivity of the conductive ferromagnetic state of high-quality epitaxial films of two CMR manganites, $\text{La}_{0.75}\text{Ca}_{0.25}\text{MnO}_3$ and $\text{Nd}_{0.7}\text{Sr}_{0.3}\text{MnO}_3$, that supports a polaronic charge-carrier effective mass $m^* = m \exp(\lambda \varepsilon_x / \hbar \omega_o)$ below T_C as also follows from the vibronic bandwidth W of eq. (29). Alexandrov et al. (2001) have developed a theory of a “polaronic Fermi liquid” in which $m^* = m \exp(A/\omega_o)$; their model corresponds to the “vibronic” state.

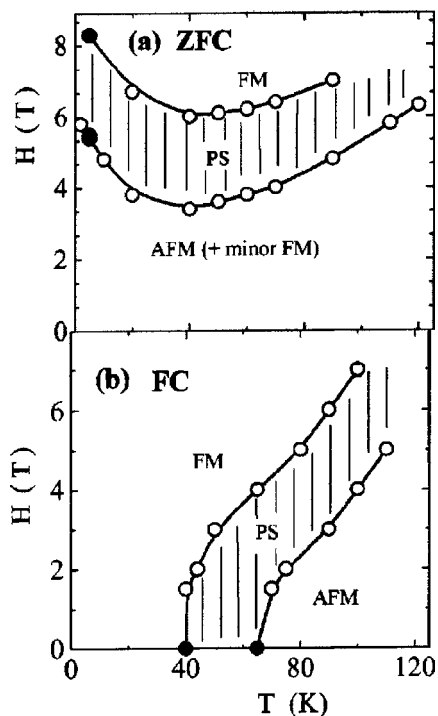


Fig. 42. Magnetic phase diagrams of $(\text{La}_{0.25}\text{Pr}_{0.75})_{0.7}\text{Ca}_{0.3}\text{Mn}^{18}\text{O}_3$ after (a) ZFC and (b) FC procedures; open circles from $M(T)$ and closed circles from NMR. PS = phase separation, after Yakubovskii et al. (2000).

Babushkina et al. (2000) examined the effect of partial $^{18}\text{O}/^{16}\text{O}$ exchange on the $x = 0.525$ sample of $\text{La}_{0.7-x}\text{Pr}_x\text{Ca}_{0.3}\text{MnO}_3$, see fig. 29. On cooling, they found the first-order transition at T_C , and T_C decreased linearly with ^{18}O content from 95 K for all ^{16}O to 50 K for 39% ^{18}O ; the residual resistivity increased. The $\rho(T)$ curves changed with increasing ^{18}O content like those of fig. 36 with decreasing pressure. Above 40% ^{18}O , the conductive ferromagnetic phase failed to percolate and remained as isolated clusters within an antiferromagnetic matrix, showing that the effective tolerance factor became $t = t_c$ at about 40% ^{18}O . Above 90% ^{18}O , the antiferromagnetic transition at T_N became second-order. Yakubovskii et al. (2000) performed magnetization and NMR studies on the ^{18}O sample of $\text{La}_{0.7-x}\text{Pr}_x\text{Ca}_{0.3}\text{MnO}_3$, $x = 0.525$. They showed that with increasing magnetic field, the conductive ferromagnetic phase grows irreversibly to beyond percolation. As shown in fig. 42, the zero-field-cooled (ZFC) ^{18}O sample exhibits a magnetic-field range in which the ferromagnetic volume fraction grew to beyond percolation whereas a sample field-cooled (FC) in $H = 7$ T has the ferromagnetic phase-separation (PS) region intersecting the temperature axis.

An intrinsic capacitance associated with the charge-ordered phase below $T_{CO} = 225$ K in $\text{Pr}_{0.67}\text{Ca}_{0.33}\text{MnO}_3$ was noted in the ac -impedance data by Rivadulla et al. (1999a); a drop in the paramagnetic susceptibility on cooling through T_{CO} would be consistent with a preferred crystallographic orientation of two-Mn Zener polarons below T_{CO} . Saraf et al. (2000) subsequently showed that strong dielectric anomalies also appear at $T_N \approx 133$ K, at the onset of spin

canting near 116 K, and at an unidentified transition at about 125 K. These anomalies appear to reflect slow reorganization responses of a cooperative lattice deformation and/or charge distribution in an electric field in the neighborhood of a transition where reorganization is occurring.

Freitas et al. (2001) have studied the dynamic properties of the magnetization of $\text{La}_{0.7-x}\text{Y}_x\text{Ca}_{0.3}\text{MnO}_3$, $0 \leq x \leq 0.15$, below a first-order metal-polaronic transition at T_C . As yttrium is added, there is a progressive appearance of cluster-glass behavior with a freezing temperature $T_f < T_C$. This behavior is characteristic of the coexistence of a ferromagnetic and an antiferromagnetic phase below T_f . Savosta and Novák (2001) have shown the coexistence of two different ferromagnetic phases below T_C in several $\text{R}_{0.7}\text{A}_{0.3}\text{MnO}_3$ compositions, including $\text{La}_{0.7}\text{Ca}_{0.3}\text{MnO}_3$. Both phases are conducting, but one contains fast charge carriers and the other slower charge carriers. We would interpret the former to be itinerant charge carriers that give a de Gennes double-exchange ferromagnetism and the latter to be polaronic charge carriers of a vibronic (polaron Fermi liquid) phase containing a large component of vibronic-superexchange ferromagnetism. The characteristic dimension of the vibronic phase was a few nm in $\text{La}_{0.7}\text{Ca}_{0.3}\text{MnO}_3$, and its volume fraction decreased with decreasing temperature. Moreover, the volume fraction of this phase at a given temperature decreased with increasing Mn–O–Mn bond angle $\theta = (180^\circ - \phi)$ for a fixed hole concentration. These data are consistent with the following interpretation of the system $\text{La}_{0.7-x}\text{Y}_x\text{Ca}_{0.3}\text{MnO}_3$ in which θ decreases with increasing x . The volume fraction of the vibronic ferromagnetic phase below T_C grows with increasing x . Ordering of the Mn(III) e orbitals below T_f transforms the vibronic ferromagnetic phase to a type-A antiferromagnetic polaronic phase. Isolated antiferromagnetic clusters create a cluster glass; they reduce the spontaneous magnetization of the sample and introduce a frustration of the magnetic interactions that increases progressively with the volume fraction of the antiferromagnetic phase. A high magnetic field may disorder the Mn(III) e orbitals so as to convert the antiferromagnetic phase back to a ferromagnetic phase.

Consistent with this interpretation is a study of the $\text{La}_{2/3}(\text{Ca}_{1-x}\text{Sr}_x)_{1/3}\text{MnO}_3$ system by Mira et al. (2002) that, together with literature data for $(\text{La}_{1-y}\text{R}_y)_{0.7}\text{A}_{0.3}\text{MnO}_3$ compounds, indicates a second critical tolerance factor $t_c^* \approx 0.98$ (based on 12-fold rather than 9-fold coordination of A sites) for the O^* -orthorhombic to R-rhombohedral transition, a first-order magnetic transition occurring at T_C in the O^* phase ($t < 0.98$) and a second-order magnetic transition occurring at T_C in the R phase ($t > 0.98$). This critical tolerance factor is to be contrasted with the $t_c = 0.955$ for the change from the second-order magnetic transition at T_N to the first-order transition at T_C that was investigated by pressure and by $^{18}\text{O}/^{16}\text{O}$ isotope exchange, fig. 41. The large CMR phenomenon as well as a first-order magnetic transition occurs in the range $t_c < t < t_c^*$ where T_C increases dramatically with t ; a discontinuous increase in the volume fraction of the more conductive ferromagnetic phase at T_C makes the magnetic transition first-order in accordance with the virial theorem, eq. (19).

In summary, the magnetic and transport properties of the $(\text{La}_{1-y}\text{R}_y)_{0.7}\text{Ca}_{0.3}\text{MnO}_3$ perovskites near the $\text{O}'\text{--}\text{O}^*$ phase boundary are extraordinarily sensitive to the tolerance factor t , the oxygen mass M_o , temperature, and pressure as well as to magnetic and electric fields. This sensitivity can be attributed to strong electron-lattice coupling associated with not only order–

disorder transitions of cooperative Jahn–Teller deformations, but also with an accompanying crossover from localized to itinerant electronic behavior of σ -bonding e electrons in the presence of localized t^3 configurations on the Mn atoms. At crossover, a hole-rich, conductive ferromagnetic phase segregates from a hole-poor polaronic phase that is antiferromagnetic where the cooperative Jahn–Teller distortions are long-range ordered, but is ferromagnetic where the distortions fluctuate. Condensation of two-Mn Zener polarons into a hole-rich, conductive ferromagnetic phase with a T_C^* higher than the T_C or T_N of its matrix and growth of the hole-rich phase to beyond its percolation threshold in an applied magnetic field in the interval $T_C < T < T_C^*$ results in the CMR phenomenon. A discontinuous increase in the volume fraction of the hole-rich phase on cooling through T_C contracts the volume discontinuously and makes the magnetic transition first-order; retention of two fluctuating ferromagnetic phases below T_C suppresses the phonons and makes the conductivity vibronic rather than itinerant. Orbital ordering in the hole-poor minority phase may occur at low temperatures to introduce magnetic frustration and cluster-glass behavior. The $O'-O^*$ phase boundary depends upon the oxygen-vibration frequency; $\omega_o > \tau_h^{-1}$ gives polaronic conduction and $\omega_o < \tau_h^{-1}$ gives itinerant-electron behavior. The $O'-O^*$ boundary and phase segregation occur where $\omega_o \approx \tau_h^{-1}$. The oxygen vibrations of interest have two components, perpendicular and parallel to a Mn–O–Mn bond axis, that harden as the bond angle $\theta = (180^\circ - \phi)$ decreases, and an $\omega_o(\phi)$ enters the vibronic bandwidth W of eq. (29) for the two-phase region. Moreover, the transitions occur where $W \approx \hbar\omega_o$, which means that the phenomena vary sensitively with the tolerance factor t . The CMR phenomenon and a first-order magnetic transition are found for 30% holes in the MnO_3 array in the interval $0.955 < t < 0.98$ where T_C increases dramatically with t ; this critical range of tolerance factors does not change significantly in systems with varying hole concentration.

3.5. The system $La_{1-x}Sr_xMnO_3$

The phase diagram of $La_{1-x}Sr_xMnO_3$, fig. 43, has been constructed from data taken from several different sources (Urushibara et al., 1995; Kawano et al., 1996; Zhou et al., 1997, 2001b; Moritomo et al., 1997b; Dabrowski et al., 1999a; Xiong et al., 1999; Zhou and Goodenough, 2000; G.-L. Liu et al., 2001). Measurements of the temperature dependence of the transport properties and magnetic susceptibility under hydrostatic pressure have proved particularly helpful in determining, without changing composition, the nature of the transitions between competing phases that have been found in the range $0.10 \leq x \leq 0.20$.

In the range $0 < x < 0.1$, the canted-spin antiferromagnetic phase is a small-polaron conductor, which classifies it as an insulator (CAFI). Below T_N , the antiferromagnetic component of the type-A magnetic order, eq. (14) and table 1, is oriented along the b -axis, the weak ferromagnetic component along the c -axis, and the Dzialoshinskii vector D_{ij} is along the a -axis in space group $Pbnm$. A ^{139}La study by Kumagai et al. (1999) has revealed the presence below T_N of ferromagnetic droplets appearing as a second phase by $x = 0.05$. Hennion et al. (2000) have observed with elastic and inelastic neutron scattering from an untwinned $x = 0.06$ single crystal the presence of ferromagnetic droplets three (001) layers thick with an in-plane diameter of about 17 Å; the droplets are separated by distances ≤ 38 Å within the (001) planes.

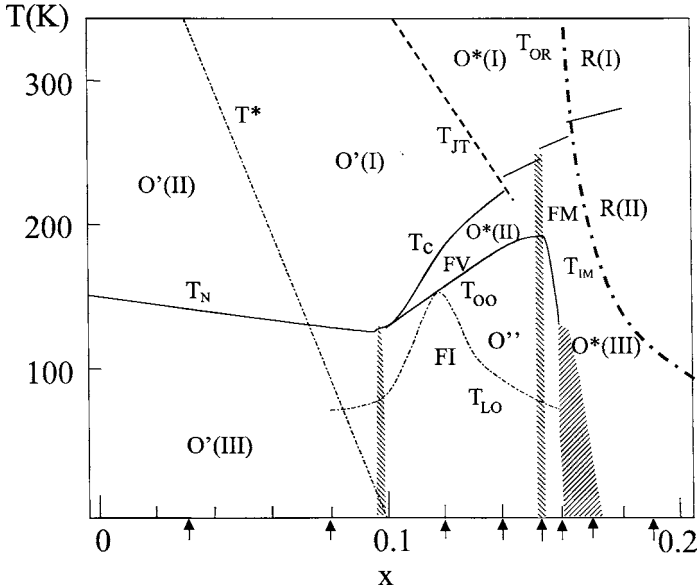


Fig. 43. Phase diagram for $\text{La}_{1-x}\text{Sr}_x\text{MnO}_3$, $0 \leq x \leq 0.20$, after Zhou and Goodenough (2001a).

These hole-rich droplets represent a ferromagnetic second phase having $T_C < T_N$; the volume fraction of this minority phase grows with increasing x , and in the range $0.1 \leq x \leq 0.13$ the droplets are condensed into large clusters having $T_C > T_N$. The crossover from $T_C < T_N$ to $T_C > T_N$ occurs at about $x = 0.10$ near a point where the 2D orbital order-disorder transition (or onset of orbitally disordered clusters) at T^* (same T^* as in fig. 14) crosses T_N .

The compositional dependence of the structural $O'-O^*$ transition at T_{JT} and the O^*-R transition at T_{OR} can be clearly followed by monitoring the temperature dependence of the resistance (Mandal et al., 2001); monitoring the variation with x of the higher-order transition at T^* from the resistance curve $R(T)$ is more subtle and has been accomplished with further aid from the thermoelectric power $\alpha(T)$ measured on single crystals (Zhou and Goodenough, 2000). The transition from polaronic to itinerant electronic behavior in the paramagnetic R-rhombohedral phase has not been studied.

In the narrow compositional range $0.10 \leq x \leq 0.13$, a spin-glass behavior is found in very low applied magnetic fields below a spin-freezing temperature T_f . The spin-glass character of the magnetic ordering is manifested in the magnetic susceptibility (Skumryev et al., 2000) as well as in the collapse of the Λ anomaly in the specific heat of the $x = 0.10$ sample at the magnetic-ordering temperature, fig. 44. However, the spin glass is converted to a ferromagnetic phase in a modest applied magnetic field with $T_C \approx T_f$; the volume fraction of the ferromagnetic phase grows at the expense of the O' antiferromagnetic phase in an applied magnetic field, and the sample becomes "ferromagnetic" where the volume fraction of the ferromagnetic phase exceeds the percolation threshold. It is only below a T_{OO} that the samples become fully ferromagnetic. The transition at T_{OO} is first-order, see the C_p data for $x = 0.11$ and $x = 0.12$, where there is a discontinuous change in the ferromagnetic volume fraction on

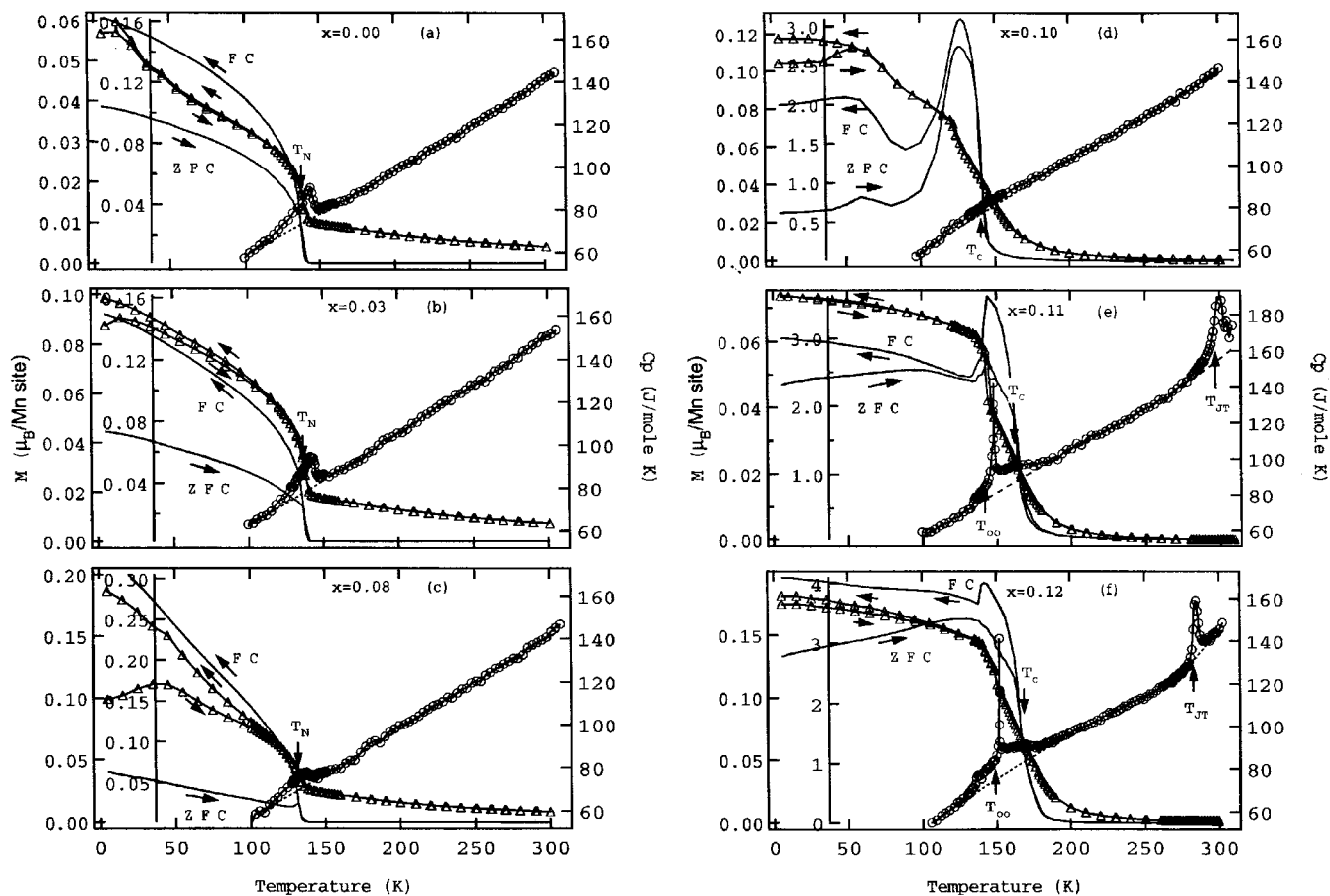


Fig. 44. Magnetization $M(T)$ in $H = 20$ Oe and 5 kOe; specific heat $C_p(T)$ for $\text{La}_{1-x}\text{Sr}_x\text{MnO}_3$, $0 \leq x \leq 0.19$: O = C_p ; $\Delta = M(T)$ in 5 kOe; simple solid line = $M(T)$ in 20 Oe. Arrows indicate warming vs. cooling curves, after G.-L. Liu et al. (2001).

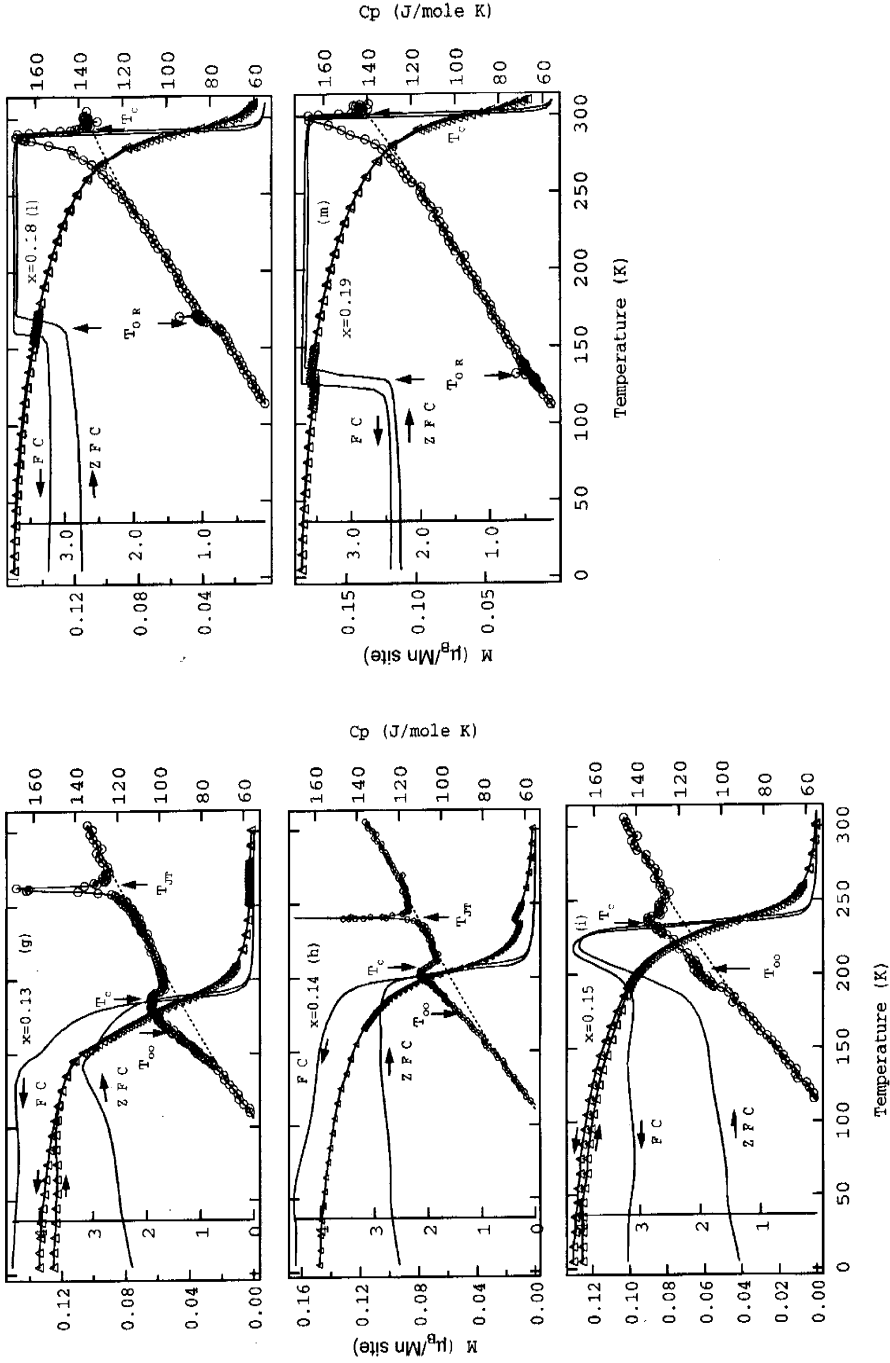


Fig. 44. Continued.

cooling through T_{OO} . For $x \geq 0.13$, the system becomes ferromagnetic below T_C in zero applied magnetic field, and the transition at T_{OO} becomes second-order. In fig. 43, the FI phase appearing below T_{OO} is labeled O'' -orthorhombic.

The ferromagnetic-insulator (FI) phase appearing below T_{OO} is both charge and orbitally ordered. Klingeler et al. (2002) who have also tracked the changes in the specific-heat anomalies appearing in the range $T_{OO} \leq T \leq T_C$, pointed out that the entropy changes can be accounted for with only the calculated changes in spin entropy and concluded that the phase changes must be driven by the exchange interactions. Therefore, the character of the orbital and charge order below T_{OO} and how it supports 3D ferromagnetic interatomic interactions is an important question that remains controversial. Whether the first-order transition at T_{OO} in $x = 0.125$ is due to charge ordering as originally reported by Yamada et al. (1996) or to an orbitally ordered state as proposed by Endoh et al. (1999) appears to have been resolved by Yamada et al. (2000), who provided evidence for both orbital and charge ordering, but with the charge ordering appearing as a c -axis charge-density wave (CDW) of opposite phase on neighboring c -axis Mn–O–Mn columns to give a unit-cell size $(\sqrt{2} \times \sqrt{2} \times 4)_{\text{cubic}}$. Ordering of long and short Mn–O bonds in the (001) planes as in LaMnO_3 gives the ferromagnetic planar interactions of the type-A antiferromagnetic structure. Ordering of the holes into static CDWs along the c -axis rows can give ferromagnetic coupling along the c -axis as well. In the interval $0.05 \leq x \leq 0.10$, the ferromagnetic plate-like second phase consists of hole-rich regions in which ferromagnetic coupling between ferromagnetic planes replaces the antiferromagnetic coupling of the type-A antiferromagnetic matrix.

Transitions between the competing phases existing at $x = 1/8$ have been tracked by high-frequency conductivity measurements (F. Mayr et al., 2000) and exposure to X-rays has been shown (Casa et al., 2001) to induce conductive transitions with memory at temperatures $T < T_{OO}$.

In the range $0.13 \leq x \leq 0.15$, T_C and T_{OO} increase with x ; T_C undergoes a first-order jump where it crosses T_{JT} . In the paramagnetic range $T_C < T < T_{JT}$, the O' structure signals an ordering of the occupied e orbitals of the matrix into the (001) planes, but either the in-plane order fluctuates or there are orbitally disordered clusters within the matrix ($T > T^*$). Three-dimensional orbital fluctuations dominate in the interval $T_{OO} < T < T_C$ where the system is a ferromagnetic vibronic conductor (FV). The greater orbital disorder is stabilized by ferromagnetic vibronic superexchange that supplements the Zener double exchange.

The resistivity data of fig. 45(a) reflect the transitions T_{JT} , T_C , T_{OO} , and T_{OR} . On cooling, the step increase at T_{JT} shows the transition changes from second-order for $x = 0.12$ and 0.13 to first-order at $x = 0.14$ where it approaches T_C . This change is also evident in the specific-heat anomaly of fig. 44. Rozenberg et al. (1994) have predicted that such a change should occur at a transition from localized to itinerant electronic behavior. The resistivity drops on cooling through T_C as a result of reduction of the spin-disorder scattering; it increases abruptly on cooling through the first-order transition at T_{OO} in the $x = 0.11$ and 0.12 samples. By $x = 0.14$, the transition at T_{OO} is no longer first-order and is only marked by a smooth minimum in $\rho(T)$. For $x > 0.15$, the minimum in $\rho(T)$ at T_{OO} is less sharp and drops sharply with increasing x . Moreover, the metallic conductivity in the interval $T_{OO} < T < T_C$ changes abruptly from vibronic to itinerant; a pressure experiment on a single-

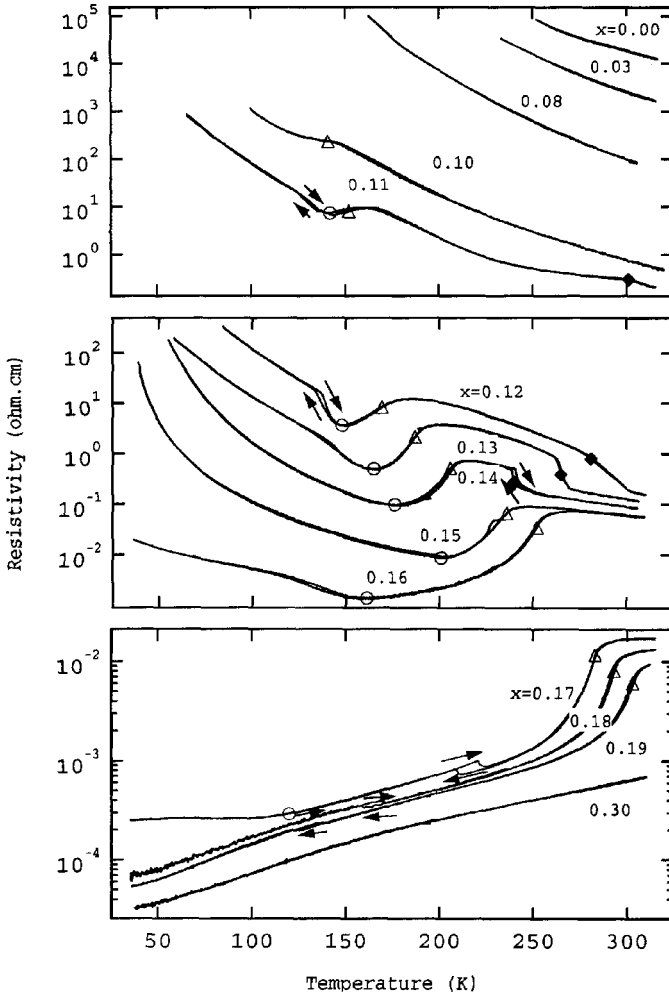


Fig. 45. (a) Resistivity vs. temperature for melt-grown single-crystal samples of $\text{La}_{1-x}\text{Sr}_x\text{MnO}_3$. Critical points; $\blacklozenge = T_{JT}$ where $|d\rho/dT|$ is a maximum; $\triangle \approx T_f$ or T_C where $d\rho/dT$ is a maximum; $\circ = T_{OO}$ where $\rho(T)$ is a local minimum. T_{OR} = midpoint of thermal hysteresis below T_C for $0.17 \leq x \leq 0.19$. Arrows indicate heating and cooling at thermal hysteresis loops, after G.-L. Liu et al. (2001).

crystal $x = 0.14$ sample (Zhou and Goodenough, 2000) showed the transition from vibronic to itinerant electronic behavior is first-order, which conforms to prediction from the virial theorem of eq. (19), see fig. 45(b). Although the FI phase below T_{OO} changes character on crossing the vibronic-itinerant electronic transition in the O^* phase, becoming more conductive in the range $0.15 < x < 0.17$ where the temperature of the transition from FI to ferromagnetic metal (FM) decreases with increasing x , nevertheless a spinodal segregation into FI and FM phases at this first-order transition was only detected in pressure measurements made on a single-crystal $x = 0.16$ sample (Zhou et al., 2001b). In the interval $0.13 \leq x \leq 0.15$, the FV to FI transition occurs over an extended temperature interval where the magnetic-exchange driving force for orbital order is sharply reduced at a ferromagnetic-ferromagnetic transition.

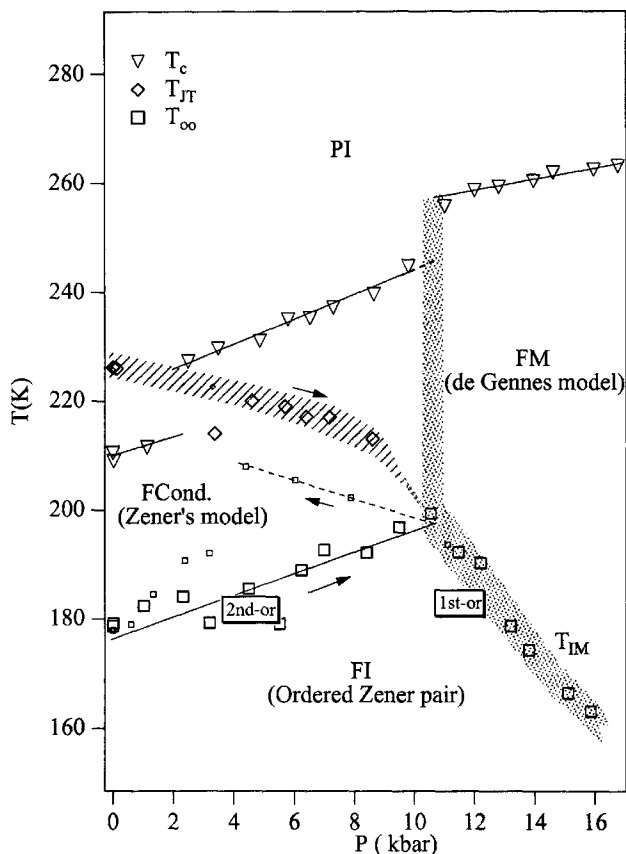


Fig. 45. (b) Pressure-temperature phase diagram below room temperature for $\text{La}_{0.86}\text{Sr}_{0.14}\text{MnO}_3$, after Zhou and Goodenough (2000).

The CMR phenomenon, not indicated in fig. 43, occurs above T_C in the O' phase; it is largest at $x \approx 0.12$ where isolated FV O^* clusters in a paramagnetic O' matrix grow to beyond percolation in an applied magnetic field. This evolution with x of physical properties bears a striking resemblance to that which occurs with δ in the $\text{LaMnO}_{3+\delta}$ samples. Uhlenbruch et al. (1999) and Nojiri et al. (1999) have shown that the FI phase below T_{OO} is stabilized relative to the FV phase by an applied magnetic field as can be expected for an exchange-driven transition. Senis et al. (1998) and Martínez et al. (2000) report that the FI phase is also stabilized by pressure whereas the FI phase in the $\text{LaMnO}_{3+\delta}$ system was suppressed by pressure. This observation signals that the charges are more localized in the FI phase of $\text{LaMnO}_{3+\delta}$.

The data of fig. 43 reveal three distinguishable ferromagnetic phases: FV, FI, and FM. The ferromagnetic interactions in the FV phase are composed of vibronic superexchange supplemented by Zener double exchange; the interactions in the FM phase may be classified as de Gennes double exchange. Those in the (001) planes of the FI phase appear to be conventional superexchange interactions whereas those along the c -axis CDWs are unconventional.

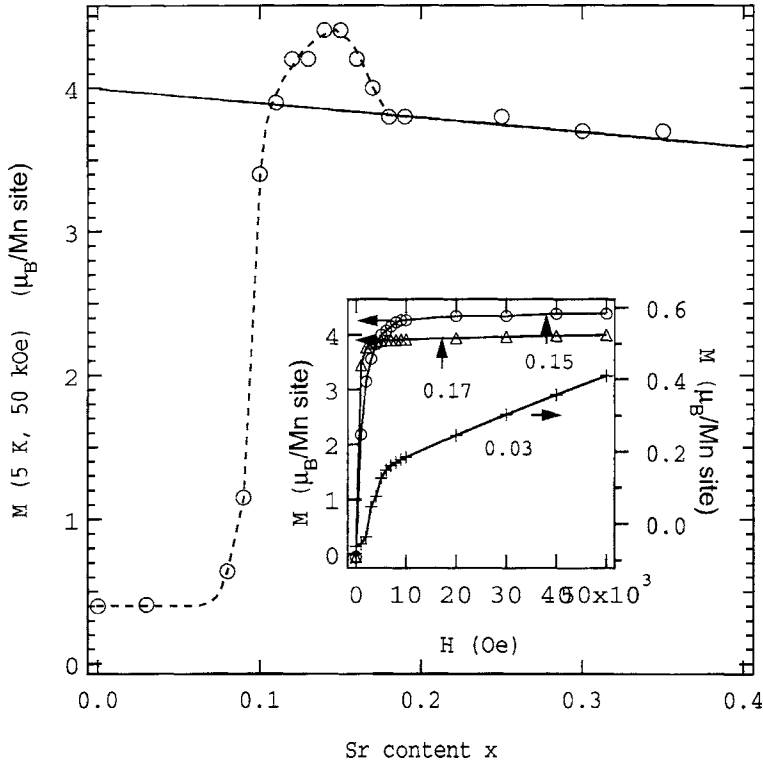


Fig. 46. Magnetization at 5 K in 50 kOe for $\text{La}_{1-x}\text{Sr}_x\text{MnO}_3$, $0 \leq x \leq 0.35$. Solid line: $(4-x)\mu_B/\text{Mn}$. Dashed line is a guide to the eye. Inset: M (5 K) vs. applied magnetic field, after G.-L. Liu et al. (2001).

Figure 46 shows the evolution with x of the magnetization at 5 K in 50 kOe. The abrupt change from canted-spin to frustrated ferromagnet at $x = 0.10$ is dramatic. Significant also is the observation that the saturation magnetization M (5 K, 50 kOe) has the spin-only theoretical value $M_S = (4-x)\mu_B/\text{Mn}$ for the FM phase $x \geq 0.18$, but it is larger in the O'' phase in the range $0.11 < x < 0.18$, reaching a maximum value of $4.4\mu_B/\text{Mn}$ at $x = 0.15$. This enhancement of the saturation magnetization is unique to the O'' phase of the $\text{La}_{1-x}\text{Sr}_x\text{MnO}_3$ system; it has not been observed in the $\text{La}_{1-x}\text{Ca}_x\text{MnO}_3$ system where the insulator O'' phase does not occur. Although the orbital angular momentum is quenched in lowest-order perturbation theory at both Mn(III) and Mn(IV) in octahedral sites, the data indicate that where the Mn(III) e electrons are localized, an orbital contribution to the atomic moment is introduced by higher-order terms; where the electrons of e -orbital parentage are itinerant, the orbital contribution is suppressed. The orbital contribution is progressively suppressed as the mean hole mobility in the O'' phase increases with x in the range $0.15 < x < 0.18$.

Neutron-scattering experiments by Vasiliu-Doloc et al. (1998a) on an $x = 0.15$ sample showed the ferromagnetic order below $T_C = 235$ K developed a canted-spin structure below

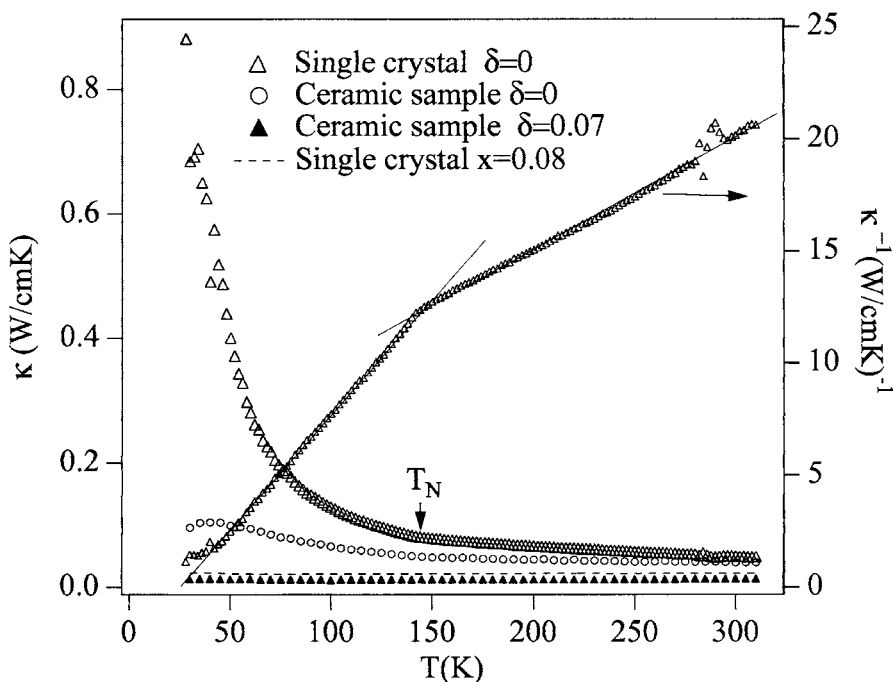


Fig. 47. Temperature dependence of the thermal conductivity $\kappa(T)$ for selected single-crystal compositions of the system $\text{La}_{1-x}\text{Sr}_x\text{MnO}_3$. (a) $x = 0, 0.08$ and $\text{LaMnO}_{3+\delta}$ ($\delta = 0$ and 0.07); the lines in κ^{-1} vs. T for $x = 0$ are linear fitting.

a $T_{CA} = 205$ K. Pressure experiments on an $x = 0.14$ single crystal showed a first-order jump in T_C where T_{JT} crosses T_C at about 2 kbar (Zhou and Goodenough, 2000) see fig. 45(b); at ambient pressure the two ferromagnetic phases would have $T_C \approx 205$ K and 235 K on either side of the transition at T_{JT} . Therefore, the change at 205 K may be attributed to crossing T_{JT} in a phase a little more hole rich than $x = 0.14$. The long-wavelength magnetic excitations were conventional spin waves, but an anomalously strong quasielastic component developed at small wave vector above about 200 K where the two magnetic phases coexist. Asamitsu et al. (1995, 1996) have shown that an $x = 0.170$ sample can be switched from the O^* -orthorhombic to the R-rhombohedral structure by the application of an external magnetic field; the switching is reversible or irreversible depending on the temperature. Campbell et al. (1997) have confirmed the phenomenon on a single-crystal $x = 0.165$ sample with neutron diffraction. The $x = 0.17$ composition sits in the FI-FM two-phase region.

The temperature dependence of the thermal conductivity for selected single-crystal compositions over the range $0 \leq x \leq 0.12$ are shown in fig. 47 (Zhou and Goodenough, 2001a, 2001b). They were chosen to probe the changes occurring on crossing the several phase transitions shown in fig. 43. Whereas the $x = 0$ compound exhibits a strong phonon component, $\kappa(T)$ is strongly suppressed at all temperatures in the $x = 0.08$ samples where holes, partic-

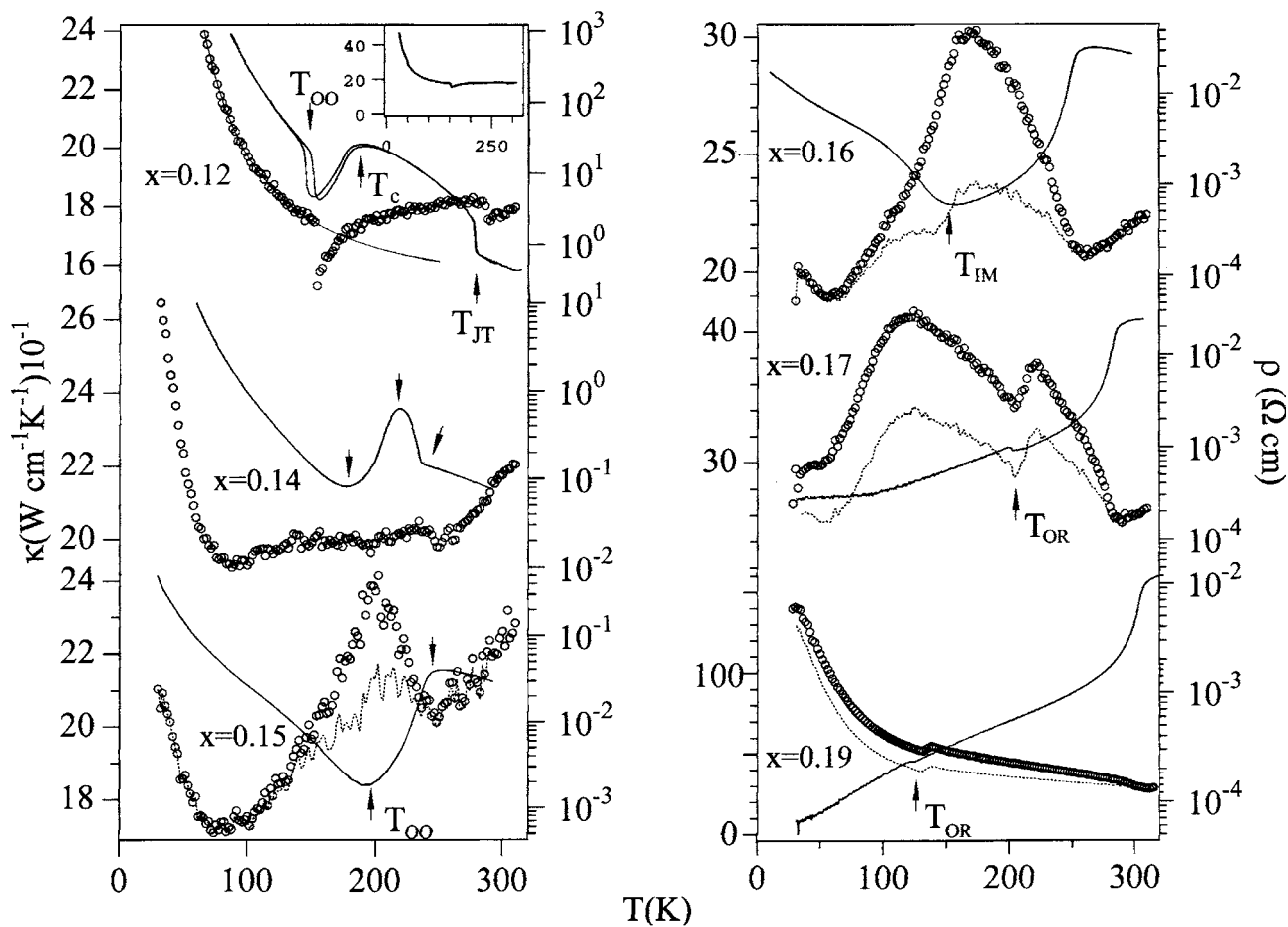


Fig. 47. (b) $x = 0.12, 0.14, 0.15, 0.16, 0.17, 0.19$: open circles for $\kappa(T)$, dashed line is $\kappa - \kappa_e$ where the electronic component κ_e was obtained from the Wiedermann-Franz Law, solid line is for resistivity $\rho(T)$, after Zhou and Goodenough (2001a).

ularly mobile holes, introduce orbital fluctuations that eliminate the phonon contribution. In the $x = 0.12$ sample, $\kappa(T)$ is extremely small in the O^* phase above T_{OO} ; there is only a small increase in $\kappa(T)$ on cooling through T_{JT} where the orbital disorder changes from 3D to 2D on entering the O' phase above T^* and there is a smooth decrease on cooling through T_C where two-phase fluctuations and vibronic superexchange retain Mn–O bond-length fluctuations. However, on cooling through the first-order transition at T_{OO} , a phonon contribution to $\kappa(T)$ is restored as a result of orbital and charge ordering in the FI phase. The $x = 1/8$ phase below T_{OO} appears to have a charge commensurability; where the transition at T_{OO} is second-order ($0.14 \leq x \leq 0.16$), the phonons are only restored at the lower transition temperature T_{LO} of fig. 43 where charge commensurability probably occurs. In the $x = 0.14$ sample, a $T_{JT} \approx T_C$ masks the jump in $\kappa(T)$ on cooling through T_{JT} . In the $x = 0.16$ sample, $\kappa(T)$ is suppressed in the orbitally fluctuating O^* phase above T_C , but it increases on cooling through T_C into the FM phase where the electrons become itinerant rather than vibronic. However, on cooling through the insulator-metal transition at T_{IM} , $\kappa(T)$ is again suppressed, which contrasts with cooling through T_{OO} in $x = 0.12$. In the $x = 0.17$ crystal, spin-lattice interactions suppress $\kappa(T)$ above T_C , see fig. 19 (Zhou and Goodenough, 2002a); the decrease in $\kappa(T)$ on cooling below 110 K is due to the appearance of two-phase fluctuations, see fig. 43. There is also a drop in $\kappa(T)$ on cooling through T_{OR} ; the rhombohedral phase does not support any orbital fluctuations within the metallic matrix. Note the change of scale for the $x = 0.19$ crystal where $\kappa(T)$ exhibits a strong phonon component below T_C . These data demonstrate the utility of monitoring $\kappa(T)$ to determine the existence of bond-length fluctuations.

Figure 48 extends the phase diagram of $\text{La}_{1-x}\text{Sr}_x\text{MnO}_3$ to include the region $0.2 \leq x \leq 1.0$. Optical studies of the ferromagnetic ground state of single-crystal samples with $0.15 \leq x \leq 0.4$ have revealed that the low-energy optical conductivity changes with decreasing x from Drude-like for $x > 0.2$ to incoherent broad features for $x < 0.2$ with spectral weight transferred to the mid-infrared region (Saitoh et al., 2000). Temperature-dependent reflectivity spectra on a single-crystal $x = 0.175$ sample showed a crossover with decreasing temperature from incoherent to coherent behavior (Takenaka et al., 1999, 2000). Analysis of the relaxation of the uniform-precession magnons into other spin-wave modes in an electron-spin-resonance (ESR) experiment on $x = 0.33$ samples did not require the introduction of magnetocrystalline anisotropy or chemical inhomogeneities; the data could be fit to a model in which the relaxation was due to demagnetizing fields at pores or between grains in polycrystalline materials or from surface irregularities in single crystals (Rivadulla et al., 1999b). Vasiliu-Doloc et al. (1998b) have used cold-neutron triple-axis measurements of single-crystal $x = 0.2$ and 0.3 samples to investigate the long-wavelength spin dynamics. They found that both systems behave like isotropic ferromagnets at low temperatures. However, an anomalously strong quasielastic central peak develops and dominates the fluctuation spectrum as $T \rightarrow T_C$. It appears that the coexistence of spin-wave excitations and spin diffusion is a common characteristic in manganese-oxide perovskites and may be related to phase fluctuations responsible for the CMR phenomenon. These data are consistent with earlier studies of the magnetization $M(T)$ in the FM phase near $x = 0.3$ that showed a decrease of $M(T)$ with increasing temperature compatible with spin-wave excitations (Smolyaninova et al., 1997) but the spin dynamics near T_C showed evidence of strong electron-lattice interactions (Fernández-

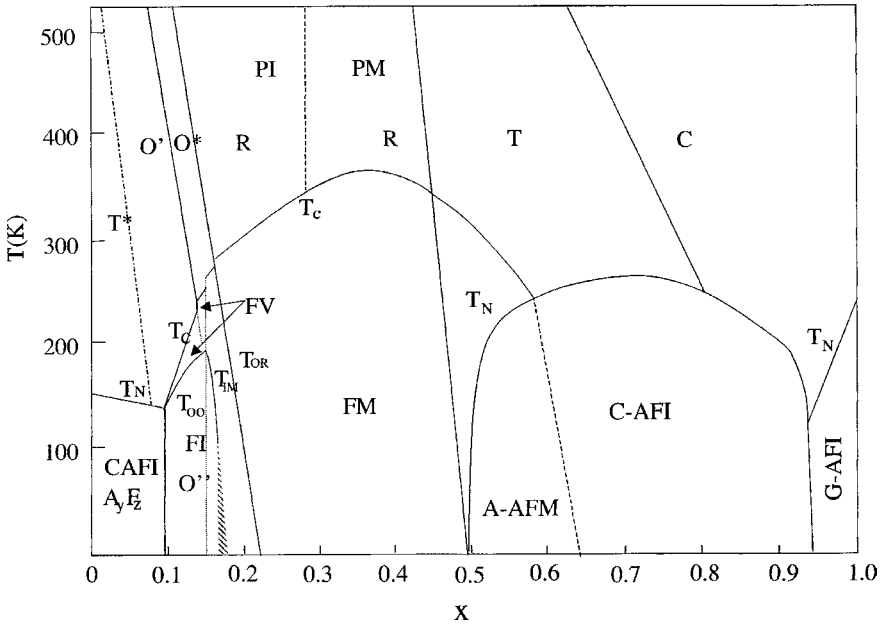


Fig. 48. Phase diagram of $\text{La}_{1-x}\text{Sr}_x\text{MnO}_3$, $0 \leq x \leq 0.7$, after Zhou and Goodenough (2001a); B. Dabrowski (private communication).

Baca et al., 1998). The volume of an $x = 0.3$ sample showed a smooth contraction on cooling through T_C (Martin et al., 1996).

Several research groups place the boundary between the FM and AFM phases beyond $x = 0.5$; this boundary varies sensitively with the method of sample preparation. Fujishiro et al. (1998) place it in the range $0.48 < x < 0.50$. As discussed in more detail in sect. 3.7, several phases compete with one another in the $\text{R}_{0.5}\text{A}_{0.5}\text{MnO}_3$ samples ($R = \text{lanthanide}$, $A = \text{alkaline earth}$), the more stable varying with the tolerance factor t . In the $\text{R}_{1-x}\text{Sr}_x\text{MnO}_3$ system, a relatively large tolerance factor stabilizes a competition between the FM phase with 3D itinerant electrons and a type-A AFM phase in which the occupied e orbitals become ordered into the (001) planes to give 2D itinerant electrons in these planes and antiferromagnetic superexchange coupling between planes as in the type-A (CAFI) insulating phase in LaMnO_3 . Dho et al. (2001) investigated the thermal hysteresis of magnetization and resistivity at T_N in the range $0.5 \leq x \leq 0.6$. They observed a normal counter-clockwise hysteresis (T_N higher on heating, lower on cooling) for the magnetic transition, but the resistivity $\rho(T)$ showed an anomalous clockwise thermal hysteresis in the compositional range where a $T_N < T_C$ is found. From these experiments, it is apparent that a two-phase region extends either side of the magnetic AFM-FM transition temperature T_N .

As the tolerance factor increases with x to $t = 1$, the room-temperature symmetry changes from orthorhombic to rhombohedral to tetragonal to cubic. With $x \geq 0.8$, a $t > 1$ stabilizes a

hexagonal polytype, but the cubic phase may be obtained by quenching a reduced $\text{LaMnO}_{3-\delta}$ to room temperature and then oxidizing at lower temperatures. A type-C antiferromagnetic order reported for the range $0.65 < x < 0.95$ includes two-phase regions on either sides of a narrower single phase, but the boundaries of the fluctuating two-phase regions have not been mapped. The type-C antiferromagnetic order, table 1, consists of ferromagnetic Mn–O–Mn chains along the c -axis with antiferromagnetic coupling between the chains. This type of magnetic order reflects an ordering of the e electrons into a 1D c -axis majority-spin σ^* band below T_N that is occupied by $(1 - x)$ electrons per formula unit; the 1D band may support a charge-density wave.

3.6. The system $\text{La}_{1-x}\text{Ca}_x\text{MnO}_3$

The relative stabilities of the competing phases in the manganese-oxide perovskites depend critically on the tolerance factor t , which is smaller in the $\text{La}_{1-x}\text{Ca}_x\text{MnO}_3$ system than in $\text{La}_{1-x}\text{Sr}_x\text{MnO}_3$. A smaller t generates a greater bending of the $(180^\circ - \phi)$ Mn–O–Mn bond, and the R-rhombohedral phase is only found at higher temperatures. The O^* –R transition temperature T_{OR} of the phase diagram of fig. 49 is taken from Uehara et al. (private communication) and Cheong and Chen (1998). Early studies of the properties of the system were plagued by a variable oxygen stoichiometry, particularly for compositions with smaller x . Dabrowski et al. (1999b, 1999c) have made a careful study of the conditions under which cation vacancies are formed and their influence on the physical properties of the $\text{La}_{1-x}\text{Ca}_x\text{MnO}_3$ system.

As in the $\text{La}_{1-x}\text{Sr}_x\text{MnO}_3$ system, the O' – O^* transition at T_{JT} decreases sharply with x . Although the disproportionation reaction occurring at T_{JT} in LaMnO_3 is retained at smaller values of x , it is found at a $T_{\text{D}} > T_{\text{JT}}$. Unlike the $\text{La}_{1-x}\text{Sr}_x\text{MnO}_3$ system, the concentration of mobile small polarons and the activation energy of their mobility change little at T_{JT} . Therefore, T_{JT} is not tracked by monitoring the resistivity, but by following the evolution with x of the O' – O^* structural transition or the associated specific-heat anomaly. The O^* phase is pseudocubic, but the $\text{MnO}_{6/2}$ octahedra are rotated ca. 20° about the b -axis (space group $Pbnm$) relative to the ideal cubic-perovskite structure (Faaland et al., 1998) and locally cooperative Jahn–Teller deformations sustain a $c/a \approx \sqrt{2}$. High-resolution neutron powder diffraction (Radaelli et al., 1996, 1997a; García-Muñoz et al., 1997) extended X-ray absorption fine structure (EXAFS) (Subías et al., 1998) and optical-conductivity spectra (Jung et al., 1998) have established the presence of dynamic distortions of the $\text{MnO}_{6/2}$ octahedra in the O^* phase above T_{C} and a dramatic suppression of these distortions in the ferromagnetic metallic (FM) phase below T_{C} .

Above T_N or T_{C} , the conductivity of the O' and O^* phases fit the adiabatic dielectric-polaron model $\alpha = (A/T) \exp(-E_a/kT)$ over the entire doping range (Worledge et al., 1998). However, thermoelectric-power data show that the charge carriers evolve from small polarons to two-manganese Zener polarons with increasing x (see discussion of fig. 31). These polarons are to be distinguished from the second phase into which they progressively condense on cooling as a result of a spinodal phase segregation into hole-rich ferromagnetic, vibronic (FV) clusters within a paramagnetic O' or O^* matrix. (These clusters are mistakenly referred to as conventional magnetic polarons in some of the literature.) The speckled area of fig. 49 denotes the spinodal region, but this region has not been systematically mapped by experiment.

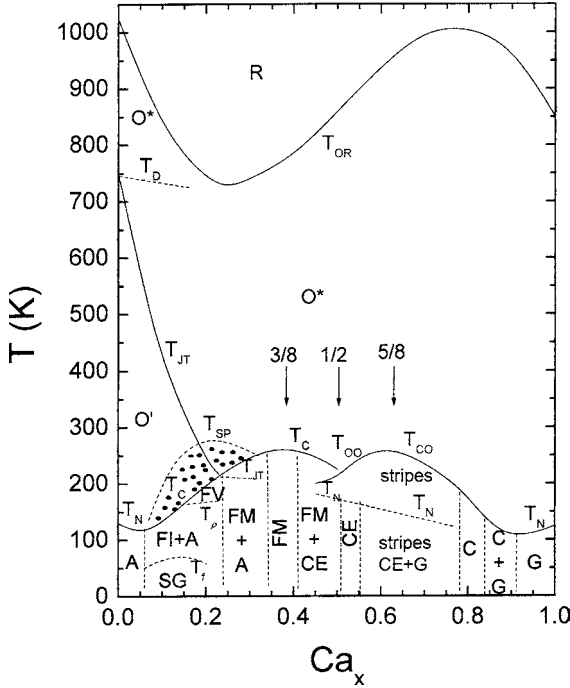


Fig. 49. Temperature - x phase diagram of $\text{La}_{1-x}\text{Ca}_x\text{MnO}_3$.

The hole-rich clusters grow with x and with decreasing temperature; and below a critical temperature $T_{sp} > T_N$ or T_C , they become superparamagnetic FV clusters. An external magnetic field stabilizes the FV phase relative to the paramagnetic matrix in the interval $T_C < T < T_{sp}$; and where the clusters grow to beyond percolation in the applied field, the resistance drops to give a “colossal negative magnetoresistance”, which is known as the CMR phenomenon. Moreover, the volume fraction of the FV phase grows to beyond percolation on cooling to a $T_C > T_N$, and a first-order phase change occurs at T_C due to a discontinuous increase in the volume fraction of the FV phase in the internal molecular field present below T_C . As the volume fraction of the FV phase at a given T grows with increasing x , T_C increases until the magnetic transition at T_C becomes second-order.

The initial substitution of Ca for La is charge-compensated by the introduction of Mn(IV) ions that, at lower temperatures, become trapped at one of the 8 nearest neighbors to a Ca^{2+} ion (Matsumoto, 1970b; Alonso et al., 2001). Elastic and inelastic neutron scattering have indicated that by $x = 0.05$, hole-rich ferromagnetic droplets form within the CAFI matrix with a correlation length $\xi \approx 8\text{--}10 \text{ \AA}$ (Hennion et al., 1997). Local ferromagnetic order only requires an inversion of the c -axis interactions within a droplet, which can occur for hole-rich droplets. The existence of ferromagnetic clusters within the CAFI O' matrix was found below T_N over the range $0.05 \leq x \leq 0.10$ with evidence that the phase segregation extends into the paramagnetic phase (Moussa et al., 1999). Direct evidence for phase segregation above as well as below T_C or T_N in the interval $0.05 \leq x \leq 0.3$ has also been found with Mössbauer

spectroscopy (Chechersky et al., 1997, 1999a, 2001; Nath et al., 2000; Hannover et al., 2000) and Mn K-edge EXAFS (Lanzara et al., 1998). Allodi et al. (1997, 1998a), Papavassiliou et al. (1999), and Dho et al. (1999a) have used ^{139}La and ^{55}Mn NMR to show the growth of the volume fraction of a ferromagnetic phase in the paramagnetic matrix with increasing x . Heffner et al. (2001) used muon-spin-relaxation measurements on a series of samples in the range $0 \leq x \leq 0.10$; fast relaxation rates were assigned to the ferromagnetic regions, which is consistent with FV behavior, and a slow Mn relaxation rate to the antiferromagnetic matrix. Markovich et al. (2002) employed several techniques on an $x = 0.18$ single crystal to demonstrate the existence of a ferromagnetic second phase both above and below T_C and growth of the ferromagnetic volume fraction not only in an applied magnetic field, but also under hydrostatic pressure. Hydrostatic pressure stabilizes the phase of smaller volume, which indicates the ferromagnetic phase has vibronic σ -bonding states, i.e., it is an FV phase, whereas the matrix contains localized electrons in orbitally ordered states. However, the CMR phenomenon only occurs where the volume fraction of the ferromagnetic FV phase approaches percolation in the paramagnetic phase and achieves percolation on cooling through a $T_C > T_N$ (Biotteau et al., 2001). On the other hand, Congeduti et al. (2001) found, with Raman spectroscopy from a polycrystalline $x = 0.25$ sample, an abrupt transition at ca. 7.5 GPa to an orbitally ordered phase, and Meneghini et al. (2002) monitored the resistance of the same sample to show that the transition prevents transformation under pressure from the FV to the FM phase. Although pressure increases the tolerance factor, the FM phase was not reached because pressure also stabilizes orbital order, but probably as an ordering of two-manganese Zener polarons as in the low-temperature O'' phase of the $\text{La}_{1-x}\text{Sr}_x\text{MnO}_3$ system. The transition to poorer conductivity at higher pressures was also noted by Okuda et al. (2000) and by J.-M. Li et al. (2001).

On cooling through T_C in the range $0.10 \leq x \leq 0.30$, there is a first-order volume contraction associated with a discontinuous increase in the volume fraction of the more conductive FV and FM phases (Radaelli et al., 1996; Huang et al., 1998) where electrons tunnel from Mn(III) to Mn(IV) neighbors in a time $\tau_h \leq \omega_0^{-1}$. In contrast, the transition from the paramagnetic phase to the CAFI phase at T_N is second-order with a smooth evolution of the volume. The charge carriers in the CAFI matrix remain polaronic. On cooling through T_C in the range $0.25 \leq x \leq 0.45$, the FV phase changes to the ferromagnetic metallic (FM) phase, but no study has been made of whether this transition is first-order as in $\text{La}_{1-x}\text{Sr}_x\text{MnO}_3$. However, Lynn et al. (1996), Erwin et al. (1997), and Dai et al. (2000) have used inelastic neutron scattering to study the evolution with temperature of the spin dynamics in the ferromagnetic phase; they found that the FM phase behaves as an ideal isotropic ferromagnet at low temperatures, but it develops an anomalous spin-diffusion component above ca. 200 K that progressively dominates the spin-fluctuation spectrum as the temperature increases to T_C . This behavior signals a transition from the FM toward the FV state as T increases to T_C . Dai et al. (2001) also studied the evolution of diffuse scattering from magnetic and lattice fluctuations in single-crystal $x = 0.15, 0.20$, and 0.30 compositions. The $x = 0.30$ sample showed an unambiguous transition to a FM phase on cooling through T_C whereas the $x = 0.15$ and 0.20 crystals exhibited a transition on cooling through T_C to a phase with strong electron-lattice interactions, which we identify with the FV phase. The FV-FM transition occurs near the crossover of T_{JT} and T_C

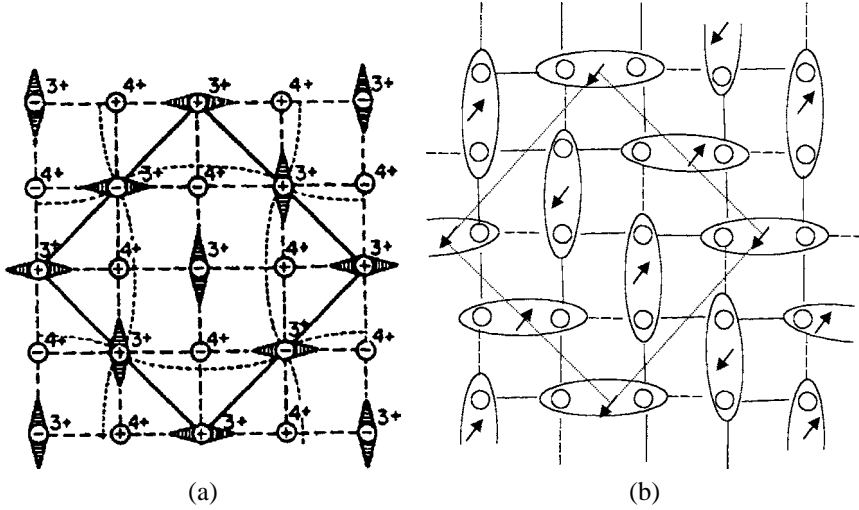


Fig. 50. Type-CE antiferromagnetic order in a - b planes; antiferromagnetic coupling above c -axis in space group $Pbnm$; (a) ordering of localized occupied e orbitals after Goodenough (1955), and (b) ordering of Zener polarons.

in the range $0.20 < x < 0.25$, which is at a higher x than in the $\text{La}_{1-x}\text{Sr}_x\text{MnO}_3$ as expected for smaller tolerance factor t .

As in the $\text{La}_{1-x}\text{Sr}_x\text{MnO}_3$ system, the percolating conductive FV matrix containing an antiferromagnetic second phase converts to a ferromagnetic-insulator (FI) phase below a T_{OO} in the compositional range $0.10 < x < 0.25$. A sound-velocity anomaly at T_{OO} and at T_{C} allows tracking of these temperatures vs. x (Fujishiro et al., 1999). Transport measurements (G. Zhao et al., 2000; Hong et al., 2001) have revealed polaronic conduction in the FI phase, but not in the FM phase.

The coexistence of two competing phases sensitive to light, to external magnetic or electric fields, and to pressure has led to many studies by a variety of techniques of the peculiar properties of samples in the range $0.10 \leq x \leq 0.35$ (Ilsavskii et al., 2001; Fisher et al., 2001; Gordon et al., 2000; Gordon et al., 2002; Cordero et al., 2002; Ren et al., 2001; Hudspeth et al., 2002; Zuo and Tao, 2001; Reutler et al., 2000; Raquet et al., 2000; Zhu et al., 1999; Hueso et al., 1999; Causa et al., 1998; Kumar et al., 2002; Lobad et al., 2001; Mayr et al., 2001; Yoon et al., 1998; Papavassiliou et al., 2001; Huhtinen et al., 2000; Yuzhelevski et al., 2001).

On the opposite side of the maximum in T_{C} vs. x at $x = 3/8$, the FM phase competes with a type-CE antiferromagnetic phase having the magnetic and charge order of fig. 50(a). In the range $0.4 < x \leq 0.5$, the FM and type-CE phases coexist (Moritomo, 1999). The phase diagram shows a $T_{\text{CO}} < T < T_{\text{C}}$. Here also an external magnetic field stabilizes the conductive FM phase relative to the type-CE antiferromagnetic-insulator (AFI) as is illustrated in fig. 51 for $\text{Nd}_{0.5}\text{Sr}_{0.5}\text{MnO}_3$ (Shimomura et al., 1999). The metamagnetism of the CE phase provides another type of CMR phenomenon.

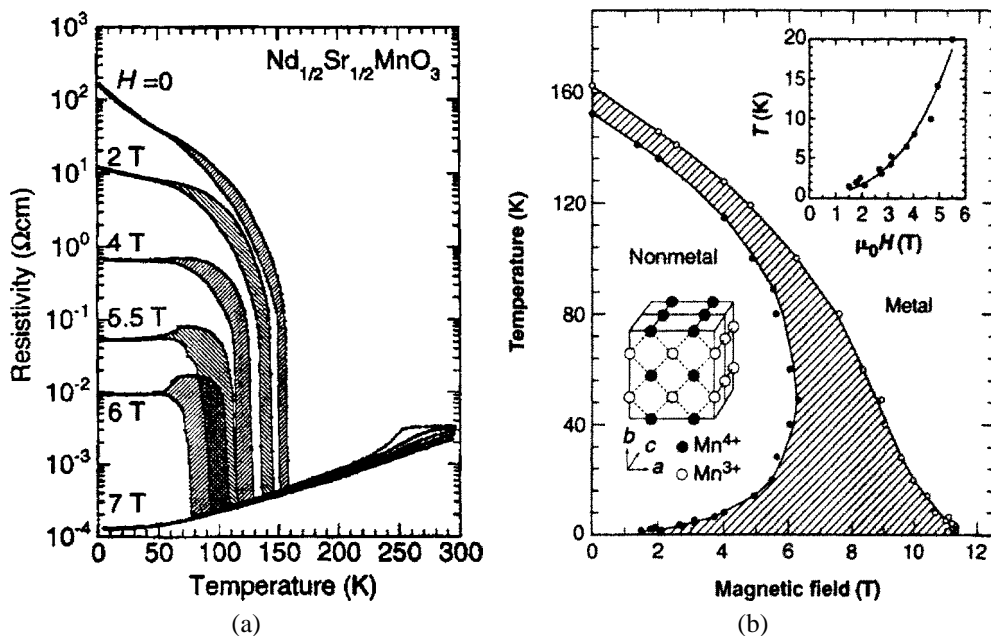


Fig. 51. (a) Temperature dependence of the resistivity $\rho(T)$ of $\text{Nd}_{0.5}\text{Sr}_{0.5}\text{MnO}_3$ under various magnetic fields. (b) Temperature-field phase diagram; after Shimomura et al. (1999).

Whereas the type-CE AFI phase competes with the FM phase in the range $0.4 < x \leq 0.5$ of $\text{La}_{1-x}\text{Ca}_x\text{MnO}_3$, reduction of the tolerance factor by substitution of Pr for La in $\text{La}_{5/8-x}\text{Pr}_x\text{Ca}_{3/8}\text{MnO}_3$ introduces already at small x a charge-ordered second phase (Kim et al., 2000a); $\text{Pr}_{5/8}\text{Ca}_{3/8}\text{MnO}_3$ undergoes charge ordering below a $T_{\text{CO}} \approx 225$ K that becomes an AFI phase below a $T_{\text{N}} \approx 175$ K (Dediu et al., 2000). In this sample, the Curie temperature of any FM minority phase is $T_{\text{C}} < T_{\text{CO}}$. The $(\text{La}_{1-y}\text{Pr}_y)_{0.67}\text{Ca}_{0.33}\text{MnO}_3$ system shows a similar percolation transition from a FM for $y = 0$ to an orbital and charge-ordered insulator for $y > 0.75$, see sect. 3.4; the volume fraction of the conductive, ferromagnetic phase grows on lowering the temperature (Kim et al., 2000a; Dediu et al., 2000; Uehara et al., 1999; Podzorov et al., 2000; Babushkina et al., 1999). Smolyaninova et al. (2002) have studied the influence of isotope exchange on a number of samples in the $\text{La}_{1-x}\text{Ca}_x\text{MnO}_3$ and $(\text{La}_{1-y}\text{Pr}_y)_{0.67}\text{Ca}_{0.33}\text{MnO}_3$ systems. The most prominent isotope shift of the transition temperatures is in the two-phase compositions; the two-phase fluctuations are thus shown to be accommodated by cooperative, dynamic oxygen displacements perpendicular and/or along the $(180^\circ - \phi)$ Mn–O–Mn bond axes.

The predicted charge and orbital ordering of fig. 50(a) for the CE phase (Wollan and Koehler, 1955; Goodenough, 1955) was thought to be fully corroborated (Radaelli et al., 1995, 1997b). However, as discussed in detail in sect. 3.7 for the $\text{R}_{0.5}\text{A}_{0.5}\text{MnO}_3$ compositions, it is necessary to distinguish the type-CE phase appearing below a $T_{\text{N}} \leq T_{\text{CO}} < T_{\text{C}}$

from that stabilized below a $T_N < T_{CO}$ where the Curie temperature for the competing FM phase is $T_C < T_{CO}$. Rivadulla et al. (2002) predicted that the charge and orbital ordering of fig. 50(a) occurs where there is a $T_{CO} > T_C$, but that the ferromagnetic zig-zag chains contain the two-manganese Zener pairs of fig. 50(b) where a dominant FM phase makes $T_C > T_{CO}$. $\text{La}_{0.5}\text{Ca}_{0.5}\text{MnO}_3$ has a $T_N \leq T_{CO} < T_C$, and a recent single-crystal neutron-diffraction study (Daoud-Aladine et al., 2002) has shown independently that indeed the CE phase below T_N contains the ordering of Zener polarons indicated in fig. 50(b). However, the competition in $\text{La}_{0.5}\text{Ca}_{0.5}\text{MnO}_3$ between the FM phase with $T_C > T_{CO}$ and the charge-ordered phase with $T_{CO} > T_C$ is made complicated by an extreme sensitivity of the critical temperatures and the respective volume fractions on the oxygen stoichiometry (Y.G. Zhao et al., 2002; Levy et al., 2000), the grain size of the polycrystalline samples (Levy et al., 2000; Freitas et al., 2002), and thermal cycling (Uehara and Cheong, 2000) as well as on the Ca concentration x . A variety of techniques have been used to characterize this situation.

Huang et al. (2000) examined with neutron diffraction three polycrystalline samples with $x = 0.47, 0.50,$ and 0.52 . They reported single-phase paramagnetic materials with a spinodal phase segregation occurring below a first-order orbital-ordering (OO) transition at $T_{OO} < T_C$. In the interval $T_{OO} < T < T_C$, the FM phase coexisted with a paramagnetic phase that underwent the first-order transition at T_{OO} . The $x = 0.47$ sample had a $T_C = 265$ K and a $T_{OO} = 230$ K. The OO phase had the smaller volume fraction, and the volume fraction of the FM phase increased on the formation of the OO phase. Below a Néel temperature $T_N = 160$ K of the OO phase, the diffraction peaks sharpened and the structure could be indexed as that of the type-CE AFI phase. The volume fraction of the FM phase remained 0.6 to lowest temperatures in the $x = 0.47$ sample; it decreased with increasing x , but was still present as a minority phase in the $x = 0.52$ sample. However, a diffraction experiment does not detect phase fluctuations that may be occurring in the paramagnetic phase above T_C . Kim et al. (2000b) noted a suppression of the conductivity $\sigma(T)$ and of the phonon component of the thermal conductivity as well as a broadening of the diffraction peaks to temperatures as high as 900 K, and Naler et al. (2002) used inelastic light scattering to show strong fluctuation effects persisting in an $x = 0.50$ sample to at least $2T_{OO}$. In another experiment, Kim et al. (2002) used optical spectroscopy to monitor the gap Δ that is opened at the Fermi energy by stabilization of the CE AFI phase. They found a $2\Delta/kT_{OO} \approx 30$ for $x = 0.5$ that decreased rapidly with increasing x even though T_{OO} had a broad maximum at about $x = 0.62$. They also noted that an optical pseudogap is present well above T_{CO} , setting in below a $T^* \approx 600$ K where independent evidence for phase fluctuations had been found. The existence of two-phase fluctuations persisting well into the paramagnetic temperature range appears to be well-established.

The coexistence of the two phases to lowest temperatures near $x = 0.5$ has also been demonstrated indirectly by ultrasonic sound velocity (Zheng et al., 2001) as well as by magnetization and conductivity measurements (Y.G. Zhao et al., 2002; Levy et al., 2000; Xiao et al., 1996; Schiffer et al., 1995; Roy et al., 1998, 1999) and more directly by ^{119}Sn and ^{57}Fe Mössbauer spectroscopies (Simopoulos et al., 2001; Kallias et al., 1999), electron diffraction (Chen and Cheong, 1996; Mori et al., 1998a), NMR (Dho et al., 1999b; Allodi et al., 1998b, 2000; Yoshinari et al., 1999; Papavassiliou et al., 1997), and infrared (Liu et al., 1998) spectroscopies. Mori et al. (1998a) showed that in their $x = 0.5$ sample the length scale of the two

phases increased on cooling from 100–120 Å at 200 K to 500–600 Å at 125 K before converting below 95 K to an OO type-CE AFI matrix. The critical magnetic field for conversion of the metamagnetic CE AFI phase to the FM phase was found to be about 8 T on increasing an external magnetic field H and 3 T on lowering the field (Freitas et al., 2002). Moreover, Huang et al. (2000) reported that the volume fraction of the FM phase increased more for a given H field if the sample was cooled in the magnetic field than if warmed in that field after cooling in zero field. Uehara and Cheong (2000) showed that the extent of the first-order conversion from one phase to another in an applied field depends on the rate of cooling or heating and on aging to relieve the internal stresses associated with the volume changes that occur; the phase transition is not martensitic. The electron-diffraction study of Chen and Cheong (1996) revealed domains of incommensurate charge ordering in the FM matrix in the range $T_{OO} < T < T_C$ with a first-order change at T_{OO} to long-range ordering of the commensurate OO phase below T_{OO} . The existence of two phases was not due to any inhomogeneity in the Ca-ion distribution and did not appear to be due to a segregation into hole-rich and hole-poor domains; it reflects a competition between orbital order and disorder similar to that found in $\text{LaMn}_{0.5}\text{Ga}_{0.5}\text{O}_3$. Dark-field images at 95 K showed CE domains a few thousand angstroms in diameter separated by twin boundaries parallel to a Mn–O–Mn bond axis. The OO phase was found (Smolyaninova et al., 1998) to have a large excess specific heat compared to the FM phase; this excess entropy can only originate from excitations of nonmagnetic origin. Application of a magnetic field of 8.5 T, which transformed the resistivity to a metallic temperature dependence, left the specific heat unchanged with no evidence of a kT term from mobile charge carriers. The mobile charge carriers apparently remain strongly coupled to the oxygen vibrations and therefore behave as vibrons. Further evidence of the strong electron coupling to the oxygen vibrational modes comes from $^{18}\text{O}/^{16}\text{O}$ isotope exchange, which increases T_{CO} of $\text{La}_{0.5}\text{Ca}_{0.5}\text{MnO}_3$ by 9 K in zero magnetic field (Zhao et al., 1999) and of $\text{Nd}_{0.5}\text{Sr}_{0.5}\text{MnO}_3$ by 21 K (Mahesh and Itoh, 1999). Raman spectra show an anomalous softening of the 494 cm^{-1} and 604 cm^{-1} modes below T_{CO} (Granado et al., 1998).

The two-manganese Zener polarons appear to order in a charge-ordered (CO) phase in the range $0.5 < x \leq 0.75$. Mori et al. (1998a, 1998b) have observed in thin films planes of a $\text{La}_{0.5}\text{Ca}_{0.5}\text{MnO}_3$ -type phase alternating with planes of a CaMnO_3 -type phase, see fig. 52, in a series of $x = n/(n + 2)$ planes, where n is the number of Mn(IV) planes in the CaMnO_3 slab. On the other hand, high-resolution synchrotron X-ray and neutron powder diffraction on bulk $x = 0.67$ samples suggested an ordering of Mn^{3+} ions separated as far apart as possible in the basal planes (Radaelli et al., 1999; Fernández-Díaz et al., 1999); however, such a “Wigner crystal” model is inconsistent with the formation of Zener polarons, which can be accommodated in the model of Mori et al. (1998a, 1998b).

The superlattice reflections of the CO phase for $x = 0.80$ were noticeably broader than those of the lower- x compositions (Chen and Cheong, 1996; Chen et al., 1997; Li et al., 1999). Therefore Pissas et al. (2002) used powder neutron diffraction to study whether charge ordering was actually present in $x = 0.80$ and 0.85 samples. They found a transition from the O^* -orthorhombic paramagnetic phase to a monoclinic $P2_1/n$ antiferromagnetic phase containing two distinguishable Mn sites below a $T_N = T_{OO} = 210\text{ K}$ for $x = 0.80$ and 160 K for $x = 0.85$; the low-temperature data showed ferromagnetic Mn–O–Mn chains coupled antipar-

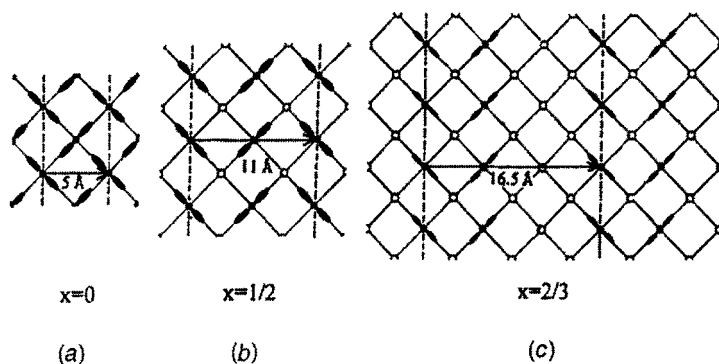


Fig. 52. Charge and orbital ordering in the orthorhombic basal plane for (a) $x = 0$, (b) $x = 0.5$ for localized e orbitals, and (c) Mori et al. (1998a, 1998b) model for $x = 2/3$.

allel to one another (type-C antiferromagnetic order of table 1) with the magnetic moment of ca. $2.5\mu_B$ oriented along the chains. They found no evidence of charge ordering as Mn(III) ions, but the magnetic order signals an ordering of the e electrons into the ferromagnetic chains. A contraction of the Mn–O bonds along the ferromagnetic chains on cooling through T_N implies, therefore, an ordering of the e electrons along the c -axis above T_N ; the contraction can then be understood from the virial theorem if the transition at T_N involves a transition from localized e to 1D itinerant σ_{\parallel}^* electrons along the chains; these electrons appear to stabilize, in addition, a commensurate charge-density wave. The reduction in the magnitude of the measured magnetic moment on the Mn atoms is characteristic of antiferromagnets.

3.7. $R_{0.5}A_{0.5}MnO_3$

The $R_{0.5}A_{0.5}MnO_3$ compositions with $A =$ alkaline earth have a fixed ratio Mn(IV)/Mn(III) = 1, but it is possible to pass from localized to itinerant electronic behavior on the MnO_3 array by varying the mean size of the A -site cations and hence the geometric tolerance factor t . In this family, the evolution of the competing phases at the crossover tolerance factor $t = t_c$ is made complex by the existence of charge and orbital ordering of localized electrons competing with ordering of Zener pairs in the crossover region $t = t_c \pm \Delta t$. In addition, an orbital ordering at $t = t_c + \Delta t'$ constrains itinerant σ^* electrons to the (001) planes to give a type-A antiferromagnetic metallic (AFM) phase that competes with ordering of Zener pairs in a type-CE AFI phase on one side and a FMM phase on the other side that has 3D itinerant σ^* electrons.

Several groups have presented temperature vs. tolerance factor phase diagrams (Rivadulla et al., 2002; Kuwahara and Tokura, 1998; Rao et al., 1998; Damay et al., 1999; Krupicka et al., 1999). Kuwahara and Tokura (1998) and Rivadulla et al. (2002) had stoichiometric single-crystal data and were the only groups to recognize the existence of a critical tolerance factor t_c separating localized from itinerant electronic behavior; their two phase diagrams are shown in fig. 53. Tokura et al. (1996) were also the first to report the existence of a narrow, ferromag-

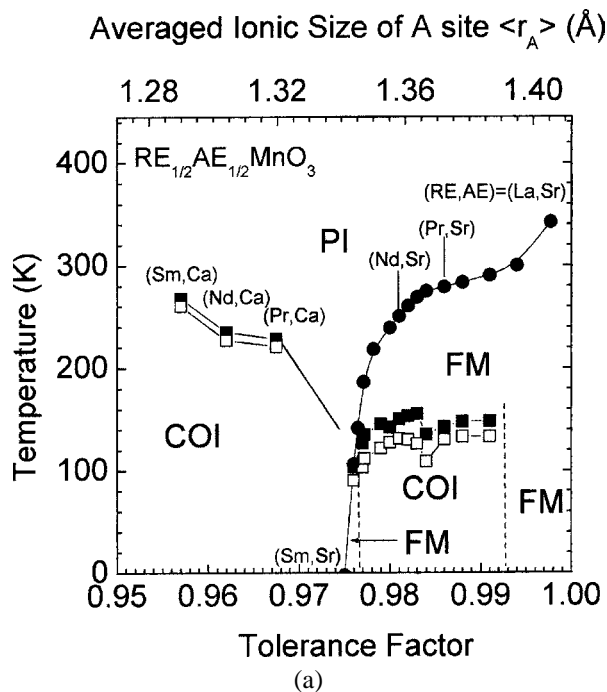


Fig. 53. Temperature-tolerance factor phase diagrams for $R_{0.5}A_{0.5}MnO_3$ from (a) Kuwahara and Tokura (1998), and (b) Rivadulla et al. (2002). In (a), PI = paramagnetic insulator, COI = charge-ordered insulator, FM = ferromagnetic metal. In (b), SP = superparamagnetic, SRCO = short-range charge-ordered fluctuations, I = CE AFI of figs. 50(a) and 52(b), II = ferromagnetic metal (FMM), FMV = ferromagnetic vibronic, PM = paramagnetic, III = CE AFI of figs. 50(b) and 57, IV = Type-A antiferromagnetic metal (AFM), V = FMM; shaded boundaries are estimates.

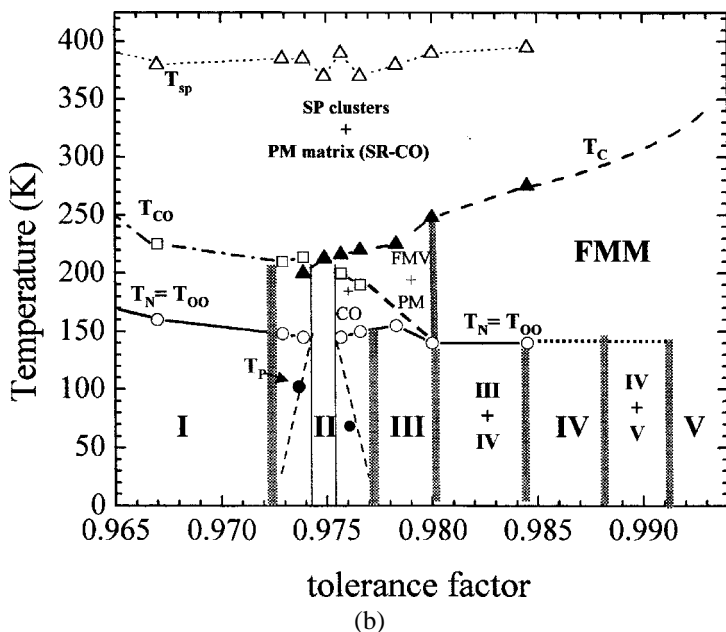


Fig. 53. Continued.

netic metallic (FMM) phase inserted between two antiferromagnetic type-CE insulator phases that they identified as COI in their diagram. They made no distinction between the two COI phases as they assumed the type-CE antiferromagnetic order necessarily implied a charge ordering as Mn(III) and Mn(IV) ions. Therefore, they considered the FMM phase to represent a metastable state appearing at a quantum critical point (QCP) where two-phase fluctuations suppress not only charge order (CO), but also orbital order (OO) and magnetic order. But such a critical point occurs at a crossover from localized to itinerant electronic behavior, so the assumption that the two CE AFI phases either side of $t = t_c$ both contain CO turns out to be invalid. Burgy et al. (2002) have modeled the QCP behavior by introducing quenched disorder into the Hamiltonian describing the competition between the COI and FMM phases. Rivadulla et al. (2002) chose to study the system $\text{Pr}_{0.5}(\text{Ca}_{1-x}\text{Sr}_x)_{0.5}\text{MnO}_3$ having a smaller variance σ^2 of the A-site-cation sizes; they found a stable FMM phase of larger volume at the critical tolerance factor t_c .

We interpret the more complete phase diagram of fig. 53(b) within the framework of a transition from localized to itinerant electronic behavior in the range $0.972 < t < 0.992$ that includes $t = t_c \approx 0.975$. (We calculate t using 12-fold coordination of the A-site cations.) Although such a transition is first-order in accordance with deduction from the virial theorem, nevertheless orbital ordering and cooperative bond-length adjustments allow it to occur in steps, beginning with the formation of molecular orbitals within two-Mn Zener polarons, transforming next to 1D metallic chains and then to 2D metallic planes before 3D itinerant-electron behavior is achieved. In the $\text{R}_{0.5}\text{A}_{0.5}\text{MnO}_3$ family, the 1D itinerant-electron chains are replaced by a charge-density-wave zig-zag chain of ordered Zener polarons.

Above T_{sp} of fig. 53(b), the paramagnetic susceptibility has Curie–Weiss behavior with a Weiss constant $\theta > 250$ K, which is indicative of ferromagnetic exchange interactions where there are orbital fluctuations and/or Zener double exchange. A deviation of the susceptibility from Curie–Weiss behavior on cooling below T_{sp} is characteristic of short-range ferromagnetic order or the onset of superparamagnetism. The thermoelectric-power data $\alpha(T)$ indicate the presence of about 20% two-Mn Zener polarons, which would have a strong ferromagnetic double-exchange coupling within a pair. We therefore conclude that ferromagnetic order within Zener polarons gives rise to superparamagnetism below T_{sp} . This phenomenon is characteristic of all compositions in a range of t spanning the critical tolerance factor $t_c \approx 0.975$.

On cooling samples with $t < 0.972$, a charge-ordering transition occurs at $T_{\text{CO}} \approx 225$ K; an orbital ordering below T_{OO} is accompanied by the onset of type-CE antiferromagnetic order below a $T_{\text{N}} = T_{\text{OO}} \approx 160$ K. In this phase I of fig. 53(b), a CO of Mn(III) and Mn(IV) ions breaks up the Zener pairs to stabilize localized electrons. Therefore, the orbital and charge ordering of this CE AFI phase is expected to have the classical (Goodenough, 1955) localized-electron order of fig. 50(a). Samples with $t \geq 0.992$ are metallic ferromagnets (FMM) below T_{C} to lowest temperatures, phase V. Between phases I and V there is a transition from localized to itinerant electrons of e-orbital parentage.

The transition temperatures T_{CO} for the CO phase and T_{C} for the FM phase cross at the critical tolerance factor $t_c \approx 0.975$ where a unique FMM phase II appears. As can be seen in fig. 54, the room-temperature volume of phase II is larger than anticipated for a smooth evolution of unit-cell volume with increasing t ; at $t = t_c$ with $\text{Mn(IV)}/\text{Mn(III)} = 1$, A-cation

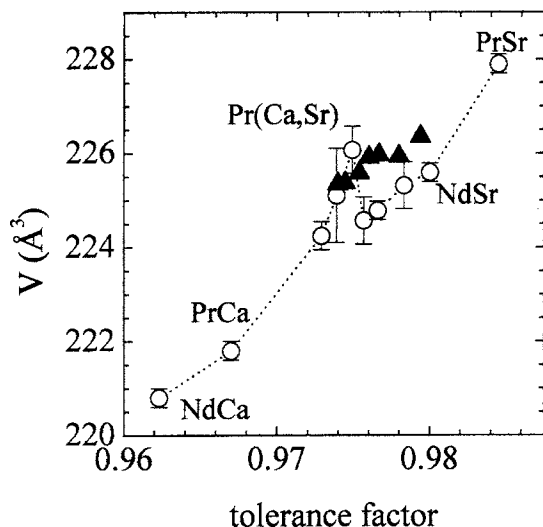


Fig. 54. Evolution of the room-temperature volume vs. tolerance factor of single-crystal $\text{Pr}_{0.5}(\text{Ca}_{1-x}\text{Sr}_x)_{0.5}\text{MnO}_3$ (open circles) after Rivadulla et al. (2002), and $(\text{Nd}_{1-x}\text{Sm}_x)_{0.5}\text{Sr}_{0.5}\text{MnO}_3$ (closed triangles) after Kuwahara et al. (1997).

displacements apparently stabilize a larger volume so as to straighten the Mn–O–Mn bond angle sufficiently to give an effective tolerance factor $t_{\text{eff}} \geq 0.992$. Comparison of figs. 53(a) and (b) shows that a larger variance σ^2 of the A-site-cation size suppresses T_C of phase II and, indeed, may suppress all order to lowest temperatures. Rivadulla et al. (2002) have shown that small deviations from unity of the Mn(IV)/Mn(III) ratio and hydrostatic pressure also suppress phase II.

Near $t = 0.980$, there is a discontinuous change in T_C ; by analogy with the transition at $x = 0.15$ in $\text{La}_{1-x}\text{Sr}_x\text{MnO}_3$, this discontinuity probably represents a change from vibronic to itinerant electronic behavior in the ferromagnetic phase, i.e., FMV to FMM. Vibronic conduction occurs where there are cooperative bond-length fluctuations associated with the coexistence of two phases, a minority paramagnetic (PM) phase that undergoes a CO transition below T_{CO} and a majority FMV phase having a $T_C > T_{\text{CO}}$. The FMM phase II appearing at $t = t_c$ is single-phase.

On lowering the temperature in the range $0.980 < t < 0.992$, the FMM phase transforms completely, or partially, to a type-A antiferromagnetic metallic (A AFM) phase IV in which orbital order constrains itinerant σ^* electrons and de Gennes double exchange to the (001) planes; the interactions between (001) planes are antiferromagnetic by $t^3\text{--O--}t^3$ superexchange as occurs in LaMnO_3 where all the 3d electrons at Mn(III) remain localized.

In the range $0.972 < t < 0.980$, the competition between stable phases is greatest; this competition results in the coexistence of two fluctuating phases. The phase fluctuations may suppress all long-range order at $t = t_c$ or, if the atomic displacements become static, may stabilize a unique single phase having 3D itinerant electrons of e-orbital parentage in a single FMM phase, phase II. The suppression of all long-range order corresponds to QCP behavior. QCP behavior or the appearance of phase II of larger volume at $t = t_c$ occurs at the crossover from a minority FMV phase in a majority CO matrix to a minority CO phase in a majority

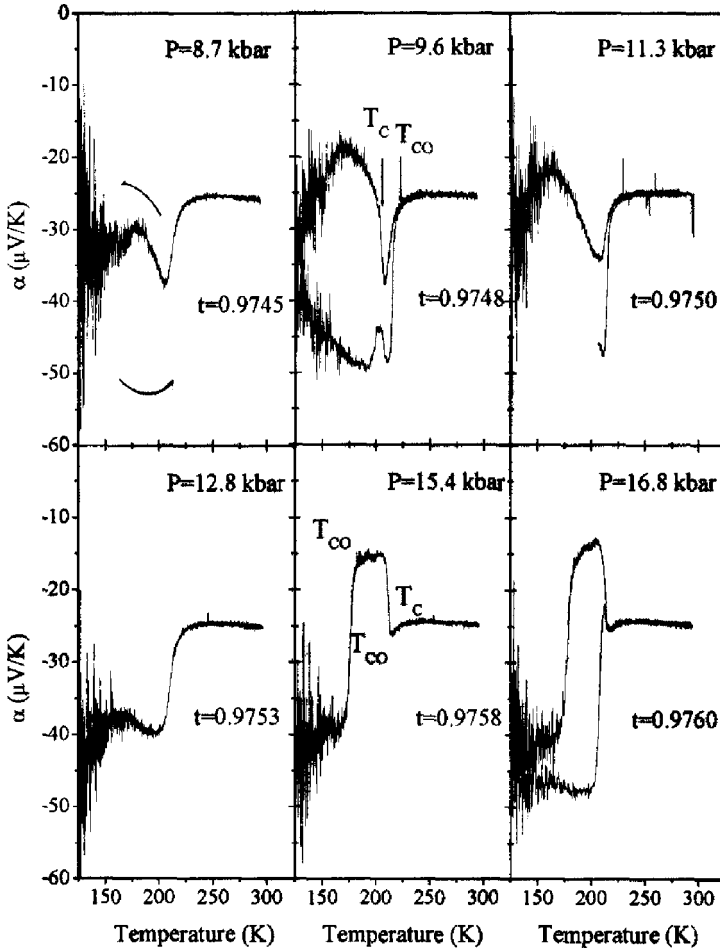


Fig. 55. Effects of hydrostatic pressure on the temperature dependence of the thermoelectric power $\alpha(T)$ for $\text{Pr}_{0.5}(\text{Ca}_{0.9}\text{Sr}_{0.1})_{0.5}\text{MnO}_3$, after Rivadulla et al. (2002).

FMV matrix. Although pressure increases t in the crossover region because of the larger compressibility of the Mn–O bond where it has a double-well equilibrium bond length, it was not possible to obtain the higher volume FMM phase II by applying pressure to a $t = 0.973 < t_c$ sample (Rivadulla et al., 2002). Figure 55 shows the evolution with pressure of the thermoelectric power $\alpha(T)$; a crossover from a $T_{\text{CO}} > T_c$ at 8.7 kbar to $T_c > T_{\text{CO}}$ at 15.4 kbar is evident, crossover occurring near 13 kbar (fig. 56). In this experiment, the magnitude of $\alpha(T)$ increases in the CO insulator phase and decreases in the conductive FMV phase. This situation indicates that a distinction must be made between the CE AFI phase I below $T_N = T_{\text{OO}}$ and the CE AFI phase III appearing below $T_N = T_{\text{OO}}$. Whereas the classical model of fig. 50(a)

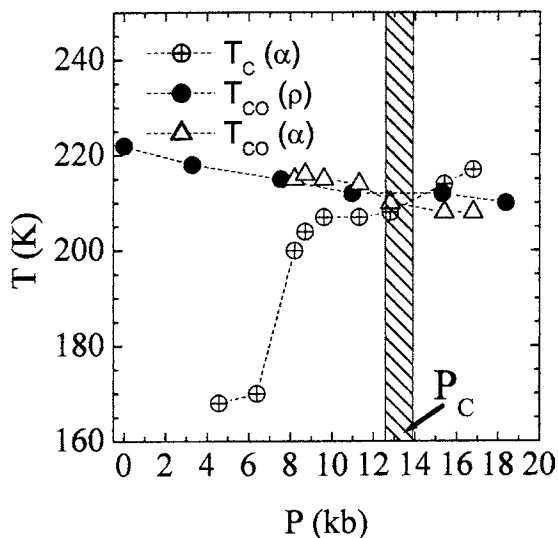


Fig. 56. Evolution with pressure of the critical temperatures for $\text{Pr}_{0.5}(\text{Ca}_{0.9}\text{Sr}_{0.1})_{0.5}\text{MnO}_3$, after Rivadulla et al. (2002).

should apply to phase I, phase III appears on the itinerant-electron side of t_c and represents the next step in the break-up with decreasing bandwidth from 3D to 2D σ^* bands to Zener polarons. Therefore phase III was predicted to represent an ordering of Zener polarons (Rivadulla et al., 2002). Independent direct evidence for such an ordering in a CE AFI phase has been provided by Daoud-Aladine et al. (2002) with neutron diffraction on a $\text{Pr}_{0.6}\text{Ca}_{0.4}\text{MnO}_3$ crystal; on lowering t , the 2D $(x^2 - y^2)\sigma^*$ bands of the type-A AFM phase IV breaks up into the charge-density-wave pattern of ordered Zener polarons shown in fig. 57.

The competition between the FMM phase and paramagnetic CO phase is already manifest in phase I where a modest applied magnetic field stabilizes the FMM phase relative to the CO paramagnetic phase. Figure 58 shows typical magnetization, $M(T)$, resistivity, $\rho(T)$, and thermoelectric power, $\alpha(T)$, curves for $\text{Pr}_{0.5}(\text{Sr}_{0.9}\text{Ca}_{0.1})_{0.5}\text{MnO}_3$ ($t \approx 0.973$). The sharp drop in $M(T)$ for $H = 0$ on cooling through $T_{\text{CO}} \approx 225$ K reflects a break-up of the superparamagnetic Zener polarons in the CO phase I, and the smaller maximum in $M(T)$ at $T_{\text{N}} = T_{\text{OO}} = 150$ K marks the onset of the CE AFI magnetic and orbital order. The thermal hysteresis in the $\rho(T)$ curve (inset) shows that the transition at T_{CO} is first-order and therefore cannot be described as a simple order-disorder transition. The $\alpha(T)$ curve is temperature-independent above T_{CO} , which is characteristic of polaron conduction; and from eq. (26), $\alpha = -28$ $\mu\text{V}/\text{K}$ corresponds to about 20% Zener polarons above T_c . The abrupt increase in the magnitude of $\alpha(T)$ on cooling through T_{CO} and $T_{\text{N}} = T_{\text{OO}}$ is due to a progressive trapping out of mobile electrons with increasing charge ordering. The maximum in $|\alpha(T)|$ appears to correspond to a growth with decreasing T in a conductive FM minority phase below 100 K. Figure 58(b) shows the change in $M(T)$ in an applied magnetic field in the range $3 \text{ T} \leq H \leq 5 \text{ T}$. In an $H = 4.5 \text{ T}$, long-range CO is completely suppressed in the range $T_{\text{N}} < T < T_{\text{CO}}$ for $H = 0$; the saturation magnetization approaches the spin-only $3.5\mu_{\text{B}}/\text{Mn}$ just above T_{N} . However, orbital ordering below $T_{\text{OO}} = T_{\text{N}}$ stabilizes the CE AFI phase, which

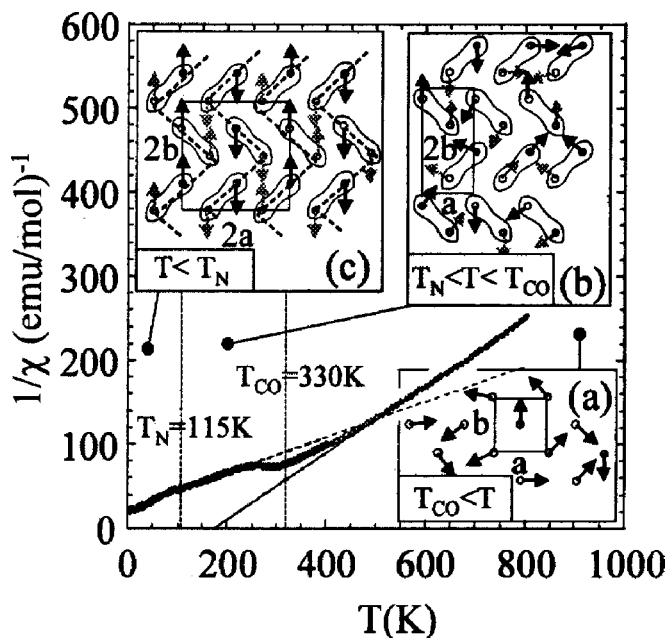


Fig. 57. Inverse magnetic susceptibility $1/\chi(T)$ of $Y_{0.5}Ca_{0.5}MnO_3$ and schematic picture of the magnetic state: (a) PM above T_{CO} with formation of Zener polarons setting in below 450 K; (b) PM Zener polarons order between T_{CO} and T_N ; (c) CE AFI structure below T_N , after Daoud-Aladine et al. (2002).

probably means it reestablishes the static CO. A similar behavior was found by Kuwahara and Tokura (1998) in $Pr_{0.5}Ca_{0.5}MnO_3$, but in higher magnetic fields as a consequence of a smaller tolerance factor t .

Like $Pr_{0.5}Ca_{0.5}MnO_3$, $Nd_{0.5}Ca_{0.5}MnO_3$ corresponds to phase I with $T_{CO} = 250$ K and $T_N = T_{OO} = 160$ K (Millange et al., 2000). In this compound, ESR data showed no trace of a FM second phase imbedded in the CO phase in zero magnetic field (Dupont et al., 2001). Nevertheless, a high-temperature Curie–Weiss paramagnetism with a positive Weiss constant shows ferromagnetic correlations are present above T_{CO} in this compound also. Moreover, a ferromagnetic phase is stabilized by an applied magnetic field in the temperature interval $T_N = T_{OO} < T < T_{CO}$. Millange et al. (2000) used neutron diffraction, magnetic susceptibility, and resistivity of polycrystalline samples to study, in particular, the magnetic behavior in the range $T_N = T_{OO} < T < T_{CO}$; they found the low-field susceptibility was typical of an antiferromagnet whereas no magnetic order could be detected by neutron diffraction, which suggests the presence of short-range antiferromagnetic fluctuations. Joshi et al. (2002) found a progressive motional narrowing of their ESR linewidth on heating in the interval $T_N = T_{OO} < T < T_{CO}$ and deduced a polaron activation energy $E_a = 0.1$ eV associated with the orbital fluctuations that suppress the long-range magnetic order. The introduction in zero applied magnetic field of microdomain FM clusters at oxygen vacancies or Cr-atom dopants has also been studied in $Nd_{0.5}Ca_{0.5}MnO_{3+\delta}$ and $Nd_{0.5}(Ca_{0.5-x}Cr_x)MnO_3$ (Frontera et al., 2000; Kimura et al., 1999; Machida et al., 2000, 2002; Chang et al., 2002).

$Pr_{0.5}Sr_{0.5}MnO_3$ corresponds to phase IV with a type-A AFM phase appearing below a $T_N = T_{OO} < T_C$ (Kawano et al., 1997; Damay et al., 1998; Llobet et al., 1999). In this phase,

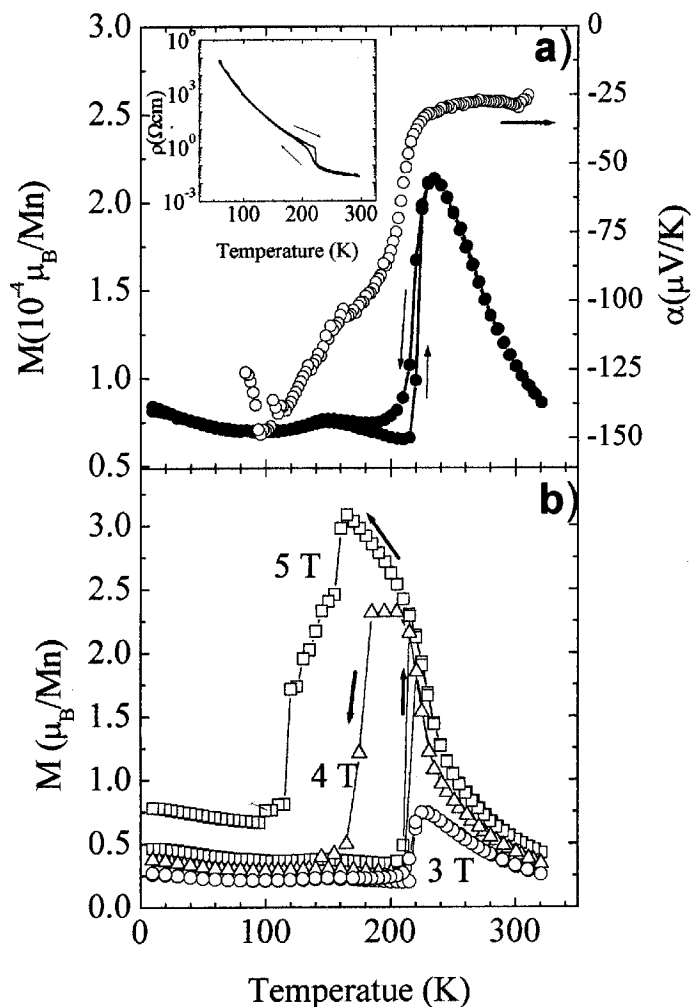


Fig. 58. (a) Temperature dependence of the magnetization $M(T)$ of $\text{Pr}_{0.5}(\text{Ca}_{0.9}\text{Sr}_{0.1})_{0.5}\text{MnO}_3$ taken on heating in a field $H = 10$ Oe after cooling in zero field (ZFC) and in $H = 10$ Oe (FC). Inset: Resistivity $\rho(T)$ on cooling and warming. (b) $M(T)$ on cooling in fields of 3 T and 5 T and on cooling and heating in 4 T, after Rivadulla et al. (2002).

the FMM phase is stabilized to low temperatures by an applied magnetic field of a few Tesla. Allodi et al. (2000) have shown with ^{55}Mn NMR that the FM phase develops from zero field by the nucleation of microscopic ferromagnetic domains. At the threshold field, the NMR spectrum changes discontinuously into that of a homogeneous, fully aligned ferromagnetic state.

Substituting smaller rare-earth ions in $\text{R}_{0.5}\text{Sr}_{0.5}\text{MnO}_3$ increases the A-site variance as well as reducing t . Whereas $\text{La}_{0.5}\text{Sr}_{0.5}\text{MnO}_3$ is a phase V FMM, $\text{Pr}_{0.5}\text{Sr}_{0.5}\text{MnO}_3$ corresponds to phase IV, stabilizing the type-A AFM phase below $T_N = T_{OO}$, and $\text{Nd}_{0.5}\text{Sr}_{0.5}\text{MnO}_3$ contains the coexistence of phases III and IV below $T_N = T_{OO} \approx 150$ K (Kajimoto et al., 1999; Kuwahara et al., 1995), but an insulator-metal transition to the FMM phase is still induced by an

applied magnetic field. Zvyagin et al. (2000) have observed with ultrasonic measurements a significant acoustic-mode softening in the FMM phase, which signals the presence of orbital and/or phase fluctuations in the FMM phase. $\text{Sm}_{0.5}\text{Sr}_{0.5}\text{MnO}_3$ and $\text{Gd}_{0.5}\text{Sr}_{0.5}\text{MnO}_3$ have a $T_{\text{CO}} \approx 250 \text{ K} > T_{\text{N}} = T_{\text{OO}}$ characteristic of $t < t_c$ in the two phase region I + II (Shames et al., 2002; García-Landa et al., 1998). A neutron-diffraction study has shown that $\text{Tb}_{0.5}\text{Sr}_{0.5}\text{MnO}_3$ has the CE AFI magnetic structure of phase I at 10 K (Machida et al., 2001). On the other hand, $\text{Ho}_{0.5}\text{Sr}_{0.5}\text{MnO}_3$ shows only short-range order below $T_{\text{N}} = T_{\text{OO}} \approx 90 \text{ K}$ as a result of the internal strains associated with the large A-site-cation variance (Autret et al., 2002).

The coexistence of two phases in the interval $0.972 < t < 0.980$ has been demonstrated by several techniques. For example, Krupicka et al. (2001) found, with ^{55}Mn NMR, FM inclusions within the CE AFI phase for $\text{Pr}_{0.5}\text{Ca}_{0.35}\text{Sr}_{0.15}\text{MnO}_3$ whereas they observed a PM phase coexisting with a FM phase just below T_{C} . The volume fraction of the FM phase IV increased with decreasing temperature until it abruptly vanished below $T_{\text{N}} = T_{\text{OO}}$; the CE AFI phase below $T_{\text{N}} = T_{\text{OO}}$ would be phase III consisting of ordered Zener polarons. The PM phase corresponds to the minority phase having a T_{CO} .

A $\text{Pr}_{0.5}(\text{Ca}_{0.85}\text{Sr}_{0.15})_{0.5}\text{MnO}_3$ crystal with $t = 0.974$ probes the two-phase region below T_{CO} at the approach to t_c from the localized-electron side. The $\rho(T)$ curve, inset of fig. 59, shows a $T_{\text{CO}} \approx 220 \text{ K}$. However, unlike the $t = 0.973$ sample of fig. 58, the $M(T)$ curve

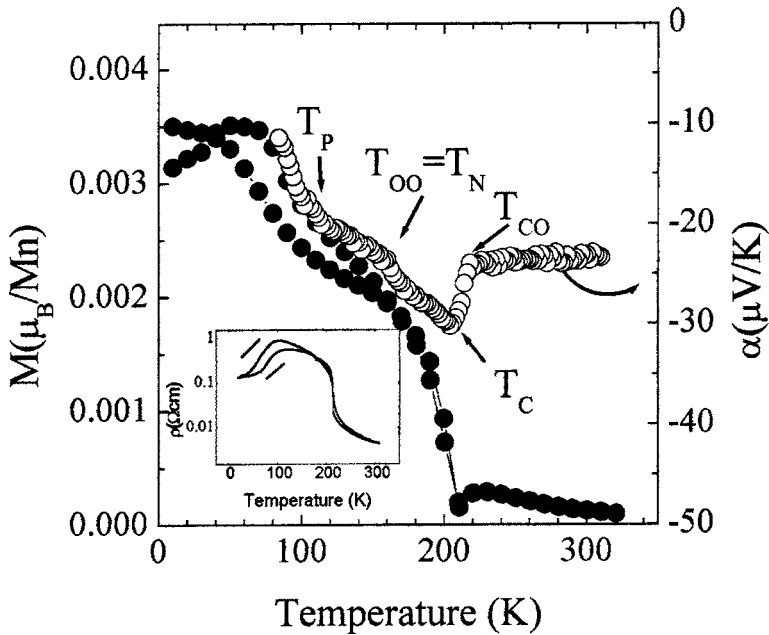


Fig. 59. Magnetization $M(T)$ in $H = 10 \text{ Oe}$ after ZFC and FC in 10 Oe (closed circles) and thermoelectric power $\alpha(T)$ (open circles) for single-crystal $\text{Pr}_{0.5}(\text{Ca}_{0.85}\text{Sr}_{0.15})_{0.5}\text{MnO}_3$. Inset: Resistivity $\rho(T)$ on cooling and warming, after Rivadulla et al. (2002).

for $t = 0.974$ in an $H = 10$ Oe reveals a ferromagnetic minority phase appearing below $T_C = 210$ K. The volume fraction of this phase grows as the temperature is lowered, reaching a percolation threshold at a $T_p \approx 100$ K below which $M(T)$ increases more sharply with decreasing temperature. The $\rho(T)$ curve shows a change to a lower resistivity below T_p , which is consistent with percolation of a more conductive phase below T_p . The onset of type-CE antiferromagnetic order below $T_N = T_{OO} \approx 150$ K of the CO phase retards the growth of the FM minority phase and introduces a thermal hysteresis into $M(T)$ and $\rho(T)$. The change in $\alpha(T)$ at T_{CO} is reduced because the volume fraction of the majority phase is reduced; inflections in $\alpha(T)$ are found at $T_{OO} = T_N$ and T_p as expected from this model.

Figure 60 shows that the ferromagnetic phase is more easily stabilized by a magnetic field relative to the CE AFI phase at temperatures $T < T_p$; in the $t = 0.973$ phase, the CE AFI phase remains stable in applied fields that are strong enough to convert the CO phase to a FM phase in the interval $T_N = T_{OO} < T < T_{CO}$ whereas the $t = 0.974$ crystal has its CE AFI phase less stable relative to the FM phase than the CO phase in the interval $T_N = T_{OO} < T < T_{CO}$. This inversion of the relative stabilities of the two phases relative to a disordering in an applied magnetic field as t approaches t_c from the localized-electron side is noteworthy; it suggests that the stability of ordering of localized orbitals as against the formation of Zener polarons decreases more rapidly as t approaches t_c than the coulombic stabilization associated with ordering of localized Mn(III) and Mn(IV) ions. However, application of an $H = 4$ T completely

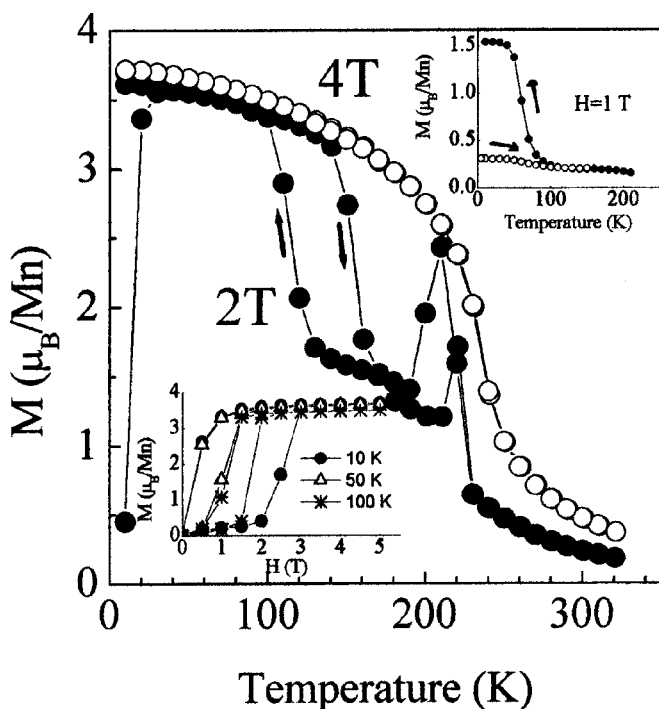


Fig. 60. Effect of an applied magnetic field on the magnetization $M(T)$ of $\text{Pr}_{0.5}(\text{Ca}_{0.85}\text{Sr}_{0.15})_{0.5}\text{MnO}_3$. Upper inset: Open circles measured during cooling in $H = 1$ T after ZFC from 320 K down to 5 K and warming up to 150 K in zero field; solid circles measured in the same way after warming up to 210 K. Lower inset: M vs. H at different temperatures $T < T_p$, after Rivadulla et al. (2002).

suppresses phase I; this phase is metamagnetic below $T_N = T_{OO}$ with an AF-FM insulator-conductor transition occurring at T_p on cooling in $H = 2$ T whereas the FM phase is retained on heating in $H = 2$ T to the zero-field magnetic transition at $T_{OO} = T_N$.

The upper inset of fig. 60 shows two $M(T)$ curves taken on cooling in a field $H = 1$ T after a rapid ZFC to 5 K and warming to 150 K or to 210 K. After warming to 150 K before $H = 1$ T is applied, the field-cooled (FC) magnetization remains very small (open circles); the crystal remains in the AF state. However, after warming to 210 K before $H = 1$ T is applied, the FC $M(T)$ curve (closed circles) increases sharply on cooling through T_p . The metamagnetism of the AF phase at $H = 1$ T is then seen to require nucleation within it of a FM phase that grows below T_p . Rapid cooling to 5 K in zero field apparently does not provide time for the ferromagnetic clusters to nucleate to an irreversible size. Uehara and Cheong (2000) have shown how cooling rate and aging in a magnetic field can drastically influence the volume fraction ratio of FM/CO phases that coexist in a wide temperature interval in the system $\text{La}_{5/8-y}\text{Pr}_y\text{Ca}_{3/8}\text{MnO}_3$.

The lower inset of fig. 60 shows M vs. H hysteresis for $0 \leq H \leq 5$ T at three different temperatures after a ZFC. At 10 K, the metamagnetic transition occurs in the interval $2 \text{ T} \leq H \leq 3 \text{ T}$ on increasing H ; it returns to a spin-glass or canted-spin-AF state on decreasing H below 1 T. At 50 K, the metamagnetic transition occurs in the interval $0.5 \text{ T} < H < 1.5 \text{ T}$ in conformity with the upper inset. At $100 \text{ K} \approx T_p$, the metamagnetic transition occurs at a larger magnetic field, $1.5 \text{ T} < H < 1.8 \text{ T}$ on increasing H and returns to a spin-glass or canted-spin-AF state at about $H = 1$ T on reducing H . This remarkable shift confirms that growth of the FM phase at the expense of the AF phase is greatly facilitated below T_p .

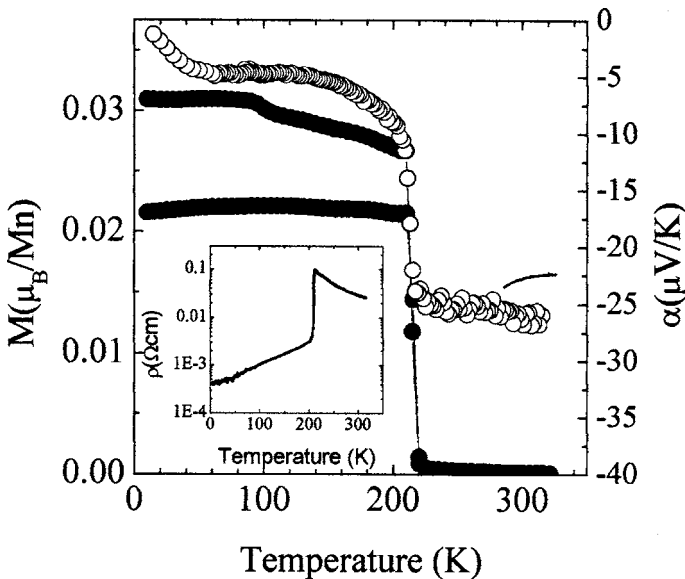


Fig. 61. Magnetization $M(T)$ in $H = 10$ Oe after ZFC and FC in 10 Oe (closed circles); thermoelectric power $\alpha(T)$ (open circles) for $\text{Pr}_{0.5}(\text{Ca}_{0.8}\text{Sr}_{0.2})_{0.5}\text{MnO}_3$ ($t = 0.975$). Inset: $\rho(T)$ showing abrupt metal-insulator transition at $T_C \approx 215$ K, after Rivadulla et al. (2002).

Figure 61 shows the ZFC and FC $M(T)$ curves for the FMM phase II, which show a first-order transition at T_C where the bond-length fluctuations become frozen out to restore the phonon contribution to the thermal conductivity, fig. 62. In the I + II two-phase samples $t = 0.973$ and $t = 0.974$, phase II is suppressed and phase fluctuations inhibit phonon formation below T_{CO} or T_C . Tokura et al. (1996) applied hydrostatic pressure to the FM phase II of $(Nd_{0.125}Sm_{0.875})_{0.5}Sr_{0.5}MnO_3$ having $t \approx t_c$; they reported the appearance of a CE AFI second phase having a volume fraction that increased with pressure below $T_{OO} = T_N$. Since pressure

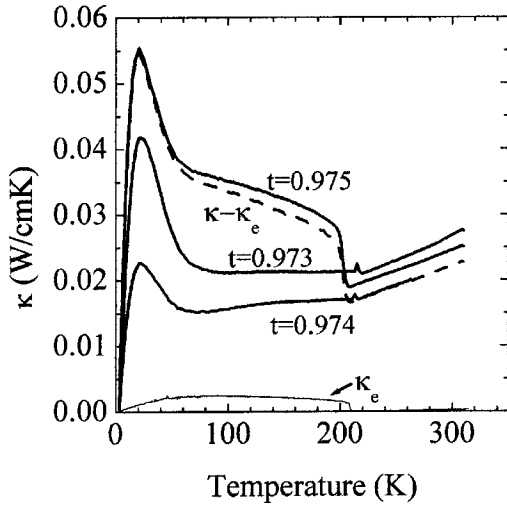


Fig. 62. Thermal conductivities $\kappa(T)$ for $Pr_{0.5}(Ca_{1-x}Sr_x)_{0.5}MnO_3$, $x = 0.10, 0.15, 0.20$. The electronic component κ_e for the most conductive sample ($x = 0.20$) is also shown, after Rivadulla et al. (2002).

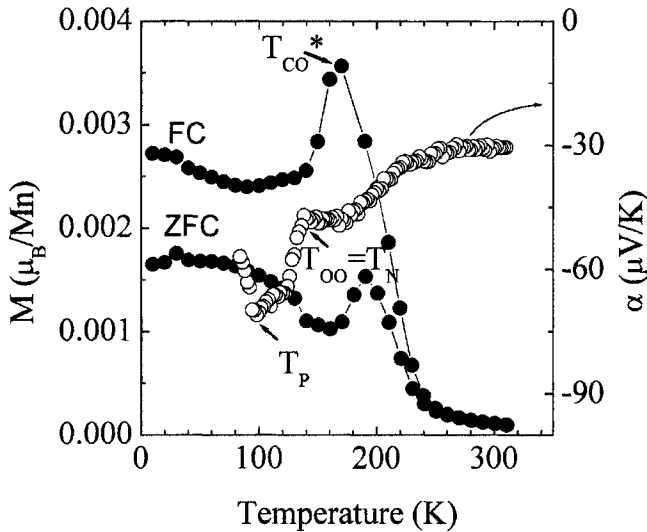


Fig. 63. Magnetization $M(T)$ in $H = 10$ Oe after ZFC and FC in 10 Oe (closed circles); thermoelectric power $\alpha(T)$ (open circles) for $Pr_{0.5}(Ca_{0.75}Sr_{0.25})_{0.5}MnO_3$ ($t = 0.976$), after Rivadulla et al. (2002).

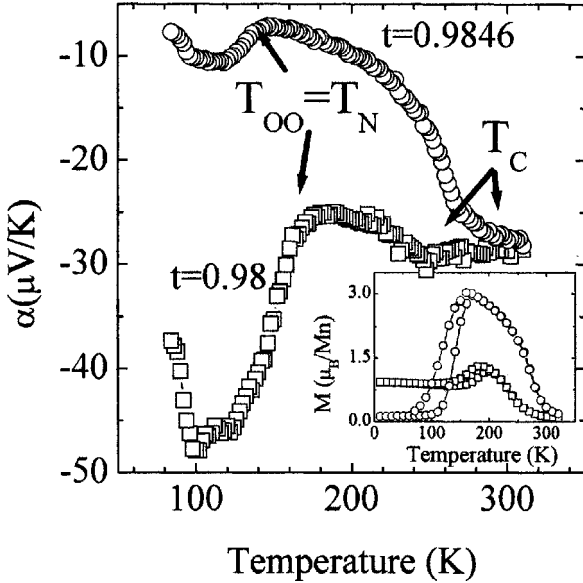


Fig. 64. Thermoelectric power $\alpha(T)$ and magnetization $M(T)$ in $H = 1$ T after ZFC and FC for $\text{Pr}_{0.5}(\text{Ca}_{0.5}\text{Sr}_{0.5})_{0.5}\text{MnO}_3$ ($t = 0.980$) (open squares) and $\text{Pr}_{0.5}(\text{Ca}_{0.25}\text{Sr}_{0.75})_{0.5}\text{MnO}_3$ ($t = 0.985$) (open circles), after Rivadulla et al. (2002).

increases t and suppresses phase II, pressure stabilizes phase III in the two-phase domain FMV + III.

Figure 63 shows $\alpha(T)$ and both ZFC and FC $M(T)$ in 10 Oe for a $t = 0.976$ crystal lying in the two-phase region between phases II and III. This figure is to be compared with figs. 58 and 60. A $T_C \approx 230$ K for the FMV matrix is only a little higher than the T_{CO} of the minority phase; below T_{CO} , the volume fraction of the CO phase competes with that of the FM phase and appears to become dominant in the interval $T_p < T < T_{OO} = T_N$ of that phase.

Finally, fig. 64 shows $M(T)$ in $H = 1$ T and $\alpha(T)$ curves for samples $\text{Pr}_{0.5}(\text{Ca}_{0.5}\text{Sr}_{0.5})_{0.5}\text{MnO}_3$ ($t = 0.980$) and $\text{Pr}_{0.5}(\text{Ca}_{0.25}\text{Sr}_{0.75})_{0.5}\text{MnO}_3$ ($t \approx 0.9846$). The former has a majority phase III with a minority phase IV; a sharp increase in $|\alpha(T)|$ occurs between T_p and $T_{OO} = T_N$. The latter is primarily phase IV with a small volume fraction of phase III. The apparent suppression of $M(T)$ in the $t = 0.980$ sample is due to the smaller temperature interval $T_{OO} = T_N < T < T_C$.

4. Conclusions

The rare-earth ions in the $\text{R}_{1-x}\text{A}_x\text{MnO}_3$ perovskites have their primary influence on physical properties through the geometric tolerance factor t that determines the bending of the $(180^\circ - \phi)$ Mn–O–Mn bond angle to achieve matching of the equilibrium A–O and Mn–O bond lengths. The variance σ^2 of the A-site-cation size plays an important, but secondary role. In this family, the tolerance factor can be varied so as to change the character of

the σ -bonding electrons of e-orbital parentage at high-spin Mn(III) ions from localized to itinerant behavior while the π -bonding t^3 configurations remain localized with a spin $S = 3/2$.

The twofold orbital degeneracy of the e electrons at octahedral-site Mn(III) induces local Jahn–Teller site distortions that may locally fluctuate cooperatively or order into a long-range, cooperative static deformation of the lattice. The orbital degeneracy may also be removed where the σ -bonding electrons are itinerant. Whereas itinerant electrons of e-orbital parentage would normally occupy 3D σ^* bands, orbital ordering may constrain these electrons (1) to 2D $x^2 - y^2\sigma^*$ bands or (2) to 1D $(3z^2 - r^2)\sigma^*$ bands that tend to form charge-density waves, or (3) to two-Mn $\text{Mn}^{3.5+}\text{-O-Mn}^{3.5+}$ Zener polarons. Electrons in 3D σ^* bands couple the localized $S = 3/2$ spins ferromagnetically via de Gennes double exchange. Constraining the itinerant electrons to 2D planes or 1D chains allows de Gennes ferromagnetic double-exchange coupling only in the metallic planes or chains; perpendicular superexchange interactions couple the ferromagnetic units antiferromagnetically. Ferromagnetic double-exchange coupling within a Zener polaron may result in superparamagnetic clusters where the polarons are disordered in a paramagnetic phase, and ordering of the Zener polarons into linear or zig-zag chains gives ferromagnetic superexchange interactions between polarons of a chain, but antiferromagnetic superexchange interactions perpendicular to the chains.

Where the e electrons are localized, orbital fluctuations introduce vibronic ferromagnetic Mn(III)–O–Mn(III) and Mn(III)–O–Mn(IV) interactions, but long-range cooperative orbital ordering constrains the ferromagnetic interactions to planes or chains with antiferromagnetic superexchange interactions between the ferromagnetic elements. Moreover, localized electrons in mixed-valent MnO_3 arrays experience strong coulomb interactions that give short-range charge-order fluctuations or long-range charge ordering. Optimization of the exchange and coulomb forces produces long-range charge and orbital ordering at lower temperatures.

The crossover from localized to itinerant electronic behavior is first-order, and the consequent double-well potential for the equilibrium Mn–O bond length can be accommodated in the perovskite structure by cooperative oxygen displacements perpendicular and/or along a Mn–O–Mn bond axis. Cooperative bond-length fluctuations permit the coexistence of competing phases in what appears to a diffraction experiment to be a single phase. Where an external input stabilizes one competing phase relative to another, the bond-length fluctuations allow one phase to grow at the expense of another at lower temperatures. Bond-length fluctuations may also suppress long-range order altogether to give quantum critical behavior at a QCP. In addition, bond-length fluctuations are associated with disorder of a cooperative Jahn–Teller distortion, and these fluctuations can allow partial, fluctuating disproportionation of 2Mn(III) into Mn(IV) and Mn(II) . The result of all these competitions is a rich array of physical phenomena to be explored and exploited. An appropriate choice of rare-earth and alkaline-earth A-site cations can change physical properties dramatically and allow the design of materials with unusual physical properties that may prove technologically useful.

References

- Adams, C.P., Lynn, J.W., Mukovskii, Y.M., Arsenov, A.A., Shulyatev, D.A., 2000. *Phys. Rev. Lett.* **85**, 3954.
- Ahn, K.H., Millis, A.J., 2001. *Phys. Rev. B* **64**, 115103.
- Alexandrov, A.S., Zhao, G.-M., Keller, H., Lorenz, B., Wang, Y.S., Chu, C.W., 2001. *Phys. Rev. B* **64**, 140404.
- Allen, P.B., Perebeinos, V., 1999. *Phys. Rev. Lett.* **83**, 4828.
- Allen, P.B., Perebeinos, V., 2001. *Nature* **410**, 155.
- Allodi, G., De Renzi, R., Guidi, G., Lucci, F., Pieper, M.W., 1997. *Phys. Rev. B* **56**, 6036.
- Allodi, G., De Renzi, R., Guidi, G., 1998a. *Phys. Rev. B* **57**, 1024.
- Allodi, G., De Renzi, R., Licci, F., Pieper, M.W., 1998b. *Phys. Rev. Lett.* **81**, 4736.
- Allodi, G., De Renzi, R., Solzi, M., Kamenev, K., Balakrishnan, G., Pieper, M.W., 2000. *Phys. Rev. B* **61**, 5924.
- Allodi, G., Castelli Guidi, M., De Renzi, R., Caneiro, A., Pinsard, L., 2001. *Phys. Rev. Lett.* **87**, 127206.
- Alonso, J., Arroyo, A., González-Calbet, J.M., Vallet-Regí, M., Martínez, J.L., Rojo, J.M., Hernando, A., 2001. *Phys. Rev. B* **64**, 172410.
- Anane, A., Renard, J.-P., Reversat, L., Dupas, C., Veillet, P., Viret, M., Pinsard, L., Revcolevschi, A., 1999. *Phys. Rev. B* **59**, 77.
- Anderson, P.W., 1959. *Phys. Rev.* **115**, 2.
- Anderson, P.W., Hasegawa, H., 1955. *Phys. Rev.* **100**, 675.
- Archibald, W., Zhou, J.-S., Goodenough, J.B., 1996. *Phys. Rev. B* **53**, 14445.
- Arima, T., Tokura, Y., Torrance, J.B., 1993. *Phys. Rev. B* **48**, 17006.
- Asamitsu, A., Moritomo, Y., Tomioka, Y., Arima, T., Tokura, Y., 1995. *Nature* **373**, 407.
- Asamitsu, A., Moritomo, Y., Kumai, R., Tomioka, Y., Tokura, Y., 1996. *Phys. Rev. B* **54**, 1716.
- Asamitsu, A., Tomioka, Y., Kuwahara, H., Tokura, Y., 1997. *Nature (London)* **388**, 50.
- Autret, C., Martin, C., Maignan, A., Hervieu, M., Raveau, B., André, G., Bourée, F., 2002. *J. Solid State Chem.* **165**, 65.
- Babushkina, N.A., Belova, L.M., Khomskii, D.I., Kugel, K.I., Gorbenko, O.Yu., Kaul, A.R., 1999. *Phys. Rev. B* **59**, 6994.
- Babushkina, N.A., Taldenkov, A.N., Belova, L.M., Chistotina, E.A., Gorbenko, O.Yu., Kaul, A.R., Kugel, K.I., Khomskii, D.I., 2000. *Phys. Rev. B* **62**, R6081.
- Bertaut, E.F., 1963. In: Rado, G.T., Suhl, H. (Eds.), *Magnetism: A Treatise on Modern Theory and Materials*. Academic Press, New York. Chap. 4.
- Billinge, S.J.L., Proffen, Th., Petkov, V., Sarrao, J.L., Kycia, S., 2000. *Phys. Rev. B* **62**, 1203.
- Biotteau, G., Hennion, M., Moussa, F., Rodríguez-Carvajal, J., Pinsard, L., Revcolevschi, A., Mukovskii, Y.M., Shulyatev, D., 2001. *Phys. Rev. B* **64**, 104421.
- Björnsson, P., Rübhausen, M., Bäckström, J., Käll, M., Ericksson, S., Eriksen, J., Börjesson, L., 2000. *Phys. Rev. B* **61**, 1193.
- Bloch, D., 1966. *J. Phys. Chem. Solids* **27**, 881.
- Brinks, H.W., Rodríguez-Carvajal, J., Fjellvåg, H., Kjekshus, A., Hauback, B.C., 2001. *Phys. Rev. B* **63**, 094411.
- Burgy, J., Mayr, M., Martin-Mayor, V., Moreo, A., Dagotto, E., 2002. *Phys. Rev. Lett.* **87**, 277202.
- Campbell, A.J., Balakrishnan, G., Lees, M.R., Paul, D.McK., McIntyre, G.J., 1997. *Phys. Rev. B* **55**, R8622.
- Casa, D., Keimer, B., Zimmermann, M.V., Hill, J.P., Habermeier, H.U., Razavi, F.S., 2001. *Phys. Rev. B* **64**, 100404.
- Causa, M.T., Tovar, M., Caneiro, A., Prado, F., Ibañez, G., Ramos, C.A., Butera, A., Alascio, B., Obradors, X., Piñol, S., Rivadulla, F., Vázquez-Vázquez, C., López-Quintela, M.A., Rivas, J., Tokura, Y., Oseroff, S.B., 1998. *Phys. Rev. B* **58**, 3233.
- Cestelli Guidi, M., Allodi, G., De Renzi, R., Guidi, G., Hennion, M., Pinsard, L., Amato, A., 2001. *Phys. Rev. B* **64**, 064414.
- Chahara, K.I., Ohno, T., Kasai, M., Kozono, Y., 1993. *Appl. Phys. Lett.* **63**, 1990.
- Chang, C.W., Debnath, A.K., Lin, J.G., 2002. *Phys. Rev. B* **65**, 024422.
- Chechersky, V., Nomura, K., Nath, A., Ju, H., Greene, R.L., 1997. *Low Temp. Phys.* **23**, 549.
- Chechersky, V., Nath, A., Isaac, I., Franck, J.P., Ghosh, K., Ju, H., Greene, R.L., 1999a. *Phys. Rev. B* **59**, 497.
- Chechersky, V., Nath, A., Isaac, I., Franck, J.P., Ghosh, K., Greene, R.L., 1999b. *Phys. Rev. B* **60**, 3005.
- Chechersky, V., Nath, A., Michel, C., Hervieu, M., Ghosh, K., Greene, R.L., 2000. *Phys. Rev. B* **62**, 5316.
- Chechersky, V., Nath, A., Isaac, I., Franck, J.P., Ghosh, K., Greene, R.L., 2001. *Phys. Rev. B* **63**, 052411.
- Chen, Y.-R., Allen, P.B., 2001. *Phys. Rev. B* **64**, 064401.
- Chen, C.H., Cheong, S.-W., 1996. *Phys. Rev. Lett.* **76**, 4042.

- Chen, C.H., Cheong, S.-W., Hwang, H.Y., 1997. *J. Appl. Phys.* **81**, 4326.
- Cheong, S.W., Chen, C.H., 1998. In: Rao, C.N.R., Raveau, B. (Eds.), *Colossal Magnetoresistance, Charge Ordering and Related Properties of Manganese Oxides*. World Scientific, Singapore.
- Chmaissem, O., Dabrowski, B., Kolesnik, S., Mais, J., Brown, D.E., Kruk, R., Prior, P., Pyles, B., Jorgensen, J.D., 2001. *Phys. Rev. B* **64**, 134412.
- Chun, S.H., Salamon, M.B., Tomioka, Y., Tokura, Y., 2000. *Phys. Rev. B* **61**, R9225.
- Congeduti, A., Postorino, P., Caramagno, E., Nardone, M., Kumar, A., Sarma, D.D., 2001. *Phys. Rev. Lett.* **86**, 1251.
- Cordero, F., Castellano, C., Cantelli, R., Ferretti, M., 2002. *Phys. Rev. B* **65**, 012403.
- Cox, D.E., Radaelli, P.G., Marezio, M., Cheong, S.-W., 1998. *Phys. Rev. B* **57**, 3305.
- Dabrowski, B., Xiong, X., Bukowski, Z., Dybziński, R., Klamut, P.W., Siewenie, J.E., Chmaissem, O., Shaffer, J., Kimball, C.W., Jorgensen, J.D., Short, S., 1999a. *Phys. Rev. B* **60**, 7006.
- Dabrowski, B., Klamut, P.W., Bukowski, Z., Dybziński, R., Siewenie, J.E., 1999b. *J. Solid State Chem.* **144**, 461.
- Dabrowski, B., Dybziński, R., Bukowski, Z., Chmaissem, O., 1999c. *J. Solid State Chem.* **146**, 448.
- Dagotto, E., Yunoki, S., Malrezzi, A.L., Moreo, A.M., Hu, J., Capponi, S., Poilblanc, D., Furukawa, N., 1998. *Phys. Rev. B* **58**, 6414.
- Dai, P., Fernandez-Baca, J.A., Wakabayashi, N., Plummer, E.W., Tomioka, Y., Tokura, Y., 2000. *Phys. Rev. Lett.* **85**, 2553.
- Dai, P., Fernandez-Baca, J.A., Plummer, E.W., Tomioka, Y., Tokura, Y., 2001. *Phys. Rev. B* **64**, 224429.
- Damay, F., Martin, C., Hervieu, M., Maignan, A., Raveau, B., André, G., Bourée, F., 1998. *J. Magn. Mater.* **184**, 71.
- Damay, F., Martin, C., Maignan, A., Hervieu, M., Raveau, B., Jiráček, Z., André, G., Bourée, F., 1999. *Chem. Mater.* **11**, 536.
- Daoud-Aladine, M., Rodríguez-Carvajal, J., Pinsard-Gaudart, L., Fernández-Díaz, M.T., Revcolevschi, A., 2002. *Phys. Rev. Lett.* **89**, 097205.
- de Gennes, P.-G., 1960. *Phys. Rev.* **118**, 141.
- De Teresa, J.M., Blasco, J., Ibarra, M.R., García, J., Marquina, C., Algarabel, P.A., del Moral, A., 1996a. *J. Appl. Phys.* **79**, 5175.
- De Teresa, J.M., Ibarra, M.R., Blasco, J., García, J., Maquina, C., Algarabel, P.A., Arnold, Z., Kamenev, K., 1996b. *Phys. Rev. B* **54**, 1187.
- De Teresa, J.M., Ibarra, M.R., Algarabel, P.A., Ritter, C., Marquina, C., Blasco, J., García, J., del Moral, A., Arnold, Z., 1997. *Nature (London)* **386**, 256.
- Dediu, V., Ferdeghini, C., Matocota, F.C., Nozar, P., Ruani, G., 2000. *Phys. Rev. Lett.* **84**, 4489.
- Dessau, D.S., Shen, Z.X., 1998. In: Takura, Y. (Ed.), *Colossal Magnetoresistive Oxides*. World Scientific, Singapore.
- Dho, J., Kim, I., Lee, S., Kim, K.H., Lee, H.J., Jung, J.H., Noh, T.W., 1999a. *Phys. Rev. B* **59**, 492.
- Dho, J., Kim, I., Lee, S., 1999b. *Phys. Rev. B* **60**, 14545.
- Dho, J., Kim, W.S., Hur, N.H., 2001. *Phys. Rev. Lett.* **87**, 187201.
- Dupont, F., Millange, F., de Brion, S., Janossy, A., Chouteau, G., 2001. *Phys. Rev. B* **64**, 220403(R).
- Dzialoshinskii, I.E., 1958. *J. Phys. Chem. Solids* **4**, 214.
- Egami, T., 2001. *Struct. Bond.* **98**, 115.
- Egami, T., Louca, D., 1999. *J. Supercond.* **12**, 23.
- Egami, T., Louca, D., 2002. *Phys. Rev. B* **65**, 094422.
- Egami, T., Louca, D., McQueeney, R.J., 1997. *J. Supercond.* **10**, 323.
- Emin, D., 1998. In: Hundley, M., Nickel, J., Ramesh, R., Tokura, Y. (Eds.), *Science and Technology of Magnetic Oxides*. Mat. Res. Soc., Pittsburgh, p. 163.
- Endoh, Y., Hirota, K., Ishihara, S., Okamoto, S., Murakami, Y., Nishizawa, A., Fukuda, T., Kimura, H., Nojiri, H., Kaneko, K., Maekawa, S., 1999. *Phys. Rev. Lett.* **82**, 4328.
- Erwin, R.W., Lynn, J.W., Borchers, J.A., Peng, J.L., Greene, R.L., 1997. *J. Appl. Phys.* **81**, 5487.
- Faaland, S., Knudsen, K.D., Einarsrud, M.A., Rørmark, L., Høier, R., Grande, T., 1998. *J. Solid State Chem.* **140**, 320.
- Fäth, M., Freisem, S., Menovsky, A.A., Tomioka, Y., Aarts, J., Mydosh, J.A., 1999. *Science* **285**, 1540.
- Fernández-Baca, J.A., Dai, P., Hwang, H.Y., Kloc, C., Cheong, S.-W., 1998. *Phys. Rev. Lett.* **80**, 4012.
- Fernández-Díaz, M.T., Martínez, J.L., Alonso, J.M., Herrero, E., 1999. *Phys. Rev. B* **59**, 1277.
- Fiebig, M., Miyano, K., Tomioka, Y., Tokura, Y., 1998. *Science* **280**, 1925.
- Fiebig, M.K., Miyano, Y., Tomioka, Y., Tokura, Y., 1999. *J. Appl. Phys.* **85**, 5561.
- Fisher, R.A., Bouquet, F., Phillips, N.E., Franck, J.P., Zhang, G., Gordon, J.E., Marcenat, C., 2001. *Phys. Rev. B* **64**, 134425.
- Fontcuberta, J., Laukhin, V., Obradors, X., 1998. *Appl. Phys. Lett.* **72**, 2607.
- Franck, J.P., Isaac, I., Chen, W., Chrzanowski, J., Irwin, J.C., Homes, C.C., 1999. *J. Supercond.* **12**, 263.
- Franck, J.P., Isaac, I., Lawrie, D.D., 2001. *Phys. Rev. B* **64**, 214412.

- Freitas, R.S., Ghivelder, L., Damay, F., Dias, F., Cohen, L.F., 2001. *Phys. Rev. B* **64**, 144404.
- Freitas, R.S., Ghivelder, L., Levy, P., Parisi, F., 2002. *Phys. Rev. B* **65**, 104403.
- Frontera, C., García-Muñoz, J.L., Llobet, A., Ritter, C., Alonso, J.A., Rodríguez-Carvajal, J., 2000. *Phys. Rev. B* **62**, 3002.
- Fujishiro, H., Ikebe, M., Konno, Y., 1998. *J. Phys. Soc. Japan* **67**, 1799.
- Fujishiro, H., Fukase, T., Ikebe, M., Kikuchi, T., 1999. *J. Phys. Soc. Japan* **68**, 1469.
- Fujishiro, H., Ohshiden, S., Ikebe, M., 2000. *J. Phys. Soc. Japan* **69**, 2082.
- García-Landa, B., De Teresa, J.M., Ibarra, M.R., Ritter, C., Drost, R., Lees, M.R., 1998. *J. Appl. Phys.* **83**, 7664.
- García-Muñoz, J.L., Suaaidi, M., Fontcuberta, J., Rodríguez-Carvajal, J., 1997. *Phys. Rev. B* **55**, 34.
- Geertsma, W. (1979). Thesis, University of Groningen, The Netherlands.
- Goodenough, J.B., 1955. *Phys. Rev.* **100**, 564.
- Goodenough, J.B., 1963. In: *Magnetism and the Chemical Bond*. Interscience-Wiley, New York.
- Goodenough, J.B., 1992. *Ferroelectrics* **130**, 77.
- Goodenough, J.B., 1997. *J. Appl. Phys.* **81**, 5330.
- Goodenough, J.B., 1999. *Aust. J. Phys.* **52**, 266.
- Goodenough, J.B., Loeb, A.L., 1955. *Phys. Rev.* **98**, 391.
- Goodenough, J.B., Zhou, J.-S., 1997. *Nature (London)* **386**, 229.
- Goodenough, J.B., Zhou, J.-S., 1998. *Mater. Res. Soc. Symp. Proc.* **494**, 335.
- Goodenough, J.B., Zhou, J.-S., 2001. *Struct. Bond.* **98**, 17.
- Goodenough, J.B., Wold, A., Arnott, R.J., Menyuk, N., 1961. *Phys. Rev.* **124**, 373.
- Goodenough, J.B., Longo, J.M., Kafalas, J.A., 1968. *Mater. Res. Bull.* **3**, 471.
- Goodenough, J.B., Kafalas, J.A., Longo, J.M., 1972. In: Hagenmuller, P. (Ed.), *Preparative Methods in Solid State Chemistry*. Academic Press, New York. Chap. 1.
- Goodenough, J.B., Dass, R.I., Zhou, J.-S., 2002. *Solid State Science* **4**, 297.
- Gordon, I., Wagner, P., Das, A., Vanacken, J., Moshchalkov, V.V., Bruynseraede, Y., Schuddinck, W., Van Tendeloo, G., Ziese, M., Borghs, G., 2000. *Phys. Rev. B* **62**, 11633.
- Gordon, J.E., Marcenat, C., Franck, J.P., Isaac, I., Zhang, G., Lortz, R., Meingast, C., Bouquet, F., Fisher, R.A., Phillips, N.E., 2002. *Phys. Rev. B* **65**, 024441.
- Granado, E., Moreno, N.O., García, A., Sanjurjo, J.A., Rettori, C., Torriani, I., Oseroff, S.B., Neumeier, J.J., McClellan, K.J., Cheong, S.-W., Tokura, Y., 1998. *Phys. Rev. B* **58**, 11435.
- Granado, E., Sanjurjo, J.A., Rettori, C., Neumeier, J.J., Oseroff, S.B., 2000. *Phys. Rev. B* **62**, 11304.
- Granado, E., Moreno, N.O., Martinho, H., García, A., Sanjurjo, J.A., Torriani, I., Rettori, C., Neumeier, J.J., Oseroff, S.B., 2001. *Phys. Rev. Lett.* **86**, 5385.
- Hannoyer, B., Marest, G., Greneche, J.M., Ravi Bathe, Patil, S.I., Ogale, S.B., 2000. *Phys. Rev. B* **61**, 9613.
- Heffner, R.H., Sonier, J.E., MacLaughlin, D.E., Nieuwenhuys, G.J., Ehlers, G., Mezei, F., Cheong, S.-W., Gardner, J.S., Röder, H., 2000. *Phys. Rev. Lett.* **85**, 3285.
- Heffner, R.H., Sonier, J.E., MacLaughlin, D.E., Nieuwenhuys, G.J., Luke, G.M., Uemura, Y.J., Ratcliff II, W., Cheong, S.-W., Balakrishnan, G., 2001. *Phys. Rev. B* **63**, 094408.
- Hennion, M., Moussa, F., Rodríguez-Carvajal, J., Pinsard, L., Revcolevschi, A., 1997. *Phys. Rev. B* **56**, R497.
- Hennion, M., Moussa, F., Biotteau, G., Rodríguez-Carvajal, J., Pinsard, L., Revcolevschi, A., 2000. *Phys. Rev. B* **61**, 9513.
- Hong, C.S., Kim, W.S., Hur, N.H., 2001. *Phys. Rev. B* **63**, 092504.
- Huang, Q., Santoro, A., Lynn, J.W., Erwin, R.W., Borchers, J.A., Peng, J.L., Greene, R.L., 1997. *Phys. Rev. B* **55**, 14987.
- Huang, Q., Santoro, A., Lynn, J.W., Erwin, R.W., Borchers, J.A., Peng, J.L., Ghosh, K., Greene, R.L., 1998. *Phys. Rev. B* **58**, 2684.
- Huang, Q., Lynn, J.W., Erwin, R.W., Santoro, A., Dender, D.C., Smolyaninova, V.N., Ghosh, K., Greene, R.L., 2000. *Phys. Rev. B* **61**, 8895.
- Hubbard, J., 1963. *Proc. Roy. Soc. (London) A* **276**, 238.
- Hudspeth, H.D., Sharifi, F., Guilaran, I.J., Xiong, P., von Molnár, S., 2002. *Phys. Rev. B* **65**, 052405.
- Hueso, L.E., Rivas, J., Rivadulla, F., López-Quintela, M.A., 1999. *J. Appl. Phys.* **86**, 3881.
- Huhtinen, H., Laiho, R., Lähderanta, E., Vlasenko, L.S., Vlasenko, M.P., Zakhvalinskii, V.S., 2000. *Phys. Rev. B* **62**, 11614.
- Hwang, H.Y., Cheong, S.-W., Radaelli, P.G., Marezio, M., Batlogg, B., 1995. *Phys. Rev. Lett.* **75**, 914.
- Ilsavskii, Y., Goltsev, A., Dyakonov, K., Popov, V., Yakhkind, E., Dyakonov, V.P., Gierlowski, P., Klimov, A., Lewandowski, S.J., Szymczak, H., 2001. *Phys. Rev. Lett.* **87**, 146602.
- Ishihara, E., Inoue, J., Maekawa, S., 1997. *Phys. Rev. B* **55**, 8280.
- Jaime, M., Salamon, M.B., 1999. In: Kaplan, T.A., Mahanti, S.D. (Eds.), *Physics of Manganites*. Kluwer Academic, Plenum, New York, p. 243.

- Jiráček, Z., Krupická, S., Simsa, Z., Dlouhá, M., Vratislav, S., 1985. *J. Magn. Magn. Mater.* **53**, 153.
- Jiráček, Z., Hejtmánek, J., Pollert, E., Marysko, M., Dlouhá, M., Vratislav, S., 1997. *J. Appl. Phys.* **81**, 5790.
- Jonker, G.H., van Santen, J.H., 1950. *Physica* **16**, 337.
- Joshi, J.P., Gupta, R., Sood, A.K., Bhat, S.V., Raju, A.R., Rao, C.N.R., 2002. *Phys. Rev. B* **65**, 024410.
- Jung, J.H., Kim, K.H., Noh, T.W., Choi, E.J., Yu, J., 1998. *Phys. Rev. B* **57**, R11043.
- Kajimoto, R., Yoshizawa, H., Kawano, H., Kuwahara, H., Tokura, Y., Ohoyama, K., Ohashi, M., 1999. *Phys. Rev. B* **60**, 9506.
- Kallias, G., Pissas, M., Devlin, E., Simopoulos, A., Niarchos, D., 1999. *Phys. Rev. B* **59**, 1272.
- Kanamori, J., 1959. *J. Phys. Chem. Solids* **10**, 87.
- Kanamori, J., 1960. *J. Appl. Phys.* **31**, 14S.
- Kataoka, M., 2001. *J. Phys. Soc. Japan* **70**, 2353.
- Katsufuji, T., Mori, S., Masaki, M., Moritomo, Y., Yamamoto, N., Takagi, H., 2001. *Phys. Rev. B* **64**, 104419.
- Kawano, H., Kajimoto, R., Kubota, M., Yoshizawa, Y., 1996. *Phys. Rev. B* **53**, 2202.
- Kawano, H., Kajimoto, R., Yoshizawa, H., Tomioka, Y., Kuwahara, H., Tokura, Y., 1997. *Phys. Rev. Lett.* **78**, 4253.
- Kim, K.H., Jung, J.H., Noh, T.W., 1998. *Phys. Rev. Lett.* **81**, 1517.
- Kim, K.H., Uehara, M., Hess, C., Sharma, P.A., Cheong, S.-W., 2000a. *Phys. Rev. Lett.* **84**, 2961.
- Kim, K.H., Uehara, M., Cheong, S.-W., 2000b. *Phys. Rev. B* **62**, R11945.
- Kim, K.H., Lee, S., Noh, T.W., Cheong, S.-W., 2002. *Phys. Rev. Lett.* **88**, 167204.
- Kimura, T., Tomioka, Y., Kumai, R., Okimoto, Y., Tokura, Y., 1999. *Phys. Rev. Lett.* **83**, 3940.
- Kiryukin, V., Casa, D., Hill, J.P., Keimer, B., Vigliante, A., Tomioka, Y., Tokura, Y., 1997. *Nature (London)* **386**, 813.
- Klingeler, R., Geck, J., Gross, R., Pinsard-Gaudart, L., Revcolevschi, A., Uhlenbruck, S., Büchner, B., 2002. *Phys. Rev. B* **65**, 174404.
- Koehler, W.C., Wollan, E.O., Wilkinson, M.K., 1960. *Phys. Rev.* **118**, 58.
- Krupická, S., Marysko, M., Jiráček, Z., Hejtmánek, J., 1999. *J. Magn. Magn. Mater.* **206**, 45.
- Krupická, S., Jiráček, Z., Hejtmánek, J., Marysko, M., Novák, P., Savosta, M.M., Sonntag, R., 2001. *J. Phys. Condens. Matter* **13**, 6813.
- Kumagai, K., Iwai, A., Tomioka, Y., Kuwahara, H., Tokura, Y., Yakubovskii, A., 1999. *Phys. Rev. B* **59**, 97.
- Kumar, D., Sankar, J., Narayan, J., Singh, R.K., Majumdar, A.K., 2002. *Phys. Rev. B* **65**, 094407.
- Kusters, R.M., Singleton, J., Keen, D.A., McGreevy, R., Hayes, W., 1989. *Physica B* **155**, 362.
- Kuwahara, H., Tokura, Y., 1998. In: Rao, C.N.R., Raveau, B. (Eds.), *Colossal Magnetoresistance, Charge Ordering and Related Properties of Manganese Oxides*. World Scientific, Singapore.
- Kuwahara, H., Tomioka, Y., Asamitsu, A., Moritomo, Y., Tokura, Y., 1995. *Science* **270**, 961.
- Kuwahara, H., Moritomo, Y., Tomioka, Y., Asamitsu, A., Kasai, M., Kumai, R., 1997. *Phys. Rev. B* **56**, 9386.
- Lanzara, A., Saini, N.L., Brunelli, M., Natali, F., Bianconi, A., Radaelli, P.G., Cheong, S.-W., 1998. *Phys. Rev. Lett.* **81**, 878.
- Laukhin, V., Fontcuberta, J., García-Muñoz, J.L., Obradors, X., 1997. *Phys. Rev. B* **56**, R10009.
- Lees, M.R., Barratt, J., Balakrishnan, G., Paul, D.McK., Dewhurst, C.D., 1996. *J. Phys. Condens. Matter* **8**, 2967.
- Levy, P., Parisi, F., Polla, G., Vega, D., Leyva, G., Lanza, H., Freitas, R.S., Ghivelder, L., 2000. *Phys. Rev. B* **62**, 6437.
- Li, J.-M., Huan, C.H.A., Du, Y.-W., Feng, D., Shen, Z.X., 2001. *Phys. Rev. B* **63**, 024416.
- Li, J.Q., Uehara, M., Tsuruta, C., Matsui, Y., Zhao, Z.X., 1999. *Phys. Rev. Lett.* **82**, 2386.
- Liu, G.-L., Zhou, J.-S., Goodenough, J.B., 2001. *Phys. Rev. B* **64**, 144414.
- Liu, H.L., Cooper, S.L., Cheong, S.-W., 1998. *Phys. Rev. Lett.* **81**, 4684.
- Liu, X.J., Moritomo, Y., Machida, A., Nakamura, A., Tanaka, H., Kawai, T., 2001a. *Phys. Rev. B* **63**, 115105.
- Liu, X.J., Moritomo, Y., Nakamura, A., Tanaka, H., Kawai, T., 2001b. *J. Phys. Soc. Japan* **70**, 3466.
- Liu, X.J., Moritomo, Y., Nakamura, A., Tanaka, H., Kawai, T., 2001c. *Phys. Rev. B* **64**, 100401.
- Llobet, A., García-Muñoz, J.L., Frontera, C., Ritter, C., 1999. *Phys. Rev. B* **60**, R9889.
- Loa, I., Adler, P., Grzechnik, A., Syassen, K., Schwarz, U., Hanfland, M., Rozenberg, G.Kh., Gorodetsky, P., Pasternak, M.P., 2001. *Phys. Rev. Lett.* **87**, 125501.
- Lobad, A.I., Averitt, R.D., Taylor, A.J., 2001. *Phys. Rev. B* **63**, 060410(R).
- Lotgering, F.K., 1970. *Philips Res. Rep.* **25**, 8.
- Louca, D., Egami, T., 1999. *Phys. Rev. B* **59**, 6193.
- Louca, D., Egami, T., Brosha, E.L., Röder, H., Bishop, A.R., 1997. *Phys. Rev. B* **56**, R8475.
- Louca, D., Egami, T., Dmowski, W., Mitchell, J.F., 2001. *Phys. Rev. B* **64**, 180403(R).

- Lu, Q., Chen, C.-C., de Lozanne, A., 1997. *Science* **276**, 2006.
- Lynn, J.W., Erwin, R.W., Borchers, J.A., Huang, Q., Santoro, A., Peng, J.-L., Li, Z.Y., 1996. *Phys. Rev. Lett.* **76**, 4046.
- MacDonald, D.K.C., 1962. *Thermoelectricity: An Introduction to the Principles*. Wiley, New York.
- Machida, A., Moritomo, Y., Nishibori, E., Takata, M., Sakata, M., Ohoyama, K., Mori, S., Yamamoto, N., Nakamura, A., 2000. *J. Phys. Soc. Japan* **69**, 3536.
- Machida, A., Moritomo, Y., Ohoyama, K., Nakamura, A., 2001. *J. Phys. Soc. Japan* **70**, 3739.
- Machida, A., Moritomo, Y., Ohoyama, K., Katsufuji, T., Nakamura, A., 2002. *Phys. Rev. B* **65**, 064435.
- Mahesh, R., Itoh, M., 1999. *J. Solid State Chem.* **144**, 232.
- Mandal, P., Bandyopadhyay, B., Ghosh, B., 2001. *Phys. Rev. B* **64**, 180405.
- Markovich, V., Rosenberg, E., Gorodetsky, G., Revzin, B., Pelleg, J., Felner, I., 2000. *Phys. Rev. B* **62**, 14186.
- Markovich, V., Rozenberg, E., Gorodetsky, G., Greenblatt, M., McCarroll, W.H., 2001. *Phys. Rev. B* **63**, 054423.
- Markovich, V., Rozenberg, E., Shames, A.I., Gorodetsky, G., Fita, I., Suzuki, K., Puzniak, R., Shulyatev, D.A., Mukovskii, Ya.M., 2002. *Phys. Rev. B* **65**, 144402.
- Martin, M.C., Shirane, G., Endoh, Y., Hirota, K., Moritomo, Y., Tokura, Y., 1996. *Phys. Rev. B* **53**, 14285.
- Martínez, B., Senis, R., Balcells, L.L., Laukhin, V., Fontcuberta, J., Pinsard, L., Revcolevschi, A., 2000. *Phys. Rev. B* **61**, 8643.
- Matsumoto, G.H., 1970a. *IBM J. Res. Develop.* **14**, 258.
- Matsumoto, G., 1970b. *J. Phys. Soc. Japan* **29**, 606.
- Mayr, F., Hartinger, C., Paraskevopoulos, M., Pimenov, A., Hemberger, J., Loidl, A., Mukhin, A.A., Balbashov, A.M., 2000. *Phys. Rev. B* **62**, 15673.
- Mayr, M., Moreo, A., Vergés, J.A., Arispe, J., Feiguin, A., Dogotto, E., 2001. *Phys. Rev. Lett.* **86**, 135.
- McIlroy, D.N., Waldfried, C., Zhang, J., Choi, J.-W., Foong, F., Liou, S.H., Dowben, P.A., 1996. *Phys. Rev. B* **54**, 17438.
- Meneghini, C., Levy, D., Mobilio, S., Ortolani, M., Nuñez-Reguero, M., Kumar, A., Sarma, D.D., 2002. *Phys. Rev. B* **65**, 012111.
- Millange, F., De Brion, S., Chouteau, G., 2000. *Phys. Rev. B* **62**, 5619.
- Millis, A.J., Littlewood, P.B., Shraiman, B.J., 1995. *Phys. Rev. Lett.* **74**, 5144.
- Mira, J., Rivas, J., Rivadulla, F., Vázquez-Vázquez, C., López Quintela, M.A., 1999. *Phys. Rev. B* **60**, 2998.
- Mira, J., Fondado, A., Hueso, L.E., Rivasibid, J., Rivadulla, F., López Quintela, M.A., 2000. *Phys. Rev. B* **61**, 5857.
- Mira, J., Rivas, J., Hueso, L.E., Rivadulla, F., López Quintela, M.A., Señaris Rodríguez, M.A., Ramos, C.A., 2002. *Phys. Rev. B* **65**, 024418.
- Miyano, K., Tanaka, T., Tomioka, Y., Tokura, Y., 1997. *Phys. Rev. Lett.* **78**, 4257.
- Mizokawa, T., Khomskii, D.I., Sawatzky, G.A., 1999. *Phys. Rev. B* **60**, 7309.
- Mori, S., Chen, C.H., Cheong, S.-W., 1998a. *Phys. Rev. Lett.* **81**, 3972.
- Mori, S., Chen, C.H., Cheong, S.-W., 1998b. *Nature (London)* **392**, 473.
- Moritomo, Y., 1999. *Phys. Rev. B* **60**, 10374.
- Moritomo, Y., Kuwahara, H., Tomioka, Y., Tokura, Y., 1997a. *Phys. Rev. B* **55**, 7549.
- Moritomo, Y., Asamitsu, A., Tokura, Y., 1997b. *Phys. Rev. B* **56**, 12190.
- Moritomo, Y., Machida, A., Nishibori, E., Takata, M., Sakata, M., 2001. *Phys. Rev. B* **64**, 214409.
- Moriya, T., 1960. *Phys. Rev.* **120**, 91.
- Mott, N.F., 1949. *Proc. Phys. Soc. (London) A* **62**, 416.
- Moussa, F., Hennion, M., Biotteau, G., Rodríguez-Carvajal, J., Pinsard, L., Revcolevschi, A., 1999. *Phys. Rev. B* **60**, 12299.
- Murakami, Y., Hill, J.P., Gibbs, D., Blume, M., Koyama, I., Tanaka, M., Kawata, H., Arima, T., Tokura, Y., Hirota, K., Endoh, Y., 1998. *Phys. Rev. Lett.* **81**, 582.
- Mydosh, J.A., 1993. *Spin Glasses: An Experimental Introduction*. Taylor & Francis, London.
- Nagaev, E.L., 1999. *Aust. J. Phys.* **52**, 305.
- Nagaev, E.L., 2001a. *Phys. Rep.* **346**, 387.
- Nagaev, E.L., 2001b. *Phys. Rev. B* **64**, 144409.
- Naler, S., Rübhausen, M., Yoon, S., Cooper, S.L., Kim, K.H., Cheong, S.-W., 2002. *Phys. Rev. B* **65**, 092401.
- Nath, A., Chechersky, V., Greene, R.L., 2000. *J. Solid State Chem.* **155**, 116.
- Neumeier, J.J., Cohn, J.L., 2000. *Phys. Rev. B* **61**, 14319.
- Neumeier, J.J., Hundley, M.F., Thompson, J.D., Heffner, R.H., 1995. *Phys. Rev. B* **52**, R7006.
- Neumeier, J.J., Cornelius, A.L., Andres, K., 2001. *Phys. Rev. B* **64**, 172406.
- Nojiri, H., Kaneko, K., Motokawa, M., Hirota, K., Endoh, Y., Takahashi, K., 1999. *Phys. Rev. B* **60**, 4142.
- Ogawa, K., Wei, W., Miyano, K., Tomioka, Y., Tokura, Y., 1998. *Phys. Rev. B* **57**, R15033.
- Okuda, T., Tomioka, Y., Asamitsu, A., Tokura, Y., 2000. *Phys. Rev. B* **61**, 8009.
- Oliver, M.R., Dimmock, J.O., McWhorter, A.L., Reed, T.B., 1972. *Phys. Rev. B* **5**, 1078.

- Overend, N., Zhou, J.-S., Goodenough, J.B., unpublished.
- Papavassiliou, G., Fardis, M., Milia, F., Simopoulos, A., Kallias, G., Pissas, M., Niarchos, D., Ioannidis, N., Dimitropoulos, C., Dolinsek, J., 1997. *Phys. Rev. B* **55**, 15000.
- Papavassiliou, G., Fardis, M., Belesi, M., Pissas, M., Panagiotopoulos, I., Kallias, G., Niarchos, D., Dimitropoulos, C., Dolinsek, C., 1999. *Phys. Rev. B* **59**, 6390.
- Papavassiliou, G., Belesi, M., Fardis, M., Dimitropoulos, C., 2001. *Phys. Rev. Lett.* **87**, 177204.
- Perebeinos, V., Allen, P.B., 2000. *Phys. Rev. Lett.* **85**, 5178.
- Perebeinos, V., Allen, P.B., 2001. *Phys. Rev. B* **64**, 085118.
- Pinsard-Gaudart, L., Rodríguez-Carvajal, J., Daoud-Aladine, A., Goncharenko, I., Medarde, M., Smith, R.I., Revcolevschi, A., 2001. *Phys. Rev. B* **64**, 064426.
- Pissas, M., Kallias, G., Hofmann, M., Többens, D.M., 2002. *Phys. Rev. B* **65**, 064413.
- Podzorov, V., Uehara, M., Gershenson, M.E., Koo, T.Y., Cheong, S.-W., 2000. *Phys. Rev. B* **61**, R3784.
- Poepplmeier, K.R., Leonowicz, M.E., Scanlon, J.C., Longo, J.M., 1982a. *J. Solid State Chem.* **45**, 71.
- Poepplmeier, K.R., Leonowicz, M.E., Longo, J.M., 1982b. *J. Solid State Chem.* **44**, 89.
- Quezel, S., Rossat-Mignod, J., Bertaut, E.F., 1974. *Solid State Commun.* **14**, 941.
- Quezel, S., Tcheou, F., Rossat-Mignod, J., Quezel, G., Roudaut, E., 1977. *Physica B & C* **86–88 B**, 916.
- Quezel-Ambrunat, S., 1968. *Bull. Soc. Fr. Mineral. Cristallogr.* **91**, 339.
- Quijada, M.A., Cerne, J., Simpson, J.R., Drew, H.D., Ahn, K.H., Millis, A.J., Shreekala, R., Ramesh, R., Rajeswari, M., Venkatesan, T., 1998. *Phys. Rev. B* **58**, 16093.
- Quijada, M.A., Simpson, J.R., Vasiliu-Doloc, L., Lynn, J.W., Drew, H.D., Mukovskii, Y.M., Karabashev, S.G., 2001. *Phys. Rev. B* **64**, 224426.
- Radaelli, P.G., Cox, D.E., Marezio, M., Cheong, S.-W., Schiffer, P.E., Ramirez, A.P., 1995. *Phys. Rev. Lett.* **75**, 4488.
- Radaelli, P.G., Marezio, M., Hwang, H.Y., Cheong, S.-W., Batlogg, B., 1996. *Phys. Rev. B* **54**, 8992.
- Radaelli, P.G., Iannone, G., Marezio, M., Hwang, H.Y., Cheong, S.-W., Jorgensen, J.D., Argyriou, D.N., 1997a. *Phys. Rev. B* **56**, 8265.
- Radaelli, P.G., Cox, D.E., Marezio, M., Cheong, S.-W., 1997b. *Phys. Rev. B* **55**, 3015.
- Radaelli, P.G., Cox, D.E., Capogna, L., Cheong, S.-W., Marezio, M., 1999. *Phys. Rev. B* **59**, 14440.
- Rao, C.N.R., Arulraj, A., Santosh, P.N., Cheetham, A.K., 1998. *Chem. Mater.* **10**, 2714.
- Raquet, B., Anane, A., Wirth, S., Xiong, P., von Molnár, S., 2000. *Phys. Rev. Lett.* **84**, 4485.
- Reller, A., Thomas, J.M., Jefferson, D.A., Uppal, M.K., 1984. *Proc. Roy. Soc. (London)* **394**, 223.
- Ren, Y.H., Zhang, X.H., Lüpke, G., Schneider, M., Onellion, M., Perakis, I.E., Hu, Y.F., Qi Li, 2001. *Phys. Rev. B* **64**, 144401.
- Reutler, P., Bensaid, A., Herbstritt, F., Höfener, C., Marx, A., Gross, R., 2000. *Phys. Rev. B* **62**, 11619.
- Rivadulla, F., López-Quintela, M.A., Hueso, L.E., Jardón, C., Fondado, A., Rivas, J., Causa, M.T., Sánchez, R.D., 1999a. *Solid State Commun.* **110**, 179.
- Rivadulla, F., López-Quintela, M.A., Hueso, L.E., Rivas, J., Causa, M.T., Ramos, C., Sánchez, R.D., Tovar, M., 1999b. *Phys. Rev. B* **60**, 11922.
- Rivadulla, F., López-Quintela, M.A., Mira, J., Rivas, J., 2001. *Phys. Rev. B* **64**, 052403.
- Rivadulla, F., Winkler, E., Zhou, J.-S., Goodenough, J.B., 2002. *Phys. Rev. B* (in press).
- Rodríguez-Carvajal, J., Hennion, M., Moussa, F., Moudén, A.H., Pinsard, L., Revcolevschi, A., 1998. *Phys. Rev. B* **57**, R3189.
- Romero, D.B., Moritomo, Y., Mitchell, J.F., Drew, H.D., 2001. *Phys. Rev. B* **63**, 132404.
- Roy, M., Mitchell, J.F., Ramirez, A.P., Schiffer, P., 1998. *Phys. Rev. B* **58**, 5185.
- Roy, M., Mitchell, J.F., Ramirez, A.P., Schiffer, P., 1999. *J. Phys. Condens. Matter* **11**, 4843.
- Roy, M., Mitchell, J.F., Ramirez, A.P., Schiffer, P., 2000. *Phys. Rev. B* **62**, 13876.
- Rozenberg, M.J., Kotliar, G., Zhang, X.Y., 1994. *Phys. Rev. B* **49**, 10181.
- Ruddlesden, S.N., Popper, P., 1957. *Acta Crystallogr.* **10**, 538.
- Ruddlesden, S.N., Popper, P., 1958. *Acta Crystallogr.* **11**, 54.
- Saitoh, E., Asamitsu, A., Okimoto, Y., Tokura, Y., 2000. *J. Phys. Soc. Japan* **69**, 3614.
- Saitoh, E., Okamoto, S., Takahashi, K.T., Tobe, K., Yamamoto, K., Kimura, T., Ishihara, S., Maekawa, S., Tokura, Y., 2001. *Nature* **410**, 180.
- Sakaie, K.E., Slichter, C.P., Lin, P., Jaime, M., Salamon, M.B., 1999. *Phys. Rev. B* **59**, 9382.
- Saraf, L.V., Ogale, S.B., Chen, Z., Godfrey, R.P., Venkatesan, T., Ramesh, R., 2000. *Phys. Rev. B* **62**, R11961.

- Savosta, M.M., Novák, P., 2001. *Phys. Rev. Lett.* **87**, 137204.
- Schiffer, P., Ramirez, A.P., Bao, W., Cheong, S.-W., 1995. *Phys. Rev. Lett.* **75**, 3336.
- Senis, R., Laukhin, V., Martínez, B., Fontcuberta, J., Obradors, X., Arsenov, A.A., Mukovskii, Y.M., 1998. *Phys. Rev. B* **57**, 14680.
- Shames, A.I., Yakabovsky, A., Amelichev, V., Gorbunenko, O., Kaul, A., 2002. *Solid State Commun.* **121**, 103.
- Shannon, R.D., Prewitt, C.T., 1969. *Acta Crystallogr. B* **25**, 725.
- Shannon, R.D., Prewitt, C.T., 1970. *Acta Crystallogr. B* **26**, 1046.
- Shimomura, S., Tajima, K., Wakabayashi, N., Kobayashi, S., Kuwahara, H., Tokura, Y., 1999. *J. Phys. Soc. Japan* **68**, 1943.
- Shrivastava, K.N., Jaccarino, V., 1976. *Phys. Rev. B* **13**, 299.
- Simopoulos, A., Kallias, G., Devlin, E., Pissas, M., 2001. *Phys. Rev. B* **63**, 054403.
- Skumryev, V., Nogués, J., Muñoz, J.S., Martínez, B., Senis, R., Fontcuberta, J., Pinsard, L., Revcolevschi, A., Mukovskii, Y.M., 2000. *Phys. Rev. B* **62**, 3879.
- Smith, D.W., 1969. *J. Chem. Phys.* **50**, 2784.
- Smolyaninova, V.N., Hamilton, J.J., Greene, R.L., Mukovskii, Y.M., Karabashev, S.G., Balbashov, A.M., 1997. *Phys. Rev. B* **55**, 5640.
- Smolyaninova, V.N., Ghosh, K., Greene, R.L., 1998. *Phys. Rev. B* **58**, R14725.
- Smolyaninova, V.N., Biswas, A., Fournier, P., Lofland, S., Zhang, X., Zhao, G., Greene, R.L., 2002. *Phys. Rev. B* **65**, 104419.
- Srivastava, S., Pandey, N., Padhan, P., Budhani, R.C., 2000. *Phys. Rev. B* **62**, 13868.
- Stankiewicz, J., Sesé, J., García, J., Blasco, J., Rillo, C., 2000. *Phys. Rev. B* **61**, 11236.
- Subías, G., García, J., Blasco, J., Proietti, M.G., 1998. *Phys. Rev. B* **57**, 748.
- Szabo, G. (1969). Ph.D. Thesis, University of Lyon, France.
- Takenaka, K., Sawaki, Y., Sugai, S., 1999. *Phys. Rev. B* **60**, 13011.
- Takenaka, K., Sawaki, Y., Shiozaki, R., Sugai, S., 2000. *Phys. Rev. B* **62**, 13864.
- Tichy, R.S., Goodenough, J.B., 2002. *Solid State Sciences* **4**, 661.
- Tobe, K., Kimura, T., Okimoto, Y., Tokura, Y., 2001. *Phys. Rev. B* **64**, 184421.
- Tokura, Y., Kuwahara, H., Moritomo, Y., Tomioka, Y., Asamitsu, A., 1996. *Phys. Rev. Lett.* **76**, 3184.
- Tomioka, Y., Asamitsu, A., Moritomo, Y., Tokura, Y., 1995. *J. Phys. Soc. Japan* **64**, 3626.
- Tomioka, Y., Asamitsu, A., Kuwahara, H., Moritomo, Y., Tokura, Y., 1996. *Phys. Rev. B* **53**, R1689.
- Tomioka, Y., Asamitsu, A., Tokura, Y., 2001. *Phys. Rev. B* **63**, 024421.
- Töpfer, J., Goodenough, J.B., 1997a. *Eur. J. Solid State Inorg. Chem.* **34**, 467.
- Töpfer, J., Goodenough, J.B., 1997b. *J. Solid State Chem.* **130**, 117.
- Töpfer, J., Doumerc, J.-P., Grenier, J.-C., 1996. *J. Mater. Chem.* **6**, 1511.
- Troyanchuk, O.Ya., Kasper, N.V., Szymczak, H., Nabialek, A., 1997. *Low Temp. Phys.* **23**, 300.
- Uehara, M., Cheong, S.-W., 2000. *Europhys. Lett.* **52**, 674.
- Uehara, M., Mori, S., Chen, C.H., Cheong, S.-W., 1999. *Nature* **399**, 560.
- Uehara, M., Kim, T.H., Cheong, S.-W., private communication.
- Uhlenbruch, S., Teipen, R., Klingeler, R., Büchner, B., Friedt, O., Hücker, M., Kierspel, H., Niemöller, T., Pinsard, L., Revcolevschi, A., Gross, R., 1999. *Phys. Rev. Lett.* **82**, 185.
- Urushibara, A., Moritomo, Y., Arima, T., Asamitsu, A., Kido, G., Tokura, Y., 1995. *Phys. Rev. B* **51**, 14103.
- van den Brink, J., 2001. *Phys. Rev. Lett.* **87**, 217202.
- Van Roosmalen, J.A.M., Cordfunke, E.H.P., 1994. *J. Solid State Chem.* **110**, 106.
- Vasiliu-Doloc, L., Lynn, J.W., Moudden, A.H., de Leon-Guevara, A.M., Revcolevschi, A., 1997. *J. Appl. Phys.* **81**, 5491.
- Vasiliu-Doloc, L., Lynn, J.W., Moudden, A.H., de Leon-Guevara, A.M., Revcolevschi, A., 1998a. *Phys. Rev. B* **58**, 14913.
- Vasiliu-Doloc, L., Lynn, J.W., Mukovskii, Y.M., Arsenov, A.A., Shulyatev, D.A., 1998b. *J. Appl. Phys.* **83**, 7342.
- von Helmolt, R., Wecker, J., Holzapfel, B., Schultz, L., Samwer, K., 1993. *Phys. Rev. Lett.* **71**, 2331.
- Wiebe, C.R., Greedan, J.E., Gardner, J.S., Zeng, Z., Greenblatt, M., 2001. *Phys. Rev. B* **64**, 064421.
- Wold, A., Arnott, R.J., 1959. *J. Phys. Chem. Solids* **9**, 176.
- Wollan, E.O., Koehler, W.C., 1955. *Phys. Rev.* **100**, 545.
- Wood, V.E., Austin, A.E., Collings, E.W., Brog, W.C., 1973. *J. Phys. Chem. Solids* **34**, 859.
- Worledge, W.C., Miéville, L., Geballe, T.H., 1998. *Phys. Rev. B* **57**, 15267.
- Xiao, G., McNiff Jr., E.J., Gong, G.Q., Gupta, A., Canedy, C.L., Sun, J.Z., 1996. *Phys. Rev. B* **54**, 6073.

- Xiong, X., Dabrowski, B., Chmaissem, O., Bukowski, Z., Kolesnik, S., Dybzinski, R., Kimball, C.W., Jorgensen, J.D., 1999. *Phys. Rev. B* **60**, 10186.
- Yakubovskii, A., Kumagai, K., Furukawa, Y., Babushkina, N., Taldenkov, A., Kaul, A., Gorbenco, O., 2000. *Phys. Rev. B* **62**, 5337.
- Yamada, Y., Hino, O., Nohdo, S., Kanao, R., Inami, T., Katano, S., 1996. *Phys. Rev. Lett.* **77**, 904.
- Yamada, Y., Suzuki, J., Oikawa, K., Katano, S., Fernandez-Baca, J.A., 2000. *Phys. Rev. B* **62**, 11600.
- Yoon, S., Liu, H.L., Schollerer, G., Cooper, S.L., Han, P.D., Payne, D.A., Cheong, S.-W., Fisk, Z., 1998. *Phys. Rev. B* **58**, 2795.
- Yoshinari, Y., Hammel, P.C., Thompson, J.D., Cheong, S.-W., 1999. *Phys. Rev. B* **60**, 9275.
- Yoshizawa, H., Kawano, H., Tomioka, Y., Tokura, Y., 1995. *Phys. Rev. B* **52**, R13145.
- Yoshizawa, H., Kawano, H., Tomioka, Y., Tokura, Y., 1996. *J. Phys. Soc. Japan* **65**, 1043.
- Yudin, V.M., Gavrilishina, A.I., Artem'eva, M.V., Bryzhina, M.F., 1966. *Soviet Phys. Solid State* **7**, 1856.
- Yuzhelevskii, Y., Markovich, V., Dikovskiy, V., Rozenberg, E., Gorodetsky, G., Jung, G., Shulyatev, D.A., Mukovskii, Ya.M., 2001. *Phys. Rev. B* **64**, 224428.
- Zaanen, J., Sawatzky, G.A., 1987. *Can. J. Phys.* **65**, 1262.
- Zener, C., 1951. *Phys. Rev.* **82**, 403.
- Zhao, G., Ghosh, K., Keller, H., Greene, R.L., 1999. *Phys. Rev. B* **59**, 81.
- Zhao, G., Smolyaninova, V., Prellier, W., Keller, H., 2000. *Phys. Rev. Lett.* **84**, 6086.
- Zhao, G.-M., Conder, K., Keller, H., Müller, K.A., 1996. *Nature (London)* **381**, 676.
- Zhao, G.-M., Hunt, M.B., Keller, H., 1997a. *Phys. Rev. Lett.* **78**, 955.
- Zhao, G.-M., Keller, H., Hofer, J., Shengalaya, A., Müller, K.A., 1997b. *Solid State Commun.* **104**, 57.
- Zhao, G.-M., Kang, D.J., Prellier, W., Rajeswari, M., Keller, H., Venkatesan, T., Greene, R.L., 2001. *Phys. Rev. B* **63**, 060402.
- Zhao, Y.G., Li, J.J., Shreekala, R., Drew, H.D., Chen, C.L., Cao, W.L., Lee, C.H., Rajeswari, M., Ogale, S.B., Ramesh, R., Baskaran, G., Venkatesan, T., 1998. *Phys. Rev. Lett.* **81**, 1310.
- Zhao, Y.G., Cai, W., Zhao, J., Zhang, X.P., Cao, B.S., Zhu, M.H., Zhang, L.W., Ogale, S.B., Wu, T., Venkatesan, T., Lu, L., Mandal, T.K., Gopalakrishnan, J., 2002. *Phys. Rev. B* **65**, 144406.
- Zheng, R.K., Zhu, C.F., Xie, J.Q., Li, X.G., 2001. *Phys. Rev. B* **63**, 024427.
- Zhou, J.-S., Goodenough, J.B., 1998. *Phys. Rev. Lett.* **80**, 2665.
- Zhou, J.-S., Goodenough, J.B., 1999. *Phys. Rev. B* **60**, R15002.
- Zhou, J.-S., Goodenough, J.B., 2000. *Phys. Rev. B* **62**, 3834.
- Zhou, J.-S., Goodenough, J.B., 2001a. *Phys. Rev. B* **64**, 024421.
- Zhou, J.-S., Goodenough, J.B., 2001b. In: Kaplan, M.D., Zimmermann, G.O. (Eds.), *Vibronic Interactions: Jahn-Teller Effect in Crystals and Molecules*. Kluwer Academic Publishers, The Netherlands, p. 15.
- Zhou, J.-S., Goodenough, J.B., 2002a. *Phys. Rev. Lett.* **89**, 087201.
- Zhou, J.-S., Goodenough, J.B., 2002b. *Phys. Rev. B* **66**, 052401.
- Zhou, J.-S., Archibald, W., Goodenough, J.B., 1996. *Nature (London)* **381**, 770.
- Zhou, J.-S., Goodenough, J.B., Asamitsu, A., Tokura, Y., 1997. *Phys. Rev. Lett.* **79**, 3234.
- Zhou, J.-S., Yin, H.Q., Goodenough, J.B., 2001a. *Phys. Rev. B* **63**, 184423.
- Zhou, J.-S., Liu, G.L., Goodenough, J.B., 2001b. *Phys. Rev. B* **63**, 172416.
- Zhu, C., Zheng, R., Su, J., He, J., 1999. *Appl. Phys. Lett.* **74**, 3504.
- Zimmermann, M.V., Nelson, C.S., Kim, Y.-J., Hill, J.P., Gibbs, D., Nakao, H., Wakabayashi, Y., Murakami, Y., Tokura, Y., Tomioka, Y., Arima, T., Kao, C.-C., Casa, D., Venkataraman, C., Gog, Th., 2001. *Phys. Rev. B* **64**, 064411.
- Zuo, J.M., Tao, J., 2001. *Phys. Rev. B* **63**, 060407(R).
- Zvyagin, S., Schwenk, H., Lüthi, B., Kamenev, K.V., Balakrishnan, G., Paul, D.Mck., Kamenev, V.I., Pashkevich, Yu.G., 2000. *Phys. Rev. B* **62**, R6104.

Chapter 215

PARAMAGNETIC NMR LANTHANIDE INDUCED SHIFTS FOR EXTRACTING SOLUTION STRUCTURES

Claude PIGUET

Department of Inorganic, Analytical and Applied Chemistry, University of Geneva,
30 quai E. Ansermet, CH-1211 Geneva 4, Switzerland

E-mail: Claude.Piguet@chiam.unige.ch

Carlos F.G.C. GERALDES

Department of Biochemistry, Faculty of Science and Technology, and
Centre of Neurosciences, University of Coimbra, 3000 Coimbra, Portugal

E-mail: gerald@ci.uc.pt

Contents

List of symbols	354	2.4.1. Calculation of the anisotropic part of the magnetic susceptibility tensor with structural models	373
1. Introduction	355	2.4.2. The model-free methods	376
2. Theory	358	2.4.2.1. Reilley's method	376
2.1. Nuclear relaxation in paramagnetic lanthanide complexes for extracting <i>R</i> -nucleus distances	358	2.4.2.2. Crystal-field independent methods	377
2.1.1. Lanthanide-induced contact relaxation	359	2.4.2.3. The special case of rhombic systems	379
2.1.2. Lanthanide-induced dipolar relaxation	361	3. Application of the model-free methods to axial monometallic lanthanide complexes with sterically rigid ligands	380
2.1.3. Lanthanide-induced Curie-spin relaxation	362	3.1. Complexes with threefold symmetry	381
2.2. Contact shifts and through-bond spin delocalisation in paramagnetic lanthanide complexes	364	3.1.1. $[R(L^1-2H)_3]^{3-}$ ($L^1 =$ oxydiacetic acid)	381
2.3. Pseudo-contact shifts and through-space interactions in paramagnetic lanthanide complexes	366	3.1.2. $[R(L^2)_3]^{3+}$ ($L^2 =$ 2,6-bis(benzimidazole)pyridine)	384
2.3.1. Origin and modeling of magnetic anisotropy in paramagnetic lanthanide complexes	368	3.1.3. $[R(L^3)_3]^{3+}$ ($L^3 =$ 2,6-pyridinedicarboxylic acid-bis-diethylamide)	387
2.4. Separation of contact and pseudo-contact contributions in paramagnetic lanthanide complexes	372	3.1.4. $[R(L^4)]^{3+}$ and $[R(L^4+H)]^{4+}$ ($L^4 =$ tris{2-[<i>N</i> -methylcarbamoyl-6-(<i>N,N</i> -diethylcarbamoyl)pyridine-2]ethyl}amine)}	390

3.1.5. $[RM(L^5)_3]^{5/6+}$ ($M = Zn, Co$; $L^5 = 2\text{-}\{6\text{-}[N,N\text{-diethylcarbox-}]\}$ $\text{amido}\text{-pyridin-2-yl}\text{-}1,1'\text{-dimeth-}$ $\text{yl-}5,5'\text{-methylene-}2'\text{-}(5\text{-methyl-}$ $\text{pyridin-2-yl})\text{bis}(1H\text{-benzimidazole})$) 393	3.2.5. Comparison of the structures of the $[R(L^{10}\text{-}4H)]^-$, $[R(L^{11})]^{3+}$ and $[R(L^{12}\text{-}8H)]^{5-}$ complexes 437
3.1.6. $[R(L^6)]^{3+}$ ($L^6 = \text{azacryptand}$, see fig. 26) 401	3.2.6. $[R(L^{13}\text{-}2H)_2]^-$ ($L^{13} = \text{phtaloc-}$ anine) 440
3.1.7. $[R(L^7\text{-}2H)_3]^{3-}$ ($L^7 = 2,6\text{-pyri-}$ $\text{dinedicarboxylic acid and deriva-}$ tives) 404	4. Application of the model-free methods to axial bimetallic lanthanide complexes with sterically rigid ligands 443
3.1.8. $[R(L^8\text{-}3H)]$ ($L^8 = 1,4,7\text{-triazacy-}$ $\text{clononane-}N,N',N''\text{-triacetic acid}$) 410	4.1. Complexes with threefold symmetry 444
3.2. Complexes with fourfold symmetry 415	4.1.1. $[R_2(L^{14}\text{-}2H)_3]$ ($L^{14} = \text{bis}\{1\text{-}$ $\text{ethyl-}2\text{-}[6'\text{-carboxy}]\text{pyridin-}2'\text{-yl}\}$ $\text{benzimidazol-}5\text{-yl}\}$ methane) 444
3.2.1. $[R(L^9\text{-}H)_4]^-$ ($L^9 = \text{dithiometh-}$ $\text{ylphosphinic acid and dithiophos-}$ $\text{phorus acid and dithiophosphorus}$ acid derivatives) 415	4.2. Complexes with fourfold symmetry 448
3.2.2. $[R(L^{10}\text{-}4H)]^-$ ($L^{10} = 1,4,7,10\text{-}$ $\text{tetraazacyclododecane-}N,N',N'',$ $N'''\text{-tetraacetic acid}$) 419	4.2.1. $[R_2(L^{15}\text{-}2H)_3]$ ($L^{15} = \text{octaethyl-}$ porphyrin) 448
3.2.3. $[R(L^{11})]^{3+}$ ($L^{11} = 1,4,7,10\text{-}$ $\text{tetraazacyclododecane-}1,4,7,10\text{-}$ $\text{tetrakis}(N,N\text{-diethylacetamide})$) 426	5. Application of the model-free methods to axial trimetallic lanthanide complexes with steri- cally rigid ligands 453
3.2.4. $[R(L^{12}\text{-}8H)]^{5-}$ ($L^{12} = 1,4,7,10\text{-}$ $\text{tetraazacyclododecane-}1,4,7,10\text{-}$ $\text{tetrakis}(\text{methylenephosphonic}$ $\text{acid})$) 430	5.1. Complexes with threefold symmetry 454
	5.1.1. $[R_3(L^{16}\text{-}3H)_2(OH_2)_6]^{3+}$ ($L^{16} =$ $1,3,5\text{-triamino-}1,3,5\text{-tridesoxy-cis-}$ inositol) 454
	5.1.2. $[R_3(L^{17})_3]^{9+}$ ($L^{17} = 2,6\text{-bis}\{1\text{-}$ $\text{ethyl-}2\text{-}[6\text{-}(N,N'\text{-diethylcarba-}$ $\text{moyl})\text{-pyridin-}2\text{-yl}]\text{benzimidazol-}$ $5\text{-methylene-}\}$ (2-ethyl-benzimida- $\text{zol-}5\text{-yl})\}$ pyridine) 455
	6. Conclusions 459
	References 460

List of symbols

A_i	Fermi hyperfine constant for a nucleus i	$\langle S_z \rangle$	expectation value of S_z
B_q^k	crystal-field parameters of rank k	T_1	longitudinal nuclear relaxation time
C_q^k	spherical tensor operators of rank k	T_2	transversal nuclear relaxation time
C_j	Bleaney's factor of lanthanide j (scaled to -100 for Dy(III))	$\text{Tr}(\chi)$	trace of the magnetic susceptibility tensor
F_i	contact term of the nucleus i	β	Bohr magneton
g_e	Landé factor	χ	magnetic susceptibility tensor
G_i	axial geometrical factor of the nucleus i	χ_0	isotropic part of the magnetic susceptibility ten- sor
H_i	rhombic geometrical factor of the nucleus i	$\chi_{\alpha\beta}$	$\alpha\beta$ component of the magnetic susceptibility tensor
H_0	applied magnetic field	δ_j^{bulk}	bulk paramagnetic shift induced by a lanthanide j
J	total angular momentum quantum number	δ_{ij}^{exp}	hyperfine chemical shift for a nucleus i in a complex of a lanthanide j
$\langle J_z \rangle$	expectation value of J_z	δ_i^{dia}	diamagnetic shift in ppm for a nucleus i
k	Boltzmann constant		
N_A	Avogadro's number		
r_i	R -nucleus i distance		
S	spin quantum number		

$\delta_{ij}^{\text{para}}$	paramagnetic hyperfine chemical shift in ppm for a nucleus i in a complex of a lanthanide j	ϕ_i	spherical coordinate of nucleus i
δ_{ij}^{c}	paramagnetic contact shift in ppm for a nucleus i in a complex of a lanthanide j	μ_{eff}	effective electronic magnetic momentum in μ_{B}
δ_{ij}^{pc}	paramagnetic pseudo-contact shift in ppm for a nucleus i in a complex of a lanthanide j	θ_i	spherical coordinate of nucleus i
ΔE_{CF}	crystal-field splitting of the ground J multiplet in cm^{-1}	τ_{c}	characteristic correlation time
γ	magnetogyric ratio	τ_{e}	electron spin relaxation characteristic time
		τ_{r}	rotational characteristic time
		τ_{m}	chemical exchange characteristic time
		ω	Larmor precession frequency in Hz
		ζ	spin orbit coupling constant

1. Introduction

Intense research activities during the last decade have demonstrated that a judicious combination of dative bonds (i.e., coordination bonds) with non-covalent interactions (i.e., electrostatic, hydrogen bonds, hydrophobic forces, etc.) provides well-defined and structurally rigid metal-containing architectures in which the geometrical and electronic structures can be finely tuned (Piguet et al., 1997; Lehn, 2000; Steed and Atwood, 2000; Swiegers and Malefetse, 2000; Holliday and Mirkin, 2001). Planned chemical, mechanical and electronic functions may be further implemented to produce supramolecular devices and machines (Piguet and Bünzli, 1998; Kahn, 2000; Balzani et al., 2000). The pronounced stereo-electronic preferences of d-block transition metal ions associated with their peculiar d^n -electronic configurations have been systematically exploited to control the final molecular or supramolecular architectures according to the *Lock and Key* concept (Leininger et al., 2000; Fujita et al., 2001). The versatile coordination properties of 4f-block ions (i.e., the lanthanides $R(\text{III})$) often prevent their use as templating agents in sophisticated molecular or supramolecular assemblies and the structural programming of the metallic sites remains challenging. On the other hand, the *Induced fit* concept takes advantage of specific non-covalent inter-strand interactions to control the size, the shape and the geometry of the metallic site, thus leading to discrete lanthanide-containing edifices in which a rational design of the associated functions relies on the chemist's capacity (i) to impose specific metallic environments and supramolecular structures and (ii) to extract reliable electronic and geometric informations in order to iteratively improve molecular programming (Piguet and Bünzli, 1999; Fu and Turro, 1999; Bruce et al., 2000; Parker, 2000; Piguet et al., 2000; Zhang et al., 2001; Bünzli and Piguet, 2002). The latter point is crucial because minute structural variations may induce (i) drastic size-discriminating effects along the lanthanide series (Petoud et al., 1997), (ii) new optical properties (Gamelin and Güdel, 2000) and huge magnetic anisotropies (Mironov et al., 2001). The characterisation of solid state structures of intermediate sizes has benefited from the recent development of array detectors and the crystallization processes leading to large semi-rigid supramolecular edifices remains the limiting factor for extracting reliable geometrical informations in this context. However, considerable structural changes

may occur between solid-state and solution (solvation, relaxation of packing constraints, dissociation, etc.) and it is crucial to extract reliable structural and electronic data in solution if self-assembly processes are to be improved. As a result of their peculiar inner-shell $4f^n$ -electronic configurations, the lanthanides display electrostatic metal–ligand bonds with minor covalency and unpaired spin delocalisation is very limited. $R(\text{III})$ ($R = \text{Ce}–\text{Yb}$) can be thus considered as paramagnetic dots which affect the magnetic properties of the molecular or supramolecular edifices in a predictable way. For a synthetic chemist, paramagnetism is often considered as a severe handicap for interpreting NMR spectra because (i) the bulk magnetic susceptibility translates the NMR spectrum by a constant (Lölicher and Scheffold, 1972), (ii) the NMR signals are severely broadened by the increased nuclear relaxation induced by the electronic magnetic momentum and (iii) the hyperfine chemical shift of each proton i drastically depends on its topological and geometrical location with respect to the paramagnetic centre (Bertini and Luchinat, 1996). However, detailed structural and electronic informations can be gained from paramagnetic contributions to the NMR data if an adequate modeling of the magnetic properties is available.

Firstly, Evans (1959) and Evans et al. (1971) have established that the bulk paramagnetic susceptibility for a complex of a lanthanide j affects the chemical shifts of all nuclei by a constant value δ_j^{bulk} (in ppm) which is given by eq. (1)

$$\delta_j^{\text{bulk}} = \left(\frac{\mu_{\text{eff}}}{2.828} \right)^2 \cdot \frac{s_f \cdot c}{T} \cdot 10^3, \quad (1)$$

μ_{eff} is the effective electronic magnetic momentum (in Bohr magnetons), T is the absolute temperature (in K), c is the molar concentration of the paramagnetic lanthanide complex (in $\text{mol} \cdot \text{dm}^{-3}$) and s_f is the shape factor of the magnet ($s_f = 4\pi/3$ for a cylindrical sample in a superconducting magnet (Baker et al., 1988)) and $2.828 = \sqrt{3k/(N_A\beta^2)}$. This term vanishes when a frequency-locked spectrometer is used together with an internal standard as a reference for chemical shifts, two conditions which are usually met when recording NMR spectra (Peters et al., 1996). However, δ_j^{bulk} can be of interest for the determination of effective electronic magnetic momenta (μ_{eff}) and associated isotropic paramagnetic susceptibilities ($\chi_0 = (1/3)\text{Tr}(\chi)$, eq. (2)) of lanthanide complexes in solution after corrections for solvent effects (Grant, 1995) and diamagnetic contributions (Piguet, 1997). Recently, the measurement of δ_j^{bulk} induced by paramagnetic lanthanide MRI contrast agents has been used for addressing their in vivo concentrations (Corsi et al., 2001).

$$\mu_{\text{eff}} = 2.828\sqrt{\chi_0 \cdot T}. \quad (2)$$

Secondly, the lanthanide induced relaxation (LIR) responsible for the broadening of the NMR signals (i.e., the decrease of characteristic longitudinal (T_1) and transversal (T_2) nuclear relaxation times) can be traced back to fluctuations of the magnetic field induced by variations of the electronic magnetic momenta due to electronic relaxation, molecular tumbling and chemical exchange processes. Theoretical background has been given by Solomon (1955) and Bloembergen and Morgan (1961), and the recent developments of slow-relaxing Gd(III) complexes working as contrast agents for magnetic resonance

imaging (MRI) have contributed to improve theoretical modeling (Peters et al., 1996; Aime et al., 1998; Babailov and Krieger, 1998; Caravan et al., 1999; Geraldes, 1999; Sharp, 2001). As far as the elucidation of molecular structures of lanthanide complexes in solution is concerned, fast-relaxing paramagnetic ions ($R = \text{Ce} - \text{Yb}$, except Gd) are better candidates for extracting lanthanide-nucleus i distances from the electronic-induced paramagnetic dipolar and spin-Curie contributions to the nuclear relaxation processes (Bertini et al., 1993a; Aime et al., 1992a). A short description of this technique together with relevant applications for exploring the solution structures of axial lanthanide complexes is proposed in the next section, although the relaxation processes are not the central theme of this review. Finally, the hyperfine paramagnetic lanthanide induced shift (LIS, $\delta_{ij}^{\text{para}}$) contains crucial informations about (i) electronic structures and spin delocalisation (via the contact contribution δ_{ij}^{c}) and (ii) molecular structures and magnetic anisotropies (via the pseudo-contact contribution δ_{ij}^{pc}) (Sherry and Geraldes, 1989; Bertini and Luchinat, 1996; Peters et al., 1996; Forsberg, 1996). The experimental hyperfine shift of a nucleus i in a paramagnetic complex of a lanthanide j (δ_{ij}^{exp} in ppm) can be partitioned according to eq. (3) in which δ_i^{dia} corresponds to the underlying diamagnetic shift measured for the analogous $4f^0$ ($R = \text{La}, \text{Y}$) or $4f^{14}$ configurations ($R = \text{Lu}$) and δ_j^{bulk} is the bulk paramagnetic susceptibility ($\delta_j^{\text{bulk}} = 0$ when an internal reference is used)

$$\delta_{ij}^{\text{exp}} = \delta_i^{\text{dia}} + \delta_j^{\text{bulk}} + \delta_{ij}^{\text{para}} = \delta_i^{\text{dia}} + \delta_j^{\text{bulk}} + \delta_{ij}^{\text{c}} + \delta_{ij}^{\text{pc}}. \quad (3a)$$

The hyperfine paramagnetic contribution (LIS, $\delta_{ij}^{\text{para}}$) corresponding to the sum of contact (through-bond) and pseudo-contact (through-space) effects is easily obtained from the experimental NMR data:

$$\text{LIS} = \delta_{ij}^{\text{para}} = \delta_{ij}^{\text{c}} + \delta_{ij}^{\text{pc}} = \delta_{ij}^{\text{exp}} - \delta_i^{\text{dia}}. \quad (3b)$$

Since the first observations by Hinckley (1969) demonstrating the ability of lanthanide chelates to induce paramagnetic LIS shifts, theoretical modeling has established the physical origins of the contact (Golding and Halton, 1972; Pinkerton et al., 1985) and pseudo-contact (Bleaney, 1972; Bleaney et al., 1972; Golding and Pyykkö, 1973; Stout and Gutowsky, 1976; Horrocks, 1977; McGarvey, 1979) contributions. Interestingly, for a given paramagnetic lanthanide, δ_{ij}^{c} depends exclusively on the magnitude of the spin delocalisation mediated by scalar Fermi interactions, and thus reflects the topology and the nature of the chemical bonds separating the paramagnetic lanthanide and the nucleus under investigation. On the other hand, δ_{ij}^{pc} results from the residual isotropic dipolar coupling between the electronic and nuclear magnetic momenta which depends on the molecular magnetic anisotropy induced by the lanthanide and the geometrical position of the nucleus under investigation. This second term contains the geometrical informations required to extract molecular structures in solution and much efforts have been focused on reliable and physically-meaningful separations of these two contributions from the experimental LIS (Reilley et al., 1975, 1976; Desreux and Reilley, 1976; Kemple et al., 1988; Forsberg et al., 1995; Lisowski et al., 1995a). Once reliable pseudo-contact terms are at hand, the complicated dependence of δ_{ij}^{pc} on the internal coordinates and

on the anisotropic part of the magnetic susceptibility tensor (see sect. 2.3) requires some preliminary assumptions. If (i) a large number of reliable pseudo-contact shifts are accessible and (ii) an efficient modeling of the three-dimensional structure is accessible (as in proteins), the calculation of the magnetic susceptibility tensors from an initial structural model followed by iterative non-linear least-squares fits provides the desired structural and magnetic informations (structure-dependent method: Kemple et al. (1988), Forsberg et al. (1995), Lisowski et al. (1995a)). For lanthanide complexes of intermediate size, contact contributions are rarely negligible and it is necessary to use a reliable a priori model of the magnetic anisotropy produced by the lanthanide site in order to extract the missing structural informations (model-free method, Bleaney (1972)). Both approaches have been addressed in two recent reviews by Forsberg (1996) and Peters et al. (1996) who conclude that structure-dependent techniques are better suited for solving solution structures since the magnetic anisotropy is obtained as a fitted parameter. However, the difficult structural and geometrical modeling of semi-rigid supramolecular edifices of intermediate size containing numerous weak non-covalent interactions and dative bonds (Fraternali and Wipff, 1997; Ulrich et al., 1997; Berny et al., 1999) combined with the extreme sensitivity of programmed functions to minor structural changes in lanthanide complexes have led to a revival of the model-free techniques for detecting crystal-field variations and structural changes (Ren and Sherry, 1996; Platas et al., 1999; Rigault et al., 2000a, 2000b). Since the seminal reviews of Forsberg (1996) and Peters et al. (1996), the application of the classical structure-independent one-nucleus method for axial lanthanide complexes has shown some limitations (Rigault and Piguet, 2000) and further developments including two- and three-nuclei techniques (Platas et al., 1999; Geraldes et al., 2001) based on original concepts previously introduced by Reuben (1982) and Spiliadis and Pinkerton (1982) have been implemented for establishing isostructurality and electronic structures (Ren and Sherry, 1996; Platas et al., 1999; Rigault et al., 2000a, 2000b).

This review focuses on the use and limitations of the model-free methods in axial paramagnetic supramolecular mono- and polymetallic lanthanide-containing complexes. A comprehensive survey of the systems with three- and fourfold symmetry for which these techniques have been applied is proposed together with a detailed discussion of the limitations of Bleaney's approach for the modeling of paramagnetic anisotropies and the detection of structural changes along the lanthanide series.

2. Theory

2.1. Nuclear relaxation in paramagnetic lanthanide complexes for extracting *R*-nucleus distances

For any nucleus *i* of a paramagnetic lanthanide complex in the absence of significant chemical exchange, the experimental longitudinal ($1/T_{1i}^{\text{exp}}$) and transversal ($1/T_{2i}^{\text{exp}}$) nuclear relaxation rates are given by eqs. (4), (5) in which T_i^{dia} corresponds to the characteristic relaxation times of the same nucleus *i* in the analogous diamagnetic complex (*R* = La, Y, Lu) and T_i^{para} are

the paramagnetic contributions induced by the lanthanide metal ion (Peters et al., 1996),

$$\frac{1}{T_{1i}^{\text{exp}}} = \frac{1}{T_{1i}^{\text{dia}}} + \frac{1}{T_{1i}^{\text{para}}}, \quad (4)$$

$$\frac{1}{T_{2i}^{\text{exp}}} = \frac{1}{T_{2i}^{\text{dia}}} + \frac{1}{T_{2i}^{\text{para}}}. \quad (5)$$

The paramagnetic contributions $1/T_i^{\text{para}}$, often termed as lanthanide-induced relaxation (LIR), arise from inner-sphere and outer-sphere mechanisms, the latter being negligible for molecular or supramolecular complexes in which the nuclei under investigation are embedded into bulky and semi-rigid organic ligand strands exhibiting slow chemical exchange (Peters et al., 1996; Platas et al., 1999). The paramagnetic inner-sphere relaxation may be traced back to the fluctuating magnetic field produced by the electronic magnetic momentum which induces nuclear spin transitions for nuclei whose magnetic momentum interacts with the electronic magnetic momentum (Solomon, 1955; Bloembergen and Morgan, 1961; Bertini and Luchinat, 1996; Peters et al., 1996). This electron–nucleus interaction is randomly modulated by a characteristic correlation time τ_c which depends on the electron spin relaxation (τ_e , Sharp et al. (2001)), molecular tumbling (τ_r) and chemical exchange (τ_m). Since only the rate constants are additive, τ_c is given by eq. (6), and it is dominated by the shortest correlation time, τ_c being even smaller than this one (Clementi and Luchinat, 1998)

$$\frac{1}{\tau_c} = \frac{1}{\tau_e} + \frac{1}{\tau_r} + \frac{1}{\tau_m}. \quad (6)$$

For semi-rigid molecular and supramolecular complexes considered in this review, the nuclei under investigation only exhibit slow chemical exchange and τ_m does not significantly contribute to τ_c ($\tau_m \gg \tau_e, \tau_r$). It will not be considered further in the discussion. The interaction between the electronic and nuclear magnetic momenta has two physical origins: contact (through-bond) and dipolar (through-space) effects, but three different mechanisms (one for contact and two for dipolar effects) are responsible for the increase of both the longitudinal (i.e., the decay of the z -component of the nuclear magnetisation) and the transversal nuclear relaxation rates (i.e., the loss of coherence of nuclear magnetisation in the xy -plane controlling the line width of the NMR signals $\Delta\nu^{1/2} = 1/(\pi T_{2i}^{\text{exp}})$).

2.1.1. Lanthanide-induced contact relaxation

Unpaired electronic density can be delocalized onto the various nuclei of the complex via through-bond scalar hyperfine interactions involving occupied orbitals containing s -character (direct interaction or polarization according to the Fermi mechanism, Wertz and Bolton (1986)). Random electron relaxation thus produces a flip–flop mechanism which affects the nuclear spin and increases nuclear relaxation processes (Bertini and Luchinat, 1996). Since these interactions are isotropic, they do not depend on molecular tumbling and τ_e is the only relevant correlation time for non-exchanging semi-rigid complexes. Moreover, only electronic spin can be delocalized via hyperfine interactions (no orbital contribution) and the contact re-

laxations given by eqs. (7), (8) involve the spin quantum number S (Bloembergen, 1957).

$$\frac{1}{T_{1i}^{\text{para-contact}}} = \frac{S(S+1)}{3} \left(\frac{A_i}{\hbar} \right)^2 \left(\frac{2\tau_e}{1 + \omega_S^2 \tau_e^2} \right), \quad (7)$$

$$\frac{1}{T_{2i}^{\text{para-contact}}} = \frac{S(S+1)}{3} \left(\frac{A_i}{\hbar} \right)^2 \left(\tau_e + \frac{\tau_e}{1 + \omega_S^2 \tau_e^2} \right), \quad (8)$$

A_i is the Fermi hyperfine constant (in Hz) and ω_S is the Larmor precession frequency of the unpaired electrons (in Hz). As a result of the very limited covalency of the lanthanide–ligand bonds, A_i are small and only nuclei close to the metallic centre are significantly affected. Along the lanthanide series, $R(\text{III}) = \text{Gd}(\text{III})$ ($S = 7/2$ and $\tau_e \approx 10^{-8}$ – 10^{-9} s, tables 1, 2) is the unique metal ion for which spin momenta (S) and electronic relaxation time (τ_e) are large enough to produce significant contact contributions. Since $\omega_S^2 \tau_e^2$ is extremely large for $\text{Gd}(\text{III})$ complexes, the contact contribution to the longitudinal relaxation ($1/T_{1i}^{\text{para-contact}}$) is negligible, but the existence of a non-dispersive term for the transverse contact contribution (eq. (8)) implies that this mechanism may dominate the transverse relaxation of water molecules bound to MRI contrasts agents (Aime et al., 1998, 1999a; Caravan et al., 1999). For the other lanthanides ($R = \text{Ce}$ – Yb except Gd), the fast electronic relaxation ($\tau_e \approx 10^{-13}$ s, table 2) strongly limits contact contributions which can be neglected for the modeling of nuclear relaxation processes in these complexes.

Table 1
Electronic characteristics of $R(\text{III})$ free ions

Config.	Ions	Ground state	g_J^a	$\mu_{\text{eff}}/\text{B.M.}$	ζ^b/cm^{-1}	1st excited state	Energy state separation $/\text{cm}^{-1}$
4f ¹	Ce ³⁺	² F _{5/2}	6/7	2.54	737	² F _{7/2}	2200
4f ²	Pr ³⁺	³ H ₄	4/5	3.58	879	³ H ₅	2100
4f ³	Nd ³⁺	⁴ I _{9/2}	8/11	3.62	1030	⁴ L _{11/2}	1900
4f ⁴	Pm ³⁺	⁵ I ₄	3/5	2.68	1190	⁵ I ₅	1600
4f ⁵	Sm ³⁺	⁶ H _{5/2}	2/7	0.85	1361	⁶ H _{7/2}	1000
4f ⁶	Eu ³⁺	⁷ F ₀	5	0	1436	⁷ F ₁	300
4f ⁷	Gd ³⁺	⁸ S _{7/2}	2	7.94	1755	⁶ P _{7/2}	30000
4f ⁸	Tb ³⁺	⁷ F ₆	3/2	9.72	1965	⁷ F ₅	2000
4f ⁹	Dy ³⁺	⁶ H _{15/2}	4/3	10.65	2189	⁶ H _{13/2}	3300
4f ¹⁰	Ho ³⁺	⁵ I ₈	5/4	10.61	2436	⁵ I ₇	5300
4f ¹¹	Er ³⁺	⁴ I _{15/2}	6/5	9.58	2700	⁴ I _{13/2}	6500
4f ¹²	Tm ³⁺	³ H ₆	7/6	7.56	2817	³ H ₅	5700
4f ¹³	Yb ³⁺	² F _{7/2}	8/7	4.54	3288	² F _{5/2}	10000

^a $g_J = 1 + \frac{J(J+1) + S(S+1) - L(L+1)}{2J(J+1)}$. The latter formula is not valid for $J = 0$ and the mathematical limit $g_J = 5$ is given for $\text{Eu}(\text{III})$ in its ground state ⁷F₀ (Kahn, 1993).

^b Taken from Golding and Halton (1972).

Table 2
Electronic (τ_e) and rotational (τ_r) correlation relaxation times for $R(\text{III})$ aqua-complexes

Config.	Ions	τ_e (10^{-12} s, 312 K) ^a	τ_e (10^{-12} s, 298 K) ^b	τ_r (10^{-12} s, 298 K) ^b
4f ¹	Ce ³⁺	0.09	–	–
4f ²	Pr ³⁺	0.057	0.082	63
4f ³	Nd ³⁺	0.115	–	–
4f ⁴	Pm ³⁺	–	–	–
4f ⁵	Sm ³⁺	0.045	0.079	67
4f ⁶	Eu ³⁺	0.009	–	–
4f ⁷	Gd ³⁺	–	10^3 – 10^4 ^c	41 ^d
4f ⁸	Tb ³⁺	0.203	–	–
4f ⁹	Dy ³⁺	0.299	0.39	63
4f ¹⁰	Ho ³⁺	0.194	0.27	65
4f ¹¹	Er ³⁺	0.238	0.31	61
4f ¹²	Tm ³⁺	0.369	–	–
4f ¹³	Yb ³⁺	0.137	0.22	68

^aTaken from Alsaadi et al. (1980c, 1980d).

^bTaken from Bertini et al. (1993a).

^cTaken from Bertini et al. (1993b).

^dTaken from Powell et al. (1996).

2.1.2. Lanthanide-induced dipolar relaxation

According to the classic description of the through-space coupling between two point dipoles, the nuclear and electronic magnetic momenta produce a dipolar interaction which depends on their separation and orientation (Bertini and Luchinat, 1996). Since the electronic magnetic momentum is 2–3 orders of magnitude larger than the nuclear momenta, the interest is restricted to the fluctuation of the magnetic field provided by the unpaired electron spins which can induce nuclear transitions via dipolar coupling. The modulation of this interaction results from electronic relaxation (τ_e) and molecular tumbling (τ_r) leading to the correlation time $\tau_c^{-1} = \tau_e^{-1} + \tau_r^{-1}$ in the absence of chemical exchange. The Solomon equations (eqs. (9), (10)) model this dipolar contribution assuming that the nuclear Larmor precession frequency (ω_I) is negligible with respect to the electronic Larmor frequency ($\omega_S \gg \omega_I$) (Solomon, 1955; Bertini and Luchinat, 1996)

$$\frac{1}{T_{1i}^{\text{para-dipolar}}} = \frac{2}{15} \left(\frac{\mu_0}{4\pi} \right)^2 \frac{\gamma_I \mu_{\text{eff}}^2 \beta^2}{r_i^6} \left(\frac{3\tau_c}{1 + \omega_I^2 \tau_c^2} + \frac{7\tau_c}{1 + \omega_S^2 \tau_c^2} \right), \quad (9)$$

$$\frac{1}{T_{2i}^{\text{para-dipolar}}} = \frac{1}{15} \left(\frac{\mu_0}{4\pi} \right)^2 \frac{\gamma_I \mu_{\text{eff}}^2 \beta^2}{r_i^6} \left(4\tau_c + \frac{3\tau_c}{1 + \omega_I^2 \tau_c^2} + \frac{13\tau_c}{1 + \omega_S^2 \tau_c^2} \right), \quad (10)$$

$\mu_0/4\pi$ is the magnetic permeability of vacuum, γ_I is the nuclear magnetogyric ratio, β is the Bohr magneton and r_i is the $R(\text{III})$ -nucleus i distance. For molecular and supramolecular complexes of intermediate size discussed in this review, $\tau_r \approx 10^{-11}$ – 10^{-9} s (Aime et al., 1992a; Caravan et al., 1999; Rigault et al., 2000b) and $\tau_e \ll \tau_r$ for all lanthanide com-

plexes except those with $R = \text{Gd}$. However, the electron-nuclear spin coupling is so effective for Gd(III) complexes that high-resolution NMR spectra cannot be recorded as a result of the considerable dipolar paramagnetic contribution to the nuclear relaxation processes. This lanthanide is thus never used for the analysis of hyperfine shift data (LIS) discussed in this review and its peculiar effect on relaxation processes will not be further considered here. Detailed and comprehensive treatments of relaxation processes in Gd(III) complexes can be found in excellent recent reviews by Peters et al. (1996), Aime et al. (1998) and Caravan et al. (1999). For $R = \text{Ce} - \text{Yb}$ (except $R = \text{Gd}$), the modulation of the dipolar electron-nuclear interaction by molecular tumbling is thus negligible and $\tau_c \cong \tau_e$. Finally, τ_e is usually so short for fast-relaxing $R(\text{III})$ that $\omega_I^2 \tau_c^2 \ll 1$ and $\omega_S^2 \tau_c^2 \ll 1$ (low-field or fast-motion limit, Bertini and Luchinat (1996)) and eqs. (9), (10) simplify to eq. (11)

$$\frac{1}{T_{1i}^{\text{para-dipolar}}} = \frac{1}{T_{2i}^{\text{para-dipolar}}} = \frac{4}{3} \left(\frac{\mu_0}{4\pi} \right)^2 \frac{\gamma_I \mu_{\text{eff}}^2 \beta^2}{r_i^6} \tau_e. \quad (11)$$

This equation justifies the qualitative statement that the shorter the electronic relaxation times, the smaller paramagnetic effects on nuclear relaxation. It also predicts that the dipolar contribution is maximum for strongly paramagnetic lanthanides (via μ_{eff}) and for nuclei located close to the metal ion (via r_i).

2.1.3. Lanthanide-induced Curie-spin relaxation

In deriving the contact and dipolar contributions induced by the unpaired electrons (eqs. (7)–(11)), the small difference in the population of the electron spin levels according to the Boltzmann distribution has been neglected (Bertini and Luchinat, 1996). However, this difference accounts for the existence of a time-average magnetic momentum $\langle \mu \rangle$. The time-average excess of spin along the quantization z -axis $\langle S_z \rangle$ is called the expectation value of the S_z operator and is given by eq. (12) (Bertini and Luchinat, 1996; Bertini et al., 2002)

$$\langle S_z \rangle = \frac{\sum_{M_S=-S}^S \langle S, M_S | S_z | S, M_S \rangle \exp(-g_e \beta H_0 M_S / kT)}{\sum_{M_S=-S}^S \exp(-g_e \beta H_0 M_S / kT)} = -\frac{g_e \beta H_0 S(S+1)}{3kT}, \quad (12)$$

g_e is the Landé factor and H_0 is the applied magnetic field responsible for the removing of the degeneracy of the M_S spin levels. For lanthanide complexes, $\langle S_z \rangle$ must be replaced by $\langle J_z \rangle$ because of the considerable orbital contribution to the total angular momentum. The associated static electronic magnetic momentum is given by $\langle \mu \rangle = -g_e \beta \langle S_z \rangle$ and it interacts with the nuclear spins via dipolar mechanism. Random modulation of this interaction through molecular tumbling (τ_r) may induce nuclear spin transitions and contributes to nuclear relaxation. This second dipolar mechanism described by eqs. (13), (14) is termed Curie-spin relaxation in order to reflect its relationship with the static magnetic susceptibility given by the Curie law

$$\frac{1}{T_{1i}^{\text{para-Curie}}} = \frac{6}{5} \left(\frac{\mu_0}{4\pi} \right)^2 \frac{\gamma_I^2 \mu_{\text{eff}}^4 \beta^4 H_0^2}{r_i^6 (3kT)^2} \left(\frac{\tau_r}{1 + \omega_I^2 \tau_r^2} \right), \quad (13)$$

$$\frac{1}{T_{2i}^{\text{para-Curie}}} = \frac{1}{5} \left(\frac{\mu_0}{4\pi} \right)^2 \frac{\gamma_I^2 \mu_{\text{eff}}^4 \beta^4 H_0^2}{r_i^6 (3kT)^2} \left(4\tau_r + \frac{3\tau_r}{1 + \omega_I^2 \tau_r^2} \right). \quad (14)$$

The mathematical forms of the Curie-spin contributions are similar to those found for transient dipolar contributions (eqs. (9)–(11), dependence on r_i^{-6}) except that (i) they increase with magnetic field (via H_0^2) and (ii) they are more sensitive to the nuclear magnetogyric ratio and electronic magnetic momentum. The Curie-spin contribution is often much smaller than the dipolar contribution except for ^1H NMR experiments (large γ_I) performed at high magnetic field (large H_0) for bulky (large τ_r) and strongly paramagnetic (large μ_{eff}) complexes. However, fast-relaxing lanthanide complexes (i.e., possessing very short τ_e , $R = \text{Ce–Yb}$, except Gd) of intermediate size considered in this review often fulfill these criteria and the Curie contributions (eqs. (13), (14)) become comparable with transient dipolar contributions (eq. (11)). The associated total paramagnetic contribution $1/T_i^{\text{para}}$ to the nuclear relaxation processes (eqs. (4), (5)) in the absence of chemical exchange thus corresponds to the sum of these two dipolar contributions and is given by eqs. (15), (16).

$$\frac{1}{T_{1i}^{\text{para}}} = \frac{4}{3} \left(\frac{\mu_0}{4\pi} \right)^2 \frac{\gamma_I \mu_{\text{eff}}^2 \beta^2}{r_i^6} \tau_e + \frac{6}{5} \left(\frac{\mu_0}{4\pi} \right)^2 \frac{\gamma_I^2 \mu_{\text{eff}}^4 \beta^4 H_0^2}{r_i^6 (3kT)^2} \left(\frac{\tau_r}{1 + \omega_I^2 \tau_r^2} \right), \quad (15)$$

$$\frac{1}{T_{2i}^{\text{para}}} = \frac{4}{3} \left(\frac{\mu_0}{4\pi} \right)^2 \frac{\gamma_I \mu_{\text{eff}}^2 \beta^2}{r_i^6} \tau_e + \frac{1}{5} \left(\frac{\mu_0}{4\pi} \right)^2 \frac{\gamma_I^2 \mu_{\text{eff}}^4 \beta^4 H_0^2}{r_i^6 (3kT)^2} \left(4\tau_r + \frac{3\tau_r}{1 + \omega_I^2 \tau_r^2} \right). \quad (16)$$

When τ_r is determined by an independent experiment such as dipolar relaxation measurements in analogous diamagnetic complexes (Wasylishen, 1987), the magnetic field dependence of $1/T_i^{\text{para}}$ is relevant for extracting R -nuclei distances (r_i) at a fixed temperature in solution. Least-squares fits of $1/T_{1i}^{\text{para}}$ vs $H_0^2/(1 + \omega_I^2 \tau_r^2)$ (eq. (15), Burns and LaMar (1982)) or $1/T_{2i}^{\text{para}}$ vs $H_0^2(4\tau_r + 3\tau_r/(1 + \omega_I^2 \tau_r^2))$ (eq. (16), or vs H_0^2 when $\omega_I^2 \tau_r^2 \ll 1$, Allegrozzi et al. (2000)) allow the simultaneous estimation of r_i from the slope and τ_e from the intercept. A linear combination of eqs. (15) and (16) has been proposed to remove τ_e from the fitting process thus leading to the determination of r_i at a single magnetic field (eq. (17), Aime et al. (1992a)), but this technique requires the accurate determination of T_{2i}^{para} which is often prevented by unresolved scalar coupling in supramolecular lanthanide complexes (Carr–Purcell–Meiboom–Gill pulse sequence (Meiboom and Gill, 1958) or line-width analysis (Rigault et al., 2000b)).

$$\frac{1}{T_{2i}^{\text{para}}} - \frac{1}{T_{1i}^{\text{para}}} = \frac{1}{5} \left(\frac{\mu_0}{4\pi} \right)^2 \frac{\gamma_I^2 \mu_{\text{eff}}^4 \beta^4 H_0^2}{r_i^6 (3kT)^2} \left(4\tau_r + \frac{3\tau_r}{1 + \omega_I^2 \tau_r^2} \right). \quad (17)$$

When τ_r is unknown, it can be adjusted together with τ_e and r_i by using non-linear least-squares fits of eqs. (15), (16) as similarly described for the treatment of NMRD profiles (Bertini et al., 1995; Ruloff et al., 1998; Toth et al., 1998), but a much simpler approach considers that both dipolar and Curie-spin contribution depend on r_i^{-6} . When a nucleus for which the R -nucleus distance r_{ref} can be estimated either from crystal structure or gas-phase modeling is used as a reference, eq. (15) reduces to its simplest form (eq. (18)) and relative R -nucleus i distances are accessible without estimations of τ_e and τ_r (Barry et al., 1971;

Forsberg, 1996; Brink et al., 1996)

$$\frac{T_{li}^{\text{para}}}{T_{\text{lref}}^{\text{para}}} = \left(\frac{r_i}{r_{\text{ref}}} \right)^6. \quad (18)$$

The latter technique is particularly appreciated by coordination chemists because of its simple mathematical formulation and the limited amount of experimental data to be collected (longitudinal relaxation times at a single magnetic field obtained by the inversion–recovery method (Vold et al., 1968)). However, the a priori choice of a reference distance (r_{ref}) requires a partial modeling of the complex and the extracted distances strongly depend on the accuracy of this original choice.

2.2. Contact shifts and through-bond spin delocalisation in paramagnetic lanthanide complexes

Since electrons relax orders of magnitude faster than nuclei, the nucleus in each of its M_I energy level only senses an average static magnetic momentum $\langle \mu \rangle = -g_e \beta \langle S_z \rangle$ which results from the slight excess of electron population in the $M_S = -1/2$ state. In paramagnetic NMR, the nucleus under investigation is rarely that bearing the unpaired electrons. Delocalisation of the spin density occurring either through direct Fermi hyperfine interaction or polarization of occupied s-containing molecular orbitals (Wertz and Bolton, 1986; Lisowski et al., 1995b), produces an additional magnetic field ΔH generated at the nucleus by the fraction of electron magnetic momentum located at the nucleus itself. Since the nuclear resonance frequency (i.e., the chemical shift) depends on the total magnetic field, this mechanism provides a contact contribution to the paramagnetic shift of a nucleus i (δ_i^c) which is given by eq. (19) (Bertini and Luchinat, 1996).

$$\delta_i^c = \frac{\Delta H}{H_0} = \frac{A_i}{\hbar \gamma_I H_0} \langle S_z \rangle. \quad (19)$$

Substituting the value $\langle S_z \rangle$ given by eq. (12) for a pure spin contribution arising from the metallic centre into eq. (19) gives eq. (20) which predicts (i) a T^{-1} dependence of δ_i^c and (ii) large contact shifts for strongly paramagnetic complexes possessing efficient spin delocalisation

$$\delta_i^c = \frac{A_i}{\hbar} \cdot \frac{g_e \beta S(S+1)}{3\gamma_I kT}. \quad (20)$$

Strictly speaking, δ_i^c is not isotropic when g_e varies with molecular orientation (i.e., the magnetic susceptibility tensor is anisotropic), but typical values for proton hyperfine anisotropy amounts to $\approx 10^5$ Hz which is much smaller than τ_r^{-1} in solution, thus leading to the observation of average isotropic contact shifts (g_e should be therefore replaced by \bar{g} in eq. (20), Bertini and Luchinat (1996)). For lanthanides, the contact contribution is strongly limited by the minute covalency of the metal–ligand bonds and only weak spin delocalisation involves the 6s metal orbital which in turn slightly polarizes the 4f orbitals (Lewis et al., 1962; Lisowski et al., 1995b). Therefore contact contributions only affect nuclei topologically close

to the lanthanide metal ion and the hyperfine constants A_i rapidly decrease with increasing separation (A_i is usually negligible for a $R(\text{III})$ -nucleus separation larger than three bonds). Equation (19) holds for lanthanide complexes because the spin expectation value $\langle S_z \rangle$ explicitly considers the populations of the ground and excited J manifold levels together with second-order terms mixing excited states with the ground state (Golding and Halton, 1972). For each J manifold, the expectation value $\langle S_z \rangle_J$ is given by eq. (21) and a Boltzmann distribution for the populations of the involved levels allows the calculation of $\langle S_z \rangle$ (eq. (22), $\lambda = \pm\zeta/2S$ in which ζ is the spin orbit coupling constant collected in table 1)

$$\langle S_z \rangle_J = -\frac{\beta H_0}{3kT} \left[g_J(g_J - 1)J(J + 1) + \left(\frac{2kT}{\lambda} \right) (g_J - 1)(g_J - 2) \right], \quad (21)$$

$$\langle S_z \rangle = \frac{\sum_J \langle S_z \rangle_J (2J + 1) \exp(-\lambda J(J + 1)/2kT)}{\sum_J (2J + 1) \exp(-\lambda J(J + 1)/2kT)}. \quad (22)$$

Numerical calculations of $\langle S_z \rangle$ at 300 K obtained with eq. (22) for all $R(\text{III})$ free ions are collected in table 3 (Golding and Halton, 1972). Pinkerton et al. (1985) have demonstrated that $\langle S_z \rangle$ are relatively insensitive to the choice of various sets of reported spin-orbit coupling constants. Moreover, except for $R = \text{Sm}$ and Eu , $\langle S_z \rangle$ displays a minor dependence on the temperature and the data calculated at 300 K (table 3) are amenable for a reliable treatment of contact shifts in solution around room temperature. The close proximity of excited states possessing different J manifolds for $\text{Sm}(\text{III})$ requires a precise calculation of $\langle S_z \rangle$ at each temperature as is the case for $R = \text{Eu}$. However, the latter metal brings some specific complications associated with the absence of a well-defined g_J value for its $J = 0$ ground state. Golding

Table 3
Spin expectation values^a $\langle S_z \rangle$ and Bleaney's factors^b C for $R(\text{III})$ free ions at 300 K, and rhombic proportionality factors^c C^{rhombic}

Config.	Ions	$\langle S_z \rangle$	C	C^{rhombic}
4f ¹	Ce ³⁺	-0.98	-6.3	-
4f ²	Pr ³⁺	-2.97	-11.0	-0.6
4f ³	Nd ³⁺	-4.49	-4.2	-2.3
4f ⁴	Pm ³⁺	-4.01	2.0	-
4f ⁵	Sm ³⁺	0.06	-0.7	-
4f ⁶	Eu ³⁺	10.68	4.0	3.4
4f ⁷	Gd ³⁺	31.50	0.0	-
4f ⁸	Tb ³⁺	31.82	-86	7.7
4f ⁹	Dy ³⁺	28.55	-100	-55.7
4f ¹⁰	Ho ³⁺	22.63	-39	-13.6
4f ¹¹	Er ³⁺	15.37	33	-3.8
4f ¹²	Tm ³⁺	8.21	53	-34.0
4f ¹³	Yb ³⁺	2.59	22	4.7

^aTaken from Golding and Halton (1972).

^bValues relative to $C_{\text{Dy}} = -100$ including mixing with excited states (Bleaney, 1972; Bleaney et al., 1972).

^cValues relative to $C_{\text{Dy}} = -100$ (Reuben and Elgavish, 1980).

and Halton (1972) used the mathematical limit $g_J = 5$ for $\text{Eu}(^7\text{F}_0)$ (Kahn, 1993) in order to obtain $\langle S_z \rangle = 10.68$ reported in table 3. Pinkerton et al. (1985) proposed $g_{J=0} = 4.4$ from experimental fits of contact contributions, thus leading to $\langle S_z \rangle = 7.57$ at 300 K. This uncertainty may limit the determination of hyperfine constants for $\text{Eu}(\text{III})$ complexes. Interestingly, $\langle S_z \rangle$ can be positive or negative for $R(\text{III})$ ions and may considerably differ from the spin-only value owing to the large orbital contributions. On the other hand, the use of $\langle S_z \rangle$, and not $\langle J_z \rangle$, is adequate because only the spin is delocalized onto the molecules (Bertini and Luchinat, 1996). Equations (21), (22) assume that (i) $kT >$ Zeeman splitting and (ii) crystal-field effects are negligible ($\Delta E_{\text{CF}} < kT$). The first hypothesis is justified for NMR measurements around room temperature, but the second one is more debatable, particularly for lanthanide complexes with 'soft' donor ligands providing large crystal-field effects $\Delta E_{\text{CF}} > 400 \text{ cm}^{-1}$ (Mironov et al., 2000). However, the extremely narrow range of μ_{eff} observed at room temperature for lanthanide complexes displaying various structures and geometries (Kahn, 1993; Bünzli, 1998; Kaltsoyannis and Scott, 1999) suggest that crystal-field splitting has only minor effects on $\langle S_z \rangle$. The recent success of the application of the two-nuclei crystal-field independent method (eq. (51)) for the evaluation of isostructurality in rigid axial supramolecular complexes also supports this conclusion (Rigault et al., 2000a, 2000b), but, to the best of our knowledge, a detailed modeling of $\langle S_z \rangle$ for specific crystal-field potentials has not been considered in the literature.

2.3. Pseudo-contact shifts and through-space interactions in paramagnetic lanthanide complexes

Since the spin delocalisation in lanthanide complexes is small (see sect. 2.1), the unpaired electrons can be considered as spatially confined onto the metal, thus producing an electronic magnetic point dipole which may interact with peripheral nuclear magnetic momenta via dipolar interactions (eq. (23), Bertini and Luchinat (1996)).

$$E_{\text{dip}} = -\left(\frac{\mu_0}{4\pi}\right) \frac{1}{r^3} \left[3 \frac{(\langle \mu \rangle \cdot r)(\mu_{I\kappa} \cdot r)}{r^2} - (\langle \mu \rangle \cdot \mu_{I\kappa}) \right], \quad (23)$$

E_{dip} is the energy of the dipolar interaction between the electronic magnetic momentum of the electron (represented by its average value $\langle \mu \rangle$) and the nuclear magnetic momentum (represented by its projection along the magnetic field $\mu_{I\kappa}$) and r is the separation between the two magnetic point dipoles. E_{dip} varies for two nuclear spin states differing by $\Delta M_I = \pm 1$ ($\mu_{I\kappa}$ depends on the orientation of the nuclear spin vector) which affects the condition of resonance of this nucleus, and thus produces a dipolar contribution δ^{dip} to the chemical shift given by eq. (24), which reduces to eq. (25) for a magnetically isotropic compound

$$\delta^{\text{dip}} = \frac{E_{\text{dip}}(M_I) - E_{\text{dip}}(M_{I+1})}{\hbar \gamma_I H_0}, \quad (24)$$

$$\delta^{\text{dip}} = \frac{1}{4\pi N_A r_i^3} \chi (3 \cos^2(\gamma) - 1), \quad (25)$$

χ is the magnetic susceptibility tensor, γ is the angle between the metal-nucleus vector r and the external magnetic field. Integration of eq. (25) over all molecular orientations averages

zero and no dipolar shift is expected for molecules possessing an isotropic magnetic susceptibility tensor ($\chi_{xx} = \chi_{yy} = \chi_{zz}$) in solution. However, for an axially anisotropic electronic magnetic momentum ($\chi_{\parallel} \neq \chi_{\perp}$), eq. (25) becomes eq. (26) and integration over all molecular orientations is no longer zero (Bertini et al., 2002). In the latter equation α is the angle of the z axis with the external field direction, θ is the angle between the metal-nucleus vector and the z axis and Ω defines the position of the metal-nucleus vector on the basal plane of the revolution cone defined by the rotation of the metal-nucleus vector about the z -axis (Bertini and Luchinat, 1996)

$$\delta^{\text{dip}} = \frac{1}{4\pi N_A r_i^3} [\chi_{\parallel} \cos^2 \alpha (3 \cos^2 \theta - 1) + \chi_{\perp} \sin^2 \alpha (3 \sin^2 \theta \cos^2 \Omega - 1) + \frac{3}{4} (\chi_{\parallel} - \chi_{\perp}) \sin 2\alpha \sin 2\theta \cos \Omega]. \quad (26)$$

Since this dipolar interaction remains in isotropic media as similarly found for the contact shift (see sect. 2.1), it is often termed as the pseudo-contact shift. For the general case of a complex possessing an anisotropic magnetic susceptibility tensor, Kemple et al. (1988) show that the pseudo-contact shift δ_i^{pc} of a nucleus i is given by eq. (27) where r_i , θ_i and ϕ_i are the spherical coordinates of the resonating nucleus in an arbitrary axes system with the lanthanide metal ion $R(\text{III})$ located at the origin (fig. 1)

$$\delta_i^{\text{pc}} = \frac{1}{2N_A r_i^3} [(\chi_{zz} - \frac{1}{3} \text{Tr} \chi)(3 \cos^2 \theta_i - 1) + (\chi_{xx} - \chi_{yy})(\sin^2 \theta_i \cos 2\phi_i)] + \frac{1}{N_A r_i^3} [\chi_{xy}(\sin^2 \theta_i \sin 2\phi_i) + \chi_{xz}(\sin 2\theta_i \cos \phi_i) \chi_{yz}(\sin 2\theta_i \sin \phi_i)]. \quad (27)$$

In the principal magnetic axes system, the magnetic susceptibility tensor is diagonal and the three last terms of eq. (27) vanish, thus leading to eq. (28) for the pseudo-contact shifts (Horrocks and Sipe, 1972; Bertini et al., 2002).

$$\delta_i^{\text{pc}} = \frac{1}{2N_A r_i^3} [(\chi_{zz} - \frac{1}{3} \text{Tr} \chi)(3 \cos^2 \theta_i - 1) + (\chi_{xx} - \chi_{yy})(\sin^2 \theta_i \cos 2\phi_i)]. \quad (28)$$

Finally, for axial complexes (i.e., complexes possessing a C_4 axis), $\chi_{xx} = \chi_{yy}$ and eq. (28) reduces to eq. (29) in the principal magnetic axes system (Forsberg, 1996).

$$\delta_i^{\text{pc}} = \frac{1}{3N_A r_i^3} [(\chi_{zz} - \chi_{xx})(3 \cos^2 \theta_i - 1)]. \quad (29)$$

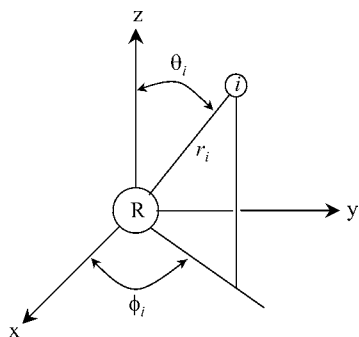


Fig. 1. Spherical coordinates r_i , θ_i and ϕ_i for a nucleus i in an arbitrary xyz reference frame with the lanthanide metal ion $R(\text{III})$ located at the origin.

Equations (27)–(29) imply that pseudo-contact shifts δ_i^{pc} are maximum for complexes displaying large molecular magnetic anisotropies and that structural and geometrical informations can be extracted from the so-called non-linear geometrical factors G_i (eq. (30)) and H_i (eq. (31)) (Forsberg, 1996; Peters et al., 1996)

$$G_i = \frac{3 \cos^2 \theta_i - 1}{r_i^3}, \quad (30)$$

$$H_i = \frac{\sin^2 \theta_i \cos 2\phi_i}{r_i^3}. \quad (31)$$

Interestingly, Hawkes et al. (1973) suggested that eq. (29) also holds for stereochemically labile lanthanide complexes exhibiting fast dynamic interconversions in solution, an experimental observation theoretically justified by Horrocks (1974) for lanthanide shift reagents existing in solution as a set of rapidly interconverting isomers. In a seminal paper, Briggs et al. (1972) demonstrated that the use of the simplified eq. (29) is justified for complexes displaying fast equilibria between at least three rotamers. In the latter case, δ_i^{pc} is proportional to G_i by a factor which is a complicated combination of axial ($\chi_{zz} - (1/3)\text{Tr}\chi$) and rhombic ($\chi_{xx} - \chi_{yy}$) magnetic anisotropies. The term ‘effective axial symmetry’ is used for describing these complexes.

2.3.1. Origin and modeling of magnetic anisotropy in paramagnetic lanthanide complexes

Large paramagnetic anisotropies and associated pseudo-contact shifts are expected when orbital contributions to the ground state is considerable because such contributions are orientation dependent (Bertini and Luchinat, 1996). For lanthanide metal ions, the combination of spin (S) and orbital (L) contributions to the total angular momentum (J) (modulated via the spin-orbit coupling) produces considerable magnetic anisotropy when crystal-field effects due to coordinated ligands remove the spherical symmetry around the metal. The terms of the magnetic susceptibility tensors $\chi_{\alpha\beta}$ can be obtained by using eq. (32) (Gerloch and McMeeking, 1975) which corresponds to the general form of the Van Vleck formula, the latter being defined in the principal magnetic axes system (Kahn, 1993)

$$\chi_{\alpha\beta} = \frac{N_A}{\sum_i \exp(-E_i/kT)} \sum_i \left\{ \sum_j \frac{\langle i|\mu_\alpha|j\rangle\langle j|\mu_\beta|i\rangle}{kT} - \sum_j \frac{\langle i|\mu_\alpha|j\rangle\langle j|\mu_\beta|i\rangle + \langle i|\mu_\beta|j\rangle\langle j|\mu_\alpha|i\rangle}{E_i - E_j} \right\} \exp(-E_i/kT), \quad (32)$$

$\alpha, \beta = x, y$ or z , E_i is the energy of the crystal-field state $|i\rangle$ produced by the non-spherical arrangement of the donor atoms coordinated to $R(\text{III})$ and μ_α ($\alpha = x, y, z$) are the components of the operator of the total magnetic momentum μ . The energies of the wave functions $|i\rangle$ of crystal-field states in a lanthanide complex are obtained from the diagonalisation of the model Hamiltonian $H = H_0 + H_{\text{CF}}$ where H_0 is the free-ion Hamiltonian and H_{CF} is the crystal-field Hamiltonian (Mironov et al., 2001, 2002). The latter is usually written in terms of phenomenological B_q^k crystal-field parameters and C_q^k spherical tensor operators (eq. (33),

Görller-Walrand and Binnemans (1996))

$$H_{CF} = \sum_{kq} B_q^k C_q^k. \quad (33)$$

Mironov et al. (2001, 2002) have followed this approach to compute theoretical magnetic anisotropies

$$\Delta\chi = \chi_{zz} - \frac{1}{2}(\chi_{xx} + \chi_{yy}) = \frac{3}{2} \left(\chi_{zz} - \frac{1}{3} \text{Tr} \chi \right)$$

at 298 K for eight-coordinate (Mironov et al., 2001) and nine-coordinate (Mironov et al., 2002) lanthanide complexes possessing arbitrary (but reasonable) crystal-field parameters. Figure 2 shows typical magnetic anisotropies $\Delta\chi$ calculated for various distortions of an eight-coordinate cubic lanthanide complex.

Such exact calculations require accurate structural, geometric and electronic parameters for the R -ligand bonds and for the metallic coordination spheres which are usually not accessible for coordination complexes in solution. Only solid-state structures for which X-ray crystal structures and B_q^k parameters have been determined, can be satisfyingly modeled with this approach (Görller-Walrand and Binnemans, 1996; Hopkins et al., 1996, 1998). Moreover, no analytical formula expressing $\Delta\chi$ as a function of B_q^k and metal-centred electronic properties can be introduced into eqs. (27)–(29) for extracting solution structures from NMR pseudo-contact shifts. In order to overcome this limitation, Bleaney (1972) has proposed a high-temperature expansion of the magnetic susceptibility tensor given by eq. (32) in a power series in the inverse temperature. The first term in T^{-1} corresponds to the isotropic magnetic susceptibility $\chi_0 = (1/3) \text{Tr} \chi$ of the free lanthanide ion (eq. (34))

$$\chi_0 = \frac{1}{3} \text{Tr} \chi = \frac{N_A g_J^2 \beta^2}{3kT} J(J+1). \quad (34)$$

The second terms in T^{-2} (eqs. (35)–(37)) correspond to the anisotropic part of the magnetic susceptibility related to the C_q^k operators of rank two ($k=2$) associated with crystal field parameters $A_2^0\langle r^2 \rangle$ and $A_2^2\langle r^2 \rangle$ (which are related to conventional B_q^k parameters by $B_0^2 = 2A_2^0\langle r^2 \rangle$ and $B_2^2 = (2/3)^{1/2} A_2^2\langle r^2 \rangle$) (Görller-Walrand and Binnemans, 1996))

$$\chi_{xx} - \chi_0 = \frac{N_A \beta^2}{30(kT)^2} \langle r^2 \rangle (A_2^0 - A_2^2) (1+p) \xi, \quad (35)$$

$$\chi_{yy} - \chi_0 = \frac{N_A \beta^2}{30(kT)^2} \langle r^2 \rangle (A_2^0 + A_2^2) (1+p) \xi, \quad (36)$$

$$\chi_{zz} - \chi_0 = -\frac{N_A \beta^2}{30(kT)^2} \langle r^2 \rangle 2A_2^0 (1+p) \xi. \quad (37)$$

The quantity ξ is given in eq. (38) where $\langle J \| \alpha \| J \rangle$ is a numerical coefficient tabulated by Bleaney (1972) for each $4f^n$ -electronic configuration

$$\xi = g_J^2 \langle J \| \alpha \| J \rangle J(J+1)(2J-1)(2J+3). \quad (38)$$

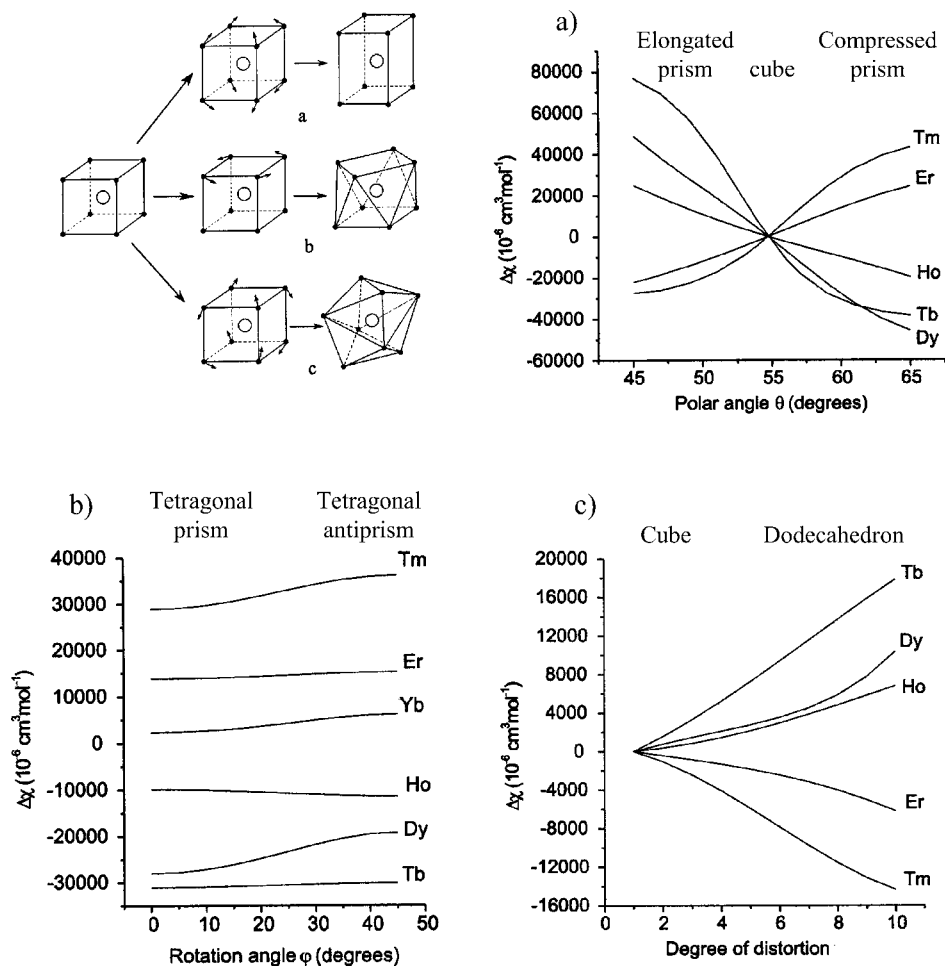


Fig. 2. Variations of the computed magnetic anisotropies $\Delta\chi$ with respect to the distortion of a cube toward (a) elongated and compressed tetragonal prisms, (b) a tetragonal antiprism and (c) a dodecahedron (adapted from Mironov et al. (2001)).

The factor $(1 + p)$ in eqs. (35)–(37) reflects the contribution of thermally populated excited multiplets of the lanthanide ion which is small for all lanthanides at 300 K except for Sm(III) and Eu(III). In the latter case, the energy of the first excited states are close enough from the ground state to require specific calculations at each temperature. Combinations of eqs. (35)–(37) allows the calculation of the magnetic anisotropy in eq. (39) which predicts that $\Delta\chi$ depends only on the B_0^2 crystal-field parameter. The sign and the magnitude of the magnetic anisotropies along an isostructural series of lanthanide complexes possessing identical B_0^2 parameter only depend on ξ which is positive for $R = \text{Eu, Er, Tm, Yb}$, negative for Ce, Pr ,

Nd, Tb, Dy and maximum for $R = \text{Dy}$ (Bleaney, 1972),

$$\begin{aligned}\Delta\chi &= \chi_{zz} - \frac{1}{2}(\chi_{xx} + \chi_{yy}) = \frac{3}{2}\left(\chi_{zz} - \frac{1}{3}\text{Tr}\chi\right) = -\frac{N_A\beta^2}{10(kT)^2}\langle r^2 \rangle A_2^0(1+p)\xi \\ &= -\frac{N_A\beta^2}{20(kT)^2}B_0^2(1+p)\xi.\end{aligned}\quad (39)$$

If the energy of the crystal-field splitting ΔE_{CF} produced by the B_q^k parameters is much smaller than the thermal energy ($kT \approx 200 \text{ cm}^{-1}$ at 300 K), all the crystal-field levels of the ground state have comparable thermal populations and the T^{-2} term of the power series is adequate for modeling the magnetic anisotropy (Bleaney, 1972; Mironov et al., 2002). Substitution of eqs. (35)–(37) into eq. (28) gives eq. (40) in terms of $A_2^q\langle r^2 \rangle$ which can be transformed into eq. (41) with conventional B_q^k parameters

$$\delta_i^{\text{pc}} = -\frac{\beta^2(1+p)\xi}{60(kT)^2}\left(\frac{1}{r_i^3}\right)\left[A_2^0\langle r^2 \rangle(3\cos^2\theta_i - 1) + A_2^2\langle r^2 \rangle(\sin^2\theta_i \cos 2\phi_i)\right], \quad (40)$$

$$\delta_i^{\text{pc}} = -\frac{\beta^2(1+p)\xi}{120(kT)^2}\left(\frac{1}{r_i^3}\right)\left[B_0^2(3\cos^2\theta_i - 1) + \sqrt{6}B_2^2(\sin^2\theta_i \cos 2\phi_i)\right]. \quad (41)$$

The first numerical terms $C = -\beta^2(1+p)\xi/(120(kT)^2)$ are often referred to as Bleaney's factors and their relative values (scaled to $C_{\text{Dy}} = -100$) have been tabulated at 300 K for any $4f^n$ configurations including excited states contributions (table 3, Bleaney et al. (1972)). Finally, the introduction of the geometrical factors defined by eqs. (30), (31) together with C into eq. (41) gives the classical eq. (42) for the pseudo-contact shifts according to Bleaney's approach (Forsberg, 1996)

$$\delta_i^{\text{pc}} = C(B_0^2G_i + \sqrt{6}B_2^2H_i). \quad (42)$$

However, a systematic survey of the crystal-field splitting in lanthanide complexes shows that $\Delta E_{\text{CF}} \approx 300\text{--}400 \text{ cm}^{-1}$ is usual and the high-temperature assumption $\Delta E_{\text{CF}} < kT$ is not fully satisfied. Therefore, C_q^k operators of rank four ($k = 4$) and rank six ($k = 6$) cannot be neglected (Morrison and Leavitt, 1982; Görrler-Walrand and Binnemans, 1996; Mironov et al., 2000). According to Bleaney's approach, the T^{-n} series does not converge at T^{-2} and further terms must be considered. Golding and Pyykkö (1973) included rank four and rank six crystal-field parameters (B_q^k , $k = 4, 6$) for the specific calculations of the magnetic susceptibilities in crystal-field potentials with D_{3h} and C_{3v} symmetries. They found that corrections to the T^{-2} term are within 20% for $R\text{Cl}_3$ compounds. Later, McGarvey (1979) derived the complete forms of the T^{-3} terms which depend on B_q^k , $k = 2, 4, 6$. Since these equations would occupy almost one complete printed page, the reader is referred to the original publication. Application to $R\text{Cl}_3$ and $R(\text{O}_3\text{SOEt})_3$ shows less than 10% deviation from classical Bleaney's approach (i.e., a power series limited to T^{-2}) and it was concluded that the T^{-3} term (or higher order terms) can be neglected (Stout and Gutowsky, 1976). However, the crystal-field splittings experienced by $R(\text{III})$ in $R\text{Cl}_3$ or in $R(\text{O}_3\text{SOEt})_3$ are among the smallest reported (Görrler-Walrand and Binnemans, 1996) and high-temperature Bleaney's

hypothesis $\Delta E_{CF}/kT < 1$ is satisfied. The recent exact calculations of $\Delta\chi$ by Mironov et al. (2001, 2002) with eqs. (32), (33) for lanthanide complexes with arbitrary crystal-field parameters and geometries show that Bleaney's approach is insufficient to model cases for which $\Delta E_{CF} > kT$. For instance, the distortion of an eight-coordinate tetragonal prismatic complex toward a tetragonal antiprism does not affect B_0^2 and no variation of $\Delta\chi$ is expected from eq. (39). The computed changes of $\Delta\chi$ for $R = Dy, Tm$ and Yb (fig. 2b) are thus clearly beyond Bleaney's theory (fig. 2b, Mironov et al. (2001)) as is the significant deviation of the magnetic anisotropy from the predicted T^{-2} behaviour noticed by Horrocks (1977) for solid $Yb(III)$ complexes. It can be concluded that Bleaney's approach is restricted to complexes with small crystal-field splitting in a narrow temperature range around 300 K, the reference temperature at which the C factors have been computed (table 3). However, to the best of our knowledge, no systematic investigation of the corrections resulting from T^{-3} terms has been investigated except for the seminal work of McGarvey (1979).

2.4. Separation of contact and pseudo-contact contributions in paramagnetic lanthanide complexes

The substitution of eqs. (19) and (28) into eq. (3) shows that the paramagnetic shift induced by a lanthanide j at a nucleus i is given by eq. (43)

$$\begin{aligned} LIS &= \delta_{ij}^{\text{para}} = \delta_{ij}^{\text{c}} + \delta_{ij}^{\text{pc}} \\ &= \frac{A_i}{\hbar\gamma_I H_0} \langle S_z \rangle_j + \frac{1}{2N_A r_i^3} \left[\left(\chi_{zz}^j - \frac{1}{3} \text{Tr} \chi^j \right) (3 \cos^2 \theta_i - 1) \right. \\ &\quad \left. + (\chi_{xx}^j - \chi_{yy}^j) (\sin^2 \theta_i \cos 2\phi_i) \right]. \end{aligned} \quad (43)$$

The use of the definitions of the geometrical factors G_i (eq. (30)) and H_i (eq. (31)) together with the contact term $F_i = A_i/(\hbar\gamma_I H_0)$ for the nucleus i leads to the well-established eq. (44) in the principal magnetic axes system

$$\delta_{ij}^{\text{para}} = \delta_{ij}^{\text{c}} + \delta_{ij}^{\text{pc}} = F_i \langle S_z \rangle_j + \frac{1}{2N_A} \left[\left(\chi_{zz}^j - \frac{1}{3} \text{Tr} \chi^j \right) G_i + (\chi_{xx}^j - \chi_{yy}^j) H_i \right]. \quad (44)$$

The contact and the pseudo-contact contributions are constituted by the product of two terms depending respectively on the lanthanide j ($\langle S_z \rangle_j$ and χ^j) and on the nucleus i (F_i , G_i and H_i). Since $\langle S_z \rangle_j$ is poorly affected by crystal-field effects, the values tabulated for the free ions (Golding and Halton, 1972; table 3) hold for all complexes and the contact term is easily factorized. On the other hand, χ^j depends on the specific electronic structure of the lanthanide ion ($4f^n$ configuration) combined with specific crystal-field potentials produced by the surrounding ligands. Except for Bleaney's approach (see sects. 2.3.1 and 2.4.2), no straightforward a priori prediction can be made for χ^j and the treatment of pseudo-contact terms requires an initial assumption of the molecular structures in order to calculate a set of G_i and H_i which are then used to extract the anisotropic part of the paramagnetic susceptibility tensor ($\chi_{zz} - (1/3) \text{Tr} \chi$, $\chi_{xx} - \chi_{yy}$) via least-squares fitting processes (Forsberg, 1996). Non-linear least-square fits may be further applied in order to simultaneously

refine the geometrical factors and the components of the magnetic tensor (Forsberg, 1996; Peters et al., 1996).

2.4.1. Calculation of the anisotropic part of the magnetic susceptibility tensor with structural models

In the absence of contact contribution ($F_i = 0$), the LIS purely reflects the pseudo-contact contributions and eqs. (27), (28) are ideally suited for extracting the experimental anisotropic part of the magnetic susceptibility tensor as long as a reasonable structural model is available. Kemple et al. (1988) reported a detailed ^1H NMR study of lanthanide complexes [$R(\text{indole-EDTA})$] ($R = \text{La, Pr, Nd, Er, Yb}$) and [$R(\text{benzyl-EDTA})$] ($R = \text{La, Pr, Yb, Lu}$; fig. 3). Decoupling experiments, 2D-COSY spectra and relaxation measurements (T_1, T_2) allowed an unambiguous assignment of the protons and reasonable molecular structures were obtained by molecular mechanics (MM2 force field). Using an arbitrary Cartesian frame (x, y, z axes) with $R(\text{III})$ at the origin, the geometrical factors G_i and H_i were calculated from the polar coordinates (r_i, θ_i and ϕ_i , fig. 1). As a first approximation, all contact contributions were set to zero and linear least-squares fits according to eq. (27) for 13 aliphatic protons used as a basis gave the five components of the traceless part of the magnetic susceptibility tensor ($\chi_{zz} - (1/3)\text{Tr}\chi, \chi_{xx} - \chi_{yy}, \chi_{xy}, \chi_{yz}, \chi_{yz}; 13 \times 5$ fit). Diagonalisation of the latter tensor gave a set of Euler angles that relates the principal magnetic axes system to the original arbitrary Cartesian frame.

The quality of the fitting process for the complex of a lanthanide j is measured by the agreement factor AF_j defined in eq. (45) (Wilcott et al., 1972)

$$AF_j = \sqrt{\frac{\sum_i (\delta_{ij}^{\text{obs}} - \delta_{ij}^{\text{calc}})^2}{\sum_i (\delta_{ij}^{\text{obs}})^2}}. \quad (45)$$

Kemple et al. (1988) found $AF_{\text{Pr}} = 0.147$, $AF_{\text{Nd}} = 0.346$ and $AF_{\text{Eu}} = 0.765$ which were not satisfying and required corrections for the contact contributions of protons close to the metal centre. By introducing a minimal set of five different contact shifts for the protons of the acetate arms and of the ethylene bridge as fitting parameters ($\delta_{ij}^c = F_i \langle S_z \rangle_j$), the original $13 \text{ observables} \times 5$ fitted parameters were transformed into a 13×10 fit and multilinear least-squares fits with eq. (44) gave $AF_{\text{Pr}} = 0.032$, $AF_{\text{Nd}} = 0.031$ and $AF_{\text{Eu}} = 0.031$. Since the contact contributions are obtained and adjusted as scalar parameters in eq. (44), any proton for which contact is allowed does not contribute to the determination of the magnetic

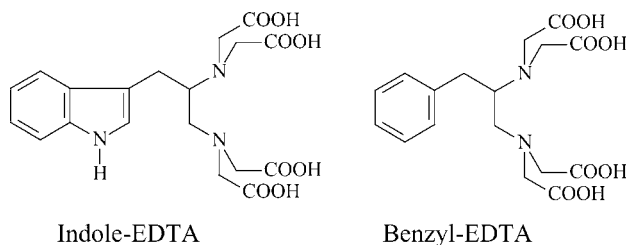


Fig. 3. Structures of substituted EDTA ligands.

susceptibility tensor. Therefore, this approach requires a large number of protons sufficiently remote from the paramagnetic lanthanide and for which $F_i = 0$, but no assumption regarding the orientation of the molecular coordinates system and the principal magnetic axes system is required, a great advantage for low-symmetry complexes. Significant rhombic distortions was observed for $[R(\text{indole-EDTA})]$ and $[R(\text{benzyl-EDTA})]$ (i.e., $\chi_{xx} - \chi_{yy} \neq 0$) and the orientation of the principal magnetic axes with respect to the molecular coordinates system varied for the different lanthanide complexes. Recently, Bertini et al. (2001) have applied this procedure for extracting the anisotropic part of the magnetic susceptibility tensor of the dicalcium protein calbindin D_{9k} in which a lanthanide metal ion has been incorporated into the C-terminal calcium binding site. From 1097 pure pseudo-contact shifts ($F_i = 0$) combined with molecular modeling obtained by molecular mechanics, the anisotropic part of the magnetic susceptibility tensor $\chi_{zz} - (1/3) \text{Tr} \chi$ and $\chi_{xx} - \chi_{yy}$ (two parameters), together with the orientation of the principal magnetic axes (three parameters) have been determined for $R = \text{Ce-Yb}$, except Pm and Gd. Non-linear least-squares fits simultaneously provide refined positions for the NMR active nuclei. The average agreement factor $\overline{AF} = (1/n) \sum_{j=1}^n AF_j$ for all lanthanides amounts to $\overline{AF} = 0.16$. Forsberg et al. (1995) have developed a computer program which allows the systematic permutation of the observed pseudo-contact shifts (δ_{ij}^{pc}) to different sets of protons when assignment is problematic. Basically following the procedure of Kemple et al. (1988), a structural model obtained by molecular mechanics is used for calculating the magnetic susceptibility tensor according to eq. (27) for each possible permutation. The associated agreement factors AF_j (eq. (45)) are then used as criteria for selecting the most probable assignment which minimizes AF_j . Subsequent diagonalisation or reorientation of the magnetic axes provides the anisotropic part of the magnetic susceptibility tensor in the principal magnetic axes system. Application to the axial C_4 -symmetrical complexes $[R(\text{L}^{11})]^{3+}$ (see sect. 3.2.3) by Forsberg et al. (1995) ($R = \text{Pr-Yb}$ except Gd) has demonstrated that, as expected from symmetry arguments, the magnetic tensor is axially symmetric ($\chi_{zz} - (1/3) \text{Tr} \chi = 3269 \cdot 10^{-6} \text{ cgs} \cdot \text{mol}^{-1}$ and $\chi_{xx} - \chi_{yy} = 0$) and the z axis coincides with the molecular C_4 axis (0.001° deviation). Ultimate refinements of the molecular geometry requires the explicit consideration of contact contributions to the observed LIS and Forsberg et al. (1995) used a complicated approach in which $\chi_{zz} - (1/3) \text{Tr} \chi$, G_i and F_i are simultaneously varied in eq. (44) in order to minimize the agreement factor AF for n nuclei in m lanthanide complexes ($n \times m$ simultaneous equations). When one structural factor G_1 is known from the structural model, a set of F_i values could be obtained which were used to extract pure pseudo-contact shifts according to $\delta_{ij}^{\text{pc}} = \delta_{ij}^{\text{para}} - \delta_{ij}^{\text{c}} = \delta_{ij}^{\text{para}} - F_i \langle S_z \rangle_j$. The final refinement of the structure then used least-squares fits of eq. (29) in the principal magnetic axes system. In a parallel contribution, Lisowski et al. (1995a) used a closely related strategy for investigating the solution structures of the pseudo-axial texaphyrin complexes $[R(\text{texa})X_2]$ ($X = \text{NO}_3^-$, diphenylphosphate; $R = \text{Ce-Yb}$ except Pm and Gd) shown on fig. 4. Pure ^1H NMR pseudo-contact shifts δ_{ij}^{pc} were fitted with eq. (28) by using the crystal structure of $[\text{Gd}(\text{texa})(\text{NO}_3)_2]$ as a structural model. Since the principal magnetic z and x axes were fixed in the molecular symmetry C_s plane, only three parameters $\chi_{zz} - (1/3) \text{Tr} \chi$, $\chi_{xx} - \chi_{yy}$ and an angle α defining the location of the lanthanide metal above the average macrocyclic plane were varied by



Fig. 4. Structure and reference frame for the dimethoxy tetraethyl dimethyl trivalent lanthanide texaphyrin. The α angle measures the out-of-plane location of $R(\text{III})$ with respect to the mean macrocyclic plane (adapted from Lisowski et al. (1995a)).

using non-linear least-squares techniques in order to obtain the best fit which minimized AF_j for each complex (α is the angle between the x axis and the $R\text{-N}_{\text{central pyrrole}}$ bond, fig. 4).

Systematic calculations with different sets of protons belonging to the complexes showed that the incorporation of the imino protons in the fitting process significantly increased AF_j because contact contributions could not be neglected for these nuclei. Exclusion of the latter protons from the fitting process gave $0.07 \leq AF_j \leq 0.26$, α angles in the range $5\text{--}30^\circ$ and magnetic parameters $\chi_{zz} - (1/3)\text{Tr } \chi$ and $\chi_{xx} - \chi_{yy}$ of comparable magnitudes pointing to considerable rhombic distortion in each lanthanide complex. The latter result demonstrated that the intuitive assignment of pseudo-axial symmetry (i.e., C_4 -symmetry) to the $[R(\text{texa})X_2]$ is not justified. Computation of pure pseudo-contact shifts δ_{ij}^{PC} for the imino protons by using eq. (28) and the experimental magnetic anisotropy tensor in the principal magnetic axes system, allowed the separation of their contact contribution according to eq. (44) ($\delta_{ij}^{\text{c}} = \delta_{ij}^{\text{para}} - \delta_{ij}^{\text{PC}} = F_i \langle S_z \rangle_j$). Interestingly, plots of δ_{ij}^{c} vs free-ions $\langle S_z \rangle_j$ values (table 3) showed the expected straight line (slope = F_i) which confirmed (i) the good quality of the calculated anisotropic part of the magnetic susceptibility tensor and (ii) the negligible dependence of $\langle S_z \rangle_j$ on the crystal-field splitting around room temperature. Lisowski et al. (1995b) proposed identical calculations for non-H atoms in $[R(\text{texa})X_2]$ and were able to obtain reliable contact shifts for all ^{13}C and ^{31}P nuclei. Detailed σ and π -mechanisms for spin delocalisation could be addressed with this technique, but the main conclusions concerned the extreme sensitivity of both ^{31}P and ^1H chemical shifts to changes in axial ligations ($X = \text{nitrate}$ or diphenylphosphate) which was mediated by the variation of the crystal-field parameters affecting the magnetic susceptibility tensor.

The direct experimental determination of the anisotropic part of the magnetic susceptibility tensor from a set of pure pseudo-contact shifts according to eqs. (27), (28) has the considerable advantage of requiring no assumption on the symmetry of the magnetic susceptibility tensor. Paramagnetic LIS for axial and rhombic complexes can be satisfyingly modeled. The estimation of the contact contributions either by simultaneous fitting processes (Kemple et al.,

1988) or by comparison with experimental LIS (Lisowski et al., 1995a, 1995b) allows a reliable separation of contact and pseudo-contact contributions. However, this approach requires (i) a large number of nuclei displaying pure pseudo-contact contributions and (ii) an accurate a priori structural model for the complex in solution, two conditions which are often limiting when considering supramolecular lanthanide complexes of intermediate size.

2.4.2. The model-free methods

When no assumption is made on the solution structure, the determination of the desired geometrical factors G_i and H_i requires the a priori separation of the contact and pseudo-contact contributions to the LIS. Bleaney's approach limited to the T^{-2} term and summarized by eqs. (40)–(42) (see sect. 2.3.1) is well-suited for this purpose since the anisotropic part of the magnetic susceptibility tensor can be modeled by a judicious combination of an electronic factor depending only on the electronic configuration of the lanthanide j (i.e., Bleaney's factors C_j in table 3) and the crystal-field parameters of rank two for the complexes. Substituting the pseudo-contact contribution of eq. (42) into eq. (44) gives eq. (46) which reduces to eq. (47) for axial systems ($B_2^2 = 0$, Reilley et al. (1975), Bryden and Reilley (1982)). Interestingly, the spherical crystal-field operator C_2^2 and the associated B_2^2 parameter are not involved for systems possessing at least a C_3 axis (Görrler-Walrand and Binnemans, 1996) and eq. (47) also holds for lanthanide complexes displaying trigonal symmetry. We have consequently limited the complexes considered in this review to those possessing at least a C_3 or a C_4 axis and for which effective axial symmetry can be applied (eq. (47)). It is worth noting that the assignment of axial symmetry to trigonal complexes is valid when the T^{-n} series is limited to $n = 2$ (Bleaney's hypothesis, Bleaney (1972)), but it can be extended for $n = 3$ because the third-order coefficient of the rhombic term (H_i) still vanishes when all B_q^k are zero except B_2^0 , B_0^4 , B_0^6 , B_3^4 , B_3^6 and B_6^6 (McGarvey, 1979)

$$\delta_{ij}^{\text{para}} = \delta_{ij}^{\text{c}} + \delta_{ij}^{\text{pc}} = F_i \langle S_z \rangle_j + C_j (B_0^2 G_i + \sqrt{6} B_2^2 H_i), \quad (46)$$

$$\delta_{ij}^{\text{para}} = F_i \langle S_z \rangle_j + C_j B_0^2 G_i. \quad (47)$$

2.4.2.1. *Reilley's method.* Since $\langle S_z \rangle_j$ and C_j do not depend on the crystal-field splitting (see sects. 2.2 and 2.3.1), Reilley et al. (1975) first proposed to rearrange eq. (46) into two linear forms (eqs. (48), (49)) for testing isostructurality along the lanthanide series

$$\frac{\delta_{ij}^{\text{para}}}{\langle S_z \rangle_j} = F_i + \frac{C_j}{\langle S_z \rangle_j} (B_0^2 G_i + \sqrt{6} B_2^2 H_i), \quad (48)$$

$$\frac{\delta_{ij}^{\text{para}}}{C_j} = (B_0^2 G_i + \sqrt{6} B_2^2 H_i) + F_i \frac{\langle S_z \rangle_j}{C_j}. \quad (49)$$

Although these two equations are mathematically identical, eq. (48) should be used when $\delta_{ij}^{\text{para}}$ is dominated by the pseudo-contact contribution and eq. (49) should be used when $\delta_{ij}^{\text{para}}$ is dominated by contact effects, thus maximizing the slopes of the resulting straight lines (Reuben and Elgavish, 1980). Plots of $\delta_{ij}^{\text{para}} / \langle S_z \rangle_j$ vs $C_j / \langle S_z \rangle_j$ (eq. (48)) or $\delta_{ij}^{\text{para}} / C_j$ vs

$\langle S_z \rangle_j / C_j$ (eq. (49)) along the lanthanide series at a fixed temperature are expected to give straight lines and any deviations point to structural changes affecting the ‘structural term’ $B_0^2 G_i + \sqrt{6} B_2^2 H_i$ (Reilly et al., 1975; Sherry and Gerald, 1989). However this simple interpretation assumes that (i) the hyperfine constant (A_i and hence the F_i term) and the crystal-field parameters B_0^2 and B_2^2 do not vary along the lanthanide series, (ii) the T^{-2} term is sufficient for describing the molecular magnetic anisotropy and (iii) the stepwise lanthanide contraction occurring when going from $R = \text{Ce}$ to Yb has negligible effects on the structural term. Peters (1986) has theoretically addressed the last point and geometrical G_i factors for axial complexes modeled with molecular mechanics have been computed. The smooth contraction of the R -ligand distances often results in a minor break occurring between $R = \text{Eu}$ and $R = \text{Tb}$ in the plot of $\delta_{ij}^{\text{para}} / \langle S_z \rangle_j$ vs $C_j / \langle S_z \rangle_j$ because the monotonous change in G_i is amplified by the large values of C_j characterising the second part of the lanthanide series (table 3). It is thus concluded that both linear plots $\delta_{ij}^{\text{para}} / \langle S_z \rangle_j$ vs $C_j / \langle S_z \rangle_j$ (eq. (48)) and $\delta_{ij}^{\text{para}} / C_j$ vs $\langle S_z \rangle_j / C_j$ (eq. (49)) should simultaneously display a break along the lanthanide series to be indicative of a significant structural change (fig. 5).

2.4.2.2. *Crystal-field independent methods.* The invariance of crystal-field parameters is more problematic since the experimental B_q^k parameters of lanthanide complexes in the solid state usually exhibit significant variations along the lanthanide series resulting from the contraction of the 4f orbitals (Freeman and Watson, 1962; Görrler-Walrand and Binnemans, 1996). Moreover, an abrupt change around the middle of the series, sometimes referred to as the ‘gadolinium break’ effect has been evidenced in $\text{Na}_3[\text{Yb}_{1-x}\text{R}_x(\text{L}^7-2\text{H})_3] \cdot \text{NaClO}_4 \cdot 10\text{H}_2\text{O}$ (see sect. 3.1.7, Hopkins et al. (1996)), and $\text{Na}_3[\text{R}(\text{L}^1-2\text{H})_3] \cdot 2\text{NaClO}_4 \cdot 6\text{H}_2\text{O}$ (see sect. 3.1.1, Hopkins et al. (1998)). Related effects are thus expected for lanthanide complexes in solution and efforts have been made to remove the influence of crystal-field parameters (Reuben, 1982; Spiliadis and Pinkerton, 1982). In axial complexes (i.e., possessing at least a C_3 axis),¹ the simultaneous consideration of the chemical shifts of two nuclei i and k provides two equations (eqs. (47), (50)) from which Bleaney’s factor C_j and the crystal field parameter B_0^2 can be removed by a judicious mathematical substitution in order to give eq. (51) (Spiliadis and Pinkerton, 1982; Platas et al., 1999)

$$\delta_{kj}^{\text{para}} = F_k \langle S_z \rangle_j + C_j B_0^2 G_k, \quad (50)$$

$$\frac{\delta_{ij}^{\text{para}}}{\langle S_z \rangle_j} = \left(F_i - F_k \frac{G_i}{G_k} \right) + \frac{G_i}{G_k} \cdot \frac{\delta_{kj}^{\text{para}}}{\langle S_z \rangle_j}. \quad (51)$$

Plots of $\delta_{ij}^{\text{para}} / \langle S_z \rangle_j$ vs $\delta_{kj}^{\text{para}} / \langle S_z \rangle_j$ are ideally suited for testing structural changes occurring along the lanthanide series in axial complexes because straight lines are expected as long as the slope $R_{ik} = G_i / G_k$ and the intercept $F_i - F_k R_{ik}$ do not vary. Structural changes affect the slope

$$R_{ik} = \frac{G_i}{G_k} = \frac{(3 \cos^2 \theta_i - 1)}{(3 \cos^2 \theta_k - 1)} \cdot \frac{r_k^3}{r_i^3}$$

¹ All complexes for which effective axial symmetry can be applied (eq. (47), see sect. 2.4.2).

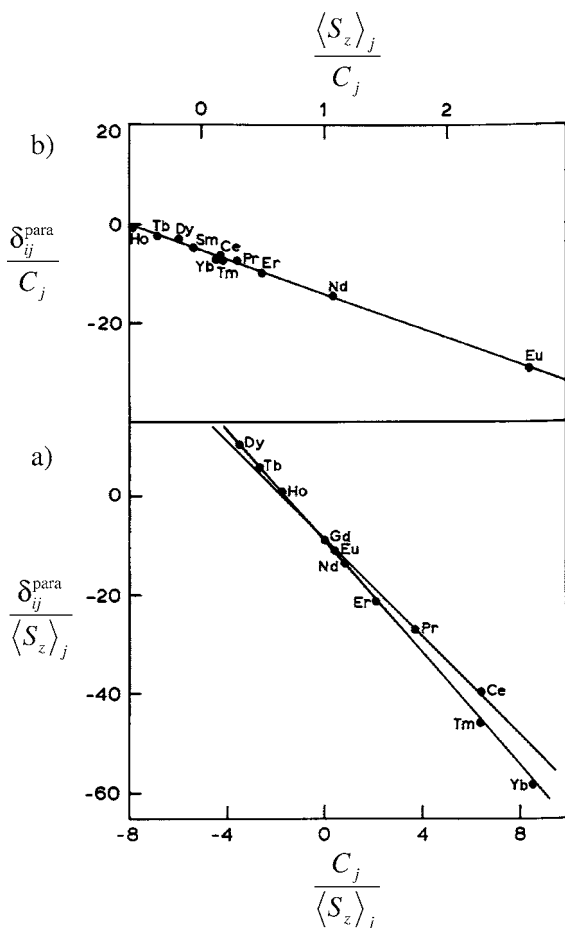


Fig. 5. Plots of (a) $\delta_{ij}^{para} / \langle S_z \rangle_j$ vs $C_j / \langle S_z \rangle_j$ (eq. (48)) and (b) δ_{ij}^{para} / C_j vs $\langle S_z \rangle_j / C_j$ (eq. (49)) for the carboxylate carbons in simulated nine-coordinate tricapped trigonal prismatic $[R(\text{OOCCH}_3)_3(\text{OH}_2)_3]$ complexes (re-drawn from Peters (1986)).

and can be easily detected, but crystal-field changes which are not associated with significant structural variations have no effect. Changes in the intercept are more difficult to interpret since $F_i - F_k R_{ik}$ depends on geometrical factors (via R_{ik}) and hyperfine constants (via F_i and F_k). In favourable cases, the prior analysis of the slope R_{ik} allows to draw reliable conclusions concerning possible variations of the hyperfine constants along the lanthanide series (Platas et al., 1999; Rigault et al., 2000b). Although $\langle S_z \rangle_j$ is relatively independent from crystal-field effects around room temperature (see sect. 2.2), Geraldes et al. (2001) have proposed to remove it by solving simultaneously eqs. (47), (50), (52) for three different nuclei i, k, l in the same lanthanide complex. Straightforward algebraic substitutions and transformations give eq. (53) where $R_{ik} = G_i / G_k$ and $S_{ik} = F_i / F_k$

$$\delta_{ij}^{para} = F_l \langle S_z \rangle_j + C_j B_0^2 G_l, \quad (52)$$

$$\frac{\delta_{ij}^{\text{para}}}{\delta_{kj}^{\text{para}}} = \frac{(S_{lk}R_{ik} - S_{ik}R_{lk})}{(S_{lk} - R_{lk})} + \frac{(S_{ik} - R_{ik})}{(S_{lk} - R_{lk})} \cdot \frac{\delta_{lj}^{\text{para}}}{\delta_{kj}^{\text{para}}} \quad (53)$$

Plotting $\delta_{ij}^{\text{para}}/\delta_{kj}^{\text{para}}$ against $\delta_{lj}^{\text{para}}/\delta_{kj}^{\text{para}}$ along the lanthanide series should yield a straight line of slope

$$\alpha = \frac{(S_{ik} - R_{ik})}{(S_{lk} - R_{lk})}$$

and an intercept

$$\beta = \frac{(S_{lk}R_{ik} - S_{ik}R_{lk})}{(S_{lk} - R_{lk})},$$

provided that S_{ik} , S_{lk} , R_{ik} and R_{lk} are invariant. Since the simple eq. (53) only requires experimental LIS data for testing isostructurality, its use seems promising as long as three different NMR-active nuclei are available in the complex. However, both the slope (α) and the intercept (β) are complicated non-linear combinations of geometrical G_i factor and contact F_i terms. Deviations from linearity are difficult to interpret and accidental compensation effects cannot be ruled out when strict linear behaviours are observed (Ouali et al., 2002).

2.4.2.3. The special case of rhombic systems. The removal of crystal-field parameters according to the two-nuclei (eq. (51)) and the three-nuclei (eq. (53)) methods is strictly limited to axial complexes for which eq. (47) holds (i.e., possessing at least a C_3 axis). The explicit consideration of the rhombic term $C_j\sqrt{6}B_2^2H_i$ in Bleaney's approach (eq. (42)) significantly complicates the derivation of crystal-field independent equations which requires at least three different nuclei. To the best of our knowledge, no analytical form has been reported in the literature for rhombic systems. Reuben and Elgavish (1980) have suggested that eq. (42) is only a poor approximation for rhombic systems and a better modeling of the pseudo-contact contribution requires two experimental factors C_j^{axial} and C_j^{rhombic} (eq. (54)),

$$\delta_i^{\text{pc}} = C_j^{\text{axial}}G_i + C_j^{\text{rhombic}}H_i \quad (54)$$

Since C_j^{axial} is proportional to $\chi_{zz} - (1/3)\text{Tr}\chi$ and C_j^{rhombic} is proportional to $\chi_{xx} - \chi_{yy}$ in the principal magnetic axes system (eq. (28)), Reuben and Elgavish (1980) used the experimental diagonalised magnetic susceptibility tensors reported by Horrocks and Sipe (1972) for solid-state $[R(\text{dipivaloylmethane})_3(4\text{-picoline})_2]$ complexes in order to compute the proportionality factors C_j^{axial} and C_j^{rhombic} scaled to $C_{\text{Dy}}^{\text{axial}} = -100$. Interestingly they notice that the axial factors C_j^{axial} satisfyingly match original Bleaney's C_j factors, but C_j^{rhombic} have only poor correlations with C_j pointing to the limit of theoretical Bleaney's approach which predicts a single factor ($C_j^{\text{axial}} = C_j^{\text{rhombic}}$, eq. (42), table 3). Two linear forms (eqs. (55), (56)) can be derived from eq. (54) for nuclei displaying no contact contributions ($F_i = 0$)

$$\frac{\delta_i^{\text{pc}}}{C_j^{\text{axial}}} = G_i + H_i \frac{C_j^{\text{rhombic}}}{C_j^{\text{axial}}}, \quad (55)$$

$$\frac{\delta_i^{\text{pc}}}{C_j^{\text{rhombic}}} = H_i + G_i \frac{C_j^{\text{axial}}}{C_j^{\text{rhombic}}}. \quad (56)$$

Plots of $\delta_i^{\text{pc}}/C_j^{\text{axial}}$ vs $C_j^{\text{rhombic}}/C_j^{\text{axial}}$ (eq. (55)) or $\delta_i^{\text{pc}}/C_j^{\text{rhombic}}$ vs $C_j^{\text{axial}}/C_j^{\text{rhombic}}$ (eq. (56)) are expected to be linear within an isostructural series. The fitting process has been applied to non-axial lanthanide shifts reagents and leads to improved linear correlations (Reuben and Elgavish, 1980), but the origin of the deviation from the strict T^{-2} terms was not addressed. We can infer that the different behaviours of C_j^{axial} and C_j^{rhombic} along the lanthanide series result from higher-order T^{-n} terms ($n \geq 3$) which are neglected in original Bleaney's approach, but which are required to reliably model complexes possessing large crystal-field splittings ($\Delta E_{\text{CF}}/kT < 1$). Since the C_j^{rhombic} factors proposed by Reuben and Elgavish (1980) originate from the specific crystal-field splitting of one reference complex [$R(\text{dipivolumethane})_3(4\text{-picoline})_2$], their systematic use for all lanthanide complexes is doubtful and this approach, to the best of our knowledge, has not been put on again for the structure-independent analysis of LIS data.

3. Application of the model-free methods to axial monometallic lanthanide complexes with sterically rigid ligands

The three following criteria have been selected for discussing the application of the model-free methods to lanthanide complexes.

- (1) Lanthanide complexes with axial symmetry (i.e., possessing at least a threefold axis, see sect. 2.4.2) are exclusively considered because the principal magnetic z axis coincides with the molecular symmetry axis (Forsberg et al., 1995) and the $C_{\pm 2}^2$ spherical tensor operators do not contribute to the crystal-field potentials (Görrler-Walrand and Binne-mans, 1996). The rhombic term of Bleaney's approach $\sqrt{6}B_2^2H_i$ (eqs. (42), (46)) thus vanishes and the crystal-field independent methods (eqs. (51), (53)) can be used without complications.
- (2) The use of sterically rigid ligands ensures the formation of well-defined coordination spheres which strongly limit dynamic behaviours occurring in solution on the NMR time scale.
- (3) Multidentate chelating ligands produce stable lanthanide complexes in solution. At concentrations compatible with NMR measurements, partial decomplexation is negligible and exchange processes involving either the free ligand or complexes with different stoichiometries are ignored because highly unequally populated sites do not significantly affect NMR spectra (Pons and Millet, 2001). Under these conditions, the experimental paramagnetic lanthanide-induced chemical shifts $\delta_{ij}^{\text{para}}$ are obtained directly from the NMR spectra recorded under the slow-exchange regime at a single concentration. When significant decomplexation occurs (see sect. 3.1.1), the shifts for bound ligands can be extrapolated from fast-exchange NMR spectra recorded upon successive additions of small portions of $R(\text{III})$ to the ligand solution (Peters et al., 1996).

3.1. Complexes with threefold symmetry

3.1.1. $[R(L^1-2H)_3]^{3-}$ ($L^1 = \text{oxydiacetic acid}$)

The thermodynamic properties of the successive complexes $[R(L^1-2H)_n]^{(3-2n)+}$ ($n = 1, 2, 3$) in water have been studied extensively by Grenthe (1973) and the associated cumulative stability constants β_n show only limited stability for the D_3 -symmetrical triple-helical complexes $[R(L^1-2H)_3]^{3-}$ in solution (Martell and Smith, 1977). For a total ligand concentration of $0.2 \text{ mol} \cdot \text{dm}^{-3}$ and a stoichiometric ratio $\text{La}/[\text{L}^1-2\text{H}]^{2-} = 0.33$, one calculates the following ligand distribution: $[\text{La}(\text{L}^1-2\text{H})_3]^{3-}$ (91%), $[\text{La}(\text{L}^1-2\text{H})_2]^-$ (6%) and $[\text{L}^1-2\text{H}]^{2-}$ (3%). As decomplexation cannot be completely neglected, Peters (1988) has extrapolated experimental paramagnetic shifts for bound ligands $\delta_{ij}^{\text{para}}$ for $[R(\text{L}^1-2\text{H})_3]^{3-}$ ($R = \text{La-Lu}$, except Pm and Gd) from fast-exchange spectra at 346 K ($0.067 \text{ mol} \cdot \text{dm}^{-3}$ in water). The observed ^1H , ^{13}C and ^{17}O NMR data confirm the formation of D_3 -symmetrical triple-helical complexes $[R(\text{L}^1-2\text{H})_3]^{3-}$ in solution in agreement with the solid-state crystal structures reported for $\text{Na}_3[R(\text{L}^1-2\text{H})_3] \cdot 2\text{NaClO}_4 \cdot 6\text{H}_2\text{O}$ ($R = \text{La-Lu}$) which show $R(\text{III})$ to be coordinated by nine oxygen donors in pseudo-tricapped trigonal prismatic arrangements (Hopkins et al., 1998; fig. 6).

Interestingly, Peters (1988) notices that the methylene protons are enantiotopic for the light lanthanides ($R = \text{Ce-Dy}$) and become diastereotopic for $R = \text{Ho-Yb}$ which implies a dynamic intramolecular interconversion between the two helical enantiomers P - $[R(\text{L}^1-2\text{H})_3]^{3-} \rightleftharpoons M$ - $[R(\text{L}^1-2\text{H})_3]^{3-}$ occurring at a moderate rate on the NMR time scale. The observation of two resolved signals for the methylene protons for the heavy lanthanides $R = \text{Ho-Yb}$ reflects the larger pseudo-contact contributions induced in the second part of the lanthanide series and a slower exchange rate due to stronger lanthanide-ligand bonds. A rough estimate of $\Delta G^\ddagger = 54 \text{ kJ/mol}$ is obtained from the measurements of the coalescence temperatures for $R = \text{Tm, Yb}$. In excess of ligand ($R/[\text{L}^1-2\text{H}]^{2-} < 0.33$), fast dynamic intermolecular processes involving ligand exchanges in the first coordination sphere are also detected on the NMR time scale. At a given temperature, the rate of ligand exchange de-

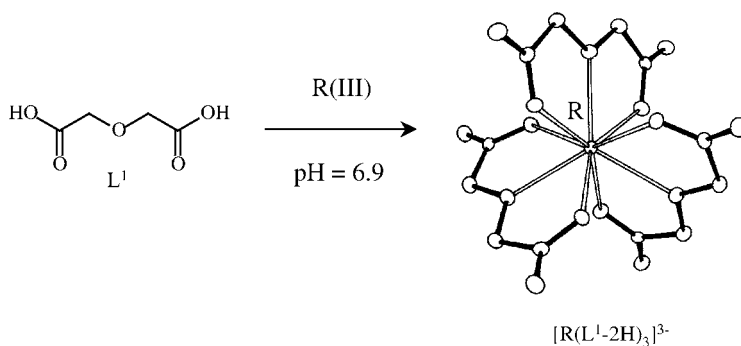


Fig. 6. Schematic formation of the D_3 -symmetrical complexes $[R(\text{L}^1-2\text{H})_3]^{3-}$ in water. The representation of $[R(\text{L}^1-2\text{H})_3]^{3-}$ corresponds to the crystal structure of $\text{Na}_3[\text{Eu}(\text{L}^1-2\text{H})_3] \cdot 2\text{NaBF}_4 \cdot 6\text{H}_2\text{O}$ (adapted from Fronczek et al. (1981)).

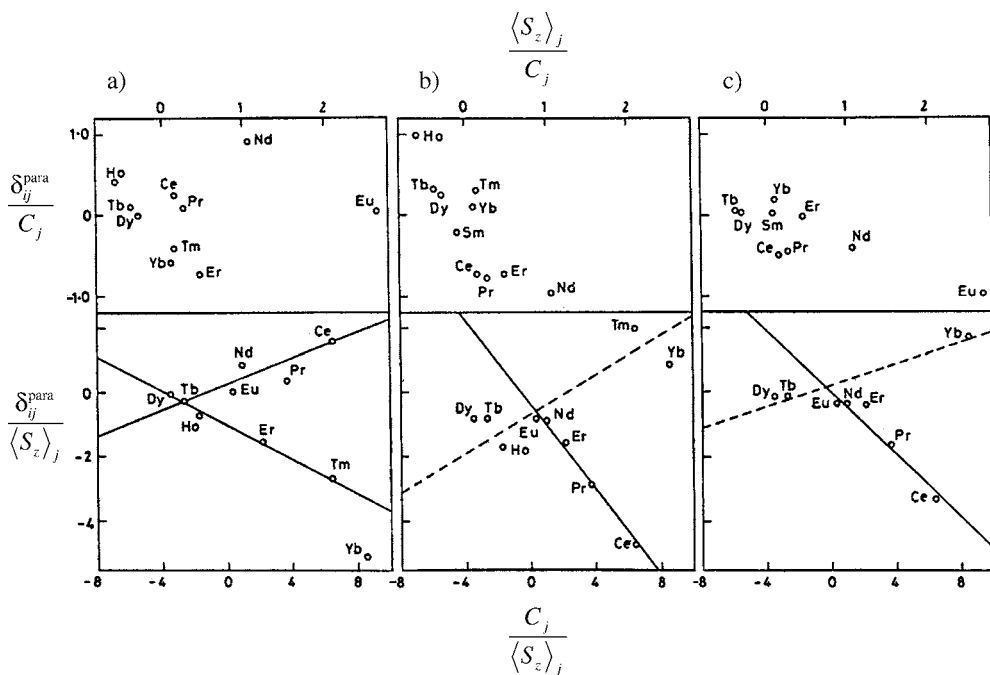


Fig. 7. Plots of $\delta_{ij}^{para}/\langle S_z \rangle_j$ vs $C_j/\langle S_z \rangle_j$ (eq. (48)) and δ_{ij}^{para}/C_j vs $\langle S_z \rangle_j/C_j$ (eq. (49)) along the lanthanide series for various nuclei in $[R(L^1-2H)_3]^{3-}$ (water, 346 K). (a) Carbon of the carbonyl group, (b) carbon of the methylene group, (c) protons of the methylene groups (redrawn from Peters (1988)).

creases with decreasing size of $R(III)$. Plots of $\delta_{ij}^{para}/\langle S_z \rangle_j$ vs $C_j/\langle S_z \rangle_j$ (eq. (48)) and δ_{ij}^{para}/C_j vs $\langle S_z \rangle_j/C_j$ (eq. (49)) along the lanthanide series for $[R(L^1-2H)_3]^{3-}$ show scattered diagrams for which unambiguous linear correlations are limited to $\delta_{ij}^{para}/\langle S_z \rangle_j$ vs $C_j/\langle S_z \rangle_j$ with $R = Ce-Eu$ (fig. 7).

Surprisingly, Bleaney's factors C_j determined at 300 K (table 3) are used without corrections for the treatment of the experimental NMR data recorded at 343 K. This approximation is probably justified for most $R(III)$ except for $R = Sm$ and Eu (see sect. 2.3), but the poor correlations exhibited by the δ_{ij}^{para}/C_j vs $\langle S_z \rangle_j/C_j$ plots might result from inadequate values of C_j (the $Sm(III)$ data have been excluded from the mathematical analysis, but the $Eu(III)$ data have been considered, fig. 7). The abrupt break of the plots according to eq. (48) occurring near the middle of the series (i.e., between $R = Eu$ and $R = Tb$) is ascribed to a structural change involving nine-coordinate D_3 -symmetrical complexes $[R(L^1-2H)_3]^{3-}$ similar to those found in the crystal structure for $R = Ce-Eu$, and eight-coordinate complexes $[R(L^1-2H)_3]^{3-}$ with low symmetry for $R = Tb-Yb$. Since the three ligands remain equivalent on the NMR time scale for $R = Tb-Yb$, Peters (1988) proposes fast on-off equilibria of the non-coordinated carboxylate group (fig. 8).

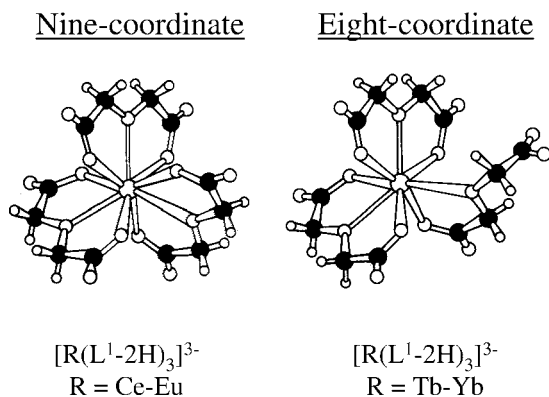


Fig. 8. Schematic representation of the two different solutions structures observed by NMR for $[R(L^1-2H)_3]^{3-}$ (adapted from Peters (1988)).

These results strongly contrast with solid-state structures of $Na_3[R(L^1-2H)_3] \cdot 2NaClO_4 \cdot 6H_2O$ ($R = La-Lu$) in which similar nine-coordinate $R(III)$ ions are located at sites of D_3 point-group symmetry along the complete lanthanide series (Hopkins et al., 1998). On the other hand, detailed spectroscopic investigations performed on these crystals provide crystal-field parameters B_q^k ($k = 2, q = 0; k = 4, q = 0, 3; k = 6, q = 0, 3, 6; R = Nd, Sm, Eu, Gd, Tb, Dy, Ho, Er$) which exhibit the expected monotonous decrease of the crystal-field interaction strength S_{CF} along the lanthanide series (contraction of the 4f electron charge distribution, Carnall et al., 1989). However, an unexpected abrupt variation of S_{CF} (mainly due to B_q^k of rank four and six) is detected near the middle of the lanthanide series (Hopkins et al., 1998; fig. 9).

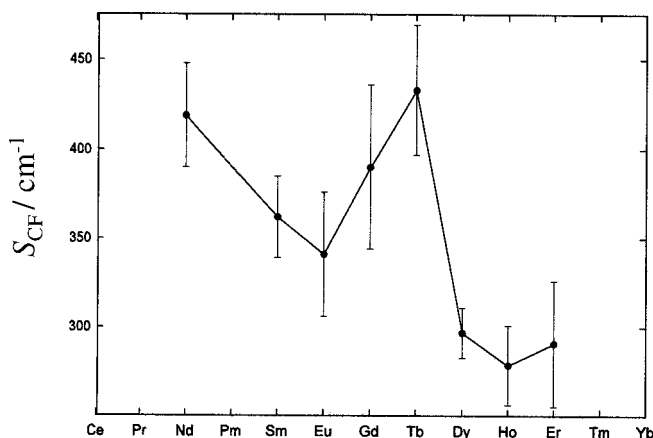


Fig. 9. Plot of the crystal-field interaction strength quantities $S_{CF} = \sqrt{\frac{1}{3} \sum_k \frac{1}{2k+1} [(B_0^k)^2 + 2 \sum_{m>0} |B_m^k|^2]}$ for eight $Na_3[R(L^1-2H)_3] \cdot 2NaClO_4 \cdot 6H_2O$ systems (redrawn from Hopkins et al. (1998)).

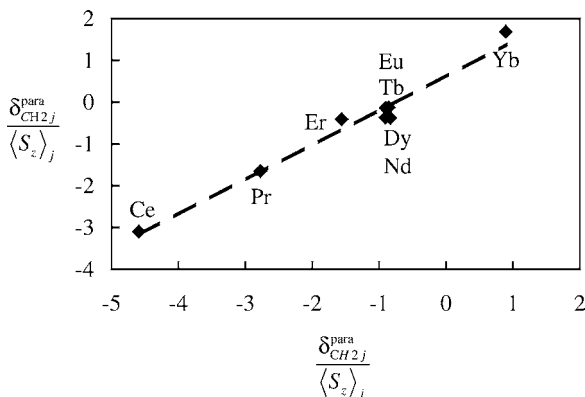


Fig. 10. Crystal-field independent plot of $\delta_{ij}^{para}/\langle S_z \rangle_j$ vs $\delta_{kj}^{para}/\langle S_z \rangle_j$ (eq. (51)) for the carbon (CH_2) and the protons (CH_2) of the methylene groups in $[R(L^1-2H)_3]^{3-}$ (D_2O , 346 K, drawn from data reported by Peters (1988)).

Although the B_q^k parameters obtained in the solid state are only indicative for those relevant in solution, their abrupt variations near the middle of the series is expected to produce a break in the linear plot $\delta_{ij}^{para}/\langle S_z \rangle_j$ vs $C_j/\langle S_z \rangle_j$ according to eq. (48) without resorting to a major structural change. To the best of our knowledge, no analysis of these data using the crystal-field independent two-nuclei technique (eq. (51)) has been reported, but plots of $\delta_{ij}^{para}/\langle S_z \rangle_j$ vs $\delta_{kj}^{para}/\langle S_z \rangle_j$ based on the data reported by Peters (1988) suggest the existence of a single straight line for $R = Ce$ – Yb compatible with an approximate isostructural series in solution (fig. 10). Since geometrical factors G_i calculated from the crystal structure of $Na_3[Ce(L^1-2H)_3] \cdot 2NaClO_4 \cdot 6H_2O$ closely match those found in solution for $R = Ce$ – Eu (Peters, 1988), we can tentatively infer that no major structural change indeed occurs in solution and the nine-coordinate D_3 -symmetrical structure found in the solid-state is a satisfying model for $[R(L^1-2H)_3]^{3-}$ along the complete lanthanide series in water. The abrupt break near the middle of the series originates from variations of the crystal-field parameters which parallel those evidenced in the solid-state.

3.1.2. $[R(L^2)_3]^{3+}$ ($L^2 = 2,6$ -bis(benzimidazole)pyridine)

The tridentate ligand L^2 possesses heterocyclic nitrogen donors exhibiting only a limited affinity for $R(III)$, and no complexation occurs in water. However, efficient coordination is restored in less competing solvents leading to the successive formation of $[R(L^2)_n]^{3+}$ ($n = 1, 2, 3$) in acetonitrile (Piguet et al., 1993). The two first successive stability constants K_n ($n = 1, 2$) show only minor variations along the lanthanide series, while K_3 increases with increasing atomic number, reaches a maximum around $R = Gd(III)$ and suddenly decreases, eventually producing poorly stable $[R(L^2)_3]^{3+}$ complexes for the smaller lanthanides (Petoud et al., 1997). This fascinating size-discriminating effect favouring the complexation of mid-range $R(III)$, results from the modulation of intramolecular interstrand interactions involving π – π stacking between aromatic benzimidazole groups in the D_3 -symmetrical $[R(L^2)_3]^{3+}$ complexes (fig. 11). For the large lanthanides ($R = La$ – Gd), attractive interstrand π -stacking stabilizes the final triple helical complexes, but further contraction of the ionic radii for $R = Tb$ – Lu induces considerable repulsive van der Waals interactions.

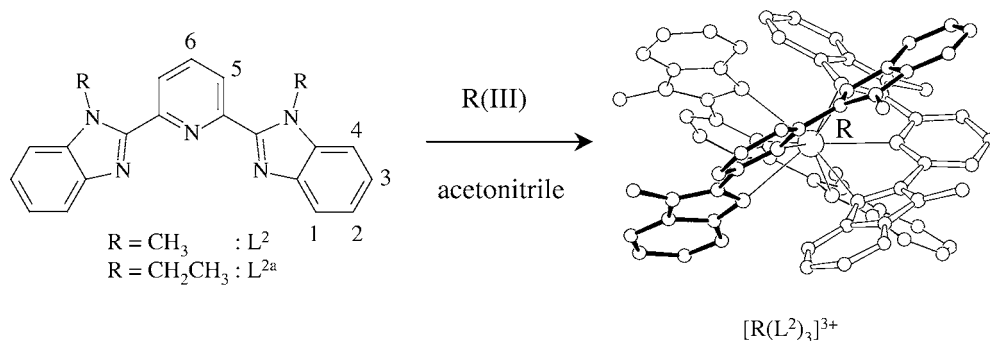


Fig. 11. Schematic formation of the D_3 -symmetrical complexes $[\text{R}(\text{L}^2)_3]^{3+}$ in acetonitrile with numbering scheme. The representation of $[\text{R}(\text{L}^2)_3]^{3+}$ corresponds to the crystal structure of $[\text{Eu}(\text{L}^2)_3](\text{ClO}_4)_3$ (Piguet et al., 1993).

For large concentrations of ligand compatible with NMR measurements ($\geq 0.015 \text{ mol} \cdot \text{dm}^{-3}$), the stability constants predict that $[\text{R}(\text{L}^2)_3]^{3+}$ are quantitatively formed ($> 98\%$) for $R = \text{Ce-Tb}$. For smaller lanthanides, partial decomplexation occurs as demonstrated by the appearance of small new peaks in the spectrum of $[\text{Dy}(\text{L}^2)_3]^{3+}$ (Petoud et al., 1997). Although NMR spectra show three sets of resolved signals corresponding to $[\text{Dy}(\text{L}^2)_3]^{3+}$, $[\text{Dy}(\text{L}^2)_2]^{3+}$ and L^2 under slow-exchange regime at 298 K, the authors have restricted their analysis to $R = \text{Ce-Dy}$. As inferred from the crystal structure of $[\text{Eu}(\text{L}^2)_2]^{3+}$, the ^1H and ^{13}C NMR data demonstrate that the threefold symmetry is maintained in solution. Moreover, the replacement of methyl groups in L^2 by ethyl groups in L^{2a} provides diastereotopic probes in $[\text{R}(\text{L}^{2a})_3]^{3+}$ which systematically display two separated signals for the methylene protons in complete agreement with the expected helical wrapping of the strands and an average D_3 point group symmetry in solution. Plots of $\delta_{ij}^{\text{para}} / \langle S_z \rangle_j$ vs $C_j / \langle S_z \rangle_j$ (eq. (48)) and $\delta_{ij}^{\text{para}} / C_j$ vs $\langle S_z \rangle_j / C_j$ (eq. (49)) for $[\text{R}(\text{L}^2)_3]^{3+}$ ($R = \text{Ce-Dy}$) give linear correlations arising from a single isostructural series (fig. 12). Multi-linear least-square fits of eq. (47) using $\langle S_z \rangle_j$ and C_j factors of table 3 provide contact F_i and pseudo-contact $B_0^2 G_i$ terms collected in table 4. The agreement factor AF_i for a nucleus i for an isostructural series of n different lanthanide complexes is given by eq. (57) (Wilcott et al., 1972)

$$AF_i = \sqrt{\frac{\sum_{j=1}^n (\delta_{ij}^{\text{obs}} - \delta_{ij}^{\text{calc}})^2}{\sum_{j=1}^n (\delta_{ij}^{\text{obs}})^2}} \quad (57)$$

The AF_i factors for $[\text{R}(\text{L}^2)_3]^{3+}$ ($R = \text{Ce-Dy}$) are satisfying except for C2 and C3 which undergo minor to negligible paramagnetic shifts (table 4). Interestingly, the sizeable F_i terms (i.e., hyperfine constants) observed for H1 and H5 suggest significant spin delocalisation for nuclei separated by four bonds from the paramagnetic centre, an effect ascribed to efficient delocalisation within heterocyclic N-donor ligands (Petoud et al., 1997). For H3 and C3, the pseudo-contact terms $B_0^2 G_i$ are only marginally different from zero in complete agreement with their location close to the magic angle $\theta_i = 54.7^\circ$ for which $G_i = 0$ ($\theta_{\text{C3}} = 57.8^\circ$ and

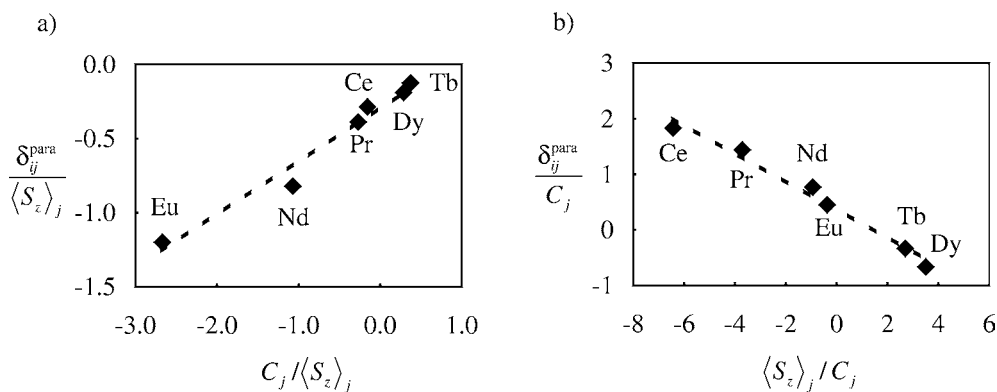


Fig. 12. Plots of (a) $\delta_{ij}^{\text{para}}/\langle S_z \rangle_j^2$ vs $C_j/\langle S_z \rangle_j^2$ (eq. (48)) and (b) $\delta_{ij}^{\text{para}}/C_j$ vs $\langle S_z \rangle_j/C_j$ (eq. (49)) for H5 in $[R(L^2)_3]^{3+}$ ($R = \text{Ce-Dy}$, CD_3CN , 298 K, drawn from data reported by Petoud et al. (1997)).

Table 4

Computed values for contact (F_i), pseudo-contact ($B_0^2 G_i$) terms and agreement factors (AF_i) for ^1H - and ^{13}C -nuclei in complexes $[R(L^2)_3]^{3+}$ ($R = \text{Ce-Dy}$, CD_3CN , 298 K, Petoud et al. (1997)). See fig. 11 for the atom-numbering scheme

	H1	H2	H3	H4	H5	H6	CH3
F_i	-0.41(12)	-0.05(2)	-0.006(5)	0.16(1)	0.42(6)	0.26(4)	0.14(3)
$B_0^2 G_i$	0.87(4)	0.094(7)	-0.008(2)	-0.111(3)	-0.30(2)	-0.22(1)	-0.25(1)
AF_i	0.04	0.06	0.05	0.06	0.10	0.08	0.05
	C1	C2	C3	C4	C5	C6	CH3
F_i	0.26(10)	-0.26(4)	0.07(3)	0.33(2)	3.38(19)	-0.93(14)	0.36(3)
$B_0^2 G_i$	0.25(3)	0.11(1)	0.002(9)	-0.124(7)	-0.46(6)	-0.30(5)	-0.28(1)
AF_i	0.08	0.25	0.25	0.12	0.07	0.06	0.06

$\theta_{\text{H3}} = 59^\circ$ in the crystal structure of $[\text{Eu}(\text{L}^2)_3]^{3+}$). Although no analysis of these data using the crystal-field independent two-nuclei technique (eq. (51)) has been reported, plots of $\delta_{ij}^{\text{para}}/\langle S_z \rangle_j^2$ vs $\delta_{kj}^{\text{para}}/\langle S_z \rangle_j^2$ based on the data reported by Petoud et al. (1997) suggest the existence of a single straight line for $R = \text{Ce-Dy}$, thus confirming isostructurality (fig. 13).

Finally, the anisotropic part of the axial magnetic susceptibility tensor $\chi_{zz}^j - (1/3) \text{Tr} \chi^j$ has been computed following the method of Kemple et al. (1988) applied to axial complexes for which the principal magnetic z axis corresponds to the molecular threefold axis. Equation (44) reduces to eq. (58) and multi-linear least-squares fits based on geometrical factors G_i obtained from the crystal structure of $[\text{Eu}(\text{L}^2)_3]^{3+}$ and using 13 paramagnetic shifts and eleven contact contributions (all carbons and five protons, 13×11 fits) give magnetic anisotropies $\chi_{zz}^j - (1/3) \text{Tr} \chi^j$ which display only qualitative agreement with Bleaney's factor C_j (Petoud et al., 1997). This poor correlation is not diagnostic for the rejection of Bleaney's approach, but it can be assigned to the very limited set of nuclei (H2 and H3) for which pure pseudo-contact contributions are observed and which are prominent for the calculation of the magnetic

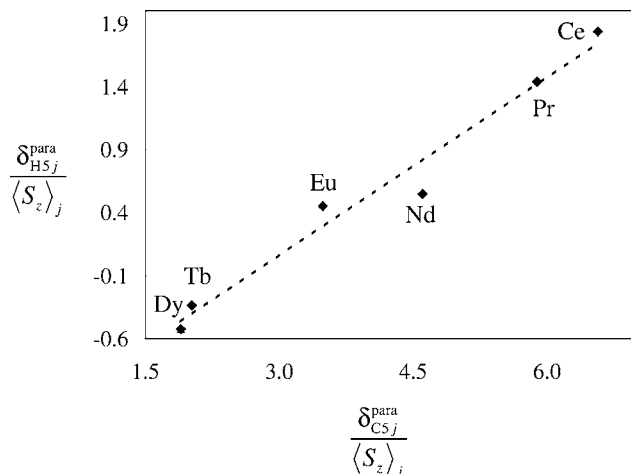


Fig. 13. Crystal-field independent plot of $\delta_{ij}^{para}/\langle S_z \rangle_j$ vs $\delta_{kj}^{para}/\langle S_z \rangle_j$ (eq. (51)) for the C5–H5 pair in $[R(L^2)_3]^{3+}$ ($R = \text{Ce–Dy}$, CD_3CN , 298 K, drawn from data reported by Petoud et al. (1997)).

anisotropy

$$\delta_{ij}^{para} = \delta_{ij}^c + \delta_{ij}^{pc} = \delta_{ij}^c + \frac{1}{2N_A} \left[\left(\chi_{zz}^j - \frac{1}{3} \text{Tr} \chi^j \right) G_i \right]. \quad (58)$$

The authors conclude that $[R(L^2)_3]^{3+}$ ($R = \text{Ce–Dy}$) are isostructural in solution and adopt a structure reminiscent to that found in the crystal structure of $[\text{Eu}(\text{L}^2)_3]^{3+}$. The aromatic backbone acts as an efficient relay for spin delocalisation and/or spin polarization which allows contact contributions to operate at long distances.

3.1.3. $[R(L^3)_3]^{3+}$ ($L^3 = 2,6\text{-pyridinedicarboxylic acid-bis-diethylamide}$)

The replacement of the two benzimidazole side arms of L^2 by two neutral carboxamide groups in L^3 provides a tridentate NO_2 chelate which exhibits significant affinity for $R(\text{III})$ in acetonitrile despite its increased flexibility (Renaud et al., 1997). The stability constants for the complexes $[R(L^3)_n]^{3+}$ ($R = \text{La–Lu}$, $n = 1, 2, 3$) are comparable to those found for light lanthanides with L^2 ($[R(L^2)_n]^{3+}$, $R = \text{La–Gd}$, $n = 1, 2, 3$), but K_3 for $[R(L^3)_3]^{3+}$ monotonously increases when going from Gd to Lu in agreement with the well-known electrostatic trend (Choppin, 1989). No specific size-discriminating effect is detected and the triple helical complexes $[R(L^2)_3]^{3+}$ are quantitatively formed ($\geq 98\%$) in acetonitrile for a total ligand concentration of $0.15 \text{ mol} \cdot \text{dm}^{-3}$ and $R/L^3 = 0.33$ (Renaud et al., 1997). The ^1H and ^{13}C NMR data imply the existence of three equivalent ligand strands on the NMR time scale and the separated ^1H NMR signal detected for the methylene protons of the ethyl groups of the carboxamide side arms ($R = \text{Y, Lu}$) points to the formation of D_3 -symmetrical complexes in solution reminiscent of the crystal structures obtained for $[R(L^3)_3]^{3+}$ ($R = \text{La, Eu}$, fig. 14).

Variable-temperature NMR measurements for $[R(L^3)_3]^{3+}$ ($R = \text{La, Sm, Y, Lu}$) in acetonitrile firmly establish dynamic interconversion between the D_3 -symmetrical helical enantiomers $P\text{-}[R(L^3)_3]^{3+} \rightleftharpoons M\text{-}[R(L^3)_3]^{3+}$. The coalescence temperature increases with de-

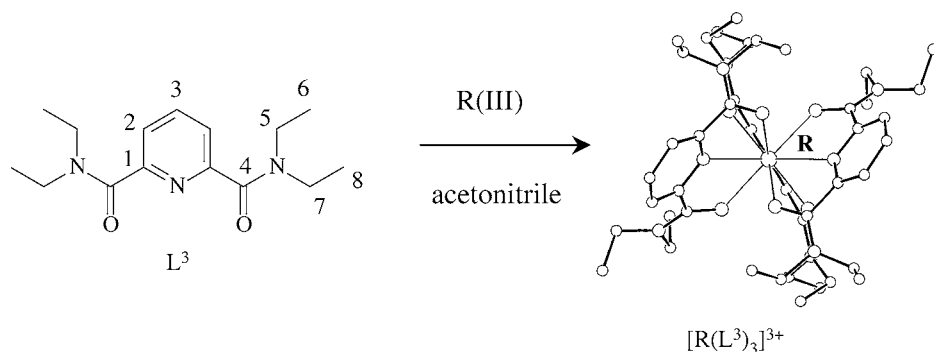


Fig. 14. Schematic formation of the D_3 -symmetrical complexes $[R(L^3)_3]^{3+}$ in acetonitrile with numbering scheme. The representation of $[R(L^3)_3]^{3+}$ corresponds to the crystal structure of $[Eu(L^3)_3](CF_3SO_3)_3(THF)_2$ (Renaud et al., 1997).

creasing ionic radii and the calculated free energies of activation at these temperatures follow the same trend $\Delta G^\ddagger(\text{Sm}, T = 263 \text{ K}) = 55 \text{ kJ/mol}$, $\Delta G^\ddagger(\text{Y}, T = 318 \text{ K}) = 73 \text{ kJ/mol}$ and $\Delta G^\ddagger(\text{Lu}, T = 333 \text{ K}) = 78 \text{ kJ/mol}$. For $R = \text{La}$, the coalescence temperature lies below 233 K and only a maximum activation energy can be estimated ($\Delta G^\ddagger(\text{La}) < 55 \text{ kJ/mol}$). Plots of $\delta_{ij}^{\text{para}}/\langle S_z \rangle_j$ vs $C_j/\langle S_z \rangle_j$ (eq. (48)) and $\delta_{ij}^{\text{para}}/C_j$ vs $\langle S_z \rangle_j/C_j$ (eq. (49)) for ^1H and ^{13}C NMR data of $[R(L^3)_3]^{3+}$ ($R = \text{Ce} - \text{Yb}$, except Pm, Gd, Dy, Ho) display an abrupt deviation from linearity between $R = \text{Tb}$ and $R = \text{Er}$ and require two different straight lines (fig. 15). Two different isostructural series are considered for $R = \text{Ce} - \text{Tb}$ and $\text{Er} - \text{Yb}$, and two sets of contact F_i and pseudo-contact $B_0^2 G_i$ terms are obtained according to least-squares fits of eq. (47) (table 5, Renaud et al. (1997)).

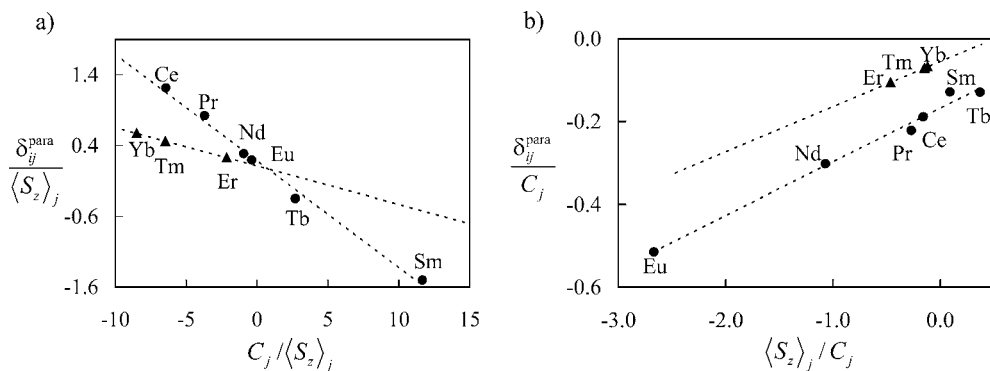


Fig. 15. Plots of (a) $\delta_{ij}^{\text{para}}/\langle S_z \rangle_j$ vs $C_j/\langle S_z \rangle_j$ (eq. (48)) and (b) $\delta_{ij}^{\text{para}}/C_j$ vs $\langle S_z \rangle_j/C_j$ (eq. (49)) for H_2 in $[R(L^3)_3]^{3+}$ ($R = \text{Ce} - \text{Yb}$, CD_3CN , 298 K, redrawn from Renaud et al. (1997)).

Table 5

Computed values for contact (F_i), pseudo-contact ($B_0^2 G_i$) terms and agreement factors (AF_i) for ^1H - and ^{13}C -nuclei in complexes $[\text{R}(\text{L}^3)_3]^{3+}$ ($R = \text{Ce} - \text{Yb}$, CD_3CN , 298 K, Renaud et al. (1997)). See fig. 14 for the atom-numbering scheme

Series $R = \text{Ce} - \text{Tb}$						
	H2	H3	H6	H8	C1	C2
F_i	0.129(4)	0.11(1)	0.023(7)	0.00(2)	0.25(9)	3.01(9)
$B_0^2 G_i$	-0.177(2)	-0.160(5)	-0.006(3)	0.118(6)	-0.53(4)	-0.40(3)
AF_i	0.01	0.04	0.49	0.05	0.07	0.04
	C3	C4	C5	C6	C7	C8
F_i	-1.02(3)	0.6(1)	0.31(5)	-0.07(3)	0.23(5)	-0.11(3)
$B_0^2 G_i$	-0.22(1)	0.16(5)	0.00(2)	0.064(9)	0.02(2)	0.06(1)
AF_i	0.02	0.11	0.13	0.20	0.16	0.31
Series $R = \text{Er} - \text{Yb}$						
	H2	H3	H6	H8	C1	C2
F_i	0.110(1)	0.14(1)	0.01(1)	-0.26(9)	0.9(4)	2.495(1)
$B_0^2 G_i$	-0.054(1)	-0.044(4)	-0.003(4)	-0.01(3)	-0.14(9)	-0.034(1)
AF_i	0.00	0.02	0.33	0.20	0.13	0.00
	C3	C4	C5	C6	C7	C8
F_i	-0.82(2)	1.1(4)	-0.21(2)	-0.267(4)	0.19(6)	0.30(4)
$B_0^2 G_i$	-0.072(1)	-0.4(1)	-0.045(4)	-0.014(1)	0.03(2)	0.09(1)
AF_i	0.01	0.08	0.06	0.01	0.24	0.13

The significant hyperfine constants (F_i terms) observed for the protons of the pyridine ring (H2 and H3) parallel those reported for $[\text{R}(\text{L}^2)_3]^{3+}$ and confirms efficient spin delocalisation onto the heterocyclic aromatic ring. Attempts to extract the axial magnetic anisotropies $\chi_{zz}^j - (1/3) \text{Tr} \chi^j$ with eq. (58) and using the crystal structure of $[\text{Eu}(\text{L}^3)_3]^{3+}$ as a model only fail because pure pseudo-contact contributions are limited to the two terminal methyl protons. Their versatile locations within each strand in the crystal structure of $[\text{Eu}(\text{L}^3)_3]^{3+}$ do not allow the calculation of reliable D_3 -average geometrical G_i factors. The crystal-field and structure-independent method (eq. (51)) has been applied for unambiguously demonstrating that a structural change occurs along the lanthanide series. Plots of $\delta_{ij}^{\text{para}} / \langle S_z \rangle_j$ vs $\delta_{kj}^{\text{para}} / \langle S_z \rangle_j$ indeed display systematic abrupt breaks between $R = \text{Tb}$ and Er leading to two different sets of structural terms $R_{ik} = G_i / G_k$ (fig. 16, Rigault et al. (2000a)). Comparison between R_{ik} terms observed in solution and those calculated from the crystal structure of $[\text{Eu}(\text{L}^3)_3]^{3+}$ shows only limited agreement (table 6), but quantitative statistical analyses suggest that the regular triple-helical arrangement of the strands observed in the solid state better fits the solution structure of the light lanthanides ($R = \text{Ce} - \text{Tb}$, Rigault et al. (2000a)). It was noticed that the dramatic discrepancies observed for pairs involving the C4 atom result from its location close to the magic angle ($\theta_{\text{C4}} = 54.9^\circ$ in the crystal structure of $[\text{Eu}(\text{L}^3)_3]^{3+}$). Since $G_{\text{C4}} \approx 0$, extreme sensitivity of $R_{\text{C4},k}$ terms for minor structural changes is expected. Finally, Renaud et al. (1997) have used relaxation measurements and eq. (18) to extract $R - \text{H}_i$ and $R - \text{C}_i$ distances which indeed slightly differ for $R = \text{Ce}$ and $R = \text{Yb}$. Renaud et al. (1997) and Rigault et al. (2000a) conclude that a structural change is firmly established for $[\text{R}(\text{L}^3)_3]^{3+}$ near the

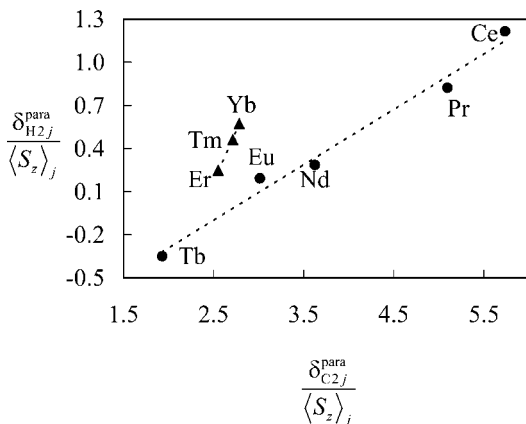


Fig. 16. Crystal-field independent plot of $\delta_{ij}^{\text{para}}/\langle S_z \rangle_j$ vs $\delta_{kj}^{\text{para}}/\langle S_z \rangle_j$ (eq. (51)) for the C2–H2 pair in $[R(L^3)_3]^{3+}$ ($R = \text{Ce–Yb}$, acetonitrile, 298 K, redrawn from Rigault et al. (2000a)).

Table 6

Minimal set of structural term $R_{ik} = G_i/G_k$ obtained from plots of $\delta_{ij}^{\text{para}}/\langle S_z \rangle_j$ vs $\delta_{kj}^{\text{para}}/\langle S_z \rangle_j$ according to eq. (51) for $[R(L^3)_3]^{3+}$ (CD_3CN , 298 K) (Rigault et al., 2000a).^a See fig. 14 for the atom-numbering scheme

	H2–H3	H2–C1	H2–C2	H2–C3	H2–C4
R_{ik} (Ce–Tb) ^b	0.93(5)	0.33(3)	0.39(3)	0.91(4)	–0.7(3)
R_{ik} (Er–Yb) ^c	1.02(9)	0.14(8)	1.38(6)	0.65(4)	0.08(2)
R_{ik} ($[\text{Eu}(L^3)_3]^{3+}$) ^d	1.018	0.213	0.499	0.591	16.321

^aA complete set of R_{ik} data can be generated according to $R_{ik} = R_{im} \cdot R_{mk}$.

^bValues for the first isostructural series (Sm has been removed because of its faint paramagnetism).

^cValues for the second isostructural series.

^dCalculated from the crystal structure of $[\text{Eu}(L^3)_3](\text{CF}_3\text{SO}_3)_3(\text{THF})_2$.

middle of the lanthanide series. Its assignment to specific variations of structural parameters in the triple-helical complexes has been delayed until a similar behaviour observed by Ouali et al. (2002) for $[\text{R}(L^7-2\text{H})_3]^{3-}$, could be ascribed to fast oscillations of the central pyridine ring occurring for large $R(\text{III})$ ions, $R = \text{Ce–Tb}$, a process which also affects $[\text{R}(L^3)_3]^{3+}$ (see sect. 3.1.7 and fig. 33).

3.1.4. $[\text{R}(L^4)]^{3+}$ and $[\text{R}(L^4+H)]^{4+}$ ($L^4 = \text{tris}\{2-[N\text{-methylcarbamoyl-}(6-(N,N\text{-diethylcarbamoyl})\text{pyridine-2ethyl})\text{amine}]\}$)

In order to limit flexibility, three tridentate binding units similar to L^3 have been connected to a covalent tri(2-aminoethyl)amine (TREN) tripod to give the nonadentate podand L^4 . Upon reaction with $R(\text{III})$ ($R = \text{La–Eu}$, Yb, Lu, Y) in acetonitrile/nitromethane (1:1), the NMR spectra confirm the formation of the expected C_3 -symmetrical complexes $[\text{R}(L^4)]^{3+}$ (Renaud et al., 1999). The methylene protons are systematically diastereotopic at 298 K. For the diamagnetic cations $R = \text{Y}$, Lu, no coalescence is observed in the accessible temperature range (233–343 K), but the rate of helical interconversion increases with increasing ionic radii and $[\text{La}(L^4)]^{3+}$ shows coalescence at 323 K, thus pointing to a fast $P\text{-}[\text{La}(L^4)]^{3+} \rightleftharpoons M\text{-}$

$[\text{La}(\text{L}^4)]^{3+}$ isomerisation process on the NMR time scale. Compared to the parent complexes $[\text{La}(\text{L}^3)]^{3+}$ which display enantiotopic methylene protons for $T > 233 \text{ K}$ (see sect. 3.1.3), the introduction of the covalent TREN tripod in $[\text{La}(\text{L}^4)]^{3+}$ significantly slows down the helical interconversion process. Protonation of the apical nitrogen atom produces the C_3 -symmetrical podates $[\text{R}(\text{L}^4+\text{H})]^{4+}$ which display only marginally faster racemisation processes. Although some steric constraints induced by the tripod limit the thermodynamic stability of the podates $[\text{R}(\text{L}^4)]^{3+}$ and $[\text{R}(\text{L}^4+\text{H})]^{4+}$, stability constants confirm their quantitative formation for a total ligand concentration of $0.05 \text{ mol} \cdot \text{dm}^{-3}$ and a stoichiometric ratio $R : \text{L}^4 = 1.0$ (Renaud et al., 1999; fig. 17).

Plots of $\delta_{ij}^{\text{para}} / \langle S_z \rangle_j$ vs $C_j / \langle S_z \rangle_j$ (eq. (48)) and $\delta_{ij}^{\text{para}} / C_j$ vs $\langle S_z \rangle_j / C_j$ (eq. (49)) for ^1H and ^{13}C NMR data of $[\text{R}(\text{L}^4)]^{3+}$ and $[\text{R}(\text{L}^4+\text{H})]^{4+}$ ($R = \text{Ce}, \text{Pr}, \text{Nd}, \text{Sm}, \text{Eu}, \text{Yb}$) show linear cor-

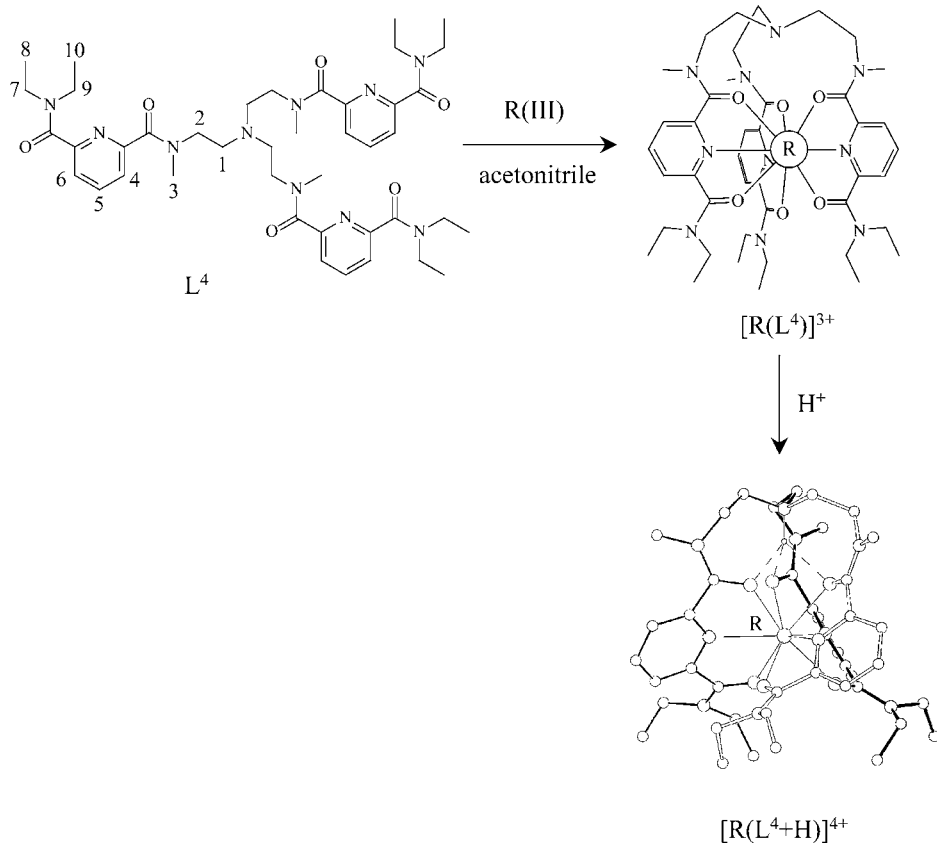


Fig. 17. Schematic formation of the C_3 -symmetrical podates $[\text{R}(\text{L}^4)]^{3+}$ and $[\text{R}(\text{L}^4+\text{H})]^{4+}$ in acetonitrile with numbering scheme. The representation of $[\text{R}(\text{L}^4+\text{H})]^{4+}$ corresponds to the crystal structure of $[\text{Eu}(\text{L}^4+\text{H})](\text{CF}_3\text{SO}_3)_3(\text{PF}_6)(\text{CH}_3\text{CN})_{0.5}$ (Renaud et al., 1999).

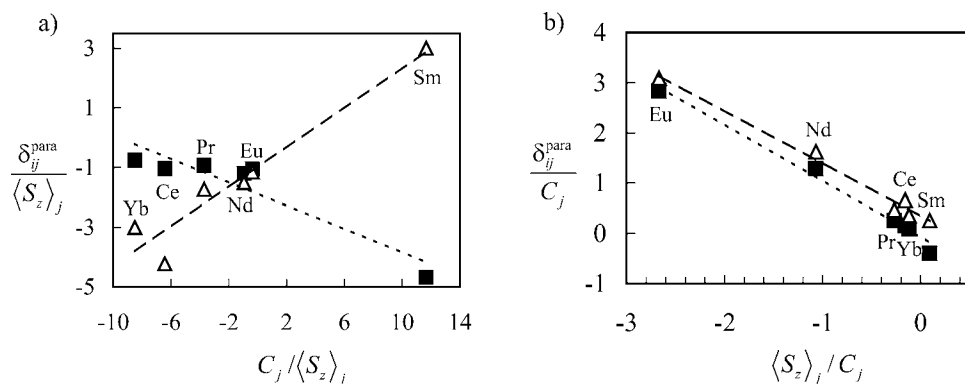


Fig. 18. Plots of (a) $\delta_{ij}^{\text{para}} / \langle S_z \rangle_j$ vs $C_j / \langle S_z \rangle_j$ (eq. (48)) and (b) $\delta_{ij}^{\text{para}} / C_j$ vs $\langle S_z \rangle_j / C_j$ (eq. (49)) for C5 in $[R(L^4)]^{3+}$ (■) and $[R(L^4+H)]^{4+}$ (△) ($R = \text{Ce-Eu, Yb, CD}_3\text{CN/CD}_3\text{NO}_2$ (1:1), 298 K, redrawn from Renaud et al. (1999)).

Table 7

Computed values for contact (F_i), pseudo-contact ($B_0^2 G_i$) terms and agreement factors (AF_i) for ^1H - and ^{13}C -nuclei in the podates $[R(L^4)]^{3+}$ and $[R(L^4+H)]^{4+}$ ($R = \text{Ce-Eu, Yb, CD}_3\text{CN/CD}_3\text{NO}_2$ (1:1), 298 K, Renaud et al. (1999)). See fig. 17 for the atom-numbering scheme

$[R(L^4)]^{3+}$							
	H3	H4	H5	H6	H8	H10	
F_i	0.04(1)	0.13(4)	0.10(4)	0.17(3)	0.01(1)	0.001(2)	
$B_0^2 G_i$	0.016(6)	-0.02(2)	-0.03(2)	0.01(1)	-0.002(3)	-0.004(7)	
AF_i	0.44	0.36	0.46	0.27	0.61	0.93	
	C1	C3	C4	C5	C6	C8	C10
F_i	0.09(8)	0.08(3)	3.4(4)	-1.1(4)	3.2(3)	-0.1(2)	-0.06(3)
$B_0^2 G_i$	0.11(4)	0.01(2)	0.2(2)	-0.04(2)	0.0(1)	0.002(7)	0.01(1)
AF_i	0.54	0.39	0.18	0.06	0.15	0.08	0.44
$[R(L^4+H)]^{4+}$							
	H3	H4	H5	H6	H8	H10	
F_i	-0.01(1)	0.08(7)	0.04(5)	0.1(4)	0.01(1)	0.03(6)	
$B_0^2 G_i$	-0.00(1)	0.20(4)	0.13(2)	0.10(2)	-0.024(4)	-0.2(3)	
AF_i	0.97	0.31	0.31	0.31	0.24	0.25	
	C1	C3	C4	C5	C6	C8	C10
F_i	0.2(2)	0.3(6)	2.8(2)	-1.1(1)	3.0(2)	-0.13(1)	-0.01(5)
$B_0^2 G_i$	-0.41(9)	-0.04(3)	0.4(1)	0.24(4)	0.28(9)	0.00(1)	-0.16(2)
AF_i	0.33	0.30	0.15	0.11	0.12	0.15	0.24

relations for all the paramagnetic lanthanides studied (fig. 18). The separation of the contact and pseudo-contact contributions according to eq. (47) for each nuclei in the two complexes show very similar contact F_i terms, but significantly different pseudo-contact $B_0^2 G_i$ terms which explains the different slopes obtained on fig. 18a (table 7). Calculation of geometrical

factors G_i from the crystal structure of $[\text{Eu}(\text{L}^4+\text{H})]^{4+}$ combined with a detailed analysis of the sign of the $B_0^2 G_i$ terms in the two complexes suggest that the position of $R(\text{III})$ is slightly shifted toward the lone pair of the apical nitrogen in $[\text{R}(\text{L}^4)]^{3+}$, while $R(\text{III})$ is moved away from the apical site upon protonation in $[\text{R}(\text{L}^4+\text{H})]^{4+}$. Although possible variations of B_0^2 have not been considered by the authors, the existence of a single isostructural series for $[\text{R}(\text{L}^4)]^{3+}$ and $[\text{R}(\text{L}^4+\text{H})]^{4+}$ strongly contrasts with the structural change assigned to the parent complexes $[\text{R}(\text{L}^3)]^{3+}$. This peculiar behaviour of the podates has been ascribed to the improved structural control imposed by the rigid tripod (Renaud et al., 1999). The limited available set of paramagnetic shifts collected for $[\text{R}(\text{L}^4)]^{3+}$ and $[\text{R}(\text{L}^4+\text{H})]^{4+}$ in the second part of the lanthanide series ($R = \text{Yb}$) prevents the application of the crystal-field independent technique (eq. (51)), but attempts to estimate magnetic anisotropies $\chi_{zz}^j - (1/3) \text{Tr} \chi^j$ with eq. (58) give only poorly reliable results because, among the available 13 LIS for protons and carbons, the contact contributions of only three carbons C1, C8 and C10 can be neglected.

3.1.5. $[\text{RM}(\text{L}^5)_3]^{5/6+}$ ($M = \text{Zn}, \text{Co}$; $\text{L}^5 = 2\{-[N,N\text{-diethylcarboxamido}]\text{-pyridin-2-yl}\}$ $-1,1'\text{-dimethyl-5,5'-methylene-2'-(5-methylpyridin-2-yl)bis(1H-benzimidazole)}$)

The use of unsymmetrical tridentate binding units for the complexation of nine-coordinate $R(\text{III})$ is strongly limited by the head-to-head-to-head (HHH) \leftrightarrow head-to-head-to-tail (HHT) isomerism resulting from the two different possible arrangements of the strands in $[\text{RL}_3]$ complexes. Covalent tripods are rarely used in this context because severe steric constraints often prevent the regular wrapping of the strands required for meridional tri-coordination (Renaud et al., 1999; Bretonnière et al., 2000; see sect. 3.1.4). Piguet et al. (1996) have taken advantage of the virtues of thermodynamic self-assembly for preparing pure d-f heterobimetallic complexes in which threefold symmetry (i.e., a strict HHH arrangement of the tridentate binding units) results from the use of a flexible non-covalent tripod. The segmental ligand L^5 has been designed for this purpose since it possesses a NN bidentate binding unit coded for the coordination of soft d-block ions and an unsymmetrical NNO tridentate binding unit coded for the coordination of 4f-block ions (Piguet et al., 2000). Upon stoichiometric mixing of L^5 (3 eq.) with $\text{Zn}(\text{II})$ (1 eq.) and $R(\text{III})$ (1 eq.) in acetonitrile, the C_3 -symmetrical triple-stranded helicates (HHH)- $[\text{RZn}(\text{L}^5)_3]^{5+}$ are quantitatively formed for total ligand concentrations larger than $10^{-4} \text{ mol} \cdot \text{dm}^{-3}$ (fig. 19). In these systems, the d-block ions is pseudo-octahedrally six-coordinated by the three bidentate binding unit, thus providing a non-covalent tripod which organizes the helical wrapping of the three tridentate chelates for their coordination to the pseudo-tricapped trigonal prismatic lanthanides.

When diamagnetic $\text{Zn}(\text{II})$ is introduced into the non-covalent tripod, $R(\text{III})$ is the only source of paramagnetism and the paramagnetic NMR data can be analyzed with the usual model-free methods. As a result of (i) the tight wrapping of the three ligand strands in (HHH)- $[\text{RZn}(\text{L}^5)_3]^{5+}$ and (ii) the strong metal–ligand interactions associated with multiple interactions (Prins et al., 2001; Swiegers and Malefetse, 2001), the dynamic interconversion between the helical enantiomers PP - $[\text{RZn}(\text{L}^5)_3]^{5+} \rightleftharpoons MM$ - $[\text{RZn}(\text{L}^5)_3]^{5+}$ is blocked on the NMR time scale in the temperature range accessible in acetonitrile (233–343 K). All methylene protons remain diastereotopic and the ^1H NMR spectra reflect the quantitative formation of

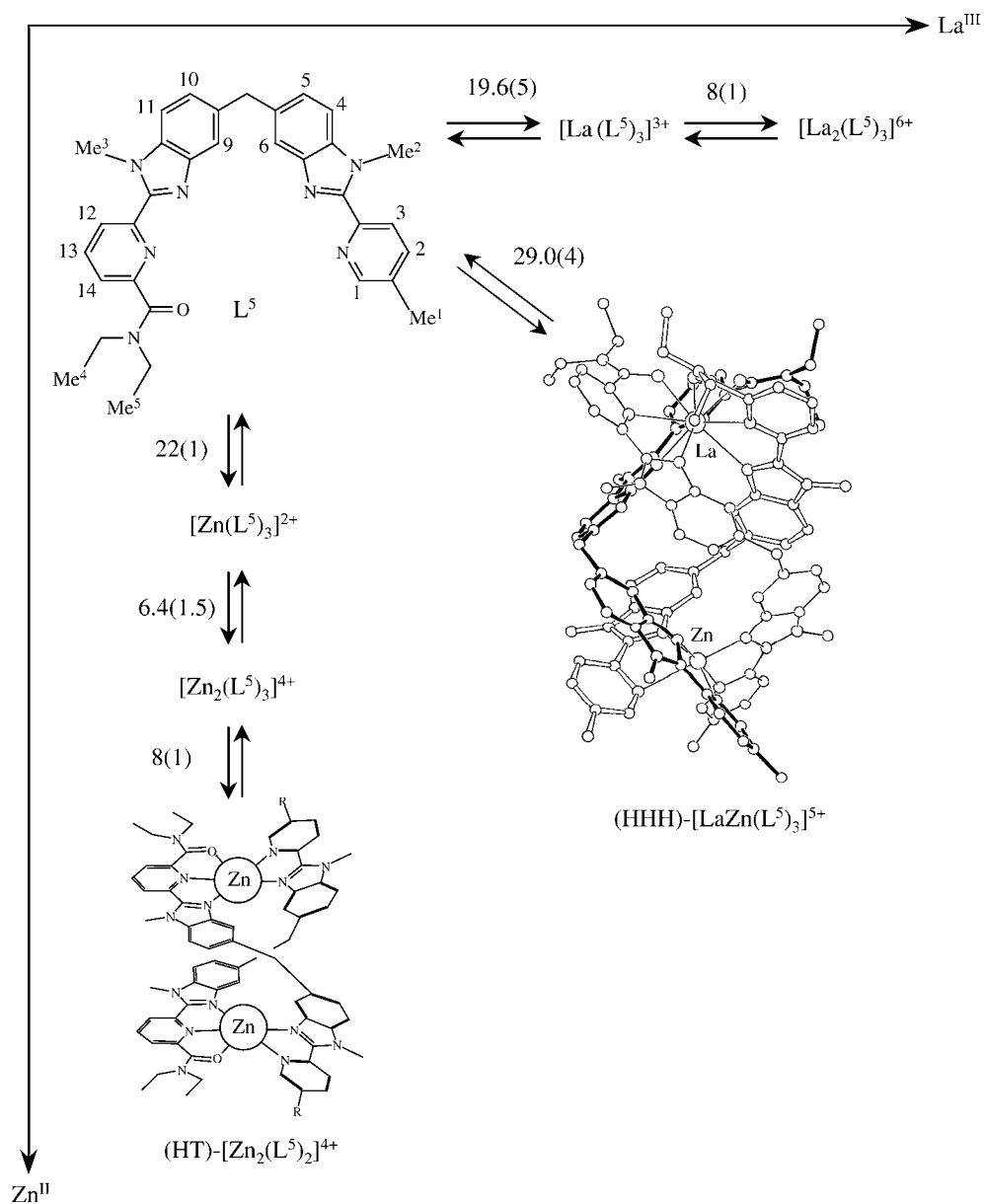


Fig. 19. Self-assembly of L^5 with La^{III} and Zn^{II} in acetonitrile. The stability constant for each defined equilibrium is given as $\log(K)$. The representation of $[LaZn(L^5)_3]^{5+}$ corresponds to the crystal structure of $[EuZn(L^5)_3](CF_3SO_3)_3(ClO_4)(CH_3CN)_4$ (Piguet et al., 1996).

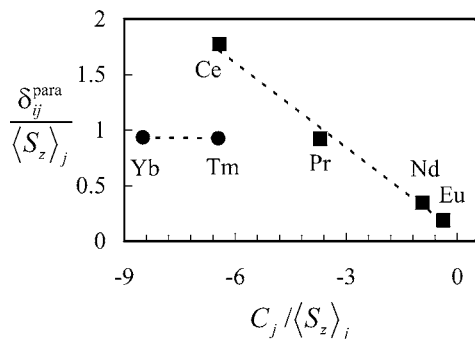


Fig. 20. Plots of $\delta_{ij}^{para} / \langle S_z \rangle_j$ vs $C_j / \langle S_z \rangle_j$ (eq. (48)) for H13 in $[RZn(L^5)_3]^{5+}$ ($R = Ce, Pr, Nd, Eu, Tm, Yb$, 298 K, drawn from data reported by Piguet et al. (1996)).

Table 8

Computed values for contact (F_i), pseudo-contact ($B_0^2 G_i$) terms and agreement factors (AF_i) for 1H -nuclei in the complexes $[RZn(L^5)_3]^{5+}$ ($R = Ce, Pr, Nd, Eu, Tm, Yb, CD_3CN$, 298 K, Piguet et al. (1996)). See fig. 19 for the atom-numbering scheme

	Bidentate binding unit										
	Me1	Me2	H1	H2	H3	H4	H5	H6			
F_i	-0.015	-0.018	-0.029	-0.020	-0.024	-0.029	-0.022	-0.105			
$B_0^2 G_i$	0.037	0.055	0.067	0.038	0.061	0.051	0.030	0.0304			
AF_i	0.13	0.13	0.12	0.10	0.11	0.09	0.08	0.14			
	Tridentate binding unit										
	Me3	H9	H10	H11	H12	H13	H14	H17	H18	H19	H20
F_i	0.060	-0.248	-0.03	0.143	0.335	0.178	0.337	0.144	-0.003	-0.039	-0.255
$B_0^2 G_i$	-0.202	0.903	0.017	-0.078	-0.250	-0.207	-0.242	-0.118	-0.030	0.057	0.737
AF_i	0.17	0.15	0.27	0.09	0.11	0.09	0.10	0.10	0.14	0.11	0.14

the C_3 -symmetrical complexes $[RZn(L^5)_3]^{5+}$ ($R = La, Ce, Pr, Nd, Sm, Eu, Tm, Yb, Lu$) in solution (Piguet et al., 1996). Although plots of $\delta_{ij}^{para} / \langle S_z \rangle_j$ vs $C_j / \langle S_z \rangle_j$ (eq. (48)) and δ_{ij}^{para} / C_j vs $\langle S_z \rangle_j / C_j$ (eq. (49)) for 1H NMR data suggest that $R = Tm, Yb$ do not belong to the straight line found for $R = Ce-Eu$ (fig. 20), multi-linear least-squares fits of eq. (47) considering a single isostructural series ($R = Ce-Yb$) have been applied for the separation of contact and pseudo-contact contributions (F_i and $B_0^2 G_i$ terms are collected in table 8).

It is thus not surprising that only poor agreement factors AF_i are obtained, but the triple-stranded helical complex possesses enough protons with negligible contact contributions to allow reliable calculations of the magnetic anisotropies $\chi_{zz}^j - (1/3) \text{Tr} \chi^j$ for each studied lanthanide (eq. (58)). Among twelve available aromatic protons, six are connected to the bidentate binding unit and exhibit no contact contribution. Multi-linear 12×6 fits using the geometrical factors G_i obtained from the crystal structure of $[EuZn(L^5)_3]^{5+}$ give $\chi_{zz}^j - (1/3) \text{Tr} \chi^j$ values for $R = Ce, Pr, Nd, Eu, Tm, Yb$ which are in qualitative good agreement with Bleaney's C_j factors (Piguet et al., 1996). It was concluded that (i) the crystal structure of $[EuZn(L^5)_3]^{5+}$ is a satisfying structural model for the complete lanthanide series and (ii) helication of the strands and coordination to d-block ions ensures a rigid and well-defined coordination site for

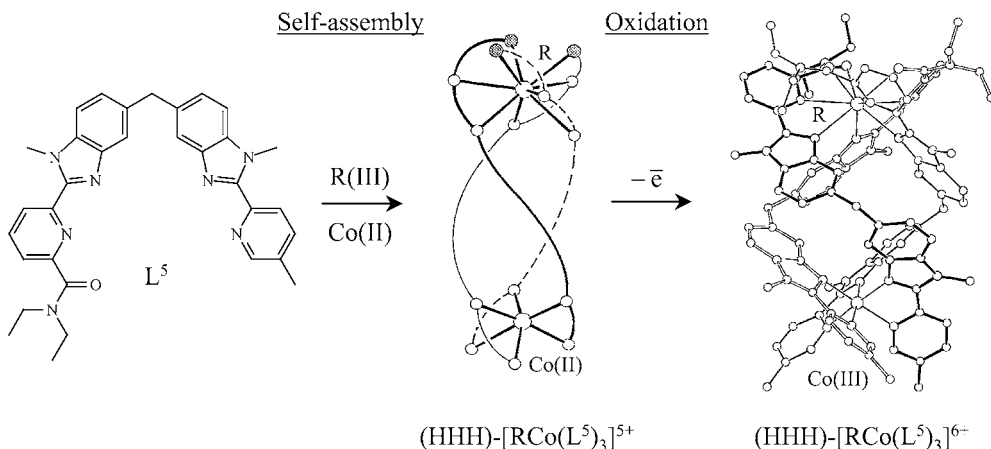


Fig. 21. Self-assembly of $(\text{HHH})\text{-}[\text{RCo}^{\text{II}}(\text{L}^5)_3]^{5+}$ followed by oxidation (post-modification) to give $(\text{HHH})\text{-}[\text{RCo}^{\text{III}}(\text{L}^5)_3]^{6+}$. The representation of $[\text{RCo}(\text{L}^5)_3]^{6+}$ corresponds to the crystal structure of $[\text{LaCo}(\text{L}^5)_3](\text{ClO}_4)_{5.5}(\text{OH})_{0.5}(\text{CH}_3\text{CN})_4(\text{H}_2\text{O})_2$ (adapted from Rigault et al. (1998)).

$R(\text{III})$. The latter point has been exploited for investigating possible variations of crystal-field parameters within isostructural series of rigid complexes. In order to design highly rigid helicates programmed for displaying a single isostructural series in solution, the kinetically inert diamagnetic $\text{Co}(\text{III})$ (d^6 low spin) has been introduced into the non-covalent tripod by using a self-assembly process with oxidative post-modification (Rigault et al., 1998; fig. 21).

No decomplexation occurs in acetonitrile ($10^{-1}\text{--}10^{-5}$ mol \cdot dm $^{-3}$) and the almost identical crystal structures obtained for lanthanide ions of extreme sizes $(\text{HHH})\text{-}[\text{RCo}(\text{L}^5)_3]^{6+}$ ($R = \text{La}, \text{Lu}$) strongly suggest that the considerable rigidity of the wrapped ligand strands minimizes structural variations associated with the lanthanide contraction (fig. 22, Rigault et al. (2000b)).

The ^1H NMR spectra of $(\text{HHH})\text{-}[\text{RCo}(\text{L}^5)_3]^{6+}$ ($R = \text{La}\text{--}\text{Lu}$, except Pm, Gd) confirm the quantitative formation of rigid C_3 -symmetrical complexes displaying systematic diastereotopic methylene protons between 233–343 K in acetonitrile. Field-dependent T_1 and T_2 relaxation measurements for $(\text{HHH})\text{-}[\text{RCo}(\text{L}^5)_3]^{6+}$ ($R = \text{Tb}, \text{Tm}$) fitted with eq. (15) (fig. 23a) and eq. (16) (fig. 23b) respectively give $R\text{--}H_i$ distances very close to those found in the solid state in agreement with negligible structural changes occurring along the lanthanide series in solution (Rigault et al., 2000b).

Magnetic anisotropies $\chi_{zz}^j - (1/3) \text{Tr} \chi^j$ for $R = \text{Ce}\text{--}\text{Yb}$ except Pm, Gd ($0.002 \leq AF_j \leq 0.06$, table 9) have been computed with eq. (58) and using five contact contributions δ_{ij}^c ($i = \text{H9}, \text{H11}\text{--}\text{H14}$) and the geometrical G_i factors obtained from the crystal structures of $(\text{HHH})\text{-}[\text{RCo}(\text{L}^5)_3]^{6+}$ ($R = \text{La}, \text{Lu}$). A qualitative good agreement ($AF = 0.23$) is obtained between the experimental magnetic anisotropies (scaled to -100 for $\text{Dy}(\text{III})$ and corrected for the variation of the crystal-field parameter near the middle of the series (*vide supra*, table 9) and Bleaney's factors (table 3). Further non-linear least-squares refinements of the molecular

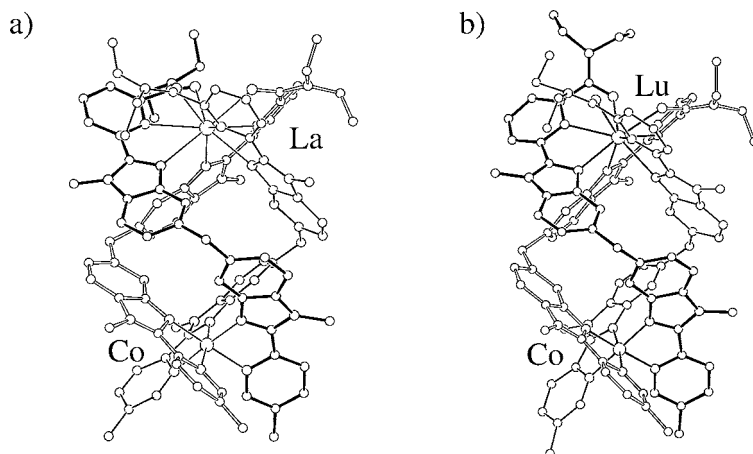


Fig. 22. Perspective views of (a) (HHH)-[LaCo^{III}(L⁵)₃]⁶⁺ and (b) (HHH)-[LuCo^{III}(L⁵)₃]⁶⁺ perpendicular to the pseudo-C₃ axis in the crystal structures of [LaCo(L⁵)₃](ClO₄)_{5.5}(OH)_{0.5}(CH₃CN)₄(H₂O)₂ and [LuCo(L⁵)₃](CF₃SO₃)₆(H₂O)(CH₃CN)₂ (adapted from Rigault et al. (2000b)).

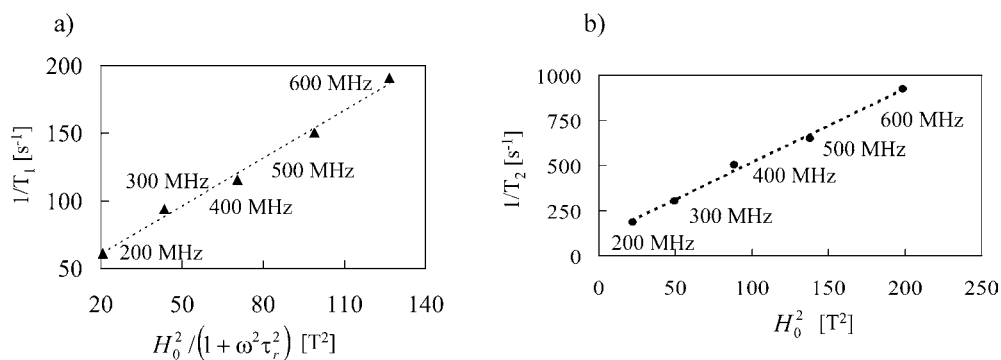


Fig. 23. Plot of (a) $1/T_{1i}^{\text{para}}$ vs $(H_0^2/(1 + \omega^2\tau_r^2))$ (eq. (15)) and $1/T_{2i}^{\text{para}}$ vs H_0^2 (eq. (16)) for H12 in (HHH)-[TbCo^{III}(L⁵)₃]⁶⁺ (acetonitrile, 298 K, redrawn from Rigault et al. (2000b)).

structure using the crystal structure of (HHH)-[LuCo(L⁵)₃]⁶⁺ as the initial model and simultaneously varying the axial coordinates θ_i and r_i and $\chi_{zz}^j - (1/3) \text{Tr} \chi^j$ (the contact contribution for H9, H11–H14 are fixed and calculated from the F_i terms of table 10: $\delta_{ij}^c = F_i \langle S_z \rangle_j$) show only minor changes for minimizing the square of the error between calculated and experimental pseudo-contact shifts. However, the final agreement of the computed magnetic anisotropies (corrected for the variation of the crystal-field parameter) and Bleaney's factors slightly improves ($AF = 0.20$). Rigault et al. (2000b) conclude that no significant structural change

Table 9
Axial magnetic anisotropies for $(\text{HHH})\text{-}[\text{RCo}^n(\text{L}^5)_3]^{(3+n)+}$ ($n = 2, 3$) in acetonitrile (Rigault et al., 2000b)^a

	$(\text{HHH})\text{-}[\text{RCo}^{\text{III}}(\text{L}^5)_3]^{6+}$		$(\text{HHH})\text{-}[\text{RCo}^{\text{II}}(\text{L}^5)_3]^{5+}$	
	$\chi_{zz}^j - (1/3) \text{Tr } \chi^j / \text{ppm} \cdot \text{\AA}^3$	Scaled C_j ^b	$\chi_{zz}^j - (1/3) \text{Tr } \chi^j / \text{ppm} \cdot \text{\AA}^3$	Scaled C_j ^b
Ce	413(10)	-5.2(1)	597(185)	-6(2)
Pr	666(13)	-8.0(2)	866(196)	-10(2)
Nd	300(8)	-3.8(1)	501(131)	-5.5(1.4)
Eu	-342(9)	4.3(1)	-532(169)	6(2)
Tb	4518(92)	-91(2)	5330(126)	-94(3)
Dy	4941(150)	-100(3)	5668(189)	-100(3)
Ho	2660(44)	-53(1)	3258(143)	-57(3)
Er	-562(18)	11.4(4)	-664(113)	12(2)
Tm	-1614(44)	32.7(9)	-2107(54)	37(1)
Yb	-651(19)	13.2(4)	-764(81)	13(2)

^aValues corrected for crystal-field effects.

^bRatios relative to $C_{\text{Dy}} = -100$.

occurs along the lanthanide series and that both crystal structures $((\text{HHH})\text{-}[\text{RCo}(\text{L}^5)_3]^{6+}$, $R = \text{La, Lu}$) are satisfying structural models.

The analyses of the ¹H-NMR data with the crystal-field independent technique (eq. (51)) display straight lines for plots of $\delta_{ij}^{\text{para}} / \langle S_z \rangle_j$ vs $\delta_{kj}^{\text{para}} / \langle S_z \rangle_j$ in complete agreement with isostructurality along the complete lanthanide series and no significant change of the G_i factors (fig. 24).

Plots of $\delta_{ij}^{\text{para}} / \langle S_z \rangle_j$ vs $C_j / \langle S_z \rangle_j$ (eq. (48)) and $\delta_{ij}^{\text{para}} / C_j$ vs $\langle S_z \rangle_j / C_j$ (eq. (49)) using crystal-field dependent techniques show systematic abrupt breaks near the middle of the lanthanide series (between $R = \text{Eu}$ and $R = \text{Tb}$) which imply a concomitant change of the contact F_i and pseudo-contact $B_0^2 G_i$ terms (table 10, fig. 25). Since G_i is essentially invariant, an abrupt variation of the crystal-field parameter B_0^2 is required to rationalize the NMR data.

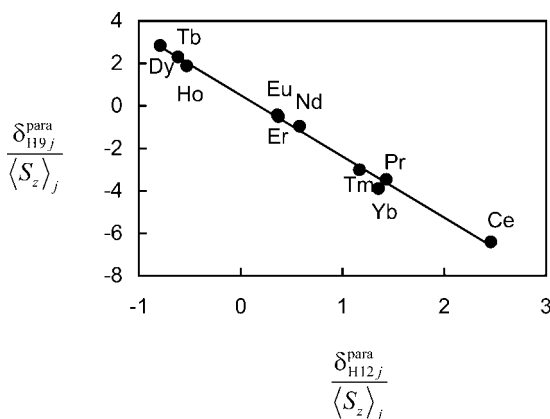


Fig. 24. Crystal-field independent plot of $\delta_{ij}^{\text{para}} / \langle S_z \rangle_j$ vs $\delta_{kj}^{\text{para}} / \langle S_z \rangle_j$ (eq. (51)) for the H9-H12 pair in $(\text{HHH})\text{-}[\text{RCo}^{\text{III}}(\text{L}^5)_3]^{6+}$ ($R = \text{Ce-Yb}$, acetonitrile, 298 K, redrawn from Rigault and Piguet (2000)).

Table 10

Computed values for contact (F_i), pseudo-contact ($B_0^2 G_i$) terms for ^1H nuclei in the complexes (HHH)- $[\text{RCo}^{\text{III}}(\text{L}^5)_3]^{6+}$ and (HHH)- $[\text{RCo}^{\text{II}}(\text{L}^5)_3]^{5+}$ ($R = \text{Ce-Eu}$ and $R = \text{Tb-Yb}$, CD_3CN , 298 K, Rigault et al. (2000b)).

See fig. 19 for the atom-numbering scheme

		Bidentate binding unit								
Compd		Me1	Me2	H1	H2	H3	H4	H5	H6	
$[\text{RCo}^{\text{III}}(\text{L}^5)_3]^{6+}$	F_i	-0.01(1)	-0.01(1)	-0.01(1)	-0.01(1)	-0.01(1)	-0.01(1)	-0.01(1)	-0.05(1)	
$R = \text{Ce-Eu}$	$B_0^2 G_i$	0.035(3)	0.060(3)	0.071(3)	0.038(1)	0.058(2)	0.068(1)	0.060(1)	0.29(1)	
$[\text{RCo}^{\text{III}}(\text{L}^5)_3]^{6+}$	F_i	0.03(1)	0.05(1)	0.06(1)	0.03(1)	0.05(1)	0.05(1)	0.04(1)	0.22(2)	
$R = \text{Tb-Yb}$	$B_0^2 G_i$	0.021(1)	0.038(1)	0.045(5)	0.024(1)	0.036(1)	0.046(1)	0.043(3)	0.177(1)	
$[\text{RCo}^{\text{II}}(\text{L}^5)_3]^{5+}$	F_i	0.07(2)	-0.01(1)	0(0)	0.01(1)	0.07(5)	0.02(2)	-0.02(1)	-0.15(7)	
$R = \text{Ce-Eu}$	$B_0^2 G_i$	0.08(2)	0.027(6)	0(0)	0.022(5)	-0.10(4)	0.01(2)	0.058(6)	0.48(6)	
$[\text{RCo}^{\text{II}}(\text{L}^5)_3]^{5+}$	F_i	0.03(1)	0.03(1)	0.05(1)	0.026(5)	-0.01(2)	0.02(1)	0.04(1)	0.30(5)	
$R = \text{Tb-Yb}$	$B_0^2 G_i$	0.026(3)	0.044(2)	0.050(3)	0.030(2)	0.053(6)	0.051(3)	0.037(2)	0.20(2)	
		Tridentate binding unit								
Compd		H9	H10	H11	H12	H13	H14	Me3	Me4	Me5
$[\text{RCo}^{\text{III}}(\text{L}^5)_3]^{6+}$	F_i	-0.07(3)	-0.01(1)	0.12(1)	0.24(1)	0.09(2)	0.17(1)	0.00(1)	-0.02(2)	0.00(2)
$R = \text{Ce-Eu}$	$B_0^2 G_i$	0.93(3)	0.067(4)	-0.019(6)	-0.33(1)	-0.23(1)	-0.15(1)	-0.149(2)	0.33(2)	-0.09(2)
$[\text{RCo}^{\text{III}}(\text{L}^5)_3]^{6+}$	F_i	0.79(4)	0.06(1)	0.09(1)	-0.11(3)	0.06(2)	-0.02(3)	-0.16(1)	0.29(3)	-0.04(2)
$R = \text{Tb-Yb}$	$B_0^2 G_i$	0.58(1)	0.038(2)	-0.007(3)	-0.20(1)	-0.132(8)	-0.097(9)	-0.096(5)	0.20(1)	-0.041(7)
$[\text{RCo}^{\text{II}}(\text{L}^5)_3]^{5+}$	F_i	-0.11(5)	-0.03(1)	0.10(1)	0.24(2)	0.09(2)	0.17(1)	-0.06(2)	0.02(2)	-0.06(3)
$R = \text{Ce-Eu}$	$B_0^2 G_i$	0.94(4)	0.080(7)	0.001(6)	-0.35(1)	-0.24(2)	-0.16(1)	-0.16(1)	-0.11(2)	0.38(3)
$[\text{RCo}^{\text{II}}(\text{L}^5)_3]^{5+}$	F_i	0.76(7)	0.05(1)	0.10(1)	0.02(1)	0.08(3)	0.06(3)	-0.16(2)	-0.06(2)	0.31(4)
$R = \text{Tb-Yb}$	$B_0^2 G_i$	0.64(2)	0.041(2)	-0.001(2)	-0.276(5)	-0.20(1)	-0.133(9)	-0.109(6)	-0.038(6)	0.24(1)

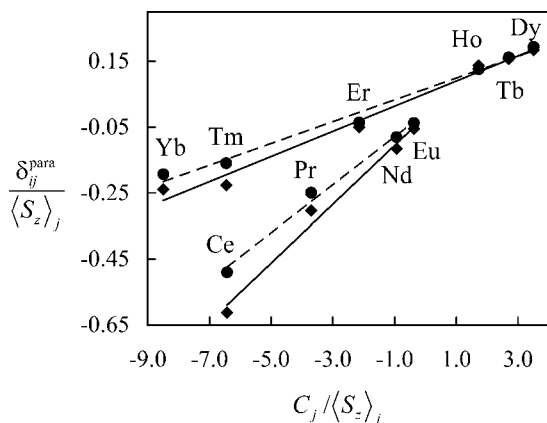


Fig. 25. Plots of $\delta_{ij}^{\text{para}}/\langle S_z \rangle_j$ vs $C_j/\langle S_z \rangle_j$ (eq. (48)) for H10 in (HHH)- $[\text{RCo}^{\text{III}}(\text{L}^5)_3]^{6+}$ (●) and (HHH)- $[\text{RCo}^{\text{II}}(\text{L}^5)_3]^{5+}$ (◆) ($R = \text{Ce-Yb}$, acetonitrile, 298 K, redrawn from Rigault et al. (2000b)).

A plot of $B_0^2 G_i (R = \text{Ce-Eu})$ vs $B_0^2 G_i (R = \text{Tb-Yb})$ gives a straight line whose slope corresponds to the ratio of the crystal-field parameters

$$\frac{B_0^2 (R = \text{Ce-Eu})}{B_0^2 (R = \text{Tb-Yb})} = 1.6(2)$$

(Rigault and Piguet, 2000). The decrease of B_0^2 with the lanthanide contraction matches the expected reduced interaction between metal-centred 4f and ligand donor orbitals. The observation of an abrupt change in the crystal-field parameters near the middle of the lanthanide series, sometimes referred to as the ‘gadolinium break’ is reminiscent of related changes established for B_q^k in crystals of $\text{Na}_3[\text{R}(\text{L}^{1-2\text{H}})_3] \cdot 2\text{NaClO}_4 \cdot 6\text{H}_2\text{O}$ (Hopkins et al., 1998; Görrler-Walrand and Binnemans, 1996; Rigault and Piguet, 2000; fig. 9). For six-rank parameters ($k = 6$), the remarkable discontinuity between the first and second half of the lanthanide series is an indication for the need to include two-electron operators in the crystal-field Hamiltonian (Judd, 1979), but its origin remains obscure for second-rank parameters (Görrler-Walrand and Binnemans, 1996; Rigault and Piguet, 2000). It is difficult to simply assign this abrupt variation of the B_0^2 parameters to deviation from Bleaney’s approach, because the experimental magnetic anisotropies determined for $(\text{HHH})\text{-}[\text{RCo}(\text{L}^5)_3]^{6+}$ satisfyingly match the C_j factors, a strong support for limiting the T^{-n} series to the second-order term. Surprisingly, the concomitant change of the contact term F_i observed according to eqs. (48), (49) (table 10) has negligible effects on the intercept $F_i - F_k R_{ik}$ of linear plots obtained according to eq. (51) (fig. 24). Specific compensation effects have been demonstrated for $(\text{HHH})\text{-}[\text{RCo}(\text{L}^5)_3]^{6+}$ (Rigault et al., 2000b), but variations of F_i terms are expected to produce two parallel straight lines for $\delta_{ij}^{\text{para}}/\langle S_z \rangle_j$ vs $\delta_{kj}^{\text{para}}/\langle S_z \rangle_j$ as demonstrated for the cryptate $[\text{R}(\text{L}^6)]^{3+}$ (see sect. 3.1.6, Platas et al. (1999)).

Reduction of Co(III) into Co(II) provides a second fast-relaxing paramagnetic centre (Co(II), d^7 high spin, $S = 3/2$) within the triple-stranded helicates $(\text{HHH})\text{-}[\text{RCo}(\text{L}^5)_3]^{5+}$ and this strongly affects the ^1H -NMR spectra. Since no intermetallic R-Co(II) magnetic coupling can be detected at 298 K, the paramagnetic shifts induced by the two metallic centres are additive and eq. (59) holds if no major structural change occurs between $(\text{HHH})\text{-}[\text{RCo}^{\text{II}}(\text{L}^5)_3]^{5+}$ and $(\text{HHH})\text{-}[\text{RCo}^{\text{III}}(\text{L}^5)_3]^{6+}$ (Rigault et al., 2000b)

$$\delta_{ij}^{\text{para}}(\text{RCo(II)}) = \delta_i^{\text{para}}(\text{LaCo(II)}) + \delta_{ij}^{\text{para}}(\text{RCo(III)}). \quad (59)$$

Satisfying predictions for the NMR spectra of $(\text{HHH})\text{-}[\text{RCo}^{\text{II}}(\text{L}^5)_3]^{5+}$ are obtained which allow the complete assignment of the ^1H NMR signals in strongly paramagnetic lanthanide-containing complexes. Detailed model-free analyses (eqs. (48), (49), (51)) using the complex $(\text{HHH})\text{-}[\text{LaCo}^{\text{II}}(\text{L}^5)_3]^{5+}$ as the ‘diamagnetic’ reference (eq. (3)), evidence very similar structural properties for $(\text{HHH})\text{-}[\text{RCo}^{\text{II}}(\text{L}^5)_3]^{5+}$ and $(\text{HHH})\text{-}[\text{RCo}^{\text{III}}(\text{L}^5)_3]^{6+}$ despite the relative 36% increase of the ionic radius when going from Co(III) (d^6 low spin) to Co(II) (d^7 high spin, Shannon (1976)). As far as paramagnetic lanthanide induced shifts are concerned, a closely related concomitant abrupt change of the hyperfine constants (via F_i) and of the crystal-field parameter

$$\frac{B_0^2(R = \text{Ce–Eu})}{B_0^2(R = \text{Tb–Yb})} = 1.6(3)$$

is observed for $(\text{HHH})\text{-}[\text{RCo}^{\text{II}}(\text{L}^5)_3]^{5+}$ (table 10, fig. 25), together with comparable magnetic anisotropies (table 9). Rigault et al. (2000b) conclude that the triple-stranded helicates are rigid enough to maintain very similar solution structures when the size of the f- and d-block

ions is varied within an acceptable range. However, the one-nucleus crystal-field dependent methods (eqs. (48), (49)) cannot be used for detecting structural changes because of unpredictable abrupt variations of the crystal-field parameter along the lanthanide series. The two-nuclei crystal-field independent technique (eq. (51)) should be preferred and systematically applied when using model-free analyses.

3.1.6. $[R(L^6)]^{3+}$ ($L^6 = azacryptand$, see fig. 26)

The capping of both termini of three tridentate chelating units with covalent tripods provides highly rigid macrobicyclic receptors (i.e., cryptands), which are ideally suited for investigating variations of crystal-field parameters within isostructural series. Platas et al. (1999) have iso-

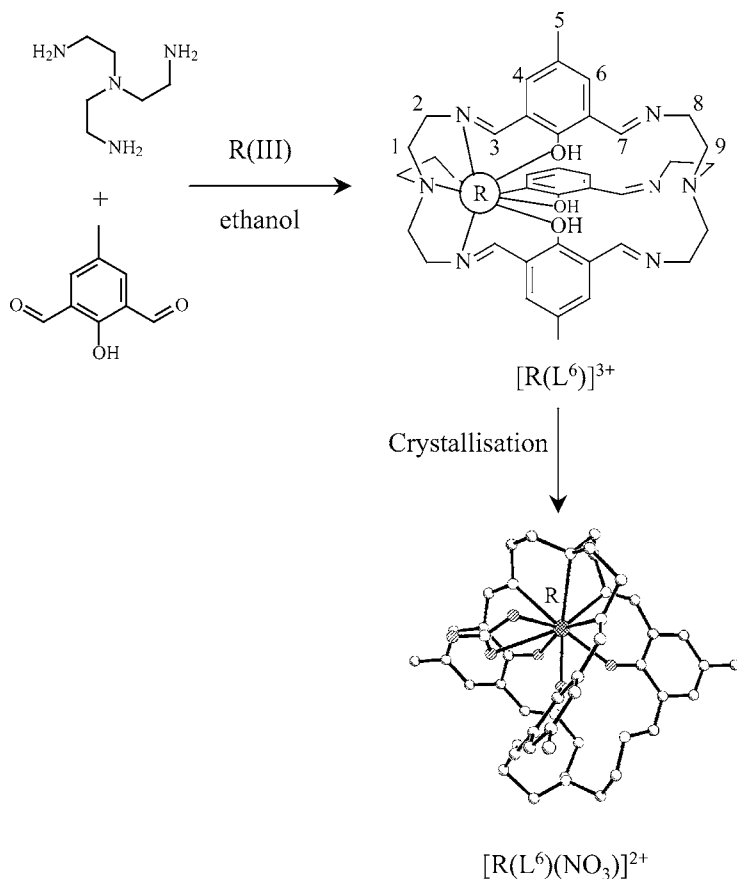


Fig. 26. Template formation of the C_3 -symmetrical cryptates $[R(L^6)]^{3+}$ in water with numbering scheme. The representation of $[R(L^6)(NO_3)]^{2+}$ corresponds to the crystal structure of $[Eu(L^6)(NO_3)](NO_3)_2(H_2O)_4$ (Platas et al., 1999).

lated the monometallic cryptates $[R(L^6)(NO_3)](NO_3)_2$ from the one-pot template reaction of tris(2-aminoethyl)amine (TREN) tripods with tridentate 2,6-diformyl-4-methylphenol in the presence of $R(NO_3)_3$. Crystal structures of $[R(L^6)(NO_3)](NO_3)_2$ ($R = Ce, Nd, Eu, Y$) show the formation of pseudo-trigonal complexes in which the lanthanide is placed asymmetrically at one end of the cavity, the four nitrogen atoms of one TREN tripod, three oxygen of the protonated phenols and two oxygen atoms of a bidentate nitrate ensuring nine-coordination (fig. 26). No major structural change is observed in the solid state for a relative lanthanide contraction of 11% (i.e., Y(III) displays an ionic radius comparable to that of Ho(III), Shannon (1976)), but threefold symmetry is removed by the coordination of the nitrate counter-anion.

Dissolution of the complexes in D_2O ($5 \cdot 10^{-3} \text{ mol} \cdot \text{dm}^{-3}$, $pD = 5.8$, 298 K) provides strict C_3 -symmetry on the NMR time scale in line with decomplexation of the nitrate anion or fast on-off exchange mechanisms. Since no decomplexation of the macrobicyclic occurs under these conditions, relaxation and hyperfine NMR shifts have been collected at a single concentration. Dynamic intramolecular $\delta \rightleftharpoons \lambda$ conformational interconversion of the five-membered chelate rings rapidly exchange H_{2axial} with $H_{2equatorial}$ on the NMR time scale. A detailed Eyring analysis of the line shape for $[La(L^6)]^{3+}$ gives $\Delta G^\ddagger = 70(3) \text{ kJ/mol}$ at 298 K, a kinetics barrier comparable to that found for the same conformational interconversion occurring in $[La(L^{10}-4H)]^-$ (60.7 kJ/mol, see sect. 3.2.2). Plots of $\delta_{ij}^{para}/\langle S_z \rangle_j$ vs $C_j/\langle S_z \rangle_j$ (eq. (48)) and δ_{ij}^{para}/C_j vs $\langle S_z \rangle_j/C_j$ (eq. (49)) for 1H NMR data of $[R(L^6)_3]^{3+}$ ($R = Ce-Yb$, except Pm, Gd) display an abrupt deviation from linearity between $R = Eu$ and $R = Tb$ and require two different straight lines (fig. 27). Two different isostructural series are considered for $R = Ce-Tb$ and $Er-Yb$, and two sets of contact F_i and pseudo-contact $B_0^2 G_i$ terms are obtained according to least-squares fits of eq. (47) (table 11, Platas et al. (1999)).

The simultaneous least-squares fits of lanthanide induced relaxation (LIR, T_1) according to eq. (18) and lanthanide induced shifts (LIS) according to eq. (47) with the crystal structures of $[R(L^6)(NO_3)](NO_3)_2$ as starting molecular models display only minor shift of $R(III)$ from its original location. For the lighter lanthanides ($R = Ce-Eu$), the best fit shows a slight shift

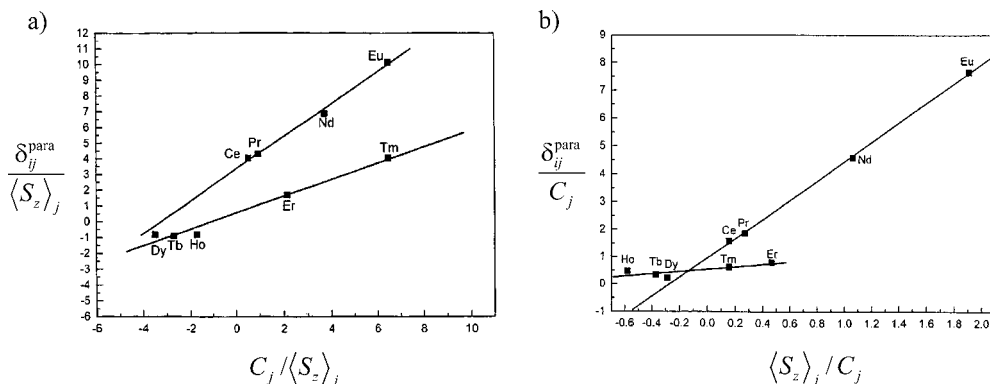


Fig. 27. Plots of (a) $\delta_{ij}^{para}/\langle S_z \rangle_j$ vs $C_j/\langle S_z \rangle_j$ (eq. (48)) and (b) δ_{ij}^{para}/C_j vs $\langle S_z \rangle_j/C_j$ (eq. (49)) for H3 in $[R(L^6)]^{3+}$ ($R = Ce-Yb$, D_2O , 298 K, adapted from Platas et al. (1999)).

Table 11
 Computed values for contact (F_i), pseudo-contact ($B_0^2 G_i$) terms for ^1H -nuclei in the complexes $[\text{R}(\text{L}^6)]^{3+}$ ($R = \text{Ce}-\text{Yb}, \text{D}_2\text{O}, 298 \text{ K}, \text{Platas et al. (1999)}$). See fig. 26 for the atom-numbering scheme

Series $R = \text{Ce}-\text{Eu}$							
	H1 _{ax}	H1 _{eq}	H2 _{ax}	H2 _{eq}	H3	H4	H5
F_i	1.81(28)	1.30(25)	0.55(13)	0.4(1)	3.48(6)	0.25(4)	0.01(2)
$B_0^2 G_i$	-2.05(22)	-1.78(15)	-0.06(4)	-0.01(4)	1.03(5)	0.49(4)	0.18(1)
	H6	H7	H8 _{ax}	H8 _{eq}	H9 _{ax}	H9 _{eq}	
F_i	0.21(1)	0.06(1)	0.15(6)	0.11(6)	0.21(6)	0.65(6)	
$B_0^2 G_i$	0.13(1)	-0.13(1)	-0.75(5)	-0.50(7)	-0.54(6)	-0.44(7)	
Series $R = \text{Tb}-\text{Yb}$							
	H1 _{ax}	H1 _{eq}	H2 _{ax}	H2 _{eq}	H3	H4	H5
F_i	0.33(32)	0.42(34)	0.79(13)	0.33(5)	0.57(17)	0.40(15)	-0.11(1)
$B_0^2 G_i$	-1.06(9)	-0.95(11)	-0.09(5)	-0.05(2)	0.52(5)	0.55(5)	0.06(1)
	H6	H7	H8 _{ax}	H8 _{eq}	H9 _{ax}	H9 _{eq}	
F_i	a	a	a	a	a	a	
$B_0^2 G_i$	a	a	a	a	a	a	

^aNot determined.

of $R(\text{III})$ toward the apical nitrogen atom of the TREN tripod (0.3 Å) and an angle of 5° between the principal magnetic z axis and the $R-\text{N}_{\text{apical}}$ vector (0° is expected for an axial system). Similar results are obtained for the heavy lanthanides $R = \text{Tb}-\text{Yb}$ except for a strict alignment of the magnetic z axis and the $R-\text{N}_{\text{apical}}$ direction. Platas et al. (1999) conclude that the cryptates $[\text{R}(\text{L}^6)_3]^{3+}$ are rigid in solution and no major structural change occurs in solution near the middle of the series. The break observed according to eqs. (48), (49) is thus assigned to a concomitant variation of F_i and B_0^2 as similarly suggested for (HHH)- $[\text{RCo}(\text{L}^5)_3]^{6+}$ (see sect. 3.1.5). The application of the crystal-field independent technique (eq. (51)) supports this statement and two parallel straight lines corresponding to the $R = \text{Ce}-\text{Eu}$ and $R = \text{Tb}-\text{Yb}$ series are observed for plots of $\delta_{ij}^{\text{para}}/\langle S_z \rangle_j$ vs $\delta_{kj}^{\text{para}}/\langle S_z \rangle_j$ (fig. 28). Since the slopes correspond to $R_{ik} = G_i/G_k$, no structural change occurs near the middle of the lanthanide series, but the variations of the hyperfine constants result in different intercepts $F_i - F_k R_{ik}$. Finally, a plot of $B_0^2 G_i (R = \text{Ce}-\text{Eu})$ vs $B_0^2 G_i (R = \text{Tb}-\text{Yb})$ gives a straight line whose slope corresponds to the ratio of the crystal-field parameters

$$\frac{B_0^2(R = \text{Ce}-\text{Eu})}{B_0^2(R = \text{Tb}-\text{Yb})} = 1.9(1).$$

The strict analogy between the behaviours of the rigid helicates (HHH)- $[\text{RCo}(\text{L}^5)_3]^{5/6+}$ and the cryptates $[\text{R}(\text{L}^6)]^{3+}$ strongly suggest that the ‘gadolinium break’ effect is a common trend when analysing paramagnetic NMR data (Rigault and Piguet, 2000).

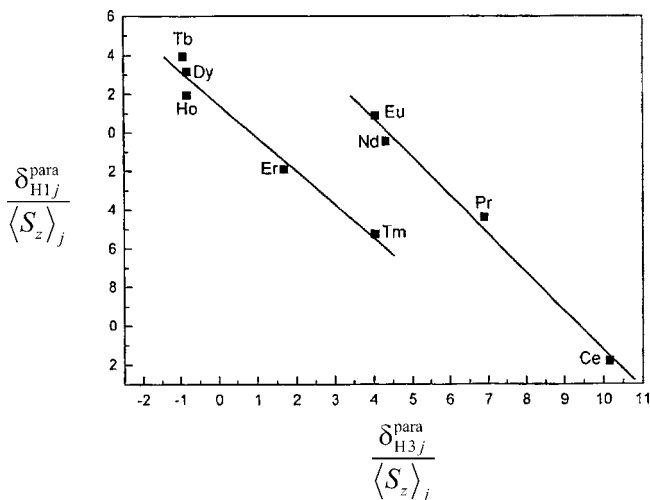


Fig. 28. Crystal-field independent plot of $\delta_{ij}^{\text{para}} / (S_z)_j$ vs $\delta_{kj}^{\text{para}} / (S_z)_j$ (eq. (51)) for the H1–H3 pair in $[R(L^6)]^{3+}$ ($R = \text{Ce–Yb}$, D_2O , 298 K, adapted from Platas et al. (1999)).

Finally, plots of $\delta_{ij}^{\text{para}} / \delta_{kj}^{\text{para}}$ vs $\delta_{ij}^{\text{para}} / \delta_{kj}^{\text{para}}$ according to the three-nuclei method (eq. (53)) confirm the break occurring near the middle of the series and the experimental slopes

$$\frac{(S_{ik} - R_{ik})}{(S_{lk} - R_{lk})}$$

and intercepts

$$\frac{(S_{lk}R_{ik} - S_{ik}R_{lk})}{(S_{lk} - R_{lk})}$$

can be satisfactorily predicted from F_i terms obtained with eqs. (48), (49) and R_{ik} terms obtained with eq. (51) (fig. 29, Geraldes et al. (2001)).

3.1.7. $[R(L^7-2H)_3]^{3-}$ ($L^7 = 2,6\text{-pyridinedicarboxylic acid and derivatives}$)

According to the systematic observation of abrupt variations of the second-rank crystal-field parameter near the middle of the lanthanide series in rigid threefold complexes on one side (see sects. 3.1.5 and 3.1.6) and the structural change evidenced in $[R(L^3)_3]^{3+}$ between $R = \text{Tb}$ and $R = \text{Er}$ on the other side (see sect. 3.1.3), the strict isostructurality combined with the invariance of B_0^2 proposed by Donato and Martin (1972) and Reilley et al. (1975) for the closely related complexes $[R(L^7-2H)_3]^{3-}$ in D_2O become suspicious and deserve to be re-examined. As discussed for $[R(L^1-2H)_n]^{(3-2n)+}$ ($n = 1, 2, 3$, see sect. 3.1.1), the thermodynamic properties of $[R(L^7-2H)_n]^{(3-2n)+}$ ($n = 1, 2, 3$) have been extensively studied by Grenthe (1961) leading to calculated ligand speciations of $[R(L^7-2H)_3]^{3-}$ (95%), $[R(L^7-2H)_2(\text{OH}_2)_3]^-$ (3%) and $[L^7-2H]^{2-}$ (2%) for a total ligand concentration of $0.03 \text{ mol} \cdot \text{dm}^{-3}$ and a stoichiometric ratio $R/L^7 = 0.33$ (water, pH = 6, 298 K). In excess of ligand ($R/L^7 = 0.25$), fast intermolecular ligand-exchange processes on the NMR time scale are detected for $[\text{La}(L^7-2H)_3]^{3-}$ (D_2O , 283–353 K), while the stronger R -ligand

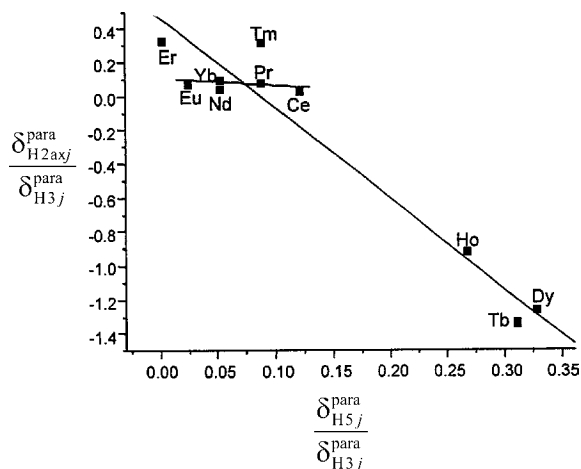


Fig. 29. Plot of $\delta_{ij}^{\text{para}}/\delta_{kj}^{\text{para}}$ vs $\delta_{lj}^{\text{para}}/\delta_{kj}^{\text{para}}$ according to the three-nuclei method (eq. (53)) for the triad H2_{ax}-H3-H5 in $[R(L^6)]^{3+}$ ($R = \text{Ce}-\text{Yb}$, D₂O, 298 K, redrawn from Geraldès et al. (2001)).

dative bonds with smaller rare earth ions ($R = \text{Y}, \text{Lu}$) provide distinct ^1H NMR signals at 283 K for free and complexed ligands (Alsaadi et al., 1980a). Ouali et al. (2002) have obtained $\Delta G^\ddagger([\text{Y}(\text{L}^7-2\text{H})_3]^{3-}) = 68(1)$ and $\Delta G^\ddagger([\text{Lu}(\text{L}^7-2\text{H})_3]^{3-}) = 74(1)$ kJ/mol at the coalescence temperatures (318 and 348 K respectively) for this intermolecular ligand-exchange process together with a smaller value $\Delta G^\ddagger([\text{La}(\text{L}^7-2\text{H})_3]^{3-}) \leq 59$ kJ/mol in agreement with the original trend proposed by Peters (1988) for the closely related oxydiacetate complexes $[R(\text{L}^1-2\text{H})_3]^{3-}$. However, the equilibrium quantities of $[R(\text{L}^7-2\text{H})_2(\text{OH})_2]^{3-}$ and $[\text{L}^7-2\text{H}]^{2-}$ are small enough to be neglected for NMR measurements obtained at high concentration and for $R/\text{L}^7 = 0.33$ (Pons and Millet, 2001). The observed ^1H and ^{13}C NMR data confirm the formation of D_3 -symmetrical triple-helical complexes $[R(\text{L}^7-2\text{H})_3]^{3-}$ and $[R(\text{L}^{\text{a}}-2\text{H})_3]^{3-}$ in solution (Reilley et al., 1975) in agreement with the numerous solid-state crystal structures reported for $(\text{cation})_3[R(\text{L}^7-2\text{H})_3]$ along the complete lanthanide series which show $R(\text{III})$ in pseudo-tricapped trigonal prismatic sites, six oxygen atoms of the carboxylate groups occupying the vertices of the trigonal prism and the three nitrogen atoms of the pyridine rings capping the rectangular faces (Hopkins et al., 1996; Harrowfield et al., 1995; fig. 30).

The introduction of diastereotopic probes in $[R(\text{L}^{7b}-2\text{H})_3]^{3-}$ shows two separated ^1H NMR signals for the methylene protons for $R = \text{Eu}, \text{Tm}$ and Yb which coalesce around 298 K (Ouali et al., 2002). The associated free energies of activation $\Delta G^\ddagger([\text{Eu}(\text{L}^{7b}-2\text{H})_3]^{3-}) = 63(1)$ kJ/mol, $\Delta G^\ddagger([\text{Tm}(\text{L}^{7b}-2\text{H})_3]^{3-}) = 64(1)$ kJ/mol and $\Delta G^\ddagger([\text{Yb}(\text{L}^{7b}-2\text{H})_3]^{3-}) = 60(1)$ kJ/mol point to a minor dependence of the racemisation process $P-[R(\text{L}^{7b}-2\text{H})_3]^{3-} \rightleftharpoons M-[R(\text{L}^{7b}-2\text{H})_3]^{3-}$ on the size of $R(\text{III})$ as similarly observed by Peters (1988) for $[R(\text{L}^1-2\text{H})_3]^{3-}$. The first-order rate constants for the ground-state helical racemisation process ($k_{\text{rac}}^{298\text{K}} = 50-200 \text{ s}^{-1}$) are in good agreement with those obtained in the excited state by polarized luminescence for $[R(\text{L}^7-2\text{H})_3]^{3-}$ ($R = \text{Eu}, \text{Tb}$, Huskowska and Riehl (1995)). Finally, ^1H relaxation measurements (Alsaadi et al., 1980b) and time-resolved luminescence (An et al., 2000) for $[R(\text{L}^7-2\text{H})_3]^{3-}$ demonstrate that no water molecule interacts

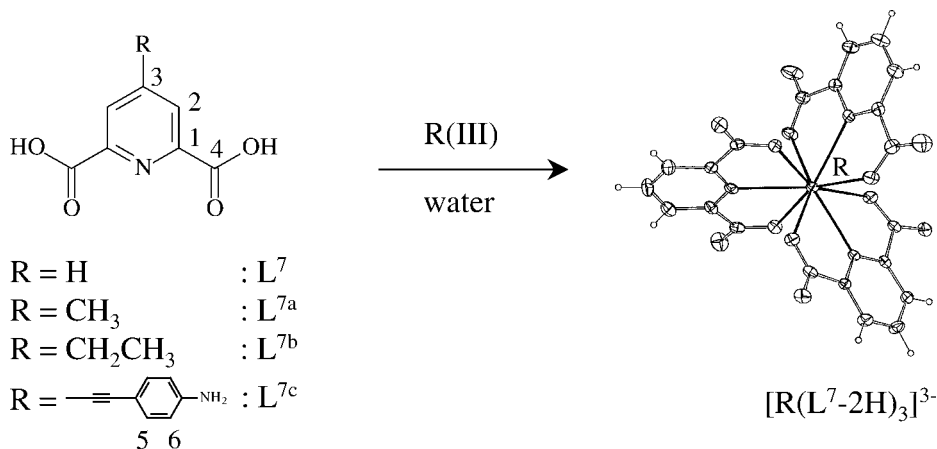


Fig. 30. Schematic formation of the D_3 -symmetrical complexes $[R(L^7-2H)_3]^{3-}$ in water with numbering scheme. The representation of $[R(L^7-2H)_3]^{3-}$ corresponds to the crystal structure of $[Cr(\text{sarcophagine})][La(L^7-2H)(H_2O)_8]$ (Harrowfield et al., 1995).

with $R(III)$ in the first coordination sphere along the complete lanthanide series, thus leading to well-defined D_3 -symmetrical triple helices in solution. Original plots of $\delta_{ij}^{\text{para}}/\langle S_z \rangle_j$ vs $C_j/\langle S_z \rangle_j$ (eq. (48)) and $\delta_{ij}^{\text{para}}/C_j$ vs $\langle S_z \rangle_j/C_j$ (eq. (49)) for 1H and ^{13}C NMR data of $[R(L^7-2H)_3]^{3-}$ ($R = Pr, Eu, Tb\text{--}Yb$) reported by Reilley et al. (1975, 1976) suggested linear behaviours compatible with isostructurality (i.e., invariance of G_i) and invariances of F_i and B_0^2 along the complete lanthanide series. Moreover, least-squares fits of the molecular structure based on G_i calculated for the crystal structures of $(\text{cation})_3[R(L^7-2H)_3]$ showed only minor variations between solid-state and solution structures. Similar conclusions have been proposed by Platas-Iglesias et al. (2001) for 1H NMR data of $[R(L^{7c}-2H)_3]^{3-}$ ($R = Nd, Eu, Tb\text{--}Yb$) except that the existence of a single isostructural series is further supported by linear correlations obtained with the crystal-field independent technique (eq. (51), fig. 31a), and minor variations of F_i between $R = Dy$ and $R = Ho$ are detected according the one-nucleus techniques (eqs. (48), (49), fig. 31b).

In both model-free analyses of $[R(L^7-2H)_3]^{3-}$ (Reilley et al., 1975) and $[R(L^{7c}-2H)_3]^{3-}$ (Platas-Iglesias et al., 2001), only two members of the first part of the lanthanide series are considered ($R = Pr, Eu$ for Reilley et al. (1975) and $R = Nd, Eu$ for Platas-Iglesias et al. (2001)), which strongly limits detection of breaks between light and heavy lanthanides according to eqs. (48), (49) and (51). Moreover, these reports contrast with the significant variations of the ratio of pseudo-contact contributions $\delta_{H2j}^{\text{pc}}/\delta_{H3j}^{\text{pc}}$ noticed by Alsaadi et al. (1980a) between light and heavy lanthanides in their original treatment of NMR data collected for $[R(L^7-2H)_n]^{(3-2n)+}$ ($n = 1, 2, 3$) at different stoichiometric ratios. A new complete set of 1H and ^{13}C NMR data for $[R(L^7-2H)_3]^{3-}$ ($R = Ce\text{--}Yb$, except Pm, Gd , 298 K, $pD = 6.0$, 300 MHz) has been collected by Ouali et al. (2002) and analyzed with eqs. (48), (49), (51). Plots of $\delta_{ij}^{\text{para}}/\langle S_z \rangle_j$ vs $\delta_{kj}^{\text{para}}/\langle S_z \rangle_j$ (eq. (51)) systematically display two different straight lines

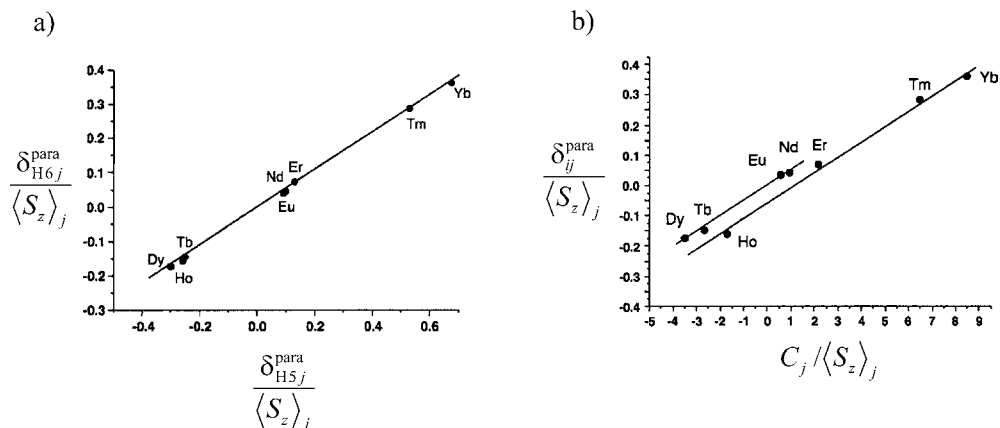


Fig. 31. (a) Crystal-field independent plot of $\delta_{ij}^{para} / \langle S_z \rangle_j$ vs $\delta_{kj}^{para} / \langle S_z \rangle_j$ (eq. (51)) for the H5–H6 pair and (b) plot of $\delta_{ij}^{para} / \langle S_z \rangle_j$ vs $C_j / \langle S_z \rangle_j$ for H6 in $[R(L^{7c}-2H)_3]^{3-}$ ($R = Nd, Eu, Tb-Yb, D_2O, 298\text{ K}$, redrawn from Platas-Iglesias et al. (2001)).

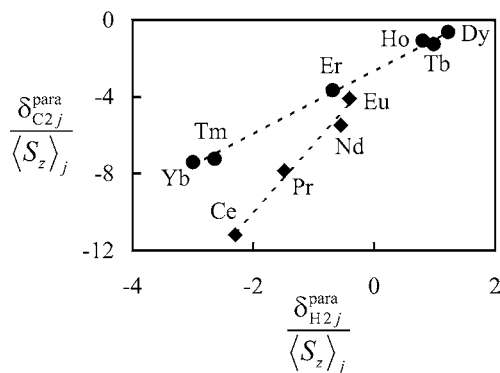


Fig. 32. Crystal-field independent plot of $\delta_{ij}^{para} / \langle S_z \rangle_j$ vs $\delta_{kj}^{para} / \langle S_z \rangle_j$ (eq. (51)) for the H2–C2 pair in $[R(L^7-2H)_3]^{3-}$ ($R = Ce-Yb, D_2O, 298\text{ K}$, redrawn from Ouali et al. (2002)).

for $R = Ce-Eu$ and $R = Tb-Yb$ (fig. 32) in contrast with the original treatment of Reilley et al. (1975), but in line with the observation of Alsaadi et al. (1980a). Two different isostructural series are observed and the R_{ik} terms calculated from the crystal structures of $[R(L^7-2H)_3]^{3-}$ ($R = La, Lu$, Harrowfield et al. (1995)) compare well with those found in solution for $R = Tb-Yb$, but not for $R = Ce-Eu$ (table 12). Extensive molecular modeling shows that the latter R_{ik} terms result from oscillations of the central pyridine rings displaying considerable amplitude for light $R(III)$ ($|\alpha(O-C4-C1-N)| \geq 46^\circ$, fig. 33). For $R = Tb-Yb$, the stronger $R-N_{pyridine}$ bonds limit oscillations and only minor displacements from the equilibrium position can be detected. Although related distortions are not observed in the crystal structures of $[R(L^7-2H)_3]^{3-}$ ($R = La, Lu$), large torsions of the pyridine rings are exemplified in the

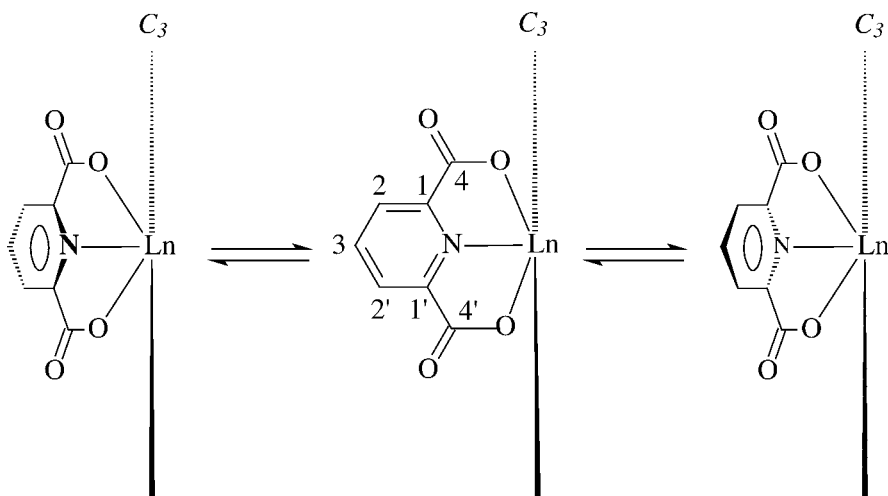


Fig. 33. Oscillations of the pyridine rings in the complexes of $[R(L^7-2H)_3]^{3-}$ with large lanthanides ($R = \text{Ce-Eu}$, adapted from Ouali et al. (2002)).

Table 12

Minimal set of geometric ratio $R_{ik} = G_i/G_k$ obtained from plots of $\delta_{ij}^{\text{para}}/\langle S_z \rangle_j$ vs $\delta_{kj}^{\text{para}}/\langle S_z \rangle_j$ according to eq. (51) for $[R(L^7-2H)_3]^{3-}$ (D_2O , 298 K, pD = 6, Ouali et al. (2002)).^a See fig. 30 for the atom-numbering scheme

	H2-H3	H2-C1	H2-C2	H2-C3	H2-C4
R_{ik} (Ce-Eu) ^b	0.98(4)	0.23(1)	0.28(3)	0.36(4)	1(1)
R_{ik} (Tb-Yb) ^c	1.15(1)	0.20(1)	0.60(2)	0.64(2)	1(5)
R_{ik} ($[\text{La}(L^7-2H)_3]^{3-}$) ^d	1.13	0.22	0.53	0.65	1.22
R_{ik} ($[\text{Lu}(L^7-2H)_3]^{3-}$) ^d	1.11	0.21	0.51	0.63	2.66

^aA complete set of R_{ik} data can be generated according to $R_{ik} = R_{im} \cdot R_{mk}$. Errors obtained according to multilinear least-squares fits are given between parentheses.

^bValues for the first isostructural series (Sm has been removed because of its faint paramagnetism).

^cValues for the second isostructural series.

^dCalculated for the crystal structures of $[\text{Cr}(\text{sarcophagine})][R(L^7-2H)_3]$ after averaging to D_3 -symmetry.

crystal structure of the analogous complex $[\text{La}(L^3)_3]^{3+}$ ($26.8^\circ \leq |\alpha(\text{O}-\text{C4}-\text{C1}-\text{N})| \leq 43.8^\circ$, Renaud et al. (1997)).

Plots of $\delta_{ij}^{\text{para}}/\langle S_z \rangle_j$ vs $C_j/\langle S_z \rangle_j$ (eq. (48)) and $\delta_{ij}^{\text{para}}/C_j$ vs $\langle S_z \rangle_j/C_j$ (eq. (49)) for ^1H and ^{13}C NMR data of $[R(L^7-2H)_3]^{3-}$ ($R = \text{Ce-Yb}$, except Pm, Gd) show an abrupt break near the middle of the lanthanide series assigned to concomitant variations of the contact F_i and pseudo-contact $B_0^2 G_i$ terms (table 13, fig. 34, Ouali et al. (2002)).

Since eq. (51) has established the existence of a structural change (oscillation of the pyridine rings) between $R = \text{Eu}$ and $R = \text{Tb}$ for $[R(L^7-2H)_3]^{3-}$, the origin of the concomitant changes of F_i and $B_0^2 G_i$ does not require further justifications. However, the geometrical fac-

Table 13

Computed values for contact (F_i), pseudo-contact ($B_0^2 G_i$) terms and agreement factors (AF_i) for ^1H - and ^{13}C -nuclei in complexes $[\text{R}(\text{L}^7\text{-2H})_3]^{3-}$ (D_2O , 298 K, pD = 6, Ouali et al. (2002)). See fig. 30 for the atom-numbering scheme

Compd		H2	H3	C1	C2	C3	C4
$R = \text{Ce-Eu}$	F_i	-0.28(1)	-0.30(3)	-0.75(4)	-3.7(2)	0.98(9)	-0.6(1)
	$B_0^2 G_i$	-0.32(1)	-0.30(2)	-1.32(3)	-1.2(2)	-0.80(8)	-0.1(1)
$R = \text{Tb-Yb}$	F_i	0.03(7)	0.02(6)	0.3(4)	-2.6(2)	1.2(1)	-1.2(2)
	$B_0^2 G_i$	-0.36(2)	-0.31(2)	-1.7(1)	-0.58(7)	-0.59(3)	-0.53(6)
	AF_i^a	0.09	0.09	0.10	0.14	0.05	0.22

^a AF_i is calculated by using $\delta_{ij}^{\text{calc}}$ obtained for $R = \text{Ce-Eu}$ and $R = \text{Tb-Yb}$.

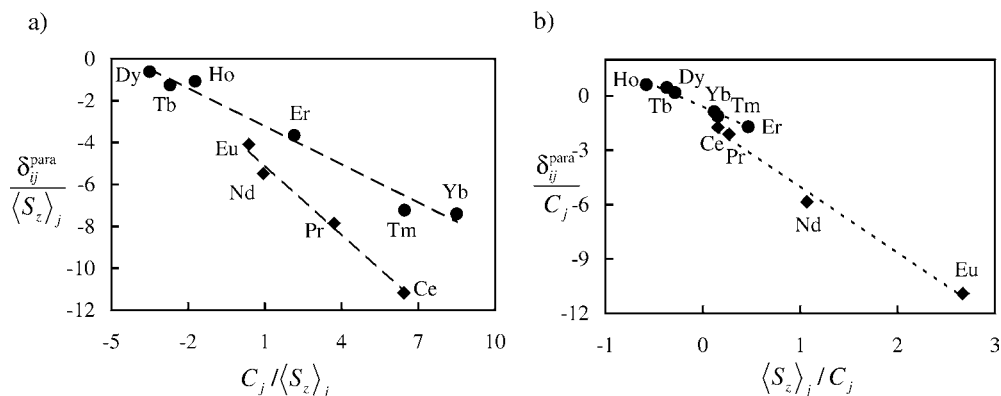


Fig. 34. Plots of (a) $\delta_{ij}^{\text{para}} / \langle S_z \rangle_j$ vs $C_j / \langle S_z \rangle_j$ (eq. (48)) and (b) $\delta_{ij}^{\text{para}} / C_j$ vs $\langle S_z \rangle_j / C_j$ (eq. (49)) for C2 in $[\text{R}(\text{L}^7\text{-2H})_3]^{3-}$ ($R = \text{Ce-Yb}$, D_2O , 298 K, adapted from Ouali et al. (2002)).

tor G_i can be calculated from the molecular models and changes of the crystal-field parameter can be addressed. The use of $G_{\text{C}3}$ as a reference taken from the two structural models allows the estimation of all remaining G_i factors from the experimental R_{ik} terms obtained for the two isostructural series (table 12). B_0^2 are computed from the pseudo-contact terms $B_0^2 G_i$ collected in table 13, thus leading to

$$\frac{B_0^2(R = \text{Ce-Eu})}{B_0^2(R = \text{Tb-Yb})} = 1.5(1).$$

The latter ratio parallels a similar trend observed for $[\text{R}(\text{L}^7\text{-2H})_3]^{3-}$ doped in single hexagonal crystals of $\text{Na}_3[\text{Yb}_{1-x}\text{R}_x(\text{L}^7\text{-2H})_3] \cdot \text{NaClO}_4 \cdot 10\text{H}_2\text{O}$, and for which $B_0^2 = -272 \text{ cm}^{-1}$ ($R = \text{Eu}$), $B_0^2 = -140 \text{ cm}^{-1}$ ($R = \text{Tb}$) and $B_0^2 = -198 \text{ cm}^{-1}$ ($R = \text{Dy}$) which correspond to an average ratio

$$\frac{B_0^2(R = \text{Eu})}{B_0^2(R = \text{Tb-Dy})} = 1.6(1)$$

(Hopkins et al., 1996). Finally, plots of $\delta_{ij}^{\text{para}}/\delta_{kj}^{\text{para}}$ vs $\delta_{lj}^{\text{para}}/\delta_{kj}^{\text{para}}$ according to the three-nuclei method (eq. (53)) confirm the abrupt break occurring near the middle of the series (Ouali et al., 2002). The experimental slopes

$$\frac{(S_{ik} - R_{ik})}{(S_{lk} - R_{lk})}$$

and intercepts

$$\frac{(S_{lk}R_{ik} - S_{ik}R_{lk})}{(S_{lk} - R_{lk})}$$

depend on F_i and G_i parameters and they can be satisfactorily predicted from F_i terms obtained with eqs. (48), (49) and G_i terms resulting from the combination of structural modeling and eq. (51). Compared to the original report of Reilley et al. (1975) proposing the invariance of G_i , F_i and B_0^2 along the complete lanthanide series, the recent re-examination of the new complete set of NMR data by Ouali et al. (2002) reaches opposite conclusions and eventually establishes a concomitant change of G_i , F_i and B_0^2 between $R = \text{Eu}$ and $R = \text{Tb}$. This discrepancy originates from (i) the too limited set of data collected by Reilley et al. (1975) for the light lanthanides and (ii) by fortuitous compensation effects produced by the concomitant variations of G_i and B_0^2 for H2, H3 and C3 which indeed provide invariant pseudo-contact terms $B_0^2 G_i$ along the complete series for these NMR signals. A similar treatment applied to the analogous complexes $[R(\text{L}^3)_3]^{3+}$ indicates that related oscillations of the pyridine rings are responsible for the observed structural changes. Although only a rough molecular modeling has been proposed for $[R(\text{L}^3)_3]^{3+}$, a similar behaviour is evidenced with a concomitant change of G_i , F_i and B_0^2 between $R = \text{Tb}$ and $R = \text{Er}$ and an approximate ratio

$$\frac{B_0^2(R = \text{Ce-Tb})}{B_0^2(R = \text{Er-Yb})} = 3(1)$$

(Ouali et al., 2002).

3.1.8. $[R(\text{L}^8-3\text{H})]$ ($\text{L}^8 = 1,4,7\text{-triazacyclononane-}N,N',N''\text{-triacetic acid}$)

The potentially hexadentate triaza macrocyclic ligand L^8 (its trianion form is also known as NOTA^{3-}) forms thermodynamically quite stable $[R(\text{L}^8-3\text{H})(\text{H}_2\text{O})_q]$ complexes in aqueous solution, with $\log \beta_1$ values increasing from 13.4 for $R = \text{La}$ to 15.9 for $R = \text{Lu}$ (Cacheris et al., 1987). Although none of the complexes of the series has so far been isolated and characterized in the solid state by X-ray crystallography, the ligand structure makes these chelates good candidates for C_3 symmetry. A study of the lanthanide(III) induced ^{17}O shifts of water solutions of these complexes has shown that their hydration number q changes across the lanthanide series, from $q = 3-4$ in the first half ($R = \text{Ce-Eu}$) to $q = 3$ in the second half of the series ($R = \text{Dy-Yb}$) (Bryden et al., 1981). This is consistent with the fluorescence data available for the Eu^{3+} complex in aqueous solution, where two different species are observed in equilibrium (Bryden et al., 1981).

The ^1H and ^{13}C NMR spectra of the whole series of $[R(\text{L}^8-3\text{H})(\text{H}_2\text{O})_q]$ complexes have been also analyzed in terms of their structure and dynamics in solution (Geraldés et al., 1985;

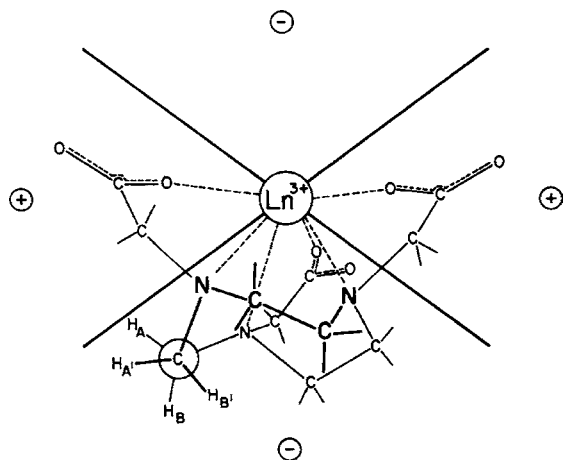


Fig. 35. Schematic representation of L^8 (NOTA) coordinated to a lanthanide ion (one of the acetate arms is not shown for clarity) with a geometry in accordance with the best fit of the LIR and LIS data, illustrating the dipolar angle effect (+ and - indicate the sign of the geometric factor G_i) (Sherry et al., 1986).

Sherry et al., 1986). In particular, the ^1H and ^{13}C LIS values have been reported for all the paramagnetic ions except Ce, Pm and Gd in D_2O ($10^{-1} \text{ mol} \cdot \text{dm}^{-3}$, $\text{pH} = 6.0$ and 343 K , Sherry et al. (1986)). The symmetry of the spectra obtained shows that the chelates indeed have C_3 symmetry in solution, and the absolute values and signs of the LIS values are clear indication that $R(\text{III})$, although bound to the three N-atoms and to the carboxylate oxygens, does not fit inside the macrocyclic cavity but is located well above (2.2 \AA) the plane of the three nitrogens (fig. 35). All ethylenediamine groups in the 9-membered macrocyclic ring adopt an identical gauche conformation, either δ or λ , leading to one of two possible square [333] conformations. The fast interconversions between the two gauche conformations of the ethylene bridges, corresponding to a high conformational flexibility of the macrocycle, explain their AA'XX' proton spectrum at all temperatures.

Plots of $\delta_{ij}^{\text{para}} / \langle S_z \rangle_j$ vs $C_j / \langle S_z \rangle_j$ (eq. (48)) and $\delta_{ij}^{\text{para}} / C_j$ vs $\langle S_z \rangle_j / C_j$ (eq. (49)) for ^1H and ^{13}C NMR data of $[R(L^8-3\text{H})(\text{H}_2\text{O})_q]$ ($R = \text{Pr}-\text{Yb}$, except Pm, Gd) show an abrupt break near the middle of the lanthanide series reflecting variations of the F_i and $B_0^2 G_i$ parameters (table 14, fig. 36, Sherry et al. (1986)). On the basis of these results, as well as of the ^{17}O NMR and luminescence data, the original work assumed that B_0^2 did not change and that two groups of solution structures were present, with a change of ligand coordination number or hydration number at Tb. The simultaneous least-squares fits of lanthanide induced relaxation (LIR, T_1) according to eq. (18) and lanthanide induced shifts (LIS) according to eq. (47) with a chemical model for the $[R(L^8-3\text{H})(\text{H}_2\text{O})_q]$ chelates based on the modified crystal structure of the Cr^{3+} complex gave different best fit structures. While for the later ions ($R = \text{Dy}-\text{Yb}$) the ligand is hexa-coordinated with three inner-sphere water molecules (fig. 35), it is concluded that the earlier chelates ($R = \text{Pr}-\text{Eu}$) adopt a structural mixture of hexa- and penta-coordinate (with one free acetate arm) ligands with three and four inner-sphere water molecules, respectively.

The application of the two-nuclei crystal-field independent technique and the three-nuclei method provide convincing evidence for the proposed structural subdivision of the $[R(L^8-3\text{H})(\text{H}_2\text{O})_q]$ complexes (Geraldès et al., 2003). All the plots of $\delta_{ij}^{\text{para}} / \langle S_z \rangle_j$ vs $\delta_{kj}^{\text{para}} / \langle S_z \rangle_j$

Table 14

Computed values for contact (F_i), pseudo-contact ($B_0^2 G_i$) terms and R^2 values, according to eq. (48), comparison of R_{ik} and $(F_i - R_{ik} F_k)$ parameters calculated directly according to eq. (51), and α and β parameters calculated directly according to eq. (53), with those obtained from the above F_i and $B_0^2 G_i$ terms, for ^1H - and ^{13}C -nuclei in complexes $[R(\text{L}^8\text{-3H})(\text{H}_2\text{O})_q]$ ($R = \text{Pr-Yb}$, D_2O , $\text{pD} = 6.0$, 343 K , Sherry et al. (1986)). See fig. 35 for the atom-numbering scheme

Compd		H _a	H _{N'}	H _{N''}	C _O	C _a	C _N
$R = \text{Pr-Tb}^{\text{a}}$	F_i	0.37	0.36	0.38	-3.19	-2.37	-4.15
	$B_0^2 G_i$	-0.12	-0.23	-1.18	3.37	0.30	-2.32
	R^2	0.914	0.704	0.552	0.999	0.881	0.985
Compd		H _a	H _{N'}	H _{N''}	C _O	C _a	C _N
$R = \text{Dy-Yb}^{\text{b}}$	F_i	0.75	0.15	0.97	-4.15	-3.00	-0.58
	$B_0^2 G_i$	0.04	-0.08	-0.43	2.06	0.33	-0.27
	R^2	0.799	0.730	0.905	0.914	0.704	0.552
Compd		C _N -C _O	C _a -C _O	C _a -C _N	H _{N'} -H _a	H _{N'} -H _{N''}	H _{N''} -H _a
$R = \text{Pr-Tb}^{\text{a}}$	$R_{ik}(\text{exp})$	-0.69	0.11	-0.16	1.02	0.15	7.35
	$(F_i - F_k R_{ik})(\text{exp})$	-6.35	-2.18	-3.18	-0.13	0.25	-2.62
	R^2	0.976	0.917	0.958	0.956	0.991	0.970
	$R_{ik}(\text{calc})$	-0.69	0.09	-0.13	1.92	0.20	9.83
	$(F_i - F_k R_{ik})(\text{calc})$	-6.32	-2.09	-2.91	-0.35	0.28	-3.26
Compd		C _N -C _O	C _a -C _O	C _a -C _N	H _{N'} -H _a	H _{N'} -H _{N''}	H _{N''} -H _a
$R = \text{Dy-Yb}^{\text{b}}$	$R_{ik}(\text{exp})$	-0.17	0.18	-1.05	-0.22	0.05	-3.71
	$(F_i - F_k R_{ik})(\text{exp})$	-0.90	-2.42	-3.36	0.36	-0.11	3.87
	R^2	0.901	0.937	0.958	0.908	0.953	0.962
	$R_{ik}(\text{calc})$	-0.13	0.16	-1.22	-2.00	0.19	-10.75
	$(F_i - F_k R_{ik})(\text{calc})$	-1.12	-2.34	-3.71	1.65	-0.14	8.99
Compd		$i = \text{C}_\text{N}; k = \text{C}_\text{a}; l = \text{C}_\text{O}$			$i = \text{H}_\text{N}'; k = \text{H}_\text{a}; l = \text{H}_\text{N}''$		
$R = \text{Pr-Tb}^{\text{a}}$	$\alpha(\text{exp})$	-0.97			16.76		
	$\beta(\text{exp})$	2.96			-10.43		
	R^2	0.981			0.895		
	$\alpha(\text{calc})$	-1.38			9.33		
	$\beta(\text{calc})$	2.99			8.72		
Compd		$i = \text{C}_\text{N}; k = \text{C}_\text{a}; l = \text{C}_\text{O}$			$i = \text{H}_\text{N}'; k = \text{H}_\text{a}; l = \text{H}_\text{N}''$		
$R = \text{Dy-Yb}^{\text{b}}$	$\alpha(\text{exp})$	-0.24			16.05		
	$\beta(\text{exp})$	0.31			-1.58		
	R^2	0.960			0.961		
	$\alpha(\text{calc})$	-0.21			5.65		
	$\beta(\text{calc})$	0.40			-6.39		

^aValues for the first isostructural series (except Ce and Sm).

^bValues for the second isostructural series.

(eq. (51)), which eliminate the effect of any changes of B_0^2 , either involving the three types of carbon nuclei or the three types of protons, systematically display two different straight lines for $R = \text{Pr-Tb}$ and $R = \text{Dy-Yb}$ (fig. 37a), confirming that the F_i and G_i parameters change abruptly at Tb. There is generally a good agreement of experimental and calculated R_{ik} and

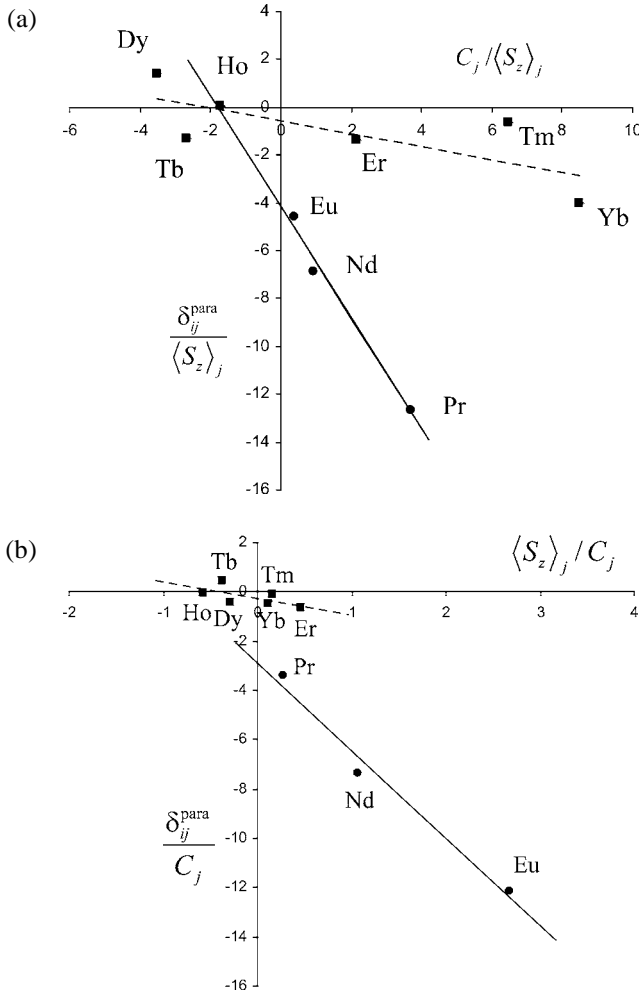


Fig. 36. Plots of (a) $\delta_{ij}^{para} / \langle S_z \rangle_j$ vs $C_j / \langle S_z \rangle_j$ and (b) δ_{ij}^{para} / C_j vs $\langle S_z \rangle_j / C_j$ for C_N in $[R(L^8-3H)(H_2O)_q]$ ($R = Pr-Tb, Dy-Yb, D_2O, 343 K$, redrawn from Sherry et al. (1986)).

$(F_i - F_k R_{ik})$ parameters (table 14). Since in the present system G_i values change, B_0^2 ratios,

$$\frac{B_0^2(R = Ce-Tb)}{B_0^2(R = Dy-Yb)},$$

could not be obtained. Plots of $\delta_{ij}^{para} / \delta_{kj}^{para}$ vs $\delta_{lj}^{para} / \delta_{kj}^{para}$ (eq. (53)) (see fig. 37b) confirm the abrupt break near the middle of the series. The experimental slope

$$\alpha = \frac{(S_{ik} - R_{ik})}{(S_{lk} - R_{lk})}$$

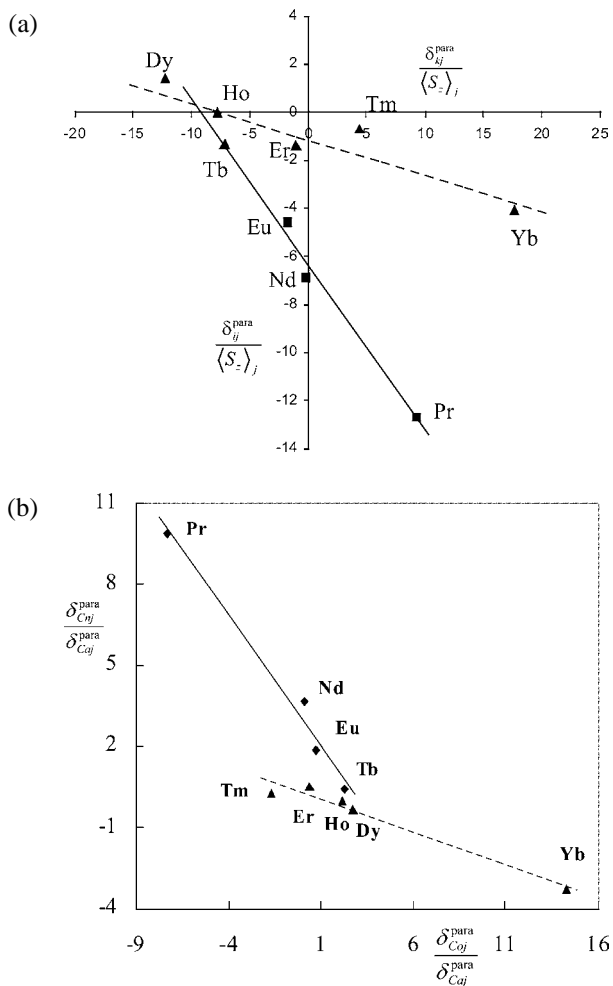


Fig. 37. (a) Crystal-field independent plot of $\delta_{ij}^{\text{para}} / \langle S_z \rangle_j$ vs $\delta_{kj}^{\text{para}} / \langle S_z \rangle_j$ for the C_N - C_O pair; (b) plot of $\delta_{ij}^{\text{para}} / \delta_{kj}^{\text{para}}$ vs $\delta_{C_Oj}^{\text{para}} / \delta_{C_Nj}^{\text{para}}$ according to the three-nuclei method for the triad C_N , C_O and C_a in $[R(L^8-3H)(H_2O)_q]$, $R = \text{Ce}-\text{Yb}$, D_2O , 298 K (redrawn from Geraldes et al. (2003)).

and intercept

$$\beta = \frac{(S_{lk}R_{ik} - S_{ik}R_{lk})}{(S_{lk} - R_{lk})}$$

parameters are in satisfactory agreement with those calculated from predicted from F_i and G_i terms obtained from the other methods (table 14).

The results described here firmly support the literature conclusion of a structural change between the light and heavy $[R(L^8-3H)(H_2O)_q]$ complexes. In this case, the breaks in the plots likely reflect a change in the geometric terms, G_i and F_i , as they are independent of any concomitant changes of the crystal field parameter.

3.2. Complexes with fourfold symmetry

3.2.1. $[R(L^9-H)_4]^-$ ($L^9 =$ dithiomethylphosphinic acid and dithiophosphorus acid and dithiophosphorus acid derivatives)

A large number of lanthanide complexes of the type $[R(L^9-H)_4]^-$ have been isolated and characterized in the solid state by X-ray crystallography, where the ligand $[L^9-H]^-$, with two sulphur donor atoms and general formula $R_2PS_2^-$, is a dithiophosphinate (e.g., $R = Me$) or a dithiophosphonate ($R = OMe, OEt, OPr^i$) (Pinkerton and Schwarzenbach, 1981; Spiliadis et al., 1982, 1983). The crystal structures show that the lanthanide is coordinated to eight sulphur atoms with coordination geometries ranging between the regular D_{2d} dodecahedron, favored by alkoxy substituents at phosphorus, and a dodecahedron distorted towards the D_2 square antiprism, favored by alkyl substituents. However for each ligand no structural change was observed along the lanthanide series in the solid state.

^{31}P and 1H LIS data have been reported for these $[R(S_2PR_2)_4]^-$ complexes in CD_2Cl_2 solution ($R = Ce-Yb$, except Pm and Gd). Measurements were carried out at 299 K for all complexes ($R = OEt$ ($S_2P(OEt)_2^- = O,O'$ -diethyl dithiophosphate) (Pinkerton and Earl, 1978); $R = CH_3$, Spiliadis and Pinkerton (1982); $R = OMe, OPr^i$, Spiliadis and Pinkerton (1983)) and also at 233 K for $R = OEt$ (Pinkerton and Earl, 1978). The observed NMR data fit an effectively axial symmetric coordination model in which the lanthanide ion is chelated by four $S_2PR_2^{2-}$ molecules in a bidentate fashion (through the two sulfur atoms). These data were analysed using a simplified version of eq. (51) by plotting $\delta_{ij}^{para}/\langle S_z \rangle_j$ vs $\delta_{kj}^{para}/\langle S_z \rangle_j$, where i is the ^{31}P nucleus and k are the CH_2 and CH_3 protons and assuming no contact contribution to the LIS values of these protons. In this case $F_k = 0$ and eq. (51) reduces to eq. (60) and the plots gave directly as intercepts the values of the hyperfine coupling constant to the ^{31}P nucleus, F_P , and as slopes the geometric ratios $R_{Pk} = \frac{G_P}{G_k}$.

$$\frac{\delta_{Pj}^{para}}{\langle S_z \rangle_j} = F_P + \frac{G_P}{G_k} \cdot \frac{\delta_{kj}^{para}}{\langle S_z \rangle_j}. \quad (60)$$

Breaks were observed in such plots for all the compounds studied, between Tb and Dy for the $R = Me$ compound, and between Dy and Ho for the alkoxy derivatives. These breaks were assigned to structural (R_{Pk} values) and ^{31}P coupling constant (F_P) changes along the lanthanide series, although no difference in the solid state structures of the complexes along the series has been detected (Pinkerton and Earl, 1978; Spiliadis and Pinkerton, 1982, 1983). Large decreases of coupling constants were observed, e.g., from 1.52 MHz to 0.86 MHz for the $R = OEt$ derivative, while for $R = Me$ the values were smaller but still decreasing along the series (1.09 MHz to 0.51 MHz). The R_{Pk} values also decreased very much along the lanthanide series due to a substantial decrease of the dipolar shift of the ^{31}P nucleus, consistent with a change in solution of the coordination polyhedron from a dodecahedral to a square antiprismatic structure.

Plots of $\delta_{ij}^{para}/\langle S_z \rangle_j$ vs $C_j/\langle S_z \rangle_j$ (eq. (48)) and δ_{ij}^{para}/C_j vs $\langle S_z \rangle_j/C_j$ (eq. (49)) for the LIS data of the $[R(S_2P(OEt)_2)_4]^-$ complexes at 299 K and 233 K show breaks at Tb, reflecting variations of the F_i and $B_0^2 G_i$ terms (table 15, fig. 38, Geraldès et al. (2003)). It can be seen

Table 15

Computed values for contact (F_i), pseudo-contact ($B_0^2 G_i$) terms and R^2 values, according to eq. (48), comparison of R_{ik} and $(F_i - R_{ik} F_k)$ parameters calculated directly according to eq. (51), and α and β parameters calculated directly according to eq. (53), with those obtained from the above F_i and $B_0^2 G_i$ terms, for ^1H - and ^{31}P -nuclei in complexes $[R(\text{L}^9\text{-H})_4]^-$ ($R = \text{Ce-Yb}$, $[\text{L}^9\text{-H}]^- = \text{S}_2\text{P}(\text{OEt})_2^-$, CD_2Cl_2 , Pinkerton and Earl (1978))

Compd	T = 253 K			T = 296 K			
	CH ₂	CH ₃	P	CH ₂	CH ₃	P	
$R = \text{Ce-Eu}^{\text{a}}$	F_i	0.35	0.12	56.43	0.18	0.07	49.38
	$B_0^2 G_i$	0.37	0.13	22.65	0.21	0.07	14.83
	R^2	0.928	0.920	0.923	0.950	0.931	0.962
$R = \text{Tb-Yb}^{\text{b}}$	F_i	-0.35	-0.13	49.90	-0.23	-0.09	38.90
	$B_0^2 G_i$	0.56	0.20	-0.10	0.28	0.10	-0.48
	R^2	0.988	0.986	0.994	0.967	0.947	0.994
Compd	CH ₂	CH ₃	P	CH ₂	CH ₃	P	
$R = \text{Ce-Eu}^{\text{a}}$	$R_{ik}(\text{exp})$		0.36	^c	0.37	86.03	
	$(F_i - F_k R_{ik})(\text{exp})$		-0.01	^c	-0.01	56.31	
	R^2		0.999	^c	0.998	0.826	
	$R_{ik}(\text{calc})$		0.34	^c	0.35	200.4	
	$(F_i - F_k R_{ik})(\text{calc})$		0.00	^c	0.00	36.16	
	$R = \text{Tb-Yb}^{\text{b}}$	$R_{ik}(\text{exp})$		0.37	^c	0.37	-3.31
$(F_i - F_k R_{ik})(\text{exp})$			-0.01	^c	-0.01	39.81	
R^2			0.998	^c	0.998	0.276	
$R_{ik}(\text{calc})$			0.35	^c	0.37	-1.07	
$(F_i - F_k R_{ik})(\text{calc})$			0.00	^c	-0.01	38.74	
Compd		$i = \text{CH}_3; k = \text{P}; l = \text{CH}_2$			$i = \text{CH}_3; k = \text{P}; l = \text{CH}_2$		
$R = \text{Ce-Eu}^{\text{a}}$	$\alpha(\text{exp})$		0.36		0.36		
	$\beta(\text{exp})$		0.00		0.00		
	R^2		0.999		0.999		
	$\alpha(\text{calc})$		0.34		0.35		
	$\beta(\text{calc})$		0.09		0.00		
	$R = \text{Tb-Yb}^{\text{b}}$	$\alpha(\text{exp})$		0.36		0.36	
$\beta(\text{exp})$			0.00		0.00		
R^2			0.999		0.999		
$\alpha(\text{calc})$			0.37		0.37		
$\beta(\text{calc})$			0.00		0.00		

^a Values for the first isostructural series (except Sm).

^b Values for the second isostructural series.

^c Not determined.

that proton F_k values are very small and F_P values, as well as R_{Pk} values indeed decrease drastically at Tb, in particular, the large F_P couplings by about 50% in the second part of the R series.

The plots of $\delta_{ij}^{\text{para}} / \langle S_z \rangle_j$ vs $\delta_{kj}^{\text{para}} / \langle S_z \rangle_j$ (eq. (51)) for $i = \text{CH}_3$ and $k = \text{CH}_2$ give a single straight line identical at both temperatures indicating that the structural change is not reflected

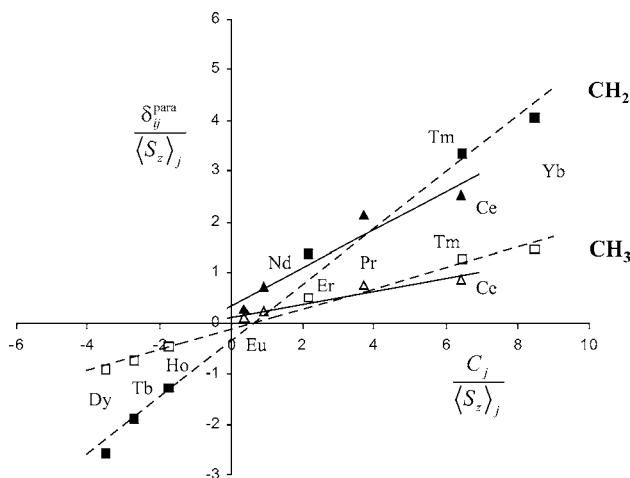


Fig. 38. Plot of $\delta_{ij}^{para} / \langle S_z \rangle_j$ vs $C_j / \langle S_z \rangle_i$ for CH_3 and CH_2 protons in $[R(\text{L}^9\text{-H})_4]^-$, $[\text{L}^9\text{-H}]^- = \text{S}_2\text{P}(\text{OEt})_2^-$ ($R = \text{Ce}\text{-Yb}$, CD_2Cl_2 , 253 K, adapted from Pinkerton and Earl (1978), Geraldes et al. (2003)).

in the proton G_i and F_i parameters, e.g., $G_{\text{CH}_3}/G_{\text{CH}_2}$ is constant (fig. 39a). However, plots with $i = \text{P}$ and $k = \text{CH}_2$ or CH_3 , identical to those discussed above using eq. (60) (fig. 39b), gave breaks at Tb, confirming that the F_i and G_i parameters change abruptly at Tb. There is generally a good agreement of experimental and calculated R_{ik} and $(F_i - F_k R_{ik})$ parameters (table 15). In the fitting of the early R plots, Eu and Sm are excluded due to the contribution of excited states to the $\langle S_z \rangle$ and C_j parameters. Since in the present system G_i values change, the B_0^2 ratios

$$\frac{B_0^2(R = \text{Ce-Tb})}{B_0^2(R = \text{Dy-Yb})}$$

could not be obtained.

Plots of $\delta_{ij}^{para} / \delta_{kj}^{para}$ vs $\delta_{lj}^{para} / \delta_{kl}^{para}$ (eq. (53)) with $i = \text{CH}_3$, $l = \text{CH}_2$ and $k = \text{P}$ give a single straight line along the lanthanide series (fig. 39c), with experimental slopes and intercepts identical at both temperatures ($\alpha = 0.366$; $\beta = 0$) (table 15). This is not surprising given that the temperature-dependent parameters, B_0^2 , $\langle S_z \rangle_j$ and C_j , are all absent from eq. (53). The experimental

$$\alpha = \frac{(S_{\text{CH}_3\text{P}} - R_{\text{CH}_3\text{P}})}{(S_{\text{CH}_2\text{P}} - R_{\text{CH}_2\text{P}})}$$

and

$$\beta = \frac{(S_{\text{CH}_2\text{P}}R_{\text{CH}_3\text{P}} - S_{\text{CH}_3\text{P}}R_{\text{CH}_2\text{P}})}{(S_{\text{CH}_2\text{P}} - R_{\text{CH}_2\text{P}})}$$

parameters are in satisfactory agreement with those calculated from F_i and G_i values obtained by the other methods (table 15). However, plots according to eq. (53) with other combinations, such as for $i = \text{P}$, $l = \text{CH}_3$ and $k = \text{CH}_2$, give breaks, and thus confirm the structural and coupling constants change. The reason why the first plot is not sensitive to the structural

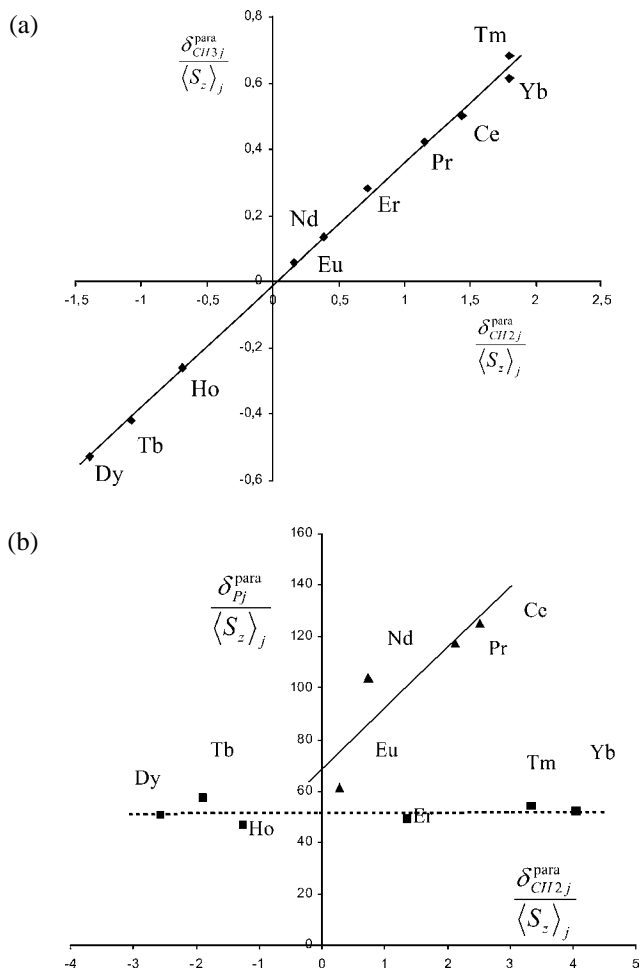


Fig. 39. Crystal-field independent plot of $\delta_{ij}^{para} / \langle S_z \rangle_j$ vs $\delta_{kj}^{para} / \langle S_z \rangle_j$ (a) for the CH₃-CH₂ pair; (b) for the P-CH₂ pair; (c) Plot of $\delta_{ij}^{para} / \delta_{kj}^{para}$ vs $\delta_{ij}^{para} / \delta_{kj}^{para}$ for the CH₃, CH₂, P triad at 253 K (Δ) and 296 K (\blacklozenge). Data for $[R(L^9-H)_4]^-$, $[L^9-H]^- = S_2P(OEt)_2^-$ ($R = Ce-Yb$, CD_2Cl_2 , 296 K, adapted from Pinkerton and Earl (1978), Geraldes et al. (2003)).

change is that $\beta = 0$ which implies that

$$\frac{F_{CH_2}}{F_{CH_3}} = \frac{G_{CH_2}}{G_{CH_3}}$$

and these ratios do not change along the series. This example illustrates that both the two nuclei and three nuclei methods may accidentally not reflect structural and/or F_i changes for

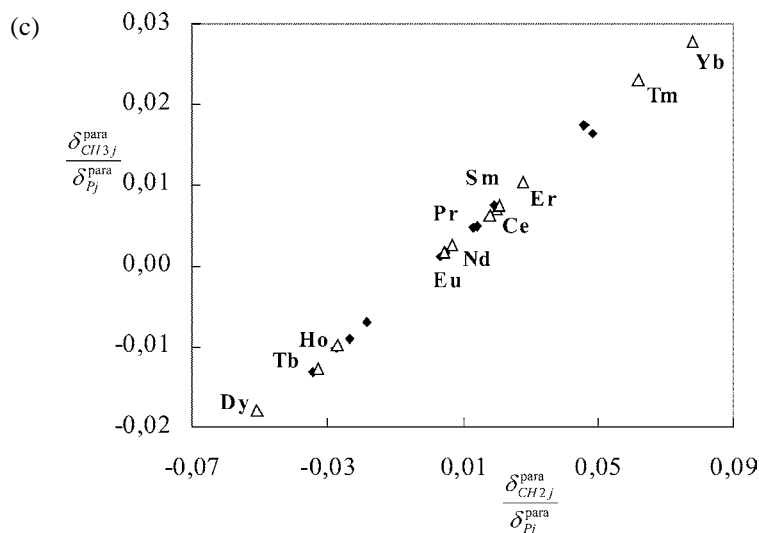


Fig. 39. Continued.

some of the combinations of nuclei used in the plots. Thus, it is important to analyse all the possible combinations.

3.2.2. $[R(L^{10}-4H)]^-$ ($L^{10} = 1,4,7,10$ -tetraazacyclododecane- N,N',N'',N''' -tetraacetic acid)

The eight donor atoms of the macrocyclic ligand L^{10} (usually known as DOTA) may produce square antiprismatic eight-coordinated structures, with the four ring nitrogens defining one of the square faces in the coordination polyhedron and the four coordinated pendant arm oxygens defining the other one (fig. 40). The twist angle α between the planes formed by the four oxygens and the four nitrogens can be positive or negative, leading to two possible isomers, the square antiprismatic (SAP) (designated M') and the inverted SAP (m'). In these two isomers, the macrocyclic rings have the same conformation and the difference between them is in the layout of the pendant arms. In these structures two structurally independent elements of chirality are present defined by the pendant arm $C_4-C_3-N-C_1$ and ring $N-C_1-C_2-N$ torsion angles (fig. 41). The 12-membered macrocyclic ring may adopt two enantiomeric square [3333] conformations, given as $\delta\delta\delta\delta$ and $\lambda\lambda\lambda\lambda$ (with respect to each five-membered ring chelate), and the pendant arms may be arranged in either a clockwise (Δ) or counterclockwise (Λ) manner, leading to four possible stereoisomers. These constitute two diastereoisomers each with enantiomeric pairs which are not distinguishable by NMR spectroscopy in solution: M' with enantiomers $\Lambda(\delta\delta\delta\delta)$ and $\Delta(\lambda\lambda\lambda\lambda)$, and m' with enantiomers $\Delta(\delta\delta\delta\delta)$ and $\Lambda(\lambda\lambda\lambda\lambda)$ (fig. 42).

X-ray crystal structures have been determined for a series of $[R(L^{10}-4H)]^-$ chelates, defining nine-coordinate capped square antiprismatic (CSAP) or inverted capped square antiprismatic structures. The acetate arms of the L^{10} or DOTA ligand are arranged in a propeller-like fashion above the basal plane made up of the four N donor atoms, which encompass the

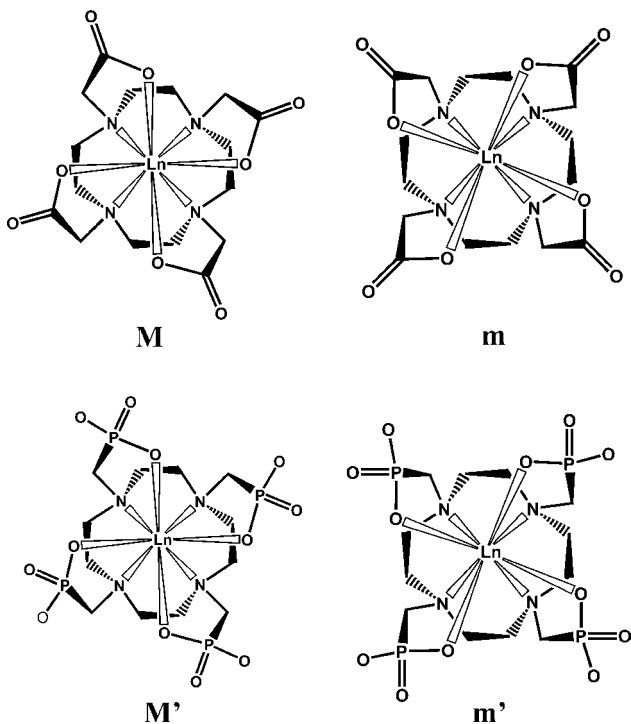


Fig. 40. Schematic representation of the M and m isomers, as well as of the M' and m' isomers, for tetraazamacrocyclic complexes of R(III) (adapted from Geraldes et al. (2003)).

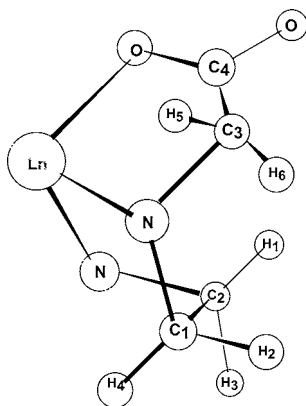


Fig. 41. Model of a part of the structure of complexes $[R(L^{10}-4H)]^{-}$ in the $\Delta(\lambda\lambda\lambda)$ enantiomeric form of the M isomer. Symmetry-related atoms are not shown for clarity. The numbering scheme for hydrogen and carbon/phosphorous atoms is also shown. H5 denotes the pro-R and H6 the pro-S pendant arm methylene proton (adapted from Ren et al. (2002)).

$R(III)$ ion, defining another plane above it, and thereby generating a C_4 symmetry axis in these complexes. The X-ray structures of the $[R(L^{10}-4H)]^{-}$ complexes with $R = \text{Eu, Gd, Y}$ and Lu are CSAP, with twist angles α of $ca\ 39^\circ$ (Spirlet et al., 1984; Dubost et al., 1991; Chang et al., 1993; Parker et al., 1994; Aime et al., 1996; Benetollo et al., 1999), whereas the La complex adopts an inverted CSAP structure in which $\alpha = -22^\circ$ (Aime et al., 1997a). The

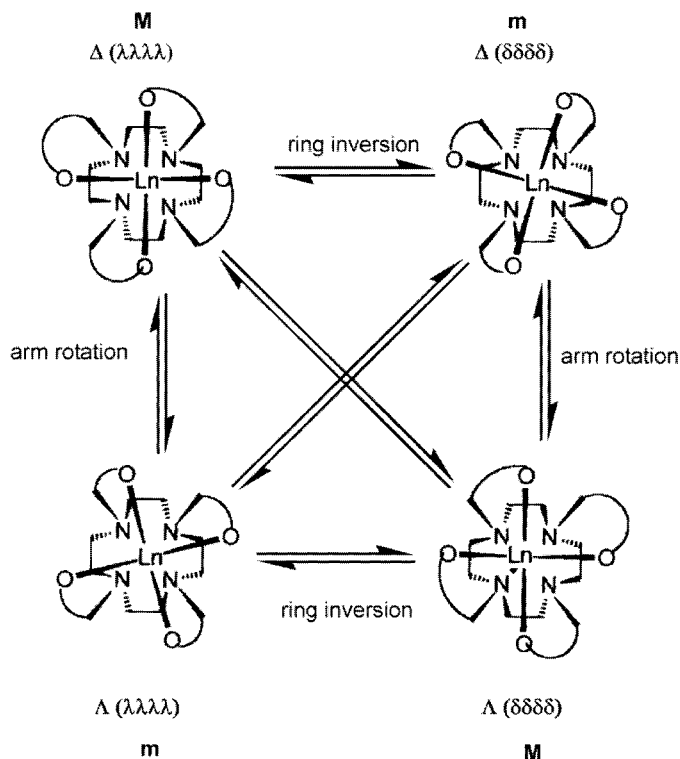


Fig. 42. Schematic representation of the structures and dynamics of $[R(L^{10}-4H)]^-$ complexes, looking down along the *R*-water O bond. The water molecule is omitted for clarity (adapted from Frulano et al. (2002)).

numbering scheme for the hydrogen and carbon atoms is shown in fig. 41, which schematically represents part of the structure of the complexes in the $\Delta(\lambda\lambda\lambda\lambda)$ enantiomeric form of the **M** isomer, where H5 denotes the pro-*R* and H6 the pro-*S* pendant arm methylene protons. This notation is in agreement with solution NMR work for the L^{10} (DOTA) complexes (Aime et al., 1992b; Marques et al., 1995).

The ^1H and ^{13}C NMR spectra of the $[R(L^{10}-4H)]^-$ ($R = \text{La-Lu}$, except Pm and Gd) complexes in D_2O at $\text{pH} = 7$ at different temperatures have been published and the LIS values for both ^1H and ^{13}C nuclei were reported (Desreux, 1980; Aime et al., 1992a, 1992b, 1997b; Hoeft and Roth, 1993; Marques et al., 1995). The ^1H and ^{13}C NMR spectra exhibit two sets of resonances corresponding to the presence of two slowly interconverting coordination isomers, one set of resonances having constantly larger frequency shifts than the other group. The isomer displaying larger shifts corresponds to a nine-coordinate CSAP structure **M**, while the isomer displaying smaller shifts is either a nine-coordinate inverted CSAP **m** (from La to Ho), or an eight-coordinate inverted SAP **m'** structure (Er to Lu) (Aime et al., 1992a, 1992b, 1997b). In addition to the frequency difference, the two isomers also differ in population. The relative intensities observed for the two sets of NMR resonances showed that while the **m** isomer dominates for the larger cations, La–Nd, the **M** isomer becomes the most stable for the smaller cations Sm–Ho, with a gradual increase of the **M**/**m** ratio from

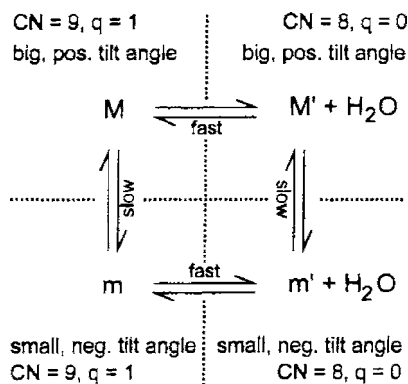


Fig. 43. Conformational and coordination equilibria for the $[R(L^{10-4H})]^-$ complexes in aqueous solution (adapted from Aime et al. (1997a)).

La to Ho. In all these cases, the isomerization process is purely conformational, as shown by the near zero reaction volumes obtained by high-pressure NMR (Aime et al., 1997b). Then, a steady decrease of the M population occurs from Er to Lu. The large positive isomerization volumes obtained show that the minor isomer results now from a fast water dissociation process superimposed on the conformational rearrangement leading to an eight-coordinate square antiprismatic (SAP) geometry, m' and a decrease of the M/ m' ratio (fig. 43) (Aime et al., 1997b). Besides the size of the $R(\text{III})$ ion, the relative concentrations of the two species, also depend on temperature, pressure and on the concentration of added inorganic salts. High concentrations of non-coordinating salts stabilize the m form relative to M.

The solution structure of the CSAP isomer M is consistent with the X-ray crystal structures of the Eu, Gd, Y, Ho and Lu complexes of L^{10} , while the structure of the inverted CSAP isomer is consistent with the X-ray structures of its La complex. This similarity between the solid state and the solution structures of the isomers was initially shown by the excellent agreement between the Yb induced ^1H shifts (of the M isomer), which are assumed to be almost purely of pseudocontact origin (eq. (29)), and shifts calculated from the X-ray structure of the Eu complex, applying the axial model, since that structure has a C_4 symmetry axis (Desreux, 1980). Later, this approach was extended to the shifts of the m' isomer of the Yb complex, supported by the comparison of the experimental distances between the $R(\text{III})$ ion and the ligand protons in the M and m' isomers of the Tb–Yb complexes, evaluated through the Curie relaxation contribution (eqs. (15)–(17)), and calculated from structural models (Aime et al., 1992a, 1992b). It was concluded that the structure of the macrocyclic rings is the same in both isomers, and that the difference between the two is in the layout of the acetate arms. This difference in the arrangement of the acetates leads to a twisted capped square antiprismatic structure (twisted or inverted CSAP) which contains a layout of the acetate arms that is inverted with respect to that in the main isomer, corresponding to a negative and smaller twist angle between the N_4 and O_4 planes. The use of variable temperature ^{13}C NMR on the Nd^{3+} -complex and ^1H EXSY on the Yb-complex (Aime et al., 1992b), and for the Eu and Yb complexes (Hoeft and Roth, 1993), demonstrated the exchange processes occurring between the isomers in solution. The dynamics of this system is summarized in fig. 42. The four stereoisomers (two pairs of enantiomers) can interconvert in solution by either ring inversion ($(\delta\delta\delta\delta) \rightleftharpoons (\lambda\lambda\lambda\lambda)$) or ac-

etate arm rotation ($\Delta \rightleftharpoons \Lambda$). Either process alone results in exchange between the CSAP and twisted CSAP geometries and both processes combined, either in succession or concerted, result in an exchange between enantiomeric pairs (see fig. 42). A thorough quantitative analysis of variable temperature ^1H EXSY and variable temperature ^{13}C NMR studies were performed on $[\text{Yb}(\text{L}^{10})]^-$ by completely solving the dynamic matrix (Jacques and Desreux, 1994). It was shown that each species in the dynamic equilibrium is exchanging with all other species and that, for this system, arm rotation is faster than ring inversion, reflecting the high rigidity of the $R(\text{III})$ complexes of DOTA.

The ^1H and ^{13}C LIS data available for the M and m isomers of the $[\text{R}(\text{L}^{10}-4\text{H})]^-$ complexes were analyzed by plots of $\delta_{ij}^{\text{para}}/\langle S_z \rangle_j$ vs $C_j/\langle S_z \rangle_j$ (eq. (48)) and $\delta_{ij}^{\text{para}}/C_j$ vs $\langle S_z \rangle_j/C_j$ (eq. (49)) (Ren et al., 2002). Because Sm, as usual, was excluded from these plots, and, due to population limitations, ^1H and ^{13}C LIS values of the M isomer were only available for $R = \text{Nd}-\text{Eu}$ in the first half of the lanthanide series, and ^{13}C LIS values for m in the second half of the series were only available for Yb (m'), in these cases not enough $R(\text{III})$ data were available for a definite conclusion. However, with the available data, breaks between light and heavy lanthanide ions were observed in most of these plots (see fig. 44 for some examples), as reported before (Marques et al., 1995), reflecting variations of the contact F_i and pseudo-contact $B_0^2 G_i$ parameters. Systematic deviations were also observed for Tm and Yb from the linear correlations defined by the other $R(\text{III})$ ions within the second half of the series. The linear correlation coefficient R^2 and the values of F_i and $B_0^2 G_i$ were evaluated for each proton and ^{13}C nucleus using those equations by subdivision of the lanthanides into two subgroups (Ce–Eu and Tb–Yb) and without such a subdivision (Ce–Yb) (table 16). All the protons and ^{13}C nuclei of the m isomer show poor linear correlations for the (Ce–Yb) data ($R^2 < 0.83$), which, due to the breaks, improve significantly when the data is divided in two groups, although the deviations at Tm and Yb give relatively low R^2 values except for H1, H5 and H6 of the m isomer, where the improvement is much better ($R^2 \sim 0.94-0.97$ for (Tb–Yb)). The M isomer shows less significant breaks, as $0.98 > R^2 > 0.92$ for (Ce–Yb) does not improve much in the (Tb–Yb) data.

The same sets of LIS data were also plotted according to eq. (51), as $\delta_{ij}^{\text{para}}/\langle S_z \rangle_j$ vs $\delta_{kj}^{\text{para}}/\langle S_z \rangle_j$, which eliminate the effect of any changes of B_0^2 (fig. 45). These plots again often do not follow a single linear correlation, but show breaks between light and heavy lanthanide ions, although much less significant than for the previous plots. The R_{ik} and $(F_i - R_{ik} F_k)$ parameters were evaluated using that equation by subdivision of the lanthanides into two subgroups (Ce–Eu and Tb–Yb) and without such a subdivision. Their values (and R^2 values) are shown in table 17. Without subdivision, the (Ce–Yb) data gave poor R^2 values for H2, H3, C2 and C4, good R^2 values for H4 and C3, and very good R^2 values (> 0.99) for H5 and H6. For all the complexes studied, R^2 values for all nuclei improved upon separation of the data in two groups (e.g., (Tb–Yb) data gave $R^2 > 0.985$ in all cases), but the breaks are only statistically significant for H4, H3, H2, C4 and C2. The R_{ik} and $(F_i - R_{ik} F_k)$ parameters evaluated directly with eq. (51) (table 17) and indirectly using the F_i and $B_0^2 G_i$ values from eq. (48) (table 16) were compared. The agreement is extremely good for all the R_{ik} ratios and only reasonably good for $(F_i - R_{ik} F_k)$, due to larger errors in the calculated F_i values.

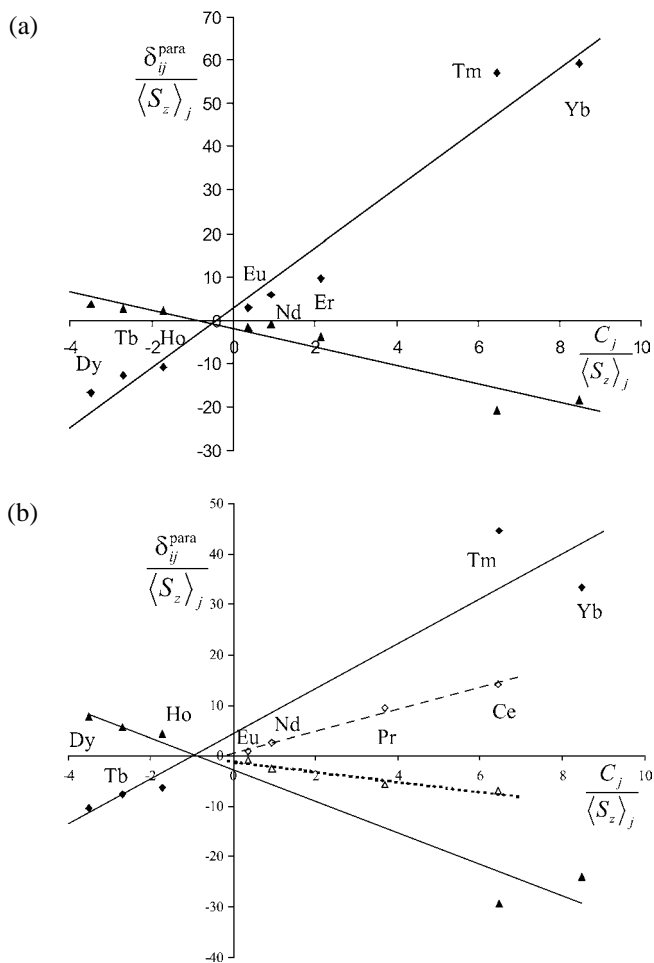


Fig. 44. Plots of $\delta_{ij}^{\text{para}}/\langle S_z \rangle_j$ vs $C_j/\langle S_z \rangle_j$ for H4 (◆) and H6 (▲) of (a) M isomer ($R = \text{Nd–Yb}$); (b) m/m' isomer ($R = \text{Ce–Yb}$) of $[\text{R}(\text{L}^{10}\text{-4H})]^-$ (D_2O , $\text{pH} = 7$, adapted from Geraldes et al. (2003)).

The breaks observed in these plots indicate that the F_i and R_{ik} parameters change at the middle of the series, together with changes of B_0^2 . The breaks of the plots according to eq. (51) are smaller relative to the plots according to eq. (48) because of the absence of B_0^2 in the later plots, as well as the presence of geometric ratios R_{ik} , which may be significantly less affected by smaller structural effects on G_i values due to the lanthanide contraction (Ren et al., 2002).

Various plots of $\delta_{ij}^{\text{para}}/\delta_{kj}^{\text{para}}$ vs $\delta_{lj}^{\text{para}}/\delta_{kj}^{\text{para}}$ (eq. (53)) were made for the ^{13}C shifts of the M isomer. With $i = \text{C3}$ or C4 , $l = \text{C1}$ and $k = \text{C2}$, single straight lines are obtained along the R ($R = \text{Pr, Nd, Sm, Eu, Tb, Dy, Ho, Er, Yb}$) series. For example, for $i = \text{C4}$, a good linear correlation with $R^2 = 0.999$ is obtained (fig. 45b) with $\alpha = -2.408$ and $\beta = 2.799$ values (table 18). Other plots of this type give a single line along the R series, such as for $i = \text{C2}$, $l = \text{C1}$ and $k = \text{C3}$, but other combinations give more or less pronounced breaks, such as for

Table 16

Computed values for contact (F_i), pseudo-contact ($B_0^2 G_i$) terms and R^2 values, according to eq. (48), for ^1H - and ^{13}C -nuclei in complexes $[\text{R}(\text{L}^{10}\text{-4H})^-]$, for the M isomer ($R = \text{Nd-Yb}$) and m/m' isomer ($R = \text{Ce-Yb}$) (D_2O , $\text{pH} = 7$, Ren et al. (2002)). See fig. 41 for the atom-numbering scheme

Compd		H1	H2	H3	H4	H5	H6
M isomer	F_i	-0.48	-0.49	-1.41	0.95	-0.78	-2.15
$R = \text{Nd-Eu}^{\text{a}}$	$B_0^2 G_i$	-1.48	0.40	1.48	5.27	-3.05	1.37
	R^2	1.000	1.000	1.000	1.000	1.000	1.000
Compd		H1	H2	H3	H4	H5	H6
M isomer	F_i	-2.14	-0.63	-0.25	3.77	-3.37	-2.53
$R = \text{Tb-Yb}^{\text{b}}$	$B_0^2 G_i$	-2.64	1.01	1.20	6.88	-4.75	-2.13
	R^2	0.934	0.983	0.984	0.969	0.943	0.938
Compd		H1	H2	H3	H4	H5	H6
m isomer	F_i	-0.52	-0.59	-1.09	0.53	-0.41	-1.18
$R = \text{Ce-Eu}^{\text{a}}$	$B_0^2 G_i$	-0.68	-0.12	0.39	2.19	-0.51	-0.98
	R^2	0.947	0.115	0.832	0.989	0.968	0.923
Compd		H1	H2	H3	H4	H5	H6
m isomer	F_i	-2.04	-0.47	-0.08	4.50	-1.95	-2.75
$R = \text{Tb-Yb}^{\text{b}}$	$B_0^2 G_i$	-1.77	0.64	0.76	4.45	-1.50	-3.10
	R^2	0.963	0.548	0.871	0.919	0.971	0.943
Compd		C1	C2	C3	C4		
M isomer	F_i	-0.10	2.54	5.51	3.56		
$R = \text{Nd-Eu}^{\text{a}}$	$B_0^2 G_i$	8.51	1.59	-8.39	-2.94		
	R^2	1.000	1.000	1.000	1.000		
Compd		C1	C2	C3	C4		
M isomer	F_i	3.63	3.27	2.53	-1.54		
$R = \text{Tb-Yb}^{\text{b}}$	$B_0^2 G_i$	4.09	1.11	-4.68	-6.70		
	R^2	0.979	0.959	0.940	0.985		
Compd		C1	C2	C3	C4		
m isomer	F_i	4.64	3.33	1.87	2.41		
$R = \text{Ce-Eu}$	$B_0^2 G_i$	4.93	2.59	0.23	0.42		
	R^2	0.985	0.984	0.050	0.166		

^aValues for the first isostructural series (except Sm).

^bValues for the second isostructural series.

$i = \text{C4}$, $l = \text{C1}$ and $k = \text{C3}$, and for $i = \text{C2}$ or C3 , $l = \text{C1}$ and $k = \text{C4}$ (see table 17 for the experimental α and β values, Geraldès et al. (2003)). This is in agreement with the detected changes of F_i and G_i parameters at the middle of the R series and again illustrates the fact that in this case still some of the plots according to eq. (53) may be accidentally linear. In the case of the ^{13}C shifts of the m isomer, the data available only for Pr, Nd and Eu gives linear plots within the first half of the R series (see table 18).

Plots of $\delta_{ij}^{\text{para}}/\delta_{kj}^{\text{para}}$ vs $\delta_{lj}^{\text{para}}/\delta_{kj}^{\text{para}}$ (eq. (53)) obtained for the ^1H LIS data of the M and m isomers, e.g., for $i = \text{H3}$, H5 and H6 , $l = \text{H1}$ and $k = \text{H4}$ support these conclusions (see fig. 45c for the m isomer). All these plots show two linear parts with breaks in the middle of the series and table 18 compares the α and β values calculated for the two isomers.

Table 17

Comparison of R_{ik} and $(F_i - R_{ik}F_k)$ parameters calculated directly according to eq. (51), with those obtained from the F_i and $B_0^2G_i$ values obtained from eq. (48) (table 16) for the ^1H - and ^{13}C -nuclei in complexes $[R(\text{L}^{10}\text{-4H})]^-$, for the M isomer ($R = \text{Nd}\text{-Yb}$) and m/m' isomer ($R = \text{Ce}\text{-Yb}$) (D_2O , pH = 7, Ren et al. (2002)). See fig. 41 for the atom-numbering scheme

Compd		H2-H1	H3-H1	H4-H1	H5-H1	H6-H1	C2-C1	C3-C1	C4-C1
M isomer	R_{ik} (exp)	-0.27	-1.00	-3.56	2.06	-0.93	0.19	-0.99	-0.35
$R = \text{Pr}\text{-Eu}^{\text{a}}$	$(F_i - F_k R_{ik})$ (exp)	-0.62	-1.89	-0.78	0.22	-2.60	2.56	5.42	3.52
	R^2	0.960	0.973	0.989	0.999	0.997	1.000	1.000	1.000
	R_{ik} (calc)	-0.27	-1.00	-3.56	2.06	-0.93	0.19	-0.99	-0.35
	$(F_i - F_k R_{ik})$ (calc)	-0.62	-1.62	-0.75	0.21	-2.60	2.56	5.42	3.53
Compd		H2-H1	H3-H1	H4-H1	H5-H1	H6-H1	C2-C1	C3-C1	C4-C1
M isomer	R_{ik} (exp)	-0.37	-0.44	-2.56	1.79	0.81	0.26	-1.15	-1.63
$R = \text{Tb}\text{-Yb}^{\text{b}}$	$(F_i - F_k R_{ik})$ (exp)	-1.34	-1.10	-1.42	0.42	-0.84	2.36	6.77	4.33
	R^2	0.963	0.972	0.990	0.999	0.999	0.924	0.977	0.998
	R_{ik} (calc)	-0.38	-0.45	-2.61	1.80	0.81	0.27	-1.14	-1.64
	$(F_i - F_k R_{ik})$ (calc)	-1.44	-1.21	-1.82	0.48	-0.80	2.29	6.67	5.05
Compd		H2-H1	H3-H1	H4-H1	H5-H1	H6-H1	C2-C1	C3-C1	C4-C1
m isomer	R_{ik} (exp)	-0.42	-0.59	-3.12	0.73	1.46	0.53	0.07	0.11
$R = \text{Ce}\text{-Eu}^{\text{a}}$	$(F_i - F_k R_{ik})$ (exp)	-1.29	-1.43	-0.90	-0.05	-0.39	0.89	1.36	1.72
	R^2	0.871	0.941	0.980	0.988	0.998	1.000	0.118	0.267
	R_{ik} (calc)	0.18	-0.57	-3.22	0.75	1.44	0.53	0.05	0.09
	$(F_i - F_k R_{ik})$ (calc)	-0.50	-1.39	-1.14	-0.02	-0.43	0.87	1.63	1.99
Compd		H2-H1	H3-H1	H4-H1	H5-H1	H6-H1	C2-C1	C3-C1	C4-C1
m isomer	R_{ik} (exp)	-0.37	-0.44	-2.57	0.85	1.77	^c	^c	^c
$R = \text{Tb}\text{-Yb}^{\text{b}}$	$(F_i - F_k R_{ik})$ (exp)	-12.4	-1.02	-0.85	-0.23	-0.90	^c	^c	^c
	R^2	0.979	0.966	0.990	0.999	0.997	^c	^c	^c
	R_{ik} (calc)	-0.36	-0.43	-2.51	0.85	1.75	^c	^c	^c
	$(F_i - F_k R_{ik})$ (calc)	-1.20	-0.96	-0.62	-0.22	-0.82	^c	^c	^c

^a Values for the first isostructural series (except Sm).

^b Values for the second isostructural series.

^c Not determined.

3.2.3. $[R(\text{L}^{11})]^{3+}$ ($\text{L}^{11} = 1,4,7,10\text{-tetraazacyclododecane}$ -1,4,7,10-tetrakis(*N,N*-diethylacetamide))

Although no crystal structure is available for any of the $[R(\text{L}^{11})]^{3+}$ complexes, where L^{11} is the DOTA-like tertiary tetraamide derivative DOTEA, the known crystal structures of $R(\text{III})$ complexes for various DOTA-like achiral primary and secondary tetraamide derivatives (fig. 46) are available. These structures are variable, with m structures for $[\text{La}(\text{DOTAM})(\text{H}_2\text{O})]^{3+}$ (Morrow et al., 1993) and $[\text{Eu}(\text{DOTAM})(\text{H}_2\text{O})]^{3+}$ (Amin et al., 1994) (twist angles between the planes of the O_4 and N_4 atoms of -26.5° and -30° , respectively), and M structures for $[\text{R}(\text{DTMA})(\text{H}_2\text{O})]^{3+}$ ($R = \text{Gd}, \text{Dy}$, twist angles of *ca* 40°) (Bianchi et al., 2000; Aime et al., 1999b). However, in solution it was found that the m/M isomer ratio increased from 0.19 for $[\text{Eu}(\text{DOTA})]^-$, to 0.25 for the primary tetraamide derivative $[\text{Eu}(\text{DOTAM})]^{3+}$, to 0.31 for the secondary tetraamide $[\text{Eu}(\text{DTMA})]^{3+}$, and to 2 for the tertiary tetraamide $[\text{Eu}(\text{DOTTA})]^{3+}$, indicating that increasing steric demand at the bound metal ion favors the inverted square antiprismatic structure m (Aime et al., 1999b).

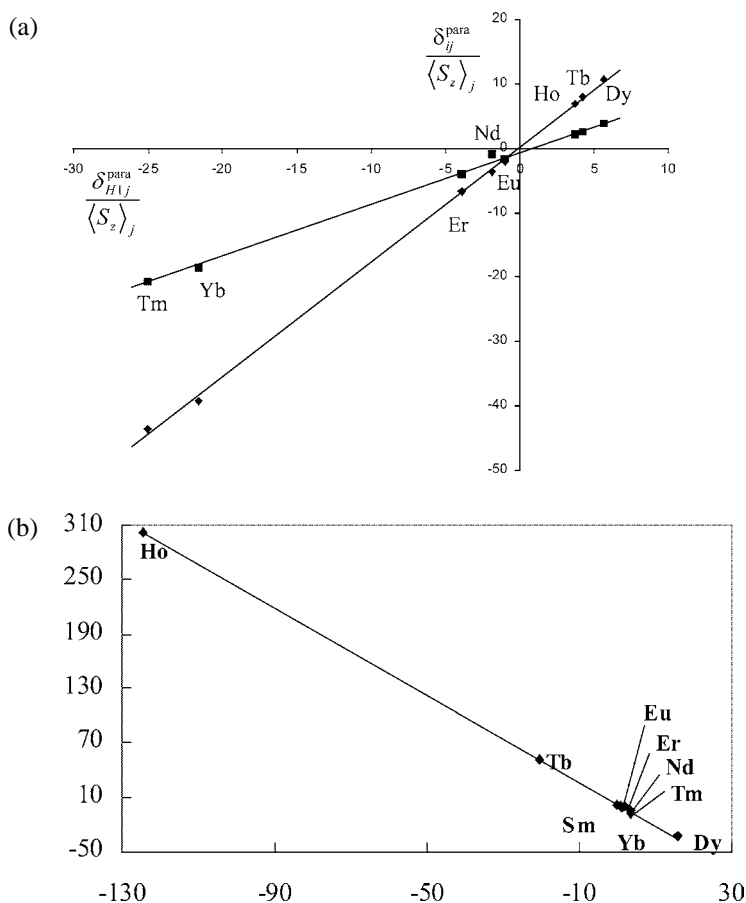


Fig. 45. (a) Crystal-field independent plots of $\delta_{ij}^{\text{para}}/\langle S_z \rangle_j$ vs $\delta_{kj}^{\text{para}}/\langle S_z \rangle_j$ for the H5–H1 (◆) and H6–H1 (■) pairs of the M isomer; Plots of $\delta_{ij}^{\text{para}}/\delta_{kj}^{\text{para}}$ vs $\delta_{Hij}^{\text{para}}/\delta_{Hkj}^{\text{para}}$; (b) for the C4, C1, C2 triad of the M isomer; (c) for the H_i , H_1 , H_4 triads ($H_i = H_3$ (◆), H_5 (▲), H_6 (●)) of the m isomer ($[R(L^{10}\text{-}4\text{H})]^-$, D_2O , $\text{pH} = 7$, adapted from Geraldes et al. (2003)).

The ^1H and ^{13}C LIS values of the $[R(L^{11})]^{3+}$ ($R = \text{Ce}–\text{Yb}$ except Pm and Gd) complexes, were obtained in CD_3CN at 253 K (the ^{13}C LIS data are available only for Pr , Nd , Sm and Eu complexes) (Forsberg et al., 1995), where only one set of NMR signals was found in solution. The ^1H LIS data were first analysed using plots of $\delta_{ij}^{\text{para}}/\langle S_z \rangle_j$ vs $C_j/\langle S_z \rangle_j$ (eq. (48)) and $\delta_{ij}^{\text{para}}/C_j$ vs $\langle S_z \rangle_j/C_j$ (eq. (49)). The shift data for the Tm complex significantly deviated from those of other complexes, and the plots showed breaks near the middle of the lanthanide series, reflecting variations of the F_i and $B_0^2G_i$ parameters. The geometric factor values derived from the two subgroups differed by as much as 30% for the six protons located three bonds

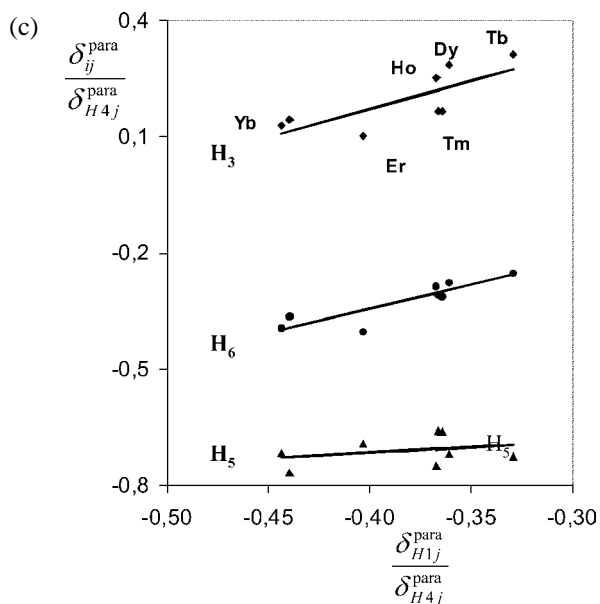
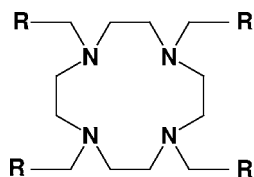


Fig. 45. Continued.



R = CONH₂ **DOTAM**
R = CONHMe **DTMA**
R = CONMe₂ **DOTTA**
R = CONEt₂ **DOTEA : L¹¹**

Fig. 46. Chemical structure of various DOTA-like tetramide derivative ligands.

away from the lanthanide ions (H1–H6) and the corresponding differences in the hyperfine coupling constant were as much as 600% (Forsberg et al., 1995). The ¹H LIS data were also analysed taking the magnetic anisotropy constant $D_1 = (\chi_{zz} - (1/3)\text{Tr}\chi) = C_j B_0^2$ as a variable and comparing the data with the geometric factor values obtained from a structure of these complexes derived by a MM2 calculation using specified geometric restrictions. This calculated structure was of the CSAP (M) type, with a twist angle of 47° between the planes of the O₄ and N₄ atoms. The results further suggested a significant difference in G_i values between the light and heavy $[R(L^{11})]^{3+}$ complexes. The derived $(\chi_{zz} - (1/3)\text{Tr}\chi)$ values for the series of $[R(L^{11})]^{3+}$ complexes did not follow the trend of Bleaney's C_j constants, which was interpreted as due to a change of the crystal field parameter B_0^2 along the lanthanide series, with the largest value for Tm.

Table 18

Comparison of α and β parameters calculated directly according to eq. (53), with those obtained from the F_i and $B_0^2G_i$ values obtained from eq. (48) (table 16) for the ^1H - and ^{13}C -nuclei in complexes $[\text{R}(\text{L}^{10}\text{-4H})]^-$, for the M isomer ($R = \text{Nd-Yb}$) and m/m' isomer (Ce-Yb) (D_2O , pH = 7, Ren et al. (2002), Gerales et al. (2003)). See fig. 41 for the atom-numbering scheme

Compd		$k = \text{H4}; l = \text{H1}$				$k = \text{C2}; l = \text{C1}$		$k = \text{C3}; l = \text{C1}$	$k = \text{C4}; l = \text{C1}$	
		$i = \text{H2}$	$i = \text{H3}$	$i = \text{H5}$	$i = \text{H6}$	$i = \text{C3}$	$i = \text{C4}$	$i = \text{C2}$	$i = \text{C2}$	$i = \text{C3}$
M isomer	$\alpha(\text{exp})$	c	c	c	c	-2.04	-2.41	0.67	c	c
$R = \text{Pr-Eu}^{\text{a}}$	$\beta(\text{exp})$	c	c	c	c	2.50	2.80	0.42	c	c
	R^2	c	c	c	c	0.999	1.00	0.98	c	c
Compd		$i = \text{H2}$	$i = \text{H3}$	$i = \text{H5}$	$i = \text{H6}$	$i = \text{C3}$	$i = \text{C4}$	$i = \text{C2}$	$i = \text{C2}$	$i = \text{C3}$
M isomer	$\alpha(\text{exp})$	3.11	2.17	0.80	3.00	-2.04	-2.41	0.67	1.43	0.64
$R = \text{Tb-Yb}^{\text{b}}$	$\beta(\text{exp})$	1.28	0.97	-0.37	0.80	2.50	2.80	0.42	0.59	1.13
	R^2	0.975	0.976	0.976	0.97	0.999	1.00	0.98	0.712	0.50
Compd		$k = \text{H4}; l = \text{H1}$				$k = \text{C3}; l = \text{C1}$				
		$i = \text{H2}$	$i = \text{H3}$	$i = \text{H5}$	$i = \text{H6}$	$i = \text{C2}$		$i = \text{C4}$		
m isomer	$\alpha(\text{exp})$	1.48	1.88	2.20	0.40	0.73		0.22		
$R = \text{Ce-Eu}^{\text{a}}$	$\beta(\text{exp})$	0.44	0.74	0.22	-0.12	-0.94		-0.39		
	R^2	0.67	0.93	1.00	0.98	0.98		0.72		
Compd		$k = \text{H4}; l = \text{H1}$				$k = \text{C3}; l = \text{C1}$				
		$i = \text{H2}$	$i = \text{H3}$	$i = \text{H5}$	$i = \text{H6}$	$i = \text{C2}$		$i = \text{C4}$		
m isomer	$\alpha(\text{exp})$	1.74	1.54	-0.01	1.25	c		c		
$R = \text{Tb-Yb}^{\text{b}}$	$\beta(\text{exp})$	0.86	0.80	-0.72	0.17	c		c		
	R^2	0.60	0.69	0.11	0.96	c		c		

^aValues for the first isostructural series (except Sm).

^bValues for the second isostructural series.

^cNot determined.

Despite this analysis of the observed LIS values, which led to a solution structure of these complexes of the CSAP (M) type, there is some conflicting evidence from the solution structure analysis of the other tertiary tetraamide complex $[\text{Eu}(\text{DOTTA})]^{3+}$, with a m/M isomer ratio of 2 (Aime et al., 1999b). Therefore we re-analyzed the ^1H LIS data, as well as the ^{13}C LIS data ($R = \text{Pr, Nd, Eu}$, excluding Sm) for the $[\text{R}(\text{L}^{11})]^{3+}$ complexes, first through plots of $\delta_{ij}^{\text{para}}/\langle S_z \rangle_j$ vs $C_j/\langle S_z \rangle_j$ (eq. (48)) and $\delta_{ij}^{\text{para}}/C_j$ vs $\langle S_z \rangle_j/C_j$ (eq. (49)) (Ren et al., 2002), and using the H5 and H6 assignments of fig. 41, which led to some re-assignments of the original data (Forsberg et al., 1995). Again breaks between light and heavy lanthanide ions were observed in most of those plots (see fig. 47) reflecting variations of the contact F_i and pseudo-contact $B_0^2G_i$ parameters. Systematic deviations were also observed for Tm and Yb from the linear correlations defined by the other $R(\text{III})$ ions within the second half of the series. The evaluated values of F_i and $B_0^2G_i$ (and R^2 values) are shown in table 19. The LIS data were also plotted according to eq. (51), as $\delta_{ij}^{\text{para}}/\langle S_z \rangle_j$ vs $\delta_{kj}^{\text{para}}/\langle S_z \rangle_j$, eliminating the effect of any changes of B_0^2 (fig. 48a). These plots again show much less significant breaks between light and heavy lanthanide ions than for the previous plots. The evaluated R_{ik} and $(F_i - R_{ik}F_k)$ parameters (and R^2 values) are shown in table 19. Again relative sensitivity of the nuclei to the breaks was $\text{H5, H6} \ll \text{H4} < \text{H2, H3}$. Their values evaluated directly by eq. (51) and indirectly

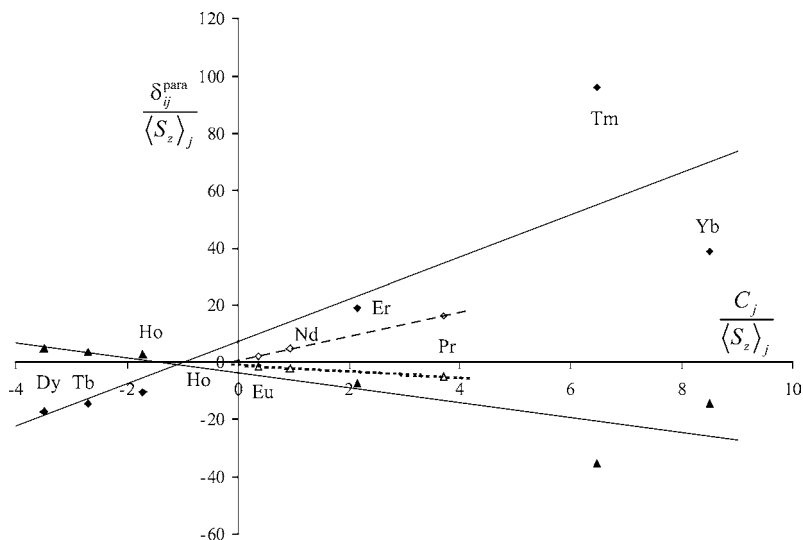


Fig. 47. Plots of $\delta_{ij}^{\text{para}}/\langle S_z \rangle_j$ vs $C_j/\langle S_z \rangle_j$ for H4 (◆) and H6 (▲) of $[R(L^{11})]^{3+}$ ($R = \text{Ce–Yb}$, D_2O , $\text{pH} = 7$, adapted from Forsberg et al. (1995), Geraldes et al. (2003)).

using the F_i and $B_0^2 G_i$ values from eq. (48) (table 19) gave extremely good agreement for all the R_{ik} ratios and only reasonably good for $(F_i - R_{ik} F_k)$. Still, the breaks observed in the plots indicate that the F_i and R_{ik} parameters change at the middle of the series, together with changes of B_0^2 .

Figure 48b shows ^1H LIS data plotted according to $\delta_{ij}^{\text{para}}/\delta_{kj}^{\text{para}}$ vs $\delta_{lj}^{\text{para}}/\delta_{kj}^{\text{para}}$ (eq. (53)) for $i = \text{H3, H5}$ and H6 , $l = \text{H1}$ and $k = \text{H4}$, which exhibit a break between the light (Pr–Eu) and the heavy lanthanide (Tb–Yb) complexes, thereby confirming the changes of the proton F_i and/or G_i parameters at the middle of the series. Table 19 summarizes the α and β values calculated from the ^1H LIS data of the $[R(L^{11})]^{3+}$ complexes for the light and heavy sub-series of lanthanide ions.

3.2.4. $[R(L^{12}-8\text{H})]^{5-}$ ($L^{12} = 1,4,7,10\text{-tetraazacyclododecane-1,4,7,10-tetrakis(methylenephosphonic acid)}$)

The ^1H , ^{13}C and ^{31}P LIS for the $[R(L^{12}-8\text{H})]^{5-}$ complexes (except $R = \text{Pm, Gd}$) (where $L^{12}-8\text{H}$ is DOTP^{8-} , the tetrakis(methylenephosphonate) analog of DOTA, fig. 40) have been reported at 298 K in D_2O at $\text{pH} = 10$ (Geraldes et al., 1992). Water ^{17}O NMR shift measurements of $[\text{Dy}(L^{12}-8\text{H})]^{5-}$ revealed that this complex lacks an inner-sphere water molecule (Ren and Sherry, 1996), which is in agreement with the crystal structure of the $[\text{Tm}(L^{12}-8\text{H})]^{5-}$ complex (Paulus et al., 1995), where the coordination polyhedron of Tm is described as a twisted square antiprism (TSAP), m^7 , with the four ring nitrogens defining one of its square faces and the four coordinated phosphonate oxygens defining the other one. Structurally very similar to the $[R(L^{10}-4\text{H})]^-$ complexes, the methylene phosphonate arms of the

Table 19

Computed values for contact (F_i), pseudo-contact ($B_0^2 G_i$) terms and R^2 values, according to eq. (48), comparison of R_{ik} and $(F_i - R_{ik} F_k)$ parameters calculated directly according to eq. (51), and α and β parameters calculated directly according to eq. (53), with those obtained from the above F_i and $B_0^2 G_i$ terms, for ^1H - and ^{13}C -nuclei in complexes $[\text{R}(\text{L}^{11})]^{3+}$ ($R = \text{Ce}-\text{Yb}$, D_2O , $\text{pH} = 7$, Forsberg et al. (1995), Ren et al. (2002), Geraldes et al. (2003)).

The stom-numbering scheme is similar to that of fig. 41

Compd		H1	H2	H3	H4	H5	H6		
$R = \text{Ce}-\text{Eu}^{\text{a}}$	F_i	-0.31	-1.18	-1.56	0.74	-1.56	-0.95		
	$B_0^2 G_i$	-1.43	0.80	0.62	4.15	0.62	-1.08		
	R^2	0.999	0.996	0.977	0.998	0.977	0.998		
Compd		H1	H2	H3	H4	H5	H6		
$R = \text{Tb}-\text{Yb}^{\text{b}}$	F_i	-4.06	0.05	-0.62	7.44	-0.62	-3.69		
	$B_0^2 G_i$	-3.28	1.17	0.90	7.38	0.90	-2.58		
	R^2	0.706	0.790	0.744	0.718	0.744	0.704		
Compd		C1	C2	C3	C4				
$R = \text{Ce}-\text{Eu}^{\text{a}}$	F_i	4.25	3.56	3.11	2.99				
	$B_0^2 G_i$	3.59	1.56	-2.44	-2.54				
	R^2	0.978	0.920	0.992	0.934				
Compd		C1	C2	C3	C4				
$R = \text{Tb}-\text{Yb}^{\text{b}}$	F_i	c	c	c	c				
	$B_0^2 G_i$	c	c	c	c				
	R^2	c	c	c	c				
Compd		H2-H1	H3-H1	H4-H1	H5-H1	H6-H1	C2-C1	C3-C1	C4-C1
$R = \text{Ce}-\text{Eu}^{\text{a}}$	$R_{ik}(\text{exp})$	-0.65	-0.52	-2.97	1.92	0.86	0.44	-0.66	-0.66
	$(F_i - F_k R_{ik})(\text{exp})$	-1.61	-1.95	-0.36	0.72	-0.42	1.62	5.75	5.55
	R^2	0.999	0.998	1.000	1.000	1.000	0.980	0.940	0.840
	$R_{ik}(\text{calc})$	-0.56	-0.43	-2.90	-0.43	0.76	0.43	-0.68	6.01
	$(F_i - F_k R_{ik})(\text{calc})$	-1.35	-1.69	-0.16	-1.69	-0.71	1.73	6.00	3.53
Compd		H2-H1	H3-H1	H4-H1	H5-H1	H6-H1	C2-C1	C3-C1	C4-C1
$R = \text{Tb}-\text{Yb}^{\text{b}}$	$R_{ik}(\text{exp})$	-0.33	-0.27	-2.27	1.61	0.79	c	c	c
	$(F_i - F_k R_{ik})(\text{exp})$	-1.20	-1.66	-1.49	1.04	-0.49	c	c	c
	R^2	0.986	0.994	0.999	1.000	1.000	c	c	c
	$R_{ik}(\text{calc})$	-0.36	-0.27	-2.25	-0.27	0.79	c	c	c
	$(F_i - F_k R_{ik})(\text{calc})$	-1.51	-1.72	-1.70	-1.72	-0.48	c	c	c
$k = \text{H4}; l = \text{H1}$									
Compd		$i = \text{H2}$	$i = \text{H3}$	$i = \text{H5}$	$i = \text{H6}$				
$R = \text{Ce}-\text{Eu}^{\text{a}}$	$\alpha(\text{exp})$	14.09	17.40	-0.35	8.01				
	$\beta(\text{exp})$	4.94	6.01	-0.72	2.42				
	R^2	0.934	0.926	0.015	0.94				
$k = \text{H4}; l = \text{H1}$									
Compd		$i = \text{H2}$	$i = \text{H3}$	$i = \text{H5}$	$i = \text{H6}$				
$R = \text{Tb}-\text{Yb}^{\text{b}}$	$\alpha(\text{exp})$	1.40	1.91	0.16	1.41				
	$\beta(\text{exp})$	0.78	0.98	-0.64	0.27				
	R^2	0.90	0.832	1.000	0.91				

^aValues for the first isostructural series (except Sm).

^bValues for the second isostructural series.

^cNot determined.

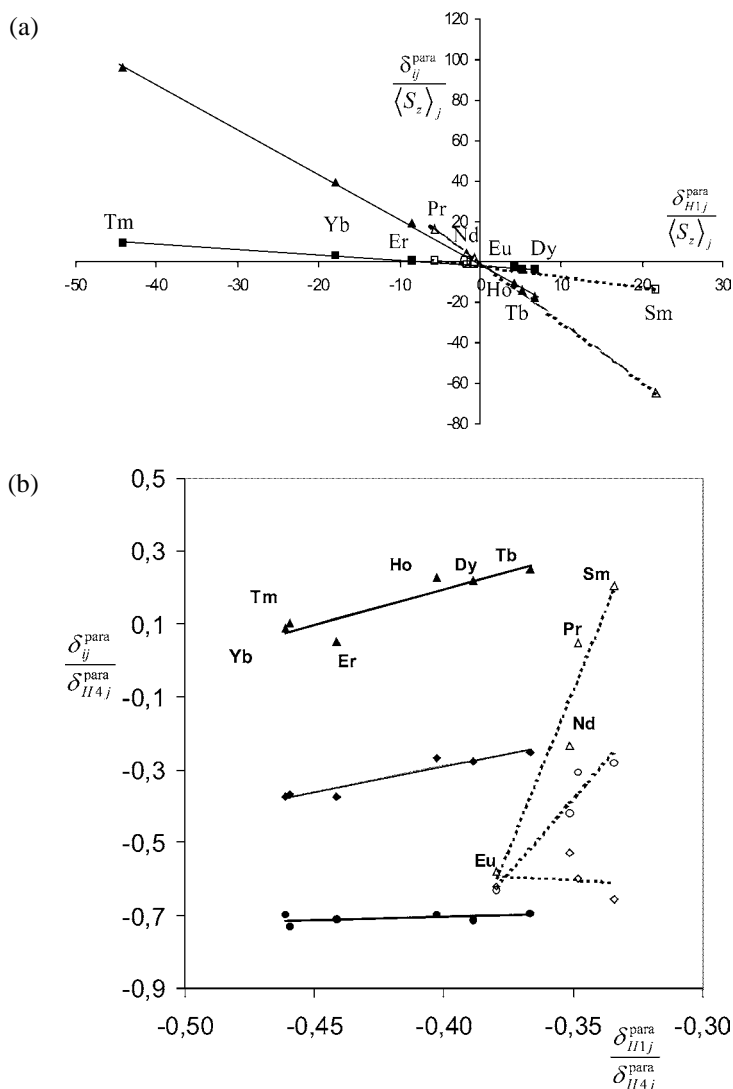


Fig. 48. (a) Plots of $\delta_{ij}^{para} / \langle S_z \rangle_j$ vs $\delta_{H1j}^{para} / \langle S_z \rangle_j$ for the H3–H1 (■) and H4–H1 (◆) pairs; (b) Plots of $\delta_{ij}^{para} / \delta_{H4j}^{para}$ vs $\delta_{H1j}^{para} / \delta_{H4j}^{para}$ for the H_i , H1, H4 triads ($H_i = H_3$ (▲), H_5 (●), H_6 (◆)) of $[R(L^{11})]^{3+}$ ($R = Ce\text{--}Yb$, D_2O , $pH = 7$, adapted from Geraldes et al. (2003)).

DOTP ligand are arranged in a propeller-like fashion above the basal plane made up of the four N donor atoms which encompass the $R(III)$ ion, thereby generating a C_4 symmetry axis in these complexes (fig. 40). Four of the residual negative charges are localized on the phos-

phonate oxygen atoms, which are directed away from the lanthanide coordination site with the fifth averaged over the bound oxygens in the coordination cage. These highly charged anionic complexes have four protonation steps over the pH range of 3–10, such that $[R(L^{12-7H})]^{4-}$ is the predominant species at pH = 7.4, leading to significantly pH dependent LIS values (Sherry et al., 1996). Thus, besides pH = 10, the LIS values at pH 7 and 3 were also analyzed. Unlike the DOTA complexes, only one set of resonances was observed in solution by 1H , ^{13}C and ^{31}P NMR for the $[R(L^{12-8H})]^{5-}$ complexes, which thus exist in solution as racemic mixtures, M' (square antiprism, SAP) ($\Delta(\delta\delta\delta\delta)$ and $\Delta(\lambda\lambda\lambda\lambda)$) or m' (twisted square antiprism, TSAP) ($\Delta(\delta\delta\delta\delta)$ and $\Delta(\lambda\lambda\lambda\lambda)$) (fig. 42), the two enantiomers of either case furnishing indistinguishable NMR signals at room temperature using conventional NMR techniques. Chiral NMR resolution, using the formation of diastereomeric adducts between the two enantiomers of $[R(L^{12-8H})]^{5-}$ and a chiral substrate, has provided indirect, albeit conclusive, evidence for the existence of these two enantiomers. The ion-pair interactions between $[R(L^{12-8H})]^{5-}$ and the chiral organic base, N-methyl-D-(-)-glucamine (MEG), were investigated using 1H , ^{13}C and ^{31}P NMR. Addition of MEG to a solution of $[Eu(L^{12-8H})]^{5-}$ lifted the signal degeneracy of the NMR spectra, resulting in doubling of the corresponding signals (Aime et al., 1999c). Similar spectral resolution in the 1H NMR spectrum of $[Eu(L^{12-8H})]^{5-}$ was achieved by the addition of the chiral transition metal complex, (+)-[Co(en) $_3$] $^{3+}$ (Sherry et al., 1996; Ren et al., 1997).

The 1H , ^{13}C and ^{31}P LIS data (pH = 10) were analysed by plotting the data for the $[R(L^{12-8H})]^{5-}$ according to eq. (48), $\delta_{ij}^{para}/\langle S_z \rangle_j$ vs $C_j/\langle S_z \rangle_j$, and eq. (49), δ_{ij}^{para}/C_j vs $\langle S_z \rangle_j/C_j$ (Geraldes et al., 1992). Breaks between light and heavy lanthanide ions were observed in those plots, reflecting variations of the contact F_i and pseudo-contact $B_0^2 G_i$ terms. Systematic deviations were also observed for Tm and Yb from the linear correlations defined by the other R(III) ions within the second half of the series. These parameters were evaluated from those plots by subdivision of the lanthanides into two subgroups (Ce–Eu and Tb–Yb) and without such a subdivision (but excluding the Tm data). In the initial analysis, the B_0^2 values were considered to be constant, and the G_i values, obtained without the lanthanide subdivision, were used together with distance ratios obtained from 1H NMR T_1 relaxation data. The geometric factors G_i for each nucleus were calculated from the minimized structure of $[R(L^{12-8H})]^{5-}$ using a MMX force field (average R–N and R–O bond lengths of 2.70 and 2.35 Å, respectively) and an axial symmetry model, as well as the R(III)-proton distance ratios. An optimum fit of the LIS and relaxation data was obtained for a SAP configuration, M' (Geraldes et al., 1992), in disagreement with the later reported m' single crystal structure of the $[Tm(L^{12-8H})]^{5-}$ complex (Paulus et al., 1995). However, in this NMR study the assignments of the H5 and H6 protons was opposite to the one adopted in the present review for all the tetraazamacrocyclic compounds (fig. 41), and therefore their reassignments have to be made. With this reassignment, the 1H and ^{13}C LIS data available for the $[R(L^{12-8H})]^{5-}$ complexes at pH = 10, 7 and 3 were reanalyzed (Ren et al., 2002). First, plots of $\delta_{ij}^{para}/\langle S_z \rangle_j$ vs $C_j/\langle S_z \rangle_j$ (eq. (48)) and δ_{ij}^{para}/C_j vs $\langle S_z \rangle_j/C_j$ (eq. (49)) were obtained, giving breaks at Tb (fig. 49), reflecting variations of F_i and $B_0^2 G_i$. The values obtained from these plots are shown in table 20. Then plots according to eq. (51), $\delta_{ij}^{para}/\langle S_z \rangle_j$ vs $\delta_{kj}^{para}/\langle S_z \rangle_j$, again show

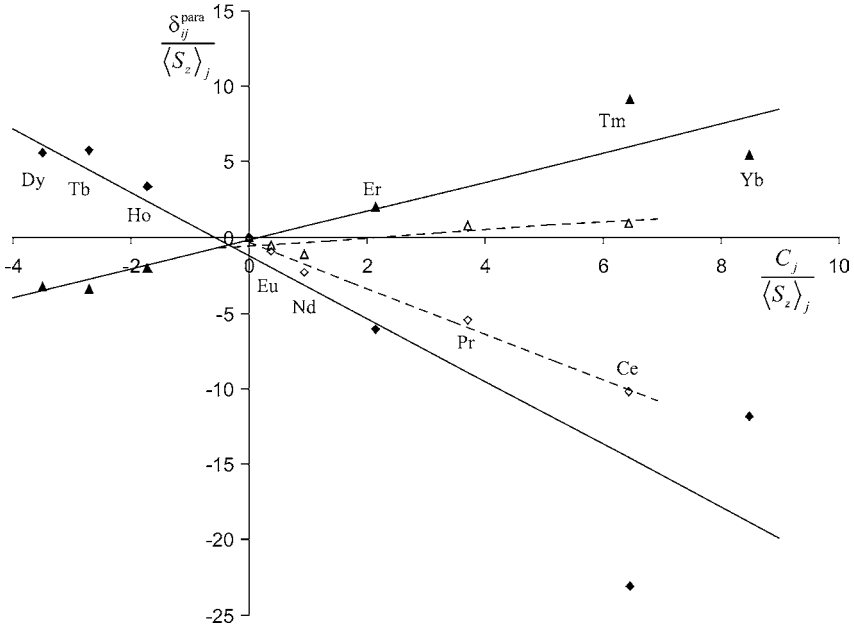


Fig. 49. Plots of $\delta_{ij}^{para} / \langle S_z \rangle_j$ vs $C_j / \langle S_z \rangle_j$ for H1 (◆) and H3 (▲) of $[R(L^{12}-8H)]^{5-}$ ($R = Ce-Yb, D_2O, pH = 10$, adapted from Ren et al. (2002)).

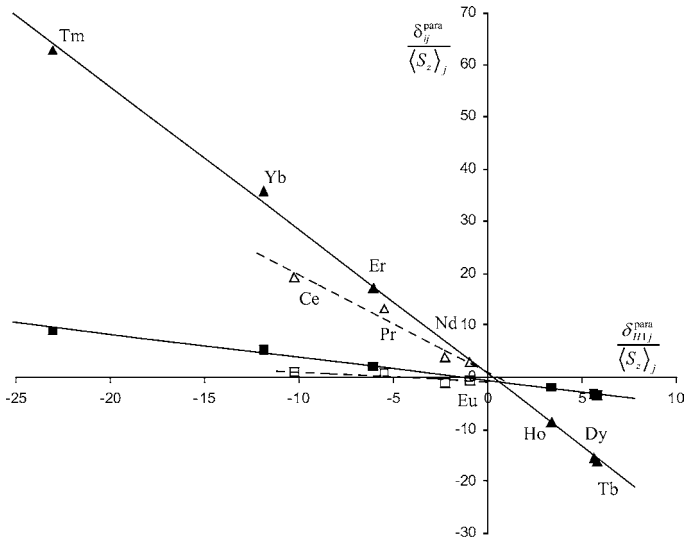


Fig. 50. Plots of $\delta_{ij}^{para} / \langle S_z \rangle_j$ vs $\delta_{H1j}^{para} / \langle S_z \rangle_j$ for the H3-H1 (■) and H4-H1 (▲) pairs of $[R(L^{12}-8H)]^{5-}$ ($R = Ce-Yb, D_2O, pH = 10$, adapted from Ren et al. (2002)).

Table 20

Computed values for contact (F_i), pseudo-contact ($B_0^2 G_i$) terms and R^2 values, according to eq. (48), comparison of R_{ik} and $(F_i - R_{ik} F_k)$ parameters calculated directly according to eq. (51), and α and β parameters calculated directly according to eq. (53), with those obtained from the above F_i and $B_0^2 G_i$ terms, for ^1H , ^{13}C and ^{31}P -nuclei in complexes $[\text{R}(\text{L}^{12}\text{-8H})]^{5-}$ ($R = \text{Ce-Yb}$, D_2O , $\text{pH} = 10$, Galdes et al. (1992, 2003), Ren et al. (2002). The atom-numbering scheme is similar to that of fig. 41

Compd		H1	H2	H3	H4	H5	H6		
$R = \text{Ce-Eu}^{\text{a}}$	F_i	-0.31	-0.44	-0.54	1.15	-0.36	-0.52		
	$B_0^2 G_i$	-1.52	0.47	0.26	2.95	-1.13	-2.80		
	R^2	0.991	0.831	0.643	0.985	0.983	0.998		
Compd		H1	H2	H3	H4	H5	H6		
$R = \text{Tb-Yb}^{\text{b}}$	F_i	-1.19	0.29	-0.15	3.75	-1.30	-2.49		
	$B_0^2 G_i$	-2.08	1.17	0.95	5.85	-1.65	-4.33		
	R^2	0.815	0.876	0.874	0.846	0.814	0.812		
Compd		C1	C2	C3	P				
$R = \text{Ce-Eu}^{\text{a}}$	F_i	3.99	2.98	1.71	4.34				
	$B_0^2 G_i$	2.28	0.92	-1.88	-1.06				
	R^2	0.990	0.985	0.999	0.796				
Compd		C1	C2	C3	P				
$R = \text{Tb-Yb}^{\text{b}}$	F_i	3.91	1.85	-1.15	-2.16				
	$B_0^2 G_i$	3.71	1.00	-4.54	-4.59				
	R^2	0.817	0.760	0.834	0.893				
Compd		H2-H1	H3-H1	H4-H1	H5-H1	H6-H1	C2-C1	C3-C1	Cp-C1
$R = \text{Ce-Eu}^{\text{a}}$	$R_{ik}(\text{exp})$	-0.34	-0.21	-1.86	0.73	1.84	0.41	-0.82	-0.47
	$(F_i - F_k R_{ik})(\text{exp})$	-0.81	-0.91	1.05	-0.22	0.03	1.35	4.97	6.25
	R^2	0.795	0.715	0.963	0.988	0.994	0.995	0.999	0.825
	$R_{ik}(\text{calc})$	-0.54	-0.17	-1.94	0.74	1.84	0.40	-0.82	-0.46
	$(F_i - F_k R_{ik})(\text{calc})$	-0.54	-0.61	0.57	-0.13	-0.01	1.34	4.98	6.22
Compd		H2-H1	H3-H1	H4-H1	H5-H1	H6-H1	C2-C1	C3-C1	Cp-C1
$R = \text{Tb-Yb}^{\text{b}}$	$R_{ik}(\text{exp})$	-0.54	-0.44	-2.76	0.79	2.08	0.28	-1.21	-1.18
	$(F_i - F_k R_{ik})(\text{exp})$	-0.28	-0.62	0.65	-0.36	-0.01	0.71	3.51	2.10
	R^2	0.992	0.993	0.998	1.000	1.000	0.995	0.999	0.987
	$R_{ik}(\text{calc})$	-0.56	-0.46	-2.81	0.79	2.08	0.27	-1.22	-1.24
	$(F_i - F_k R_{ik})(\text{calc})$	-0.19	-0.67	0.47	-0.36	-0.01	0.76	3.58	2.45
Compd		$k = \text{H4}; l = \text{H1}$				$k = \text{C2}; l = \text{C1}$			
		$i = \text{H2}$	$i = \text{H3}$	$i = \text{H5}$	$i = \text{H6}$	$i = \text{C3}$	$i = \text{P}$		
$R = \text{Ce-Eu}^{\text{a}}$	$\alpha(\text{exp})$	1.07	0.99	1.25	0.64	-2.42	-2.15		
	$\beta(\text{exp})$	0.56	0.47	-0.28	-0.05	4.04	4.12		
	R^2	0.393	0.26	0.977	0.925	0.997	0.981		
	$\alpha(\text{calc})$	-2.21	-1.55	0.29	2.15	-2.30	-2.29		
	$\beta(\text{calc})$	-0.98	-1.08	-0.24	0.09	3.68	4.62		

continued on next page

Table 20, *continued*

Compd		$k = \text{H4}; l = \text{H1}$				$k = \text{C2}; l = \text{C1}$	
		$i = \text{H2}$	$i = \text{H3}$	$i = \text{H5}$	$i = \text{H6}$	$i = \text{C3}$	$i = \text{P}$
$R = \text{Tb-Yb}^{\text{b}}$	$\alpha(\text{exp})$	1.07	0.99	1.25	0.64	-2.42	-2.15
	$\beta(\text{exp})$	0.56	0.47	-0.28	-0.05	4.04	4.12
	R^2	0.393	0.263	0.977	0.925	0.997	0.981
	$\alpha(\text{calc})$	-3.15	-3.22	1.64	1.95	-2.45	-2.45
	$\beta(\text{calc})$	-4.59	-1.06	-0.88	0.09	4.57	4.57

^aValues for the first isostructural series (except Sm).

^bValues for the second isostructural series.

less significant breaks at Tb (fig. 50). The calculated R_{ik} and $(F_i - R_{ik}F_k)$ parameters (and R^2 values) are also shown in table 20. Again, the relative sensitivity of the various nuclei to the breaks was: $\text{H5, H6} \ll \text{H4, C3} < \text{H2, H3, C2}$ and P. The R_{ik} and $(F_i - R_{ik}F_k)$ parameters evaluated directly by eq. (51) and indirectly using the F_i and $B_0^2G_i$ values from eq. (48) were compared (see table 20). The agreement is extremely good for all the R_{ik} ratios and only reasonably good for $(F_i - R_{ik}F_k)$. Again, the breaks observed in these plots indicate that the F_i and R_{ik} parameters change at the middle of the series, together with changes of B_0^2 .

A previous analysis of the ^1H , ^{13}C and ^{31}P LIS data for the $[\text{R}(\text{L}^{12}\text{-8H})]^{5-}$ complexes within the second half of the series ($R = \text{Tb-Yb}$) using Reuben's crystal-field parameter independent method (Reuben, 1982) has come to the conclusion that these complexes are isostructural (G_i constant) and that F_i are invariant along the second half of the series (Ren and Sherry, 1996), showing that the deviations in the plots according to eqs. (48) and (49) (fig. 49) in Tb-Yb, in particular for Tm and Yb, also reflect changes of B_0^2 within this half-series. Assuming that H4 has no contact shift contribution, F_i and $R_{i\text{H4}} = G_i/G_{\text{H4}}$ values were obtained for $i = \text{C1, C2, CP}$ and P nuclei, as well as the B_0^2 values for the Tb-Yb complexes. The results have shown that B_0^2 changes significantly along the Tb-Yb half-series of complexes, with the largest value for Tm and the smallest for Yb (Ren and Sherry, 1996).

Figure 51a shows the ^{13}C LIS data of C3 when plotted according to $\delta_{ij}^{\text{para}}/\delta_{kj}^{\text{para}}$ vs $\delta_{lj}^{\text{para}}/\delta_{kj}^{\text{para}}$ (eq. (53)) for $i = \text{C3, } l = \text{C1}$ and $k = \text{C2}$, where all data points ($n = 11$) fall on a straight line. The ^{31}P LIS data when plotted in the same way ($i = \text{P, } l = \text{C1}$ and $k = \text{C2}$) also show a good linear relationship. Table 20 summarizes the α and β values obtained directly from these plots, which agree quite reasonably with those calculated from the F_i and $B_0^2G_i$ parameters obtained from Reilly's plots (table 20). However, like before, plots using other combinations give more or less pronounced breaks, such as for $i = \text{C4, } l = \text{C1}$ and $k = \text{C3}$, and for $i = \text{C2}$ or $\text{C3, } l = \text{C1}$ and $k = \text{C4}$ (Geraldès et al., 2003). This is again in agreement with the detected changes of F_i and G_i parameters at the middle of the R series and it illustrates the appearance of accidentally linear plots according to eq. (53).

These conclusions are supported by plots of the ^1H LIS data according to eq. (53), obtained for $i = \text{H2, H3, H5}$ and $\text{H6, } l = \text{H1}$ and $k = \text{H4}$. While the plots are reasonably linear for $i = \text{H5}$ and H6 (fig. 51b), they show large deviations from linearity for $i = \text{H2}$ and H3 (see table 21 for the α and β values).

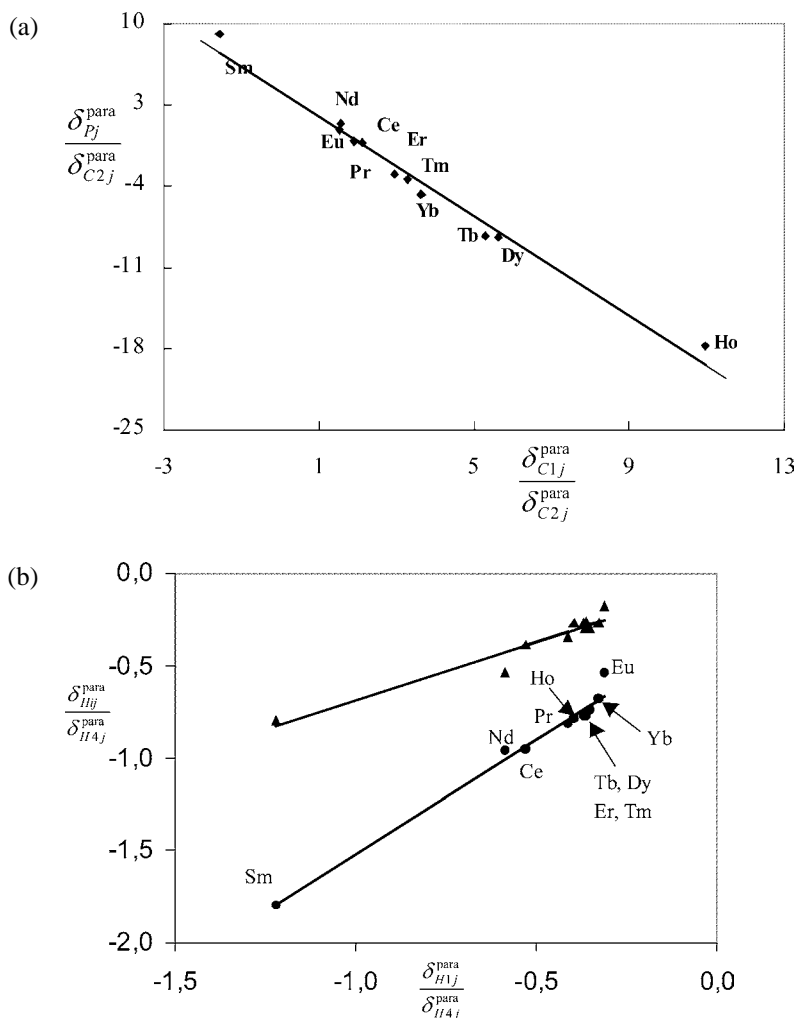


Fig. 51. Plots of $\frac{\delta_{ij}^{para}}{\delta_{kj}^{para}}$ vs $\frac{\delta_{lj}^{para}}{\delta_{kj}^{para}}$ (a) for the C3, C1, C2 triad; (b) for the Hi, H1, H4 triads (Hi = H5 (▲), H6 (●)) of $[R(L^{12}-8H)]^{5-}$ ($R = Ce-Yb$, D_2O , $pH = 7$, adapted from Geraldès et al. (2003)).

3.2.5. Comparison of the structures of the $[R(L^{10}-4H)]^-$, $[R(L^{11})]^{3+}$ and $[R(L^{12}-8H)]^{5-}$ complexes

As described in the previous sections, the solution LIS data analysis for $[R(L^{10}-4H)]^-$ (M and m isomers), $[R(L^{11})]^{3+}$ and $[R(L^{12}-8H)]^{5-}$ ($pH = 10, 7$ and 3) using the one nucleus, two nuclei and three nuclei methods gave quite comparable results. Their solution structures were systematically compared using the parameter data obtained from the last two graphical methods and listed in table 21 (Geraldès et al., 2003; Ren et al., 2002). In this table,

Table 21

Comparison of the parameters for the ^1H LIS of the R -tetraazamacrocyclic complexes $[\text{R}(\text{L}^{10}\text{-4H})]^-$ (M and m), $[\text{R}(\text{L}^{11})]^{3+}$ and $[\text{R}(\text{L}^{12}\text{-8H})]^{5-}$ obtained using the graphical methods based on eqs. (51) and (53) (Ren et al., 2002; Geraldes et al., 2003)

Compd.	R_{21}	$F_2 - R_{21}F_1$	R_{31}	$F_3 - R_{31}F_1$	R_{41}	$F_4 - R_{41}F_1$	R_{51}	$F_5 - R_{51}F_1$	R_{61}	$F_6 - R_{61}F_1$
$R = \text{Ce-Eu}$										
$[\text{R}(\text{L}^{12}\text{-8H})]^{5-}$	-0.34	-0.81	-0.21	-0.91	-1.86	1.05	0.86	-0.22	0.86	0.03
$[\text{R}(\text{L}^{10}\text{-4H})]^-$ (M)	-0.27	-0.62	-1.00	-1.89	-3.56	-0.78	0.86	0.22	-0.93	-2.60
$[\text{R}(\text{L}^{10}\text{-4H})]^-$ (m)	-0.42	-1.29	-0.59	-1.43	-3.12	-0.90	0.86	-0.05	0.86	-0.39
$[\text{R}(\text{L}^{11})]^{3+}$	-0.65	-1.61	-0.52	-1.95	-2.97	-0.36	1.92	0.72	0.86	-0.42
$R = \text{Tb-Yb}$										
$[\text{R}(\text{L}^{12}\text{-8H})]^{5-}$	-0.54	-0.28	-0.44	-0.62	-2.76	0.65	0.79	-0.36	2.08	-0.01
$[\text{R}(\text{L}^{10}\text{-4H})]^-$ (M)	-0.37	-1.34	-0.44	-1.10	-2.56	-1.42	1.79	0.42	0.81	-0.84
$[\text{R}(\text{L}^{10}\text{-4H})]^-$ (m)	-0.37	-1.24	-0.44	-1.02	-2.57	-0.85	0.85	-0.23	1.77	-0.90
$[\text{R}(\text{L}^{11})]^{3+}$	-0.33	-1.20	-0.27	-1.66	-2.27	-1.49	1.61	1.04	0.79	-0.49
$k = \text{H4}; l = \text{H1}$	$i = \text{H2}$		$i = \text{H3}$		$i = \text{H5}$		$i = \text{H6}$			
	α	β	α	β	α	β	α	β		
$R = \text{Ce-Eu}$										
$[\text{R}(\text{L}^{12}\text{-8H})]^{5-}$	1.07	0.56	0.99	0.47	1.25	-0.278	0.64	-0.05		
$[\text{R}(\text{L}^{10}\text{-4H})]^-$ (M)	a	a	a	a	a	a	a	a		
$[\text{R}(\text{L}^{10}\text{-4H})]^-$ (m)	1.48	0.444	1.88	0.74	2.20	0.22	0.40	-0.12		
$[\text{R}(\text{L}^{11})]^{3+}$	14.09	4.94	17.40	6.01	-0.35	-0.72	8.01	2.42		
$R = \text{Tb-Yb}$										
$[\text{R}(\text{L}^{12}\text{-8H})]^{5-}$	1.07	0.56	0.99	0.47	1.25	-0.28	0.64	-0.05		
$[\text{R}(\text{L}^{10}\text{-4H})]^-$ (M)	3.11	1.28	2.17	0.97	0.80	-0.37	3.00	0.80		
$[\text{R}(\text{L}^{10}\text{-4H})]^-$ (m)	0.86	0.60	1.54	0.80	-0.01	-0.72	1.25	0.16		
$[\text{R}(\text{L}^{11})]^{3+}$	1.40	0.78	1.91	0.98	0.16	-0.64	1.41	0.27		

^aNot determined.

the R_{ik} geometric ratios for the H1–H6 protons, relative to H1, and the R'_{ik} ratios for the C1–C4 carbons (C4 replaced by P atom in $[\text{R}(\text{L}^{12}\text{-8H})]^{5-}$), relative to C1 are of high structural importance. The sign of R_{ik} is different for the H1, H5 and H6 relative to H2, H3 and H4, and of C1 and C2 relative to C3 and C4(P), showing that these two groups of protons and carbon/phosphorus nuclei have distinct locations in the complexes relative to the dipolar shift cone defined by $3 \cos^2 \theta = 1$. The absolute magnitude of the ring R_{ik} ratios follow the order $\text{H4} > \text{H1} > \text{H2} > \text{H3}$ for the $[\text{R}(\text{L}^{11})]^{3+}$ and $[\text{R}(\text{L}^{12}\text{-8H})]^{5-}$ complexes, and $\text{H4} > \text{H1} > \text{H3} > \text{H2}$ for the M and m isomers of the $[\text{R}(\text{L}^{10}\text{-4H})]^-$ complexes. The acetate proton ratios also differ significantly, with $\text{H5} > \text{H6}$ for the $[\text{R}(\text{L}^{10}\text{-4H})]^-$ (M) and $[\text{R}(\text{L}^{11})]^{3+}$ complexes, and $\text{H6} > \text{H5}$ for the $[\text{R}(\text{L}^{10}\text{-4H})]^-$ (m) and $[\text{R}(\text{L}^{12}\text{-8H})]^{5-}$ complexes. Although the proton shifts of the $[\text{R}(\text{L}^{12}\text{-8H})]^{5-}$ complexes are significantly pH dependent, with a decrease of the dipolar shifts when the pH drops from 10 to 3 (Ren et al., 2002), the four protonation steps undergone by the phosphonate groups at their unbound oxygens does not cause a variation of the complex geometry, as the R_{ik} are nearly invariant from $\text{pH} = 10$ to $\text{pH} = 3$ ($< \pm 4\%$). Such large decreases of dipolar shifts with pH decrease are attributed to a decrease of the crystal field parameter B_0^2 upon protonation. As described before,

the B_0^2 values for the Tb–Yb complexes of $[R(L^{12}-8H)]^{5-}$ have been obtained assuming that H4 has no contact shift contribution, showing that B_0^2 changes significantly along the Tb–Yb half-series of complexes, with the largest value for Tm and the smallest for Yb (Ren and Sherry, 1996). However, these quantitative values must be seen with some caution, as the assumption that F_{H4} is negligible for the $[R(L^{12}-8H)]^{5-}$ complexes is doubtful (see table 20). On the other hand, calculation of B_0^2 ratios,

$$\frac{B_0^2(R = \text{Ce–Eu})}{B_0^2(R = \text{Dy–Yb})},$$

which is obtained by assuming constant G_i values along the series and taking the slope of a linear plot of $B_0^2 G_i$ ($R = \text{Ce–Tb}$) vs $B_0^2 G_i$ ($R = \text{Ce–Tb}$), could not be undertaken, since in the present systems G_i values display only small changes along the $R(\text{III})$ series.

Comparing the experimental and calculated R_{ik} values for each proton in the four complexes studied (table 22), in particular for the two isomers, M and m, of $[R(L^{10}-4H)]^-$, which result from different arrangements of the four pendant arms around the $R(\text{III})$ ion, one concludes that these ratios are quite constant for the ring protons in all complexes, in accordance with very similar macrocyclic ring conformations. The differences between M and m forms occur in the H5 and H6 protons of the pendant arms, with very good agreement of experimental and calculated data for the $[R(L^{10}-4H)]^-$ complexes (also with the X-ray results) and for the $[R(L^{11})]^{3+}$ complexes, where the calculated structure is M (Forsberg et al., 1995). For the $[R(L^{12}-8H)]^{5-}$ complexes, the re-assignment of these protons indicates that they have a m' solution conformation, in agreement with calculated values for models of the M' and m' conformations and with the X-ray crystal structure.

Further information about the structure of these macrocyclic complexes is provided in table 23, which compares the experimental Yb–H distances normalized to H1 (r_{Hi}/r_{H1}) ob-

Table 22

Comparison of experimental and calculated geometric ratios $R_{k1} = G_k/G_{H1}$ for H1–H6 protons of $[R(L^{10}-4H)]^-$ (M and m), $[R(L^{11})]^{3+}$ and $[R(L^{12}-8H)]^{5-}$

		H1	H2	H3	H4	H5	H6
$[R(L^{10}-4H)]^-$ (M)	Exp. ^a	1.00	–0.31	–0.44	–2.56	1.79	0.81
	Calc. ^a	1.00	–0.41	–0.45	–2.73	1.82	0.86
$[R(L^{10}-4H)]^-$ (m)	Exp. ^a	1.00	–0.37	–0.44	–2.57	0.85	1.77
	Calc. ^a	1.00	–0.26	–0.29	–2.26	0.89	1.63
$[R(L^{11})]^{3+}$	Exp. ^b	1.00	–0.33	–0.27	–2.27	1.61	0.79
	Calc. ^b	1.00	–0.35	–0.27	–2.29	1.65	0.79
$[R(L^{12}-8H)]^{5-}$ (M')	Exp. ^c	1.00	–0.54	–0.44	–2.76	0.79	2.08
	Calc. ^d	1.00	–0.65	–0.51	–3.15	2.29	0.92
(m')	Calc. ^d	1.00	–0.63	–0.46	–2.89	0.87	2.41

^aAime et al. (1992b).

^bForsberg et al. (1995).

^cGeraldes et al. (1992).

^dCalculated for models of M' and m' structures (Ren et al., 2002). The m' structure was obtained based on the crystal structure of $[\text{Tm}(L^{12}-8H)]^{5-}$ and the M' structure by changing m' to give a twist angle of $+39^\circ$.

Table 23

Comparison of experimental and calculated Yb–Hi distance ratios relative to H1, r_{Hi}/r_{H1} , for H1–H6 protons of $[R(L^{10}-4H)]^-$ (M and m), $[R(L^{11})]^{3+}$ and $[R(L^{12}-8H)]^{5-}$

		H1	H2	H3	H4	H5	H6
$[R(L^{10}-4H)]^-$ (M)	Exp. ^a	1.00	1.19	1.21	0.96	1.04	1.16
	Calc. ^a	1.00	1.17	1.17	0.99	0.99	1.15
$[R(L^{10}-4H)]^-$ (m)	Exp. ^a	1.00	1.17	1.19	0.95	1.02	1.05
	Calc. ^a	1.00	1.17	1.17	0.99	0.99	0.98
$[R(L^{11})]^{3+}$	Exp. ^b	1.00	1.13	1.13	0.90	1.01	1.19
	Calc. ^b	1.00	1.19	1.19	0.99	0.98	1.16
$[R(L^{12}-8H)]^{5-}$ (M')	Exp. ^c	1.00	1.16	1.16	0.95	1.22	0.98
	Calc. ^d	1.00	1.19	1.19	1.01	0.96	1.17
(m')	Calc. ^d	1.00	1.21	1.21	1.04	1.18	0.93

^aAime et al. (1992b).

^bForsberg et al. (1995).

^cGeraldes et al. (1992).

^dCalculated for models of M' and m' structures (Ren et al., 2002).

tained using the proton T_1 relaxation times from the literature and eq. (18), with the relative distances calculated for the M and m/m' forms of the $[R(L^{10}-4H)]^-$ complexes and the M form of the $[R(L^{11})]^{3+}$ complex. There is no significant differences in the relative distances of the ring protons for all these Yb complexes, which also agree with the calculated values. Due to the different arrangements of the pendant acetate arms around the Yb ion, the calculated Yb–H distances of H5 and H6 in the M and m/m' forms differ quite substantially: while H5 is closer to Yb than H6 in M, their distances to Yb are about the same in m/m'. The experimental results for the $[R(L^{10}-4H)]^-$ M and m/m' isomers agree very well with the predicted values, and the experimental results for the $[R(L^{11})]^{3+}$ complex is consistent with a M form in solution. In the case of $[R(L^{12}-8H)]^{5-}$, the experimental data also agrees with the values calculated for a m' form (Ren et al., 2002).

Finally it is worth noting that a comparison of the α and β values, obtained from plots of the ^1H LIS for the acetate protons in the three complexes according to eq. (53), for $i = \text{H5}$ and H6 , with $l = \text{H1}$ and $k = \text{H4}$ (table 21), is not indicative of their structure being either SAP (M) or TSAP (m or m'), despite these structures only differ in the arrangement of the pendant arms around the metal ion. Those α and β parameters do not reflect those structural changes directly, probably as a result of their very indirect structural dependence on the R_{iH4} ($i = \text{H5}$ and H6) geometric ratio (eq. (53)), which is mixed with dependence on the R_{H1H4} geometric ratio and hyperfine coupling constants ratios S_{iH4} and S_{H1H4} , which significantly change for the various complexes (table 21). This reduces the structural diagnostic power of the three nuclei method based on eq. (53).

3.2.6. $[R(L^3-2H)_2]^-$ ($L^3 = \text{phtalocyanine}$)

Considerable interest has been focused on the physico-chemical properties of sandwich complexes of lanthanide(III) ions with two macrocyclic conjugated rings such as phtalocyanine. Several X-ray crystallographic studies on Nd(III) (Kasuga et al., 1980) and Lu(III) (Mous-

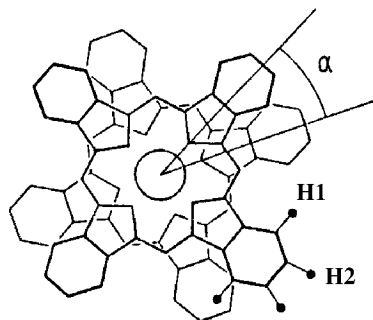


Fig. 52. The structure of $[R(L^{13}-2H)_2]^{-}$, with the twist angle α , $\alpha = 45^\circ$ for the D_{4d} form, and 0° for the D_{4h} form (adapted from Konami et al. (1989)).

savi et al., 1988) complexes have been carried out for $H[Nd(L^{13}-2H)_2]$, $[N(^nBu)_4][Lu(L^{13}-2H)_2]$ and $H[Lu(L^{13}-2H)_2]$. These reveal quite similar solid-state structures, where the $R(III)$ cation is 8-coordinated by the isoindole nitrogen atoms of the two phthalocyanine rings in quasi square antiprismatic geometries (D_{4d} symmetry), with staggering angles α between the two stacked phthalocyanines (fig. 52) of 45° , 43° and 41° , respectively. The benzimidazole groups are somewhat tilted, giving a slightly bowl-type deformation of the phthalocyanine macrocycles towards the lanthanide ion. Slight distortions of some of these sandwich structures, with small deviations of the mean planes of the two phthalocyanines from parallel positions, were assigned to ion packing in the crystals.

The proton NMR spectra of the $[N(^nBu)_4][R(L^{13}-2H)_2]$ ($R = Pr-Lu$ except Pm, Gd) complexes in CD_3CN solution at room temperature are very simple in the aromatic region, with only one H1 and one H2 resonance of the phthalocyanine rings, indicating that the complexes have a C_4 axis in solution (Konami et al., 1989). This is compatible with a D_{4h} square prismatic or a D_{4d} square antiprismatic geometry, depending whether the two stacked phthalocyanines are eclipsed or staggered, or fast interconversion between the two. The splitting of the Q band observed in the UV-vis absorption spectra of the $R = Pr, Lu$ complexes in CD_3CN solution excludes the D_{4h} structure. From the LIS values of the H1 and H2 protons in the paramagnetic complexes, plots of $\delta_{ij}^{para}/\langle S_z \rangle_j$ vs $C_j/\langle S_z \rangle_j$ (eq. (48)) and δ_{ij}^{para}/C_j vs $\langle S_z \rangle_j/C_j$ (eq. (49)) were obtained, which showed breaks near the middle of the lanthanide series and also significant deviations from linearity within each of the two subfamilies of lanthanides, reflecting variations of the coupling constant F_i and the pseudo-contact term $B_0^2 G_i$ (fig. 53a and table 24). In the original work, $B_0^2 G_i$ values were identified with G_i and single F_i and G_i values were obtained for H1 and H2 along the lanthanide series which did not fully agree with our analysis (table 24, Konami et al. (1989)). Fitting of the geometrical dependence of the experimentally derived R_{ik} ratios to a chemical model of the $[R(L^{13}-2H)_2]^{-}$ complexes based on the crystal structures of the Nd and Lu compounds gave an average distance between the two rings in the sandwich compound of 2.54 \AA and an average R-N distance of 2.31 \AA (Konami et al., 1989). However, the data analysis available does not prove isostructurality in solution.

A plot of $\delta_{ij}^{para}/\langle S_z \rangle_j$ vs $\delta_{kj}^{para}/\langle S_z \rangle_j$ (eq. (51)) for $i = H2$ and $j = H1$, according to the two-nuclei crystal-field independent technique, which eliminates the effect of any changes

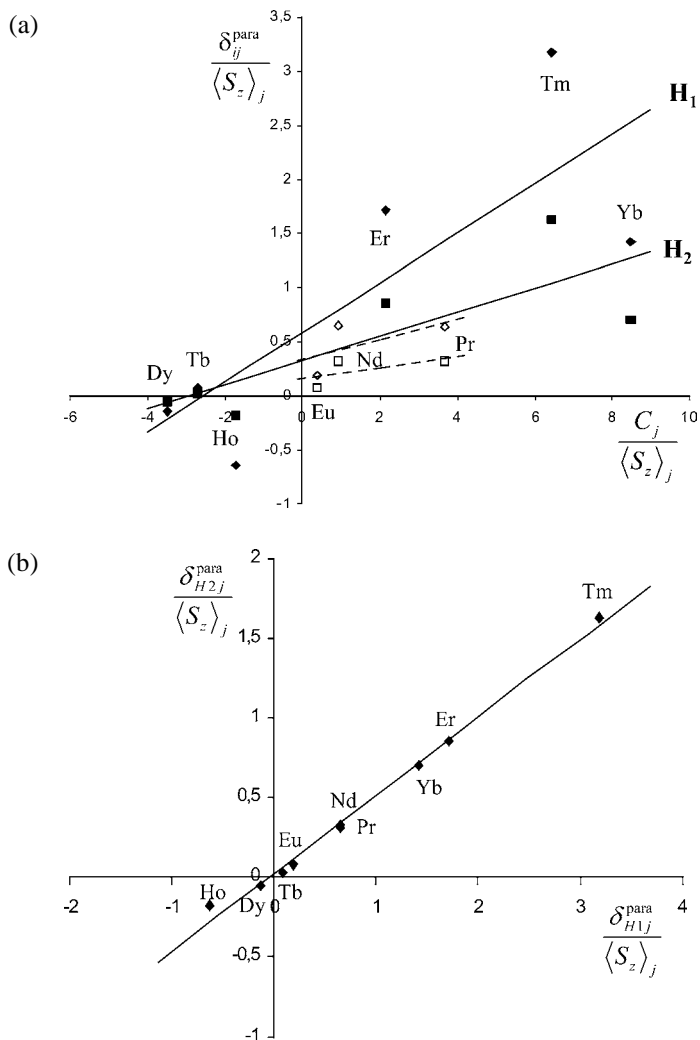


Fig. 53. (a) Plots of $\delta_{ij}^{para}/\langle S_z \rangle_j$ vs $C_j/\langle S_z \rangle_j$ for H1 (◆) and H2 (■) and (b) plot of $\delta_{ij}^{para}/\langle S_z \rangle_j$ vs $\delta_{kj}^{para}/\langle S_z \rangle_j$ for the H1–H2 (◆) pair in $[R(L^{13}\text{-}2H)_2]^-$ ($R = \text{Pr}\text{-Yb}$, CD_3CN , adapted from Konami et al. (1989), Geraldes et al. (2003)).

in B_0^2 , gives a single straight line along the lanthanide series (fig. 53b), confirming that the complexes are isostructural and that the B_0^2 parameter and F_i change along the series. There is generally a good agreement between experimental and calculated R_{ik} and $(F_i - F_k R_{ik})$ parameters (table 24).

Table 24

Computed values for contact (F_i), pseudo-contact ($B_0^2 G_i$) terms and R^2 values, according to eq. (48) and comparison of R_{ik} and $(F_i - R_{ik} F_k)$ parameters calculated directly according to eq. (51) with those obtained from the above F_i and $B_0^2 G_i$ terms, for ^1H -nuclei in complexes $[\text{R}(\text{L}^{13}\text{-2H})_2]^-$ ($\text{R} = \text{Pr-Yb}$, CD_3CN , Konami et al. (1989), Geraldès et al. (2003)). See fig. 52 for the atom-numbering scheme

Parameter	Compd	H1	H2	Compd	H1	H2	Compd	H1	H2
F_i	$\text{R} = \text{Pr-Eu}^{\text{a}}$	0.34	0.16	$\text{R} = \text{Tb-Yb}^{\text{b}}$	0.59	0.33	$\text{R} = \text{Pr-Yb}$	0.44	0.24
$B_0^2 G_i$		0.09	0.06		0.23	0.11		0.22	0.11
R^2		0.380	0.426		0.649	0.652		0.601	0.600
	Compd	H2-H1		Compd	H2-H1		Compd	H2-H1	
$R_{ik}(\text{exp})$	$\text{R} = \text{Pr-Eu}^{\text{a}}$	0.52		$\text{R} = \text{Tb-Yb}^{\text{b}}$	0.48		$\text{R} = \text{Pr-Yb}$	0.49	
$(F_i - F_k R_{ik})(\text{exp})$		0.01			0.02			0.03	
R^2		0.994			0.994			0.993	
$R_{ik}(\text{calc})$		0.67			0.48			0.50	
$(F_i - F_k R_{ik})(\text{calc})$		-0.07			0.05			0.02	

^aValues for the first isostructural series (except Sm).

^bValues for the second isostructural series.

4. Application of the model-free methods to axial bimetallic lanthanide complexes with sterically rigid ligands

Axial symmetry according to Bleaney's approach is maintained in polymetallic lanthanide complexes when the metals lie on the molecular threefold or fourfold axes. For n magnetically non-coupled lanthanide ions packed along the symmetry axis, contact and pseudo-contact contributions can be considered as additive and the original model-free equation (eq. (47)) is transformed into eq. (61) in which the sum runs over the n paramagnetic centres, each being located at the origin of its own reference frame associated with a specific set of axial coordinates θ_i^m and r_i^m (the z axis corresponds to the molecular symmetry axis, fig. 54),

$$\delta_{ij}^{\text{para}} = \delta_{ij}^{\text{c}} + \delta_{ij}^{\text{pc}} = \sum_{m=1}^n [F_i^m \langle S_z \rangle_j^m + C_j^m B_0^{2m} G_i^m]. \quad (61)$$

For homopolymetallic axial complexes, the spin expectation values and Bleaney's factors are identical for all metallic sites ($\langle S_z \rangle_j^m = \langle S_z \rangle_j$ and $C_j^m = C_j$) and can be factorized out to give eq. (62) which can be linearized according to the method proposed by Reilley et al. (1975) for monometallic complexes (eqs. (63), (64), Elhabiri et al. (1999)),

$$\delta_{ij}^{\text{para}} = \left(\sum_{m=1}^n F_i^m \right) \langle S_z \rangle_j + \left(\sum_{m=1}^n B_0^{2m} G_i^m \right) C_j, \quad (62)$$

$$\frac{\delta_{ij}^{\text{para}}}{\langle S_z \rangle_j} = \left(\sum_{m=1}^n F_i^m \right) + \left(\sum_{m=1}^n B_0^{2m} G_i^m \right) \frac{C_j}{\langle S_z \rangle_j}, \quad (63)$$

$$\frac{\delta_{ij}^{\text{para}}}{C_j} = \left(\sum_{m=1}^n B_0^{2m} G_i^m \right) + \left(\sum_{m=1}^n F_i^m \right) \frac{\langle S_z \rangle_j}{C_j}. \quad (64)$$

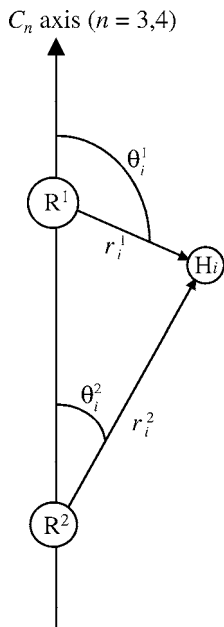


Fig. 54. Axial coordinates considered in bimetallic axial lanthanide complexes (adapted from Rigault et al. (2000a)).

The derivation of a general crystal-field independent method for polymetallic lanthanide complexes related to eq. (51) is precluded by the consideration of variable numbers of different crystal-field parameters (maximum n) depending on the exact symmetry of the axial complex (see sect. 4.1.1, Rigault et al. (2000a)).

4.1. Complexes with threefold symmetry

4.1.1. $[R_2(L^{14}-2H)_3]$ ($L^{14} = \text{bis}\{1\text{-ethyl-2-[6'-carboxy]pyridin-2'-yl}\}$ *benzimidazol-5-yl)methane*)

Reaction of the bis-tridentate receptor $[L^{14}-2H]^{2-}$ with $R(ClO_4)_3$ in water produces the highly stable homobimetallic triple-stranded helicates $[R_2(L^{14}-2H)_3]$ ($R = \text{La-Tb}$ except Pm and $R = \text{Er-Yb-Lu}$, $\log \beta_{[R_2(L^{14}-2H)_3]} = 51(4)$, Elhabiri et al. (1999)). ^1H NMR spectra point to rigid D_3 -symmetrical complexes for which exchange between the helical enantiomers is slow on the NMR time scale (i.e., the methylene protons of the ethyl residues are systematically diastereotopic, fig. 55).

The considerable intermetallic separation (8.81–8.83 Å in the crystal structures of $[\text{Eu}_2(L^{14}-2H)_3]$ and $[\text{Tb}_2(L^{14}-2H)_3]$) prevents magnetic coupling and the ‘isolating’ methylene spacer separating the two tridentate units restrict through-bond contact interactions for a given nucleus i to a single paramagnetic centre. Under these conditions and for D_3 -symmetrical bimetallic lanthanide complexes (i.e., $B_0^{21} = B_0^{22} = B_0^2$), eqs. (62)–(64) simplify to eqs. (65)–(67)

$$\delta_{ij}^{\text{para}} = F_i \langle S_z \rangle_j + B_0^2 (G_i^1 + G_i^2) C_j, \quad (65)$$

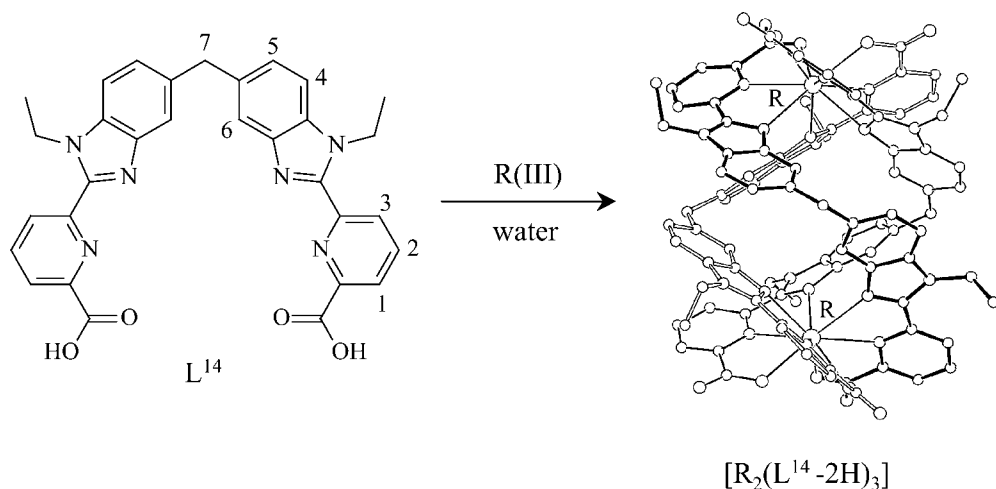


Fig. 55. Schematic formation of the D_3 -symmetrical complexes $[R_2(L^{14}-2H)_3]$ in water with numbering scheme. The representation of $[R_2(L^{14}-2H)_3]$ corresponds to the crystal structure of $[Eu_2(L^{14}-2H)_3](H_2O)_{20.5}$ (Elhabiri et al., 1999).

Table 25

Computed values for contact (F_i), pseudo-contact ($B_0^2(G_i^1 + G_i^2)$) terms and agreement factors (AF_i) for 1H -nuclei in complexes $[R_2(L^{14}-2H)_3]$ (D_2O , 298 K, Elhabiri et al. (1999)). See fig. 55 for the atom-numbering scheme

Compd		H1	H2	H3	H4	H5	H6	H7
$R = Ce-Tb$	F_i	0.32(4)	0.21(4)	0.36(5)	0.13(1)	0.011(2)	-1.7(2)	-0.02(1)
	$B_0^2(G_i^1 + G_i^2)$	-0.38(3)	-0.32(1)	-0.35(2)	-0.05(3)	0.032(8)	0.76(7)	0.086(4)
	AF_i	0.03	0.04	0.08	0.04	0.06	0.35	0.11
$R = Er-Yb$	F_i	-0.47(2)	-0.15(3)	-0.46(2)	0.07(3)	0.07(5)	1.99(2)	-0.11(4)
	$B_0^2(G_i^1 + G_i^2)$	-0.41(6)	-0.30(4)	-0.42(7)	0.058(9)	-0.004(9)	2.07(4)	0.11(1)
	AF_i	0.20	0.18	0.19	0.08	0.04	0.002	0.06

$$\frac{\delta_{ij}^{para}}{\langle S_z \rangle_j} = F_i + B_0^2(G_i^1 + G_i^2) \frac{C_j}{\langle S_z \rangle_j}, \quad (66)$$

$$\frac{\delta_{ij}^{para}}{C_j} = B_0^2(G_i^1 + G_i^2) + F_i \frac{\langle S_z \rangle_j}{C_j}. \quad (67)$$

Plots of $\delta_{ij}^{para} / \langle S_z \rangle_j$ vs $C_j / \langle S_z \rangle_j$ (eq. (66)) and δ_{ij}^{para} / C_j vs $\langle S_z \rangle_j / C_j$ (eq. (67)) for the 1H NMR data of $[R_2(L^{14}-2H)_3]$ ($R = Ce-Tb$ except Pm and $R = Er-Yb$) display an abrupt deviation from linearity between $R = Tb$ and $R = Er$ and require two different straight lines (fig. 56). Two different isostructural series have been considered for $R = Ce-Tb$ and $Er-Yb$, and two sets of contact F_i and pseudo-contact $B_0^2(G_i^1 + G_i^2)$ terms are obtained according to least-squares fits of eq. (65) (table 25, Elhabiri et al. (1999)).

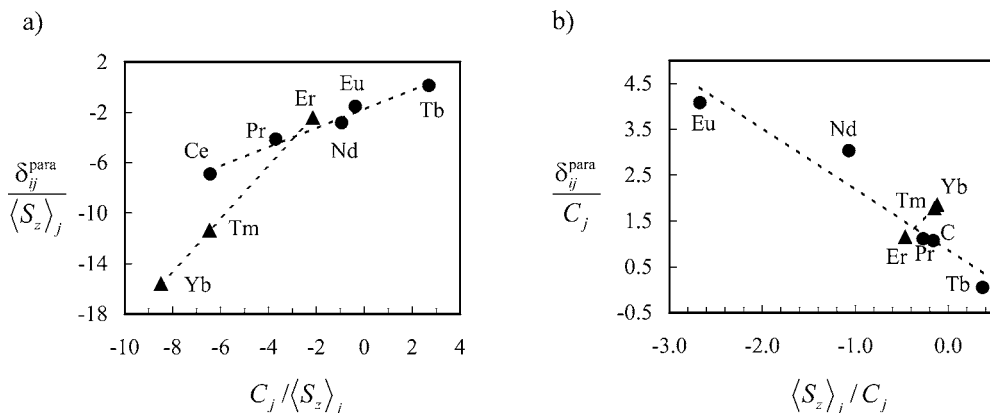


Fig. 56. Plots of (a) $\delta_{ij}^{para} / \langle S_z \rangle_j$ vs $C_j / \langle S_z \rangle_j$ (eq. (66)) and (b) δ_{ij}^{para} / C_j vs $\langle S_z \rangle_j / C_j$ (eq. (67)) for H6 in $[R_2(L^{14}-2H)_3]$ ($R = \text{Ce-Eu, Er-Yb, D}_2\text{O, 298 K}$, adapted from Rigault et al. (2000a)).

The crystal-field parameter B_0^2 can be removed when eq. (65) is expressed for two different nuclei i and k (Rigault et al., 2000a). The resulting crystal-field independent eq. (68) is very similar to eq. (51) except that global geometrical factors $(G_i^1 + G_i^2)$ replace G_i .

$$\frac{\delta_{ij}^{para}}{\langle S_z \rangle_j} = \left(F_i - F_k \frac{(G_i^1 + G_i^2)}{(G_k^1 + G_k^2)} \right) + \frac{(G_i^1 + G_i^2)}{(G_k^1 + G_k^2)} \cdot \frac{\delta_{kj}^{para}}{\langle S_z \rangle_j}. \quad (68)$$

Plots of $\delta_{ij}^{para} / \langle S_z \rangle_j$ vs $\delta_{kj}^{para} / \langle S_z \rangle_j$ (eq. (68)) for the various pairs of paramagnetic NMR shifts in $[R_2(L^{14}-2H)_3]$ show three different behaviours depending on the protons involved (fig. 57, Rigault et al. (2000a)). Firstly, no obvious correlation is observed for pairs involving H5 which can be explained by the peculiar location of this proton in the triple-stranded helicate. According to the D_3 -averaged crystal-structure of $[\text{Eu}_2(\text{L}^{14}-2\text{H})_3]$, the axial coordinates amount to $\theta_{\text{H}5}^1 = 54.1^\circ$ and $\theta_{\text{H}5}^2 = 55.0^\circ$ which are both close to the magic angle (54.7°) and lead to a dramatic sensitivity to faint structural changes along the lanthanide series as similarly observed for H11 in $[\text{RCo}(\text{L}^5)_3]^{6+}$ (see sect. 3.1.5) and C4 in $[\text{R}(\text{L}^3)_3]^{3+}$ (see sect. 3.1.3). Nevertheless, this observation points to possible minor geometrical changes from one lanthanide to the other, but it is not diagnostic for significant structural variations occurring along the lanthanide series. Secondly, pairs involving protons H1-3,6,7 display a single straight line for the complete lanthanide series (Ce–Yb, fig. 57a) which indicates that (i) no significant structural variation occurs along the complete lanthanide series and (ii) changes in the crystal field parameters affect the linearity of the one-nucleus methods.

Thirdly, related plots according to eq. (68) involving H4 clearly exhibit two straight lines, one for the large (Ce–Tb) and one for the small (Er–Yb) lanthanide ions with an abrupt transition between them (fig. 57b). This behaviour contrasts with that observed for H1-3,6,7 and apparently leads to opposite conclusions in which two different structural arrangements should be invoked. However, both metallic centres significantly contribute to the paramagnetic shift

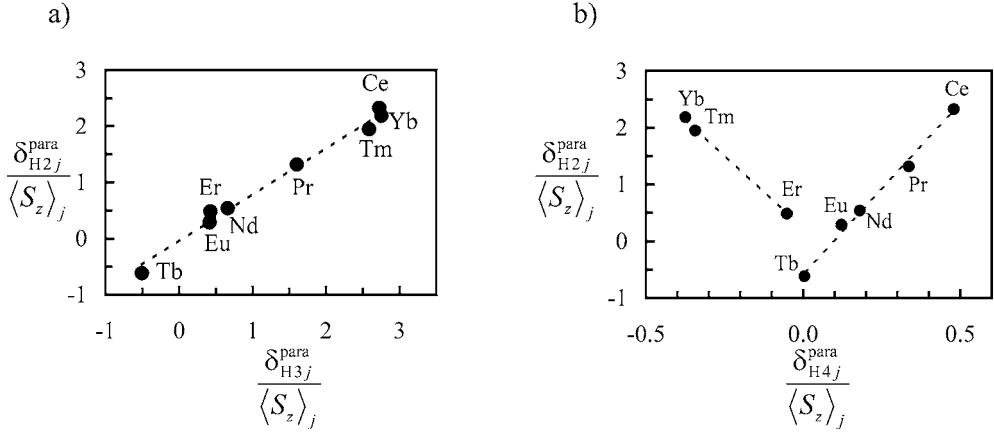


Fig. 57. Crystal-field independent plots of (a) $\delta_{H2j}^{para} / \langle S_z \rangle_j$ vs $\delta_{H3j}^{para} / \langle S_z \rangle_j$ (eq. (68)) for the H2–H3 and (b) H2–H4 pairs in $[R_2(L^{14}-2H)_3]$ ($R = Ce-Tb, Er-Yb, D_2O, 298 K$, adapted from Rigault et al. (2000a)).

of H4 ($G_{H4}^1/G_{H4}^2 = 0.58$) and the θ_{H4}^i angles ($i = 1, 2$) are distributed on both sides of the magic angles (49.1° and 63.0° according to the crystal structure of $[Eu_2(L^{14}-2H)_3]$). The paramagnetic shift of H4 is thus particularly sensitive to minor structural variations as a result of its peculiar geometrical location. Theoretical computed R_{ik} factors obtained when the $R \cdots R$ distance is increased by stepwise increment of $\approx 0.2 \text{ \AA}$ from 8.4 \AA to 9.2 \AA indeed show small variations for $Hi-Hk$ pairs ($i \neq k$ and $i, k = 1, 2, 3, 6, 7$), but $Hi-H4$ pairs ($i \neq 4$) exhibit drastic changes which confirm their extreme sensitivity to minor structural changes (fig. 58).

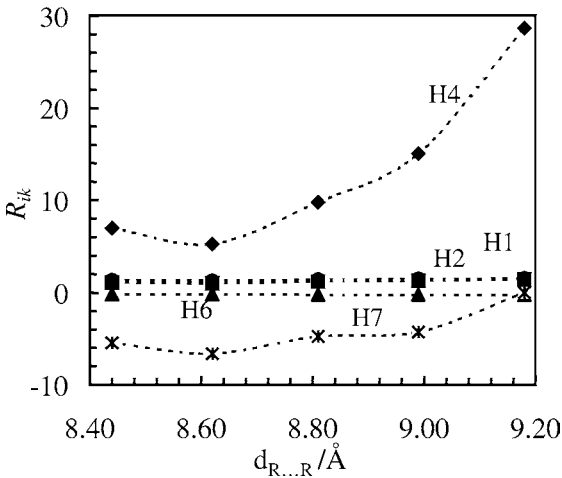


Fig. 58. Computed R_{ik} factors for pairs H3– H_k ($k = 1, 2, 4, 6, 7$) in the crystal structure of $[Eu_2(L^{14}-2H)_3]$ (the intermetallic distance d varies from 8.4 to 9.2 \AA , adapted from Rigault et al. (2000a)).

The R_{ik} factors found in solution are in good agreement with those calculated from the averaged D_3 -symmetrical crystal structure leading to an agreement factor $AF = 0.17$, and to the conclusion that the crystal structure of $[\text{Eu}_2(\text{L}^{14}-2\text{H})_3]$ is a satisfying model for the complexes in solution along the complete lanthanide series. The breaks observed according to the one-nucleus methods (eqs. (66), (67), fig. 56) have been assigned to concomitant changes of F_i and B_0^2 occurring between $R = \text{Tb}$ and $R = \text{Er}$, but the minor variation of the slopes for the two straight lines obtained for $\delta_{ij}^{\text{para}} / \langle S_z \rangle_j$ vs $C_j / \langle S_z \rangle_j$ plots (eq. (66), fig. 56a) suggests a ratio of crystal-field parameters close to unity (Rigault et al., 2000a). A plot of $B_0^2(G_i^1 + G_i^2)_{R=\text{Ce}-\text{Tb}}$ vs $B_0^2(G_i^1 + G_i^2)_{R=\text{Er}-\text{Yb}}$ excluding H5 gives a rough linear correlation with

$$\frac{B_0^2(R = \text{Ce}-\text{Tb})}{B_0^2(R = \text{Er}-\text{Yb})} = 0.8(2).$$

Finally, global geometrical factors $G_i^1 + G_i^2$ calculated from the crystal structure of $[\text{Eu}_2(\text{L}^{14}-2\text{H})_3]$ have been used for estimating magnetic anisotropies $\chi_{zz}^j - (1/3) \text{Tr} \chi^j$ with eq. (69) and using four contact contributions δ_{ij}^c ($i = \text{H1, H2, H3, H6}$, Elhabiri et al. (1999)). Since only three protons display no contact contribution, only rough estimations of $\chi_{zz}^j - (1/3) \text{Tr} \chi^j$ are obtained and no comparison with Bleaney's factors has been performed,

$$\delta_{ij}^{\text{para}} = \delta_{ij}^c + \frac{1}{2N_A} \left[\left(\chi_{zz}^j - \frac{1}{3} \text{Tr} \chi^j \right) (G_i^1 + G_i^2) \right]. \quad (69)$$

Isostructurality along the complete lanthanide series has been ultimately confirmed by relaxation measurements. For the bimetallic complexes $[\text{R}_2(\text{L}^{14}-2\text{H})_3]$, each nucleus undergoes the sum of two dipolar and two Curie-spin paramagnetic contributions to their longitudinal relaxation rate. Thus eq. (18) is no longer valid and must be replaced with eq. (70) which takes into account the effect of the two paramagnetic centres (fig. 54, Elhabiri et al. (1999)),

$$\frac{T_{li}^{\text{para}}}{T_{l\text{ref}}^{\text{para}}} = \left(\frac{(r_{\text{ref}}^1)^6 + (r_{\text{ref}}^2)^6}{(r_i^1)^6 + (r_i^2)^6} \right) \cdot \left(\frac{(r_i^1)^6 \cdot (r_i^2)^6}{(r_{\text{ref}}^1)^6 \cdot (r_{\text{ref}}^2)^6} \right). \quad (70)$$

Taking the r_i^n distances observed in the crystal structure of $[\text{Eu}_2(\text{L}^{14}-2\text{H})_3]$ and H3 as an internal reference, the calculated ratios

$$\left(\frac{(r_{\text{ref}}^1)^6 + (r_{\text{ref}}^2)^6}{(r_i^1)^6 + (r_i^2)^6} \right) \cdot \left(\frac{(r_i^1)^6 \cdot (r_i^2)^6}{(r_{\text{ref}}^1)^6 \cdot (r_{\text{ref}}^2)^6} \right)$$

closely match the experimental terms $T_{li}^{\text{para}}/T_{l\text{ref}}^{\text{para}}$ obtained for $R = \text{Ce, Pr, Nd, Yb}$, henceforth confirming that $[\text{Eu}_2(\text{L}^{14}-2\text{H})_3]$ is a satisfying structural model.

4.2. Complexes with fourfold symmetry

4.2.1. $[\text{R}_2(\text{L}^{15}-2\text{H})_3]$ ($\text{L}^{15} = \text{octaethylporphyrin}$)

Early efforts in the synthesis and characterisation of lanthanide(III) porphyrin coordination compounds led to monoporphyrimates such as $[\text{R}(\text{TPP})(\text{acac})(\text{H}_2\text{O})_2]$ (where $(\text{TPP})^{2-}$

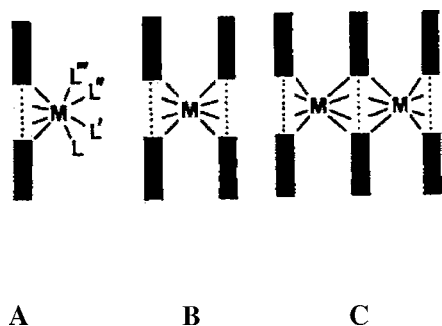


Fig. 59. Configurations of (A) mono-tetrapyrroles [$R(L^{15}-2H)LL'L''L'''$], (B) bis-tetrapyrroles [$R(L^{15}-2H)_2$] and (C) tris-tetrapyrroles [$R_2(L^{15}-2H)_3$] (adapted from Buchler et al. (1986)).

is 5,10,15,20-tetraphenylporphyrin and H(acac) is acetylacetonate) representing coordination type A of square antiprismatic geometry (fig. 59) (Wong et al., 1974; Wong and Horrocks, 1975). A protonated bis-porphyrinate, H[Pr(TTP)₂], was also obtained but could not be crystallised and characterised structurally (Buchler et al., 1983). However, the use of octaethylporphyrin ($[L^{15}-2H]^{2-}$ or $(OEP)^{2-}$) afforded the entire series of double-decker sandwich compounds [$R(L^{15}-2H)_2$] ($R = La-Lu$ except Pm) (coordination type B) and triple-decker dimetallic compounds [$R_2(L^{15}-2H)_3$] ($R = La-Gd$ except Pm) (coordination type C) of square antiprismatic geometry (fig. 59) (Buchler et al., 1986).

The crystal structures of the Ce compounds of both series, [$Ce(L^{15}-2H)_2$] and [$Ce_2(L^{15}-2H)_3$], were obtained by X-ray crystallography. In the first compound, the Ce(IV) ion has a square antiprismatic coordination polyhedron formed by the eight nitrogen atoms of the two staggered porphyrin rings, with rotational angle $\alpha = 41.8^\circ$ (fig. 60a). The crystal structure of the dimetallic compound [$Ce_2(L^{15}-2H)_3$] consists of a small stack of three ligand dianions separated by two Ce(III) ions, which define a C_4 symmetry axis. Due to the presence of an inversion center located between the two Ce(III) ions, the two external rings have the same orientation with respect to the internal macrocycle. Each ion is surrounded by eight nitrogen atoms, four of which belonging to the external and four to the internal porphyrinate ring. The coordination polyhedron is more distorted from the ideal square antiprism than in the monometallic compound, as the mean rotational angle of the two macrocycles is $\alpha = 24.5^\circ$ (fig. 60b). Furthermore, the Ce(III) ions are closer to the $4N_p$ mean planes of the external rings (1.394 Å) than of the internal ring (1.876 Å) and the $4N_p$ mean-plane separation is

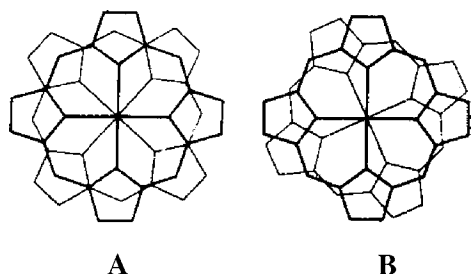


Fig. 60. Stick bond model projection of [$Ce(L^{15}-2H)_2$] (A) and [$Ce_2(L^{15}-2H)_3$] (B), showing the respective relative rotations of the different macrocyclic units (adapted from Buchler et al. (1986)).

approximately 3.27 Å (Buchler et al., 1986). There is also a strong C_{4v} doming of the outer rings, which also helps to relax inter-ring alkyl crowding.

The ^1H NMR spectra of the dimetallic compounds $[R_2(\text{L}^{15}-2\text{H})_3]$ ($R = \text{La-Eu}$ except Pm) were reported in CCl_4 at 293 K (Buchler et al., 1986, 1988, 1989), while the ^{13}C NMR spectra of the corresponding $R = \text{La, Ce}$ and Pr compounds were recorded in $\text{CCl}_4/\text{CD}_2\text{Cl}_2$ or $\text{CCl}_4/\text{C}_6\text{D}_6$ mixtures (Buchler et al., 1992). The LIS values of the methyl (CH_3), methylene (CH_2) and methine (CH) proton resonances of the outer- and inner rings were obtained for the paramagnetic complexes, relative to the diamagnetic La complex. Since the outer rings do not possess a symmetry plane, the outer ring CH_2 protons are diastereotopic and two resonances result. As all nuclei of these complexes experience additive LIS effects from the two paramagnetic centers, which have negligible electron spin interactions between them, it is not surprising that the relative LIS values were larger for all the protons of the inner ring, which experience the closer magnetic influence of the two paramagnetic centers.

In a structural analysis of the observed proton LIS values for the Ce(III) dimetallic complex, the contact contribution was neglected (Buchler et al., 1989). Axial dipolar contributions from the two Ce ions were added using eq. (65) which reduces to eqs. (71), (72) for the outer ring and inner ring protons, respectively (Ce(1) is proximal to and Ce(2) is distal to the outer ring)

$$\delta_{ij}^{\text{para}} = \delta_{ij}^{\text{dip,Ce(1)}} + \delta_{ij}^{\text{dip,Ce(2)}} = B_0^2(G_i^1 + G_i^2)C_j, \quad (71)$$

$$\delta_{ij}^{\text{para}} = 2\delta_{ij}^{\text{dip,Ce(1)}} = 2B_0^2G_i^1C_j. \quad (72)$$

As $\delta_{ij}^{\text{dip,Ce(1)}} > \delta_{ij}^{\text{dip,Ce(2)}}$, the inner ring dipolar shifts are larger than those of the outer ring. A solution geometry for $[\text{Ce}_2(\text{L}^{15}-2\text{H})_3]$ was searched for which there was a reasonable agreement between experimental dipolar shift ratios and calculated geometric factor ratios, using as geometrical model the single crystal structure of the compound. The degree of doming of the outer rings and the outer Ce positions were increased systematically, as well as alkyl group bond rotation. The geometric factors were calculated for the protons and used in the solution structural search. This procedure gave compelling evidence for inter-ring steric crowding and subsequent limited rotation of the outer ring alkyl groups such that the outer $\beta\text{-CH}_3$ groups stay far away from the inner ring alkyl groups to minimize inter-ring steric crowding.

We proceeded to verify if the approximation of neglecting the contact contribution to the ^1H LIS values is warranted. Plots of $\delta_{ij}^{\text{para}}/\langle S_z \rangle_j$ vs $C_j/\langle S_z \rangle_j$ (eq. (66)) and $\delta_{ij}^{\text{para}}/C_j$ vs $\langle S_z \rangle_j/C_j$ (eq. (67)) for the ^1H NMR data of $[R_2(\text{L}^{15}-2\text{H})_3]$ ($R = \text{Ce, Pr, Nd, Eu}$) do not give very good linear correlations (fig. 61a). The irregularities are possibly due to deviations of the relative dipolar shift values from relative Bleaney's constants C_j , in particular for the Ce and Pr ions and inner-ring protons, as observed before (Buchler et al., 1992). The contact F_i and pseudo-contact $B_0^2(G_i^1 + G_i^2)$ terms, obtained according to least-squares fits of eq. (65), indicate that some of the protons do have non-negligible contact shifts (table 26).

All the plots of $\delta_{ij}^{\text{para}}/\langle S_z \rangle_j$ vs $\delta_{kj}^{\text{para}}/\langle S_z \rangle_j$ (eq. (68)) for the various pairs of proton LIS values of $[R_2(\text{L}^{15}-2\text{H})_3]$ give good linear correlations (fig. 61b) indicating that the complexes are isostructural and that the irregularities of the LIS values are due to changes of the crystal field

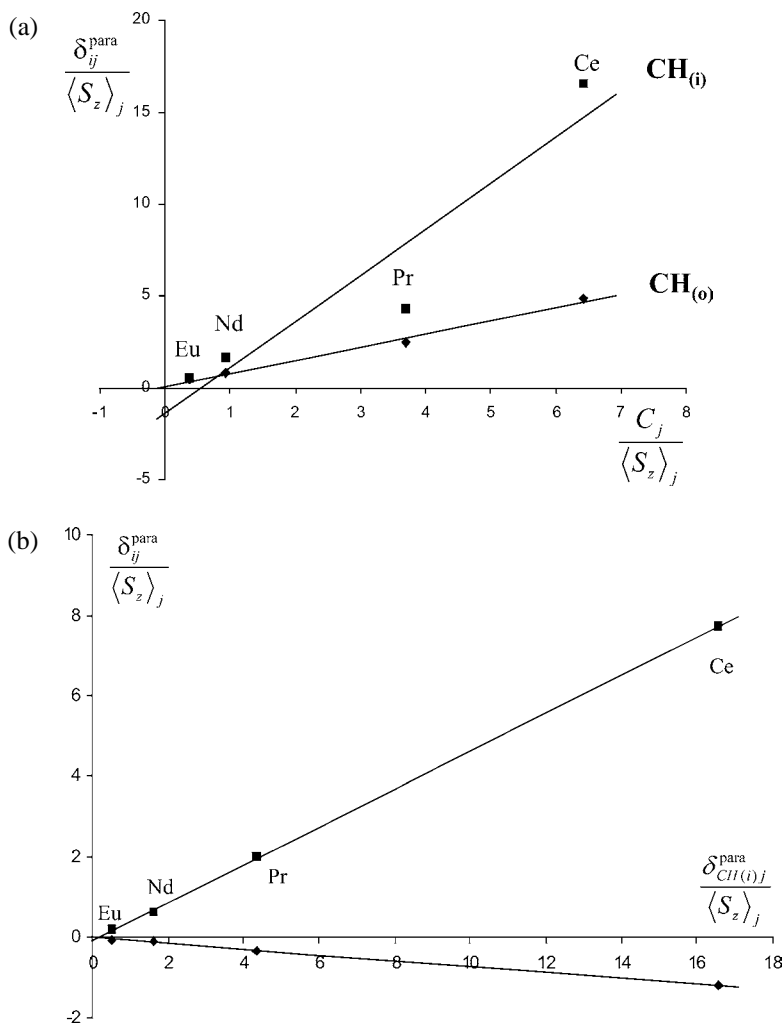


Fig. 61. Plots of (a) $\delta_{ij}^{\text{para}}/\langle S_z \rangle_j$ vs $C_j/\langle S_z \rangle_j$ for $\text{CH}_{(i)}$ (■) and $\text{CH}_{(o)}$ (◆); (b) $\delta_{ij}^{\text{para}}/\langle S_z \rangle_j$ vs $\delta_{kj}^{\text{para}}/\langle S_z \rangle_j$ for the $\text{CH}_3(o)\text{-CH}_{(i)}$ (◆) and $\text{CH}_3(i)\text{-CH}_{(i)}$ (■) pairs; (c) $\delta_{ij}^{\text{para}}/\delta_{kj}^{\text{para}}$ vs $\delta_{ij}^{\text{para}}/\delta_{kj}^{\text{para}}$ for the $\text{CH}_3(i)\text{-CH}_2(i)\text{-CH}_{(i)}$ (■) and $\text{CH}_3(o)\text{-CH}_2(i)\text{-CH}_{(i)}$ (▲) triads (data for the complexes $[\text{R}_2(\text{L}^{15}\text{-2H})_3]$ ($\text{R} = \text{Ce-Eu}$), CCl_4 , 293 K, adapted from Buchler et al. (1992), Geraldès et al. (2003)).

parameter B_0^2 . However, the agreement of experimental and calculated R_{ik} and $(F_i - F_k)R_{ik}$ parameters is not always good, in particular for the CH_2 protons (table 26). All the calculated geometric terms G_i have the same sign except the outer-ring CH_3 protons (outside the dipolar cone). The R_{ik} values obtained by the above method give very good agreement with the calculated geometric factors (Buchler et al., 1989) except for $\text{CH}_2(i)$. Plots of $\delta_{ij}^{\text{para}}/\delta_{kj}^{\text{para}}$ vs

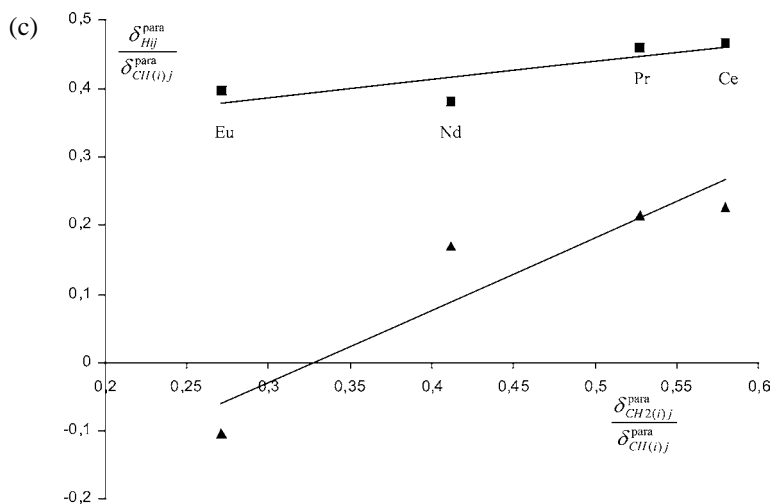


Fig. 61. Continued.

$\delta_{ij}^{para} / \delta_{kj}^{para}$ (eq. (53)) according to the three nuclei method are also affected by the irregularities of the dipolar shifts found in the Reilly method (fig. 61c and table 26).

The ^{13}C NMR spectra of the $[R_2(L^{15}\text{-}2\text{H})_3]$ ($R = \text{La}, \text{Ce}, \text{Pr}$) complexes were obtained in a $\text{CCl}_4/\text{CD}_2\text{Cl}_2$ mixture, yielding ^{13}C LIS values for the α , β , methine (CH), methylene (CH_2) and methyl (CH_3) carbons of the inner and outer rings (Buchler et al., 1992). ^{13}C LIS values in aromatic systems can have three contributions:

$$\delta_{ij}^{para} = \delta_{ij}^c + \delta_{ij}^{\text{MCdip}} + \delta_{ij}^{\text{LCdip}}, \quad (73)$$

where the presence of a significant contact shift, δ_{ij}^c , reflects spin density delocalization onto the porphyrin carbon atoms, leading to a ligand-centered dipolar shift, $\delta_{ij}^{\text{LCdip}}$, besides the traditional metal-centered dipolar shift, $\delta_{ij}^{\text{MCdip}}$. The $\delta_{ij}^{\text{MCdip}}$ term is the easiest to estimate assuming axial magnetic symmetry (a) the geometric terms from the solution geometry established above (Buchler et al. (1989) were used) (b) the magnetic anisotropy for the Ce(III) complex was obtained from plots of the proton LIS values, assumed to be purely metal-centered dipolar, versus the respective geometric terms, yielding $(\chi_{\parallel} - \chi_{\perp}) = 2980 \times 10^{-6} \text{ cm}^3 \cdot \text{mol}^{-1}$ per Ce, which is then valid for the ^{13}C LIS. Comparison of the calculated $\delta_{ij}^{\text{MCdip}}$ values with the observed LIS shows very good qualitative agreement, except for the α -carbon nuclei, the closest to the Ce ions, in particular for the outer rings. This is indicative of the presence of contact shifts and ligand-centered dipolar shifts, from direct 4f orbital overlap and/or indirect spin polarization of the 6s or 6p orbitals involving a low-lying (π or π^*) porphyrin molecular orbital. However separation of the contact and ligand-centered dipolar contributions was not possible (Buchler et al., 1992).

Table 26

Computed values for contact (F_i), pseudo-contact ($B_0^2(G_i^1 + G_i^2)$) terms and R^2 values, according to eq. (65) and comparison of R_{ik} and $(F_i - R_{ik} F_k)$ parameters calculated directly according to eq. (68) with those obtained from the above F_i and $B_0^2(G_i^1 + G_i^2)$ terms, for ^1H -nuclei in complexes $[R_2(\text{L}^{15}\text{-2H})_3]$ ($R = \text{Ce-Eu}$, CCl_4 , 293 K, Buchler et al. (1992), Geraldes et al. (2003))^a

Compd		$\text{CH}_3(\text{o})$	$\text{CH}_3(\text{i})$	$\text{CH}_2(\text{o}_1)$	$\text{CH}_2(\text{o}_2)$	$\text{CH}_2(\text{i})$	$\text{CH}(\text{o})$	$\text{CH}(\text{i})$
$R = \text{Ce-Eu}^b$	F_i	-0.18	-0.75	0.31	0.02	0.03	0.08	-1.40
	$B_0^2(G_i^1 + G_i^2)$	0.10	1.18	0.13	0.08	0.02	0.71	2.50
	R^2	0.892	0.896	0.829	0.535	0.535	0.991	0.894
Compd		$\text{CH}_3(\text{o})\text{-CH}(\text{i})$		$\text{CH}_3(\text{i})\text{-CH}(\text{i})$		$\text{CH}_2(\text{o}_1)\text{-CH}(\text{i})$		
$R = \text{Ce-Eu}^b$	$R_{ik}(\text{exp})$		-0.07		0.47		0.26	
	$(F_i - F_k R_{ik})(\text{exp})$		0.00		-0.08		-0.11	
	R^2		0.999		0.999		0.997	
	$R_{ik}(\text{calc})$		0.04		0.47		0.07	
	$(F_i - F_k R_{ik})(\text{calc})$		-0.12		-0.09		0.33	
	$R_{ik}(\text{calc})^b$		-0.07		0.47		0.23	
Compd		$\text{CH}_2(\text{o}_2)\text{-CH}(\text{i})$		$\text{CH}_2(\text{i})\text{-CH}(\text{i})$		$\text{CH}(\text{o})\text{-CH}(\text{i})$		
$R = \text{Ce-Eu}^b$	$R_{ik}(\text{exp})$		0.10		0.03		0.26	
	$(F_i - F_k R_{ik})(\text{exp})$		-0.17		-0.09		0.69	
	R^2		0.974		0.793		0.944	
	$R_{ik}(\text{calc})$		0.03		0.00		0.28	
	$(F_i - F_k R_{ik})(\text{calc})$		0.06		0.03		0.47	
	$R_{ik}(\text{calc})^b$		0.18		0.60		0.32	
$k = \text{CH}_2(\text{i}); l = \text{CH}(\text{i})$								
Compd		$i = \text{CH}(\text{o})$	$i = \text{CH}_3(\text{i})$	$i = \text{CH}_3(\text{o})$	$i = \text{CH}_2(\text{o}_1)$	$i = \text{CH}_2(\text{o}_2)$		
$R = \text{Ce-Eu}^b$	$\alpha(\text{exp})$	-1.45	0.27	0.11	1.06	-0.25		
	$\beta(\text{exp})$	1.19	0.31	-0.13	-0.35	0.28		
	R^2	0.499	0.706	0.499	0.862	0.254		

^aThe following numbering scheme is used: o = outer ring, i = inner ring, CH_3 = methyl, CH_2 = methylene (labels 1 and 2 correspond to the different diastereotopic protons) and CH = methine.

^bValues for the first isostructural series (except Sm).

5. Application of the model-free methods to axial trimetallic lanthanide complexes with sterically rigid ligands

Axial symmetry in trimetallic lanthanide complexes requires the location of the metal ions along the molecular threefold or fourfold axes. Since the terminal coordination sites are different from the central coordination site for symmetry reasons, two different crystal-field parameters $B_0^{2\text{terminal}}$ and $B_0^{2\text{central}}$ must be considered. Equation (61) holds for the general case of three ($n = 3$) magnetically non-coupled lanthanide metal ions packed along the symmetry axis and eqs. (62)–(64) can be used for homotrimetallic axial complexes. To the best of our knowledge, only one partial study of the NMR data for a D_3 -symmetrical axial trimetallic complex has been reported (Bocquet et al., 2002; Floquet et al., 2003; see sect. 5.1.2). The D_{3h} -symmetrical complexes $[R_3(\text{L}^{16}\text{-3H})_2(\text{OH}_2)_6]^{3+}$ do not fit the requirements for axial symmetry since the metal ions are located on mirror planes and not on the threefold axis, but

the authors have applied pseudo-axial symmetry for their mathematical treatment (Chapon et al., 2001; see sect. 5.1.1).

5.1. Complexes with threefold symmetry

5.1.1. $[R_3(L^{16}-3H)_2(OH_2)_6]^{3+}$ ($L^{16} = 1,3,5$ -triamino-1,3,5-trideoxy-cis-inositol)

The ligand 1,3,5-triamino-1,3,5-trideoxy-cis-inositol (L^{16}) reacts with $R(III)$ in water to give quantitatively the D_{3h} -symmetrical trinuclear sandwich-type complexes $[R_3(L^{16}-3H)_2(OH_2)_6]^{3+}$ (Hedinger et al., 1998; fig. 62). Toth et al. (1998) have used the gadolinium complex $[Gd_3(L^{16}-3H)_2(OH_2)_6]^{3+}$ as a model for investigating polymetallic MRI contrast agents and the selective formation of heterometallic analogues with lower symmetries $[R_2R'(L^{16}-3H)_2(OH_2)_6]^{3+}$ (C_{2v} point group) and $[RR'R''(L^{16}-3H)_2(OH_2)_6]^{3+}$ (C_s point group) has been demonstrated by Chapon et al. (2002).

As far as NMR studies are concerned, 2D-EXSY spectra show that the complexes exhibit fast intramolecular rotation of the ligand with respect to the lanthanide ions on the NMR time scale, which corresponds to the rotations of the cyclohexane backbones about the threefold axis in the homotrimetallic complexes $[R_3(L^{16}-3H)_2(OH_2)_6]^{3+}$ (Chapon et al., 2002). Only two 1H NMR signals are detected for protons H1 and H2, and plots of $\delta_{ij}^{para} / \langle S_z \rangle_j$ vs $C_j / \langle S_z \rangle_j$ (eq. (74)) and δ_{ij}^{para} / C_j vs $\langle S_z \rangle_j / C_j$ (eq. (75)) for $[R_3(L^{16}-3H)_2(OH_2)_6]^{3+}$ ($R = Pr$ – Yb except Pm and Gd) display linear correlations which have been assigned to isostructurality along the complete lanthanide series (Chapon et al., 2001; fig. 63),

$$\frac{\delta_{ij}^{para}}{\langle S_z \rangle_j} = \sum_{m=1}^3 F_i^m + \left[\sum_{m=1}^3 (B_0^2 G_i^m + \sqrt{6} B_2^2 H_i^m) \right] \frac{C_j}{\langle S_z \rangle_j}, \quad (74)$$

$$\frac{\delta_{ij}^{para}}{C_j} = \sum_{m=1}^3 (B_0^2 G_i^m + \sqrt{6} B_2^2 H_i^m) + \left[\sum_{m=1}^3 F_i^m \right] \frac{\langle S_z \rangle_j}{C_j}. \quad (75)$$

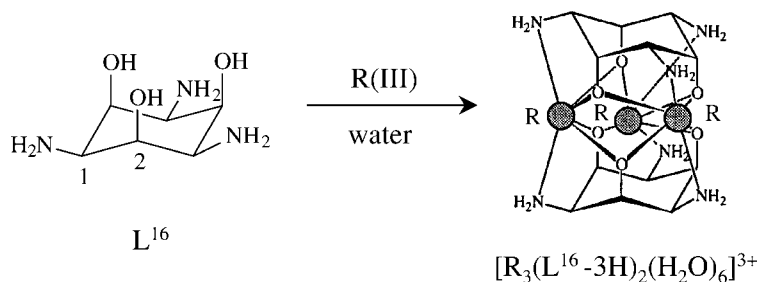


Fig. 62. Schematic formation of the D_{3h} -symmetrical complexes $[R_3(L^{16}-3H)_2(OH_2)_6]^{3+}$ in water with numbering scheme. The representation of the complex corresponds to the crystal structure of $[Gd_3(L^{16}-3H)_2(H_2O)_6]Cl_3 \cdot 3H_2O$, but the water molecules (two per $R(III)$) have been omitted for clarity (Hedinger et al., 1998).

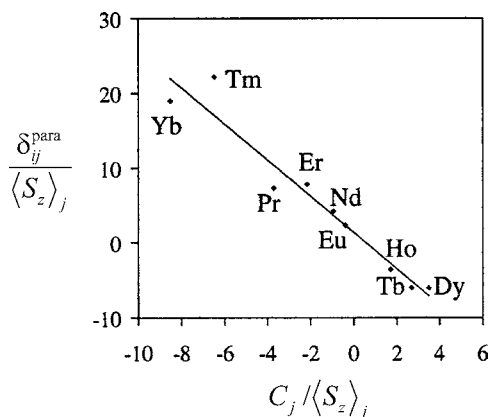


Fig. 63. Plot of $\delta_{ij}^{\text{para}} / \langle S_z \rangle_j^2$ vs $C_j / \langle S_z \rangle_j$ (eq. (74)) for H1 in $[R_3(L^{16}-3H)_2(OH_2)_6]^{3+}$ ($R = \text{Pr}-\text{Yb}$, D_2O , 298 K, adapted from Chapon et al. (2001)).

Since in the crystal structure the metallic sites are not located on the threefold axis (but on mirror planes), the rhombic term $\sqrt{6}B_2^2H_i$ in eqs. (46), (48), (49) cannot be neglected and eqs. (74), (75) hold. However, it is worth noting that the $\delta_{ij}^{\text{para}} / \langle S_z \rangle_j^2$ vs $\delta_{kj}^{\text{para}} / \langle S_z \rangle_j^2$ plot for H1–H2 in $[R_3(L^{16}-3H)_2(OH_2)_6]^{3+}$ ($R = \text{Pr}-\text{Yb}$ except Pm and Gd) indeed gives a straight line which strongly suggest that the rotation of the cyclohexane backbone provides ‘effective axial symmetry’ in solution (Chapon, 2001; Briggs et al., 1972).

5.1.2. $[R_3(L^{17})_3]^{9+}$ ($L^{17} = 2,6\text{-bis}\{1\text{-ethyl-2-[6-(N,N'-diethylcarbamoyl)-pyridin-2-yl]benzimidazol-5-methylene}\text{-}(2\text{-ethyl-benzimidazol-5-yl})\}\text{pyridine}$)

Strict axial symmetry results from the alignment of the three lanthanide ions defining the threefold axis in the self-assembled D_3 -symmetrical triple-stranded helicates $[R_3(L^{17})_3]^{9+}$. Thermodynamic studies display the quantitative formation of the trimetallic helicates in acetonitrile at concentrations compatible with NMR measurements. Variable-temperature ^1H NMR spectra of $[R_3(L^{17})_3]^{9+}$ ($R = \text{La}, \text{Y}, \text{Lu}$, 233–343 K) show diastereotopic methylene protons, in line with the formation of the expected rigid D_3 -symmetrical structure on the NMR time scale (Bocquet et al., 2002; fig. 64). Paramagnetic spectra for $R = \text{Ce}-\text{Eu}$, Yb have been assigned with classical NOE and COSY techniques, but detailed assignments for $R = \text{Tb}-\text{Tm}$ require more sophisticated relaxation measurements which have limited structural analyses to the paramagnetic light lanthanides ($R = \text{Ce}-\text{Tb}$, Floquet et al. (2003)).

Since (i) no magnetic coupling occurs at room temperature between the $R(\text{III})$ ions lying at distances larger than 4 Å and (ii) the tridentate binding units are separated by methylene bridges in L^{17} which are poor electronic relays, the contact contributions δ_{ij}^c result from through-bond *Fermi* interactions with a single metallic center and eq. (61) reduces to eq. (76) for $[R_3(L^{17})_3]^{9+}$ in which S_i is defined in eq. (77). Different crystal-field parameters for the central RN_9 ($B_0^{2\text{central}}$) and the two terminal RN_6O_3 ($B_0^{2\text{terminal}}$) metallic sites are required together with three geometrical factors $G_i^m = (3 \cos^2(\theta_i^m) - 1) / (r_i^m)^3$ defined in fig. 65 ($m = 1, 2, 3$). Equations (78), (79) correspond to the linear forms of eq. (76) used for testing

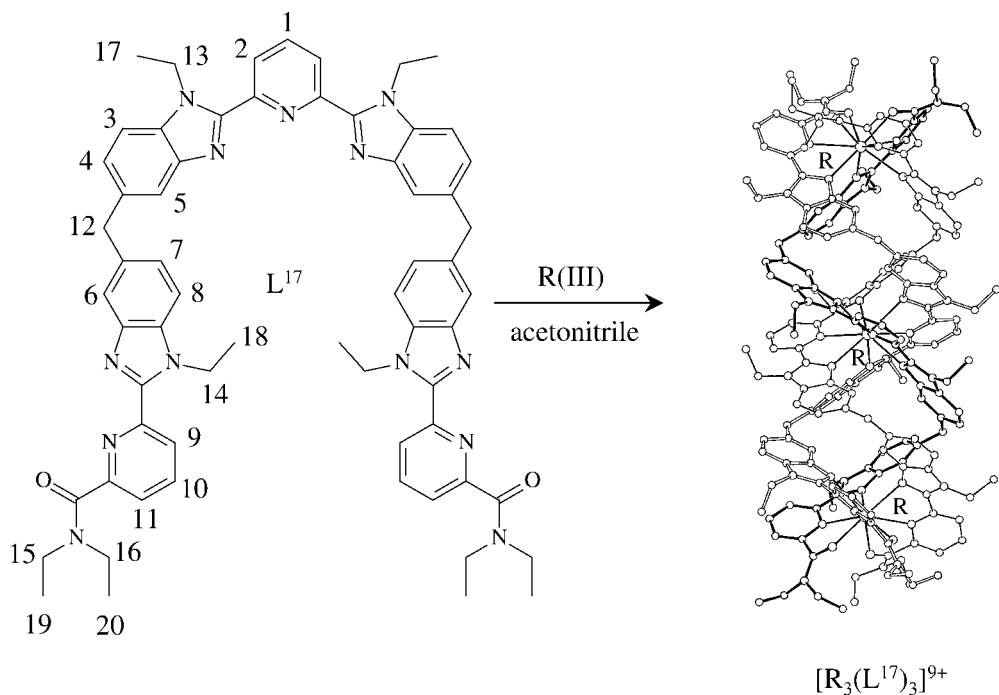


Fig. 64. Schematic formation of the D_3 -symmetrical complexes $[R_3(L^{17})_3]^{9+}$ in acetonitrile. The representation of the complex corresponds to the crystal structure of $[Eu_3(L^{17})_3](CF_3SO_3)_9(CH_3CN)_9(H_2O)_2$ (Bocquet et al., 2002).

isostructurality (Floquet et al., 2003),

$$\delta_{ij}^{\text{para}} = F_i \langle S_z \rangle_j + C_j S_i, \quad (76)$$

$$S_i = (B_0^{\text{central}} G_i^1 + B_0^{\text{terminal}} (G_i^2 + G_i^3)), \quad (77)$$

$$\frac{\delta_{ij}^{\text{para}}}{\langle S_z \rangle_j} = F_i + S_i \frac{C_j}{\langle S_z \rangle_j}, \quad (78)$$

$$\frac{\delta_{ij}^{\text{para}}}{C_j} = S_i + F_i \frac{\langle S_z \rangle_j}{C_j}. \quad (79)$$

Plots of $\delta_{ij}^{\text{para}} / \langle S_z \rangle_j$ vs $C_j / \langle S_z \rangle_j$ (eq. (78)) and $\delta_{ij}^{\text{para}} / C_j$ vs $\langle S_z \rangle_j / C_j$ (eq. (79)) are linear for all aromatic protons (H1–H11) and for the methyl groups (Me17–Me20) along the series $R = \text{Ce–Eu}$ in agreement with the existence of an isostructural series (fig. 66). A first set of F_i and S_i factors obtained with eq. (76) has been used for predicting the ^1H NMR spectra of $[R_3(L^{17})_3]^{9+}$ for the strongly paramagnetic lanthanides ($R = \text{Tb–Yb}$). Comparison between predictions and experimental data is only satisfying for the first member of the second series $[\text{Tb}_3(L^{17})_3]^{9+}$, thus allowing a complete assignment for this complex and its consideration

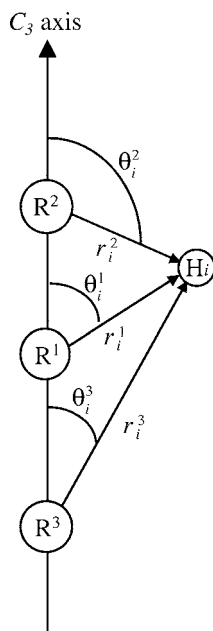


Fig. 65. Axial coordinates considered in trimetallic axial lanthanide complexes (adapted from Floquet et al. (2003)).

Table 27

Computed values for contact (F_i) and pseudo-contact $S_i = (B_0^{2\text{central}} G_i^1 + B_0^{2\text{terminal}} (G_i^2 + G_i^3))$ terms and agreement factors (AF_i) for aromatic and methyl protons in complexes $[R_3(L^{17})_3]^{9+}$ ($R = \text{Ce-Tb}$, CD_3CN , 298 K, Floquet et al. (2003)). See fig. 64 for the atom-numbering scheme

	H1	H2	H3	H4	H5	H6	H7	H8
F_i	-0.18(3)	-0.42(6)	-0.10(1)	0.043(4)	0.45(7)	0.6(1)	0.031(3)	-0.26(3)
S_i	-0.08(1)	-0.03(2)	0.025(2)	0.095(1)	1.20(2)	1.20(3)	0.068(1)	0.05(1)
AF_i	0.23	0.12	0.07	0.02	0.04	0.05	0.02	0.05
	H9	H10	H11	Me17	Me18	Me19	Me20	
F_i	-0.28(5)	-0.07(4)	-0.16(3)	0.01(4)	-0.01(2)	-0.02(1)	0.11(2)	
S_i	-0.27(1)	-0.23(1)	-0.17(1)	-0.06(1)	-0.158(4)	-0.025(4)	0.470(5)	
AF_i	0.18	0.04	0.04	0.29	0.05	0.33	0.01	

for the calculations of the final set of F_i and S_i factors collected in table 27. For $R = \text{Dy-Yb}$, the experimental ^1H NMR spectra do not fit those predicted with eq. (76), which indicate a change of F_i and S_i near the middle of the lanthanide series. Detailed analyses using crystal-field independent equations related to eq. (51), but extended to trimetallic complexes, are currently in progress to detect possible changes of crystal-field parameters occurring near the middle of the series.

For $R = \text{Ce-Tb}$, the *Wilcott* agreement factors (eq. (57)) are acceptable for all aromatic protons ($0.02 < AF_i < 0.23$, table 27), but the large AF_i values observed for Me17 and Me19 result from minor paramagnetic shifts associated with negligible spin delocalization (F_i) and dipolar effects (S_i). The F_i values are negligible for protons separated from the

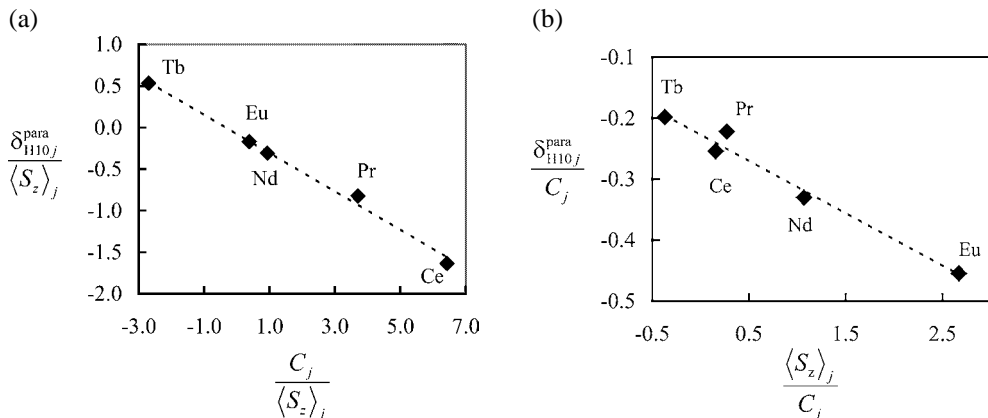


Fig. 66. Plots of (a) $\delta_{ij}^{para}/\langle S_z \rangle_j$ vs $C_j/\langle S_z \rangle_j$ (eq. (78)) and (b) δ_{ij}^{para}/C_j vs $\langle S_z \rangle_j/C_j$ (eq. (79)) for H10 in $[R_3(L^{17})_3]^{9+}$ ($R = \text{Ce–Tb}$, CD_3CN , 298 K, adapted from Floquet et al. (2003)).

paramagnetic center by more than five bonds, thus justifying that the contact contribution can be limited to a single magnetic center in $[R_3(L^{17})_3]^{9+}$. Interestingly, F_i for the central pyridine protons H1 and H2 are larger than those found for the related protons of the terminal pyridine groups H9–H11 which strongly suggests improved spin delocalization onto the bis(benzimidazole)pyridine units. The structural factor S_i is difficult to interpret because it combines two crystal-field and three geometrical parameters. The maximum values found for H5 and H6 confirm the tight helical wrapping of the strands which forces them to point inside the triple helix and close to the metal ions (i.e., $(r_i^n)^{-3}$ are large). The larger values of S_i observed for H9–H11 compared with those obtained for the central pyridine (H1–H2) are responsible for the strong paramagnetic shift experienced by the terminal pyridine ring, but its eventual assignment to specific geometrical parameters requires the evaluation of the crystal-field parameters. Taking the crystal structure of $[\text{Eu}_3(\text{L}^{17})_3]^{9+}$ as a structural model for the solution structure, the geometrical factors G_i^m ($m = 1, 2, 3$) have been calculated and a multi-linear least-squares fit of S_i versus G_i^1 and $G_i^2 + G_i^3$ for the eleven aromatic protons H1–H11 gives $B_0^{2\text{central}} = -48(3)$ and $B_0^{2\text{terminal}} = -70(3)$. The quality of the linear correlation is satisfying leading to an agreement factor $AF_S = 0.06$ between calculated and experimental S_i factors which indicates that only minor structural changes occur between the solid-state and the solution structures in these rigid polymetallic helicates. We can now rationalize the origin of the larger values observed for S_{H9-H11} compared to S_{H1-H2} which results from a combination of (i) the larger crystal-field effects associated with the terminal sites ($|B_0^{2\text{terminal}}| > |B_0^{2\text{central}}|$) and (ii) the larger compensation effect resulting from opposite paramagnetic contributions in the central metallic site (i.e., G_i^1 and $G_i^2 + G_i^3$ display opposite signs for all pyridine protons, but the absolute value of the ratios $|B_0^{2\text{central}} G_i^1 / B_0^{2\text{terminal}} (G_i^2 + G_i^3)| = 1.7\text{--}1.8$ are smaller for H1–H2 than $|B_0^{2\text{terminal}} (G_i^2 + G_i^3) / B_0^{2\text{central}} G_i^1| = 5.8\text{--}6.9$ for H9–H11). We conclude from

the analysis of NMR data that the triple-stranded helical structure is maintained in solution for $R = \text{La}$ to Lu and that isostructurality characterizes the first part of the lanthanide series ($R = \text{Ce}$ – Tb). However, an abrupt change of the crystal-field parameters near the middle of the lanthanide series prevents the analysis of strongly paramagnetic complexes ($R = \text{Dy}$ – Yb) with the one-nucleus technique (eq. (76), Floquet et al. (2003)).

6. Conclusions

This survey of the applications of the model-free methods to axial lanthanide complexes with semi-rigid multidentate chelates demonstrates that any behaviour may occur along the lanthanide series. Structural changes are usually observed for flexible complexes in which dynamic motions produce significant distortions whose magnitude is controlled by the strength of the R –ligand interactions ($[\text{R}(\text{L}^3)_3]^{3+}$, $[\text{R}(\text{L}^7-2\text{H})_3]^{3-}$). On the other hand, the considerable rigidity imposed by podand ($[\text{R}(\text{L}^4)_3]^{3+}$), non-covalent podand $[\text{RM}(\text{L}^5)_3]^{5/6+}$ or macrobicyclic ($[\text{R}(\text{L}^6)_3]^{3+}$) ligands ensures well-defined coordination sites and isostructurality along the complete lanthanide series. Surprisingly, the branched macrocyclic complexes $[\text{R}(\text{L}^{10}-4\text{H})]^-$, $[\text{R}(\text{L}^{11})]^{3+}$ and $[\text{R}(\text{L}^{12}-8\text{H})]^{5-}$ are rigid enough to display different conformational isomers existing as non-interconverting species on the NMR time scale, but they adapt their cavity to the lanthanide contraction to such an extent that minor but significant variations of the F_i and R_{ik} parameters are systematically detected near the middle of the series. However, the most striking observations concern the rather systematic detection of concomitant changes in the crystal-field parameter B_0^2 and hyperfine constants (A_i) near the middle of the lanthanide series for rigid, semi-rigid and flexible complexes. At first sight, such break could be traced back to the failure of Bleaney's approach for modeling magnetic anisotropies. Although one cannot exclude that some specific amplifications of minor structural changes result from the larger C_j factors in the second part of the lanthanide series, the parallel variations of B_q^k observed by electronic spectroscopy in the solid state and the good correlations obtained between the C_j factors and the experimental anisotropic parts of the susceptibility magnetic tensors ($\chi_{zz}^j - (1/3) \text{Tr} \chi^j$) for axial complexes, strongly support the view that Bleaney's approach (i.e., a series limited to T^{-2}) is a satisfying approximation. It remains that the multidentate ligands considered in this review often provide large crystal-field splittings which probably do not satisfy the high-temperature hypothesis $\Delta E_{\text{CF}}/kT < 1$. To the best of our knowledge, no attempt has been made to introduce the next T^{-3} term for the treatment of paramagnetic NMR data, despite the solid theoretical background proposed by McGarvey (1979). Further experimental justifications of the use of the limited high-temperature expansion for the magnetic susceptibility tensor is now required, but the recent successful applications of crystal-field independent techniques (eqs. (51), (53), (68)) in axial complexes bring some support to the classical model-free approach (i.e., limited to T^{-2}) because the removal of the crystal-field parameter is only justified within Bleaney's approach. We are convinced that further extensions toward rhombic systems and supramolecular poly-metallic complexes are within reach and recent applications to bi- and trimetallic systems

open fascinating perspectives for the design of lanthanide-containing paramagnetic probes with tuneable anisotropies.

References

- Aime, S., Barbero, L., Botta, M., Ermondi, G., 1992a. *J. Chem. Soc., Dalton Trans.*, 225.
- Aime, S., Botta, M., Ermondi, G., 1992b. *Inorg. Chem.* **31**, 4291.
- Aime, S., Barge, A., Botta, M., Fasano, M., Ayala, J.D., Bombieri, G., 1996. *Inorg. Chim. Acta* **246**, 423.
- Aime, S., Barge, A., Benetollo, F., Bombieri, G., Botta, M., Uggeri, F., 1997a. *Inorg. Chem.* **36**, 4287.
- Aime, S., Botta, M., Fasano, M., Marques, M.P.M., Geraldes, C.F.G.C., Pubanz, D., Merbach, A.E., 1997b. *Inorg. Chem.* **36**, 2059.
- Aime, S., Botta, M., Fasano, M., Terreno, E., 1998. *Chem. Soc. Rev.* **27**, 19.
- Aime, S., Botta, M., Fasano, M., Terreno, E., 1999a. *Acc. Chem. Res.* **32**, 941.
- Aime, S., Barge, A., Bruce, J.I., Botta, M., Howard, J.A.K., Moloney, J.M., Parker, D., de Sousa, A.S., Woods, M., 1999b. *J. Am. Chem. Soc.* **121**, 5762.
- Aime, S., Botta, M., Crich, S.G., Terreno, E., Anelli, P.L., Uggeri, F., 1999c. *Chem. Eur. J.* **5**, 1261.
- Allegrozzi, M., Bertini, I., Janik, M.B.L., Lee, Y.-M., Liu, G., Luchinat, C., 2000. *J. Am. Chem. Soc.* **122**, 4154.
- Alsaadi, B.M., Rossotti, F.J.C., Williams, R.J.P., 1980a. *J. Chem. Soc., Dalton Trans.*, 597.
- Alsaadi, B.M., Rossotti, F.J.C., Williams, R.J.P., 1980b. *J. Chem. Soc., Dalton Trans.*, 813.
- Alsaadi, B.M., Rossotti, F.J.C., Williams, R.J.P., 1980c. *J. Chem. Soc., Dalton Trans.*, 2147.
- Alsaadi, B.M., Rossotti, F.J.C., Williams, R.J.P., 1980d. *J. Chem. Soc., Dalton Trans.*, 2151.
- Amin, S., Morrow, J.R., Lake, C.H., Churchill, M.R., 1994. *Angew. Chem. Int. Ed. Engl.* **33**, 773.
- An, Y., Berry, M.T., van Veggel, F.C.J.M., 2000. *J. Phys. Chem. A* **104**, 11243.
- Babailov, S.P., Krieger, Y.G., 1998. *J. Struct. Chem.* **39**, 580.
- Baker, M.V., Field, L.D., Hambley, T.W., 1988. *Inorg. Chem.* **27**, 2872.
- Balzani, V., Credi, A., Raymo, F.M., Stoddart, J.F., 2000. *Angew. Chem. Int. Ed.* **39**, 3348.
- Barry, C.D., North, A.C.T., Glasel, J.A., Williams, R.J.P., Xavier, A.V., 1971. *Nature* **232**, 236.
- Benetollo, F., Bombieri, G., Aime, S., Botta, M., 1999. *Acta Cryst. C* **55**, 353.
- Berny, F., Muzet, N., Troxler, L., Dedieu, A., Wipff, G., 1999. *Inorg. Chem.* **38**, 1244.
- Bertini, I., Capozzi, F., Luchinat, C., Nicastro, G., Xia, Z.J., 1993a. *Phys. Chem.* **97**, 6351.
- Bertini, I., Turano, P., Vila, A.J., 1993b. *Chem. Rev.* **93**, 2833.
- Bertini, I., Galas, O., Luchinat, C., Parigi, G., 1995. *J. Magn. Reson.* **113**, 151.
- Bertini, I., Luchinat, C., 1996. *Coord. Chem. Rev.* **150**, 1.
- Bertini, I., Janik, M.B.L., Lee, Y.-M., Luchinat, C., Rosato, A., 2001. *J. Am. Chem. Soc.* **123**, 4181.
- Bertini, I., Luchinat, C., Parigi, G., 2002. *Prog. Nucl. Magn. Res.* **40**, 249.
- Bianchi, A., Calabi, L., Giorgi, C., Losi, P., Mariani, P., Paoli, P., Rossi, P., Valtancoli, B., Virtuani, M., 2000. *J. Chem. Soc., Dalton Trans.*, 697.
- Bleaney, B., 1972. *J. Magn. Reson.* **8**, 91.
- Bleaney, B., Dobson, C.M., Levine, B.A., Martin, R.B., Williams, R.J.P., Xavier, A.V., 1972. *J. Chem. Soc., Chem. Commun.*, 791.
- Bloembergen, N., 1957. *J. Chem. Phys.* **27**, 572.
- Bloembergen, N., Morgan, L.O., 1961. *J. Chem. Phys.* **34**, 842.
- Bocquet, B., Bernardinelli, G., Ouali, N., Floquet, S., Renaud, F., Hopfgartner, G., Piguet, C., 2002. *Chem. Commun.*, 930.
- Bretonnière, Y., Wietzke, R., Lebrun, C., Mazzanti, M., Pécaut, J., 2000. *Inorg. Chem.* **39**, 3499.
- Briggs, J.M., Moss, G.P., Randall, E.W., Sales, K.D., 1972. *J. Chem. Soc., Chem. Commun.*, 1180.
- Brink, J.M., Rose, R.A., Holz, R.C., 1996. *Inorg. Chem.* **35**, 2878.
- Bruce, J.I., Dickins, R.S., Govenlock, L.J., Gunnlaugsson, T., Lopinski, S., Lowe, M.P., Parker, D., Peacock, R.D., Perry, J.J.B., Aime, S., Botta, M., 2000. *J. Am. Chem. Soc.* **122**, 9674.
- Bryden, C.C., Reilley, C.N., 1982. *Anal. Chem.* **54**, 610.
- Bryden, C.C., Reilley, C.N., Desreux, J.F., 1981. *Anal. Chem.* **53**, 1418.
- Buchler, J.W., Kappellmann, H.-G., Knoff, M., Lay, K.-L., Pfeiffer, S., 1983. *Z. Naturforsch. B: Anorg. Chem., Org. Chem.* **38B**, 1339.

- Buchler, J.W., deCian, A.D., Fischer, J., Kihn-Botulinski, M., Paulus, H., Weiss, R., 1986. *J. Am. Chem. Soc.* **108**, 3652.
- Buchler, J.W., deCian, A.D., Fischer, J., Kihn-Botulinski, M., Weiss, R., 1988. *Inorg. Chem.* **27**, 339.
- Buchler, J.W., Kihn-Botulinski, M., Löffler, J., Wicholas, M., 1989. *Inorg. Chem.* **28**, 3770.
- Buchler, J.W., Löffler, J., Wicholas, M., 1992. *Inorg. Chem.* **31**, 524.
- Bünzli, J.-C.G., 1998. In: Saez Puche, R., Caro, P. (Eds.), *Rare Earths*. Editorial Complutense S.A., Madrid, p. 223.
- Bünzli, J.-C.G., Piguët, C., 2002. *Chem. Rev.* **102**, 1897.
- Burns, P.D., LaMar, G.N., 1982. *J. Magn. Reson.* **46**, 61.
- Cacheris, W.P., Nickle, S.K., Sherry, A.D., 1987. *Inorg. Chem.* **26**, 958.
- Caravan, P., Ellison, J.J., McMurry, T.J., Lauffer, R.B., 1999. *Chem. Rev.* **99**, 2293.
- Carnall, W.T., Goodman, G.L., Rajnak, K., Rana, R.S., 1989. *J. Chem. Phys.* **90**, 3443.
- Chang, C.A., Francesconi, L.C., Malley, M.F., Kumar, K., Gougoutas, J.Z., Tweedle, M.F., Lee, D.W., Wilson, L.J., 1993. *Inorg. Chem.* **32**, 3501.
- Chapon D., 2001. PhD thesis, University Joseph Fourier, Grenoble, p. 130.
- Chapon, D., Husson, C., Delangle, P., Lebrun, C., Votéro, P.J.A., 2001. *J. Alloys Compd.* **323–324**, 128.
- Chapon, D., Delangle, P., Lebrun, C., 2002. *J. Chem. Soc., Dalton Trans.*, 68.
- Choppin, G., 1989. In: Bünzli, J.-C.G., Choppin, G. (Eds.), *Lanthanide Probes in Life, Chemical and Earth Sciences, Theory and Practice*. Elsevier, Amsterdam, ch. 1.
- Clementi, V., Luchinat, C., 1998. *Acc. Chem. Res.* **31**, 351.
- Corsi, D.M., Platas-Iglesias, C., van Bekkum, H., Peters, J.A., 2001. *Magn. Reson. Chem.* **39**, 723.
- Desreux, J.F., 1980. *Inorg. Chem.* **19**, 1319.
- Desreux, J.F., Reilley, C.N., 1976. *J. Am. Chem. Soc.* **98**, 2105.
- Donato, H., Martin, R.B., 1972. *J. Am. Chem. Soc.* **94**, 4129.
- Dubost, J.P., Leger, J.M., Langlois, M.H., Meyer, D., Schaefer, M.C.R., 1991. *Academie Sci., Ser. II Univers.* **312**, 329.
- Elhabiri, M., Scopelliti, R., Bünzli, J.-C.G., Piguët, C., 1999. *J. Am. Chem. Soc.* **121**, 10747.
- Evans, D.F., 1959. *J. Chem. Soc.*, 2003.
- Evans, D.F., Fazakerley, G.V., Phillips, R.F., 1971. *J. Chem. Soc. A*, 1931.
- Floquet, S., Ouali, N., Bocquet, B., Bernardinelli, G., Imbert, D., Bünzli, J.C.-G., Hopfgartner, G., Piguët, C., 2003. *Chem. Eur. J.*, in press.
- Forsberg, J.H., Delaney, R.M., Zhao, Q., Harakas, G., Chandran, R., 1995. *Inorg. Chem.* **34**, 3705.
- Forsberg, J.H., 1996. In: Gschneidner, K.A., Eyring, L. (Eds.), *Handbook on the Physics and Chemistry of Rare Earths*, Vol. 23. Elsevier, Amsterdam, p. 1, ch. 153.
- Fraternali, F., Wipff, G., 1997. *J. Phys. Org. Chem.* **10**, 292.
- Freeman, A.J., Watson, R.E., 1962. *Phys. Rev. B.* **127**, 2058.
- Fronczek, F., Banerjee, A.K., Watkins, S.F., Schwartz, R.W., 1981. *Inorg. Chem.* **20**, 2745.
- Frullano, L., Rohovec, J., Peters, J.A., Geraldes, C.F.G.C., 2002. *Top. Curr. Chem.* **221**, 26.
- Fu, P.K.L., Turro, C.J., 1999. *J. Am. Chem. Soc.* **121**, 1.
- Fujita, M., Umemoto, K., Yoshizawa, M., Fujita, N., Kusakawa, T., Biradha, K., 2001. *Chem. Commun.*, 509.
- Gamelin, D.R., Güdel, H.U., 2000. *Acc. Chem. Res.* **33**, 235.
- Geraldes, C.F.G.C., 1999. In: Pous, M. (Ed.), *NMR in Supramolecular Chemistry*. Kluwer Academic, Amsterdam, p. 133.
- Geraldes, C.F.G.C., Alpoim, M.C., Marques, M.P.M., Sherry, A.D., Singh, M., 1985. *Inorg. Chem.* **24**, 3876.
- Geraldes, C.F.G.C., Sherry, A.D., Kiefer, G.E., 1992. *J. Magn. Reson.* **97**, 290.
- Geraldes, C.F.G.C., Zhang, S., Platas, C., Rodriguez-Blas, T., de Blas, A., Sherry, A.D., 2001. *J. Alloys Compd.* **323–324**, 824.
- Geraldes, C.F.G.C., Zhang, S., Sherry, A.D., 2003. *Bioinorg. Chem. App.*, in press.
- Gerloch, M., McMeeking, R.F., 1975. *J. Chem. Soc., Dalton Trans.*, 2443.
- Golding, R.M., Halton, M.P., 1972. *Aust. J. Chem.* **25**, 2577.
- Golding, R.M., Pykkö, P., 1973. *Mol. Phys.* **26**, 1389.
- Görrler-Walrand, C., Binnemans, K., 1996. In: Gschneidner, K.A., Eyring, L. (Eds.), *Handbook on the Physics and Chemistry of Rare Earths*, Vol. 23. Elsevier, Amsterdam, p. 121, ch. 155.
- Grant, D.H., 1995. *J. Chem. Educ.* **72**, 39.
- Grenthe, I., 1961. *J. Am. Chem. Soc.* **83**, 360.
- Grenthe, I., 1973. *Acta Chem. Scand.* **27**, 2453 and references therein.
- Harrowfield, J.M., Kim, Y., Skelton, B.W., White, A.H., 1995. *Aust. J. Chem.* **48**, 807 and references therein.
- Hawkes, G.E., Leibfritz, D., Roberts, D.W., Roberts, J.D., 1973. *J. Am. Chem. Soc.* **95**, 1659.

- Hedinger, R., Ghisletta, M., Hegetschweiler, K., Toth, E., Merbach, A.E., Sessoli, R., Gatteschi, D., Gramlich, V., 1998. *Inorg. Chem.* **37**, 6698.
- Hinckley, C.C., 1969. *J. Am. Chem. Soc.* **91**, 5160.
- Hoefst, S., Roth, K., 1993. *Chem. Ber.* **126**, 869.
- Holliday, B.J., Mirkin, C.A., 2001. *Angew. Chem. Int. Ed.* **40**, 2022.
- Hopkins, T.A., Bolender, J.P., Metcalf, D.H., Richardson, F.S., 1996. *Inorg. Chem.* **35**, 5356 and references therein.
- Hopkins, T.A., Metcalf, D.H., Richardson, F.S., 1998. *Inorg. Chem.* **37**, 1401 and references therein.
- Horrocks Jr., W.deW., 1974. *J. Am. Chem. Soc.* **96**, 3022.
- Horrocks Jr., W.deW., 1977. *J. Magn. Reson.* **26**, 333.
- Horrocks Jr., W.deW., Sipe, J.P., 1972. *Science* **177**, 994.
- Huskowska, E., Riehl, J.P., 1995. *Inorg. Chem.* **34**, 5615 and references therein.
- Jacques, V., Desreux, J.F., 1994. *Inorg. Chem.* **33**, 4048.
- Judd, B.R., 1979. *J. Lumin.* **18/19**, 604.
- Kahn, O., 1993. *Molecular Magnetism*. VCH Publishers, New York.
- Kahn, O., 2000. *Acc. Chem. Res.* **33**, 647.
- Kaltsayannis, N., Scott, P., 1999. *The f-Elements*. Oxford University Press.
- Kasuga, K., Tutui, M., Peterson, R.C., Tatsumi, T., VanOpdenbosch, N., Pepe, G., Meyer Jr., E.F., 1980. *J. Am. Chem. Soc.* **102**, 4835.
- Kemple, M.D., Ray, B.D., Lipkowitz, K.B., Prendergast, F.G., Rao, B.D.N., 1988. *J. Am. Chem. Soc.* **110**, 8275.
- Konami, H., Hatano, M., Tajiri, A., 1989. *Chem. Phys. Lett* **160**, 163.
- Lehn, J.-M., 2000. *Chem. Eur. J.* **6**, 2097.
- Leininger, S., Olenyuk, B., Stang, P.J., 2000. *Chem. Rev.* **100**, 853.
- Lewis, W.B., Jackson, J.A., Lemons, J.F., Taube, H., 1962. *J. Chem. Phys.* **36**, 694.
- Lisowski, J., Sessler, J.L., Lynch, V., Mody, T.D., 1995a. *J. Am. Chem. Soc.* **117**, 2273.
- Lisowski, J., Sessler, J.L., Mody, T.D., 1995b. *Inorg. Chem.* **34**, 4336.
- Lölicher, J., Scheffold, R., 1972. *J. Chem. Educ.* **49**, 646.
- Marques, M.P.M., Geraldes, C.F.G.C., Sherry, A.D., Merbach, A.E., Powell, H., Pubanz, D., Aime, S., Botta, M., 1995. *J. Alloys Compd.* **225**, 303.
- Martell, A.E., Smith, R.M., 1977. *Critical Stability Constants*, Vol. 3. Plenum Press, New York, p. 134.
- McGarvey, B.R., 1979. *J. Magn. Reson.* **33**, 445.
- Meiboom, S., Gill, D., 1958. *Rev. Sci. Instrum.* **29**, 688.
- Mironov, V.S., Galyametdinov, Y.G., Ceulemans, A., Binnemans, K., 2000. *J. Chem. Phys.* **113**, 10293.
- Mironov, V.S., Galyametdinov, Y.G., Ceulemans, A., Görrler-Walrand, C., Binnemans, K., 2001. *Chem. Phys. Lett.* **345**, 132.
- Mironov, V.S., Galyametdinov, Y.G., Ceulemans, A., Görrler-Walrand, C., Binnemans, K., 2002. *J. Chem. Phys.* **116**, 4673.
- Morrison, C.A., Leavitt, R.P., 1982. In: Gschneidner, K.A., Eyring, L. (Eds.), *Handbook on the Physics and Chemistry of Rare Earths*, Vol. 5. Elsevier, Amsterdam, p. 461, ch. 46.
- Morrow, J.R., Amin, S., Lake, C.H., Churchill, M.R., 1993. *Inorg. Chem.* **32**, 4566.
- Moussavi, M., De Cian, A., Fischer, J., Weiss, R., 1988. *Inorg. Chem.* **27**, 1287.
- Ouali, N., Bocquet, B., Rigault, S., Morgantini, P.-Y., Weber, J., Piguet, C., 2002. *Inorg. Chem.* **41**, 1436.
- Parker, D., 2000. *Coord. Chem. Rev.* **205**, 109.
- Parker, D., Pulkody, K., Smith, F.C., Batsanov, A., Howard, J.A.K., 1994. *J. Chem. Soc., Dalton Trans.*, 689.
- Paulus, E.F., Juretschke, P., Lang, J., 1995. 3. Jahrestag der Deutschen Gesellschaft für Kristallographie, Darmstadt.
- Peters, J.A., 1986. *J. Magn. Res.* **68**, 240.
- Peters, J.A., 1988. *J. Chem. Soc., Dalton Trans.*, 961.
- Peters, J.A., Huskens, J., Raber, D.J., 1996. *Prog. NMR Spectroscopy* **28**, 283.
- Petoud, S., Bünzli, J.-C.G., Renaud, F., Piguet, C., Schenk, K.J., Hopfgartner, G., 1997. *Inorg. Chem.* **36**, 5750.
- Piguet, C., 1997. *J. Chem. Educ.* **74**, 815.
- Piguet, C., Bünzli, J.-C.G., Bernardinelli, G., Williams, A.F., 1993. *Inorg. Chem.* **32**, 4139.
- Piguet, C., Bünzli, J.-C.G., Bernardinelli, G., Hopfgartner, G., Petoud, S., Schaad, O., 1996. *J. Am. Chem. Soc.* **118**, 6681.
- Piguet, C., Bernardinelli, G., Hopfgartner, G., 1997. *Chem. Rev.* **97**, 2005.
- Piguet, C., Bünzli, J.-C.G., 1998. *Chimia* **52**, 579.
- Piguet, C., Bünzli, J.-C.G., 1999. *Chem. Soc. Rev.* **28**, 347.
- Piguet, C., Edler, C., Rigault, S., Bernardinelli, G., Bünzli, J.-C.G., Hopfgartner, G., 2000. *J. Chem. Soc., Dalton Trans.*, 3999.
- Pinkerton, A.A., Earl, W.L., 1978. *J. Chem. Soc., Dalton Trans.*, 267.
- Pinkerton, A.A., Schwarzenbach, D., 1981. *J. Chem. Soc., Dalton Trans.*, 1470.
- Pinkerton, A.A., Rossier, M., Spiliadis, S., 1985. *J. Magn. Reson.* **64**, 420.

- Platas, C., Avecilla, F., de Blas, A., Gernaldes, C.F.G.C., Rodriguez-Blas, T., Adams, H., Mahia, J., 1999. *Inorg. Chem.* **38**, 3190.
- Platas-Iglesias, C., Pigué, C., André, N., Bünzli, J.-C.G., 2001. *J. Chem. Soc., Dalton Trans.*, 3084.
- Pons, M., Millet, O., 2001. *Prog. Nucl. Magn. Reson. Spec.* **38**, 267.
- Powell, D.H., Ni Dhubhghaill, O.M., Pubanz, D., Helm, L., Lebedev, Y.S., Schlaepfer, W., Merbach, A.E., 1996. *J. Am. Chem. Soc.* **118**, 9333.
- Prins, L.J., Reinhoudt, D.N., Timmerman, P., 2001. *Angew. Chem. Int. Ed.* **40**, 2382.
- Reilley, C.N., Good, B.W., Desreux, J.F., 1975. *Anal. Chem.* **47**, 2110.
- Reilley, C.N., Good, B.W., Allendoerfer, R.D., 1976. *Anal. Chem.* **48**, 1446.
- Ren, J., Sherry, A.D., 1996. *J. Magn. Reson. B* **111**, 178.
- Ren, J., Springer, C.S., Sherry, A.D., 1997. *Inorg. Chem.* **36**, 3493.
- Ren, J., Zhang, S., Sherry, A.D., Gernaldes, C.F.G.C., 2002. *Inorg. Chim. Acta* **339**, 273.
- Renaud, F., Pigué, C., Bernardinelli, G., Bünzli, J.-C.G., Hopfgartner, G., 1997. *Chem. Eur. J.* **3**, 1646.
- Renaud, F., Pigué, C., Bernardinelli, G., Bünzli, J.-C.G., Hopfgartner, G., 1999. *J. Am. Chem. Soc.* **121**, 9326.
- Reuben, J., 1982. *J. Magn. Reson.* **50**, 233.
- Reuben, J., Elgavish, G.A., 1980. *J. Magn. Res.* **39**, 421.
- Rigault, S., Pigué, C., 2000. *J. Am. Chem. Soc.* **122**, 9304.
- Rigault, S., Pigué, C., Bernardinelli, G., Hopfgartner, G., 1998. *Angew. Chem. Int. Ed. Engl.* **37**, 169.
- Rigault, S., Pigué, C., Bünzli, J.-C.G., 2000a. *J. Chem. Soc., Dalton Trans.*, 2045.
- Rigault, S., Pigué, C., Bernardinelli, G., Hopfgartner, G., 2000b. *J. Chem. Soc., Dalton Trans.*, 4587.
- Ruloff, R., Muller, R.N., Pubanz, D., Merbach, A.E., 1998. *Inorg. Chim. Acta* **275–276**, 15.
- Shannon, R.D., 1976. *Acta Crystallogr. A* **32**, 751.
- Sharp, R., 2001. *Nucl. Magn. Res.* **30**, 477.
- Sharp, R., Lohr, L., Miller, J., 2001. *Prog. Nucl. Magn. Reson. Spec.* **38**, 115.
- Sherry, A.D., Singh, M., Gernaldes, C.F.G.C., 1986. *J. Magn. Reson.* **66**, 511.
- Sherry, A.D., Gernaldes, C.F.G.C., 1989. In: Bünzli, J.-C.G., Choppin, G. (Eds.), *Lanthanide Probes in Life, Chemical and Earth Sciences, Theory and Practice*. Elsevier, Amsterdam, ch. 4.
- Sherry, A.D., Ren, J., Huskens, J., Brücher, E., Tóth, É., Gernaldes, C.F.G.C., Castro, M.M.C.A., Cacheris, W.P., 1996. *Inorg. Chem.* **35**, 4604.
- Solomon, I., 1955. *Phys. Rev.* **9**, 559.
- Spiliadis, S., Pinkerton, A.A., 1982. *J. Chem. Soc., Dalton Trans.*, 1815.
- Spiliadis, S., Pinkerton, A.A., 1983. *Inorg. Chim. Acta* **75**, 125.
- Spiliadis, S., Pinkerton, A.A., Schwarzenbach, D., 1982. *J. Chem. Soc., Dalton Trans.*, 1809.
- Spiliadis, S., Pinkerton, A.A., Schwarzenbach, D., 1983. *Inorg. Chim. Acta* **75**, 115.
- Spirlet, M.-R., Rebizant, J., Desreux, J.F., Loncin, M.-F., 1984. *Inorg. Chem.* **23**, 359.
- Steed, J.W., Atwood, J.L., 2000. *Supramolecular Chemistry*. Wiley, Chichester.
- Stout, E.W., Gutowsky, H.S., 1976. *J. Magn. Reson.* **24**, 389.
- Swiegers, G.F., Malefetse, T.J., 2000. *Chem. Rev.* **100**, 3483.
- Swiegers, G.F., Malefetse, T.J., 2001. *J. Incl. Phen., Macrocycl. Chem.* **40**, 253.
- Toth, E., Helm, L., Merbach, A.E., Hedinger, R., Hegetschweiler, K., Janossy, A., 1998. *Inorg. Chem.* **37**, 4104.
- Ulrich, G., Ziessel, R., Manet, I., Guardigli, M., Sabbatini, N., Fraternali, F., Wipff, G., 1997. *Chem. Eur. J.* **3**, 1815.
- Vold, R.L., Waugh, J.S., Klein, M.P., Phelps, D.E., 1968. *J. Chem. Phys.* **43**, 3831.
- Wasylishen, R.E., 1987. In: Dybowski, C., Lichters, R.L. (Eds.), *NMR Spectroscopy*. Dekker, New York–Basle, p. 45.
- Wertz, J.E., Bolton, J.R., 1986. *Electron Spin Resonance*. Chapman and Hall, New York–London, chaps. 3–5.
- Wilcott, M.R., Lenkinski, R.E., Davis, R.E., 1972. *J. Am. Chem. Soc.* **94**, 1742.
- Wong, C.P., Venteicher, R.F., Horrocks Jr., W.deW., 1974. *J. Am. Chem. Soc.* **96**, 7149.
- Wong, C.P., Horrocks Jr., W.deW., 1975. *Tetrahedron Lett.*, 2637.
- Zhang, S., Kovacs, Z., Burgess, S., Aime, S., Terreno, E., Sherry, A.D., 2001. *Chem. Eur. J.* **7**, 288.

Chapter 216

LANTHANIDE AND ACTINIDE SOLUTION CHEMISTRY AS STUDIED BY TIME-RESOLVED EMISSION SPECTROSCOPY

Isabelle BILLARD

Institut de Recherches Subatomiques, Chimie Nucléaire,

B.P. 28, 67037 Strasbourg cedex 2, France

Contents

List of symbols	466	3.7.4. Discussion on the use of a Förster mechanism	484
1. Introduction	466	3.8. Third interpretation: Empirical law for long range interactions	484
2. Basic principles of Time-Resolved Emission Spectroscopy (TRES)	467	3.9. Conclusion on the question of hydration numbers and related topics	485
2.1. Physical basis	467	4. Reaction rate constants as studied by TRES	485
2.2. Experimental	469	4.1. Theoretical approach	485
2.3. Data analysis	470	4.1.1. Stern–Volmer formula	485
3. Physico-chemical modifications of the solution: Influence on the spectroscopic parameters	471	4.1.2. Diffusion or activation-controlled reaction	486
3.1. Introduction	471	4.1.3. Diffusion-controlled reaction: Smoluchowsky approach	487
3.2. Changes of solvent: Experimental data	471	4.1.4. Ionic strength effects	487
3.3. Addition of supporting electrolytes: Experimental data	473	4.1.5. Electron transfer: Rehm–Weller equation	488
3.4. Temperature changes: Experimental data	474	4.1.6. Time-dependent reaction rate constant and other modifications of the Stern–Volmer formula	488
3.5. General comments on the experimental data	475	4.2. Experimental data and links to theory	489
3.6. First interpretation: Solvent effects onto the first hydration sphere	475	4.3. Conclusion on the study of reaction constants with TRES	492
3.6.1. Initial model: Solvated Eu^{3+} (or other lanthanide ions) in various solvents	475	5. Equilibrium constants and complexation as studied by TRES	493
3.6.2. First extension: Lanthanide and curium complexes in solution	477	5.1. Solvation/complexation: A brief introduction	493
3.6.3. Second extension: Solutions with supporting electrolytes	479	5.2. Experimental data: Effects of complexation on the spectroscopic parameters	493
3.6.4. Discussion: Determination of the hydration number by TRES	480	5.2.1. Absorption	494
3.7. Second interpretation: Förster mechanism	483	5.2.2. Lifetime values and decay spectra	494
3.7.1. General theoretical approach	483	5.2.3. Excitation spectra and luminescence quantum yield	495
3.7.2. Use of a simplified formalism	483		
3.7.3. Explicit use of the Förster mechanism	484		

5.2.4. Emission spectra	496	5.7. Conclusion on the determination of equilibrium constants by TRES	506
5.3. General considerations	497	6. Analytical applications of TRES: A few examples	506
5.3.1. Photophysical point of view and related experimental data	497	6.1. Trace amount determination of lanthanides and actinides	506
5.3.2. Chemical point of view and related experimental data	499	6.2. Trace amount determination of other ions	508
5.4. General kinetic scheme	501	6.3. Luminescent lanthanide sensors	508
5.5. Main results and physical implications	502	7. General conclusion	509
5.6. Discussion: Application to lanthanides and actinides	504	References	510

List of symbols

$\tau_{\text{obs}}, \tau_{\text{obs}}^{\text{H}_2\text{O}}, \tau_{\text{obs}}^{\text{D}_2\text{O}}$	experimental lifetimes of a luminescent probe. When necessary, the solvent is indicated as a superscript	$N_{\text{H}_2\text{O}}$	hydration number
$k_{\text{obs}}, k_{\text{obs}}^{\text{H}_2\text{O}}, k_{\text{obs}}^{\text{D}_2\text{O}}$	experimental decay rate of a luminescent probe. When necessary, the solvent is indicated as a superscript	$k_{\text{SV}}, k_{\text{diff}}, k_{\text{act}}$	Stern–Volmer reaction rate, diffusion contribution and activation contribution
$k_{\text{rad}}, k_{\text{nrad}}$	decay rate of the radiative and non-radiative process	k_{B}	Boltzmann constant
Q, Q_0	luminescence quantum yield	T	temperature
$[\text{M}^*](t)$	concentration of the excited state M^* at time t	η	viscosity
I, I_0	luminescence intensity	ε	dielectric constant
		K, K_{app}	equilibrium constants
		$k_{\text{M}}, k_{\text{ML}}$	experimental lifetimes of species M and ML
		NEA	Nuclear Energy Agency

1. Introduction

Time-Resolved Emission Spectroscopy (TRES) is being increasingly used for the study of various chemical aspects of lanthanides and actinides in solution. These studies are related to deactivation mechanisms, luminescence enhancement, determination of equilibrium reaction rate constants, hydration numbers and analytical aspects such as the detection of trace amounts of species. In the case of actinides, the studies mainly deal with problems related to questions of nuclear fuel reprocessing and waste disposals. In this frame, some lanthanides, especially europium, are also studied as some of them are considered as good analogues of actinides. On the other hand, uranyl photophysics in solution has long been studied on more fundamental grounds. These include kinetic aspects of the Stern–Volmer type and non-radiative deactivation mechanisms. As a whole, lanthanide and actinide luminescence in solution as studied by TRES is of interest to a large community of scientists for both fundamental and applied aspects.

This chapter deals with experimental TRES results and theoretical approaches that are relevant to the question of lanthanides and actinides solution chemistry. In this sense, this chapter

does not intend to present a comprehensive bibliography but details publications that are of interest either from a theoretical or an experimental viewpoint. Publications dealing with solids will not be reviewed, except in few cases where such studies are of great interest for the general topics of this chapter.

In principle, the luminescent species relevant to this work are:

Lanthanides: Ce(III), Nd(III), Sm(III), Eu(II), Eu(III), Gd(III), Tb(III), Dy(III), Ho(III), Er(III), Yb(III).

Actinides: U(VI), Np(VI), Am(III), Cm(III), Bk(III), Cf(III), Es(III).

However, for many of these species, some peculiarities strongly limit the number of published data. From the actinide list above, Np(VI) luminescence has been observed and characterized only in solid matrix (Dewey and Hopkins, 2000). Bk, Cf and Es are hardly available in large quantities and few papers have appeared on Am(III), due to its very short luminescence lifetime, so that in practice, actinide luminescence studies are more or less restricted to U(VI) and Cm(III). Similarly, the extensive lanthanide list above is restricted mostly to Eu(III), Gd(III) and Tb(III), with fewer papers devoted to the other lanthanides. Note that Eu(II), although luminescent, is not stable in solution under “normal” conditions which limits the number of studies. As a consequence, this chapter reflects the tendencies described above by presenting examples mostly from Eu(III), Gd(III), Tb(III) and from U(VI) and Cm(III) studies. In solution, these ions are solvated so that either the subscript “aq” or “soln” will be used, depending on the solvent of interest.

Finally, it is understood that the reader is aware of the basic principles of solution chemistry of lanthanides and actinides. Besides all the information published in the previous issues of this Handbook for lanthanides, excellent reviews exist on these topics, either on a general (Katz et al., 1986; Bünzli and Choppin, 1989; Grenthe, 1992; Choppin, 1997; Bünzli, 1998) or an historical perspective (Morss and Fuger, 1992).

2. Basic principles of Time-Resolved Emission Spectroscopy (TRES)

2.1. Physical basis

For the general notions required, the reader is referred to a comprehensive publication (Birks, 1970). The brief presentation in this section aims only at setting basic principles.

Once a species, M, has absorbed a photon of energy $h\nu$, an excited state is created, M^* . Deactivation back to the ground state occurs through multiple steps, including very fast non-radiative processes that schematically correspond to energy transfers to the solvent. Radiative deactivation may also occur, leading to the emission of a photon of energy $h\nu'$. Due to the non-radiative processes, $h\nu' < h\nu$ (Stokes shift). The emission spectrum is composed of bands, that are characteristics of the species.

Besides the emission spectrum, the lifetime of the excited state is an important feature. Many organic fluorescent molecules display “very short” lifetimes, in the pico- to nanosecond range, while the species of interest in this chapter (except Am(III) and Eu(II)) have rather “long” lifetimes, in the micro- to millisecond range. This lifetime value results from the combination of the two types of processes evoked above (radiative and non-radiative), together

with the selection rules prevailing (e.g., “forbidden” transitions). This is described through eq. (1):

$$\tau_{\text{obs}}^{-1} = k_{\text{obs}} = k_{\text{rad}} + k_{\text{nrad}}, \quad (1)$$

where τ_{obs} is the lifetime of the excited state, k_{obs} the global deactivation rate. The term k_{rad} in eq. (1) corresponds to an intrinsic phenomenon which is due to the electronic configuration, while the term k_{nrad} stands for non-radiative deactivation processes, which depend on many factors, such as temperature, solvent etc. This aspect will be detailed in sect. 3. In the following, either τ or k values will be used. The fluorescent quantum yield, Q , is defined as:

$$Q = \frac{k_{\text{rad}}}{k_{\text{rad}} + k_{\text{nrad}}}. \quad (2a)$$

From eqs. (1), (2a) one easily derives the following equations that are of practical use:

$$k_{\text{nrad}} = \frac{k_{\text{rad}}(1 - Q)}{Q}, \quad k_{\text{rad}} = Qk_{\text{obs}}. \quad (2b)$$

In practice, it is very difficult to measure an *absolute* fluorescent quantum yield and experimentalists usually limit themselves to measure the *relative* fluorescence yields.

Turning to the basic kinetic aspects of the deactivation process, the equation describing the time-dependence of the excited species population, noted $M^*(t)$, is:

$$\frac{d[M^*](t)}{dt} = -(k_{\text{rad}} + k_{\text{nrad}})[M^*](t), \quad (3)$$

from which one readily derives:

$$[M^*](t) = [M^*](0) \exp[-(k_{\text{rad}} + k_{\text{nrad}})t], \quad (4)$$

where $[M^*](0)$ is the amount of excited state at time zero. The time dependence of $[M^*](t)$ is a decaying exponential and $k_{\text{obs}} = (k_{\text{rad}} + k_{\text{nrad}})$ is the decay rate of the excited state. However, the experimentalist has not directly access to $[M^*](t)$ but only to the photons emitted by M^* . The time dependence of the measured signal is therefore:

$$S(t) = \frac{dh\nu'}{dt} = k_{\text{rad}}[M^*](t). \quad (5)$$

This signal is also an exponential of rate k_{obs} but the instantaneous amount of photons collected by the detector is related to k_{rad} , not to $(k_{\text{rad}} + k_{\text{nrad}})$. The global fluorescence intensity of M^* , defined as the integral of all photons emitted is equal to:

$$I = \int_0^\infty \frac{dh\nu'}{dt} dt = \frac{k_{\text{rad}}}{(k_{\text{rad}} + k_{\text{nrad}})} [M^*](0) = Q[M^*](0). \quad (6)$$

The measured intensity is a function of the total number of excited species created by the excitation pulse and of the luminescence quantum yield, Q . In other words, for a given lifetime, the Q value determines the ease of detection of a given species. The notion of radiative vs. non radiative pathways is in fact very important as will be detailed below (sects. 3–5).

In conclusion of this very brief description, the signature of an excited species in a given solution is composed of the emission spectrum and the lifetime value. This corresponds to 3D experimental data (intensity, wavelength, time) as is schematically depicted in fig. 1.

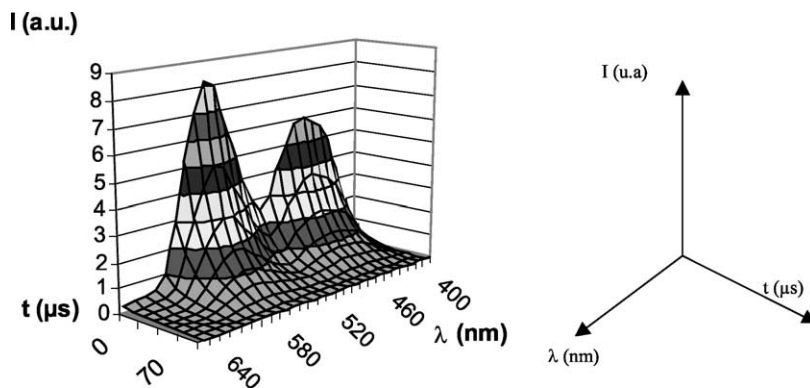


Fig. 1. Schematic view of the 3D experimental data collected in Time-Resolved Emission Spectroscopy.

2.2. Experimental

Most of the time-resolved emission spectroscopy setups are “home made” in the sense that they are built from individual devices (laser, detection system, ...) hence they are not of a “plug and press” type, so that their exact characteristics may vary from one installation to the other. Some of these differences have no impact on the overall capabilities of the system but some have a drastic influence on the way the collected data are processed and analysed. This aspect will be detailed in the next section, while this section deals with a general description of the apparatus. The most basic type of apparatus will be described, with no reference to sophisticated techniques such as Time Correlated Single Photon Counting or Circularly Polarized Luminescence devices.

The excitation is performed by use of a pulsed laser delivering an appropriate wavelength. Due to the intense beam delivered, care should be taken to avoid multiple photon absorption and filter effects, due to a too large absorption of light. For lanthanide ions, as their absorption spectra are composed of rather narrow bands, an exact match between the laser wavelength and the absorption band is requested, so that a dye (liquid) or OPO (solid) laser is needed (for a complete set of absorption spectra of the lanthanides, see Carnall (1979)). For lanthanide complexes the absorption spectra partially overlap with those of the free ions, so that usually the same excitation wavelength can be used to induce the fluorescence of both species. Fine tuning across the excitation spectra is possible (Wu and Horrocks, 1996). In this sense, Cm(III) is very similar to Eu(III). The particular case of excitation through energy transfer (antenna effect) will be discussed in sect. 5. In the case of the uranyl ion, the absorption spectrum is rather broad, so the third (355 nm) or fourth (266 nm) harmonic of a Nd:YAG laser can be used. The emission at 337 nm from a N_2 laser is also possible. For all these lasers, the duration of the pulse is of the order of a few nanoseconds, which is three or more orders of magnitude below the lifetime of the fluorescent probe under study. Therefore, the excitation process can be considered as instantaneous. The liquid sample, in a quartz cuvette, is kept in a thermoregulated chamber. The luminescence is emitted isotropically and its intensity is small

as compared to the laser excitation pulse. Therefore, detection should be performed at right angle with respect to the laser beam direction, in order to avoid detector saturation.

Schematically, two main systems can be used to collect 3D fluorescence data (time, wavelength, number of photons, see fig. 1). In a first type of system, light is directed into a monochromator connected to a photomultiplier tube and then to a fast oscilloscope (PM detection). The experimentalist thus collects luminescence decays at various wavelengths. This system is known to be very efficient for luminescence decay acquisition but is very time-consuming for the acquisition of emission spectra. In the second type of system, light is directed to a diode array detector (or CCD camera) and a subsequent electronic detection device (diode detection). The experimentalist collects emission spectra at various delay times (time zero for the pulse entering in the sample). This system is very efficient for emission data acquisition but, on the other hand, time-consuming for luminescence decay acquisitions. From this very schematic description, it appears that a system combining the two types of detections would be the optimum.

Finally, it has to be noted that whatever the detection chain used, the overall efficiency of the system is rarely constant over the whole acquisition range. The wavelength-dependent efficiency is not always taken into account in the published data. This has *a priori* no effect on the lifetime values but renders difficult any comparison of emission spectra from one laboratory to another. Certified data are increasingly needed and requested by institutions, customers and the public. In the future more attention should be paid to corrected spectra, controlled data etc, even in basic research.

2.3. Data analysis

In principle, emission spectra are easy to characterize through the position of the maxima. In contrast, luminescence decay analysis is not straightforward. As will be detailed later in this chapter, luminescence decays may be either mono- or multi-exponential and the determination of their exact nature is of paramount importance (see sect. 5). In the case of diode detection systems, the “physical” signal, as provided by the sample, is modified by the detection chain. In particular, it is integrated over short time delays, so that the ability of computer programs to extract lifetime values from such data set depends on the choice of these time delays and on the way they cover the time range of interest. Other difficulties may arise from the chemical nature of the sample: In some cases, the luminescence decay *should* be multi-exponential, because of the phenomena involved in the solution under study, but the decay *seems* monoexponential, because some of the luminescent species emit with a very low intensity, as compared to the others. Another possible intricate situation is when the lifetime values are close to one another. A complete description of the difficulties possibly encountered is out of the scope of this chapter and the reader is referred to a specific publication on this question (Sharman et al., 1999). Other methods for multiexponential decay analysis are summarized in Bare et al. (2002). Furthermore, a recent round-robin test performed on aqueous solutions of U(VI) evidenced that, at least for the programs tested, improvements are required when more than two components are observed, in decays or emission spectra (Billard et al., 2003a). In this context, mathematical methods such as chemometrics (Adams, 1995) or global analysis

(Janssens et al., 1990) or mixed methods (Al-Soufi et al., 2001) appear to be very promising in the field.

3. Physico-chemical modifications of the solution: Influence on the spectroscopic parameters

3.1. Introduction

In this section, experimental data on the spectroscopic changes observed upon modifications of the medium surrounding the luminescent probe will be first presented. These changes do *not* include inner-sphere complexation of the probe itself, a topic examined in detail in sect. 5. However, the term “luminescent probe” may refer to a complex, for which the lifetime changes induced by modifications of the surrounding medium are investigated. The various models and empirical approaches that have been used to interpret the data will then be presented and discussed.

3.2. Changes of solvent: Experimental data

The lifetime values of the luminescent probe in various solvents (either as a solvated ion or in a complexed form) are taken from the literature. However, considering the numerous publications available on lanthanide organic complexes (mostly of Eu(III)) that have been studied in water and in D₂O or some other solvents, it is out of the scope of this work to cite them all. Only some studies, which lead to very general conclusions of interest for the discussions below, are presented. In some cases, experiments have been performed in mixtures of two solvents, in various proportions. When specified in the publications, the decays are said to be strictly monoexponential.

For the aqueous or solvated Eu(III) ion, tremendous variations of the lifetime are observed by changing the solvent as well as by using a deuterated analog of a given solvent. Some lifetime values are displayed in table 1. Similarly, strong modifications of the $\text{Eu}^{3+}_{\text{solv}}$ lifetime are observed in mixtures such as H₂O/CH₃COCH₃, H₂O/acetonitrile, H₂O/dioxane (Tanaka et al., 1988), H₂O/D₂O (Haas and Stein, 1971b), H₂O/DMF, H₂O/DMSO (Lis and Choppin, 1991) as a function of the water content. In H₂O/ethanol mixtures, modifications of both the lifetime and the emission spectrum are observed when EuCl₃ is used, while no modifications of the emission spectra are detected for Eu(ClO₄)₃ (Lochhead et al., 1994). Such modifications of the lifetime when passing from water to another solvent are also observed for the other solvated lanthanide ions (Carnall, 1979; Bünzli and Choppin, 1989; Kimura et al., 2001b). Some recent results are displayed in table 2. In the case of R(III) complexes, a strong influence of deuteration or solvent changes are observed (Bryden and Reilley, 1982; De Sa et al., 1993; Klink et al., 2000; Schuurmans and Lagendijk, 2000). Actually, in the case of Eu(III) complexes, it happens that the lifetime in D₂O is always larger than the lifetime in H₂O.¹ In some cases, modifications of the emission spectra are also observed.

¹ In the paper by Balzani and Sabbatini (1986), table 3, the larger lifetime in H₂O as compared to D₂O is a typing error.

Table 1
Lifetime values of $\text{Eu}^{3+}_{\text{solV}}$ in various solvents

Solvent	τ (μs)	Ref.
H_2O	110	a
D_2O	3600 or 4100	a or d
CH_3OH	267 or 230	a or c
CH_3OD	1408	a
CD_3OD	4100	c
CH_3CN	191 ^a or 775 or 210	a or b or d
CD_3CN	1400	b
Dioxane	159	a
Dimethylformamide (DMF)	1567 or 1700	a or c
$\text{DMF-}d_7$	2300	c
$(\text{CH}_3)_2\text{SO}$	1500 or 1700	b or c
$(\text{CD}_3)_2\text{SO}$	2850 or 3200	b or c
CH_3COCH_3	182	a

^aPresence of crystallised water.

References

- (a) Tanaka et al. (1988) (c) Kimura et al. (2001b)
 (b) Haas and Stein (1971a) (d) Bünzli and Choppin (1989)

Experimental conditions

- (a) $T = 25^\circ\text{C}$, hydrated EuCl_3 salt in D_2O or H_2O , $\text{Eu}(\text{ClO}_4)_3$ in CH_3CN and CD_3CN , $[\text{Eu}^{3+}] = 10^{-2}$ M;
 (b) room temperature, perchlorate salt, $[\text{Eu}^{3+}]$ from 0.01 to 0.05 M;
 (c) $T = 25^\circ\text{C}$, perchlorate salt, $[\text{Eu}^{3+}] = 10^{-2}$ M;
 (d) room temperature, perchlorate salt, $[\text{Eu}^{3+}] < 0.1$ M.

Table 2

Experimental lifetimes (μs) of some lanthanide ions in various solvents (from Kimura et al. (2001b)). Experimental conditions: $T = 25^\circ\text{C}$, perchlorate salt, $[\text{R}(\text{III})] = 10^{-2}$ M. Theoretical radiative lifetimes (τ_{rad} , in μs) from Carnall (1979)

	H_2O	D_2O	MeOH	MeOD- d_4	DMF	DMF- d_7	DMSO	DMSO- d_6	τ_{rad}
Nd	0.032	0.17	0.054	0.40	0.49	2.0	2.0	12	420
Sm	2.7	64	4.6	93	20	250	22	610	6260
Tb	430	4100	890	5200	1900	2000	2800	3200	9020
Dy	2.5	43	3.6	69	14	170	12	330	1850

Table 3

Lifetime of solvated Cm^{3+} in various solvents.
From Kimura et al. (2001b)

Solvent	τ (μs)
H_2O	60
D_2O	1200
MeOH	190
MeOD- d_4	800
DMF	420
DMF- d_7	770
DMSO	870
DMSO- d_6	1100

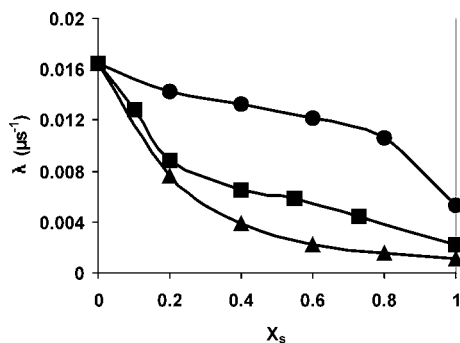


Fig. 2. Variations of k_{obs} (μs^{-1}) for Cm(III) as a function of X_s , the mole fraction of the solvent in water. (●) methanol/water. (■) DMF/water. (▲) DMSO/water. Re-drawn from Kimura et al. (2001b).

Fewer papers have appeared for U(VI). In the case of the solvated ion, the solvent effect onto the lifetime is not drastic, with a factor of roughly two between H₂O and D₂O (Allsopp et al., 1979). For uranyl complexes in various solvents, see Yayamura et al. (1994). For Cm(III) and Am(III), the bibliography is somewhat scarce (Beitz, 1991; Kimura and Choppin, 1994; Kimura et al., 2001b). In the case of Cm³⁺_{solv}, see table 3 for some recent values.

In general, the variations of $k_{obs} = \tau_{obs}^{-1}$ are not a linear function of the molar fraction of one of the solvents in the mixture, whatever the ion studied. Typical curves are displayed in fig. 2 for curium, considered as a typical example, also representative of Eu(III). From the wealth of data measured so far, it appears that linear variations of k_{obs} are obtained only in the case of H₂O/D₂O mixtures, whatever the luminescent ions. In particular, in the case of H₂O/DMF or H₂O/DMSO mixtures, a linearity is obtained for τ_{obs} , not for k_{obs} , up to 5 mol% (Lis and Choppin, 1991).

3.3. Addition of supporting electrolytes: Experimental data

In this section, lifetime values (and in few cases, data on emission spectra) are collected for a luminescent probe in a given solvent, to which variable amounts of supporting electrolytes have been added. To the best of our knowledge, such experiments have been performed only for aquo ions (never for complexes), in H₂O or D₂O, but in two cases. Although the term “supporting electrolyte” implies no chemical reactivity towards the probe, results involving chloride based electrolytes, for which a complexation process is sometimes evoked in the case of lanthanides, are also presented in this section. When discussed at all in the literature, decay spectra are said to be monoexponential.

In the case of lanthanides, all authors agree that the addition of perchlorate salts (NaClO₄, LiClO₄ or HClO₄) leads to a lifetime decrease for Sm³⁺, Eu³⁺, Tb³⁺ or Dy³⁺ in H₂O (Breen and Horrocks, 1983; Lis and Choppin, 1992; Kimura and Kato, 1998; Nehlig et al., 2003). In D₂O, the Eu(III) lifetime in presence of perchlorate based electrolytes decreases from roughly 4 ms (0.01 M) to 2.7 ms (above 8 M) (Lis and Choppin, 1992). The situation is more controversial in the case of chloride salts. According to some authors, the Eu(III) lifetime slightly decreases in H₂O solutions by addition of NaCl, LiCl or HCl (Lis and Choppin, 1992; Nehlig et al., 2003; Arisaka et al., 2002), while other authors observed no variation for

Eu^{3+} and Tb^{3+} and a very slight increase for Sm^{3+} or Dy^{3+} (Tanaka and Yamashita, 1984; Kimura and Kato, 1998). An effect of the cation associated to the chloride ion has been observed, as lifetime increases for increasing amounts of CsCl (Nehlig et al., 2003) while it decreases with LiCl in H_2O solutions (Nehlig et al., 2003; Arisaka et al., 2002). Spectral modifications (excitation and emission) parallel these lifetime changes in the few publications where these spectroscopic parameters have been measured (Breen and Horrocks, 1983; Nehlig et al., 2003). Finally, we note two publications where the effects of chloride based electrolytes have been examined in a $\text{H}_2\text{O}/\text{CH}_3\text{OH}$ mixture for Eu^{3+} (Arisaka et al., 2001, 2002).

In the case of U(VI) in H_2O , drastic lifetime changes are observed in the case of perchlorate based electrolytes (NaClO_4 , HClO_4 and mixtures of both), that have been experimentally studied in detail (Bouby et al., 1999; Rustenholtz et al., 2001). For example, the UO_2^{2+} lifetime increases from $\approx 2 \mu\text{s}$ ($[\text{HClO}_4] = 10^{-2} \text{ M}$) to $90 \mu\text{s}$ ($[\text{HClO}_4] = 10 \text{ M}$). Similarly to the europium case, an effect of the electrolyte cation has been observed: HClO_4 induces a lifetime increase, while NaClO_4 leads to a lifetime decrease. Furthermore, the effect of a given amount of NaClO_4 depends on the amount of HClO_4 . In such experiments, no spectral shift is observed. To our knowledge, no such experiments are available for Am^{3+} or Cm^{3+} , apart from one study for the system $\text{Cm}^{3+}_{\text{aq}}/\text{LiCl}$ (Arisaka et al., 2002). Note however that chloride ions are known to form inner-sphere complexes with Cm^{3+} and Am^{3+} (Allen et al., 2000) so that chloride based salts cannot be considered as supporting electrolytes in this case.

3.4. Temperature changes: Experimental data

Surprisingly, studies devoted to temperature effects (in the liquid range) as such are very limited.

Interesting results were obtained on the temperature dependence of the lifetime of an Eu(III) amino-diphosphonate complex, in H_2O and D_2O (Holz et al., 1990b). In both solvents, the lifetime decreases as temperature increases and this was ascribed to an additional (photoinduced) deexcitation pathway due to some ligand energy levels.

In the case of uranyl, most of the available studies have been performed using rather high concentrations of nitrate salts of U(VI) (e.g., 0.2 M in Allsopp et al. (1979)) for which temperature-dependent complexation occurs (Grenthe, 1992). In addition, NO_3^- is liable to complex radiolysis reactions that are also temperature-dependent (Mack and Bolton, 1999) so that the results of such studies may be an intricate combination of various temperature effects on the solvated UO_2^{2+} ion. Only one recent study has been performed with U(VI) using perchlorate salts, in sufficiently acidic solution (by use of HClO_4) so that no anion complexation occurs. Thus, the results appear strictly ascribable to temperature effects onto UO_2^{2+} (Eliet et al., 1995). The lifetime changes follow a typical Arrhenius plot in the range 288–333 K, with an activation energy of $(43.5 \pm 1.8) \text{ kJ mol}^{-1}$, independent of the total HClO_4 concentration. A very interesting feature of the decays is their non-exponential behavior at 288 K. Unfortunately, such studies have not been further detailed and the overall conclusions are rather limited, especially with respect to the emission spectra.

3.5. *General comments on the experimental data*

From the wealth of data outlined in the above sections, it can be seen that the lifetime is very sensitive to many physico-chemical changes in the surrounding medium of the luminescent probe (that should not lead to inner-sphere complexation, treated apart, see sect. 5), while the emission spectra are more or less not affected. Considering the brief theoretical approach of sect. 2.1, such changes are most probably only ascribable to changes in the k_{nrad} term of eq. (1), which substantiates the absence of significant changes in the emission spectra.

It is therefore tempting to search for a relationship linking the observed decay rate, k_{obs} , to one basic physico-chemical parameter that is varied in a given experimental series. If possible, in order to be "user-friendly", such a relationship should be as simple as possible, i.e., linear. Unfortunately, such an approach, to our opinion, is most of the time hopeless and may be misleading in certain cases. The nature of the effects observed will hamper any establishment of such a relationship, as the problem is obviously multiparametric in nature. Actually, changing the solvent or adding supporting electrolytes leads to modifications of many (if not all) physico-chemical properties of the medium, such as viscosity, density, dielectric constant, refractive index, conductivity, ion mobility, etc. However, usually one focusses on only one of these properties, not on their simultaneous variations. A plot of k_{obs} as a function of *any* of these parameters will most likely lead to smooth or even linear variations, that may have no physical meaning, however. None of these parameters can be considered as the only "good" parameter and the joint variation of any physico-chemical parameter and the luminescence data must be examined with great caution before concluding on the existence of any real physical correlation.

We would like, however, to moderate the pessimistic view that has been developed above by noting that actually, one-to-one correlations *are* experimentally obtained and that a first approach to the problem, by seeking for linear correlations, is a necessary step towards the comprehensive understanding of the multiparametric phenomena involved.

In the following, interpretation of the experimental variations detailed in sects. 3.2 and 3.3 are presented and discussed.

3.6. *First interpretation: Solvent effects onto the first hydration sphere*

This interpretation has been first proposed in the mid 1960s by three groups of authors and since that time has been modified and extended in several steps that will be presented in a chronological order.

3.6.1. *Initial model: Solvated Eu^{3+} (or other lanthanide ions) in various solvents*

Depending on the group of authors, such an interpretation is strictly limited to the lifetime variations of solvated lanthanides ($\text{Sm}^{3+}_{\text{solv}}$, $\text{Eu}^{3+}_{\text{solv}}$, $\text{Tb}^{3+}_{\text{solv}}$ and $\text{Dy}^{3+}_{\text{solv}}$) in $\text{D}_2\text{O}/\text{H}_2\text{O}$ mixtures (Heller, 1966) or in other mixed solvents (Haas and Stein, 1971a, 1971b). For the latter, in addition to studies of ions such as $\text{Eu}^{3+}_{\text{solv}}$ and $\text{Gd}^{3+}_{\text{solv}}$ (Kropp and Windsor, 1965), attempts have been made to also include the case of europium complexes with sulfate or acetate (Kropp and Windsor, 1967) and this will be quoted in sect. 3.6.2. Two groups developed very similar reasonings (Kropp and Windsor, 1965; Haas and Stein, 1971a, 1971b).

In D₂O/H₂O mixtures (Heller, 1966), the k_{obs} variations are ascribed to changes in the deactivation processes induced by OH and OD vibrations, which in turn leads to a decomposition of the expression of k_{nrad} (see eq. (2)) in a sum of terms:

$$Q = \frac{k_{\text{rad}}}{k_{\text{rad}} + k_{\text{nrad}}} = \frac{k_{\text{rad}}}{k_{\text{rad}} + k_{\text{H}}[\text{H}]^n + k_{\text{D}}[\text{D}]^m + \sum k_i[\text{Q}_i]}, \quad (7)$$

where k_{H} and k_{D} correspond to the contributions of H and D atoms to the overall value of k_{nrad} , respectively; $[\text{H}]^n$ and $[\text{D}]^m$ are the concentrations of these atoms with empirical powers and the last term takes into account the effect of other quenching species Q_i , if present (e.g., impurities). Such an approach will be also used for the Stern–Volmer equation, see sect. 4.1.1. This equation is purely phenomenological, since it does not assume any particular quenching mechanism. Assuming that $\sum k_i[\text{Q}_i]$ is negligible and denoting Q_0 the fluorescence quantum yield in a solution of D₂O, one obtains readily:

$$\frac{Q_0}{Q} = 1 + \frac{k_{\text{H}}}{k_{\text{rad}} + k_{\text{D}}[\text{D}]^m} [\text{H}]^n. \quad (8)$$

In this publication (Heller, 1966), the author measured the luminescence intensity ratio, denoted by I_0/I , which is proportional to Q_0/Q (cf. eq. (6) and sect. 2.1). For the experiments described, the I_0/I plot as a function of the H₂O concentration is linear in the very narrow range investigated (up to 8% of H₂O). On this basis, the author concluded that $n = 1$ and $m = 0$ in eq. (8). From the value $n = 1$, it is then deduced that “the radiationless relaxations studied involve only a single hydrogen atom”, which “leaves the OH bond as the only acceptable species”. Other species, like H₂O, HDO, H₂O·nD₂O and other aggregates are therefore not taken into consideration.

The other group of publications corresponds to a two-step reasoning which is summarised as follows. In the first step, the authors studied various pure solvents, such as H₂O, D₂O, CH₃CN, CH₃OH (Haas and Stein, 1971a; Kropp and Windsor, 1965). Using perchlorate salts of europium(III), the authors obtained the value k_{nrad} for various solvents by use of eq. (2b). From the values obtained, the authors divide the solvents into three groups, according to their quenching efficiencies, which are tentatively related to their chemical formula. In the second step, the authors restrict their study to the case of Eu(ClO₄)₃ in CH₃CN, in which variable amounts of water are added (Haas and Stein, 1971b). The quantum yield of such solutions depends on the water concentration and is written as:

$$Q = \frac{k_{\text{rad}}}{k_{\text{rad}} + k_{\text{nrad}} + k_{\text{H}}[\text{H}_2\text{O}]}. \quad (9)$$

In this equation, it is assumed that the effect of the added water can be simply described through the term $k_{\text{H}}[\text{H}_2\text{O}]$, where k_{H} is the bimolecular rate of deactivation of excited europium through OH bonds and $[\text{H}_2\text{O}]$ is the water concentration. Again, Q and k_{rad} are experimentally measured so that:

$$\frac{k_{\text{rad}}}{Q} - k_{\text{rad}} = k_{\text{nrad}} + k_{\text{H}}[\text{H}_2\text{O}]. \quad (10)$$

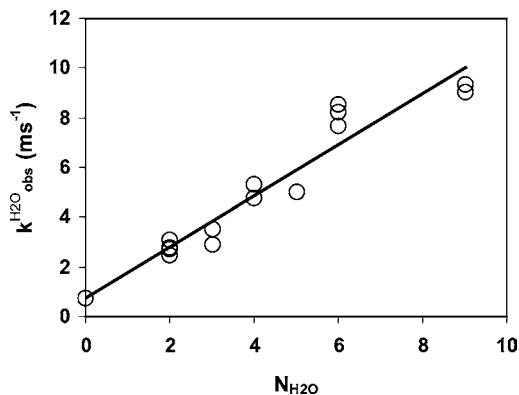


Fig. 3. Variations of $k_{\text{obs}}^{\text{H}_2\text{O}}$ (ms^{-1}) for some Eu(III) solid compounds as a function of the number of water molecules in the first coordination sphere (X-ray measurements). Solid line: linear regression for the data. Redrawn from Horrocks and Sudnick (1983).

The experimental parameter $[k_{\text{rad}}/Q] - k_{\text{rad}}$ is not a linear function of the water content in the whole range of concentration so that the authors restricted the fit to the narrow range for which a linear plot is obtained, assuming that k_{nrad} is independent of the water content. The derived value² is $k_{\text{H}} = 1100 \text{ M}^{-1} \text{ s}^{-1}$ (Haas and Stein, 1971b). This value is then related to the global quenching ability of water towards Eu(III), as determined in the first step. Assuming that the deactivation mechanism quantified in the first step can be only ascribed to the water molecules in the first hydration sphere, the average hydration number of Eu(III) in pure water is thus equal to 9, which is in good agreement with the values obtained by other techniques.

3.6.2. First extension: Lanthanide and curium complexes in solution

Since the 1980s, the concepts of the previous studies have been extended on the basis of a detailed experimental work (Horrocks and Sudnick, 1983). Note however that such an extension was clearly envisioned in a former paper (Kropp and Windsor, 1967).

First, various solid state compounds of Eu(III) and Tb(III) have been synthesized with a known number of coordinated water molecules in the first hydration sphere. X-ray diffraction experiments lead to the characterization of the structure of each compound. The decay rates of these solids, $k_{\text{obs}}^{\text{H}_2\text{O}}$, have been measured and plotted as a function of the number of water molecules in the first hydration sphere (see fig. 3).

As can be seen from fig. 3, the $k_{\text{obs}}^{\text{H}_2\text{O}}$ values are a linear function of the number of water molecules, up to 9, to a good approximation. Thus, on the basis of the publications discussed in sect. 3.6.1, Horrocks and co-workers derive:

$$k_{\text{obs}}^{\text{H}_2\text{O}} = k_{\text{rad}} + k_{\text{nrad}} + N_{\text{H}_2\text{O}} k_{\text{H}_2\text{O}}, \quad (11)$$

where k_{rad} is the intrinsic decay rate and k_{nrad} represents all the deactivation pathways other than energy transfers through OH vibrations. The deactivation processes occurring through OH vibrations are described in the last term, where $N_{\text{H}_2\text{O}}$ is the number of water molecules in the first coordination sphere, and $k_{\text{H}_2\text{O}}$ is the decay rate due to one water molecule. Assuming

² In the cited publication, the unit (s^{-1}) is erroneous and has been corrected in this text.

that the term $(k_{\text{rad}} + k_{\text{nrad}})$ is equal to the decay rate of the luminescent probe in D_2O , $k_{\text{obs}}^{\text{D}_2\text{O}}$, this allows the determination of $k_{\text{H}_2\text{O}}$ for Eu(III) and Tb(III):

$$k_{\text{H}_2\text{O}} = \frac{(k_{\text{obs}}^{\text{H}_2\text{O}} - k_{\text{obs}}^{\text{D}_2\text{O}})}{N_{\text{H}_2\text{O}}}, \quad (12a)$$

$$N_{\text{H}_2\text{O}} = \alpha (k_{\text{obs}}^{\text{H}_2\text{O}} - k_{\text{obs}}^{\text{D}_2\text{O}}). \quad (12b)$$

The conclusion drawn is that for solid compounds, eqs. (11), (12) apply and may be used for the determination of the number of water molecules in an unknown solid compound. The authors estimate the uncertainty to ± 0.5 water molecule.

Second, Horrocks and coworkers, and after them many others, have applied eq. (11) to Eu(III) or Tb(III) compounds in *aqueous solutions*, in order to determine the number of water molecules in the first hydration sphere. The measurements were performed with TRES assuming that the decay rate is a function of the water molecules in the first hydration sphere only. Similar studies leading to calibration laws of the type of eq. (12b) have been performed for Sm, Tb and Dy (Kimura and Kato, 1995, 1998) or Cm (Beitz, 1991; Kimura and Choppin, 1994). For Cm, the decay rate is measured in water/ D_2O mixtures of known composition and for solid compounds doped with Cm. The crystallographic structures of these compounds have not been determined but assumed (Kimura and Choppin, 1994). Following this method, non-integer values of $N_{\text{H}_2\text{O}}$ are often found. Besides the uncertainty of the method, this is ascribed to the fact that $N_{\text{H}_2\text{O}}$ is an average of the dynamical equilibrium occurring in solution between water molecules of the first hydration sphere and of the bulk.

The method described above requires two measurements of the same compound: one in D_2O and one in H_2O . Therefore, in a third step, the method has been simplified by using a general calibration law for which only the experimental value in H_2O is needed:

$$N_{\text{H}_2\text{O}} = Ak_{\text{obs}}^{\text{H}_2\text{O}} + B. \quad (13)$$

A and B are constants that can be determined for a given luminescent probe (i.e., Eu or Tb). Various values of A and B can be found in the literature and are presented in table 4. In this table, each expression is only referenced once, although it may have been used in numerous papers. More sophisticated expressions (see sect. 3.6.4) have not been included. Table 4 also displays the numerical values used in eq. (12b) (derived from Horrocks and Sudnick (1983)) for Eu(III) and Tb(III). The studies by Bryden and Reilley (1982), Wang and Horrocks (1997), Wang et al. (1999), already cited in the experimental section and others (Albin et al., 1984; Barthelemy and Choppin, 1989; Shin and Choppin, 1999), correspond to this approach, either in its "exact" (eq. (12b)) or "simplified" (eq. (13)) version. Finally, note that the authors using this method ascribe the decay rate changes mostly to the "water molecules" but that some authors use the more general term of "OH bonds".

This method has been further extended to non aqueous solvents, such as C_6H_6 , where the number of H_2O molecules in the first hydration sphere is deduced from the measurement of decay rates of some Eu complexes extracted in C_6H_6 (Lis et al., 1991). In another paper, eq. (12b) has been adapted to methanol, by replacing $k_{\text{obs}}^{\text{H}_2\text{O}}$ ($k_{\text{obs}}^{\text{D}_2\text{O}}$) by $k_{\text{obs}}^{\text{MeOH}}$ ($k_{\text{obs}}^{\text{MeOD}}$) (Holz et

Table 4

Numerical expression of eqs. (12b) and (13) used in the literature for various ions in water solutions (k_{obs} expressed in ms^{-1})

Ion	$N_{\text{H}_2\text{O}}$	Ref.
Nd(III)	$3.58 k_{\text{obs}} - 1.97$	a
Sm(III)	$0.026 k_{\text{obs}} - 1.6$	b
	$0.0254 k_{\text{obs}} - 0.37$	a
Eu(III)	$1.1 k_{\text{obs}} - 0.71$	b
	$1.05 k_{\text{obs}} - 0.44$	a
	$1.07 k_{\text{obs}} - 0.62$	c
	$1.05 k_{\text{obs}} - 0.70$	d
	$1.05 (k_{\text{obs}}^{\text{H}_2\text{O}} - k_{\text{obs}}^{\text{D}_2\text{O}})$	e
Tb(III)	$4.0 k_{\text{obs}} - 1.0$	b
	$4.03 k_{\text{obs}} - 0.87$	a
	$4.2 (k_{\text{obs}}^{\text{H}_2\text{O}} - k_{\text{obs}}^{\text{D}_2\text{O}})$	e
	$0.024 k_{\text{obs}} - 1.3$	b
	$0.021 k_{\text{obs}} - 0.6$	a
Am(III)	$2.56 \times 10^{-4} k_{\text{obs}} - 1.43$	a
Cm(III)	$0.65 k_{\text{obs}} - 0.88$	c
	$0.612 k_{\text{obs}} - 0.48$	a

References

- (a) Kimura et al. (2001b) (c) Kimura et al. (1998) (e) Horrocks and Sudnick (1983).
 (b) Kimura and Kato (1995) (d) Barthelemy and Choppin (1989)

al., 1991) and the same method has been used in CHCl_3 (Hasegawa et al., 1999). Numerical values obtained for $\text{H}_2\text{O}/\text{D}_2\text{O}$ mixtures have been directly applied to $\text{H}_2\text{O}/\text{DMSO}$, $\text{H}_2\text{O}/\text{DMF}$, $\text{H}_2\text{O}/\text{MeOH}$ and other mixtures (Kimura et al. 2001a, 2001b).

It is interesting to note that the same type of interpretation (i.e., the role of OH oscillators in the k_{nrad} term) has been proposed for the Eu^{2+} lifetime changes induced by complexation with various cryptands and crown-ethers in methanol (for a review of this question, see Jiang et al., 1998). The experimental data are presented in sect. 5, which is devoted to spectroscopic changes induced by complexation. In the case of Eu^{2+} luminescence in solution, data are scarce because Eu(II) is easily oxidised into Eu(III) . Thus, the quantitative interpretation of the data in terms of an equation such as eq. (12b) has not been performed. However, in view of the interesting discussion that has been initiated by Jiang and co-workers, these results will be discussed below in sect. 3.6.4.

3.6.3. Second extension: Solutions with supporting electrolytes

Some authors attempted a description of the lifetimes changes induced by the addition of supporting electrolytes (sect. 3.3) by use of either the “exact” or “simplified” method proposed by Horrocks (Lis and Choppin, 1992; Kimura and Kato, 1998). By using eq. (12b) or eq. (13), one obtains an apparent increase in the calculated hydration number $N_{\text{H}_2\text{O}}$ as a function of the electrolyte concentration, which is surprising (from 9 to 11 in the case of Eu^{3+} in $\text{HClO}_4/\text{H}_2\text{O}$ solutions, for example). In order to overcome this difficulty, it was suggested that the inner hydration number remains constant with an increasing quenching of the excited state as a

function of the salt concentration. The increase would be due to stronger interactions of the Eu(III) ion with the OH oscillators already present in the inner coordination sphere (Lis and Choppin, 1992). This stronger metal-water interaction in the primary sphere would result from smaller interaction with water molecules in the outer hydration sphere caused by the increasing concentration of ions.

3.6.4. Discussion: Determination of the hydration number by TRES

In the original papers, the important question of the possible hydrolysis of the solvated ion in the D₂O/H₂O mixtures is not addressed. It is assumed however that whatever the composition of the solvent, the aquo ion is, by far, the dominating species. From an experimental viewpoint, the initial D₂O concentration in the D₂O/H₂O mixture is controlled but the existence of HDO is not discussed. In one of these papers (Heller, 1966), the OH bond is considered as the only acceptable species responsible for the decay rate changes while H₂O, H₂O.nD₂O and aggregates are not considered at all; it is therefore somewhat difficult to conceive the exact nature of these OH bonds. In two papers (Haas and Stein, 1971a, 1971b), the attribution of the non radiative effects to the water molecules in the first hydration sphere is (strictly speaking) restricted to the case where the k_{obs} variations are linear, which corresponds to a somewhat limited number of experiments, as was discussed in the experimental section. Finally, in the last paper (Kropp and Windsor, 1965), the deactivation process is clearly ascribed to OH and CH bonds. To conclude on this first interpretation, it should be emphasised that these studies are the first ones addressing a difficult question, as the experimental section has shown. The physical bases included in eq. (7) appear reasonable, as it explicitly states that *all* the solvent molecules participate in the deactivation process. Furthermore, the assumption of specific deactivation efficiencies for all types of solvents is realistic. It should be noted that the absence of linearity of the k_{obs} plots above a few water percents (except for the H₂O/D₂O mixtures) is a strong indication that all solvent molecules do not interact in an identical and independent way.

Therefore, the extension made by Horrocks and collaborators (Horrocks and Sudnick, 1983) and by many other authors appears questionable. First, note that the interpretation of the lifetime values in solids is a rather difficult task. Tremendous Eu(III) lifetimes changes in solids (from 1–2 ms to 50 μ s, for example) have been ascribed to changes in the symmetry of the emitting center, a higher symmetry inducing a slower decay (Gaft et al., 2000a; 2000b, 2001). Second, all the studies based on eq. (13) rely on the assumption that the non-radiative deactivation process in solution is solely due to the water molecules in the first hydration sphere, while by use of eq. (12b), which requires the measurement of $k_{\text{obs}}^{\text{D}_2\text{O}}$ and $k_{\text{obs}}^{\text{H}_2\text{O}}$, the assumption is that the other non-radiative contributions are equal in H₂O and D₂O (and thus may not be negligible). The assumption embedded in eq. (13) is clearly an abusive extension of the results obtained by Haas and Stein (1971a, 1971b) and is in contradiction with the work of Kropp and Windsor (1965). This assumption totally neglects the role of other solvent molecules and anions as well as the non-linear variations of k_{obs} in the case of non-aqueous mixtures. This last criticism applies to a limited number of papers but the general tendency with time evolves towards an extension of the so-called Horrocks' method to various media such as non-aqueous liquid systems (Hasegawa et al., 1999; Holz et al., 1991;

Lis et al., 1991), ion-exchange resins (Takahashi et al., 1997; Kimura et al., 1998; Arisaka et al., 2001, 2002) or hydrated zeolites (Suib et al., 1984) for which the direct use of eq. (12b) should be considered with caution.

Actually, if H₂O were the only cause of deactivation, this would imply that the lifetime of a given R(III) ion in all solvents (except water) should be close to its radiative lifetime. Table 1 shows that the solvated Eu(III) lifetime is solvent dependent (radiative Eu³⁺ lifetime: 9.7 ms, from Carnall, 1979), tables 2 and 3 give a similar information for other R(III) solvated ions and Cm³⁺_{solv}, respectively. Examination of these tables shows that the contribution of D₂O molecules to the deactivation pathways cannot be neglected, as that of any other solvent.

Turning to the case of R(III) complexes, it should be first noted that the theoretical radiative lifetime of a given R(III) complex may be (very) different from that of the solvated ion (Werts et al., 2002). Therefore, the lifetime values of R(III) complexes in various solvents should be interpreted with caution. However, some experimental facts are in contradiction with eq. (13): (i) the deactivation efficiency of a ligand can be even lower than that of D₂O: in one case, an Eu(III) complex in D₂O has a lifetime ($\tau_{\text{obs}} = 4.66$ ms) larger than that of Eu³⁺_{aq} in D₂O (Elhabiri et al., 1999); (ii) the lifetime of a Tb complex in D₂O is *decreased* by further complexation with various anions such as OH⁻, NO₃⁻, CH₃CO₂⁻, HCO₃⁻, citrate or CO₃²⁻ (Dickins et al., 1998). In fact, the radiative lifetime value of a given complex is rather difficult to derive and very few calculations (or data) are available so that comparison between k_{rad} and k_{obs} values is only possible for Eu-dipicolinate complexes (Werts et al., 2002) (see table 5). Nevertheless, it can be seen that the ligand has an important impact onto the lifetime, even in D₂O (see table 5). In particular, it was shown in a very detailed study on Eu, Gd, Tb and Yb (Beeby et al., 1999), that the -OH, -NH and -CH bonds have an effect. A similar study has

Table 5

Experimental lifetime values of various Eu(III) complexes in pure D₂O. Radiative lifetime values for some species

Complex	$\tau_{\text{obs}}^{\text{D}_2\text{O}}$ (μs)	τ_{rad} (μs) theoretical/(experimental)
Eu ³⁺ _{aq}	3970 (a)	7700/(9500) (d)
[Eu(dpa)] ⁺	3560 (a)	4900/(6000) (d)
[Eu(dpa) ₂] ⁻	3270 (a)	
[Eu(dpa) ₃] ²⁻	3320 (a)	3100/(4300) (d)
[Eu(dota)] ⁻	2400 (b)	
[Eu(nota)]	1700 (b)	
[EuL] ⁻	2083 (c)	
[EuL'] ⁻	1850 (c)	

dpa: dipicolinate;

dota: 1,4,7,10-tetraazacyclododecane-1,4,7,10-tetraacetate;

nota: 1,4,7-triazacyclononane-1,4,7-triacetate;

L: 1,4,7,10-tetrakis(benzylphosphinate)-1,4,7,10-tetraazacyclododecane;

L': 1,4,7,10-tetrakis(methylphosphinate)-1,4,7,10-tetraazacyclododecane.

References

- (a) An et al. (2000) (c) Beeby et al. (1999)
 (b) Supkowski and Horrocks (1999) (d) Werts et al. (2002)

been limited to the –NH bond (Hnatejko et al., 2000). It was also shown that closely diffusing second-sphere solvent molecules have an influence onto the lifetime (Dickins et al., 1996; Beeby et al., 1999). A study considering all these effects can be found in Supkowski and Horrocks (1999). As a matter of fact, for a given ion, the large variations observed in the numerical values of B in eq. (13)—which is in units of (water) molecules—shed some doubts on the reliability of such a formulation (see table 4), unless a careful calibration is made and the equation used only for a given type of complex in a given solvent.

In the case of solutions of supporting electrolytes, the use of the calibration relationship appears inadequate. The fact that the Eu^{3+} lifetime is changing by addition of NaClO_4 in D_2O (see sect. 3.3) is by itself an indication that the H_2O molecules are not the only cause of the non-radiative deactivation process or, at least, that this is an indirect effect of the water molecules. As is quoted in sect. 3.6.3, in some cases, the calculated hydration number is increasing when the electrolyte concentration is increasing, which is difficult to link to other experimental findings, although some doubts on that question have been raised (Kanno and Hiraishi, 1982; Kanno and Yokoyama, 1996). The qualitative explanation suggested an increasing quenching ability of each OH bond as a function of salt concentration is not in line with the physical concept of eq. (13) which is based on a quenching contribution of each OH oscillators *independent* of all others and limited to the first hydration sphere. In the case of chloride based electrolytes, a detailed discussion on this point can be found in Nehlig et al. (2003). Recent experiments show that the structure of electrolyte solutions (in H_2O or D_2O) is very complex so that the notion of a single type of first hydration sphere appears somewhat doubtful (Laenen and Thaller, 2001; Max and Chapados, 2002; Stangret and Gampe, 2002). Similarly, in the specific case of ethanol/ H_2O mixtures, it is well-known that hydrophobic aggregation takes place and is strongly dependent on the nature of the various introduced ions (Sacco and Holz, 1997; Sacco et al., 1998) so that the rather naive image of an homogeneous medium, which is actually embedded in eq. (13), has to be revised.

Another fundamental questionable point can be raised by considering the temperature-dependent lifetime data of an $\text{Eu}(\text{III})$ complex (Holz et al., 1990b) (see section 3.4). One can take advantage of the $k_{\text{obs}}^{\text{D}_2\text{O}}$ and $k_{\text{obs}}^{\text{H}_2\text{O}}$ values that have been measured in the temperature range 278–363 K, in order to calculate the $N_{\text{H}_2\text{O}}$ variations as a function of T , by use of eq. (12b). While $N_{\text{H}_2\text{O}}$ is equal to 2.15 at $T = 278$ K, it raises as a function of T and reaches a value of 12 at $T = 363$ K. This latter value seems unphysically large. This most probably means that other deactivation pathways are available at high T . Conversely, it means that at *any* temperature, one has to discriminate between the contribution of such a phenomenon and of the envisioned OH oscillator effect, which appears a very difficult task that has never been discussed, to our knowledge.

In the case of the $\text{Eu}(\text{II})$ luminescence in methanol, the available data, that refer to the lifetime increase through complexation (see sect. 5) have been tentatively explained within the frame of OH bonds exclusion from the first $\text{Eu}(\text{II})$ solvation shell. Interestingly, the values of τ_{obs} and τ_{rad} for various $\text{Eu}(\text{II})$ complexes in methanol were obtained. The discussion above has shown the great interest of such measurements which, in the case of $\text{Eu}(\text{II})$, are difficult to perform due to the instability of divalent europium, and which should be more systematically performed in the case of trivalent europium. As compared to the solvated Eu^{2+} ion

in methanol, the various complexes studied (mainly crown-ethers) display rather similar radiative decay rates and lower non-radiative deactivation rates. From these results, the authors concluded that water molecules in the first solvation sphere are responsible for the deactivation pathways (Jiang et al., 1998). However, we do not agree with this conclusion: Similarly to the case of Eu^{3+} luminescence, comparison has to be made, for a given complex, between τ_{obs} and τ_{rad} values, whilst the comparison between the τ_{obs} values of the complex and of $\text{Eu}^{2+}_{\text{solv}}$ does not provide insight into this question, as explained above. The experimental data in methanol evidence a large effect of the type of ligand (for a given stoichiometry) onto the lifetime, as in the Eu(III) case.

3.7. *Second interpretation: Förster mechanism*

3.7.1. *General theoretical approach*

The work of Förster deals with the problem of the energy transfer (non-radiative pathway) from a donor D^* (created by absorption of a photon) to an acceptor A (see Förster (1959) for a good start in this theory, see Blasse (1990) for general aspects on the influence of ligands on luminescence and for a deeper look at the mathematics, see Voltz (1968)). Depending on the energy level matches between D^* and A, such a transfer is more or less efficient so that by modifications of the energy levels of A, either an inhibition or an enhancement of the fluorescence of D^* can be envisioned. The main physical parameters that are derived from the mathematical treatment are the energy transfer rate and R , the mean distance of interaction between D^* and A. The transfer efficiency varies, in a first approximation, as $(1/R)^6$. Other parameters of importance are the refractive index of the medium and the overlap between the emission spectrum of D^* and the absorption spectrum of A. Although this theory is very general, Förster clearly stated that the following two cases can be described within this framework:

- (i) Energy transfer between independent species in solution (no chemical bond).
- (ii) Energy transfer between independent electronic systems of a given species.

Therefore, the effect of a solvent onto the lifetime of a luminescent probe is ascribable to case (i) and the ligand effect to case (ii). In the first case, experiments have shown that the typical interaction distance is of the order of 70 Å while it is 5 to 10 Å in the second case. The Förster theory is more accurate than the empirical formulation discussed in sect. 3.6.2. The following sections discuss the use that has been made of the Förster formalism.

3.7.2. *Use of a simplified formalism*

Based on the experimental evidences discussed in sect. 3.6.4 of an effect of the ligand onto the lifetime, numerous publications have appeared that refer to the Förster's theory (De Sa et al., 1993; Beeby et al., 1999; Supkowski and Horrocks, 1999; An et al., 2000). However, this theory is not applied in order to derive the transfer rate constant or the mean interaction distance value but only to justify the search for relationships between the observed decay rate and the number of OH, CH or NH bonds of the ligand, plus a global parameter for the solvent. Thus, although based on a very different theoretical approach, one deals with equations similar to eq. (11), with more terms, as in the following example (Beeby et al., 1999):

$$k_{\text{obs}} = k_{\text{rad}} + k_{\text{sol}} + k_{\text{CH}} + k_{\text{NH}} + k_{\text{OH}} + k_{\text{C=O}}. \quad (14)$$

3.7.3. *Explicit use of the Förster mechanism*

In other studies, the aim is to determine whether the non-radiative deactivation mechanism is actually a Förster mechanism (other mechanisms, that have not been detailed in this paper, may lead to lifetime changes, especially at short interaction distances: Dexter mechanism or electron transfer, for example), and, if so, to derive the physical parameters relevant to this approach. For example, in the case of some heteronuclear lanthanide complexes, it was shown that the decrease of the donor quantum yield is not ascribable to a Förster mechanism (Tanaka and Ishibashi, 1996). In this very interesting study, both the fluorescence decrease of the donor and the increase of the acceptor luminescence have been followed versus time. For other lanthanide complexes, a Förster mechanism has been assumed, in order to derive the mean interaction distance (Clarkson et al., 2000). Similarly, impressive results are obtained in the case of proteins (or other biological molecules) bound to lanthanides (Tb or Eu), where the distance between the absorbing chromophore and the luminescent metallic center has been measured (Horrocks and Sudnick, 1981). In one case, an unusual energy transfer (Förster's theory) from a counter-ion towards Eu, Tb or Dy has been proposed, although the possible effect of the crown-ether cage was not fully ruled out (Tran and Zhang, 1990). Finally, although the mechanism is a Dexter transfer according to the authors, it is worth mentioning a study in xerogels doped with lanthanides (Buddhudu et al., 1999).

Note that in the case where the Förster mechanism concerns an organic species transferring its energy to the lanthanide center to which it is bound, this is often referred to as the "antenna effect" and the ligand is sometimes called a sensitiser. Such an effect becomes efficient provided that the organic chromophore possesses a triplet excited state close to but at least 1700 cm^{-1} above that of the lanthanide emissive state (Parker and Williams, 1996).

3.7.4. *Discussion on the use of a Förster mechanism*

Although the theoretical approach appears to be valid, one may regret that some studies lead to equations that are not, *in nature*, very different from the empirical Horrocks' method. In addition, as quoted by the authors of a very detailed work on this question (Beeby et al., 1999), the values of the k_{HX} parameters in eq. (14) ($X = \text{O}, \text{C}$ or N), were obtained for a specific donor-acceptor distance. They should be corrected for the $(1/R)^6$ term for other ligands, which considerably lowers the general interest of eq. (14).

In contrast, studies aiming at determining the exact nature of the non-radiative deactivation mechanism and the corresponding mean distance of interaction appear to be more in line with the Förster theory spirit and may be regarded as a fascinating attempt in this field. However, applications appear rather limited as far as the question of the hydration sphere determination is concerned.

3.8. *Third interpretation: Empirical law for long range interactions*

It may appear very tempting to apply the Förster's formalism to the question of electrolyte effects onto the lifetime. However, some features of this effect render the use of the Förster's theory difficult: experiments with Eu have shown that the observed variations cannot be reproduced solely on the basis of the refractive index changes, a term included in the Förster's

expression (Schuermans and Legendijk, 2000). In addition, the non additive effect of anions and cations (see sect. 3.3, UO_2^{2+} case) is not included in the theory, which does not explicitly lead to an expression for the lifetime variations as a function of the electrolyte concentration. Therefore an empirical expression for the k_{nrad} variations has been proposed in the specific case of UO_2^{2+} in perchlorate based electrolyte solutions (Billard et al., 2001). It is based on the physical input of the Förster's mechanism, i.e., on long-range interactions and energy transfers between the probe and the surrounding medium. The proposed expression contains a polynomial basis, which accounts for the increase in τ_{obs} as a function of $[\text{H}^+]$, together with additional polynomial, logarithmic and exponential terms involving $[\text{ClO}_4^-]$ and $[\text{H}^+]$ in order to reproduce the effect of electrolytes composed of a mixture of HClO_4 and NaClO_4 (Billard et al., 2001). This empirical law was shown to be compatible with quenching experiments (see sect. 4 for a definition), thus demonstrating that this effect is actually due to k_{nrad} changes only. Similarly, empirical laws may also be found for the lanthanide case, although no study of this type has been performed yet. Considering the rather smooth k_{obs} variations observed (Nehlig et al., 2003), it is most probable that second order polynomial expressions relating the concentration of the electrolyte ions to the k_{obs} value would be sufficient to reproduce the k_{obs} variation observed in the lanthanide case. However, such empirical formulations have little interest *as such*: the important fact is that this electrolyte effect has been identified as being of physical instead of chemical nature. Obviously, such an approach is of no help for the determination of hydration sphere numbers and a comprehensive theoretical treatment of such effects is still needed.

3.9. Conclusion on the question of hydration numbers and related topics

The spectroscopic characteristics of actinide and lanthanide luminescent probes are sensitive to numerous parameters, such as modifications of solvent composition, addition of supporting electrolytes, temperature changes etc. Therefore, TRES appears as an interesting tool for the chemist, because it provides sensitive experimental data. However, the interactions between the probe and the surrounding medium (in a wide sense) appear to be intricate and difficult to handle. In this sense, attempts to describe lifetime variations as a function of a unique parameter, the hydration sphere number, have shown their limitations. On the other hand, the open questions related to Förster's mechanism are a vivid and still not fully explored field.

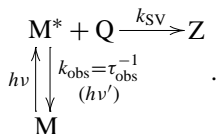
4. Reaction rate constants as studied by TRES

In this section, the use of TRES for the study of a reaction rate constant will be discussed. In a first step, the theoretical aspects will be presented and in a second step, the experimental data, mostly concerning U(VI), will be detailed.

4.1. Theoretical approach

4.1.1. Stern–Volmer formula

The general frame is that of a reaction between an excited luminescent probe, M^* , and another species, denoted by Q, following the scheme:



It will be assumed that Q does not absorb the excitation light and does not react with the ground-state M. The decay rate of M* in the absence of Q will be denoted k_{M} . Such a chemical scheme is independent of any effective mechanism for the interaction between M* and Q (Birks, 1970). It only states that, in the presence of Q, an additional deactivation pathway is present, through the creation of Z, which may be non-luminescent. By use of classical kinetic laws, one derives:

$$\frac{d[\text{M}^*]}{dt} = -k_{\text{M}}[\text{M}^*] - k_{\text{SV}}[\text{Q}][\text{M}^*]. \quad (15)$$

Supposing, which is correct most of the time, that Q is in large excess as compared to M*, and that k_{SV} is time-independent, one obtains:

$$[\text{M}^*](t) = [\text{M}^*](0) \exp(-[k_{\text{M}} + k_{\text{SV}}[\text{Q}]t]). \quad (16)$$

Therefore, in the presence of Q, the observed decay rate of M* is equal to:

$$k_{\text{obs}} = k_{\text{M}} + k_{\text{SV}}[\text{Q}]. \quad (17)$$

This is known as the Stern–Volmer equation, where k_{SV} is the bimolecular reaction rate constant (in units of $\text{M}^{-1} \text{s}^{-1}$). From an experimental viewpoint, the plot of k_{obs} as a function of [Q] is a straight line, of slope k_{SV} : the lifetime decreases as a function of [Q]. The global luminescence intensity of M* as a function of [Q] is equal to:

$$I = \int_0^{\infty} \frac{dh\nu'}{dt} dt = \int_0^{\infty} k_{\text{M}}[\text{M}^*](t) dt = \frac{k_{\text{M}}}{k_{\text{M}} + k_{\text{SV}}[\text{Q}]} [\text{M}^*](0) = \frac{k_{\text{M}}}{k_{\text{obs}}} [\text{M}^*](0). \quad (18)$$

This shows that the luminescence intensity decreases as a function of [Q] (Q is called a luminescence inhibitor or “quencher”), in parallel to the lifetime variation: no additional information is obtained by measurement of I as compared to lifetime measurements. In particular, the emission spectrum of M* is not distorted (no spectral shift) when Q is added to the solution. The exact chemical nature of Z cannot be deduced from the luminescence measurement of M* because the spectroscopic characteristics of Z do not appear in eqs. (15)–(18). Finally, it should be noted that, strictly speaking, the term “luminescence inhibition” and the Stern–Volmer equation should apply solely to experiments for which *both* the lifetime and the luminescence intensity decrease in parallel as a function of the concentration of a “quencher”. Finally, note that Stern–Volmer constants having a negative value have no physical meaning (Kessler, 1998).

4.1.2. Diffusion or activation-controlled reaction

Solution reaction kinetics may be decomposed into two contributions. The first one arises from the diffusion of the reactants and the second one corresponds to the chemical reaction itself.

When the chemical reaction step occurs very rapidly (virtually instantaneously upon collision of the reactants), one speaks of a diffusion-controlled reaction and in this case, the reaction rate constant is typically on the order of $10^{10} \text{ M}^{-1} \text{ s}^{-1}$. When the chemical reaction is slow as compared to the collisional process, the reaction is often called an activation-controlled reaction because a high activation energy is needed to yield the products. The rate constant is thus on the order of $1 \text{ M}^{-1} \text{ s}^{-1}$. In the general case, the reaction rate constant is a combination of the two processes and is described by the following expression:

$$\frac{1}{k_{\text{SV}}} = \frac{1}{k_{\text{diff}}} + \frac{1}{k_{\text{act}}}, \quad (19)$$

where k_{diff} and k_{act} are the reaction rates of the diffusion and activation steps, respectively.

4.1.3. Diffusion-controlled reaction: Smoluchowsky approach

A detailed presentation can be found in Steinfeld et al. (1999). In the case of neutral reactants, at infinite dilution, the expression of k_{diff} is:

$$k_{\text{diff}} = \frac{2k_{\text{B}}T(r_1 + r_2)^2}{3\eta r_1 r_2} \quad (20)$$

where k_{B} is the Boltzmann constant, T is the temperature, η stands for the viscosity and r_1 and r_2 are the ionic radii of the reactants. This equation is often called the Smoluchowsky relation but may present some slight differences from one author to the other, due to the various approximations made in the calculations. If the reactants are charged moieties, one has to consider the potential between them, which leads to another expression, sometimes referred to as the Debye expression:

$$k_{\text{diff}} = \frac{2k_{\text{B}}T(r_1 + r_2)^2}{3\eta r_1 r_2} \frac{-z_1 z_2 e^2}{\varepsilon k_{\text{B}}T \left[1 - \exp\left(\frac{z_1 z_2 e^2}{\varepsilon k_{\text{B}}T(r_1 + r_2)}\right) \right]} \frac{1}{(r_1 + r_2)}, \quad (21)$$

where ε is the dielectric constant of the solution and z_1, z_2 the charges of the moieties. Some numerical applications allow to set limits for the k_{diff} values. For neutral species, the maximum value of k_{diff} (cf. eq. (20)) is on the order of $6 \times 10^9 \text{ M}^{-1} \text{ s}^{-1}$. For charged reactants, this value is increased by a factor 2 to 5 if the charges are of the same sign and is decreased by a factor of 0.2 for moieties of opposite sign.

4.1.4. Ionic strength effects

If the two reactants are embedded in an electrolyte solution, the effects of the Coulomb attraction/repulsion terms are to be taken into account in the k_{SV} expression. These correction terms are different in nature whether one considers the diffusion or activation contributions to k_{SV} or not.

For diffusion-controlled reactions the global effect of the electrolyte is to counterbalance the electrostatic effects between the reactants: the reaction rate will be increased for moieties of the same sign and will be decreased for moieties of opposite sign. The work of Debye and Hückel, based on the approximation that the solution is diluted enough to consider that

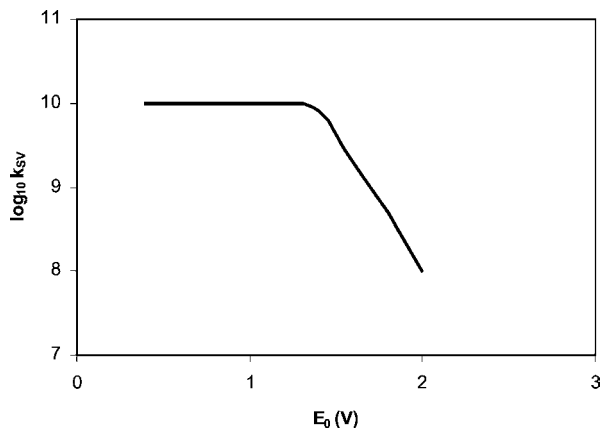


Fig. 4. Schematic plot of $\log_{10} k_{SV}$ as a function of the ionization potential (E_0, V) of quenchers of similar chemical structures.

the electrolyte ions are not “too close” to each other, leads to the extended Debye–Hückel expression:

$$\log_{10} k_{SV} = \log_{10} k_0 + 1.02z_1z_2\sqrt{I}, \quad (22)$$

where k_0 is the k_{SV} value as calculated in the absence of supporting electrolyte and I is the ionic strength of the solution. Considering the approximations made to obtain this expression, its limit of validity is roughly equal to 0.1 M.

In the case of an activation-controlled process, the supporting electrolyte modifies the activation coefficients of the reactants and it is out of the scope of this work to enter in the mathematical treatment. A detailed approach of this case can be found in Simonin and Hendrawan (2001).

4.1.5. Electron transfer: Rehm–Weller equation

In the above sections, nothing was said about the type of reaction between M^* and Q . This is because the Stern–Volmer equation is model independent, as explained above and also because eqs. (20)–(22) are for a diffusion-controlled reaction. Some information can be obtained regarding an electron transfer from various quenchers of similar chemical structures towards M^* . In this case, one may derive a relationship between k_{SV} (as obtained from eq. (17)) and the ionization potential of these inhibitors. This is the Rehm–Weller equation, which is schematically depicted in fig. 4. In this plot, the plateau value corresponds to k_{diff} . For a general overview of problems related to electron transfers, see Pouliquen and Wintgens (1988) (in French).

4.1.6. Time-dependent reaction rate constant and other modifications of the Stern–Volmer formula

One of the basic hypotheses which sustains the Stern–Volmer equation is that the reaction rate constant, k_{SV} , is time-independent. This is clearly an approximation. By assuming a time-dependent k_{SV} , integration of eq. (15) becomes tedious. Fortunately, this time-dependence is

effective only at very short times as compared to the lanthanide and actinide excited state lifetimes, which allows one to neglect this dependence. However, this fundamental question (and also the spatial dependence of the reaction rate constant) is of great interest and is the subject of numerous theoretical and experimental works. In particular, Marcus' theory shows that, for very negative ionization potentials, the plateau of the Rehm–Weller semi-empirical approach is no longer valid (inverted Marcus region) and that the electron transfer rate should display a bell shape as a function of the ionization potential. The reader will find some recent advances on this questions in Scully et al. (1992), Tachiya and Murata (1992), Molski (1994), Berezhkovskii et al. (1998), Molski et al. (1998), Sikorski et al. (1998), Agmon and Gopich (1999).

It is also possible that the properties of the solution induce some modifications of eq. (17). This is the case for example of a fluorescent probe attached onto a polyelectrolyte: in this case, the high local concentration of ions strongly influences the rate constant so that eq. (17) is no longer valid. For one typical recent example of such a phenomenon with phenanthrene, see Morrison et al. (1996).

4.2. *Experimental data and links to theory*

Numerous ions quench either the R(III) or U(VI) luminescence but most of the data available concern uranyl probes. Table 6 displays a selection of k_{SV} values. Numerous additional k_{SV} values for various alcohols/U(VI) systems can be found in the very comprehensive and interesting work of Cunningham and Srijaranai (1990), where k_{SV} values vary from $\sim 10^6 \text{ M}^{-1} \text{ s}^{-1}$ to $1.5 \times 10^9 \text{ M}^{-1} \text{ s}^{-1}$ in H_2O . Other values can also be found for an impressive list of quenchers of $[\text{UO}_2\text{F}_4]^{2-}$ (Billing et al., 1991). A wealth of data can be found in Moriyasu et al. (1977b) for U(VI) in various complexing media such as H_3PO_4 1 M. Among the somewhat unusual media in which such studies have been performed with U(VI), one can find concentrated HNO_3 aqueous solutions (Katsumura et al., 1989) and supercritical CO_2 (Addleman and Wai, 1999). Note a very interesting study on enantioselective quenching for Eu(III), by use of the rather confidential time-resolved chiroptical luminescence technique (Metcalfe et al., 1990). Nothing on this topics is known for Cm^{3+} .

Although experimental k_{SV} values of some ions (NO_2^- with Ce^{3+} or I^- with UO_2^{2+} , for example) come close to the maximum value calculated from the Smoluchowsky equation (cf. eq. (21)), most of the inhibitors presented in table 6 do not correspond to diffusion-controlled reactions, as the k_{SV} values are more than two orders of magnitude below the maximum (N_3^- with Eu^{3+} or Dy^{3+} with UO_2^{2+} , for example). A solvent effect has been observed, with a k_{SV} value in D_2O higher by a factor of two than that in H_2O for Eu^{3+} quenched by N_3^- ions, but no explanation has been provided (Lis et al., 2001). No isotope or solvent effect has been found for alcohols and U(VI) (Cunningham and Srijaranai, 1990). Attention is drawn on the beautiful work about k_{SV} values for various U(VI) complexes (Park et al., 1990) and also on a similar work, devoted to a more limited series of inhibitors (Lopez and Birch, 1997). Note that the smaller values obtained for uranyl complexes as compared to $\text{UO}_2^{2+}_{\text{aq}}$ are ascribable to a larger radius of this reactant, which limits its diffusion. Finally, some publications have presented k_{SV} values for UO_2^{2+} using NO_3^- or SO_4^{2-} as U(VI) counter-ions. As these anions

Table 6
 k_{SV} values ($M^{-1} s^{-1}$) for various luminescence inhibitors. The solvent is H_2O , unless specified

Probe	Inhibitor	Experimentals	k_{SV} ($M^{-1} s^{-1}$)	Ref.
Eu^{3+}_{aq}	NO_2^-	$[R^{3+}] = 0.1 M$; chloride salt; $T = 25^\circ C$	6.4×10^6	a
	N_3^-	$[R^{3+}] = 10^{-2} M$; perchlorate salt	2.6×10^5 (H_2O)	b
			5.3×10^5 (D_2O)	
Ce^{3+}_{aq}			2.8×10^{10}	
Dy^{3+}_{aq}	NO_2^-	$[R^{3+}] = 0.1 M$; chloride salt; $T = 25^\circ C$	4.7×10^8	a
Sm^{3+}_{aq}			3×10^8	
Gd^{3+}_{aq}	N_3^-	$[R^{3+}] = 10^{-2} M$; perchlorate salt	7×10^6	b
	N_3^-	$[R^{3+}] = 10^{-2} M$; perchlorate salt	5.7×10^4	b
Tb^{3+}_{aq}	NO_2^-	$[R^{3+}] = 10^{-3} M$; chloride salt	1.3×10^9	a
	Cl^-		1.8×10^9	
	Br^-	$I = 3 M$; pH = 3.4;	4.1×10^9	
$UO_2^{2+}_{aq}$	SCN^-	$T = 25^\circ C$; $[UO_2^{2+}] = 10^{-2} M$; perchlorate salt	4.8×10^9	c
	I^-	perchloric medium	6.2×10^9	
			4.8×10^9	d
	Ag^+	$[HClO_4] = 1 M$; $T = 25^\circ C$; $[UO_2^{2+}] = 10^{-2} M$	3.3×10^9	e
			$[UO_2^{2+}] = 4.6 \times 10^{-2} M$; perchloric media	2×10^9
	Dy^{3+}	$I = 3 M$; $[UO_2^{2+}] = 5 \times 10^{-3} M$	3.5×10^6	
	Gd^{3+}	$[HClO_4] = 2.5 M$; $[UO_2^{2+}] = 5 \times 10^{-3} M$	6.4×10^6	f
Eu^{3+}	$[HClO_4] = 0.4 M$; $I = 1 M$; $[UO_2^{2+}] = 5 \times 10^{-3} M$	3×10^5		
$[(UO_2)_2(OH)_2]^{2+}$	Cl^-	pH = 3.4; $I = 3 M$;	2.2×10^8	
	Br^-	$T = 25^\circ C$;	2.2×10^9	
	I^-	perchlorate salt;	5.8×10^9	c
	SCN^-	$[UO_2^{2+}] = 10^{-2} M$	4.1×10^9	
	Ag^+	$[UO_2^{2+}] = 4.6 \times 10^{-2} M$	2.6×10^9	d
$[UO_2F_4]^{2-}$	NO_2^-		2.6×10^8	
	I^-		1.5×10^9	
	Br^-	room temperature;	1.5×10^9	
	Cl^-	$[UO_2^{2+}] = 10^{-2} M$	3.5×10^6	g
	SCN^-		1.4×10^9	
	N_3^-		3.5×10^8	
	Cl^-		1.8×10^7	
	Br^-	$I = 1.13 M$; $[UO_2^{2+}] = 10^{-2} M$	8.9×10^8	
$UO_2(H_2PO_4)_2$	I^-		3×10^9	
	SCN^-		1.9×10^9	
	Cl^-		4.5×10^7	
	Br^-		8.5×10^8	
	I^-	$I = 2.2 M$; $[UO_2^{2+}] = 10^{-2} M$	2×10^9	c
	SCN^-		1.6×10^9	

continued on next page

Table 6, continued from previous page

Probe	Inhibitor	Experimentals	k_{SV} ($M^{-1} s^{-1}$)	Ref.
UO ₂ SO ₄	Cl ⁻	$I = 1.03 \text{ M}; [\text{UO}_2^{2+}] = 10^{-2} \text{ M}$	3.8×10^8	
	Br ⁻		2.5×10^9	
	I ⁻		4.6×10^9	
	SCN ⁻		3.8×10^9	

References

- (a) Tanaka et al. (1993) (d) Lopez and Birch (1997) (g) Billing et al. (1991)
 (b) Lis et al. (2001) (e) Moriyasu et al. (1977b)
 (c) Park et al. (1990) (f) Yamamura et al. (1999)

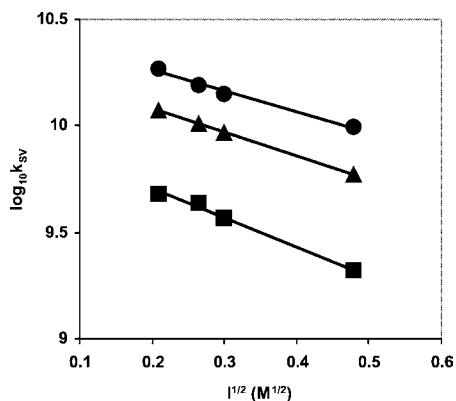


Fig. 5. Logarithmic plot of k_{SV} as a function of $(I)^{1/2}$ for various UO₂²⁺ inhibitors: (●) I⁻; (▲) Br⁻; (■) Cl⁻. Redrawn from Yokoyama et al. (1976).

are well-known U(VI) complexing agents, caution should be paid on the exact attribution of the k_{SV} constant to UO₂²⁺_{aq} or to a complex species (Burrows, 1990). In some publications about the fluorescence of Eu(III) complexes, reference is made to the Stern–Volmer equation, although the authors clearly state that only the luminescence intensity decreases as a function of the “inhibitor”, while the lifetime remains constant (Parker et al., 1998; Parker, 2000).

Ionic strength effects onto the k_{SV} constant, as described by eq. (22), have been observed long ago, mainly for U(VI) (Yokoyama et al., 1976; Moriyasu et al., 1977b; Yamamura et al., 1999) but also for various lanthanides in the excellent work of Tanaka et al. (1993). Over the limited range of ionic strength investigated, it appears that eq. (22) is able to reproduce the experimental k_{SV} variations, as illustrated in fig. 5 for the UO₂²⁺ case. A recent work dealing with a wide range of ionic strength (10^{-2} to 9 M) shows that the k_{SV} variations cannot be reproduced by this simple equation in this whole concentration range (Simonin et al., 2003).

The ionic strength effect is not limited to k_{SV} variation as described by eq. (22). The addition of large amounts of electrolytes may also modify the quencher solubility and thus its efficiency. This effect has been used by some authors, in systems very different from those examined in this work, in order to determine the association constant of the inhibitor salt (Mac, 1997; Mac and Tokarczyk, 1999): as the electrolyte concentration is increased, the quencher ion associates, so that the effective concentration of the inhibitor ion decreases, leading to a downward curvature of the Stern–Volmer plot. Such a curvature can be quantitatively related

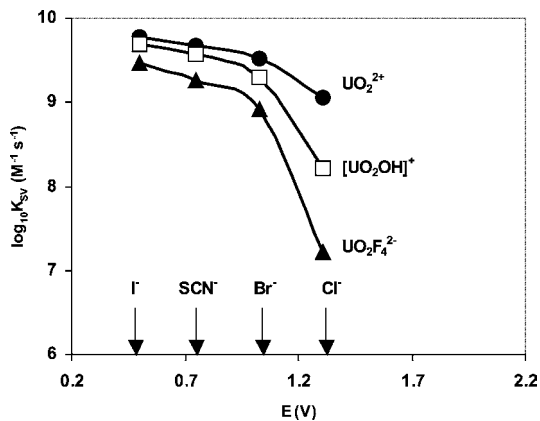


Fig. 6. Rehm-Weller plots for halogenide and pseudohalogenide inhibitors of some uranyl complexes. Redrawn from Park et al. (1990).

to the association constant of the inhibitor salt. This idea sustains the study of the inhibition of Eu(III) by NO_2^- , which may be present in its associated HNO_2 form (no quenching efficiency) or in its dissociated NO_2^- form (maximum quenching efficiency) depending on pH (Tanaka et al., 1993).

Numerous authors have shown that the Rehm-Weller equation is valid for the fluorescence inhibition of various U(VI) species with alkenes (Park and Tomiyasu, 1992), heteroatomic (Park and Tomiyasu, 1993) or halogenated compounds (Burrows, 1990), as is illustrated in fig. 6. This corresponds to the so-called normal Marcus region (which is thus also correctly described through the Rehm-Weller equation). This implies that an electron transfer occurs in such systems, from the inhibitor to the U(VI) species, leading to U(V), which disproportionates into U(IV) and U(VI). In one case at least, U(IV) has been observed, which strongly supports the proposed mechanism (Park et al., 1991; Park and Tomiyasu, 1992). Finally, lanthanides inhibit the UO_2^{2+} fluorescence, most probably through an electron transfer (Yamamura et al., 1993, 1999). Apart from electron transfers at short distances that have been evidenced for some lanthanides (Tanaka et al., 1993), energy transfers through a Förster-type mechanism can also be responsible for the quenching (Tanaka et al., 1993). Finally, note an unusual paper where a theoretical approach related to the Marcus' theory is applied to the reduction of lanthanide ions by hydrated electrons (Lee et al., 1998).

4.3. Conclusion on the study of reaction constants with TRES

TRES is a valuable method to determine rate constants in the very specific case of a reaction between an excited species and a quencher. The theoretical approaches are easily applicable and lead to interesting results on various aspects of such reactions. Another type of reaction rate constant can be studied by TRES but is rather anecdotal: in the case where a ligand, L, reacts very slowly (on the order of hours to months) with the luminescent probe, the formation of the complex can be followed by TRES (for example, see Wu et al. (1996), Bazzicalupi et al. (2001)).

5. Equilibrium constants and complexation as studied by TRES

The measurement of equilibrium constants is a crucial aspect in lanthanide and actinide chemistry. Several techniques are available for such determination (spectrophotometry, potentiometry, solvent extraction, electrospray mass-spectrometry, ...), among which TRES is commonly used in the case of reaction studies of luminescent lanthanides with organic ligands (Richardson, 1982; Parker and Williams, 1996). The high sensitivity of TRES (see sect. 6) allows quantitative measurements of very dilute solutions, which facilitates the handling of highly radioactive materials such as Cm.

In this section, the experimental changes in the luminescence characteristics of lanthanides and actinides upon complexation will first be presented. Most of the work reviewed deals with aqueous solutions. The theoretical background will then be detailed and linked to the experiments. The consequences will be discussed in the last part of this section.

5.1. Solvation/complexation: A brief introduction

As noted previously in this chapter, an ion in solution is not “free” but is solvated by solvent molecules. Usually, one refers to the first solvation sphere but one may also define, for the sake of convenience, a second, a third etc solvation spheres, which are looser than the first one. In fact, besides the first solvation sphere, this notion is highly dependent on the technique used to determine it and the reader is referred to a review on this subject (Hinton and Amis, 1971). As explained before, in this chapter, we adopt the notation X_{solv} for the solvated ion X. Strictly speaking, a solvated ion is *complexed* by the solvent molecules and this is particularly true for water as a solvent (Spencer et al., 1999). However, usually speaking, the term complexation only refers to the chemical acts that lead to an ion surrounded by at least one moieties different from the solvent, as long as a chemical interaction exists between them. Note that this new entity, which is called a complex, is *also* solvated but the subscript “solv” is usually omitted in this case (and is indeed omitted in this chapter). The notion of solvation and complexation are dynamic ones, as the ligand and the solvent molecules exchange with the bulk. Turning to the mechanism of complexation, two types of complexes can be envisioned: outer- and inner-sphere complexes. In the former case, the ligand and the central ion are separated by at least one solvent molecule. To form an inner-sphere complex, the entering ligand can expulse a solvent molecule (monodentate case) from the first solvation sphere, so that the coordination number remains constant but a change in the coordination may also occur (reorganisation of the solvation sphere). Reviews exist on this subject for lanthanides (Bünzli and Milicic-Tang, 1995; Choppin, 1997; Bünzli, 1998) and for actinides (Nash and Sullivan, 1998).

5.2. Experimental data: Effects of complexation on the spectroscopic parameters

For lanthanides, the wide question of the changes in the spectroscopic characteristics upon complexation has been already detailed in other publications (Bünzli and Choppin, 1989; Choppin and Peterman, 1998) but, to our knowledge, no similar work exists for actinides. Thus, in this chapter, the general trends will be presented for the various spectroscopic parameters with some emphasis on the actinide case, whenever possible.

5.2.1. Absorption

As was stressed above, in case of direct excitation of the lanthanides, the differences in the absorption spectra between the solvated ion and the complex formed are usually considered as slight but allow nevertheless the use of spectrophotometry for speciation purposes (for a recent example, see Giroux et al. (2000)). In the case of U(VI), the absorption changes observed upon complexation have often been used to determine equilibrium constants (for the classical example of U(VI) hydrolysed species, see Dai et al. (1998), Meinrath (1998)). For curium, no information of this kind is available: the low molar absorption coefficient implies the use of solutions with high total curium concentrations, which are almost impossible to handle nowadays due to safety reasons. The absorption spectra of curium are known only for aqueous solutions of HClO_4 (Carnall et al., 1958), HCl , H_2SO_4 and HNO_3 (Pascal, 1962).

Another way of exciting the probe of interest in its complexed form is through the so-called “antenna-effect”, a notion relevant only for lanthanides and curium complexed to organic ligands. The basic principle is that of a Förster mechanism (see sect. 3.7.3): the ligand is excited with UV light and the energy is transferred to the metallic center, which then emits its specific luminescence. For very good publications on this aspect in the lanthanide case, the reader is referred to Parker and Williams (1996) and Bünzli (2003) and for an example in the case of curium, see Panak et al. (1995). Some applications of this phenomenon will be presented in sect. 6.

5.2.2. Lifetime values and decay spectra

As can be deduced from sect. 2.1, complexation leads to lifetime changes. Again, due to the large number of studies devoted to very specific organic ligands of the lanthanides (for some examples, see Klink et al. (2000), Latva et al. (1997), Steemers et al. (1995), Wang and Horrocks (1997), Elhabiri et al. (1999) and others cited elsewhere in this chapter), it is out of the scope of this chapter to review them all. A short list of lifetime values for some Eu(III) complexes (in D_2O) has already been presented in table 5. The general trend is an increase of the lifetime through complexation. The range available is very large: for Eu(III) in H_2O solution for example, values from 119 μs (with terephthalate, 1:1 complex, Wang et al. (1999)) to 1 ms (with a macrocyclic ligand, Wang and Horrocks (1997)) or 3.9 ms (dipicolinate ligand, An et al. (2000)) can be found. Similarly, large variations in lifetime values can be found for a series of Eu(III) complexes extracted in C_6H_6 (Lis et al., 1991).

Eu^{2+} luminescence deserves a special mention (see sect. 3.6.4 for a discussion of the data presented here). While $\text{Eu}^{2+}_{\text{aq}}$ is known to be non-luminescent in water (Sabbatini et al., 1982), it emits weakly in methanol and the luminescence is greatly enhanced through complexation in this solvent (Jiang et al., 1998). In one case, a very weak emission has been observed in water for a Eu(II) complex (Sabbatini et al., 1984). As compared to the Eu^{3+} luminescence characteristics, Eu^{2+} always displays a rather short lifetime in methanol (in the range of 2 ns for solvated Eu^{2+} and up to 800 ns when complexed with 15C5).³ The detailed studies by Jiang and co-workers also provide data for the quantum yields, the radiative and non radiative contribution to τ_{obs} together with the emission spectra (Jiang et al., 1998).

³ Furthermore, the emission range is in the green part of the visible spectrum (roughly from 380 to 500 nm).

For actinides, the general trend is also to an increase in the lifetime value upon complexation but the available range is more limited: for example, the 1:1 sulfato complex of U(VI) displays $\tau_{\text{obs}} = 4.3 \mu\text{s}$ (Geipel et al., 1996), $\text{UO}_2\text{F}_{2\text{aq}}$ is quoted with $\tau_{\text{obs}} = 250 \mu\text{s}$ (Beitz and Williams, 1997), while the first two sulfato Cm^{3+} complexes present lifetimes equal to 88 μs and 95 μs (Fanghänel and Kim, 1998). However, this lifetime increase is not systematic and some carbonato U(VI) complexes have short lifetimes or exhibit no fluorescence (Bernhard et al., 2001). In fact, a recent study on the application of TRES to U(VI) aqueous speciation has revealed that the lifetime of U(VI) complexes depends on the nature of the electrolytes added to the solution (Billard et al., 2003a). This effect is most probably similar to that discussed for solvated ions (see sect. 3.3) but has never, to our knowledge, been examined in details for lanthanide complexes. Nothing is known for Cm complexes on that question. In conclusion, the lifetime measured in solution is not an intrinsic (i.e., characteristic) parameter of a given species and precise indications should be given on the exact composition of the solution for the sake of comparison.

The question of the decay behavior is not unimportant and will be discussed in the theoretical part in details (see also the discussion on data analysis in sect. 2.3). It is therefore of interest to review the experimental evidences on this point. For europium, depending on the ligand, the luminescence decays are either mono- or multi-exponential in the range of ligand concentration where both the solvated ion and the complex exist in solution (Ermolaev and Gruzdev, 1984; Horrocks and Sudnick, 1983; Wang et al., 1999). For all the (inorganic) ligands investigated with U(VI), the decay spectra are multiexponential, although two studies indicate a monoexponential behavior for U(VI)/ F^- (Beitz and Williams, 1997) and U(VI)/ OH^- (Meinrath et al., 2000). Note however that for these last two systems, such a monoexponential behavior was not confirmed in a recent round-robin test (Billard et al., 2003a). For Cm^{3+} , it seems that inorganic ligands lead to a monoexponential behavior in solution (a bi-exponential behavior has been observed for Cm^{3+} embedded in a calcite lattice (Stumpf and Fanghänel, 2002)), while organic ones lead to a multiexponential behavior, whatever the ligand concentration is (Panak et al., 1995; Klenze, 2001).

5.2.3. *Excitation spectra and luminescence quantum yield*

Due to the modifications of the electronic cloud induced by complexation, the quantum yield and the excitation spectrum are also modified. As the direct determination of the absolute quantum yield is very difficult to achieve, one usually finds in the literature quantum yield values determined by comparison to well-known standards, such as quinine sulfate. For example, some values can be found in Georges (1993) or in Klink et al. (2000) for some europium complexes but may be found also in many other papers on lanthanide luminescence. Studies on the correlations between the photophysical properties of a given type of europium complexes and the energy levels can be found in Latva et al. (1997), Klink et al. (2000). A correlation has been found between the excitation properties and the stoichiometry of various Eu(III) complexes (Choppin and Wang, 1997). Note that the changes in the excitation maximum induced by complexation usually amount to a few tenths of nanometers, which requires high resolution for detection. In the case of Eu(III), a correlation has been found between the frequency

of the ${}^5D_0 \leftrightarrow {}^7F_0$ transition and the nephelauxetic parameters of the coordinating atoms (Frey and Horrocks, 1995).

Very little is known on these topics for actinides, as it seems that the determination of quantum yields is not a common feature in this case: To the best of our knowledge, a single publication gives a few values of luminescence quantum yields in various media for uranyl (Katsumura et al., 1989) and nothing is known for Cm.

5.2.4. Emission spectra

In parallel to these lifetime changes, complexation induces tremendous modifications of the emission spectra, that have been examined for lanthanides in dedicated papers (for example, Hnatejko et al., 2000) or reviewed (Bünzli and Choppin, 1989). Briefly, for Eu(III), taken as a typical example of R(III) ions, the emission arises from the ${}^5D_0 \rightarrow {}^7F_J$ transitions, from which the ${}^5D_0 \rightarrow {}^7F_2$ (around 616 nm) exhibits hypersensitivity. Therefore, the wealth of information experimentally obtained is highly dependent on the scanning step used and a high resolution is needed to make the best of an emission spectrum (Bünzli and Choppin, 1989). However, even in the case of a low resolution, the changes are spectacular, as illustrated in fig. 7.

When specific information on the symmetry of the complex is not sought (or needed), the ratio, R , of the intensity of the ${}^5D_0 \rightarrow {}^7F_2$ transition to that of the ${}^5D_0 \rightarrow {}^7F_1$ (around 592 nm) can be used as an indicator of complexation. For $\text{Eu}^{3+}_{\text{aq}}$, this ratio is equal to 0.36 (Kim et al., 1994). The R value depends on the symmetry of the complex (Bünzli and Choppin, 1989), and values around 10 for complex with low symmetry are not rare (Lis et al., 1991). Conversely, low R value can be obtained, such as 0.67 for a centrosymmetric complex at room temperature (Klink et al., 2000) or 0.21 for a T_h symmetry ($T = 77$ K) (Bünzli et al., 1999).

For U(VI), complexation usually induces a red shift (typically of 3 to 5 nm) of the emission spectra. For Cm(III), complexation also induces red-shifts of a few nm of the whole spectra so that complexation is observed mainly as a shoulder of increasing importance as the ligand concentration is increased (Fanghänel and Kim, 1998).

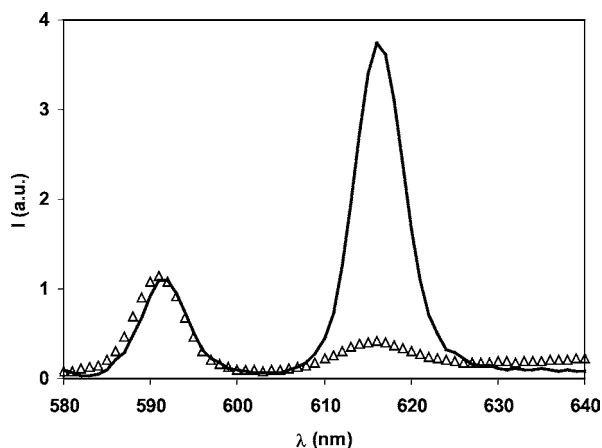


Fig. 7. Emission spectrum of $\text{Eu}^{3+}_{\text{aq}}$ in slightly acidic aqueous (pH = 2) solution (Δ) and of its 1:1 complex with acetate (solid line). Units are arbitrary and the two spectra have been normalised at 592 nm.

5.3. General considerations

Obviously, TRES, by creating excited species, may be a very useful tool to study excited state chemistry (kinetics, equilibrium, etc.) but, as these excited species arise from the ground state ones, TRES may also give an insight into the ground-state speciation.

In the case of lanthanides studied by TRES, it has always been considered that the reactivity of the excited-state simply mimic that of the ground-state (Horrocks and Sudnick, 1983; Ermolaev and Gruzdev, 1984). To our knowledge, a single group raised some doubts on this question (Marcantonatos et al., 1982) but the experimental evidences on which this hypothesis was proposed appear somehow thin. In contrast, diverging opinions are found for the uranyl case: photophysicists have long been interested in the UO_2^{2+*} reactivity, which is considered to be *very* different from the reactivity of the UO_2^{2+} ground-state (Jørgensen and Reisfeld, 1982; Baird and Kemp, 1997). In the radiochemistry field, however, it is mostly assumed that ground-state uranyl reactions only govern the speciation and that the various species formed, once excited, *do not* interact: the hypothesis of the UO_2^{2+} excited-state reactivity has hardly been evoked in radiochemical studies (Beitz and Williams, 1997; Meinrath et al., 2000). Finally, for Cm^{3+} , although studies are relevant to the radiochemistry field only, it is assumed that Cm excited-state reactivity exists and is similar to that of the ground-state.

These opinions may appear rather contradictory at first glance and it is the hope of the author to show in the following sections that they are in fact just two faces of a same problem. Therefore, before presenting the general theoretical treatment which allows to actually reconcile these various approaches, the experimental evidences on which these opinions are based will be shortly presented and their main basis summarized.

5.3.1. Photophysical point of view and related experimental data

One of the main reasons of the interest in uranyl photophysics is that the photoexcited uranyl ion is one of the most oxidizing species known. Thus, two types of studies can be performed, either focussing on the photoreduction of U(VI) or on the oxidation of various moieties by U(VI)^* . NMR (Rykov et al., 1991) or UV-Visible spectrophotometry can be used to follow the photoreduction/oxidation process. The species U(V) and/or U(IV) have been observed in various solutions such as $\text{H}_2\text{SO}_4/\text{H}_2\text{O}/\text{XeO}_3$ (Khamidullina et al., 1994), lactic acid in water (Yokoyama et al., 1974) or in dry acetone (Sandhu et al., 1990). A special mention should be made on the ease of U(VI) photoreduction by alcohols (Bell and Billings, 1975; Katsumura et al., 1989; Cunningham and Srijaranai, 1990; Nagaishi et al., 2002) and on the complexity of the envisioned schemes (Arvis et al., 1983; Katsumura et al., 1989). Large effects of dissolved oxygen (Cunningham and Srijaranai, 1990; Rykov et al., 1991), of NO_3^- (Katsumura et al., 1989) and of the irradiation time are found (Burrows et al., 1992; Khamidullina et al., 1994), which render the overall phenomenon difficult to describe. Catalytic oxidation of cyclohexane has been observed (Mooney et al., 1988). Although very interesting, such studies are not perfectly in line with the general topic of this chapter and will not be discussed further.

Pioneer studies have been performed in the late 1970s about various aspects of uranyl luminescence in solution, which appears to be sensitive to pH, temperature and to the addition

of quenchers (in a wide sense). For a recent review on this subject (including solid state) see Baird and Kemp (1997). Below $\text{pH} = 2$, the decay spectra were claimed to present a biexponential behavior, correlated to significant changes in the emission spectra. This was ascribed to the appearance of a new emitting center (Deschaux and Marcantonatos, 1979). The exact nature of this new emitting center was the subject of numerous publications, both on theoretical and experimental aspects (Marcantonatos, 1977, 1978, 1980; Marcantonatos and Pawlowska, 1989). Two models were put forward to describe the experiments: the group of Marcantonatos and co-workers suggested an exciplex, $(\text{U}_2\text{O}_4\text{H}^{4+})^*$, and the group of Burrows and co-workers proposed a distinct excited state, noted X^* , linked to UO_2^{2+*} by a reversible crossing mechanism (Miguel et al., 1984). The experiments on which this last hypothesis relied were made at higher pH value, typically from 3 to 4.5. A discussion was therefore started whether the observed changes at low and high pH values could possibly be due to the same phenomena. The theoretical aspects were rather detailed, including in some cases over 30 parameters in order to reproduce the entire set of data (Marcantonatos, 1980). Arguments in favor of either of the two models were proposed, based on the experimental emission spectra and oscillator strength theory, and electronic assignments were suggested. However, none of these publications paid enough attention to three problems related to the way the experiments were performed and which severely hamper the discussion on the possible existence of an exciplex or any other excited species: (i) most of these experiments were performed with high uranyl concentrations (0.1 M in Miguel et al. (1984) or 1 M in Azenha et al. (1991), for example) and the counter-ion was usually NO_3^- , which is a well-known complexing agent of uranyl (Grenthe, 1992); (ii) the NO_3^- ion is known to absorb the excitation wavelengths used, leading to the creation of radicals with a complex photophysics (Mack and Bolton, 1999); (iii) above $\text{pH} = 3$, the hydrolysis of the *ground-state* UO_2^{2+} ion is a well-known phenomenon, which has not been considered at all in the first studies. All these problems shed doubts on the interpretations implying the formation of an exciplex or a reversible crossing mechanism, although the theory by itself is perfectly correct. In a very courageous paper, the group of Burrows admitted that its interpretation was misleading and that it is not necessary to consider an exciplex to interpret TRES data above pH 3, which were most probably ascribable to the excitation of hydrolysed ground-state species (Azenha et al., 1991). On the other hand, the experimental data of Marcantonatos and co-workers at low pH could not be reproduced by other groups (Park et al., 1990; Eliet et al., 1995) when NO_3^- counter-ions were avoided so that the hypothesis of an exciplex formation $(\text{U}_2\text{O}_4\text{H}^{4+})^*$ was abandoned in the early 1990s.

Finally, on more general grounds, it is important to note that numerous photophysical studies are devoted to the determination of rate constants reactions between excited species (for two examples, see Laws and Brand (1979), Al-Soufi et al. (2001)). In such studies, it is taken for granted that if only ground-state chemistry is involved, simple relationships are to be found between the amplitudes of the emission spectra and the concentrations of the ground-state species and that the observed lifetimes represent the distinct decay rates of the non-interacting species. In contrast, in the case of excited state reactions, it is clear that neither of these simple relationships exist (Beechem et al., 1985).

5.3.2. *Chemical point of view and related experimental data*

From the experimental data briefly described in sect. 5.1, one sees that TRES has considerable potential for the study of complexation reactions and thus for the determination of the equilibrium constant K . This objective has been the subject of a large number of publications so that only some of them will be reviewed here and the main aspects of this question, together with the so far unanswered questions, will be discussed.

The determination of equilibrium constants from TRES experiments for lanthanide systems was first described independently by Horrocks and Sudnick (1983) and Ermolaev and Gruzdev (1984). Based on the hypothesis of the similarity of the excited and ground state reactivity, it was said that TRES easily gives access to the equilibrium constant of the ground-state, K , for fast and slow photochemical processes; for intermediate rates of photochemical processes, it was said that no information on K can be derived. However, the original papers did not provide a clear experimental evidence of this statement. Nevertheless, the method has been extensively used for K -determination and some studies, by displaying excellent agreements between the equilibrium constants derived from TRES and by other means, have clearly shown the great interest of the method for lanthanide systems (see table 7 for some values). However, it has to be noted that the number of comparative studies of this kind for the lanthanide case is, actually, very limited, as comparison is often made with values for Sm or Gd (Gruzdev, 1983; Albin et al., 1984) or for chemical conditions that differ significantly (Wu and Horrocks, 1997).

Table 7

Equilibrium constants, β_x , as determined by TRES and other techniques for some Eu(III) and U(VI) systems. β_x is defined for the reaction: $M + xL \rightleftharpoons ML_x$ (unless specified); $\beta_x = (ML_x)/[(M)(L)^x]$

System M/L	Experimentals	K by TRES	K by other means	Ref.
Eu ³⁺ /hemimellitate	TRES: pH \leq 5.5	$\beta_1 = 10^{5.25}$	$\beta_1 = 10^{5.08}$	TRES: (a)
Eu ³⁺ /pyromellitate	other: potentiometry, $I = 0.1$ M; $T = 298$ K	$\beta_1 = 10^{5.81}$	$\beta_1 = 10^{4.86}$	other: (b)
UO ₂ ²⁺ /SO ₄ ²⁻	TRES: recalculated at $I = 0$ M	$\beta_1 = 10^{3.35}$	$\beta_1 = 10^{3.15}$	TRES: (c)
	other: recalculated at $I = 0$ M	$\beta_2 = 10^{4.21}$	$\beta_2 = 10^{4.14}$	other: (e)
UO ₂ ²⁺ /NO ₃ ⁻	TRES: I from 0.3 to 6.4 M	$\beta_1 = 10^{-0.47}$	$\beta_1 = 10^{0.3}$	TRES: (d)
	other: recalculated at $I = 0$ M			other: (e)
UO ₂ ²⁺ /HPO ₄ ²⁻	TRES: $T = 20$ °C;	$\beta_1 = 10^{19.53}$	$\beta_1 = 10^{19.87}$	TRES: (f)
^a	recalculated at $I = 0$ M	$\beta_2 = 10^{22.31}$	$\beta_2 = 10^{22.58}$	other: (f)
	other: potentiometry; $T = 22$ °C;			
	recalculated at $I = 0$ M			

^a β_x is defined for the reactions: UO₂²⁺ + PO₄³⁻ + H⁺ \rightleftharpoons UO₂(HPO₄)

UO₂²⁺ + PO₄³⁻ + 2H⁺ \rightleftharpoons UO₂(H₂PO₄)⁺

References

- | | | |
|---------------------------|---------------------------|----------------------------|
| (a) Wang et al. (1999) | (c) Geipel et al. (1996) | (e) Grenthe (1992) |
| (b) Choppin et al. (1994) | (d) Couston et al. (1995) | (f) Brendler et al. (1996) |

Table 8

Equilibrium constants, β_x , as determined by TRES and other techniques for some Cm(III) systems. β_x is defined for the reaction: $M + xL \rightleftharpoons ML_x$; $\beta_x = (ML_x)/[(M)(L)^x]$

System M/L	Experimentals	K by TRES	K by other means	Ref.
Cm^{3+}/SO_4^{2-}	TRES: $I = 2$ M; $T = 25$ °C other: extraction, pH = 3; $I = 2$ M; $T = 25$ °C	$\beta_1 = 6.68^a$ $\beta_2 = 2.51$	$\beta_1 = 22$ $\beta_2 = 73$	TRES: (a) other: (b)
Cm^{3+}/Cl^-	TRES: I from 2.27 to 6 molal Other: ion exchange	$0.02 < \beta_1 < 0.046$ $7 \times 10^{-4} < \beta_2 < 10^{-2}$	$\beta_1 = 1.6$ $\beta_2 = 0.9$	TRES: (g) other: (b)
Cm^{3+}/F^-	TRES: $T = 25$ °C; $I = 0.5$ molal Other: extraction; pH = 3.6, $I = 0.5$ M	$\beta_1 = 316^b$	$\beta_1 = 2.2 \times 10^3$	TRES: (c) other: (b)
Cm^{3+}/OH^-	TRES: recalculated at $I = 0$ M; $T = 25$ °C other: diluted medium; $T = 25$ °C	$\beta_1 = 10^{6.44}$	$\beta_1 = 10^{6.3}$	TRES: (a) other: (e)

^aThis system has been studied by TRES in the range of ionic strength from 10^{-2} to 6 molal, but β_x values are displayed only for $I = 2$ M, to allow comparison with other data from the literature.

^bThe β_1 value at $I = 0.5$ M has been interpolated from the data provided in Ref. (c) to allow comparison with other data from the literature.

References

- (a) Fanghänel and Kim (1998) (d) Wimmer et al. (1992) (g) Fanghänel et al. (1995)
 (b) Katz et al. (1986) (e) Fuger (1992)
 (c) Aas et al. (1999) (f) Grenthe (1992)

In more recent years, the method has been directly applied to various systems containing curium: complexing anion such as F^- (Aas et al., 1999), OH^- (Wimmer et al., 1992; Fanghänel et al., 1994), 5-sulfo-salicylate (Klenze et al., 1998), CO_3^{2-} (Fanghänel et al., 1998a, 1998b) and SO_4^{2-} (Paviet et al., 1996) have been investigated. In these papers, reference to the theoretical result obtained on lanthanide systems is clear. Unfortunately, comparison between equilibrium constants as determined by TRES and other techniques is very difficult for curium systems: in the past, solvent extraction or ion exchange were used (Katz et al., 1986) but these techniques require a large amount of radioactive material. Thus, TRES appears nowadays to be the only available technique, so that comparison with determinations performed using other techniques is only possible for a very limited number of systems. The comparison reveals some discrepancies, as illustrated in table 8. In the case of the Cm^{3+}/Cl^- system, the rather large discrepancies are attributed to the fact that TRES is sensitive to inner-sphere complexes only, while other techniques do not make distinction between inner- and outer-sphere complexes, thus leading to an enhanced equilibrium constant, as compared to TRES (Fanghänel et al., 1995). However, this argument is not valid for sulfate complexation. In order to overcome the lack of stability constant data for Cm^{3+} , tentative comparisons have been made with known values for Pu or Am (Cm^{3+}/Cl^- system, Fanghänel et al. (1995)) or with values for Tb, Sm, Am and Pu ($Cm^{3+}/$ sulfosalicylate system, Klenze et al. (1998)).

At the same time, uranyl reactivity has been studied by TRES without any reference to the theoretical results mentioned above for the lanthanides, as it was more or less clearly assumed that the uranyl excited-state reactivity is negligible (Geipel et al., 1996; Lopez and Birch,

1997; Moulin et al., 1998; Rutsch et al., 1999; Eliet et al., 2000). As a matter of fact, the value of the equilibrium constant as determined by TRES for some uranyl systems are in very good agreement with the value obtained by other means (see table 7). A very limited number of papers on uranyl reactivity as followed by TRES suggested that the photoreactivity is not negligible ($U(VI)/F^-$ in Beitz and Williams, 1997 and $U(VI)/OH^-$ in Meinrath et al., 2000) but these results were not firmly assessed in a recent round-robin test (Billard et al., 2003a).

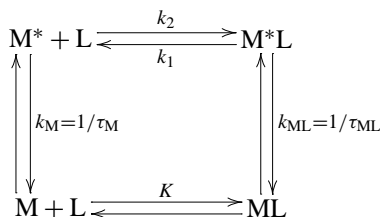
5.4. General kinetic scheme

Considering the literature review above, it is necessary to develop a comprehensive view that may apply to any system, whatever the luminescent probe is, each system being considered as one specific case of a more general theory. In this section, we first discuss the general scheme of (photo)chemical equations needed to describe a TRES experiment as well as a simplified scheme without photophysical reactions. The theoretical conditions to derive equilibrium constants from TRES data are discussed for the R(III), U(VI), and Cm(III) cases and are related to the experimental data presented above.

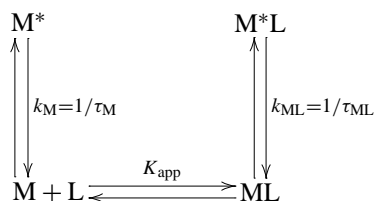
A solution is supposed to contain two species, M and L, which form a 1:1 complex. The general reaction scheme after pulsed laser excitation of M can be described as in scheme 1.

K is the equilibrium constant in the ground state, $k_{1,2}$ are the reaction rate constants in the excited state and $k_{M,ML}$ are the intrinsic fluorescence decay rates of M^* and M^*L , respectively. In this scheme, M is the fluorescent probe and it is assumed that complexation, although modifying the electronic configuration of M, still allows for luminescence to occur. In contrast, L is assumed not to absorb at the excitation wavelength. A typical TRES experiment consists in measuring time-resolved emission spectra as a function of the ligand concentration up to a large excess with respect to the concentration of the metal ion. Scheme 1 corresponds to the general situation where both ground-state and excited state reactions occur. One of the questions raised by Horrocks and Sudnick (1983) or Ermolaev and Gruzdev (1984) is under which conditions scheme 1, which leads to rather complicated rate equations, can be approximated by scheme 2, which neglects excited state reactions.

In this model, K_{app} stands for the *apparent* equilibrium constant. Whether or not K_{app} is a good approximation for the constant K in scheme 1 is clearly an important question for experiments studying ground-state complexation reactions. As a whole, these two schemes and the conditions under which model 2 is a good approximation for model 1 (with the advantage



Scheme 1. Comprehensive photochemical kinetic scheme describing a TRES experiment.



Scheme 2. Simplified kinetic scheme without photochemical processes.

of an easier manipulation) correspond to the photophysical and chemical points of view discussed in sects. 5.3.1 and 5.3.2. The detailed mathematical treatment of these two schemes can be found elsewhere (Billard et al., 2003a) for time-independent reaction rate constants k_1 and k_2 and, for example, in Molski and Boens (1997), Molski et al. (1998) for time-dependent reaction rate constants. Note that the question of time and space-dependence of k_1 and k_2 , although very important and difficult to solve (see sect. 4.1.6 for a insight onto this question), does not have to be considered here because such a phenomenon occurs on the pico- and sub-picosecond time scale, which is far below the time resolution of usual TRES setups and the usual lifetimes of the luminescent probes of interest in this chapter. Therefore, this point will not be discussed further. It is out of the scope of this text to enter into the minute analysis of the mathematics and only the main results will be presented, focussing on the physical implications.

5.5. Main results and physical implications

The time dependences of M^* and M^*L for schemes 1 and 2 are:

$$\text{Scheme 1: } [M^*](t) = A \exp(\Lambda_1 t) + B \exp(\Lambda_2 t) \quad (23a)$$

$$[M^*L](t) = C \exp(\Lambda_1 t) + D \exp(\Lambda_2 t)$$

$$\text{Scheme 2: } [M^*](t) = [M^*](0) \exp(-k_M t) \quad (23b)$$

$$[M^*L](t) = [M^*L](0) \exp(-k_{ML} t)$$

where Λ_1 and Λ_2 have negative values and are given by the roots of a second order polynomial, which depends on $[L]$, k_M , k_{ML} , k_1 and k_2 in a complex way:

$$\Lambda_{1,2} = -\frac{1}{2}(k_M + k_{ML} + k_2[L] + k_1) \pm \sqrt{(k_M + k_{ML} + k_2[L] + k_1)^2 - 4[(k_{ML} + k_1)(k_M + k_2[L]) - k_1 k_2]}. \quad (24)$$

For scheme 1, the luminescence decay, i.e. the time dependence of the sum of M^* and M^*L , reflects two decaying modes that are not specific to the two luminescing moieties M^* and M^*L : the two excited species both decay with two different lifetime values, $(-1/\Lambda_1)$ and $(-1/\Lambda_2)$, that are a function of $[L]$ (eq. (24)).⁴ In contrast, in the case of model 2, each decaying species is characterized by its own lifetime, $1/k_M$ or $1/k_{ML}$, both independent of $[L]$. Conversely, one may consider the emission spectra and the intensities, J_i^1 or J_i^2 , associated with the emitting species M^* and M^*L under the frame of model 1 or 2:

$$\text{Scheme 1: } J_1^1 = -\frac{A k_{\text{rad},1}}{\Lambda_1} - \frac{B k_{\text{rad},1}}{\Lambda_2} \quad (25a)$$

$$J_2^1 = -\frac{C k_{\text{rad},2}}{\Lambda_1} - \frac{D k_{\text{rad},2}}{\Lambda_2}$$

⁴ As a consequence, attempt to use eq. (12b) to get an insight into the hydration number in this case is meaningless (Holz et al., 1990a).

$$\text{Scheme 2: } J_1^2 = \frac{k_{\text{rad},1}\alpha[\text{M}]}{\lambda_1} \quad (25\text{b})$$

$$J_2^2 = \frac{k_{\text{rad},2}\beta[\text{ML}]}{\lambda_2}$$

where α and β are defined as follows:

$$[\text{M}^*](0) = \alpha[\text{M}],$$

$$[\text{M}^*\text{L}](0) = \beta[\text{ML}].$$

In both models, the two species M^* and M^*L have their own characteristic emission spectra, the intensities of which depend upon $[\text{L}]$. In other words, the total emission spectrum is the weighted sum of the individual contributions, which have very different expressions whether one considers model 1 or 2 (see eqs. (25a) and (25b)).

Therefore, the emitting species M^* and M^*L can in principle be identified from a decomposition of the total emission spectrum, and thus TRES experiments are mainly based on the evaluation of emission spectra rather than luminescence decays. However, a detailed analysis of the decays allows one to derive important information that cannot be obtained through the emission spectra, as will be explained below. In the frame of model 2, it is easily shown that the expressions of the relative contributions of the two species to the global emission spectrum contain only one unknown parameter, K_{app} , while the equivalent expressions under the frame of model 1 are much more complex. This raises the question as to whether model 2 can be considered a reasonable approximation of the more complex scheme 1. This issue can be discussed qualitatively on the basis of three distinct cases of model 1, depending on the importance of photochemical reactions.

(i) If reactions in the excited state are negligible, i.e., if k_1 and k_2 are small as compared to the decay rates of the excited species (regime A), model 2 is obviously expected to be a good approximation of model 1. In this case, no significant mixing occurs before the majority of excited species has decayed to their respective ground states. One obtains:

$$K_{\text{app}} = K. \quad (26)$$

This result is in agreement with those obtained by Horrocks and Sudnick (1983) and Ermolaev and Gruzdev (1984). Furthermore, under the frame of model 1 for slow excited state processes, the decays are multiexponential and the lifetimes do not vary significantly with $[\text{L}]$.

(ii) If the rate constants of the photochemical processes are on the same order of magnitude as those of the intrinsic decays (regime B), model 2 is not expected to be a good approximation for model 1. Again, this qualitative result is in agreement with the study of Horrocks and Sudnick (1983), even though the mathematical expressions presented in their work do not seem to be correct (Billard et al., 2003a). Under the frame of model 1, the decays are multiexponential but the photochemical processes induce a non negligible scrambling of the excited species, so that the lifetimes depend on $[\text{L}]$, one decreasing and the other one increasing as $[\text{L}]$ increases.

(iii) The third case corresponds to rapid photochemical processes, where the equilibrium between the excited species is attained before a noticeable amount has decayed (regime C).

In this case, it can be shown that one of the two lifetimes ($-1/\Lambda_1$) or ($-1/\Lambda_2$) vanishes, so that the luminescence decays appear monoexponential (model 1). Although this scenario differs considerably from the assumptions of model 2, one can nevertheless fit the experimental emission spectra by use of model 2 in order to obtain an apparent equilibrium constant K_{app} . The question remains as to the relationship between the derived K_{app} value and the various parameters of the kinetic scheme 1. An expression of K_{app} , based on a qualitative reasoning, can be obtained, by successively considering the three important steps of light absorption, equilibrium and decay to the ground state: the quantities of $[M^*]$ and $[M^*L]$ generated by laser excitation depend upon the equilibrium constant K and the photoabsorption coefficients α and β , a point already mentioned in Moriyasu et al. (1977a). The information on K which is contained in the values $[M^*](0)$ and $[M^*L](0)$ is then lost due to the rapid photochemical processes defined by the equilibrium constant in the excited state, K^* , which instantaneously leads to new values of $[M^*]$ and $[M^*L]$. Therefore, K_{app} is proportional to K^* . For given values of K and K^* , an increase in α (all other parameters being unchanged) will create an increased amount of $[M^*](0)$ which will be counterbalanced by an increased complexation through K^* . Conversely, an increase in β will induce an enhanced dissociation of M^*L . Therefore, K_{app} is proportional to the ratio (α/β) . Finally, the time dependence of $[M^*]$ and $[M^*L]$ is governed by two processes, the depletion by deactivation (k_M and k_{ML}) and the equilibrium reaction ($K^* = k_2/k_1$). Assuming $k_M > k_{ML}$, deactivation occurs predominantly via the channel $M^* \rightarrow M$. Thus, more photons come from the M^* decay than expected if no dissociation of M^*L would occur. With these considerations in mind, model 2 can be regarded as an approximation of scheme 1 with the following expression of K_{app} :

$$K_{\text{app}} = K^* \frac{\alpha}{\beta} \frac{\tau_M}{\tau_{ML}}. \quad (27)$$

This qualitative result can be applied to any luminescent chemical system. It differs from the relation proposed in Horrocks and Sudnick (1983), which does not include the term $(\alpha/\beta)(\tau_M/\tau_{ML})$. Finally, in the case of fast photochemical processes, the decays are monoexponential but the single lifetime is a function of $[L]$ (see eq. (24)), and varies from $\tau_M([L] = 0 \text{ M})$ to τ_{ML} (L in large excess).

In conclusion, the behavior of the luminescence decays allows one to determine to which regime (A, B or C) corresponds the system under study. For A and C regimes, the analysis of the emission spectra allows one to derive a value of K_{app} , which can be easily related to K^* in the latter case and to K in the former.

5.6. Discussion: Application to lanthanides and actinides

In the case of lanthanides, the 4f electrons, which are involved in the photoexcitation process, are strongly shielded. Hence one may assume that:

$$K^* \approx K. \quad (28)$$

This yields:

$$K_{\text{app}} \approx K \frac{\alpha}{\beta} \frac{\tau_M}{\tau_{ML}}. \quad (29)$$

From the literature review proposed in sect. 5.2.3 regarding the decay behavior, the following conclusions can be drawn:

- (i) Uranyl systems correspond to regime A or B, with the possible exception of the F^- ligand.
- (ii) Europium systems belonging to either one of the three regimes have been reported.
- (iii) Curium systems fall within regime C for all inorganic ligands investigated so far.

Depending on the element of interest (R(III), U(VI) or Cm(III)), these results lead to different implications for the K_{app} values as determined by TRES and how they can be related to K (eqs. (26)–(29)).

For the uranium systems (except for F^- , which is a doubtful case), the value of K_{app} , determined by TRES and calculated according to model 2, is in fact equal to K (see eq. (26)). This is confirmed in the case of the UO_2^{2+}/SO_4^{2-} system (Geipel et al., 1996) by the very good agreement between the equilibrium constants as recommended by the Nuclear Energy Agency (NEA) and the value from TRES (table 7).

In the case of europium complexation, depending on the type of ligand, TRES experiments give access directly to K (regime A) or cannot be used to derive K (regime B). For a system that falls within regime C, the determination of K is feasible, provided that the term $(\alpha/\beta)(\tau_M/\tau_{ML})$ is measured or known: in fact, for the very few Eu(III) systems for which the K_{app} value derived by TRES has been compared to the value derived by other techniques (see table 7), it happens that τ_{ML} values are below 140 μs (Albin et al., 1984; Wang et al., 1999) while $\tau_M \approx 110 \mu s$ (lifetime of Eu^{3+}_{aq}). This yields $\tau_M/\tau_{ML} \approx 1-1.3$. In addition, the strong shielding of the 4f electrons in lanthanide elements results in small variations of the absorption coefficient upon complexation (Bryden and Reilley, 1982; Clarkson et al., 2000; Giroux et al., 2000), which would give $\alpha/\beta \approx 1$ for the excitation wavelengths used in these studies. Hence, the term $(\alpha/\beta)(\tau_M/\tau_{ML})$ is expected to be close to unity. This explains the agreement obtained between equilibrium constants measured by TRES and other techniques (Wang et al., 1999). Finally, it is often noted in the literature, as a general remark, that the emission lifetimes in water for Eu (but also for Gd or Tb) are long enough, as compared to the ligand and water exchange rates, to consider that the lanthanide ion in its excited state reaches thermodynamic equilibrium with the ligand in solution. This remark is perfectly correct for regime C but is not applicable to regime A: as europium systems are found for which the luminescence decays are multiexponential, this means that k_1 and k_2 are small enough to avoid equilibrium between the excited species taking place within their lifetimes. Again, attention should be paid to the decay behavior in order to characterise the system.

For the systems curium/inorganic ligands studied, on the other hand, the K_{app} values derived by TRES are proportional to K^* rather than to K (see eq. (27)). To our knowledge, no simple relationship between K^* and K has been derived for 5f elements and the assumption $K^* \approx K$ simply relies on the similarities in the chemistry of 4f and 5f elements, a point which does not appear to be straightforward (Choppin, 1983). However, the question of a difference between K and K^* is not unimportant, as this difference can be very large in some systems, e.g., $K^* = 10^{-2.8}$ and $K = 10^{-9.5}$ for deprotonation of 2-naphtol (Laws and Brand, 1979).

In addition, even under the assumption $K^* \approx K$, the needed (α/β) value is difficult to determine experimentally, because of the large amounts of Cm required for such a measurement. As a whole, although no precise information on possible differences between K^* and K can be given presently for Cm, it appears that the question of estimating the possible difference between these two quantities remains unanswered. This point is of a certain relevance for calculations of the migration of curium in the environment (Nitzsche et al., 2000). In this respect, some doubts have been shed on the K values determined by TRES for the two systems $\text{Cm}^{3+}/\text{CO}_3^{2-}$ and $\text{Cm}^{3+}/\text{SO}_4^{2-}$ by some authors (Felmy and Rai, 1999).

5.7. Conclusion on the determination of equilibrium constants by TRES

TRES appears to be a sensitive tool to follow lanthanide and actinide complexation in solution, because most of the spectroscopic parameters are influenced by complexation. It has been shown that caution should be paid to the type of photochemical processes occurring in solution in order to correctly analyse the data. Taking account this important point, TRES is an interesting technique for the determination of equilibrium constants. From a more fundamental viewpoint, one may wonder why inorganic ligands lead to regime A with U(VI) and to regime C with Cm(III).

However, the effective experimental problems encountered in the determination of K -values with TRES have not been discussed yet. These problems are of two distinct types. First, as already stressed, the correct analysis of a luminescence decay (i.e., mono- or multi-exponential behaviour) is not a straightforward task, as has been shown in the case of well-defined U(VI) systems (Billard et al., 2003a). In the case where more than two luminescent species are present in solution, overlap of the different emission spectra is also a problem, which limits the number of "ideal" systems to be studied. As a whole, it should be emphasized that TRES, although attractive, is not an "easy" technique and requires much effort, patience and great caution in data analysis. Second, nothing has been said in this section about the possible bias that can be generated by the photodegradation of the ligand, due to too intense irradiation. This point has to be avoided in TRES experiments but cannot be foreseen for a given ligand, especially organic or biological ones. A few publications of general interest are suggested on this point: Lao (1996), Holz et al. (1999), Nijegorodov and Mabbs (2000), together with publications directly related to this problem for lanthanide or actinide systems (Matsumoto and Azuma, 1988; Bouby et al., 1998; Morgenstern et al., 2000; Monsallier et al., 2001).

6. Analytical applications of TRES: A few examples

6.1. Trace amount determination of lanthanides and actinides

When looking for R(III) determination, use can be made of the "antenna effect" already discussed in sect. 3.7, provided the lanthanide of interest is luminescent. The basic principle is to add a given organic ligand, which will ensure a high complexation constant with the lanthanide together with an efficient UV absorption and energy transfer to the R(III)

ion. The lanthanide luminescence can thus be detected down to the 10^{-10} M range, depending on the ligand and on the lanthanide. Note that the luminescence is so intense in most cases that time-resolved devices are usually not needed to achieve detection. A previous review has collected a large number of data on this question, to which the reader is referred (Horrocks and Albin, 1984); more recent papers on this topics present detection limits in the range 10^{-8} to 10^{-9} M, depending on the element (Berregi et al., 1999; Peter et al., 1992) and down to 0.11 ppt in the case of co-luminescence (Jenkins and Murray, 1996). Table 9 displays selected detection limits obtained for various lanthanides and actinides.

Another possibility is to take advantage of the effect of various supporting electrolytes (in a wide sense) that act as luminescence enhancers, as discussed in sect. 3.3, such as phosphoric acid. This method has been investigated in details both for lanthanides and actinides

Table 9
Detection limits for the determination of lanthanides and actinides as determined by TRES

Element	Experimentals	Limit of detection	Ref.
All RE (but Pm), La, Yb	calcein complexation; 6.0 < pH < 9.2,	5.2×10^{-8} M (Lu); 9×10^{-8} M (Ho); 6.9×10^{-7} M (La)	
Mixtures of RE	depending on the element	4.5×10^{-8} M (total concentration)	(a)
Eu	DPA complexation; 7 < pH < 11	14 ppt	
	DPA plus columinescence (Yb)	0.11 ppt	(b)
	3 M K ₂ CO ₃ medium	$0.1 \mu\text{g l}^{-1}$	(c)
Tb	DPA complexation; 7 < pH < 11	2.4 ppt	(b)
	DPA plus columinescence (Yb)	0.056 ppt	
	DPA plus columinescence (Yb)	$1 \mu\text{g l}^{-1}$	(c)
Sm	DPA complexation; 7 < pH < 11	140 ppt	(b)
	3 M K ₂ CO ₃ medium	$1.5 \mu\text{g l}^{-1}$	(c)
Dy	DPA complexation; 7 < pH < 11	640 ppt	
	DPA plus columinescence (Yb)	53 ppt	(b)
	3 M K ₂ CO ₃ medium	$0.5 \mu\text{g l}^{-1}$	(c)
U		10 pptr	(d)
	concentrated H ₃ PO ₄	1 ng l^{-1}	(e)
Am	TTA-TOPO/triton X-100	$\approx 10^{-8}$ M	(f)
	3 M K ₂ CO ₃ medium	5×10^{-11} M	(g)
Cm	TTA-TOPO/triton X-100	4×10^{-13} M	(h)

DPA: 2,6-pyridinedicarboxylic acid;

TTA: thenoyltrifluoroacetone;

TOPO: tri-n-octylphosphine oxide.

References

- | | | |
|-------------------------------|-----------------------------|----------------------------|
| (a) Berregi et al. (1999) | (d) Kaminski et al. (1981) | (g) Decambox et al. (1989) |
| (b) Jenkins and Murray (1996) | (e) Brina and Miller (1992) | |
| (c) Berthoud et al. (1989) | (f) Thouvenot et al. (1993) | (h) Moulin et al. (1991b) |

in various media of interest to the nuclear fuel cycle industry, such as solutions containing U and Pu (Berthoud et al., 1988; Moulin et al., 1996), human urines (Decambox et al., 1991) or blood (Scapolan et al., 1998) but also for natural waters (Moulin et al., 1990). The commercial complexing agent called “fluran”, which is widely used for uranium detection, is a purified (uranium free) mixture of $\text{Na}_4\text{P}_2\text{O}_7$ and NaH_2PO_4 (buffer at $\text{pH} = 7$).⁵ For lanthanides, depending on the element, the detection limit is from $0.1 \mu\text{g l}^{-1}$ to $50 \mu\text{g l}^{-1}$ (Berthoud et al., 1989). For Cm, detections limits as low as 5×10^{-11} M (carbonated medium, Decambox et al., 1989) or 5×10^{-13} M (micellar system, Moulin et al., 1991b) were obtained. A summary of some detection limits can be found in Moulin et al. (1991a).

In the specific case of the determination of trace amounts of actinides, it is interesting to compare the results obtained by TRES to those obtained by other techniques. This very brief presentation is based on a very detailed and comprehensive lecture on radioactive ultra-trace determination in the environment (Aupiais, 2001, in French). In order to detect radioactive traces in environmental samples, various techniques are available (α and β liquid scintillation, γ spectrometry, mass spectrometry, ...), which most of the time are coupled to a pre-concentration of the sample. Such methods allow isotope discrimination, which is impossible with TRES. Another restriction of TRES as compared to the other techniques available is that TRES is strictly limited to luminescent elements. On the other hand, liquid scintillation is a rather time-consuming method as compared to TRES. For example, detection limits with α liquid scintillation are equal to 2×10^{-10} mol for ^{238}U and 9×10^{-19} mol for ^{244}Cm but the acquisition time is on the order of a few days, to be compared with TRES acquisition times of a few minutes. In the case of Cm, the advantage of α liquid scintillation is clear but TRES appears to be competitive in the case of U, if no isotopic discrimination is required.

6.2. Trace amount determination of other ions

The Stern–Volmer equation (see sect. 4) may be used to determine small amounts of a species which would behave as an inhibitor of a given luminescent probe. The detection limit depends, among other parameters, on k_M and on the detection limits of the setup. The potentials of this method for analytical purposes are discussed, on a general aspect, in Borissevitch (1999), Rakicioglu et al. (1998) and the specific cases of Eu(III) or U(VI) are presented in Georges (1993), Lopez and Birch (1996), Kessler (1998). For example, a detection limit of 7 ng l^{-1} for Cu^{2+} is obtained (Lopez and Birch, 1996). Numerous factors may render the method difficult to apply: besides the variations of k_{SV} as a function of ionic strength, if more than one quencher is present in solution, it becomes difficult to determine their individual concentrations. This problem has been studied in the case of solutions that more or less mimic the nuclear fuel solutions in Katsumura et al. (1989).

6.3. Luminescent lanthanide sensors

This subject is very important, vivid and passionating and has generated a wealth of specific publications and reviews. Although related to the main topics of this chapter, because of the

⁵ Mix equal volumes of solution A ($\text{Na}_4\text{P}_2\text{O}_7$ $C = 5 \times 10^{-3}$ M) and solution B (NaH_2PO_4 $C = 0.4$ M) before use. If necessary, adjust to $\text{pH} = 7$.

use of lanthanide luminescence, it is out of the scope of this chapter to make a comprehensive presentation of this subject. Therefore, we will restrict ourselves to a short presentation, making reference to a limited number of recent reviews on the subject to which the reader is referred to gain deeper information. For an historical perspective, see Soini and Lövgren (1987).

The basic idea is to take advantage of the antenna effect (as described in sect. 3.7). The sensitiser, owing to its specific chemical structure, may be sensitive to changes in the solution (for example, protonation/deprotonation as a function of pH, presence/absence of a given moiety which will modify energy levels of the antenna through complexation). The energy transfer to the lanthanide will reflect these changes, and therefore the complex (antenna + lanthanide) will act as a sensor of some specific physico-chemical changes. This principle is very general and can be used with other metal ions than lanthanides. A recent review on this aspect for heavy and transition metal ions can be found in Rurack (2001). The physical principles detailed elsewhere in this chapter (Förster–Dexter mechanism, Stern–Volmer law, electron transfer, ...) directly apply to lanthanide sensors as detailed in two recent reviews on the subject (Parker, 2000; Bazin et al., 2001). Usually, the changes in the luminescence intensity is monitored but in the case of fluoroimmunoassays, detection by use of time-resolved setups can also be of great interest (Hemmilä and Webb, 1997; Hemmilä and Mikkala, 2001). Note that detection through lifetime changes is also possible (Bare et al., 2002). In some cases, detection limits are very good (10^{-18} mol) (Hemmilä and Webb, 1997). In order to improve the sensitivity and the panel of sensors, the question then remains on how to design specific sensors.

So far, lanthanide-based sensors have been successfully used for drug screening, assays and diagnostics as reviewed in Hemmilä and Webb (1997). Sensors for pH, pO_2 and some anions (Cl^- , CO_3^{2-} , ...) have been tested as exemplified in Parker et al. (1998), Bazzicalupi et al. (2001). In the case where protonation/deprotonation of part of the ligand (in its excited state) is the sensor basis, the pK_a of interest is that of the excited state, which may differ from that of the ground-state, as explained in sect. 5 (Parker et al., 1998; Blair et al., 2001).

7. General conclusion

Through the various aspects treated here, the author hopes she has convinced the reader of the wide interest of TRES both for applied and fundamental aspects of lanthanide and actinide chemistry in solution. In particular, it was shown that theoretical approaches can be confronted to experimental data in fields as different as electron and energy transfers, ion interactions or photochemistry for example. In addition, TRES can be of great interest to the determination of equilibrium constants. Although nothing has been said in this chapter about micellar systems, colloids, solids and interfaces (in a wide sense), TRES is also a tool of large potential for the analysis of these media. TRES has been demonstrated to be of great interest for the study of U(VI) dissolved in supercritical CO_2 (see, for example, the very good paper of Addleman and Wai, 1999). Other systems with high interest for TRES studies are Room Temperature Ionic

Liquids (RTILs) and molten salts, two types of liquid media gaining increasing interest in various fields of chemistry: in addition to their general interest in “green chemistry” (RTILs) and in the nuclear fuel reprocessing industry (molten salts), their characteristics render them attractive for TRES experiments: they are transparent, photostable, and they can dissolve rather large amounts of various salts. Under such conditions, it is very probable that TRES will be used in the near future for the study of these liquids (Billard et al., 2003b).

References

- Aas, W., Steinle, E., Fanghänel, T., Kim, J.I., 1999. *Radiochim. Acta* **84**, 85.
- Adams, M.J., 1995. *Chemometrics in Analytical Spectroscopy*. The Royal Society of Chemistry, Cambridge.
- Addleman, R.S., Wai, C.M., 1999. *Phys. Chem. Chem. Phys.* **1**, 783.
- Agmon, N., Gopich, I.V., 1999. *Chem. Phys. Lett.* **302**, 399.
- Albin, M., Farber, G.K., Horrocks, W.deW. Jr., 1984. *Inorg. Chem.* **23**, 1648.
- Allen, P., Bucher, J., Shuh, D., Edelstein, N., Craig, I., 2000. *Inorg. Chem.* **39**, 595.
- Allsopp, S.R., Cox, A., Kemp, T.J., Reed, W.J., Carassiti, V., Traverso, O., 1979. *J. Chem. Soc., Faraday Trans. I* **75**, 342.
- Al-Soufi, W., Novo, M., Mosquera, M., 2001. *Appl. Spectrosc.* **55**, 630.
- An, Y., Berry, M.T., van Veggel, F.C.J.M., 2000. *J. Phys. Chem. A* **104**, 11243.
- Arisaka, M., Kimura, T., Suganuma, H., Yoshida, Z., 2001. *Radiochim. Acta* **89**, 593.
- Arisaka, M., Kimura, T., Suganuma, H., Yoshida, Z., 2002. *Radiochim. Acta* **90**, 193.
- Arvis, M., Keller, N., Folcher, G., Hickel, B., 1983. *J. Photochem.* **21**, 313.
- Aupiais, J., 2001. In: *La mesure des radioéléments à l'état de traces dans l'environnement*. Ed. CEA, Méjannes-le-Clap, France.
- Azenha, M.E., Burrows, H.D., Formosinho, S.J., Miguel, M.G., Daramagnyan, A.P., Khudiakov, I.V., 1991. *J. Lum.* **48/49**, 522.
- Baird, C.P., Kemp, T.J., 1997. *Prog. Reaction Kin.* **22**, 87.
- Balzani, V., Sabbatini, N., 1986. *Chem. Rev.* **86**, 319.
- Bare, W.D., Mack, N.H., Xu, W., Demas, J.N., DeGraff, B.A., 2002. *Anal. Chem.* **74**, 2198.
- Barthelemy, P.P., Choppin, G.R., 1989. *Inorg. Chem.* **28**, 3354.
- Bazin, H., Préaudat, M., Trinquet, E., Mathis, G., 2001. *Spectrochim. Acta A* **57**, 2197.
- Bazzicalupi, C., Bencini, A., Berni, E., Bianchi, A., Giorgi, C., Fusi, V., Valtancoli, B., Lodeiro, C., Roque, A., Pina, F., 2001. *Inorg. Chem.* **40**, 6172.
- Beeby, A., Clarkson, I., Dickins, R., Faulkner, S., Parker, D., Royle, L., de Sousa, A., Williams, J., Woods, M., 1999. *J. Chem. Soc., Perkin Trans. II*, 493.
- Beechem, J.M., Ameloot, M., Brand, L., 1985. *Chem. Phys. Lett.* **120**, 466.
- Beitz, J.V., 1991. *Radiochim. Acta* **52**, 35.
- Beitz, J.V., Williams, C., 1997. *J. Alloys Compounds* **250**, 375.
- Bell, J., Billings, M., 1975. *J. Inorg. Nucl. Chem.* **37**, 2529.
- Berezhkovskii, A.M., D'yakov, Y.A., Zitserman, V.Y., 1998. *J. Chem. Phys.* **109**, 4182.
- Bernhard, G., Geipel, G., Reich, T., Brendler, V., Amayri, S., Nitsche, H., 2001. *Radiochim. Acta* **89**, 511.
- Berregi, I., Durand, J.S., Casado, J.A., 1999. *Talanta* **48**, 719.
- Berthoud, T., Decambox, P., Kirsch, B., Mauchien, P., Moulin, C., 1988. *Anal. Chem.* **60**, 1296.
- Berthoud, T., Decambox, P., Kirsch, B., Mauchien, P., Moulin, C., 1989. *Anal. Chim. Acta* **220**, 235.
- Billard, I., Rustenholtz, A., Sémon, L., Lützenkirchen, K., 2001. *Chem. Phys.* **270**, 345.
- Billard, I., Ansoborlo, E., Apperson, K., Arpigny, S., Azeha, A.E., Birch, D., Bros, P., Burrows, H., Choppin, G.R., Couston, L., Dubois, V., Fanghänel, T., Geipel, G., Hubert, S., Kim, J.I., Kimura, T., KlENZE, R., Kronenberg, A., Kumke, M., Lagarde, G., Lamarque, G., Lis, S., Madic, C., Meinrath, G., Moulin, C., Nagaishi, R., Parker, D., Planque, G., Scherbaum, F., Simoni, E., Sinkov, S., Viallesoubranne, C., 2003a. *Appl. Spect.*, accepted.
- Billard, I., Moutiers, G., Labet, A., El Azzi, A., Gailard, C., Mariet, C., Lützenkirchen, K., 2003b. *Inorg. Chem.*

- Billing, R., Zakharaova, G.V., Atabekyan, L.S., Hennig, H., 1991. *J. Photochem. Photobiol. A* **59**, 163.
- Birks, J., 1970. *Photophysics of Aromatic Molecules*. Wiley-Interscience, London.
- Blair, S., Lowe, M.P., Mathieu, C.E., Parker, D., Senanayake, P.K., Katakya, R., 2001. *Inorg. Chem.* **40**, 5860.
- Blasse, G., 1990. *Photochem. Photobiol.* **52**, 417.
- Borissevitch, I.E., 1999. *J. Lum.* **81**, 219.
- Bouby, M., Billard, I., MacCordick, J., Rossini, I., 1998. *Radiochim. Acta* **80**, 95.
- Bouby, M., Billard, I., Bonnenfant, A., Klein, G., 1999. *Chem. Phys.* **240**, 353.
- Breen, P.J., Horrocks, W.deW. Jr., 1983. *Inorg. Chem.* **22**, 536.
- Brendler, V., Geipel, G., Bernhard, G., Nitsche, H., 1996. *Radiochim. Acta* **74**, 75.
- Brina, R., Miller, A.G., 1992. *Anal. Chem.* **64**, 1413.
- Bryden, C.C., Reilley, C.N., 1982. *Anal. Chem.* **54**, 610.
- Buddhudu, S., Morita, M., Murakami, S., Rau, D., 1999. *J. Lum.* **83/84**, 199.
- Bünzli, J.-C.G., 1998. In: Saez-Puche, R., Caro, P. (Eds.), *Rare Earths*. Editorial Complutense, Madrid, p. 223.
- Bünzli, J.-C.G., 2003. In: Liu, G.K. (Ed.), *Spectroscopic Properties of Rare Earths in Optical Materials*. Springer-Verlag, Berlin, in press.
- Bünzli, J.-C.G., Choppin, G.R., 1989. *Lanthanide Probes in Life, Chemical and Earth Sciences: Theory and Practice*. Elsevier, Amsterdam.
- Bünzli, J.-C.G., Milicic-Tang, A., 1995. In: Gschneider, K.A., Eyring, L. (Eds.), *Handbook on the Physics and Chemistry of Rare Earths*. Elsevier Science, Amsterdam, ch. 145.
- Bünzli, J.-C.G., Petoud, S., Moret, E., 1999. *Spec. Lett.* **32**, 155.
- Burrows, H.D., 1990. *Inorg. Chem.* **29**, 1549.
- Burrows, H.D., Cardoso, A.C., Formosinho, S.J., Gil, A.M.P.C., Miguel, M.G., 1992. *J. Photochem. Photobiol. A* **68**, 279.
- Carnall, W.T., 1979. In: Gschneider, K.A. Jr., Eyring, L. (Eds.), *Handbook on the Physics and Chemistry of Rare Earths: Non-metallic Compounds I*. North Holland, Amsterdam, ch. 24.
- Carnall, W.T., Fields, P.R., Stewart, D.C., Keenan, T.K., 1958. *J. Inorg. Nucl. Chem.* **6**, 213.
- Choppin, G.R., 1983. *J. Less-Common Met.* **93**, 323.
- Choppin, G.R., 1997. *J. Alloys Compounds* **249**, 1.
- Choppin, G.R., Peterman, D.R., 1998. *Coord. Chem. Rev.* **174**, 283.
- Choppin, G.R., Wang, Z., 1997. *Inorg. Chem.* **36**, 249.
- Choppin, G.R., Rizkalla, E.N., El-Ansi, T.A., Dadgar, A., 1994. *J. Coord. Chem.* **31**, 297.
- Clarkson, I.M., Beeby, A., Bruce, J.I., Govenloch, L.J., Lowe, M.P., Mathieu, C.E., Parker, D., Senanayake, K., 2000. *New J. Chem.* **24**, 377.
- Couston, L., Pouyat, D., Moulin, C., Decambox, P., 1995. *Appl. Spectrosc.* **49**, 349.
- Cunningham, J., Srijaranai, S., 1990. *J. Photochem. Photobiol. A* **55**, 219.
- Dai, S., Burleigh, M.C., Simonson, J.M., Mesmer, R.E., Xue, Z.L., 1998. *Radiochim. Acta* **81**, 195.
- De Sa, G.F., Nunes, L.H.A., Wang, Z.M., Choppin, G.R., 1993. *J. Alloys Compounds* **196**, 17.
- Decambox, P., Mauchien, P., Moulin, C., 1989. *Radiochim. Acta* **48**, 23.
- Decambox, P., Mauchien, P., Moulin, C., 1991. *Appl. Spectrosc.* **45**, 116.
- Deschaux, M., Marcantonatos, M.D., 1979. *Chem. Phys. Lett.* **63**, 283.
- Dewey, H.J., Hopkins, T.A., 2000. *AIP Conf. Proc.* **532**, 307.
- Dickins, R.S., Parker, D., de Sousa, A.S., Williams, J.A.G., 1996. *Chem. Commun.*, 697.
- Dickins, R.S., Gunnlaugsson, T., Parker, D., Peacock, R.D., 1998. *Chem. Commun.*, 1643.
- Elhabiri, M., Scopelliti, R., Bünzli, J.-C.G., Pigué, C., 1999. *J. Am. Chem. Soc.* **121**, 10747.
- Eliet, V., Bidoglio, G., Omenetto, N., Parma, L., Grenthe, I., 1995. *J. Chem. Soc. Faraday Trans.* **91**, 2275.
- Eliet, V., Grenthe, I., Bidoglio, G., 2000. *Appl. Spectrosc.* **54**, 99.
- Ermolaev, V.L., Gruzdev, V.P., 1984. *Inorg. Chim. Acta* **95**, 179.
- Fanghänel, T., Kim, J.I., 1998. *J. Alloys Compounds* **271/273**, 728.
- Fanghänel, T., Kim, J.I., Paviet, P., Klenze, R., Hauser, W., 1994. *Radiochim. Acta* **66/67**, 81.
- Fanghänel, T., Kim, J.I., Klenze, R., Kato, Y., 1995. *J. Alloys Compounds* **225**, 308.
- Fanghänel, T., Weger, H., Konnecke, T., Neck, V., Paviet-Hartmann, P., Steinle, E., Kim, J.I., 1998a. *Radiochim. Acta* **82**, 47.
- Fanghänel, T., Weger, H.T., Schubert, G., Kim, J.I., 1998b. *Radiochim. Acta* **82**, 55.
- Felmy, A.R., Rai, D., 1999. *J. Sol. Chem.* **28**, 533.
- Förster, T., 1959. *Discuss. Faraday Soc.* **27**, 7.
- Frey, S.T., Horrocks, W.deW. Jr., 1995. *Inorg. Chim. Acta* **229**, 383.
- Fuger, J., 1992. *Radiochim. Acta* **58**, 81.
- Gaft, M., Panczer, G., Reisfeld, R., Shinno, I., 2000a. *J. Alloys Compounds* **300/301**, 267.

- Gaft, M., Panczer, G., Reisfeld, R., Shinno, I., Champagnon, B., Boulon, G., 2000b. *J. Lum.* **87/89**, 1032.
- Gaft, M., Panczer, G., Reisfeld, R., Uspensky, E., 2001. *Phys. Chem. Minerals* **28**, 347.
- Geipel, G., Brachmann, A., Brendler, V., Bernhard, G., Nitsche, H., 1996. *Radiochim. Acta* **75**, 199.
- Georges, J., 1993. *Analyst* **118**, 1481.
- Giroux, S., Rubini, P., Henry, B., Aury, S., 2000. *Polyhedron* **19**, 1567.
- Grenthe, I., 1992. *Chemical Thermodynamics of Uranium*. North-Holland, Amsterdam.
- Gruzdev, V.P., 1983. *Russian J. Inorg. Chem.* **28**, 1712.
- Haas, Y., Stein, G., 1971a. *J. Phys. Chem.* **75**, 3668.
- Haas, Y., Stein, G., 1971b. *J. Phys. Chem.* **75**, 3677.
- Hasegawa, Y., Ishiwata, E., Ohnishi, T., Choppin, G.R., 1999. *Anal. Chem.* **71**, 5060.
- Heller, A., 1966. *J. Am. Chem. Soc.* **88**, 2058.
- Hemmilä, I., Webb, S., 1997. *Drug Discovery Today* **2**, 373.
- Hemmilä, I., Mukkala, V.M., 2001. *Critical Rev. Clinical Lab. Sci.* **38**, 441.
- Hinton, J.F., Amis, E.S., 1971. *Chem. Rev.* **71**, 627.
- Hnatejko, Z., Lis, S., Elbanowski, M., 2000. *J. Alloys Compounds* **300/301**, 38.
- Holz, R.C., Klakamp, S.L., Chang, C.A., Horrocks, W.deW. Jr., 1990a. *Inorg. Chem.* **29**, 2651.
- Holz, R.C., Meister, G.E., Horrocks, W.deW. Jr., 1990b. *Inorg. Chem.* **29**, 5183.
- Holz, R.C., Chang, C.A., Horrocks, W.deW. Jr., 1991. *Inorg. Chem.* **30**, 3270.
- Holzer, W., Penzkofer, A., Pichlmaier, M., Bradley, D., Blau, W., 1999. *Chem. Phys.* **248**, 273.
- Horrocks, W.deW. Jr., Albin, M., 1984. *Prog. Inorg. Chem.* **31**, 1.
- Horrocks, W.deW. Jr., Sudnick, D.R., 1981. *Acc. Chem. Res.* **14**, 384.
- Horrocks, W.deW. Jr., Sudnick, D.R., 1983. *J. Am. Chem. Soc.* **101**, 334.
- Horrocks, W.deW. Jr., Arkle, V.K., Liotta, F.J., Sudnick, D.R., 1983. *J. Am. Chem. Soc.* **105**, 3455.
- Janssens, L.D., Boens, N., Ameloot, M., De Schryver, F.C., 1990. *J. Phys. Chem.* **94**, 3564.
- Jenkins, A.L., Murray, G.M., 1996. *Anal. Chem.* **68**, 2974.
- Jiang, J., Higashiyama, N., Machida, K., Adachi, G., 1998. *Coord. Chem. Rev.* **170**, 1.
- Jørgensen, C.K., Reisfeld, R., 1982. *Struct. Bond.* **50**, 122.
- Kaminski, R., Purcell, F.J., Russavage, E., 1981. *Anal. Chem.* **53**, 1093.
- Kanno, H., Hiraishi, J., 1982. *J. Phys. Chem.* **86**, 1488.
- Kanno, H., Yokoyama, H., 1996. *Polyhedron* **15**, 1437.
- Katsumura, Y., Abe, H., Yotsuyanagi, T., Ishigure, K., 1989. *J. Photochem. Photobiol. A* **50**, 183.
- Katz, J.J., Seaborg, G.T., Morss, L.R., 1986. *The Chemistry of Actinide Elements*. Chapman and Hall, London.
- Kessler, M.A., 1998. *Anal. Chim. Acta* **364**, 125.
- Khamidullina, L.A., Lotnik, S.V., Kazakov, V.P., 1994. *High Energy. Chem.* **28**, 122.
- Kim, J.I., Klenze, R., Wimmer, H., Runde, W., Hauser, W., 1994. *J. Alloys Compounds* **213**, 333.
- Kimura, T., Choppin, G.R., 1994. *J. Alloys Compounds* **213**, 313.
- Kimura, T., Kato, Y., 1995. *J. Alloys Compounds* **225**, 284.
- Kimura, T., Kato, Y., 1998. *J. Alloys Compounds* **278**, 92.
- Kimura, T., Kato, Y., Takeishi, H., Choppin, G.R., 1998. *J. Alloys Compounds* **271/273**, 719.
- Kimura, T., Nagaishi, R., Kato, Y., Yoshida, Z., 2001a. *J. Alloys Compounds* **323/324**, 164.
- Kimura, T., Nagaishi, R., Kato, Y., Yoshida, Z., 2001b. *Radiochim. Acta* **89**, 125.
- Klenze, R., 2001. Private communication.
- Klenze, R., Panak, P., Kim, J.I., 1998. *J. Alloys Compounds* **271/273**, 746.
- Klink, S.I., Graves, L., Reinhoudt, D.N., van Veggel, F., Werts, M.H.V., Geurts, F.A.J., Hofstraat, J.W., 2000. *J. Phys. Chem. A* **104**, 5457.
- Kropp, J.L., Windsor, M.W., 1965. *J. Chem. Phys.* **42**, 1599.
- Kropp, J.L., Windsor, M.W., 1967. *J. Phys. Chem.* **71**, 477.
- Laenen, R., Thaller, A., 2001. *Chem. Phys. Lett.* **349**, 442.
- Lao, K., 1996. *J. Phys. Chem.* **100**, 4693.
- Latva, M., Takalo, H., Mukkala, V.M., Matachescu, C., Rodriguez-Ubis, J.C., Kankare, J., 1997. *J. Lum.* **75**, 149.
- Laws, W.R., Brand, L., 1979. *J. Phys. Chem.* **83**, 795.
- Lee, K.P., Park, K.S., Kang, D.W., Yamada, Y., Ohno, S.I., 1998. *J. Radioanal. Nucl. Chem.* **235**, 17.
- Lis, S., Choppin, G.R., 1991. *Anal. Chem.* **63**, 2542.
- Lis, S., Choppin, G.R., 1992. *Mat. Chem. Phys.* **31**, 159.
- Lis, S., Mathur, J.N., Choppin, G.R., 1991. *Sol. Extr. Ion Exch.* **9**, 637.
- Lis, S., Kimura, T., Yoshida, Z., 2001. *J. Alloys Compounds* **323/324**, 125.
- Lochhead, M.J., Wamsley, P.R., Bray, K.L., 1994. *Inorg. Chem.* **33**, 2000.
- Lopez, M., Birch, D.J.S., 1996. *Analyst* **121**, 905.

- Lopez, M., Birch, D.J.S., 1997. *Chem. Phys. Lett.* **268**, 125.
- Mac, M., 1997. *J. Photochem. Photobiol. A* **107**, 107.
- Mac, M., Tokarczyk, B., 1999. *Chem. Phys. Lett.* **304**, 309.
- Mack, J., Bolton, J.R., 1999. *J. Photochem. Photobiol., A* **128**, 1.
- Marcantonatos, M.D., 1977. *Inorg. Chim. Acta* **24**, 37.
- Marcantonatos, M.D., 1978. *Inorg. Chim. Acta* **26**, 41.
- Marcantonatos, M.D., 1980. *J. Chem. Soc., Faraday Trans. I* **76**, 1093.
- Marcantonatos, M.D., Deschaux, M., Vuilleumier, J.J., 1982. *Chem. Phys. Lett.* **91**, 149.
- Marcantonatos, M.D., Pawlowska, M.M., 1989. *J. Chem. Soc., Faraday Trans. I* **85**, 2481.
- Matsumoto, A., Azuma, N., 1988. *J. Phys. Chem.* **92**, 1830.
- Max, J.J., Chapados, C., 2002. *J. Chem. Phys.* **116**, 4626.
- Meinrath, G., 1998. *J. Alloys Compounds* **275/277**, 777.
- Meinrath, G., Lis, S., Stryla, Z., Noubactep, C., 2000. *J. Alloys Compounds* **300/301**, 107.
- Metcalf, D.H., Snyder, S.W., Demas, J.N., Richardson, F.S., 1990. *J. Phys. Chem.* **94**, 7143.
- Miguel, M.G., Formosinho, S.J., Cardoso, A.C., Burrows, H.D., 1984. *J. Chem. Soc., Faraday Trans. I* **80**, 1735.
- Molski, A., 1994. *Chem. Phys.* **182**, 203.
- Molski, A., Boens, N., 1997. *J. Phys. Chem. A* **101**, 5124.
- Molski, A., Boens, N., Ameloot, M., 1998. *J. Phys. Chem. A* **102**, 807.
- Monsallier, J.M., Scherbaum, F.J., Buckau, G., Kim, J.I., Kumbe, M.U., Specht, H., Frimmel, F.H., 2001. *J. Photochem. Photobiol., A* **138**, 55.
- Mooney, W., Chauveau, F., Tran-Thi, T.H., Folcher, G., Giannotti, C., 1988. *J. Chem. Soc. Perkin Trans. II*, 1479.
- Morgenstern, M., Klenze, R., Kim, J.I., 2000. *Radiochim. Acta* **88**, 7.
- Moriyasu, M., Yokoyama, Y., Ideka, S., 1977a. *J. Inorg. Nucl. Chem.* **39**, 2199.
- Moriyasu, M., Yokoyama, Y., Ikeda, S., 1977b. *J. Inorg. Nucl. Chem.* **39**, 2205.
- Morrison, M.E., Dorfman, R.C., Webber, S.E., 1996. *J. Phys. Chem.* **100**, 15187.
- Morss, L.R., Fuger, J., 1992. *Transuranium Elements: A Half Century*. American Chemical Society, Washington, DC.
- Moulin, C., Beaucaire, C., Decambox, P., Mauchien, P., 1990. *Anal. Chim. Acta* **238**, 291.
- Moulin, C., Decambox, P., Mauchien, P., 1991a. *Journal de Physique IV* **1**, 677.
- Moulin, C., Decambox, P., Mauchien, P., 1991b. *Anal. Chim. Acta* **254**, 145.
- Moulin, C., Decambox, P., Mauchien, P., Pouyat, D., Couston, L., 1996. *Anal. Chim. Acta* **68**, 3204.
- Moulin, C., Laszak, I., Moulin, V., Tondre, C., 1998. *Appl. Spectrosc.* **52**, 528.
- Nagaishi, R., Katsumura, Y., Ishigure, K., Aoyagi, H., Yoshida, Z., Kimura, T., Kato, Y., 2002. *J. Photochem. Photobiol. A* **146**, 157.
- Nash, K.L., Sullivan, J.C., 1998. *J. of Alloys Compounds* **271/273**, 712.
- Nehlig, A., Elhabiri, M., Billard, I., Albrecht-Gary, A.M., Lützenkirchen, K., 2003. *Radiochim. Acta* **91**, 37.
- Nijegorodov, N., Mabbs, R., 2000. *Spectrochim. Acta* **56**, 2157.
- Nitzsche, O., Meinrath, G., Merkel, B., 2000. *J. Contam. Hydrol.* **44**, 223.
- Panak, P., Klenze, R., Kim, J.I., Wimmer, H., 1995. *J. Alloys Compounds* **225**, 261.
- Park, Y.Y., Tomiyasu, H., 1992. *J. Photochem. Photobiol. A* **64**, 25.
- Park, Y.Y., Tomiyasu, H., 1993. *J. Photochem. Photobiol. A* **74**, 11.
- Park, Y.Y., Sakai, Y., Abe, R., Ishii, T., Harada, M., Kojima, T., Tomiyasu, H., 1990. *J. Chem. Soc., Faraday Trans.* **86**, 55.
- Park, Y.Y., Harada, M., Tomiyasu, H., 1991. *J. Nucl. Sci. Technol.* **28**, 418.
- Parker, D., 2000. *Coord. Chem. Rev.* **205**, 109.
- Parker, D., Williams, J., 1996. *J. Chem. Soc., Dalton Trans.*, 3613.
- Parker, D., Senanayake, P.K., Williams, J.A.G., 1998. *J. Chem. Soc., Perkin Trans. II*, 2129.
- Pascal, P., 1962. *Nouveau Traité de Chimie Minérale*. Masson, Paris.
- Paviet, P., Fanghänel, T., Klenze, R., Kim, J.I., 1996. *Radiochim. Acta* **74**, 99.
- Peter, S., Panigrahi, B.S., Viswanathan, K.S., Mathews, C.K., 1992. *Anal. Chim. Acta* **260**, 135.
- Pouliquen, J., Wintgens, V., 1988. *J. Chim. Phys.* **85**, 455.
- Rakicioglu, Y., Young, M., Schulman, S., 1998. *Anal. Chim. Acta* **359**, 269.
- Richardson, F., 1982. *Chem. Rev.* **82**, 541.
- Rurack, K., 2001. *Spectrochim. Acta A* **57**, 2161.
- Rustenholtz, A., Billard, I., Duplâtre, G., Lützenkirchen, K., Sémon, L., 2001. *Radiochim. Acta* **89**, 83.
- Rutsch, M., Geipel, G., Brendler, V., Bernhard, G., Nitsche, H., 1999. *Radiochim. Acta* **86**, 135.

- Rykov, S., Khudyakov, I., Skakovsky, E., Burrows, H.D., Formosinho, S., Miguel, M., 1991. *J. Chem. Soc., Perkin Trans. II*, 835.
- Sabbatini, N., Ciano, M., Dellonte, S., Bonazzi, A., Balzani, V., 1982. *Chem. Phys. Lett.* **90**, 265.
- Sabbatini, N., Ciano, M., Dellonte, S., Bonazzi, A., Bolletta, F., Balzani, V., 1984. *J. Phys. Chem.* **88**, 1534.
- Sacco, A., Holz, M., 1997. *J. Chem. Soc. Faraday Trans.* **93**, 1101.
- Sacco, A., De Cillis, F.M., Holz, M., 1998. *J. Chem. Soc., Faraday Trans.* **94**, 2089.
- Sandhu, S., Singh, R., Chawla, S., 1990. *J. Photochem. Photobiol. A* **52**, 65.
- Scapolan, S., Ansoborlo, E., Moulin, C., Madic, C., 1998. *J. Alloys Compounds* **271/273**, 106.
- Schuurmans, F.J.P., Lagendijk, A., 2000. *J. Chem. Phys.* **113**, 3310.
- Scully, A.D., Hirayama, S., Hachisu, D., Tominaga, T., 1992. *J. Phys. Chem.* **96**, 7333.
- Sharman, K.S., Periasamy, A., Ashworth, H., Demas, J.N., Snow, N.H., 1999. *Anal. Chem.* **71**, 947.
- Shin, H., Choppin, G.R., 1999. *Radiochim. Acta* **86**, 167.
- Sikorski, M., Krystkowiak, E., Steer, R.P., 1998. *J. Photochem. Photobiol. A* **117**, 1.
- Simonin, J.P., Hendrawan, H., 2001. *Phys. Chem. Chem. Phys.* **3**, 4286.
- Simonin, J.P., Billard, I., Hendrawan, H., Bernard, O., Lützenkirchen, K., Sémon, L., 2003. *Phys. Chem. Chem. Phys.* **5**, 520.
- Soini, E., Lövgren, T., 1987. *Critical Rev. Anal. Chem.* **18**, 105.
- Spencer, S., Gagliardi, L., Handy, C., Ioannou, A.G., Skylaris, C.-K., Willets, A., Simper, A., 1999. *J. Phys. Chem. A* **103**, 1831.
- Stangret, J., Gampe, T., 2002. *J. Phys. Chem. A* **106**, 5393.
- Steemers, F., Verboom, W., Reinhoudt, D., Van der Tol, E., Verhoeven, J., 1995. *J. Am. Chem. Soc.* **117**, 9408.
- Steinfeld, J., Francisco, J., Hase, W., 1999. In: Steinfeld, J., Francisco, J., Hase, W. (Eds.), *Chemical Kinetics and Dynamics*. Prentice-Hall, Upper Saddle River.
- Stumpf, T., Fanghänel, T., 2002. *J. Colloid Interface Sci.* **249**, 119.
- Suib, S.L., Zerger, R.P., Stucky, G.D., Morrison, T.I., Shenoy, G.K., 1984. *J. Chem. Phys.* **80**, 2203.
- Supkowski, R.M., Horrocks, W.deW. Jr., 1999. *Inorg. Chem.* **38**, 5616.
- Tachiya, M., Murata, S., 1992. *J. Phys. Chem.* **96**, 8441.
- Takahashi, K., Kimura, T., Kato, Y., Minai, Y., Tomi-naga, T., 1997. *Chem. Commun.*, 223.
- Tanaka, F., Ishibashi, T., 1996. *J. Chem. Soc., Faraday Trans.* **92**, 1105.
- Tanaka, F., Yamashita, S., 1984. *Inorg. Chem.* **23**, 2044.
- Tanaka, F., Kawasaki, Y., Yamashita, S., 1988. *J. Chem. Soc., Faraday Trans. I*, 1083.
- Tanaka, F., Ishibashi, T., Okamoto, M., 1993. *J. Photochem. Photobiol. A* **74**, 15.
- Thouvenot, P., Hubert, S., Moulin, C., Decambox, P., Mauchien, P., 1993. *Radiochim. Acta* **61**, 15.
- Tran, C.D., Zhang, W., 1990. *Anal. Chem.* **62**, 835.
- Voltz, R., 1968. *Radiat. Res. Rev.* **1**, 301.
- Wang, Y., Horrocks, W.deW. Jr., 1997. *Inorg. Chim. Acta* **263**, 309.
- Wang, Z.M., van de Burgt, L.J., Choppin, G.R., 1999. *Inorg. Chim. Acta* **293**, 167.
- Werts, M.H.V., Jukes, R.T.F., Verhoeven, J.W., 2002. *Phys. Chem. Chem. Phys.* **4**, 1542.
- Wimmer, H., Klenze, R., Kim, J.I., 1992. *Radiochim. Acta* **56**, 79.
- Wu, S., Horrocks, W.deW. Jr., 1996. *Anal. Chem.* **68**, 394.
- Wu, S., Horrocks, W.deW. Jr., 1997. *J. Chem. Soc., Dalton Trans.*, 1497.
- Wu, S.L., Franklin, S.J., Raymond, K.N., Horrocks, W.deW. Jr., 1996. *Inorg. Chem.* **35**, 162.
- Yamamura, T., Park, Y.Y., Tomiyasu, H., 1993. *J. Alloys Compounds* **193**, 186.
- Yayamura, T., Iwata, S., Iwamaru, S.I., Tomiyasu, H., 1994. *J. Chem. Soc., Faraday Trans.* **90**, 3253.
- Yamamura, T., Fazekas, Z., Harada, M., Tomiyasu, H., 1999. *Phys. Chem. Chem. Phys.* **1**, 3491.
- Yokoyama, Y., Moriyasu, M., Ikeda, S., 1974. *J. Inorg. Nucl. Chem.* **36**, 385.
- Yokoyama, Y., Moriyasu, M., Ikeda, S., 1976. *J. Inorg. Nucl. Chem.* **38**, 1329.

Chapter 217

**OPTICAL STUDIES OF NON-METALLIC COMPOUNDS
UNDER PRESSURE**

Thomas TRÖSTER

Universität Paderborn, FB 6 / Physik, 33095 Paderborn, Germany

Contents

List of symbols and abbreviations	515	4.6.1. Multiple sites/glasses	555
1. Introduction	516	4.6.2. Phase transitions	556
2. High pressure technique	517	5. Intensities and lifetimes of f-f transitions	559
3. Survey of experimental data	520	5.1. General considerations	559
4. Energy levels	520	5.2. Absorption studies	562
4.1. Theoretical background	520	5.3. Luminescence studies	562
4.2. Line shifts	527	5.3.1. Influence of $4f^{N-1}5d^1$ configura-	
4.3. Nephelauxetic effect	529	tions	563
4.4. Crystal-field splittings	535	5.3.2. Influence of charge transfer states	567
4.4.1. Crystal-field parameters	535	5.3.3. Energy transfer processes in insu-	
4.4.2. Local distortions	540	lators	572
4.4.3. Superposition model	541	5.3.4. Energy transfer processes in semi-	
4.4.4. Ab initio calculations	545	conductors	577
4.4.5. Correlation crystal fields	547	6. Electron-phonon interaction	580
4.4.6. Excited states	548	7. Conclusions	582
4.5. Pressure sensors	552	Acknowledgement	583
4.6. Structural probes	555	References	583

List of symbols and abbreviations

$\bar{B}_k(R)$	intrinsic crystal-field parameters	HOMO	Highest Occupied Molecular Orbital
B_q^k	crystal-field parameters	I	intensity
$C_q^{(k)}$	tensor operators	J	total angular momentum
CFCM	central-field covalency model	L	total orbital angular momentum
CTS	charge transfer state	LUMO	Lowest Unoccupied Molecular Orbital
DAC	diamond anvil cell	n	refractive index
D_{ED}	electric dipole strength	N	renormalisation coefficient
D_{MD}	magnetic dipole strength	p	pressure
e	elementary charge	$R_j, \vartheta_j, \varphi_j$	ligand coordinates
F^k	Slater parameters	S	crystal-field strength
G_{iQ}^K	correlation crystal-field parameters	S	total spin angular momentum

SCCF	spin-correlated crystal field	κ	isothermal compressibility
SRCM	symmetry-restricted covalency model	Γ	linewidth
t_k	power law exponent	Γ_1	irreducible representation
W	transition rate	λ	wavelength
Z^*	effective nuclear charge	μ	crystal quantum number
α, β, γ	two-body configuration interaction parameters	ν	wavenumber
α_P	polarizability	ω	phonon frequency
β_R	branching ratio	τ_R	radiative lifetime
ε	dielectric function	ζ	spin-orbit coupling parameter
		$\Omega_{2,4,6}$	Judd–Ofelt intensity parameters

1. Introduction

Ever since the foundations of spectroscopy were laid the problem of the relationship between the optical spectra emitted or absorbed by matter and the microscopic properties of the matter has been regarded as a fundamental problem. A class of very interesting systems with this regard is provided by non-metallic compounds of rare-earth ions with partially filled 4f shells. Their rich electronic structure is only weakly perturbed by the environment and provides a detailed fingerprint of the surrounding arrangement of atoms and their interactions with the f-electrons.

Valuable insight has been obtained by measuring the spectra of rare-earth ions in various host lattices. However, with respect to the relation of energy levels and host lattice structure, the presence of different ligands and local distortions around the impurity ion in each host lattice and the limited number of isostructural crystals available for spectroscopic studies restrict the empirical information thus obtainable.

High pressure techniques, in contrast, offer a more powerful method for such studies. By applying pressure one can vary the interatomic distances continuously and thereby study the crystal structure dependence of the f-electron states directly. A second, equally interesting possibility is based on the different sensitivities of the energies of electronic states on interatomic distances. These specific sensitivities allows the experimentalist to alter the energy difference between two states and thus to get unique information about their mutual influence.

The first published work on the pressure dependence of optical spectra of solids seems to be of Paetzold (1940), who has studied the effect of pressure on absorption spectra of praseodymium nitrate, ruby, and other minerals between 1938 and 1939. To generate a maximum pressure of 0.1 GPa the samples were subjected to pressurised nitrogen. Using the same high pressure apparatus, Hellwege and Schröck-Vietor (1955) studied the pressure dependence of the absorption spectra of EuZn-nitrate. These authors, for the first time, applied the crystal-field Hamiltonian formalism for the analysis of the high pressure spectroscopic results.

The development of a squeezer apparatus for optical studies by Drickamer and his co-workers (Fitch et al., 1957) and almost at the same time the development of the diamond anvil cell (DAC) (Weir et al., 1959; Jamieson et al., 1959) provided real breakthrough in the

experimental study of lanthanide crystal fields under high pressure in general. Since then, different rare-earth ions in various compounds have been investigated and in many studies the pressure dependence of the crystal-field and free-ion parameters were determined and interpreted. Recently, Bray (2001) has compiled several examples of luminescence properties of transition metal and lanthanide systems under pressure.

The aim of this chapter is to present a review of the high pressure optical studies on rare-earth ions in non-metallic compounds. Other methods, as for example neutron scattering, magnetic resonance techniques or Mößbauer spectroscopy will not be considered here, unless they provide additional valuable information to the optical studies. It will be demonstrated that the problem of host lattice structural dependence of $4f^N$ states can be effectively tackled by high pressure techniques and hopefully the interest for further, more refined high pressure studies of this problem can be stimulated.

In the next section the rare-earth compounds that have been studied by optical means under pressure so far will be reviewed. Then, after a brief introduction of the most commonly used high pressure device, the diamond anvil cell, sect. 4 presents a discussion of the pressure-induced changes of the crystal-field levels and their interpretation. In sects. 5 and 6 some aspects of the dynamical effects under pressure are discussed. These include lifetime and intensity measurements, the influence due to excited configurations and charge transfer bands, and the electron-phonon coupling.

2. High pressure technique

A huge variety of different approaches to generate high pressures has been developed in the last century. In general, the devices depend on the type of materials under consideration (gas, liquid or solid), the desired temperature and pressure ranges, the pressure-generating mechanisms, and the experimental methods that are to be used. For detailed information about different types of high-pressure systems, the interested reader is referred to some very good text books and reviews dealing with various high-pressure techniques and methods (Eremets, 1996; Holzapfel and Isaacs, 1997).

Roughly, one can distinguish between three different categories of high-pressure devices. Hydraulic systems are used for the compression of fluids where the fluid either acts as the sample itself or as a pressure-transmitting medium. The pressure range for these systems is usually limited to pressures below 2 GPa. Second, piston-cylinder devices are used for the compression of large-volume ($> 1\text{mm}^3$) solid samples. Pressures of around 10 GPa are achievable with this method.

The third and most important category contains all types of opposed-anvil systems. The underlying idea in this case is quite simple. Because pressure is defined as force per area, a given force applied to the large sides of opposed conical anvils will result in an enlarged pressure between the small sides of the anvils. To reach very high pressures, the anvil material of course should be as hard as possible. Thus, starting in the 1970s, diamonds were used as the anvils which allowed for extending the pressure range up to several hundred GPa. At the same time, diamonds exhibit superior features as optical windows. They are transparent from

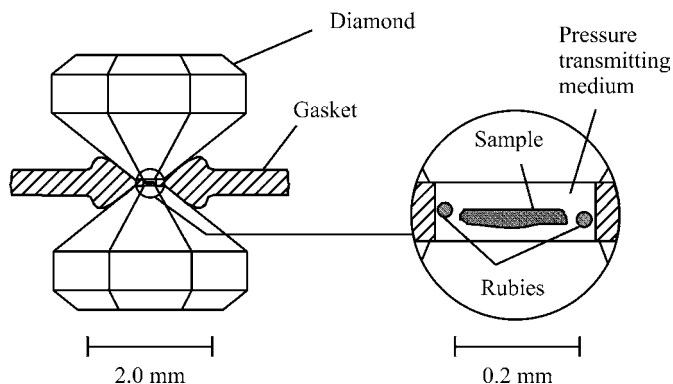


Fig. 1. Principle of the pressure-generating method with opposed diamond anvils. The enlargement on the right side shows the central hole of the gasket filled with rubies, a sample, and a pressure-transmitting medium.

the far infrared to the vacuum ultraviolet and their intrinsic luminescence can be negligible when carefully selected.

Meanwhile, the diamond anvil cell (DAC) has become the dominant device in high-pressure research. Although optical studies build up a big part of research performed with DACs, nearly every method used to study physical properties of matter has been successfully employed also in high-pressure DACs. Examples are electrical measurements (Gonzalez et al., 1986), X-ray diffraction (Hazen and Finger, 1982; Holzapfel, 1989), X-ray absorption (Tolentino et al., 1990), Mössbauer spectroscopy (Lübbbers et al., 2000), neutron scattering (Vettier, 1989), resonance techniques (Sakai and Pifer, 1985).

The principle of pressure-generation with opposed diamond anvils is shown in fig. 1. A gasket with a central hole is placed between the two diamond tips to provide a sample chamber which can be filled with a pressure-transmitting medium to maintain hydrostatic conditions. Furthermore, the sample chamber is loaded with the sample and some pressure sensor.

Different materials have been used for the gasket, depending on the maximum pressure desired and the experimental method to be employed. Common materials are all sorts of stainless steels, as for example Inconel X750. For pressures in the 100 GPa region, Re or Mo gaskets are used because of their higher strength. In the case of X-ray experiments, Be with its low atomic number has the advantage of low absorbance.

The most common pressure sensor for optical studies is ruby ($\text{Al}_2\text{O}_3:\text{Cr}^{3+}$, Piermarini et al. (1975)), whose strong R_1 and R_2 luminescence line shifts under pressure have been calibrated up to 180 GPa at room temperature (Mao et al., 1978; Mao, 1989). At low temperatures the line position has to be corrected by a known temperature-induced shift (Noack and Holzapfel, 1979). Besides ruby also other sensors utilizing rare-earth ions have been proposed and discussed in literature (Shen et al., 1991). In most of these cases the pressure induced shifts of luminescence lines are used to determine the pressure (see sect. 4.5).

One of the problems that has to be tackled in high pressure physics is the difficulty to provide truly hydrostatic or at least nearly hydrostatic conditions at very high pressure. In a DAC this requirement is fulfilled by the encapsulating fluid. As soon as this fluid solidifies at a certain pressure, however, the pressure and stress distribution within the medium can become non-uniform. The same applies in the case of solids with low shear strengths, as for example

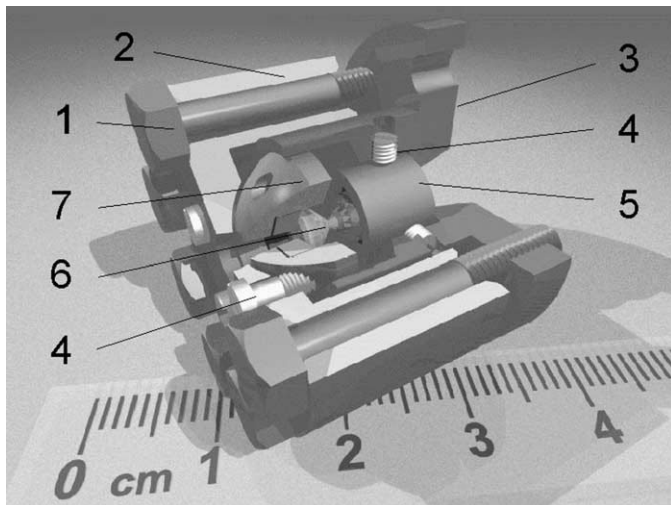


Fig. 2. Intersection of a miniature diamond anvil cell (from Michael (2000)). The pressure range extends up to 35 GPa at room as well as at low temperatures. 1 – Screws for pressure generation, 2 – cell body, 3 – piston, 4 – adjustment screws, 5 – diamond support, 6 – diamond, 7 – tilting diamond mount hemisphere.

NaCl, which are sometimes used as the pressure transmitting medium. The unknown magnitude of the deviant stresses in such systems has often cast serious doubts on the interpretation of the measurements.

Piermarini et al. (1973) have studied the hydrostatic limits of different liquids and solids by measuring the pressure gradient in the medium across the anvil diameter and observing the line shape of the R_1 , R_2 -lines of ruby. In the case of the line shape a broadening indicates local uniaxial components of the stress, due to its influence on the position of the lines. Thus, the broadening is a measure for the deviations from purely hydrostatic conditions. Other indicators for estimating the value of hydrostaticity are the splitting of the R_1 and R_2 lines of ruby and the lattice parameters of a crystal relative to the loading direction (Asaumi and Ruoff, 1986).

The best medium with regard to hydrostatic conditions found by Piermarini et al. (1973) was a 4:1 methanol–ethanol mixture. In this case hydrostatic conditions were maintained up to a pressure of around 10 GPa. Other common media are a 16:3:1 mixture of methanol–ethanol–water with a hydrostatic limit of 14.5 GPa (Fujishiro et al., 1982), argon or neon with limits of 9 GPa and 16 GPa, respectively (Bell and Mao, 1981) or helium with a maximum value of 70 GPa (Eremets, 1996).

A serious limitation is imposed to high-pressure experiments by the small size of the samples. Typical dimensions of the samples are in the range $200 \times 200 \times 40 \mu\text{m}$. This small size causes weak signals and, especially in the case of absorption spectroscopy, it can be very difficult or even impossible to study doped samples.

Various types of DACs have been developed within the past decades. An overview of different cells is given for example by Jayaraman (1983). As an example to demonstrate the capabilities of DACs, fig. 2 presents an cutaway view of a miniature cell used at the University of Paderborn. The cell was designed for magnetic resonance studies with maximum pressures of up to 35 GPa. To use it within magnetic fields, it is completely made of a non-magnetic Be–Co

alloy. The small size and mass permits the efficient use also in standard cryostats. The support of the diamond anvils is made from boron carbide, a material which is nonconductive at low temperatures and allows the micro wave to enter the cell without significant attenuation.

3. Survey of experimental data

By far the largest part of the experimental results presented in this work, has been obtained with the aid of optical studies. Only in exceptional cases other methods, like electron-spin resonance or neutron scattering, have been employed to get information about energy levels under pressure. Obviously, these methods must be used in the case of non-transparent materials, where optical methods are not suitable.

Before continuing, some words must be said with regard to the terms “rare earths” and “f elements” used in this chapter. The term rare earths includes the elements Sc, Y and the lanthanides La through Lu. However, this chapter solely deals with divalent or trivalent rare-earth ions which are optically active, i.e., possess a partially filled f-shell. Thus, although the term rare earths is used in this chapter, it should be kept in mind that the elements Sc, Y, La, and Lu are excluded. In some exceptional cases the more general term f elements will be used, as for example when high pressure studies on actinide ions with a partially filled 5f shell are discussed. There are only few studies on 5f elements in non-metallic compounds under pressure, however, it seems interesting to compare the results found for these ions with those for the 4f-elements.

To provide an overview of the rare-earth compounds which have been studied under pressure so far, table 1 lists the compounds, with respect to the doped ion and with the respective references. Obviously, Eu has been studied under pressure in much more host matrices than any of the other elements. This situation is similar to the observations made by Görrler-Walrand and Binnemans (1996), who reviewed the experimental data on spectroscopic properties of trivalent lanthanide ions doped into crystalline host matrices at ambient pressure. They found that Nd and Eu alone built up around 50% of all studies.

The optical studies performed on most samples of table 1 were aimed at different aspects of the f-electron properties. A considerable amount of the work was concerned with the energy level shifts under pressure. From these shifts, variations of free-ion parameters, crystal-field parameters or crystal-field strengths with pressure have been deduced. Other studies concentrated on changes in lifetimes or intensities, the efficiency of energy transfer between rare earths or rare earths and other impurities or on electron–phonon coupling effects under pressure. The various aspects investigated under high pressure will be presented within the next sections.

4. Energy levels

4.1. Theoretical background

When an f-element ion is embedded in a crystal, the free-ion energy levels, characterized by the total angular momentum J , are affected in two different ways. On one hand the energy

Table 1

Non-metallic rare-earth compounds studied under high pressure. In almost all cases the energy level shifts as a function of pressure have been determined. The second column gives details concerning the measurements and evaluations made. In particular the following abbreviations are used: L: Luminescence-, A: Absorption-, E: Excitation-, S: Site-selective spectroscopy, O: Other methods, EPC: Electron-Phonon Coupling, Int: Intensities, LT: Lifetime, CFP: Crystal-Field Parameters, FIP: Free-Ion Parameters, IP: Intrinsic Parameters, ET: Energy Transfer

Compound	Studies	Reference
Ce³⁺		
CaF ₂ :Ce ³⁺	A	Drotning and Drickamer (1973)
CeAs	O	Okayama et al. (1993), Yoshizawa et al. (1995), Oohara et al. (1995)
Ce(C ₂ H ₅ SO ₄) ₃ ·9H ₂ O	O, EPC	Krygin and Prokhorov (1987a)
CeP	O	Kohgi et al. (1993), Naka et al. (1994), Yoshizawa et al. (1995)
Eu(C ₂ H ₅ SO ₄) ₃ ·9H ₂ O:Ce ³⁺	O, CFP	Krygin et al. (1983), Krygin and Prokhorov (1984)
Y(C ₂ H ₅ SO ₄) ₃ ·9H ₂ O:Ce ³⁺	O, CFP	Krygin et al. (1983), Krygin and Prokhorov (1984)
Pr³⁺		
CaF ₂ :Pr ³⁺	L, CFP, IP	Kennedy (1980), Kennedy and Campbell (1980)
CeF ₃ :Pr ³⁺	A, FIP	Voloshin and Krimnus (1977)
GdOCl:Pr ³⁺	L, E, FIP, CFP, IP	Bungenstock et al. (2000a, 2000b)
La(C ₂ H ₅ SO ₄) ₃ ·9H ₂ O:Pr ³⁺	L, A, FIP, CFP, EPC	Voloshin and Krimnus (1977), Voloshin and Ivchenko (1980), Voloshin (1986)
LaCl ₃ :Pr ³⁺	L, A, E, Int, FIP, CFP, IP	Keating and Drickamer (1961a), Gregorian and Holzapfel (1984), Umland et al. (1985, 1986), Gregorian et al. (1986, 1989, 1991), Voloshin (1988), Umland (1989), Tröster et al. (1993), Tröster (1999)
LaOCl:Pr ³⁺	L, E, FIP, CFP, IP	Bungenstock et al. (1998, 2000b), Tröster and Holzapfel (1998)
PrBr ₃	A	Wilmarth et al. (1989)
PrCl ₃	L, A, Int, FIP, CFP, IP	Keating and Drickamer (1961a), Wilmarth et al. (1989), Tröster et al. (1993)
Pr(C ₂ H ₅ SO ₄) ₃ ·9H ₂ O	A, Int	Keating and Drickamer (1961a), Voloshin and Ivchenko (1980), Voloshin (1982), Krygin et al. (1984)
PrF ₃	A, Int	Keating and Drickamer (1961a)
Pr(NO ₃) ₃ ·6H ₂ O	A	Paetzold (1940)
PrO ₂	O	Hu et al. (1994)
PrOCl	L, A, FIP, CFP, IP	Bungenstock et al. (2000b)
PrSb	O, CFP	Vettier et al. (1977), Vettier (1989)
PrX (X = N, P, As, Sb, S, Se)	O	Schirber et al. (1978)
SrF ₂ :Pr ³⁺	L, CFP, IP	Kennedy (1980), Kennedy and Campbell (1980)
YBa ₂ Cu ₃ O ₇ :Pr ³⁺	O, EPC	Voloshin (1990)
Nd³⁺		
Gd ₃ Ga ₅ O ₁₂ :Nd ³⁺	L, O	Hua et al. (1996)
Gd ₃ Sc ₂ Ga ₃ O ₁₂ :Nd ³⁺	L, O	Hua et al. (1996)
La(C ₂ H ₅ SO ₄) ₃ ·9H ₂ O:Nd ³⁺	O, CFP	Krygin et al. (1986), Krygin and Prokhorov (1987b)

continued on next page

Table 1, *continued*

Compound	Studies	Reference
LaCl ₃ :Nd ³⁺	L, E, O, FIP, CFP, IP	Tröster et al. (1990, 1993), Gregorian et al. (1991), Krygin et al. (1992), Jayasankar et al. (1993), Tröster (1999)
LaF ₃ :Nd ³⁺	L, FIP	Voloshin et al. (1975)
NdBa ₂ Cu ₃ O ₇	O, EPC	Goncharov et al. (1994)
NdBr ₃	A	Wilmarth et al. (1989)
Nd(C ₂ H ₅ SO ₄) ₃ ·9H ₂ O	A, Int	Keating and Drickamer (1961a)
NdCl ₃ ·6H ₂ O	L, A, Int, FIP	Keating and Drickamer (1961a), Voloshin et al. (1975)
NdCl ₃	L, A, Int, FIP, CFP, IP	Keating and Drickamer (1961a), Peterson et al. (1986), Tröster et al. (1993)
NdF ₃	A, Int	Keating and Drickamer (1961a)
NdP ₅ O ₁₄	A, L, LT	Merkle et al. (1981)
Pb ₂ Sr ₂ NdCu ₃ O ₈	O, EPC	Goncharov et al. (1994)
Y ₃ Al ₅ O ₁₂ :Nd ³⁺	L, O	Hua et al. (1996), Hua and Vohra (1997)
YAlO ₃ :Nd ³⁺	L	Barnett et al. (1973), Hua and Vohra (1997)
Y(C ₂ H ₅ SO ₄) ₃ ·9H ₂ O:Nd ³⁺	O, CFP	Krygin et al. (1986), Krygin and Prokhorov (1987b)
YP ₅ O ₁₄ :Nd ³⁺	L, A, LT	Merkle et al. (1981)
Sm²⁺		
BaF ₂ :Sm ²⁺	L, CFP	Kennedy (1980)
BaFCl:Sm ²⁺	L, CFP, IP, EPC	Shen et al. (1990), Shen and Holzapfel (1993, 1995a, 1995c, 1995d, 1996), Shen and Bray (1998a, 1999)
CaF ₂ :Sm ²⁺	L, A, CFP, EPC	Wang and Drickamer (1973), Kennedy (1980), Kennedy and Campbell (1980)
CaFCl:Sm ²⁺	L, O, CFP, IP	Oppenländer et al. (1989), Shen and Holzapfel (1995a, 1995b, 1995c, 1996), Shen and Bray (1998a, 1999)
CsSmI ₃	L	Chen et al. (1994c)
SmFCl	A, X-ray	Bolduan et al. (1985)
SmSe	O	Neuenschwander and Wachter (1990)
SmS	O	Neuenschwander and Wachter (1990)
SrB ₄ O ₇ :Sm ²⁺	L, E, LT	Lacam and Chateau (1989), Leger et al. (1990), Urošević et al. (1992), Datchi et al. (1997)
SrF ₂ :Sm ²⁺	L, CFP, IP, EPC	Kennedy (1980), Kennedy and Campbell (1980), Yoo et al. (1991)
SrFCl _{0.5} Br _{0.5} :Sm ²⁺	L, LT	Jovanić (2001)
SrFCl:Sm ²⁺	L, Int, LT, FIP, CFP, IP	Shen et al. (1990, 1991, 1997), Gregorian et al. (1991), Lorenz et al. (1994), Shen and Holzapfel (1995a, 1995c, 1995d, 1996), Jovanić et al. (1997a, 1997b), Shen and Bray (1998a, 1999)
Sm³⁺		
Chelates:Sm ³⁺	L, Int, ET	Hayes and Drickamer (1982)
49.5 H ₃ BO ₃ –49.5 LiF– 1.0 Sm ₂ O ₃	L, LT	Jayasankar et al. (2000), Lavin et al. (2002a)

continued on next page

Table 1, *continued*

Compound	Studies	Reference
Sm(C ₂ H ₅ SO ₄) ₃ ·9H ₂ O	A, Int	Keating and Drickamer (1961a)
Sm ₂ [Pt(CN) ₄] ₃ ·18H ₂ O	L, Int, ET	Yersin and Stock (1982)
Y ₃ Al ₅ O ₁₂ :Sm ³⁺	L, Int	Hess and Exarhos (1989), Bi et al. (1990), Hess and Schiferl (1990, 1992), Liu and Vohra (1993, 1994), Yusa et al. (1994)
Eu²⁺		
BaBr ₂	L	Tröster et al. (2002)
Ba ₂ SiO ₄ :Eu ²⁺	L, Int, LT	Tyner and Drickamer (1977)
CaAl ₂ O ₄ :Eu ²⁺	L, Int, LT	Tyner and Drickamer (1977)
CaBPO ₅ :Eu ²⁺	L, Int, LT	Tyner and Drickamer (1977)
Ca ₂ P ₂ O ₇ :Eu ²⁺	L, Int, LT	Tyner and Drickamer (1977)
CdF ₂ :Eu ²⁺	O, CFP	Rewaj and Krupski (1980)
EuF ₂	A	Wang and Drickamer (1973)
EuO	A, O	Zimmer et al. (1984)
SrAl ₂ O ₄ :Eu ²⁺	L, Int, LT	Tyner and Drickamer (1977)
SrBPO ₅ :Eu ²⁺	L, Int, LT	Tyner and Drickamer (1977)
ZnS:Eu ²⁺	L, Int	Wang et al. (1984)
Eu³⁺		
90B ₂ O ₃ -10Na ₂ O-	L	Soga et al. (1988)
1Eu ₂ O ₃ (glass)		
Ca(PO ₃) ₂ :Eu ³⁺ (glass)	L, CFP, Int	
CaF ₂ :Eu ³⁺	S, O, CFP	Radliński and Silversmith (1986), Wright et al. (1995), Olsen et al. (1996)
Chelates:Eu ³⁺	L, Int, ET	Hayes and Drickamer (1982)
Eu[Au(CN) ₂] ₃ ·3H ₂ O	L, Int, ET	Yersin et al. (1998)
Eu benzoylacetate	L, LT, Int, ET	Voloshin et al. (1976), Voloshin and Savutskii (1976)
Eu ₂ O ₃	L, FIP	Chen et al. (1992b, 1992c, 1994b), Stump et al. (1993)
EuOCl	L, A, LT	Del Cul et al. (1991)
Eu(OH) ₃	L, CFP	Chen et al. (1994a, 1995)
EuPO ₄	L, LT, CFP	Chen et al. (1997)
EuP ₅ O ₁₄	L, LT, FIP, ET	Huber et al. (1977), Blanzat et al. (1984)
Eu ₂ [Pt(CN) ₄] ₃ ·18H ₂ O	L, Int, ET	Yersin et al. (1979)
EuSe	O	Neuenschwander and Wachter (1990)
EuVO ₄	L	Chen et al. (1994d)
Eu ₂ Zn ₃ (NO ₃) ₁₂ ·xH ₂ O	A, CFP	Hellwege and Schröck-Vietor (1955)
EuZrF ₇	L	Lavin et al. (2002b)
GdOBr:Eu ³⁺	L, FIP, CFP	Chi et al. (1997)
GdOCl:Eu ³⁺	L, FIP, CFP	Liu et al. (1998a)
Gd ₂ O ₂ S:Eu ³⁺	L, FIP, CFP	Chi et al. (1998a, 1998b)
LaOBr:Eu ³⁺	L, FIP, CFP	Chi et al. (1990), Wang and Bulou (1995), Shen and Holzapfel (1995a)
LaOCl:Eu ³⁺	L, FIP, CFP, Int	Fonger and Struck (1970), Chi et al. (1986), Wang and Bulou (1993), Shen and Holzapfel (1995a)

continued on next page

Table 1, *continued*

Compound	Studies	Reference
$\text{La}_2\text{O}_2\text{S}:\text{Eu}^{3+}$	L, LT, CFP	Fonger and Struck (1970), Webster and Drickamer (1980a, 1980b), Wang et al. (1992), Gleason et al. (1993)
$\text{Na}_5\text{Eu}(\text{MoO}_4)_4$	L, CFP	Guo et al. (1991)
$\text{Na}_5\text{Eu}(\text{WO}_4)_4$	L, CFP	Guo et al. (1991)
$\text{Na}_2\text{O}\cdot 2\text{SiO}_2:\text{Eu}^{3+}$ (glass)	L, S, LT, CFP, EPC	Lochhead and Bray (1995), Monteil et al. (2000)
$\text{Y}_3\text{Al}_5\text{O}_{12}:\text{Eu}^{3+}$	L	Arashi and Ishigame (1982)
$\text{SrF}_2:\text{Eu}^{3+}$	S	Wright et al. (1995)
$\text{Y}_2\text{O}_3:\text{Eu}^{3+}$	L, LT	Jovanić et al. (1996)
$\text{Y}_2\text{O}_2\text{S}:\text{Eu}^{3+}$	L, Int, FIP, CFP	Fonger and Struck (1970), Webster and Drickamer (1980a), Wang et al. (1984), Liu et al. (1988, 1998b), Nishimura et al. (1991)
$\text{YVO}_4:\text{Eu}^{3+}$	L, LT	Chen et al. (1992a, 1992d)
Gd³⁺		
$\text{CaF}_2:\text{Gd}^{3+}$	A, O, CFP	Wang and Drickamer (1973), Kasatochkin and Yakovlev (1977)
$\text{CdF}_2:\text{Gd}^{3+}$	O, CFP	Rewaj and Krupski (1978)
Chelates: Gd^{3+}	L, Int, ET	Hayes and Drickamer (1982)
$\text{CsCaF}_3:\text{Gd}^{3+}$	O, CFP	Rewaj et al. (1992)
Gd benzoylacetate		Voloshin et al. (1976)
$\text{La}(\text{C}_2\text{H}_5\text{SO}_4)_3\cdot 9\text{H}_2\text{O}:\text{Gd}^{3+}$	O, CFP	Lukin et al. (1981)
$\text{RbCaF}_3:\text{Gd}^{3+}$	O, CFP	Rewaj et al. (1992)
$\text{RbCdF}_3:\text{Gd}^{3+}$	O, CFP	Rewaj et al. (1992)
$\text{TlCdF}_3:\text{Gd}^{3+}$	O, CFP	Rewaj et al. (1992)
Tb³⁺		
$\text{CaF}_2:\text{Tb}^{3+}$	A	Drotning and Drickamer (1973)
Chelates: Tb^{3+}	L, Int, ET	Hayes and Drickamer (1982)
$\text{La}_2\text{O}_2\text{S}:\text{Tb}^{3+}$	L, E, Int, LT	Gleason et al. (1993)
$\text{TbP}_5\text{O}_{14}$	L, LT, CFP, ET	Blanzat et al. (1984), Chi et al. (1988)
Tb^{3+} in solutions	L, Int, LT	Baumann and Bilal (1986)
$\text{Y}_3\text{Al}_5\text{O}_{12}:\text{Tb}^{3+}$	L, CFP	Liu et al. (1986)
Dy²⁺		
$\text{CaF}_2:\text{Dy}^{2+}$	A	Wang and Drickamer (1973)
Ho³⁺		
HoCl_3	A, Int	Keating and Drickamer (1961a)
Er³⁺		
$\text{CaF}_2:\text{Er}^{3+}$	L, CFP, IP, EPC	Kennedy (1980), Kennedy and Campbell (1980)
$\text{ErBa}_2\text{Cu}_3\text{O}_x$	O, CFP	Mesot et al. (1990)
$\text{Er}(\text{C}_2\text{H}_5\text{SO}_4)_3\cdot 9\text{H}_2\text{O}$	A, Int	Keating and Drickamer (1961a)
ErCl_3	A, Int	Keating and Drickamer (1961a)
$\text{GaAs}:\text{Er}^{3+}$	L, Int, ET	Takarabe et al. (1995, 1997), Takarabe (1996), Culp et al. (1997), Hogg et al. (1997a, 1997b)

continued on next page

Table 1, *continued*

Compound	Studies	Reference
GaP:Er ³⁺	L, E, Int, ET	Culp et al. (1996)
LiNbO ₃ :Er ³⁺	S, CFP	Dierolf et al. (2000, 2003)
Si:Er ³⁺	L, Int, ET	Jantsch et al. (1996), Przybylinska et al. (1996)
SrF ₂ :Er ³⁺	L, EPC	Kennedy (1980), Kennedy and Campbell (1980)
Tm²⁺		
CaF ₂ :Tm ²⁺	A	Wang and Drickamer (1973)
SrF ₂ :Tm ²⁺	A	Wang and Drickamer (1973)
TmSe	O	Neuenschwander and Wachter (1990)
TmTe	O	Neuenschwander and Wachter (1990)
Tm³⁺		
Cs ₂ NaTmCl ₆	O, EPC	Mak et al. (2002)
LiTmF ₄	O, EPC	Kupchikov et al. (1982)
TmCl ₃	A, Int	Keating and Drickamer (1961a)
Y ₃ Al ₅ O ₁₂ :Tm ³⁺	L, ET	Wamsley and Bray (1994a, 1994b, 1995), Shen et al. (2000)
Yb³⁺		
InP:Yb ³⁺	L, Int, ET	Stapor et al. (1991), Taguchi et al. (1994), Takarabe et al. (1994), Takarabe (1996)
YbO	A, O	Syassen et al. (1985)
YbS	A, O	Syassen et al. (1985)

levels are shifted to lower energies (a so-called red shift) and on the other hand the $(2J + 1)$ -fold degeneracy is partially or totally lifted. Although the term “crystal” has been used here, these effects are not restricted to crystals only. Any surrounding that breaks the spherical symmetry of the free ion can lead to a shift and splitting of the energy levels. Thus, the following considerations apply also to other materials like glasses or liquids where a long-range order does not exist.

The first step to calculate the energy levels of f-element ions is the calculation of the free-ion energy levels. Within the central field generated by the nucleus and the closed shells, all f-states are still degenerated. However, various interactions occurring in the f-electron system lead to a partial splitting of these states. The most important interaction is the Coulomb interaction, giving rise to terms characterized by the spin quantum number S and the angular momentum quantum number L . A further splitting occurs through the spin-orbit interaction which couples different terms and generates the $^{2S+1}L_J$ multiplets, where J denotes the total angular momentum. Due to the coupling of different terms, the quantum numbers S and L lose their meaning. However, because in most cases a large part of the intermediate coupled wavefunction is determined by one single term, the S - L -classification is usually still preserved. In a phenomenological scheme the various interactions contributing to the Hamiltonian are split into unknown radial parts which are treated as adjustable parameters and the angular parts which can be calculated exactly. The matrix elements of the free-ion Hamil-

tonian H_{FI} can then be written as follows:

$$\begin{aligned} \langle |H_{\text{FI}}| \rangle = & \sum_k F^k f_k + \zeta \left\langle \left| \sum_i s_i l_i \right| \right\rangle + \alpha L(L+1) + \beta G(G_2) + \gamma G(R_7) + \sum_\lambda T^\lambda t_\lambda \\ & + \sum_k P^k p_k + \sum_k M_k m_k. \end{aligned} \quad (1)$$

The radial parts of the Hamiltonian which are treated as free parameters are represented by the Slater parameters F^k ($k = 0, 2, 4, 6$) (Coulomb interaction), the spin-orbit coupling parameter ζ , two-body and three-body configuration interaction parameters α , β , γ and T_λ ($\lambda = 2, 3, 4, 6, 7, 8$), respectively, the spin-spin and spin-other-orbit interactions parameters M_k ($k = 0, 2, 4$), and the electrostatically correlated spin-orbit interaction parameters P^k ($k = 2, 4, 6$). The corresponding expectation values of the angular parts are denoted by f_k , t_λ , p_k , and m_k . l_i and s_i are the spin and orbital angular momentum of the i th electron, and $G(G_2)$ and $G(R_7)$ are the eigenvalues of Casimir's operators for the groups G_2 and R_7 . For a detailed description of the free-ion Hamiltonian see, for example, Wybourne (1965) or Goldschmidt (1978).

In the second step, the crystal-field potential is introduced to the Hamiltonian. The potential in the one-electron approximation can be written as follows:

$$H_{\text{CF}} = \sum_{k,q} B_q^k C_q^{(k)}. \quad (2)$$

The $C_q^{(k)}$ are tensor operators, whose matrix elements again can be calculated exactly, whereas the crystal-field parameters B_q^k are regarded as adjustable parameters. The number of parameters for this potential is greatly reduced by the parity and triangular selection rules and finally by the point symmetry for the f-element ion in the crystal. Detailed information about the crystal-field potential has been given for example by Görrler-Walrand and Binnemans (1996).

Due to the so-called J -mixing within the crystal field, multiplets with different J values are coupled. However, similar to the free-ion case, the levels are still designated by the principal $2S+1L_J$ component of the crystal-field wavefunction. For the further labeling of levels split by the crystal field, either the irreducible representation Γ_i (Bethe, 1929) to which the particular wavefunction belongs or the crystal quantum number μ defined by Hellwege (1949) are most commonly used.

The parametrization of the total Hamiltonian discussed above is utilized in almost all studies on energy levels of f elements in crystals at ambient as well as at high pressure. However, taking into account only the free-ion Hamiltonian from eq. (1), one already would have to determine not less than 20 parameters from the energy levels. Practically, this is not possible for the limited data sets available under pressure. Thus, in almost all cases only the most important Slater and spin-orbit coupling parameters in addition to the crystal-field parameters have been determined. This procedure turned out to give an adequate description of the pressure-induced energy level shifts in most cases. In the following sections the effect of pressure on these parameters is presented. Extensions of the crystal-field model towards relaxing

the one-electron approximation or including configuration interactions will be considered in sects. 4.4.5 and 4.4.6.

Before discussing the changes of free-ion and crystal-field parameters, it should be mentioned that pressure in principle is not the most suitable quantity to characterize the observed changes. Actually, the cause for the increasing interaction strength under pressure is more directly related to the decreasing distances between f-electrons and ligands. Decreasing distances are related to a decreasing volume V which is related to pressure through the isothermal compressibility κ of the material:

$$\kappa = -\frac{1}{V} \left(\frac{\partial V}{\partial P} \right)_T. \quad (3)$$

Applying the same pressure to different materials results in different changes of the volume and distances. The larger κ , the larger will be the reduction of volume and thus the effect of pressure. Therefore, if a comparison of different materials is made, it is not appropriate to compare the pressure shifts, but one should compare them for the same changes of interatomic distances.

4.2. Line shifts

In almost all cases, the absorption and luminescence lines of f elements shift to lower energies under pressure (one of the very few exceptions is presented in sect. 4.5 and fig. 10). This general trend is caused by an overall contraction of the f configuration and thus by a reduction in the energy difference between ground and excited state multiplets. This effect is related to decreasing Coulomb and spin-orbit interactions under pressure which will be discussed quantitatively in the next sections. Superimposed on the reduction in multiplet splittings is a change in their individual splittings. Usually, these crystal-field splittings increase under pressure, however, in many cases also decreasing splittings have been observed.

An example of observed line shifts for $\text{LaCl}_3:\text{Pr}^{3+}$ is given in fig. 3. In this case excitation spectra have been recorded up to around 8 GPa at 20 K (Tröster, 1994). The dominant red shift of the $^3\text{H}_4 \rightarrow ^1\text{D}_2$ transition lines and a slighter change in the respective splittings is clearly visible. The assignment of the various lines can be gathered from the energy level scheme schematically depicted on the right side of fig. 3. The changes in the splittings are the reason for different shifts of transitions between the same two multiplets.

From the line shifts, the corresponding variations of the energy levels can be derived. Thereby, the shift of the center of gravity (CG) of the $^1\text{D}_2$ multiplet with respect to the ground state $^3\text{H}_4(2)$ and the changes of the $^1\text{D}_2$ crystal-field splittings with respect to the CG can be treated separately. The variations of the crystal-field splittings of $^1\text{D}_2$ with respect to the CG are shown in fig. 4. The CG shift of $^1\text{D}_2$ can be described by the polynomial function $E_{\text{CG}} = a_0 + a_1 p + a_2 p^2$ with $a_0 = 16730.4 \text{ cm}^{-1}$, $a_1 = -17.18 \text{ cm}^{-1}/\text{GPa}$, and $a_2 = 0.246 \text{ cm}^{-1}/\text{GPa}^2$. The total shift up to 8 GPa thus amounts to -122 cm^{-1} .

Typical values for the observed red shifts of f-element transitions range between a few $\text{cm}^{-1}/\text{GPa}$ and some tenth of $\text{cm}^{-1}/\text{GPa}$. The particular value strongly depends on the energy of the luminescent multiplet and the f element under consideration. Some characteristic

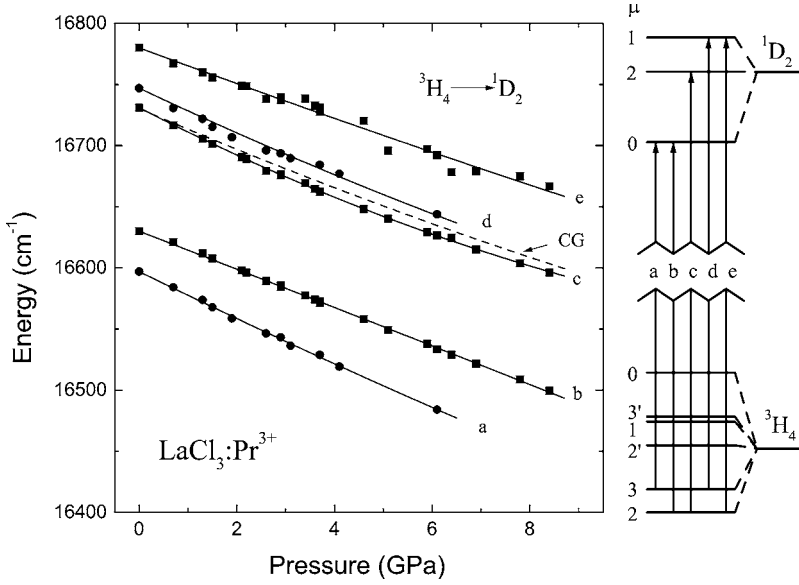


Fig. 3. Shift of the excitation line peaks of $\text{LaCl}_3:\text{Pr}^{3+}$ under pressure at 20 K. The assignment of the lines can be gathered from the level diagram on the right side. CG denotes the center of gravity of the 1D_2 multiplet.

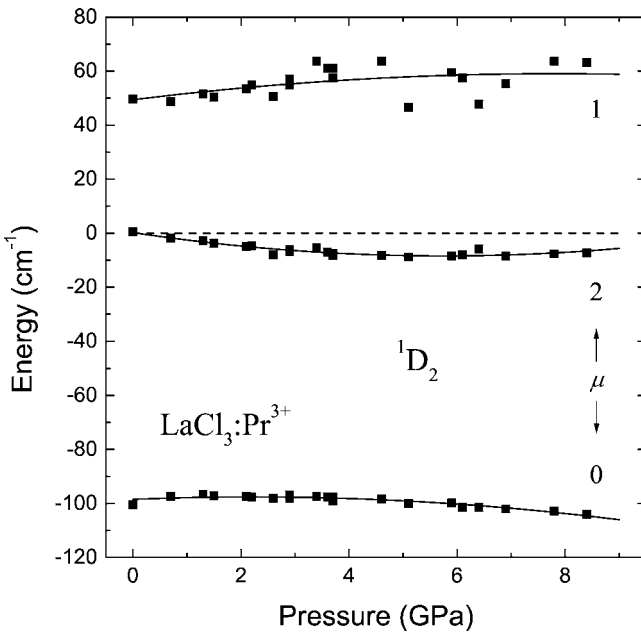


Fig. 4. Crystal-field split levels of the 1D_2 multiplet of $\text{LaCl}_3:\text{Pr}^{3+}$ under pressure, drawn with respect to the center of gravity fixed to zero (dashed line).

Table 2

Selected average values for line shifts of different f elements under pressure. In all cases only the average linear coefficient is given, slight deviations are neglected

Ion	Host	Transition	ν_0 (cm ⁻¹)	$d\nu/dp$ (cm ⁻¹ /GPa)	Pressure range (GPa)	Reference
Pr ³⁺	LaCl ₃	³ P ₀ → ³ H ₄	20473.0	-22.9	0-8	1
	LaOCl	³ P ₀ → ³ H ₄	20267.8	-20.5	0-21	2
Nd ³⁺	LaCl ₃	² D _{3/2} → ⁴ I _{9/2}	21161.9	-11.2	0-8	3
Sm ²⁺	SrB ₄ O ₇	⁵ D ₀ → ⁷ F ₀	14589.8	-5.4	0-20	4
	SrFCl	⁵ D ₀ → ⁷ F ₀	14486	-22.4	0-20	5
Sm ³⁺	Y ₃ Al ₅ O ₁₂	Y ₁	16189.1	-8.0	0-20	6
Eu ³⁺	EuPO ₄	⁵ D ₀ → ⁷ F ₀	17274.0	-2.1	0-6	7
	Y ₃ Al ₅ O ₁₂	⁵ D ₀ → ⁷ F ₁	16932	-5.7	0-7	8
Er ³⁺	LiNbO ₃	⁴ F _{9/2} → ⁴ I _{15/2}	15143.7	-2.8	0-10	9
Tb ³⁺	Y ₃ Al ₅ O ₁₂	⁵ D ₄ → ⁷ F ₆	20146	-3.5	0-8	10
U ³⁺	LaCl ₃	² D _{3/2} ← ⁴ I _{9/2}	15822.6	-65.3	0-8	3

References

- Gregorian et al. (1989)
- Bungenstock et al. (1998)
- Tröster (1994)
- Lacam and Chateau (1989)
- Shen et al. (1991)
- Bi et al. (1990)
- Chen et al. (1997)
- Arashi and Ishigame (1982)
- Dierolf et al. (2003)
- Liu et al. (1986)

average values are summarized in table 2. The specific case of the actinide ion U³⁺ doped into LaCl₃ has been included in table 2 to demonstrate the much larger shifts observable for this 5f element. This difference simply corresponds to the more extended 5f wavefunction with respect to the 4f wavefunctions of the lanthanides.

4.3. Nephelauxetic effect

In sects. 4.1 and 4.2 the red shift of the free-ion levels due to either the incorporation of the f element into the crystal or due to the application of high pressure has been discussed. This effect is called nephelauxetic effect (Jørgensen and Reisfeld, 1977) and can be accounted for by a reduction of the free-ion parameters. Effectively, the transition from the free ion to the ion in the crystal can be thought of as increasing the spherically symmetric part of the crystal field from zero to one. In high-pressure experiments, the interaction between the f-electrons and their environment and thus the spherically symmetric part of the crystal fields is increased further, which thus should cause a continued decrease of the free-ion parameters. Actually, this is what has been observed in all high-pressure experiments performed till now. Following these considerations, the high-pressure induced decrease of free-ion parameters is the same as the nephelauxetic effect and can thus be used to learn more about the nature of this effect.

The reduction of the free-ion parameters has been ascribed to different mechanisms, where in general two types of models can be distinguished. On the one hand, one has the most often used wavefunction renormalisation or covalency models, which consider an expansion of the open-shell orbitals in the crystal (Jørgensen and Reisfeld, 1977). This expansion follows either from a covalent admixture with ligand orbitals (symmetry-restricted covalency mechanism) or from a modification of the effective nuclear charge Z^* , due to the penetration of the ligand electron clouds into the metal ion (central-field covalency mechanism).

The symmetry-restricted covalency model (SRCM) leads to:

$$\Delta F^k \propto N^4 \quad \text{and} \quad \Delta \zeta \propto N^2, \quad (4)$$

where N is a renormalisation coefficient, expressible as a sum including overlap integrals and covalency parameters (Newman et al., 1984). The central-field covalency model (CFCM) predicts (Goldschmidt, 1978):

$$\Delta F^k \propto Z^* \quad \text{and} \quad \Delta \zeta \propto Z^{*3}. \quad (5)$$

On the other hand, electrostatic models regard the ligands or the whole crystal as polarizable units and thereby lead to weaker Coulomb and spin-orbit interactions. In a dielectric screening model (DSM) from Morrison et al. (1967) the f element is placed within an empty sphere with radius R_S which is embedded into an infinite medium with dielectric constant ε . This leads to a reduction ΔF^k of the Slater parameters (Newman, 1973):

$$\Delta F^k = \frac{(\varepsilon - 1)(r^k)^2}{\left(\frac{k}{k+1} + \varepsilon\right)R_S^{2k+1}}. \quad (6)$$

In most high-pressure experiments, only the covalency models have been taken into account. The likely reason for this is the arbitrary nature of the sphere radius R_S used in the electrostatic model.

One of the first studies on the changes of free-ion parameters under pressure has been performed by Huber et al. (1977). They investigated the luminescence of $\text{EuP}_5\text{O}_{14}$ up to 40 GPa at room temperature. From the energy level variations the change of the Slater parameter F_2 and the spin-orbit coupling parameter ζ was determined, whereby the analysis was restricted to pressures below 10 GPa due to uniaxial stresses at higher pressures. According to their results, both free-ion parameters decreased under pressure, though the Slater parameter F_2 showed a much weaker change than the spin-orbit coupling parameter ζ . This result supports the CFC model for the nephelauxetic effect. However, the quantitative results should be taken with some precaution because the theoretical analysis neglected contributions as for example intermediate coupling effects or J -mixing.

A further system which has been studied under high pressure is $R_2\text{O}_2\text{S}$ ($R = \text{Y, La, Gd}$) doped with Eu^{3+} . Wang et al. (1992) have measured the luminescence spectra of $\text{La}_2\text{O}_2\text{S}:\text{Eu}^{3+}$ under pressures up to 13 GPa at room temperature. In the analysis of the observed energy level shifts, Wang et al. (1992) used the intermediate coupling wavefunctions and partly included J -mixing effects. The relative shifts of the Slater parameters F_k ($k = 2, 4, 6$) and the spin-orbit coupling parameter ζ up to 13 GPa were about -0.38% and -0.20% , respectively. Thus, the shift for the F_k parameters was twice as large as for ζ , which supports the SRC model, in contrast to the results for $\text{EuP}_5\text{O}_{14}$.

Nearly identical results were obtained also for $\text{Y}_2\text{O}_2\text{S}:\text{Eu}^{3+}$ (Liu et al., 1998a) and $\text{Gd}_2\text{O}_2\text{S}:\text{Eu}^{3+}$ (Chi et al., 1998a, 1998b). In both cases the reduction of the free-ion parameters was about -0.40% for F_2 and -0.20% for ζ up to pressures of 13 GPa and 14.8 GPa, respectively. Considering the two different covalency models, the authors concluded that the SRC model describes the nephelauxetic effect more reasonably than the CFC model.

The rare-earth trichlorides belong to the best studied systems at ambient as well as at high pressure. Voloshin et al. (1975) studied the effect of pressure on the free-ion parameters of $\text{NdCl}_3 \cdot 6\text{H}_2\text{O}$ up to 2.3 GPa. They found reductions of -0.26% , -0.29% , -0.12% , and -0.25% for F_2 , F_4 , F_6 , and ζ , respectively. Such variations can be explained neither by the CFC nor by the SRC model alone.

In a study on $\text{LaCl}_3:\text{Pr}^{3+}$ the corresponding changes up to 8 GPa were -1.2% , -0.6% , -0.7% , and -0.3% (Gregorian et al., 1986, 1989). It was pointed out that these changes could be described by the SRC but certainly not by the CFC model. However, Gregorian et al. (1989) discussed several weak points of the SRC model, which could not describe other experimental observations. One problem for example is, that the “nephelauxetic ratio” $\beta = (F_k)_{\text{complex}}/(F_k)_{\text{free}}$ from which the so-called “covalency factors” are determined, is defined to be independent of k , in contrast to the experimentally observed distinct differences in the relative decreases of F_2 , F_4 , and F_6 parameters. Furthermore, ab initio calculations for Pr^{3+} in PrCl_3 predicted that these covalency contributions are an order of magnitude too small to account for the reduction (Newman, 1973). In view of these problems, Gregorian et al. (1989) also considered the DS model. They assumed a proportionality between the spherical cavity radius R_S and the mean $\text{Pr}^{3+}-\text{Cl}^-$ distance under pressure and found that up to about 70% of the change of the F_k could be accounted for by the 3% variation of this radius in the pressure range up to 8 GPa.

Further high pressure studies concerning this problem have been performed on the compounds NdCl_3 , $\text{LaCl}_3:\text{Nd}^{3+}$, PrCl_3 , $\text{LaCl}_3:\text{Pr}^{3+}$ (Tröster et al., 1993), and $\text{LaCl}_3:\text{U}^{3+}$ (Tröster et al., 1995). The results for the changes in the free-ion parameters for these materials are summarized in table 3.

The results for the pure material PrCl_3 have larger uncertainties because of a very small data set available under pressure (Tröster et al., 1993). The actinide ion U^{3+} provides an interesting possibility to compare 5f with 4f elements and thus has been included in table 3. The essential quantitative differences to the lanthanide ion Nd^{3+} are due to the more extended 5f-wavefunctions and result mainly in smaller Coulomb interactions, a larger spin-orbit coupling and larger crystal-field splittings. Corresponding to the more extended wavefunction, a larger shift of the energy levels is observed for U^{3+} , as mentioned already in the beginning of sect. 4.2.

According to table 3 some trends which are valid for all these systems can be noted:

- (1) the shifts of the Slater parameters are larger or comparable to the shift of the spin-orbit coupling parameter,

Table 3

Relative changes $\Delta P/P$ of free-ion parameters (in %) for Nd^{3+} , Pr^{3+} (Tröster et al., 1993) and U^{3+} (Tröster et al., 1995) in different hosts up to a pressure of 8 GPa

Parameter	$\text{LaCl}_3:\text{Nd}^{3+}$	NdCl_3	$\text{LaCl}_3:\text{Pr}^{3+}$	PrCl_3	$\text{LaCl}_3:\text{U}^{3+}$
$\Delta F^2/F^2$	-0.7(1)	-0.7(1)	-1.1(1)	-2.0(4)	-6.6(8)
$\Delta F^4/F^4$	-0.3(2)	-0.4(2)	-0.8(2)	-0.2(15)	-5.3(14)
$\Delta F^6/F^6$	-0.4(1)	-0.3(1)	-0.9(2)	-3.9(17)	-3.2(19)
$\Delta\zeta/\zeta$	-0.4(1)	-0.3(1)	-0.4(1)	-0.5(1)	-1.0(7)

Table 4

Experimental results for the Slater parameter reductions of Nd^{3+} , Pr^{3+} , and U^{3+} (Tröster et al., 1995) in LaCl_3 under pressure up to 8 GPa in comparison with results from the dielectric screening model. All values in cm^{-1}

Parameter	Nd^{3+}		Pr^{3+}		U^{3+}	
	Expt.	Calc.	Expt.	Calc.	Expt.	Calc.
ΔF^2	-477	-298	-683	-323	-2622	-659
ΔF^4	-204	-109	-398	-129	-1766	-435
ΔF^6	-155	-150	-198	-195	-737	-750

- (2) distinct differences in the shifts of the Slater parameters with different k are present, and
 (3) the total shift increases according to the order $\text{Nd}^{3+} < \text{Pr}^{3+} \ll \text{U}^{3+}$.

The last point is not very surprising because it proves that pressure effects are stronger the more extended the wavefunction is. Thus, the order $\text{Nd}^{3+} < \text{Pr}^{3+} < \text{U}^{3+}$ simply reflects an increasing extension of the f-wavefunction. Point (1) can be explained if the SRC model is valid in these cases, because it predicts a stronger variation of the F_k compared to ζ . However, following the discussion by Gregorian et al. (1989), the SRC model has some drawbacks, for example it cannot explain the different shifts for different k parameters as noted in point (2).

Tröster et al. (1995) also considered the DS model, whereby the radius R_S was assumed to be proportional to a mean metal ion – chloride ion distance R_M . As ambient pressure values they used ratios R_S/R_M of 0.417 for Nd^{3+} , 0.424 for Pr^{3+} , and 0.500 for U^{3+} . With these values the absolute changes of the Slater parameters have been calculated up to 8 GPa as shown in table 4.

It must be emphasized that both the absolute values for the ΔF^k and the ratios $\Delta F^{k'}/\Delta F^k$ depend strongly on the choice of R_S at ambient pressure. Nevertheless, it can be seen from table 4 that this simple model can partly produce shifts that are in the correct order of magnitude. However, these calculations can not be regarded as a definite prove for the relevance of the DS model since in fact a “true” value for R_S could be completely different to the value used here, which then may result in even negligible shifts. Furthermore, the relatively large discrepancies for U^{3+} , where covalency effects can be expected to be especially important, indicate that precisely these cannot be disregarded.

Similar to the rare-earth trichlorides, also different ternary MYX compounds have been studied thoroughly under high pressure. The results for the pressure-induced changes of the Slater parameter F^2 and the spin–orbit coupling parameter ζ of these and other compounds are presented in table 5. Due to the difficulties with the DS model, the evaluation of the parameter shifts has been performed only in terms of the two covalency models. Assuming small changes for the free-ion parameters, the relative changes were approximated by:

$$\frac{\Delta F^k}{F^k} = 4 \frac{\Delta N}{N} + \frac{\Delta Z^*}{Z^*} \quad \text{and} \quad \frac{\Delta \zeta}{\zeta} = 2 \frac{\Delta N}{N} + 3 \frac{\Delta Z^*}{Z^*}. \quad (7)$$

The first parts are derived from the SRC model, the second parts from the CFC model. A useful quantity to distinguish both models is the covalency ratio CR (Bungenstock et al., 2000b):

$$CR = \frac{\Delta F^k}{F^k} \bigg/ \frac{\Delta \zeta}{\zeta}. \quad (8)$$

Table 5

Relative decrease of the free-ion parameters F_2 and ζ , the renormalisation factor N and the effective nuclear charge Z^* for Pr^{3+} , Nd^{3+} , Eu^{3+} , Sm^{2+} , and U^{3+} in different host lattices under pressures up to 8 GPa. The covalency ratio CR is a measure of the relative importance of the CFC or SRC models (see text). Rows 0–5 GPa, 5–10 GPa, and 10–15 GPa give the CR value of $\text{LaOCl}:\text{Pr}^{3+}$ for different pressure regions

Ion	Compound	$\Delta F^2/F^2$ (%)	$\Delta\zeta/\zeta$ (%)	CR	$\Delta N/N$ (%)	$\Delta Z^*/Z^*$ (%)	Ref.
Eu^{3+}	LaOX ($X = \text{Cl}, \text{Br}$)	-0.31	-0.62	0.49	-0.03	-0.19	Shen and Holzapfel (1995a)
	LaOCl	-0.78	-0.73	1.07	-0.16	-0.14	Wang and Bulou (1995)
	LaOBr	-0.96	-0.84	1.14	-0.20	-0.14	Wang and Bulou (1995)
	GdOCl	-0.30	-0.38	0.79	-0.05	-0.09	Liu et al. (1998a)
	GdOBr	-0.26	-0.45	0.56	-0.03	-0.13	Chi et al. (1997)
	$\text{Gd}_2\text{O}_2\text{S}$	-0.26	-0.18	1.44	-0.06	-0.02	Chi et al. (1998a)
Nd^{3+}	LaCl_3	-0.70	-0.40	1.75	-0.17	-0.02	Tröster et al. (1993)
	NdCl_3	-0.70	-0.30	2.33	-0.18	0.02	Tröster et al. (1993)
Pr^{3+}	LaOCl	-0.77	-0.60	1.28	-0.17	-0.09	Bungenstock et al. (1998)
	0–5 GPa			1.22			
	5–10 GPa			1.48			
	10–15 GPa			1.99			
	PrOCl	-0.90	-0.52	1.74	-0.21	-0.03	Bungenstock et al. (2000b)
	GdOCl	-0.91	-0.46	1.95	-0.23	-0.01	Bungenstock et al. (2000a)
	LaCl_3	-1.00	-0.50	2.00	-0.25	0.00	Tröster et al. (1993)
Sm^{2+}	MFCl ($M = \text{Ba}, \text{Sr}, \text{Ca}$)	-1.17	-0.39	3.00	-0.31	0.08	Shen and Holzapfel (1995a)
U^{3+}	LaCl_3	-6.60	-1.00	6.60	-1.88	0.92	Tröster et al. (1995)

If only the CFC model is responsible for the decrease of the free-ion parameters, CR should be equal to 0.33, if only the SRC model is important, CR should be equal to 2. An intermediate value between 0.33 and 2 would indicate that both types of contributions are essential.

According to table 5, in all cases except for some Eu^{3+} compounds, the decrease for F^2 is larger than for ζ . Thus, the SRC model plays the dominant role. In the case of some Eu^{3+} compounds on the contrary, the spin-orbit coupling parameter decrease more strongly than the Slater parameter, which leads to the conclusion that the CFC model is dominating here.

The Eu^{3+} ion is, compared with Pr^{3+} , Nd^{3+} , Sm^{2+} , and U^{3+} , the ion with the least expanded 4f wavefunction. Therefore, one can conclude that the SRC model becomes increasingly more important when the wavefunction is expanded. This view is supported very strikingly by the data for U^{3+} , whose 5f wavefunction is much more expanded than the 4f wavefunctions of the other ions in table 5. For U^{3+} , the decrease of F^2 with respect to ζ is very large indicating that the classical CFC model does not play any significant role anymore.

These observations fit also to the behavior in different pressure regions, as indicated in table 5 for the three regions 0–5 GPa, 5–10 GPa, and 10–15 GPa for $\text{LaOCl}:\text{Pr}^{3+}$. The increasing influence of the SRC model with increasing pressure is a consequence of the progressive expansion of the wavefunctions. The different values for the same ion in different host crystals also confirm this general trend. For example, the sequence $\text{LaOCl}:\text{Pr}^{3+}$, $\text{PrOCl}:\text{Pr}^{3+}$, and $\text{GdOCl}:\text{Pr}^{3+}$ of isostructural hosts corresponds to decreasing local distances around the Pr^{3+}

ion and thus to an increasing internal pressure. The wave functions of the f-electrons are thus expanding throughout this sequence, as shown by a decrease in the free-ion parameters at ambient pressure (Bungenstock et al., 2000b). Accordingly, the value CR increases from LaOCl:Pr^{3+} to PrOCl:Pr^{3+} and to GdOCl:Pr^{3+} and the same trend is observed also under pressure.

An open question concerns some positive values for $\Delta Z^*/Z^*$ listed in table 5. Positive values for this quantity are related to a value larger than two for CR . A value larger than two means, that even the SRC model cannot account for the much stronger changes in the Slater parameters with respect to the spin-orbit coupling parameter. These unusually strong changes can be described in the combined model only if the effective nuclear charge increases.

It is not clear whether an increase in the effective nuclear charge is reasonable. In principle, such an increase could be explained by an increased covalency between the inner shell electrons and the ligands, leading to a charge transfer from inner shells to the ligands and thus to an increase of the effective nuclear charge Z^* for the f-electrons. This effect could be called “anti-screening”.

On the other hand, if the effective nuclear charge does not change at all at high pressures, it would mean that the SRC model cannot describe the situation at strong compression or for strongly expanded wave functions.

Some exceptions from the general trends have to be commented on. First, the results from Wang and Bulou (1995) are quite different to the results from Shen and Holzapfel (1995a) for LaOX:Eu^{3+} ($X = \text{Cl, Br}$). Although the value for CR found by Wang and Bulou (1995) is still lower than for all the other ions, it is distinctly larger than the value found by Shen and Holzapfel (1995a). One possible explanation is the fact that Wang and Bulou (1995) did not assume fixed ratios for F_4/F_2 and F_6/F_2 but allowed the parameters to vary independently. However, because only two different terms, namely ${}^5\text{D}$ and ${}^7\text{F}$ have been observed under pressure, a large uncertainty is imposed on the parameters F_4 and F_6 , which was emphasized also by the authors. Thus, in principle only one Slater parameter can be determined. The pressure-induced variations of F_4 and F_6 found by Wang and Bulou (1995) are much smaller than the variation of F_2 . This means, that a fixed ratio would lead to a smaller variation of F_2 which in turn would bring the CR values closer to the values from Shen and Holzapfel (1995a).

Large values for CR are also found in the case of $\text{Gd}_2\text{O}_2\text{S:Eu}^{3+}$ (Chi et al., 1998a). However, in this case the spin-orbit coupling parameter shows a strong nonlinear behavior with a steep drop in the beginning and a nearly constant value at higher pressures. The reason for this peculiar behavior was not addressed but should give rise to some care when using these values.

An interesting improvement of the SRC model has been discussed by Wang and Bulou (1995). They considered simplified expansion factors used in the Hartree-Fock radial wavefunctions for the f-electrons. With these factors it was possible to introduce a k dependence for the pressure-induced change of different Slater parameters. This procedure would remove the weak point of the model which could not account for the observed k -dependence of the parameters under pressure.

In summary, the analysis of the free-ion parameters of different materials under pressure have led to a coherent picture. The nephelauxetic effect can be described by a combination of the CFC and SRC models and depends on the expansion of the f-electron wavefunctions. Only at very high pressures or in the case of strongly expanded wavefunctions the SRC and CFC models could not provide a completely adequate description of the observed variations.

4.4. *Crystal-field splittings*

By far most work on the optical properties of the f shells under pressure concentrated on the mechanisms that cause the crystal-field splittings of the free-ion levels. Whereas in the case of the nephelauxetic effect pressure always reduces the free-ion parameters and thus generates a red shift of the multiplets, it is not straightforward to explain how the crystal field and thus the splittings change with increasing pressure. In principle, pressure moves the ions in the lattice closer to each other, which increases the interactions between the f-electrons and their ligands. Correspondingly, an increase of the crystal-field splitting can be expected. In actual high-pressure experiments, however, it was also observed that the crystal-field splittings decreased with increasing pressure (see, for example, Bungenstock et al. (1998)).

At first glance such a result seems peculiar, but a closer look to the crystal-field parameters introduced in sect. 4.1 reveals that not only the interaction strength of f-electrons and ligands but also structural information is contained therein. Actually, it is a change in the structural parameters which can be responsible for an overall decreasing crystal-field strength, although the pure interactions between f-electrons and ligands monotonically increase with decreasing ion separations. In the following section the changes of the crystal-field parameters and the crystal-field strength under pressure is presented for various compounds. To extract the physical origin of the crystal fields, the subsequent sections will discuss the problem of local distortions, extract the structural information from the parameters by using the superposition model and finally relate the intrinsic parameters of this model to ab initio calculations. A last part will be devoted to the special case of glasses, where a strong inhomogenous broadening makes the evaluation of the data much more difficult.

4.4.1. *Crystal-field parameters*

Crystal-field parameters have been determined under pressure in a large amount of f-element compounds. Besides the optical methods, which have been employed in most cases, some work has been done using neutron scattering or magnetic resonance methods. These methods do not allow for the determination of more than the ground states, however, they can be used also in cases of non-transparent materials. For example, neutron scattering was used under pressure to study the high- T_C compounds $\text{ErBa}_2\text{Cu}_3\text{O}_x$. In these materials charge redistributions in the CuO_2 planes led to distinct changes of the 2nd order crystal-field parameter under pressure (Mesot et al., 1990). A further example is a high-pressure study on PrSb , where it was demonstrated that a simple point charge model approach to the crystal-field parameters appeared to break down (Vettier et al., 1977).

Magnetic resonance studies have been performed in a number of different materials. In most cases the pressure dependence of the spin-Hamiltonian crystal-field parameters have

been determined, as for example for Gd^{3+} in fluoroperovskite crystals (Rewaj et al., 1992), Gd^{3+} and Eu^{2+} in CdF_2 (Rewaj and Krupski, 1978, 1980), and Eu^{2+} in CaF_2 (Radliński and Silversmith, 1986). This method was also employed in the case of some ethylsulfate (ES) compounds, in particular for lanthanum ES doped with Gd^{3+} (Lukin et al., 1981), yttrium and europium ES doped with Ce^{3+} (Krygin et al., 1983), and yttrium and lanthanum ES doped with Nd^{3+} (Krygin et al., 1986).

A much more detailed picture about the crystal-field splittings and in turn about crystal-field parameters is provided by optical means. In some cases much more than a hundred spectral lines can be observed and assigned at ambient pressure. The situation is usually worse in high-pressure experiments because very small dimensions of the samples prevent the detection of weaker lines. In addition, pressure-induced broadening can lead to a strong overlapping and consequently to difficulties to resolve the lines. Nevertheless, in general the number of transitions and energy levels determined under pressure still exceed the number of crystal-field parameters by far. Thus, in many studies the pressure dependence of the crystal-field parameters was readily determined.

In the previous section it was shown that the changes of the free-ion parameters within a common pressure range between atmospheric pressure and 10 GPa do not exceed a few percent. On the contrary, the changes of the crystal-field parameters often are one or even two orders of magnitude larger within the same pressure range. For example, Chi et al. (1988) studied TbP_5O_{14} up to a pressure of 8 GPa. The site symmetry of the Tb^{3+} ion is C_{4v} , thus 5 crystal-field parameters B_0^2 , B_0^4 , B_4^4 , B_0^6 , and B_4^6 were considered. Their respective changes of the absolute values under pressure up to 8 GPa were 38%, 30%, 19%, 22%, and 89%. These changes demonstrate the strong effect of pressure in general and also the distinct differences for individual parameters.

A well-known and thoroughly studied system at ambient as well as at high pressure is $LaCl_3$ doped with various rare-earth ions. Anhydrous $LaCl_3$, as well as other lanthanide trichlorides, crystallizes in the hexagonal UCl_3 type structure. The lanthanum ion is coordinated by 9 chloride ions arranged on a tricapped trigonal prism as illustrated in fig. 5. The capping anions are referred to as equatorial, whereby an angle δ denotes the angular deviation of the equatorial ions from the normal to the prism faces. If δ is not equal to zero, the site symmetry of the lanthanide ion is C_{3h} . However, in the case of $LaCl_3$ δ is very small, therefore, an effective site symmetry D_{3h} is commonly used. According to D_{3h} symmetry, the crystal-field potential can be written as:

$$H_{CF} = B_0^2 C_0^{(2)} + B_0^4 C_0^{(4)} + B_0^6 C_0^{(6)} + B_6^6 (C_6^{(6)} + C_{-6}^{(6)}). \quad (9)$$

The pressure-induced variations of these crystal-field parameters for $LaCl_3:Pr^{3+}$ (Gregorian et al., 1989; Tröster et al., 1993) are represented in fig. 6 by the solid lines. The dashed lines show the effects due to configuration interaction. These effects will be discussed later in sect. 4.4.6. Further high-pressure studies on $LaCl_3:Nd^{3+}$ (Tröster et al., 1990, 1993) and $LaCl_3:U^{3+}$ (Tröster et al., 1995) were aimed at testing the transferability of crystal-field parameter shifts for different f elements. In this series, the relatively simple $4f^2$ configuration of Pr^{3+} is compared with the more complicated $4f^3$ configuration of Nd^{3+} and the formally equivalent $5f^3$ configuration of the actinide ion U^{3+} . Indeed the high pressure investigations for Nd^{3+} and

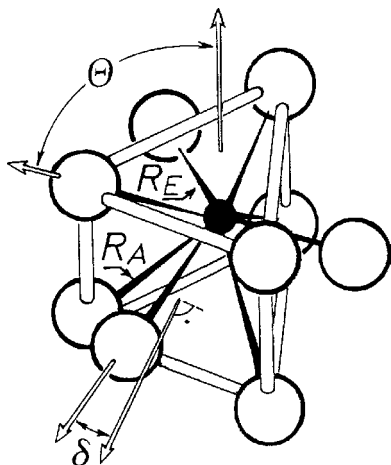


Fig. 5. Coordination polyhedron of the Cl ligands around La in LaCl_3 . R_E and R_A denote the equatorial and apical La-Cl bond distances. The angle θ denotes the polar angle of the apical anions and δ the deviation from the normal to the prism faces of the equatorial anions (from Gregorian et al. (1989)).

U^{3+} in LaCl_3 resulted in very similar shifts as those depicted in fig. 6. In all cases the absolute values of B_0^6 and B_6^6 increased. Furthermore, the parameter B_0^4 is the least affected parameter with a slight decrease in all cases. Distinct differences exist only for the parameter B_0^2 , which shows a minimum for the lanthanides, but a simple increase for the actinide ion.

Comparing only the two lanthanides, a very similar behavior under pressure could be established. In the case of U^{3+} at least the qualitative behavior, except for B_0^2 , also matched that of the lanthanides. Quantitatively, the absolute shifts for the actinide ion were larger, a result that could be expected from the much more expanded wavefunctions of the 5f shell. It should be noted, however, that the relative changes were also very similar compared to the lanthanides.

Further interesting and intensively studied systems are provided by MYX compounds. In particular, the crystal-field parameters have been determined for $\text{ROY}:\text{Eu}^{3+}$ ($R = \text{La, Gd}$; $Y = \text{Br, Cl}$), $\text{ROCl}:\text{Pr}^{3+}$ ($R = \text{La, Pr, Gd}$) and $\text{MFCl}:\text{Sm}^{2+}$ ($M = \text{Ba, Ca, Sr}$). For the corresponding references see table 1. As an example for these compounds, fig. 7 shows the crystal-field parameter shifts up to 16 GPa for $\text{ROCl}:\text{Pr}^{3+}$ ($R = \text{La, Pr, Gd}$) obtained by Bungenstock et al. (2000b). The Pr^{3+} ion in ROCl is surrounded by four O^{2-} and five Cl^- ions. According to the site symmetry C_{4v} five crystal-field parameters must be taken into account:

$$H_{\text{CF}} = B_0^2 C_0^{(2)} + B_0^4 C_0^{(4)} + B_4^4 (C_4^{(4)} + C_{-4}^{(4)}) + B_0^6 C_0^{(6)} + B_4^6 (C_4^{(6)} + C_{-4}^{(6)}). \quad (10)$$

The qualitative as well as quantitative changes of the parameters shown in fig. 7 are very similar in the three cases. Striking is the apparent continuation of the parameter shifts found for $\text{LaOCl}:\text{Pr}^{3+}$ in PrOCl or $\text{GdOCl}:\text{Pr}^{3+}$. This behavior can be related to the fact that the doped Pr^{3+} ion is smaller than the replaced La ion in LaOCl . This causes a “negative” internal pressure compared to the pure substance PrOCl . Similarly, in GdOCl the Pr^{3+} ion is larger than Gd^{3+} , resulting in a “positive” internal pressure compared to PrOCl . The application of external pressure to $\text{LaOCl}:\text{Pr}^{3+}$ then subsequently creates a structural environment similar to the ambient pressure environments of PrOCl and $\text{GdOCl}:\text{Pr}^{3+}$.

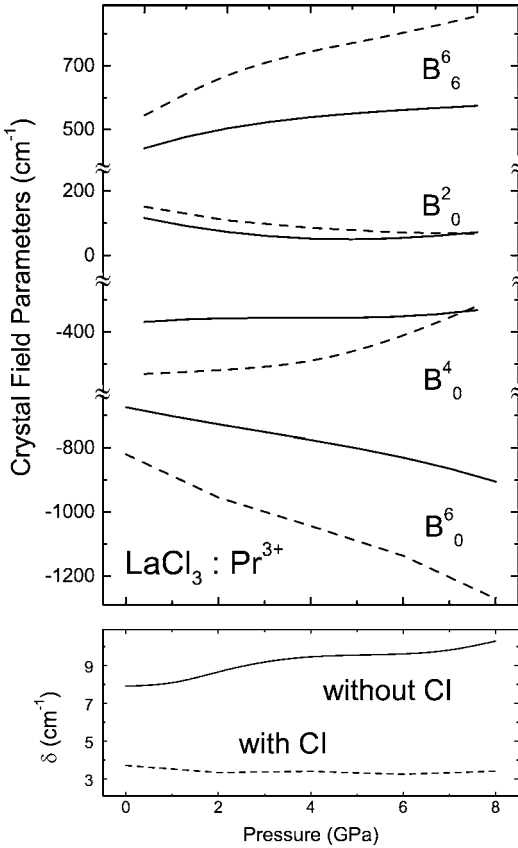


Fig. 6. Variation of the crystal-field parameters of $\text{LaCl}_3:\text{Pr}^{3+}$ under pressure. Solid lines correspond to the conventional one-electron crystal field, utilizing only the $4f^2$ wavefunctions as the basis set. δ denotes the mean deviation as defined in the text. Dashed lines represent the results derived from the inclusion of the $4f^15d^1$ configuration interactions.

Although it is not possible to directly compare the individual crystal-field parameters obtained for different hosts, it is possible to define an overall scalar crystal-field strength S which is independent of the specific crystal structure. The strength parameter S can be calculated according to (Chang et al., 1982):

$$S = \left\{ \frac{1}{3} \sum_k \frac{1}{2k+1} \left[B_{k0}^2 + 2 \sum_{q>0} (\Re B_{kq}^2 + \Im B_{kq}^2) \right] \right\}^{1/2}. \tag{11}$$

In a good approximation the maximum splitting of distinct $^{2S+1}L_J$ multiplets depends linearly on the crystal-field strength. Due to enhanced interactions between f-electrons and ligands, S is expected to increase under pressure, a behavior, which indeed was found for many materials. Wang et al. (1992) have studied the crystal-field strength for Eu^{3+} in $\text{La}_2\text{O}_2\text{S}$ and found an increase from 314 cm^{-1} to 363 cm^{-1} up to 13 GPa. Similarly, for $\text{Y}_2\text{O}_2\text{S}:\text{Eu}^{3+}$ an increase from 364 cm^{-1} to 395 cm^{-1} up to 10 GPa was noticed. In the case of $\text{YAG}:\text{Tb}^{3+}$ S changed from 711 cm^{-1} at ambient pressure to 768 cm^{-1} at 8.2 GPa. A much stronger variation of the crystal-field strength from 269 cm^{-1} at ambient pressure to 380 cm^{-1} at 5 GPa

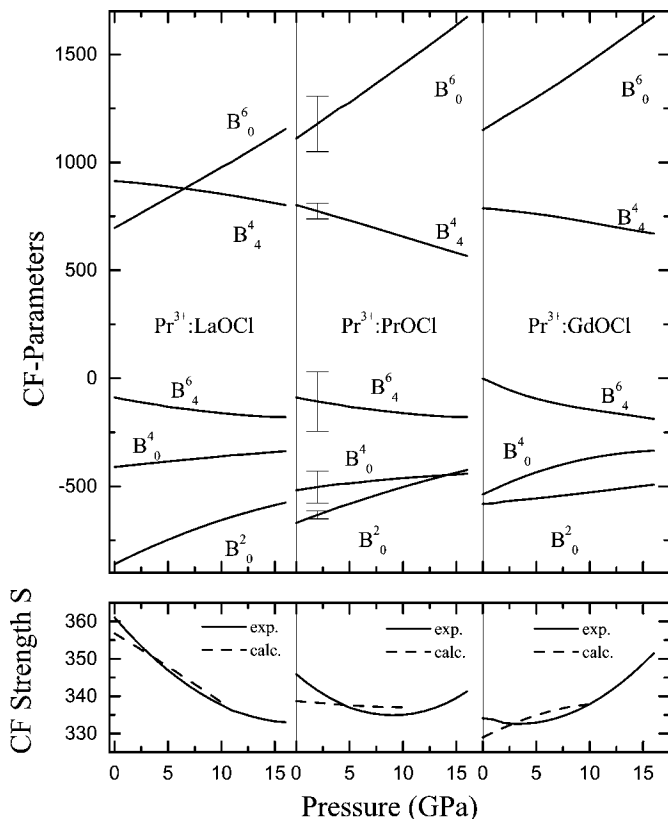


Fig. 7. Variation of the crystal-field parameters and the crystal-field strength of $\text{ROCl}:\text{Pr}^{3+}$ ($R = \text{La, Pr, Gd}$) under pressure. The dashed lines show a superposition model calculation of the crystal-field strength.

was observed for $\text{Na}_5\text{Eu}(\text{MoO}_4)_4$ (Guo et al., 1991). Although this simply seems to indicate distinct differences with respect to $\text{La}_2\text{O}_2\text{S}$ or YAG, definite conclusions can be drawn only after the specific changes of the interatomic distances, due to the particular compressibilities, have been taken into account.

Besides the crystal-field parameter shifts, fig. 7 also shows the variation of the crystal-field strength for $\text{ROCl}:\text{Pr}^{3+}$. Obviously, the crystal-field strength is distinctly decreasing in the case of $\text{LaOCl}:\text{Pr}^{3+}$ up to 15 GPa and slightly decreasing for $\text{GdOCl}:\text{Eu}^{3+}$ up to 10 GPa. The initial decrease for $\text{GdOCl}:\text{Eu}^{3+}$ was observed also by Liu et al. (1998b). In addition, a similar behavior was found for $\text{LaOBr}:\text{Eu}^{3+}$ up to 13 GPa (Chi et al., 1990) and $\text{GdOBr}:\text{Eu}^{3+}$ up to 12 GPa (Chi et al., 1997).

The possibility of a decreasing crystal-field strength with increasing pressure has been mentioned in the beginning of sect. 4.4. There it was argued that a change in the structural parameters can occur in such a way that the overall crystal-field strength decreases although the interactions between f-electrons and ligands increase with decreasing distances. This assumption is confirmed by a calculation of the crystal-field strength, shown by the dashed lines in fig. 7. For the calculation, the superposition model (sect. 4.4.3) and the pressure-induced

structural changes of the $ROCl$ host lattices (Bungenstock et al., 2001) have been utilized. In the superposition model the crystal-field parameters are calculated as a sum of products of so-called intrinsic parameters and geometrical factors. The intrinsic parameters represent the interactions between the f-electrons and one ligand and indeed were found to increase under pressure. However, the geometrical factors compensated this increase and in fact resulted in the calculated decrease under pressure.

4.4.2. Local distortions

To relate the f-element spectra or equivalently the crystal-field parameters to the structure of the host lattice, a detailed knowledge of the distances and angles of the atomic arrangement is required. In this respect, local distortions arising from a size mismatch between doped and substituted ions impose serious limitations on the determination of the parameter-structure relationship. Usually, at ambient pressure different hosts are used to generate different structural environments around the same f element. This enables the experimentalist to deduce a parameter-structure relation from the spectral data of the particular hosts. This procedure, however, suffers from the problem of unknown and in particular different local distortions for each host.

On the other hand, parameter-structure relations determined from shifts under pressure are somewhat more reliable, because one and the same local distortion is present which in addition affects the parameter changes only if the distortions themselves considerably change under pressure. Nevertheless, the problem of local distortions cannot be neglected in high-pressure experiments. Local distortions are present, if the distances or angles from the doped rare-earth ion to the ligands deviate from those of the pure sample. In principle, the whole information about the local distortions is contained in the spectra of the doped ions themselves. Thus, once the problem of the dependence of spectra on the distances is solved, it should be possible to derive the distortions directly from the spectra. The application of high pressure is directed towards the solution of exactly this problem, therefore high pressure could provide possibilities to determine local distortions.

With these considerations in mind, Gregorian et al. (1989) proposed a model which allows to derive the local distortions for Pr^{3+} in $LaCl_3$ from high-pressure experiments. The basic assumption of this model is that the local coordination polyhedra of the Pr^{3+} ion in two different host lattices with the same type of ligand complexes should be identical, as soon as all multiplet centroids of the Pr^{3+} ion are energetically equal in both hosts.

To illustrate this method, fig. 8 shows the dependence of the 3P_0 multiplet of Pr^{3+} in RCl_3 ($R = La, Pr, Nd, Gd$) on the host lattice equatorial bond distances R_E and apical bond distances R_A (see fig. 5) at ambient pressure (circles) as well as at high pressure for $LaCl_3:Pr^{3+}$ (triangles). The structural data under high pressure have been determined by single-crystal X-ray diffraction studies (Gregorian et al., 1989). According to fig. 8, the energies of the 3P_0 multiplet of Pr^{3+} in $LaCl_3$ at 0.9 GPa and $PrCl_3$ at ambient pressure coincide with one another. Simultaneously, the distances R_E are equal in both lattices, but a distinct difference exists for the distance R_A . However, according to the assumption that identical energies are synonymous with an identical local geometry, it must be concluded that the local distance R_A

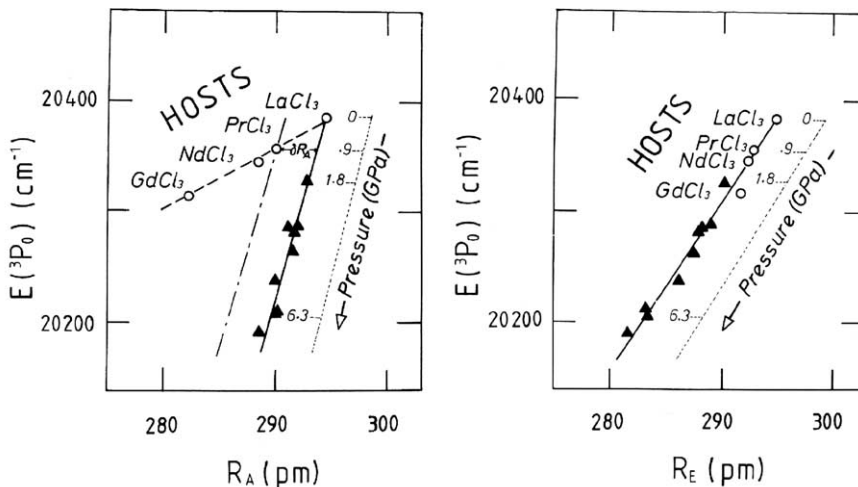


Fig. 8. Energy of the 3P_0 multiplet of $\text{LaCl}_3:\text{Pr}^{3+}$ as a function of the host lattice equatorial and apical La-Cl distances (from Gregorian et al., 1989). The circles correspond to the multiplet energies of Pr^{3+} in RCl_3 ($R = \text{La}, \text{Pr}, \text{Nd}, \text{Gd}$) and the respective host-lattice bond distances at ambient pressure. Triangles denote the high-pressure data for $\text{LaCl}_3:\text{Pr}^{3+}$.

for Pr^{3+} in LaCl_3 at 0.9 GPa is identical with the distance in PrCl_3 at ambient pressure. Thus, the local distortion δR_A can be simply read from the difference of the two host lattice values.

The same considerations were used by Gregorian et al. (1989) to determine the local distortions for all structural parameters for $\text{LaCl}_3:\text{Pr}^{3+}$ and for $\text{GdCl}_3:\text{Pr}^{3+}$. This model has been applied also for $\text{LaCl}_3:\text{Nd}^{3+}$ (Tröster et al., 1993), $\text{ROCl}:\text{Pr}^{3+}$ ($R = \text{La}, \text{Gd}$) (Bungenstock et al., 2000b). In both cases the optical high-pressure studies have been compared to results for the pure substances NdCl_3 and PrOCl .

A further possibility to derive local distortions can be based on models like the superposition model, which explicitly relate the crystal-field parameters to structural parameters. This has been done for $\text{CaFCl}:\text{Sm}^{2+}$ (Shen and Holzapfel, 1995b) and $\text{MFCl}:\text{Sm}^{2+}$ ($M = \text{Ba}, \text{Sr}, \text{Ca}$) (Shen and Holzapfel, 1996). These results will be discussed in the next section.

4.4.3. Superposition model

The crystal-field parameters introduced in sect. 4.1 still contain all the structural information about the local environment. Therefore, a direct comparison of crystal-field parameters derived from different hosts, even with the same site symmetry, is not reasonable. In addition, the crystal-field parameters cannot be directly related to the distance and angle variations induced by the high-pressure application. Widely used models which extract the structural information from the crystal-field parameters are the angular-overlap (Jørgensen et al., 1963) and superposition model (Bradbury and Newman, 1967). In the case of f elements, the superposition model has been employed widely for the analysis of crystal-field parameters.

The underlying assumption of the superposition model is that the one-electron crystal field is additive and can be regarded as a superposition of the contributions from individual ions

in the crystal. No specific assumptions are made on the kind of interactions between the f-electrons and their ligands. Within this model, the crystal-field parameters can be related to so-called intrinsic parameters \bar{B}_k and geometrical factors K_{kq} :

$$B_q^k = \sum_j \bar{B}_k(R_j) K_{kq}(\vartheta_j, \varphi_j). \quad (12)$$

The intrinsic parameters \bar{B}_k depend only on the distance R_j and on the kind of ligand j located at $(R_j, \vartheta_j, \varphi_j)$. The effect of pressure on the geometrical factors can be calculated once the structural changes under pressure have been determined for example by X-ray diffraction experiments. For the distance dependence of the intrinsic parameters \bar{B}_k a simple power law is commonly assumed:

$$\bar{B}_k^L(R^L) = \bar{B}_k^L(R_0^L) \left(\frac{R_0^L}{R^L} \right)^{t_k^L}. \quad (13)$$

The quantities $\bar{B}_k^L(R_0^L)$ and t_k^L are treated as adjustable parameters and R_0^L is a reference distance that can be chosen arbitrarily. In principle, the number of ligand shells considered for the calculation of intrinsic parameters is not limited, however, it is usually assumed that only the nearest neighbors of the rare-earth ion contribute significantly to the crystal-field potential. Thus, especially long-range interactions like electrostatic interactions are not accounted for explicitly. Because these interactions are most important for $k = 2$ parameters, in many cases only the $k = 4, 6$ intrinsic parameters have been considered.

At ambient pressure a large amount of work has been done to derive intrinsic parameters of rare-earth ions doped into different host crystals. For a detailed account of the superposition model and the ambient pressure results see, for example, Newman (1971), Newman and Ng (1989) and Garcia and Faucher (1995). According to eq. (13), the intrinsic parameters for a given ligand depend only on the distance between the rare-earth ion and the ligand. The determination of intrinsic parameters thus requires a variation of this distance, which naturally favors the application of high pressure. Despite this obvious possibility, only a limited number of intrinsic parameter studies under pressure has been published. This is simply explained by the number of different and partly sophisticated methods (optical spectroscopy, X-ray diffraction, extended X-ray absorption fine structure) that must be employed simultaneously at high pressure to one and the same sample to get all the information necessary.

The systems that have been studied in detail under pressure are LaCl_3 doped with Pr^{3+} , Nd^{3+} (Tröster et al., 1995), and U^{3+} (Tröster et al., 1995), ROCl ($R = \text{La, Pr, Gd}$) doped with Pr^{3+} (Bungenstock et al., 2000b), and MFCl ($M = \text{Ba, Ca, Sr}$) doped with Sm^{2+} (Shen and Holzapfel, 1995c, 1995d). In the case of LaCl_3 only one type of ligands exists and thus only one set of intrinsic parameters has to be determined. The results for this system for the intrinsic parameters $\bar{B}_k^{\text{Cl}}(R_0^{\text{Cl}})$ and t_k^{Cl} for Pr^{3+} , Nd^{3+} and U^{3+} are summarized in table 6.

As can be seen from table 6 the crystal-field strength for U^{3+} at ambient pressure, represented by $\bar{B}_k^{\text{Cl}}(R_0^{\text{Cl}})$, is about twice as large as the value for the lanthanides. In spite of this remarkable difference, the distance dependences are nearly the same in all cases. The apparent difference in the case of t_4 for $\text{LaCl}_3:\text{Nd}^{3+}$ is either due to uncertainties in the determination

Table 6

Intrinsic crystal-field parameters $\overline{B}_{4,6}(R_0)$ (in cm^{-1}) and power law exponents $t_{4,6}$ for chloride ligands for Pr^{3+} , Nd^{3+} , and U^{3+} in LaCl_3 . $R_0 = 295$ pm

	$\overline{B}_4(R_0)$	t_4	$\overline{B}_6(R_0)$	t_6
Pr^{3+}	287(22)	5(4)	258(28)	7(2)
Nd^{3+}	254(28)	2(4)	271(32)	6(2)
U^{3+}	507(47)	7(4)	585(52)	5(2)

Table 7

Intrinsic crystal-field parameters (in cm^{-1}) for chloride and oxygen ligands for Pr^{3+} in ROCl ($R = \text{La}, \text{Pr}, \text{Gd}$). ΔB_q^k represent special shifts for B_0^4 and B_4^4

$R_0^{\text{Cl}} = 316$ pm	$\overline{B}_2^{\text{Cl}}(R_0^{\text{Cl}})$	t_2^{Cl}	$\overline{B}_4^{\text{Cl}}(R_0^{\text{Cl}})$	t_4^{Cl}	$\overline{B}_6^{\text{Cl}}(R_0^{\text{Cl}})$	t_6^{Cl}	ΔB_0^4	ΔB_4^4
$\text{LaOCl}:\text{Pr}^{3+}$	906(26)	5(2)	172(25)	10(2)	181(43)	11(2)	351	327
$\text{PrOCl}:\text{Pr}^{3+}$	908(36)	5(2)	189(28)	13(2)	308(28)	10(2)	205	226
$\text{GdOCl}:\text{Pr}^{3+}$	898(84)	5(2)	163(31)	12(2)	298(43)	9(2)	150	190
$R_0^{\text{O}} = 235$ pm	$\overline{B}_2^{\text{O}}(R_0^{\text{O}})$	t_2^{O}	$\overline{B}_4^{\text{O}}(R_0^{\text{O}})$	t_4^{O}	$\overline{B}_6^{\text{O}}(R_0^{\text{O}})$	t_6^{O}		
$\text{LaOCl}:\text{Pr}^{3+}$	2229(177)	-1(1)	722(69)	8(3)	214(24)	12(2)		
$\text{PrOCl}:\text{Pr}^{3+}$	1819(189)	-1(2)	705(47)	7(3)	272(50)	10(2)		
$\text{GdOCl}:\text{Pr}^{3+}$	1607(70)	-1(2)	693(23)	9(2)	236(22)	11(3)		

of the local distortions according to the model described in sect. 4.4.2 (Tröster et al., 1995) or to the neglect of correlation effects (see sect. 4.4.5).

In contrast to the LaCl_3 case, for ROCl two different ligands must be taken into account. In this host the Pr^{3+} ion is surrounded by four O^{2-} and five Cl^- ions. The four O^{2-} ions are located in a plane below the central ion at a distance R_0 , four Cl^- ions in a plane above the central ion at a distance R_{Cl} , and one Cl^- ion above the Cl^- plane at a distance $R_{\text{Cl}'}$. Within the superposition model, the sum of the contributions from these ligands for the crystal-field parameters B_q^k can be written as:

$$\begin{aligned} B_0^k &= 4\overline{B}_k^{\text{O}}(R_0)K_{k0}^{\text{O}} + 4\overline{B}_k^{\text{Cl}}(R_{\text{Cl}})K_{k0}^{\text{Cl}} + \overline{B}_k^{\text{Cl}'}(R_{\text{Cl}'})K_{k0}^{\text{Cl}'} \quad \text{and} \\ B_4^k &= 4\overline{B}_k^{\text{O}}(R_0)K_{k4}^{\text{O}} + 4\overline{B}_k^{\text{Cl}}(R_{\text{Cl}})K_{k4}^{\text{Cl}}. \end{aligned} \quad (14)$$

For every ligand (Cl and O) a set of three intrinsic parameters exists. The results for the intrinsic parameters determined from the crystal-field parameter shifts up to 10 GPa are presented in table 7. Local distortions have been estimated according to the model described in sect. 4.4.2. Although only the immediate neighbors of the Pr^{3+} ion have been considered, the $k = 2$ parameters have also been derived by Bungenstock et al. (2000b). The results for these parameters, however, have to be taken with some precaution due to the problems of long-range interactions mentioned before.

Within the estimated uncertainties, table 7 shows that a common set of intrinsic parameters for $k = 6$ can be found which describes all samples studied there. One remarkable difference is observed only in the case of $\overline{B}_6^{\text{Cl}}(R_0^{\text{Cl}})$ for $\text{LaOCl}:\text{Pr}^{3+}$. However, this difference was caused simply by the use of different data sets in the determination of the crystal-field parameters.

Table 8

Intrinsic crystal-field parameters $\overline{B}_{4,6}(R_0)$ (in cm^{-1}) and power law exponents $t_{4,6}$ for chloride and fluoride ligands for Sm^{2+} in BaFCl and SrFCl. $R_0 = 311.4$ pm for chloride and $R_0 = 249.6$ pm for fluoride ions

	$\overline{B}_4(R_0)$	t_4	$\overline{B}_6(R_0)$	t_6
$\text{Sm}^{2+}\text{-Cl}^-$	124(14)	14(4)	152(16)	10(3)
$\text{Sm}^{2+}\text{-F}^-$	245(25)	6(2)	172(18)	5(1)

Once identical data sets for all three samples were used, very similar values were also obtained for $\overline{B}_6^{\text{Cl}}(R_0^{\text{Cl}})$.

More serious difficulties were encountered in the case of the intrinsic parameters $\overline{B}_4^{\text{F}}$. In that case two further parameters ΔB_0^4 and ΔB_4^4 had to be introduced into the fitting procedure to get a reasonable description of the experimental crystal-field parameters. The additional parameters represent pressure independent constants, added to the calculated crystal-field parameters. Bungenstock et al. (2000b) discussed various possible sources of this problem and finally concluded that their high pressure data for hosts with two different ligands required modifications of the superposition model, possibly related to long-range electrostatic or ligand–ligand interactions which are not included in the model.

Similar results were obtained by Shen and Holzapfel (1995d). They studied Sm^{2+} in BaFCl and SrFCl under pressures up to 8 GPa. The structure of both hosts is identical to LaOCl and thus eq. (14) can be applied also in this case, with the only difference of fluoride ions replacing the oxide ions. The results for the $k = 4, 6$ intrinsic parameters for both types of ions are listed in table 8. When they compared their results with other literature values, they noted much larger t_k exponents for the chloride but much smaller intrinsic parameters for the fluoride ions. Shen and Holzapfel (1995d) argued that ligand–ligand interactions could remove these discrepancies by increasing the values of $\overline{B}_k^{\text{Cl}}$ and simultaneously decreasing the values of $\overline{B}_k^{\text{F}}$. They also pointed out that on the basis of some investigations for PrCl_3 which included ligand–ligand overlap effects (Curtis and Newman, 1970), one can expect contributions to the intrinsic parameters on the order of 10%. However, it would not be surprising if the interactions show up more strongly in systems like MFCl or LaOCl, where two kinds of ligands contribute to the crystal-field parameters.

Though some limitations of the superposition model have been revealed by the high pressure studies, in general a reasonable description of the crystal-field parameters can be achieved. In particular this is the case when results for isostructural hosts are compared, where a common set of parameters usually is sufficient to describe the pressure variations for all hosts. This fact has been used to derive local distortions for Sm^{2+} in CaFCl (Shen and Holzapfel, 1995b) and Sm^{2+} in BaFCl (Shen and Holzapfel, 1996). In both cases, the intrinsic crystal-field parameters determined from a high-pressure study on SrFCl: Sm^{2+} were used as a starting point. In this sample, local distortions could be safely neglected due to the facts that the ionic radii of Sm^{2+} and Sr^{2+} are almost identical and the structural parameters for SmFCl and SrFCl are very similar.

According to the superposition model the intrinsic parameters found for SrFCl: Sm^{2+} were simply transferred to either CaFCl: Sm^{2+} or BaFCl: Sm^{2+} . Then, combining the intrinsic parameters with crystal-field parameters gained from optical high pressure studies on CaFCl: Sm^{2+}

and BaFCl:Sm^{2+} , it was possible to adjust the local structural parameters around the Sm^{2+} ion. As the result a shortening of the $\text{Sm}^{2+}-\text{Cl}^-$ and $\text{Sm}^{2+}-\text{F}^-$ distances by -7 pm and -6 pm in BaFCl (Shen and Holzapfel, 1996) and a lengthening by $+3.4$ pm and $+3.5$ pm in CaFCl (Shen and Holzapfel, 1995b) was found. These results are fully consistent with the expectation of shorter distances in BaFCl because of the smaller ionic radius of Sm^{2+} compared to Ba^{2+} and longer distances in CaFCl because of the larger ionic radius of Sm^{2+} compared to Ca^{2+} .

As a last remark, it should be mentioned that also a few evaluations of the crystal-field parameters of Pr^{3+} in LaCl_3 in the scope of the angular overlap model have been made. Umland et al. (1985) and Umland (1989) used the angular overlap model to calculate the crystal-field splittings of $\text{LaCl}_3:\text{Pr}^{3+}$ under pressure. In addition, Gregorian et al. (1989) derived the parameters of both models and found that both approaches were capable to successfully describe the high-pressure results.

4.4.4. *Ab initio calculations*

The intrinsic parameters discussed in the previous section open a practicable possibility to analyze the fundamental interactions occurring between the f-electrons and the ligands. In an ab initio calculation for the system $\text{Pr}^{3+}-\text{Cl}^-$, Newman and Ng (1986) took into account five different mechanisms contributing to the intrinsic crystal-field parameters at various $\text{Pr}^{3+}-\text{Cl}^-$ distances. These were point charges, charge penetration, exchange, p and s overlap, and p and s covalency.

Gregorian et al. (1989) compared the theoretical results from Newman and Ng (1986) with their experimentally determined intrinsic parameters from a high-pressure study. They found that the theoretical values $\overline{B}_k^{\text{Cl}}(R_0^{\text{Cl}})$ at ambient pressure were significantly smaller than the experimental values. However, the variation of the theoretical values agreed very well with the experimental results, especially if the large cancellations between the different theoretical contributions are taken into account.

Following the approach suggested by Newman and Ng (1986), an improved ab initio calculation of the intrinsic crystal-field parameters for the systems $\text{Pr}^{3+}-\text{Cl}^-$ (Shen and Holzapfel, 1994) and $\text{Nd}^{3+}-\text{Cl}^-$ (Shen, 1994) has been presented. The comparison of these results with experimental intrinsic parameters derived for $\text{LaCl}_3:\text{Pr}^{3+}$ and $\text{LaCl}_3:\text{Nd}^{3+}$ (Tröster et al., 1993) is shown in fig. 9. Similar to the observations made by Gregorian et al. (1989), it is obvious that the ambient pressure values of the theoretical calculations are too small, yet the distance dependence is reasonably reproduced.

Shen and Bray (1998b) also performed ab initio calculations of the intrinsic crystal-field parameters for the systems $\text{Sm}^{2+}-\text{Cl}^-$ and $\text{Sm}^{2+}-\text{F}^-$. Again the same formalism as in the case of the LaCl_3 calculations was used. The calculated parameters were compared with experimental results from high pressure studies on $M\text{FCl:Sm}^{2+}$ ($M = \text{Sr}, \text{Ba}$). The slight differences observed between theoretical and experimental parameters were attributed to the use of free-ion 4f wavefunctions, which are less expanded compared to the actual wavefunctions in the crystal (see sect. 4.3) and neglect of ligand–ligand and $4f^5 5d^1$ configuration interactions.

Despite small deviations between the ab initio calculations and experimental high-pressure results, in general it can be noticed that the contributions considered in the calculations ac-

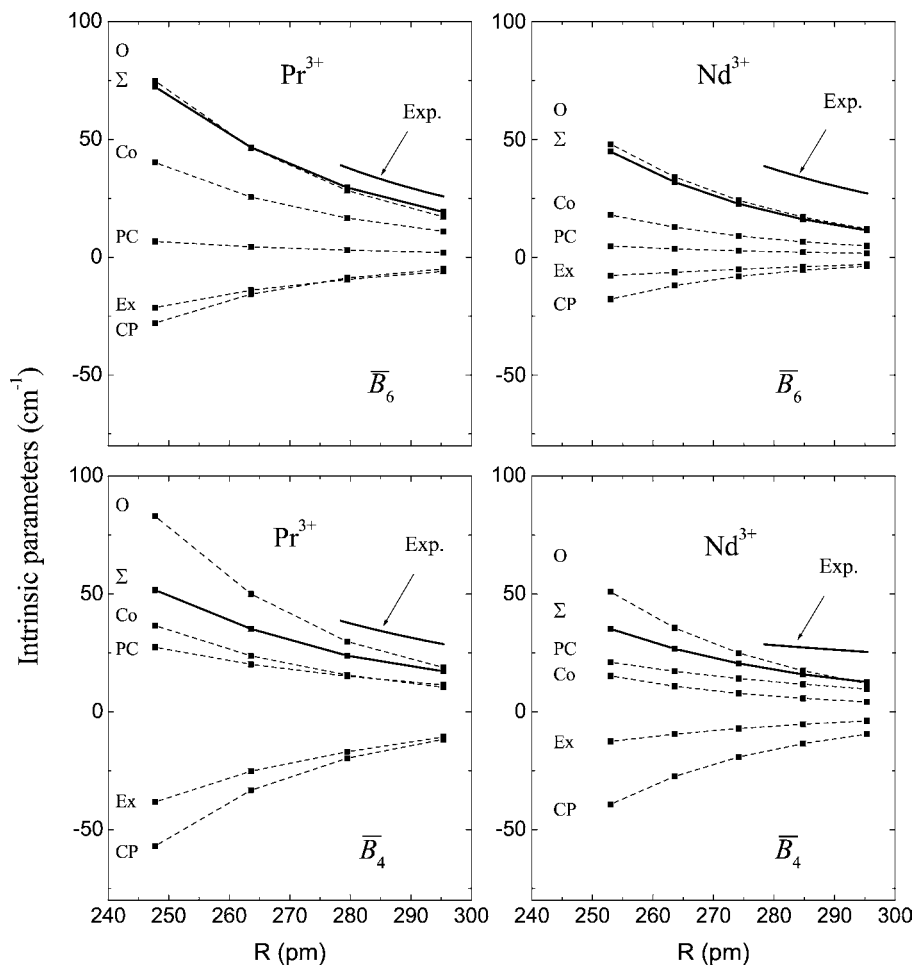


Fig. 9. Ab initio calculations of the intrinsic parameters for the systems $\text{Pr}^{3+}-\text{Cl}^-$ (Shen and Holzappel, 1994) and $\text{Nd}^{3+}-\text{Cl}^-$ (Shen, 1994). Dashed lines denote the individual contributions: CP – Charge Penetration, Ex – Exchange, PC – Point Charges, O – s, p Overlap, Co – s, p Covalency. Σ marks the sum of all contributions. The experimental results were taken from table 7 (Tröster et al., 1993; Tröster, 1994).

count for the primary effects responsible for the crystal-field potential. These observations point to the importance of overlap and covalency contributions and in addition justify the assumptions of the superposition model as reasonable approximations of the given situation.

Finally, the interesting case of a negative exponent t_2^O found for the $\text{Pr}^{3+}-\text{O}^{2-}$ system (see table 7) in $\text{ROCl}:\text{Pr}^{3+}$ ($R = \text{La, Pr, Gd}$) (Bungenstock et al., 2000b) should be mentioned. Shen (1994) also performed ab initio calculations for this system and in fact he found a negative value for t_2^O (for details, see Bungenstock, 1999). This agreement can be regarded as

an interesting confirmation of the ab initio calculations as well as the superposition model. However, these results should not be taken too seriously, because of the problems connected especially with the $k = 2$ parameters, as discussed in the previous section. In addition, the same calculation produced a much too small ambient pressure value $\overline{B}_2^O(R_0^O)$ compared to the experimental value.

4.4.5. Correlation crystal fields

In sect. 4.1 the one-electron crystal-field model for the f^N configurations was introduced. Though this model is very successful in providing a description of the crystal-field splittings, certain “anomalous” multiplets are poorly fitted. Prominent examples are the 1D_2 multiplet of Pr^{3+} , the $^2H(2)_{11/2}$ multiplet of Nd^{3+} , and the 3K_8 multiplet of Ho^{3+} . Almost independent of the host crystal, the calculated crystal-field levels of these multiplets show a much larger deviation from the experimental ones than all the other levels.

Improvement of the crystal-field splitting calculation has been achieved by two different approaches. On one hand the basis set of wavefunctions was extended to include also excited configurations. This approach will be dealt with in sect. 4.4.6. On the other hand, the one-electron approximation has been relaxed to take into account electron correlation effects. The original formulation of the correlation crystal-field parameterization has been proposed by Bishton and Newman (1968). Judd (1977) and Reid (1987) redefined the operators to ensure their mutual orthogonality:

$$H_{\text{OCCF}} = \sum_{i,K,Q} G_{iQ}^K g_{iQ}^{(K)}. \quad (15)$$

As for the one-electron crystal field, the G_{iQ}^K are treated as parameters, whereas the angular parts $g_{iQ}^{(K)}$ can be calculated exactly. Again, the number of terms which have to be considered can be reduced by the site symmetry. However, this number is much larger here than for the one-electron crystal field. Actually, even for an octahedral site symmetry, 41 parameters are left, which cannot be determined from the experimental data. To tackle this problem, different approaches have been proposed. On one hand, it is possible to assume a certain type of interaction that is mainly responsible for the correlation effects. This leads to special correlations with less parameters, as for example the spin- or orbitally-correlated crystal fields or the δ -function model. For a more detailed description of such models see, for example, Reid and Newman (2000).

On the other hand, a more practical approach is to analyze the various parameters with respect to their influence on the “anomalous” multiplets. According to this procedure Li and Reid (1990) could show that taking into account only the parameters G_{10AQ}^4 , a pronounced improvement for the description of the $^2H(2)_{11/2}$ multiplet of Nd^{3+} could be achieved. To study the dependence of correlation effects on the interatomic distances, Jayasankar et al. (1993) analyzed spectroscopic data for $\text{LaCl}_3:\text{Nd}^{3+}$ at pressures up to 10 GPa. Using the superposition model, they could derive the distance dependences of the intrinsic parameters \overline{B}_4 and \overline{G}_{10A}^4 which are multiplied by the same geometrical factor. In contrast to earlier assumptions (Reid, 1987), Jayasankar et al. (1993) could show that the correlation intrinsic parame-

ter changed much more with pressure than the one-electron intrinsic parameter. Assuming a power law dependence of the correlation intrinsic parameter, an exponent of $t_4^{\text{OCCF}} \approx 15$, compared to a value of $t_4 \approx 5$ for the one-electron intrinsic parameter, was found.

Another possibility to address the problem of the correlation crystal fields is an approach based on different wavefunctions for the spin-up and spin-down electrons. This spin-correlated crystal-field model merely doubles the number of crystal-field parameters and thus can be applied in most cases. Shen and Holzapfel (1995c) presented a high pressure study on spin-correlated crystal fields in $M\text{FCl}:\text{Sm}^{2+}$ ($M = \text{Ba}, \text{Sr}, \text{Ca}$). In particular, they considered the splitting ratio R of the $^5\text{D}_1$ and $^7\text{F}_1$ multiplets, which should be equal to 0.298 within the conventional one-electron crystal-field theory and independent of the host crystal. In a first step, Shen and Holzapfel (1995c) considered ambient pressure as well as high pressure data of the isoelectronic Eu^{3+} ion. In this case they found a ratio of $R = 0.238$, which could be explained by taking into account a spin-correlated crystal-field parameter $c_2 = -0.007(3)$.

However, applying the same model to the high-pressure results for Sm^{2+} , extreme deviations were encountered. The authors attributed these deviations to a breakdown of the spin-correlated crystal-field model for Sm^{2+} . As the reason for this failure, configuration interactions with the $4f^5 5d^1$ configuration were determined. These interactions are expected to be much stronger for Sm^{2+} , because the energy of the excited configuration is much lower (at about $20\,000\text{ cm}^{-1}$) than in the case of Eu^{3+} (at about $50\,000\text{ cm}^{-1}$).

Recently, the δ -function model has also been employed to analyze high-pressure results on $\text{LaCl}_3:\text{Pr}^{3+}$ and $\text{LaCl}_3:\text{Nd}^{3+}$ (Burdick and Tröster, 2003). This model assumes the dominant contributions to the correlation crystal field interactions arising from paired electrons within the same orbital. It has been shown that this model is capable to greatly improve the description of “anomalous” multiplets like the $^1\text{D}_2$ multiplet of Pr^{3+} at ambient pressure (Burdick and Richardson, 1997).

Applying the model to the high-pressure data also distinctly improved the quality of the fits for both samples and at all pressures. A striking example is the $^1\text{D}_2$ multiplet of Pr^{3+} , where the rms error rises from 14.8 cm^{-1} at ambient pressure to a maximum value of 20.1 cm^{-1} at 8 GPa, when using solely the one-electron crystal-field parameters. On the contrary, if the δ -function model is included, a maximum rms error of only 0.9 cm^{-1} is found at ambient pressure and even smaller values are found at higher pressures.

Furthermore, a very interesting property of these fits concerns the one-electron crystal-field parameter B_0^4 of Nd^{3+} in LaCl_3 . In this case large difficulties were encountered in deriving the intrinsic parameter \bar{B}_4 because of much too small variations of B_0^4 of only 1% from ambient pressure to 8 GPa (see sect. 4.4.3 and table 6). On the other hand, taking into account the δ -function model, the change of B_0^4 distinctly increases to more than 10% from ambient pressure to 8 GPa. This clearly improves the values of the intrinsic parameter and points out the ability of the model to significantly improve the energy level calculations.

4.4.6. Excited states

High-pressure research on trivalent f elements is mostly concerned with the energy levels of the f^N configurations. This is mainly due to the fact that the energies necessary to access higher-lying states are within the VUV region, where the diamonds start to absorb the ra-

diation. The situation is much better in the case of divalent f elements whose excited states are much lower in energy. In principle, two different kinds of high energy states have been observed, on one hand charge transfer states, involving the excitation of an electron from a ligand orbital to the f^N configuration and, on the other hand, excited configurations of the f element itself, like the $f^{N-1}d^1$ configurations.

Besides the general interest on excited states, they can also strongly affect the properties of the f-electrons. For example, the two-body and three-body configuration interaction parameters α , β , γ and T_λ ($\lambda = 2, 3, 4, 6, 7, 8$), which are used in the free-ion Hamiltonian describe the influence of excited configurations on the centroids of the f^N multiplets. A further prominent influence of excited states is the interaction with $f^{N-1}d^1$ configurations, which is accepted to be responsible for the observed intensities of f-f transitions. In the past, high pressure studies have been performed especially on the influence of the $4f^{N-1}5d^1$ configurations. After presenting these studies, a brief discussion about the few high pressure studies on charge transfer states will follow.

The outstanding properties of f electrons stem from the fact that they are shielded from the crystal fields by outer closed sub-shells. For d electrons the situation is different, their wavefunction is much more expanded which causes a much stronger interaction with the lattice. Consequently, the $4f^{N-1}5d^1$ configurations show broad absorption and luminescence bands, in contrast to the sharp f-f transitions. The stronger interaction with the lattice also causes more pronounced pressure effects. Especially the energy shifts of the excited $4f^{N-1}5d^1$ configuration are usually an order of magnitude larger than in the case of the f-electrons. Shifts of the luminescence lines from $4f^{N-1}5d^1 \rightarrow 4f^N$ transitions are summarized in table 9.

According to table 9 an average shift of the f-d configuration can be determined to be around $-130 \text{ cm}^{-1}/\text{GPa}$. This is approximately five times larger than the average shift of the f-f transitions which is on the order of $-25 \text{ cm}^{-1}/\text{GPa}$. The f-d configuration of U^{4+} shifts faster compared to the 4f elements, a result which is not unexpected if the already larger shift of the f-f transitions (see sect. 4.2) is taken into account.

It is conspicuous that the excited configurations always shift to lower energies, with the only exception of CsSmI_3 . In this sample, the f-d configuration of Sm^{2+} is lower in energy than the 5D_0 multiplet and thus the luminescence is completely quenched at ambient pressure. However, at a pressure of 16.4 GPa Chen et al. (1994c) observed some new lines which they assigned to f-f transitions. According to this assignment the authors argued that the f-d configuration must have shifted to energies above the 5D_0 multiplet to allow f-f transitions to become visible. However, from the results presented by Chen et al. (1994c) it is not quite clear whether the f-d configuration really shows a continuous shift, because only a single spectrum recorded at 16.4 GPa is discussed. In addition, the authors assume a reversible first-order phase transition to occur under pressure which of course could be made responsible for a discrete jump of the f-d configuration. Thus, the positive value of the shift given in table 9 requires some further confirmation.

A similar effect as in the case of CsSmI_3 has been observed by Yoo et al. (1991). In their study on the Sm^{2+} ions in SrF_2 they could demonstrate an electronic crossover connected with a phase transition starting at pressures around 4.5 GPa. At this pressure, the f-d configuration shifted below the 5D_0 multiplet.

Table 9

Ambient pressure luminescence peaks and their pressure shifts for transitions from the $4f^{N-1}5d^1$ configurations to the ground state of the $4f^N$ configuration. Values marked with an asterisk correspond to the onset of the lowest energy luminescence line. In the case of UO_2 , excitation energies were determined

Ion	Ground State	Host	E (cm^{-1})	Shift ($\text{cm}^{-1}/\text{GPa}$)	Pressure range (GPa)	Reference
Ce^{3+}	$4f^1$	CaF_2	32900	-143	0-7	1
Pr^{3+}	$4f^2$	LaOCl	45000	-30*	0-10	2
Sm^{2+}	$4f^6$	CaF_2	16100	-113	0-8	3
			23500	-106	0-8	4
		CsSmI_3	35150	-113	0-8	5
			12500*	+200*	0-16	4
			16600*	-200*	0-9	5
			14800*	-149*	0-13	6
Eu^{2+}	$4f^7$	BaBr_2	24700	-225	0-10	7
			19600	-127	0-10	8
		Ba_2SiO_4	22900	-290	0-10	8
		CaAl_2O_4	24800	-150	0-10	8
		$\text{Ca}_2\text{P}_2\text{O}_7$	23300	-70	0-10	8
		EuF_2	30300	-175	0-8	3
		CaF_2	14000	-156	0-8	3
Dy^{2+}	$4f^{10}$	CaF_2	17250	-138	0-8	3
			21800	-94	0-8	3
			35500	-119	0-8	3
			16850	-106	0-8	3
			24400	-119	0-8	3
Tm^{2+}	$4f^{13}$	CaF_2	17500	-100	0-8	3
			24850	-150	0-8	3
		SrF_2	20160	-282	0-15	9
			20160	-282	0-15	9

References

1. Drotning and Drickamer (1973)
2. Tröster and Holzapfel (1998)
3. Wang and Drickamer (1973)
4. Chen et al. (1994c)
5. Bolduan et al. (1985)
6. Yoo et al. (1991)
7. Tröster et al. (2002)
8. Tyner and Drickamer (1977)
9. Syassen et al. (1986)

Apart from the interest in the properties of the excited configurations themselves, their influence on the f-electrons has been studied extensively. As mentioned in the beginning of this section, mixing with excited configurations is responsible for the observed intensities of f-f transitions. This feature will be discussed in sect. 5.3.1. The influence on the center of gravity of the multiplets is also taken into account in most studies via the two-body and three-body configuration interaction parameters.

However, relatively new is the inclusion of excited configurations to improve the description of the crystal field split levels within the f configuration.

In this respect, it was demonstrated for example for Pr^{3+} (Garcia and Faucher, 1989) and Nd^{3+} (Faucher and Moune, 1997), that the crystal-field level calculations both in general and for the "anomalous" multiplets, could be greatly improved by taking into account the $4f^{N-1}5d^1$ and $4f^{N-1}6p^1$ configurations. The effects due to configuration interactions are specifically interesting for high-pressure experiments because the large red shift of the excited configurations should lead to a distinct increase in the interactions.

In sect. 4.4.1 the pressure-induced variations of the crystal-field parameters of $\text{LaCl}_3:\text{Pr}^{3+}$ were shown in fig. 6. In this case the “anomalous” multiplet $^1\text{D}_2$ could also be measured under pressure (Tröster et al., 1993), which opened a possibility to study the configuration interactions as a function of pressure. Including the $4f^15d^1$ configuration in the energy level fits and leaving only the energy distance to the $4f^2$ configuration as an adjustable parameter, the mean deviation δ decreased from around 8 cm^{-1} to less than 4 cm^{-1} at ambient pressure (Tröster and Holzapfel, 2002).

Furthermore, the observed increase of δ under pressure completely vanishes (see fig. 6). The mean deviation is defined as:

$$\delta = \sqrt{\frac{(E_{\text{Calc.}} - E_{\text{Exp.}})^2}{N}}, \quad (16)$$

where N is the number of energies measured. The energy distance between both configurations was found to decrease with increasing pressure, however, the rate of around $1000 \text{ cm}^{-1}/\text{GPa}$ seems to be too large compared to the typical values given in table 9. Nevertheless, this basically reasonable behavior points to the importance of configuration interactions also for the energies of the $4f^2$ levels. It should be stressed that the conventional crystal-field parameters within the f -configuration partly show distinct changes when including the configuration interaction. The strongest deviation is found for B_0^4 , where a distinct pressure-induced change of its value is observed only if the configuration interaction is taken into account (see fig. 6). This behavior is very similar to what was observed in the case of the δ -function model as discussed in sect. 4.4.5 and may also remove the difficulties encountered for the determination of the $k = 4$ intrinsic parameters.

Further high-pressure studies on configuration interactions have been performed for $\text{LaOCl}:\text{Pr}^{3+}$ taking into account the $4f^{N-1}6p^1$ configuration (Bungenstock, 1999) and $\text{LiYF}_4:\text{Pr}^{3+}$ taking into account the $4f^{N-1}5d^1$ and $4f^{N-1}6p^1$ configuration (Tröster and Lavin, 2003). In both cases distinct improvements of the rms deviations at ambient as well as at high pressures have been obtained. The absolute values of the crystal-field parameters within the $4f$ configuration changed up to 50%, however, their pressure variations showed only minor differences.

The only system that has been studied in some detail with respect to charge transfer states under pressure is $\text{R}_2\text{O}_2\text{S}:\text{Eu}^{3+}$ ($R = \text{La}, \text{Y}$). Webster and Drickamer (1980a) observed a blue-shift of the absorption maximum of the charge transfer band in $\text{La}_2\text{O}_2\text{S}:\text{Eu}^{3+}$ with a rate of approximately $200 \text{ cm}^{-1}/\text{GPa}$. The charge transfer state is believed to be formed here with the transfer of an electron from the sulfide S^{2-} to the Eu^{3+} ion. The shift of the charge transfer state in $\text{Y}_2\text{O}_2\text{S}:\text{Eu}^{3+}$ was found to be larger than in $\text{La}_2\text{O}_2\text{S}:\text{Eu}^{3+}$ with a rate of approximately $250 \text{ cm}^{-1}/\text{GPa}$.

Further studies on these bands by Wang et al. (1984) and Gleason et al. (1993) mainly concentrated on the influence on the intensities and lifetimes of the f - f transitions. These effects will be discussed in sect. 5.3.2. The influence on the energy levels within the f configuration was not addressed.

4.5. Pressure sensors

The line shifts of f-f transitions discussed in sect. 4.2, offer an interesting possibility to establish high pressure gauges. As mentioned in sect. 2, ruby is still the most widely used gauge for pressure determination. However, some deficiencies caused a continuous search for improved sensor materials. Especially the temperature induced broadening and quenching limits the application of ruby to below 500 °C.

New sensors should solve this problem, but at the same time should still preserve the advantages of ruby, namely the strong luminescence efficiency and the strong line shift with increasing pressure relative to the given linewidth.

Some general requirements for a luminescence pressure sensor can be formulated as follows:

- the lines should show a large shift with pressure (measure: $d\lambda/dp$),
- the temperature dependent line shift should be as small as possible (measure: $d\lambda/dT$),
- for high sensitivity and precision, the linewidth Γ should be small compared to the line shift (measure: $\Gamma^{-1} d\lambda/dp$),
- the spectrum should consist of a single line,
- no significant broadening or weakening of the line should occur.

Due to these requirements, special attention has been paid to rare-earth sensors because the shielding of the f-electrons produces very sharp lines which are less sensitive to the environment compared to the 3d electrons of Cr^{3+} .

One of the first studies taking into account rare-earth ions as a pressure sensor by Barnett et al. (1973) used Nd^{3+} doped into YAIO_3 . The pressure coefficients $d\lambda/dp$ and temperature coefficients $d\lambda/dT$ were compared there for several potential luminescence sensors up to 10 GPa. As expected, the temperature shift of the $R_2 \rightarrow Z_2$ line at 875.3 nm, belonging to the ${}^4F_{3/2} \rightarrow {}^4I_{9/2}$ transitions of Nd^{3+} (for the nomenclature see, for example, Dieke, 1968), was indeed approximately an order of magnitude smaller than for the Cr^{3+} doped samples. However, at the same time the pressure coefficient for Nd^{3+} was found to be much smaller.

As shown in sect. 4.2, in almost all cases of rare earth doped compounds a red shift of the optical transitions is observed, due to decreasing spin-orbit and Coulomb interactions under pressure. However, in the case of Nd^{3+} doped into YAIO_3 , Barnett et al. (1973) observed a blue shift of the ${}^4F_{3/2} \rightarrow {}^4I_{9/2}$ transitions. This peculiar behavior was taken up by Hua and Vohra (1997), who studied the ${}^4F_{3/2} \rightarrow {}^4I_{9/2}$ transitions in the same host YAIO_3 as well as in $\text{Y}_3\text{Al}_5\text{O}_{12}$ (YAG) in the extended pressure range up to 80 GPa. From the observed line shifts they deduced the energies of the two crystal-field levels of ${}^4F_{3/2}$, R_1 and R_2 , as a function of pressure as shown in fig. 10. Corresponding to the blue shift of the luminescence lines, both levels showed a continuous shift to higher energies in YAIO_3 , in contrast to the case of YAG, where both levels shift to lower energies, as expected.

Hua and Vohra (1997) did not give an explanation why the levels in YAIO_3 behave completely different to what is usually observed. In principle, the observed blue shift of these levels point to increasing Coulomb and spin-orbit coupling interactions, which should be connected with an increasing local volume (see also sect. 4.3). Whether such a behavior is reasonable or not could be answered only by further investigations as for example using

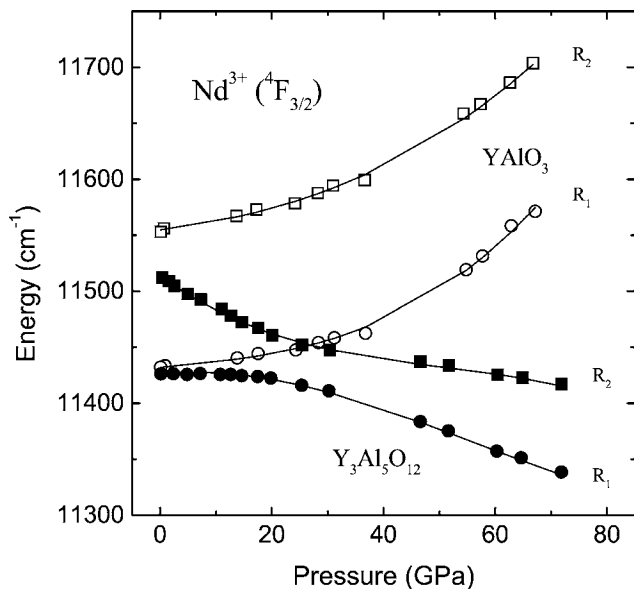


Fig. 10. Effect of pressure on the ${}^4F_{3/2}$ crystal-field levels in $YAlO_3$ and $Y_3Al_5O_{12}$. The solid lines are polynomial fits to the data (from Hua and Vohra (1997)).

high-pressure X-ray diffraction studies. In any case, Hua and Vohra (1997) noted that the ${}^4F_{3/2} \rightarrow {}^4I_{9/2}$ transitions may be suitable as a pressure gauge in diamond anvil research at ultrahigh pressure. One of the main advantages of this system is that there is no interference with the diamond luminescence as in the case of ruby above 100 GPa.

A further requirement for a pressure sensor is the stability of the host lattice at high pressures and temperatures. This requirement strongly narrows the range of possible candidates for high-pressure sensors. From X-ray diffraction experiments under pressure, it was found that YAG is stable at least up to 69 GPa at room temperature (Liu and Vohra, 1993). This is one of the reasons why doped YAG was chosen by many researchers as a promising host for pressure calibrants.

One of the best studied sensor material is YAG doped with Sm^{3+} , whose most intense luminescence feature is a doublet at 16186.5 cm^{-1} and 16231.5 cm^{-1} (Y_1 and Y_2 lines). This doublet has been studied at room temperature up to a maximum pressure of 180 GPa (Bi et al., 1990; Yusa et al., 1994; Liu and Vohra, 1994) and it was found that the pressure-induced peak shift is comparable to the R_1 shift of ruby. At the same time, the temperature-induced shift is almost two orders of magnitude smaller than the observed shift for the R_1 peak. In fact, measurements at elevated temperatures up to 900°C and 10 GPa (Hess and Exarhos, 1989; Hess and Schiferl, 1990) as well as studies at temperatures above 400°C up to 25 GPa, indicated that the pressure could be determined from the Sm^{3+} luminescence without any temperature correction in this range (Hess and Schiferl, 1992).

Besides the Sm^{3+} ion, the Eu^{3+} ion was also studied in YAG (Arashi and Ishigame, 1982). In this case the ${}^5D_0 \rightarrow {}^7F_1$ transitions were monitored up to a temperature of 700°C and a pressure of 7 GPa. The results for the temperature and pressure-induced line shifts were

Table 10
Selected characteristic values for different pressure sensors. Values in parentheses are estimated

Material	Transition	λ (nm)	$d\lambda/dp$ (nm/GPa)	$d\lambda/\Gamma dp$ (1/GPa)	$d\lambda/dT$ (nm/10 ³ K)	$(d\lambda/\Gamma dp)$ / $(d\lambda/dT)10^3$ K /nm GPa	Reference
Cr ³⁺ :Al ₂ O ₃	² E → ⁴ A ₂	694.2	0.365	0.49	6.8	0.072	1
Cr ³⁺ :YAlO ₃	² E → ⁴ A ₂	722.8	0.70	0.7	7.6	0.092	1
Nd ³⁺ :YAlO ₃	⁴ F _{3/2} → ⁴ I _{9/2}	875.3	-0.13	-0.065	0.001	65	1
Eu ³⁺ :YAG	⁵ D ₀ → ⁷ F ₁	590.6	0.197	(0.8)	-0.54	0.002	2
Sm ³⁺ :YAG	Y ₁	617.8	0.30	0.23	0.23	1	3
Sm ²⁺ :SrB ₄ O ₇	⁵ D ₀ → ⁷ F ₀	685.4	0.255	1.7	-0.1	17	4
Sm ²⁺ :SrFCl	⁵ D ₀ → ⁷ F ₀	690.3	1.10	5.8	-2.3	2.5	5

References

1. Barnett et al. (1973)
2. Arashi and Ishigame (1982)
3. Hess and Exarhos (1989)
4. Lacam and Chateau (1989)
5. Shen et al. (1991)

similar to YAG:Sm³⁺. However, the two strongest lines in the luminescence spectrum were approaching each other with increasing pressure, resulting in a strong overlap and thus an increased error in the line position determination already at 6 GPa.

Another luminescence sensor, SrB₄O₇:Sm²⁺ has been suggested by Lacam and Chateau (1989). The advantage of using Sm²⁺ instead of Sm³⁺ is the occurrence of the well-isolated singlet transition ⁵D₀ → ⁷F₀ at 685.41 nm at ambient conditions. Also in this case the pressure-induced shift was similar to ruby, whereas the temperature-induced shift was much smaller. The stability of the host was proven up to 108 GPa (Leger et al., 1990) and the shift of the ⁵D₀ → ⁷F₀ transition has been calibrated in a hydrostatic medium (helium) up to 124 GPa (Datchi et al., 1997).

Another promising material is SrFCl:Sm²⁺. Shen et al. (1991) and Lorenz et al. (1994) have studied the pressure-induced shift of the ⁵D₀ → ⁷F₀ transition of the Sm²⁺ ion up to 20 GPa at room temperature and determined also the temperature-induced line shift up to 370 °C at ambient pressure. According to these studies the line shift under pressure is approximately three times larger than for ruby. At the same time, the temperature dependence was found to be about three times smaller. From the point of view of sensitivity SrFCl:Sm²⁺ is the best sensor studied so far. However, the main drawback here is the intensity decrease under pressure, which is due to an enhanced interaction of the ⁵D₀ energy level with the 4f⁵5d¹ configuration. The decrease already starts at around 10 GPa, limiting the use of this sensor to this lower pressure range.

Some characteristic values of the pressure sensors mentioned here have been summarized in table 10. As mentioned before, the value $\Gamma^{-1}d\lambda/dp$, denoting the sensitivity of the sensor with respect to a pressure change, is the highest for SrFCl:Sm²⁺. However, if an experiment requires high pressures and high temperatures, a closer look at the value of $\Gamma^{-1}d\lambda/dp/(d\lambda/dT)$ is necessary. This value can be regarded as a measure for the overall performance of the sensor with respect to pressure and temperature. From this point of view YAlO₃:Nd³⁺ would be the best sensor due to its extremely low temperature shifts.

4.6. *Structural probes*

In many cases the crystal structure of a rare-earth compound studied under high pressure is a priori known. In such studies the quality of the theoretical link between structure and spectra can be tested. However, a different possibility would be to use the experimentally determined spectral variations in connection with a theoretical approach to derive information about the local structure of the rare-earth ions. Such an attempt has been made in sect. 4.4.2, where the local distortions have been derived either directly from the spectra or by applying the superposition model. Similarly, high pressure studies have been used to get information about the structure in more complicated cases of multiple sites or glasses. In addition, the spectra of rare-earth ions have been used to detect phase transitions that often occur under pressure. Results of such studies will be discussed in the next two sections.

4.6.1. *Multiple sites/glasses*

The high pressure studies presented so far only considered compounds with a single, well-defined site for the rare-earth ion. However, in contrast to this case, many materials exhibit either a discrete variety of different sites or even a continuous distribution of sites, a situation typically encountered in glasses.

In the case of different, but spectroscopically still resolvable sites, it is possible to study the effects of pressure on each individual site. Such an attempt has been made by Dierolf et al. (2000) for Er^{3+} ions doped into stoichiometric LiNbO_3 . In this case a special spectroscopic technique, a combined excitation-emission spectroscopy, allowed to observe the pressure shifts of slightly different sites. From the shifts, the variations of the crystal-field parameters could be determined. These variations include all the information necessary to derive characteristics of the structure of each site (Dierolf et al., 2003).

Also in the case of semiconductors rare-earth ions often occupy different sites. For example, in GaAs at least 10 different types of Er^{3+} centers can be present simultaneously within the sample (Wolford and Bradley, 1985). Hogg et al. (1997a, 1997b) have studied the luminescence spectra of different Er^{3+} centers under hydrostatic pressures. They recognized some new centers which became optically active under pressure. In addition, it was shown that one center exhibited a configurational change at an elevated pressure (Hogg et al., 1997a).

Further work mainly concentrated on high-pressure effects on glasses doped with f elements. Soga et al. (1988) investigated densified glass specimens of $90 \text{ B}_2\text{O}_3\text{--}10 \text{ Na}_2\text{O--}1 \text{ Eu}_2\text{O}_3$ obtained by applying pressures up to 6 GPa. They noted that pressure first eliminates the atomic scale voids, usually appearing when the glass is quenched from high temperatures. Above 2 GPa no voids were formed during the quenching process. Furthermore, the fluctuation of local fields around Eu^{3+} was increased by high-pressure application. This behavior was attributed to the distortion of the glass network, which was accompanied with wide variations of bond length and angle.

Lochhead and Bray (1995) studied Eu^{3+} doped sodium disilicate glass with a high-pressure fluorescence line-narrowing technique. This technique was used to characterize the local structure of the Eu^{3+} ions up to a pressure of 21 GPa. For the crystal-field analysis they assumed a C_{2v} site symmetry which allowed for a complete splitting of the crystal-field components. The crystal-field strength was determined according to eq. (11). The effect of pressure

on the ${}^7F_0 \rightarrow {}^5D_0$ excitation was strongly dependent on the pressure range. From ambient pressure to ~ 4.7 GPa a red shift of approximately 0.12 nm/GPa was observed. From this pressure up to around 15 GPa the peak position remained unchanged and above 15 GPa a further small red shift was noticed. The bandwidth was constant up to around 7 GPa and increased above that pressure.

The interpretation of the high-pressure results presented by Lochhead and Bray (1995) was different for the two characteristic pressure regions below and above 4 GPa. Besides the already mentioned red shift, characteristic features below 4 GPa were an overall crystal-field strength decrease, and a lengthening of the luminescence lifetimes. Lochhead and Bray (1995) explained these results by minor structural changes like simple distortions of the Si–O–Si intertetrahedral angles and a small increase of the overall Eu–O bond covalency. They also noted a possible increase of higher-lying d-state energies relative to those of the f states under pressure.

The high-pressure regime from 4 GPa to 21 GPa is characterized by a simultaneous increase of the overall crystal-field strength and the ${}^7F_0 \rightarrow {}^5D_0$ linewidth, along with a shortening of the luminescence lifetimes. In addition, the nearly unchanged ${}^7F_0 \rightarrow {}^5D_0$ peak position up to 15 GPa suggested that high-field Eu^{3+} sites are created in this pressure range. These high-field sites appear on the high-energy side of the ${}^7F_0 \rightarrow {}^5D_0$ band, which explains the broadening of the band while the peak position remains the same.

The application of pressure to silicate glasses results in a gradual coordination change to five- and six-coordinate species of Si. A proposed mechanism for this coordination increase is through the consumption of nonbridging oxygens. Nonbridging oxygens are covalently bonded to one Si atom ($\text{Si}-\text{O}^-$) rather than to two Si atoms ($\text{Si}-\text{O}-\text{Si}$). In analogy to this process, Lochhead and Bray (1995) argued that a decrease in the nonbridging oxygen concentration should lead to an increase in the Eu^{3+} site crystal-field strength and thus to a blue shift or broadening of the ${}^7F_0 \rightarrow {}^5D_0$ band.

Because of the decreasing concentration, the number of coordinating nonbridging oxygens is decreasing. At the same time, the few remaining nonbridging oxygens are drawn closer to the Eu^{3+} ions than they would be in the ambient pressure high coordination state to satisfy its overall electrostatic and covalent energy requirements. As the result the high crystal field Eu^{3+} sites are associated with a low local concentration of nonbridging oxygens, low coordination numbers, and short Eu–O bonds. Conversely, weak field sites are characterized by a high local concentration of nonbridging oxygens, high coordination numbers, and long Eu–O bonds. These experimental results were completely confirmed by a molecular dynamics simulation by Monteil et al. (2000).

4.6.2. Phase transitions

The splitting of free-ion levels by the action of a crystal field depends on the symmetry of the crystal field which in turn reflects the symmetry of the arrangement of the neighboring ions. This property can thus be used to get evidence about the point group symmetry of a site in a given solid once the splitting of the free-ion multiplets have been determined (see, for example, sect. 5.8 of Görller-Walrand and Binnemans (1996)). This can be a very useful

feature in high-pressure experiments because many materials undergo phase transitions which usually alter the site symmetry.

In a stoichiometric compound, the symmetry reflected by the splitting is identical with the point symmetry of the site occupied by the rare-earth ion in the solid. However, in the case of rare-earth ions being dopants, the reflected symmetry can, but must not, be identical with the point group symmetry of the substituted ion (Denning et al., 1976). This problem arises because the splitting is dominated mainly by the crystal-field potential due to the nearest neighbors of the f element (Mishimura and Kushida, 1991). Thus, the splitting mainly reflects the symmetry of the arrangement of the ligand ions. Their positions, however, can deviate from the usual positions in the undoped material especially if the rare-earth ion replaces an ion of a distinctly different size. Therefore, the optical site symmetry deduced from the energy level splittings of the doped ion can be different from the real site symmetry of the host.

Numerous studies about phases and phase transitions detected by optical investigations of f elements have been published by Haire, Peterson, and co-workers. In many cases they used the Eu^{3+} ion to correlate the luminescence properties with structural changes. The Eu^{3+} ion exhibits a variety of characteristic transitions serving as a fingerprint for the structure (Chen et al., 1992e). However, in view of the problematic situation with respect to the local symmetry in the case of doped ions mentioned above, there has been some discussion on whether the Eu^{3+} ion or f elements in general can be used as indicators of the actual host structure or not (Tanner and Rudowicz, 1993; Stump et al., 1993). In summary, it must be concluded that the spectral/structural correlation has limitations especially in the case of doped ions where deviations between local and real site symmetry may readily occur.

To test the feasibility of the Eu^{3+} ion luminescence method to identify phase transitions, Chen et al. (1992b, 1994b) have performed high-pressure studies on the lanthanide sesquioxide Eu_2O_3 under pressure. In this stoichiometric compound the problem of local distortions is ruled out. The lanthanide sesquioxides show only three different crystal structures at ambient conditions, denoted by A, B, and C. The sesquioxides of the larger lanthanide cations tended to be hexagonal (A-type), those of the smallest cubic (C-type), and that of the intermediate-sized cations monoclinic (B-type). Some of the sesquioxides, including Eu_2O_3 , can exhibit both the B and C structures at ambient conditions.

In a high pressure study on C-type Eu_2O_3 at room temperature, Chen et al. (1992b) observed distinct changes in the luminescence spectrum of the Eu^{3+} ion at around 8 GPa. From a comparison with the ambient pressure spectrum of B-type Eu_2O_3 , they concluded that the observed changes were due to a phase transition to the B-type monoclinic structure. Such a transition had already been observed by Hoekstra (1966). In a further study, starting with B-type Eu_2O_3 , Chen et al. (1994b) observed spectral changes at pressures around 4 GPa. The spectra taken above 4 GPa were found to be similar to the spectrum of the Eu^{3+} ion in an A-type hexagonal La_2O_3 host crystal. Therefore, the observed changes were attributed to a phase transition from B- to A-type structure.

Another interesting example is a crystalline to amorphous phase transition in $\text{Eu}(\text{OH})_3$ (Chen et al., 1994a) at room temperature. The initial structure is the UCl_3 -type structure (space group $P6_3/m$) which was confirmed by X-ray diffraction. Figure 11 shows that broad bands appear under pressure and completely replace the former sharp lines at around 5.5 GPa. The

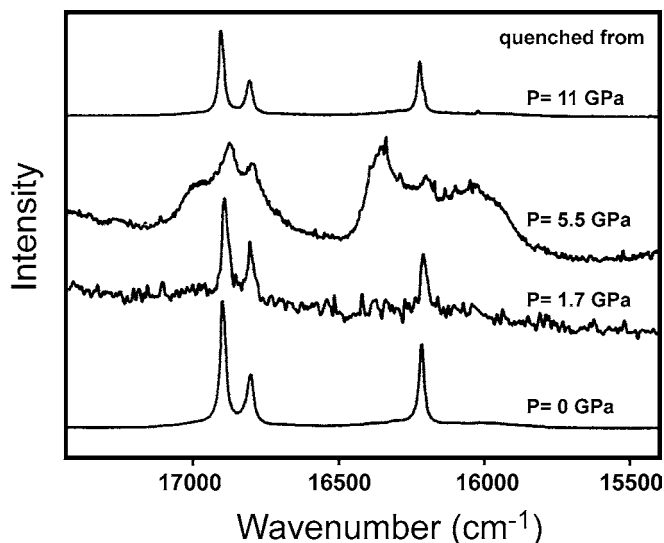


Fig. 11. Luminescence spectra from initially crystalline $\text{Eu}(\text{OH})_3$ at different pressures (from Chen et al. (1994a)). Amorphization is observed at 5.5 GPa. The transition is reversible as shown by the spectrum quenched from 11 GPa.

broad bands are characteristic for a sample in an amorphous state (Chen et al., 1995). The transition is completely reversible which can be seen by the spectrum quenched from 11 GPa in fig. 11.

As in the case of $\text{Eu}(\text{OH})_3$ the UCl_3 -type structure can be found in various lanthanide and actinide (lanact) trihalide compounds. Excluding the trifluorides, only four different crystal structures can be observed in lanact trihalides. These structures can be ordered according to an increasing $M^{3+}:X^-$ radius ratio such as: BiI_3 -type rhombohedral [6] \rightarrow AlCl_3 -type monoclinic [6] \rightarrow PuBr_3 -type orthorhombic [8] \rightarrow UCl_3 -type hexagonal [9] (Beck and Gladrow, 1979). The numbers in brackets give the respective coordination numbers of the lanact ion. With increasing pressure the radius ratio increases because of the much softer halide ions compared to the metal ions. Thus, according to this increase and the pressure-coordination rule from Neuhaus (1964), it can be expected that high pressure phase transitions should follow the same order.

With high pressure X-ray diffraction experiments Beck and Gladrow (1979, 1983) could reproduce a part of this series. In particular, they observed transitions from the AlCl_3 -structure and BiI_3 -structure to the PuBr_3 -structure. Several optical studies, utilizing the f-element luminescence or absorption, could also support phase transitions of lanact trihalides following this sequence: AlCl_3 -type \rightarrow PuBr_3 -type: CfBr_3 (Peterson et al., 1985, 1987); BiI_3 -type \rightarrow PuBr_3 -type: AmI_3 (Haire et al., 1985); PuI_3 , CmI_3 (Haire et al., 1987). Beck and Gladrow (1979) pointed out that a transition from the PuBr_3 -structure to the UCl_3 -structure can not be realized due to the higher packing efficiency ($\Sigma V_{\text{ions}}/V_{\text{cell}}$) in the PuBr_3 -structure.

Deviating from the above structural series, Wilmarth et al. (1989) reported phase transitions from the UCl_3 -structure to the PuBr_3 -structure in the case of PrCl_3 and PrBr_3 , deduced from high pressure absorption and Raman studies. The same transition was observed also in the case of CfCl_3 (Peterson et al., 1986; Young et al., 1990) and CmCl_3 (Del Cul et al., 1992). In

principle, such a transition promotes a higher packing efficiency, however, it does not fit to the pressure-coordination rule nor to the radius ratio order of the structures. In all cases the phase transitions were proposed because of slight changes in the absorption spectra in connection with Raman spectra. For example, in the case of PrCl_3 (UCl_3 -structure) above 15.5 GPa a more symmetric shape of the ${}^3\text{H}_4 \rightarrow {}^1\text{D}_2$ band and a loss of intensity in and a lack of resolution of the ${}^3\text{H}_4 \rightarrow {}^1\text{I}_6$ absorption band in relation to the ${}^3\text{H}_4 \rightarrow {}^3\text{P}_1$ absorption band resulted in a spectrum very similar to the orthorhombic PrBr_3 (PuBr_3 -structure) spectrum. In addition, Raman spectra gave further evidence that a phase transition had occurred around 15 GPa. However, from the very slight changes in the absorption spectra under pressure alone, it seems to be difficult to unambiguously propose an UCl_3 to PuBr_3 phase transition in these cases.

In several optical studies on PrBr_3 , NdBr_3 , CeBr_3 , and CeCl_3 a new higher pressure phase beyond the PuBr_3 -type structure has been observed (Peterson, 1994). Further studies on $\text{LaCl}_3:\text{Pr}^{3+}$ (Gregorian et al., 1989) and $\text{La}(\text{C}_2\text{H}_5\text{SO}_4)_3 \cdot 9\text{H}_2\text{O}$ (lanthanum ethylsulfate) doped with Pr^{3+} (Voloshin and Ivchenko, 1980; Voloshin, 1982), both exhibiting the UCl_3 -structure at ambient conditions, also revealed phase transitions to a yet unidentified high-pressure structure. The interpretation of this new structure has been tackled in different ways. Gregorian et al. (1989) used the critical ionic radii which mark the stability ranges of the six different lanthanide halide structures (Greis and Petzel, 1974; Beck and Gladrow, 1979). Relating these radii to the structural data obtained under pressure, they found indications of a possible phase transition to the LaF_3 -structure at around 10 GPa. This result fitted well to the first observation of new unknown lines at around 8 GPa. On the contrary, Voloshin (1988) interpreted the results for $\text{LaCl}_3:\text{Pr}^{3+}$ and also for lanthanum ethylsulfate: Pr^{3+} (Voloshin, 1986) in terms of vibronic states. He argued that the reduction in the distance between f element and its ligands leads to a participation of the f orbitals in the chemical bond. This would cause a vanishing of the pure electronic transitions and the appearance of vibronic lines. In the general case the symmetry should be lowered and all degeneration should be lifted.

In summary, these examples clearly show that the luminescence spectra of the f elements definitely have the ability to indicate a phase transition, however, unambiguous conclusions about the structure of the new phases are quite difficult to draw and may be restricted to special cases.

5. Intensities and lifetimes of f-f transitions

5.1. General considerations

Most electronic transitions between different states of the f-electrons are dominated by electric dipole transitions. Only in exceptional cases like $\text{Eu}(\text{III})$, magnetic dipole transitions are found to be as strong as electric dipole transitions. However, in the case of an f element, electric-dipole transitions between the $4f^N$ states are forbidden because the parity of initial and final state is conserved. Only when the f element is embedded in a crystal providing a point group symmetry that does not contain the inversion operation, these transitions can be observed readily.

In an actual experiment, two different physical quantities connected with electric (or magnetic) dipole transitions are accessible via optical studies, on the one hand the intensities of the

transitions and on the other hand the lifetimes of the excited levels. For transitions between different J multiplets, where the crystal-field split levels of the initial multiplet are equally occupied, the experimental quantities can be easily related to the oscillator strengths used in the parameter calculations. In the case of absorption spectroscopy the integrated area of a transition peak I_0 can be compared directly to the experimental oscillator strength P according to (Görller-Walrand and Binnemans, 1998):

$$I_0 = \frac{8\pi^3}{hc} \frac{N_A}{2303} \nu_0 \frac{1}{3} \left[D_{ED} \frac{(n^2 + 2)^2}{9n} + D_{MD} \cdot n \right] \frac{1}{2J + 1} \quad \text{and}$$

$$P = \frac{8\pi^2 m_e c \nu_0}{h e^2} \frac{1}{3} \left[D_{ED} \frac{(n^2 + 2)^2}{9n} + D_{MD} \cdot n \right] \frac{1}{2J + 1} = 2303 \frac{m_e c^2}{\pi N_A e^2} I_0, \quad (17)$$

where h is Planck's constant, c the speed of light, N_A Avogadro's constant, ν_0 the wavenumber at the absorption maximum, n the refractive index of the material, J the total angular momentum of the ground multiplet, m_e the electron mass, e the elementary charge, and D the dipole strength in a randomly oriented system. The dipole strength can be calculated from the matrix element of the dipole operator $\widehat{\mathbf{O}}$ (MD or ED operator):

$$D = |\langle \Psi_i | \widehat{\mathbf{O}} | \Psi_f \rangle|^2. \quad (18)$$

In the case of luminescence transitions it is usually not appropriate to use the absolute intensities because non-radiative processes such as multiphonon decay or energy transfer processes can effectively change the observed intensities. Similarly, also the experimentally measured lifetime is not suitable because non-radiative processes can effectively shorten the lifetime. However, the radiative branching ratios β_R can still be compared with the calculations. These ratios denote the relative intensities for transitions from the same initial to different final multiplets.

Only if non-radiative processes can be discarded, as for example in cases of diluted f elements with multiplets lying well above the next lowest levels, the radiative lifetimes τ_R can be compared with theoretical calculations. In this case the radiative lifetime is inversely proportional to the oscillator strength of the transition.

The remaining problem in the calculation of intensities and radiative lifetimes is the calculation of the dipole or, in other words, the oscillator strength matrix element in eq. (18). To calculate this element, Judd (1962) and Ofelt (1962) proposed the transition oscillator strengths being due to the mixing of the $4f^{N-1}nd^1$ and $4f^{N-1}ng^1$ configurations into the $4f^N$ configuration by the crystal field. Because this mixing introduces components of different parities, the transitions become allowed. Although this theory has been widely and successfully employed to describe the total oscillator strengths of transitions between different J multiplets, it has been pointed out that also other mechanisms as for example mixing with ligand states will contribute to the observed oscillator strengths (Poon and Newman, 1984).

In the scope of the Judd–Ofelt theory three parameters Ω_2 , Ω_4 , and Ω_6 are commonly used to describe the transitions between J multiplets. For this case, the contributions from individual crystal field split levels of a given multiplet are simply summed up. To account for individual transitions, effective transition operators can be used to derive a parametrization

analogous to the crystal-field Hamiltonian. This procedure introduces parameters A_{ip}^λ , which can be used to calculate the Judd–Ofelt parameters. For a detailed account of this subject see, for example, Görrler-Walrand and Binnemans (1998) and Reid (2000).

As discussed, intensities and lifetimes are related to the oscillator strengths of the f-f transitions which in turn are connected to the mixing of excited configurations $4f^{N-1}nd^1$, $4f^{N-1}ng^1$ or ligand states to the $4f^N$ configuration. The mixing results from configuration interactions due to the odd-parity crystal-field components in the first case and overlap and covalency contributions in the second case. These considerations form the starting-point of high-pressure experiments.

The application of high pressure to f-element compounds should change the configuration interaction as well as the interactions with the ligands. Thus, both intensities and lifetimes should be influenced by pressure. The direction and magnitude of this influence, however, is difficult to forecast because pressure will act in different ways. The mixture with excited configurations is determined by the energy difference and the size of the matrix elements of the crystal-field potential between the configurations.

Obviously, the intensity of a transition depends on the amount of this mixing which can be increased (decreased) by decreasing (increasing) the energy difference to the excited configurations or increasing (decreasing) odd-parity components of the crystal-field potential. Overlap and covalency contributions can be expected to increase under pressure, leading to enhanced mixing and oscillator strengths. However, the increased interaction with the ligands may also lead to enhanced non-radiative decay in case of luminescence measurements, which then would diminish the intensities and lifetimes.

It should be noted that also the refractive index in eq. (17) will change under pressure. This change can be estimated by the Lorenz local-field model, where the refractive index n is related to the atomic polarizability α_P and the density of the material ρ by the Lorentz–Lorenz relation:

$$\frac{n^2 - 1}{n^2 + 1} = \frac{4\pi N_A}{3} \alpha_P \rho. \quad (19)$$

According to eq. (19) the refractive index increases with increasing density (increasing pressure) and increasing polarizability. However, this model is exactly valid only for point dipoles in a cubic arrangement. Therefore, the reliability of this model with respect to quantitative predictions is limited in many cases (Eremets, 1996). A further difficulty here is to estimate the change of the polarizability under pressure.

Johannsen (1997) performed high-pressure experiments on alkali halides to determine the changes of the refractive index with increasing density. According to his results, an increase of the density by around 20% causes an increase of the refractive index of less than 3%. Such a change would increase the intensity of a transition by less than 10% and can thus explain only slight changes in the intensities.

In the following sections it will be shown that a careful analysis of the high pressure effects on intensities and lifetimes can yield valuable information about various aspects of physical interactions leading to the observed intensities and lifetimes. At first, absorption studies will be presented which have the advantage that the observed intensities can be related di-

rectly to the oscillator strengths. In the subsequent section luminescence studies will be discussed where it is possible to study effects due to configuration interactions or energy transfer processes.

5.2. Absorption studies

Only a few absorption studies under pressure with respect to the intensities of f-f transitions can be found in the literature. A systematic and comprehensive study of rare-earth ions in ionic crystals has been performed by Keating and Drickamer (1961a). They studied rare-earth trichlorides, trifluorides, and ethylsulfates at room temperature up to pressures of 18 GPa by means of absorption spectroscopy. The rare earths studied were Pr^{3+} , Nd^{3+} , Sm^{3+} , Ho^{3+} , Er^{3+} , and Tm^{3+} . In all cases they observed an increase of the intensities by approximately 40%. To explain this result, they assumed the crystal-field potential arising from point charges only. In this case the potential contains odd-parity terms proportional to R_1^{-4} , R_1^{-5} , and R_1^{-6} , where R_1 is the distance between the nucleus of the rare-earth ion and the charge e_i of a ligand ion. Estimating a volume reduction of 15–20% at 10 GPa and taking into account only the most important R_1^{-4} term, Keating and Drickamer (1961a) could obtain a theoretical intensity increase of about 45%, in good agreement with the experimentally determined increase. Therefore, they concluded that the increase in intensity was due to an increased mixing of 5d and 4f orbitals due to an increase of the mixing potential.

To extend these studies, Keating and Drickamer (1961b) also investigated UF_3 and UF_4 . In the case of UF_3 the results were similar to the rare-earth fluorides, in particular an increase in intensity could be observed for all transitions. However, for UF_4 they observed increasing as well as decreasing intensities for different lines under pressure. The U^{4+} ion in UF_4 is situated in a position which is only slightly distorted from having a center of symmetry. Thus, the odd-parity components of the crystal-field potential can be quite small and one has to search for other mechanisms contributing to the intensities which can cause the observed decrease under pressure. One mechanism is the mixing of f- and d-orbitals by lattice vibrations. According to Keating and Drickamer (1961b) the mixing is proportional to $(r_0/r)^2 V_e$, where V_e is the even part of the crystalline potential, r_0 denotes the amplitude of vibration of the metal nucleus, and r is the radius of the f orbital. The intensity is proportional to the square of this quantity. Under pressure, V_e and r can be expected to increase, whereas r_0 can be assumed to decrease. In total, this quantity may therefore increase or decrease, depending on the size of the various contributions. Because at the same time the mixing via the odd-parity components of the crystal field can be quite small, it may easily occur that some of the intensities, which are dominated by the lattice vibration mixing show a decreasing intensity under pressure.

5.3. Luminescence studies

In luminescence studies it can often be observed that intensities decrease with increasing pressure. A decreasing luminescence intensity can be ascribed to two main effects. On one hand, the excitation efficiency can decrease due to a pressure-induced shift of absorption bands away from a fixed excitation energy. This effect can be minimized either by a tunable excitation source or by exciting into a band, whose shift is negligible compared to its width.

On the other hand, the luminescence quantum efficiency can decrease. Apart from a decrease of the oscillator strengths themselves, many other mechanisms can cause such reduced quantum efficiencies, as, for example, enhanced electron–phonon coupling, generation of new paths for deexcitation or energy transfer processes. In fact, these processes will not affect the oscillator strengths of the transition but simply influence the occupation of the excited level. Therefore, the oscillator strength of a given transition may still increase under pressure, however, this increase is completely covered up by a fast depletion of the excited level.

The lifetime of an excited level can be used here to distinguish between a change in the oscillator strength or the occupation of an excited level. A decreasing oscillator strength is connected with an increasing lifetime and vice versa. Thus, if the lifetime of a level is decreasing under pressure, the intensity must increase. However, if on the contrary a decreasing intensity is observed, some depletion process must be present and dominate a possible increase in the oscillator strength. Besides depletion also filling processes may occur under pressure. Such a process would require some long-living reservoir which slowly fills the excited level. As a result, a strong enhancement of the intensity may be observed, independent of a change in the oscillator strengths.

The measurement of a lifetime is much more accurate and reliable than the measurement of the absolute luminescence intensity under pressure. Therefore, the majority of studies on f-element compounds reported on pressure-dependent lifetimes only. The compounds studied so far can be found in table 1. In most cases a decrease of the lifetime under pressure has been observed. The following sections will treat the changes in lifetimes or intensities according to the mechanisms responsible for the observed variations.

5.3.1. Influence of $4f^{N-1}5d^1$ configurations

Excited $4f^{N-1}5d^1$ configurations can influence the f-f transitions in two different ways: first, a thermal excitation from excited $4f^N$ states to the $4f^{N-1}5d^1$ configuration can lead to a quenching of the f-f luminescence and decreasing lifetimes, and second, an increased (decreased) mixing of $4f^{N-1}5d^1$ to the $4f^N$ wavefunctions can cause increasing (decreasing) intensities and decreasing (increasing) lifetimes.

One of the best studied systems is SrFCl doped with Sm^{2+} . Jovanić et al. (1997a) studied the lifetime of the $^5D_0 \rightarrow ^7F_0$ transition of the Sm^{2+} ion as a function of pressure and found a pronounced exponential decrease from approximately 1.4 ms to 0.5 ms up to 10 GPa. In a subsequent paper they used the Lorentz–Lorentz equation (eq. (9)) to attribute the observed decrease of the lifetime to changes of the refractive index under pressure (Jovanić et al., 1997b). The same explanation was also applied to the case of the mixed crystal $\text{SrFCl}_{0.5}\text{Br}_{0.5}:\text{Sm}^{2+}$, where a similar decrease of the lifetime was noted (Jovanić, 2001). Although in both cases a good agreement between calculated and experimental values was reached, the model used is clearly oversimplified. Despite many assumptions on polarizabilities, dipole matrix elements and others, Jovanić et al. (1997b) neglected all other radiative transitions from 5D_0 . Taking into account these transitions, which contribute to the overall transition probability and henceforth to the lifetime, one would have to consider for example different factors for the energies, the wavelength dependence of the refractive index, and a completely different factor for the magnetic dipole transition $^5D_0 \rightarrow ^7F_1$ (see eq. (17)).

In addition, from structural data for SrFCl (Shen et al., 1994) under pressure, the increase of the density of SrFCl up to 10 GPa can be calculated to be approximately 13%. Comparing this increase with the high-pressure experiments on the refractive index of the alkali halides (Johannsen, 1997), one can expect a small change of perhaps 2% of the refractive index. Such a change should decrease the lifetime by no more than a few percent. Nevertheless, the studies from Jovanić and coworkers at least indicate that the change of the refractive index under pressure may give rise to some corrections of quantitative evaluations of pressure effects.

The lowest state of the $4f^5 5d^1$ configuration of SrFCl:Sm²⁺ is located only at around 19 000 cm⁻¹ above the ⁷F₀ ground state of the $4f^6$ configuration (Shen and Bray, 1998a). Under pressure, the energy distance between both configurations is rapidly decreasing. This should provide a unique possibility to study the influence of this configuration on intensities and lifetimes of the f-f transitions. Following these considerations, Shen et al. (1997) and Shen and Bray (1998a, 1999) have presented a detailed investigation on SrFCl:Sm²⁺ and CaFCl:Sm²⁺.

They considered two effects, on one hand the mixing of the wavefunctions of the $4f^6$ and $4f^5 5d^1$ configurations and on the other hand the nonradiative crossover between levels of both configurations. To analyze the nonradiative crossover, they used the single configurational coordinate (SCC) energy level diagram for Sm²⁺ in SrFCl depicted in fig. 12. The missing ⁷F_J ($J = 0, \dots, 6$) multiplets would be placed directly below the ⁵D_J ($J = 0, \dots, 2$) multiplets with the minimum of the ⁷F₀ parabola at the zero of energy. The ⁵D_J ($J = 0, \dots, 2$) multiplets have small Franck–Condon offsets relative to the ground ⁷F₀ multiplet, in contrast to the much larger Franck–Condon offset for the excited $4f^5 5d^1$ configuration.

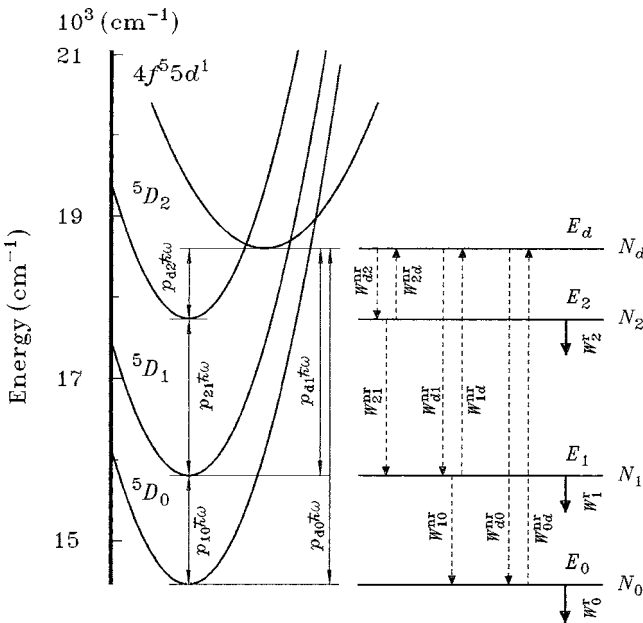


Fig. 12. Single configurational coordinate energy level diagram for SrFCl:Sm²⁺ (from Shen and Bray (1998a)). For details see text.

The quantities used in fig. 12 are the energies E relative to the ground state 7F_0 , the energy differences $p\hbar\omega$ between different states, where $\hbar\omega$ is the energy of the single optical phonon associated with the diagram and p is the number of phonons bridging the respective energy gaps, the populations N , and radiative W^r and nonradiative W^{nr} transition rates. All quantities are characterized by indices d , J or J' or combinations thereof, where d denotes the $4f^55d^1$ configuration and J , J' different 5D_J multiplets.

Studying the intensities and lifetimes as a function of temperature first, Shen and Bray (1998a) could fit the radiative and nonradiative rates depicted in fig. 12 to the experimentally observed variations. They obtained excellent agreement of calculated and experimental results. In particular, it was shown that quenching of the 5D_2 luminescence with increasing temperature between 50 K and 100 K is due to a thermally induced ${}^5D_2 \rightarrow 4f^55d^1 \rightarrow {}^5D_{1,0}$ crossover. Further quenching of the 5D_1 luminescence at temperatures above 100 K, could be assigned to a thermally induced ${}^5D_1 \rightarrow 4f^55d^1 \rightarrow {}^5D_0$ process and a direct ${}^5D_1 \rightarrow {}^5D_0$ multiphonon relaxation process.

In a second step, Shen and Bray (1998a) studied the changes of the 5D_0 and 5D_1 lifetimes of $\text{SrFCl}:\text{Sm}^{2+}$ and $\text{CaFCl}:\text{Sm}^{2+}$ under pressure. In both systems they observed an exponential decrease as shown in fig. 13 for the case of the 5D_0 lifetime at room temperature. According to their analysis of the temperature effects, the measured lifetime of the ${}^5D_0 \rightarrow {}^7F_0$ transition represents an almost pure radiative lifetime. A strong decrease under pressure therefore indicates an increase in the radiative rate W_J^r . This in turn was attributed to an increased elec-

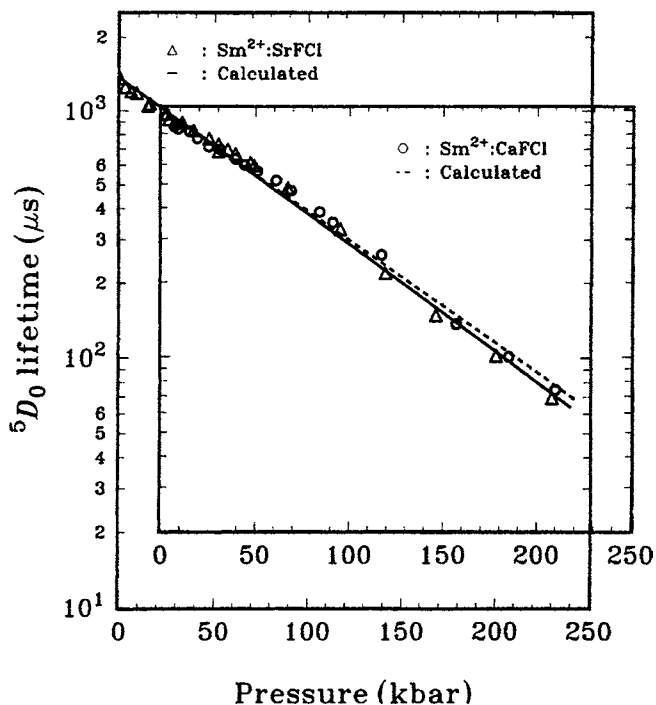


Fig. 13. Calculated and experimental results for the pressure dependence of the RT 5D_0 lifetimes of $\text{SrFCl}:\text{Sm}^{2+}$ and $\text{CaFCl}:\text{Sm}^{2+}$ (from Shen and Bray (1998a)). The data for $\text{CaFCl}:\text{Sm}^{2+}$ are shifted with respect to those of $\text{SrFCl}:\text{Sm}^{2+}$ by a pressure of 2.2 GPa. The solid and dashed curves were calculated as explained in the text.

tronic $4f^55d^1$ admixture resulting from a shift of the $4f^55d^1$ configuration to lower energy with pressure.

To study this admixture in detail, Shen and Bray (1998a) calculated the radiative rates taking into account electric and magnetic dipole transitions. While magnetic dipole transitions are allowed within the $4f$ shell, electric dipole transitions depend on the size of the wavefunction mixing due to odd crystal-field terms. In their calculation, Shen and Bray (1998a) considered the conventional Judd–Ofelt electric dipole contribution, designated as the 2nd electric dipole contribution, as well as a 3rd electric dipole contribution suggested by Wybourne (1968). This contribution takes into account the spin–orbit coupling of multiplets with different spin states in the excited configuration. This coupling, in connection with the odd crystal-field terms, is capable of mixing different spin states to the multiplets of the $4f^6$ configuration, thus relaxing the spin selection rule for the ${}^5D_0 \rightarrow {}^7F_0$ transition.

Only three quantities, two odd crystal-field parameters B_0^1 and B_0^3 and the energy distance E_d between the two configurations, were used as parameters in the calculations to describe the changes of the 5D_0 lifetime. Performing the fits, Shen and Bray (1998a) assumed a linear dependence of B_0^1 , B_0^3/B_0^1 , and E_d on pressure. As the result for the pressure dependence of these quantities they finally found (p in GPa, E_d and B_0^k in cm^{-1}):

$$\begin{aligned} E_d &= 18630 - 230(2)p, \\ 10^{10} B_0^1 &= 56(2) + 6.4(6)p, \\ B_0^3/B_0^1 &= 104(8) - 7.0(8)p. \end{aligned} \quad (20)$$

The calculated lifetimes, taking into account these shifts, are included in fig. 13 as dashed and solid lines. They show an excellent agreement with the experimental values. The pressure shift of $-230 \text{ cm}^{-1}/\text{GPa}$ of the excited $4f^55d^1$ configuration, deduced from the lifetime calculations, also agrees well with the experimental value of $-200 \text{ cm}^{-1}/\text{GPa}$ for pure SmFCl given by Bolduan et al. (1985). This gives strong evidence that taking into account magnetic and the two electric dipole contributions is necessary to completely describe the behavior of the 5D_0 lifetime. In particular, this result shows that the spin–orbit coupling within the excited configuration gives an important contribution for the mixing of the wavefunctions via the odd crystal-field parameters. More difficulties arose in the case of the calculated 5D_1 lifetime under pressure, which showed only poor agreement with experiment. The reasons for this disagreement were not understood, but were tentatively related to a breakdown of the closure approximation used in the model.

Gleason et al. (1993) presented a study on $\text{La}_2\text{O}_2\text{S:Tb}^{3+}$ and $\text{Gd}_2\text{O}_2\text{S:Tb}^{3+}$ under pressure. Tb^{3+} has a similar energy level structure to Sm^{2+} , the main difference is a reversed order of the multiplets with respect to the total angular momentum J . Accordingly, the ground state is 7F_6 and the multiplet with the highest energy of the 7F term is 7F_0 , located at approximately 6000 cm^{-1} above the ground state. The next highest multiplets are 5D_4 and 5D_3 , at around 20000 cm^{-1} and 26500 cm^{-1} , respectively. The $4f^75d^1$ configuration lies only about 2000 cm^{-1} above the 5D_3 multiplet.

Under pressure, Gleason et al. (1993) observed a strong decrease of the 5D_3 lifetime, which was attributed to a nonradiative transfer to the excited $4f^75d^1$ configuration. This configuration

was shown to rapidly shift with a rate of $-460 \text{ cm}^{-1}/\text{GPa}$ to lower energies. Considering the nonradiative transfer in the SCC model, they could successfully describe the pressure-induced variation of the lifetime of the ${}^5\text{D}_3$ multiplet.

The lifetime of the lower-lying, isolated ${}^5\text{D}_4$ multiplet of Tb^{3+} should be determined mainly by radiative transitions, similar to the case of the ${}^5\text{D}_0$ multiplet of Sm^{2+} . However, in the case of Tb^{3+} no change of the lifetime and hence of the radiative rate, was observed under pressures up to 5 GPa. This indicates that the mixing with the excited $4f^75d^1$ configuration does not change, despite of the large shift with pressure. One reason may simply be that the energy difference between the ${}^5\text{D}_4$ multiplet and the $4f^75d^1$ configuration for Tb^{3+} is larger at ambient pressure than in the case of $\text{SrFCl}:\text{Sm}^{2+}$. However, due to the strong shift, this difference becomes comparable to Sm^{2+} at around 5 GPa. Thus, a change of the lifetime should have been observed in this pressure range. The obvious differences may indicate for example a different variation of the odd crystal-field parameters for $\text{La}_2\text{O}_2\text{S}:\text{Tb}^{3+}$. Another possibility is that the spin-orbit coupling contribution, which was very important for the change in the lifetime of ${}^5\text{D}_0$ of Sm^{2+} , does not play any significant role in the case of the ${}^5\text{D}_4$ multiplet of Tb^{3+} . This could mean that the spin-orbit coupling contribution is not important either specifically for the ${}^5\text{D}_4$ multiplet or for Tb^{3+} in general.

5.3.2. Influence of charge transfer states

Similar to the influence of the excited $4f^{N-1}5d^1$ configurations, charge transfer states (CTS) can affect the lifetimes and intensities of f-f transitions in two different ways. On one hand the possibility for nonradiative energy transfer from an excited level of the $4f^N$ configuration to the CTS is enabled and on the other hand the wavefunctions of the CTS can be mixed to the $4f^N$ configuration. The lifetimes of the f-f transitions should decrease with increasing nonradiative energy transfer or increasing wavefunction mixing. Furthermore, the intensities should decrease with increasing nonradiative transfer but increase with enhanced wavefunction mixing.

A system which has been studied in some detail under pressure is $\text{R}_2\text{O}_2\text{S}:\text{Eu}^{3+}$ ($R = \text{Y, La}$). The configurational coordinate diagram of $\text{Y}_2\text{O}_2\text{S}:\text{Eu}^{3+}$ is shown in fig. 14. In many regards the energy level scheme is similar to the isoelectronic Sm^{2+} in SrFCl (see sect. 5.3.1). The main difference is that the first excited state is not an intrinsic ionic state of the rare-earth ion itself, but an extended state involving the wavefunctions of the ligand orbitals. It is therefore interesting to look for possible differences in the high pressure behavior.

A detailed analysis of this system at ambient pressure has been performed by Fonger and Struck (1970) and Struck and Fonger (1970). They studied the intensities and lifetimes of the ${}^5\text{D}_J$ multiplets as a function of temperature and attributed the observed changes to thermally promoted transitions ${}^5\text{D} \rightarrow \text{CTS}$ followed by return crossovers to lower ${}^5\text{D}$ states. Such a process is indicated by arrows in fig. 14. On the contrary, Wickersheim et al. (1968) have reported similar measurements, but tried to explain the successive quenching of the ${}^5\text{D}$ states through multiphonon emission.

To get further evidence about which model is more appropriate, Webster and Drickamer (1980a) have measured the luminescence efficiency of $\text{La}_2\text{O}_2\text{S}:\text{Eu}^{3+}$ and $\text{Y}_2\text{O}_2\text{S}:\text{Eu}^{3+}$ and the lifetimes of the lanthanum compound under pressures up to 12 GPa. Intensities and life-

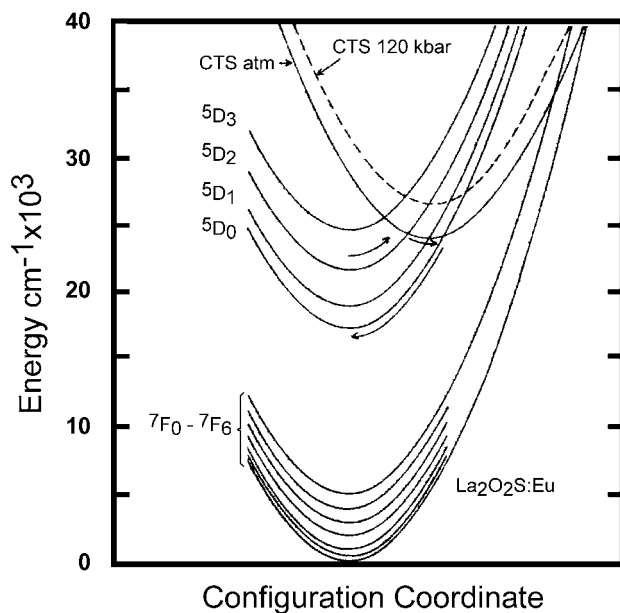


Fig. 14. Configurational coordinate diagram for $\text{La}_2\text{O}_2\text{S}:\text{Eu}^{3+}$ showing the position of the charge transfer state (CTS) at ambient and high pressure (from Webster and Drickamer (1980a)). The arrows indicate the $5\text{D}_J \rightarrow \text{CTS} \rightarrow 5\text{D}_{J'}$ ($J > J'$) relaxation pathway. (10 kbar = 1 GPa).

times of $\text{La}_2\text{O}_2\text{S}:\text{Eu}^{3+}$ and $\text{Y}_2\text{O}_2\text{S}:\text{Eu}^{3+}$ were also measured by Gleason et al. (1993) and Wang et al. (1984), respectively, who got mainly the same results as Webster and Drickamer (1980a). To exclude effects due to energy transfer between different Eu^{3+} ions, Webster and Drickamer (1980a) their discussion on the results for the sample with the lowest Eu^{3+} concentration of 0.1%. For higher concentrations up to 3% they could prove that a damping of the pressure effects occurred, however, the basic findings were the same.

To explain the high-pressure results, Webster and Drickamer (1980a) slightly modified the model from Struck and Fonger (1970). They took into account an activation energy $E_{i \text{ act}}$, related to the energy difference between the 5D_i level and the CTS, and various nonradiative processes. To determine the crucial position of the CTS under pressure, Webster and Drickamer (1980a) performed absorption studies and found a blue shift of the CTS at a rate of approximately $180 \text{ cm}^{-1}/\text{GPa}$. The position of the CTS at 12 GPa is shown in fig. 14. Taking into account this large shift, the $5\text{D} \rightarrow \text{CTS} \rightarrow 5\text{D}$ high-pressure model predicts distinct changes of the 5D_J lifetimes and intensities.

Actually, the main effects on the intensities of the $5\text{D}_J \rightarrow 7\text{F}_0$ ($J = 0, 1, 2, 3$) transitions of $\text{La}_2\text{O}_2\text{S}:\text{Eu}^{3+}$ under pressure are found to perfectly match with the $5\text{D} \rightarrow \text{CTS} \rightarrow 5\text{D}$ model. In particular, Webster and Drickamer (1980a) found that the emissions from 5D_0 and 5D_1 decreased in intensity with increasing pressure. On the contrary, the very weak 5D_2 emission increased by a large factor, stayed approximately constant between 2 GPa and 8 GPa and finally decreased above 8 GPa. The emission of 5D_3 appeared at about 5–6 GPa and increased rapidly in intensity.

The results for $\text{Y}_2\text{O}_2\text{S}:\text{Eu}^{3+}$ differed quantitatively from the results for $\text{La}_2\text{O}_2\text{S}:\text{Eu}^{3+}$, but this could be explained simply by the difference in location of the charge transfer state and

its shift with pressure. Finally, it should be noted that the changes in the lifetimes of the 5D_J multiplets could also be described with the above model. The high-pressure results therefore clearly support the model of luminescence quenching due to a ${}^5D \rightarrow \text{CTS} \rightarrow {}^5D$ crossover in favor of nonradiative decay.

Further systems in which the nonradiative energy transfer from ligand states to f elements has been studied in detail are the $[\text{Pt}(\text{CN})_4]_3$ and $[\text{Au}(\text{CN})_2]_3$ complexes. In particular, Yersin and coworkers have studied $\text{Eu}_2[\text{Pt}(\text{CN})_4]_3 \cdot 18\text{H}_2\text{O}$ (Yersin et al., 1979), $\text{Sm}_2[\text{Pt}(\text{CN})_4]_3 \cdot 18\text{H}_2\text{O}$ (Yersin and Stock, 1982), and $\text{Eu}[\text{Au}(\text{CN})_2]_3 \cdot 3\text{H}_2\text{O}$ (Yersin et al., 1998).

These systems are of great interest to energy transfer investigations since they exhibit extraordinary properties which mainly result from the unusual arrangement of the $[\text{Pt}(\text{CN})_4]_3^{2-}$ and $[\text{Au}(\text{CN})_2]_3$ complexes, acting as donors. In the case of $R_2[\text{Pt}(\text{CN})_4]_3 \cdot 18\text{H}_2\text{O}$, the $[\text{Pt}(\text{CN})_4]_3$ complexes are arranged in linear stacks, leading to highly coupled electronic wavefunctions along the stacking axis (*c*-axis). The rare-earth ions are the acceptors located between the stacks. The $[\text{Au}(\text{CN})_2]_3$ complexes in $\text{Eu}[\text{Au}(\text{CN})_2]_3 \cdot 3\text{H}_2\text{O}$ form two-dimensional layers alternating with layers of rare-earth ions. The low-energy states of the dicyanoaurates(I) as well as the tetracyanoplatinates(II) can be traced to the Au (Pt) 5d, 6s HOMO and the Au (Pt) 6p, CN π^* LUMO, respectively (Yersin and Gliemann, 1978). Due to the strong electronic interaction between the complexes, valence and conduction bands develop. Finally, strong electron-hole interactions lead to excitonic states with a binding energy of up to 4000 cm^{-1} (Eichhorn et al., 1981).

One of the outstanding properties of these substances is the extreme tunability of the electronic states under high pressure. In many cases a red shift on the order of $2000 \text{ cm}^{-1}/\text{GPa}$ has been observed (Yersin and Riedl, 1995). In addition, an effective nonradiative energy transfer from the cyano donor complexes to the f elements has been observed. In the case of $\text{Eu}[\text{Au}(\text{CN})_2]_3 \cdot 3\text{H}_2\text{O}$ this process even totally quenches the otherwise very intense and broad emission from the $[\text{Au}(\text{CN})_2]^-$ layers. However, because of the very strong red shift of the donor electronic states, it is possible to shift the donor states over different levels of the f element. Especially, resonant and nonresonant energy transfer conditions can be achieved to study the transfer mechanism.

Figure 15 shows the emission spectra of single crystal $\text{Eu}[\text{Au}(\text{CN})_2]_3 \cdot 3\text{H}_2\text{O}$ at various pressures (Yersin et al., 1998). At ambient pressure only luminescence from the Eu^{3+} ion (${}^5D_0 \rightarrow {}^7F_J$ and some weak transitions from 5D_1) but no luminescence from the donor can be observed. However, at pressures above approximately 1 GPa at 20 K, a very weak emission occurs and grows in with increasing pressure. This effect is a consequence of a pressure-induced tuning off of the nonradiative energy transfer from the dicyanoaurate(I) donors to the Eu^{3+} acceptors. Taking into account the pressure dependence of the donor emission band, it is possible to extrapolate the ambient pressure position to be about $23600 \pm 300 \text{ cm}^{-1}$.

The transfer rate P_{D-A} between donor D and acceptor A can be expressed by (Förster, 1951; Dexter, 1953):

$$P_{D-A} = F(R) \int f_D^e(\bar{\nu}) f_A^a(\bar{\nu}) d\bar{\nu}. \quad (21)$$

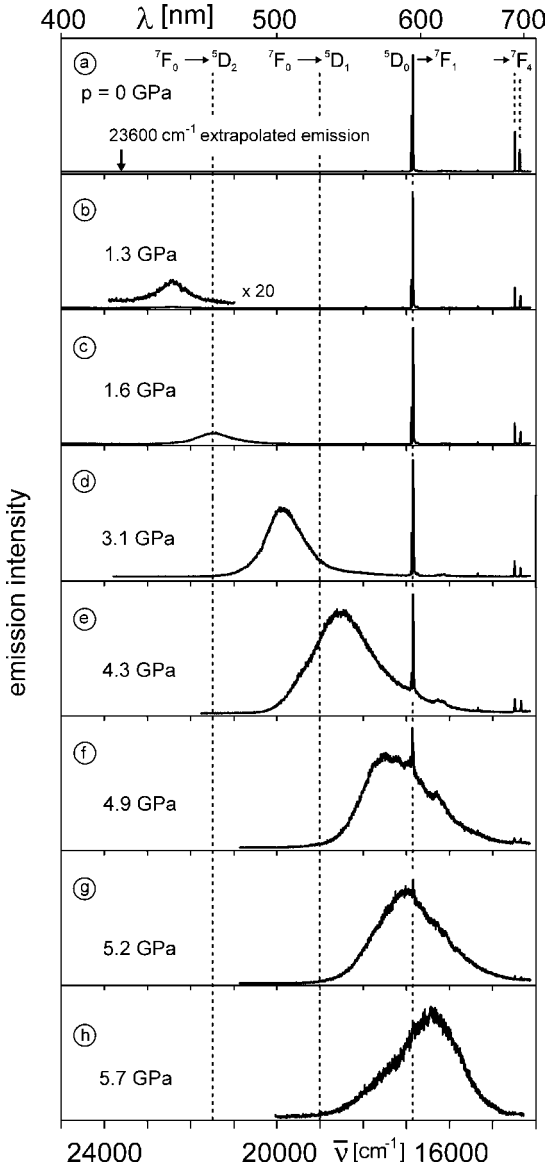


Fig. 15. Luminescence spectra of single-crystal $\text{Eu}[\text{Au}(\text{CN})_2]_3 \cdot 3\text{H}_2\text{O}$ at various pressures ($T = 20 \text{ K}$, $\lambda_{\text{exc}} = 363.8 \text{ nm}$). With increasing pressure, the energy transfer from the dicynoaurates donors to the Eu^{3+} acceptors can successively be tuned off. The vertical lines characterize positions of Eu^{3+} absorptions and emissions, respectively (from Yersin et al. (1998)). (10 kbar = 1 GPa).

The integral is the spectral overlap integral of the donor emission $f_D^e(\bar{\nu})$ with the acceptor absorption profile $f_A^a(\bar{\nu})$ for resonance condition. $F(R)$ summarizes the essential mechanisms, like the Dexter (1953) exchange or the Förster (1951) multipole mechanism with their specific R distance dependences.

According to eq. (21), resonance energy transfer can occur only if the spectral overlap integral differs from zero. At ambient pressure, this is the case for only two multiplets of Eu^{3+} , ${}^5\text{L}_6$ and ${}^5\text{D}_3$, with estimated barycenters near 25100 cm^{-1} and 24300 cm^{-1} , respectively. With increasing pressure, the spectral overlap integral with these multiplets is tuned to zero, leading to the appearance of the donor emission. With further increasing pressure, the overlap integral is continuously tuned on and subsequently off with the lower lying multiplets of Eu^{3+} in the order ${}^5\text{D}_2$ (maximum overlap at around 1.6 GPa), ${}^5\text{D}_1$ (3.9 GPa) and ${}^5\text{D}_0$ (5.3 GPa). At 1.6 GPa the intensity of the donor emission increased by a factor of 10, although the spectral overlap with ${}^5\text{D}_2$ reached its maximum. This clearly reveals that the energy transfer is much more efficient to ${}^5\text{D}_3$ than to ${}^5\text{D}_2$. At the highest pressures the overlap is zero with all but the lowest ${}^5\text{D}_0$ multiplet. Under these conditions no f-f luminescence could be observed at all, showing that no energy transfer from the donor to the ${}^5\text{D}_0$ multiplet occurs.

Similar examples for energy transfer from ligand localized levels to highly localized 4f levels are represented by the rare-earth chelates. Voloshin and Savutskii (1976) studied europium benzoylacetate under pressures up to 6 GPa. Exciting the triplet level they could observe the luminescence from the Eu^{3+} ion. It was possible to describe the observed initial increase in the quantum yield of the Eu^{3+} luminescence up to 2.5 GPa and the following decrease by the exchange resonance theory (Dexter, 1953). A more detailed study on different *Tris* chelates of Sm^{3+} , Eu^{3+} , Gd^{3+} , and Tb^{3+} with β -diketonates was performed by Hayes and Drickamer (1982), where the most dramatic effects of pressure on energy transfer phenomena were found for the Eu^{3+} chelates.

A schematic diagram of the ligand localized and Eu^{3+} excited energy levels are shown in fig. 16. The ligand levels are denoted with *S* and *T* for the singlet and triplet states, respectively.

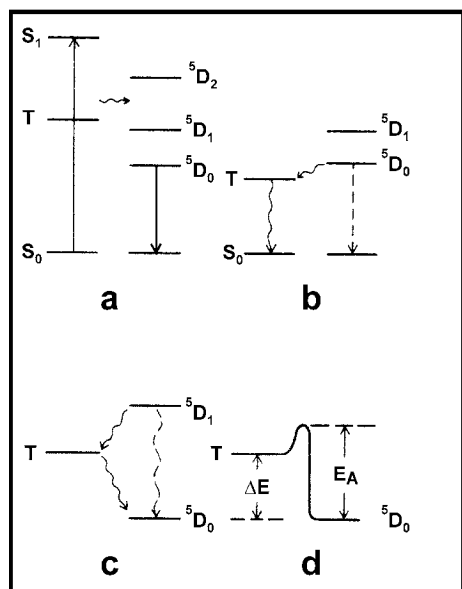


Fig. 16. Energy transfer processes in Eu chelates (from Hayes and Drickamer (1982)). Wiggly arrows represent nonradiative processes. Solid and dashed arrows represent radiative processes, with a lesser probability for the dashed arrows; a, b, c, d: see text.

tively. Under pressure both levels show a strong red shift. The shift of the lower-lying triplet levels was 1400 cm^{-1} for Thenoyltrifluoroacetylacetonone (TTF) and 1000 cm^{-1} for Dibenzoylmethide (DBM) up to 4 GPa. The simultaneous shift of the 5D_J multiplets of Eu^{3+} is more than one order of magnitude smaller.

Figure 16 also indicates the various optical processes that were observed in europium chelates in the study of Hayes and Drickamer (1982). Part (a) illustrates the excitation of the singlet ligand state, followed by a relaxation to the triplet state and a subsequent energy transfer process which induces the emission of the Eu^{3+} ion. Part (c) shows the situation at higher pressures, when the triplet level lies between 5D_1 and 5D_0 . In this case a relaxation from the excited 5D_1 to the 5D_0 multiplet can occur via the intermediate triplet level under proper conditions. Finally, part (b) and (d) indicate a thermal deactivation process back to the ligand localized levels. This process already occurs with the triplet level above 5D_0 (see part d) and is responsible for a pronounced quenching of the 5D_0 luminescence at higher pressures for EuDBM.

One of the aims of the high pressure studies of Hayes and Drickamer (1982) was to test this triplet quenching hypothesis (Sato and Wada, 1970). According to part (d) of fig. 16, an activation energy E_A is needed to transfer the energy stored in 5D_0 to the triplet level. This energy can be slightly larger than the energy difference ΔE between 5D_0 and the triplet level (Struck and Fonger, 1975). Assuming that the quenching of the 5D_0 luminescence in EuDBM can be related with this process, a one-to-one correspondence of the red shift of the triplet energy and the change in the activation energy should be found. Under pressure exactly this behavior was found, which definitely confirmed the triplet quenching process as the main mode of thermal deactivation in these systems.

5.3.3. Energy transfer processes in insulators

In the preceding section the pressure effects on the energy transfer from electronic states of constituents of the host lattice to the f element have been discussed. Different to this case, another source of energy transfer can be the electronic state of some point defect in the host lattice which will be considered now. As simple examples, the point defect can be another f element (either of the same or a different kind) or a transition metal element.

Pressure effects on the energy transfer between f elements of the same kind were studied by Merkle et al. (1981) for the case of $\text{Nd}^{3+}\text{-Nd}^{3+}$ pairs in $\text{Nd}_x\text{Y}_{1-x}\text{P}_5\text{O}_{14}$ ($x = 1, 0.1$). This material was studied in detail because of its potential use as a stoichiometric laser material. An outstanding property is a very weak concentration quenching of the luminescence. The total luminescence decay rate of the ${}^4F_{3/2}$ multiplet in $\text{Nd}_x\text{Y}_{1-x}\text{P}_5\text{O}_{14}$ ($x = 1, 0.1$) under pressure is shown in fig. 17. Obviously the stoichiometric compound shows a much larger increase of the decay rate than the doped compound.

Merkle et al. (1981) discussed three possible mechanisms of the pressure-enhanced decay rate: an increase of the radiative decay rate of each Nd^{3+} ion, an increase of the nonradiative decay rate of each Nd^{3+} ion, or an increase in the interaction between Nd^{3+} ions leading to luminescence quenching. The nonradiative decay rates for the ${}^4F_{3/2}$ multiplet were estimated to contribute less than 20% to the total decay rate (Powell et al., 1980) at ambient pressure.

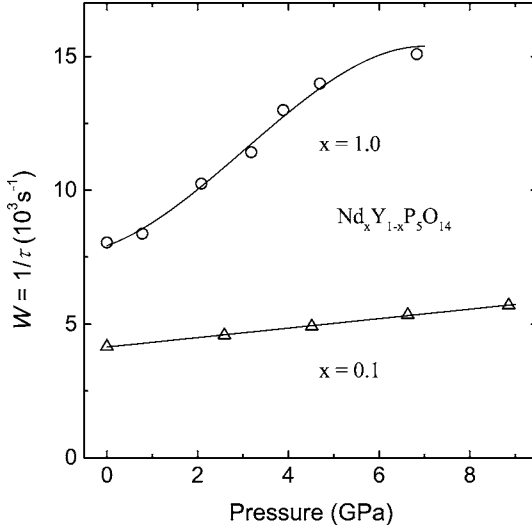


Fig. 17. Total luminescence decay rate of ${}^4F_{3/2}$ in $\text{Nd}_x\text{Y}_{1-x}\text{P}_5\text{O}_{14}$ for $x = 0.1$ and 1.0 , as a function of pressure (from Merkle et al. (1981)).

Because it is very unlikely that pressure can cause an increase of this small contribution to the extent necessary to explain the $\text{NdP}_5\text{O}_{14}$ data, the second possibility was ruled out.

The increase in the radiative decay rate of ${}^4F_{3/2}$ under pressure was estimated from the measured absorption strength of the ${}^4I_{9/2} \rightarrow {}^4F_{3/2}$ transitions and the relative luminescence intensities for $\text{NdP}_5\text{O}_{14}$. It was found that an increase by a factor of about 1.2(4) can be expected. However, this value is much smaller than the observed increase (see fig. 17) and thus cannot be used to explain the experimental results. Because it has been shown that the oscillator strengths for Nd^{3+} transitions in $\text{Nd}_x\text{La}_{1-x}\text{P}_5\text{O}_{14}$ are independent of the Nd^{3+} concentration (Auzel, 1976), it can be assumed that the change in the radiative decay rate with pressure should also depend little on concentration. Therefore, the same estimated increase of 1.2(4) for the stoichiometric compound can be expected also in the case of the doped sample. Indeed, in this case the experimental result agrees well with the prediction. This clearly reveals that in the case of the stoichiometric compound a further mechanism, which is not due to single-ion processes, must contribute to the increased decay rates.

Merkle et al. (1981) considered two multi-ion quenching processes that are possible in this case, namely a cross-relaxation between pairs of Nd^{3+} ions and energy migration to sinks. A possible strong increase of the cross-relaxation mechanism $\text{Nd}({}^4F_{3/2}) + \text{Nd}({}^4I_{9/2}) \rightarrow \text{Nd}({}^4I_{15/2}) + \text{Nd}({}^4I_{15/2})$ could be ruled out because of various spectral properties observed under pressure. The final possibility therefore was an increased energy migration to traps. To check the plausibility of this hypothesis, Merkle et al. (1981) used a simple diffusion model, where the rate of energy transfer to traps is proportional to the energy diffusion coefficient, D , which can be calculated for resonant dipole-dipole interaction by (Trlifaj, 1958):

$$W^{\text{mig}} \propto D \propto a^{-4} W_{\text{ion}}^2 \Delta \nu_{\text{hom}}^{-1} \quad (22)$$

Here the average lattice spacing is denoted by a , W_{ion} is the single-ion transition rate and $\Delta\nu_{\text{hom}}$ is the homogeneous linewidth which is used to approximate the spectral overlap integral between the two interacting ions. As the result, the decay rate due to migration should increase by a factor of 2.4(1.0) up to 6.8 GPa. Correcting the data from fig. 17 for the change of the radiative decay rate one finds an experimental increase by a factor of 2.2(3). This value is in close agreement with the prediction from eq. (22). Therefore, Merkle et al. (1981) concluded that energy migration is the dominant effect leading to an increase in the decay rates of $\text{NdP}_5\text{O}_{14}$ under pressure.

Similar conclusions were drawn by Blanzat et al. (1984) who studied $\text{Tb}_x\text{La}_{1-x}\text{P}_5\text{O}_{14}$, $\text{Eu}_x\text{La}_{1-x}\text{P}_5\text{O}_{14}$ and mixed single crystals $\text{Tb}_x\text{Eu}_{1-x}\text{P}_5\text{O}_{14}$ under pressure. By selective excitation of the $^5\text{D}_4$ multiplet of Tb^{3+} the luminescence of Eu^{3+} could be observed due to an efficient $\text{Tb}^{3+} \rightarrow \text{Eu}^{3+}$ energy transfer. Under pressure the lifetime of the Eu^{3+} luminescence decreased which was interpreted by a weak back-transfer from Eu^{3+} to Tb^{3+} due to the increased overlapping of the $^5\text{D}_4$ multiplet of Tb^{3+} with the $^5\text{D}_2$ multiplet of Eu^{3+} .

The decay of the Tb^{3+} luminescence in the mixed crystals is dominated by a very fast energy diffusion process to the Eu^{3+} acceptors at ambient pressure, leading to a single-exponential decay. The decay time increases with increasing Tb^{3+} concentration which is characteristic for a diffusion-limited relaxation mechanism since the average distance required for energy to migrate to an Eu^{3+} ion is increased. At higher pressures the direct $\text{Tb}^{3+} \rightarrow \text{Eu}^{3+}$ energy transfer is strongly enhanced, resulting in an initial non-exponential decay. Consistent with a dominant energy diffusion process, the decay time of the following exponential part decreases with increasing pressure due to decreasing average distances to the Eu^{3+} ions. In summary, the work of Blanzat et al. (1984) supports the conclusions of Merkle et al. (1981) who identified the energy migration mechanism as the dominant energy transfer mechanism in $\text{NdP}_5\text{O}_{14}$.

In the beginning of sect. 5.3 it was mentioned that besides depletion processes due to enhanced non-radiative decay, filling processes due to some long-living reservoir may also occur. $\text{La}_2\text{O}_2\text{S}$ doped with Eu^{3+} represents such a case. Two types of traps are responsible there for the slow energy release, one type forming a shallow and the other a deep storage. The phosphorescence of this material was studied by Webster and Drickamer (1980b) under pressures up to 6 GPa. They approximated the decay curves of the Eu^{3+} luminescence as the sum of two exponential terms, belonging to the shallow and deep traps, respectively. Under pressure they observed an increase of both lifetimes of the detrapping processes. These lifetimes depend on the activation energy necessary for detrapping and thus can be used to determine the activation energy as a function of pressure. In their study, Webster and Drickamer (1980b) found that both activation energies increased under pressure. It was argued that the formation of the charge transfer state represents the detrapping process. This assumption is supported by the high pressure studies where energy could be stored in the traps at high pressure for an apparently indefinite length of time and appeared as emission from the Eu^{3+} ion on the sudden release of pressure, a phenomenon similar to thermoluminescence.

A technological interesting possibility is the energy transfer from transition-metal ions to f elements. Transition-metal ions offer broad absorption bands which can be easily excited by flashlamps. A subsequent energy transfer to an f element can then result in a sharp emission

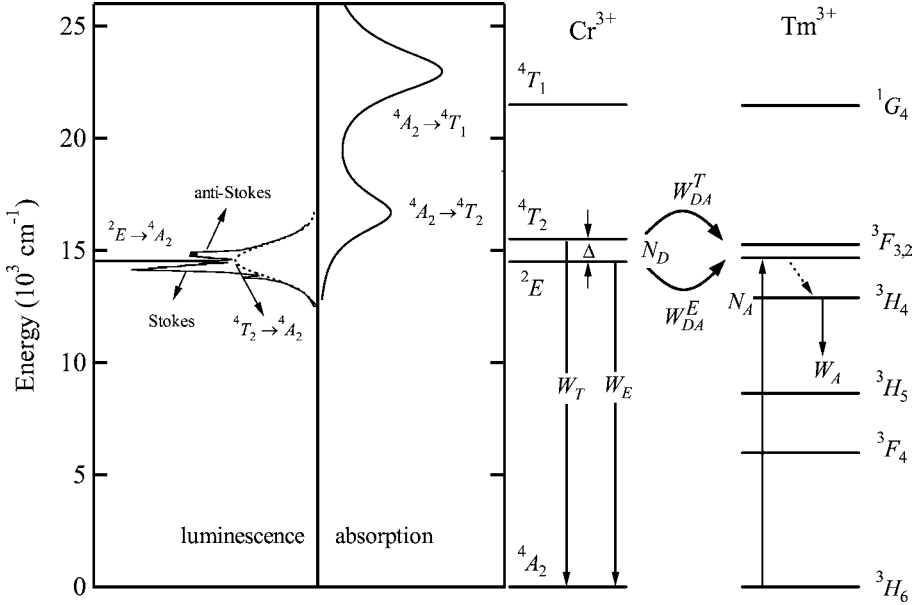


Fig. 18. Schematic energy level diagrams of Cr^{3+} and Tm^{3+} in YAG showing the energy transfer from Cr^{3+} to Tm^{3+} . The absorption and luminescence spectra of $\text{YAG}:\text{Cr}^{3+}$ (0.5 at.%) are shown at ambient pressure and room temperature (from Shen et al. (2000)).

in the near infrared. Such a process may be used to develop efficient laser materials. A typical system of this type is $\text{Cr}^{3+}:\text{Tm}^{3+}:\text{Y}_3\text{Al}_5\text{O}_{12}$ (YAG). This material has been studied under high pressure by Wamsley and Bray (1994a, 1995) and Shen et al. (2000).

A schematic energy-level diagram of Cr^{3+} and Tm^{3+} in YAG together with the luminescence and absorption spectra of Cr^{3+} are shown in fig. 18. Three primary $\text{Cr}^{3+} \rightarrow \text{Tm}^{3+}$ energy transfer pathways can be identified: thermally activated energy transfer from the ${}^4\text{T}_2$ state (${}^4\text{T}_2$ ET), thermally activated energy transfer from the ${}^2\text{E}$ anti-Stokes phonon sidebands (${}^2\text{E}$ anti-Stokes ET), and temperature-independent energy transfer from the zero phonon and Stokes phonon sidebands of the ${}^2\text{E}$ state (${}^2\text{E}$ Stokes ET).

In a first step Shen et al. (2000) studied the temperature dependence of the Cr^{3+} luminescence. Setting up the dynamic rate equations for the $\text{Cr}^{3+}-\text{Tm}^{3+}$ system, the number N_D of Cr^{3+} donor ions in the thermally coupled ${}^4\text{T}_2-{}^2\text{E}$ excited states can be calculated according to

$$N_D(t) = N_D(0)e^{-W_D t} e^{-P_{\text{DA}}(t)}$$

$$\text{with } P_{\text{DA}}(t) = \sum_s N_s \ln(1 - C_A + C_A e^{-W_{\text{DA}}(R_s)t}). \quad (23)$$

Here $N_D(0)$ is the number of donors excited at $t = 0$, W_D is the intracenter decay rate of the coupled ${}^4\text{T}_2-{}^2\text{E}$ states of Cr^{3+} , C_A is equivalent to the acceptor doping concentration, N_s is

the number of equivalent acceptor sites in the coordination shell s at a distance R_s from the donor, and $W_{DA}(R_s)$ is the donor–acceptor transfer rate which is assumed to be the same for all acceptor ions in the same shell s . In their analysis, Shen et al. (2000) took into account the first eight acceptor coordination shells of the Cr^{3+} ion and a dipole–dipole energy transfer mechanism. For an accurate description of the decay curves of the Cr^{3+} luminescence, it was shown that all three transfer pathways described above had to be taken into account. In particular, three temperature regions could be distinguished by the relative weight of the pathways: at temperatures below ~ 75 K neither the ${}^4\text{T}_2$ state nor the ${}^2\text{E}$ anti-Stokes phonon sidebands contributed significantly to the decay, resulting in a constant W_{DA} transfer rate due to ${}^2\text{E}$ Stokes ET. With increasing temperature the increasing ${}^2\text{E}$ anti-Stokes phonon sidebands lead to an enhanced transfer rate. With further increasing temperature above ~ 175 K the thermal population of the ${}^4\text{T}_2$ state becomes appreciable, resulting in a even stronger increase of the energy transfer rate.

The temperature dependence of the energy transfer rate W_{DA} is related to a changing occupation of the ${}^2\text{E}$ anti-Stokes phonon sidebands and the ${}^4\text{T}_2$ state. On the contrary, pressure significantly increases the energy separation Δ between the ${}^4\text{T}_2$ and ${}^2\text{E}$ states, whereas the energy of the zero phonon and the vibronic ${}^2\text{E} \rightarrow {}^4\text{A}_2$ transitions of Cr^{3+} change only weakly with pressure. Thus, pressure almost solely influences the occupation of the ${}^4\text{T}_2$ state and with it its contribution to the energy transfer rate, but does not affect the other contributions connected with the ${}^2\text{E}$ state.

According to these considerations, Shen et al. (2000) took advantage of this situation by artificially eliminating the energy transfer due to the ${}^4\text{T}_2$ state by the application of high pressure. They first studied the decay curves of the Cr^{3+} luminescence under pressure at room-temperature and analyzed them with eq. (23). Assuming again a dipole–dipole transfer mechanism and taking into account the first eight acceptor coordination shells, they obtained the $\text{Cr}^{3+} \rightarrow \text{Tm}^{3+}$ transfer rate W_{DA} as a function of pressure, as shown in fig. 19.

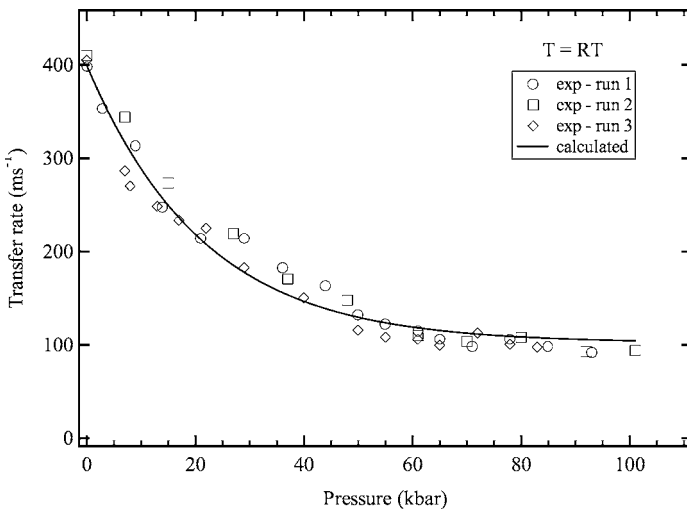


Fig. 19. Room temperature $\text{Cr}^{3+} \rightarrow \text{Tm}^{3+}$ transfer rate W_{DA} in Cr^{3+} (0.7 at.): Tm^{3+} (2 at.):YAG as a function of pressure (from Shen et al. (2000)). W_{DA} was obtained from fits to the experimental decay curves at different pressures assuming dipole–dipole energy transfer. The solid line has been calculated as described in the text. (10 kbar = 1 GPa).

The pressure dependence of W_{DA} can be divided into different regions. From ambient pressure to around 4 GPa a very fast decrease of the transfer rate can be noted. This range corresponds to the decreasing occupation of the 4T_2 state with increasing energy separation Δ under pressure. Above approximately 6 GPa a leveling off can be observed, indicating that now only the temperature and pressure independent part of the 2E Stokes ET contribute to the transfer rate. The solid curve in fig. 19 represents a calculation of the transfer rate taking into account the three pathways for energy transfer and the pressure-induced increase of the energy separation Δ (Wamsley and Bray, 1994b). Obviously a very good agreement with the data was obtained.

The importance of the three different pathways for energy transfer can now be isolated by considering three cases:

- (1) The limiting transfer rate at ambient pressure and low temperatures $W_{DA} \sim 10 \text{ ms}^{-1}$ can be regarded as a measure for 2E Stokes ET.
- (2) The limiting high-pressure transfer rate at room temperature $W_{DA} \sim 95 \text{ ms}^{-1}$ contains 2E Stokes ET as well as 2E anti-Stokes ET. Because both contributions do not change with pressure, they can be directly related to ambient pressure room temperature conditions.
- (3) The ambient pressure, room temperature rate of $W_{DA} \sim 400 \text{ ms}^{-1}$ represents a sum of all three contributions. Subtracting the value obtained in case two directly indicates the importance of the 4T_2 ET part.

Finally, in a last step Shen et al. (2000) also analyzed the spectra and decay curves of the Tm^{3+} ions. On the basis of the luminescence spectra they noted that Tm^{3+} ions located in the first coordination shell of the Cr^{3+} ions (C-type) showed a distinctly different spectral pattern compared to the almost similar patterns of more distant Tm^{3+} ions (N'-type). Studying the decay curves of both types of Tm^{3+} ions at different temperatures, they could show that the energy transfer from the Cr^{3+} ions to the C-type ions is much faster than to the N'-type ions. However, at room temperature the energy transfer to the N'-type ions dominate, which is due to an overall strongly increased energy transfer (participation of the 4T_2 state) and a saturation of the transfer to C-type ions. This case is described by the Inokuti–Hirayama model for energy transfer, where a random distribution of acceptor sites is assumed (Inokuti and Hirayama, 1965). At higher pressures, where the energy transfer due to the 4T_2 state is eliminated again, the overall transfer rate decreases and thus the energy transfer to the C-type ions gains importance. Similar to the low-temperature case, the Inokuti–Hirayama model then starts to breakdown because the inherent assumptions of the model are no longer fulfilled.

5.3.4. Energy transfer processes in semiconductors

In the case of semiconductors doped with f elements a different kind of an energy transfer process can be observed, namely from extended band states or excitonic states to the highly localized f-element states. Such a process is different from the cases discussed in the preceding sections, where the energy transfer from point defects (or at the most molecular states) was considered. The interest in semiconductors doped with f elements is obvious, because of their potential to combine sharp f-element luminescence with the possibility of simple electrical excitation via the semiconductor host. However, a quenching of the luminescence with

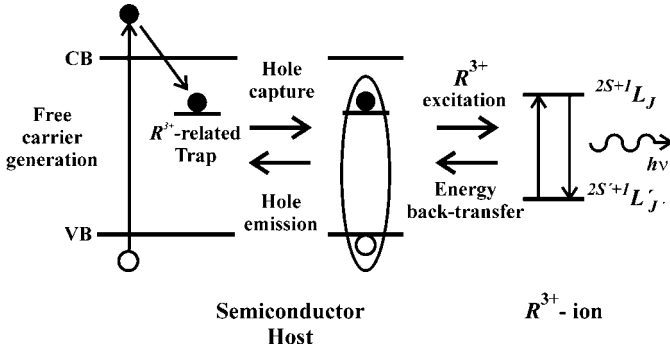


Fig. 20. Energy back-transfer model describing the energy transfer between the semiconductor host and the lanthanide ion R^{3+} (Culp et al., 1997; Takarabe et al., 1995).

increasing temperature and the very low efficiencies found for f elements in semiconductors already at room temperature, prevented them from the use as opto-electronic devices.

To address the problem of low efficiencies, one needs a better understanding of the nature of f-element centers in the semiconductor lattice, their energy level structure in relationship to the host band structure and the relevant excitation mechanisms. In this respect, high pressure offers the unique possibility to study energy transfer processes while continuously shifting the host band edges with respect to the f-element energy levels. Despite this advantage, only few systems have been studied under pressure so far. These include some systems doped with the Er^{3+} ion, where the technological interest is due to the emission in the infrared region at $1.54 \mu\text{m}$, a wavelength which matches the minimum loss of silica fibers. Another system is InP:Yb^{3+} which has the advantage that the Yb^{3+} ions form only one kind of luminescence centers in the InP host and in addition, with only one f-electron missing in the 4f shell, Yb^{3+} possesses the simplest electronic structure of all f elements.

The excitation mechanism of the f elements in semiconductors can be illustrated by fig. 20. Through carrier injection or a host photoexcitation process electrons and holes are created. The f element, acting as an electron or hole trap catches a carrier and becomes negatively or positively charged. The Coulombic potential of the charged center subsequently attracts a further carrier of opposite charge, leading to an exciton bound at the f-element center. Finally, the exciton transfers its energy to the 4f-shell by a nonradiative recombination.

Taking into account an energy back-transfer mechanism as indicated in fig. 20 it was also possible to explain the observed temperature quenching of the f-f luminescence in InP:Yb^{3+} as well as in GaAs:Er^{3+} . During the energy back-transfer process at higher temperatures, the energy of the excited rare-earth ion is used to once again create an e-h pair by phonon-assisted nonradiative recombination (a variety of the Auger effect) at the rare-earth ion (Taguchi et al., 1994). This e-h pair can then recombine or completely dissociate and thus quench the f-f luminescence.

A first test of this model was performed with pressure experiments on InP:Yb^{3+} . Here the Yb^{3+} ion introduces an electron trap to the semiconductor host. The pressure-induced shift of the ${}^2F_{5/2} \rightarrow {}^2F_{7/2}$ intra 4f shell transitions amounts to 0.96 meV/GPa up to 4 GPa (Stapor et al., 1991), while the bandgap energy of InP increases by 85 meV/GPa (Trommer et al., 1980).

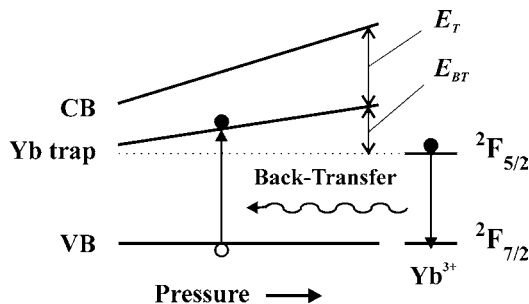


Fig. 21. Change of the Yb^{3+} trap level under pressure. The Yb^{3+} ground state is arbitrarily aligned with the valence band (Culp et al., 1997; Takarabe et al., 1995).

This behavior is schematically shown in fig. 21, where the change in the ${}^2\text{F}_{5/2}-{}^2\text{F}_{7/2}$ splitting, being about two orders of magnitude smaller than the bandgap rise, has been neglected.

Two energies in fig. 21 are important quantities for the luminescence behavior. First, the energy E_T represents the binding energy of the rare earth bound exciton with respect to the conduction band and second, E_{BT} , the necessary energy for back-transfer, corresponds to the difference between the bound exciton recombination energy and the ${}^2\text{F}_{5/2} \rightarrow {}^2\text{F}_{7/2}$ transition energy of the Er^{3+} ion. Assuming a thermal equilibrium between the bound e-h pairs and the excited Yb^{3+} ions, the intensity ratio of the band-edge related emission I_{InP} due to the bound e-h pairs and the Yb^{3+} luminescence I_{Yb} depends on the energy E_{BT} (Takarabe, 1996).

Measuring the variations of the intensity ratio $I_{\text{InP}}/I_{\text{Yb}}$ under pressure, Takarabe (1996) was able to determine the energy difference E_{BT} and found a pressure-induced shift of 70 meV/GPa which is close to the shift of the band-edge related luminescence due to the bound e-h pairs. Furthermore, under pressure it was possible to completely recover the thermally quenched luminescence of the Yb^{3+} ion at temperatures of 220 K and 260 K (Takarabe et al., 1994) as well as at room temperature (Takarabe, 1996). The minimum pressure at which the luminescence could be observed again was shown to increase with increasing temperature. All these facts fitted well to the proposed back-transfer model, which was thus strongly supported by the pressure experiments.

The same model has been applied also to GaAs:Er^{3+} (Takarabe et al., 1995, 1997; Hogg et al., 1997b; Culp et al., 1997) under pressure. In addition to the intensity measurements, Culp et al. (1997) also studied the lifetime of the ${}^4\text{I}_{13/2} \rightarrow {}^4\text{I}_{15/2}$ transition of Er^{3+} in GaAs. At ambient pressure, a temperature study revealed that the lifetime at first did slightly increase with increasing temperature, although the intensity was already decreasing. Only above 150 K did the lifetime start to decrease. This result is still consistent with the back-transfer model if additionally the dissociation of the bound exciton is taken into account. This process requires a second different activation energy which is needed to remove the Coulombic bound hole from the negatively charged trap. The dissociation can occur already at lower temperatures, preventing the energy transfer from the exciton to the f element. Accordingly, only the intensity, but not the lifetime changes. At higher temperatures the back-transfer process is added to the dissociation which then decreases both intensity and lifetime. To account for both processes under pressure, Culp et al. (1997) considered a two-process quenching model

of the form:

$$X = \frac{X_0}{1 + A_1 \exp\left(-\frac{E_1}{kT}\right) + A_2 \exp\left(-\frac{E_2}{kT}\right)}, \quad (24)$$

where E_1 and E_2 denote the activation energies and X is either the intensity or the lifetime of the Er^{3+} luminescence. As the result they obtained $E_1 = 13.4 \pm 0.3$ meV, which was assigned to the exciton dissociation process and $E_2 = 115.8 \pm 3.4$ meV, which was assigned to the back-transfer process. Under a pressure of 4.2 GPa, the quenching of the luminescence was reduced by nearly an order of magnitude at room temperature, an observation which is identical to the case of InP:Yb^{3+} (Takarabe, 1996). A further fit of the activation energies at 4.2 GPa gave an almost constant value for $E_1 = 10.4 \pm 3.0$ meV, a result which fits to the assumption of this activation energy being due to the Coulombic electron-hole binding energy. The change of the second activation energy was estimated to lie between +6 and +50 meV/GPa. This value is very uncertain due to the already weak effects of the back-transfer process. However, it is comparable to the experimental shift found for the Er^{3+} related trap in GaAs:Er,O of 36 meV/GPa (Takarabe et al., 1995) and to theoretical calculations, giving values of 24 meV/GPa (Chadi and Chang, 1988) and 10–40 meV/GPa (Ren et al., 1982).

The luminescence intensity of the Er^{3+} ion under pressure has also been studied in Si. This semiconductor possesses an indirect bandgap, contrary to the cases discussed above. At ambient pressure, the 4f-4f luminescence of the Er^{3+} ion in Si is quenched at temperatures exceeding 100 K, but contrary to the case of direct bandgaps, indirect bandgaps decrease with increasing pressure. Therefore, provided the energy back-transfer model can be applied here, the observed quenching temperature for the Er^{3+} ion should decrease under pressure. In high-pressure experiments, Przybylinska et al. (1996) and Jantsch et al. (1996) observed exactly the opposite, namely an increase of the quenching temperature with pressure. However, this behavior was not attributed to a breakdown of the back-transfer model but to the existence of deep oxygen related levels which mediated the energy transfer process.

As in the case of Si, GaP is also a semiconductor with an indirect bandgap. Culp et al. (1996) have studied the Er^{3+} ion doped into GaP under pressures up to 5 GPa. Contrary to the cases discussed above, the Er^{3+} luminescence does not show a pronounced quenching with increasing temperature. In addition, the Er^{3+} emission intensity is considerably stronger when exciting with below-bandgap energies, which promotes carriers directly to the Er^{3+} related trap, than with above-bandgap energies, where the free carriers which are created subsequently have to be captured by the Er^{3+} trap. Under pressure, the above-bandgap excitation became as effective as the below-bandgap excitation. This behavior was explained by the fact that competitive capture of free carriers by deep levels, responsible for the lower efficiency for above-bandgap excitation at ambient pressure, is significantly reduced with increasing pressure.

6. Electron–phonon interaction

In general, due to the localized and screened nature of the 4f-electrons, their interaction with phonons is weak. However, this interaction affects the 4f states in many different ways and

can give important contributions in specific cases. In principle, the interaction influences the energy levels as well as the transition probabilities between different states. A quite common feature is the thermal line broadening, however, the energy levels can also be shifted or split by the electron–phonon interaction. Furthermore, transitions between 4f states involving the creation or annihilation of phonons (phonon sidebands) can be observed. A pronounced effect on the intensities can be noted also for specific transitions where the luminescence can be quenched completely via nonradiative transitions through multiphonon relaxation or a quenching process involving charge transfer states or $4f^{N-1}5d^1$ configurations (see sects. 5.3.1 and 5.3.2). On the other hand, phonons in crystals with a rare-earth site symmetry including an inversion center, can be the only source to mix configurations with an odd parity to the 4f-states and thus allow for the zero-phonon transitions.

In sects. 5.3.1 and 5.3.2 the electron–phonon coupling was necessary to mediate an energy transfer process but no attempt was made to discuss the coupling strength between an electronic level and a lattice vibration itself. In fact, this coupling strength has been the subject of very few high pressure studies and thus will be considered only briefly in this section. One of the first studies was performed by Voloshin (1986), who reported on the intensity changes of vibronic lines for Pr^{3+} in lanthanum ethylsulfate under pressures up to 2.5 GPa. Furthermore, a qualitative experiment has been presented by Shen and Holzapfel (1993), who studied the phonon sidebands of the transitions ${}^5\text{D}_0 \rightarrow {}^7\text{F}_{1,2}$ and ${}^5\text{D}_1 \rightarrow {}^7\text{F}_1$ of the Sm^{2+} ion in BaFCl under pressures up to 8 GPa at 20 K. The bandshape of the sidebands was similar for all transitions, however, they noted a strong enhancement of the phonon sidebands under pressure solely for the ${}^5\text{D}_1 \rightarrow {}^7\text{F}_1$ transition. This enhancement reflected an increasing electron–phonon coupling under pressure.

Changing electron–phonon couplings have been observed also for $\text{Cs}_2\text{NaTmCl}_6$. In this case the relative intensities of different Raman lines showed an anomalous behavior under pressure, which has been qualitatively interpreted as due to an electron–phonon coupling of the $a\Gamma_5$ electronic state with the $\Gamma_1 + \nu_5(t_{2g})$ vibronic state (Mak et al., 2002).

Likewise qualitative studies have been performed for two different glasses. Lochhead and Bray (1995) used high pressure to characterize the local structure of Eu^{3+} ions in sodium disilicate glass. Their luminescence and lifetime studies revealed two different pressure regimes with different behavior of intensities and lifetimes. In the high-pressure regime from 4 GPa to the maximum pressure of 21 GPa achieved in their experiment, a decrease of the ${}^5\text{D}_0 \rightarrow {}^7\text{F}_0$ lifetime from approximately 2.5 ms down to 1.4 ms is accompanied by a decrease in the luminescence signal and an increase in the linewidth. These observations could be explained by an enhanced nonradiative decay under pressure, which in turn was related to an increased coupling to local vibrations because of shorter Eu–O bonds. Similar results were reported by Jayasankar et al. (2000) in a high pressure study on Sm^{3+} in lithium fluoroborate glass. They also attributed a decrease in the decay time of the ${}^4\text{G}(4)_{5/2} \rightarrow {}^6\text{H}_J$ transition from 1.3 ms at ambient pressure to 0.6 ms at 21 GPa to an increased coupling to local vibrations.

The electron–phonon interaction has been studied also in a LiTmF_4 crystal by Kupchikov et al. (1982). They have measured Raman and infrared reflection spectra under pressures up to 1.2 GPa and at temperatures ranging from 4.2 K to 300 K. The interaction of optical phonons with electronic excitations in this system of rare-earth ions was detected by anomalous tem-

Table 11

Bare crystal-field (CF) and phonon (ph) energies and the CF–phonon coupling constant V at ambient pressure and the corresponding pressure coefficients for the compounds $\text{NdBa}_2\text{Cu}_3\text{O}_7$ and $\text{Pb}_2\text{Sr}_2\text{NdCu}_3\text{O}_8$ (Goncharov et al., 1994). CE and SC refer to ceramic and single-crystal samples, respectively

Substance	ν_{CF} (cm^{-1})	$d\nu_{\text{CF}}/dP$ ($\text{cm}^{-1}/\text{GPa}$)	ν_{ph} (cm^{-1})	$d\nu_{\text{ph}}/dP$ ($\text{cm}^{-1}/\text{GPa}$)	V (cm^{-1})	dV/dP ($\text{cm}^{-1}/\text{GPa}$)
$\text{Pb}_2\text{Sr}_2\text{NdCu}_3\text{O}_8$ SC	319	3.47	293	2.67	25.5(4)	0.29(7)
$\text{NdBa}_2\text{Cu}_3\text{O}_7$ CE	295	3.0	293	3.0	25	–
$\text{NdBa}_2\text{Cu}_3\text{O}_7$ CE	300	2.68	308	2.37	26.7(3)	0.16(3)
$\text{NdBa}_2\text{Cu}_3\text{O}_7$ SC	297	2.46	307	2.80	28.1(3)	0.26(4)

perature and pressure dependences of some lines in the lattice vibration spectra. Using a microscopic theory, Kupchikov et al. (1982) could determine binding parameters between rare-earth ions and optical phonons and use these parameters to estimate shifts in lattice vibrational lines as a function of temperature and pressure.

A quantitative analysis of the electron–phonon coupling was performed by Goncharov et al. (1994) on the Nd-containing cuprates $\text{NdBa}_2\text{Cu}_3\text{O}_7$ and $\text{Pb}_2\text{Sr}_2\text{NdCu}_3\text{O}_8$. Here the effect of pressure on the coupling between a Nd^{3+} crystal-field excitation and a CuO_2 -plane oxygen phonon (B_{1g}) near 300 cm^{-1} was investigated up to 14 GPa. In both samples the interaction between an excited level of the $^4I_{9/2}$ ground multiplet and the out-of-plane oxygen vibration leads to a doublet structure in the Raman spectra. While in the case of $\text{NdBa}_2\text{Cu}_3\text{O}_7$ the bare crystal-field excitation is lower in energy than the phonon frequency, the opposite is found for $\text{Pb}_2\text{Sr}_2\text{NdCu}_3\text{O}_8$.

The motivation of the high-pressure experiments arose from the fact that the application of pressure results in simultaneous changes of the crystal-field and phonon energies and their energy differences. From the frequencies and intensities of the coupled excitations under pressure, it is possible to derive the pressure dependence of the bare crystal-field energy level and the coupling constant using a two-level coupling model (Thalmeier and Fulde, 1982). The change of the coupling constant can subsequently be related to the corresponding changes of the interatomic distances. According to the two-level coupling model, the bare crystal-field excitation ω_{CF} and phonon ω_{ph} frequencies and the coupling constant V can be expressed as

$$\omega_{\text{CF}} = \frac{\nu_1 k + \nu_2}{1 + k}, \quad \omega_{\text{ph}} = \frac{\nu_1 + \nu_2 k}{1 + k} \quad \text{and} \quad V = \frac{1}{2} \cdot \sqrt{(\nu_1 - \nu_2)^2 - (\omega_{\text{ph}} - \omega_{\text{CF}})^2}, \quad (25)$$

where ν_1 and ν_2 denote the line positions and k is their oscillator strength ratio. The results for the pressure-induced changes of the bare energies and the coupling constant are summarized in table 11. It is obvious that the crystal-field splittings as well as the electron–phonon coupling increase with increasing pressure for both samples, regardless of the relative ordering of the bare crystal-field level and the phonon energy.

7. Conclusions

The development of the diamond anvil cell opened an easy, fast, and reliable possibility to study optical spectra as a function of applied pressure. With this elegant method, the energy

level scheme, transition probabilities and intensities, energy transfer processes and many other properties of ions in crystals can be related to the structural parameters of the host lattice. Besides the structural relationship, an important feature concerns the ability of pressure to "tune" energies of various electronic states in a different manner. This allows to alter energy differences and to explicitly study their respective influence on the state under investigation.

While ambient pressure studies must rely on discrete changes of crucial parameters, the high pressure method is capable of generating continuous changes of interatomic distances or relative energies of different electronic states. Moreover, at the same time the chemical composition of the rare-earth compound is conserved under pressure, while ambient pressure studies usually have to consider different compounds. In this sense, the application of high pressure can solve physical problems which can not be accessed by any other method.

The main emphasis in this chapter was put on the optical investigations under high pressure. These studies reveal a considerable part of the energy level scheme and can be used also to study lifetimes and intensities. All these quantities are related to and influenced by the electronic states of the other constituents in the crystal. However, it should be noted that many other physical methods have been employed in connection with high-pressure devices.

Although the high-pressure method itself is rather simple to use, high-pressure physics is still a somewhat "exotic" tool for investigating rare-earth compounds. This seems rather surprising if the unique possibilities for example for the determination of intrinsic crystal-field parameters are considered. In many cases, theories explicitly predict certain distance dependences, which can be verified straightforward by the application of pressure, which continuously alters the interatomic distances.

The knowledge of fundamental relations between the properties of rare earths and the electronic and physical structure of the host compound is essential for the development of improved or new materials. However, up to now only a rather small amount of high-pressure studies compared to ambient pressure studies has been performed. It is hoped that this chapter has demonstrated the ability of high-pressure physics in exploring fundamental relationships especially for rare-earth ions and will stimulate further experimental and theoretical work in this area.

Acknowledgement

Financial support under grants from the Deutsche Forschungsgemeinschaft (DFG) is gratefully acknowledged. The author wishes to thank W.B. Holzapfel (Universität Paderborn, Germany) for his continuous support during the past years and W. Sievers (Universität Paderborn, Germany) for editorial help.

References

- Arashi, H., Ishigame, M., 1982. *Jpn. J. Appl. Phys.* **21**, 1647.
Asaumi, K., Ruoff, A.L., 1986. *Phys. Rev. B* **33**, 5633.
Auzel, F., 1976. *IEEE J. Quantum Electron.* **QE-12**, 258.
Barnett, J.D., Block, S., Piermarini, G.J., 1973. *Rev. Sci. Instrum.* **44**, 1.
Baumann, M., Bilal, B.A., 1986. *Z. Naturforsch.* **41a**, 974.

- Beck, H.P., Gladrow, E., 1979. *Z. Anorg. Allg. Chem.* **453**, 79.
- Beck, H.P., Gladrow, E., 1983. *Z. Anorg. Allg. Chem.* **502**, 178.
- Bell, P.M., Mao, H.K., 1981. *Carnegie Institute Washington Yearbook* **80**, 404.
- Bethe, H.A., 1929. *Ann. Physik* **3**, 133.
- Bi, Q., Brown, J.M., Sato-Sorensen, Y., 1990. *J. Appl. Phys.* **68**, 5357.
- Bishton, S.S., Newman, D.J., 1968. *J. Chem. Phys. Lett.* **1**, 616.
- Blanzat, B., Tercier, N., Denis, J.P., Barthou, C., 1984. *J. de Phys.* **45**, C8-71.
- Bolduan, F., Hochheimer, H.D., Beck, H.P., 1985. *Phys. Stat. Sol. (b)* **127**, 673.
- Bradbury, M.I., Newman, D.J., 1967. *Chem. Phys. Lett.* **1**, 44.
- Bray, K.L., 2001. *High Pressure Probes of Electronic Structure and Luminescence Properties of Transition Metal and Lanthanide Systems*. In: Yersin, H. (Ed.), *Topics in Current Chemistry*, Vol. **213**. Springer-Verlag, Berlin, Heidelberg.
- Bungenstock, C., 1999. Ph.D. Thesis (Paderborn).
- Bungenstock, C., Tröster, Th., Holzapfel, W.B., Bini, R., Ulivi, L., Cavalieri, S., 1998. *J. Phys.: Condens. Matter* **10**, 9329.
- Bungenstock, C., Tröster, Th., Holzapfel, W.B., Fini, L., Santoro, M., 2000a. *J. Phys.: Condens. Matter* **12**, 6959.
- Bungenstock, C., Tröster, Th., Holzapfel, W.B., 2000b. *Phys. Rev. B* **62**, 7945.
- Bungenstock, C., Reiß, G., Nessel, F., Giefers, H., Nowitzke, G., Wortmann, G., Holzapfel, W.B., Haines, J., Léger, J.M., 2001. To be published.
- Burdick, G.W., Richardson, F.S., 1997. *J. Alloys Compd.* **250**, 293.
- Burdick, G.W., Tröster, Th. 2003. To be published.
- Chadi, D.J., Chang, K.J., 1988. *Phys. Rev. Lett.* **61**, 873.
- Chang, N.C., Gruber, J.B., Leavitt, R.P., Morrison, C.A., 1982. *J. Chem. Phys.* **76**, 3877.
- Chen, G., Stump, N.A., Haire, R.G., Peterson, J.R., Abraham, M.M., 1992a. *Solid State Commun.* **84**, 313.
- Chen, G., Stump, N.A., Haire, R.G., Peterson, J.R., 1992b. *J. Alloys Compd.* **181**, 503.
- Chen, G., Haire, R.G., Peterson, J.R., 1992c. *High Press. Res.* **6**, 371.
- Chen, G., Stump, N.A., Haire, R.G., Peterson, J.R., Abraham, M.M., 1992d. *J. Phys. Chem. Solids* **53**, 1253.
- Chen, G., Haire, R.G., Peterson, J.R., 1992e. *Appl. Spectrosc.* **46**, 273.
- Chen, G., Stump, N.A., Haire, R.G., Peterson, J.R., 1994a. *Solid State Commun.* **89**, 1005.
- Chen, G., Stump, N.A., Haire, R.G., Burns, J.B., Peterson, J.R., 1994b. *High Press. Res.* **12**, 83.
- Chen, G., Wang, S., Haire, R.G., Peterson, J.R., 1994c. *Appl. Spectroscopy* **48**, 1026.
- Chen, G., Haire, R.G., Peterson, J.R., Abraham, M.M., 1994d. *J. Phys. Chem. Solids* **55**, 313.
- Chen, G., Haire, R.G., Peterson, J.R., 1995. *J. Phys. Chem. Solids* **56**, 1095.
- Chen, G., Hölsa, J., Peterson, J.R., 1997. *J. Phys. Chem. Solids* **58**, 2031.
- Chi, Y., Liu, S., Shen, W., Wang, L., Zou, G., 1986. *Physica* **139–140B**, 555.
- Chi, Y., Liu, S., Zhang, H., Wang, L., 1988. *J. Lumin.* **40–41**, 303.
- Chi, Y., Liu, S., Wang, Q., Wang, L., Zou, G., 1990. *High Press. Res.* **3**, 150.
- Chi, Y., Liu, S., Li, H., Zhao, X., Wang, L., 1997. *J. Alloys Compd.* **256**, 1.
- Chi, Y., Liu, S., Wang, Q., Wang, L., 1998a. *Physica B* **245**, 293.
- Chi, Y., Liu, S., Wang, L., Zou, G., Wang, Q., 1998b. *Rev. High Pressure Sci. Technol.* **7**, 754.
- Culp, T.D., Wang, X.Z., Kuech, T.F., Wessels, B.W., Bray, K.L., 1996. In: Coffa, S., Polman, A., Schwartz, R.N. (Eds.), *Rare Earth Doped Semiconductors II*. In: *MRS Symposium Proceedings*, Vol. **422**. Materials Research Society, Pittsburgh, p. 101.
- Culp, T.D., Hömmerich, U., Redwing, J.M., Kuech, T.F., Bray, K.L., 1997. *J. Appl. Phys.* **82**, 368.
- Curtis, M.M., Newman, D.J., 1970. *J. Chem. Phys.* **52**, 1340.
- Datchi, F., LeToullec, R., Loubeyre, P., 1997. *J. Appl. Phys.* **81**, 3333.
- Del Cul, G.D., Murray, G.M., Nave, S.E., Chang, C.-T.P., Begun, G.M., Peterson, J.R., 1991. *Eur. J. Solid State Inorg. Chem.* **28**, 155.
- Del Cul, G.D., Haire, R.G., Peterson, J.R., 1992. *J. Alloys Compd.* **181**, 63.
- Denning, R., Snellgrove, T., Woodwark, D., 1976. *Mol. Phys.* **32**, 419.
- Dexter, D.L., 1953. *J. Chem. Phys.* **21**, 836.
- Dieke, G.H., 1968. *Spectra and Energy Levels of Rare-earth Ions in Crystals*. Wiley, New York.
- Dierolf, V., Kutsenko, A.B., Sandmann, C., Tröster, Th., Corradi, G., 2000. *J. Lumin.* **87–89**, 989.
- Dierolf, V., Sandmann, C., Tröster, Th., Corradi, G., 2003. To be published.
- Drotning, W.D., Drickamer, H.G., 1973. *J. Chem. Phys.* **59**, 3482.

- Eichhorn, M., Willig, F., Yersin, H., 1981. *Chem. Phys. Lett.* **81**, 371.
- Eremets, M., 1996. *High-Pressure Experimental Methods*. Oxford University Press Inc., New York.
- Faucher, M.D., Moune, O.K., 1997. *J. Alloys Compd.* **250**, 306.
- Fitch, R.A., Slykhouse, T.E., Drickamer, H.G., 1957. *J. Opt. Soc. Am.* **47**, 1015.
- Fonger, W.H., Struck, C.W., 1970. *J. Chem. Phys.* **52**, 6364.
- Förster, T., 1951. *Fluoreszenz organischer Verbindungen*. Vandenhoeck und Rupprecht, Göttingen, Germany.
- Fujishiro, I., Piermarini, G.J., Block, S., Munro, R.G., 1982. Viscosities and glass transition pressures in the methanol-ethanol-water system. In: Backman, C.M., Johansson, T., Terner, L. (Eds.), *High Pressure in Research and Industry*. In: Proc. 8th AIRAPT Conference, Uppsala, Vol. **II**, pp. 608-611.
- Garcia, D., Faucher, M., 1989. *J. Chem. Phys.* **91**, 7461.
- Garcia, D., Faucher, M., 1995. Crystal field in non-metallic (rare earth) compounds. In: Gschneidner Jr., K.A., Eyring, L. (Eds.), *Handbook on the Physics and Chemistry of Rare Earths*, Vol. **21**. North-Holland, Amsterdam, pp. 263-304 (ch. 144).
- Gleason, J.K., Offen, H.W., Turley, W.D., 1993. *Inorg. Chem.* **32**, 639.
- Goldschmidt, Z.B., 1978. Atomic properties (free atom). In: Gschneidner Jr., K.A., Eyring, L. (Eds.), *Handbook on the Physics and Chemistry of Rare Earths*, Vol. **1**. North-Holland, Amsterdam, p. 1 (ch. 1).
- Goncharov, A.F., Struzhkin, V.V., Ruf, T., Syassen, K., 1994. *Phys. Rev. B* **50**, 13841.
- Gonzalez, J., Besson, J.M., Weill, G., 1986. *Rev. Sci. Instrum.* **57**, 106.
- Görrler-Walrand, C., Binnemans, K., 1996. Rationalization of crystal-field parametrization. In: Gschneidner Jr., K.A., Eyring, L. (Eds.), *Handbook on the Physics and Chemistry of Rare Earths*, Vol. **23**. North-Holland, Amsterdam, pp. 121-283 (ch. 155).
- Görrler-Walrand, C., Binnemans, K., 1998. Spectral intensities of f-f transitions. In: Gschneidner Jr., K.A., Eyring, L. (Eds.), *Handbook on the Physics and Chemistry of Rare Earths*, Vol. **25**. North-Holland, Amsterdam, pp. 101-264 (ch. 167).
- Gregorian, T., Holzapfel, W.B., 1984. *J. de Phys.* **45**, C8-41.
- Gregorian, T., d'Amour-Sturm, H., Holzapfel, W.B., 1986. *Physica B* **139-140**, 550.
- Gregorian, T., d'Amour-Sturm, H., Holzapfel, W.B., 1989. *Phys. Rev. B* **39**, 12497.
- Gregorian, T., Shen, Y.R., Tröster, Th., Holzapfel, W.B., 1991. *J. Solid State Inorg. Chem.* **28**, 117.
- Greis, O., Petzel, T., 1974. *Z. Anorg. Allg. Chem.* **403**, 1.
- Guo, C., Li, B., He, Y., Cui, H., 1991. *J. Lumin.* **48-49**, 489.
- Haire, R.G., Benedict, U., Young, J.P., Peterson, J.R., Begun, G.M., 1985. *J. Phys. C: Solid State Phys.* **18**, 4595.
- Haire, R.G., Young, J.P., Peterson, J.R., Benedict, U., 1987. *J. Less-Common Met.* **133**, 167.
- Hayes, A.V., Drickamer, H.G., 1982. *J. Chem. Phys.* **76**, 114.
- Hazen, R.M., Finger, L.W., 1982. *Comparative Crystal Chemistry*. Wiley, New York.
- Hellwege, K.H., 1949. *Ann. Physik* **4**, 95.
- Hellwege, K.H., Schröck-Vietor, W., 1955. *Z. Phys.* **143**, 451.
- Hess, N.J., Exarhos, G.J., 1989. *High Press. Res.* **2**, 57.
- Hess, N.J., Schiferl, D., 1990. *J. Appl. Phys.* **68**, 1953.
- Hess, N.J., Schiferl, D., 1992. *J. Appl. Phys.* **71**, 2082.
- Hoekstra, H.R., 1966. *Inorg. Chem.* **5**, 754.
- Hogg, R.A., Takahei, K., Taguchi, A., Takarabe, K., Mizushima, T., Minomura, S., 1997a. *J. Appl. Phys.* **82**, 813.
- Hogg, R.A., Takahei, K., Taguchi, A., 1997b. *Phys. Rev. B* **56**, 10255.
- Holzapfel, W.B., 1989. In: Polian, A., Loubeyre, P., Boccara, N. (Eds.), *Simple Molecular Systems at Very High Density*. Plenum Press, New York, pp. 257-276.
- Holzapfel, W.B., Isaacs, N.S., 1997. *High-Pressure Techniques in Chemistry and Physics*. Oxford University Press, New York.
- Hu, Z., Bertram, S., Kaindl, G., 1994. *Phys. Rev. B* **49**, 39.
- Hua, H., Vohra, Y.K., 1997. *Appl. Phys. Lett.* **71**, 2602.
- Hua, H., Mirov, S., Vohra, Y.K., 1996. *Phys. Rev. B* **54**, 6200.
- Huber, G., Syassen, K., Holzapfel, W.B., 1977. *Phys. Rev. B* **15**, 5123.
- Inokuti, M., Hirayama, F., 1965. *J. Chem. Phys.* **43**, 1978.
- Jamieson, J.C., Lawson, A.W., Nachtrieb, N.D., 1959. *Rev. Scientific Instr.* **30**, 1016.
- Jantsch, W., Przybylinska, H., Skierbiszewski, C., Lanzertorfer, S., Palmetshofer, L., 1996. In: Coffa, S., Polman, A., Schwartz, R.N. (Eds.), *Rare Earth Doped Semiconductors II*. In: MRS Symposium Proceedings, Vol. **422**. Materials Research Society, Pittsburgh, p. 101.
- Jayaraman, A., 1983. *Rev. Mod. Phys.* **55**, 65.

- Jayasankar, C.K., Reid, M.F., Tröster, Th., Holzapfel, W.B., 1993. *Phys. Rev. B* **48**, 5919.
- Jayasankar, C.K., Babu, P., Tröster, Th., Holzapfel, W.B., 2000. *J. Lumin.* **91**, 33.
- Johannsen, P.G., 1997. *Phys. Rev. B* **55**, 6856.
- Jørgensen, C.K., Reisfeld, R., 1977. *Lasers and Excited States of Rare Earths*. Springer, Berlin.
- Jørgensen, C.K., Pappalardo, R., Schmidtke, H., 1963. *J. Chem. Phys.* **39**, 1422.
- Jovanić, B.R., 2001. *J. Lumin.* **92**, 161.
- Jovanić, B.R., Radenkovic, B., Zekovic, Lj.D., 1996. *J. Phys.: Condens. Matter* **8**, 4107.
- Jovanić, B.R., Radenkovic, B., Zekovic, Lj.D., 1997a. *Solid State Commun.* **101**, 119.
- Jovanić, B.R., Radenkovic, B., Zekovic, Lj.D., 1997b. *Solid State Commun.* **104**, 91.
- Judd, B.R., 1962. *Phys. Rev.* **127**, 750.
- Judd, B.R., 1977. *J. Chem. Phys.* **66**, 3163.
- Kasatochkin, S.V., Yakovlev, E.N., 1977. *High Temp. – High Press.* **8**, 615.
- Keating, K.B., Drickamer, H.G., 1961a. *J. Chem. Phys.* **34**, 143.
- Keating, K.B., Drickamer, H.G., 1961b. *J. Chem. Phys.* **34**, 140.
- Kennedy, R.J., 1980. *J. Phys. C: Solid St. Phys.* **13**, 5353.
- Kennedy, R.J., Campbell, J.A., 1980. *J. Phys. C: Solid St. Phys.* **13**, 5341.
- Kohgi, M., Osakabe, T., Mori, N., Takahashi, H., Okayama, Y., Yoshizawa, H., Ohara, Y., Ikeda, S., Suzuki, T., Haga, Y., 1993. *Physica B* **186–188**, 393.
- Krygin, I.M., Prokhorov, A.D., 1984. *Sov. Phys. JETP* **59**, 344.
- Krygin, I.M., Prokhorov, A.D., 1987a. *Sov. Phys. JETP* **65**, 311.
- Krygin, I.M., Prokhorov, A.D., 1987b. *Sov. Phys. Solid State* **29**, 368.
- Krygin, I.M., Neilo, G.N., Prokhorov, A.D., 1983. *Sov. Phys. JETP* **57**, 1307.
- Krygin, I.M., Neilo, G.N., Prokhorov, A.D., 1984. *Sov. Phys. Solid State* **26**, 1125.
- Krygin, I.M., Neilo, G.N., Prokhorov, A.D., 1986. *Sov. Phys. Solid State* **28**, 634.
- Krygin, I.M., Neilo, G.N., Prokhorov, A.D., Izotov, A.I., 1992. *Sov. Phys. Solid State* **34**, 260.
- Kupchikov, A.K., Malkin, B.Z., Rzaev, D.A., Ryskin, A.I., 1982. *Sov. Phys. Solid State* **24**, 1348.
- Lacam, A., Chateau, C., 1989. *J. Appl. Phys.* **66**, 366.
- Lavin, V., Martin, I.R., Jayasankar, C.K., Tröster, Th., 2002a. *Phys. Rev. B* **66**, 064207.
- Lavin, V., Tröster, Th., Rodriguez-Mendoza, U.R., Martin, I.R., Rodriguez, V.D., 2002b. *High Pressure Research* **22**, 111.
- Leger, J.M., Chateau, C., Lacam, A., 1990. *J. Appl. Phys.* **68**, 2351.
- Li, C.L., Reid, M.F., 1990. *Phys. Rev. B* **42**, 1903.
- Liu, J., Vohra, Y.K., 1993. *Solid State Commun.* **88**, 417.
- Liu, J., Vohra, Y.K., 1994. *Appl. Phys. Lett.* **64**, 3386.
- Liu, S., Chi, Y., Ma, L., Wang, L., Zou, G., 1986. *Physica B* **139–140**, 559.
- Liu, S., Chi, Y., Wang, L., 1988. *J. Lumin.* **40–41**, 395.
- Liu, S., Chi, Y., Zhao, X., Wang, L., Zou, G., 1998a. *Rev. High Pressure Sci. Technol.* **7**, 712.
- Liu, S., Chi, Y., Gao, C., Wang, L., Zou, G., 1998b. *Rev. High Pressure Sci. Technol.* **7**, 757.
- Lochhead, M.J., Bray, K.L., 1995. *Phys. Rev. B* **52**, 15763.
- Lorenz, B., Shen, Y.R., Holzapfel, W.B., 1994. *High Press. Res.* **12**, 91.
- Lübbbers, R., Rupprecht, K., Wortmann, G., 2000. *Hyperfine Interactions* **128**, 115.
- Lukin, S.N., Neilo, G.N., Prokhorov, A.D., Tsintsadze, G.A., 1981. *Sov. Phys. Solid State* **23**, 1789.
- Mak, C.S.K., Tanner, P.A., Tröster, Th., Xia, S., 2002. *J. Phys. Chem. Solids* **63**, 1623.
- Mao, H.K., 1989. In: Polian, A., Loubeyre, P., Boccaro, N. (Eds.), *Simple Molecular Systems at Very High Density*. Plenum Press, New York, pp. 221–236.
- Mao, H.K., Bell, P.M., Shaner, J.W., Steinberg, D.J., 1978. *J. Appl. Phys.* **49**, 3276.
- Merkle, L.D., Spain, I.L., Powell, R.C., 1981. *J. Phys. C: Solid State Phys.* **14**, 2027.
- Mesot, J., Staub, U., Allenspach, P., Furrer, A., Mutka, H., Vettier, C., 1990. In: Kuzmany, H., Mehring, M., Fink, J. (Eds.), *Electronic Properties of High-TC Superconductors and Related Compounds*, Vol. **99**. Springer Verlag Berlin, Heidelberg, pp. 244–247.
- Michael, K., 2000. Ph.D. Thesis (Paderborn).
- Mishimura, G., Kushida, T., 1991. *J. Phys. Soc. Japan* **60**, 683.
- Monteil, A., Bernard, C., Chaussedent, S., Ferrari, M., Balu, N., Obriot, J., 2000. *J. Lumin.* **87–89**, 691.
- Morrison, C., Mason, D.R., Kikuchi, C., 1967. *Phys. Lett.* **24A**, 607.
- Naka, T., Matsumoto, T., Okayama, Y., Mori, N., Haga, Y., Suzuki, T., 1994. *Physica B* **199–200**, 551.
- Neuenschwander, J., Wachter, P., 1990. *Physica B* **160**, 231.
- Neuhaus, A., 1964. *Chimia* **18**, 93.
- Newman, D.J., 1971. *Theory of lanthanide crystal fields*. *Adv. Phys.* **20**, 197.
- Newman, D.J., 1973. *J. Phys. Chem. Solids* **34**, 541.
- Newman, D.J., Ng, B., 1986. *J. Phys. C: Solid State Phys.* **19**, 389.

- Newman, D.J., Ng, B., 1989. The superposition model of crystal fields. *Rep. Prog. Phys.* **52**, 699.
- Newman, D.J., Ng, B., Poon, Y.M., 1984. *J. Phys. C: Solid State Phys.* **17**, 5577.
- Nishimura, G., Tanaka, M., Kurita, A., Kushida, T., 1991. *J. Lumin.* **48–49**, 473.
- Noack, R.A., Holzapfel, W.B., 1979. In: Timmerhaus, K.D., Barber, M.S. (Eds.), *High Pressure Science and Technology*, Vol. **1**. Plenum, New York, p. 748.
- Ofelt, G.S., 1962. *J. Chem. Phys.* **37**, 511.
- Okayama, Y., Ohara, Y., Mitsuda, S., Takahashi, H., Yoshizawa, H., Osakabe, T., Kohgi, M., Haga, Y., Suzuki, T., Mori, N., 1993. *Physica B* **186–188**, 531.
- Olsen, L.R., Wright, A.O., Wright, J.C., 1996. *Phys. Rev. B* **53**, 14135.
- Oohara, Y., Okayama, Y., Mitsuda, S., Takahashi, H., Yoshizawa, H., Mori, N., Osakabe, T., Haga, Y., Kohgi, M., Suzuki, T., 1995. *Physica B* **213–214**, 116.
- Oppenländer, A., Vial, J.-C., Macfarlane, R.M., Chaminade, J.-P., 1989. *J. Lumin.* **42**, 331.
- Paetzold, H.K., 1940. *Ann. Phys.* **37**, 470.
- Peterson, J.R., 1994. *J. Alloys Compd.* **213–214**, 394.
- Peterson, J.R., Young, J.P., Haire, R.G., Begun, G.M., Benedict, U., 1985. *Inorg. Chem.* **24**, 2466.
- Peterson, J.R., Young, J.P., Haire, R.G., Benedict, U., 1986. *Physica B* **144**, 85.
- Peterson, J.R., Haire, R.G., Benedict, U., Young, J.P., 1987. *J. Less-Common Met.* **33**, 143.
- Piermarini, G.J., Block, S., Barnett, J.D., 1973. *J. Appl. Phys.* **44**, 5377.
- Piermarini, G.J., Block, S., Barnett, J.D., Forman, R.A., 1975. *J. Appl. Phys.* **46**, 2774.
- Poon, Y.M., Newman, D.J., 1984. *J. Phys. C: Solid State Phys.* **17**, 4319.
- Powell, R.C., Neikirk, D.P., Sardar, D., 1980. *J. Opt. Soc. Am.* **70**, 486.
- Przybylinska, H., Jantsch, W., Lanzerstorfer, S., Skierbiszewski, C., Palmesthofer, L., 1996. In: Scheffner, M., Zimmermann, R. (Eds.), *The Physics of Semiconductors*. World Scientific, Singapore, pp. 3025–3037.
- Radliński, A.P., Silversmith, A.J., 1986. *Phys. Rev. B* **34**, 86.
- Reid, M.F., 1987. *J. Chem. Phys.* **87**, 2875.
- Reid, M.F., 2000. In: Newman, D.J., Ng, B. (Eds.), *Transition intensities, Crystal Field Handbook*. University Press, Cambridge, pp. 190–226 (ch. 10).
- Reid, M.F., Newman, D.J., 2000. Effects of electron correlation on crystal field splittings. In: Newman, D.J., Ng, B. (Eds.), *Crystal Field Handbook*. Cambridge University Press, pp. 120–139 (ch. 6).
- Ren, S.Y., Dow, J.D., Wohlford, D.J., 1982. *Phys. Rev. B* **25**, 7661.
- Rewaj, T., Krupski, M., 1978. *Phys. Stat. Sol. (b)* **88**, K65.
- Rewaj, T., Krupski, M., 1980. *Phys. Stat. Sol. (b)* **99**, 285.
- Rewaj, T., Krupski, M., Kuriata, J., Buzare, J.Y., 1992. *J. Phys.: Condens. Matter* **4**, 9909.
- Sakai, N., Pifer, J.H., 1985. *Rev. Sci. Instrum.* **56**, 726.
- Sato, S., Wada, M., 1970. *Bull. Chem. Soc. Jpn.* **43**, 1955.
- Schirber, J.E., Weaver, H.T., Ginley, D.S., 1978. *J. Appl. Phys.* **49**, 1469.
- Shen, Y.R., 1994. Private communication.
- Shen, Y.R., Bray, K.L., 1998a. *Phys. Rev. B* **58**, 11944.
- Shen, Y.R., Bray, K.L., 1998b. *Phys. Rev. B* **58**, 5305.
- Shen, Y.R., Bray, K.L., 1999. *Mat. Sci. Forum* **315–317**, 243.
- Shen, Y.R., Holzapfel, W.B., 1993. *J. Alloys Compd.* **192**, 53.
- Shen, Y.R., Holzapfel, W.B., 1994. *J. Phys.: Condens. Matter* **6**, 2367.
- Shen, Y.R., Holzapfel, W.B., 1995a. *Phys. Rev. B* **52**, 12618.
- Shen, Y.R., Holzapfel, W.B., 1995b. *J. Phys.: Condens. Matter* **7**, 6241.
- Shen, Y.R., Holzapfel, W.B., 1995c. *Phys. Rev. B* **51**, 6127.
- Shen, Y.R., Holzapfel, W.B., 1995d. *Phys. Rev. B* **51**, 15752.
- Shen, Y.R., Holzapfel, W.B., 1996. In: Trzeciakowski, W. (Ed.), *High Pressure Science and Technology*. World Scientific, Singapore, pp. 576–578.
- Shen, Y.R., Gregorian, T., Tröster, Th., Schulte, O., Holzapfel, W.B., 1990. *High Press. Res.* **3**, 144.
- Shen, Y.R., Gregorian, T., Holzapfel, W.B., 1991. *High Press. Res.* **7**, 73.
- Shen, Y.R., Englisch, U., Chudinovskikh, L., Porsch, F., Haberkorn, R., Beck, H.P., Holzapfel, W.B., 1994. *J. Phys.: Condens. Matter* **6**, 3197.
- Shen, Y.R., Bray, K.L., Holzapfel, W.B., 1997. *J. Lumin.* **72–74**, 266.
- Shen, Y.R., Riedener, T., Bray, K.L., 2000. *Phys. Rev. B* **61**, 11460.
- Soga, N., Hirao, K., Yoshimoto, M., Yamamoto, H., 1988. *J. Appl. Phys.* **63**, 4451.
- Stapor, A., Kozanecki, A., Reimann, K., Syassen, K., Weber, J., Moser, M., Scholz, F., 1991. *Acta Phys. Pol. A* **79**, 315.
- Struck, C.W., Fonger, W.H., 1970. *J. Lumin.* **1–2**, 456.
- Struck, C.W., Fonger, W.H., 1975. *J. Lumin.* **10**, 1.

- Stump, N.A., Chen, G., Haire, R.G., Peterson, J.R., 1993. *Appl. Spectrosc.* **47**, 1951.
- Syassen, K., Winzen, H., Zimmer, H.G., Tups, H., Leger, J.M., 1985. *Phys. Rev. B* **32**, 8246.
- Syassen, K., Winzen, H., Benedict, U., 1986. *Physica B* **144**, 91.
- Taguchi, A., Takahei, K., Horikoshi, Y., 1994. *J. Appl. Phys.* **76**, 7288.
- Takarabe, K., 1996. *Phys. Stat. Sol. (b)* **198**, 211.
- Takarabe, K., Minomura, S., Taguchi, A., Takahei, K., 1994. *Mat. Sci. Forum* **143–147**, 731.
- Takarabe, K., Mizushima, T., Minomura, S., Taguchi, A., Takahei, K., 1995. *Mat. Sci. Forum* **196–201**, 645.
- Takarabe, K., Mizushima, T., Minomura, S., Hogg, R.A., Taguchi, A., Takahei, K., 1997. *Appl. Phys. Lett.* **71**, 93.
- Tanner, P.A., Rudowicz, C., 1993. *Appl. Spectrosc.* **47**, 127.
- Thalmeier, P., Fulde, P., 1982. *Phys. Rev. Lett.* **49**, 1588.
- Tolentino, H., Baudelet, F., Dartyge, E., Fontaine, A., Lena, A., Tourillon, G., 1990. *Nucl. Instrum. Methods A* **289**, 307.
- Trlifaj, M., 1958. *J. Physique* **8**, 510.
- Trommer, R., Müller, H., Cardona, M., Vogl, P., 1980. *Phys. Rev. B* **21**, 4869.
- Tröster, Th., 1994. Ph.D. Thesis (Universität Paderborn).
- Tröster, Th., 1999. VUV Spectroscopy of Pr^{3+} and Nd^{3+} in LaCl_3 . In: Materlik, G., Schneider, J.R., Schulte-Schrepping, H., Franz, H. (Eds.), *HASYLAB Annual Report, Part 1. Hamburger Synchrotronstrahlungslabor HASYLAB, Hamburg*.
- Tröster, Th., Holzapfel, W.B., 1998. VUV Spectroscopy of Pr^{3+} under Pressure. In: Laasch, W., Materlik, G., Schneider, J.R., Schulte-Schrepping, H. (Eds.), *HASYLAB Annual Report, Part 1. Hamburger Synchrotronstrahlungslabor HASYLAB, Hamburg*.
- Tröster, Th., Holzapfel, W.B., 2002. *Phys. Rev. B* **66**, 075114.
- Tröster, Th., Lavin, V., 2003. *J. Lumin.* **101**, 241.
- Tröster, Th., Gregorian, T., Johannsen, P.G., Holzapfel, W.B., 1990. *High Press. Res.* **3**, 147.
- Tröster, Th., Gregorian, T., Holzapfel, W.B., 1993. *Phys. Rev. B* **48**, 2960.
- Tröster, Th., Holzapfel, W.B., Goffart, J., 1995. *Phys. Rev. B* **51**, 14892.
- Tröster, Th., Spaeth, J.-M., Schweizer, S., 2002. *J. Lumin.* **99**, 343.
- Tyner, C.E., Drickamer, H.G., 1977. *J. Chem. Phys.* **67**, 4116.
- Urland, W., 1989. *J. Less-Common Met.* **148**, 151.
- Urland, W., Hochheimer, H.D., Kourouklis, G.A., Kremer, R., 1985. *Solid State Commun.* **55**, 649.
- Urland, W., Hochheimer, H.D., Kourouklis, G.A., Kremer, R., 1986. *Physica B* **139–140**, 553.
- Urošević, V.V., Jaksic, Z.M., Zekovic, Lj.D., Jovanić, B.R., 1992. *High Press. Res.* **9**, 251.
- Vettier, C., 1989. *J. Less-Common Met.* **149**, 13.
- Vettier, C., McWhan, D.B., Blount, E.I., Shirane, G., 1977. *Phys. Rev. Lett.* **39**, 1028.
- Voloshin, V.A., 1982. *Solid State Commun.* **42**, 347.
- Voloshin, V.A., 1986. *Sov. Phys. JETP* **63**, 782.
- Voloshin, V.A., 1988. *Physica B* **154**, 111.
- Voloshin, V.A., 1990. *Physica C* **168**, 506.
- Voloshin, V.A., Krimm, M.G., 1977. *Phys. Stat. Sol. (b)* **82**, 695.
- Voloshin, V.A., Savutskii, A.I., 1976. *High Temp. – High Press.* **8**, 607.
- Voloshin, V.A., Ivchenko, L.A., 1980. *JETP Letters* **32**, 100.
- Voloshin, V.A., Kulagin, N.A., Ovander, L.N., Prudnikov, A.M., 1975. *Opt. Spectrosc.* **39**, 334.
- Voloshin, V.A., Savutskii, A.I., Kasyanov, A.I., 1976. *Opt. Spectrosc.* **40**, 346.
- Wamsley, P.R., Bray, K.L., 1994a. *J. Lumin.* **60–61**, 188.
- Wamsley, P.R., Bray, K.L., 1994b. *J. Lumin.* **59**, 11.
- Wamsley, P.R., Bray, K.L., 1995. *J. Lumin.* **63**, 31.
- Wang, P.J., Drickamer, H.G., 1973. *J. Chem. Phys.* **58**, 4444.
- Wang, Q., Bulou, A., 1993. *J. Phys.: Condens. Matter* **5**, 7657.
- Wang, Q., Bulou, A., 1995. *Solid State Commun.* **94**, 309.
- Wang, L., Zhang, Z., Chi, Y., Liu, S., 1984. In: Homan, C., MacCrone, R.K., Whalley, E. (Eds.), *High Pressure in Science and Technology. In: MRS Symposia Proceedings, Vol. 22. North-Holland, New York*, pp. 345–348. pt. 3.
- Wang, Q., Lun, L., Zhang, D., Chi, Y., Wang, L., 1992. *J. Phys.: Condens. Matter* **4**, 6491.
- Webster, G.A., Drickamer, H.G., 1980a. *J. Chem. Phys.* **72**, 3740.
- Webster, G.A., Drickamer, H.G., 1980b. *J. Chem. Phys.* **72**, 4661.
- Weir, C.E., Lippincott, E.R., Van Valkenburg, A., Bunting, E.N., 1959. *Journal of Research of the National Bureau of Standards* **63A**, 55.
- Wickersheim, K.A., Buchanan, R.A., Yates, E.C., 1968. In: *Proc. Seventh Rare Earth Research Conf., Coronado, CA*, p. 835.
- Wilmarth, W.R., Begun, G.M., Haire, R.G., Young, J.P., Peterson, J.R., 1989. *Appl. Spectrosc.* **43**, 1038.
- Wolford, D.J., Bradley, J.A., 1985. *Solid State Commun.* **53**, 1069.

- Wright, A.O., Olsen, L.R., Wright, J.C., 1995. *Chem. Phys. Lett.* **244**, 395.
- Wybourne, B.G., 1965. *Spectroscopic properties of Rare Earths*. Wiley, New York.
- Wybourne, B.G., 1968. *J. Chem. Phys.* **48**, 2596.
- Yersin, H., Gliemann, G., 1978. In: Miller, J.S., Epstein, A.J. (Eds.), *Synthesis and Properties of Low-Dimensional Materials*, Vol. **313**. New York Academy of Sciences, pp. 539–559.
- Yersin, H., Stock, M., 1982. *J. Chem. Phys.* **76**, 2136.
- Yersin, H., Riedl, U., 1995. *Inorg. Chem.* **34**, 1642.
- Yersin, H., Ammon, W.v., Stock, M., Gliemann, G., 1979. *J. Lumin.* **18–19**, 774.
- Yersin, H., Trümbach, D., Strasser, J., Patterson, H.H., Assefa, Z., 1998. *Inorg. Chem.* **37**, 3209.
- Yoo, C.S., Radousky, H.B., Holmes, N.C., Edelstein, N.M., 1991. *Phys. Rev. B* **44**, 830.
- Yoshizawa, H., Okayama, Y., Oohara, Y., Takahashi, H., Mori, N., Mitsuda, S., Osakabe, T., Kohgi, M., Haga, Y., Suzuki, T., 1995. *J. Phys. Soc. Jpn.* **64**, 617.
- Young, J.P., Peterson, J.R., Haire, R.G., Wilmarth, W.R., Begun, G.M., 1990. *High Press. Res.* **2**, 391.
- Yusa, H., Yagi, T., Arashi, H., 1994. *J. Appl. Phys.* **75**, 1463.
- Zimmer, H.G., Takemura, K., Syassen, K., Fischer, K., 1984. *Phys. Rev. B* **29**, 2350.

AUTHOR INDEX

- Aarts, J., see Fäth, M. 298
- Aas, W. 500
- Abbasov, A.S., see Geydarova, E.N. 85
- Abd-Elmeguid, M.M., see Bauer, E. 24
- Abdusalamova, M.N. 36, 37, 135
- Abdusalamova, M.N., see Abulkhaev, V.D. 37, 94
- Abe, H., see Katsumura, Y. 489, 496, 497, 508
- Abe, K., see Aoki, Y. 17–19
- Abe, K., see Keller, L. 17, 23
- Abe, K., see Sugawara, H. 18
- Abe, R., see Park, Y.Y. 489, 491, 492, 498
- Abe, Y., see Sato, H. 6, 8, 12, 17, 18, 22, 23
- Abe, Y., see Sugawara, H. 8, 9, 23
- Abraham, M.M., see Chen, G. 523, 524
- Abrikosov, N.Kh., see Dudkin, L.D. 29
- Abulkhaev, V.D. 37, 94
- Achard, J.C., see Ravot, D. 57
- Adachi, G., see Jiang, J. 479, 483, 494
- Adachi, T., see Shirotani, I. 7–9, 12
- Adamo, C. 183, 186–189
- Adams, C.P. 298
- Adams, H., see Platas, C. 358, 359, 377, 378, 400–404
- Adams, M.J. 470
- Addleman, R.S. 489, 509
- Adler, P., see Loa, I. 268
- Adroja, D.T. 60, 61, 118
- Adroja, D.T., see Malik, S.K. 48, 56, 60, 69, 77, 81, 85, 89, 108, 118
- Adroja, D.T., see Thornton, M.J. 124
- Afanas'ev, Y.A., see Khanaev, E.I. 209, 213
- Afanas'ev, Y.A., see Storozhenko, T.P. 215–217
- Agmon, N. 489
- Ahn, K.H. 267, 268
- Ahn, K.H., see Quijada, M.A. 296
- Ahnen, T., see Petzel, T. 234, 235
- Aime, S. 357, 360–363, 420–422, 426, 429, 433, 439, 440
- Aime, S., see Benetollo, F. 420
- Aime, S., see Bruce, J.I. 355
- Aime, S., see Marques, M.P.M. 421, 423
- Aime, S., see Zhang, S. 355
- Ajtony, Z., see Kaposi, O. 196, 240
- Akishin, P.A. 224
- Akita, K., see Sekine, C. 13
- Al-Soufi, W. 471, 498
- Alascio, B., see Causa, M.T. 326
- Albering, J.H. 76, 90
- Albin, M. 478, 499, 505
- Albin, M., see Horrocks Jr., W.deW. 507
- Albrecht-Gary, A.M., see Nehlig, A. 473, 474, 482, 485
- Aldred, A.T., see Shaked, H. 84, 87, 89, 90, 127, 129
- Aléonard, S., see Labeau, M. 203
- Alexandrov, A.S. 308
- Algarabel, P.A., see De Teresa, J.M. 298–300
- Aliev, F.G. 118
- Aliev, I.I., see Sadygov, F.M. 75
- Aliev, O.M. 55, 77, 78, 80, 91, 92
- Aliev, O.M., see Rustamov, P.G. 74, 77, 92
- Aliyev, I.Ya., see Geydarova, E.N. 85
- Aliyev, O.M., see Sadygov, F.M. 36
- Allegrozzi, M. 363
- Allen, P. 474
- Allen, P.B. 268, 269
- Allen, P.B., see Chen, Y.-R. 285
- Allen, P.B., see Perebeinos, V. 268
- Allendoerfer, R.D., see Reilley, C.N. 357, 406
- Allenspach, P., see Mesot, J. 524, 535
- Allodi, G. 288, 325, 328, 337
- Allodi, G., see Cestelli Guidi, M. 264
- Allsopp, S.R. 473, 474
- Almai, M., see De Kozak, A. 202
- Alonso, J. 324
- Alonso, J.A., see Frontera, C. 336
- Alonso, J.M., see Fernández-Díaz, M.T. 329
- Alpoim, M.C., see Geraldès, C.F.G.C. 410
- Alsaadi, B.M. 361, 405–407
- Altmeyer, R.O. 37
- Amato, A., see Cestelli Guidi, M. 264
- Amayri, S., see Bernhard, G. 495
- Amelichev, V., see Shames, A.I. 338
- Ameloot, M., see Beechem, J.M. 498
- Ameloot, M., see Janssens, L.D. 471

- Ameloot, M., see Molski, A. 489, 502
Amin, S. 426
Amin, S., see Morrow, J.R. 426
Amis, E.S., see Hinton, J.F. 493
Amitsuka, H., see Sekine, C. 20
Ammon, W.v., see Yersin, H. 523, 569
An, Y. 405, 481, 483, 494
Anane, A. 291
Anane, A., see Raquet, B. 326
Anderson, P.W. 31, 256, 258
André, G. 123
André, G., see Autret, C. 338
André, G., see Damay, F. 330, 336
André, N., see Platas-Iglesias, C. 406, 407
Andreev, A.V., see Matsuda, T.D. 17
Andres, K., see Neumeier, J.J. 278
Anelli, P.L., see Aime, S. 433
Ansoborlo, E., see Billard, I. 470, 495, 501–503, 506
Ansoborlo, E., see Scapolan, S. 508
Antonio, M.A., see Xue, J.S. 12
Aoki, K., see Sugawara, H. 18
Aoki, Y. 17–19
Aoki, Y., see Keller, L. 17, 23
Aoki, Y., see Matsuda, T.D. 17
Aoki, Y., see Sato, H. 6, 8, 12, 17, 18, 22, 23
Aoki, Y., see Sugawara, H. 8, 9, 23
Aoyagi, H., see Nagaishi, R. 497
Apperson, K., see Billard, I. 470, 495, 501–503, 506
Arai, F., see Kimura, S. 130
Arashi, H. 524, 529, 553, 554
Arashi, H., see Yusa, H. 523, 553
Archibald, W. 294, 295, 300
Archibald, W., see Zhou, J.-S. 300–302
Argyriou, D.N., see Radaelli, P.G. 299, 323
Arima, T. 279
Arima, T., see Asamitsu, A. 319
Arima, T., see Murakami, Y. 263
Arima, T., see Urushibara, A. 311
Arima, T., see Zimmermann, M.V. 264
Arisaka, M. 473, 474, 481
Arispe, J., see Mayr, M. 326
Arkle, V.K., see Horrocks Jr., W.deW. 499, 501
Armitage, J.G.M., see Thornton, M.J. 124
Arnold, Z., see De Teresa, J.M. 298, 300
Arnott, R.J., see Goodenough, J.B. 265, 267, 269, 270
Arnott, R.J., see Wold, A. 289
Arpigny, S., see Billard, I. 470, 495, 501–503, 506
Arroyo, A., see Alonso, J. 324
Arsenov, A.A., see Adams, C.P. 298
Arsenov, A.A., see Senis, R. 317
Arsenov, A.A., see Vasiliu-Doloc, L. 321
Artem'eva, M.V., see Yudin, V.M. 276
Arulraj, A., see Rao, C.N.R. 330
Arvis, M. 497
Asamitsu, A. 291, 319
Asamitsu, A., see Kuwahara, H. 333, 337
Asamitsu, A., see Moritomo, Y. 311
Asamitsu, A., see Okuda, T. 325
Asamitsu, A., see Saitoh, E. 321
Asamitsu, A., see Tokura, Y. 330, 341
Asamitsu, A., see Tomioka, Y. 291, 294, 297
Asamitsu, A., see Urushibara, A. 311
Asamitsu, A., see Zhou, J.-S. 311
Asaumi, K. 519
Ashworth, H., see Sharman, K.S. 470
Assefa, Z., see Morrison, H.G. 151, 205
Assefa, Z., see Yersin, H. 523, 569, 570
Atabekyan, L.S., see Billing, R. 489, 491
Atwood, J.L., see Steed, J.W. 355
Aune, R.E., see Stolyarova, V.L. 235
Aupiais, J. 508
Aury, S., see Giroux, S. 494, 505
Austin, A.E., see Wood, V.E. 275
Autret, C. 338
Auzel, F. 573
Avecilla, F., see Platas, C. 358, 359, 377, 378, 400–404
Averitt, R.D., see Lobad, A.I. 326
Ayala, J.D., see Aime, S. 420
Azehna, A.E., see Billard, I. 470, 495, 501–503, 506
Azenha, M.E. 498
Azuma, N., see Matsumoto, A. 506
Babailov, S.P. 357
Babu, P., see Jayasankar, C.K. 522, 581
Babushkina, N., see Yakubovskii, A. 309
Babushkina, N.A. 308, 309, 327
Bäckström, J., see Björnsson, P. 268
Baetslé, L.H. 149
Baev, A.G., see Novikov, G.I. 236
Baginskii, A.V., see Lyapunov, K.M. 164, 165, 176
Bagirova, S.D., see Geydarova, E.N. 85
Baglio, J.A., see Struck, C.W. 196
Baird, C.P. 497, 498
Baker, F.B. 214
Baker, M.V. 356
Balakrishnan, G., see Allodi, G. 328, 337
Balakrishnan, G., see Campbell, A.J. 319

- Balakrishnan, G., see Heffner, R.H. 325
 Balakrishnan, G., see Lees, M.R. 291
 Balakrishnan, G., see Zvyagin, S. 338
 Balbashov, A.M., see Mayr, F. 315
 Balbashov, A.M., see Smolyaninova, V.N. 321
 Balcells, L.I., see Martínez, B. 317
 Balthazar, K., see Kaposi, O. 196, 240
 Balu, N., see Monteil, A. 524, 556
 Balzani, V. 355, 471
 Balzani, V., see Sabbatini, N. 494
 Bandyopadhyay, B., see Mandal, P. 312
 Banerjee, A.K., see Fronczek, F. 381
 Bao, W., see Schiffer, P. 328
 Barbero, L., see Aime, S. 357, 361, 363, 421, 422
 Bare, W.D. 470, 509
 Barge, A., see Aime, S. 420, 422, 426, 429
 Barnett, J.D. 522, 552, 554
 Barnett, J.D., see Piermarini, G.J. 518, 519
 Barone, V., see Adamo, C. 186, 189
 Barratt, J., see Lees, M.R. 291
 Barry, C.D. 363
 Barthelemy, P.P. 478, 479
 Bartholin, H., see Burret, P. 55
 Bartholin, H., see Rossat-Mignod, J. 55, 57
 Barthou, C., see Blanzat, B. 523, 524, 574
 Basch, H., see Stevens, W.J. 148
 Baskaran, G., see Zhao, Y.G. 296
 Basov, D.N., see Dilley, N.R. 26
 Basov, D.N., see Dordevic, S.V. 8, 12, 17, 26, 27
 Batlogg, B., see Hwang, H.Y. 290, 291
 Batlogg, B., see Radaelli, P.G. 323, 325
 Batsanov, A., see Parker, D. 420
 Baudalet, F., see Tolentino, H. 518
 Bauer, E. 24
 Bauer, E.D. 8, 12, 13, 15–17, 21, 22, 24
 Bauer, E.D., see Dilley, N.R. 15, 26
 Bauer, E.D., see Dordevic, S.V. 8, 12, 17, 26, 27
 Bauer, E.D., see Gajewski, D.A. 13
 Bauer, E.D., see Maple, M.B. 22
 Baumann, M. 524
 Bazin, H. 509
 Bazzicalupi, C. 492, 509
 Beale Jr., A.F., see Westrum Jr., E.F. 154, 157
 Beaucaire, C., see Moulin, C. 508
 Beaudry, B.J., see Spedding, F.H. 164, 165, 176, 178
 Beck, H.P. 558, 559
 Beck, H.P., see Bolduan, F. 522, 550, 566
 Beck, H.P., see Shen, Y.R. 564
 Becke, A.D. 148
 Beeby, A. 481–484
 Beeby, A., see Clarkson, I.M. 484, 505
 Beechem, J.M. 498
 Begun, G.M., see Daniel, J.F. 151, 205
 Begun, G.M., see Del Cul, G.D. 523
 Begun, G.M., see Haire, R.G. 558
 Begun, G.M., see Peterson, J.R. 558
 Begun, G.M., see Wilmarth, W.R. 521, 522, 558
 Begun, G.M., see Young, J.P. 558
 Beitz, J.V. 473, 478, 495, 497, 501
 Belesi, M., see Papavassiliou, G. 325, 326
 Bell, J. 497
 Bell, P.M. 519
 Bell, P.M., see Mao, H.K. 518
 Belova, L.M., see Babushkina, N.A. 308, 309, 327
 Bencini, A., see Bazzicalupi, C. 492, 509
 Bencze, L. 186, 226, 235
 Benedict, U., see Haire, R.G. 558
 Benedict, U., see Peterson, J.R. 522, 558
 Benedict, U., see Syassen, K. 550
 Benetollo, F. 420
 Benetollo, F., see Aime, S. 420, 422
 Bennington, S., see Keppens, V. 11
 Bensaid, A., see Reutler, P. 326
 Berezhkovskii, A.M. 489
 Berger, S., see Bauer, E. 24
 Bernard, C., see Monteil, A. 524, 556
 Bernard, O., see Simonin, J.P. 491
 Bernardinelli, G., see Bocquet, B. 453, 455, 456
 Bernardinelli, G., see Floquet, S. 453, 455–459
 Bernardinelli, G., see Piquet, C. 355, 384, 385, 393–395
 Bernardinelli, G., see Renaud, F. 387–393, 408
 Bernardinelli, G., see Rigault, S. 358, 361, 363, 366, 378, 396–400
 Bernhard, G. 495
 Bernhard, G., see Brendler, V. 499
 Bernhard, G., see Geipel, G. 495, 499, 500, 505
 Bernhard, G., see Rutsch, M. 501
 Berni, E., see Bazzicalupi, C. 492, 509
 Berny, F. 358
 Berregi, I. 507
 Berry, M.T., see An, Y. 405, 481, 483, 494
 Bertaut, E.F. 258
 Bertaut, E.F., see Quezel, S. 275
 Berthoud, T. 507, 508
 Bertini, I. 356, 357, 359, 361–364, 366–368, 374
 Bertini, I., see Allegrozzi, M. 363
 Bertram, S., see Hu, Z. 521
 Besenbruch, G., see Kent, R.A. 234
 Besenbuch, G. 235
 Besson, J.M., see Gonzalez, J. 518

- Bethe, H.A. 526
 Bettonville, S. 217, 219, 221
 Bhat, S.V., see Joshi, J.P. 336
 Bi, Q. 523, 529, 553
 Bianchi, A. 426
 Bianchi, A., see Bazzicalupi, C. 492, 509
 Bianconi, A., see Lanzara, A. 295, 325
 Bidoglio, G., see Eliet, V. 474, 498, 501
 Biefeld, R.M. 235
 Bilal, B.A., see Baumann, M. 524
 Billard, I. 470, 485, 495, 501–503, 506, 510
 Billard, I., see Bouby, M. 474, 506
 Billard, I., see Nehlig, A. 473, 474, 482, 485
 Billard, I., see Rustenholtz, A. 474
 Billard, I., see Simonin, J.P. 491
 Billing, R. 489, 491
 Billinge, S.J.L. 304
 Billings, M., see Bell, J. 497
 Bini, R., see Bungenstock, C. 521, 529, 533, 535
 Binnemans, K., see Görrler-Walrand, C. 369, 371, 376, 377, 380, 400, 520, 526, 556, 560, 561
 Binnemans, K., see Mironov, V.S. 355, 366, 368–372
 Biotteau, G. 325
 Biotteau, G., see Hennion, M. 311
 Biotteau, G., see Moussa, F. 324
 Biradha, K., see Fujita, M. 355
 Birch, D., see Billard, I. 470, 495, 501–503, 506
 Birch, D.J.S., see Lopez, M. 489, 491, 500, 508
 Birks, J. 467, 486
 Bishop, A.R., see Louca, D. 263
 Bishton, S.S. 547
 Biswas, A., see Smolyaninova, V.N. 327
 Björnsson, P. 268
 Blacquère, R.J.H., see Cordfunke, E.H.P. 152, 207, 209
 Blair, S. 509
 Blanzat, B. 523, 524, 574
 Blasco, J., see De Teresa, J.M. 298–300
 Blasco, J., see Stankiewicz, J. 292
 Blasco, J., see Subías, G. 323
 Blasse, G. 483
 Blau, W., see Holzer, W. 506
 Bleaney, B. 357, 358, 365, 369, 371, 376
 Bloch, D. 279, 281
 Block, S., see Barnett, J.D. 522, 552, 554
 Block, S., see Fujishiro, I. 519
 Block, S., see Piermarini, G.J. 518, 519
 Bloembergen, N. 356, 359, 360
 Blonska, A., see Hennig, C. 215
 Blount, E.I., see Vettier, C. 521, 535
 Blume, M., see Murakami, Y. 263
 Bocquet, B. 453, 455, 456
 Bocquet, B., see Floquet, S. 453, 455–459
 Bocquet, B., see Ouali, N. 379, 390, 405–410
 Bodak, O., see Sologub, O. 41–43, 45, 46, 48, 49, 51–54, 56–63, 66–69, 72–76, 79–93, 102, 119–123, 133
 Bodak, O.I., see Pankevich, Yu.V. 52, 59, 66, 73
 Bodak, O.I., see Pecharsky, V.K. 40, 45, 52, 53, 59, 66, 67, 73, 79, 82, 84, 86, 88, 89, 92, 98, 100, 106, 109, 138, 139
 Bodak, O.I., see Skolozdra, R.V. 41, 46, 53, 59, 60, 67, 73, 80, 82, 84, 86–88, 132, 133
 Bodak, O.I., see Stetskiy, A.O. 55, 109, 111
 Bodnar, R.E. 37
 Boens, N., see Janssens, L.D. 471
 Boens, N., see Molski, A. 489, 502
 Bogacz, A., see Gaune-Escard, M. 151, 166–168, 179, 203–206, 222, 223
 Boghosian, S. 184
 Bogner, J., see Leithe-Jasper, A. 26
 Bolduan, F. 522, 550, 566
 Bolender, J.P., see Hopkins, T.A. 369, 377, 405, 410
 Bolletta, F., see Sabbatini, N. 494
 Bollore, G. 43, 47, 49, 50, 55, 57, 58, 60, 62, 69, 71, 72, 74, 75, 110
 Bolton, J.R., see Mack, J. 474, 498
 Bolton, J.R., see Wertz, J.E. 359, 364
 Bombieri, G., see Aime, S. 420, 422
 Bombieri, G., see Benetollo, F. 420
 Bommer, H. 174, 210–215, 217–221
 Bommer, H., see Hohmann, E. 210–214, 216, 218, 220, 222
 Bonazzi, A., see Sabbatini, N. 494
 Bonnenfant, A., see Bouby, M. 474
 Booiij, A.S., see Cordfunke, E.H.P. 181, 210, 211, 213, 218
 Booiij, A.S., see Furkaliouk, M.Y. 210
 Booiij, A.S., see Kovács, A. 228
 Boonk, L., see Evers, C.B.H. 15, 23
 Boonk, L., see Evers, Ch.B.H. 65, 71, 72, 74, 76, 77, 95
 Borchers, J.A., see Erwin, R.W. 325
 Borchers, J.A., see Huang, Q. 289, 325
 Borchers, J.A., see Lynn, J.W. 299, 325
 Borghs, G., see Gordon, I. 326
 Borissevitch, I.E. 508
 Börjesson, L., see Björnsson, P. 268
 Borodulenko, G.P., see Korshunov, B.G. 204, 205
 Borrrmann, H., see Günselius, H. 151

- Borsese, A. 36
 Borsese, A., see Borzone, G. 36
 Borshchevsky, A., see Caillat, T. 29
 Borshchevsky, A., see Chen, B. 13
 Borshchevsky, A., see Fleuriat, J.-P. 3, 11, 13, 27, 29
 Borshchevsky, A., see Watcharapasorn, A. 6, 7, 12, 13, 29
 Borstel, G., see Slebarski, A. 45, 59, 60, 100, 113
 Borzone, G. 36, 37, 135, 136
 Borzone, G., see Borsese, A. 36
 Borzone, G., see Cacciamani, G. 135
 Borzone, G., see Ferro, R. 37, 135
 Botta, M., see Aime, S. 357, 360–363, 420–422, 426, 429, 433, 439, 440
 Botta, M., see Benetollo, F. 420
 Botta, M., see Bruce, J.I. 355
 Botta, M., see Marques, M.P.M. 421, 423
 Bouby, M. 474, 506
 Boulon, G., see Gaft, M. 480
 Bouquet, F., see Fisher, R.A. 326
 Bouquet, F., see Gordon, J.E. 326
 Bourée, F., see André, G. 123
 Bourée, F., see Autret, C. 338
 Bourée, F., see Damay, F. 330, 336
 Boutonnet, R., see Labeau, M. 203
 Brachmann, A., see Geipel, G. 495, 499, 500, 505
 Bradbury, M.I. 541
 Bradley, D., see Holzer, W. 506
 Bradley, J.A., see Wolford, D.J. 555
 Brand, L., see Beechem, J.M. 498
 Brand, L., see Laws, W.R. 498, 505
 Braun, D., see Jeitschko, W. 2, 4, 6, 7, 15
 Braun, D.J. 2, 4, 7, 11, 15, 44, 47, 49, 52, 56, 57, 59, 60, 62, 69, 71, 76–78
 Braun, D.J., see Evers, C.B.H. 15, 23
 Braun, D.J., see Evers, Ch.B.H. 65, 71, 72, 74, 76, 77, 95
 Braun, D.J., see Grandjean, F. 8, 13, 23, 24
 Bray, K.L. 517
 Bray, K.L., see Culp, T.D. 524, 525, 578–580
 Bray, K.L., see Lochhead, M.J. 471, 524, 555, 556, 581
 Bray, K.L., see Shen, Y.R. 522, 525, 545, 564–566, 575–577
 Bray, K.L., see Wamsley, P.R. 525, 575, 577
 Bredig, M.A., see Dworkin, A.S. 151, 152, 166–168, 179–181, 200, 203–209, 222, 223
 Breen, P.J. 473, 474
 Brendler, V. 499
 Brendler, V., see Bernhard, G. 495
 Brendler, V., see Geipel, G. 495, 499, 500, 505
 Brendler, V., see Rutsch, M. 501
 Brese, N.E., see Gordon, R.A. 56, 95
 Bretonnière, Y. 393
 Brewer, L., see Lewis, G.N. 182
 Briggs, J.M. 368, 455
 Brina, R. 507
 Brink, J.M. 364
 Brinks, H.W. 275, 276
 Brog, W.C., see Wood, V.E. 275
 Bros, P., see Billard, I. 470, 495, 501–503, 506
 Brosha, E.L., see Louca, D. 263
 Brown, D. 152
 Brown, D., see Fuger, J. 219, 220
 Brown, D., see Hurtgen, C. 210, 212–214, 216, 218, 220
 Brown, D.E., see Chmisseem, O. 278, 280
 Brown, E., see Porter, B. 200, 201
 Brown, J.M., see Bi, Q. 523, 529, 553
 Bruce, J.I. 355
 Bruce, J.I., see Aime, S. 426, 429
 Bruce, J.I., see Clarkson, I.M. 484, 505
 Brücher, E., see Sherry, A.D. 433
 Brunelli, M., see Lanzara, A. 295, 325
 Brunetti, B. 195, 236–240
 Brunetti, B., see Piacente, V. 195, 237, 239, 240
 Brunetti, B., see Villani, A.R. 195, 236, 238–240
 Bruynseraede, Y., see Gordon, I. 326
 Bryden, C.C. 376, 410, 471, 478, 505
 Brylak, M. 42, 43, 48, 50, 56, 58, 61, 62, 69, 72, 75, 81, 83, 85, 87, 89, 90
 Brylyak, M., see Wollesen, P. 43, 44, 46, 48, 49, 51, 52, 54, 57–61, 63, 66, 68, 70, 72, 73, 75, 80, 83
 Bryzhina, M.F., see Yudin, V.M. 276
 Buchanan, R.A., see Wickersheim, K.A. 567
 Büchel, D. 151, 206
 Bucher, J., see Allen, P. 474
 Buchler, J.W. 449–453
 Büchner, B., see Klingeler, R. 315
 Büchner, B., see Uhlenbruch, S. 317
 Buckau, G., see Monsallier, J.M. 506
 Buddhudu, S. 484
 Budhani, R.C., see Srivastava, S. 291, 292
 Bud'ko, S.L., see Fisher, I.R. 90, 91, 134, 135, 137
 Bukhtiyarov, V.V., see Korshunov, B.G. 204
 Bukowski, Z., see Dabrowski, B. 311, 323
 Bukowski, Z., see Xiong, X. 311
 Bulou, A., see Wang, Q. 523, 533, 534
 Bungenstock, C. 521, 529, 532–535, 537, 540–544, 546, 551

- Bunting, E.N., see Weir, C.E. 516
 Bünzli, J.-C.G. 355, 366, 467, 471, 472, 493, 494, 496
 Bünzli, J.-C.G., see Elhabiri, M. 443–445, 448, 481, 494
 Bünzli, J.-C.G., see Floquet, S. 453, 455–459
 Bünzli, J.-C.G., see Petoud, S. 355, 384–387
 Bünzli, J.-C.G., see Piguet, C. 355, 384, 385, 393–395
 Bünzli, J.-C.G., see Platas-Iglesias, C. 406, 407
 Bünzli, J.-C.G., see Renaud, F. 387–393, 408
 Bünzli, J.-C.G., see Rigault, S. 358, 366, 389, 390, 444, 446–448
 Burdick, G.W. 548
 Burdukovskaya, G.G., see Kudin, L.S. 193, 237, 238
 Burgess, J. 221
 Burgess, S., see Zhang, S. 355
 Burgy, J. 332
 Burkhard, W.J., see Corbett, J.D. 208
 Burleigh, M.C., see Dai, S. 494
 Burlet, P. 55
 Burlet, P., see Rossat-Mignod, J. 55, 57
 Burnashev, O.R., see Abdusalamova, M.N. 36, 37, 135
 Burnett, J.L. 215
 Burns, J.B., see Chen, G. 523, 557
 Burns, P.D. 363
 Burrows, H., see Billard, I. 470, 495, 501–503, 506
 Burrows, H.D. 491, 492, 497
 Burrows, H.D., see Azenha, M.E. 498
 Burrows, H.D., see Miguel, M.G. 498
 Burrows, H.D., see Rykov, S. 497
 Burton, G.D., see Thoma, R.E. 201–203, 206, 207
 Buschow, K.J., see Mentink, S.A.M. 54
 Butera, A., see Causa, M.T. 326
 Butman, M.F., see Kudin, L.S. 193, 237, 238
 Buzare, J.Y., see Rewaj, T. 524, 536

 Cacciamani, G. 135
 Cacciamani, G., see Ferro, R. 37, 135
 Cacciamani, G., see Riani, P. 93
 Cacheris, W.P. 410
 Cacheris, W.P., see Sherry, A.D. 433
 Cader, M.S.R., see Greis, O. 149, 150, 166, 200–203
 Cahill, J.A., see Kishenbaum, A.D. 178
 Cai, W., see Zhao, Y.G. 328
 Caillat, T. 29
 Caillat, T., see Chen, B. 13
 Caillat, T., see Fleurial, J.-P. 3, 11, 13, 27, 29
 Caillat, T., see Nolas, G.S. 11
 Caillat, T., see Watcharapasorn, A. 6, 7, 12, 13, 29
 Calabi, L., see Bianchi, A. 426
 Calvert, L.D., see Villars, P. 37
 Camp, F.E., see Hirayama, C. 239, 240
 Campbell, A.J. 319
 Campbell, J.A., see Kennedy, R.J. 521, 522, 524, 525
 Canedy, C.L., see Xiao, G. 328
 Caneiro, A., see Allodi, G. 288
 Caneiro, A., see Causa, M.T. 326
 Canfield, P.C., see Fisher, I.R. 90, 91, 134, 135, 137
 Cantelli, R., see Cordero, F. 326
 Cao, B.S., see Zhao, Y.G. 328
 Cao, W.L., see Zhao, Y.G. 296
 Capogna, L., see Radaelli, P.G. 329
 Capozzi, F., see Bertini, I. 357, 361
 Capponi, S., see Dagotto, E. 261
 Caramagno, E., see Congeduti, A. 325
 Carassiti, V., see Allsopp, S.R. 473, 474
 Caravan, P. 357, 360–362
 Cardona, M., see Trommer, R. 578
 Cardoso, A.C., see Burrows, H.D. 497
 Cardoso, A.C., see Miguel, M.G. 498
 Carlson, G.L., see Hirayama, C. 196, 197, 239
 Carnall, W.T. 160, 161, 383, 469, 471, 472, 481, 494
 Casa, D. 315
 Casa, D., see Kiryukin, V. 291
 Casa, D., see Zimmermann, M.V. 264
 Casado, J.A., see Berregi, I. 507
 Castellano, C., see Cordero, F. 326
 Castelli Guidi, M., see Allodi, G. 288
 Castle, P.M., see Hirayama, C. 196, 197, 239, 240
 Castro, M.M.C.A., see Sherry, A.D. 433
 Causa, M.T. 326
 Causa, M.T., see Rivadulla, F. 309, 321
 Cava, R.J. 56
 Cavalieri, S., see Bungenstock, C. 521, 529, 533, 535
 Cerne, J., see Quijada, M.A. 296
 Cesaro, S.N., see Bencze, L. 186, 226, 235
 Cesaro, S.N., see Feltrin, A. 186, 191, 227–229, 231
 Cestelli Guidi, M. 264
 Ceulemans, A., see Mironov, V.S. 355, 366, 368–372
 Chadi, D.J. 580
 Chahara, K.I. 290
 Chakoumakos, B.C. 8

- Chakoumakos, B.C., see Dilley, N.R. 26
 Chakoumakos, B.C., see Keppens, V. 11
 Chakoumakos, B.C., see Sales, B.C. 7, 9–11, 13, 29, 31
 Chaminade, J.-P., see Oppenländer, A. 522
 Champagnon, B., see Gaft, M. 480
 Chan, J.Y. 37, 90, 134
 Chandran, R., see Forsberg, J.H. 357, 358, 374, 380, 427–431, 439, 440
 Chang, C.-T.P., see Del Cul, G.D. 523
 Chang, C.A. 420
 Chang, C.A., see Holz, R.C. 478, 480, 502
 Chang, C.W. 336
 Chang, K.J., see Chadi, D.J. 580
 Chang, N.C. 538
 Chapados, C., see Max, J.J. 482
 Chapon, D. 454, 455
 Chapon, L., see Ravot, D. 10, 11, 13
 Charlu, T.V. 164, 165
 Charlu, T.V., see Besenbuch, G. 235
 Charvillat, J.-P. 57, 61, 71, 75, 81
 Chateau, C., see Lacam, A. 522, 529, 554
 Chateau, C., see Leger, J.M. 522, 554
 Chau, R., see Bauer, E.D. 13, 16
 Chau, R., see Gajewski, D.A. 13
 Chaudhuri, A.K., see Charlu, T.V. 164, 165
 Chaussecent, S., see Monteil, A. 524, 556
 Chauveau, F., see Mooney, W. 497
 Chawla, S., see Sandhu, S. 497
 Chechersky, V. 295, 296, 298, 305, 325
 Chechersky, V., see Nath, A. 325
 Cheetham, A.K., see Rao, C.N.R. 330
 Chen, B. 13
 Chen, B., see Morelli, D.T. 11
 Chen, C.-C., see Lu, Q. 298
 Chen, C.H. 328, 329
 Chen, C.H., see Cheong, S.W. 323
 Chen, C.H., see Mori, S. 328–330
 Chen, C.H., see Uehara, M. 327
 Chen, C.L., see Zhao, Y.G. 296
 Chen, G. 522–524, 529, 549, 550, 557, 558
 Chen, G., see Stump, N.A. 523, 557
 Chen, H.J., see Zhang, J.S. 65, 73
 Chen, J.W., see Torikachvili, M.S. 6, 8, 17, 22
 Chen, L., see Tang, X. 29, 30
 Chen, W., see Franck, J.P. 307
 Chen, Y.-R. 285
 Chen, Z., see Saraf, L.V. 309
 Cheong, S.-W., see Chen, C.H. 328, 329
 Cheong, S.-W., see Cox, D.E. 291
 Cheong, S.-W., see Fernández-Baca, J.A. 321
 Cheong, S.-W., see Granado, E. 329
 Cheong, S.-W., see Heffner, R.H. 298, 325
 Cheong, S.-W., see Hwang, H.Y. 290, 291
 Cheong, S.-W., see Kim, K.H. 327, 328
 Cheong, S.-W., see Lanzara, A. 295, 325
 Cheong, S.-W., see Liu, H.L. 328
 Cheong, S.-W., see Mori, S. 328–330
 Cheong, S.-W., see Naler, S. 328
 Cheong, S.-W., see Podzorov, V. 327
 Cheong, S.-W., see Radaelli, P.G. 299, 323, 325, 327, 329
 Cheong, S.-W., see Schiffer, P. 328
 Cheong, S.-W., see Uehara, M. 323, 327–329, 340
 Cheong, S.-W., see Yoon, S. 326
 Cheong, S.-W., see Yoshinari, Y. 328
 Cheong, S.W. 323
 Chernogorenko, V.B., see Kobzenko, G.F. 36
 Chi, Y. 523, 524, 530, 533, 534, 536, 539
 Chi, Y., see Liu, S. 523, 524, 529, 530, 533, 539
 Chi, Y., see Wang, L. 523, 524, 551, 568
 Chi, Y., see Wang, Q. 524, 530, 538
 Chistotina, E.A., see Babushkina, N.A. 308, 309
 Chmaisseem, O. 278, 280
 Chmaisseem, O., see Dabrowski, B. 311, 323
 Chmaisseem, O., see Xiong, X. 311
 Choi, E.J., see Jung, J.H. 323
 Choi, J.-W., see McIlroy, D.N. 295
 Choppin, G.R. 387, 467, 493, 495, 499, 505
 Choppin, G.R., see Barthelemy, P.P. 478, 479
 Choppin, G.R., see Billard, I. 470, 495, 501–503, 506
 Choppin, G.R., see Bünzli, J.-C.G. 467, 471, 472, 493, 496
 Choppin, G.R., see De Sa, G.F. 471, 483
 Choppin, G.R., see Hasegawa, Y. 479, 480
 Choppin, G.R., see Kimura, T. 473, 478, 479, 481
 Choppin, G.R., see Lis, S. 471, 473, 478–481, 494, 496
 Choppin, G.R., see Shin, H. 478
 Choppin, G.R., see Wang, Z.M. 478, 494, 495, 499, 505
 Chouteau, G., see Dupont, F. 336
 Chouteau, G., see Millange, F. 336
 Chrétien, A., see De Kozak, A. 201
 Christensen, A.L., see King, E.G. 154, 164, 176, 178, 200
 Chrzanowski, J., see Franck, J.P. 307
 Chu, C.W., see Alexandrov, A.S. 308
 Chudinovskikh, L., see Shen, Y.R. 564
 Chuiko, A.G., see Abdusalamova, M.N. 37
 Chuiko, A.G., see Abulkhaev, V.D. 94

- Chun, S.H. 298
 Churchill, M.R., see Amin, S. 426
 Churchill, M.R., see Morrow, J.R. 426
 Ciach, S. 236, 237
 Ciano, M., see Sabbatini, N. 494
 Clarkson, I., see Beeby, A. 481–484
 Clarkson, I.M. 484, 505
 Clementi, V. 359
 Cohen, L.F., see Freitas, R.S. 310
 Cohn, J.L., see Neumeier, J.J. 283
 Cohn, J.L., see Nolas, G.S. 11
 Coldea, R., see Keppens, V. 11
 Collings, E.W., see Wood, V.E. 275
 Conder, K., see Zhao, G.-M. 305, 307
 Congeduti, A. 325
 Cooper, S.L., see Liu, H.L. 328
 Cooper, S.L., see Naler, S. 328
 Cooper, S.L., see Yoon, S. 326
 Corbett, J.D. 5, 208, 209
 Corbett, J.D., see Druding, L.F. 204, 208
 Corbett, J.D., see Ganguli, A.K. 42, 110
 Corbett, J.D., see Guloy, A.M. 49
 Corbett, J.D., see Mee, J.E. 208
 Cordero, F. 326
 Cordfunke, E.H.P. 152, 171, 172, 174, 181,
 207–211, 213, 218, 220, 221
 Cordfunke, E.H.P., see Furkaliouk, M.Y. 210, 211,
 220, 222
 Cordfunke, E.H.P., see Van Roosmalen, J.A.M.
 267
 Cordier, G. 43, 44, 46
 Cordier, G., see Sologub, O. 43, 46, 47, 51, 54, 60,
 68, 74, 103
 Cornelius, A.L., see Neumeier, J.J. 278
 Corradi, G., see Dierolf, V. 525, 529, 555
 Corsi, D.M. 356
 Cortes, R., see Grandjean, F. 13
 Cousseins, J.C., see Labeau, M. 203
 Couston, L. 499
 Couston, L., see Billard, I. 470, 495, 501–503, 506
 Couston, L., see Moulin, C. 508
 Cox, A., see Allsopp, S.R. 473, 474
 Cox, D.E. 291
 Cox, D.E., see Radaelli, P.G. 327, 329
 Cox, J.D. 173
 Craig, I., see Allen, P. 474
 Credi, A., see Balzani, V. 355
 Crich, S.G., see Aime, S. 433
 Cripe, D.M., see Robinson, M. 200
 Crosswhite, H., see Dieke, G.H. 154, 160
 Crosswhite, H.M., see Dieke, G.H. 154, 160
 Cui, H., see Guo, C. 524, 539
 Culp, T.D. 524, 525, 578–580
 Cundari, T.R. 148, 185, 189
 Cunningham, B.B., see Burnett, J.L. 215
 Cunningham, B.B., see Lohr, H.R. 210, 212
 Cunningham, J. 489, 497
 Curtis, M.M. 544
 Daane, A.H., see Spedding, F.H. 149, 200–209
 Dabrowski, B. 311, 323
 Dabrowski, B., see Chmaissem, O. 278, 280
 Dabrowski, B., see Xiong, X. 311
 Dadgar, A., see Choppin, G.R. 499
 Dagotto, E. 261
 Dagotto, E., see Burgy, J. 332
 Dai, P. 325
 Dai, P., see Fernández-Baca, J.A. 321
 Dai, P., see Keppens, V. 11
 Dai, S. 494
 Daire, M. 215
 Dalichaouch, Y., see Torikachvili, M.S. 6, 8, 17, 22
 Damay, F. 330, 336
 Damay, F., see Freitas, R.S. 310
 Damien, D., see Charvillat, J.-P. 57, 61, 71, 75, 81
 d'Amour-Sturm, H., see Gregorian, T. 521, 529,
 531, 532, 536, 537, 540, 541, 545, 559
 Daniel, J.F. 151, 205
 Dannebrock, M.E. 10, 21, 23, 24
 Daoud-Aladine, A., see Pinsard-Gaudart, L. 268,
 280
 Daoud-Aladine, M. 328, 335, 336
 Daramagnyan, A.P., see Azenha, M.E. 498
 Darling, T.W., see Dilley, N.R. 26
 Dartyge, E., see Tolentino, H. 518
 Das, A., see Gordon, I. 326
 Das, A., see Vijaya Lakshmi, K. 121, 124
 Dass, R.I., see Goodenough, J.B. 272–274
 Datchi, F. 522, 554
 Davis, R.E., see Wilcott, M.R. 373, 385
 de Blas, A., see Geraldès, C.F.G.C. 358, 378, 404,
 405
 de Blas, A., see Platas, C. 358, 359, 377, 378,
 400–404
 de Brion, S., see Dupont, F. 336
 De Brion, S., see Millange, F. 336
 De Cian, A., see Moussavi, M. 440
 De Cillis, F.M., see Sacco, A. 482
 de Gennes, P.-G. 258
 De Kozak, A. 201, 202
 de Leon-Guevara, A.M., see Vasiliu-Doloc, L.
 299, 318

- de Lozanne, A., see Lu, Q. 298
- De Renzi, R., see Allodi, G. 288, 325, 328, 337
- De Renzi, R., see Cestelli Guidi, M. 264
- De Sa, G.F. 471, 483
- De Schryver, F.C., see Janssens, L.D. 471
- de Sousa, A., see Beeby, A. 481–484
- de Sousa, A.S., see Aime, S. 426, 429
- de Sousa, A.S., see Dickins, R.S. 482
- De Teresa, J.M. 298–300
- De Teresa, J.M., see García-Landa, B. 338
- Deakin, L. 133
- Debnath, A.K., see Chang, C.W. 336
- Decambox, P. 507, 508
- Decambox, P., see Berthoud, T. 507, 508
- Decambox, P., see Couston, L. 499
- Decambox, P., see Moulin, C. 507, 508
- Decambox, P., see Thouvenot, P. 507
- deCian, A.D., see Buchler, J.W. 449, 450
- Dedieu, A., see Berny, F. 358
- Dediu, V. 327
- DeGraff, B.A., see Bare, W.D. 470, 509
- DeKock, C.W., see Lesiecki, M. 186, 224
- DeKock, C.W., see Wesley, R.D. 186, 191, 224, 225
- Del Cul, G.D. 523, 558
- del Moral, A., see De Teresa, J.M. 298, 299
- Delacote, D., see Rossat-Mignod, J. 55, 57
- Delaney, R.M., see Forsberg, J.H. 357, 358, 374, 380, 427–431, 439, 440
- Delange, P., see Chapon, D. 454, 455
- Delaplane, R.G., see Wasse, J.C. 179
- Delfino, S., see Borzone, G. 36
- Deline, T.A. 161, 163
- Dellonte, S., see Sabbatini, N. 494
- DeLong, L.E. 6, 8, 9
- Demas, J.N., see Bare, W.D. 470, 509
- Demas, J.N., see Metcalf, D.H. 489
- Demas, J.N., see Sharman, K.S. 470
- DeMattei, R.C., see Watcharapasorn, A. 6, 12, 13, 29
- Dender, D.C., see Huang, Q. 328, 329
- Denis, J.P., see Blanzat, B. 523, 524, 574
- Denning, R. 557
- Deschaux, M. 498
- Deschaux, M., see Marcantonatos, M.D. 497
- Desreux, J.F. 357, 421, 422
- Desreux, J.F., see Bryden, C.C. 410
- Desreux, J.F., see Jacques, V. 423
- Desreux, J.F., see Reilley, C.N. 357, 376, 377, 404–407, 410, 443
- Desreux, J.F., see Spirlet, M.-R. 420
- Dessau, D.S. 268
- Dettingmeijer, J.H. 196, 240
- Deventer, E.V., see Rudzitis, E. 215, 219
- Devlin, E., see Kallias, G. 328
- Devlin, E., see Simopoulos, A. 328
- Dewalsky, M.V., see Jeitschko, W. 15, 23, 24
- Dewey, H.J. 467
- Dewhurst, C.D., see Lees, M.R. 291
- Dexter, D.L. 569–571
- Dho, J. 322, 325, 328
- Di Bella, S. 185
- Dias, F., see Freitas, R.S. 310
- Dickey, R.P., see Bauer, E.D. 8, 12, 15, 17
- Dickins, R., see Beeby, A. 481–484
- Dickins, R.S. 481, 482
- Dickins, R.S., see Bruce, J.I. 355
- Dieke, G.H. 154, 160, 552
- Dielis, H.R., see Dettingmeijer, J.H. 196, 240
- Dierolf, V. 525, 529, 555
- Dietrich, L., see Wollesen, P. 43, 44, 46, 48, 49, 51, 52, 54, 57–61, 63, 66, 68, 70, 72, 73, 75, 80, 83
- Dikovsky, V., see Yuzhelevski, Y. 326
- Dilley, N.R. 15, 26
- Dilley, N.R., see Bauer, E.D. 8, 12, 13, 15–17
- Dilley, N.R., see Dordevic, S.V. 8, 12, 17, 26, 27
- Dilley, N.R., see Gajewski, D.A. 13
- Dimitropoulos, C., see Papavassiliou, G. 325, 326, 328
- Dimmock, J.O., see Oliver, M.R. 252
- DiSalvo, F.J., see Gordon, R.A. 56, 95, 97, 100, 113
- Dlouhá, M., see Jiráček, Z. 275, 291
- Dmowski, W., see Louca, D. 304
- Dobson, C.M., see Bleaney, B. 357, 365, 371
- Dogotto, E., see Mayr, M. 326
- Dolg, M. 148, 183, 187–189
- Dolinsek, C., see Papavassiliou, G. 325
- Dolinsek, J., see Papavassiliou, G. 328
- Donato, H. 404
- Donni, A., see Keller, L. 17, 23
- Dordevic, S., see Dilley, N.R. 26
- Dordevic, S.V. 8, 12, 17, 26, 27
- Dorfman, R.C., see Morrison, M.E. 489
- Doumerc, J.-P., see Töpfer, J. 286, 287, 289
- Dow, J.D., see Ren, S.Y. 580
- Dowben, P.A., see McIlroy, D.N. 295
- Drew, H.D., see Quijada, M.A. 269, 296
- Drew, H.D., see Romero, D.B. 268
- Drew, H.D., see Zhao, Y.G. 296
- Drickamer, H.G., see Drotning, W.D. 521, 524, 550

- Drickamer, H.G., see Fitch, R.A. 516
 Drickamer, H.G., see Hayes, A.V. 522–524, 571, 572
 Drickamer, H.G., see Keating, K.B. 521–525, 562
 Drickamer, H.G., see Tyner, C.E. 523, 550
 Drickamer, H.G., see Wang, P.J. 522–525, 550
 Drickamer, H.G., see Webster, G.A. 524, 551, 567, 568, 574
 Drobot, D.V., see Korshunov, B.G. 204, 205
 Drobot, D.V., see Pashinkin, A.S. 237
 Drost, R., see García-Landa, B. 338
 Drotning, W.D. 521, 524, 550
 Druding, L.F. 204, 208
 Druding, L.F., see Corbett, J.D. 208
 Du, Y.-W., see Li, J.-M. 325
 Dubois, V., see Billard, I. 470, 495, 501–503, 506
 Dubost, J.P. 420
 Dudareva, A.G., see Molodkin, A.K. 208
 Dudchik, G.P. 236–238
 Dudchik, G.P., see Makhmadmurodov, A. 195, 239
 Dudek, H. 206
 Dudkin, L.D. 29
 Dunner, J. 77, 95
 Dupas, C., see Anane, A. 291
 Duplâtre, G., see Rustenholtz, A. 474
 Dupont, F. 336
 Durand, J.S., see Berregi, I. 507
 Dwight, A.E. 37, 40–42, 72, 76, 79, 81–90, 92, 93
 Dwight, A.E., see Shaked, H. 84, 87, 89, 90, 127, 129
 Dworkin, A.S. 151, 152, 166–168, 179–181, 200, 203–209, 222, 223
 Dyakonov, K., see Ilisavskii, Y. 326
 Dyakonov, V.P., see Ilisavskii, Y. 326
 D'yakov, Y.A., see Berezhkovskii, A.M. 489
 Dybzinski, R., see Dabrowski, B. 311, 323
 Dybzinski, R., see Xiong, X. 311
 Dzialoshinskii, I.E. 258
- Earl, W.L., see Pinkerton, A.A. 415–418
 Ebel, T., see Albering, J.H. 76, 90
 Ebel, T., see Evers, C.B.H. 15, 23
 Ebel, T., see Evers, Ch.B.H. 65, 71, 72, 74, 76, 77, 95
 Edder, C., see Piguët, C. 355, 393
 Edelstein, N., see Allen, P. 474
 Edelstein, N.M., see Yoo, C.S. 522, 549, 550
 Edvalson, J.H., see Hornbostel, M.D. 8
 Effantim, J.M., see Rossat-Mignod, J. 55, 57
 Efimov, M.E., see Furkaliouk, M.Y. 216
 Egami, T. 261, 263, 292, 304
 Egami, T., see Louca, D. 263, 304
 Ehlers, G., see Heffner, R.H. 298
 Ehrlich, A.C., see Nolas, G.S. 11
 Ehrlich, S., see Oppermann, H. 210
 Eichhorn, M. 569
 Eick, H.A., see Biefeld, R.M. 235
 Einarsrud, M.A., see Faaland, S. 323
 El Azzi, A., see Billard, I. 510
 El-Ansi, T.A., see Choppin, G.R. 499
 Elbanowski, M., see Hnatejko, Z. 482, 496
 Elgavish, G.A., see Reuben, J. 365, 376, 379, 380
 Elhabiri, M. 443–445, 448, 481, 494
 Elhabiri, M., see Nehlig, A. 473, 474, 482, 485
 Eliet, V. 474, 498, 501
 Eliseev, A.A., see Abdusalamova, M.N. 37
 Ellenwood, R.E., see Ferguson, M.J. 48, 57, 61, 70, 102
 Ellison, J.J., see Caravan, P. 357, 360–362
 Elzinga, G.D., see Cordfunke, E.H.P. 152, 207, 208
 Emin, D. 293
 Endoh, Y. 315
 Endoh, Y., see Martin, M.C. 322
 Endoh, Y., see Murakami, Y. 263
 Endoh, Y., see Nojiri, H. 317
 Englisch, U., see Shen, Y.R. 564
 Eremets, M. 517, 519, 561
 Ericksson, S., see Björnsson, P. 268
 Eriksen, J., see Björnsson, P. 268
 Ermolaev, V.L. 495, 497, 499, 501, 503
 Ermondi, G., see Aime, S. 357, 361, 363, 421, 422, 439, 440
 Erwin, R.W. 325
 Erwin, R.W., see Huang, Q. 289, 325, 328, 329
 Erwin, R.W., see Lynn, J.W. 299, 325
 Evans, D.F. 356
 Evers, C.B.H. 15, 23
 Evers, C.B.H., see Dannebrock, M.E. 10, 21, 23, 24
 Evers, C.B.H., see Jeitschko, W. 15, 23, 24
 Evers, Ch.B.H. 65, 71, 72, 74, 76, 77, 95
 Evseeva, G.V. 236
 Exarhos, G.J., see Hess, N.J. 523, 553, 554
 Eyring, L., see Machlan, G.R. 214, 215, 221
 Ezhov, Y.S. 230
- Faaland, S. 323
 Fahey, J.A., see Morss, L.R. 214, 218
 Fanghänel, T. 495, 496, 500
 Fanghänel, T., see Aas, W. 500

- Fanghänel, T., see Billard, I. 470, 495, 501–503, 506
- Fanghänel, T., see Paviet, P. 500
- Fanghänel, T., see Stumpf, T. 495
- Farber, G.K., see Albin, M. 478, 499, 505
- Fardis, M., see Papavassiliou, G. 325, 326, 328
- Fasano, M., see Aime, S. 357, 360, 362, 420–422
- Faslyeva, N.D., see Abdusalamova, M.N. 37
- Fäth, M. 298
- Faucher, M., see Garcia, D. 542, 550
- Faucher, M.D. 550
- Faulkner, S., see Beeby, A. 481–484
- Fazakerley, G.V., see Evans, D.F. 356
- Fazekas, Z., see Yamamura, T. 491, 492
- Fazlyeva, N.D., see Abdusalamova, M.N. 36, 37
- Fedorov, P.P., see Sobolev, B.P. 150, 200–203
- Feigelson, R.S., see Watcharapasorn, A. 6, 7, 12, 13, 29
- Feiguin, A., see Mayr, M. 326
- Feldman, J.L. 11
- Felmy, A.R. 506
- Felner, I., see Markovich, V. 287
- Feltrin, A. 186, 191, 227–229, 231
- Feltrin, A., see Bencze, L. 186, 226, 235
- Feng, D., see Li, J.-M. 325
- Ferdeghini, C., see Dediu, V. 327
- Ferguson, M.J. 43, 47–50, 57, 58, 61–63, 70, 72, 75, 79, 82, 84, 102, 103
- Ferguson, M.J., see Bollore, G. 43, 47, 49, 50, 55, 57, 58, 60, 62, 69, 71, 72, 74, 75, 110
- Ferguson, M.J., see Raju, N.P. 43
- Fernández-Baca, J.A. 321
- Fernandez-Baca, J.A., see Dai, P. 325
- Fernandez-Baca, J.A., see Yamada, Y. 315
- Fernández-Díaz, M.T. 329
- Fernández-Díaz, M.T., see Daoud-Aladine, M. 328, 335, 336
- Ferrari, M., see Monteil, A. 524, 556
- Ferretti, M., see Cordero, F. 326
- Ferro, R. 37, 135
- Ferro, R., see Borsese, A. 36
- Ferro, R., see Borzone, G. 36, 37, 135, 136
- Ferro, R., see Cacciamani, G. 135
- Ferro, R., see Flandorfer, H. 91, 92, 118
- Ferro, R., see Marazza, R. 41, 48, 56, 61, 69, 74, 81, 83, 85, 87, 88, 91, 106
- Ferro, R., see Riani, P. 41, 85, 87, 88, 91, 93
- Ferro, R., see Rossi, D. 49, 57, 71, 76
- Feuersanger, A.E., see Struck, C.W. 196, 239, 240
- Ficalora, P., see Hastie, J.W. 193, 197, 236, 237
- Fiebig, M. 291
- Fiebig, M.K. 291
- Field, L.D., see Baker, M.V. 356
- Fields, P.R., see Carnall, W.T. 494
- Finger, L.W., see Hazen, R.M. 518
- Fini, L., see Bungenstock, C. 521, 533
- Fink, H., see Seifert, H.J. 203, 204
- Finkelshtein, L.D., see Aliev, O.M. 77, 78, 91
- Fischer, H.O. 49, 58, 62
- Fischer, J., see Buchler, J.W. 449, 450
- Fischer, J., see Moussavi, M. 440
- Fischer, K., see Zimmer, H.G. 523
- Fischer, P., see Keller, L. 17, 23
- Fisher, I.R. 90, 91, 134, 135, 137
- Fisher, R.A. 326
- Fisher, R.A., see Gordon, J.E. 326
- Fisk, Z., see Yoon, S. 326
- Fita, I., see Markovich, V. 325
- Fitch, R.A. 516
- Fitzgibbon, G.C. 210, 212, 215–217
- Fitzgibbon, G.C., see Baker, F.B. 214
- Fitzgibbon, G.C., see Huber Jr., E.J. 218
- Fjellvåg, H., see Brinks, H.W. 275, 276
- Flandorfer, H. 91, 92, 118, 127
- Fletcher, S., see Brown, D. 152
- Fleurial, J.-P. 3, 11, 13, 27, 29
- Fleurial, J.-P., see Caillat, T. 29
- Fleurial, J.-P., see Chen, B. 13
- Fleurial, J.-P., see Watcharapasorn, A. 6, 7, 12, 13, 29
- Floquet, S. 453, 455–459
- Floquet, S., see Bocquet, B. 453, 455, 456
- Flotow, H.E. 154, 157
- Flotow, H.E., see Lyon, W.G. 154, 157, 162–164, 166
- Flynn, J.P., see Spedding, F.H. 210–212, 215, 216, 219
- Foecker, A.J., see Jeitschko, W. 15, 23, 24
- Folcher, G., see Arvis, M. 497
- Folcher, G., see Mooney, W. 497
- Fondado, A., see Mira, J. 295
- Fondado, A., see Rivadulla, F. 309
- Fonger, W.H. 523, 524, 567
- Fonger, W.H., see Struck, C.W. 567, 568, 572
- Fontaine, A., see Tolentino, H. 518
- Fontcuberta, J. 299
- Fontcuberta, J., see García-Muñoz, J.L. 323
- Fontcuberta, J., see Laukhin, V. 299
- Fontcuberta, J., see Martínez, B. 317
- Fontcuberta, J., see Senis, R. 317
- Fontcuberta, J., see Skumryev, V. 312
- Foong, F., see McIlroy, D.N. 295

- Forman, R.A., see Piermarini, G.J. 518
 Formosinho, S., see Rykov, S. 497
 Formosinho, S.J., see Azenha, M.E. 498
 Formosinho, S.J., see Burrows, H.D. 497
 Formosinho, S.J., see Miguel, M.G. 498
 Fornasini, M.L., see Borzone, G. 37, 135, 136
 Fornasini, M.L., see Merlo, F. 91, 92
 Forsberg, J.H. 357, 358, 364, 367, 368, 371–374, 380, 427–431, 439, 440
 Förster, T. 483, 569, 570
 Fort, D., see Thornton, M.J. 124
 Fournier, P., see Smolyaninova, V.N. 327
 Fragalá, I., see Di Bella, S. 185
 Fragalá, I.L., see Lanza, G. 189
 Francesconi, L.C., see Chang, C.A. 420
 Francisco, J., see Steinfeld, J. 487
 Franck, J.P. 307
 Franck, J.P., see Chechersky, V. 295, 296, 305, 325
 Franck, J.P., see Fisher, R.A. 326
 Franck, J.P., see Gordon, J.E. 326
 Franklin, S.J., see Wu, S.L. 492
 Franzen, H.F., see Mozharivskiy, Yu. 37, 41, 42, 80, 81, 83, 85, 87–90, 93
 Franzen, H.F., see Zeng, L. 48
 Fraternali, F. 358
 Fraternali, F., see Ulrich, G. 358
 Frederick, N.A., see Bauer, E.D. 21, 22
 Frederick, N.A., see Maple, M.B. 22
 Freeman, A.J. 377
 Freeman, E.J., see Bauer, E.D. 8, 12, 15, 17, 24
 Freeman, E.J., see Dilley, N.R. 15, 26
 Freeman, E.J., see Gajewski, D.A. 13
 Freeman, E.J., see Keppens, V. 11
 Freibert, F., see Dilley, N.R. 26
 Freisem, S., see Fäth, M. 298
 Freitas, R.S. 310, 328, 329
 Freitas, R.S., see Levy, P. 328
 Frey, S.T. 496
 Frick, B. 94, 140
 Friedt, O., see Uhlenbruch, S. 317
 Frimmel, F.H., see Monsallier, J.M. 506
 Fronczek, F. 381
 Frontera, C. 336
 Frontera, C., see Llobet, A. 336
 Frullano, L. 421
 Fu, P.K.L. 355
 Fuger, J. 171, 219, 220, 500
 Fuger, J., see Bettonville, S. 217, 219, 221
 Fuger, J., see Hurtgen, C. 210, 212–214, 216, 218, 220
 Fuger, J., see Merli, L. 174, 210, 213, 216, 220–222
 Fuger, J., see Morss, L.R. 467
 Fujishiro, H. 276, 322, 326
 Fujishiro, I. 519
 Fujita, M. 355
 Fujita, N., see Fujita, M. 355
 Fukase, T., see Fujishiro, H. 326
 Fukuda, T., see Endoh, Y. 315
 Fukushima, K., see Iwadate, Y. 179
 Fulde, P., see Thalmeier, P. 582
 Furkaliouk, M.Y. 210, 211, 216, 217, 220–222
 Furkaliouk, M.Y., see Cordfunke, E.H.P. 213, 218
 Furkalyuk, M.Y., see Leonidov, V.Y. 218
 Furrer, A., see Mesot, J. 524, 535
 Furukawa, N., see Dagotto, E. 261
 Furukawa, Y., see Yakubovskii, A. 309
 Fusi, V., see Bazzicalupi, C. 492, 509
 Gaft, M. 480
 Gagliardi, L., see Spencer, S. 493
 Gaillard, C., see Billard, I. 510
 Gajewski, D.A. 13
 Gajewski, D.A., see Keppens, V. 11
 Galas, O., see Bertini, I. 363
 Galatanu, A., see Bauer, E. 24
 Galchenko, I.E., see Korshunov, B.G. 204, 205
 Galli, M., see Bauer, E. 24
 Galyametdinov, Y.G., see Mironov, V.S. 355, 366, 368–372
 Gamanovich, N.M. 219
 Gambino, R.J. 94
 Gamelin, D.R. 355
 Gampe, T., see Stangret, J. 482
 Ganguli, A.K. 42, 110
 Ganzjuk, A.L., see Skolozdra, R.V. 41, 46, 53, 59, 60, 67, 73, 80, 82, 84, 86–88, 132, 133
 Gao, C., see Liu, S. 524, 539
 García, A., see Granado, E. 284, 329
 Garcia, D. 542, 550
 García, J., see De Teresa, J.M. 298–300
 García, J., see Stankiewicz, J. 292
 García, J., see Subías, G. 323
 García-Landa, B. 338
 García-Muñoz, J.L. 323
 García-Muñoz, J.L., see Frontera, C. 336
 García-Muñoz, J.L., see Laukhin, V. 299
 García-Muñoz, J.L., see Llobet, A. 336
 Gardner, J.S., see Heffner, R.H. 298
 Gardner, J.S., see Wiebe, C.R. 282
 Gardner, P.J. 168
 Garton, G. 205

- Garvin, D., see Parker, V.B. 173
 Gatteschi, D., see Hedinger, R. 454
 Gaune-Escard, M. 151, 166–168, 179, 203–206, 222, 223
 Gaune-Escard, M., see Rycerz, L. 166, 168, 179, 180, 204–206, 222, 223
 Gavrichev, K.S. 161, 163
 Gavrichev, K.S., see Gorbunov, V.E. 157, 158, 160
 Gavrichev, K.S., see Tolmach, P.I. 157, 158, 160
 Gavrilishina, A.I., see Yudin, V.M. 276
 Geballe, T.H., see Worledge, W.C. 323
 Geck, J., see Klingeler, R. 315
 Geertsma, W. 277
 Geidarova, E.A. 42, 71, 75, 85
 Geidarova, E.A., see Rustamov, P.G. 81, 83
 Geidarova, E.A., see Sadygov, F.M. 75
 Geipel, G. 495, 499, 500, 505
 Geipel, G., see Bernhard, G. 495
 Geipel, G., see Billard, I. 470, 495, 501–503, 506
 Geipel, G., see Brendler, V. 499
 Geipel, G., see Rutsch, M. 501
 Georges, J. 495, 508
 Geraldès, C.F.G.C. 357, 358, 378, 404, 405, 410, 411, 414, 415, 417, 418, 420, 424, 425, 427, 429–433, 435–440, 442, 443, 451, 453
 Geraldès, C.F.G.C., see Aime, S. 421, 422
 Geraldès, C.F.G.C., see Frullano, L. 421
 Geraldès, C.F.G.C., see Marques, M.P.M. 421, 423
 Geraldès, C.F.G.C., see Platas, C. 358, 359, 377, 378, 400–404
 Geraldès, C.F.G.C., see Ren, J. 420, 423–426, 429, 431, 433–435, 437–440
 Geraldès, C.F.G.C., see Sherry, A.D. 357, 377, 411–413, 433
 Gerard, A., see Grandjean, F. 8, 13, 23, 24
 Gerloch, M. 368
 Gershenson, M.E., see Podzorov, V. 327
 Gershikov, A.G., see Spiridonov, V.P. 227
 Geurts, F.A.J., see Klink, S.I. 471, 494–496
 Geydarova, E.N. 85
 Ghisletta, M., see Hedinger, R. 454
 Ghivelder, L., see Freitas, R.S. 310, 328, 329
 Ghivelder, L., see Levy, P. 328
 Ghosh, B., see Mandal, P. 312
 Ghosh, K., see Chechersky, V. 295, 296, 298, 305, 325
 Ghosh, K., see Huang, Q. 325, 328, 329
 Ghosh, K., see Malik, S.R. 95
 Ghosh, K., see Smolyaninova, V.N. 329
 Ghosh, K., see Zhao, G. 329
 Giannotti, C., see Mooney, W. 497
 Gibbs, D., see Murakami, Y. 263
 Gibbs, D., see Zimmermann, M.V. 264
 Gibson, J.K. 192, 234
 Giefers, H., see Bungenstock, C. 540
 Gierlowski, P., see Ilisavskii, Y. 326
 Gietmann, C. 194, 196, 197, 207, 209, 238–240
 Gil, A.M.P.C., see Burrows, H.D. 497
 Gill, D., see Meiboom, S. 363
 Ginley, D.S., see Schirber, J.E. 521
 Giorgi, C., see Bazzicalupi, C. 492, 509
 Giorgi, C., see Bianchi, A. 426
 Girichev, G.V. 227–229
 Girichev, G.V., see Giricheva, N.I. 184, 186, 190, 191, 193, 227–229, 232
 Girichev, G.V., see Zakharov, A.V. 184, 186, 190, 191, 195, 229, 232
 Giricheva, N.I. 184, 186, 190, 191, 193, 227–229, 232
 Giricheva, N.I., see Girichev, G.V. 229
 Giricheva, N.I., see Zakharov, A.V. 184, 186, 190, 191, 195, 229, 232
 Giroux, S. 494, 505
 Gladrow, E., see Beck, H.P. 558, 559
 Glasel, J.A., see Barry, C.D. 363
 Gleason, J.K. 524, 551, 566, 568
 Gliemann, G., see Yersin, H. 523, 569
 Glybin, V.P., see Gamanovich, N.M. 219
 Godart, C., see Flandorfer, H. 91, 92, 118, 127
 Godart, C., see Leithe-Jasper, A. 26
 Godart, C., see Patil, S. 53, 80, 133
 Godfrey, R.P., see Saraf, L.V. 309
 Godzaev, E.M., see Rustamov, P.G. 77
 Goffart, J., see Tröster, Th. 531–533, 536, 542, 543
 Gog, Th., see Zimmermann, M.V. 264
 Gogadze, N.G. 201–203
 Golding, R.M. 357, 360, 365, 366, 371, 372
 Goldschmidt, Z.B. 526, 530
 Goldsmid, H.J. 28, 29
 Goldsmid, H.J., see Nolas, G.S. 28
 Goltsev, A., see Ilisavskii, Y. 326
 Golushina, L.N., see Gavrichev, K.S. 161, 163
 Golushina, L.N., see Tolmach, P.I. 157, 158, 160
 Goncharenko, I., see Pinsard-Gaudart, L. 268, 280
 Goncharov, A.F. 522, 582
 Gong, G.Q., see Xiao, G. 328
 Gonzalez, J. 518
 González-Calbet, J.M., see Alonso, J. 324
 Good, B.W., see Reilley, C.N. 357, 376, 377, 404–407, 410, 443

- Goodenough, J.B. 250, 251, 256, 261–263, 265, 267, 269, 270, 272–274, 277, 282, 293, 296, 298, 326, 327, 332
 Goodenough, J.B., see Archibald, W. 294, 295, 300
 Goodenough, J.B., see Liu, G.-L. 311, 313, 316, 318
 Goodenough, J.B., see Overend, N. 303
 Goodenough, J.B., see Rivadulla, F. 328, 330–335, 337–342
 Goodenough, J.B., see Tichy, R.S. 277
 Goodenough, J.B., see Töpfer, J. 269, 286, 288, 289
 Goodenough, J.B., see Zhou, J.-S. 264, 265, 268, 269, 271, 272, 276–282, 284, 300–302, 305–308, 311, 312, 316, 317, 319–322
 Goodman, G.L., see Carnall, W.T. 383
 Gopalakrishnan, J., see Zhao, Y.G. 328
 Gopich, I.V., see Agmon, N. 489
 Gorbenko, O., see Shames, A.I. 338
 Gorbenko, O., see Yakubovskii, A. 309
 Gorbenko, O.Yu., see Babushkina, N.A. 308, 309, 327
 Gorbunov, V.E. 157, 158, 160
 Gorbunov, V.E., see Gavrichev, K.S. 161, 163
 Gorbunov, V.E., see Tolmach, P.I. 157, 158, 160
 Gordon, I. 326
 Gordon, J.E. 326
 Gordon, J.E., see Fisher, R.A. 326
 Gordon, R.A. 56, 95, 97, 100, 113
 Görrler-Walrand, C. 369, 371, 376, 377, 380, 400, 520, 526, 556, 560, 561
 Görrler-Walrand, C., see Mironov, V.S. 355, 368–372
 Gorodetsky, G., see Markovich, V. 287, 325
 Gorodetsky, G., see Yuzhelevski, Y. 326
 Gorodetsky, P., see Loa, I. 268
 Goryushkin, V.F. 180, 182, 205, 206, 209, 223
 Goryushkin, V.F., see Furkaliouk, M.Y. 216, 217, 220, 221
 Goryushkin, V.F., see Gavrichev, K.S. 161, 163
 Goryushkin, V.F., see Gorbunov, V.E. 157, 158, 160
 Goryushkin, V.F., see Kiseleva, T.V. 204
 Goryushkin, V.F., see Laptev, D.M. 203, 204
 Goryushkin, V.F., see Monaenkova, A.S. 218
 Goryushkin, V.F., see Pogrebnoi, A.M. 193, 194, 236, 237
 Goryushkin, V.F., see Poshevneva, A.I. 182, 208
 Goryushkin, V.F., see Tiflova, L.A. 216
 Goryushkin, V.F., see Tolmach, P.I. 157, 158, 160
 Goryushkina, Y.V., see Poshevneva, A.I. 182, 208
 Goto, T., see Sekine, C. 15, 25, 26
 Goto, T., see Tang, X. 29, 30
 Goudiakas, J., see Bettonville, S. 217, 219, 221
 Gougoutas, J.Z., see Chang, C.A. 420
 Govenlock, L.J., see Clarkson, I.M. 484, 505
 Govenlock, L.J., see Bruce, J.I. 355
 Gramlich, V., see Hedinger, R. 454
 Granado, E. 263, 284, 329
 Grande, T., see Faaland, S. 323
 Grandjean, F. 8, 13, 23, 24
 Grandjean, F., see Long, G.J. 13
 Grandjean, F., see Lyon, W.G. 154, 157, 162–164, 166
 Grant, D.H. 356
 Graves, D.T., see Myers, C.E. 182, 184, 186, 192, 194
 Graves, L., see Klink, S.I. 471, 494–496
 Greedan, J.E., see Raju, N.P. 43
 Greedan, J.E., see Wiebe, C.R. 282
 Greenblatt, M., see Markovich, V. 287
 Greenblatt, M., see Wiebe, C.R. 282
 Greene, R.L., see Chechersky, V. 295, 296, 298, 305, 325
 Greene, R.L., see Erwin, R.W. 325
 Greene, R.L., see Huang, Q. 289, 325, 328, 329
 Greene, R.L., see Nath, A. 325
 Greene, R.L., see Smolyaninova, V.N. 321, 327, 329
 Greene, R.L., see Zhao, G. 329
 Greene, R.L., see Zhao, G.-M. 308
 Gregorian, T. 521, 522, 529, 531, 532, 536, 537, 540, 541, 545, 559
 Gregorian, T., see Shen, Y.R. 518, 522, 529, 554
 Gregorian, T., see Tröster, Th. 521, 522, 531, 533, 536, 541, 545, 546, 551
 Greis, O. 149, 150, 166, 200–203, 559
 Greis, O., see Petzel, T. 235
 Greneche, J.M., see Hannover, B. 325
 Grenier, J.-C., see Töpfer, J. 286, 287, 289
 Grenthe, I. 381, 404, 467, 474, 498–500
 Grenthe, I., see Eliet, V. 474, 498, 501
 Groen, P.C. 186, 190, 228, 229, 231
 Grønqvold, F., see Westrum Jr., E.F. 154
 Gross, R., see Klingeler, R. 315
 Gross, R., see Reutler, P. 326
 Gross, R., see Uhlenbruch, S. 317
 Gruber, J.B., see Chang, N.C. 538
 Gruber, J.B., see Wells Jr., J.C. 186, 227, 229, 230
 Grund, I. 40, 42, 96
 Gruzdev, V.P. 499

- Gruzdev, V.P., see Ermolaev, V.L. 495, 497, 499, 501, 503
- Grytsiv, A., see Bauer, E. 24
- Grzechnik, A., see Loa, I. 268
- Gschneidner, K.A., see Adroja, D.T. 60, 61, 118
- Gschneidner Jr., K.A. 171, 199
- Gschneidner Jr., K.A., see Niu, X.J. 82
- Guardigli, M., see Ulrich, G. 358
- Güdel, H.U., see Gamelin, D.R. 355
- Guertin, R.P., see Meisner, G.P. 6, 12
- Guertin, R.P., see Torikachvili, M.S. 6, 8, 17, 22
- Guidi, G., see Allodi, G. 325
- Guidi, G., see Cestelli Guidi, M. 264
- Guilaran, L.J., see Hudspeth, H.D. 326
- Guloy, A.M. 49
- Gunnlaugsson, T., see Bruce, J.I. 355
- Gunnlaugsson, T., see Dickins, R.S. 481
- Gunseliuss, H. 151
- Guo, C. 524, 539
- Gupta, A., see Xiao, G. 328
- Gupta, L.C., see Patil, S. 53, 56, 80, 133
- Gupta, R., see Joshi, J.P. 336
- Guseinov, G.A., see Kuliev, A.N. 74
- Guseinov, G.G., see Aliev, O.M. 77
- Guseinov, M.S., see Aliev, O.M. 77
- Guseinov, M.S., see Rustamov, P.G. 77
- Gutowsky, H.S., see Stout, E.W. 357, 371
- Guzik, A. 54, 113
- Guzik, A., see Kaczmarek, K. 80
- Gvelesiani, G.G. 210, 214
- Gvelesiani, G.G., see Yashvili, T.S. 215
- Haas, Y. 471, 472, 475–477, 480
- Haberkorn, R., see Shen, Y.R. 564
- Habermeier, H.U., see Casa, D. 315
- Hachisu, D., see Scully, A.D. 489
- Haga, Y., see Kohgi, M. 521
- Haga, Y., see Naka, T. 521
- Haga, Y., see Okayama, Y. 521
- Haga, Y., see Oohara, Y. 521
- Haga, Y., see Yoshizawa, H. 521
- Haines, J., see Bungenstock, C. 540
- Haire, R.G. 558
- Haire, R.G., see Chen, G. 522–524, 549, 550, 557, 558
- Haire, R.G., see Del Cul, G.D. 558
- Haire, R.G., see Gibson, J.K. 192, 234
- Haire, R.G., see Morrison, H.G. 151, 205
- Haire, R.G., see Peterson, J.R. 522, 558
- Haire, R.G., see Stump, N.A. 523, 557
- Haire, R.G., see Wilmarth, W.R. 521, 522, 558
- Haire, R.G., see Young, J.P. 558
- Halton, M.P., see Golding, R.M. 357, 360, 365, 366, 372
- Hamaya, N., see Shirohata, I. 13
- Hambley, T.W., see Baker, M.V. 356
- Hamilton, J.J., see Smolyaninova, V.N. 321
- Hammel, P.C., see Yoshinari, Y. 328
- Han, P.D., see Yoon, S. 326
- Handy, C., see Spencer, S. 493
- Hanfland, M., see Loa, I. 268
- Hannay, M.H. 236
- Hannay, M.H., see Myers, C.E. 237
- Hannoyer, B. 325
- Hansen, L.D., see Baker, F.B. 214
- Harada, M., see Park, Y.Y. 489, 491, 492, 498
- Harada, M., see Yamamura, T. 491, 492
- Harakas, G., see Forsberg, J.H. 357, 358, 374, 380, 427–431, 439, 440
- Hargittai, M. 184, 186, 190, 191, 224, 228–230, 232
- Hargittai, M., see Molnár, J. 185, 186, 190, 191, 230–232
- Harima, H. 8, 9
- Harima, H., see Sugawara, H. 8, 9, 23
- Harris, A.L. 204
- Harrison, E.R. 236, 238
- Harrowfield, J.M. 405–407
- Hartinger, C., see Mayr, F. 315
- Hartjes, K. 44, 53, 59, 66, 73, 79, 82, 84, 86, 88, 89, 92, 106, 115–117
- Haschke, J.M., see Deline, T.A. 161, 163
- Haschke, J.M., see Greis, O. 149, 150
- Hase, W., see Steinfeld, J. 487
- Hasegawa, H., see Anderson, P.W. 258
- Hasegawa, Y. 479, 480
- Hastie, J.W. 186, 191, 193, 197, 224, 225, 236, 237
- Hastie, J.W., see Hauge, R.H. 186, 225, 226
- Hatano, M., see Konami, H. 441–443
- Hauback, B.C., see Brinks, H.W. 275, 276
- Hauge, R.H. 186, 225, 226
- Hauge, R.H., see Hastie, J.W. 186, 191, 224, 225
- Hauser, W., see Fanghänel, T. 500
- Hauser, W., see Kim, J.I. 496
- Hautot, D., see Long, G.J. 13
- Hawkes, G.E. 368
- Hayashi, M., see Nanba, T. 20
- Hayes, A.V. 522–524, 571, 572
- Hayes, W., see Kusters, R.M. 290
- Hazen, R.M. 518
- He, J., see Zhu, C. 326
- He, Y., see Guo, C. 524, 539

- Hedinger, R. 454
Hedinger, R., see Toth, E. 363, 454
Hedo, M., see Sugawara, H. 8, 9, 23
Heffner, R.H. 298, 325
Heffner, R.H., see Neumeier, J.J. 299
Hegetschweiler, K., see Hedinger, R. 454
Hegetschweiler, K., see Toth, E. 363, 454
Hejtmánek, J., see Jirák, Z. 275
Hejtmánek, J., see Krupicka, S. 330, 338
Heller, A. 475, 476, 480
Hellwege, K.H. 516, 523, 526
Helm, L., see Powell, D.H. 361
Helm, L., see Toth, E. 363, 454
Hemberger, J., see Mayr, F. 315
Hemmilä, I. 509
Henderson, D.C. 162, 164, 203
Henderson, D.C., see Spedding, F.H. 162, 164, 165, 176, 178, 200–203
Hendrawan, H., see Simonin, J.P. 488, 491
Hennig, C. 213–215
Hennig, H., see Billing, R. 489, 491
Hennion, M. 311, 324
Hennion, M., see Biotteau, G. 325
Hennion, M., see Cestelli Guidi, M. 264
Hennion, M., see Moussa, F. 324
Hennion, M., see Rodríguez-Carvajal, J. 263, 275
Henry, B., see Giroux, S. 494, 505
Herbsttritt, F., see Reutler, P. 326
Hernando, A., see Alonso, J. 324
Herrero, E., see Fernández-Díaz, M.T. 329
Herrmannsdorfer, T., see Keller, L. 17, 23
Hervieu, M., see Autret, C. 338
Hervieu, M., see Chechersky, V. 298
Hervieu, M., see Damay, F. 330, 336
Hess, C., see Kim, K.H. 327
Hess, N.J. 523, 553, 554
Hickel, B., see Arvis, M. 497
Hiebl, K., see Flandorfer, H. 91, 92, 118, 127
Hiebl, K., see Sologub, O. 41, 43, 45–49, 51–54, 56–63, 66–69, 72–76, 79–84, 86–89, 91, 93, 103, 119–122
Hiebl, K., see Weitzer, F. 44, 59, 65, 73
Higashiyama, N., see Jiang, J. 479, 483, 494
Hill, J.P., see Casa, D. 315
Hill, J.P., see Kiryukin, V. 291
Hill, J.P., see Murakami, Y. 263
Hill, J.P., see Zimmermann, M.V. 264
Hilpert, K. 149, 239
Hilpert, K., see Gietmann, C. 194, 196, 197, 207, 209, 238–240
Hilscher, G., see Bauer, E. 24
Hinckley, C.C. 357
Hino, O., see Yamada, Y. 315
Hinton, J.F. 493
Hirai, T., see Tang, X. 29, 30
Hiraishi, J., see Kanno, H. 482
Hirao, K., see Soga, N. 523, 555
Hirayama, C. 196, 197, 239, 240
Hirayama, F., see Inokuti, M. 577
Hirayama, S., see Scully, A.D. 489
Hirayama, T., see Lee, C.H. 20
Hirota, K., see Endoh, Y. 315
Hirota, K., see Martin, M.C. 322
Hirota, K., see Murakami, Y. 263
Hirota, K., see Nojiri, H. 317
Hnatejko, Z. 482, 496
Ho, P.-C., see Bauer, E.D. 21, 22
Ho, P.-C., see Maple, M.B. 22
Hochheimer, H.D., see Bolduan, F. 522, 550, 566
Hochheimer, H.D., see Urland, W. 521, 545
Hodges, J., see Grandjean, F. 24
Hoelt, S. 421, 422
Hoekstra, H.R. 557
Höfener, C., see Reutler, P. 326
Hofer, J., see Zhao, G.-M. 305, 307
Hoffman, W.K. 45, 48, 53, 56, 59, 61, 67, 69, 73–75, 77, 79, 82, 84, 86, 88, 99, 139
Hofmann, M., see Pissas, M. 329
Hofstraat, J.W., see Klink, S.I. 471, 494–496
Hogg, R.A. 524, 555, 579
Hogg, R.A., see Takarabe, K. 524, 579
Hohmann, E. 210–214, 216, 218, 220, 222
Hohmann, E., see Bommer, H. 174, 210–215, 217–221
Høier, R., see Faaland, S. 323
Holah, D.G., see Brown, D. 152
Holley Jr., C.E., see Baker, F.B. 214
Holley Jr., C.E., see Fitzgibbon, G.C. 210, 212, 215–217
Holley Jr., C.E., see Huber Jr., E.J. 218
Holliday, B.J. 355
Holmes, N.C., see Yoo, C.S. 522, 549, 550
Holokhonova, L.I., see Rezukhina, T.N. 209, 212
Hölsa, J., see Chen, G. 523, 529
Holz, M., see Sacco, A. 482
Holz, R.C. 474, 478, 480, 482, 502
Holz, R.C., see Brink, J.M. 364
Holzapfel, B., see von Helmolt, R. 290
Holzapfel, W.B. 517, 518
Holzapfel, W.B., see Bungenstock, C. 521, 529, 532–535, 537, 540–544, 546

- Holzapfel, W.B., see Gregorian, T. 521, 522, 529, 531, 532, 536, 537, 540, 541, 545, 559
- Holzapfel, W.B., see Huber, G. 523, 530
- Holzapfel, W.B., see Jayasankar, C.K. 522, 547, 581
- Holzapfel, W.B., see Lorenz, B. 522, 554
- Holzapfel, W.B., see Noack, R.A. 518
- Holzapfel, W.B., see Shen, Y.R. 518, 522, 523, 529, 533, 534, 541, 542, 544–546, 548, 554, 564, 581
- Holzapfel, W.B., see Tröster, Th. 521, 522, 531–533, 536, 541–543, 545, 546, 550, 551
- Holzer, W. 506
- Homes, C.C., see Franck, J.P. 307
- Hömmerich, U., see Culp, T.D. 524, 578, 579
- Hong, C.S. 326
- Honma, T., see Matsuda, T.D. 17
- Hope, H., see Chan, J.Y. 37
- Hope, H., see Stetson, N.T. 15
- Hopfgartner, G., see Bocquet, B. 453, 455, 456
- Hopfgartner, G., see Floquet, S. 453, 455–459
- Hopfgartner, G., see Petoud, S. 355, 384–387
- Hopfgartner, G., see Piguet, C. 355, 393–395
- Hopfgartner, G., see Renaud, F. 387–393, 408
- Hopfgartner, G., see Rigault, S. 358, 361, 363, 366, 378, 396–400
- Hopkins, T.A. 369, 377, 381, 383, 400, 405, 410
- Hopkins, T.A., see Dewey, H.J. 467
- Hori, M., see Shirovani, I. 13
- Horikoshi, Y., see Taguchi, A. 525, 578
- Hornbostel, M.D. 8
- Horrocks Jr., W.deW. 357, 367, 368, 372, 379, 477–480, 484, 495, 497, 499, 501, 503, 504, 507
- Horrocks Jr., W.deW., see Albin, M. 478, 499, 505
- Horrocks Jr., W.deW., see Breen, P.J. 473, 474
- Horrocks Jr., W.deW., see Frey, S.T. 496
- Horrocks Jr., W.deW., see Holz, R.C. 474, 478, 480, 482, 502
- Horrocks Jr., W.deW., see Supkowski, R.M. 481–483
- Horrocks Jr., W.deW., see Wang, Y. 478, 494
- Horrocks Jr., W.deW., see Wong, C.P. 449
- Horrocks Jr., W.deW., see Wu, S. 469, 499
- Horrocks Jr., W.deW., see Wu, S.L. 492
- Hossain, Z., see Patil, S. 53, 80, 133
- Houshiar, M., see Thornton, M.J. 124
- Howard, J.A.K., see Aime, S. 426, 429
- Howard, J.A.K., see Parker, D. 420
- Hu, J., see Dagotto, E. 261
- Hu, S., see Meisner, G.P. 11
- Hu, S., see Morelli, D.T. 11
- Hu, Y.F., see Ren, Y.H. 326
- Hu, Z. 521
- Hua, H. 521, 522, 552, 553
- Huan, C.H.A., see Li, J.-M. 325
- Huang, Q. 289, 325, 328, 329
- Huang, Q., see Lynn, J.W. 299, 325
- Hubbard, J. 260
- Hubbard, W.N., see Fuger, J. 171
- Hubbard, W.N., see Johnson, G.K. 209, 210, 212, 213, 215–217, 219, 220
- Hubbard, W.N., see Lyon, W.G. 154, 157, 162–164, 166
- Huber, G. 523, 530
- Huber Jr., E.J. 218
- Huber Jr., E.J., see Fitzgibbon, G.C. 212, 215
- Hubert, S., see Billard, I. 470, 495, 501–503, 506
- Hubert, S., see Thouvenot, P. 507
- Hubert, T.D., see Montgomery, R.L. 214
- Hücker, M., see Uhlenbruch, S. 317
- Hudspeth, H.D. 326
- Hueso, L.E. 326
- Hueso, L.E., see Mira, J. 295, 310
- Hueso, L.E., see Rivadulla, F. 309, 321
- Huhtinen, H. 326
- Hulliger, F. 48, 49, 78, 94, 140
- Hulliger, F., see Frick, B. 94, 140
- Hulliger, F., see Ott, H.R. 55
- Hundley, M.F., see Neumeier, J.J. 299
- Hunt, M.B., see Zhao, G.-M. 305, 307
- Huntelaar, M.E., see Cordfunke, E.H.P. 152, 207, 208
- Hur, N.H., see Dho, J. 322
- Hur, N.H., see Hong, C.S. 326
- Hurtgen, C. 210, 212–214, 216, 218, 220
- Hushagen, R.W., see Bollore, G. 43, 47, 49, 50, 55, 57, 58, 60, 62, 69, 71, 72, 74, 75, 110
- Hushagen, R.W., see Ferguson, M.J. 43, 47, 49, 50, 58, 62, 63, 72, 79, 82, 84
- Hushagen, W., see Ferguson, M.J. 49, 57, 61, 70, 75, 103
- Huskens, J., see Peters, J.A. 356–359, 362, 368, 373, 380
- Huskens, J., see Sherry, A.D. 433
- Huskowska, E. 405
- Husson, C., see Chapon, D. 454, 455
- Hutchinson, F. 179
- Hwang, H.Y. 290, 291
- Hwang, H.Y., see Chen, C.H. 329
- Hwang, H.Y., see Fernández-Baca, J.A. 321
- Hwang, H.Y., see Radaelli, P.G. 299, 323, 325
- Hyer, E.J., see Hornbostel, M.D. 8

- Iannone, G., see Radaelli, P.G. 299, 323
 Ibañez, G., see Causa, M.T. 326
 Ibarra, M.R., see De Teresa, J.M. 298–300
 Ibarra, M.R., see García-Landa, B. 338
 Ideka, S., see Moriyasu, M. 504
 Igarashi, K. 203–205
 Ikebe, M., see Fujishiro, H. 276, 322, 326
 Ikeda, S., see Kohgi, M. 521
 Ikeda, S., see Moriyasu, M. 489, 491
 Ikeda, S., see Yokoyama, Y. 491, 497
 Ikezawa, M., see Kimura, S. 130
 Il'ina, L.D., see Khanaev, E.I. 209, 213, 214
 Ilisavskii, Y. 326
 Imbert, D., see Floquet, S. 453, 455–459
 Inaba, T., see Sekine, C. 20, 24
 Inada, Y., see Sugawara, H. 18
 Inagawa, I., see Sekine, C. 13
 Inami, T., see Yamada, Y. 315
 Inokuti, M. 577
 Inoue, J., see Ishihara, E. 269
 Inoue, M., see Sekine, C. 24
 Ioannidis, N., see Papavassiliou, G. 328
 Ioannou, A.G., see Spencer, S. 493
 Ippolitov, E.G., see Gogadze, N.G. 201–203
 Ippolitov, E.G., see Rezukhina, T.N. 209, 212
 Ippolitov, E.G., see Zhigarnovskii, B.M. 201, 203
 Ireland, J.R., see Kim, S.-J. 92
 Irwin, J.C., see Franck, J.P. 307
 Isaac, I., see Chechersky, V. 295, 296, 305, 325
 Isaac, I., see Franck, J.P. 307
 Isaac, I., see Gordon, J.E. 326
 Isaacs, N.S., see Holzapfel, W.B. 517
 Ishibashi, T., see Tanaka, F. 484, 491, 492
 Ishigame, M., see Arashi, H. 524, 529, 553, 554
 Ishigure, K., see Katsumura, Y. 489, 496, 497, 508
 Ishigure, K., see Nagaishi, R. 497
 Ishihara, E. 269
 Ishihara, S., see Endoh, Y. 315
 Ishihara, S., see Saitoh, E. 269
 Ishii, M., see Lee, C.H. 20
 Ishii, T., see Park, Y.Y. 489, 491, 492, 498
 Ishikawa, M. 41, 101
 Ishikawa, M., see Kanai, K. 13
 Ishikawa, M., see Takeda, N. 8, 12, 15–17, 21, 23, 24
 Ishiwata, E., see Hasegawa, Y. 479, 480
 Itoh, M., see Mahesh, R. 329
 Ivchenko, L.A., see Voloshin, V.A. 521, 559
 Iwadate, Y. 179
 Iwai, A., see Kumagai, K. 311
 Iwamaru, S.I., see Yayamura, T. 473
 Iwata, S., see Yayamura, T. 473
 Izotov, A.I., see Krygin, I.M. 522
 Jaccarino, V., see Shrivastava, K.N. 279, 280
 Jackson, J.A., see Lewis, W.B. 364
 Jacques, V. 423
 Jaime, M. 300
 Jaime, M., see Sakaie, K.E. 296
 Jaksic, Z.M., see Urosevic, V.V. 522
 Jamieson, J.C. 516
 Janik, M.B.L., see Allegrozzi, M. 363
 Janik, M.B.L., see Bertini, I. 374
 Janosy, A., see Dupont, F. 336
 Janosy, A., see Toth, E. 363, 454
 Janssens, L.D. 471
 Jantsch, W. 525, 580
 Jantsch, W., see Przybylinska, H. 525, 580
 Jardón, C., see Rivadulla, F. 309
 Jasien, P.G., see Stevens, W.J. 148
 Jayaraman, A. 519
 Jayasankar, C.K. 522, 547, 581
 Jayasankar, C.K., see Lavin, V. 522
 Jefferson, D.A., see Reller, A. 282
 Jeitschko, W. 2, 4, 6, 7, 15, 23, 24
 Jeitschko, W., see Albering, J.H. 76, 90
 Jeitschko, W., see Altmeyer, R.O. 37
 Jeitschko, W., see Braun, D.J. 2, 4, 7, 11, 15, 44, 47, 49, 52, 56, 57, 59, 60, 62, 69, 71, 76–78
 Jeitschko, W., see Brylak, M. 42, 43, 48, 50, 56, 58, 61, 62, 69, 72, 75, 81, 83, 85, 87, 89, 90
 Jeitschko, W., see Dannebrock, M.E. 10, 21, 23, 24
 Jeitschko, W., see Evers, C.B.H. 15, 23
 Jeitschko, W., see Evers, Ch.B.H. 65, 71, 72, 74, 76, 77, 95
 Jeitschko, W., see Grandjean, F. 8, 13, 23, 24
 Jeitschko, W., see Hartjes, K. 44, 53, 59, 66, 73, 79, 82, 84, 86, 88, 89, 92, 106, 115–117
 Jeitschko, W., see Hoffman, W.K. 45, 48, 53, 56, 59, 61, 67, 69, 73–75, 77, 79, 82, 84, 86, 88, 99, 139
 Jeitschko, W., see Kaiser, J.W. 4, 15, 52
 Jeitschko, W., see Marchand, R. 76, 79
 Jeitschko, W., see Rühl, R. 76, 90
 Jeitschko, W., see Schmidt, T. 94, 135, 140
 Jeitschko, W., see Wollesen, P. 43, 44, 46, 48, 49, 51, 52, 54, 57–61, 63, 66, 68, 70, 72, 73, 75, 80, 83
 Jenkins, A.L. 507
 Jezierski, A., see Slebarski, A. 45, 59, 60, 100, 113
 Jia, Y.Q. 184
 Jiang, J. 479, 483, 494

- Jin, R., see Sales, B.C. 11
 Jirák, Z. 275, 291
 Jirák, Z., see Damay, F. 330
 Jirák, Z., see Krupicka, S. 330, 338
 Johannsen, P.G. 561, 564
 Johannsen, P.G., see Tröster, Th. 522, 536
 Johansson, B. 199
 Johnson, C.E., see Kim, K.-Y. 170, 171
 Johnson, D.C., see Hornbostel, M.D. 8
 Johnson, G.K. 209, 210, 212, 213, 215–217, 219, 220
 Johnson, G.K., see Lyon, W.G. 154, 157, 162–164, 166
 Jones, D.A. 200–203
 Jonker, G.H. 265
 Jorda, J.L., see Ishikawa, M. 41, 101
 Jørgensen, C.K. 497, 529, 541
 Jørgensen, J.D., see Chmaissem, O. 278, 280
 Jørgensen, J.D., see Dabrowski, B. 311
 Jørgensen, J.D., see Radaelli, P.G. 299, 323
 Jørgensen, J.D., see Xiong, X. 311
 Joshi, J.P. 336
 Joubert, L. 182, 183, 187–189
 Jovanić, B.R. 522, 524, 563
 Jovanić, B.R., see Urosevic, V.V. 522
 Ju, H., see Chechersky, V. 295, 296, 325
 Judd, B.R. 400, 547, 560
 Jukes, R.T.F., see Werts, M.H.V. 481
 Jun-Hao, X., see Chen, B. 13
 Jung, G., see Yuzhelevski, Y. 326
 Jung, J.H. 323
 Jung, J.H., see Dho, J. 325
 Jung, J.H., see Kim, K.H. 296
 Junod, A., see Ishikawa, M. 41, 101
 Juretschke, P., see Paulus, E.F. 430, 433
- Kachmarska, K., see Skolozdra, R.V. 52, 112, 113, 117, 120–123
 Kacprzak, L., see Massalski, T.B. 36
 Kaczmarska, K. 80, 112, 113
 Kaczmarska, K., see Guzik, A. 54
 Kaczorowski, D., see Leithe-Jasper, A. 26
 Kaeser, M., see Nolas, G.S. 29, 30
 Kafalas, J.A., see Goodenough, J.B. 250, 251, 277, 282
 Kahn, O. 355, 360, 366, 368
 Kaindl, G., see Hu, Z. 521
 Kaiser, J.W. 4, 15, 52
 Kajimoto, R. 337
 Kajimoto, R., see Kawano, H. 311, 336
 Käll, M., see Björnsson, P. 268
- Kallias, G. 328
 Kallias, G., see Papavassiliou, G. 325, 328
 Kallias, G., see Pissas, M. 329
 Kallias, G., see Simopoulos, A. 328
 Kaltsoyannis, N. 366
 Kamada, M., see Kimura, S. 130
 Kamenev, K., see Allodi, G. 328, 337
 Kamenev, K., see De Teresa, J.M. 300
 Kamenev, K.V., see Zvyagin, S. 338
 Kamenev, V.I., see Zvyagin, S. 338
 Kaminski, R. 507
 Kana'an, A., see Kent, R.A. 234
 Kanai, K. 13
 Kanamori, J. 263
 Kanao, R., see Yamada, Y. 315
 Kanatsidis, M.G., see Kim, S.-J. 92
 Kanazawa, M., see Kim, Y.C. 217, 220
 Kaneko, K., see Endoh, Y. 315
 Kaneko, K., see Nojiri, H. 317
 Kang, D.J., see Zhao, G.-M. 308
 Kang, D.W., see Lee, K.P. 492
 Kang, S.H., see Kim, Y.C. 214, 215, 221
 Kankare, J., see Latva, M. 494, 495
 Kannewurf, C.R., see Kim, S.-J. 92
 Kanno, H. 482
 Kanoda, K., see Shirotani, I. 7, 9, 21
 Kanoda, K., see Uchiumi, T. 7–9, 12
 Kao, C.-C., see Zimmermann, M.V. 264
 Kapala, J. 190, 191, 193, 232, 233, 236, 237
 Kaposi, O. 196, 240
 Kappelmann, H.-G., see Buchler, J.W. 449
 Karabashev, S.G., see Quijada, M.A. 269
 Karabashev, S.G., see Smolyaninova, V.N. 321
 Karagodina, A.M., see Molodkin, A.K. 208
 Kasai, M., see Chahara, K.I. 290
 Kasai, M., see Kuwahara, H. 333
 Kasatochkin, S.V. 524
 Kasaya, M. 49, 57, 58, 62, 129–132
 Kasaya, M., see Katoh, K. 130, 132
 Kasaya, M., see Kimura, S. 130
 Kasaya, M., see Suzuki, H. 58, 78
 Kasper, N.V., see Troyanchuk, O.Ya. 275
 Kasuga, K. 440
 Kasyanov, A.I., see Voloshin, V.A. 523, 524
 Katak, R., see Blair, S. 509
 Katano, S., see Yamada, Y. 315
 Kataoka, M. 263
 Kato, Y., see Fanghänel, T. 500
 Kato, Y., see Kimura, T. 471–474, 478, 479, 481
 Kato, Y., see Nagaishi, R. 497
 Kato, Y., see Takahashi, K. 481

- Katoh, K. 118, 130, 132
 Katoh, K., see Kasaya, M. 49, 57, 58, 62, 129–132
 Katoh, K., see Kimura, S. 130
 Katoh, T., see Suzuki, H. 58, 78
 Katsufuji, T. 275
 Katsufuji, T., see Machida, A. 336
 Katsumura, Y. 489, 496, 497, 508
 Katsumura, Y., see Nagaishi, R. 497
 Katz, J.J. 467, 500
 Kaul, A., see Shames, A.I. 338
 Kaul, A., see Yakubovskii, A. 309
 Kaul, A.R., see Babushkina, N.A. 308, 309, 327
 Kauzlarich, S.M., see Chan, J.Y. 37, 90, 134
 Kauzlarich, S.M., see Fisher, I.R. 90, 91, 134, 135, 137
 Kauzlarich, S.M., see Rehr, A. 76, 111
 Kauzlarich, S.M., see Stetson, N.T. 15
 Kauzlarich, S.M., see Xue, J.S. 12
 Kawai, T., see Liu, X.J. 299
 Kawakami, T., see Shirohani, I. 9, 10
 Kawano, H. 311, 336
 Kawano, H., see Kajimoto, R. 337
 Kawano, H., see Yoshizawa, H. 291
 Kawasaki, Y., see Tanaka, F. 471, 472
 Kawata, H., see Murakami, Y. 263
 Kazakov, V.P., see Khamidullina, L.A. 497
 Keating, K.B. 521–525, 562
 Keen, D.A., see Kusters, R.M. 290
 Keenan, T.K., see Carnall, W.T. 494
 Keimer, B., see Casa, D. 315
 Keimer, B., see Kiryukin, V. 291
 Keller, H., see Alexandrov, A.S. 308
 Keller, H., see Zhao, G. 326, 329
 Keller, H., see Zhao, G.-M. 305, 307, 308
 Keller, L. 17, 23
 Keller, N., see Arvis, M. 497
 Kemp, T.J., see Allsopp, S.R. 473, 474
 Kemp, T.J., see Baird, C.P. 497, 498
 Kemple, M.D. 357, 358, 367, 373–375, 386
 Kennedy, R.J. 521, 522, 524, 525
 Kent, R.A. 234
 Keppens, V. 11
 Keppens, V., see Chakoumakos, B.C. 8
 Keppens, V., see Sales, B.C. 7, 9–11, 13, 29, 31
 Kessler, M.A. 486, 508
 Khairulin, R.A. 178, 202
 Khairulin, R.A., see Stankus, S.V. 150, 200–203
 Khamidullina, L.A. 497
 Khanaev, E.I. 209, 213, 214
 Khanaev, E.I., see Storozhenko, T.P. 215–217
 Khasaev, J.P., see Rustamov, P.G. 74, 77
 Khasanshin, I.V., see Kudin, L.S. 193, 237
 Kholokhova, L.I. 211, 213, 215, 216, 221
 Khomskii, D.I., see Babushkina, N.A. 308, 309, 327
 Khomskii, D.I., see Mizokawa, T. 263
 Khudiakov, I.V., see Azenha, M.E. 498
 Khudyakov, I., see Rykov, S. 497
 Kido, G., see Urushibara, A. 311
 Kiefer, G.E., see Geraldes, C.F.G.C. 430, 433, 435, 439, 440
 Kierspel, H., see Uhlenbruch, S. 317
 Kihn-Botulinski, M., see Buchler, J.W. 449–452
 Kijowski, J., see Burgess, J. 221
 Kikuchi, C., see Morrison, C. 530
 Kikuchi, T., see Fujishiro, H. 326
 Kim, I., see Dho, J. 325, 328
 Kim, J.I. 496
 Kim, J.I., see Aas, W. 500
 Kim, J.I., see Billard, I. 470, 495, 501–503, 506
 Kim, J.I., see Fanghänel, T. 495, 496, 500
 Kim, J.I., see Klenze, R. 500
 Kim, J.I., see Monsallier, J.M. 506
 Kim, J.I., see Morgenstern, M. 506
 Kim, J.I., see Panak, P. 494, 495
 Kim, J.I., see Paviet, P. 500
 Kim, J.I., see Wimmer, H. 500
 Kim, K.-Y. 170, 171
 Kim, K.H. 296, 327, 328
 Kim, K.H., see Dho, J. 325
 Kim, K.H., see Jung, J.H. 323
 Kim, K.H., see Naler, S. 328
 Kim, K.Y., see Johnson, G.K. 209, 210, 212, 213, 215–217, 219, 220
 Kim, S.-J. 92
 Kim, T.H., see Uehara, M. 323
 Kim, W.S., see Dho, J. 322
 Kim, W.S., see Hong, C.S. 326
 Kim, Y., see Harrowfield, J.M. 405–407
 Kim, Y.-J., see Zimmermann, M.V. 264
 Kim, Y.C. 213–215, 217, 219–221
 Kimball, C.W., see Dabrowski, B. 311
 Kimball, C.W., see Xiong, X. 311
 Kimura, H., see Endoh, Y. 315
 Kimura, S. 130
 Kimura, S., see Shirohani, I. 13
 Kimura, T. 336, 471–474, 478, 479, 481
 Kimura, T., see Arisaka, M. 473, 474, 481
 Kimura, T., see Billard, I. 470, 495, 501–503, 506
 Kimura, T., see Lis, S. 489, 491
 Kimura, T., see Nagaishi, R. 497
 Kimura, T., see Saitoh, E. 269

- Kimura, T., see Takahashi, K. 481
 Kimura, T., see Tobe, K. 266, 269
 King, E.G. 154, 164, 176, 178, 200
 Kinoshita, M., see Shirofani, I. 7–9, 12
 Kirsch, B., see Berthoud, T. 507, 508
 Kiryukin, V. 291
 Kiseleva, T.V. 204
 Kiseleva, T.V., see Laptev, D.M. 203, 204, 210–212, 216
 Kishenbaum, A.D. 178
 Kjekshus, A., see Brinks, H.W. 275, 276
 Klakamp, S.L., see Holz, R.C. 502
 Klamut, P.W., see Dabrowski, B. 311, 323
 Klein, G., see Bouby, M. 474
 Klein, M.P., see Vold, R.L. 364
 Kleinke, H. 37
 Klenze, R. 495, 500
 Klenze, R., see Billard, I. 470, 495, 501–503, 506
 Klenze, R., see Fanghänel, T. 500
 Klenze, R., see Kim, J.I. 496
 Klenze, R., see Morgenstern, M. 506
 Klenze, R., see Panak, P. 494, 495
 Klenze, R., see Paviet, P. 500
 Klenze, R., see Wimmer, H. 500
 Klimov, A., see Ilisavskii, Y. 326
 Klingeler, R. 315
 Klingeler, R., see Uhlenbruch, S. 317
 Klink, S.I. 471, 494–496
 Kloc, C., see Fernández-Baca, J.A. 321
 Klose, H., see Vogel, R. 36
 Klüfers, P. 77, 91
 Knoff, M., see Buchler, J.W. 449
 Knudsen, K.D., see Faaland, S. 323
 Kobayashi, S., see Shimomura, S. 326, 327
 Kobzenko, G.F. 36
 Koehler, W.C. 259
 Koehler, W.C., see Wollan, E.O. 262, 327
 Kohgi, M. 521
 Kohgi, M., see Kasaya, M. 131, 132
 Kohgi, M., see Okayama, Y. 521
 Kohgi, M., see Oohara, Y. 521
 Kohgi, M., see Yoshizawa, H. 521
 Kojima, T., see Park, Y.Y. 489, 491, 492, 498
 Kok-Scheele, A., see Konings, R.J.M. 208
 Kolenda, M., see André, G. 123
 Kolesnik, S., see Chmaissem, O. 278, 280
 Kolesnik, S., see Xiong, X. 311
 Kolonits, M., see Molnár, J. 185, 186, 190, 191, 230–232
 Komarov, S.A., see Ezhov, Y.S. 230
 Konami, H. 441–443
 Konings, R.J.M. 156, 208
 Konings, R.J.M., see Cordfunke, E.H.P. 171, 172, 174, 220, 221
 Konings, R.J.M., see Kovács, A. 183–186, 189, 190, 227–230
 Konings, R.J.M., see Molnár, J. 185, 186, 190, 191, 230–232
 Konnecke, T., see Fanghänel, T. 500
 Konno, Y., see Fujishiro, H. 322
 Koo, T.Y., see Podzorov, V. 327
 Korshunov, B.G. 204, 205
 Korshunov, B.G., see Pashinkin, A.S. 237
 Kotliar, G., see Rozenberg, M.J. 261, 315
 Kotov, M.G., see Khanaev, E.I. 209, 213
 Kotzyba, G., see Jeitschko, W. 15, 23, 24
 Kourouklis, G.A., see Urland, W. 521, 545
 Kovács, A. 183–186, 189–191, 198, 227–230, 232, 233
 Kovacs, Z., see Zhang, S. 355
 Koyama, I., see Murakami, Y. 263
 Koyama, Y., see Iwadate, Y. 179
 Kozanecki, A., see Stapor, A. 525, 578
 Kozono, Y., see Chahara, K.I. 290
 Kozyrkov, V.V., see Aliev, F.G. 118
 Krasnov, A.V., see Girichev, G.V. 229
 Krasnov, A.V., see Giricheva, N.I. 184, 190, 191, 193, 228, 232
 Krasnov, K.S. 227
 Krasnov, K.S., see Giricheva, N.I. 229
 Krasnova, O.G., see Girichev, G.V. 229
 Krasnova, O.G., see Giricheva, N.I. 184, 190, 191, 193, 228, 232
 Krauss, M., see Stevens, W.J. 148
 Krayevski, J.J., see Cava, R.J. 56
 Kremer, R., see Urland, W. 521, 545
 Krieger, Y.G., see Babailov, S.P. 357
 Krimnus, M.G., see Voloshin, V.A. 521
 Krohina, A.G., see Molodkin, A.K. 208
 Krok-Kowalski, J., see Büchel, D. 151, 206
 Kronenberg, A., see Billard, I. 470, 495, 501–503, 506
 Kropp, J.L. 475–477, 480
 Kruk, R., see Chmaissem, O. 278, 280
 Krupicka, S. 330, 338
 Krupicka, S., see Jiráček, Z. 291
 Krupski, M., see Rewaj, T. 523, 524, 536
 Krygin, I.M. 521, 522, 536
 Krystkowiak, E., see Sikorski, M. 489
 Krzhizhanovskaya, see Suvorov, A.V. 234
 Kubo, H., see Iwadate, Y. 179
 Kubota, M., see Kawano, H. 311

- Kudin, L.S. 193, 237, 238
 Kudin, L.S., see Pogrebnoi, A.M. 193, 194, 236, 237
 Kuech, T.F., see Culp, T.D. 524, 525, 578–580
 Kugel, K.I., see Babushkina, N.A. 308, 309, 327
 Kulagin, N.A., see Voloshin, V.A. 522, 531
 Kulagin, N.M., see Laptev, D.M. 203, 204
 Kuliev, A.N. 74
 Kumagai, K. 311
 Kumagai, K., see Yakubovskii, A. 309
 Kumai, R., see Asamitsu, A. 319
 Kumai, R., see Kimura, T. 336
 Kumai, R., see Kuwahara, H. 333
 Kumar, A., see Congeduti, A. 325
 Kumar, A., see Meneghini, C. 325
 Kumar, D. 326
 Kumar, K., see Chang, C.A. 420
 Kumbe, M.U., see Monsallier, J.M. 506
 Kumke, M., see Billard, I. 470, 495, 501–503, 506
 Kunnen, B., see Jeitschko, W. 15, 23, 24
 Kupchikov, A.K. 525, 581, 582
 Kuriata, J., see Rewaj, T. 524, 536
 Kurita, A., see Nishimura, G. 524
 Kushida, T., see Mishimura, G. 557
 Kushida, T., see Nishimura, G. 524
 Kusters, R.M. 290
 Kusukawa, T., see Fujita, M. 355
 Kutnetsov, A.Y., see Kudin, L.S. 193, 237, 238
 Kutscher, J. 208, 209
 Kutsenko, A.B., see Dierolf, V. 525, 555
 Kuwahara, H. 330, 331, 333, 336, 337
 Kuwahara, H., see Asamitsu, A. 291
 Kuwahara, H., see Kajimoto, R. 337
 Kuwahara, H., see Kawano, H. 336
 Kuwahara, H., see Kumagai, K. 311
 Kuwahara, H., see Moritomo, Y. 291
 Kuwahara, H., see Shimomura, S. 326, 327
 Kuwahara, H., see Tokura, Y. 330, 341
 Kuwahara, H., see Tomioka, Y. 291
 Kuz'ma, Yu.B., see Mozharivskij, Yu. 41, 82, 84, 86–88, 92, 111, 138, 139
 Kuznetsov, V.L. 24, 26
 Kvardakov, A.M., see Slovyanskikh, V.K. 94, 95, 140
 Kwon, Y.U., see Ganguli, A.K. 42, 110
 Kycia, S., see Billinge, S.J.L. 304

 Labeau, M. 203
 Labet, A., see Billard, I. 510
 Lacam, A. 522, 529, 554
 Lacam, A., see Leger, J.M. 522, 554
 Lacerda, A.H., see Gajewski, D.A. 13

 Laenen, R. 482
 Lafont, U., see Ravot, D. 10, 11, 13
 Lagarde, G., see Billard, I. 470, 495, 501–503, 506
 Legendijk, A., see Schuurmans, F.J.P. 471, 485
 Lähderanta, E., see Huhtinen, H. 326
 Laiho, R., see Huhtinen, H. 326
 Lake, C.H., see Amin, S. 426
 Lake, C.H., see Morrow, J.R. 426
 Lam, R. 47, 55, 60, 68, 74, 78, 80, 83, 84, 103
 Lam, R., see Deakin, L. 133
 LaMar, G.N., see Burns, P.D. 363
 Lamarque, G., see Billard, I. 470, 495, 501–503, 506
 Lang, A., see Jeitschko, W. 15, 23, 24
 Lang, J., see Paulus, E.F. 430, 433
 Langlois, M.H., see Dubost, J.P. 420
 Lanza, G. 189
 Lanza, G., see Di Bella, S. 185
 Lanza, H., see Levy, P. 328
 Lanzara, A. 295, 325
 Lanzerstorfer, S., see Jantsch, W. 525, 580
 Lanzerstorfer, S., see Przybylinska, H. 525, 580
 Lao, K. 506
 Laptev, D.M. 203, 204, 210–212, 216
 Laptev, D.M., see Kiseleva, T.V. 204
 Laszak, I., see Moulin, C. 501
 Latvia, M. 494, 495
 Lauffer, R.B., see Caravan, P. 357, 360–362
 Laukhin, V. 299
 Laukhin, V., see Fontcuberta, J. 299
 Laukhin, V., see Martínez, B. 317
 Laukhin, V., see Senis, R. 317
 Lavin, V. 522, 523
 Lavin, V., see Tröster, Th. 551
 Lawrie, D.D., see Franck, J.P. 307
 Laws, W.R. 498, 505
 Lawson, A.W., see Jamieson, J.C. 516
 Lay, K.-L., see Buchler, J.W. 449
 Leavitt, R.P., see Chang, N.C. 538
 Leavitt, R.P., see Morrison, C.A. 154, 160–162, 167, 371
 Lebedev, V.A. 36
 Lebedev, Y.S., see Powell, D.H. 361
 Lebrun, C., see Bretonnière, Y. 393
 Lebrun, C., see Chapon, D. 454, 455
 Lee, C.H. 20
 Lee, C.H., see Zhao, Y.G. 296
 Lee, Ch.-H., see Sekine, C. 13
 Lee, D.W., see Chang, C.A. 420
 Lee, H.J., see Dho, J. 325
 Lee, K.P. 492

- Lee, S., see Dho, J. 325, 328
 Lee, S., see Kim, K.H. 328
 Lee, Y.-M., see Allegrozzi, M. 363
 Lee, Y.-M., see Bertini, I. 374
 Lees, M.R. 291
 Lees, M.R., see Campbell, A.J. 319
 Lees, M.R., see García-Landa, B. 338
 Legendre, J.-J., see Joubert, L. 182, 183, 187–189
 Leger, J.M. 522, 554
 Léger, J.M., see Bungenstock, C. 540
 Leger, J.M., see Dubost, J.P. 420
 Leger, J.M., see Syassen, K. 525
 Lehn, J.-M. 355
 Leibfritz, D., see Hawkes, G.E. 368
 Leininger, S. 355
 Leithe-Jasper, A. 26, 43, 44, 51, 52, 59, 63–66, 72, 73, 79, 96, 100, 104, 138
 Leithe-Jasper, A., see Flandorfer, H. 127
 Leithe-Jasper, A., see Sologub, O. 42, 48, 56, 61, 69, 75, 81, 83, 85, 87, 88, 90, 92, 93, 102, 119, 120, 123
 Leithe-Jasper, A., see Weitzer, F. 44, 59, 65, 73
 Lelik, L., see Kaposi, O. 196, 240
 Lemons, J.F., see Lewis, W.B. 364
 Lena, A., see Tolentino, H. 518
 Lenkinski, R.E., see Wilcott, M.R. 373, 385
 Leonidov, V.Y. 218
 Leonidov, V.Y., see Furkaliouk, M.Y. 217, 220, 221
 Leonov, A.V., see Morozkin, A.V. 85
 Leonowicz, M.E., see Poepelmeier, K.R. 282
 Lesiecki, M. 186, 224
 Leśniewska, B., see André, G. 123
 LeToullec, R., see Datchi, F. 522, 554
 Levine, B.A., see Bleaney, B. 357, 365, 371
 Levy, D., see Meneghini, C. 325
 Levy, P. 328
 Levy, P., see Freitas, R.S. 328, 329
 Lewandowski, S.J., see Ilisavskii, Y. 326
 Lewis, E.A., see Baker, F.B. 214
 Lewis, G.N. 182
 Lewis, M., see Wells Jr., J.C. 186, 227, 229, 230
 Lewis, W.B. 364
 Leyva, G., see Levy, P. 328
 Lezhava, S.A. 219, 220
 Li, B., see Guo, C. 524, 539
 Li, C.L. 547
 Li, H., see Chi, Y. 523, 533, 539
 Li, J.-M. 325
 Li, J.J., see Zhao, Y.G. 296
 Li, J.Q. 329
 Li, X.G., see Zheng, R.K. 328
 Li, Z.Y., see Lynn, J.W. 299, 325
 Licci, F., see Allodi, G. 328
 Lim, M. 234
 Lin, J.G., see Chang, C.W. 336
 Lin, J.H., see Zhang, J.S. 65, 73
 Lin, P., see Sakaie, K.E. 296
 Lincoln, R.L., see Nafziger, R.H. 200
 Lindahl, C.B., see Corbett, J.D. 208
 Liotta, F.J., see Horrocks Jr., W.deW. 499, 501
 Liou, S.H., see McIlroy, D.N. 295
 Lipkowitz, K.B., see Kemple, M.D. 357, 358, 367, 373–375, 386
 Lippincott, E.R., see Weir, C.E. 516
 Lis, S. 471, 473, 478–481, 489, 491, 494, 496
 Lis, S., see Billard, I. 470, 495, 501–503, 506
 Lis, S., see Hnatejko, Z. 482, 496
 Lis, S., see Meinrath, G. 495, 497, 501
 Lisowski, J. 357, 358, 364, 374–376
 Littleton IV, R.T., see Nolas, G.S. 29, 30
 Littlewood, P.B., see Millis, A.J. 268
 Liu, G., see Allegrozzi, M. 363
 Liu, G.-L. 311, 313, 316, 318
 Liu, G.L., see Zhou, J.-S. 311, 316
 Liu, H.L. 328
 Liu, H.L., see Yoon, S. 326
 Liu, J. 523, 553
 Liu, S. 523, 524, 529, 530, 533, 539
 Liu, S., see Chi, Y. 523, 524, 530, 533, 534, 536, 539
 Liu, S., see Wang, L. 523, 524, 551, 568
 Liu, X.J. 299
 Lobet, A. 336
 Lobet, A., see Frontera, C. 336
 Loa, I. 268
 Lobad, A.I. 326
 Lochhead, M.J. 471, 524, 555, 556, 581
 Lodeiro, C., see Bazzicalupi, C. 492, 509
 Loeb, A.L., see Goodenough, J.B. 262
 Löffler, J., see Buchler, J.W. 450–453
 Lofland, S., see Smolyaninova, V.N. 327
 Lohr, H.R. 210, 212
 Lohr, L., see Sharp, R. 359
 Loidl, A., see Mayr, F. 315
 Loktyushina, N.S. 186, 228–231
 Lölliger, J. 356
 Loncin, M.-F., see Spirlet, M.-R. 420
 Long, G.J. 13
 Long, G.J., see Grandjean, F. 13
 Longo, J.M., see Goodenough, J.B. 250, 251, 277, 282

- Longo, J.M., see Poepfelmeier, K.R. 282
 Lopez, M. 489, 491, 500, 508
 López Quintela, M.A., see Mira, J. 295, 310
 López-Quintela, M.A., see Causa, M.T. 326
 López-Quintela, M.A., see Hueso, L.E. 326
 López-Quintela, M.A., see Rivadulla, F. 305, 309, 321
 Lopinski, S., see Bruce, J.I. 355
 Lorenz, B. 522, 554
 Lorenz, B., see Alexandrov, A.S. 308
 Lortz, R., see Gordon, J.E. 326
 Losi, P., see Bianchi, A. 426
 Lotgering, F.K. 267
 Lotnik, S.V., see Khamidullina, L.A. 497
 Loubeyre, P., see Datchi, F. 522, 554
 Louca, D. 263, 304
 Louca, D., see Egami, T. 263, 292
 Lövgren, T., see Soini, E. 509
 Lowe, M.P., see Blair, S. 509
 Lowe, M.P., see Bruce, J.I. 355
 Lowe, M.P., see Clarkson, I.M. 484, 505
 Lu, L., see Zhao, Y.G. 328
 Lu, Q. 298
 Lübbers, R. 518
 Lucci, F., see Allodi, G. 325
 Luchinat, C., see Allegrozzi, M. 363
 Luchinat, C., see Bertini, I. 356, 357, 359, 361–364, 366–368, 374
 Luchinat, C., see Clementi, V. 359
 Lueken, H., see Sologub, O.L. 58, 72, 106
 Luke, G.M., see Heffner, R.H. 325
 Lukin, S.N. 524, 536
 Lun, L., see Wang, Q. 524, 530, 538
 Lüpke, G., see Ren, Y.H. 326
 Lüthi, B., see Zvyagin, S. 338
 Lützenkirchen, K., see Billard, I. 485, 510
 Lützenkirchen, K., see Nehlig, A. 473, 474, 482, 485
 Lützenkirchen, K., see Rustenholtz, A. 474
 Lützenkirchen, K., see Simonin, J.P. 491
 Lyapunov, K.M. 164, 165, 176
 Lyapunov, K.M., see Khairulin, R.A. 178
 Lyapunov, K.M., see Stankus, S.V. 150, 200–203
 Lynch, V., see Lisowski, J. 357, 358, 374–376
 Lynchak, K.A., see Kobzenko, G.F. 36
 Lynn, J.W. 299, 325
 Lynn, J.W., see Adams, C.P. 298
 Lynn, J.W., see Erwin, R.W. 325
 Lynn, J.W., see Huang, Q. 289, 325, 328, 329
 Lynn, J.W., see Maple, M.B. 22
 Lynn, J.W., see Quijada, M.A. 269
 Lynn, J.W., see Vasiliu-Doloc, L. 299, 318, 321
 Lyon, W.G. 154, 157, 162–164, 166
 Lyutsarev, V.S., see Spiridonov, V.P. 227
 Lyzlov, Y.N. 203–206
 Lyzlov, Y.N., see Nisel'son, L.A. 203–205
 Lyzlov, Y.N., see Nisel'son, L.N. 236, 238
 Ma, L., see Liu, S. 524, 529
 Mabbs, R., see Nijegorodov, N. 506
 Mac, M. 491
 MacCordick, J., see Bouby, M. 506
 MacDonald, D.K.C. 302
 Macfarlane, R.M., see Oppenländer, A. 522
 Machida, A. 336, 338
 Machida, A., see Liu, X.J. 299
 Machida, A., see Moritomo, Y. 277, 284, 285
 Machida, K., see Jiang, J. 479, 483, 494
 Machlan, G.R. 214, 215, 221
 Mack, J. 474, 498
 Mack, N.H., see Bare, W.D. 470, 509
 MacLaughlin, D.E., see Heffner, R.H. 298, 325
 Madden, P.A., see Hutchinson, F. 179
 Madic, C., see Billard, I. 470, 495, 501–503, 506
 Madic, C., see Scapolan, S. 508
 Maekawa, S., see Endoh, Y. 315
 Maekawa, S., see Ishihara, E. 269
 Maekawa, S., see Saitoh, E. 269
 Magerramov, E.V., see Aliev, O.M. 55, 80
 Mahan, G. 28
 Mahan, G.D. 28
 Mahan, G.D., see Sofo, J.O. 6
 Mahesh, R. 329
 Mahia, J., see Platas, C. 358, 359, 377, 378, 400–404
 Mahl, S., see Slebarski, A. 45, 59, 60, 100, 113
 Maignan, A., see Autret, C. 338
 Maignan, A., see Damay, F. 330, 336
 Mais, J., see Chmaissem, O. 278, 280
 Majumdar, A.K., see Kumar, D. 326
 Mak, C.S.K. 525, 581
 Makhmadmurodov, A. 195, 239
 Makhmadmurodov, A., see Dudchik, G.P. 238
 Maksudova, T.F., see Aliev, O.M. 77, 78, 91, 92
 Maksudova, T.F., see Rustamov, P.G. 92
 Maldivi, P., see Adamo, C. 183, 186–189
 Malefetse, T.J., see Swiegers, G.F. 355, 393
 Malik, S.K. 48, 56, 60, 69, 77, 81, 85, 89, 108, 118
 Malik, S.K., see Adroja, D.T. 60, 61, 118
 Malik, S.K., see Mehta, A. 69
 Malik, S.K., see Menon Latica 48, 56, 61, 69
 Malik, S.K., see Vijaya Lakshmi, K. 121, 124

- Malik, S.R. 95
Malkin, B.Z., see Kupchikov, A.K. 525, 581, 582
Malley, M.F., see Chang, C.A. 420
Malrezzi, A.L., see Dagotto, E. 261
Mal'tsev, A.A., see Loktyushina, N.S. 186, 229–231
Mal'tsev, A.A., see Selivanov, G.K. 186, 189, 227
Mandal, P. 312
Mandal, T.K., see Zhao, Y.G. 328
Mandrus, D., see Bauer, E.D. 13, 16
Mandrus, D., see Chakoumakos, B.C. 8
Mandrus, D., see Feldman, J.L. 11
Mandrus, D., see Gajewski, D.A. 13
Mandrus, D., see Keppens, V. 11
Mandrus, D., see Sales, B.C. 2, 7, 9–11, 13, 26, 29, 31
Manet, I., see Ulrich, G. 358
Mao, H.K. 518
Mao, H.K., see Bell, P.M. 519
Maple, M.B. 22
Maple, M.B., see Bauer, E.D. 8, 12, 13, 15–17, 21, 22, 24
Maple, M.B., see Dilley, N.R. 15, 26
Maple, M.B., see Dordevic, S.V. 8, 12, 17, 26, 27
Maple, M.B., see Gajewski, D.A. 13
Maple, M.B., see Keppens, V. 11
Maple, M.B., see Meisner, G.P. 6, 12
Maple, M.B., see Torikachvili, M.S. 6, 8, 17, 22
Maquina, C., see De Teresa, J.M. 300
Mar, A., see Bollore, G. 43, 47, 49, 50, 55, 57, 58, 60, 62, 69, 71, 72, 74, 75, 110
Mar, A., see Deakin, L. 133
Mar, A., see Ferguson, M.J. 43, 47–50, 57, 58, 61–63, 70, 72, 75, 79, 82, 84, 102, 103
Mar, A., see Lam, R. 47, 55, 60, 68, 74, 78, 80, 83, 84, 103
Mar, A., see Mills, A.M. 47, 54, 60, 68, 74, 104, 111
Mar, A., see Raju, N.P. 43
Mar, R.W. 234
Marazza, R. 41, 48, 56, 61, 69, 74, 81, 83, 85, 87, 88, 91, 106
Marazza, R., see Riani, P. 41, 85, 87, 88, 91, 93
Marazza, R., see Rossi, D. 49, 57, 71, 76
Marcantonatos, M.D. 497, 498
Marcantonatos, M.D., see Deschaux, M. 498
Marcenat, C., see Fisher, R.A. 326
Marcenat, C., see Gordon, J.E. 326
Marchand, R. 76, 79
Marest, G., see Hannover, B. 325
Marezio, M., see Cox, D.E. 291
Marezio, M., see Hwang, H.Y. 290, 291
Marezio, M., see Radaelli, P.G. 299, 323, 325, 327, 329
Margrave, J.L., see Besenbuch, G. 235
Margrave, J.L., see Charlu, T.V. 164, 165
Margrave, J.L., see Hastie, J.W. 186, 191, 193, 197, 224, 225, 236, 237
Margrave, J.L., see Hauge, R.H. 186, 225, 226
Margrave, J.L., see Kent, R.A. 234
Margrave, J.L., see Zmbov, K.F. 234, 235
Mariani, P., see Bianchi, A. 426
Mariet, C., see Billard, I. 510
Markovich, V. 287, 325
Markovich, V., see Yuzhelevski, Y. 326
Marochko, O.Y., see Solomonik, V.G. 186
Marqina, C., see De Teresa, J.M. 298
Marques, M.P.M. 421, 423
Marques, M.P.M., see Aime, S. 421, 422
Marques, M.P.M., see Gerales, C.F.G.C. 410
Marquina, C., see De Teresa, J.M. 299
Marsel, J., see Kaposi, O. 196, 240
Martell, A.E. 381
Mårtensson, N., see Johansson, B. 199
Martin, C., see Autret, C. 338
Martin, C., see Damay, F. 330, 336
Martin, I.R., see Lavin, V. 522, 523
Martin, M.C. 322
Martin, R.B., see Bleaney, B. 357, 365, 371
Martin, R.B., see Donato, H. 404
Martin-Mayor, V., see Burgy, J. 332
Martinchuk, E.L., see Kobzenko, G.F. 36
Martínez, B. 317
Martínez, B., see Senis, R. 317
Martínez, B., see Skumryev, V. 312
Martínez, J.L., see Alonso, J. 324
Martínez, J.L., see Fernández-Díaz, M.T. 329
Martinho, H., see Granado, E. 284
Martynova, L.F., see Slovyanskikh, V.K. 94, 95, 140
Marx, A., see Reutler, P. 326
Marx, V., see Petzel, T. 234, 235
Marysko, M., see Jiráč, Z. 275
Marysko, M., see Krupicka, S. 330, 338
Masaki, M., see Katsufuji, T. 275
Mason, D.R., see Morrison, C. 530
Massalski, T.B. 36
Masuda, T.D., see Aoki, Y. 17–19
Matachescu, C., see Latva, M. 494, 495
Matacotta, F.C., see Dediu, V. 327
Mathews, C.K., see Peter, S. 507
Mathieu, C.E., see Blair, S. 509

- Mathieu, C.E., see Clarkson, I.M. 484, 505
 Mathis, G., see Bazin, H. 509
 Mathur, J.N., see Lis, S. 478, 481, 494, 496
 Matsuda, T., see Sato, H. 6, 8, 12, 17, 18, 22, 23
 Matsuda, T.D. 17
 Matsuda, T.D., see Keller, L. 17, 23
 Matsuda, T.D., see Sugawara, H. 18
 Matsuhata, H., see Lee, C.H. 20
 Matsuhira, K. 20
 Matsuhira, K., see Sekine, C. 15, 25, 26
 Matsui, Y., see Li, J.Q. 329
 Matsumoto, A. 506
 Matsumoto, G. 275, 324
 Matsumoto, G.H. 264
 Matsumoto, T., see Naka, T. 521
 Matsumoto, T., see Shirotani, I. 9, 10
 Matsushita, A., see Shirotani, I. 9, 10
 Mat'tsev, A., see Perov, P.A. 186, 227, 228
 Mauchien, P., see Berthoud, T. 507, 508
 Mauchien, P., see Decambox, P. 507, 508
 Mauchien, P., see Moulin, C. 507, 508
 Mauchien, P., see Thouvenot, P. 507
 Mauger, A., see Ravot, D. 10, 11, 13
 Max, J.J. 482
 Mayr, F. 315
 Mayr, M. 326
 Mayr, M., see Burgy, J. 332
 Mazin, I.I., see Feldman, J.L. 11
 Mazzanti, M., see Bretonnière, Y. 393
 Mazzone, D., see Borsese, A. 36
 Mazzone, D., see Riani, P. 41, 85, 87, 88, 91
 Mazzone, D., see Rossi, D. 49, 57, 71, 76
 McCarroll, W.H., see Markovich, V. 287
 McClellan, K.J., see Granada, E. 329
 McCreary, J.R. 234, 235
 McDonald, J.D., see Kent, R.A. 234
 McDonald, R., see Lam, R. 47, 60, 68, 74, 80, 83, 84, 103
 McElfresh, M.W., see Torikachvili, M.S. 6, 8, 17, 22
 McGarvey, B.R. 357, 371, 372, 376, 459
 McGreevy, R., see Kusters, R.M. 290
 McIlroy, D.N. 295
 McIntyre, G.J., see Campbell, A.J. 319
 McMasters, D.D., see Schmidt, F.A. 36
 McMeeking, R.F., see Gerloch, M. 368
 McMurry, T.J., see Caravan, P. 357, 360–362
 McNiff Jr., E.J., see Xiao, G. 328
 McQueeney, R.J., see Egami, T. 263
 McWhan, D.B., see Vettier, C. 521, 535
 McWhorter, A.L., see Oliver, M.R. 252
 Medarde, M., see Pinsard-Gaudart, L. 268, 280
 Medvedev, V.A., see Cox, J.D. 173
 Mee, J.E. 208
 Mehta, A. 69
 Meiboom, S. 363
 Meingast, C., see Gordon, J.E. 326
 Meinrath, G. 494, 495, 497, 501
 Meinrath, G., see Billard, I. 470, 495, 501–503, 506
 Meinrath, G., see Nitzsche, O. 506
 Meisner, G.P. 6, 8, 9, 11, 12, 20
 Meisner, G.P., see Chen, B. 13
 Meisner, G.P., see DeLong, L.E. 6, 8, 9
 Meisner, G.P., see Fleurial, J.-P. 3, 11, 13, 27, 29
 Meisner, G.P., see Grandjean, F. 13
 Meisner, G.P., see Long, G.J. 13
 Meisner, G.P., see Morelli, D.T. 11, 13, 29
 Meisner, G.P., see Nolas, G.S. 11
 Meisner, G.P., see Shenoy, G.K. 8
 Meisner, G.P., see Torikachvili, M.S. 6, 8, 17, 22
 Meister, G.E., see Holz, R.C. 474, 482
 Meneghini, C. 325
 Menon Latica 48, 56, 61, 69
 Menon Latica, see Malik, S.R. 95
 Menon Latica, see Vijaya Lakshmi, K. 121, 124
 Menovsky, A.A., see Fäth, M. 298
 Mentink, S.A.M. 54
 Menyuk, N., see Goodenough, J.B. 265, 267, 269, 270
 Merbach, A.E., see Aime, S. 421, 422
 Merbach, A.E., see Hedinger, R. 454
 Merbach, A.E., see Marques, M.P.M. 421, 423
 Merbach, A.E., see Powell, D.H. 361
 Merbach, A.E., see Ruloff, R. 363
 Merbach, A.E., see Toth, E. 363, 454
 Merkel, B., see Nitzsche, O. 506
 Merkle, L.D. 522, 572–574
 Merli, L. 174, 210, 213, 216, 220–222
 Merlo, F. 91, 92
 Mesmer, R.E., see Dai, S. 494
 Mesot, J. 524, 535
 Metcalf, D.H. 489
 Metcalf, D.H., see Hopkins, T.A. 369, 377, 381, 383, 400, 405, 410
 Mewis, A., see Dunner, J. 77, 95
 Mewis, A., see Klüfers, P. 77, 91
 Mewis, A., see Wenski, G. 62, 71, 78, 107
 Meyer, D., see Dubost, J.P. 420
 Meyer, G. 149
 Meyer Jr., E.F., see Kasuga, K. 440
 Mezei, F., see Heffner, R.H. 298

- Michael, K. 519
Michel, C., see Chechersky, V. 298
Michels, G., see Dunner, J. 77, 95
Michor, H., see Bauer, E. 24
Miéville, L., see Worledge, W.C. 323
Migliori, A., see Dilley, N.R. 26
Miguel, M., see Rykov, S. 497
Miguel, M.G. 498
Miguel, M.G., see Azenha, M.E. 498
Miguel, M.G., see Burrows, H.D. 497
Mikhailova, N.P., see Savin, V.D. 222
Mikhalsky, Ja.F., see Skolozdra, R.V. 52, 112, 113, 117, 120–123
Milia, F., see Papavassiliou, G. 328
Milicic-Tang, A., see Bünzli, J.-C.G. 493
Millange, F. 336
Millange, F., see Dupont, F. 336
Miller, A.G., see Brina, R. 507
Miller, C.F., see Spedding, F.H. 174, 211, 213
Miller, J., see Sharp, R. 359
Miller, M., see Hilpert, K. 239
Miller, M., see Kapala, J. 190, 191, 193, 232, 233, 236, 237
Millet, O., see Pons, M. 380, 405
Millis, A.J. 17, 26, 268
Millis, A.J., see Ahn, K.H. 267, 268
Millis, A.J., see Quijada, M.A. 296
Mills, A.M. 47, 54, 60, 68, 74, 104, 111
Minai, Y., see Takahashi, K. 481
Minami, A., see Katoh, K. 118
Minomura, S., see Hogg, R.A. 524, 555
Minomura, S., see Takarabe, K. 524, 525, 578–580
Mira, J. 295, 310
Mira, J., see Rivadulla, F. 305
Mirkin, C.A., see Holliday, B.J. 355
Mironov, K.E., see Abdusalamova, M.N. 36, 37, 135
Mironov, V.S. 355, 366, 368–372
Mirov, S., see Hua, H. 521, 522
Mishimura, G. 557
Misumi, M., see Kim, Y.C. 219
Mitchell, J.F., see Louca, D. 304
Mitchell, J.F., see Romero, D.B. 268
Mitchell, J.F., see Roy, M. 291, 328
Mitsuda, S., see Okayama, Y. 521
Mitsuda, S., see Oohara, Y. 521
Mitsuda, S., see Yoshizawa, H. 521
Miyano, K. 291
Miyano, K., see Fiebig, M. 291
Miyano, K., see Ogawa, K. 291
Miyano, Y., see Fiebig, M.K. 291
Mizokawa, T. 263
Mizushima, T., see Hogg, R.A. 524, 555
Mizushima, T., see Takarabe, K. 524, 578–580
Mobilio, S., see Meneghini, C. 325
Mochinaga, J., see Igarashi, K. 203–205
Mody, T.D., see Lisowski, J. 357, 358, 364, 374–376
Møller, C. 148
Moller, M.H., see Brylak, M. 42, 48, 56, 61, 69, 75, 81, 83, 85, 87, 89, 90
Moller, M.H., see Jeitschko, W. 15, 23, 24
Molnár, J. 185, 186, 190, 191, 230–232
Molodkin, A.K. 208
Moloney, J.M., see Aime, S. 426, 429
Molski, A. 489, 502
Monaenkova, A.S. 218
Monaenkova, A.S., see Popova, A.A. 213
Monaenkova, A.S., see Tiflova, L.A. 216
Monsallier, J.M. 506
Monteil, A. 524, 556
Montgomery, R.L. 210, 211, 214, 219
Mooney, W. 497
Moorman, J., see Spedding, F.H. 164, 165, 176, 178
Morelli, D.T. 11, 13, 29
Morelli, D.T., see Chen, B. 13
Morelli, D.T., see Fleurial, J.-P. 3, 11, 13, 27, 29
Morelli, D.T., see Grandjean, F. 13
Morelli, D.T., see Long, G.J. 13
Morelli, D.T., see Meisner, G.P. 11
Morelli, D.T., see Nolas, G.S. 3, 11, 27
Moreno, N.O., see Granado, E. 284, 329
Moreo, A., see Burgy, J. 332
Moreo, A., see Mayr, M. 326
Moreo, A.M., see Dagotto, E. 261
Moret, E., see Bünzli, J.-C.G. 496
Morgan, L.O., see Bloembergen, N. 356, 359
Morgantini, P.-Y., see Ouali, N. 379, 390, 405–410
Morgenstern, A., see Oppermann, H. 210
Morgenstern, M. 506
Mori, N., see Kohgi, M. 521
Mori, N., see Naka, T. 521
Mori, N., see Okayama, Y. 521
Mori, N., see Oohara, Y. 521
Mori, N., see Yoshizawa, H. 521
Mori, S. 328–330
Mori, S., see Katsufuji, T. 275
Mori, S., see Machida, A. 336
Mori, S., see Uehara, M. 327
Moriarity, J.L. 194, 236–238
Morita, M., see Buddhudu, S. 484

- Moritomo, Y. 277, 284, 285, 291, 311, 326
 Moritomo, Y., see Asamitsu, A. 319
 Moritomo, Y., see Katsufuji, T. 275
 Moritomo, Y., see Kuwahara, H. 333, 337
 Moritomo, Y., see Liu, X.J. 299
 Moritomo, Y., see Machida, A. 336, 338
 Moritomo, Y., see Martin, M.C. 322
 Moritomo, Y., see Romero, D.B. 268
 Moritomo, Y., see Tokura, Y. 330, 341
 Moritomo, Y., see Tomioka, Y. 291
 Moritomo, Y., see Urushibara, A. 311
 Moriya, T. 258
 Moriyasu, M. 489, 491, 504
 Moriyasu, M., see Yokoyama, Y. 491, 497
 Morozkin, A.V. 40, 81, 83–85, 87–89, 93, 108
 Morozova, V.A., see Savin, V.D. 222
 Morrison, C. 530
 Morrison, C.A. 154, 160–162, 167, 371
 Morrison, C.A., see Chang, N.C. 538
 Morrison, H.G. 151, 205
 Morrison, M.E. 489
 Morrison, T.I., see Suib, S.L. 481
 Morrow, J.R. 426
 Morrow, J.R., see Amin, S. 426
 Morss, L.R. 171, 210, 214, 217–222, 467
 Morss, L.R., see Fuger, J. 219, 220
 Morss, L.R., see Katz, J.J. 467, 500
 Moser, M., see Stapor, A. 525, 578
 Moshchalkov, V.V., see Aliev, F.G. 118
 Moshchalkov, V.V., see Gordon, I. 326
 Mosquera, M., see Al-Soufi, W. 471, 498
 Moss, G.P., see Briggs, J.M. 368, 455
 Motalov, V.B., see Kudin, L.S. 193, 237
 Motalov, V.B., see Pogrebnoi, A.M. 193, 194, 236, 237
 Motokawa, M., see Nojiri, H. 317
 Mott, N.F. 260
 Moudden, A.H., see Rodríguez-Carvajal, J. 263, 275
 Moudden, A.H., see Vasiliu-Doloc, L. 299, 318
 Moulin, C. 501, 507, 508
 Moulin, C., see Berthoud, T. 507, 508
 Moulin, C., see Billard, I. 470, 495, 501–503, 506
 Moulin, C., see Couston, L. 499
 Moulin, C., see Decambox, P. 507, 508
 Moulin, C., see Scapolan, S. 508
 Moulin, C., see Thouvenot, P. 507
 Moulin, V., see Moulin, C. 501
 Moune, O.K., see Faucher, M.D. 550
 Moussa, F. 324
 Moussa, F., see Biotteau, G. 325
 Moussa, F., see Hennion, M. 311, 324
 Moussa, F., see Rodríguez-Carvajal, J. 263, 275
 Moussavi, M. 440
 Moutiers, G., see Billard, I. 510
 Mozharivskiy, Yu. 37, 41, 42, 80–90, 92, 93, 111, 138, 139
 Mudryi, S.I., see Salamakha, P. 47, 54, 91, 98, 102
 Mukhin, A.A., see Mayr, F. 315
 Mukkala, V.M., see Hemmilä, I. 509
 Mukkala, V.M., see Latva, M. 494, 495
 Mukovskii, Y.M., see Adams, C.P. 298
 Mukovskii, Y.M., see Biotteau, G. 325
 Mukovskii, Y.M., see Quijada, M.A. 269
 Mukovskii, Y.M., see Senis, R. 317
 Mukovskii, Y.M., see Skumryev, V. 312
 Mukovskii, Y.M., see Smolyaninova, V.N. 321
 Mukovskii, Y.M., see Vasiliu-Doloc, L. 321
 Mukovskii, Ya.M., see Markovich, V. 325
 Mukovskii, Ya.M., see Yuzhelevski, Y. 326
 Müller, H., see Trommer, R. 578
 Müller, K.A., see Zhao, G.-M. 305, 307
 Müller, M., see Grund, I. 40, 42, 96
 Muller, R.N., see Ruloff, R. 363
 Muller, U. 5
 Muñoz, J.S., see Skumryev, V. 312
 Munro, R.G., see Fujishiro, I. 519
 Murakami, S., see Buddhudu, S. 484
 Murakami, Y. 263
 Murakami, Y., see Endoh, Y. 315
 Murakami, Y., see Zimmermann, M.V. 264
 Murani, A.P., see Guzik, A. 54
 Murata, S., see Tachiya, M. 489
 Muravjova, A.A. 43, 137
 Murray, G.M., see Del Cul, G.D. 523
 Murray, G.M., see Jenkins, A.L. 507
 Mustafayev, F.M., see Geydarova, E.N. 85
 Mutka, H., see Mesot, J. 524, 535
 Muzet, N., see Berny, F. 358
 Mydosh, J.A. 270
 Mydosh, J.A., see Fäth, M. 298
 Mydosh, J.A., see Mentink, S.A.M. 54
 Myers, C.E. 182, 184, 186, 192, 194, 237
 Myers, C.E., see Hannay, M.H. 236
 Nabialek, A., see Troyanchuk, O.Ya. 275
 Nachtrieb, N.D., see Jamieson, J.C. 516
 Nafziger, R.H. 200
 Nagaev, E.L. 293, 305, 307
 Nagaishi, R. 497
 Nagaishi, R., see Billard, I. 470, 495, 501–503, 506
 Nagaishi, R., see Kimura, T. 471–473, 479

- Nagarajan, R., see Patil, S. 53, 80, 133
 Naka, T. 521
 Nakamura, A., see Liu, X.J. 299
 Nakamura, A., see Machida, A. 336, 338
 Nakanishi, T., see Shirotani, I. 9, 10
 Nakao, H., see Zimmermann, M.V. 264
 Nakazawa, Y., see Shirotani, I. 7, 9, 21
 Nakazawa, Y., see Uchiumi, T. 7–9, 12
 Naler, S. 328
 Namiki, T., see Aoki, Y. 17–19
 Nanba, T. 20
 Narayan, J., see Kumar, D. 326
 Nardone, M., see Congeduti, A. 325
 Nash, K.L. 493
 Natali, F., see Lanzara, A. 295, 325
 Nath, A. 325
 Nath, A., see Chechersky, V. 295, 296, 298, 305, 325
 Naumov, V.A., see Akishin, P.A. 224
 Nave, S.E., see Del Cul, G.D. 523
 Neck, V., see Fanghänel, T. 500
 Nedyak, S., see Perov, P.A. 186, 227, 228
 Nehlig, A. 473, 474, 482, 485
 Neikirk, D.P., see Powell, R.C. 572
 Neilo, G.N., see Krygin, I.M. 521, 522, 536
 Neilo, G.N., see Lukin, S.N. 524, 536
 Nelson, C.S., see Zimmermann, M.V. 264
 Nesmeyanov, A.N. 236
 Nessel, F., see Bungenstock, C. 540
 Neuenschwander, J. 522, 523, 525
 Neuhaus, A. 558
 Neumann, H., see Klüfers, P. 77, 91
 Neumann, M., see Slebarski, A. 45, 59, 60, 100, 113
 Neumeier, J.J. 278, 283, 299
 Neumeier, J.J., see Granado, E. 263, 284, 329
 Newman, D.J. 530, 531, 542, 545
 Newman, D.J., see Bishton, S.S. 547
 Newman, D.J., see Bradbury, M.I. 541
 Newman, D.J., see Curtis, M.M. 544
 Newman, D.J., see Poon, Y.M. 560
 Newman, D.J., see Reid, M.F. 547
 Ng, B., see Newman, D.J. 530, 542, 545
 Ni, B., see Bauer, E. 24
 Ni Dhubhghaill, O.M., see Powell, D.H. 361
 Niarchos, D., see Kallias, G. 328
 Niarchos, D., see Papavassiliou, G. 325, 328
 Nibler, J.W., see Lesiecki, M. 186, 224
 Nicastro, G., see Bertini, I. 357, 361
 Nicholson, A.J.C., see Ciach, S. 236, 237
 Nickel, H., see Gietmann, C. 194, 196, 197, 207, 209, 238–240
 Nickle, S.K., see Cacheris, W.P. 410
 Niemann, U., see Hilpert, K. 149
 Niemöller, T., see Uhlenbruch, S. 317
 Nieuwenhuys, G.J., see Heffner, R.H. 298, 325
 Nieuwenhuys, G.J., see Mentink, S.A.M. 54
 Nigam, A.K., see Vijaya Lakshmi, K. 121, 124
 Nijegorodov, N. 506
 Nisel'son, L.A. 203–205
 Nisel'son, L.N. 236, 238
 Nisel'son, L.N., see Lyzlov, Y.N. 203–206
 Nishibori, E., see Machida, A. 336
 Nishibori, E., see Moritomo, Y. 277, 284, 285
 Nishimura, G. 524
 Nishizawa, A., see Endoh, Y. 315
 Nitsche, H., see Bernhard, G. 495
 Nitsche, H., see Brendler, V. 499
 Nitsche, H., see Geipel, G. 495, 499, 500, 505
 Nitsche, H., see Rutsch, M. 501
 Nitzsche, O. 506
 Niu, X.J. 82
 Niwa, K., see Shimazaki, E. 206–208, 236, 238–240
 Noack, R.A. 518
 Noakes, D.R., see Shenoy, G.K. 8
 Noël, H., see Flandorfer, H. 127
 Noël, H., see Sologub, O. 41, 42, 45, 46, 48, 49, 52, 53, 56, 58–62, 66, 67, 69, 72–76, 79–93, 102, 119–123
 Noël, H., see Weitzer, F. 44, 59, 65, 73
 Nogués, J., see Skumryev, V. 312
 Noh, T.W., see Dho, J. 325
 Noh, T.W., see Jung, J.H. 323
 Noh, T.W., see Kim, K.H. 296, 328
 Nohdo, S., see Yamada, Y. 315
 Nojiri, H. 317
 Nojiri, H., see Endoh, Y. 315
 Nojiri, S., see Sugawara, H. 18
 Nolas, G.S. 3, 11, 27–30
 Nomura, K., see Chechersky, V. 295, 296, 325
 Nordstrom, L. 6, 12, 13
 North, A.C.T., see Barry, C.D. 363
 Noubactep, C., see Meinrath, G. 495, 497, 501
 Novák, P., see Krupicka, S. 338
 Novák, P., see Savosta, M.M. 310
 Novikov, G., see Suvorov, A.V. 234
 Novikov, G.I. 236
 Novikov, G.I., see Dudchik, G.P. 236–238
 Novikov, G.I., see Polyachenok, O.G. 213, 236, 237

- Novo, M., see Al-Soufi, W. 471, 498
 Novoselova, A.V., see Shaimuradov, I.B. 202
 Novotný, P., see Söhnle, O. 173
 Nowitzke, G., see Bungenstock, C. 540
 Nozar, P., see Dediu, V. 327
 Nozawa, K., see Shirotani, I. 7–9, 12
 Nozawa, S., see Kanai, K. 13
 Nunes, L.H.A., see De Sa, G.F. 471, 483
 Nuñez-Reguero, M., see Meneghini, C. 325
 Nunziantese Cesaro, S., see Kapala, J. 190, 191, 193, 232, 233, 236, 237

 Obradors, X., see Causa, M.T. 326
 Obradors, X., see Fontcuberta, J. 299
 Obradors, X., see Laukhin, V. 299
 Obradors, X., see Senis, R. 317
 Obriot, J., see Monteil, A. 524, 556
 Oetting, F.L., see Fuger, J. 171
 Ofelt, G.S. 560
 Offen, H.W., see Gleason, J.K. 524, 551, 566, 568
 Oftedal, I. 2
 Ogale, S.B., see Hannover, B. 325
 Ogale, S.B., see Saraf, L.V. 309
 Ogale, S.B., see Zhao, Y.G. 328
 Ogale, S.B., see Zhao, Y.G. 296
 Ogawa, K. 291
 Oguro, I., see Katoh, K. 118
 Ohara, Y., see Kohgi, M. 521
 Ohara, Y., see Okayama, Y. 521
 O'Hare, P.A.G., see Flotow, H.E. 154, 157
 Ohashi, M., see Kajimoto, R. 337
 Ohnishi, T., see Hasegawa, Y. 479, 480
 Ohno, K., see Shirotani, I. 7, 9, 10, 21
 Ohno, S.I., see Lee, K.P. 492
 Ohno, T., see Chahara, K.I. 290
 Ohoyama, K., see Kajimoto, R. 337
 Ohoyama, K., see Machida, A. 336, 338
 Ohshiden, S., see Fujishiro, H. 276
 Ohta, T., see Lee, C.H. 20
 Oikawa, K., see Yamada, Y. 315
 Oishi, J., see Kim, Y.C. 213–215, 217, 219–221
 Okada, H., see Matsuda, T.D. 17
 Okada, H., see Sato, H. 6, 8, 12, 17, 18, 22, 23
 Okako, N., see Iwadata, Y. 179
 Okamoto, H., see Massalski, T.B. 36
 Okamoto, H., see Villars, P. 37
 Okamoto, M., see Tanaka, F. 491, 492
 Okamoto, S., see Endoh, Y. 315
 Okamoto, S., see Saitoh, E. 269
 Okayama, Y. 521
 Okayama, Y., see Kohgi, M. 521
 Okayama, Y., see Naka, T. 521
 Okayama, Y., see Oohara, Y. 521
 Okayama, Y., see Yoshizawa, H. 521
 Okimoto, Y., see Kimura, T. 336
 Okimoto, Y., see Saitoh, E. 321
 Okimoto, Y., see Tobe, K. 266, 269
 Okuda, T. 325
 Olenyuk, B., see Leininger, S. 355
 Oleś, A., see André, G. 123
 Oliver, M.R. 252
 Olmstead, M.M., see Chan, J.Y. 37, 90
 Olsen, L.R. 523
 Olsen, L.R., see Wright, A.O. 523, 524
 Omenetto, N., see Eliet, V. 474, 498
 Onellion, M., see Ren, Y.H. 326
 Onuki, Y., see Sugawara, H. 8, 9, 18, 23
 Oohara, Y. 521
 Oohara, Y., see Yoshizawa, H. 521
 Oppenländer, A. 522
 Oppermann, H. 210
 Oppermann, H., see Hennig, C. 213–215
 Ortolani, M., see Meneghini, C. 325
 Osakabe, T., see Kasaya, M. 131, 132
 Osakabe, T., see Kohgi, M. 521
 Osakabe, T., see Okayama, Y. 521
 Osakabe, T., see Oohara, Y. 521
 Osakabe, T., see Yoshizawa, H. 521
 Osborne, D.W., see Lyon, W.G. 154, 157, 162–164, 166
 Oseroff, S.B., see Causa, M.T. 326
 Oseroff, S.B., see Granado, E. 263, 284, 329
 Oshchepkov, D.I., see Laptev, D.M. 216
 Osin, S.B., see Loktyushina, N.S. 186, 228, 229
 Ott, H.R. 55
 Ott, H.R., see Hulliger, F. 48, 49, 78, 94
 Ouali, N. 379, 390, 405–410
 Ouali, N., see Bocquet, B. 453, 455, 456
 Ouali, N., see Floquet, S. 453, 455–459
 Ovander, L.N., see Voloshin, V.A. 522, 531
 Overend, N. 303
 Oyanagi, H., see Lee, C.H. 20
 Ozawa, T.C., see Fisher, I.R. 90, 91, 134, 135, 137

 Padhan, P., see Srivastava, S. 291, 292
 Paetzold, H.K. 516, 521
 Palmetshofer, L., see Jantsch, W. 525, 580
 Palmetshofer, L., see Przybylinska, H. 525, 580
 Panagiotopoulos, I., see Papavassiliou, G. 325
 Panak, P. 494, 495
 Panak, P., see Klenze, R. 500
 Panczer, G., see Gaft, M. 480

- Pandey, N., see Srivastava, S. 291, 292
 Pani, M., see Merlo, F. 91, 92
 Panigrahi, B.S., see Peter, S. 507
 Pankevich, Yu.V. 52, 59, 66, 73
 Pankevich, Yu.V., see Pecharsky, V.K. 40, 52, 53,
 59, 66, 67, 73, 79, 82, 84, 86, 88, 89, 92, 100,
 106, 109, 138, 139
 Paoli, P., see Bianchi, A. 426
 Papatheodorou, G.N., see Boghosian, S. 184
 Papavassiliou, G. 325, 326, 328
 Pappalardo, R., see Jørgensen, C.K. 541
 Paraskevopoulos, M., see Mayr, F. 315
 Parigi, G., see Bertini, I. 362, 363, 367
 Parisi, F., see Freitas, R.S. 328, 329
 Parisi, F., see Levy, P. 328
 Park, K.S., see Lee, K.P. 492
 Park, Y.Y. 489, 491, 492, 498
 Park, Y.Y., see Yamamura, T. 492
 Parker, D. 355, 420, 484, 491, 493, 494, 509
 Parker, D., see Aime, S. 426, 429
 Parker, D., see Beeby, A. 481–484
 Parker, D., see Billard, I. 470, 495, 501–503, 506
 Parker, D., see Blair, S. 509
 Parker, D., see Bruce, J.I. 355
 Parker, D., see Clarkson, I.M. 484, 505
 Parker, D., see Dickins, R.S. 481, 482
 Parker, V.B. 173
 Parker, V.B., see Fuger, J. 171
 Parma, L., see Eliet, V. 474, 498
 Parodi, N., see Borzone, G. 37, 135, 136
 Parodi, N., see Cacciamani, G. 135
 Pascal, P. 494
 Paschke, D., see Jeitschko, W. 15, 23, 24
 Pashinkin, A.S. 237
 Pashkevich, Yu.G., see Zvyagin, S. 338
 Pasternak, M.P., see Loa, I. 268
 Pastor, R.C. 150, 201, 202
 Patil, S. 53, 56, 80, 133
 Patil, S.I., see Hannoyer, B. 325
 Patterson, H.H., see Yersin, H. 523, 569, 570
 Paul, C., see Bauer, E. 24
 Paul, Ch., see Bauer, E. 24
 Paul, D.McK., see Campbell, A.J. 319
 Paul, D.McK., see Lees, M.R. 291
 Paul, D.McK., see Zvyagin, S. 338
 Paulose, P.L., see Patil, S. 53, 56, 80, 133
 Paulus, E.F. 430, 433
 Paulus, H., see Buchler, J.W. 449, 450
 Paviet, P. 500
 Paviet, P., see Fanghänel, T. 500
 Paviet-Hartmann, P., see Fanghänel, T. 500
 Pavlyuk, V.V. 78, 82
 Pavlyuk, V.V., see Stetskiv, A.O. 55, 109, 111
 Pavone, D., see Baker, F.B. 214
 Pawlowska, M.M., see Marcantonatos, M.D. 498
 Payne, D.A., see Yoon, S. 326
 Peacock, R.D., see Bruce, J.I. 355
 Peacock, R.D., see Dickins, R.S. 481
 Pécaut, J., see Bretonnière, Y. 393
 Pecharsky, A.O., see Niu, X.J. 82
 Pecharsky, V.K. 40, 45, 52, 53, 59, 66, 67, 73, 79,
 82, 84, 86, 88, 89, 92, 98, 100, 106, 109, 138, 139
 Pecharsky, V.K., see Adroja, D.T. 60, 61, 118
 Pecharsky, V.K., see Niu, X.J. 82
 Pecharsky, V.K., see Pankevich, Yu.V. 52, 59, 66,
 73
 Peck Jr., W.F., see Cava, R.J. 56
 Pelipets, O.V., see Giricheva, N.I. 184, 186, 190,
 191, 193, 228, 232
 Pelleg, J., see Markovich, V. 287
 Peng, J.-L., see Lynn, J.W. 299, 325
 Peng, J.L., see Erwin, R.W. 325
 Peng, J.L., see Huang, Q. 289, 325
 Pennell, R.G., see Johnson, G.K. 209, 210, 212,
 213, 215–217, 219, 220
 Penzkofer, A., see Holzer, W. 506
 Pepe, G., see Kasuga, K. 440
 Perakis, I.E., see Ren, Y.H. 326
 Perdew, J.P. 148
 Perebeinos, V. 268
 Perebeinos, V., see Allen, P.B. 268, 269
 Periasamy, A., see Sharman, K.S. 470
 Perov, P.A. 186, 227, 228
 Perry, J.J.B., see Bruce, J.I. 355
 Peter, S. 507
 Peterman, D.R., see Choppin, G.R. 493
 Peters, J.A. 356–359, 362, 368, 373, 377, 378,
 380–384, 405
 Peters, J.A., see Corsi, D.M. 356
 Peters, J.A., see Frullano, L. 421
 Peterson, J.R. 522, 558, 559
 Peterson, J.R., see Chen, G. 522–524, 529, 549,
 550, 557, 558
 Peterson, J.R., see Daniel, J.F. 151, 205
 Peterson, J.R., see Del Cul, G.D. 523, 558
 Peterson, J.R., see Haire, R.G. 558
 Peterson, J.R., see Morrison, H.G. 151, 205
 Peterson, J.R., see Stump, N.A. 523, 557
 Peterson, J.R., see Wilmarth, W.R. 521, 522, 558
 Peterson, J.R., see Young, J.P. 558
 Peterson, R.C., see Kasuga, K. 440
 Petkov, V., see Billinge, S.J.L. 304

- Petoud, S. 355, 384–387
 Petoud, S., see Bünzli, J.-C.G. 496
 Petoud, S., see Piguët, C. 393–395
 Petzel, T. 234, 235
 Petzel, T., see Greis, O. 559
 Pfeiffer, S., see Buchler, J.W. 449
 Phelps, D.E., see Vold, R.L. 364
 Phillips, N.E., see Fisher, R.A. 326
 Phillips, N.E., see Gordon, J.E. 326
 Phillips, R., see Stubblefield, C.T. 215
 Phillips, R.F., see Evans, D.F. 356
 Piacente, V. 195, 237, 239, 240
 Piacente, V., see Brunetti, B. 195, 236–240
 Piacente, V., see Villani, A.R. 195, 236, 238–240
 Picard, G., see Joubert, L. 182, 183, 187–189
 Pichlmaier, M., see Holzer, W. 506
 Pickett, W.E., see Singh, D.J. 6
 Pieper, M.W., see Allodi, G. 325, 328, 337
 Piermarini, G.J. 518, 519
 Piermarini, G.J., see Barnett, J.D. 522, 552, 554
 Piermarini, G.J., see Fujishiro, I. 519
 Pierre, J., see Guzik, A. 54, 113
 Pierre, J., see Kaczmarek, K. 80, 112, 113
 Pierre, J., see Skolozdra, R.V. 52, 112, 113, 117, 120–123
 Pifer, J.H., see Sakai, N. 518
 Piguët, C. 355, 356, 384, 385, 393–395
 Piguët, C., see Bocquet, B. 453, 455, 456
 Piguët, C., see Bünzli, J.-C.G. 355
 Piguët, C., see Elhabiri, M. 443–445, 448, 481, 494
 Piguët, C., see Floquet, S. 453, 455–459
 Piguët, C., see Quali, N. 379, 390, 405–410
 Piguët, C., see Petoud, S. 355, 384–387
 Piguët, C., see Platas-Iglesias, C. 406, 407
 Piguët, C., see Renaud, F. 387–393, 408
 Piguët, C., see Rigault, S. 358, 361, 363, 366, 378, 389, 390, 396–400, 403, 444, 446–448
 Pimenov, A., see Mayr, F. 315
 Pina, F., see Bazzicalupi, C. 492, 509
 Pinkerton, A.A. 357, 365, 366, 415–418
 Pinkerton, A.A., see Spiliadis, S. 358, 377, 415
 Piñol, S., see Causa, M.T. 326
 Pinsard, L., see Allodi, G. 288
 Pinsard, L., see Anane, A. 291
 Pinsard, L., see Biotteau, G. 325
 Pinsard, L., see Cestelli Guidi, M. 264
 Pinsard, L., see Hennion, M. 311, 324
 Pinsard, L., see Martínez, B. 317
 Pinsard, L., see Moussa, F. 324
 Pinsard, L., see Rodríguez-Carvajal, J. 263, 275
 Pinsard, L., see Skumryev, V. 312
 Pinsard, L., see Uhlenbruch, S. 317
 Pinsard-Gaudart, L. 268, 280
 Pinsard-Gaudart, L., see Daoud-Aladine, M. 328, 335, 336
 Pinsard-Gaudart, L., see Klingeler, R. 315
 Pissas, M. 329
 Pissas, M., see Kallias, G. 328
 Pissas, M., see Papavassiliou, G. 325, 328
 Pissas, M., see Simopoulos, A. 328
 Pizer, K.S., see Lewis, G.N. 182
 Plancque, G., see Billard, I. 470, 495, 501–503, 506
 Platas, C. 358, 359, 377, 378, 400–404
 Platas, C., see Gerales, C.F.G.C. 358, 378, 404, 405
 Platas-Iglesias, C. 406, 407
 Platas-Iglesias, C., see Corsi, D.M. 356
 Plesset, M.S., see Møller, C. 148
 Plummer, E.W., see Dai, P. 325
 Podzorov, V. 327
 Poepelmeier, K.R. 282
 Poettgen, R., see Gordon, R.A. 56, 95
 Pogrebnoi, A.M. 193, 194, 236, 237
 Pogrebnoi, A.M., see Kudin, L.S. 193, 237, 238
 Poilblanc, D., see Dagotto, E. 261
 Polla, G., see Levy, P. 328
 Pollert, E., see Jiráček, Z. 275
 Polyachenok, O.G. 209, 212, 213, 215, 219, 236, 237
 Polyachenok, O.G., see Dudchik, G.P. 236–238
 Polyachenok, O.G., see Makhadmurodov, A. 195, 239
 Pons, M. 380, 405
 Poon, Y.M. 560
 Poon, Y.M., see Newman, D.J. 530
 Popov, V., see Ilisavskii, Y. 326
 Popova, A.A. 213
 Popovic, A., see Bencze, L. 186, 226, 235
 Popovic, A., see Kaposi, O. 196, 240
 Popper, P., see Ruddlesden, S.N. 250
 Porsch, F., see Shen, Y.R. 564
 Porter, B. 200, 201
 Poshevneva, A.I. 182, 208
 Poshevneva, A.I., see Goryushkin, V.F. 180, 182, 205, 206, 209, 223
 Postorino, P., see Congeduti, A. 325
 Pöttgen, R., see Gordon, R.A. 56, 97, 113
 Potthast, J., see Petzel, T. 234, 235
 Pouliquen, J. 488
 Pouyat, D., see Couston, L. 499

- Pouyat, D., see Moulin, C. 508
 Powell, D.H. 361
 Powell, H., see Marques, M.P.M. 421, 423
 Powell, R.C. 572
 Powell, R.C., see Merkle, L.D. 522, 572–574
 Prado, F., see Causa, M.T. 326
 Préaudat, M., see Bazin, H. 509
 Prellier, W., see Zhao, G. 326
 Prellier, W., see Zhao, G.-M. 308
 Prendergast, F.G., see Kemple, M.D. 357, 358, 367, 373–375, 386
 Preston, S.R., see Gardner, P.J. 168
 Preuss, H., see Dolg, M. 148, 183, 187–189
 Prewitt, C.T., see Shannon, R.D. 250
 Prince, A., see Villars, P. 37
 Prins, L.J. 393
 Prior, P., see Chmaissem, O. 278, 280
 Proffen, Th., see Billinge, S.J.L. 304
 Proietti, M.G., see Subías, G. 323
 Prokhorov, A.D., see Krygin, I.M. 521, 522, 536
 Prokhorov, A.D., see Lukin, S.N. 524, 536
 Protsyk, O. 45, 53
 Prudnikov, A.M., see Voloshin, V.A. 522, 531
 Pryadun, V.V., see Aliev, F.G. 118
 Przybylinska, H. 525, 580
 Przybylinska, H., see Jantsch, W. 525, 580
 Pubanz, D., see Aime, S. 421, 422
 Pubanz, D., see Marques, M.P.M. 421, 423
 Pubanz, D., see Powell, D.H. 361
 Pubanz, D., see Ruloff, R. 363
 Pulukkody, K., see Parker, D. 420
 Purcell, F.J., see Kaminski, R. 507
 Puzniak, R., see Markovich, V. 325
 Pyatkov, V.I., see Lebedev, V.A. 36
 Pyles, B., see Chmaissem, O. 278, 280
 Pyykkö, P., see Golding, R.M. 357, 371
- Qi Li, see Ren, Y.H. 326
 Quezel, G., see Quezel, S. 275
 Quezel, S. 275
 Quezel, S., see Burlet, P. 55
 Quezel, S., see Rossat-Mignod, J. 55, 57
 Quezel-Ambrunat, S. 275
 Quijada, M.A. 269, 296
- Raber, D.J., see Peters, J.A. 356–359, 362, 368, 373, 380
 Rachmatov, O.I., see Abdusalamova, M.N. 37
 Radaelli, P.G. 299, 323, 325, 327, 329
 Radaelli, P.G., see Cox, D.E. 291
 Radaelli, P.G., see Hwang, H.Y. 290, 291
 Radaelli, P.G., see Lanzara, A. 295, 325
 Radenkovic, B., see Jovanić, B.R. 522, 524, 563
 Radliński, A.P. 523, 536
 Radousky, H.B., see Yoo, C.S. 522, 549, 550
 Rai, D., see Felmy, A.R. 506
 Rainford, B.D., see Adroja, D.T. 60, 61, 118
 Rainford, B.D., see Thornton, M.J. 124
 Rajeswari, M., see Quijada, M. 296
 Rajeswari, M., see Zhao, G.-M. 308
 Rajeswari, M., see Zhao, Y.G. 296
 Rajnak, K., see Carnall, W.T. 383
 Raju, A.R., see Joshi, J.P. 336
 Raju, N.P. 43
 Rakhmatov, O.I., see Abdusalamova, M.N. 36, 37
 Rakicioglu, Y. 508
 Ramakrishnan, S., see Malik, S.R. 95
 Raman, A., see Wang, R. 48, 49, 75
 Ramesh, R., see Quijada, M. 296
 Ramesh, R., see Saraf, L.V. 309
 Ramesh, R., see Zhao, Y.G. 296
 Ramirez, A.P., see Cava, R.J. 56
 Ramirez, A.P., see Radaelli, P.G. 327
 Ramirez, A.P., see Roy, M. 291, 328
 Ramirez, A.P., see Schiffer, P. 328
 Ramondo, F., see Hilpert, K. 239
 Ramos, C., see Rivadulla, F. 321
 Ramos, C.A., see Causa, M.T. 326
 Ramos, C.A., see Mira, J. 310
 Rana, R.S., see Carnall, W.T. 383
 Randall, E.W., see Briggs, J.M. 368, 455
 Randall, M., see Lewis, G.N. 182
 Rao, B.D.N., see Kemple, M.D. 357, 358, 367, 373–375, 386
 Rao, C.N.R. 330
 Rao, C.N.R., see Joshi, J.P. 336
 Raquet, B. 326
 Ratcliff II, W., see Heffner, R.H. 325
 Ratnikova, I.D., see Sobolev, B.P. 202
 Rau, D., see Buddhudu, S. 484
 Raveau, B., see Autret, C. 338
 Raveau, B., see Damay, F. 330, 336
 Ravi Bathe, see Hannoyer, B. 325
 Ravot, D. 10, 11, 13, 57
 Ravot, D., see Rossat-Mignod, J. 55, 57
 Ray, B.D., see Kemple, M.D. 357, 358, 367, 373–375, 386
 Raymo, F.M., see Balzani, V. 355
 Raymond, K.N., see Wu, S.L. 492
 Razavi, F.S., see Casa, D. 315
 Rebizant, J., see Spirlet, M.-R. 420
 Redwing, J.M., see Culp, T.D. 524, 578, 579

- Reed, T.B., see Oliver, M.R. 252
 Reed, W.J., see Allsopp, S.R. 473, 474
 Rehr, A. 76, 111
 Rehr, A., see Chan, J.Y. 134
 Reich, T., see Bernhard, G. 495
 Reid, M.F. 547, 561
 Reid, M.F., see Jayasankar, C.K. 522, 547
 Reid, M.F., see Li, C.L. 547
 Reilley, C.N. 357, 376, 377, 404–407, 410, 443
 Reilley, C.N., see Bryden, C.C. 376, 410, 471, 478, 505
 Reilley, C.N., see Desreux, J.F. 357
 Reimann, K., see Stapor, A. 525, 578
 Reinhoudt, D., see Steemers, F. 494
 Reinhoudt, D.N., see Klink, S.I. 471, 494–496
 Reinhoudt, D.N., see Prins, L.J. 393
 Reisfeld, R., see Gaft, M. 480
 Reisfeld, R., see Jørgensen, C.K. 497, 529
 Reiß, G., see Bungenstock, C. 540
 Reissner, M., see Leithe-Jasper, A. 26
 Reller, A. 282
 Ren, J. 358, 420, 423–426, 429–431, 433–440
 Ren, J., see Sherry, A.D. 433
 Ren, S.Y. 580
 Ren, Y.H. 326
 Renard, J.-P., see Anane, A. 291
 Renaud, F. 387–393, 408
 Renaud, F., see Bocquet, B. 453, 455, 456
 Renaud, F., see Petoud, S. 355, 384–387
 Reppke, M., see Dunner, J. 77, 95
 Reshetnikova, L.P., see Shaimuradov, I.B. 202
 Rettori, C., see Granado, E. 263, 284, 329
 Reuben, J. 358, 365, 376, 377, 379, 380, 436
 Reuter, G. 166, 167, 205
 Reutler, P. 326
 Revcolevschi, A., see Anane, A. 291
 Revcolevschi, A., see Biotteau, G. 325
 Revcolevschi, A., see Daoud-Aladine, M. 328, 335, 336
 Revcolevschi, A., see Hennion, M. 311, 324
 Revcolevschi, A., see Klingeler, R. 315
 Revcolevschi, A., see Martínez, B. 317
 Revcolevschi, A., see Moussa, F. 324
 Revcolevschi, A., see Pinsard-Gaudart, L. 268, 280
 Revcolevschi, A., see Skumryev, V. 312
 Revcolevschi, A., see Uhlenbruch, S. 317
 Revcolevschi, A., see Vasiliu-Doloc, L. 299, 318
 Revcolevschi, A., see Rodríguez-Carvajal, J. 263, 275
 Reversat, L., see Anane, A. 291
 Revzin, B., see Markovich, V. 287
 Rewaj, T. 523, 524, 536
 Rezukhina, T.N. 209, 212
 Rezukhina, T.N., see Kholokhova, L.I. 211, 213, 215, 216, 221
 Riani, P. 41, 85, 87, 88, 91, 93
 Riazance, N., see Nafziger, R.H. 200
 Richardson, F. 493
 Richardson, F.S., see Burdick, G.W. 548
 Richardson, F.S., see Hopkins, T.A. 369, 377, 381, 383, 400, 405, 410
 Richardson, F.S., see Metcalf, D.H. 489
 Riedener, T., see Shen, Y.R. 525, 575–577
 Riedi, P.C., see Thornton, M.J. 124
 Riedl, U., see Yersin, H. 569
 Riehl, J.P., see Huskowska, E. 405
 Rigault, S. 358, 361, 363, 366, 378, 389, 390, 396–400, 403, 444, 446–448
 Rigault, S., see Ouali, N. 379, 390, 405–410
 Rigault, S., see Piguet, C. 355, 393
 Rillo, C., see Stankiewicz, J. 292
 Ritter, C., see De Teresa, J.M. 298
 Ritter, C., see Frontera, C. 336
 Ritter, C., see García-Landa, B. 338
 Ritter, C., see Llobet, A. 336
 Rivadulla, F. 305, 309, 321, 328, 330–335, 337–342
 Rivadulla, F., see Causa, M.T. 326
 Rivadulla, F., see Hueso, L.E. 326
 Rivadulla, F., see Mira, J. 295, 310
 Rivas, J., see Causa, M.T. 326
 Rivas, J., see Hueso, L.E. 326
 Rivas, J., see Mira, J. 295, 310
 Rivas, J., see Rivadulla, F. 305, 309, 321
 Rivasibid, J., see Mira, J. 295
 Rizkalla, E.N., see Choppin, G.R. 499
 Roberts, D.W., see Hawkes, G.E. 368
 Roberts, J.A. 192, 197, 234
 Roberts, J.D., see Hawkes, G.E. 368
 Robinson, M. 200
 Robinson, M., see Pastor, R.C. 150, 201, 202
 Röder, H., see Heffner, R.H. 298
 Röder, H., see Louca, D. 263
 Rodewald, U.C., see Jeitschko, W. 15, 23, 24
 Rodriguez, V.D., see Lavin, V. 523
 Rodríguez-Blas, T., see Gerales, C.F.G.C. 358, 378, 404, 405
 Rodríguez-Blas, T., see Platas, C. 358, 359, 377, 378, 400–404
 Rodríguez-Carvajal, J. 263, 275
 Rodríguez-Carvajal, J., see Biotteau, G. 325
 Rodríguez-Carvajal, J., see Brinks, H.W. 275, 276

- Rodríguez-Carvajal, J., see Daoud-Aladine, M. 328, 335, 336
- Rodríguez-Carvajal, J., see Frontera, C. 336
- Rodríguez-Carvajal, J., see García-Muñoz, J.L. 323
- Rodríguez-Carvajal, J., see Hennion, M. 311, 324
- Rodríguez-Carvajal, J., see Moussa, F. 324
- Rodríguez-Carvajal, J., see Pinsard-Gaudart, L. 268, 280
- Rodríguez-Mendoza, U.R., see Lavin, V. 523
- Rodríguez-Ubis, J.C., see Latva, M. 494, 495
- Roffe, M. 205
- Rogl, P., see Bauer, E. 24
- Rogl, P., see Flandorfer, H. 91, 92, 118, 127
- Rogl, P., see Leithe-Jasper, A. 26, 43, 44, 51, 52, 59, 63, 64, 66, 72, 73, 79
- Rogl, P., see Sologub, O. 41–43, 45–49, 51–54, 56–63, 66–69, 72–76, 79–93, 102, 103, 119–123, 133
- Rogl, P., see Weitzer, F. 44, 59, 65, 73
- Rohovec, J., see Frullano, L. 421
- Rojo, J.M., see Alonso, J. 324
- Rome, J.F., see Hirayama, C. 196, 197, 239, 240
- Romero, D.B. 268
- Roque, A., see Bazzicalupi, C. 492, 509
- Rorif, F., see Merli, L. 174, 210, 213, 216, 220–222
- Rørmark, L., see Faaland, S. 323
- Rosato, A., see Bertini, I. 374
- Rose, R.A., see Brink, J.M. 364
- Rosenberg, E., see Markovich, V. 287
- Rossat-Mignod, J. 55, 57
- Rossat-Mignod, J., see Burlet, P. 55
- Rossat-Mignod, J., see Quezel, S. 275
- Rossat-Mignot, J., see Ravot, D. 57
- Rossel, C., see Torikachvili, M.S. 6, 8, 17, 22
- Rossi, D. 49, 57, 71, 76
- Rossi, D., see Marazza, R. 41, 48, 56, 61, 69, 74, 81, 83, 85, 87, 88, 91, 106
- Rossi, P., see Bianchi, A. 426
- Rossier, M., see Pinkerton, A.A. 357, 365, 366
- Rossini, I., see Bouby, M. 506
- Rossotti, F.J.C., see Alsaadi, B.M. 361, 405–407
- Rozsak, S., see Kapala, J. 190, 191, 193, 232, 233, 236, 237
- Roth, K., see Hoefl, S. 421, 422
- Roudaut, E., see Quezel, S. 275
- Rowe, D.M. 28
- Rowe, D.M., see Kuznetsov, V.L. 24, 26
- Rowley, A.J., see Hutchinson, F. 179
- Roy, M. 291, 328
- Royle, L., see Beeby, A. 481–484
- Rozenberg, E., see Markovich, V. 287, 325
- Rozenberg, E., see Yuzhelevski, Y. 326
- Rozenberg, G.Kh., see Loa, I. 268
- Rozenberg, M.J. 261, 315
- Ruani, G., see Dediu, V. 327
- Rübhausen, M., see Björnsson, P. 268
- Rübhausen, M., see Naler, S. 328
- Rubini, P., see Giroux, S. 494, 505
- Ruddlesden, S.N. 250
- Rudowicz, C., see Tanner, P.A. 557
- Rudzitis, E. 215, 219
- Ruf, T., see Goncharov, A.F. 522, 582
- Rühl, R. 76, 90
- Ruloff, R. 363
- Runde, W., see Kim, J.I. 496
- Ruoff, A.L., see Asaumi, K. 519
- Rupprecht, K., see Lübbers, R. 518
- Rurack, K. 509
- Russavage, E., see Kaminski, R. 507
- Rustamov, P.G. 74, 77, 81, 83, 92
- Rustamov, P.G., see Aliev, O.M. 55, 77, 78, 80, 91, 92
- Rustamov, P.G., see Geidarova, E.A. 42, 71, 75, 85
- Rustenholtz, A. 474
- Rustenholtz, A., see Billard, I. 485
- Rutledge, J.L., see Stubblefield, C.T. 215
- Rutsch, M. 501
- Ryan, W., see Ferguson, M.J. 49, 57, 61, 70, 75, 103
- Rycerz, L. 166, 168, 179, 180, 204–206, 222, 223
- Rycerz, L., see Gaune-Escard, M. 151, 166–168, 179, 203–206, 222, 223
- Rykov, S. 497
- Ryskin, A.I., see Kupchikov, A.K. 525, 581, 582
- Rzaev, D.A., see Kupchikov, A.K. 525, 581, 582
- Sabbatini, N. 494
- Sabbatini, N., see Balzani, V. 471
- Sabbatini, N., see Ulrich, G. 358
- Sacco, A. 482
- Sacccone, A., see Flandorfer, H. 91, 92, 118
- Sadygov, F.M. 36, 75
- Safaraliev, G.I., see Kuliev, A.N. 74
- Saini, N.L., see Lanzara, A. 295, 325
- Saito, H., see Sekine, C. 20, 23
- Saitoh, E. 269, 321
- Sakai, A., see Sekine, C. 20, 23
- Sakai, N. 518
- Sakai, Y., see Park, Y.Y. 489, 491, 492, 498
- Sakaie, K.E. 296

- Sakakibara, T., see Matsuhira, K. 20
 Sakakibara, T., see Sekine, C. 15, 20, 25, 26
 Sakata, M., see Machida, A. 336
 Sakata, M., see Moritomo, Y. 277, 284, 285
 Salamakha, P. 47, 54, 56, 66, 91, 98, 102, 109, 138, 139
 Salamakha, P., see Protsyk, O. 45, 53
 Salamakha, P., see Sologub, O. 62, 63, 65, 67–69, 137
 Salamakha, P.S., see Skolozdra, R.V. 41, 46, 53, 59, 60, 67, 73, 80, 82, 84, 86–88, 132, 133
 Salamakha, P.S., see Sologub, O.L. 58, 72, 91, 106
 Salamakha, P.S., see Zaplatynsky, O.V. 67, 69
 Salamon, M.B., see Chun, S.H. 298
 Salamon, M.B., see Jaime, M. 300
 Salamon, M.B., see Sakaie, K.E. 296
 Sales, B.C. 2, 3, 7, 9–11, 13, 26–29, 31
 Sales, B.C., see Bauer, E.D. 13, 16
 Sales, B.C., see Chakoumakos, B.C. 8
 Sales, B.C., see Dilley, N.R. 26
 Sales, B.C., see Feldman, J.L. 11
 Sales, B.C., see Gajewski, D.A. 13
 Sales, B.C., see Keppens, V. 11
 Sales, B.C., see Mahan, G. 28
 Sales, K.D., see Briggs, J.M. 368, 455
 Salmon, P.S., see Hutchinson, F. 179
 Salmon, P.S., see Wasse, J.C. 179
 Samouël, M., see De Kozak, A. 201
 Samsonova, N.D., see Aliev, O.M. 77, 78, 91
 Samwer, K., see von Helmolt, R. 290
 Sánchez, R.D., see Rivadulla, F. 309, 321
 Sandhu, S. 497
 Sandmann, C., see Dierolf, V. 525, 529, 555
 Sandrok, J., see Seifert, H.J. 204, 205
 Sanjurjo, J.A., see Granado, E. 263, 284, 329
 Sankar, J., see Kumar, D. 326
 Santoro, A., see Huang, Q. 289, 325, 328, 329
 Santoro, A., see Lynn, J.W. 299, 325
 Santoro, M., see Bungenstock, C. 521, 533
 Santosh, P.N., see Rao, C.N.R. 330
 Sanygin, V.P., see Slovyanskikh, V.K. 94, 95, 140
 Saraf, L.V. 309
 Sardar, D., see Powell, R.C. 572
 Sarma, D.D., see Congeduti, A. 325
 Sarma, D.D., see Meneghini, C. 325
 Sarrao, J.L., see Billinge, S.J.L. 304
 Sato, H. 6, 8, 12, 17, 18, 22, 23
 Sato, H., see Aoki, Y. 17–19
 Sato, H., see Keller, L. 17, 23
 Sato, H., see Matsuda, T.D. 17
 Sato, H., see Sugawara, H. 8, 9, 18, 23
 Sato, N., see Kasaya, M. 131, 132
 Sato, S. 572
 Sato, Y., see Kimura, S. 130
 Sato-Sorensen, Y., see Bi, Q. 523, 529, 553
 Savin, A., see Dolg, M. 148
 Savin, V.D. 222
 Savosta, M.M. 310
 Savosta, M.M., see Krupicka, S. 338
 Savutskii, A.I., see Voloshin, V.A. 523, 524, 571
 Sawa, H., see Katoh, K. 118
 Sawaki, Y., see Takenaka, K. 321
 Sawatzky, G.A., see Mizokawa, T. 263
 Sawatzky, G.A., see Zaanen, J. 256, 277
 Sazonov, L.A., see Nesmeyanov, A.N. 236
 Scanlon, J.C., see Poeppelmeier, K.R. 282
 Scapolan, S. 508
 Scardala, P., see Brunetti, B. 195, 236–240
 Scardala, P., see Piacente, V. 195, 237, 239, 240
 Scardala, P., see Villani, A.R. 236, 238, 240
 Schaad, O., see Piguet, C. 393–395
 Schaefer, M.C.R., see Dubost, J.P. 420
 Schaffer, H., see Cordier, G. 43, 44, 46
 Scheffold, R., see Löliger, J. 356
 Schenk, K.J., see Petoud, S. 355, 384–387
 Scherbaum, F., see Billard, I. 470, 495, 501–503, 506
 Scherbaum, F.J., see Monsallier, J.M. 506
 Schiferl, D., see Hess, N.J. 523, 553
 Schiffer, P. 328
 Schiffer, P., see Roy, M. 291, 328
 Schiffer, P.E., see Radaelli, P.G. 327
 Schirber, J.E. 521
 Schlaepfer, W., see Powell, D.H. 361
 Schmidt, F.A. 36
 Schmidt, T. 94, 135, 140
 Schmidtke, H., see Jørgensen, C.K. 541
 Schneider, A., see Kutscher, J. 208, 209
 Schneider, A., see Vogel, G. 203–205
 Schneider, M., see Ren, Y.H. 326
 Schoenes, J., see Frick, B. 94, 140
 Schollerer, G., see Yoon, S. 326
 Scholz, F., see Stapor, A. 525, 578
 Scholz, U.D., see Evers, C.B.H. 15, 23
 Scholz, U.D., see Evers, Ch.B.H. 65, 71, 72, 74, 76, 77, 95
 Schröck-Vietor, W., see Hellwege, K.H. 516, 523
 Schubert, G., see Fanghänel, T. 500
 Schuddinck, W., see Gordon, I. 326
 Schulman, S., see Rakicoglu, Y. 508
 Schulte, O., see Shen, Y.R. 522
 Schultz, L., see von Helmolt, R. 290

- Schuster, H.-U., see Grund, I. 40, 42, 96
 Schuster, H.-U., see Klüfers, P. 77, 91
 Schuster, H.U., see Fischer, H.O. 49, 58, 62
 Schuster, H.U., see Tomuschat, C. 77, 78
 Schuurmans, F.J.P. 471, 485
 Schwartz, R.W., see Fronczek, F. 381
 Schwarz, U., see Loa, I. 268
 Schwarzenbach, D., see Pinkerton, A.A. 415
 Schwarzenbach, D., see Spiliadis, S. 415
 Schweizer, S., see Tröster, Th. 523, 550
 Schwenk, H., see Zvyagin, S. 338
 Scopelliti, R., see Elhabiri, M. 443–445, 448, 481, 494
 Scott, P., see Kaltsoyannis, N. 366
 Scully, A.D. 489
 Sczepananiak, W., see Gaune-Escard, M. 151, 166–168, 179, 203–206, 222, 223
 Seaborg, G.T., see Katz, J.J. 467, 500
 Searcy, A.W., see Lim, M. 234
 Searcy, A.W., see Mar, R.W. 234
 Searcy, A.W., see Roberts, J.A. 192, 197, 234
 Searcy, A.W., see Skinner, H.B. 192, 234
 Sechovsky, V., see Matsuda, T.D. 17
 Seetharaman, S., see Stolyarova, V.L. 235
 Seifert, H., see Dudek, H. 206
 Seifert, H.J. 203–205
 Seifert, H.J., see Büchel, D. 151, 206
 Seifert, H.J., see Reuter, G. 166, 167, 205
 Seifert, H.J., see Roffe, M. 205
 Seifert, H.J., see Thiel, G. 204
 Seirania, K.B., see Sobolev, B.P. 150, 200–203
 Sekachev, Y.N., see Selivanov, G.K. 186, 189, 227
 Sekine, C. 7, 13, 15, 19–21, 23–26
 Sekine, C., see Lee, C.H. 20
 Sekine, C., see Matsuhira, K. 20
 Sekine, C., see Nanba, T. 20
 Sekine, C., see Shirota, I. 7, 9, 10, 13, 21
 Sekine, C., see Uchiumi, T. 7–9, 12
 Selivanov, G.K. 186, 189, 227
 Sémon, L., see Billard, I. 485
 Sémon, L., see Rustenholtz, A. 474
 Sémon, L., see Simonin, J.P. 491
 Senanayake, K., see Clarkson, I.M. 484, 505
 Senanayake, P.K., see Blair, S. 509
 Senanayake, P.K., see Parker, D. 491, 509
 Señaris Rodríguez, M.A., see Mira, J. 310
 Senis, R. 317
 Senis, R., see Martínez, B. 317
 Senis, R., see Skumryev, V. 312
 Sesé, J., see Stankiewicz, J. 292
 Sessler, J.L., see Lisowski, J. 357, 358, 364, 374–376
 Sessoli, R., see Hedinger, R. 454
 Settai, R., see Sugawara, H. 8, 9, 18, 23
 Sevast'yanov, V.G., see Ezhov, Y.S. 230
 Shaffer, J., see Dabrowski, B. 311
 Shahgulyev, N.S., see Sadygov, F.M. 36
 Shahkalamian, G.S., see Sobolev, B.P. 202
 Shaimuradov, I.B. 202
 Shaked, H. 84, 87, 89, 90, 127, 129
 Shakhkalamian, G.S., see Sobolev, B.P. 150
 Shames, A.I. 338
 Shames, A.I., see Markovich, V. 325
 Shand, W.A., see Jones, D.A. 200–203
 Shaner, J.W., see Mao, H.K. 518
 Shannon, R.D. 250, 400, 402
 Sharifi, F., see Hudspeth, H.D. 326
 Sharma, P.A., see Kim, K.H. 327
 Sharman, K.S. 470
 Sharp, J., see Nolas, G.S. 28
 Sharp, J.W., see Mahan, G. 28
 Sharp, J.W., see Sales, B.C. 11
 Sharp, R. 357, 359
 Shen, W., see Chi, Y. 523
 Shen, Y.R. 518, 522, 523, 525, 529, 533, 534, 541, 542, 544–546, 548, 554, 564–566, 575–577, 581
 Shen, Y.R., see Gregorian, T. 521, 522
 Shen, Y.R., see Lorenz, B. 522, 554
 Shen, Z.X., see Dessau, D.S. 268
 Shen, Z.X., see Li, J.-M. 325
 Shengalaya, A., see Zhao, G.-M. 305, 307
 Shenoy, G.K. 8
 Shenoy, G.K., see Suib, S.L. 481
 Sherry, A.D. 357, 377, 411–413, 433
 Sherry, A.D., see Cacheris, W.P. 410
 Sherry, A.D., see Geraldine, C.F.G.C. 358, 378, 404, 405, 410, 411, 414, 415, 417, 418, 420, 424, 425, 427, 429–433, 435–440, 442, 443, 451, 453
 Sherry, A.D., see Marques, M.P.M. 421, 423
 Sherry, A.D., see Ren, J. 358, 420, 423–426, 429–431, 433–440
 Sherry, A.D., see Zhang, S. 355
 Shevel'kov, V.F., see Loktyushina, N.S. 186, 228, 229
 Shevtsova, Z.N., see Korshunov, B.G. 204
 Shimazaki, E. 206–208, 236, 238–240
 Shimomura, S. 326, 327
 Shin, H. 478
 Shin, S., see Kanai, K. 13
 Shinno, I., see Gaft, M. 480
 Shiokawa, Y., see Matsuda, T.D. 17

- Shiozaki, R., see Takenaka, K. 321
- Shirane, G., see Martin, M.C. 322
- Shirane, G., see Vettier, C. 521, 535
- Shirotani, I. 7–10, 12, 13, 21
- Shirotani, I., see Lee, C.H. 20
- Shirotani, I., see Matsuhira, K. 20
- Shirotani, I., see Nanba, T. 20
- Shirotani, I., see Sekine, C. 7, 13, 15, 19–21, 23–26
- Shirotani, I., see Uchiumi, T. 7–9, 12
- Shishkin, E.A., see Abdusalamova, M.N. 37
- Shlykov, S.A., see Girichev, G.V. 229
- Shlykov, S.A., see Giricheva, N.I. 184, 186, 190, 191, 193, 227, 228, 232
- Shlykov, S.A., see Zakharov, A.V. 184, 186, 190, 191, 195, 229, 232
- Short, S., see Dabrowski, B. 311
- Shraiman, B.J., see Millis, A.J. 268
- Shreekala, R., see Quijada, M. 296
- Shreekala, R., see Zhao, Y.G. 296
- Shrivastava, K.N. 279, 280
- Shteynberg, D.B., see Sobolev, B.P. 150
- Shuh, D., see Allen, P. 474
- Shulyatev, D., see Biotteau, G. 325
- Shulyatev, D.A., see Adams, C.P. 298
- Shulyatev, D.A., see Markovich, V. 325
- Shulyatev, D.A., see Vasiliu-Doloc, L. 321
- Shulyatev, D.A., see Yuzhelevski, Y. 326
- Shumakova, T.P., see Abdusalamova, M.N. 37
- Siewenie, J.E., see Dabrowski, B. 311, 323
- Sikorski, M. 489
- Silversmith, A.J., see Radliński, A.P. 523, 536
- Simon, A., see Gunselius, H. 151
- Simoni, E., see Billard, I. 470, 495, 501–503, 506
- Simonin, J.P. 488, 491
- Simonson, J.M., see Dai, S. 494
- Simopoulos, A. 328
- Simopoulos, A., see Kallias, G. 328
- Simopoulos, A., see Papavassiliou, G. 328
- Simper, A., see Spencer, S. 493
- Simpson, J.R., see Quijada, M. 296
- Simpson, J.R., see Quijada, M.A. 269
- Simsa, Z., see Jiráč, Z. 291
- Singh, D.J. 6
- Singh, D.J., see Feldman, J.L. 11
- Singh, D.J., see Nordstrom, L. 6, 12, 13
- Singh, M., see Geraldès, C.F.G.C. 410
- Singh, M., see Sherry, A.D. 411–413
- Singh, R., see Sandhu, S. 497
- Singh, R.K., see Kumar, D. 326
- Singleton, J., see Kusters, R.M. 290
- Sinitsyn, B.V., see Sobolev, B.P. 150, 202
- Sinkov, S., see Billard, I. 470, 495, 501–503, 506
- Sipe, J.P., see Horrocks Jr., W.deW. 367, 379
- Sirvent, C., see Bauer, E.D. 8, 12, 15, 17, 24
- Sisoeva, T.F., see Rezukhina, T.N. 209, 212
- Skakovsky, E., see Rykov, S. 497
- Skelton, B.W., see Harrowfield, J.M. 405–407
- Skierbiszewski, C., see Jantsch, W. 525, 580
- Skierbiszewski, C., see Przybylinska, H. 525, 580
- Skinner, H.B. 192, 234
- Skolozdra, R., see Kaczmarska, K. 112, 113
- Skolozdra, R.V. 41, 46, 52, 53, 59, 60, 67, 73, 80, 82, 84, 86–88, 112, 113, 117, 120–123, 132, 133
- Skolozdra, R.V., see Aliev, F.G. 118
- Skolozdra, R.V., see Kobzenko, G.F. 36
- Skumryev, V. 312
- Skylaris, C.-K., see Spencer, S. 493
- Slack, G.A. 11, 29
- Slack, G.A., see Nolas, G.S. 11
- Slebarski, A. 45, 59, 60, 100, 113
- Slebarski, A., see Bauer, E.D. 8, 12, 15, 17, 24
- Slebarski, A., see Kaczmarska, K. 80, 112, 113
- Slichter, C.P., see Sakaie, K.E. 296
- Slov'ev, S.I., see Nisel'son, L.N. 236, 238
- Slovyanskikh, V.K. 94, 95, 140
- Slykhouse, T.E., see Fitch, R.A. 516
- Smith, D.F., see Walden, G.E. 166–168, 179, 222
- Smith, D.W. 280
- Smith, F.C., see Parker, D. 420
- Smith, R.I., see Pinsard-Gaudart, L. 268, 280
- Smith, R.M., see Martell, A.E. 381
- Smolyaninova, V., see Zhao, G. 326
- Smolyaninova, V.N. 321, 327, 329
- Smolyaninova, V.N., see Huang, Q. 328, 329
- Snellgrove, T., see Denning, R. 557
- Snider, W.E., see Hirayama, C. 196, 197, 239
- Snow, N.H., see Sharman, K.S. 470
- Snyder, G.J., see Watcharapasorn, A. 6, 7, 12, 13, 29
- Snyder, S.W., see Metcalf, D.H. 489
- Sobolev, B.P. 150, 200–203
- Soderholm, L., see Xue, J.S. 12
- Sofu, J.O. 6
- Soga, N. 523, 555
- Söhnel, O. 173
- Soini, E. 509
- Sologub, O. 41–43, 45–49, 51–54, 56–63, 65–69, 72–76, 79–93, 102, 103, 119–123, 133, 137
- Sologub, O., see Flandorfer, H. 127
- Sologub, O., see Protsyk, O. 45, 53
- Sologub, O., see Salamakha, P. 56, 109

- Sologub, O.L. 58, 72, 91, 106
 Solomon, I. 356, 359, 361
 Solomonik, V.G. 186
 Solzi, M., see Allodi, G. 328, 337
 Sommerer, S.O., see Cundari, T.R. 185, 189
 Sommers, J.A. 151, 157, 158, 166–168
 Song, C., see Fisher, I.R. 90, 91, 134, 135, 137
 Sonier, J.E., see Heffner, R.H. 298, 325
 Sonntag, R., see Krupicka, S. 338
 Sood, A.K., see Joshi, J.P. 336
 Spaeth, J.-M., see Tröster, Th. 523, 550
 Spain, I.L., see Merkle, L.D. 522, 572–574
 Specht, H., see Monsallier, J.M. 506
 Spedding, F.H. 149, 162, 164, 165, 174, 176, 178, 200–213, 215, 216, 219
 Spence, T.G., see Morss, L.R. 218
 Spencer, S. 493
 Spiliadis, S. 358, 377, 415
 Spiliadis, S., see Pinkerton, A.A. 357, 365, 366
 Spiridonov, V.P. 227
 Spiridonov, V.P., see Giricheva, N.I. 229
 Spirlet, M.-R. 420
 Springer, C.S., see Ren, J. 433
 Srijaranai, S., see Cunningham, J. 489, 497
 Srivastava, S. 291, 292
 Stang, P.J., see Leininger, S. 355
 Stangret, J. 482
 Stankiewicz, J. 292
 Stankus, S.V. 150, 200–203
 Stankus, S.V., see Khairulin, R.A. 178, 202
 Stankus, S.V., see Lyapunov, K.M. 164, 165, 176
 Stapor, A. 525, 578
 Staub, U., see Mesot, J. 524, 535
 Steed, J.W. 355
 Steemers, F. 494
 Steer, R.P., see Sikorski, M. 489
 Stein, G., see Haas, Y. 471, 472, 475–477, 480
 Steinberg, D.J., see Mao, H.K. 518
 Steiner, W., see Leithe-Jasper, A. 26
 Steiner, W., see Weitzer, F. 44, 59, 65, 73
 Steinfeld, J. 487
 Steinfink, H., see Bodnar, R.E. 37
 Steinfink, H., see Wang, R. 48, 49, 75
 Steinle, E., see Aas, W. 500
 Steinle, E., see Fanghänel, T. 500
 Stetskiv, A.O. 50, 55, 109, 111
 Stetson, N.T. 15
 Stevens, W.J. 148
 Stevens, W.J., see Cundari, T.R. 148
 Stewart, D.C., see Carnall, W.T. 494
 Stock, M., see Yersin, H. 523, 569
 Stoddart, J.F., see Balzani, V. 355
 Stoll, H., see Dolg, M. 148, 183, 187–189
 Stolyarova, V.L. 235
 Storozhenko, T.P. 215–217
 Storozhenko, T.P., see Khanaev, E.I. 214
 Stout, E.W. 357, 371
 Strasser, J., see Yersin, H. 523, 569, 570
 Strohecker, L.A., see Cundari, T.R. 185, 189
 Struck, C.W. 196, 239, 240, 567, 568, 572
 Struck, C.W., see Fonger, W.H. 523, 524, 567
 Struzhkin, V.V., see Goncharov, A.F. 522, 582
 Stryla, Z., see Meinrath, G. 495, 497, 501
 Stubblefield, C.T. 212, 215
 Stubblefield, C.T., see Machlan, G.R. 214, 215, 221
 Stucki, F., see Ott, H.R. 55
 Stucky, G.D., see Suib, S.L. 481
 Stump, N.A. 523, 557
 Stump, N.A., see Chen, G. 523, 524, 557, 558
 Stumpf, T. 495
 Stuve, J.M. 213, 215, 216, 219–221
 Stuve, J.M., see Montgomery, R.L. 219
 Su, J., see Zhu, C. 326
 Suaaidi, M., see García-Muñoz, J.L. 323
 Subías, G. 323
 Subramanian, P.R., see Massalski, T.B. 36
 Sudnick, D.R., see Horrocks Jr., W.deW. 477–480, 484, 495, 497, 499, 501, 503, 504
 Sugai, S., see Takenaka, K. 321
 Suganuma, H., see Arisaka, M. 473, 474, 481
 Sugawara, H. 8, 9, 18, 23
 Sugawara, H., see Aoki, Y. 17–19
 Sugawara, H., see Keller, L. 17, 23
 Sugawara, H., see Matsuda, T.D. 17
 Sugawara, H., see Sato, H. 6, 8, 12, 17, 18, 22, 23
 Suib, S.L. 481
 Suimetsu, T., see Salamakha, P. 56, 109
 Sullivan, J.C., see Nash, K.L. 493
 Sun, J.Z., see Xiao, G. 328
 Supkowski, R.M. 481–483
 Suvorov, A.V. 234
 Suzuki, H. 58, 78
 Suzuki, J., see Yamada, Y. 315
 Suzuki, K., see Markovich, V. 325
 Suzuki, T., see Kohgi, M. 521
 Suzuki, T., see Naka, T. 521
 Suzuki, T., see Okayama, Y. 521
 Suzuki, T., see Oohara, Y. 521
 Suzuki, T., see Yoshizawa, H. 521
 Sviridov, L.A., see Morozkin, A.V. 40, 81, 83–85, 87–89, 93, 108

- Swiegers, G.F. 355, 393
 Swingler, D.L., see Ciach, S. 236, 237
 Syassen, K. 525, 550
 Syassen, K., see Goncharov, A.F. 522, 582
 Syassen, K., see Huber, G. 523, 530
 Syassen, K., see Loa, I. 268
 Syassen, K., see Stapor, A. 525, 578
 Syassen, K., see Zimmer, H.G. 523
 Szabo, G. 275
 Szymczak, H., see Ilisavskii, Y. 326
 Szymczak, H., see Troyanchuk, O.Ya. 275
 Szytuła, A., see André, G. 123
 Szytuła, A., see Zigmunt, A. 61, 69, 74, 83, 85, 87
- Tachi, K., see Shirotani, I. 7–9, 12
 Tachiya, M. 489
 Taguchi, A. 525, 578
 Taguchi, A., see Hogg, R.A. 524, 555, 579
 Taguchi, A., see Takarabe, K. 524, 525, 578–580
 Tajima, K., see Shimomura, S. 326, 327
 Tajiri, A., see Konami, H. 441–443
 Takabatake, T., see Katoh, K. 118
 Takabatake, T., see Salamakha, P. 56, 109
 Takabatake, T., see Sologub, O.L. 91
 Takagi, H., see Cava, R.J. 56
 Takagi, H., see Katsufuji, T. 275
 Takahashi, H., see Kohgi, M. 521
 Takahashi, H., see Okayama, Y. 521
 Takahashi, H., see Oohara, Y. 521
 Takahashi, H., see Shirotani, I. 9, 10
 Takahashi, H., see Yoshizawa, H. 521
 Takahashi, K. 481
 Takahashi, K., see Nojiri, H. 317
 Takahashi, K.T., see Saitoh, E. 269
 Takahei, K., see Hogg, R.A. 524, 555, 579
 Takahei, K., see Taguchi, A. 525, 578
 Takahei, K., see Takarabe, K. 524, 525, 578–580
 Takalo, H., see Latva, M. 494, 495
 Takarabe, K. 524, 525, 578–580
 Takarabe, K., see Hogg, R.A. 524, 555
 Takata, M., see Machida, A. 336
 Takata, M., see Moritomo, Y. 277, 284, 285
 Takazawa, H., see Lee, C.H. 20
 Takeda, N. 8, 12, 15–17, 21, 23, 24
 Takeda, N., see Kanai, K. 13
 Takegahara, K., see Kasaya, M. 49, 57, 58, 62, 129, 130
 Takeishi, H., see Kimura, T. 479, 481
 Takemura, K., see Zimmer, H.G. 523
 Takenaka, K. 321
 Takeya, H., see Adroja, D.T. 60, 61, 118
- Takikawa, T., see Matsuhira, K. 20
 Taldenkov, A., see Yakubovskii, A. 309
 Taldenkov, A.N., see Babushkina, N.A. 308, 309
 Tanaka, F. 471, 472, 474, 484, 491, 492
 Tanaka, H., see Liu, X.J. 299
 Tanaka, M., see Murakami, Y. 263
 Tanaka, M., see Nishimura, G. 524
 Tanaka, T., see Miyano, K. 291
 Tang, J., see Shirotani, I. 9, 10
 Tang, X. 29, 30
 Tanner, P.A. 557
 Tanner, P.A., see Mak, C.S.K. 525, 581
 Tao, J., see Zuo, J.M. 326
 Tatevskii, V.M., see Akishin, P.A. 224
 Tatsumi, T., see Kasuga, K. 440
 Taube, H., see Lewis, W.B. 364
 Taylor, A.J., see Lobad, A.I. 326
 Tcheou, F., see Quezel, S. 275
 Tchuiko, A.C., see Abdusalamova, M.N. 36, 37
 Tedenac, J.C., see Ravot, D. 10, 11, 13
 Teipen, R., see Uhlenbruch, S. 317
 Tercier, N., see Blanzat, B. 523, 524, 574
 Terreno, E., see Aime, S. 357, 360, 362, 433
 Terreno, E., see Zhang, S. 355
 Tetenbaum, M., see Flotow, H.E. 154
 Thaller, A., see Laenen, R. 482
 Thalmeier, P. 582
 Thiel, G. 204
 Thiel, G., see Seifert, H.J. 203, 205
 Thiel, J., see Hornbostel, M.D. 8
 Thistlethwaite, P.J., see Ciach, S. 236, 237
 Thoma, R.E. 201–203, 206, 207
 Thomas, J.M., see Reller, A. 282
 Thompson, J.D., see Neumeier, J.J. 299
 Thompson, J.D., see Yoshinari, Y. 328
 Thompson, J.R., see Sales, B.C. 7, 9–11, 13, 29, 31
 Thorn, R.J., see McCreary, J.R. 234, 235
 Thornton, M.J. 124
 Thouvenot, P. 507
 Tichy, R.S. 277
 Tiflova, L.A. 213, 216, 218, 220, 221
 Tiflova, L.A., see Monaenkova, A.S. 218
 Timmerman, P., see Prins, L.J. 393
 Timofeev, S.S., see Abulkhaev, V.D. 94
 Tippett, L., see Cundari, T.R. 185, 189
 Tkachenko, N.L., see Sobolev, B.P. 150, 200–203
 Töbrens, D.M., see Pissas, M. 329
 Tobe, K. 266, 269
 Tobe, K., see Saitoh, E. 269
 Todo, S., see Shirotani, I. 7–9, 12, 21
 Todo, S., see Uchiumi, T. 7–9, 12

- Tokarczyk, B., see Mac, M. 491
 Tokura, Y. 330, 341
 Tokura, Y., see Arima, T. 279
 Tokura, Y., see Asamitsu, A. 291, 319
 Tokura, Y., see Causa, M.T. 326
 Tokura, Y., see Chun, S.H. 298
 Tokura, Y., see Dai, P. 325
 Tokura, Y., see Fiebig, M. 291
 Tokura, Y., see Fiebig, M.K. 291
 Tokura, Y., see Granado, E. 329
 Tokura, Y., see Kajimoto, R. 337
 Tokura, Y., see Kawano, H. 336
 Tokura, Y., see Kimura, T. 336
 Tokura, Y., see Kiryukin, V. 291
 Tokura, Y., see Kumagai, K. 311
 Tokura, Y., see Kuwahara, H. 330, 331, 336, 337
 Tokura, Y., see Martin, M.C. 322
 Tokura, Y., see Miyano, K. 291
 Tokura, Y., see Moritomo, Y. 291, 311
 Tokura, Y., see Murakami, Y. 263
 Tokura, Y., see Ogawa, K. 291
 Tokura, Y., see Okuda, T. 325
 Tokura, Y., see Saitoh, E. 269, 321
 Tokura, Y., see Shimomura, S. 326, 327
 Tokura, Y., see Tobe, K. 266, 269
 Tokura, Y., see Tomioka, Y. 291, 294, 297
 Tokura, Y., see Urushibara, A. 311
 Tokura, Y., see Yoshizawa, H. 291
 Tokura, Y., see Zhou, J.-S. 311
 Tokura, Y., see Zimmermann, M.V. 264
 Tolentino, H. 518
 Tolmach, P.I. 157, 158, 160
 Tolmach, P.I., see Gorbunov, V.E. 157, 158, 160
 Tominaga, T., see Scully, A.D. 489
 Tominaga, T., see Takahashi, K. 481
 Tomioka, Y. 291, 294, 297
 Tomioka, Y., see Asamitsu, A. 291, 319
 Tomioka, Y., see Chun, S.H. 298
 Tomioka, Y., see Dai, P. 325
 Tomioka, Y., see Fäth, M. 298
 Tomioka, Y., see Fiebig, M. 291
 Tomioka, Y., see Fiebig, M.K. 291
 Tomioka, Y., see Kawano, H. 336
 Tomioka, Y., see Kimura, T. 336
 Tomioka, Y., see Kiryukin, V. 291
 Tomioka, Y., see Kumagai, K. 311
 Tomioka, Y., see Kuwahara, H. 333, 337
 Tomioka, Y., see Miyano, K. 291
 Tomioka, Y., see Moritomo, Y. 291
 Tomioka, Y., see Ogawa, K. 291
 Tomioka, Y., see Okuda, T. 325
 Tomioka, Y., see Tokura, Y. 330, 341
 Tomioka, Y., see Yoshizawa, H. 291
 Tomioka, Y., see Zimmermann, M.V. 264
 Tomiyasu, H., see Park, Y.Y. 489, 491, 492, 498
 Tomiyasu, H., see Yamamura, T. 491, 492
 Tomiyasu, H., see Yayamura, T. 473
 Tomka, G.J., see Thornton, M.J. 124
 Tomuschat, C. 77, 78
 Tondre, C., see Moulin, C. 501
 Töpfer, J. 269, 286–289
 Torikachvili, M.S. 6, 8, 17, 22
 Torikachvili, M.S., see Meisner, G.P. 6, 12
 Torrance, J.B., see Arima, T. 279
 Torriani, I., see Granado, E. 284, 329
 Toth, E. 363, 454
 Toth, E., see Hedinger, R. 454
 Tóth, É., see Sherry, A.D. 433
 Totrova, G.A., see Gavrichev, K.S. 161, 163
 Totrova, G.A., see Gorbunov, V.E. 157, 158, 160
 Totrova, G.A., see Tolmach, P.I. 157, 158, 160
 Tourillon, G., see Tolentino, H. 518
 Tovar, M., see Causa, M.T. 326
 Tovar, M., see Rivadulla, F. 321
 Tran, C.D. 484
 Tran, V.H., see Bauer, E. 24
 Tran-Thi, T.H., see Mooney, W. 497
 Traverso, O., see Allsopp, S.R. 473, 474
 Tremel, W., see Mozharivskiy, Yu. 86, 138, 139
 Trinquet, E., see Bazin, H. 509
 Tritt, T.M., see Nolas, G.S. 3, 11, 27, 29, 30
 Trlifaj, M. 573
 Trommer, R. 578
 Tröster, Th. 521–523, 527, 529, 531–533, 536, 541–543, 545, 546, 550, 551
 Tröster, Th., see Bungenstock, C. 521, 529, 532–535, 537, 541–544, 546
 Tröster, Th., see Burdick, G.W. 548
 Tröster, Th., see Dierolf, V. 525, 529, 555
 Tröster, Th., see Gregorian, T. 521, 522
 Tröster, Th., see Jayasankar, C.K. 522, 547, 581
 Tröster, Th., see Lavin, V. 522, 523
 Tröster, Th., see Mak, C.S.K. 525, 581
 Tröster, Th., see Shen, Y.R. 522
 Troxler, L., see Berny, F. 358
 Troyanchuk, O.Ya. 275
 Trümbach, D., see Yersin, H. 523, 569, 570
 Tsintsadze, G.A., see Lukin, S.N. 524, 536
 Tsuruta, C., see Li, J.Q. 329
 Tupolev, V.S., see Molodkin, A.K. 208
 Tups, H., see Syassen, K. 525
 Turano, P., see Bertini, I. 361

- Turley, W.D., see Gleason, J.K. 524, 551, 566, 568
 Turro, C.J., see Fu, P.K.L. 355
 Tutui, M., see Kasuga, K. 440
 Tweedle, M.F., see Chang, C.A. 420
 Tyagel'sky, P.V., see Khairulin, R.A. 202
 Tyner, C.E. 523, 550
- Uchiumi, T. 7–9, 12
 Uchiumi, T., see Sekine, C. 7, 15, 19–21, 23, 25, 26
 Uchiumi, T., see Shirovani, I. 7, 9, 13, 21
 Uebach, W., see Seifert, H.J. 203, 204
 Uehara, M. 323, 327–329, 340
 Uehara, M., see Kim, K.H. 327, 328
 Uehara, M., see Li, J.Q. 329
 Uehara, M., see Podzorov, V. 327
 Uemura, Y.J., see Heffner, R.H. 325
 Ueno, K., see Lee, C.H. 20
 Uggeri, F., see Aime, S. 420, 422, 433
 Uher, C. 3, 27
 Uher, C., see Chen, B. 13
 Uher, C., see Meisner, G.P. 11
 Uher, C., see Morelli, D.T. 11
 Uhlenbruch, S. 317
 Uhlenbruck, S., see Klingeler, R. 315
 Ulivi, L., see Bungenstock, C. 521, 529, 533, 535
 Ulrich, G. 358
 Umemoto, K., see Fujita, M. 355
 Uppal, M.K., see Reller, A. 282
 Urland, W. 521, 545
 Urland, W., see Gonselius, H. 151
 Urosevic, V.V. 522
 Urushibara, A. 311
 Ushenin, S.N., see Lebedev, V.A. 36
 Uspensky, E., see Gaft, M. 480
- Vallet-Regí, M., see Alonso, J. 324
 Valtancoli, B., see Bazzicalupi, C. 492, 509
 Valtancoli, B., see Bianchi, A. 426
 van Bekkum, H., see Corsi, D.M. 356
 van de Burgt, L.J., see Wang, Z.M. 478, 494, 495, 499, 505
 van den Brink, J. 269
 Van der Tol, E., see Steemers, F. 494
 Van Roosmalen, J.A.M. 267
 van Rossum, B.J., see Mentink, S.A.M. 54
 van Santen, J.H., see Jonker, G.H. 265
 Van Tendeloo, G., see Gordon, I. 326
 Van Valkenburg, A., see Weir, C.E. 516
 van Veggel, F., see Klink, S.I. 471, 494–496
 van Veggel, F.C.J.M., see An, Y. 405, 481, 483, 494
 van Vlaanderen, P., see Cordfunke, E.H.P. 152, 207, 208
 Vanacken, J., see Gordon, I. 326
 VanOpdenbosch, N., see Kasuga, K. 440
 Vasil'ev, V.V., see Laptev, D.M. 210–212, 216
 Vasiliu-Doloc, L. 299, 318, 321
 Vasiliu-Doloc, L., see Quijada, M.A. 269
 Vassallo, P., see Brunetti, B. 195, 237, 239, 240
 Vázquez-Vázquez, C., see Causa, M.T. 326
 Vázquez-Vázquez, C., see Mira, J. 295
 Veale, C.R., see Harris, A.L. 204
 Védrine, A., see Labeau, M. 203
 Vega, D., see Levy, P. 328
 Veillet, P., see Anane, A. 291
 Venkataraman, C., see Zimmermann, M.V. 264
 Venkatesan, T., see Quijada, M. 296
 Venkatesan, T., see Saraf, L.V. 309
 Venkatesan, T., see Zhao, G.-M. 308
 Venkatesan, T., see Zhao, Y.G. 296, 328
 Venteicher, R.F., see Wong, C.P. 449
 Verboom, W., see Steemers, F. 494
 Vergés, J.A., see Mayr, M. 326
 Verhoeven, J., see Steemers, F. 494
 Verhoeven, J.W., see Werts, M.H.V. 481
 Vettier, C. 518, 521, 535
 Vettier, C., see Mesot, J. 524, 535
 Vial, J.-C., see Oppenländer, A. 522
 Viallesoubranne, C., see Billard, I. 470, 495, 501–503, 506
 Vigliante, A., see Kiryukin, V. 291
 Vijaya Lakshmi, K. 121, 124
 Vila, A.J., see Bertini, I. 361
 Villani, A.R. 195, 236, 238–240
 Villani, A.R., see Brunetti, B. 195, 236, 238, 239
 Villani, A.R., see Piacente, V. 195, 237, 239, 240
 Villars, P. 37
 Vinokurova, N.G., see Goryushkin, V.F. 182, 209
 Vinokurova, N.G., see Poshevneva, A.I. 182, 208
 Viret, M., see Anane, A. 291
 Virtuani, M., see Bianchi, A. 426
 Viswanathan, K.S., see Peter, S. 507
 Vlasenko, L.S., see Huhtinen, H. 326
 Vlasenko, M.P., see Huhtinen, H. 326
 Vogel, G. 203–205
 Vogel, R. 36
 Vogl, P., see Trommer, R. 578
 Vogt, J., see Zakharov, A.V. 184, 186, 190, 191, 195, 229, 232

- Vogt, N., see Zakharov, A.V. 184, 186, 190, 191, 195, 229, 232
 Vogt, O., see Burlet, P. 55
 Vogt, O., see Frick, B. 94, 140
 Vogt, O., see Rossat-Mignod, J. 55, 57
 Vohra, Y.K., see Hua, H. 521, 522, 552, 553
 Vohra, Y.K., see Liu, J. 523, 553
 Vold, R.L. 364
 Voloshin, V.A. 521–524, 531, 559, 571, 581
 Voltz, R. 483
 von Helmolt, R. 290
 von Molnár, S., see Hudspeth, H.D. 326
 von Molnár, S., see Raquet, B. 326
 Vorontsov, E.S., see Laptev, D.M. 203, 204
 Vottéro, P.J.A., see Chapon, D. 454, 455
 Vratislav, S., see JirákJ, Z. 275, 291
 Vuilleumier, J.J., see Marcantonatos, M.D. 497
 Vybornov, M., see Sologub, O. 43, 46, 47, 51, 54, 60, 68, 74, 103

 Wachter, P., see Neuschwander, J. 522, 523, 525
 Wada, M., see Sato, S. 572
 Wadsö, I., see Fitzgibbon, G.C. 210
 Wagman, D.D., see Cox, J.D. 173
 Wagman, D.D., see Parker, V.B. 173
 Wagner, P., see Gordon, I. 326
 Wai, C.M., see Addleman, R.S. 489, 509
 Wakabayashi, N., see Dai, P. 325
 Wakabayashi, N., see Shimomura, S. 326, 327
 Wakabayashi, Y., see Zimmermann, M.V. 264
 Walden, G.E. 166–168, 179, 222
 Waldfried, C., see McIlroy, D.N. 295
 Walker, P.J., see Garton, G. 205
 Walters, M.K., see Hutchinson, F. 179
 Wamsley, P.R. 525, 575, 577
 Wamsley, P.R., see Lochhead, M.J. 471
 Wang, L. 523, 524, 551, 568
 Wang, L., see Chi, Y. 523, 524, 530, 533, 534, 536, 539
 Wang, L., see Liu, S. 523, 524, 529, 530, 533, 539
 Wang, L., see Wang, Q. 524, 530, 538
 Wang, M.E., see Chan, J.Y. 134
 Wang, P.J. 522–525, 550
 Wang, Q. 523, 524, 530, 533, 534, 538
 Wang, Q., see Chi, Y. 523, 530, 533, 534, 539
 Wang, R. 48, 49, 75
 Wang, S., see Chen, G. 522, 549, 550
 Wang, X.Z., see Culp, T.D. 525, 580
 Wang, Y. 478, 494
 Wang, Y.S., see Alexandrov, A.S. 308
 Wang, Z., see Choppin, G.R. 495
 Wang, Z.M. 478, 494, 495, 499, 505
 Wang, Z.M., see De Sa, G.F. 471, 483
 Wasse, J.C. 179
 Wasse, J.C., see Hutchinson, F. 179
 Wasylshen, R.E. 363
 Watcharapasorn, A. 6, 7, 12, 13, 29
 Watkins, S.F., see Fronczek, F. 381
 Watson, R.E., see Freeman, A.J. 377
 Waugh, J.S., see Vold, R.L. 364
 Weaver, H.T., see Schirber, J.E. 521
 Webb, D., see Chan, J.Y. 134
 Webb, D.J., see Chan, J.Y. 90
 Webb, S., see Hemmilä, I. 509
 Webber, S.E., see Morrison, M.E. 489
 Weber, J., see Ouali, N. 379, 390, 405–410
 Weber, J., see Stapor, A. 525, 578
 Webster, G.A. 524, 551, 567, 568, 574
 Wecker, J., see von Helmolt, R. 290
 Weger, H., see Fanghänel, T. 500
 Weger, H.T., see Fanghänel, T. 500
 Wei, W., see Ogawa, K. 291
 Weill, G., see Gonzalez, J. 518
 Weir, C.E. 516
 Weiss, R., see Buchler, J.W. 449, 450
 Weiss, R., see Moussavi, M. 440
 Weitzer, F. 44, 59, 65, 73
 Wells Jr., J.C. 186, 227, 229, 230
 Wenski, G. 62, 71, 78, 107
 Werts, M.H.V. 481
 Werts, M.H.V., see Klink, S.I. 471, 494–496
 Wertz, J.E. 359, 364
 Wesley, R.D. 186, 191, 224, 225
 Wessels, B.W., see Culp, T.D. 525, 580
 Westrum Jr., E.F. 154, 157
 Westrum Jr., E.F., see Deline, T.A. 161, 163
 Westrum Jr., E.F., see Sommers, J.A. 151, 157, 158, 166–168
 White, A.H., see Harrowfield, J.M. 405–407
 White, W.T., see Xue, J.S. 12
 Wicholas, M., see Buchler, J.W. 450–453
 Wickersheim, K.A. 567
 Wickleder, M.S., see Meyer, G. 149
 Wiebe, C.R. 282
 Wiesinger, G., see Weitzer, F. 44, 59, 65, 73
 Wiesinger, W., see Leithe-Jasper, A. 26
 Wietzke, R., see Bretonnière, Y. 393
 Wilcott, M.R. 373, 385
 Wilkinson, M.K., see Koehler, W.C. 259
 Willets, A., see Spencer, S. 493
 Williams, A.F., see Piguët, C. 384, 385
 Williams, C., see Beitz, J.V. 495, 497, 501

- Williams, J., see Beeby, A. 481–484
 Williams, J., see Parker, D. 484, 493, 494
 Williams, J.A.G., see Dickins, R.S. 482
 Williams, J.A.G., see Parker, D. 491, 509
 Williams, R.J.P., see Alsaadi, B.M. 361, 405–407
 Williams, R.J.P., see Barry, C.D. 363
 Williams, R.J.P., see Bleaney, B. 357, 365, 371
 Williams, R.K., see Sales, B.C. 2, 7, 9, 11, 13, 26, 29
 Willig, F., see Eichhorn, M. 569
 Wilmarth, W.R. 521, 522, 558
 Wilmarth, W.R., see Daniel, J.F. 151, 205
 Wilmarth, W.R., see Young, J.P. 558
 Wilson, K.G. 13
 Wilson, L.J., see Chang, C.A. 420
 Wilson, M., see Hutchinson, F. 179
 Wimmer, H. 500
 Wimmer, H., see Kim, J.I. 496
 Wimmer, H., see Panak, P. 494, 495
 Windsor, M.W., see Kropp, J.L. 475–477, 480
 Winkler, E., see Rivadulla, F. 328, 330–335, 337–342
 Wintgens, V., see Pouliquen, J. 488
 Winzen, H., see Syassen, K. 525, 550
 Wipff, G., see Berny, F. 358
 Wipff, G., see Fraternali, F. 358
 Wipff, G., see Ulrich, G. 358
 Wirth, S., see Raquet, B. 326
 Wohlford, D.J., see Ren, S.Y. 580
 Wojakowski, A., see Charvillat, J.-P. 57, 61, 71, 75, 81
 Wold, A. 289
 Wold, A., see Goodenough, J.B. 265, 267, 269, 270
 Wolford, D.J. 555
 Woll, P., see Cordier, G. 43, 44, 46
 Woll, P., see Sologub, O. 43, 46, 47, 51, 54, 60, 68, 74, 103
 Wollan, E.O. 262, 327
 Wollan, E.O., see Koehler, W.C. 259
 Wollesen, P. 43, 44, 46, 48, 49, 51, 52, 54, 57–61, 63, 66, 68, 70, 72, 73, 75, 80, 83
 Wong, C.P. 449
 Wood, V.E. 275
 Woods, M., see Aime, S. 426, 429
 Woods, M., see Beeby, A. 481–484
 Woodward, F.M., see Maple, M.B. 22
 Woodwark, D., see Denning, R. 557
 Worledge, W.C. 323
 Wortmann, G., see Bungenstock, C. 540
 Wortmann, G., see Lübbers, R. 518
 Wright, A.O. 523, 524
 Wright, A.O., see Olsen, L.R. 523
 Wright, J.C., see Olsen, L.R. 523
 Wright, J.C., see Wright, A.O. 523, 524
 Wu, S. 469, 499
 Wu, S.L. 492
 Wu, T., see Zhao, Y.G. 328
 Wybourne, B.G. 526, 566
 Xavier, A.V., see Barry, C.D. 363
 Xavier, A.V., see Bleaney, B. 357, 365, 371
 Xia, S., see Mak, C.S.K. 525, 581
 Xia, Z.J., see Bertini, I. 357, 361
 Xiao, G. 328
 Xie, J.Q., see Zheng, R.K. 328
 Xiong, P., see Hudspeth, H.D. 326
 Xiong, P., see Raquet, B. 326
 Xiong, X. 311
 Xiong, X., see Dabrowski, B. 311
 Xu, W., see Bare, W.D. 470, 509
 Xue, J.S. 12
 Xue, Z.L., see Dai, S. 494
 Yagi, T., see Sekine, C. 7, 15, 19–21, 25, 26
 Yagi, T., see Shirotani, I. 7–10, 12, 21
 Yagi, T., see Uchiumi, T. 7–9, 12
 Yagi, T., see Yusa, H. 523, 553
 Yakabovskiy, A., see Shames, A.I. 338
 Yakhkind, E., see Ilisavskii, Y. 326
 Yakovlev, E.N., see Kasatochkin, S.V. 524
 Yakubovskii, A. 309
 Yakubovskii, A., see Kumagai, K. 311
 Yamada, Y. 315
 Yamada, Y., see Lee, K.P. 492
 Yamaguchi, T., see Suzuki, H. 58, 78
 Yamamoto, A., see Lee, C.H. 20
 Yamamoto, E., see Matsuda, T.D. 17
 Yamamoto, H., see Soga, N. 523, 555
 Yamamoto, K., see Saitoh, E. 269
 Yamamoto, N., see Katsufuji, T. 275
 Yamamoto, N., see Machida, A. 336
 Yamamura, T. 491, 492
 Yamashita, S., see Tanaka, F. 471, 472, 474
 Yanase, N., see Sekine, C. 13
 Yang, J., see Meisner, G.P. 11
 Yang, K.N., see Meisner, G.P. 6, 12
 Yano, H., see Kim, Y.C. 219
 Yashvili, T.S. 215
 Yashvili, T.S., see Gvelesiani, G.G. 210, 214
 Yates, E.C., see Wickersheim, K.A. 567
 Yayamura, T. 473

- Yelon, W.B., see Mehta, A. 69
 Yersin, H. 523, 569, 570
 Yersin, H., see Eichhorn, M. 569
 Yin, H.Q., see Zhou, J.-S. 269, 271, 272, 284
 Yokoya, T., see Kanai, K. 13
 Yokoyama, H., see Kanno, H. 482
 Yokoyama, M., see Sekine, C. 20
 Yokoyama, Y. 491, 497
 Yokoyama, Y., see Moriyasu, M. 489, 491, 504
 Yoo, C.S. 522, 549, 550
 Yoon, S. 326
 Yoon, S., see Naler, S. 328
 Yoshida, Z., see Arisaka, M. 473, 474, 481
 Yoshida, Z., see Kimura, T. 471–473, 479
 Yoshida, Z., see Lis, S. 489, 491
 Yoshida, Z., see Nagaishi, R. 497
 Yoshimoto, M., see Soga, N. 523, 555
 Yoshinari, Y. 328
 Yoshizawa, H. 291, 521
 Yoshizawa, H., see Kajimoto, R. 337
 Yoshizawa, H., see Kawano, H. 336
 Yoshizawa, H., see Kohgi, M. 521
 Yoshizawa, H., see Okayama, Y. 521
 Yoshizawa, H., see Oohara, Y. 521
 Yoshizawa, M., see Fujita, M. 355
 Yoshizawa, Y., see Kawano, H. 311
 Yotsuyanagi, T., see Katsumura, Y. 489, 496, 497, 508
 Young, J.P. 558
 Young, J.P., see Haire, R.G. 558
 Young, J.P., see Peterson, J.R. 522, 558
 Young, J.P., see Wilmarth, W.R. 521, 522, 558
 Young, M., see Rakicioglu, Y. 508
 Yu, J., see Jung, J.H. 323
 Yudin, V.M. 276
 Yuhasz, W.M., see Maple, M.B. 22
 Yunoki, S., see Dagotto, E. 261
 Yusa, H. 523, 553
 Yuzhelevski, Y. 326

 Zaanen, J. 256, 277
 Zaitsev, S.A., see Loktyushina, N.S. 186, 228, 229
 Zakharov, A.V. 184, 186, 190, 191, 195, 229, 232
 Zakharov, A.V., see Girichev, G.V. 229
 Zakharov, A.V., see Giricheva, N.I. 184, 186, 227
 Zakharova, G.V., see Billing, R. 489, 491
 Zakhvalinskii, V.S., see Huhtinen, H. 326
 Zalyalyutdinov, M.K., see Aliev, F.G. 118
 Zalyмова, S.A., see Goryushkin, V.F. 180, 205, 206, 223
 Zanicchi, G., see Riani, P. 41, 85, 87, 88, 91, 93

 Zapf, V.S., see Bauer, E.D. 8, 12, 15, 17, 21, 22
 Zapf, V.S., see Maple, M.B. 22
 Zaplatynsky, O.V. 67, 69, 71
 Zasorin, E.Z. 184, 185, 224–231
 Zasorin, E.Z., see Giricheva, N.I. 229
 Zavalii, I.Yu. 40, 44, 138, 139
 Zavalii, I.Yu., see Pecharsky, V.K. 45, 98
 Zekovic, Lj.D., see Jovanic, B.R. 522, 524, 563
 Zekovic, Lj.D., see Urosevic, V.V. 522
 Zener, C. 257, 258
 Zeng, L. 48
 Zeng, Z., see Wiebe, C.R. 282
 Zenkevich, L.V., see Evseeva, G.V. 236
 Zerger, R.P., see Suib, S.L. 481
 Zevtsova, Z.R., see Pashinkin, A.S. 237
 Zhang, D., see Wang, Q. 524, 530, 538
 Zhang, G., see Fisher, R.A. 326
 Zhang, G., see Gordon, J.E. 326
 Zhang, H., see Chi, Y. 524, 536
 Zhang, J., see Lam, R. 55, 78
 Zhang, J., see McLlroy, D.N. 295
 Zhang, J.S. 65, 73
 Zhang, L.W., see Zhao, Y.G. 328
 Zhang, S. 355
 Zhang, S., see Gerales, C.F.G.C. 358, 378, 404, 405, 411, 414, 415, 417, 418, 420, 424, 425, 427, 429–432, 435–438, 442, 443, 451, 453
 Zhang, S., see Ren, J. 420, 423–426, 429, 431, 433–435, 437–440
 Zhang, S.G., see Jia, Y.Q. 184
 Zhang, W., see Tran, C.D. 484
 Zhang, X., see Smolyaninova, V.N. 327
 Zhang, X.H., see Ren, Y.H. 326
 Zhang, X.P., see Zhao, Y.G. 328
 Zhang, X.Y., see Rozenberg, M.J. 261, 315
 Zhang, Z., see Wang, L. 523, 524, 551, 568
 Zhao, G. 326, 329
 Zhao, G., see Smolyaninova, V.N. 327
 Zhao, G.-M. 305, 307, 308
 Zhao, G.-M., see Alexandrov, A.S. 308
 Zhao, J., see Zhao, Y.G. 328
 Zhao, Q., see Forsberg, J.H. 357, 358, 374, 380, 427–431, 439, 440
 Zhao, X., see Chi, Y. 523, 533, 539
 Zhao, X., see Liu, S. 523, 530, 533
 Zhao, Y.G. 296, 328
 Zhao, Z.X., see Li, J.Q. 329
 Zheng, R., see Zhu, C. 326
 Zheng, R.K. 328
 Zhigarnovskii, B.M. 201, 203
 Zhigarnovskii, B.M., see Gogadze, N.G. 201–203

- Zhou, J.-S. 264, 265, 268, 269, 271, 272, 276–282,
284, 300–302, 305–308, 311, 312, 316, 317,
319–322
- Zhou, J.-S., see Archibald, W. 294, 295, 300
- Zhou, J.-S., see Goodenough, J.B. 261, 272–274,
296, 298
- Zhou, J.-S., see Liu, G.-L. 311, 313, 316, 318
- Zhou, J.-S., see Overend, N. 303
- Zhou, J.-S., see Rivadulla, F. 328, 330–335,
337–342
- Zhu, C. 326
- Zhu, C.F., see Zheng, R.K. 328
- Zhu, M.H., see Zhao, Y.G. 328
- Ziese, M., see Gordon, I. 326
- Ziessel, R., see Ulrich, G. 358
- Zimmer, H.G. 523
- Zimmer, H.G., see Syassen, K. 525
- Zimmermann, M.V. 264
- Zimmermann, M.V., see Casa, D. 315
- Zitserman, V.Y., see Berezhkovskii, A.M. 489
- Zmbov, K.F. 234, 235
- Zmbov, K.F., see Besenbuch, G. 235
- Zmbov, K.F., see Kent, R.A. 234
- Zou, G., see Chi, Y. 523, 530, 539
- Zou, G., see Liu, S. 523, 524, 529, 530, 533, 539
- Zuo, J.M. 326
- Zvyagin, S. 338
- Zygmunt, A. 61, 69, 74, 83, 85, 87
- Zygmunt, A., see Slebarski, A. 45, 59, 60, 100,
113

SUBJECT INDEX

- 1,3,5-triamino-1,3,5-trideoxy-cis-inositol 454
 1,4,7,10-tetraazacyclododecane-1,4,7,10-tetrakis
 (methylenephosphonic acid) 430
 1,4,7,10-tetraazacyclododecane-1,4,7,10-tetrakis
 (*N,N*-diethylacetamide) 426
 1,4,7,10-tetraazacyclododecane-*N,N',N'',N'''*-
 tetraacetic acid 419
 1,4,7-triazacyclononane-*N,N',N''*-triacetic acid
 410
 2,6-bis{[1-ethyl-2-[6-(*N,N'*-diethylcarbamoyl)-
 pyridin-2-yl]benzimidazol-5-methylene]-
 (2-ethyl-benzimidazol-5-yl)}pyridine 455
 2,6-bis(benzimidazole)pyridine 384
 2,6-pyridinedicarboxylic acid 404
 2,6-pyridinedicarboxylic acid-bis-diethylamide
 387
 2-[6-[*N,N*-diethylcarboxamido]-pyridin-2-yl]-
 1,1'-dimethyl-5,5'-methylene-2'-(5-meth-
 ylpyridin-2-yl)bis(1*H*-benzimidazole) 393
 2D orbital order-disorder transition 312
- A-type antiferromagnetic order 285
 ab initio calculations of intrinsic parameters 545
 absorption
 – of Cm(III) 494
 – of lanthanides 469, 494
 – of U(VI) 494
 absorption lines under pressure 527
 ADP 30
 AF-FM insulator-conductor transition 340
 agreement factor 373, 374, 385
 AIB₂ structure type 106, 139
 angular overlap model 545
 antiferromagnetic fluctuations 336
 antiferromagnetic order 20, 23, 25
 antiferromagnetic order: type-CE 338, 339
 antiferromagnetic phase converts abruptly to the
 conductive, ferromagnetic phase 305
 antiferromagnetic state can be driven irreversibly to
 a ferromagnetic conductive state 292
 antiferromagnetic superexchange interaction 256,
 276, 343
 antiferromagnetic t³-O-t³ interactions 275, 285
 antiferromagnetic t³-O-t³ superexchange
 interactions 262, 276
 antiferromagnetic to ferromagnetic transition 294
 antisymmetric exchange 258, 264
 atomic displacement parameter (ADP) 4, 11, 23
 atomic orbitals 253
 axial system 376, 377, 380
 azacryptand 401
- B₂O₃-Na₂O-Eu₂O₃ (glass) 523
 Ba₂SiO₄:Eu²⁺ 523
 Ba₅Al₂Sb₆ structure type 111
 BaAl₄ structure type 98
 BaAl₄ type related structures 141
 BaBr₂ 523
 bad metal 266, 287, 288, 302
 BaF₂:Sm²⁺ 522
 BaFCl:Sm²⁺ 522
 BaFe₄Sb₁₂ 15
 band structure 8
 BaOs₄Sb₁₂ 15
 BaRu₄Sb₁₂ 15
 bending angle ϕ 251, 256, 275, 292, 306
 bending of the (180° - ϕ) Mn-O-Mn bond angle
 323, 342
 bimetallic lanthanide complexes 443
 binary systems R-Sb 36
 bis{1-ethyl-2-[6'-carboxy]pyridin-
 2'-yl]benzimidazol-5-yl}methane) 444
 Bleaney's factors 371
 Bloch's rule 279
 bond length 183
 – LnBr₃ 183
 – LnCl₃ 183
 – LnF₃ 183
 – LnI₃ 183
 bond-bending angle 261, 292, 304
 bond-length fluctuations 261, 262, 282, 284, 304,
 321, 333, 341, 343
 Born-Haber cycle 171, 172
 Born-Landé equation 170
 bulk paramagnetic susceptibility 356

- C-type antiferromagnetic order 284
 C-type antiferromagnetic phase 283
 $\text{Ca}_{1-x}\text{La}_x\text{MnO}_3$, $0 \leq x \leq 0.2$ 283
 $\text{Ca}_{14}\text{AlSb}_{11}$ structure type 111, 138
 $\text{Ca}_2\text{P}_2\text{O}_7:\text{Eu}^{2+}$ 523
 $\text{CaAl}_2\text{O}_4:\text{Eu}^{2+}$ 523
 CaAl_2Si_2 structure type 98, 138
 CaBe_2Ge_2 structure type 99, 139
 $\text{CaBPO}_5:\text{Eu}^{2+}$ 523
 CaCrO_3 282
 $\text{CaF}_2:\text{Ce}^{3+}$ 521
 $\text{CaF}_2:\text{Dy}^{2+}$ 524
 $\text{CaF}_2:\text{Er}^{3+}$ 524
 $\text{CaF}_2:\text{Eu}^{3+}$ 523
 $\text{CaF}_2:\text{Gd}^{3+}$ 524
 $\text{CaF}_2:\text{Pr}^{3+}$ 521
 $\text{CaF}_2:\text{Sm}^{2+}$ 522
 $\text{CaF}_2:\text{Tb}^{3+}$ 524
 $\text{CaF}_2:\text{Tm}^{2+}$ 525
 $\text{CaFCl}:\text{Sm}^{2+}$ 522
 $\text{CaFe}_4\text{Sb}_{12}$ 15
 CaIn_2 structure type 106, 139
 $\text{CaMnO}_{2.94}$ 282
 CaMnO_3 256, 276, 277, 281, 282
 canted-spin 318
 canted-spin antiferromagnet 273, 340
 canted-spin antiferromagnetic insulator 273
 canted-spin antiferromagnetic phase 311
 canted-spin ferromagnetic 292
 canted-spin ferromagnetism 258
 canted-spin, type-A antiferromagnetic order 269
 $\text{Ca}(\text{PO}_3)_2:\text{Eu}^{3+}$ (glass) 523
 carrier concentration 13
 carrier mass 17
 CaTiO_3 4
 cation-anion resonance (electron-energy transfer)
 integral 277
 $\text{CdF}_2:\text{Eu}^{2+}$ 523
 $\text{CdF}_2:\text{Gd}^{3+}$ 524
 CDWs 315, 317
 CE AFI phase 328, 329, 332, 334, 335, 341
 CE domains 329
 CE phase 326–328
 Ce–Ag–Sb 56
 Ce–As–Sb 55
 Ce–Au–Sb 58
 Ce–Cd–Sb 57
 Ce–Co–Sb 52
 Ce–Cr–Sb 50
 Ce–Cu–Sb 53
 Ce–Cu–Sb, isothermal section 53, 54
 Ce–Fe–Sb 51
 Ce–Ga–Sb 54
 Ce–Ge–Sb 55
 Ce–Ge–Sb, isothermal section 55
 Ce–Hf–Sb 57
 Ce–In–Sb 57
 Ce–Li–Sb 49
 Ce–M–Sb systems 49
 Ce–Mn–Sb 50
 Ce–Mn–Sb, isothermal section 50, 51
 Ce–Ni–Sb 52
 Ce–Ni–Sb, isothermal section 52, 53
 Ce–Os–Sb 57
 Ce–Pd–Sb 56
 Ce–Pt–Sb 57
 Ce–Rh–Sb 56
 Ce–Ru–Sb 56
 Ce–Sb 36
 Ce–Se–Sb 55
 Ce–Si–Sb 50
 Ce–Si–Sb, isothermal section 50
 Ce–Sn–Sb 57
 Ce–Te–Sb 57
 Ce–Ti–Sb 50
 Ce–V–Sb 50
 Ce–Zn–Sb 54
 Ce–Zr, Nb–Sb 55
 $\text{Ce}_{0.33}\text{U}_{0.67}\text{Sb}_2$ 94
 $\text{Ce}_{0.6}\text{La}_{0.4}\text{CuSb}_2$ 122
 $\text{Ce}_{0.8}\text{La}_{0.2}\text{CuSb}_2$ 122
 $\text{Ce}_{1-x}\text{La}_x\text{RhSb}$ 95
 $\text{Ce}_{12}\text{Ga}_4\text{Sb}_{23}$ 54
 $\text{Ce}_{29}\text{Mn}_{13}\text{Sb}_{58}$ 51
 $\text{Ce}_2\text{Fe}_4\text{Sb}_5$ 52
 Ce_2GeSb_3 55, 109
 $\text{Ce}_2\text{Pd}_9\text{Sb}_3$ 56
 $\text{Ce}_2\text{Pd}_9\text{Sb}_3$ structure type 95
 Ce_2Sb 38
 $\text{Ce}_2\text{Se}_3\text{--Sb}_2\text{Se}_3$ section 55
 $\text{Ce}_2\text{Si}_3\text{Sb}_5$ 50
 $\text{Ce}_3\text{Au}_{3-x}\text{Pt}_x\text{Sb}_4$ 132, 133
 $\text{Ce}_3\text{Au}_3\text{Sb}_4$ 58, 106, 129
 $\text{Ce}_3\text{Cu}_3\text{Sb}_4$ 53, 132, 133
 Ce_3GeSb 55, 111
 Ce_3HfSb_5 57
 Ce_3NbSb_5 55
 $\text{Ce}_3\text{Pd}_6\text{Sb}_5$ 56, 113, 141
 $\text{Ce}_3\text{Pd}_6\text{Sb}_5$ structure type 97
 $\text{Ce}_3\text{Pt}_3\text{Sb}_4$ 57, 129
 $\text{Ce}_3\text{Rh}_3\text{Sb}_4$ 56, 133
 Ce_3SiSb 50

- Ce₃TiSb₅ 50
 Ce₃ZrSb₅ 55
 Ce₄Sb₃ 38
 Ce₅Ge₃Sb₂ 55
 Ce₅Sb₃ 38
 Ce₆CuSb₁₅ 54
 Ce₆Ge_{5-x}Sb_{11+x} 55, 135
 Ce₆Mn_{0.4}Sb₁₅ 103
 Ce₆MnSb₁₅ 51, 133, 134
 Ce₆ZnSb₁₅ 54, 133, 134
 Ce₈Pd₂₄Sb 56
 Ce₈Pd₂₄Sb structure type 100
 (Ce_xSb_{1-x})₂Se₃ 55
 CeAg₂Sb₂ 113
 CeAgSb₂ 56, 102, 123, 124, 128
 CeAs 521
 CeAs_xSb_{1-x} 55
 CeAuSb 58
 CeAuSb₂ 58, 121
 Ce(C₂H₅SO₄)₃·9H₂O 521
 CeCdSb₂ 57
 CeCo_{1-x}Sb₂ 52
 CeCrSb₃ 50, 72
 CeCu_{1-x}Sb₂ 53
 CeCu₂Sb₂ 113
 CeCu₆Sb₃ 53
 CeCuSb₂ 53, 120–122
 CEF 23
 CeF₃:Pr³⁺ 521
 CeFe_{0.6}Sb₂ 127
 CeFe_{1-x}Sb₂ 51
 CeFe₄As₁₂ 13, 14
 CeFe₄P₁₂ 12, 14
 CeFe₄Sb₁₂ 10, 11, 13, 14, 16, 52
 CeGa₂Al₂ structure type 99, 139, 140
 CeIn_{0.8}Sb₂ 57
 CeLi₂Sb₂ 50
 CeMn_{0.85}Sb₂ 51, 120
 CeNi_{2+x}Sb_{2-x} 53, 141
 CeNi_{2+x}Sb_{2-x} structure type 100
 CeNi_{2.36}Sb_{1.64} 100
 CeNi₂Sb₂ 53, 112
 CeNiSb 52, 116, 117
 CeNiSb₂ 52, 121, 122
 central-field covalency model CFC 530, 533
 CeOs₄As₁₂ 14
 CeOs₄P₁₂ 13, 14
 CeOs₄Sb₁₂ 14, 17, 57
 CeP 521
 CePd₂Sb₂ 56
 CePdSb 56, 118
 CePdSb₂ 56, 121
 CePdSb₃ 56
 CePtSb 57
 CeRh₂Sb₂ 56
 CeRhSb 56, 95, 109, 118
 CeRu₄As₁₂ 13, 14
 CeRu₄P₁₂ 12, 14
 CeRu₄Sb₁₂ 14–16, 56
 CeSb 38
 CeSb (HP) 38
 CeSb₂ 37, 38
 CeSb₂ (HT) 38
 CeSbTe 57
 CeScSi structure type 108, 137
 CeSe₃₀Sb₁₉ 55
 CeSn_xSb₂ 57
 CeTe_xSb_{1-x} 57
 CeVSb₃ 50
 CeVSb₃, structure type 137
 CeZn_{0.8}Sb₂ 54
 CeZn_{1-x}Sb₂ 54, 120
 CeZnSb₂ 119
 characteristic temperature 15, 26
 charge and orbital ordering 286, 327, 328, 330, 343
 charge and orbitally ordered 315
 charge disproportionation 267
 charge order 332
 charge ordering 292, 315, 327, 329, 332, 335, 343
 charge transfer state 551, 574
 charge transfer states under pressure 549, 551, 567, 568
 – La₂O₂S:Eu³⁺ 568
 – R₂O₂S:Eu³⁺ 551, 567
 charge-density wave 282, 284, 315, 323, 330, 332, 335, 343
 charge-density/spin-density wave 261
 charge-order fluctuations 343
 charge-ordered 327–329
 charge-ordered phase 309
 chelates
 – Eu³⁺ 523
 – Gd³⁺ 524
 – Sm³⁺ 522
 – Tb³⁺ 524
 chloride complexes 500
 – of Cm(III) 474
 – of lanthanides 473, 474
 cluster glass 288, 290, 310, 311
 Cm(III)
 – lifetime 473, 481

- CMR phenomenon 290, 317, 321, 324, 325
 CO 332
 CO phase 329, 332, 333, 335, 342
 CO transition 333
 CoAs₃ 2
 colossal magnetoresistance 262
 conductivity 27
 configuration interactions 536, 548, 550, 551, 561
 – LaCl₃:Pr³⁺ 551
 – LaOCl:Pr³⁺ 551
 – LiYF₄:Pr³⁺ 551
 – MFCl:Sm²⁺ 548
 configuration interactions under pressure 551
 contact contribution 364
 contact shifts 364
 cooperative Jahn–Teller distortion 268, 273
 cooperative Jahn–Teller Mn(III)-site distortions 285
 cooperative oxygen displacements 255, 304
 cooperative rotations 251, 263, 264, 275
 coordination number 493
 COP 28
 correlation crystal fields under pressure
 LaCl₃:Nd³⁺ 547
 correlation intrinsic parameter 548
 correlation of luminescence properties with
 structural changes 557
 correlation time 359
 CoSb₃ 5
 covalent mixing 260
 covalent-mixing parameters 254
 critical field 22
 cross-relaxation 573
 crossover 334
 crossover from localized to itinerant electron
 behavior 304
 crossover from localized to itinerant electronic
 behavior 250, 261, 290, 293, 299, 311, 332,
 343
 crossover from localized to vibronic behavior 288
 crossover from localized-electron to band
 magnetism 282
 crossover from polaronic to itinerant electron
 behavior 304
 crystal-field 13, 21, 366, 368, 371, 372, 377, 380,
 459
 crystal-field energies 158
 crystal-field energy
 – LnCl₃ 160
 – LnF₃ 154
 crystal-field independent methods 377
 crystal-field parameters 368
 crystal-field parameters under pressure 535, 538,
 539
 crystal-field splitting 157
 crystal-field splittings under pressure 535
 crystal-field strength under pressure 535, 538–540
 – GdOBr:Eu³⁺ 539
 – GdOCl:Eu³⁺ 539
 – La₂O₂S:Eu³⁺ 538
 – LaOBr:Eu³⁺ 539
 – LaOCl:Pr³⁺ 539
 – Na₅Eu(MoO₄)₄ 539
 – ROCl:Pr³⁺ 539
 – Y₂O₂S:Eu³⁺ 538
 – YAG:Tb³⁺ 538
 crystalline electric field 17, 18, 20, 22
 Cs₂NaTmCl₆ 525
 CsCaF₃:Gd³⁺ 524
 CsSmI₃ 522
 cubic-field splitting 254
 Curie–Weiss behavior 332
 Curie–Weiss paramagnetism 264, 336
 Curie-spin relaxation 362
 cyclotron effective mass 18

 δ -function model 547, 548, 551
 – LaCl₃:Nd³⁺ 548
 – LaCl₃:Pr³⁺ 548
 de Gennes double exchange 285, 292, 293, 310,
 317, 333, 343
 De Haas–van Alphen 18, 23
 Debye temperature 9
 diamagnetic shift 357
 diamond anvil cell 517, 519
 dicalcium protein calbindin D_{9k} 374
 dielectric screening model 530, 532
 dimensionless figure of merit 27
 direct exchange 256
 disordered orbitals 272
 displacive-type phase transition 23
 disproportionation 255, 343
 disproportionation reaction 266, 267, 273, 323
 distance dependence of intrinsic parameters 547
 distinguishable ferromagnetic phases 317
 dithiomethylphosphinic acid 415
 dithiophosphorus acid 415
 divalent europium 479, 482, 483, 494
 DOTA 419
 DOTAM 426
 DOTEAM 426
 DOTP 430
 DOTTA 426

- double-decker sandwich compound 449
double-exchange 257, 266, 267, 293, 307, 308, 332
DTMA 426
Dy–Ag–Sb 85
Dy–Au–Sb 85
Dy–Cr–Sb 84
Dy–Cu–Sb 84
Dy–Ge–Sb 84
Dy–M–Sb systems 84
Dy–Ni–Sb 84
Dy–Pd–Sb 85
Dy–Pt–Sb 85
Dy–Sb 37
Dy–Te–Sb 85
Dy–Zr–Sb 84
Dy_{0.33}U_{0.67}Sb₂ 94
Dy_{1.5}U_{1.5}Sb₇ 94
Dy₂Sb₅ 37, 39
Dy₃Au₃Sb₄ 85
Dy₃Cu₃Sb₄ 84, 133
Dy₄Sb₃(α) 39
Dy₅Ni₂Sb 84, 111
Dy₅Pd₂Sb 85
Dy₅Pt₂Sb 85
Dy₅Sb₃ 39
Dy₆Ge_{5-x}Sb_{11+x} 84, 135
DyAgSb₂ 85, 128
DyCrSb₃ 84
DyCuSb₂ 84, 121
dynamic phase segregation 282
DyNi_{2-x}Sb₂ 84
DyNiSb 84, 116
DyNiSb₂ 84, 121
DyPd₂Sb 85
DyPdSb 85
DyPtSb 85
(DySb)_{1-x}Ni_x 84
DySb₂(HT) 39
DySb(α) 39
DyTe₃Sb 85
DyZrSb 84
Dzialoshinskii vector 258, 264, 285, 311
- e_g* 5
effective axial symmetry 368, 455
effective electronic magnetic momenta 356
effective masses 28
effective nuclear charge 529, 534
Einstein frequency 11
elastic constant 11
electric quadrupole 22
electron coupling to oxygen vibrations 305
electron–crystal 30
electron–electron coulomb energies 252
electron–lattice coupling 310
electron–lattice interactions 321
electron–phonon coupling 269
electron–phonon coupling constant 582
electron–phonon interactions 268, 293, 580
– Cs₂NaTmCl₆ 581
– LiTmF₄ 581
– NdBa₂Cu₃O₇ 582
– Pb₂Sr₂NdCu₃O₈ 582
– sodium disilicate glass:Eu³⁺ 581
electron–spin interactions 293
electronic specific heat coefficient 8
emission
– of Cm(III) 496
– of lanthanides 496
– of U(VI) 474, 496–498
energy back-transfer model 578, 579
energy diffusion process 574
energy levels under pressure 520, 527, 550
energy migration 573, 574
energy shifts of excited configurations 549
energy transfer between f elements 572, 573
– Eu_xLa_{1-x}P₅O₁₄ 574
– La₂O₂S:Eu³⁺ 574
– Nd_xY_{1-x}P₅O₁₄ 572, 573
– Tb_xEu_{1-x}P₅O₁₄ 574
– Tb_xLa_{1-x}P₅O₁₄ 574
energy transfer from ligand states to f elements
569, 571
– Eu₂[Pt(CN)₄]₃·18H₂O 569
– Eu[Au(CN)₂]₃·3H₂O 570
– Eu[Au(CN)₂]₃·3H₂O 569
– rare-earth chelates 571
– Sm₂[Pt(CN)₄]₃·18H₂O 569
energy transfer from transition metal ions to f elements 574–577
– Cr³⁺:Tm³⁺:Y₃Al₅O₁₂ 575
energy transfer in insulators 572
energy transfer in semiconductors 577, 579
– GaAs:Er,O 580
– GaAs:Er³⁺ 578, 579
– GaP:Er³⁺ 580
– InP:Yb³⁺ 578, 580
– recover of quenched luminescence 579
– Si:Er³⁺ 580
energy transfer rate under pressure 576

- enthalpies of dimerisation 198
 – LnBr_3 197, 198
 – LnCl_3 198
 – LnF_3 198
 – LnI_3 198
- enthalpies of formation
 – LnBr_3 173, 192
 – LnCl_3 173, 192, 194
 – LnF_3 173, 192, 193
 – LnI_3 173, 192
- enthalpies of fusion
 – LnBr_3 181
 – LnCl_3 179, 222
 – LnF_3 177, 178
 – LnI_3 181
- enthalpies of sublimation
 – gaseous LnBr_3 238
- enthalpy increment
 – LaF_3 162
 – LnF_3 164
- enthalpy of formation 191
 – $\text{CeX}_3(\text{cr})$ 211
 – $\text{DyX}_3(\text{cr})$ 217
 – $\text{ErX}_3(\text{cr})$ 219
 – $\text{EuX}_3(\text{cr})$ 215
 – $\text{GdX}_3(\text{cr})$ 215
 – $\text{HoX}_3(\text{cr})$ 219
 – $\text{LaX}_3(\text{cr})$ 209
 – LnBr_3 172, 175
 – LnCl_3 172, 175
 – LnF_3 169, 171
 – LnI_3 172, 175
 – $\text{LuX}_3(\text{cr})$ 221
 – $\text{NdX}_3(\text{cr})$ 213
 – $\text{PrX}_3(\text{cr})$ 212
 – $\text{SmX}_3(\text{cr})$ 214
 – $\text{TbX}_3(\text{cr})$ 216
 – $\text{TmX}_3(\text{cr})$ 220
 – $\text{YbX}_3(\text{cr})$ 221
- enthalpy of formation of gaseous
 – LnBr_3 194
 – LnCl_3 193
 – LnF_3 191
 – LnI_3 196
- enthalpy of sublimation
 – gaseous LnCl_3 236
 – gaseous LnF_3 234
 – gaseous LnI_3 239
 – LnBr_3 195
 – LnCl_3 194
- entropies of fusion
 – LnBr_3 182
 – LnCl_3 180
 – LnF_3 177, 178
 – LnI_3 182
- Er–Ag–Sb 88
 Er–Au–Sb 89
 Er–Cu–Sb 88
 Er–M–Sb systems 88
 Er–Ni–Sb 88
 Er–Pd–Sb 88
 Er–Pt–Sb 89
 Er–Sb 37
 Er–Zr–Sb 88
 $\text{Er}_{0.33}\text{U}_{0.67}\text{Sb}_2$ 94
 $\text{Er}_3\text{Au}_3\text{Sb}_4$ 89
 $\text{Er}_3\text{Cu}_3\text{Sb}_4$ 88, 133
 Er_4Sb_3 39
 $\text{Er}_5\text{Ni}_2\text{Sb}$ 88
 $\text{Er}_5\text{Pd}_2\text{Sb}$ 88
 $\text{Er}_5\text{Pt}_2\text{Sb}$ 89
 Er_5Sb_3 39
 ErAgSb_2 88, 128
 $\text{ErBa}_2\text{Cu}_3\text{O}_x$ 524, 535
 $\text{Er}(\text{C}_2\text{H}_5\text{SO}_4)_3 \cdot 9\text{H}_2\text{O}$ 524
 ErCl_3 524
 ErCuSb_2 88, 119, 121
 $\text{ErNi}_{2-x}\text{Sb}_2$ 88
 ErNiSb 88, 116, 118
 ErPd_2Sb 88
 ErPdSb 88
 ErPtSb 89
 ErSb 39
 $(\text{ErSb})_{1-x}\text{Ni}_x$ 88
 ErSb_2 (HT) 39
 ErZrSb 88
- ethylsulfate compounds 536
 Eu benzoylacetate 523
 Eu–Ag–Sb 78
 Eu–Au–Sb 78
 Eu–Cu–Sb 77
 Eu–Fe–Sb 76
 Eu–Li–Sb 76
 Eu–M–Sb systems 76
 Eu–Mn–Sb 76
 Eu–Ni–Sb 76
 Eu–Os–Sb 78
 Eu–Pd–Sb 77
 Eu–Pt–Sb 78
 Eu–Ru–Sb 77
 Eu–Se–Sb 77

- Eu–Sn–Sb 78
 Eu–Te–Sb 78
 Eu–Zn–Sb 77
 Eu₁₁Sb₁₀ 39
 Eu₁₄MnSb₁₁ 76, 111, 134
 Eu₁₆Sb₁₁ 37, 39
 Eu₂O₃ 523
 Eu₂[Pt(CN)₄]₃·18H₂O 523
 Eu₂Sb₃ 38
 Eu₂Zn₃(NO₃)₁₂·xH₂O 523
 Eu₃GdSb₃ 94
 Eu₃Se₉Sb₄ 77
 Eu₄TeSb₂ 78
 Eu₅Sb₃ 39
 EuAgSb 78
 Eu[Au(CN)₂]₃·3H₂O 523
 EuAuSb 78
 Eu(C₂H₅SO₄)₃·9H₂O:Ce³⁺ 521
 EuCu_{1.75}As₂ 95
 EuCu_{1.75}As₂–EuCu₂Sb₂ region 95
 EuCu_{1.85}AsSb 95
 EuCu_{1.8}As_{1.5}Sb_{0.5} 95
 EuCu_{1.9}As_{0.85}Sb_{1.15} 95
 EuCu₂As_{0.5}Sb_{1.5} 95
 EuCu₂As_{0.65}Sb_{1.35} 95
 EuCu₂As_{0.6}Sb_{1.4} 95
 EuCu₂Sb₂ 77, 95
 EuCuSb 77
 EuF₂ 523
 EuFe₄P₁₂ 14, 23
 EuFe₄Sb₁₂ 15, 24, 76
 EuLiSb 76
 EuMn₂Sb₂ 76
 EuNi_{1.53}Sb₂ 99
 EuNi₂Sb₂ 76
 EuO 523
 EuOCl 523
 Eu(OH)₃ 523
 EuOs₄Sb₁₂ 15, 78
 EuP₅O₁₄ 523, 530
 EuPd₂Sb₂ 77
 EuPdSb 77
 EuPO₄ 523
 EuPtSb 78
 EuRu₄P₁₂ 14, 24
 EuRu₄Sb₁₂ 15, 24, 77
 EuSb₂ 38
 EuSe 523
 EuSe₄Sb₂ 77
 EuSn₃Sb₄ 78
 EuTe–Sb₂Te₃ section 78
 EuTe₄Sb₂ 78
 EuTe₇Sb₄ 78
 EuVO₄ 523
 EuZn₂Sb₂ 77
 excess entropy 156
 excess heat capacity 155
 – DyF₃ 156
 – LnCl₃ 167
 exchange energy 260
 exchange of ¹⁸O for ¹⁶O 305, 308
 exchange striction 276, 277, 284
 excited configurations under pressure 549, 567
 – CsSmI₃ 549
 – SrF₂:Sm²⁺ 549
 excited states under pressure 548
 expansion of wavefunctions 533, 535
 experimental hyperfine shift 357

 Fermi surface 9, 23
 ferrimagnetic 24
 – order 285
 ferromagnet 24
 ferromagnetic 21–24
 – exchange interactions 270
 – insulator 273
 – interactions 25
 – quantum critical point 17
 – σ -bond superexchange 275
 – superexchange 257, 267, 343
 – superexchange interactions 262
 – vibronic (FV) 287
 ferromagnetic-ferromagnetic transition 316
 field-induced phase transition 25
 figure of merit 27
 filled skutterudite 1–32
 – structure 4, 5
 fluctuating ferromagnetic phases 311
 fluctuating phases 333
 fourfold symmetry 415, 448
 free-ion parameters under pressure 530, 531
 from vibronic to itinerant electronic behavior 333
 FV phase 287, 317, 325
 FV-FM transition 325

 γ 12, 13, 17, 21, 22, 26
 G-type antiferromagnetic order 282, 283
 GaAs:Er³⁺ 524
 gadolinium break 400, 459
 GaP:Er³⁺ 525
 Gd benzoylacetate 524
 Gd–Ag–Sb 81
 Gd–Au–Sb 81

- Gd–Bi–Sb 82
 Gd–Cr–Sb 79
 Gd–Cu–Sb 80
 Gd–Fe–Sb 79
 Gd–Ge–Sb 80
 Gd–Li–Sb 78
 Gd–Li–Sb, isothermal section 78, 79
 Gd–M–Sb systems 78
 Gd–Ni–Sb 79
 Gd–Pd–Sb 81
 Gd–Pt–Sb 81
 Gd–Sb 36
 Gd–Se–Sb 80
 Gd–Te–Sb 81
 Gd–Zn–Sb 80
 Gd–Zr–Sb 81
 Gd_{0.32}U_{0.68}Sb₂ 94
 Gd_{0.5}Sr_{0.5}MnO₃ 338
 Gd_{1.5}U_{1.5}Sb₇ 94
 Gd₁₆Sb₃₉ 37, 39
 Gd_{2.31}U_{0.69}Sb₇ 94
 Gd₂LiSb 78
 Gd₂O₂S:Eu³⁺ 523, 534
 Gd₂Sb₅ 37, 39
 Gd₂Se₃–Sb₂Se₃ section 80
 Gd₃Au₃Sb₄ 81
 Gd₃Cu₃Sb₄ 80, 132, 133
 Gd₃Ga₅O₁₂:Nd³⁺ 521
 Gd₃Li₄Sb₄ 78
 Gd₃Sc₂Ga₃O₁₂:Nd³⁺ 521
 Gd₄(Bi_xSb_{1-x})₃ 82
 Gd₄Li₃Sb₄ 78
 Gd₄Sb₃ 39
 Gd₅Ni₂Sb 80
 Gd₅Pd₂Sb 81
 Gd₅Pt₂Sb 81
 Gd₅Sb₃ 39
 Gd₆Ge_{4.3}Sb_{11.7} 80
 Gd₆Ge_{5-x}Sb_{11+x} 135
 Gd₆ZnSb₁₅ 80, 133, 134
 Gd_xR_{5-x}Sb₃ 94
 (Gd_xSb_{1-x})₂Se₃ 80
 GdAgSb₂ 81, 128
 GdCrSb₃ 79
 GdCu₂Sb₂ 80
 GdCuSb₂ 80, 121
 GdFe_{1-x}Sb₂ 79
 GdFe₄P₁₂ 15, 24
 GdLi₃Sb₂ 78
 GdLi₇Sb₂ 78
 GdNi_{2-x}Sb₂ 79
 GdNi₂Sb₂ 79
 GdNiSb 79, 116
 GdNiSb₂ 79, 121
 GdOBr:Eu³⁺ 523
 GdOCl:Eu³⁺ 523
 GdOCl:Pr³⁺ 521, 533, 537
 GdPdSb 81, 118
 GdPdSb₂ 81, 121
 GdPtSb 81
 GdRu₄P₁₂ 15, 25
 GdSb (α) 39
 GdSb (β) 39
 GdSb₂ 37
 GdSb₂ (HT) 39
 GdSb₂ (LT) 39
 GdSbTe 81
 GdTe–Sb₂Te₃ section 81
 GdU₂Sb₆ 95
 GdZn_{1-x}Sb₂ 80
 GdZrSb 81
 geometrical factor 368, 372
 geometrical parameters
 – Ln₂X₆ dimers 232
 glasses under pressure 555
 – 90B₂O₃–10Na₂O–1Eu₂O₃ 555
 – coordination changes 556
 – silicate glasses 556
 – structural changes 556

 H₃BO₃–LiF–Sm₂O₃ 522
 Hall coefficient 17
 Hall measurements 8
 Hall mobility 13
 heat capacity 9, 11, 12, 16–18, 20–24, 26
 – GdCl₃ 159
 – LnF₃ 154
 – LuCl₃ 159
 heat capacity data 13
 heat capacity of gaseous
 – LnBr₃ 182
 – LnCl₃ 182
 – LnF₃ 182
 – LnI₃ 182
 heat capacity of liquid
 – LnBr₃ 177, 180, 181
 – LnCl₃ 177–179, 222
 – LnF₃ 175, 177, 178
 – LnI₃ 177, 180, 181
 heavy-fermion 13
 heavy-fermion state (HFS) 17
 heavy-fermion superconductor 22
 hexagonal polytypes 251, 277, 323

- Hf₅CuSb₃-anti type 110
 HfCuSb₂, structure type 139
 HfCuSi₂, structure type 102, 138, 140
 HFS 19
 high pressure technique 517
 high temperature heat capacity 162
 – LnBr₃ 168, 169
 – LnCl₃ 166, 169
 – LnF₃ 165
 – LnI₃ 168, 170
 high-pressure fluorescence line-narrowing 555
 high-spin 253
 Ho–Ag–Sb 87
 Ho–Au–Sb 87
 Ho–Cu–Sb 86
 Ho–M–Sb systems 86
 Ho–Ni–Sb 86
 Ho–Ni–Sb, isothermal section 86
 Ho–Pd–Sb 87
 Ho–Pt–Sb 87
 Ho–Sb 37
 Ho–Zr–Sb 87
 Ho_{0.33}U_{0.67}Sb₂ 94
 Ho_{0.5}Sr_{0.5}MnO₃ 338
 Ho_{1.47}U_{1.53}Sb₇ 94
 Ho₃Au₃Sb₄ 87
 Ho₃Cu₃Sb₄ 87, 133
 Ho₄Sb₃ 39
 Ho₅Ni₂Sb 86
 Ho₅Pd₂Sb 87
 Ho₅Pt₂Sb 87
 Ho₅Sb₃ 39
 HoAgSb₂ 87, 128
 HoCl₃ 524
 HoCuSb₂ 87, 121
 HoMnO₃ 275
 HoNi_{2-x}Sb₂ 86
 HoNiSb 86, 116, 118
 HoNiSb₂ 86, 121
 HoPd₂Sb 87
 HoPdSb 87
 HoPtSb 87
 HoSb 39
 HoSb₂ 39
 HoZrSb 87
 Hund intraatomic exchange 253
 hybridization 12, 17
 hydration number
 – of Cm(III) 479
 – of lanthanides 479
 hydration number (more specific) 475–483
 hydrostatic limits 519
 hyperfine interaction 359, 364, 377, 459
 hyperfine paramagnetic lanthanide induced shift 357
 hyperfine parameters 24
 indirect exchange 258
 inelastic neutron scattering 11, 22
 influence of 4f^{N-1}5d¹ configurations on intensities and lifetimes under pressure 563
 influence of charge transfer states on intensities and lifetimes under pressure 567
 inner-sphere relaxation 359
 InP:Yb³⁺ 525
 insulator-metal transition 287, 305
 intensities under pressure 559
 – rare-earth ethylsulfates 562
 – rare-earth trichlorides 562
 – rare-earth trifluorides 562
 – UF₃ 562
 – UF₄ 562
 interatomic interactions 256, 260
 interatomic spin–spin exchange interactions 256
 intergrowth structures 250
 intermediate valence 26
 intraatomic electron–electron interactions 260
 intraatomic exchange 286, 294
 intraatomic interactions 252, 260
 intrinsic parameters 542–546, 548
 isomer shift 24
 isotope effect 305
 isotope exchange 262, 305, 306, 310, 327, 329
 isotope shift 308
 itinerant orbiton 269
 itinerant-electron magnetism 259, 260
 Jahn–Teller deformations 267, 311, 323
 Jahn–Teller distortional 305
 Jahn–Teller distortions 263, 266, 304, 307, 311, 343
 Jahn–Teller energies 263
 Jahn–Teller orbital fluctuations 261
 Jahn–Teller orbital ordering 263, 268, 306
 Jahn–Teller ordering 262
 Jahn–Teller site deformations 293
 Jahn–Teller site distortions 255, 343
 κ_{min} 29, 30
 κ_L 29
 KHg₂ structure type 108, 138
 Kondo temperature 13

- La–Ag–Sb 48
 La–Al–Sb 43
 La–Au–Sb 49
 La–Cd–Sb 48
 La–Co–Sb 44
 La–Cr–Sb 43
 La–Cu–Sb 45
 La–Cu–Sb, isothermal section 45, 46
 La–Fe–Sb 43
 La–Ga–Sb 47
 La–Ge–Sb 47
 La–Hf–Sb 49
 La–In–Sb 48
 La–Li–Sb 42
 La–*M*–Sb systems 42
 La–Mg–Sb 42
 La–Mn–Sb 43
 La–Nb–Sb 47
 La–Ni–Sb 44
 La–Ni–Sb, isothermal section 45
 La–Os–Sb 49
 La–Pb–Sb 49
 La–Pd–Sb 48
 La–Pt–Sb 49
 La–Rh–Ge 48
 La–Ru–Sb 47
 La–Sb 36
 La–Sn–Sb 48
 La–Ti–Sb 43
 La–V–Sb 43
 La–Zn–Sb 46
 La–Zr–Sb 47
 La_{0.1}Rh₈Sb₂₄ 48
 (La_{0.25}Nd_{0.75})_{0.7}Ca_{0.3}MnO₃ 306, 308
 La_{0.4}Ce_{0.6}CuSb₂ 120
 La_{0.5}Ca_{0.5}MnO₃ 259, 328
 La_{0.5}Sr_{0.5}MnO₃ 337
 La_{0.65}Ba_{0.35}MnO₃ 295
 La_{0.7–x}Pr_xCa_{0.3}MnO₃ 290, 294, 309
 La_{0.7–x}Y_xCa_{0.3}MnO₃ 310
 La_{0.75}Ca_{0.25}MnO₃ 299, 308
 (La_{0.78}Pr_{0.22})_{2/3}Ca_{1/3}MnO₃ 305
 La_{0.7}Ca_{0.3}MnO₃ 298, 310
 La_{0.7}(Ca_{1–y}Sr_y)_{0.3}MnO₃ 294
 La_{0.7}Sr_{0.3}MnO₃ 290, 294
 La_{0.8}Ca_{0.2}MnO₃ 305
 La_{1–x}Ba_xMn_{1–x}Ti_xO₃ 267
 La_{1–x}Ca_xMnO₃ 295, 298, 307, 318, 323
 La_{1–x}Sr_xMnO₃ 260, 286, 311, 323, 326, 333
 (La_{1–y}Nd_y)_{0.7}Ca_{0.3}MnO₃ 294
 (La_{1–y}Pr_y)_{0.67}Ca_{0.33}MnO₃ 327
 (La_{1–y}Pr_y)_{0.7}Ca_{0.3}MnO₃ 294
 (La_{1–y}R_y)_{0.7}A_{0.3}MnO₃ 290, 310
 (La_{1–y}R_y)_{0.7}Ca_{0.3}MnO₃ 310
 (La_{1–y}R_y)_{2/3}(Ca_{1–x}Sr_x)_{1/3}MnO₃ 299
 La₁₂Ga₄Sb₂₃ 47
 La₁₃Ga₈Sb₁₁ 47
 La₁₃Ga₈Sb₂₁ structure type 104
 La_{2/3}(Ca_{1–x}Sr_x)_{1/3}MnO₃ 310
 La_{2/3}Ca_{1/3}MnO₃ 299, 300
 La_{2/3}Sr_{1/3}MnO₃ 295
 La₂O₂S:Eu³⁺ 524
 La₂O₂S:Tb³⁺ 524
 La₂Sb 38
 La₃Au₃Sb₄ 49, 129
 La₃Cu₃Sb₄ 46, 133
 La₃HfSb₅ 49
 La₃InGe structure type 111
 La₃Mg_{4.6}Sb₆ 43, 110
 La₃Mg_{5–x}Sb₆ structure type 110
 La₃NbSb₅ 47
 La₃Sb₂ 38
 La₃TiSb₅ 43, 110
 La₃YSb₃ 94
 La₃ZrSb₅ 47
 La_{4.89}Mg_{1.539}Sb₆ 42, 110
 La₄Mg_{4.48}Sb₇ 42, 110
 La₄Mg_{5–x}Sb₇ structure type 110
 La₄PbSb₂ 49
 La₄Sb₃ 38
 La₄SnSb₂ 48
 La_{5–y}Mg_{2–x}Sb₆ structure type 110
 La_{5/8–x}Pr_xCa_{3/8}MnO₃ 327
 La_{5/8–y}Pr_yCa_{3/8}MnO₃ 340
 La₅Pb₃Sb 49
 La₅Sb₃ 38
 La₆Co₁₃Sb 44
 La₆CuSb₁₅ 46
 La₆Ge_{2.8}Sb_{13.2} 47
 La₆Ge_{5–x}Sb_{11+x} 135
 La₆Ge_{5–x}Sb_{11+x} structure type 103
 La₆MnSb₁₅ 43
 La₆MnSb₁₅ structure type 103, 138, 140
 La₆ZnSb₁₅ 47
 LaAg₂Sb₂ 113
 LaAgSb₂ 48, 128
 LaAuSb₂ 49, 121
 La(C₂H₅SO₄)₃·9H₂O:Gd³⁺ 524
 La(C₂H₅SO₄)₃·9H₂O:Nd³⁺ 521
 La(C₂H₅SO₄)₃·9H₂O:Pr³⁺ 521
 LaCdSb₂ 48
 LaCl₃ 536, 537

- LaCl₃:Nd³⁺ 522, 531, 536
 LaCl₃:Pr³⁺ 521, 528, 531, 536, 538, 541
 LaCl₃:U³⁺ 531, 536
 LaCo_{1-x}Sb₂ 44
 LaCrSb₃ 43
 LaCu_{0.82-0.87}Sb₂ 46
 LaCu₂Sb₂ 113
 LaCu₆Sb₃ 46
 LaCuSb₂ 120, 121
 LaF₃:Nd³⁺ 522
 LaFe_{1-x}Sb₂ 43
 LaFe₄As₁₂ 9, 14
 LaFe₄P₁₂ 8, 9, 14
 LaFe₄P₁₂ structure type 95
 LaFe₄Sb₁₂ 9-11, 14, 44
 LaFe₄Sb₁₂ structure type 138
 LaGaO₃ 277
 LaGaSb₂ 47
 LaIn_{0.8}Sb₂ 48
 LaInSb₂ structure type 102
 LaLi₃Sb₂ 42
 LaLi₃Sb₂ structure type 96
 LaMn_{0.5}Ga_{0.5}O₃ 292, 294, 303, 329
 LaMn_{0.65-0.76}Sb₂ 43
 LaMn_{0.87}Sb₂ 120
 LaMn_{1-x}Al_xO₃ 273
 LaMn_{1-x}Ga_xO₃ 267, 284
 LaMn_{1-x}Ga_xO₃ and LaMn_{1-x}Sc_xO₃ 269
 LaMn_{1-x}Sc_xO₃ 268
 LaMnO₃ 256, 262, 277, 280-282, 284, 294, 323, 333
 LaMnO_{3+δ} 285, 317
 LaMnO_{3-δ} 317
 LaMSb₂ 119
 La(Ni, Sb)₄ 141
 LaNi_{1.51}Sb₂ 45, 99
 LaNi₂Sb₂ 45, 98, 113
 LaNiSb 44, 106, 115, 116
 LaNiSb₂ 45, 121
 lanthanide antimonides 7
 lanthanide arsenides 7
 lanthanide contraction 184
 lanthanide (III) halides 147-247
 lanthanide induced relaxation 356, 359
 lanthanide phosphides 6
 lanthanide-induced contact relaxation 359
 lanthanide-induced Curie-spin relaxation 362
 lanthanide-induced dipolar relaxation 361
 lanthanum trihalides 198
 LaOBr:Eu³⁺ 523
 LaOCl:Eu³⁺ 523
 LaOCl:Pr³⁺ 521, 533, 537
 LaOs₄As₁₂ 9, 14
 LaOs₄P₁₂ 9, 14
 LaOs₄Sb₁₂ 12, 14, 49
 LaOX:Eu³⁺ 534
 LaPd₂Sb₂ 48
 LaPdSb 48
 LaPdSb₂ 48, 121
 LaPt₂Ge₂ 141
 LaPt₂Ge₂ structure type 100
 LaPtSb 49
 LaRh₂Sb₂ 48
 LaRhSb 48, 95
 LaRu₄As₁₂ 9, 10, 14
 LaRu₄P₁₂ 8, 14
 LaRu₄Sb₁₂ 12, 14, 47
 LaSb 38
 LaSb (HP) 38
 LaSb₂ 38
 LaSn_xSb₂ 49
 LaSn_xSb₂ (x = 0.75) structure type 103
 LaSnSb₂ 142
 lattice constant 26
 lattice thermal conductivity 11
 LaVSb₃ 43
 LaZn_{0.6}Sb₂ 47
 LaZn_{1-x}Sb₂ 46
 LaZnSb₂ 102
 lifetime
 - non-radiative 467, 468, 475-478
 - of Cm(III) 472, 495
 - of lanthanides 471-474, 481, 482, 494, 495
 - of U(VI) 471-474, 484, 485, 494, 495
 - radiative 467, 468, 472, 481
 lifetimes under pressure 559, 565
 - CaFCl:Sm²⁺ 565
 - Gd₂O₂S:Tb³⁺ 566
 - La₂O₂S:Tb³⁺ 566
 - SrFCl:Sm²⁺ 563-565
 LiGaGe, structure type 139, 140
 ligand-ligand interactions 544, 545
 ligand-field wavefunctions 254
 ligand-fields 253
 LiNbO₃:Er³⁺ 525
 line shifts under pressure 527-529
 - LaCl₃:Pr³⁺ 527
 - LaCl₃:U³⁺ 529
 LIR 356, 359
 LIS 357, 362, 373, 375
 LiTmF₄ 525

- Ln*-*X* equilibrium bond distances
 – *LnBr*₃ 184
 – *LnCl*₃ 184
 – *LnF*₃ 184
 – *LnI*₃ 184
*Ln*₂*Cl*₆ dimers 193
*Ln*₂*X*₆ dimers 190, 197
*LnCl*₃ 158
*LnF*₃ 149, 154, 162
*LnX*₃ monomers 182
 local distortions 540, 541, 543, 544, 555
 – *MFC*:*Sm*²⁺ 541
 – *RCl*₃ 540
 – *ROCl*:*Pt*³⁺ 541
 local distortions from high-pressure experiments 540
 local structure 555
 local structure in glasses 555
 local vibrations 581
 local-density approximation (LDA) 12
 localized from itinerant electronic behavior 330
 localized to itinerant electronic behavior 330
 localized to itinerant electronic transition 282
 long-range orbital order 263, 269
 low temperature heat capacity 154, 158
 – *LnBr*₃ 161
 – *LnI*₃ 161
Lu–*Ag*–*Sb* 93
Lu–*Au*–*Sb* 93
Lu–*Cu*–*Sb* 93
Lu–*M*–*Sb* systems 92
Lu–*Ni*–*Sb* 92
Lu–*Pd*–*Sb* 93
Lu–*Pt*–*Sb* 93
Lu–*Sb* 37
Lu–*Zr*–*Sb* 93
*Lu*₃*Au*₃*Sb*₄ 93
*Lu*₃*Sb* 39
*Lu*₅*Ni*₂*Sb* 92
*Lu*₅*Pd*₂*Sb* 93
*Lu*₅*Pt*₂*Sb* 93
*Lu*₅*Sb*₃ 39
LuAgSb 93
*LuCuSb*₂ 93
 luminescence inhibition 485, 486, 489–492
 luminescence lines under pressure 527
 luminescence quantum yield 468, 495, 496
 luminescence quenching 563, 572
LuNiSb 92, 116
LuPtSb 93
LuSb 39
*LuSb*₂ 39
LuZrSb 93
 Madelung energy 252
 magnetic anisotropy 368–370, 373, 377
 magnetic polaron 293
 magnetic polarons 323
 magnetic susceptibility 8–10, 12, 13, 15, 17, 20–23, 25, 26
 magnetic susceptibility tensor 366
 magnetic transition 23
 magnetization 19, 25, 26
 magnetoresistance 290, 293, 299
 magnon scattering 22
 mass enhancement 26
 material property database 200
 mean bond energy
 – *LnBr*₃ 195, 196
 – *LnCl*₃ 194
 – *LnF*₃ 193, 195
 – *LnI*₃ 197
 melting temperature 150, 151
 – *CnBr*₃ 152
 – *LnBr*₃ 151, 206
 – *LnCl*₃ 151, 203
 – *LnF*₃ 151, 200
 – *LnI*₃ 151, 208
 metal to insulator transition 23
 metal–insulator transition (M-I) 19
 metamagnetic 17, 25, 329, 340
 metamagnetic transition 340
 metamagnetism 326, 337, 340
MFC:*Sm*²⁺ 537
MgAgAs structure type 109, 139
*MgCu*₂*Al* structure type 139
 mixed valence 24
 mixing of configurations 561
 mixing of f- and d-orbitals by lattice vibrations 562
 mixing of ligand and 4f states 561
 mixing of wavefunctions 563, 564, 567
 mixing with excited configurations 567
*MnCu*₂*Al* structure type 101
*MnO*_{6/2} octahedra are rotated 323
*Mo*₅*B*₂*Si* structure type 111, 139
 mobilities 28
 model-free method 376, 380, 443, 453, 459
 molar volume
 – *LnBr*₃ 161
 – *LnCl*₃ 159
 – *LnF*₃ 159
 – *LnI*₃ 161

- molecular geometry 182
 – of the Ln_2X_6 dimer 190
 molecular structure 183
 – Ln_2X_6 190
 molecular vibrations Ln_2X_6 191
 monometallic lanthanide complexes 380
 Mössbauer 8, 13, 24
 Mössbauer isomer shift 24
 Mott–Hubbard transition 260
 MR 299
 multiple sites under pressure 555
 – GaAs:Er³⁺ 555
 – LiNbO₃:Er³⁺ 555
 MYX compounds 532, 537
- Na₂O–2SiO₂:Eu³⁺ (glass) 524
 Na₅Eu(MoO₄)₄ 524
 Na₅Eu(WO₄)₄ 524
 narrow gap semiconductor 13
 (Nd, Pr)₂Sb 93
 (Nd, Pr)₄Sb₃ 93
 (Nd, Pr)Sb 93
 (Nd, Pr)Sb₂ 93
 Nd–Ag–Sb 69
 Nd–Ag–Sb, isothermal section 69, 70
 Nd–Au–Sb 71
 Nd–Au–Sb, isothermal section 71, 72
 Nd–Cd–Sb 69
 Nd–Cd–Sb, isothermal section 69, 70
 Nd–Co–Sb 65
 Nd–Co–Sb, isothermal section 65, 66
 Nd–Cr–Sb 62
 Nd–Cr–Sb, isothermal section 62, 63
 Nd–Cu–Sb 67
 Nd–Cu–Sb, isothermal section 67
 Nd–Fe–Sb 63
 Nd–Fe–Sb, isothermal section 63–65
 Nd–Ga–Sb 68
 Nd–Ge–Sb 68
 Nd–Hf–Sb 71
 Nd–In–Sb 70
 Nd–Li–Sb 62
 Nd–M–Sb systems 62
 Nd–Mn–Sb 63
 Nd–Mn–Sb, isothermal section 63, 64
 Nd–Ni–Sb 66
 Nd–Ni–Sb, isothermal section 66, 67
 Nd–Os–Sb 71
 Nd–Pd–Sb 69
 Nd–Pt–Sb 71
 Nd–Rh–Ge 69
- Nd–Ru–Sb 69
 Nd–Sb 36
 Nd–Sn–Sb 70
 Nd–Te–Sb 71
 Nd–Ti–Sb 62
 Nd–V–Sb 62
 Nd–Zn–Sb 67
 Nd–Zn–Sb, isothermal section 67, 68
 Nd–Zr, Nb–Sb 69
 (Nd_{0.125}Sm_{0.875})_{0.5}Sr_{0.5}MnO₃ 341
 Nd_{0.33}U_{0.67}Sb₂ 94
 Nd_{0.475}Pr_{0.475}Sb_{0.05} 93
 Nd_{0.5}(Ca_{0.5–x}Cr_x)MnO₃ 336
 Nd_{0.5}Ca_{0.5}MnO₃ 336
 Nd_{0.5}Ca_{0.5}MnO_{3+δ} 336
 Nd_{0.5}Sr_{0.5}MnO₃ 326, 337
 Nd_{0.7}Sr_{0.3}MnO₃ 308
 Nd₁₂Ga₄Sb₂₃ 68
 Nd₂₆Mn₈Sb₆₆ 63
 Nd₂₉Mn₁₃Sb₅₈ 63
 Nd₂Fe₁₇ 65
 Nd₂Sb 38
 Nd₂Te₃–Sb₂Te₃ section 71
 Nd₃Au₃Sb₄ 72
 Nd₃Cu₃Sb₄ 67, 132, 133
 Nd₃HfSb₅ 71
 Nd₃NbSb₅ 69
 Nd₃TiSb₅ 62
 Nd₃ZrSb₅ 69
 Nd₄Sb₃ 38
 Nd₅Sb₃ 38
 Nd₆CdSb₁₅ 69
 Nd₆CoSb₁₅ 66
 Nd₆Fe₁₃Sb 65, 104
 Nd₆Fe₁₃Si structure type 104, 138
 Nd₆Ge_{3.6}Sb_{12.4} 68
 Nd₆Ge_{5–x}Sb_{11+x} 135
 Nd₆ZnSb₁₅ 68
 Nd_{8+x}Sb_{19+y} 37, 38
 NdAgAs₂ structure type 102
 NdAgSb₂ 69, 128
 NdAgSb₂ structure type 138
 NdAuSb₂ 72, 121
 NdBa₂Cu₃O₇ 522
 NdBr₃ 522
 Nd(C₂H₅SO₄)₃·9H₂O 522
 NdCdSb 69
 NdCdSb₂ 69
 NdCl₃ 522, 531
 NdCl₃·6H₂O 522
 NdCo_{1–x}Sb₂ 66

- NdCo₃Sb₂ 66
 NdCrSb₃ 62
 NdCu₆Sb₃ 67
 NdCuSb₂ 67, 121
 NdF₃ 522
 NdFe_{0.6}Sb₂ 64
 NdFe_{1-x}Sb₂ 63
 NdFe_{2-x}Sb₂ 65
 NdFe₂Sb₂ 142
 NdFe₂Sb₂ structure type 100
 NdFe₃Sb₂ 65, 97, 142
 NdFe₃Sb₂ structure type 96
 NdFe₄As₁₂ 14, 23
 NdFe₄P₁₂ 14, 22
 NdFe₄Sb₁₂ 14, 23, 63
 NdIn_{0.8}Sb₂ 70
 NdLi₂Sb₂ 62
 NdMn_{0.83}Sb₂ 120
 NdMn_{1-x}Sb₂ 63
 NdMnO₃ 252
 NdNi₂Sb₂ 66
 NdNiSb 66, 116
 NdNiSb₂ 66, 121
 NdOs₄As₁₂ 14, 23
 NdOs₄P₁₂ 14, 23
 NdOs₄Sb₁₂ 14, 23, 71, 95
 NdP₅O₁₄ 522
 NdPd₂Sb₂ 69
 NdPdSb 69, 106
 NdPdSb₂ 69, 121
 NdPtSb 71
 NdPtSb (or LiGaGe) structure type 107
 NdRh₂Sb₂ 69
 NdRhSb 69, 108
 NdRu₄As₁₂ 14, 23
 NdRu₄P₁₂ 14, 23
 NdRu₄Sb₁₂ 14, 23, 69
 NdSb 38
 NdSb₂ 38
 NdSbTe 71
 NdSn_xSb₂ 70
 NdTe₃Sb 71
 NdVSb₃ 62
 NdZn_{1-x}Sb₂ 68
 NdZn₂Sb₂ 68
 nephelauxetic effect 529, 535
 neutron scattering 17, 23
 neutron scattering under pressure 535
 non-Fermi liquid (NFL) 15
 nonradiative crossover between configurations 564
 nonradiative energy transfer 567, 569
 nonradiative energy transfer to charge transfer states 567
 nonradiative transfer to excited configurations 566
 NOTA 410
 nuclear relaxation 358, 363, 448
 nuclear relaxation in paramagnetic lanthanide complexes 358
¹⁸O substitution for ¹⁶O 308
¹⁸O/¹⁶O exchange 305, 307, 309
 O^{*}-R transition 323
 O^{*}-orthorhombic to the R-rhombohedral 319
 octaethylporphyrin 448
 odd crystal-field terms under pressure 566, 567
 ODS 19
 on-site coulomb energies 260
 one-nucleus method 376, 445, 456
 OO phase 328
 optical measurements 17, 26
 optical studies under pressure 515-589
 orbital and charge disorder 290
 orbital and charge order 290, 315
 orbital and charge ordering 259, 315, 321, 332
 orbital and/or bond-length fluctuations 288
 orbital and/or phase fluctuations 338
 orbital angular momentum 318
 orbital degeneracy 253
 orbital disorder 263, 270, 321
 orbital exciton 269
 orbital fluctuations 256, 257, 261, 263, 266, 284, 285, 289, 293, 304, 315, 321, 332, 336, 343
 orbital order 325, 332, 333, 335
 orbital order and disorder 329
 orbital order-disorder transition 263
 orbital ordering 255, 267-269, 288, 308, 311, 328, 330, 332, 335, 343
 orbitally disordered 273
 orbitally fluctuating 272, 287, 290, 321
 orbitally ordered 272
 orbitally ordered Jahn-Teller state 268
 orbitally ordered state 315
 orbitally-correlated crystal fields 547
 orbitals fluctuate 272
 orbiton 268, 269
 order-disorder transitions 311, 335
 ordering of the Mn(III) e orbitals 310
 orthorhombic *Pbnm* symmetry 251
 orthorhombic to rhombohedral to tetragonal to cubic 322
 oxydiacetic acid 381
 oxygen interstitials 251
 oxygen stoichiometry 251, 265, 323, 328

- oxygen vacancies 282
 oxygen-deficient 277
 oxygen-stoichiometric 268, 269, 276

 pair-density-function analysis 261, 263
 paramagnetic NMR lanthanide included shifts
 353–463
 Pauli exclusion principle 256
 Pauli susceptibility 13
 $\text{Pb}_2\text{Sr}_2\text{NdCu}_3\text{O}_8$ 522
 PDF 304
 percolate 309
 percolating 294, 326
 percolation 293, 296, 298, 301, 309, 312, 324,
 325, 327, 339
 percolation threshold 270
 perovskite 3
 phase diagram 19
 phase fluctuations 304, 321, 328
 phase segregation 324
 phase transitions detected by f elements 557
 phase transitions under pressure 556, 558
 – $\text{Eu}(\text{OH})_3$ 558
 – sesquioxides 557
 phonon drag 303
 phonon sidebands under pressure 581
 – $\text{BaFCl}:\text{Sm}^{2+}$ 581
 phonon–glass 30
 phtalocyanine 440
 polaron 300, 308, 336
 polaron conduction 335
 polaronic 298, 305, 308, 325, 326
 polaronic conduction 257, 286, 294
 polaronic phase 310
 polaronic to itinerant-electron behavior 304
 polaronic to itinerant/vibronic 299
 polymetallic lanthanide complexes 444
 polymorphism 149
 – in the lanthanide tribromides 153
 – in the lanthanide trichlorides 152
 – in the lanthanide trifluorides 150
 – in the lanthanide triiodides 153
 – LnBr_3 152
 – LnCl_3 150
 – LnI_3 152
 potential energy curves 185
 power generation 27
 Pr–Ag–Sb 61
 Pr–Au–Sb 62
 Pr–Cd–Sb 61
 Pr–Co–Sb 59
 Pr–Cr–Sb 58
 Pr–Cu–Sb 59
 Pr–Fe–Sb 59
 Pr–Ga–Sb 60
 Pr–Ge–Sb 60
 Pr–Hf–Sb 62
 Pr–In–Sb 61
 Pr–Li–Sb 58
 Pr–M–Sb systems 58
 Pr–Mn–Sb 58
 Pr–Ni–Sb 59
 Pr–Os–Sb 62
 Pr–Pd–Sb 61
 Pr–Pt–Sb 62
 Pr–Rh–Sb 60
 Pr–Ru–Sb 60
 Pr–Sb 36
 Pr–Sn–Sb 61
 Pr–Te–Sb 61
 Pr–Ti–Sb 58
 Pr–V–Sb 58
 Pr–Zn–Sb 60
 Pr–Zr, Nb–Sb 60
 $\text{Pr}_{0.33}\text{U}_{0.67}\text{Sb}_2$ 94
 $\text{Pr}_{0.5}(\text{Ca}_{0.25}\text{Sr}_{0.75})_{0.5}\text{MnO}_3$ 342
 $\text{Pr}_{0.5}\text{Ca}_{0.35}\text{Sr}_{0.15}\text{MnO}_3$ 338
 $\text{Pr}_{0.5}\text{Ca}_{0.5}\text{MnO}_3$ 336
 $\text{Pr}_{0.5}(\text{Ca}_{0.5}\text{Sr}_{0.5})_{0.5}\text{MnO}_3$ 342
 $\text{Pr}_{0.5}(\text{Ca}_{0.85}\text{Sr}_{0.15})_{0.5}\text{MnO}_3$ 338
 $\text{Pr}_{0.5}(\text{Ca}_{1-x}\text{Sr}_x)_{0.5}\text{MnO}_3$ 332
 $\text{Pr}_{0.5}\text{Sr}_{0.5}\text{MnO}_3$ 336, 337
 $\text{Pr}_{0.5}(\text{Sr}_{0.9}\text{Ca}_{0.1})_{0.5}\text{MnO}_3$ 335
 $\text{Pr}_{0.7}\text{Ca}_{0.3}\text{MnO}_3$ 290, 294
 $\text{Pr}_{12}\text{Ga}_4\text{Sb}_{23}$ 60
 $\text{Pr}_{12}\text{Ga}_4\text{Sb}_{23}$ structure type 104
 $\text{Pr}_{2/3}\text{Ca}_{1/3}\text{MnO}_3$ 305
 Pr_2Sb 38
 $\text{Pr}_3\text{Au}_3\text{Sb}_4$ 62
 $\text{Pr}_3\text{Cu}_3\text{Sb}_4$ 60, 133
 Pr_3HfSb_5 62
 Pr_3NbSb_5 60
 $\text{Pr}_3\text{Pt}_3\text{Sb}_4$ 62, 129
 Pr_3TiSb_5 58
 Pr_3ZrSb_5 60
 Pr_4Sb_3 38
 $\text{Pr}_{5/8}\text{Ca}_{3/8}\text{MnO}_3$ 327
 Pr_5Sb_3 38
 $\text{Pr}_6\text{Fe}_{13}\text{Sb}$ 59
 $\text{Pr}_6\text{Ge}_{5-x}\text{Sb}_{11+x}$ 60, 135
 $\text{Pr}_6\text{ZnSb}_{15}$ 60, 133, 134
 PrAgSb_2 61, 128

- PrAuSb₂ 62, 121
 PrBr₃ 521
 Pr(C₂H₅SO₄)₃·9H₂O 521
 PrCd_{1-x}Sb₂ 61
 PrCdSb₂ 61
 PrCl₃ 521, 531
 PrCo_{1-x}Sb₂ 59
 PrCrSb₃ 58
 PrCu₂Sb₂ 60, 113
 PrCuSb₂ 60, 119, 121
 pressure 9
 pressure sensor 518, 552–554
 – rare-earth sensors 552
 – ruby 518, 519, 552
 – SrB₄O₇:Sm²⁺ 554
 – SrFCl:Sm²⁺ 554
 – YAG:Eu³⁺ 553
 – YAG:Nd³⁺ 553
 – YAG:Sm³⁺ 553
 – YAlO₃:Nd³⁺ 552
 pressure-generation with diamond anvils 518
 PrF₃ 521
 PrFe_{1-x}Sb₂ 59
 PrFe₄As₁₂ 14, 21
 PrFe₄P₁₂ 14, 17–19
 PrFe₄Sb₁₂ 14, 21, 59
 PrIn_{0.8}Sb₂ 61
 PrLi₂Sb₂ 58
 PrMn_{0.82}Sb₂ 58, 120
 PrMnO₃ 294
 PrNi_{1.8}Sb₂ 113
 PrNi_{2-x}Sb₂ 59
 PrNi₂Sb₂ 59, 100, 113
 PrNiSb 59, 116
 PrNiSb₂ 59, 121
 Pr(NO₃)₃·6H₂O 521
 PrO₂ 521
 PrOCl 521, 537
 PrOCl:Pr³⁺ 533
 PrOs₄As₁₂ 14, 21
 PrOs₄P₁₂ 14, 20
 PrOs₄Sb₁₂ 14, 21, 22, 62
 PrPd₂Sb₂ 61
 PrPdSb 61, 118
 PrPdSb_{0.952} 61
 PrPdSb₂ 61, 119, 121
 PrPtSb 62
 PrRh₂Sb₂ 61
 PrRhSb 60, 118
 PrRu₄As₁₂ 14, 21
 PrRu₄P₁₂ 14, 19, 20
 PrRu₄Sb₁₂ 14, 21, 60
 PrSb 38, 521, 535
 PrSb₂ 38
 PrSn_xSb₂ 61
 PrTeSb 61
 PrVSb₃ 58
 PrX (X = N, P, As, Sb, S, Se) 521
 PrZn_{1-x}Sb₂ 60
 pseudo-contact shift 366, 367
 pseudo-gap 17

 QCP behavior 333
 quadrupolar order 17
 quantum chemical computations 182
 quantum critical behavior at a QCP 343
 quantum critical point 15, 332
 quantum-critical-point fluctuations 261
 quaternary systems 95

 (R, U)₃Sb₇ 94
 (R, U)Sb₂ 94
 R–Cu(Ag, Au)–Sb, peculiarities of interaction 139
 R–d-element–Sb, peculiarities of interaction 137
 R–f-element–Sb, peculiarities of interaction 140
 R–Fe(Co, Ru, Rh, Os, Ir)–Sb, peculiarities of interaction 137
 R–Mn(Cd, Zn)–Sb, peculiarities of interaction 137
 R–Ni(Pd, Pt)–Sb, peculiarities of interaction 138
 R–p-element–Sb, peculiarities of interaction 136
 R–R'–Sb systems 93
 R–s-element–Sb, peculiarities of interaction 136
 R–Sb binary compounds 37
 R–Sb systems, peculiarities of interaction 135, 136
 R–Ti(V, Cr, Zr, Nb, Mo, Hf, Ta, W, Re)–Sb, peculiarities of interaction 137
 R–U–Sb 94
 R–U–Sb systems 94
 R_{0.5}A_{0.5}MnO₃ 327, 330
 R_{0.5}Sr_{0.5}MnO₃ 337
 R_{0.7}A_{0.3}MnO₃ 310
 R₁₁Sb₁₀ 136
 [R₂(L¹⁴–2H)₃] 444
 [R₂(L¹⁵–2H)₃] 448
 R₂O₂S:Eu³⁺ 530
 R₂Sb 136
 R₂Sb₅ 136
 R₃Au₃Sb₄ 129
 [R₃(L¹⁶–3H)₂(OH₂)₆]³⁺ 454
 [R₃(L¹⁷)₃]⁹⁺ 455
 R₄Sb₃ 136

- $R_5\text{Sb}_3$ 136
 $R_6\text{Ge}_{5-x}\text{Sb}_{11+x}$ 133
 Raman measurements 20
 Raman modes 23
 rare earth – antimony systems 35–146
 rare earth – manganese perovskites 249–351
 rare-earth compounds studied under pressure 521
 rattlers 29
 $\text{RbCaF}_3:\text{Gd}^{3+}$ 524
 $\text{RbCdF}_3:\text{Gd}^{3+}$ 524
 $[\text{R}(\text{benzyl-EDTA})]$ 373, 374
 RCl_3 530–532
 $[\text{RCo}(\text{L}^5)_3]^{5+}$ 400
 $[\text{RCo}(\text{L}^5)_3]^{6+}$ 396
 redox energy 252, 260
 reduced enthalpy increment
 – CeCl_3 168
 – GdCl_3 166
 – LaCl_3 167
 – PrCl_3 168
 – PrF_3 164
 reduction of free-ion parameters 529, 533
 reduction of Slater parameter 529, 532
 reduction of the free-ion parameters 529
 reduction of the spin–orbit coupling parameter 529
 refractive index under pressure 561, 563, 564
 refrigeration 28
 Reilly's method 376
 ReO_3 4
 representations of base vectors 259
 resistivity 8–10, 12, 13, 15–18, 20–22, 24–26
 resonance energy transfer 571
 resonance integrals 253
 rhombic system 379, 455, 459
 rhombohedral $R\bar{3}c$ symmetry 251
 $[\text{R}(\text{indole-EDTA})]$ 373, 374
 $[\text{R}(\text{L}^1\text{-2H})_3]^{3-}$ 381
 $[\text{R}(\text{L}^{10}\text{-4H})^-]$ 419, 437
 $[\text{R}(\text{L}^{11})]^{3+}$ 374, 426, 437
 $[\text{R}(\text{L}^{12}\text{-8H})]^{5-}$ 430, 437
 $[\text{R}(\text{L}^{13}\text{-2H})_2]^-$ 440
 $[\text{R}(\text{L}^2)_3]^{3+}$ 384
 $[\text{R}(\text{L}^{2a})_3]^{3+}$ 385
 $[\text{R}(\text{L}^3)_3]^{3+}$ 387, 410
 $[\text{R}(\text{L}^4\text{+H})]^{4+}$ 390
 $[\text{R}(\text{L}^4)]^{3+}$ 390
 $[\text{R}(\text{L}^6)]^{3+}$ 401
 $[\text{R}(\text{L}^7\text{-2H})_3]^{3-}$ 404, 406
 $[\text{R}(\text{L}^{7a}\text{-2H})_3]^{3-}$ 405
 $[\text{R}(\text{L}^{7b}\text{-2H})_3]^{3-}$ 405
 $[\text{R}(\text{L}^{7c}\text{-2H})_3]^{3-}$ 406
 $[\text{R}(\text{L}^8\text{-3H})]$ 410
 $[\text{R}(\text{L}^9\text{-H})_4]^-$ 415
 $r(\text{Ln-X})$ bond length
 – LnBr_3 184
 – LnCl_3 184
 – LnF_3 184
 – LnI_3 184
 $[\text{RM}(\text{L}^5)_3]^{5/6+}$ 393
 RMnO_3 275
 $\text{ROCl}:\text{Pr}^{3+}$ 537, 539
 $\text{ROY}:\text{Eu}^{3+}$ 537
 RSb 136
 RSb_2 136
 $[\text{R}(\text{texa})\text{X}_2]$ 374, 375
 Ruddlesden–Popper 250
 Ruddlesden–Popper phases 251
 $[\text{RZn}(\text{L}^5)_3]^{5+}$ 393

 $\text{Sb}_2\text{Te}_3\text{-Dy}_2\text{Te}_3$ section 85
 $\text{Sb}_2\text{Te}_3\text{-Sb}_3\text{Yb}_4$ section 92
 $\text{Sb}_2\text{Te}_3\text{-Sm}_2\text{Te}_3$ section 75
 $\text{Sb}_2\text{Te}_3\text{-SmTe}$ section 75
 $\text{Sb}_2\text{Te}_3\text{-TeYb}$ section 92
 $\text{Sb}_2\text{Te}_3\text{-Yb}$ section 92
 $\text{Sb}_7\text{Te}_4\text{Yb}$ 92
 $\text{Sb}_4\text{Te}_7\text{Yb}$ 92
 $\text{Sb}_4\text{Te}_7\text{Yb-Te}$ section 92
 $\text{Sb}_4\text{Te}_7\text{Yb-Yb}$ section 92
 Sc-Co-Sb 37
 Sc-M-Sb systems 37
 Sc-Ni-Sb 37
 Sc-Pt-Sb 40
 Sc_2Sb 38
 Sc_5Sb_3 38
 scanning calorimetry 23
 ScCoSb 37
 Schottky heat capacity 154
 Schottky peak 22
 ScNiSb 37, 109, 118
 ScPtSb 40
 ScSb 38
 Seebeck 24
 Seebeck coefficient 10, 13, 17
 segregation of orbitally disordered and orbitally ordered volumes 289
 semicovalent component of the superexchange 284
 semicovalent exchange 256, 277
 sensitized luminescence 483, 484, 494, 506–509
 separation of contact and pseudo-contact contributions 372
 Si:Er^{3+} 525

- single configurational coordinate energy level
 diagram 564, 568
- skutterudite 2
- Slater parameters under pressure 529
- Sm–Ag–Sb 75
- Sm–Au–Sb 76
- Sm–Cd–Sb 75
- Sm–Co–Sb 73
- Sm–Cr–Sb 72
- Sm–Cu–Sb 73
- Sm–Fe–Sb 72
- Sm–Ga–Sb 74
- Sm–Ge–Sb 74
- Sm–Hf–Sb 75
- Sm–*M*–Sb systems 72
- Sm–Mn–Sb 72
- Sm–Nb–Sb 74
- Sm–Ni–Sb 73
- Sm–Os–Sb 76
- Sm–Pd–Sb 74
- Sm–Pt–Sb 76
- Sm–Ru–Sb 74
- Sm–Sb 36
- Sm–Se–Sb 74
- Sm–Sn–Sb 75
- Sm–Te–Sb 75
- Sm–Ti–Sb 72
- Sm–V–Sb 72
- Sm–Zn–Sb 73
- Sm_{0.33}U_{0.67}Sb₂ 94
- Sm_{0.5}Sr_{0.5}MnO₃ 338
- Sm₁₂Ga₄Sb₂₃ 74
- Sm₂Fe₁₇ 73
- Sm₂[Pt(CN)₄]₃·18H₂O 523
- Sm₂Sb 38
- Sm₂Sb₅ 37, 38
- Sm₂SnSb₃ 75
- Sm₃Au₃Sb₄ 76
- Sm₃Cu₃Sb₄ 73, 133
- Sm₃GdSb₃ 94
- Sm₃HfSb₅ 75
- Sm₃NbSb₅ 74
- Sm₃NdSb₃ 94
- Sm₃Se₉Sb₄ 74
- Sm₃TiSb₅ 72
- Sm₄Sb₃ 38
- Sm₅Sb₃ 38
- Sm₆Fe₁₃Sb 72
- Sm₆Ge_{5–*x*}Sb_{11+*x*} 74, 135
- Sm₆ZnSb₁₅ 74, 133, 134
- SmAgSb₂ 75, 128
- small polarons 283, 285, 294, 307, 311, 323
- small to Zener polarons 308
- small-polaron/Zener-polaron 308
- SmAuSb₂ 76, 121
- Sm(C₂H₅SO₄)₃·9H₂O 523
- SmCdSb₂ 75
- SmCo_{1–*x*}Sb₂ 73
- SmCuSb₂ 73, 121
- SmFCl 522
- SmFe_{1–*x*}Sb₂ 72
- SmFe₄P₁₂ 14, 23
- SmFe₄Sb₁₂ 14, 23, 72
- SmGaSb₂ 74
- SmMn_{0.90}Sb₂ 72, 120
- SmNi₂Sb₂ 73
- SmNiO₃ 277
- SmNiSb 73, 106, 116
- SmNiSb₂ 73, 121
- SmOs₄Sb₁₂ 14, 23, 76
- SmPd₂Sb₂ 75
- SmPdSb 74
- SmPdSb₂ 74, 121
- SmPtSb 76
- SmRu₄P₁₂ 14, 23
- SmRu₄Sb₁₂ 14, 23, 74
- SmS 522
- SmSb 38
- SmSb₂ 38
- SmSbTe 75
- SmSe 522
- SmSn_{*x*}Sb₂ 75
- SmTe₃Sb 75
- SmTe₄Sb₂ 75
- SmTe₇Sb₄ 75
- SmVSb₃ 72
- SmZn_{1–*x*}Sb₂ 73
- specific heat 15
- spherical coordinates 367
- spherical tensor operators 368
- spin canting 283, 310
- spin configurations 258, 259
- spin expectation value 362, 365
- spin fluctuations 288
- spin orbit 365
- spin ordering 269
- spin waves 319, 321
- spin–orbit coupling parameter under pressure 529
- spin–phonon coupling 284
- spin-canted antiferromagnet 285
- spin-correlated crystal fields 547, 548
- *M*FCl:Sm²⁺ 548

- spin-density wave (SDW) 260
 spin-dependent resonance integrals 256
 spin-glass 270, 273, 285, 289, 290, 303, 312, 340
 spin-glass insulator 273
 spin-glass phase transforms to a ferromagnetic phase 273
 spin-glass to a ferromagnetic phase 272
 spin-independent resonance integrals 256
 spin-lattice interactions 276, 321
 spinodal phase segregation 261, 262, 282, 289, 290, 292, 316, 323, 328
 spiral-spin configuration 275, 276
 $\text{Sr}_{1-x}\text{Ca}_x\text{MnO}_3$ ($0 \leq x \leq 1$) and $\text{Sr}_{1-y}\text{Ba}_y\text{MnO}_3$ ($0 \leq y \leq 0.2$) 278
 $\text{SrAl}_2\text{O}_4:\text{Eu}^{2+}$ 523
 $\text{SrB}_4\text{O}_7:\text{Sm}^{2+}$ 522
 $\text{SrBPO}_5:\text{Eu}^{2+}$ 523
 $\text{SrF}_2:\text{Er}^{3+}$ 525
 $\text{SrF}_2:\text{Eu}^{3+}$ 524
 $\text{SrF}_2:\text{Pr}^{3+}$ 521
 $\text{SrF}_2:\text{Sm}^{2+}$ 522
 $\text{SrF}_2:\text{Tm}^{2+}$ 525
 $\text{SrFCl}_{0.5}\text{Br}_{0.5}:\text{Sm}^{2+}$ 522
 $\text{SrFCl}:\text{Sm}^{2+}$ 522
 $\text{SrFe}_4\text{Sb}_{12}$ 15
 SrMnO_3 277
 $\text{SrOs}_4\text{Sb}_{12}$ 15
 $\text{SrRu}_4\text{Sb}_{12}$ 15
 stability constant
 – of Cm(III) 499, 500, 505, 506
 – of lanthanides 499, 504, 505
 – of U(VI) 499–501, 505
 stability constant (general) 501, 502
 standard entropy 154, 158
 – EuX_3 162
 – LaX_3 162
 – LnBr_3 161, 163
 – LnCl_3 157, 159
 – LnF_3 157, 158
 – LnI_3 161, 163
 – LuX_3 162
 standard molar entropies 156
 stripes 304
 strong-correlation fluctuations 262
 structural parameters
 – LnBr_3 229
 – LnCl_3 227
 – LnF_3 224
 – LnI_3 230
 structural transition 20
 sublimation enthalpies
 – LnBr_3 196
 – LnF_3 192, 195
 – LnI_3 196, 197
 superconducting 9, 12, 21
 superconductivity 8, 9
 superconductor 21
 superexchange 256, 279, 280, 333
 superexchange interaction 259, 268, 276, 277, 317, 343
 superexchange interatomic interactions 307
 superparamagnetic 296, 324, 335, 343
 superparamagnetism 296, 332
 superposition model 539, 541, 546, 547
 – $\text{LaCl}_3:\text{Nd}^{3+}$ 542
 – $\text{LaCl}_3:\text{Pr}^{3+}$ 542
 – $\text{LaCl}_3:\text{U}^{3+}$ 542
 – $\text{MFCI}:\text{Sm}^{2+}$ 542
 – $\text{ROCl}:\text{Pr}^{3+}$ 542
 supramolecular 355, 358, 359, 361, 363, 366, 459
 symmetry-restricted covalency model SRC 530, 533
 synthesis and crystal growth 6

 t_{2g} 5
 Θ_D 9, 12, 13, 17, 21
 T_{JT} 319
 T_{OO} = orbital-ordering temperature 321
 T_{OR} = orthorhombic-rhombohedral transition temperature 321
 t = tolerance factor 339
 Tb–Ag–Sb 83
 Tb–Au–Sb 84
 Tb–Cr–Sb 82
 Tb–Cu–Sb 82
 Tb–Ge–Sb 83
 Tb–Li–Sb 82
 Tb–M–Sb systems 82
 Tb–Ni–Sb 82
 Tb–Pd–Sb 83
 Tb–Pt–Sb 83
 Tb–Sb 36
 Tb–Te–Sb 83
 Tb–Zn–Sb 83
 Tb–Zr–Sb 83
 $\text{Tb}_{0.33}\text{U}_{0.67}\text{Sb}_2$ 94
 $\text{Tb}_{0.5}\text{Sr}_{0.5}\text{MnO}_3$ 338
 $\text{Tb}_{1.5}\text{U}_{1.5}\text{Sb}_7$ 94
 Tb_2Sb_5 37, 39
 $\text{Tb}_3\text{Au}_3\text{Sb}_4$ 84
 $\text{Tb}_3\text{Cu}_3\text{Sb}_4$ 82, 133
 $\text{Tb}_4\text{Sb}_3(\alpha)$ 39

- Tb₅Ni₂Sb 82
 Tb₅Pd₂Sb 83
 Tb₅Pt₂Sb 83
 Tb₅Sb₃ 39
 Tb₆Ge_{5-x}Sb_{11+x} 83, 135
 Tb³⁺ in solutions 524
 TbAgSb₂ 83, 124, 128
 TbCrSb₃ 82
 TbCuSb₂ 82, 121
 TbLi₂Sb₂ 82
 TbNi_{2-x}Sb₂ 82
 TbNiSb 82, 116
 TbNiSb₂ 82, 121
 TbP₅O₁₄ 524, 536
 TbPdSb 83
 TbPdSb₂ 83, 119, 121
 TbPtSb 83
 TbRu₄P₁₂ 15, 25, 26
 TbSb₂ (HT) 39
 TbSb₂ (LT) 39
 TbSb(α) 39
 TbTe-Sb₂Te₃ section 83
 TbZn_{1-x}Sb₂ 83
 TbZrSb 83
 Te₂Ag₃Tl structure type 109
 ternary antimonides with the equiatomic composition 140
 ternary antimonides with the *R*:Sb ratio equal to 1:2 141
 ternary antimonides, interconnection with binary structure types 140
 tetragonal *I4/mcm* symmetry 251
 thermal conductivity 13
 thermal expansion 20
 thermoelectric couple 28
 thermoelectric generator 31
 thermoelectric properties 2, 13, 24, 26
 ThFe₄P₁₂ 15
 ThOs₄As₁₂ 15
 three-nuclei method 379
 threefold symmetry 381, 444, 454
 ThRu₄P₁₂ 15
 tight-binding 267
 tight-binding bandwidth 260, 262, 292
 time-resolved emission spectroscopy 465–514
 TiNiSi structure type 109, 138–140
 TICdF₃:Gd³⁺ 524
 Tm–Ag–Sb 90
 Tm–Au–Sb 90
 Tm–Cu–Sb 89
 Tm–*M*–Sb systems 89
 Tm–Ni–Sb 89
 Tm–Pd–Sb 89
 Tm–Pt–Sb 90
 Tm–Sb 37
 Tm–Zr–Sb 89
 Tm_{0.33}U_{0.67}Sb₂ 94
 Tm₃Au₃Sb₄ 90
 Tm₅Ni₂Sb 89
 Tm₅Pd₂Sb 89
 Tm₅Pt₂Sb 90
 Tm₅Sb₃ 39
 TmAgSb₂ 90, 123, 128
 TmCl₃ 525
 TmCuSb₂ 89, 121
 TmNiSb 89, 116, 118
 TmPdSb 89
 TmPtSb 90
 TmSb 39
 TmSb₂ 39
 TmSe 525
 TmTe 525
 TmZrSb 89
 tolerance factor 250, 261, 275, 277, 287, 290, 292–294, 299, 305, 308–311, 322, 323, 325, 326, 330, 332, 333, 342
 trace detection 508
 – of Cm(III) 507, 508
 – of lanthanides 507, 508
 – of U(VI) 507, 508
 transition at *T*_{JT} 323
 transition from a spin glass to a ferromagnetic phase 270
 transition from antiferromagnetic to ferromagnetic behavior 292
 transition from ferromagnetic insulator (FI) to ferromagnetic metal (FM) 316
 transition from localized *e* to 1D itinerant 330
 transition from localized to itinerant electronic behavior 260, 268, 304, 315, 332
 transition from localized-electron to band magnetism 281
 transition from polaronic to itinerant electronic behavior 312
 transition from the FM toward the FV state 325
 transition from vibronic to itinerant electronic behavior 316
 transition temperature 150, 151
 – *Ln*Br₃ 151, 206
 – *Ln*Cl₃ 151, 203
 – *Ln*F₃ 151, 200
 – *Ln*I₃ 151, 153, 208

- transitions under pressure
 – trihalide compounds 558
 transport gap 12
 trimetallic lanthanide complexes 453
 triple-decker dimetallic compound 449
 tris{2-[*N*-methylcarbamoyl-(6-(*N,N*-diethylcarbamoyl)pyridine-2)ethyl]amine}
 390
 two-manganese (Zener) polarons 283
 two-nuclei method 377, 446
 two-phase fluctuations 321, 327, 332
 type G 276
 type-A AFM phase 322, 335–337
 type-A antiferromagnetic 310, 315, 330, 333
 type-A antiferromagnetic order 264, 268
 type-A (CAFI) 322
 type-A canted-spin antiferromagnet 270
 type-A magnetic order 311
 type-C antiferromagnetic order 323, 330
 type-CE 332
 type-CE AFI phase 327, 328, 330
 type-CE antiferromagnetic phase 288, 326, 332,
 339
 type-CE antiferromagnetic-insulator (AFI) 326
 type-CE phase 326, 327

 U₃CrSb₅ structure type 110, 137
 UFe₄P₁₂ 15

 Van Vleck 368
 Van Vleck paramagnetism 23
 vapour pressure
 – LnBr₃ 194
 – LnCl₃ 193
 – LnI₃ 196
 vapour pressures 191
 variance 251, 278, 332, 333, 337, 338, 342
 vibrational density of states 11
 vibrational frequencies
 – Ln₂X₆ compounds 233
 – LnBr₃ 190, 229
 – LnCl₃ 186, 188, 189, 227
 – LnF₃ 186, 187, 189, 224
 – LnI₃ 190, 230
 vibrational properties 182
 vibrational spectra 183
 vibronic 304, 310, 311, 321, 325, 343
 – bandwidth 308, 311
 – conduction 292, 293, 333
 – conductor 266, 315
 – ferromagnetic phase 310
 – ferromagnetic superexchange 307
 – (FV) clusters 323
 – isotropic superexchange 267
 – Mn(III)–O–Mn(III) superexchange interaction
 272
 – phase 310
 – state 308
 – superexchange 257, 265–267, 289, 292–294,
 310, 315, 317, 321
 vibronic to itinerant 315
 vibronic-itinerant electronic transition 316
 vibrons 329
 virial theorem 261, 282, 290, 308, 310, 330, 332

 weak canted-spin ferromagnetism 264
 weak ferromagnetic component 285
 weak ferromagnetism 258
 Wilson–Sommerfeld ratio 13, 26

X–Ln–*X* bond angle
 – LnBr₃ 185
 – LnCl₃ 185
 – LnF₃ 185
 – LnI₃ 185
X–Ln–*X* equilibrium bond angles
 – Ln 184
 – LnBr₃ 184
 – LnCl₃ 184
 – LnF₃ 184
 – LnI₃ 184
 XANES 12, 13, 20, 24, 26

 Y–Ag–Sb 42
 Y–Au–Sb 42
 Y–Cu–Sb 41
 Y–Li–Sb 40
 Y–*M*–Sb systems 40
 Y–Ni–Sb 40
 Y–Ni–Sb, isothermal section 40–42
 Y–Pd–Sb 41
 Y–Pt–Sb 42
 Y–Sb 36
 Y–Te–Sb 42
 Y–Zr–Sb 40
 Y_{1–*x*}U_{*x*}Sb 94
 Y₂O₂S:Eu³⁺ 524
 Y₂O₃:Eu³⁺ 524
 Y₃Al₅O₁₂ 553
 Y₃Al₅O₁₂:Eu³⁺ 524
 Y₃Al₅O₁₂:Nd³⁺ 522
 Y₃Al₅O₁₂:Sm³⁺ 523
 Y₃Al₅O₁₂:Tb³⁺ 524

- $Y_3Al_5O_{12}:Tm^{3+}$ 525
 $Y_3Au_3Sb_4$ 42
 $Y_3Au_3Sb_4$ structure type 106, 140
 $Y_3Cu_3Sb_4$ 41, 132, 133
 Y_3Sb 38
 Y_4Sb_3 38
 $Y_5Ni_xSb_{3-x}$ 41
 Y_5Pd_2Sb 42
 Y_5Pt_2Sb 42
 Y_5Sb_3 37
 Y_5Sb_3 (HT) 38
 Y_5Sb_3 (LT) 38
 $YAgSb_2$ 42, 128
 $YAlO_3$ 553
 $YAlO_3:Nd^{3+}$ 522
 $Yb-Ag-Sb$ 92
 $Yb-Al-Sb$ 90
 $Yb-Au-Sb$ 92
 $Yb-Cd-Sb$ 91
 $Yb-Cu-Sb$ 91
 $Yb-In-Sb$ 92
 $Yb-Li-Sb$ 90
 $Yb-M-Sb$ systems 90
 $Yb-Mn-Sb$ 90
 $Yb-Ni-Sb$ 90
 $Yb-Pd-Sb$ 91
 $Yb-Pt-Sb$ 92
 $Yb-Sb$ 37
 $Yb-Se-Sb$ 91
 $Yb-Te-Sb$ 92
 $Yb-Zn-Sb$ 91
 $Yb_{11}Sb_{10}$ 39
 $Yb_{14}AlSb_{11}$ 90, 135
 $Yb_{14}MnSb_{11}$ 90, 135
 $Yb_{14}ZnSb_{11}$ 91, 134, 135
 Yb_3DySb_3 94
 Yb_3GdSb_3 94
 Yb_4Sb_3 39
 $Yb_5In_2Sb_6$ 92, 111
 Yb_5Sb_3 39
 $YBa_2Cu_3O_7:Pr^{3+}$ 521
 $YbAgSb$ 92, 118, 119
 $YbAuSb$ 92, 118, 119
 $YbCd_2Sb_2$ 91
 $YbCuSb$ 91, 118, 119
 $YbCuSb_2$ 91
 $YbFe_4Sb_{12}$ 15, 16, 26, 27
 $YbLiSb$ 90
 $YbMn_2Sb_2$ 90
 $YbNiSb$ 90, 118
 YbO 525
 $YbOs_4Sb_{12}$ 15
 $YbPd_2Sb$ 91
 $YbPdSb$ 91, 118
 $YbPtSb$ 92
 YbS 525
 $YbSb$ 39
 $YbSb_2$ 39
 $YbSe_4Sb_2$ 91
 $(YbTe)_x(Te_3Sb_2)_{1-x}$ 92
 $YbZn_2Sb_2$ 91, 98
 $Y(C_2H_5SO_4)_3 \cdot 9H_2O:Ce^{3+}$ 521
 $Y(C_2H_5SO_4)_3 \cdot 9H_2O:Nd^{3+}$ 522
 $YCrO_3$ 277, 280, 281
 $YCuSb_2$ 41, 119, 121
 YLi_3Sb_2 40, 142
 $YNiSb$ 41
 $YP_5O_{14}:Nd^{3+}$ 522
 YPd_2Sb 41, 101
 $YPdSb$ 41
 $YPtSb$ 42
 YSb 38
 YSb_2 38
 YTe_3Sb 42
 $YVO_4:Eu^{3+}$ 524
 $YZrSb$ 40, 108

Zener double exchange 292, 315, 317, 332
Zener pairs 328, 330, 332
Zener polarons 258, 283, 285, 294, 300, 308, 309, 311, 323, 325, 328, 329, 332, 335, 338, 339, 343
Zener to small polarons 300
Zener two-manganese polarons 285
Zintl compounds 5
 $ZnS:Eu^{2+}$ 523
 $ZrBeSi$ structure type 106, 139, 140
 ZT 13, 26–30